fluids

Recent Advances in Fluid Mechanics

Feature Papers

Edited by
Mehrdad Massoudi

Printed Edition of the Special Issue Published in *Fluids*

www.mdpi.com/journal/fluids

MDPI

Recent Advances in Fluid Mechanics: Feature Papers

Recent Advances in Fluid Mechanics: Feature Papers

Editor

Mehrdad Massoudi

MDPI • Basel • Beijing • Wuhan • Barcelona • Belgrade • Manchester • Tokyo • Cluj • Tianjin

Editor
Mehrdad Massoudi
Carnegie Mellon University
USA

Editorial Office
MDPI
St. Alban-Anlage 66
4052 Basel, Switzerland

This is a reprint of articles from the Special Issue published online in the open access journal *Fluids* (ISSN 2311-5521) (available at: https://www.mdpi.com/journal/fluids/special_issues/feature_papers_fluids).

For citation purposes, cite each article independently as indicated on the article page online and as indicated below:

LastName, A.A.; LastName, B.B.; LastName, C.C. Article Title. *Journal Name* **Year**, *Volume Number*, Page Range.

ISBN 978-3-0365-2000-1 (Hbk)
ISBN 978-3-0365-2001-8 (PDF)

Contents

About the Editor

Mehrdad Massoudi is an Adjunct Professor from the Department of Biomedical Engineering, Carnegie Mellon University, Pittsburgh, PA 15213, USA. Dr. Massoudi received his BS, MS, and PhD in 1979, 1982, and 1986 from the University of Pittsburgh. His research interests are in the areas of mathematical modeling of non-linear materials, non-Newtonian fluid mechanics, multiphase flows, and granular materials. He is an ASME Fellow and the Editor-in-Chief of Fluids.

fluids

Editorial

Recent Advances in Fluid Mechanics: Feature Papers

Mehrdad Massoudi

U. S. Department of Energy, National Energy Technology Laboratory (NETL), Pittsburgh, PA 15236, USA;
Mehrdad.Massoudi@netl.doe.gov

This Special Issue is a collection of top-quality papers from some of the Editorial Board Members of Fluids, Guest Editors, and leading researchers discussing new knowledge or new cutting-edge developments on all aspects of fluid mechanics. Research in Turbulence continues to be one of the active areas; other papers focus on mixing , multiphase flows and porous media , slow (creeping) flows, potential flows, non-Newtonian fluids, fluid-structure interaction, and numerical methods.

With the latest developments in turbulence modeling, Klein and Germano [1] indicate that the Large Eddy Simulation (LES) technique will be used more often in the future. By performing a multiscale dynamic analysis of the commutation error, based on the filtering approach, they illustrate the flexibility of their method, showing that, in all the cases that they considered, the commutation error was smaller than the error obtained by neglecting the commutation error.

To assess the effects of continuous transition on mixing performance, Ryu and Cookson [2] use a modified blinking vortex system with a varying degree of continuous transition; their results indicate that mixing systems, such as continuous pipe flow-based devices, might benefit from the presence of a small degree of continuous transition between discrete states.

To study gas dispersal in urban places or hilly grounds, one usually uses the two-phase flow approach or the Navier–Stokes equations. Among simpler approaches are the two-layer shallow water models for large-scale dispersions. Based on their previous studies, Chiapolino et al. [3] propose a new model and show that this new model which uses a more appropriate drag force correlation, accurately reproduces the experimental results for the case of heavy gas dispersal in quiescent air.

Koleski and Bickel [4] study the creeping flow of a Newtonian fluid in a hemispherical region. The original solution given by Lamb is not complete when the flow is restricted to a semi-infinite space. The authors also discuss the solutions of Marangoni flows due to a local source at the liquid–air interface.

Baddoo [5] presents a method for computing potential flows in planar domains; this study is based on a new class of techniques, known as “lightning solvers”, particularly suitable for flows in domains with corners. The method is then applied to a range of classical problems, including steady potential flows, vortex dynamics, and free-streamline flows.

It has been known that polymeric additives can reduce the frictional drag in turbulent flows. Rajappan and McKinley [6], through experimental measurements in a turbulent Taylor–Couette flow, show that both polymer additives and superhydrophobic walls can be used to reduce the frictional drag in wall-bounded turbulence.

Jiang et al. [7] provide a brief review of some of the recent developments in the mathematical foundations of eddy viscosity (EV) models of turbulence. After reviewing the Boussinesq conjecture, the authors suggest methods to adapt EV models to non-statistically stationary turbulence without encountering numerical instabilities such as the negative eddy viscosities. By reinterpreting the turbulence length scale, they can obtain model simplification and a stronger connection between the model and the Navier–Stokes equation.

High-rise buildings with semi-enclosed landscaped spaces are open to outdoor airflow. Mohammadi et al. [8] studied the effects of three common wind buffers (railing, hedges,

check for updates

Citation: Massoudi, M. Recent Advances in Fluid Mechanics: Feature Papers. *Fluids* **2021**, *6*, 143. https://doi.org/10.3390/fluids6040143

Received: 1 April 2021
Accepted: 3 April 2021
Published: 7 April 2021

and trees) on the performance of such skygardens by performing computational fluid dynamics (CFD) simulations using the realizable k-ε method. Their results indicate that by using the right combination and right dimension of these elements, aero-thermal comfort across the skygardens can be achieved.

Dostalík et al. [9] use some of the classical models in dilute polymeric fluids and show that they can obtain thermodynamically consistent models for non-isothermal flows of these fluids. They also look at the finite amplitude (nonlinear) stability of a stationary, spatially homogeneous state in a thermodynamically isolated system.

Zhang and Agarwal [10] use the incompressible Reynolds-Averaged Navier–Stokes (RANS) equations with realizable k-ε and WA (Wray–Agarwal) turbulence model in their numerical simulations with ANSYS Fluent to study the flow of a fountain formed by twin-jet impingement on the ground. Their results indicate that, for different Reynolds numbers, a fountain that inclines toward the jet with a smaller Reynolds number can be observed. To compensate for alterations of the turbulence structure due to the numerical treatment, Tangermann and Klein [11] use a method based on local volume forces with a control loop; they present their results for the flow around an airfoil at a high angle of attack and with massive flow separation. Obeid et al. [12] present a closed-loop control algorithm for the reduction of turbulent flow separation over NACA 0015 airfoil. The authors also perform numerical simulations using the URANS equations for various airfoil incidences with and without closed-loop control.

Fluid-solid interactions is a challenging area of research, especially if the solid component is deformable. Silva-Leon and Cioncolini [13] use flexible filaments with a rectangular cross-section and various lengths; they consider air flow at a moderate Reynolds number, corresponding to laminar and mildly turbulent flow conditions, and experimentally study the flexible filaments dynamics using fast video imaging.

By using a DNS database of statistically premixed flames subjected to unburned gas, Brearley et al. [14] show that the turbulent velocity fluctuations within the flame brush remain anisotropic, indicating a tendency toward the trailing edge of the flame brush. Their study indicates that the assumption of homogeneous isotropic turbulence may not be valid for turbulent premixed flames.

In many studies, baffle plates are used as a potential device for dampening the sloshing of propellant in rocket tanks; this may cause larger pressure fluctuations in the tank. To avoid this problem, Furuichi and Tagawa [15] consider the two-phase flow of gaseous oxygen and liquid oxygen in a spherical spacecraft tank in a non-gravitational field, with an imposed impact excitation force. Their computational studies indicate that the sloshing depends to a certain extent on the magnetic flux density at the coil center.

To accurately model transport in porous media, an important parameter is the hydrodynamic dispersion coefficient for particles, which could depend on the properties of the medium, the dispersing compound, and the flow field characteristics. Nguyen and Papavassiliou [16] use the lattice Boltzmann method (LBM) to simulate the flow in porous media and the Lagrangian particle tracking (LPT) to track the movement of individual dispersing particles. They find that the hydrodynamic dispersion coefficient depends on the effective Lagrangian Peclet number for packed beds. Most two-component (two-phase flow) studies assume that the whole mixture has one temperature and only one energy equation is required. Two-temperature theories are rare and difficult to use. Kirwan and Massoudi [17] consider a mixture of two Newtonian fluids which are at different temperatures and use standard principles, such as frame indifference, in continuum mechanics; they look at the constraints due to the Clausius–Duhem inequality and obtain inequalities involving the principal and the cross flux coefficients appearing in the constitutive relations.

Su et al. [18] develop a novel flapping mode, named partial advanced mode (PAM), which can generate a high lift force. Their numerical simulations indicate that the period-averaged lift coefficient, CL, increases up to 16% when compared to the traditional symmetrical mode.

One of the approaches used to study flow in fractured porous media is the complex variable formulations. Weijermars and Khanal [19] present a modified solution, using complex analysis methods (CAM). They show that the new approach corrects the physically unfeasible refraction of streamlines across high-permeability bands.

Kinetic instabilities of sedimentation and creaming are important issues when studying suspensions and emulsions. Pal [20] provides a brief review of the unhindered and hindered settling/creaming behaviors of conventional suspensions. The results, based on simulations, show the influence of a three-phase contact angle of nanoparticles at the oil/water interface.

Basse [21] considers the streamwise turbulence intensity definitions using smooth- and rough-wall pipe flow measurements; he also presents a procedure to calculate the turbulence intensity based on the bulk Reynolds number.

Vortex methods can be used to solve the incompressible Navier–Stokes equations in their velocity-vorticity formulation. Mimeau and Mortazavi [22] provide an overview of the Vortex Methods, which are based on Lagrangian approaches. They present detailed evaluations and developments of the mathematical framework, and they discuss the strengths and the limitations as well as some references to applications and numerical simulations using these techniques.

To study turbulence-solid surface interactions, the Rapid Distortion Theory on transversely sheared mean flows is sometimes used. Goldstein [23] provides a brief review of the general theory given in recently published papers. He uses a pair of very general conservation laws which can be used to derive upstream boundary conditions.

To study hydrocarbon migration, one can use complex analysis methods (CAM) along with Eulerian particle tracking. Weijermars et al. [24] use CAM, provide pressure field solutions, and compare their results with the independent embedded discrete fracture method (EDFM) solutions. They also provide different examples for the fast optimization of waterflood patterns and the modeling of fluid withdrawal patterns in hydraulically fractured wells.

Finally, I would like to thank all the authors who contributed to this special issue. Without their contributions and without the help of qualified reviewers, it would not have been possible to organize this special issue; we are grateful to all the anonymous reviewers for their help. A personal note of appreciation and gratitude to Ms. Sonia Guan, the Managing Editor of Fluids, and the editorial staff at the Fluids Office; without their help and assistance, Fluids would not be able to publish high-quality papers in such a short period of time.

Conflicts of Interest: The author declares no conflict of interest.

References

1. Klein, M.; Germano, M. Analysis and Modelling of the Commutation Error. *Fluids* **2020**, *6*, 15. [CrossRef]
2. Ryu, H.; Cookson, A.N. Assessing Eulerian Indicators for Predicting Mixing in a Blinking Vortex System with Varying Degrees of Continuous Transition. *Fluids* **2020**, *6*, 10. [CrossRef]
3. Chiapolino, A.; Courtiaud, S.; Lapébie, E.; Saurel, R. Modeling Heavy-Gas Dispersion in Air with Two-Layer Shallow Water Equations. *Fluids* **2020**, *6*, 2. [CrossRef]
4. Koleski, G.; Bickel, T. Stokes Equation in a Semi-Infinite Region: Generalization of the Lamb Solution and Applications to Marangoni Flows. *Fluids* **2020**, *5*, 249. [CrossRef]
5. Baddoo, P.J. Lightning Solvers for Potential Flows. *Fluids* **2020**, *5*, 227. [CrossRef]
6. Rajappan, A.; McKinley, G.H. Polymers and Plastrons in Parallel Yield Enhanced Turbulent Drag Reduction. *Fluids* **2020**, *5*, 197. [CrossRef]
7. Jiang, N.; Layton, W.; McLaughlin, M.; Rong, Y.; Zhao, H. On the Foundations of Eddy Viscosity Models of Turbulence. *Fluids* **2020**, *5*, 167. [CrossRef]
8. Mohammadi, M.; Tien, P.W.; Calautit, J.K. Influence of Wind Buffers on the Aero-Thermal Performance of Skygardens. *Fluids* **2020**, *5*, 160. [CrossRef]
9. Dostalík, M.; Málek, J.; Průša, V.; Süli, E. A Simple Construction of a Thermodynamically Consistent Mathematical Model for Non-Isothermal Flows of Dilute Compressible Polymeric Fluids. *Fluids* **2020**, *5*, 133. [CrossRef]

10. Zhang, X.; Agarwal, R.K. Numerical Simulation of Fountain Formation due to Normal and Inclined Twin-Jet Impingement on Ground. *Fluids* **2020**, *5*, 132. [CrossRef]
11. Tangermann, E.; Klein, M. Controlled Synthetic Freestream Turbulence Intensity Introduced by a Local Volume Force. *Fluids* **2020**, *5*, 130. [CrossRef]
12. Obeid, S.; Ahmadi, G.; Jha, R. NARMAX Identification Based Closed-Loop Control of Flow Separation over NACA 0015 Airfoil. *Fluids* **2020**, *5*, 100. [CrossRef]
13. Silva-Leon, J.; Cioncolini, A. Experiments on Flexible Filaments in Air Flow for Aeroelasticity and Fluid-Structure Interaction Models Validation. *Fluids* **2020**, *5*, 90. [CrossRef]
14. Brearley, P.; Ahmed, U.; Chakraborty, N.; Klein, M. Scaling of Second-Order Structure Functions in Turbulent Premixed Flames in the Flamelet Combustion Regime. *Fluids* **2020**, *5*, 89. [CrossRef]
15. Furuichi, Y.; Tagawa, T. Numerical Study of the Magnetic Damping Effect on the Sloshing of Liquid Oxygen in a Propellant Tank. *Fluids* **2020**, *5*, 88. [CrossRef]
16. Nguyen, V.; Papavassiliou, D.V. Hydrodynamic Dispersion in Porous Media and the Significance of Lagrangian Time and Space Scales. *Fluids* **2020**, *5*, 79. [CrossRef]
17. Kirwan, J.A.D.; Massoudi, M. The Heat Flux Vector(s) in a Two Component Fluid Mixture. *Fluids* **2020**, *5*, 77. [CrossRef]
18. Su, X.; Zhang, K.; Zheng, J.; Zhao, Y.; Han, R.; Zhang, J. Investigation of High Lift Force Generation of Dragonfly Wing by a Novel Advanced Mode in Hover. *Fluids* **2020**, *5*, 59. [CrossRef]
19. Weijermars, R.; Khanal, A. Flow in Fractured Porous Media Modeled in Closed-Form: Augmentation of Prior Solution and Side-Stepping Inconvenient Branch Cut Locations. *Fluids* **2020**, *5*, 51. [CrossRef]
20. Pal, R. Modeling of Sedimentation and Creaming in Suspensions and Pickering Emulsions. *Fluids* **2019**, *4*, 186. [CrossRef]
21. Basse, N.T. Turbulence Intensity Scaling: A Fugue. *Fluids* **2019**, *4*, 180. [CrossRef]
22. Mimeau, C.; Mortazavi, I. A Review of Vortex Methods and Their Applications: From Creation to Recent Advances. *Fluids* **2021**, *6*, 68. [CrossRef]
23. Goldstein, M.E. Theoretical Foundation of Rapid Distortion Theory on Transversely Sheared Mean Flows. *Fluids* **2020**, *5*, 62. [CrossRef]
24. Weijermars, R.; Khanal, A.; Zuo, L. Fast Models of Hydrocarbon Migration Paths and Pressure Depletion Based on Complex Analysis Methods (CAM): Mini-Review and Verification. *Fluids* **2020**, *5*, 7. [CrossRef]

fluids MDPI

Article

Analysis and Modelling of the Commutation Error

Markus Klein [1,*] and Massimo Germano [2]

[1] Department of Aerospace Engineering, Bundeswehr University Munich, Werner-Heisenberg-Weg 39, 85577 Neubiberg, Germany
[2] Department of Civil and Environmental Engineering, Duke University, Durham, NC 27708, USA; mg234@duke.edu
* Correspondence: markus.klein@unibw.de; Tel.:+49-89-6004-2122

Abstract: A multiscale dynamic analysis of the commutation error, based on the filtering approach is performed. The similarity multiscale hypothesis proposed by Bardina (1983) and extended by Geurts and Holm (2006) to the commutation error is examined in detail and an extension of the Germano identity to the analysis and the modelling of the commutation error is proposed. For a detailed analysis under controlled condition the method is first applied to synthetic turbulence and subsequently to the a-priori analysis of a turbulent channel flow at $Re_\tau = 590$. The results illustrate the flexibility of the dynamic modelling approach. Combined with a scale similarity assumption for the commutation error very satisfactory results have been obtained for first order derivatives and reasonable results for second order derivatives. In all cases the modelling of the commutation error resulted in smaller errors than the error obtained by neglecting the commutation error.

Keywords: large eddy simulation; commutation error; dynamic modelling; scale similarity model; a-priori analysis

check for updates

Citation: Klein, M.; Germano, M. Analysis and Modelling of the Commutation Error. *Fluids* **2021**, *6*, 15. https://doi.org/10.3390/fluids6010015

Received: 8 December 2020
Accepted: 24 December 2020
Published: 31 December 2020

1. Introduction

Turbulence modelling using the Large Eddy Simulation (LES) technique is considered advantageous over traditional methods relying on Reynolds averaging due to its inherent ability to resolve the energy carrying turbulent structures. Given the advances in computing power over the last decades, together with recent advances in numerical methods [1,2] and advanced modelling techniques [3,4] based on machine learning, it can be expected that LES will be increasingly used in the future for a variety of applications such as combustion [5,6] or two-phase flows [7–9] to name only two.

The Large Eddy Simulation of turbulent flow is affected by many errors, due to many reasons, first of all the granularity of the grid coupled with the nonlinearity of the equations. Following Reference [10], we can formalize all that in terms of a filtering approach that reads the data produced by a numerical code as a filtered database. The filtering operator representative of a given LES is characterized by a filter length, directly associated to the grid length, and a lot of information, useful both for modelling and for analysing the results, can be recovered by comparing two different simulations at two different resolution levels by means of the so called dynamic filtering approach. As recalled in the abstract, the first application of the dynamic modelling approach was presented thirty years ago at the Summer Meeting of the CTR [11], and since then a lot of different applications flourished thanks to the interest of many researchers around the world. We refer both to the cited Reference [12] and to Reference [13] for more details on that.

In order to derive the LES formalism, the Navier-Stokes equations are usually filtered with a commutative filter, that is, $\partial \overline{u} = \overline{\partial u}$ where u denotes a general variable and $\bar{\cdot}$ a general filtering operation, typically defined as a convolution integral (here for illustration in 1D) with the filter kernel G such that

$$\overline{u}(x) = \int_{-\infty}^{\infty} u(y)G(x-y)dy, \quad \int_{-\infty}^{\infty} G(x-y)dy = 1. \tag{1}$$

Examples of filter kernels in physical scace are the box filter

$$G(x-y) = \frac{1}{\Delta} \text{ if } |x-y| \leq \frac{\Delta}{2}; \quad G(x-y) = 0 \text{ otherwise} \tag{2}$$

or the Gaussian filter

$$G(x-y) = \left(\frac{6}{\pi\Delta^2}\right)^{1/2} exp\left(\frac{-6|x-y|^2}{\Delta^2}\right). \tag{3}$$

Making use of the linearity of filtering one obtains

$$\frac{\partial}{\partial t}\overline{u_i} = -\frac{\partial}{\partial x_j}\left(\overline{u_i u_j}\right) + \frac{\partial}{\partial x_j}\nu\left(\frac{\partial \overline{u_i}}{\partial x_j} + \frac{\partial \overline{u_j}}{\partial x_i}\right) - \frac{1}{\rho}\frac{\partial \overline{p}}{\partial x_i}\,. \tag{4}$$

Without loss of generality viscosity ν and density ρ are assumed to be constant. Two approaches exist to deal with the unknown correlation $\overline{u_i u_j}$ appearing in the filtered Navier-Stokes equations [14]:

$$\overline{u_i u_j} = \overline{u_i}\,\overline{u_j} + \left(\overline{u_i u_j} - \overline{u_i}\,\overline{u_j}\right) \tag{5}$$

$$\overline{u_i u_j} = \overline{\overline{u_i}\,\overline{u_j}} + \left(\overline{u_i u_j} - \overline{\overline{u_i}\,\overline{u_j}}\right). \tag{6}$$

The term in parentheses is the unknown sgs stress tensor τ_{ij}. If Equation (5) is used, a closed equation for $\overline{u_i}$ is obtained, provided a model for τ_{ij} is supplied. This equation requires no explicit filtering during the solution process. If relation (6) is used one obtains again a closed equation but this time with an additional explicit filtering operation applied to the non linear term. Therefore we call the first approach implicit filtering and the second approach explicit filtering ([15] uses the terminology triple and double decomposition).

In order to derive Equation (4) a homogeneous filter defined in an infinite domain has been assumed. Problems with the theory outlined so far can therefore arise from inhomogeneous filters or from bounded computational domains. This can be seen by differentiating Equation (1) with respect to x which gives [15]:

$$\frac{\partial \overline{u}(x)}{\partial x} = \overline{\frac{\partial u(x)}{\partial x}} + \int_{-\infty}^{\infty} u(y)\frac{\partial G(x-y)}{\partial x}dy. \tag{7}$$

Inhomogeneous filters (grids) are extensively applied in the proximity of walls or regions of strong gradients, like shear layers for example. Hence, the commutation of derivation and filtering is of particular importance for manipulating the Navier-Stokes equations and application of a non commutative filter to the governing equations results in unknown expressions for all terms.

The problem of deriving high order commutative (HOC) filters has been addressed in the past literature (e.g., References [16–18]). Vasilyev et al. [17] developed a class of HOC filters using a mapping function. In extension to that work Marsden et al. [18] proposed a more general procedure for use on unstructured meshes. These filters are defined as a linear combination of simple commutative basis filters, thus allowing to control additionally the filter shape. An implementation of this method into an unstructured solver can for example be found in Reference [19]. The underlying idea of the work mentioned above is that the commutation error can be controlled by imposing conditions on the filter moments.

However, as the primary filtering operation is not explicitly performed in a real LES [14], a general limitation of these ideas is, that these commutative filters can only be used for the secondary filtering operation, such as in Equation (6), or when using a test filter in the dynamic modelling approach. John [20] argues that the commutation error vanishes if and only if the normal stress on the boundary is zero for all times which is very unlikely. While the analysis in this work considers only spatial, time independent filters, it is worth to mention the following extensions: Leonard et al. [21] discuss the commutation error when the spatial filter varies in time, while Franke and Frank analyse the temporal commutation error [22]. The next sections discuss a framework that potentially could be used for modelling the commutation error for the primary filtering operation such as in Equation (5).

2. Multiscale Modelling

It has been mentioned in Reference [23] that the commutation error can be modelled using a scale similarity type approach. Here the main attention is not only to modelling but equally important to analyse the commutation errors with the filtering approach and the related multiscale procedure based on the Germano identity. We remark that in the framework of the filtering approach a Large Eddy Simulation of a turbulent flow is mathematically formalized as a filtered representation of a Direct Simulation. If with $\mathcal{F}$ we represent the filtering operator usually unknown and denoted with an overbar $\bar{\cdot}$, that produces the filtered LES values $\langle u_i \rangle_f$ of the velocity components, a basic problem is to understand how the filtered product $\langle u_i u_j \rangle_f$ is related to them. The filtering approach tries to resolve this problem from a multiscale point of view. We define the Generalized Central Moment, (GCM), $\tau_f(u_i, u_j)$ associated to $\langle u_i u_j \rangle_f$ as

$$\tau_f(u_i, u_j) = \langle u_i u_j \rangle_f - \langle u_i \rangle_f \langle u_j \rangle_f, \tag{8}$$

and we look to the GCM associated to $\langle \langle u_i u_j \rangle_f \rangle_g$, where $\mathcal{G}$ is an explicit test filtering operator, denoted also with a hat $\hat{\cdot}$,

$$\tau_{fg}(u_i, u_j) = \langle \langle u_i u_j \rangle_f \rangle_g - \langle \langle u_i \rangle_f \rangle_g \langle \langle u_j \rangle_f \rangle_g. \tag{9}$$

It is easy to see that the *resolved* GCM (based on resolved quantities $\langle \cdot \rangle_f$ and considering filter level g),

$$\tau_g(\langle u_i \rangle_f, \langle u_j \rangle_f) = \langle \langle u_i \rangle_f \langle u_j \rangle_f \rangle_g - \langle \langle u_i \rangle_f \rangle_g \langle \langle u_j \rangle_f \rangle_g \tag{10}$$

can alternatively be expressed by the tensor M_{ij} defined as

$$M_{ij} = \tau_{fg}(u_i, u_j) - \langle \tau_f(u_i, u_j) \rangle_g. \tag{11}$$

Inserting a model expression for τ_f and τ_{fg} with one free model parameter into Equation (11) to express M_{ij} and equating it to Equation (10) one could in principle determine this model parameter from

$$\tau_g(\langle u_i \rangle_f, \langle u_j \rangle_f) = M_{ij}. \tag{12}$$

However, each tensor component would provide a different equation and a different value of for the model parameter. If instead we contract the identity (12) with M_{ij}, following the approach of Lilly [24], we have identically

$$\tau_g(\langle u_i \rangle_f, \langle u_j \rangle_f) M_{ij} = M_{ij} M_{ij} \,. \tag{13}$$

The contraction corresponds to summation over both indices and as a result of it the resulting model parameter represents the single model parameter which provides the best approximation in a least square sense to the six equations representing the symmetric tensor components.

We remark that from the LES modelling point of view, but not only, it is very important to understand how the dynamic coefficient C

$$C = \frac{\tau_g(\langle u_i\rangle_f, \langle u_j\rangle_f)M_{ij}}{M_{ij}M_{ij}} \tag{14}$$

scales with resolved quantities. Obviously the dynamic coefficient C should be rigorously equal to one everywhere if the modelling scaling is exact, but this is not the case for a generic scaling model. As an example, we can scale M_{ij} with the similarity model of Bardina [25].

Thus we can write

$$\begin{aligned} \tau_{ss,f}(u_i, u_j) &= \tau_f(\langle u_i\rangle_f, \langle u_j\rangle_f) = \\ &= \langle\langle u_i\rangle_f\langle u_j\rangle_f\rangle_f - \langle\langle u_i\rangle_f\rangle_f\langle\langle u_j\rangle_f\rangle_f \\ &= \overline{\overline{u}_i\,\overline{u}_i} - \overline{\overline{u}_i}\,\overline{\overline{u}_j} \end{aligned} \tag{15}$$

$$\begin{aligned} \tau_{ss,fg}(u_i, u_j) &= \tau_{fg}(\langle u_i\rangle_{fg}, \langle u_j\rangle_{fg}) \\ &= \langle\langle u_i\rangle_{fg}\langle u_j\rangle_{fg}\rangle_{fg} - \langle\langle u_i\rangle_{fg}\rangle_{fg}\langle\langle u_j\rangle_{fg}\rangle_{fg} \\ &= \widehat{\overline{\widehat{\overline{u}}_i\,\widehat{\overline{u}}_i}} - \widehat{\overline{\widehat{\overline{u}}_i}}\,\widehat{\overline{\widehat{\overline{u}}_j}} \end{aligned} \tag{16}$$

and finally the parameter C_{ss} be computed with *resolved* quantities

$$C_{ss} = \frac{\tau_g(\langle u_i\rangle_f, \langle u_j\rangle_f)M_{ss,ij}}{M_{ss,ij}M_{ss,ij}} \tag{17}$$

where

$$M_{ss,ij} = \tau_{ss,fg}(u_i, u_j) - \langle\tau_{ss,f}(u_i, u_j)\rangle_g. \tag{18}$$

In this local form, the Bardina dynamic coefficient C_{ss} depends on time and space, but a global form can be conceived, averaged in time and/or eventually in homogeneous space directions.

Strangely enough this multiscale approach and the main use of the identity (12) was to *model* turbulence, and not to *analyse* its multiscale peculiarities. The reasons for that are not so simple to explain. We only remark that this attitude has prevented simple observations that could be usefully applied to LES. One of them refers to the commutation error, and that is the main contribution of this paper. Let us formally consider the GCM associated to the filtered product of a space derivative with a velocity component $\langle\partial_j u_i\rangle_f$, on filter level $\mathcal{F}$ defined as

$$\tau_f(\partial_i, u_j) = \langle\partial_i u_j\rangle_f - \partial_i\langle u_j\rangle_f = \overline{\frac{\partial u}{\partial x}} - \frac{\partial\overline{u}}{\partial x}. \tag{19}$$

If we introduce once more an explicit test filter $\mathcal{G}$, a simple extension of the identity (12) is the following

$$\tau_g(\partial_i, \langle u_j\rangle_f) = \tau_{fg}(\partial_i, u_j) - \langle\tau_f(\partial_i, u_j)\rangle_g = \left(\widehat{\overline{\frac{\partial u}{\partial x}}} - \frac{\partial\widehat{\overline{u}}}{\partial x}\right) - \left(\widehat{\overline{\frac{\partial u}{\partial x}} - \frac{\partial\overline{u}}{\partial x}}\right), \tag{20}$$

where $\tau_g(\partial_i, \langle u_j\rangle_f)$ is the *resolved* GCM given by

$$\tau_g(\partial_i, \langle u_j\rangle_f) = \langle\partial_i\langle u_j\rangle_f\rangle_g - \partial_i\langle u_j\rangle_{fg} = \left(\widehat{\frac{\partial\overline{u}}{\partial x}} - \frac{\partial\widehat{\overline{u}}}{\partial x}\right). \tag{21}$$

We can contract this identity like

$$\tau_g(\partial_i, \langle u_j\rangle_f)M_{ij} = M_{ij}M_{ij}, \tag{22}$$

where

$$M_{ij} = \tau_{fg}(\partial_i, u_j) - \langle\tau_f(\partial_i, u_j)\rangle_g = \left(\frac{\widehat{\overline{\partial u}}}{\partial x} - \frac{\partial\widehat{\overline{u}}}{\partial x}\right) - \left(\widehat{\frac{\overline{\partial u}}{\partial x} - \frac{\partial\overline{u}}{\partial x}}\right) \tag{23}$$

and also in this case it is very important to understand how the dynamic coefficient C associated to the commutation GCM,

$$C = \frac{\tau_g(\partial_i, \langle u_j\rangle_f)M_{ij}}{M_{ij}M_{ij}} \tag{24}$$

scales with resolved quantities. Obviously the candidates to this explorations are many. The scale similarity model is known to show high correlations in a-priori tests not only for isothermal flows but also for the stress, the flux modelling and the reaction rate closure in reacting flows [26–28] or two phase flows [7,8]. The problem of insufficient dissipation of the model has for example been addressed in Reference [29]. Encouraged by these results and by the work of Reference [23] we will therefore examine in some detail how the ratio C scales with the extension of the similarity model of Bardina [25]. We write

$$\tau_{ss,f}(\partial_i, \langle u_j\rangle_f) \quad = \quad \langle\partial_i\langle u_j\rangle_f\rangle_f - \partial_i\langle\langle u_j\rangle_f\rangle_f = C\left(\frac{\overline{\partial\overline{u}}}{\partial x} - \frac{\partial\overline{\overline{u}}}{\partial x}\right) \tag{25}$$

$$\tau_{ss,fg}(\partial_i, \langle u_j\rangle_{fg}) \quad = \quad \langle\partial_i\langle u_j\rangle_{fg}\rangle_{fg} - \partial_i\langle\langle u_j\rangle_{fg}\rangle_{fg} = C\left(\frac{\widehat{\overline{\partial\widehat{\overline{u}}}}}{\partial x} - \frac{\partial\widehat{\overline{\widehat{\overline{u}}}}}{\partial x}\right) \tag{26}$$

as well as

$$M_{ss,ij} = \tau_{ss,fg}(\partial_i, u_j) - \langle\tau_{ss,f}(\partial_i, u_j)\rangle_g \tag{27}$$

such that finally

$$\begin{aligned} C_{ss} \quad &= \quad \frac{\tau_g(\partial_i, \langle u_j\rangle_f)M_{ss,ij}}{M_{ss,ij}M_{ss,ij}} \\ &= \quad \frac{\left(\frac{\widehat{\partial\overline{u}}}{\partial x} - \frac{\partial\widehat{\overline{u}}}{\partial x}\right) \times \left[\left(\frac{\widehat{\overline{\partial\widehat{\overline{u}}}}}{\partial x} - \frac{\partial\widehat{\overline{\widehat{\overline{u}}}}}{\partial x}\right) - \left(\widehat{\frac{\overline{\partial\overline{u}}}{\partial x} - \frac{\partial\overline{\overline{u}}}{\partial x}}\right)\right]}{\left[\left(\frac{\widehat{\overline{\partial\widehat{\overline{u}}}}}{\partial x} - \frac{\partial\widehat{\overline{\widehat{\overline{u}}}}}{\partial x}\right) - \left(\widehat{\frac{\overline{\partial\overline{u}}}{\partial x} - \frac{\partial\overline{\overline{u}}}{\partial x}}\right)\right] \times \left[\left(\frac{\widehat{\overline{\partial\widehat{\overline{u}}}}}{\partial x} - \frac{\partial\widehat{\overline{\widehat{\overline{u}}}}}{\partial x}\right) - \left(\widehat{\frac{\overline{\partial\overline{u}}}{\partial x} - \frac{\partial\overline{\overline{u}}}{\partial x}}\right),\right]} \end{aligned} \tag{28}$$

where numerator and denominator will be space or ensemble averaged as appropriate. Averaging is a standard procedure for regularisation of the dynamic procedure (for an overview on this topic see Reference [15]). For unsteady 3D flow problems the averaging in homogeneous directions can be replaced by the Lagrangian dynamic model proposed by Meneveau et al. [30].

3. Approximations for Commutation Errors

In this section a first order approximation of the commutation error for the first and second derivative will be presented under the assumption that the filter is a differential or elliptic filter. If the filter varies in space and the filter width is formally associated to the length scale Δ one can explicitly include this dependency in Equation (7)

$$\begin{aligned}\frac{\partial \overline{u}(x,t,\Delta)}{\partial x} &= \overline{\frac{\partial u(x,t,\Delta)}{\partial x}} + \int_{-\infty}^{\infty} \frac{\partial G(\xi,\Delta)}{\partial x} u(x-\xi,t)d\xi \\ &= \overline{\frac{\partial u(x,t,\Delta)}{\partial x}} + \int_{-\infty}^{\infty} \frac{\partial \Delta}{\partial x}\frac{\partial G(\xi,\Delta)}{\partial \Delta} u(x-\xi,t)d\xi \end{aligned} \tag{29}$$

such that the commutation error can be formally expressed in one dimension as [31,32]

$$\tau_f(\partial,u) \equiv \langle \partial u\rangle_f - \partial\langle u\rangle_f = -\frac{\partial \Delta}{\partial x}\frac{\partial\langle u\rangle_f}{\partial \Delta}. \tag{30}$$

By using the overline notation we derive the following expression for the second order derivative

$$\tau(\partial,u) = \overline{\frac{\partial u}{\partial x}} - \frac{\partial \overline{u}}{\partial x} = -\frac{\partial \Delta}{\partial x}\frac{\partial \overline{u}}{\partial \Delta} \tag{31}$$

$$\tau(\partial,\partial u) = \overline{\frac{\partial}{\partial x}\frac{\partial u}{\partial x}} - \frac{\partial}{\partial x}\overline{\frac{\partial u}{\partial x}} = -\frac{\partial \Delta}{\partial x}\frac{\partial}{\partial \Delta}\overline{\frac{\partial u}{\partial x}} \tag{32}$$

$$\begin{aligned}\tau(\partial^2,u) &= \overline{\frac{\partial^2 u}{\partial x^2}} - \frac{\partial^2 \overline{u}}{\partial x^2} \\ &= \frac{\partial \tau(\partial,u)}{\partial x} - \frac{\partial \Delta}{\partial x}\frac{\partial^2 \bar{u}}{\partial \Delta \partial x} - \frac{\partial \Delta}{\partial x}\frac{\partial \tau(\partial,u)}{\partial \Delta}.\end{aligned} \tag{33}$$

The commutation error has been also examined in Reference [33]. From this last paper we can derive an estimate of the derivative of $\overline{u}$ with Δ in the case of the *elliptic* differential filter [34]

$$u = \overline{u} - \Delta^2\frac{\partial^2 \overline{u}}{\partial x^2}; \qquad \frac{\partial \overline{u}}{\partial \Delta} \sim 2\Delta\frac{\partial^2 \bar{u}}{\partial x^2}. \tag{34}$$

In this case we have as a first approximation

$$\tau(\partial,u) \approx \tau_a = -2\Delta\frac{\partial \Delta}{\partial x}\frac{\partial^2 \overline{u}}{\partial x^2}. \tag{35}$$

Similarly, the Gaussian filter and its inverse can be approximated by a differential filter [15]

$$u \approx \overline{u} - \frac{1}{24}\Delta^2\frac{\partial^2 \overline{u}}{\partial x^2}; \quad \overline{u} \approx u + \frac{1}{24}\Delta^2\frac{\partial^2 u}{\partial x^2} = u + (\Delta^*)^2\frac{\partial^2 u}{\partial x^2}; \quad \Delta^* = (1/24)^{1/2}\Delta. \tag{36}$$

From Equation (31) we get

$$\frac{\partial \tau(\partial,u)}{\partial x} = -\frac{\partial^2 \Delta}{\partial x^2}\frac{\partial \bar{u}}{\partial \Delta} - \frac{\partial \Delta}{\partial x}\frac{\partial^2 \bar{u}}{\partial \Delta \partial x} \tag{37}$$

$$\frac{\partial \tau(\partial,u)}{\partial \Delta} = -\frac{\partial \Delta}{\partial x}\frac{\partial^2 \bar{u}}{\partial \Delta^2} \tag{38}$$

and insertion in Equation (33) gives

$$\overline{\frac{\partial^2 u}{\partial x^2}} - \frac{\partial^2 \overline{u}}{\partial x^2} = -2\frac{\partial \Delta}{\partial x}\frac{\partial^2 \bar{u}}{\partial \Delta \partial x} - \frac{\partial^2 \Delta}{\partial x^2}\frac{\partial \bar{u}}{\partial \Delta} - \left(\frac{\partial \Delta}{\partial x}\right)^2\frac{\partial^2 \bar{u}}{\partial \Delta^2}. \tag{39}$$

If, using Equation (34), we write as a first approximation

$$\frac{\partial^2 \bar{u}}{\partial x \partial \Delta} = 2\Delta\frac{\partial^3 \bar{u}}{\partial x^3} + 2\frac{\partial \Delta}{\partial x}\frac{\partial^2 \bar{u}}{\partial x^2} \tag{40}$$

the first term to the right in (39) reads as

$$-2\frac{\partial\Delta}{\partial x}\frac{\partial^2\bar{u}}{\partial\Delta\partial x} = -4\Delta\frac{\partial\Delta}{\partial x}\frac{\partial^3\bar{u}}{\partial x^3} - 4\left(\frac{\partial\Delta}{\partial x}\right)^2\frac{\partial^2\overline{u}}{\partial x^2}. \tag{41}$$

One can assume that $(\partial\Delta/\partial x)^2 < (\partial\Delta/\partial x)$ and $(\partial\Delta/\partial x)^2 < \Delta(\partial\Delta/\partial x)$. Often a constant grid stretching is used such that $\partial\Delta/\partial x = const$ and $\partial^2\Delta/\partial x^2 = 0$. Under these conditions one has

$$\tau(\partial^2, u) =\approx \tau_a^2 = -4\Delta\frac{\partial\Delta}{\partial x}\frac{\partial^3\overline{u}}{\partial x^3}. \tag{42}$$

4. Analysis of Synthetic Turbulence

The commutation for the primary filter affects, apart from the temporal derivative, every term in the Navier-Stokes equations. Hence an implementation of the methodology in a real LES will be cumbersome and not straightforward on bounded domains with non-uniform meshes. For a first illustration of the methodology a simple 1D example has been chosen here, which has also the advantage that all turbulence parameters can be strictly controlled.

4.1. First Order Derivatives

The computational mesh used for illustration of the method is a stretched one-dimensional mesh with variables stored in the cell center on a domain with unity length. The first cell has a length of $\Delta x = \Delta x_1$ and the subsequent cells (50 in total) have the width $\Delta x_i = \Delta x \cdot s^{i-1}$ where s is a constant stretch factor taken as 1.05 for the example in Figure 1. In this particular case the first mesh cell has a width of $\Delta x = \Delta x_1 = 0.00239$. The discrete filter is an inhomogeneous, asymmetric box filter as illustrated in Figure 1.

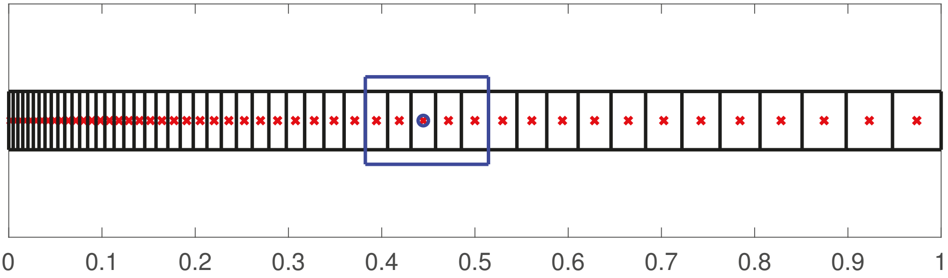

Figure 1. Illustration of the stretched 1D computational mesh with cell centred data storage and one sketched box filter.

For a given parameter p the filter around a point i_0 is given by the coefficients with the weights w_{i_0+i}:

$$w_{i_0+i} = \Delta x_{i_0+i}/w_{tot}, \quad i = -p, \ldots, p, \quad w_{tot} = \sum_{i=-p,\ldots,p} \Delta x_{i_0+i}. \tag{43}$$

All derivatives are calculated by second order accurate finite differences for non-equidistant meshes

$$\frac{\partial u_i}{\partial x} \approx \frac{u_{i+1}\Delta_-^2 - u_{i-1}\Delta_+^2 + u_i(\Delta_+^2 - \Delta_-^2)}{\Delta_-\Delta_+(\Delta_- + \Delta_+)}, \quad \Delta_- = x_i - x_{i-1},\ \Delta_+ = x_{i+1} - x_i, \tag{44}$$

where x_i denotes the midpoints of the cells. It is worth noting that this formula reduces to the standard central difference for equidistant meshes. Due to the inhomogeneous filtering operation the mesh has to be elongated in positive $(x > 1)$ and negative $(x < 0)$ direction in order to have a well-defined filtering operation for up to fourfold filtering.

Pseudo turbulent data has been generated using the digital filter based method detailed in Reference [35], where the integral turbulent length scale has been set to $L_{11} = 5\Delta x_1$ respectively $10\Delta x_1$ and the fluctuation intensity is set to unity without loss of generality. The associated two-point autocorrelation function (an equivalent of the energy spectrum) obtained by this approach resembles homogenous isotropic turbulence in a late stage [35].

The turbulent initial data has been generated on a uniform mesh and interpolated on the non-equidistant computational mesh using a cubic spline function, as illustrated in Figure 2. The derivatives of the signal shown in Figure 2 and the associated commutation error are shown in Figure 3a,b. It is worth noting that for a homogeneous symmetric filter $\tau_f = 0$ and this has been verified in the numerical implementation by setting the stretch factor to $s = 1$. We remark that the numerical gradients become smaller with larger grid size (i.e., towards the right boundary of the computational domain). The scale similarity model given by Equation (25) is shown together with the commutation error in Figure 3b using $C = 1$. Table 1 shows the performance of the model in terms of the Pearson correlation coefficient for initial data with two different length scales and two different filter width, which according to Equation (43) can be specified using the parameter p_f. Furthermore, Table 1 shows the optimal model parameter C determined from a least square fit of the model data to the real commutation error according to Equation (25). The numerical experiment has been repeated 2000 times and all data is space and ensemble averaged. In a real LES determination of the model constant C using least square fits is not possible because the commutation error is unknown. Table 1 shows also the dynamically determined model coefficient C_{ss} for different initial data and different f, g filter size pairs (p_f, p_g). It can be seen that the dynamic procedure reasonably represents the optimal model coefficient. It is also worth mentioning that in all cases the model error, using either the default value $C = 1$ or the optimal value from least square fits, has been found to be considerably smaller than the commutation error (representative of using no model) and this is demonstrated in Table 1 by the relative mean squared error (RMSE) defined as the local mean squared commutation error divided by the local mean squared value of the derivative of the signal multiplied with 100. We remark the simple extension of the dynamic procedure that can be easily generalized and implemented in different directions.

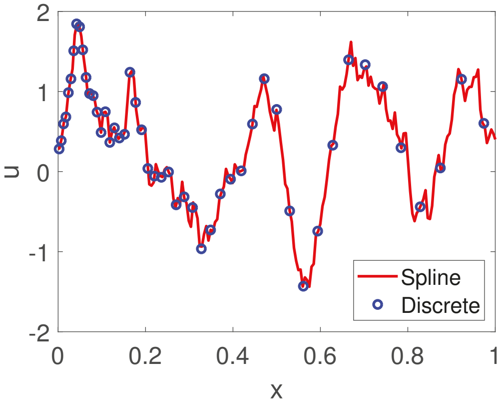

Figure 2. Spline through digital filter based pseudo turbulence and corresponding values interpolated on the computational mesh.

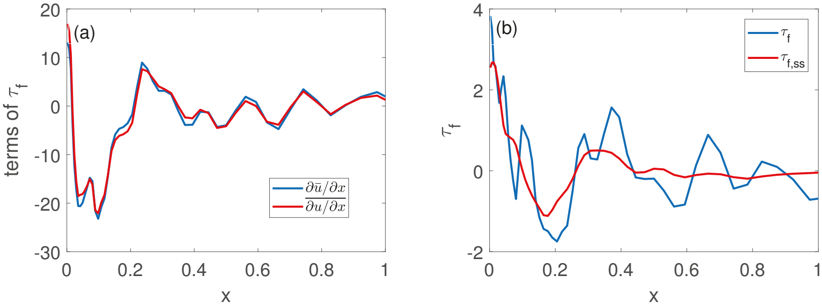

Figure 3. (**a**) (Filtered) gradients of the data (filtered data) shown in Figure 2. (**b**) Commutation error given by $\overline{\partial u/\partial x} - \partial\overline{u}/\partial x$ together with scale similarity model for the commutation error, given by Equation (25) using $C = 1$.

Table 1. Performance of model $\tau_{f,ss}$ for different initial data and different filter sizes (note that the correlation coefficient is independent of the secondary filter). Dynamically determined model coefficient C and mean squared error between commutation error and different approximations, for different initial data and different f, g filter size pairs (p_f, p_g).

Turb. Length Scale L_{11} **Filter Width Pair (p_f, p_g)**	**$5\Delta x$** **(1,2)**	**$5\Delta x$** **(5,10)**	**$10\Delta x$** **(1,2)**	**$10\Delta x$** **(5,10)**
Corr. Coeff.	0.90	0.63	0.90	0.71
Opt. C	1.39	1.56	1.37	1.38
C_{ss} dynamic	1.66	1.83	1.51	1.53
RMSE $(\tau_f - 0)$	0.16	6.36	0.09	5.02
RMSE $(\tau_f - \tau_{f,ss}, C = 1)$	0.06	4.80	0.02	3.35
RMSE $(\tau_f - \tau_{f,ss}, C_{opt})$	0.05	4.51	0.01	3.09

4.2. Second Order Derivatives

The same procedure can be automatically extended to the second derivatives. The commutation error is then given by:

$$\tau_f^2 = \overline{\frac{\partial^2 u}{\partial x^2}} - \frac{\partial^2 \overline{u}}{\partial x^2}. \tag{45}$$

The second numerical derivatives are calculated using the following formula:

$$\frac{\partial^2 u_i}{\partial x^2} \approx \frac{2(u_{i+1}\Delta_- + u_{i-1}\Delta_+ - u_i(\Delta_+ + \Delta_-))}{\Delta_-\Delta_+(\Delta_- + \Delta_+)}, \quad \Delta_- = x_i - x_{i-1},\ \Delta_+ = x_{i+1} - x_i \tag{46}$$

The scale similarity model for the second derivative reads:

$$\tau_{f,ss}^2 = C\left(\overline{\frac{\partial^2 \overline{u}}{\partial x^2}} - \frac{\partial^2 \overline{\overline{u}}}{\partial x^2}\right). \tag{47}$$

The associated filtered second derivatives and second derivatives of filtered data are illustrated in Figure 4a. The scale similarity model given by Equation (47) is shown together with the commutation error in Figure 4b using $C = 1$. It becomes immediately clear that the scale similarity assumption works less satisfactory for the second derivative compared to the first derivative. Selected results for the second derivatives are summarised in Table 2. The modelling and dynamic procedure are in analogy to the case of the first derivative.

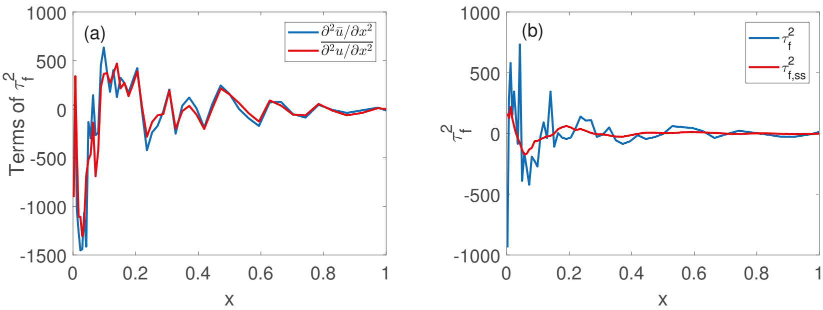

Figure 4. (**a**) (Filtered) second derivatives of the data (filtered data) shown in Figure 2. (**b**) Commutation error given by $\overline{\partial^2 u/\partial x^2} - \partial^2\bar{u}/\partial x^2$ together with scale similarity model for the commutation error, given by Equation (47) using $C = 1$.

While the correlation strengths for the second derivatives are lower compared to the first derivative and also the reduction of RMSE happens to a smaller extend, Table 2 still shows that modelling the commutation error results in a smaller error compared to the commutation error itself especially for small filter width pairs (p_f, p_g).

Table 2. Performance of model $\tau_{f,ss}^2$ for different initial data and different filter sizes (note that the correlation coefficient is independent of the secondary filter). Dynamically determined model coefficient C for different initial data and different f, g filter size pairs (p_f, p_g).

Turb. Length Scale L_{11} **Filter Width Pair (p_f, p_g)**	**$5\Delta x$** **(1,2)**	**$5\Delta x$** **(5,10)**	**$10\Delta x$** **(1,2)**	**$10\Delta x$** **(5,10)**
Corr. Coeff.	0.59	0.34	0.50	0.35
Opt. C	1.42	1.12	1.40	1.05
C_{ss} dynamic	1.75	1.45	1.81	1.02
RMSE $(\tau_f^2 - 0)$	1.75	33.41	1.47	30.94
RMSE $(\tau_f^2 - \tau_{f,ss}^2, C = 1)$	1.65	31.30	0.99	28.01
RMSE $(\tau_f^2 - \tau_{f,ss}^2, C_{opt})$	1.18	30.82	0.95	28.00

5. Analysis of Turbulent Channel Flow at $Re_\tau = 590$

Next the relations from Section 2 will be applied to DNS data. For this a-priori analysis a turbulent channel flow DNS at $Re_\tau = 590$ is considered. The equations are solved by using a finite volume technique on a cartesian mesh. The variables are located on a staggered grid. For spatial discretization second order central differences are used. Temporal discretization is an explicit third order, Runge–Kutta-method. The Poisson equation is inverted by using a direct fast solver.

For the channel flow DNS the Reynolds number, based on the wall friction velocity, has been set to $Re_\tau = 590$ similar to the DNS data of Moser et al. [36]. The extension of the computational domain in axial L_x spanwise L_y and vertical L_z direction is $6\delta \times 3\delta \times 2\delta$ where δ is the channel half width. The computational domain is resolved with $512 \times 512 \times 512$ grid points. The grid is stretched in wall normal direction with a factor of $s = 1.0125$ such that $\partial\Delta/\partial x = const$ and $\partial^2\Delta/\partial x^2 = 0$. A fixed theoretical pressure gradient is prescribed in the simulations. This results in a mesh of dimensions $\Delta x_+ = 6.91, \Delta y_+ = 3.46, \Delta z_+ = 7.6$ in the channel center and $\Delta z_+^{min} = 0.32$ at the wall. The filter width parameter has been chosen to $p = 1$ for the primary filter and $p = 2$ for the test filter. To avoid ambiguous definitions of the filter when approaching the wall, all filtering operations stay away from the wall such that with every filter operation the signal becomes a little bit shorter. Nevertheless, for the analysis presented here this is entirely irrelevant. Periodic boundary conditions are applied in axial and spanwise direction, no slip conditions at the wall. It is worth noting that the above mesh can be considered typical for a channel flow DNS. Using the filter parameter $p = 1$, that is, combining three neighbouring cells into a representative filter volume, can be considered typical for a wall resolved LES mesh. The meshes in homogeneous x, y-directions of channel flow LES/DNS are typically uniform and no commutation errors occur in this direction. Therefore only selected z-components of the different terms of the Navier-Stokes equation have been analysed. It is remarked that in contrast to the analysis in Section 4 where mean values of the signal were zero, the mean axial velocity profile for a channel flow is characterised by strong wall normal gradients in particular in the vicinity to the wall. In other words the signal to be analysed contains the mean velocity contribution which makes it more predictable. Furthermore it is remarked that the wall normal filter width for the DNS and the a-priori LES analysis is very small, presumably much smaller than characteristic turbulent length scales.

First attention is focused on the first order derivatives in the Navier-Stokes equation, that is, the convective term and the pressure gradient. Figure 5a compares the commutation error for the wall normal derivative of convective component uw with the wall normal gradient of the SGS turbulent flux. Consistent with the analysis of Reference [37] it is found that the commutation error for the convective term can have the same order of magnitude than the SGS contribution. It can further be seen from Figure 5b,d that the scale similarity model represents very well the commutation errors for the term $\partial uw/\partial z$ and the pressure gradient, where the commutation error for the pressure gradient is much smaller in magnitude. Finally, Figure 5c shows that the dynamically determined model parameter C_{ss} is very close to unity which is consistent with subfigure (b). It is argued that this result is due to the small wall normal filter width (typical for wall bounded LES/DNS) and the velocity profile being dominated by the strong mean gradients.

Terms containing second derivatives, that is, for constant viscosity and density flow the diffusion term and the pressure Laplacian appearing in the Poisson equation for the pressure, will be considered next in Figure 6. Subfigure (a) again shows a very good performance of the scale similarity model (here for the second derivative). Similar observations in regards of the performance for the pressure Laplacian can be seen in Figure 6b. In all cases shown in Figures 5 and 6 the optimal model parameter is very close to unity which has been recovered by the dynamic procedure, but is not explicitly shown here for all terms.

Finally Figure 7 illustrates that Equations (35) and (42) represent reasonable approximations for the commutation error of the first and second wall normal derivative of axial velocity in channel flows. The differential filter given in Equation (36) has been used for filtering the data.

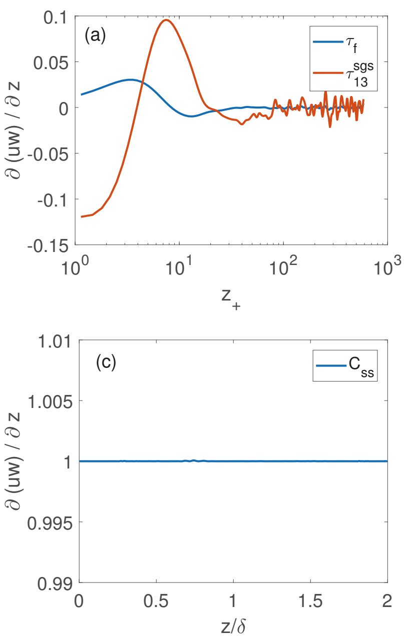

Figure 5. (**a**) Commutation error at primary filter level f for the first derivative $\partial uw/\partial z$ compared to the SGS component $\partial(\overline{uw} - \overline{u}\,\overline{w})/\partial z$ (**b**) Commutation error at primary filter level f for the first derivative $\partial uw/\partial z$ together with the corresponding scale similarity model. (**c**) Dynamic model parameter C_{ss} averaged in both homogeneous directions. (**d**) Commutation error at primary filter level f for the pressure gradient $\partial p/\partial z$ together with the corresponding scale similarity model. Without explicitly mentioning it, all results have been averaged in both homogeneous directions here and in the following figures.

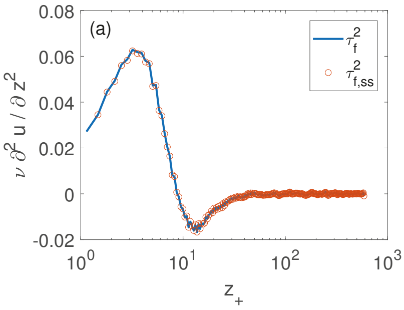

Figure 6. (**a**) Commutation error at primary filter level f for the second derivative (viscous term) $\nu\partial^2 u/\partial z^2$ together with the corresponding scale similarity model. (**b**) Commutation error at primary filter level f for the second derivative $\partial^2 p/\partial z^2$ appearing in the Poisson equation of the projection method together with the corresponding scale similarity model.

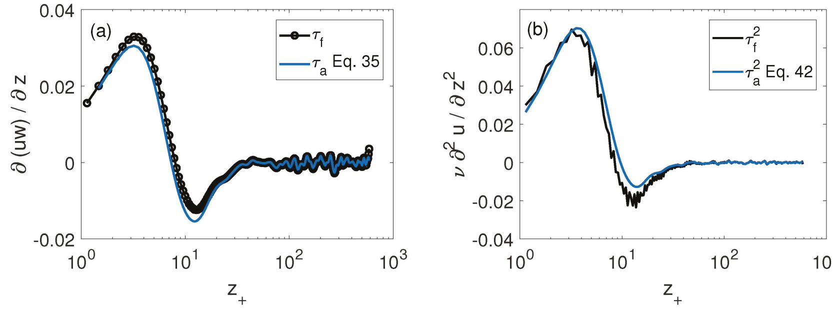

Figure 7. (**a**) Commutation error for $\partial uw/\partial z$ and (**b**) $\nu\partial^2 u/\partial z^2$ with the approximations given by Equations (35) and (42).

6. Conclusions

A large eddy simulation consists of filtering the Navier-Stokes equations in order to compute the large energy carrying motions of the flow while the smaller scales are modelled. The scale separation is formally introduced by a filtering operation. While this approach is very appealing, the filtering operation turns out to be more difficult compared to Reynolds averaging, because of the non-commutativity non only with respect to products but also with respect to derivatives in the case of anisotropic meshes.

A dynamic commutation error model has been produced by generalizing the dynamic modelling procedure. The commutation errors at two different resolution levels are defined and a multiscale identity relating them is derived. All that is in strict analogy with the well known dynamic model. The first results are promising for the future and it is remarked that the same formalism has been extended to second derivatives as well. The framework has been first applied to a synthetic turbulent flow with zero mean values and precisely controllable turbulence characteristics. The results reveal a good correlation strength of the scale similarity model and the dynamic procedure was shown to provide model coefficients close to the optimal model parameter (which cannot be calculated in a real LES in the absence of DNS data).

In a second step an a-priori analysis of a turbulent channel flow has been conducted indicating that the scale similarity models provide a very satisfactory performance with optimal model parameters very close to unity, which again was reproduced by the dynamic procedure. Selected terms of the Navier-Stokes equations have been analysed, showing that the commutation error for the first and second derivative can have a similar order of magnitude than the convective SGS contribution, which is (for the first derivative) consistent with findings from Reference [37] for a different flow configuration and different filtering technique.

In particular the results show, as remarked by Reference [12] that constraints derived from generalizations of the multiscale identities between different resolution levels may provide useful input in the specification of model parameters. Apart future more dedicated applications, the main aim of this short note should be to show the easiness and flexibility of the dynamic approach in very different modelling contexts.

Author Contributions: Conceptualization, M.G. and M.K.; methodology, M.G.; software, M.K.; formal analysis, M.K.; writing—original draft preparation, M.K. and M.G.; writing—review and editing, M.K. and M.G.; visualization, M.K. All authors have read and agreed to the published version of the manuscript.

Funding: This research received no external funding.

Institutional Review Board Statement: Not applicable for studies not involving humans.

Informed Consent Statement: Not applicable for studies not involving humans.

Data Availability Statement: Data available on reasonable request from the authors.

Conflicts of Interest: The authors declare no conflict of interest.

References

1. De Wiart, C.C.; Hillewaert, K.; Bricteux, L.; Winckelmans, G. Implicit LES of free and wall-bounded turbulent flows based on the discontinuous Galerkin/symmetric interior penalty method. *Int. J. Numer. Methods Fluids* **2015**, *78*, 335–354. [CrossRef]
2. Creech, A.; Jackson, A. Hybrid Large Eddy Simulation for low-order Discontinuous Galerkin methods using an explicit filter. *Comput. Phys. Commun.* **2021**, *260*, 107730. [CrossRef]
3. Schoepplein, M.; Weatheritt, J.; Sandberg, R.; Talei, M.; Klein, M. Application of an evolutionary algorithm to LES modelling of turbulent transport in premixed flames. *J. Comput. Phys.* **2018**, *374*, 1166 – 1179. [CrossRef]
4. Reissmann, M.; Hasslberger, J.; Sandberg, R.D.; Klein, M. Application of Gene Expression Programming to a-posteriori LES modeling of a Taylor Green Vortex. *J. Comput. Phys.* **2021**, *424*, 109859. [CrossRef]
5. Janicka, J.; Sadiki, A. Large eddy simulation of turbulent combustion systems. *Proc. Combust. Inst.* **2005**, *30*, 537–547. [CrossRef]
6. Pitsch, H. Large eddy-simulation of turbulent combustion. *Ann. Rev. Fluid Mech.* **2006**, *38*, 453–482. [CrossRef]
7. Ketterl, S.; Klein, M. A-priori assessment of subgrid scale models for large-eddy simulation of multiphase primary breakup. *Comput. Fluids* **2018**, *165*, 64–77. [CrossRef]
8. Klein, M.; Ketterl, S.; Hasslberger, J. Large eddy simulation of multiphase flows using the volume of fluid method: Part 1—Governing equations and a priori analysis. *Exp. Comput. Multiph. Flow* **2019**, *1*, 130–144. [CrossRef]
9. Long, S.; Yang, J.; Huang, X.; Li, G.; Shi, W.; Sommerfeld, M.; Yang, X. Large-eddy simulation of gas–liquid two-phase flow in a bubble column reactor using a modified sub-grid scale model with the consideration of bubble-eddy interaction. *Int. J. Heat Mass Transf.* **2020**, *161*, 120240. [CrossRef]
10. Leonard, A. Energy Cascade in Large-Eddy Simulations of Turbulent Fluid Flows. *Adv. Geophys.* **1974**, *18A*, 237–248.
11. Germano, M.; Piomelli, U.; Moin, P.; Cabot, W. A dynamic subgrid-scale eddy viscosity model. In Proceedings of the 1990 Summer Program, Stanford University, Stanford, CA, USA, December 1990; pp. 5–17. Available online: https://ui.adsabs.harvard.edu/abs/1990stun.proc....5G/abstract (accessed on 30 December 2020).
12. Meneveau, C. Germano identity-based subgrid-scale modeling: A brief survey of variations on a fertile theme. *Phys. Fluids* **2012**, *24*, 121301. [CrossRef]
13. Germano, M. Ten years of the dynamic model. In *Modern Simulation Strategies for Turbulent Flows*; Geurts, B.J., Ed.; Edwards: Philadelphia, PA, USA, 2001; pp. 173–190.
14. Lund, T. On the use of discrete filters for large eddy simulation. In *Annual Research Briefs*; Technical Report; Center for Turbulence Research: Stanford, CA, USA, 1997.
15. Sagaut, P. *Large Eddy Simulation for Incompressible Flows*; Springer: Berlin/Heidelberg, Germany, 1998.
16. Ghosal, S.; Moin, P. The basic equations for the large eddy simulation of turbulent flows in complex geometry. *J. Comput. Phys.* **1995**, *118*, 24–37. [CrossRef]
17. Vasilyev, O.; Lund, T.; Moin, P. A general class of commutative filters for LES in complex geometries. *J. Comput. Phys.* **1998**, *146*, 82–104. [CrossRef]
18. Marsden, A.; Vasilyev, O.; Moin, P. Construction of Commutative Filters for LES on Unstructured MEshes. *J. Comput. Phys.* **2002**, *175*, 584–603. [CrossRef]
19. Ciardi, M.; Sagaut, P.; Klein, M.; Dawes, W. A dynamic finite volume scheme for large-eddy simulation on unstructred grids. *J. Comput. Phys.* **2005**, *210*, 632–655. [CrossRef]
20. John, V. On large eddy simulation and variational multiscale methods in the numerical simulation of turbulent flows. *Appl. Math.* **2016**, *51*, 321–353. [CrossRef]
21. Leonard, S.; Terracol, M.; Sagaut, P. Commutation error in LES with time-dependent filter width. *Comput. Fluids* **2007**, *36*, 513–519. [CrossRef]
22. Franke, J.; Frank, W. Temporal Commutation Errors in Large-Eddy Simulation. *ZAMM J. Appl. Math. Mech.* **2001**, *81*, 467–468. [CrossRef]
23. Geurts, B.; Holm, D. Commutator errors in large-eddy simulation. *J. Phys. A Math. Gen.* **2006**, *39*, 2213–2229. [CrossRef]
24. Lilly, D. A proposed modification of the Germano subgrid-scale closure method. *Phys. Fluids* **1992**, *4*, 633–635. [CrossRef]
25. Bardino, J.; Ferziger, J.H.; Reynolds, W.C. *Improved Turbulence Models Based on Large Eddy Simulation of Homogeneous, Incompressible, Turbulent Flows*; Technical Reports Thermosciences Division; Department Mechanical Engineering, Stanford University: Stanford, CA, USA, 1983.
26. Klein, M.; Kasten, C.; Gao, Y.; Chakraborty, N. A-priori direct numerical simulation assessment of sub-grid scale stress tensor closures for turbulent premixed combustion. *Comput. Fluids* **2015**, *122*, 1–11. [CrossRef]
27. Klein, M.; Chakraborty, N.; Gao, Y. Scale similarity based models and their application to subgrid scale scalar flux modelling in the context of turbulent premixed flames. *Int. J. Heat Fluid Flow* **2016**, *57*, 91–108. [CrossRef]
28. Shamooni, A.; Cuoci, A.; Faravelli, T.; Sadiki, A. New Dynamic Scale Similarity Based Finite-Rate Combustion Models for LES and a priori DNS Assessment in Non-premixed Jet Flames with High Level of Local Extinction. *Flow Turbul. Combust* **2020**, *104*, 233–260. [CrossRef]

29. Klein, M.; Ketterl, S.; Engelmann, L.; Kempf, A.; Kobayashi, H. Regularised, parameter free scale similarity type models for Large Eddy Simulation. *Int. J. Heat Fluid Flow* **2020**, *81*, 108496. [CrossRef]
30. Meneveau, C.; Lund, T.; Cabot, W. A Lagrangian dynamic subgrid-scale model of turbulence. *J. Fluid Mech.* **1996**, *319*, 353–385. [CrossRef]
31. Iovieno, M.; Tordella, D. Variable scale filtered Navier–Stokes equations: A new procedure to deal with the associated commutation error. *Phys. Fluids* **2003**, *15*, 1926–1936. [CrossRef]
32. Chaouat, B. Commutation errors in PITM simulation. *Int. J. Heat Fluid Flow* **2017**, *67*, 138–154. [CrossRef]
33. Germano, M. On the Physical Effects of Variable Filtering lengths and times in LES. In *Advances in LES of Complex Flows*; Springer: Dordrecht, The Netherlands, 2002; pp. 3–11.
34. Germano, M. Differential filters of elliptic type. *Phys. Fluids* **1986**, *29*, 1757–1758. [CrossRef]
35. Klein, M.; Sadiki, A.; Janicka, J. A Digital Filter Based Generation of Inflow Data for Spatially Developing Direct Numerical or Large Eddy Simulations. *J. Comput. Phys.* **2003**, *186*, 652–665. [CrossRef]
36. Moser, R.D.; Kim, J.; Mansour, N.N. Direct numerical simulation of turbulent channel flow up to $Re_\tau = 590$. *Phys. Fluids* **1999**, *11*, 943–945. [CrossRef]
37. van der Bos, F.; Geurts, B.J. Commutator errors in the filtering approach to large-eddy simulation. *Phys. Fluids* **2005**, *17*, 035108. [CrossRef]

fluids

Article

Assessing Eulerian Indicators for Predicting Mixing in a Blinking Vortex System with Varying Degrees of Continuous Transition

Hyekyung Ryu and Andrew N. Cookson *

Department of Mechanical Engineering, University of Bath, Claverton Down, Bath BA2 7AY, UK; whistle2574@gmail.com
* Correspondence: a.n.cookson@bath.ac.uk; Tel.: +44-1225-386-296

Abstract: A discontinuous change in sequential velocity fields is known to generate laminar flow mixing through the mechanism of streamline crossing. However, previous research has suggested that a small degree of continuous transition between velocity fields may not necessarily be detrimental. This study therefore used a modified blinking vortex system with varying degree of continuous transition to assess the precise effect that this continuous transition has on mixing performance. This system was studied for the parameters: blinking period, vortex spacing, and the fraction of time spent in transition. Continuous Eulerian indicators were computed to investigate their correspondence with Lagrangian-based metrics, such as Intensity of Segregation, under such conditions. The results showed that up to 30% transition time yielded improvements in mixing, most notably when vortex spacing was large, and this was consistent across different time periods. The mixing prediction by the Eulerian indicators, particularly mobility, showed good agreement with actual mixing quality, albeit not perfectly, suggesting room for refinement in these metrics. Overall, the findings imply that mixing systems, such as continuous pipe flow-based devices, which are designed assuming a discontinuous change in velocity fields, might benefit from the presence of a small degree of continuous transition between discrete states.

Keywords: blinking vortex; chaotic advection; mixing; Eulerian indicators; laminar flow; stirring; streamline crossing

Citation: Ryu, H.; Cookson, A.N. Assessing Eulerian Indicators for Predicting Mixing in a Blinking Vortex System with Varying Degrees of Continuous Transition. *Fluids* **2021**, *6*, 10. https://doi.org/10.3390/fluids6010010

Received: 4 December 2020
Accepted: 26 December 2020
Published: 30 December 2020

1. Introduction

Since Aref's [1] introduction of the blinking vortex system, discontinuous change in velocity fields, embedding streamline crossing, has been known to be an effective route to laminar flow mixing by chaotic advection. This discontinuous property has been studied in other systems such as a partitioned pipe mixer [2–5], a twisted pipe [6,7], a mixer using helical geometry [8–10], etc.

The partitioned pipe mixer devised by Khakhar et al. [2] contains two rectangular plates which are orthogonally fixed in a rotating cylinder through which fluids travel by an axial pressure gradient. The fluids are mixed not only by axially superimposed streamlines but also by the baker's transform, which squeezes/stretches fluid material elements and then cuts and stacks them to create additional layers of the different fluids [11]. This device was studied further by bifurcation analysis [3], as a generalised partitioned pipe mixer [4], and as a partitioned pipe mixer with a barrier embedded, under different rotation protocols [5].

Jones et al. [6] created a twisted pipe to induce chaotic mixing by connecting in series curved pipe segments at twist angle in the range of 0 to π. The chaotic region was found to be maximised for $\pi/2$, when streamline crossing is at a maximum. Similarly, Jen et al. [7] tested twisted microchannels in T-shaped mixers from the assumption that chaotic advection could be achieved with a simple velocity field by periodically alternating the angle of the bottom in the channels.

An analogous effect has been implemented in curved channels and helical tubes. By changing the channel dimension or the sign of curvature, two different flow patterns are periodically switched like the blinking vortex, which generates chaotic mixing in the laminar regime without additional microstructures [8,9]. More recently, it was harnessed by Cookson et al. [10], as a way to generate enhanced mixing in a biological context, by concatenating in series small amplitude helical pipes. It had previously been found that small amplitude helical tubes induced swirling flow and in-plane mixing [12], and such effects could be enhanced by discontinuously connecting velocity fields from different helical amplitudes.

There are also other papers using the concept of blinking flow patterns. Chaotic mixing can be produced in cavity flows by alternatively moving the upper and lower walls [13], in channels by varying shape of grooves (a staggered herringbone mixer) [14], by embedding barriers [15], and by having a separatrix with secondary flows [16], and in a micromixer with two-layer serpentine crossing channels [17]. All mixing devices listed induce a periodic change in velocity fields to give the 'blinking' effect, thereby generating chaotic mixing. This effect was generalised theoretically by Sturman, Ottino, and Wiggins within the framework of Linked Twist Maps [18], which allowed for rigorous proofs of mixing bounds for simple mixing scenarios.

This discontinuous change in velocity fields is therefore clearly an important and useful mechanism for generating mixing. However, Cookson et al. [10] found that the strict discontinuity in velocity fields that was assumed for their design did not occur in practice, as there was a short distance over which a continuous transition between the vortical structures of each component pipe occurred. Comparing the mixing results to those from an idealised prediction where this discontinuity could be strictly enforced, showed very similar mixing values and Lagrangian structures, suggesting that some degree of continuous transition may not necessarily degrade the mechanism behind a discontinuous change. Only two such geometries were studied in this way, therefore leaving it unclear as to how general or robust this effect is. Furthermore, Lagrangian-based mixing analysis for optimisation in their study was computationally expensive.

Attempting to capture the principle mechanisms described in the theory of Linked Twist Maps, Sturman and Wiggins proposed Eulerian indicators (EIs) [19] as a means of predicting mixing performance from Eulerian properties alone. The EIs were refined by others [20,21] to handle continuously varying velocity fields, and may offer a route to accelerated design optimisation reducing need for Lagrangian calculations as the efficiency of the EIs has been proved in [16,19–22]. However, these metrics are not absolutely quantitative and different mixing devices are best predicted by a different subset of the Eulerian indicators.

Therefore, the aims of this study are to assess: (1) the impact, whether detrimental or beneficial, of a continuous transition regime on a mixing system designed around discontinuous operation, and (2) how well current Eulerian indicators are able to predict this mixing. As the degree of transition between velocity fields is not an independent variable in the helical pipe system, a modified blinking vortex model is chosen here as the simplest such mixing system and which gives control over this variable and others. The key findings are that continuous transition improved mixing when vortex spacing was large, but reduced mixing when vortex spacing was small. Such a trend was quite constant across different blinking periods although the effects of the vortex spacing were more noticeable for longer periods. Among the EIs investigated, mobility showed the best overall prediction of mixing quality but not for all cases, suggesting that current EIs may need further refinement.

2. Materials and Methods

2.1. Blinking Vortex with Continuous Transition

While Aref's blinking vortex model employs two point vortices which alternately turn on and off, thereby giving a discrete change in velocity fields, a continuous transition phase was introduced to that system here. Specifically, the point vortex can now move continuously with a constant velocity between the two fixed points for some or all of the total time, thus causing the velocity fields to change in a continuous, rather than discontinuous, manner. The period of the system, T, can be expressed as the sum of the time spent in the fixed state, t_{fixed}, and time spent in the transition state, t_{trans}, as follows:

$$T = t_{fixed} + t_{trans} \tag{1}$$

Figure 1a is a schematic of the blinking vortex system with the path of the moving vortex indicated. Figure 1b–d illustrate how the angle of a velocity vector at a given point (defined with respect to the positive x-axis) varies during a single period of the system. Figure 1b describes Aref's blinking vortex system, where the angle is constant for each fixed vortex, but experiences a discontinuous change at the half period. A pure transition model is described in Figure 1c where the angle continuously and linearly changes and returns to the initial point within a period. Figure 1d shows the change in angle for a system composed of both fixed and transition stages. To reflect the operating order of the fixed and moving vortex, Equation (1) can be more specifically stated as:

$$T = \frac{t_{fixed}}{2} + \frac{t_{trans}}{2} + \frac{t_{fixed}}{2} + \frac{t_{trans}}{2} \tag{2}$$

As in Aref's system, this model is two-dimensional, with the fluid both incompressible and inviscid. Particle motion is determined solely by advection via the velocity field, that is, with no diffusion. To clarify terms used in this paper, the vortex in static and transition stages will be defined as the fixed and moving vortex, respectively, and a vortex centre will represent the fixed vortex centre unless it is specified as the moving vortex centre.

2.2. Particle Tracking

Particle trajectories by the fixed vortex were computed by Aref's mapping [1]. The equation of motion for a particle in Aref's blinking vortex model is:

$$\dot{\bar{\zeta}} = \frac{\Gamma}{2\pi i}\frac{a^2 - R^2}{(\zeta - a)(a\zeta - R^2)} \tag{3}$$

where ζ, Γ, a, and R are a particle position, fixed/moving vortex strength, fixed vortex centre, and domain radius, respectively. The particle position can be expressed with its circular trajectory's centre ζ_c, radius ρ, and phase angle ϕ, as follows [1]:

$$\zeta = \zeta_c + \rho e^{i\phi} \tag{4}$$

Once the phase angle ϕ_t, after time t, is computed, the new position of the particle after t is [1]:

$$\zeta_t = \zeta_c + \rho e^{i\phi_t} \tag{5}$$

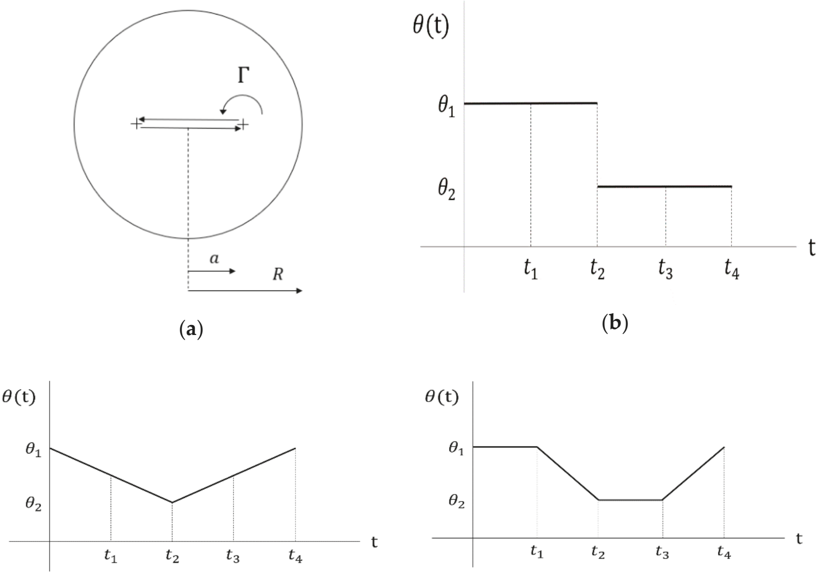

(**a**) (**b**)

(**c**) (**d**)

Figure 1. A schematic diagram of (**a**) Aref's blinking vortex model with moving vortex and the angle of velocity with respect to the positive x-axis for (**b**) Aref's blinking vortex model with motion of the point vortices between the fixed points of the original vortex positions; (**c**) pure transition model; and (**d**) a system with fixed and moving vortices. Γ, a, and R are vortex strength, vortex centre, and domain radius, respectively, and the arrows indicate the direction of the vortex or the trajectory of the moving vortex. A period from 0 to t_4 is not (necessarily) equally divided, but t_1 and $t_3 - t_2$ are identical and t_2 is half of t_4.

With $t_{fixed,\,1}$ and $t_{fixed,\,2}$ ($t_{fixed,\,1} = t_{fixed,\,2} = t_{fixed}/2$) being the first and second times spent in the stationary state within a period, the final particle position during the second fixed state, $\zeta_{fixed,2f}$, can be obtained using $\zeta_{fixed,1}$, which is calculated by Equation (5), without switching the vortex centre. With the initial position at $\zeta_{fixed,2i}$, the trajectory from $\zeta_{fixed,2i}$ to $\zeta_{fixed,2f}$ by the second fixed vortex is inverted against the domain centre or origin, which is identical, by symmetry considerations, to the trajectory from $-\zeta_{fixed,2i}$ to $-\zeta_{fixed,2f}$ by the first fixed vortex. The final position by the second vortex is obtained by returning $-\zeta_{fixed,2f}$ to $\zeta_{fixed,2f}$ by inversion again after $-\zeta_{fixed,2f}$ is calculated by the first vortex. The merits of this algorithm are that it does not require a generic time integration scheme for particle tracking and that its simulation time is independent of the period, which enables faster run-time independent of system parameters.

The particle trajectories during the vortex transition state are however computed by the MATLAB (Release 2019b, The MathWorks, Inc., Natick, MA, USA) functions *ode23* and *ode45*, which are three-stage and six-stage Runge-Kutta methods to solve ordinary differential equations, respectively. As the function names indicate, *ode23* and *ode45* include both second/third and fourth/fifth order methods in a single step, respectively. This dual order approach provides an error estimate that enables these adaptive time stepping schemes to achieve a specified tolerance, unless a fixed time step size is specified instead. The moving vortex centre varies over time as:

$$a_t = (-1)^{m+1} \cdot a \left(1 - \frac{4t}{t_{trans}}\right) \tag{6}$$

where

$$m = \begin{cases} odd\ numbers, & at\ the\ first\ moving\ stage \\ even\ numbers, & at\ the\ second\ moving\ stage \end{cases} \tag{7}$$

So that $a_t = a$ at $t = 0$ and $a_t = -a$ at $t = \frac{t_{trans}}{2}$ for the first half moving period, and $a_t = -a$ and $a_t = a$ for the second. Note that a_t is defined considering the code implementation, and, hence, the range of t is from 0 to $\frac{t_{trans}}{2}$, not to t_{trans}. In practice, *ode23* was used to calculate particle distributions, for reasons of computational efficiency as the difference in accuracy, compared to using *ode45*, was negligible under a small number of system iterations. However, Poincaré sections were drawn by *ode45* due to the much greater number of system iterations required to construct these plots. The time step was tested in the range 10^{-2} to 10^{-6} by 10^{-1}. When the time step is smaller than 10^{-4}, a decrease in RMS error was not noticeably reduced while the run-time significantly increased by a factor of up to 10. Both a smaller RMS error and shorter simulation time were achieved by allowing the solver to adjust the timestep automatically. The MATLAB code written for computing particle distributions, Poincaré sections, and Eulerian indicators is available for download in the Supplementary Materials.

2.3. Mixing Analysis and Prediction

2.3.1. Lagrangian Approaches

Mixing performance was evaluated qualitatively and quantitively by Poincaré sections and intensity of segregation, respectively. Poincaré sections provide a useful visualisation of structures underlying observed mixing behaviour. They represent a periodic sampling of particle trajectories across a large number of iterations. They may draw out a region of regular flow, often corresponding to a physical streamline or may have an unstructured region, generally corresponding to chaotic regions that are associated with good mixing. To create the Poincaré sections presented here, 15 particles were initially placed at $(x, y) = (\pm 0.05, 0)$, $(\pm 0.2, 0)$, $(\pm 0.35, 0)$, (0, 0), (0, 0.125), (0, 0.25), (0, 0.375), (0, 0.5), (0, 0.625), (0, 0.75), (0, 0.875), and (0, 1), and the system was run for 5000 iterations.

To calculate the intensity of segregation measure of mixing, an initial distribution of red and green particles (503,424 particles in total) is perfectly segregated in the left half and right half of the domain, respectively. A grid is superimposed onto the domain, permitting a local concentration, c, to be calculated within a circle located at each grid point as [19]:

$$c = \frac{number\ of\ red\ particles}{number\ of\ red\ particles + number\ of\ green\ particles} \tag{8}$$

The circle radius was chosen as 0.04 to ensure a sufficient number of particles were included and a grid size of 0.025 was selected by running convergence tests. The average concentration over the entire domain is 0.5, with the variance of concentration across the domain given by [20]:

$$\mathcal{V}(t) = \frac{1}{N_{gridpoint}} \sum_{i=1}^{N_{gridpoint}} \left(c_i(r_i, t) - c_{avg}\right)^2 \tag{9}$$

where $N_{gridpoints}$, $c_i(r_i, t)$, and c_{avg} are the number of grid points, a local concentration at (r_i, t), and the averaged concentration over the domain, respectively. The intensity of segregation is obtained by rescaling Equation (9):

$$I = 4 \cdot \mathcal{V}(t) \tag{10}$$

A value of I equal to 0 and 1 indicates a perfect mixture of particles, and perfect segregation of particles, respectively.

2.3.2. Eulerian Approaches

The chaotic nature of particle trajectories in systems with good mixing means that time steps must in general be very small to obtain acceptable accuracy, meaning that Lagrangian analysis of mixing is usually computational expensive. Eulerian based methods of mixing performance are attractive due to their much lower computational cost. The EIs devised by Sturman and Wiggins [19] (which will be called discontinuous Eulerian indicators or d-EIs) attempted to predict mixing behaviour from several properties of the discontinuously changing velocity fields produced in a system. The velocity field in Aref's blinking vortex model is [19]:

$$\dot{x} = -\frac{\Gamma}{2\pi}\left[\frac{y}{(x-a)^2+y^2} + \frac{y}{(x-R^2/a)^2+y^2}\right] \tag{11}$$

$$\dot{y} = \frac{\Gamma}{2\pi}\left[\frac{x-a}{(x-a)^2+y^2} + \frac{x-R^2/a}{(x-R^2/a)^2+y^2}\right] \tag{12}$$

By analogy to linked twist maps, Sturman and Wiggins proposed that perpendicular streamline crossing and strong shear rate applied to adjacent fluid elements would generate good mixing. The product of those two properties showed good correspondence with the actual mixing performance, although investigating only one factor would not be enough to reflect fluid movements by the velocity fields. Note that the comparison was conducted by examining the qualitative agreement between the corresponding graphs of Lagrangian and Eulerian results, not by computing numerical errors, as the EIs only enable relative comparisons and do not provide absolute values, nor are these values within a predetermined normalised range, as is the case for intensity of segregation.

Those results, however, were dependent on a discrete change of the velocity field. Therefore, the EIs modified by McIlhany and Wiggins [20] (which will be called continuous Eulerian indicators or c-EIs) were adopted in this paper to capture the characteristics of continuously varying conditions. The c-EIs have four indicators: streamline crossing, the relative rate of velocity change, mobility, and the product of the streamline crossing and mobility. With the method being based on the time-averaged scheme,

$$\begin{aligned}\tfrac{1}{T}\textstyle\int_0^T f(t)dt = \tfrac{1}{T}\ &\left[\int_0^{\frac{1}{2}t_{fixed}} f_1(t)dt + \int_{\frac{1}{2}t_{fixed}}^{\frac{1}{2}(t_{fixed}+t_{trans})} f_2(t)dt\right.\\ &\left. + \int_{\frac{1}{2}(t_{fixed}+t_{trans})}^{\frac{1}{2}(t_{fixed}+t_{trans}+t_{fixed})} f_3(t)dt + \int_{\frac{1}{2}(t_{fixed}+t_{trans}+t_{fixed})}^{T} f_4(t)dt\right]\end{aligned} \tag{13}$$

The integration was numerically calculated using the trapezium rule with a time step of 10^{-4}, with the singularities at the vortex centres, in Equations (11) and (12), excluded from the calculations.

The streamline crossing of the c-EIs is conceptually the same as one of the d-EIs but with a different mechanism, thereby giving the identical result for the pure blinking system. The angle of a velocity vector with respect to the positive x-axis is averaged by time as [20]:

$$\langle\theta(\boldsymbol{r};\epsilon)\rangle_t \equiv \frac{1}{T}\int_0^T \theta(\boldsymbol{r},t;\epsilon)dt \tag{14}$$

where $\boldsymbol{r}$ and ϵ include space and system parameter information, respectively. After Equation (14) is adjusted to be between $-\frac{\pi}{2}$ and $\frac{\pi}{2}$, the RMS value is computed, which is followed by the second rescaling, $\alpha(\boldsymbol{r};\epsilon)$, to make the range between 0 and $\frac{\pi}{2}$. The streamline crossing is obtained by a spatial average [20]:

$$\overline{\alpha}(\epsilon) = \langle\alpha\left(\boldsymbol{r};\epsilon\right)\rangle_r \tag{15}$$

The second indicator is computed by averaging the relative rate of velocity change over time and then on the domain, as follows [20]:

$$dw(\boldsymbol{r},t;\epsilon) = \lim_{\Delta t\to 0}\frac{||\boldsymbol{v}(\boldsymbol{r},t+\Delta t;\epsilon)-\boldsymbol{v}(\boldsymbol{r},t;\epsilon)||}{||\boldsymbol{v}(\boldsymbol{r},t+\Delta t;\epsilon)||+||\boldsymbol{v}(\boldsymbol{r},t;\epsilon)||} \tag{16}$$

$$\widetilde{w}(\boldsymbol{r};\epsilon) = \frac{1}{T}\int_0^T dw(\boldsymbol{r},t;\epsilon)dt \tag{17}$$

$$\zeta(\epsilon) = \langle\widetilde{w}(\boldsymbol{r};\epsilon)\rangle_{\boldsymbol{r}} \tag{18}$$

As for the mobility, the velocity for fast-changing flows and slow-changing flows are defined as [20,23]:

$$v_{fast}(\boldsymbol{r};\epsilon) \equiv \frac{1}{T}\left|\int_0^T \boldsymbol{v}(\boldsymbol{r},t;\epsilon)dt\right| \tag{19}$$

$$v_{slow}(\boldsymbol{r};\epsilon) \equiv \frac{1}{T}\int_0^T |\boldsymbol{v}(\boldsymbol{r},t;\epsilon)|dt \tag{20}$$

which is based on the notion that the cancellation of velocity vectors has greater importance for fast-changing flows. The integrated velocity magnitude can be expressed as [20]:

$$v_{sum}(\boldsymbol{r};\epsilon) \equiv \left(1-e^{-\widetilde{w}(\boldsymbol{r};\epsilon)}\right)v_{fast}(\boldsymbol{r};\ \epsilon)+e^{-\widetilde{w}(\boldsymbol{r};\epsilon)}v_{slow}(\boldsymbol{r};\ \epsilon) \tag{21}$$

which implies that $v_{fast}(\boldsymbol{r};\epsilon)$ is dominant with the high relative rate of velocity change while $v_{slow}(\boldsymbol{r};\epsilon)$ is the main contributor to $v_{sum}(\boldsymbol{r};\epsilon)$ with the low rate. To calculate the mobility, the threshold velocity is defined as [20,23]:

$$v_{thresh} = \left\langle\langle v_{sum}(\boldsymbol{r};\epsilon)\rangle_{\boldsymbol{r}}\right\rangle_{\epsilon} \tag{22}$$

If $v_{sum}(\boldsymbol{r};\epsilon)$ exceeds $v_{thresh}(\boldsymbol{r};\epsilon)$, $\mathbb{I}(\boldsymbol{r};\epsilon)$ is assigned a value of 1, and the mobility is computed by averaging $\mathbb{I}(\boldsymbol{r};\epsilon)$ on the domain, as follows [20]:

$$\mathbb{I}(\boldsymbol{r};\epsilon) = \begin{cases} 1 & if\ v_{sum}(\boldsymbol{r};\epsilon) \geq v_{thresh} \\ 0 & otherwise \end{cases} \tag{23}$$

$$\eta(\epsilon) \equiv \langle\mathbb{I}(\boldsymbol{r};\epsilon)\rangle_{\boldsymbol{r}} \tag{24}$$

The final indicator, $\gamma(\epsilon)$ is the product of the streamline crossing and mobility:

$$\gamma(\epsilon) = \overline{\alpha}(\epsilon)\eta(\epsilon) \tag{25}$$

2.4. Study Methods

As in Aref's paper, dimensionless parameters were defined as [1]:

$$\mu = \frac{\Gamma T}{2\pi R^2} \tag{26}$$

$$\nu = \frac{a}{R} \tag{27}$$

So that $\mu = T$ and $\nu = a$ when $\Gamma = 2\pi$ and $R = 1$, and the ratio of transition time to a period is:

$$r_{trans} = \frac{t_{trans}}{T} = \frac{t_{trans}}{\mu} \tag{28}$$

These three parameters were varied to observe their effects on mixing performance and how they interact to improve or worsen the mixing quality. The comparisons were carried out for both a fixed number of system iterations and for fixed total time ($= \mu \times iterations$). Lagrangian analysis was conducted mainly for the interpretation of the mixing behaviour and determination of the system parameters' effects. These results were compared to the Eulerian indicator results to assess their accuracy at predicting mixing quality.

3. Results

3.1. Lagrangian Mixing Analysis

Mixing performance was evaluated for three parameters—continuous transition time (t_{trans}), vortex spacing, and blinking period—which interact with one another, thereby providing different results with a different set of the parameters. Mixing analysis was conducted with continuous transition varying either μ or ν to observe their interactions and mainly focused on phenomena occurring between the fixed vortices where the essential effect of the continuously moving vortex appears to be focused. First, the analysis was conducted comparing results from a fixed number of iterations to discover the effects of the parameters at each μ. However, as a longer period, for an equal number of iterations, gives more time for the system to mix, the effects were re-examined, keeping the total run time constant.

3.1.1. Qualitative Analysis

Before making quantitative comparisons, it is useful to compare the mixing produced in the different systems qualitatively. Poincaré sections are visually instructive for understanding and comparing the nature of the mixing behaviour of a system, particularly for identifying islands of regular flow. Figure 2 shows Poincaré sections and particle distributions for $\mu = 1$ and $\nu = 0.5$ and includes the minimum I (or the best mixing) at $r_{trans} = 0.3$ and maximum at $r_{trans} = 0.9$. From $r_{trans} = 0.0$ to 0.3, there are no significant islands of no-mixing in the Poincaré sections, only some small islands near the circular boundary. At $r_{trans} = 0.4$, however, a noticeable island appears due to overlapped analogous streamlines around the moving vortex centre, and this island grows as r_{trans} increases. The islands observed in these Poincaré sections are spatially co-located with the areas of unmixed coloured particles in the particle distribution plots, which demonstrates that the islands are functioning as a barrier to particle transport, and thus are preventing the mixing of fluid between the inside and outside of the islands. In contrast, in the chaotic regions, it is observed that particles are well mixed.

Although Poincaré sections may provide an intuitive understanding of chaotic behaviour and mixing performance, it is somewhat difficult to clearly distinguish which system produces better mixing quality when significant differences between the Poincaré sections are not readily apparent. Such differences are quantified by the intensity of segregation (in Section 3.1.2), but it remains unsolved to explain why mixing performance does not straightforwardly increase or decrease in the presence of islands. The Poincaré sections show how well particles are mixed in the system given sufficient time, but not the rate of mixing or rate of approach to an asymptotic state.

Examining the sequence of particle distributions within a single iteration reveals the physical processes that generate the fluid mixing. Figure 3 shows snapshots of the particle distributions, within one iteration, for the best mixing case (as quantified by I), that is $r_{trans} = 0.3$ with $\mu = 1$ and $\nu = 0.5$. As seen in Figure 3a, the first half period initially contributes less directly to the fluid mixing but rather acts to bring different species near to the fixed vortices. Figure 3b reveals that the second fixed vortex in the period creates circular layers of stretched material filaments around the vortex centre, which appear to be beneficial once the moving vortex is able to take particles from one side to the other (see Figure 3c,d).

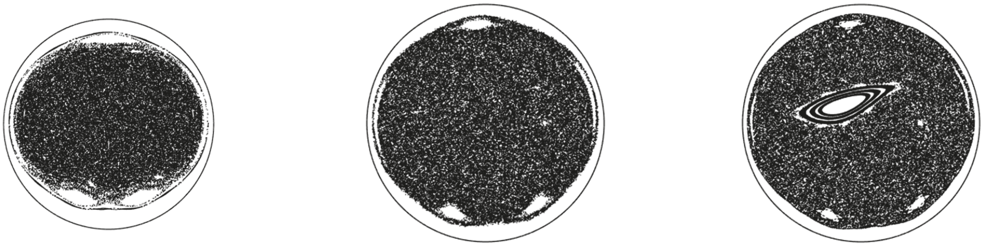

(**a**) $r_{trans} = 0.0$ (**b**) $r_{trans} = 0.3$ (**c**) $r_{trans} = 0.4$

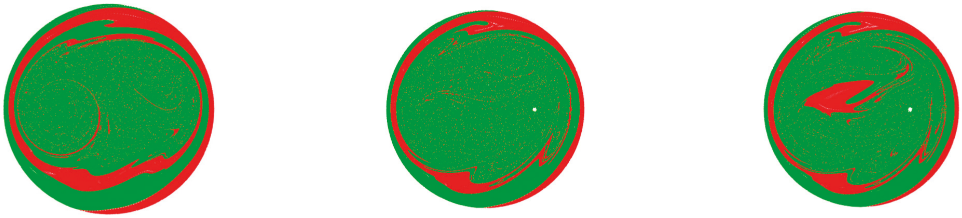

(**d**) $r_{trans} = 0.0$ (**e**) $r_{trans} = 0.3$ (**f**) $r_{trans} = 0.4$

(**g**) $r_{trans} = 0.6$ (**h**) $r_{trans} = 0.9$ (**i**) $r_{trans} = 1.0$

(**j**) $r_{trans} = 0.6$ (**k**) $r_{trans} = 0.9$ (**l**) $r_{trans} = 1.0$

Figure 2. Poincaré sections (the first and third rows) and particle distributions (the second and forth rows) with $\mu = 1$ and $\nu = 0.5$. A total of 5000 iterations were computed to construct the Poincaré sections and the particle distribution plots experience the identical total time, equal to 10.

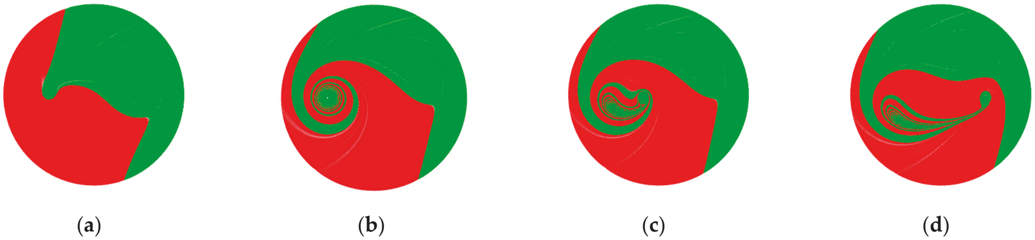

Figure 3. Particle distribution at (**a**) t = 0.5 (half period); (**b**) 0.85 (after the second fixed vortex); (**c**) 0.9 (under moving vortex); and (**d**) 1.0 (after a single period) with μ of 1, ν of 0.5, and r_{trans} of 0.3.

The mixing performance of the system was found to depend on the ratio of t_{fixed} and t_{trans}. As the stationary vortex produces filament layers while the moving vortex transports particles between the fixed vortex centres, the system's mixing performance is reduced if the time spent in either stationary or moving regimes is too short. In Figure 4, the best mixing performance is at $r_{trans} = 0.3$ while the worst is at $r_{trans} = 0.9$. When the r_{trans} is lower than 0.3, the moving vortex cannot take particles to the other side effectively due to its near-instantaneous movements, whereas the higher r_{trans} would not allow the fixed vortex to create sufficient filament layers. Given that the fixed vortex produces no layers at $r_{trans} = 0.9$ and the moving vortex creates the layer along its trace, the pure transition is more beneficial to enhance mixing quality than r_{trans} of 0.9.

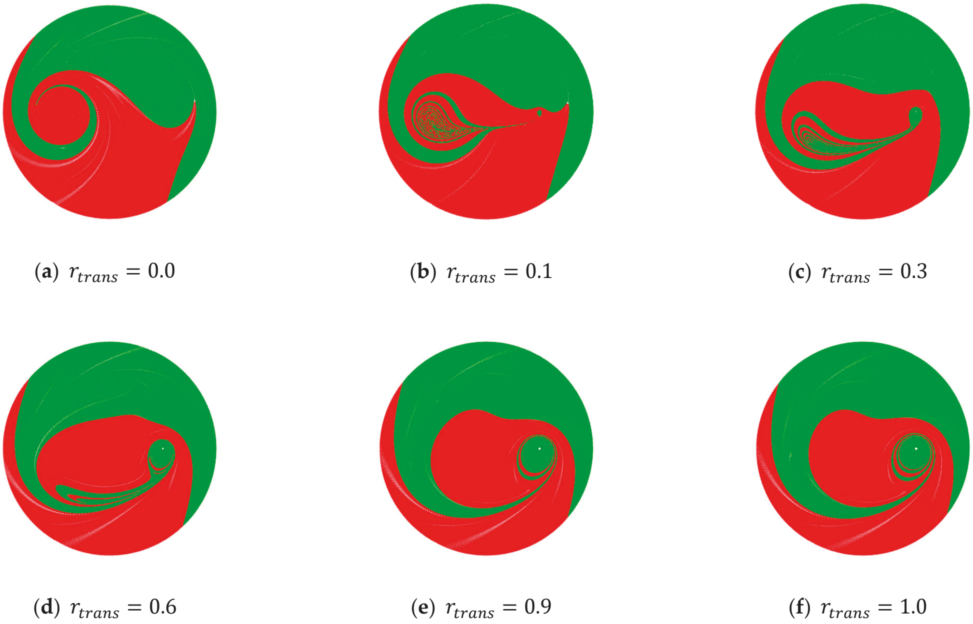
(**a**) $r_{trans} = 0.0$ (**b**) $r_{trans} = 0.1$ (**c**) $r_{trans} = 0.3$

(**d**) $r_{trans} = 0.6$ (**e**) $r_{trans} = 0.9$ (**f**) $r_{trans} = 1.0$

Figure 4. Particle distribution after one iteration with μ of 1 and ν of 0.5 with different transition time.

3.1.2. Quantitative Analysis

The coloured particle distribution plots were then analysed using the intensity of segregation metric, I, to provide a quantitative comparison of mixing performance. The effect of continuous transition and source spacing on mixing quality at each period for a fixed number of iterations of 10 is shown in Figure 5, where I is plotted against r_{trans}, varying from 0.0 to 1.0 in increments of 0.2, for different values of ν and μ. Given that a smaller value of I corresponds to better mixing performance, with the introduction of the moving vortex, the mixing quality is improved for large ν while the inverse is true for small ν. The continuous transition contributes to efficient particle transport and a decrease in discrete properties. When the vortices are adjacent, the mixing is already very effective due to the strong interactions between the point vortices, and the movement of the vortex removes the benefit of the discontinuously changing velocity fields. On the other hand, the stationary vortices positioned near the boundary (i.e., without any continuous transition) do not benefit from the discontinuous change in velocity fields due to the weak vortex interactions arising from the inverse relationship between velocity and radius. This means that the strongest part of each vortex's velocity field is in the region where only a single species (colouring) exists. This poor mixing can be enhanced by the moving vortex, which acts to physically transport particles as the vortex centre moves between the two fixed positions.

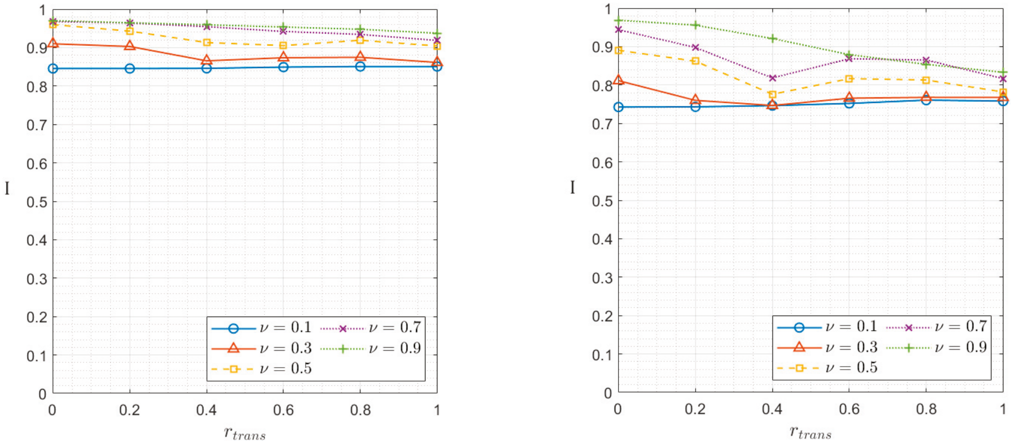

(**a**) $\mu = 0.05$ (**b**) $\mu = 0.125$

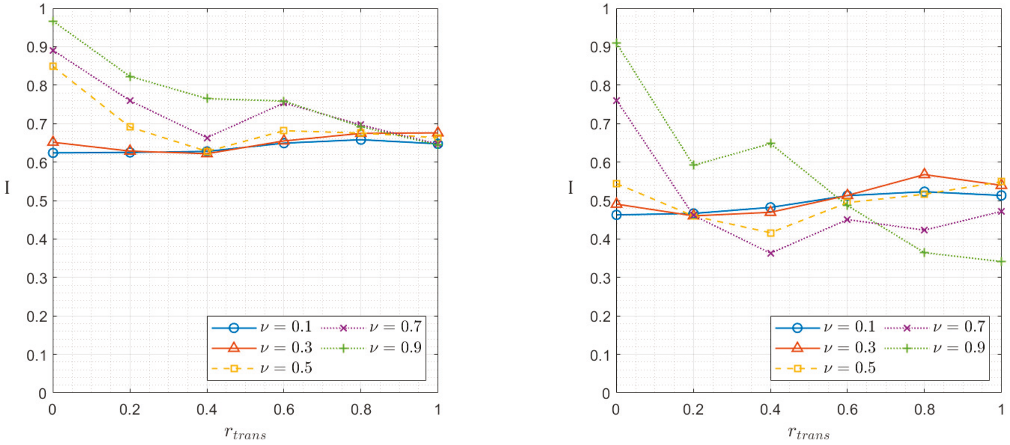

(**c**) $\mu = 0.25$ (**d**) $\mu = 0.5$

Figure 5. *Cont.*

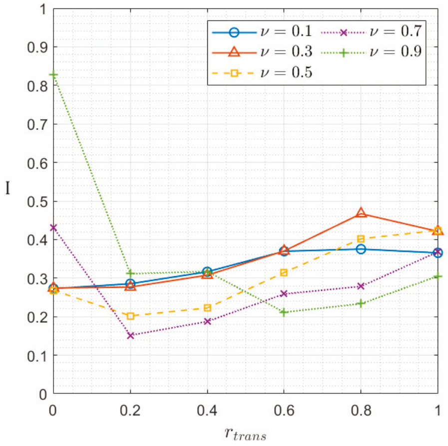

(**e**) $\mu = 1.0$

Figure 5. The effect of the transition time (r_{trans}) and fixed vortex centre (ν) on mixing performance (I) with fixed iterations of 10, which indicates that (**a**) total time is 0.5; (**b**) 1.25; (**c**) 2.5; (**d**) 5; and (**e**) 10 with different periods (μ).

Another feature of Figure 5 is that the longer period produces better mixing quality when comparing across a fixed number of iterations; for example, the performance with ν of 0.1 (blue lines in Figure 5) is improved as μ increases, which is also true for other cases. However, it does not guarantee that long periods are beneficial for mixing, in that the total time that each system experiences is different for the same number of iterations. For instance, the total time is only 0.5 for the shortest period while it is 10 for the longest of those studied here. Therefore, the better mixing performance may simply be caused by the longer total time that the system operates for and so results will also be compared for fixed total time.

The results with the same set of parameters but now with the fixed total time (equal to 10), are found in Figure 6 where the trend observed for fixed total iterations is no longer always the case. It is still true for low r_{trans}, but the improvements can be achieved with short μ as r_{trans} increases with exceptions for the large spacing. Since the mixing behaviour with zero transition is governed by discrete properties, that is streamline crossing, it is more beneficial to specify a long time period, so that a particle can escape from its previous streamline and then travel in a different direction on a new streamline as in Aref's system. In contrast, the system with pure transition is wholly driven by the moving vortex; thus, the more frequently the moving vortex stirs the fluid or the region between the fixed vortex centres experiences the stronger regions of the velocity fields, the better mixing quality can be obtained. However, the trend does not hold for the combination of large spacing and small period. In Figure 6e, an I of 0.3052 with $\mu = 1.0$ improves to 0.1099 with $\mu = 0.25$ in Figure 6c, but worsens to 0.2335 when $\mu = 0.05$ in Figure 6a. As shown in Figure 7a–f, increasing the system period produces larger islands of regular flow, thereby producing an unmixed area. The same appears the case for the large source spacing in Figure 7g–i where the island at the domain origin becomes large as μ increases. In Figure 7g, however, the seemingly chaotic region actually consists of many small-scale islands which trap particles inside separating them from the rest of the domain. Although this may be difficult to discern in a Poincaré section created with a full set of sample particles, it was found that the large chaotic regions were indeed divided into smaller chaotic regions when the Poincaré sections were created from a single particle in turn. Figure 7j shows the resultant patterns of layers of unmixed particles separated by such areas.

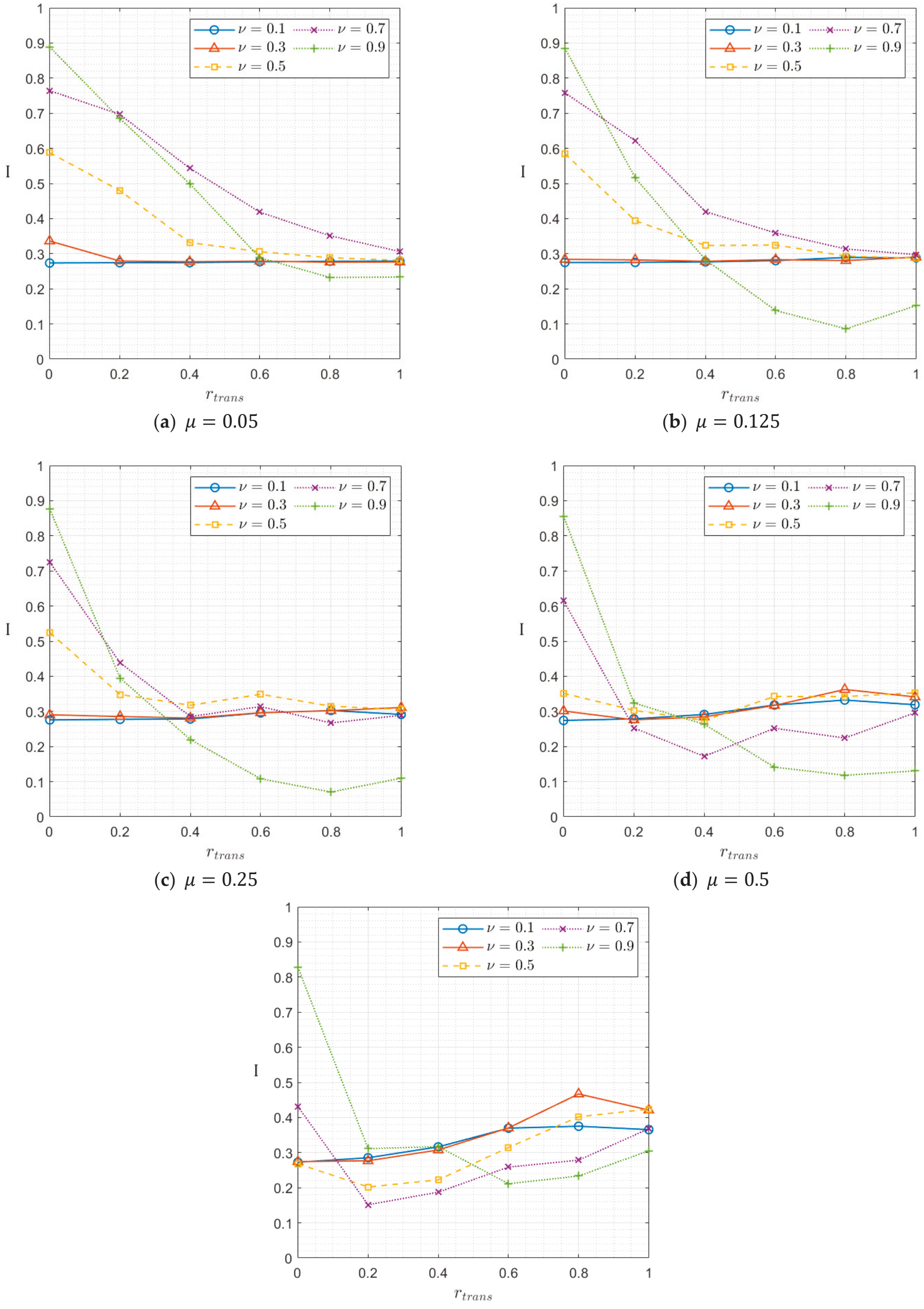

(**a**) $\mu = 0.05$ (**b**) $\mu = 0.125$

(**c**) $\mu = 0.25$ (**d**) $\mu = 0.5$

(**e**) $\mu = 1.0$

Figure 6. The effect of the transition time (r_{trans}) and fixed vortex centre (ν) on mixing performance (I) with fixed total time of 10, which indicates that (**a**) iterations are 200; (**b**) 80; (**c**) 40; (**d**) 20; and (**e**) 10 with different periods (μ). Note that Figure 6e is identical to Figure 5e.

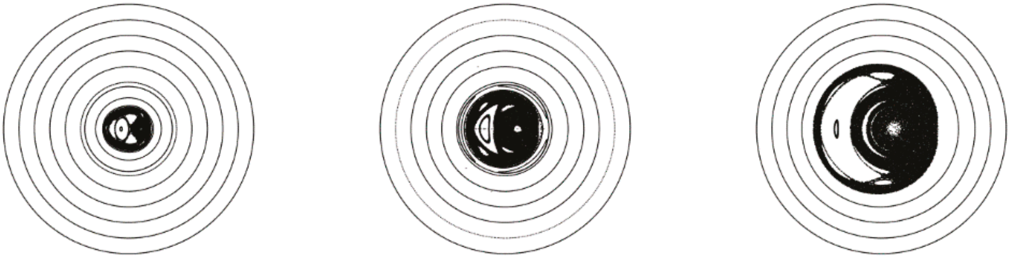

(**a**) $\mu = 0.05$ and $\nu = 0.1$ (**b**) $\mu = 0.25$ and $\nu = 0.1$ (**c**) $\mu = 1.0$ and $\nu = 0.1$

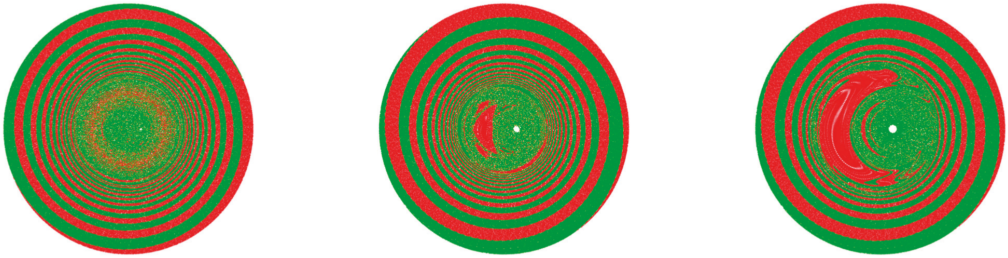

(**d**) $\mu = 0.05$ and $\nu = 0.1$ (**e**) $\mu = 0.25$ and $\nu = 0.1$ (**f**) $\mu = 1.0$ and $\nu = 0.1$

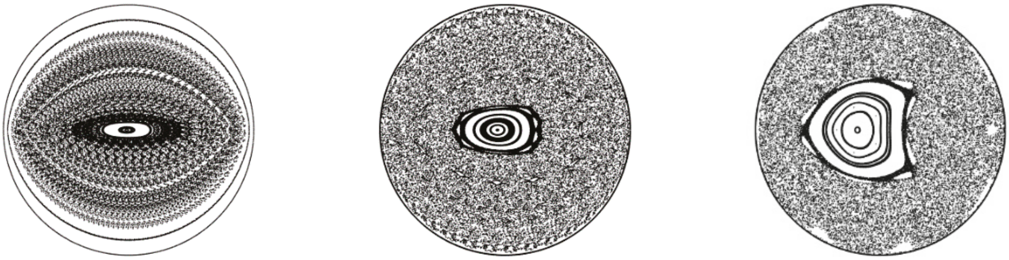

(**g**) $\mu = 0.05$ and $\nu = 0.9$ (**h**) $\mu = 0.25$ and $\nu = 0.9$ (**i**) $\mu = 1.0$ and $\nu = 0.9$

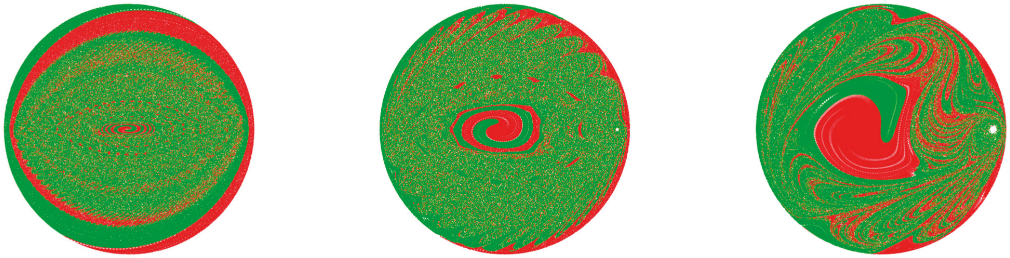

(**j**) $\mu = 0.05$ and $\nu = 0.9$ (**k**) $\mu = 0.25$ and $\nu = 0.9$ (**l**) $\mu = 1.0$ and $\nu = 0.9$

Figure 7. Poincaré sections (the first and third rows) and particle distributions (the second and forth rows) for $r_{trans} = 1$. A total of 5000 iterations were computed to construct the Poincaré sections and the particle distribution plots experience the identical total time, equal to 10.

In both Figures 5 and 6, the effect of vortex spacing appears to be qualitatively the same across the plots. The results for the pure blinking model agree with those of [1,19], that is, the conclusions that longer periods and small source spacing enhance mixing performance. As the total time of system operation is longer in the plots of Figure 6 (except for μ of 1.0 when it is equal), the results in Figure 6 reveal better mixing performance than the corresponding plots in Figure 5. Specifically, for large vortex spacing running the system for more iterations only improves mixing by less than 10%, whereas the mixing performance can be improved by up to 68% for small vortex spacing, for the pure blinking model. Vortices with a large spacing do not interact effectively (unless some continuous transition has been introduced), such that additional iterations provide little benefit. Furthermore, it is more noticeable in Figure 6 that the positive correlations between I and r_{trans} for small v do not reveal noticeable differences, compared to the broad source spacing. The continuous transition has relatively little effect on the mixing performance for small spacing while a sharp drop in I is found with even a small fraction of transition time for large spacing, as the inefficiency of the largely spaced vortex system can be significantly improved by the moving vortex. If the transition time is long enough to give the effects described in Figure 3c,d, increasing r_{trans} becomes less important afterwards. However, as for short μ, the transition time is also short in absolute terms, so the effect of r_{trans} is less significant than for long μ.

3.2. Eulerian Mixing Analysis

3.2.1. Discontinuous Eulerian Indicators

The tests with the d-EIs varying the vortex centre at different r_{trans} showed good prediction by the product of streamline crossing and shear rate, but only when the system was operated by a pure blinking vortex. With continuous transition introduced, the agreements with the actual mixing performance were mainly eliminated. The d-EIs, which capture discrete properties, were no longer suitable once r_{trans} was greater than 0.2; therefore, the c-EIs were chosen for the more thorough investigation into how to predict mixing performance for these cases. Figure 8 compares the mixing prediction of the d-EIs and c-EIs. Even in the case of the pure blinking model without continuous transition, the c-EIs provide a better prediction, albeit only for mobility.

3.2.2. Continuous Eulerian Indicators

Table 1 summaries a qualitative assessment of the strength of the correlation between various Eulerian indicators and intensity of segregation, for a range of values of vortex centre and period. The correlation was classified as Poor (P), Medium (M), and Good (G), with each table cell representing a graph of the intensity of segregation, (I) (left y-axis) and one of the Eulerian indicators ($\overline{\alpha}$, ζ, η, or γ) (right y-axis) versus the ratio of continuous transition (r_{trans}). Minor or localised discrepancies were ignored when the mixing quality was assessed as Good. For instance, the evaluation of the first plot in Figure 9a is found in Table 1 with μ of 0.05 and ν of 0.1, which is the upper left box for streamline crossing, denoted as G. Due to the c-EIs not being an absolutely quantiative measure, each evaluation was conducted with qualitative criteria instead of computing numerical errors. If the overall trend between the Lagrangian and Eulerian results was agreed, it was assessed as Medium, and if not, it was classed as Poor. Only when both the overall trend and the shape of the graph were in general agreement was the prediction classified as Good. Some examples for the classifications can be found by comparing Table 1 and Figures 9 and 10. Note that the y-axis of the c-EIs, whose correlation with mixing performance is positive, has been reversed to make clearer that the agreement with intensity of segregation indicates that the particular c-EI is a good predictor of mixing.

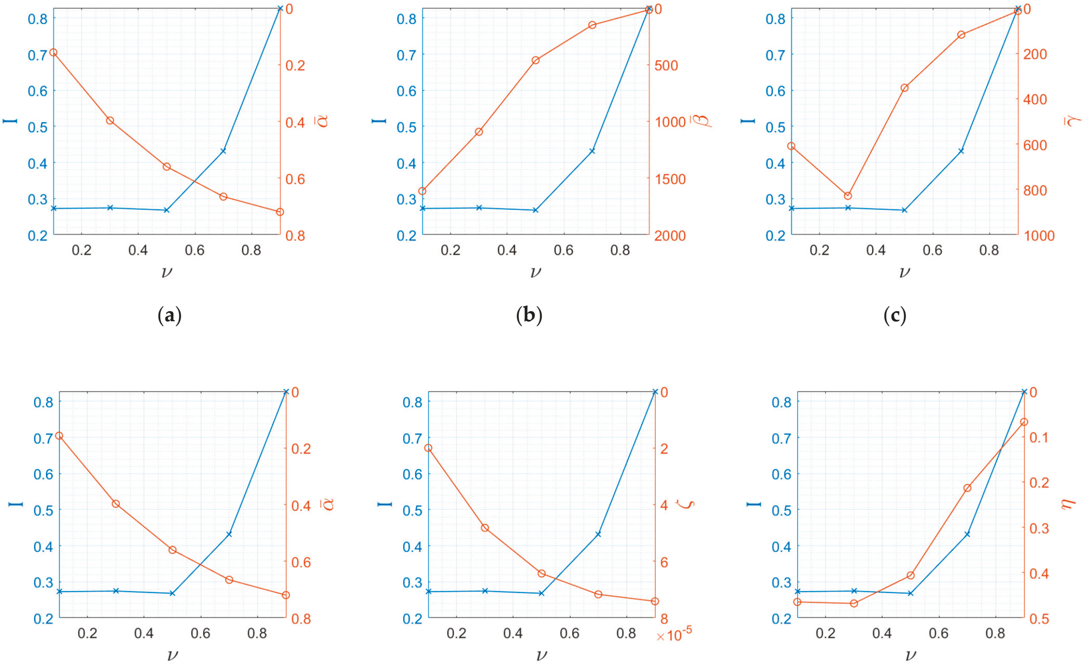

(**a**) (**b**) (**c**)

(**d**) (**e**) (**f**)

Figure 8. Comparison between d-EIs (the first row) and c-EIs (the second). The indicators are (**a**) streamline crossing; (**b**) shear rate; (**c**) the product of the streamline crossing and shear rate; (**d**) streamline crossing; (**e**) the relative rate of velocity change; and (**f**) mobility.

In Table 1, patterns dividing the classifications can be found for streamline crossing and relative rate of velocity change, although the patterns are less obvious for both mobility, and the product of streamline crossing and mobility. Configurations with the fixed iterations, denoted in the round brackets, are found not to significantly alter the trend with the fixed total time; that is, such variations do not appear globally and there were no jumps between the highest and worst assessment. In terms of the vortex spacing, it can be roughly said that the mixing performance would become worse for the small spacing while it would be improved for the large spacing as the ratio of continuous transition increases; therefore, in this case, the values of I and the c-EIs should increase and decrease, respectively, when the vortices are close, and vice versa.

For the first c-EI, streamline crossing, increasing continuous transition eliminates the discrete change of velocity fields, so perpendicular streamline crossing rarely occurs. To be more specific, the effect of the continuous transition can be interpreted as either positive or negative with respect to the angle of velocity vectors. Note that the streamline crossing metric only views the perpendicular angle as beneficial without considering the direction of velocity vectors. The angle between the velocities by two fixed vortices is almost 90° just above/below each vortex centre; for example, above the left vortex centre, the velocity by the left vortex is horizontal while one by the right vortex is almost vertical. This should be beneficial for the pure blinking model, but the angle would be divided into smaller angles with the continuous transition, meaning continuous transition has a negative effect on mixing around the vortex centres. On the other hand, the direction of the velocities between the vortex centres is almost opposite just over/below the x-axis. By dividing this angle, it can be reduced to close to 90° when only one single point of the transition is considered. Although the continuous transition would not cause the angle to be divided into approximately two right angles, it still gives a positive influence, meaning continuous transition has a positive effect on mixing between the vortex centres. Between the vortex centres, however, the velocity vectors by the left/right vortices and transition are aligned vertically on the x-axis and around the domain centre, meaning a roughly neutral effect around the domain centre. Thus, the value of streamline crossing is always small regardless of the continuous transition. When the fixed vortices are adjacent, the effect between the centres is negligible and therefore the negative effect of continuous transition dominates the calculation, thus decreasing $\bar{\alpha}$ for small vortex spacing, while both positive and negative effects combined effects are detected for a larger vortex spacing. As the region between the fixed vortices is larger, the positive effects spread first until the expansion is prohibited by the domain centre, and the value starts to decrease by the negative effects around the vortex centres (see Figure 11a–c).

Table 1. Comparisons between Lagrangian and Eulerian results for fixed total time. The agreements are assessed as Poor (P; yellow, overall trend disagreed), Medium (M; green, overall trend agreed), and Good (G; blue, overall trend and the shape of graph agreed). The indicators in parentheses represent the corresponding results for the case of fixed iterations, where this is different to the trend for fixed total time.

				μ		
		0.05	**0.125**	**0.25**	**0.5**	**1.0**
				Streamline crossing		
	0.1	G(M)	M(G)	M	G(M)	G
	0.3	P	P	M(P)	M	G
ν	0.5	P	P	P	P	M
	0.7	P	P	P	P	P
	0.9	P	P	P	P	P
				Relative rate of velocity change		
	0.1	P	P	P	P	P
	0.3	M(P)	P	P	P	P
ν	0.5	M	M	M	P	P
	0.7	G	G(M)	M	M	P
	0.9	G	M(G)	M(G)	M(G)	M
				Mobility		
	0.1	G(M)	M(G)	M	M	M
	0.3	P	P	M(P)	M	G
ν	0.5	G	G	G	P	P
	0.7	G	G(M)	M	M	P
	0.9	M(G)	M(G)	M	M(G)	M
				Product of streamline crossing and mobility		
	0.1	G(M)	M(G)	M	**G(M)↑**	**G↑**
	0.3	P	P	M(P)	M	G
ν	0.5	**P↓**	**P↓**	**P↓**	**M↑**	**M↑**
	0.7	G	G(M)	M	M	P
	0.9	M(G)	M(G)	M	M(G)	M

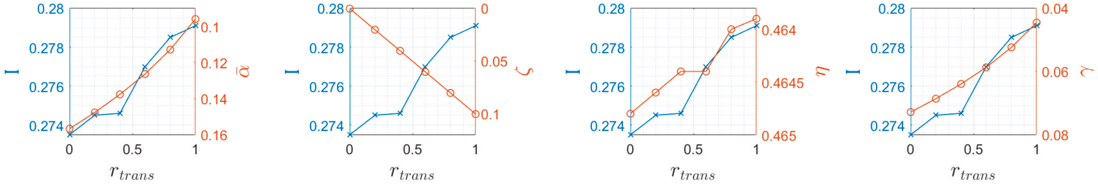

(**a**) $\nu = 0.1$

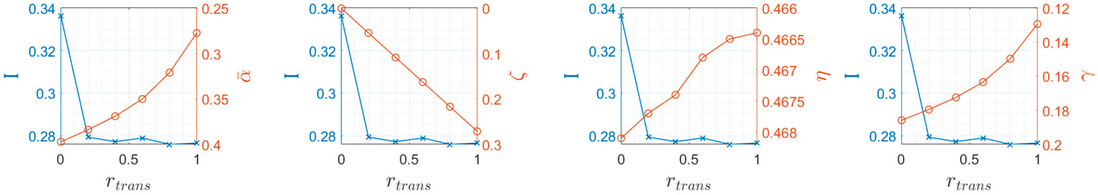

(**b**) $\nu = 0.3$

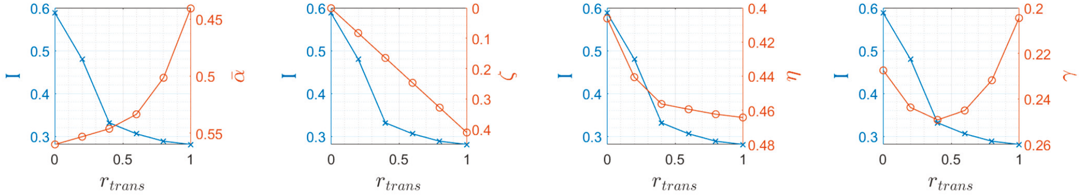

(**c**) $\nu = 0.5$

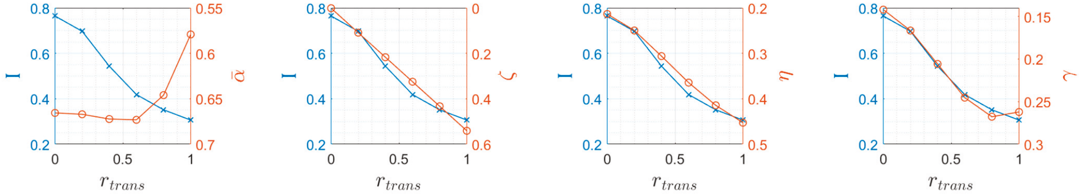

(**d**) $\nu = 0.7$

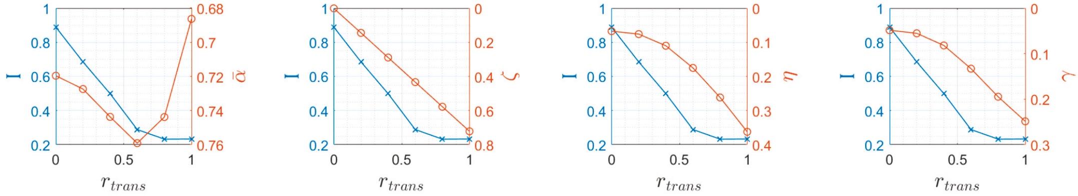

(**e**) $\nu = 0.9$

Figure 9. Comparison between I (blue lines) and c-EIs (orange lines) with μ of 0.05. From the left, the indicators are streamline crossing, the relative rate of velocity change, mobility, and the product of streamline crossing and mobility. The intensity of segregation was calculated with the identical total time, equal to 10.

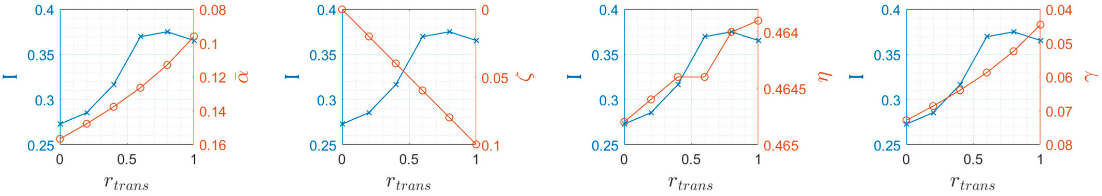

(**a**) $\nu = 0.1$

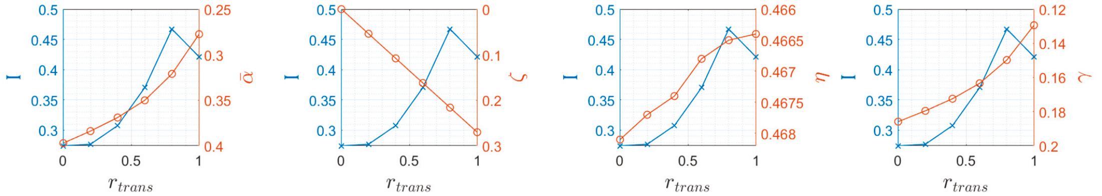

(**b**) $\nu = 0.3$

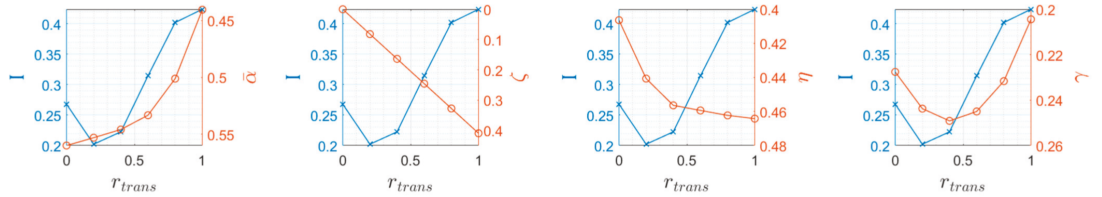

(**c**) $\nu = 0.5$

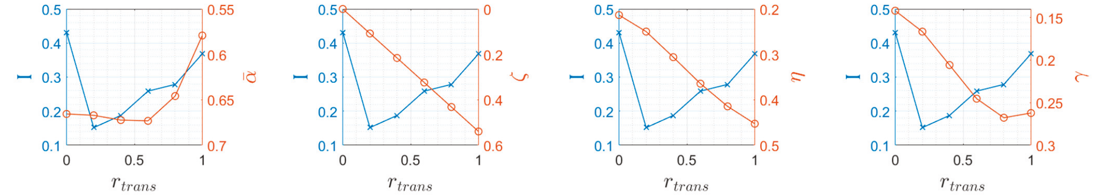

(**d**) $\nu = 0.7$

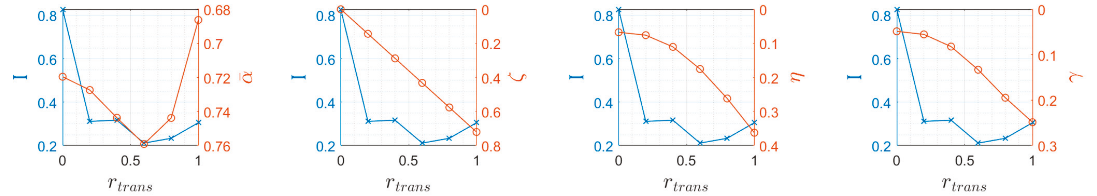

(**e**) $\nu = 0.9$

Figure 10. Comparison between I (blue lines) and c-EIs (orange lines) for $\mu = 1.0$. From the left, the indicators are streamline crossing, the relative rate of velocity change, mobility, and the product of streamline crossing and mobility. The intensity of segregation was calculated with the identical total time, equal to 10.

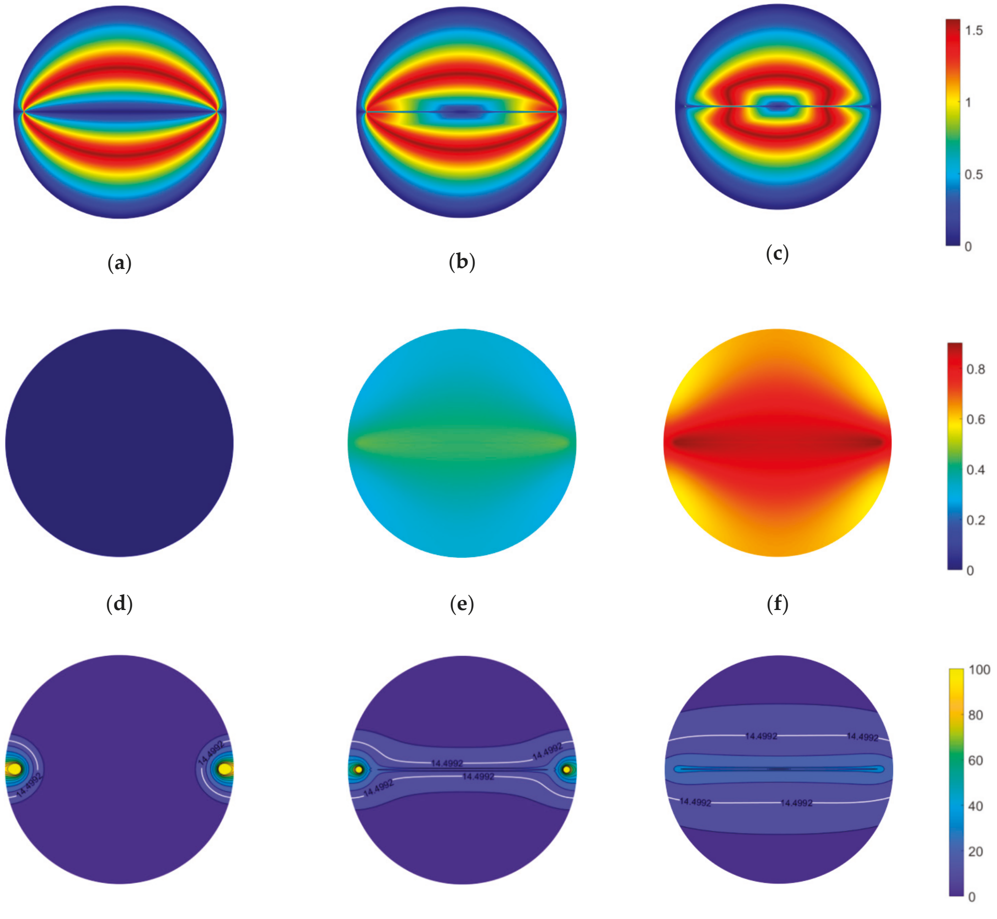

(**a**) (**b**) (**c**)

(**d**) (**e**) (**f**)

(**g**) (**h**) (**i**)

Figure 11. Time-averaged EI values over the domain for (**a**–**c**) streamline crossing and (**d**–**f**) relative rate of velocity change and (**g**–**i**) the contour of v_{sum} with μ of 1.0 and ν of 0.9. From the left, each column represents $r_{trans} = 0.0$, 0.5, and 1.0. The white line in the last row denotes v_{thresh}, equal to 14.4992. Note, the colour bar range for mobility is fixed at 0 to 100 in order to highlight the region where v_{sum} is greater than v_{thresh}.

As seen in Figures 9 and 10, the value of the relative rate of velocity change linearly increases regardless of the system parameters. Given that the velocity field has a singularity at the vortex centre, the velocity magnitude near to the centre is extremely large, and therefore the higher values of r_{trans} would result in the larger calculated values of this EI (see Figure 11d–f). As for the mobility, from Figure 11d–f and Equations (20)–(22), $\widetilde{w}$ is high around/between the vortex centres, so ν_{fast} dominates the calculation of ν_{sum} and velocity cancellation is important. For the pure blinking model, the directions of the velocity vectors by the fixed vortices are (nearly) opposite, and the differences in velocity magnitude are trivial unless the velocities are very close to the vortex centres. However, in the region around the centres where the velocities are aligned, it is not meaningful to distinguish ν_{fast} and ν_{slow} , and only the magnitude contributes to the EI. As the former effect of the continuous transition is positive and the latter would be negative, the resultant effect would be beneficial for large vortex spacing but not for the small spacing. Although a value of ν_{sum} at each point can be reduced with the continuous transition, η is computed based on the size of the region where ν_{sum} is faster than ν_{thresh} (indicated by the white contour in Figure 11g–i). Therefore, η decreases and increases for the small and large vortex spacing, respectively. Unlike for streamline crossing, the combined effect of $\overline{\alpha}$ for large ν was not observed, as the mobility is only contingent on the region having ν_{sum} bigger than ν_{thresh}. Consequently, it could be concluded that the trend of mixing performance with small and large ν would be more likely to be predicted by the first and second c-EI, respectiely, while the mobility is expected to predict both cases.

Although such graph trends are inferred by rough explanations, and the graph shape can be somewhat different, especially for I, the expectation is, notwithstanding, quite precise in Table 1. It is observed that the mixing prediction is strong at small ν for the streamline crossing while the relative rate of velocity change shows good prediction at large ν. As for the mobility, the prediction is quite well achieved overall, but is Poor in a few cases. This could be because the inversion of the trend from small to large ν is inaccurately predicted, such as is shown in the third plots in Figures 9b and 10c. Another explanation might be that the prediction of mobility appears monotonically, so that the detailed properties of the mixing behaviour are not captured well, as seen in Figure 10d.

The product of the steamline crossing and mobility was expected to provide a better prediction than the previous two c-EIs, based on the conclusions of McIlhany and Wiggins [20], which was however found to not always be the case in this study. In Table 1, the evaluations for the product of these two quantities in bold type indicates a difference from the mobility, and the up/down arrows denote an improved/worsened prediction by the product, respectively. The improvements in prediction seem to be randomly distributed, with no clear pattern, and in some case reducing the correlation between the c-EI and mixing. Overall, mobility appears to be a better predictor of mixing performance with more Good correlations and fewer Poor.

3.3. Computational Efficiency

The high computational cost of Lagrangian mixing analysis has motivated the creation of EIs. Though they are less accurate and do not provide absolute quantification of the mixing performance, their substantially lower computational cost is attractive. For particle tracking, the run-time is dependent on the number of iterations, system period, and for this study, it was also affected by the ratio of the continuous transition, as particle tracking for the fixed vortex position was computed using Aref's mapping, which has a fixed computational cost.

The total run-time for the Lagrangian approaches ranged between 5668 s and 110,234 s while it was between 1.14 s and 686 s for the c-EIs. Although the c-EIs require a longer run-time than the d-EIs (which had an averaged run time of just 0.2034 s), c-EIs can give a more precise prediction of mixing, for both discontinuous and continuous states, than the d-EIs, for a total run time still much shorter than Lagrangian-based methods.

4. Discussion

4.1. Findings and Implications

Previous research [1,19] into the blinking vortex model highlighted that vortices placed closed together and run for a long period, led to good mixing performance, which was confirmed here for cases without continuous transition. Introducing a continuous transition phase did not improve mixing for small vortex spacing, however when mixing was poor, such as for large vortex spacing, the transition regime enhanced the interaction of these vortices and improved the mixing. Similarly, in some cases the continuous transition also improved mixing performance in systems with a shorter time period.

Such findings imply that, as in [10], a complete discontinuity is not strictly necessary for good mixing in systems based on a streamline crossing principles. This is useful for engineering applications, particularly for continuous flow pipe-based systems, where a strict discontinuity may be impossible to achieve.

Discontinuous EIs were no longer accurate once more than a small amount of continuous transition was introduced to the system. The continuous EIs, mobility and the product of the streamline crossing and mobility, in general showed good agreement with the actual mixing performance. Although it was not explicitly stated whether the latter showed a better performance than the former did in [20], it did not for this study. The prediction of mixing by this product was improved in some cases and worsened in others. In contrast to the monotonic prediction of the c-EIs, the variations of I were not as simple, due to a range of physical effects, as discussed in Section 3.1.1, which the c-EIs appear unable to capture.

4.2. Limitations and Future Work

The blinking vortex model is somewhat unrealistic in that it is inviscid and contains singularities at the vortex centres. The point vortices could be renormalised to remove these singularities, though it is expected that the overall phenomena would be preserved. A more significant limitation is that there is only a single region of closed streamlines. A more complicated flow, such as one containing at least one separatrix should be tested to see if the key findings still apply.

The system parameters and the transition motion were kept simple here. However, there are many system parameters that could be varied, for example, asymmetric vortex positioning, more than two vortices, order of vortex activation, and nonlinear trajectories of the point vortices. Appropriate manipulation of the latter variable might help to reduce the size of islands of regular flow, particularly for large vortex spacing.

The c-EIs showed good performance for predicting overall mixing behaviour in the presence of the moving vortex. However, given that the assessment conducted in Table 1 was quite generous and the c-EIs were less likely to capture finer details of the mixing, it seems that further improvements are required to Eulerian indicators so that they can capture all of the flow features that contribute to mixing.

5. Conclusions

The results showed that up to 30% transition time between discrete states was either neutral or beneficial for the mixing performance, with the biggest benefit observed for cases where the mixing from the blinking protocol was poor, e.g., due to large vortex spacing. The biggest improvement in mixing, observed for r_{trans} of 0.2, was an increase of 62.4% when $\mu = 1.0$ and $\nu = 0.9$, while the worsened performance for $\nu = 0.1$ was less than 5%. This effect was generally consistent across the different blinking periods although very short blinking periods did not follow the same trend. Finally, for this system, mobility was the EI that most accurately characterised the mixing performance. However, there were still some parameter cases where its agreement with actual mixing performance was poor, with the EIs unable to capture the benefits of this small amount of transition, suggesting that improved EIs may be needed. Overall, these results suggest that mixing systems, such as continuous pipe flow-based devices, which are designed assuming a discontinuous change in velocity, might actually benefit from the presence of a small degree of continuous transition between discrete states.

Supplementary Materials: The following are available online at https://www.mdpi.com/2311-5521/6/1/10/s1, MATLAB code for performing particle tracking, generating Poincaré sections, and computing Eulerian indicators.

Author Contributions: Conceptualisation, H.R. and A.N.C.; methodology, H.R. and A.N.C.; software, H.R.; validation, H.R.; formal analysis, H.R. and A.N.C.; investigation, H.R.; writing—original draft preparation, H.R. and A.N.C.; writing—review and editing, H.R. and A.N.C.; visualisation, H.R.; supervision, A.N.C. All authors have read and agreed to the published version of the manuscript.

Funding: This research received no external funding.

Institutional Review Board Statement: Not applicable.

Informed Consent Statement: Not applicable.

Data Availability Statement: Code used to generate the data in this paper is available for download in the supplementary materials. Specific instances of this data are available on request from the corresponding author.

Conflicts of Interest: The authors declare no conflict of interest.

References

1. Aref, H. Stirring by chaotic advection. *J. Fluid Mech.* **1984**, *143*, 1–21. [CrossRef]
2. Khakhar, D.V.; Franjione, J.G.; Ottino, J.M. A case study of chaotic mixing in deterministic flows: The partitioned-pipe mixer. *Chem. Eng. Sci.* **1987**, *42*, 2909–2926. [CrossRef]
3. Ling, F.H. Chaotic mixing in a spatially periodic continuous mixer. *Phys. Fluids Fluid Dyn.* **1993**, *5*, 2147–2160. [CrossRef]
4. Mizuno, Y.; Funakoshi, M. Chaotic mixing caused by an axially periodic steady flow in a partitioned-pipe mixer. *Fluid Dyn. Res.* **2004**, *35*, 205. [CrossRef]
5. Jung, H.I.; Jung, S.Y.; Kang, T.G.; Ahn, K.H. Numerical study on the mixing in a barrier-embedded partitioned pipe mixer (BPPM) for non-creeping flow conditions. *Korea-Aust. Rheol. J.* **2018**, *30*, 227–238. [CrossRef]
6. Jones, S.W.; Thomas, O.M.; Aref, H. Chaotic advection by laminar flow in a twisted pipe. *J. Fluid Mech.* **1989**, *209*, 335–357. [CrossRef]
7. Jen, C.-P.; Wu, C.-Y.; Lin, Y.-C.; Wu, C.-Y. Design and simulation of the micromixer with chaotic advection in twisted microchannels. *Lab. Chip* **2003**, *3*, 77–81. [CrossRef]
8. Schönfeld, F.; Hardt, S. Simulation of helical flows in microchannels. *AIChE J.* **2004**, *50*, 771–778. [CrossRef]
9. Jiang, F.; Drese, K.S.; Hardt, S.; Küpper, M.; Schönfeld, F. Helical flows and chaotic mixing in curved micro channels. *AIChE J.* **2004**, *50*, 2297–2305. [CrossRef]
10. Cookson, A.N.; Doorly, D.J.; Sherwin, S.J. Efficiently Generating Mixing by Combining Differing Small Amplitude Helical Geometries. *Fluids* **2019**, *4*, 59. [CrossRef]
11. Ottino, J.M. *The Kinematics of Mixing: Stretching, Chaos, and Transport*; Cambridge University Press: Cambridge, UK, 1989; ISBN 0-521-36335-7.
12. Cookson, A.N.; Doorly, D.J.; Sherwin, S.J. Mixing Through Stirring of Steady Flow in Small Amplitude Helical Tubes. *Ann. Biomed. Eng.* **2009**, *37*, 710–721. [CrossRef] [PubMed]
13. Chien, W.-L.; Rising, H.; Ottino, J.M. Laminar mixing and chaotic mixing in several cavity flows. *J. Fluid Mech.* **1986**, *170*, 355–377. [CrossRef]
14. Stroock, A.D.; Dertinger, S.K.W.; Ajdari, A.; Mezic, I.; Stone, H.A.; Whitesides, G.M. Chaotic Mixer for Microchannels. *Science* **2002**, *295*, 647–651. [CrossRef] [PubMed]
15. Kim, D.S.; Lee, S.W.; Kwon, T.H.; Lee, S.S. A barrier embedded chaotic micromixer. *J. Micromech. Microeng.* **2004**, *14*, 798. [CrossRef]
16. McIlhany, K.L.; Wiggins, S. Optimizing mixing in channel flows: Kinematic aspects associated with secondary flows in the cross-section. *Microfluid. Nanofluidics* **2011**, *10*, 249–262. [CrossRef]
17. Hossain, S.; Lee, I.; Kim, S.M.; Kim, K.-Y. A micromixer with two-layer serpentine crossing channels having excellent mixing performance at low Reynolds numbers. *Chem. Eng. J.* **2017**, *327*, 268–277. [CrossRef]
18. Sturman, R.; Ottino, J.M.; Wiggins, S. *The Mathematical Foundations of Mixing: The Linked Twist Map as a Paradigm in Applications: Micro to Macro, Fluids to Solids*; Cambridge University Press: Cambridge, UK, 2006; ISBN 978-0-521-86813-6.
19. Sturman, R.; Wiggins, S. Eulerian indicators for predicting and optimizing mixing quality. *New J. Phys.* **2009**, *11*, 075031. [CrossRef]
20. McIlhany, K.L.; Wiggins, S. Eulerian indicators under continuously varying conditions. *Phys. Fluids* **2012**, *24*, 073601. [CrossRef]
21. McIlhany, K.L.; Guth, S.; Wiggins, S. Lagrangian and Eulerian analysis of transport and mixing in the three dimensional, time dependent Hill's spherical vortex. *Phys. Fluids* **2015**, *27*, 063603. [CrossRef]
22. McIlhany, K.L.; Mott, D.; Oran, E.; Wiggins, S. Optimizing mixing in lid-driven flow designs through predictions from Eulerian indicators. *Phys. Fluids* **2011**, *23*, 082005. [CrossRef]
23. Reza, M.M.S.; Arzani, A. A critical comparison of different residence time measures in aneurysms. *J. Biomech.* **2019**, *88*, 122–129. [CrossRef] [PubMed]

fluids

Article

Modeling Heavy-Gas Dispersion in Air with Two-Layer Shallow Water Equations

Alexandre Chiapolino [1,*], Sébastien Courtiaud [2], Emmanuel Lapébie [2] and Richard Saurel [1,3]

[1] Scientific Research and Numerical Simulation (RS2N), 371 Chemin de Gaumin, 83640 Saint-Zacharie, France; richard.saurel@univ-amu.fr
[2] Commissariat à l'Énergie Atomique et aux Energies Alternatives, Direction des Applications Militaires (CEA-DAM), CEA-Gramat, 46500 Gramat, France; sebastien.courtiaud@cea.fr (S.C.); emmanuel.lapebie@cea.fr (E.L.)
[3] Laboratory of Mechanics and Acoustics (LMA), Centrale Marseille, French National Centre for Scientific Research (CNRS), Aix-Marseille Univ, 4 Impasse Nikola Tesla, 13013 Marseille, France
* Correspondence: alexandre.chiapolino@rs2n.eu

Abstract: Computation of gas dispersal in urban places or hilly grounds requires a large amount of computer time when addressed with conventional multidimensional models. Those are usually based on two-phase flow or Navier-Stokes equations. Different classes of simplified models exist. Among them, two-layer shallow water models are interesting to address large-scale dispersion. Indeed, compared to conventional multidimensional approaches, 2D simulations are carried out to mimic 3D effects. The computational gain in CPU time is consequently expected to be tremendous. However, such models involve at least three fundamental difficulties. The first one is related to the lack of hyperbolicity of most existing formulations, yielding serious consequences regarding wave propagation. The second is related to the non-conservative terms in the momentum equations. Those terms account for interactions between fluid layers. Recently, these two difficulties have been addressed in Chiapolino and Saurel (2018) and an unconditional hyperbolic model has been proposed along with a Harten-Lax-van Leer (HLL) type Riemann solver dealing with the non-conservative terms. In the same reference, numerical experiments showed robustness and accuracy of the formulation. In the present paper, a third difficulty is addressed. It consists of the determination of appropriate drag effect formulation. Such effects also account for interactions between fluid layers and become of particular importance when dealing with heavy-gas dispersion. With this aim, the model is compared to laboratory experiments in the context of heavy gas dispersal in quiescent air. It is shown that the model accurately reproduces experimental results thanks to an appropriate drag force correlation. This function expresses drag effects between the heavy and light gas layers. It is determined thanks to various experimental configurations of dam-break test problems.

Keywords: two-layer; shallow water; hyperbolic systems; drag effects; gas dispersal; experiments

Citation: Chiapolino, A.; Courtiaud, S.; Lapébie, E.; Saurel, R. Modeling Heavy-Gas Dispersion in Air with Two-Layer Shallow Water Equations. *Fluids* **2021**, *6*, 2. https://dx.doi.org/10.3390/fluids6010002

Received: 6 November 2020
Accepted: 18 December 2020
Published: 22 December 2020

1. Introduction

1.1. Heavy-Gas Dispersal

Gas dispersal may occur in many urban places, industrial plants and natural environments. Knowledge of the flow field is important in such contexts because dispersal may carry pollutants or hazardous chemical species. For instance, certain industrial processes involve storing hazardous liquefied gases, which may be released accidentally. The release of these heavier-than-air gases is of serious interest regarding risk assessment.

From a numerical point of view, one of the difficulties is to address long-time and large-scale computations, for instance, at the scale of a city, while providing accurate results with reasonable CPU time. Multiple classes of dense-gas dispersion models are available in the literature, such as integral or box models [1,2], intermediate (SLAB-type) models [3], shallow water models [4], and multidimensional computational fluid dynamics (CFD) models [5]. Relevant literature on this subject can be found in the PhD thesis of Hankin, 1997 [4].

Integral or box models typically regard an instantaneously released cloud of dense gas as a uniform cylinder. Those are the simplest form of heavy-gas dispersion models. However, they do not have flexibility to characterize a cloud influenced by a complex terrain. They are limited by the assumption that the cloud remains as a uniform cylinder or ellipse. Such an assumption is obviously inappropriate if the cloud is channeled by topographical features into low-lying areas for example.

Multidimensional computations based on two-phase flow or Navier–Stokes equations are obviously much more complex and are capable of accounting for a complex terrain. However, their numerical resolution demands a large amount of computer time. Illustrative 3D results are provided in Hank et al. (2012, 2014) [5,6], for example.

Between the simplicity of integral or box models and the complexity of multidimensional CFD models, intermediate approaches have been proposed. Examples are SLAB-type models, where a Lagrangian description is used to track gas bubbles of a plume. Another approach is based on shallow water models [4].

Results obtained with the commonly used SLAB-type models are provided in Hanna et al., 2008 [7], for instance. Although such models admit more complex cloud geometries than integral models, they also suffer from similar drawbacks as they are inappropriate for describing a cloud influenced by complex topographies [4].

The shallow water approach has a number of advantages over other simplified models as thoroughly argued in Hankin, 1997 [4]. The main advantage of such approach is that it is able to account for complex topographies such as buildings, valleys and mountain ranges.

As only the height and speed of the dense gas layer are of interest, a single-layer shallow water model is attractive. Nevertheless, in the present heavy-gas dispersion context, the single-layer shallow water approach is inaccurate as shown in the numerical experiments of Chiapolino and Saurel, 2018 [8]. The lack of accuracy is due to the low-density ratio between the two gases. Interactions between the ambient gas and the dense gas layer are indeed important and are to be accounted for [4,8].

In this direction, the present paper presents a novel approach. The dispersal of the heavy gas in air is treated with the recent hyperbolic two-layer shallow water model of Chiapolino and Saurel, 2018 [8]. Interactions between the two gases are considered through the non-conservative terms of the momentum equations and through drag effects, occurring at the interface between the dense gas and the ambient air.

Turbulence effects are considered at the interface through the corresponding interfacial area. However, determination of proper interfacial aera is a hard task. In the present contribution, it is adjusted to address heavy gas dispersion into a quiescent atmosphere and on a flat ground. This step is indeed necessary to validate the hyperbolic two-layer shallow water model in its simple form, i.e., considering only wave propagation and drag effects.

More complex and realistic situations will be part of future investigations, such as the introduction of multidimensional and topography effects as well as turbulence. Relevant literature on the last subject is, for instance, the works of Teshukov, 2007 [9] and Richard and Gavrilyuk, 2012 [10] where a model for turbulent shear shallow water flows is derived. In this latter contribution, the rapidly varied flows studied by the authors are characterized by the presence of a turbulent structure called roller in which the turbulent energy dissipation plays a major part. This work has been continued by the same authors in [11–14], to cite a few.

However, the aforementioned references address turbulent structures with a one-layer shallow water type model. Adaptation to two-layer equations is out of the scope of the present paper but shall also be considered in future investigations.

The present approach based on two-layer shallow water equations is very different from usual atmospheric models that are unsuitable for describing a cloud of dense gas influenced by urban structures or hilly grounds. Topography effects are omitted in the present contribution for the sake of simplicity but shall be addressed in future works as well. Indeed, even in the absence of topography effects or agitated atmospheric conditions, two-layer models need modelling and validation efforts, as detailed a bit further.

It is therefore important to address first heavy-gas dispersion on a flat ground and in a quiescent atmosphere. Such task is addressed in the present paper. It is shown that the two-layer approach has nice predicting abilities. A background of two-layer shallow water models is presented hereafter.

1.2. Two-Layer Shallow Water Approach

The two-layer shallow water strategy is indeed an interesting candidate as it allows addressing 2D simulations to mimic 3D flows. The computational gain in CPU time is thereby expected to be tremendous compared to conventional multi-fluid approaches, see for example Saurel and Pantano, 2018 [15] for a review of diffuse interface capturing methods. In Chiapolino and Saurel, 2018 [8], CPU time saving factor of the order of million is reported thanks to a two-layer shallow water approach.

Two-layer (and multi-layer) shallow water models are particularly useful in some limit cases of multi-fluid and variable density flows separated by nearly horizontal interfaces. These models govern the dynamics of incompressible fluids spreading under gravity effects. It can be, for example:

- Flows of the same liquid but at different temperatures, resulting in density differences, such situations being typical of oceanic flows.
- Flows of two liquids of different densities.
- Flows of two gases evolving at low Mach number.

In this contribution, this last situation is of particular interest. As mentioned earlier, heavy-gas dispersal in urban places or hilly grounds motivates the present work.

The two-layer approach is also helpful when the height of one of the phases is arbitrarily small as there is no need to spatially resolve it. Thereby, no numerical diffusion of the nearly horizontal interface is present, and no interface tracking is needed. Such models can deal with topography effects or obstacles (not treated in the present paper). However, there are obviously some limitations with this approach:

- The vertical velocity component is neglected.
- The velocity is assumed uniform in cross sections of each layer.

Such types of modeling also involve serious difficulties. Indeed, most models are not hyperbolic, this issue having serious consequences both for wave propagation, which becomes ill-posed, and for the design of numerical methods. A second serious difficulty appears as non-conservative terms are present in the momentum equations. Recently, those difficulties have been addressed in Chiapolino and Saurel, 2018 [8] and solutions have been proposed. A third difficulty appears in the modeling of drag effects between fluid layers. This issue is addressed in the present contribution with the help of dedicated laboratory dam-break experiments.

In the frame of averaged (or homogenized) equations in fluid mechanics, the issue related to the lack of hyperbolicity appears in different types of models, such as those of non-equilibrium two-phase flows. Only a few models seem well-posed with this respect (Marble, 1963 [16], Baer and Nunziato, 1986 [17], Saurel et al., 2017 [18]). There are mainly two types of remedy to cure this issue:

- Consider compressibility of the phases and deal with pressure relaxation (Lallemand and Saurel, 2000 [19]). This approach involves sound propagation in the phases and is particularly efficient in many situations. It has been adopted in [17,18].
- Consider turbulent effects in the phases, as they result in the appearance of a "turbulent sound speed" (Forestier et al., 1997 [20], Saurel et al., 2003 [21], Lhuillier et al., 2013 [22]). In the frame of shallow water flows, these effects have been studied in Richard and Gavrilyuk, 2012 [10] and Gavrilyuk et al., 2016 [14].

In the present work, the first method is adopted, and the fluids are considered weakly compressible. The resulting model is unconditionally hyperbolic and in the limit of stiff pressure relaxation, the conventional (non-hyperbolic) two-layer model is recovered. This approach is reminiscent of the model of Abgrall and Karni, 2009 [23] except that extra pressure terms are present in the momentum equations of the new formulation. It also gives another interpretation of the relaxation approach, now based on compressibility and pressure effects.

The second issue, related to the presence of non-conservative terms in the momentum equations, has also been addressed in [8]. By examining the Riemann problem structure, it appears that local constants are present, at locations where the derivative of the Heaviside function emerges. Consequently, the non-conservative products become well-defined and a locally conservative form is obtained and used in the frame of a Harten-Lax-van Leer (HLL) type Riemann solver.

The accuracy and robustness of the new HLL-type solver has been checked against results of Abgrall and Karni, 2009 [23] as well as results obtained with a flow solver based on the VFRoe method of Gallouet and Masella, 1996 [24] as it is able to deal, to some extent, with both conservative and non-conservative systems.

The theoretical formulation of Chiapolino and Saurel, 2018 [8] and its associated HLL-type solver make consequently an interesting strategy to address large-scale gas dispersal. The 1D two-layer model has been confronted in [8] to 2D diffuse interface computations [15,25–27] and showed good agreement. However, a parameter related to the drag force was needed to match 1D and 2D averaged results in the vertical direction. In the present paper, the model is confronted to laboratory experiments, specifically designed for this aim. A drag function is proposed, with three parameters determined explicitly, enabling accurate matching of computed 1D results and experiments, in a broad range of initial conditions of two-layer dam-break test problems.

This paper is organized as follows. The two-layer model with its hyperbolic formulation is presented in Section 2. Pressure and velocity relaxation (drag effects) are introduced as well. The numerical treatment is summarized in Section 3. The experimental facility used for dam-break-type tests is presented in Section 4. Comparisons between 1D computed results and laboratory experiments are presented in Section 5, enabling building of an appropriate drag function between heavy and light fluid layers. It is shown that the hyperbolic model accurately reproduces experimental results at the price of few parameters related to the drag function. Conclusions are given in Section 6.

2. Hyperbolic Two-Layer Shallow Water Model

The model of Chiapolino and Saurel, 2018 [8] reads:

$$\left\{\begin{array}{l}
\frac{\partial h_1}{\partial t}+u_1\frac{\partial h_1}{\partial x}=\mu\frac{\left(p_1-p_0-\rho_2 g h_2\right)}{\rho_1 c_1^2},\ \mu\to+\infty,\\
\frac{\partial\left(h_1\rho_1\right)}{\partial t}+\frac{\partial\left(h_1\rho_1 u_1\right)}{\partial x}=0,\\
\frac{\partial\left(h_1\rho_1 u_1\right)}{\partial t}+\frac{\partial\left(h_1\rho_1 u_1^2+h_1 p_1\left(\rho_1,\rho_2,h_2\right)+\frac{1}{2}\rho_1 g h_1^2\right)}{\partial x}=\rho_2 g h_2\frac{\partial h_1}{\partial x}+p_0\frac{\partial h_1}{\partial x},\\
\frac{\partial h_2}{\partial t}+u_2\frac{\partial h_2}{\partial x}=\mu\frac{\left(p_2-p_0\right)}{\rho_2 c_2^2},\\
\frac{\partial\left(h_2\rho_2\right)}{\partial t}+\frac{\partial\left(h_2\rho_2 u_2\right)}{\partial x}=0,\\
\frac{\partial\left(h_2\rho_2 u_2\right)}{\partial t}+\frac{\partial\left(h_2\rho_2 u_2^2+h_2 p_2\left(\rho_2\right)+\frac{1}{2}\rho_2 g h_2^2\right)}{\partial x}=-\rho_2 g h_2\frac{\partial h_1}{\partial x}+p_0\frac{\partial h_2}{\partial x}.
\end{array}\right. \tag{1}$$

In the present paper, index 1 denotes the heaviest fluid (lower layer) and index 2 the lightest one (upper layer). The notations are conventional, h_1 and h_2 denote the heights of the two layers, ρ_1 and ρ_2 represent the densities of the fluids, u_1 and u_2 denote the fluid velocities, averaged in each layer and g represents the gravity constant. p_1 and p_2 denote the thermodynamic pressure of the fluids, given by barotropic (and convex) equations of state. An example of such an equation of state (EOS) is:

$$\begin{cases} p_1 = p_0 + \rho_2 g h_2 + c_1^2\left(\rho_1 - \rho_1^{(0)}\right), \\ p_2 = p_0 + c_2^2\left(\rho_2 - \rho_2^{(0)}\right). \end{cases} \tag{2}$$

Other options, such as Tait EOS are possible. As shown in [8], the choice of the EOS is not important, only the related fluid sound speeds c_1 and c_2 have importance. p_0 denotes the (constant) atmospheric pressure. Hydrostatic effects are then considered through the EOS of the first fluid, i.e., the heaviest layer.

Topography effects have been omitted for the sake of simplicity as well as friction with the bottom and between layers. As shown in [8], System (1) recovers the conventional but conditionally hyperbolic model of Ovsyannikov, 1979 [28] in the stiff pressure relaxation limit ($\mu \to +\infty$). Such conventional model has been examined in Abgrall and Karni, 2009 [23], Kurganov and Petrova, 2009 [29] and Monjarret, 2015 [30] and appeared hyperbolic for low velocity drift only:

$$(u_1 - u_2)^2 < (h_1 - h_2) g \left(1 - \frac{\rho_2}{\rho_1}\right).$$

In the present approach, pressure non-equilibrium effects result in an unconditionally hyperbolic formulation. Such hyperbolic system has been developed in Abgrall and Karni, 2009 [23] and an extended version in Chiapolino and Saurel, 2018 [8].

Compared to the conventional two-layer shallow water model (Ovsyannikov, 1979 [28]), two equations have been added and express the transport of the heights of the fluid layers that are assumed to vary as a function of pressure differentials.

The pressure relaxation parameter μ is related to the sound speeds and heights of fluid layers. It controls the rate at which pressure equilibrium is reached. In most situations, the relaxation time τ is of the order of $1/100$ s meaning that the relaxation parameter μ is large: $\mu \simeq \max\left(\tau_1^{-1}, \tau_2^{-1}\right)$ or alternatively $\mu \simeq \min(c_1, c_2)$. Details are provided in Chiapolino and Saurel, 2018 [8].

In practical computations, the relaxation time τ will be assumed of the same order as the computational time step and stiff pressure relaxation will be done at the end of each time step. Therefore, there is no need for a precise knowledge of the pressure relaxation parameter μ.

System (1) is hyperbolic with wave speeds u_k, $u_k + \sqrt{c_k^2 + \frac{1}{2} g h_k}$, $u_k - \sqrt{c_k^2 + \frac{1}{2} g h_k}$. This model is however relevant with respect to the physics expressed in the conventional but non-hyperbolic system of Ovsyannikov, 1979 [28], as it tends to the same equations when pressure relaxation is stiff, see [8] for details.

Consequently, as System (1) is hyperbolic, it is a good candidate to numerically approximate the conventional model with a two-step procedure:

- Resolution of the hyperbolic step, i.e., the resolution of System (1) in the absence of source terms. An HLL-type Riemann solver has been developed in Chiapolino and Saurel, 2018 [8] and is summarized in the following.
- Stiff pressure relaxation towards the hydrostatic and atmospheric pressures and reset of the heights. This step makes the solution tend to the one of the conventional models [28].

In the present context, pressure relaxation is particularly simple. It just consists of resetting the heights of the layers $h_k \to h_k^*$ and is independent of the equation of state [8]. For the lightest fluid, thanks to mass conservation, the relaxed state reads:

$$h_2^* = \frac{h_2 \rho_2}{\rho_2^{(0)}}. \tag{3}$$

For the heaviest fluid, mass conservation and hydrostatic effects result in the relaxed state:

$$h_1^* = \frac{h_1\rho_1}{\rho_1^{(0)} + \frac{\rho_2^* g h_2^*}{c_1^2}}. \tag{4}$$

In these relations, $\rho_k^{(0)}$ denotes the constant density of fluid k at atmospheric pressure and superscript * denotes the relaxed solution state.

The hyperbolic two-layer shallow water model is able to recover the solution of the conventional but non-hyperbolic two-layer system. Besides, the single-layer Saint-Venant solution is recovered as well when the flow conditions are appropriate. Such situation happens either when the height of the heaviest layer is insignificant $h_1 \to 0$ or when the effects of the surrounding fluid are negligible. This behavior appears when the density ratio between the lightest fluid and the heaviest one is very small: $r = \frac{\rho_2}{\rho_1} \ll 1$. Examples are provided in Chiapolino and Saurel, 2018 [8]. In the same reference, the importance of the two-layer model when the density ratio $r = \rho_2/\rho_1$ is arbitrary, is illustrated. Indeed, the two-layer system can deal with interactions between fluids unlike the conventional one-fluid Saint-Venant model.

Consequently, the one-layer model yields inaccurate results when the order of magnitude of the density ratio $r = \rho_2/\rho_1$ is about $[0.2 - 0.5]$, see [8] for illustrative results and further discussions. In the present paper, such situation is of particular interest as the flow involves only gases.

The two-layer model is then necessary. The present model has been confronted in [8] to 2D diffuse interface computations [15,25–27] and showed good agreement after the introduction of drag effects. Pressure (or "acoustic") drag is considered only and is modeled through velocity relaxation terms that appear in the right-hand side of the momentum equations. For non-viscous fluids, the "acoustic" drag force can be written as:

$$F = \frac{Z_1 Z_2}{Z_1 + Z_2} A_I (u_2 - u_1). \tag{5}$$

$Z_k = \rho_k c_k$ denotes the acoustic impedance of fluid k and A_I denotes the specific interfacial area. This acoustic drag effect modeling was developed in Saurel et al., 2003 [21] and Chinnayya et al., 2004 [31]. It is obtained by local interfacial pressure integration over a piece of interface. The interfacial pressure is estimated through local approximate Riemann solver for the Euler equations of gas dynamics. Let us mention that upon integration over height, the specific interfacial area A_I becomes dimensionless. In Chiapolino and Saurel, 2018 [8], A_I was considered as a constant parameter. In Section 5, a correlation based on experimental results will be built. Beforehand, let us present the HLL-type Riemann solver used during the hyperbolic step.

3. HLL-Type Riemann Solver and Godunov-Type Method

A Riemann solver based on the Rankine-Hugoniot relations, such as the HLL solver of Harten et al., 1983 [32], has been developed in [8]. This HLL-type solver is simple, accurate and robust. It is summarized in the following.

For each fluid k, the two extreme, left- and right-facing waves ($S_{L,k}$ and $S_{R,k}$ respectively) are approximated following Davis, 1988 [33] as:

$$\begin{cases} S_{L,k} = \min\left(u_{L,k} - \sqrt{c_{L,k}^2 + \frac{1}{2}gh_{L,k}}\ ,\ u_{R,k} - \sqrt{c_{R,k}^2 + \frac{1}{2}gh_{R,k}}\right), \\ S_{R,k} = \max\left(u_{L,k} + \sqrt{c_{L,k}^2 + \frac{1}{2}gh_{L,k}}\ ,\ u_{R,k} + \sqrt{c_{R,k}^2 + \frac{1}{2}gh_{R,k}}\right), \end{cases} \tag{6}$$

with $k = \{1, 2\}$. The indexes L and R denote respectively the left and right states at a given cell boundary. The two most extreme waves (S_L and S_R), used in the Riemann problem solution, are then approximated as:

$$S_L = \min\left(S_{L,1}, S_{L,2}\right),\ S_R = \max\left(S_{R,1}, S_{R,2}\right). \tag{7}$$

The two contact waves u_1 and u_2 are considered as well for the transport of the heights h_1 and h_2. Their exact Riemann problem solutions are straightforward:

$$\begin{cases} h_1^*\left(\frac{x}{t} < u_1^*\right) = h_{1,L},\ h_1^*\left(\frac{x}{t} > u_1^*\right) = h_{1,R}, \\ h_2^*\left(\frac{x}{t} < u_2^*\right) = h_{2,L},\ h_2^*\left(\frac{x}{t} > u_2^*\right) = h_{2,R}. \end{cases} \tag{8}$$

In the present section, the superscript $*$ denotes the Riemann problem solution. Relations (8) indicate that the non-conservative terms have contributions between the two extreme waves S_L and S_R, at points where h_1 and h_2 are discontinuous. More precisely, only the discontinuity in $\rho_2 g h_2 \frac{\partial h_1}{\partial x}$ needs attention, as the non-conservative terms involving the atmospheric pressure (considered constant) transform to fluxes: $p_0 \frac{\partial h_k}{\partial x} = \frac{\partial (p_0 h_k)}{\partial x}$. An analysis of the Riemann problem structure is provided in Chiapolino and Saurel, 2018 [8] and reveals that local constants appear precisely at locations where the non-conservative products need definition. Thanks to these local constants, a locally conservative formulation of the equations is obtained. Consequently, the non-conservative terms do not cause numerical difficulties during the resolution of the Riemann problem, this asset being significant.

Besides, to simplify the algorithm, a single solution state is considered for the apparent densities $\left(\rho_k h_k\right)^*$ instead of the two $\left(\rho_k h_k\right)_L^*$ and $\left(\rho_k h_k\right)_R^*$ in the same spirit as in the HLL solver for the Euler equations:

$$U_{k,\text{mass}}^* = \left(\rho_k h_k\right)^* = \frac{\left(\rho_k h_k\right)_R \left(u_{k,R} - S_R\right) - \left(\rho_k h_k\right)_L \left(u_{k,L} - S_L\right)}{S_L - S_R}. \tag{9}$$

Such approximation relying on two waves instead of three remains accurate in the present context, as the intermediate wave vanishes at the end of the pressure relaxation step. It is present only during the hyperbolic step, not in the asymptotic system resulting of pressure relaxation. Thanks to this approximation, the momentum equations become locally:

$$\begin{cases} \frac{\partial\left(h_1\rho_1 u_1\right)}{\partial t} + \frac{\partial\left(h_1\rho_1 u_1^2 + h_1\left(p_1\left(\rho_1,\rho_2,h_2\right) - p_0\right) + \frac{1}{2}\rho_1 g h_1^2 - g\left(\rho_2 h_2\right)^* h_1\right)}{\partial x} = 0 \Leftrightarrow \frac{\partial U_{1,\text{mom}}}{\partial t} + \frac{\partial F_{1,\text{mom}}}{\partial x} = 0, \\ \frac{\partial\left(h_2\rho_2 u_2\right)}{\partial t} + \frac{\partial\left(h_2\rho_2 u_2^2 + h_2\left(p_2\left(\rho_2\right) - p_0\right) + \frac{1}{2}\rho_2 g h_2^2 + g\left(\rho_2 h_2\right)^* h_1\right)}{\partial x} = 0 \Leftrightarrow \frac{\partial U_{2,\text{mom}}}{\partial t} + \frac{\partial F_{2,\text{mom}}}{\partial x} = 0. \end{cases} \tag{10}$$

Solutions in terms of conservative variables U_k^* and fluxes F_k^* are then computed by the HLL approximation:

$$U_k^* = \frac{F_{k,R} - F_{k,L} - S_R U_{k,R} + S_L U_{k,L}}{S_L - S_R}, F_k^* = \frac{F_{k,R} S_L - F_{k,L} S_R + S_L S_R \left(U_{k,L} - U_{k,R}\right)}{S_L - S_R}. \tag{11}$$

The speeds of the fluids are given by:

$$u_k^* = \frac{U_{k,\text{mom}}^*}{U_{k,\text{mass}}^*} = \frac{\left(h_k \rho_k u_k\right)^*}{\left(h_k \rho_k\right)^*}. \tag{12}$$

The various equations of System (1) are updated with a Godunov-type method (stable under the conventional CFL condition) as:

$$\left\{\begin{array}{l} h_{k,i}^{n+1} = h_{k,i}^{n} - \frac{\Delta t}{\Delta x}\left((hu)_{k,i+1/2}^{*} - (hu)_{k,i-1/2}^{*}\right) + \frac{\Delta t}{\Delta x}h_{k,i}^{n}\left(u_{k,i+1/2}^{*} - u_{k,i-1/2}^{*}\right), \\ \left(h_k\rho_k\right)_i^{n+1} = \left(h_k\rho_k\right)_i^{n} - \frac{\Delta t}{\Delta x}\left(F_{k,mass,i+1/2}^{*} - F_{k,mass,i-1/2}^{*}\right), \\ \left(h_1\rho_1u_1\right)_i^{n+1} = \left(h_1\rho_1u_1\right)_i^{n} - \frac{\Delta t}{\Delta x}\left(F_{1,mom,i+1/2}^{*} - F_{1,mom,i-1/2}^{*}\right) + \frac{\Delta t}{\Delta x}h_{1,i}^{n}\left(-g\left[(h_2\rho_2)_{i+1/2}^{*} - (h_2\rho_2)_{i-1/2}^{*}\right]\right), \\ \left(h_2\rho_2u_2\right)_i^{n+1} = \left(h_2\rho_2u_2\right)_i^{n} - \frac{\Delta t}{\Delta x}\left(F_{2,mom,i+1/2}^{*} - F_{2,mom,i-1/2}^{*}\right) + \frac{\Delta t}{\Delta x}h_{1,i}^{n}\left(g\left[(h_2\rho_2)_{i+1/2}^{*} - (h_2\rho_2)_{i-1/2}^{*}\right]\right), \end{array}\right. \tag{13}$$

where n + 1 and n denote two consecutive time steps and superscript $*$ denotes the Riemann problem solution. Indexes i and $i \pm 1/2$ denote respectively the center of the current numerical cell and its corresponding boundaries. Note that the present integration of the non-conservative terms assumes h_k constant and taken at cell center $h_{k,i}^n$.

The HLL-type solver and its associated Godunov-type scheme (13) provide accurate results, maintain height positivity even in extreme situations and are oscillation free as shown in [8]. In this reference, it is also shown that sound speeds c_k influence computed results and particularly numerical diffusion.

For the sake of clarity, let us consider a limit situation where $h_1 \to 0$. System (1) then tends to the one-layer Saint-Venant equations, in the limit of stiff pressure relaxation. The wave speeds of the two-layer model (1) involve the effective sound speeds given by $\pm\sqrt{c_k^2 + \frac{1}{2}gh_k}$ while the single-layer wave speeds involve only $\pm\sqrt{gh}$. As shown in [8], when c_k is significantly greater than $\sqrt{\frac{1}{2}gh_k}$ excessive numerical diffusion is present. However, computational results do converge towards the exact solution when the mesh is fine enough. It thus appears that large sound speeds are admissible but result in excessive numerical diffusion. Numerical experiments also reveal that the method becomes unstable when $c_k < \sqrt{\frac{1}{2}gh_k}$. They consequently suggest existence of a subcharacteristic condition. The following numerical sound speed has consequently been proposed in [8],

$$c_k = \sqrt{\theta_k \frac{1}{2} g h_k}, \text{ with } \theta_k > 1, k = \{1, 2\}, \tag{14}$$

during the hyperbolic step only, i.e., during the resolution of the Riemann problem.

θ_k is a parameter that controls numerical diffusion. In order to unambiguously fulfill the above-mentioned subcharacteristic condition, θ_k must be greater than unit. According to numerical experiments, $\theta_k \in [2, 5]$ seems to be a fair choice as it is low enough to control numerical diffusion and large enough to ensure stability (see Chiapolino and Saurel, 2018 [8] for details).

4. Experimental Apparatus

Many experimental results dealing with fluid dispersal under gravity effects are provided in the literature and compared to shallow water computations. However, most of the experiments are carried out with one or several liquids, see for example Adduce et al., 2012 [34] and references therein. Consequently, a dedicated experimental setup was designed to produce and characterize an axisymmetric flow of dense gas, and thus obtain the necessary data for the validation of the model. The principle of the experiment is similar to the one used during the full-scale trials of Thorney Island [35] and consists of filling a cylindrical container with a dense gas and releasing it instantaneously (or very fast) by letting the container's walls fall down, thus creating a gravity-driven axisymmetric flow. The current tests were performed at small scale and pure krypton was used as the dense gas. In the present section, krypton will be specifically denoted with the index "Kr". The second gas is the environmental air and will be denoted specifically with the index "a".

4.1. Description of the Experimental Setup

The experimental setup is depicted in Figure 1. It is made of a closed, 1.2-m large, cubic vessel. The vessel is not airtight and is only used to isolate the experiment from any external perturbation. Three of the lateral faces, the ceiling and the floor are transparent to have optical access. The latter is made of plexiglass whereas the other faces are made of glass. It is to be noted that the floor is supported by the aluminum frame of the vessel but also by two additional beams. The vessel is placed in an open room which means that the external conditions could not be controlled during the trials.

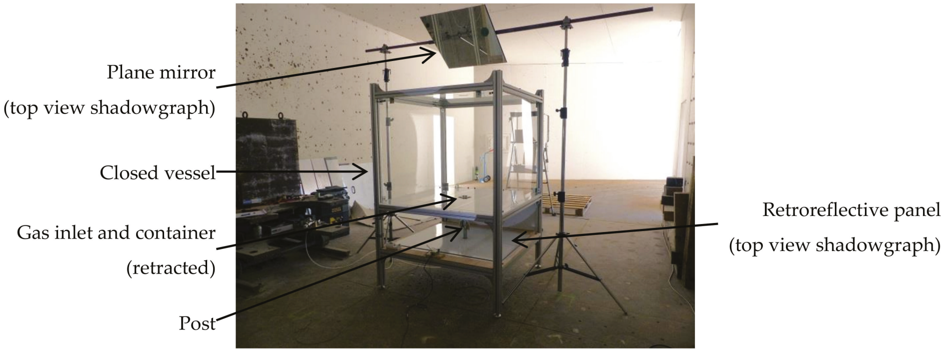

Figure 1. Global view of the experimental setup. The retro-reflective back panel was removed when the picture was taken.

The floor is equipped with a retractable metallic cylindrical container (shown in Figure 2) filled with krypton at the beginning of each trial. Its internal diameter is 99.6 mm and its height above the floor could be set to three different values: 6 cm, 11 cm and 16 cm, corresponding respectively to gas heights of 5 cm, 10 cm, and 15 cm. When retracted, the top of the container is flush with the floor. The container is installed on a post on which it could slide, and which includes the gas inlet. The container is initially maintained in position thanks to a pin, visible in Figure 2b, that is simply removed at the start of the experiment. In order to avoid the apparition of strong vibrations when the container reaches its lower position, an elastic damper is installed on the post. Besides, the rebound of the container is mitigated thanks to two sandbags placed at its bottom. The airtightness of the junction between the floor and the container is ensured by a rubber gasket and holes are made at the bottom of the container to avoid any suction effect during its descent. The gas inlet is 4 mm in diameter and a metallic part is put above it to break the krypton jet and ensure a homogeneous filling of the container from the bottom to the top with pure gas.

The resulting krypton cloud is visualized along two axes using Edgerton's (1958) shadowgraphy technique [36]. A first camera looks at the cloud in a vertical transversal plane (front view) whereas a second one looks at the cloud from above (top view). To this end, the back panel is covered with a retro-reflective material, a similar panel is placed below the floor of the vessel and a plane mirror is positioned above the vessel. The lenses of the two cameras are equipped with small mirrors to direct the light on the same axis as the camera optical axis as shown in Figure 3. The cameras used are a Phantom V2511 for the front view and a Photron Fastcam SA-Z for the top view. The frame rate is 500 Hz for both cameras. The resolution of the shadowgraphs is 0.86 mm per pixel for the front view and 0.97 mm per pixel for the top view.

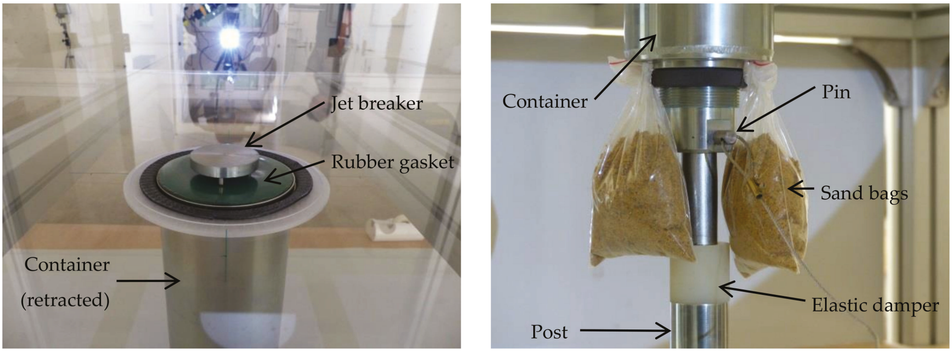

(**a**) View from above the floor (**b**) View from below the floor

Figure 2. Detailed view of the retractable, metallic, cylindrical container used to contain the dense gas at the initial state.

Figure 3. Detailed view of the lens of one of the cameras showing the small plane mirror used to direct the light on the same axis as the camera optical axis.

The amount of gas introduced inside the container is controlled with a ball flowmeter and a chronometer. Given the height h_{Kr} of krypton to be introduced, and a target value of the volumetric flow rate Q_{Kr} of krypton, the target value for the duration of the filling process t_{Kr} is determined as,

$$t_{Kr} = \frac{\pi R_c^2 h_{Kr}}{Q_{Kr}}, \tag{15}$$

where R_c is the internal radius of the container.

4.2. Course of Operations

Each test is performed as follows. First, the back panel of the vessel is removed, and the container is lowered. The bottle of krypton and the gas inlet are open, and the flowmeter is set to the target flow rate value. The gas inlet is closed, and the vessel is aerated. The container is then set to the desired height and the vessel is closed. After a few minutes (according to the estimate of Equation (15)), the container is filled with krypton. The experiment is started by removing the pin at the bottom of the container. Krypton is thereby released almost instantaneously and creates a cloud spreading on the floor. The time between the end of the filling process and the removal of the pin did not exceed a few seconds.

4.3. Processing of the Shadowgraphs

The analysis of the shadowgraphs and the extraction of the radius of the cloud have been performed automatically thanks to a dedicated tool written in Python and making use of the image processing library Scikit-Image [37]. Since the images of the top and front view differ, the processing method has been adapted to each view.

In the top view images, the cloud of krypton has a circular shape. Consequently, the processing method consists of determining a circle which fits the contours of the cloud. The processing steps are illustrated in Figure 4. First, the background of the image is subtracted (Figure 4b). The background image is calculated by taking the average of several dozens of pictures that are taken between the moment when the pin leaves the field of view and the moment when the container reaches its lowest position. The contrasts of the picture are then enhanced using a Contrast Limited Adaptive Histogram Equalization (CLAHE) technique (Figure 4c) which results in a clean picture of the cloud alone. Then two filters are applied to determine the contours of the cloud. The first one is a Frangi filter [38] (Figure 4d), which is well-adapted to circular patterns, and the second one is a Canny filter [39] (Figure 4e) which makes the image binary and facilitates the fitting step. The last step consists of determining the circle that best fits the contours of the cloud thanks to the Hough transform technique (Figure 4f). The extraction of the contours is limited by the initial contrast of the images and thus by the thickness of the cloud. As it expands, the contrast decreases and the determination of the circle becomes more difficult. Another restriction comes from the field of view of the camera which is limited by the size of the plane mirror.

(**a**) Raw image (**b**) Subtraction of the background (**c**) Contrast enhancement

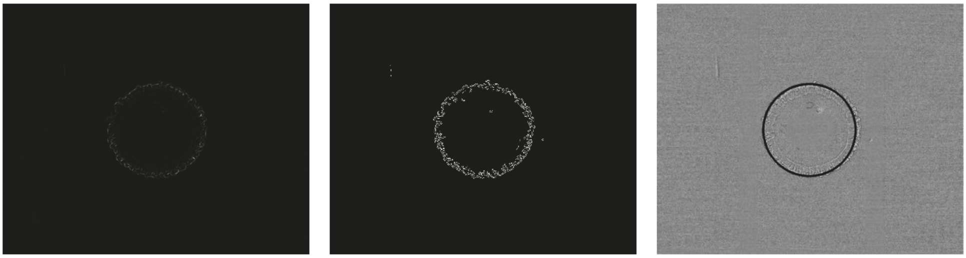

(**d**) Contour (first pass). (**e**) Contour (second pass) (**f**) Determination of the best-fit circle

Figure 4. Processing steps for the top-view shadowgraphs.

In the front view images, the cloud has a flat shape. Consequently, it is not possible to use strictly the same method to determine the radius of the cloud and the processing technique has been adapted. Instead of processing the whole image, only a horizontal line of pixels is processed. This line was taken five pixels above the floor which approximately corresponds to the height at which the head of the cloud reaches its maximum radius. The processing steps are illustrated in Figure 5. First, on each picture of the video, the line of pixels is extracted, and the background is subtracted. These lines are then assembled chronologically from top to bottom to form a kymograph (Figure 5a). The contrast of the kymograph is then enhanced using the CLAHE method (Figure 5b). The same two-edge filters [38,39] are then applied to get a binary image of the contours of the cloud. As artefacts of the background remained materialized as vertical streaks, only the vertical gradient of the image was kept (Figure 5c). In the last step, the left and right boundaries of the clouds are determined (Figure 5d). For that, the boundaries are first initialized as the boundaries of the container. Then the kymograph is processed line by line from top to bottom. The position of the left boundary on one line is chosen as the one of the leftmost contours detected on this line, in the limit of 50 pixels around the position calculated at the previous line. The symmetrical operation is performed for the right boundary. As for the processing of the images of the top view, the extraction of the contours is limited by the initial contrast of the images. Consequently, it is increasingly difficult to determine the boundaries of the cloud as it spreads. This is particularly visible in Figure 5c as fewer contours are detected as time evolves.

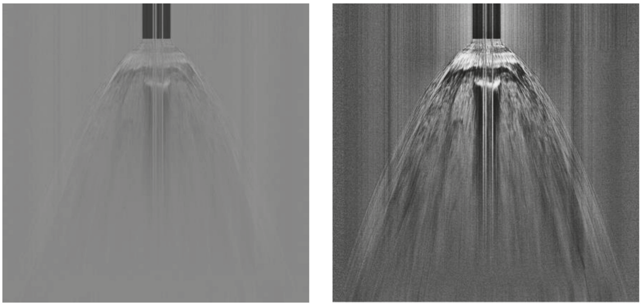

(**a**) Subtraction of the background and creation of a kymograph

(**b**) Contrast enhancement

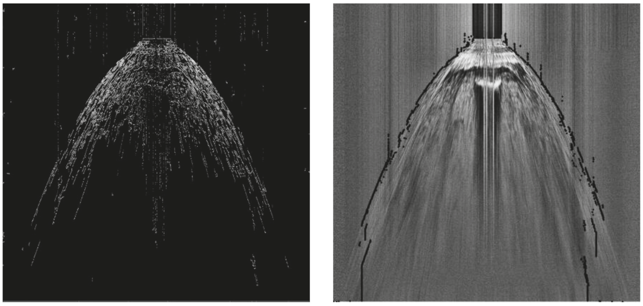

(**c**) Contour

(**d**) Determination of the cloud boundaries

Figure 5. Processing steps for the front-view shadowgraphs.

4.4. Experimental Configurations and Data

For all the tested configurations, the atmospheric pressure p_a and temperature T_a were measured near the vessel at the time of the trial. It allows calculating the actual density of krypton by using the ideal gas law:

$$\rho_{Kr} = \frac{p_a}{T_a}\frac{W_{Kr}}{\hat{R}}, \tag{16}$$

where $W_{Kr} = 83.8 \cdot 10^{-3}$ kg mol^{-1} is the molar mass of krypton and $\hat{R} = 8.314$ J/mol/K is the ideal gas constant. Pressure and temperature equilibria between krypton and atmospheric air are assumed. It could be objected that, since krypton is expanded from a high-pressure bottle, it could be colder than the atmosphere. However, krypton flows slowly in a several-meter long pipe before arriving in the container and this pipe acts as a heat exchanger. Equation (16) is only used to provide the order of magnitude of the cloud Froude and Reynolds numbers for the various container heights as will be seen in Section 4.7. Consequently, assuming pressure and temperature equilibria between krypton and air seems reasonable.

Given the duration of the filling process, t_{Kr}, and the krypton volumetric flow rate, Q_{Kr}, it is possible to determine the actual volume of krypton inside the container and then the initial height of krypton:

$$V_{Kr} = Q_{Kr} t_{Kr}, \tag{17}$$

$$h_{Kr} = \frac{V_{Kr}}{\pi R_c^2}, \tag{18}$$

with R_c the internal radius of the container. The last expression supposes that krypton does not mix substantially with air during the filling process. This point has been checked thanks to the shadowgraphs taken at the moments when the container starts to fall. Their analysis indeed shows that the height at which the separation between krypton and air begins to be visible corresponds closely to the calculated value of the height of krypton. Consequently, even if krypton happens to mix with air, the mixing is not significant.

All the experimental configurations are listed in Table 1. Three initial heights of krypton were tested and at least six trials were carried out for each height for repeatability. In the table and in the following, the experimental cases are referenced using a notation of the form “hX” where “h” is the target value for the height of krypton in centimeter and “X” is an alphabetical index. The column Δh_{Kr} corresponds to the difference between the target value of the initial height of krypton and the actual value. The uncertainties indicated with the different parameters are calculated by assuming that the duration of the filling process and the krypton flow rate are known respectively with a precision of 1 s and 0.01 L min^{-1}, which corresponds to the precision of the flowmeter. For every case, the actual initial height of krypton is close to the target value and the difference between the two is always below the calculated uncertainty, which confirms repeatability of the initial conditions.

4.5. Scaling Law

In order to compare the results obtained with the three container heights in the same frame, a scaling law will be used. The following parametrization [40] is used for the cloud radius R and time t:

$$R \to \lambda = \frac{R}{\left(R_c^2 h_0\right)^{\frac{1}{3}}} = S_r R, \tag{19}$$

$$t \to \tau = \left(S_r g\left(\frac{\rho_0}{\rho_a} - 1\right)\right)^{\frac{1}{2}} t = S_t t, \tag{20}$$

where λ and τ are the dimensionless scaled radius and time, R_c is the internal radius of the container, h_0 is the initial height of the heavy gas cloud, ρ_0 is its initial density, ρ_a is the atmospheric density and g is the acceleration due to gravity.

Therefore, the cloud area A can also be scaled according to the following relation:

$$A \rightarrow \Sigma = S_r^2 A. \tag{21}$$

Table 1. Summary of the experimental configurations and associated parameters.

Case	$\mathbf{t_{Kr}}$	$\mathbf{Q_{Kr}}$	$\mathbf{T_a}$	$\mathbf{p_a}$	$\boldsymbol{\rho_{Kr}}$	$\mathbf{V_{Kr}}$	$\mathbf{h_{Kr}}$	$\mathbf{\Delta h_{Kr}}$
		[L·min^{-1}]	**[°C]**	**[mbar]**	**[kg·m^{-3}]**	**[L]**	**[cm]**	**[cm]**
5A	1 min 34 s	0.25 ± 0.01	16.8	976	3.39	0.39 ± 0.02	5.0 ± 0.3	0.0 ± 0.3
5B	1 min 35 s	0.24 ± 0.01	16.9	976	3.39	0.38 ± 0.02	4.9 ± 0.3	-0.1 ± 0.3
5C	1 min 34 s	0.25 ± 0.01	17.8	981	3.40	0.39 ± 0.02	5.0 ± 0.3	0.0 ± 0.3
5D	1 min 35 s	0.24 ± 0.01	17.7	981	3.40	0.38 ± 0.02	4.9 ± 0.3	-0.1 ± 0.3
5E	1 min 35 s	0.24 ± 0.01	17.6	981	3.40	0.38 ± 0.02	4.9 ± 0.3	-0.1 ± 0.3
5F	1 min 36 s	0.25 ± 0.01	18.1	981	3.39	0.40 ± 0.02	5.1 ± 0.3	0.1 ± 0.3
5G	1 min 34 s	0.24 ± 0.01	18.0	981	3.40	0.38 ± 0.02	4.9 ± 0.3	-0.1 ± 0.3
5H	1 min 35 s	0.24 ± 0.01	18.3	980	3.39	0.38 ± 0.02	4.9 ± 0.3	-0.1 ± 0.3
10A	3 min 9 s	0.25 ± 0.01	18.0	980	3.39	0.79 ± 0.03	10.1 ± 0.4	0.1 ± 0.4
10B	3 min 9 s	0.24 ± 0.01	17.9	980	3.39	0.76 ± 0.03	9.8 ± 0.4	-0.2 ± 0.4
10C	3 min 8 s	0.24 ± 0.01	15.9	978	3.41	0.75 ± 0.03	9.6 ± 0.4	-0.4 ± 0.4
10D	3 min 8 s	0.25 ± 0.01	16.5	978	3.40	0.78 ± 0.03	10.0 ± 0.4	0.0 ± 0.4
10E	3 min 9 s	0.24 ± 0.01	16.3	978	3.41	0.76 ± 0.03	9.8 ± 0.4	-0.2 ± 0.4
10F	3 min 8 s	0.25 ± 0.01	16.7	978	3.40	0.78 ± 0.03	10.0 ± 0.4	0.0 ± 0.4
15A	4 min 46 s	0.24 ± 0.01	15.0	975	3.41	1.14 ± 0.05	14.6 ± 0.6	-0.4 ± 0.6
15B	4 min 45 s	0.24 ± 0.01	15.1	975	3.41	1.14 ± 0.05	14.6 ± 0.6	-0.4 ± 0.6
15C	4 min 44 s	0.25 ± 0.01	15.4	975	3.41	1.18 ± 0.05	15.1 ± 0.6	0.1 ± 0.6
15D	4 min 44 s	0.25 ± 0.01	15.5	975	3.41	1.18 ± 0.05	15.1 ± 0.6	0.1 ± 0.6
15E	4 min 44 s	0.25 ± 0.01	16.3	975	3.40	1.18 ± 0.05	15.1 ± 0.6	0.1 ± 0.6
15F	4 min 44 s	0.25 ± 0.01	16.2	975	3.40	1.18 ± 0.05	15.1 ± 0.6	0.1 ± 0.6

4.6. Expected Evolution of the Cloud

In the present cylindrical experimental setup, the heavy gas is released almost instantaneously, and the subsequent flow is axisymmetric. Box models [1,2] have been developed in this specific context. Those are however irrelevant for more complex flow configurations. They are valid only in cylindrical and axisymmetric situation such as the present one. It is consequently worth introducing such models. The experimental time evolution of the cloud, in terms of disk-shaped area, is then to be compared with these specific models. In the simplest version, the heavy gas cloud is represented as a cylindrical volume of homogeneous and constant density gas spreading on the ground. The cloud volume is thus assumed to be constant. The expansion velocity is then given by:

$$\frac{dR}{dt} = Fr\sqrt{g\frac{\rho_{Kr} - \rho_a}{\rho_a}h_{Kr}}, \tag{22}$$

where R and h_{Kr} are the instantaneous radius and height of the cloud, g is the acceleration due to gravity, ρ_{Kr} and ρ_a are the respective density of the heavy gas and air and Fr is the cloud Froude number which represents the ratio between its kinetic energy and its gravitational potential energy. From this expression, it is possible to derive an evolution equation for the disk-shaped area of the cloud:

$$\frac{dA}{dt} = 2\pi Fr\sqrt{\frac{gV_{Kr}}{\pi}\frac{\rho_{Kr} - \rho_a}{\rho_a}}, \tag{23}$$

$$A(t) = 2\pi Fr\sqrt{\frac{gV_{Kr}}{\pi}\frac{\rho_{Kr} - \rho_a}{\rho_a}}t + A_0, \tag{24}$$

with V_{Kr} being the (constant) cloud volume and A_0 the initial cloud area.

Seen from above, the present experimental cloud is expected a have a circular shape. According to Equation (24), its disk-shaped area $A(t)$ is to evolve linearly with time. Its radius $R(t)$ is consequently expected to present a parabolic time evolution. The aera and radius are indeed related through $A(t) = \pi R^2(t)$. As will be seen further in Sections 4.7 and 5.3, present experimental data verify indeed these behaviors.

In the right side of Equation (24), the Froude number is the only unknown. In the left side, the area of the cloud is known with the help of the cloud radius, experimentally measured by the methods (top and front views) presented previously and evolves linearly with time. The Froude number can consequently be extracted from Equation (24) by performing a linear regression.

Experimental results are presented in the following section. The corresponding Froude numbers are also provided. Let us recall that such simple model is only valid for cylindrical and symmetrical flows. It is here used for the sole purpose of checking the consistency of the experimental data. Indeed, such model cannot be used to address non-cylindrical flows or flows in complex geometries. The present two-layer shallow water model (1) is obviously more complex than Equation (24) but can deal with arbitrary geometrical domains. Its accuracy will be examined in Section 5.3.

4.7. Results and Discussion

Shadowgraphs taken during trial 15E and showing the expansion of the krypton cloud are shown in Figure 6. These shadowgraphs have been processed using the method described in Section 4.3 in order to remove the background and increase the contrasts. When the container reaches its lowest position (first row of Figure 6), the cloud begins to fall. The interface between air and krypton wrinkles due to the apparition of Kelvin-Helmholtz [41,42] instabilities. Then, krypton spreads on the floor. Seen from above, the cloud keeps an overall circular shape which confirms the good symmetry of the gas release. Unlike front view images may suggest, the thickness of the cloud is not uniform. Instead, it has a thick vertical “head” and is thin and flat elsewhere. Rayleigh-Taylor instabilities [43,44] can be seen on the “head” of the cloud and are caused by both the difference of density between krypton and air and deceleration of the cloud.

Using the processing technique described in Section 4.3, the temporal evolution of the cloud radius has been extracted from the shadowgraphs and the evolution of its area has been deduced. The resulting data are plotted in Figure 7a for the top view and Figure 7b for the front view. For all sets of data, the origin of time has been manually corrected in order to correspond to the end of the descent of the container. As it can be seen, the experimental setup proved to be repeatable for each initial height of gas despite its apparent simplicity. Processing of the front view images leads to more scattered data but allows following the cloud for a longer time. It is worth noting that the top view image processing tends to underestimate the cloud area above 0.08 m^2. A slight inflection can for example be seen at 0.23 s on the graphs in Figure 7 corresponding to the initial height of 15 cm. Such inflection appears because part of the cloud is then located over the two beams that support the floor of the vessel, which hinders the determination of the circle.

The growth of the cloud’s area is linear as expected (see Section 4.6). The slope of the curves however still depends on the Froude number. When the scaling law from Section 4.5 is applied, all the plots almost collapse on a single line as shown in Figure 8. These results confirm the good behavior of experimental data and their validity for the validation of the two-layer model (1).

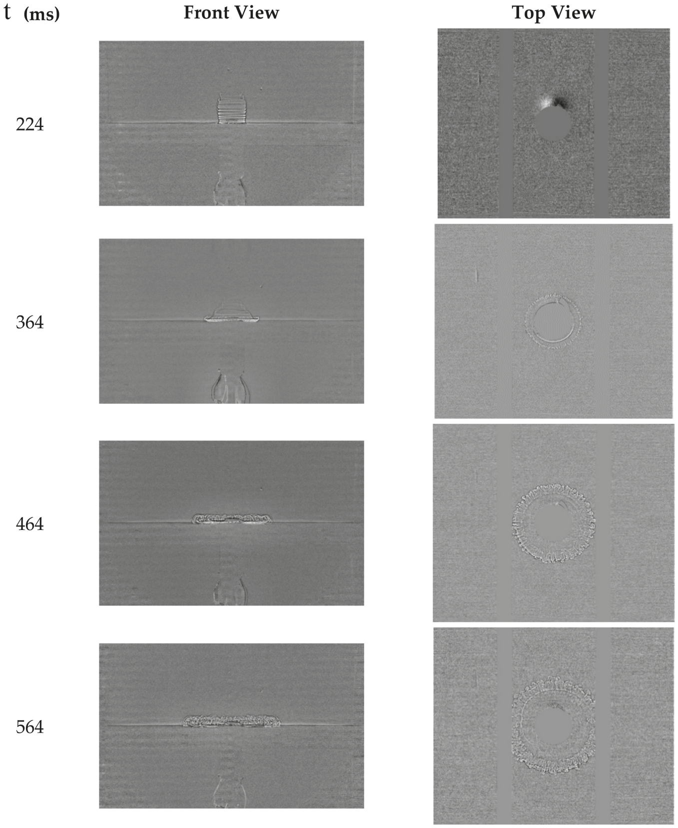

Figure 6. Shadowgraphs (front view and top view) of trial 15E showing the evolution of the krypton cloud. For each row, the front and top view pictures are taken at the same time. The origin of time corresponds to the beginning of the descent of the container.

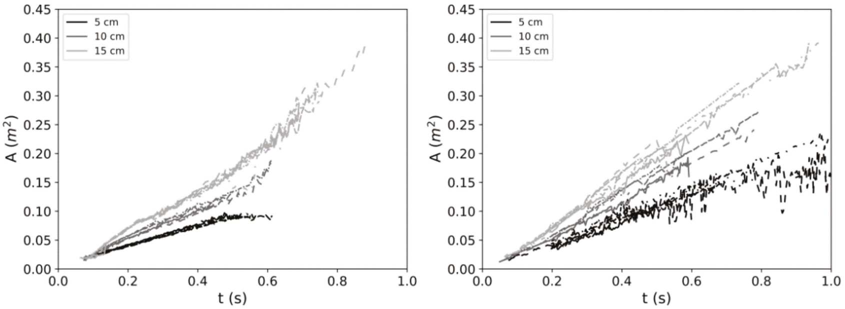

(**a**) Top view (**b**) Front view

Figure 7. Temporal evolution of the cloud area measured on the shadowgraphs.

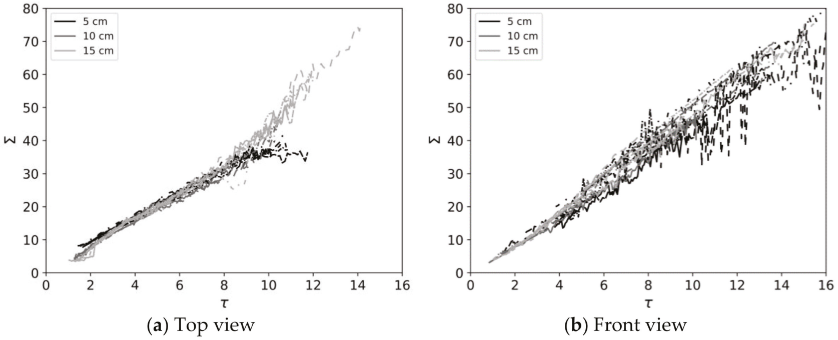

(**a**) Top view (**b**) Front view

Figure 8. Temporal evolution of the cloud area (defined by Equation (21)) measured on the shadowgraphs in scaled coordinates.

From the evolution of the cloud area, the Froude number has been determined for every configuration by performing a linear regression using Equation (24). Regarding front view images, as they could contain some noise, a filtering step was performed before applying linear regression. By comparing the determined cloud radius with the front view pictures, it was noticed that the noise corresponded mostly to an underestimation of the radius. This is due to turbulent structures located inside the cloud instead of its boundaries. Consequently, instead of performing directly linear regression on the data output by the processing script, it was decided to perform it on the upper envelope of the curves. This method appeared to be effective even on very noisy signals. The determined value of the Froude number is given for each configuration in Table 2. Top view data for trial 5B and trial 10B do not appear in the table because of data transfer issues.

Table 2. Froude number calculated from the processing of the shadowgraphs.

Case	Froude Number [–]			
	Top View	**Front View–Left**	**Front View–Right**	**Average**
5A	0.61	0.80	0.70	0.70
5B	-	0.79	0.65	0.72
5C	0.63	0.72	0.78	0.71
5D	0.58	0.80	0.63	0.67
5E	0.61	0.82	0.75	0.73
5F	0.61	0.71	0.58	0.63
5G	0.58	0.71	0.69	0.66
5H	0.61	0.76	0.73	0.70
10A	0.63	0.78	0.81	0.74
10C	0.57	0.79	0.73	0.70
10D	0.62	0.77	0.81	0.73
10E	0.61	0.86	0.93	0.80
10F	0.63	0.86	0.71	0.73
15A	0.80	0.80	1.01	0.87
15B	0.81	1.00	0.84	0.88
15C	0.77	0.81	0.93	0.84
15D	0.81	0.80	0.85	0.82
15E	0.72	0.90	0.82	0.81
15F	0.75	0.87	0.96	0.86

From the data given in Table 2, the average Froude number was calculated for each initial height of krypton. The results are given in Table 3. The associated standard deviation was also calculated to give an estimation of the uncertainty. As it can be noticed, the average Froude number tends to increase with the initial cloud height, which shows that the conversion of potential energy into kinetic energy tends to be more efficient when the cloud is initially higher.

Table 3. Average Froude number for each initial height and associated standard deviation.

h_{Kr} [cm]	Average Fr [–]	Standard Deviation [–]
5	0.69	0.03
10	0.74	0.03
15	0.85	0.03

As the configuration of the current trials is similar to the one studied at Thorney Island [35] and only differs in scale, it is of interest to compare the results of both experiments. The trials of Thorney Island (Phase I) consisted of the instantaneous release of a dense gaseous mixture of dichlorofluoromethane and nitrogen initially contained in a twelve-sided, 14-m wide and 13-m high container, which corresponds to an initial volume of 2000 m^3. The evolution of the cloud radius and area was estimated thanks to aerial photographs taken from a helicopter located 300 m above the test site [35]. The analysis of the collected data allowed to determine that the cloud Froude number was 1.05 ± 0.12 [1]. This value is higher than the ones found during the current trials, which tends to corroborate the previous observation made about the Froude number.

It is highly likely that viscous effects play a more prominent role at small scale than at full scale. The cloud Reynolds number, representing the ratio between inertial and viscous effects, reads,

$$\mathrm{Re} = \frac{\rho_a u R}{\mu_a}, \tag{25}$$

where u is the cloud front velocity and μ_a is the viscosity of air. According to Equation (22), the cloud's expansion velocity obeys,

$$R\frac{dR}{dt} = Ru = \mathrm{Fr}\sqrt{\frac{gV_{Kr}}{\pi}\frac{\rho_{Kr} - \rho_a}{\rho_a}} = K. \tag{26}$$

Hence, the expression of the cloud Reynolds number becomes,

$$\mathrm{Re} = \frac{\rho_a}{\mu_a}K, \tag{27}$$

with $\rho_a = \frac{p_a}{T_a}\frac{W_a}{\hat{R}}$ and $W_a = 29 \cdot 10^{-3}$ kg.mol^{-1}. For the current trials, the value of the constant is $K \simeq 0.06$ m^2/s for $h_{Kr} = 15$ cm, $K \simeq 0.05$ m^2/s for $h_{Kr} = 10$ cm and $K \simeq 0.03$ m^2/s for $h_{Kr} = 5$ cm. The cloud Reynolds number is thus smaller for small heights of container and viscous effects are indeed more prominent in that case. In the case of the Thorney Island trials [35], $K \simeq 68$ m^2/s, which tends to confirm the previous conclusion.

In the frame of the validation of the two-layer model, it means that, although the current experimental results can indeed be used as a reference for comparison, attention shall be paid in future work to scale effects.

Numerical results of the present two-layer shallow water model (1) are compared to experimental data in the next section. In this specific cylindrical symmetry context, simpler models such as (23) and (24), provide good results, assuming known Froude number. However, such simplified models become irrelevant for non-cylindrical situations and are unable to deal with more complex geometries. The two-layer shallow water approach becomes more appropriate.

5. Numerical Results with Two-Layer Model and Laboratory Experiments Comparison

5.1. Two-Layer Flow Model with Cylindrical Symmetry

The present laboratory experiments involve a cylindrical gas column. Consequently, cylindrical symmetry is introduced in the 1D equations of System (1). The corresponding system is presented in Appendix A.

5.2. Velocity Relaxation

Numerical experiments have been carried out in order to find the best values of the interfacial area A_I (see Section 2, Equation (5)) for each dam-break configuration. For each test, multiple values of A_I (constant during time step Δt) have been necessary to match computational and experimental results. Based on these numerical experiments, the following function has been determined:

$$A_I(t) = A_I(h_0)e^{-\frac{t}{\tau}} + A_{I0}. \tag{28}$$

$A_I(h_0)$ represents the initial interfacial area. It consequently depends on the initial height h_0 of the krypton column. τ represents the "system's time constant" and A_{I0} is a positive constant ensuring that the interfacial area $A_I(t)$ remains non-zero during time evolution. The present drag function may be conveniently written with the following parameters,

$$A_I(t) = a.h_0 e^{-b.t} + c, \tag{29}$$

where h_0 is the initial height of the krypton column and a, b, c are three positive constants. The interfacial area is then expressed under the form of a correlation depending on time and requiring three parameters.

According to numerical experiments, parameters $a = 0.2\ \mathrm{m}^{-1}, b = 12.5\ \mathrm{s}^{-1}, c = 5.10^{-5}$ are a fair choice. The present interfacial law consequently reads,

$$A_I(t) = 0.2\ h_0 e^{-12.5\ t} + 5.10^{-5}, \tag{30}$$

for all initial conditions of two-layer dam-break test problems.

5.3. Results and Comparisons

The experiments consist of a cylindrical krypton column of diameter 10 cm. Under gravity effects, gas dispersal occurs into the surrounding atmospheric air. Experimental results are provided in terms of position (radius R) of the krypton front. Three initial column heights are used, namely 5, 10 and 15 cm. The experimental apparatus consists of a glass-made cubic enclosure of dimension $1.2 \times 1.2 \times 1.2\ \mathrm{m}^3$. However, for symmetry reasons, the following 1D computations only consider half of the domain. These initial data correspond to the ones of the experiments of Section 4.

Initial conditions consequently consist of a 0.6-m wide computational domain with a discontinuity located at $x_0 = 0.05$ m. On the left of the discontinuity, initial heights are $h_1 = 0.05,\ 0.10,\ 0.15$ m and $h_2 = 1.2 - h_1$. On the right, the initial heights are $h_1 = 10^{-6}$ m and $h_2 = 1.2$ m. Initial densities are $\rho_1 = 3.506\ \mathrm{kg/m^3}$ for the krypton and $\rho_2 = 1.29\ \mathrm{kg/m^3}$ for the air. The gravity constant is $g = 9.81\ \mathrm{m/s^2}$. Fluids are initially at rest $u_1 = u_2 = 0$ m/s. Reflective boundary conditions are used (symmetry condition on the left and wall on the right). Acoustic impedances $Z_k = \rho_k c_k = (\rho_k c_k)_{atm}$ are considered constant and are computed with $\rho_1 = 3.506\ \mathrm{kg/m^3}$ and $c_1 = 218$ m/s for the krypton and $\rho_2 = 1.29\ \mathrm{kg/m^3}$ and $c_2 = 340$ m/s for the air. The atmospheric pressure is $p_0 = 101325$ Pa. The "sound speed" numerical parameters are $\theta_1 = \theta_2 = 2$ for both fluids during the hyperbolic step.

Computed results' accuracy is improved with the Monotonic-Upwind-Scheme-for-Conservation-Laws (MUSCL) type second order scheme (see for example Chiapolino et al., 2017 [27]) using van Leer's limiter [45]. The computational domain is made of 1000 cells $(M = 1000)$. The CFL number is CFL $= 0.8$. The computed position of the krypton front is specifically determined according to,

$$h_{1,i} h_{2,i} > \varepsilon. \tag{31}$$

This indicator notifies height variations at cell center i. Relation (31) is used from right $(i = M)$ to left $(i = 1)$. When a height variation of $\varepsilon = 10^{-10}$ m^2 is recorded, the krypton front position is considered at $\frac{x_i + x_{i+1}}{2}$ where x_i and x_{i+1} represent locations of the cell centers i and $i + 1$.

Numerical results are compared to experimental data in Figures 9–11. Experimental results are extracted from multiple series of tests resulting in various (grey lines) curves in the following graphs. The dam-break test problem is first considered with a 5-cm high initial krypton column. Corresponding results are shown in Figure 9.

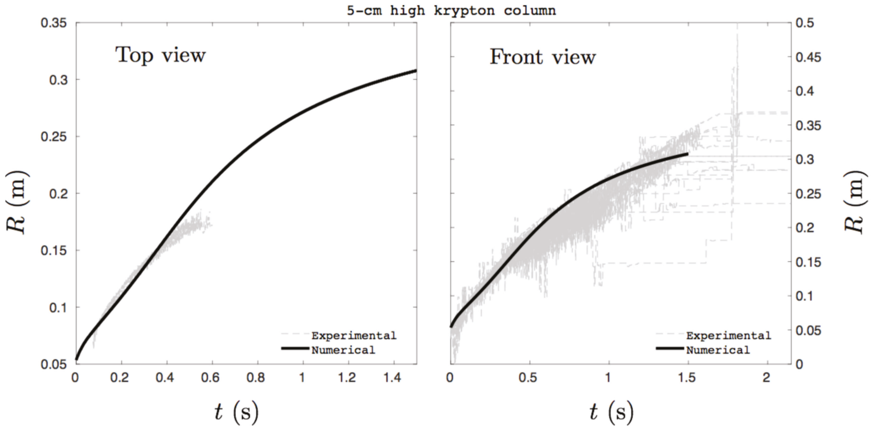

Figure 9. Temporal evolution of the krypton front position. Comparison of the one-dimensional solution of the present two-layer shallow water model versus experimental data. The initial krypton column is 5-cm high. Computed results are in good agreement with experimental measurements.

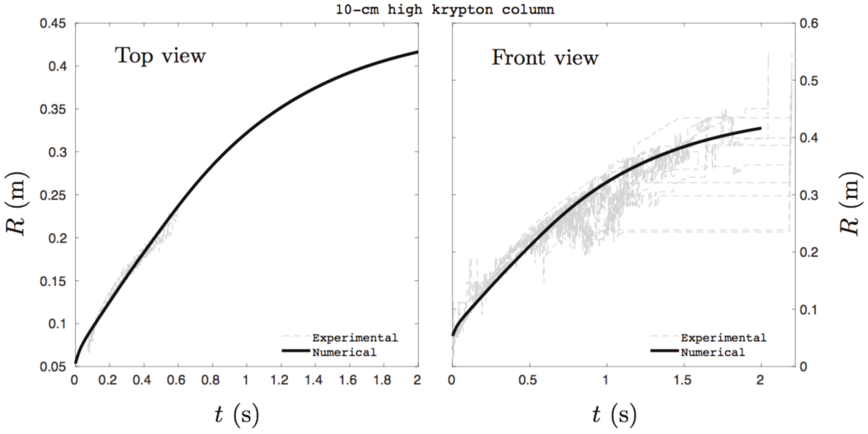

Figure 10. Temporal evolution of the krypton front position. Comparison of the one-dimensional solution of the present two-layer shallow water model versus experimental data. The initial krypton column is 10-cm high. Computed results are in good agreement with experimental measurements.

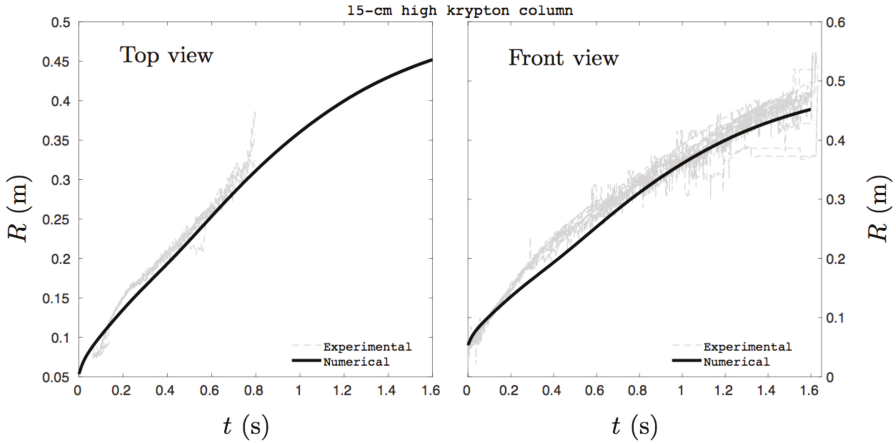

Figure 11. Temporal evolution of the krypton front position. Comparison of the one-dimensional solution of the present two-layer shallow water model versus experimental data. The initial krypton column is 15-cm high. Computed results are in good agreement with experimental measurements.

Good agreement between numerical and experimental results is observed. The test is now repeated with a 10-cm high initial krypton column. Corresponding results are shown in Figure 10.

Again, good agreement is observed. The test is finally repeated with a 15-cm high initial krypton column. Corresponding results are shown in Figure 11.

Once more, good agreement between numerical and experimental results is obtained. Those results indicate that the present hyperbolic two-layer shallow water model accurately reproduces experimental results at the price of few parameters related to the drag function.

In the three studied configurations, Relation (30) inserted in the acoustic drag force model (5) enables fairly accurate comparison of computed and experimental results. These small-scale comparisons show model's ability to predict large-scale dispersal of dense gases when drag effects are properly adjusted.

5.4. Concluding Remarks

The present approach based on two-layer shallow water equations appears promising. The agreement between experimental and computational results is good. It is obtained nowadays at the price of a few parameters related to the interfacial aera function, summarizing drag and turbulence effects at the interface separating the dense gas and the ambient one. A more sophisticated interfacial area will be needed in the future to address more complex situations and large-scale configurations. However, the present work shows that the two-layer approach has nice predicting abilities.

Topography effects, encountered in urban places or hilly grounds, have not been considered for the sake of simplicity. The model with its drag modeling has then been successfully compared to experimental data in its simplest form. This step was necessary before addressing more complex configurations.

Nevertheless, introduction of topography effects into two-layer shallow water equations is possible and will be part of future investigations. This flexibility is real asset of the two-layer shallow water approach, compared to other simplified box or SLAB-type models that are inappropriate for describing a gas cloud evolving in complex topographies [4].

The multi-D CFD approach is able to account for complex terrains but is much more complex and much more time-consuming than the present two-layer shallow water strategy. The corresponding equations have been recently revisited in Chiapolino and Saurel, 2018 [8] with an unconditionally hyperbolic formulation. In the same contribution, the importance of the two-layer property of the model, resulting in interaction terms, is illustrated. Indeed, in the present heavy-gas dispersal context, a single-layer model is too inaccurate, at least without extra terms [4]. Numerical resolution of the present two-layer model is about one million times faster than common multi-D CFD computations [8] and is robust and accurate if properly adjusted.

6. Conclusions

Heavy-gas dispersion modeling has been addressed in this paper. From a numerical point of view, one of the difficulties is related to long-time and large-scale computations, for instance a city scale, while providing accurate results with reasonable CPU time.

The present method differs from models commonly used in heavy-gas dispersion [7] as it relies on a two-layer shallow water approach. This approach seems more appropriate than box or SLAB-type models to address heavy-gas dispersal in urban places or hilly grounds. Indeed, among the aforementioned methods, introduction of topography effects is possible only with the two-layer approach. Such task has not been addressed in the present paper for the sake of simplicity but shall be part of future investigations. Computed results are indeed promising and highlight the predicting abilities of the two-layer shallow water approach.

Interactions between the ambient fluid and the dense layer is significant in this heavy-gas dispersal context and a single-layer model is inaccurate [8], at least without extra terms [4]. In the present contribution, these fluid interactions are accounted for through the non-conservative terms of the recent hyperbolic two-layer shallow water model of Chiapolino and Saurel, 2018 [8] and through drag effects that play a significant role. Particularly, creation of an interfacial aera is significant as it summarizes turbulent structures appearing at the interface and controls the dispersion speed of the dense gas cloud.

A set of laboratory experiments involving a dense gas has been specifically designed to address determination of the interfacial aera. Thanks to the experiments, an interfacial area function with few parameters has been determined and yields a good agreement between numerical and experimental results.

Computed results highlight the ability of the two-layer shallow water approach to address heavy-gas dispersal. However, a more sophisticated determination of the interfacial area will be needed in the future to address real configurations such as gas dispersal in a city, for instance. This interfacial area modeling is an important research work mainly related to friction between fluid layers that depends on interfacial instabilities. Such topics shall also be part of future investigations.

Most two-layer shallow water models are only conditionally hyperbolic, resulting in serious consequences both for wave propagation, which becomes ill-posed, and for the design of numerical methods. The present two-layer shallow water is unconditionally hyperbolic and consequently presents a solid base for many future developments. Indeed, in addition to the above-mentioned prospects, this research work can be continued in many other directions. Among them are the extension of the hyperbolic model to more than two fluids, the introduction of mass transfer between layers describing ascending effects or the modeling of thin and heterogeneous layers such as the free surface of the ocean (water-air mixing zone).

Author Contributions: A.C.: Investigation, Validation, Writing, Editing, Review, Software. S.C.: Investigation, Validation, Writing, Editing, Experiments. E.L.: Investigation, Validation, Writing, Editing. R.S.: Investigation, Validation, Writing, Editing, Review, Supervision. All authors have read and agreed to the published version of the manuscript.

Funding: This research received no external funding.

Acknowledgments: The authors wish to acknowledge the technical teams from CEA Gramat for their contribution to the conception of the experimental setup and the success of the experiments.

Conflicts of Interest: The authors declare no conflict of interest.

Appendix A.

Appendix A.1. Two-Layer Flow Model with Cylindrical Symmetry

In the present work, cylindrical symmetry is considered through geometric source terms resulting from the integration of the two-layer shallow water equations on a cylindrical control volume. For the sake of space restriction, calculation details are omitted and only the final system is given as

$$\begin{cases} \frac{\partial h_1}{\partial t} + u_1 \frac{\partial h_1}{\partial r} = 0, \\ \frac{\partial(h_1 \rho_1)}{\partial t} + \frac{\partial(h_1 \rho_1 u_1)}{\partial r} = -\frac{h_1 \rho_1 u_1}{r}, \\ \frac{\partial(h_1 \rho_1 u_1)}{\partial t} + \frac{\partial(h_1 \rho_1 u_1^2 + h_1 (p_1 - p_0) + \frac{1}{2} \rho_1 g h_1^2)}{\partial r} = \rho_2 g h_2 \frac{\partial h_1}{\partial r} - \frac{h_1 \rho_1 u_1^2}{r}, \\ \frac{\partial h_2}{\partial t} + u_2 \frac{\partial h_2}{\partial r} = 0, \\ \frac{\partial(h_2 \rho_2)}{\partial t} + \frac{\partial(h_2 \rho_2 u_2)}{\partial r} = -\frac{h_2 \rho_2 u_2}{r}, \\ \frac{\partial(h_2 \rho_2 u_2)}{\partial t} + \frac{\partial(h_2 \rho_2 u_2^2 + h_2 (p_2 - p_0) + \frac{1}{2} \rho_1 g h_1^2)}{\partial r} = -\rho_2 g h_2 \frac{\partial h_1}{\partial r} - \frac{h_2 \rho_2 u_2^2}{r}. \end{cases} \tag{A1}$$

Let us recall that index 1 denotes the heavy fluid (krypton) and index 2 the light one (air). Here, r is the radial direction and the terms $-\frac{h_k \rho_k u_k}{r}$ and $-\frac{h_k \rho_k u_k^2}{r}$ are discretized, after the hyperbolic step, as:

$$\begin{aligned} -\frac{h_k \rho_k u_k}{r} &\to -\frac{1}{R_i} \frac{(h_k \rho_k u_k)^*_{i+1/2} + (h_k \rho_k u_k)^*_{i-1/2}}{2}, \\ -\frac{h_k \rho_k u_k^2}{r} &\to -\frac{1}{R_i} \frac{(h_k \rho_k u_k^2)^*_{i+1/2} + (h_k \rho_k u_k^2)^*_{i-1/2}}{2}, \end{aligned} \tag{A2}$$

where the radius R_i is the location of the center of cell i and the superscript $*$ denotes the Riemann problem solution (Section 3). Pressure relaxation is then achieved as in Section 2 followed by velocity relaxation. This step is addressed hereafter.

A.2. Velocity Relaxation

Drag effects are now included in the momentum equations (as seen in Section 2) as source terms:

$$\begin{cases} \frac{\partial(h_1 \rho_1)}{\partial t} = 0, \\ \frac{\partial(h_1 \rho_1 u_1)}{\partial t} = \frac{Z_1 Z_2}{Z_1 + Z_2} A_I (u_2 - u_1), \\ \frac{\partial(h_2 \rho_2)}{\partial t} = 0 \\ \frac{\partial(h_2 \rho_2 u_2)}{\partial t} = -\frac{Z_1 Z_2}{Z_1 + Z_2} A_I (u_2 - u_1). \end{cases} \tag{A3}$$

When the interfacial area A_I is considered as constant, as well as acoustic impedances $Z_k = \rho_k c_k = (\rho_k c_k)_{atm}$ solution of System (A3) is determined explicitly as:

$$\begin{cases} (u_2)_t = \frac{(h_1 \rho_1 u_1 + h_2 \rho_2 u_2)^n + (h_1 \rho_1)^n (u_2 - u_1)^n e^{(cst A_I \, \Delta t)}}{(h_1 \rho_1)^n + (h_2 \rho_2)^n}, \\ (u_1)_t = (u_2)_t - (u_2 - u_1)^n e^{(cst A_I \, \Delta t)}, \end{cases} \tag{A4}$$

with

$$cst = -\frac{Z_1 Z_2}{Z_1 + Z_2} \left(\frac{1}{(h_1 \rho_1)^n} + \frac{1}{(h_2 \rho_2)^n} \right). \tag{A5}$$

The conservative variables of the momentum equations are then updated after the hyperbolic step, the cylindrical correction step, and pressure relaxation as:

$$\begin{cases} (h_1 \rho_1 u_1)^{n+1} = (h_1 \rho_1)^{n+1} (u_1)_t, \\ (h_2 \rho_2 u_2)^{n+1} = (h_2 \rho_2)^{n+1} (u_2)_t, \end{cases} \tag{A6}$$

where $(u_1)_t$ and $(u_2)_t$ are given by (A4).

In the present contribution, the interfacial area has been determined in Section 5 as a function of time:

$$A_I(t) = a.h_0 e^{-b.t} + c, \tag{A7}$$

where h_0 is the initial height of the krypton column and a, b, c are three positive constants.

However, System (A3) still admits explicitly solution as:

$$\begin{cases} (u_2)_t = \dfrac{(h_1\rho_1 u_1 + h_2\rho_2 u_2)^n + (h_1\rho_1)^n (u_2 - u_1)^n e^{cst(\frac{a.h_0}{-b} e^{-b.t_0}(e^{-b\Delta t}-1)+c\Delta t)}}{(h_1\rho_1)^n + (h_2\rho_2)^n}, \\ (u_1)_t = (u_2)_t - (u_2 - u_1)^n e^{cst(\frac{a.h_0}{-b} e^{-b.t_0}(e^{-b\Delta t}-1)+c\Delta t)}, \end{cases} \tag{A8}$$

with t_0 the current time. The conservative variables of the momentum equations are then updated with the help of Equation (A6).

References

1. Brighton, P.W.M.; Prince, A.J.; Webber, D.M. Determination of cloud area and path from visual and concentration records. *J. Hazard. Mater.* **1985**, *11*, 155–178. [CrossRef]
2. Deaves, D.M. Dense gas dispersion modelling. *J. Loss Prev. Process Ind.* **1992**, *5*, 219–227. [CrossRef]
3. Ermak, D.L. *User's Manual for SLAB: An Atmospheric Dispersion Model for Denser-Than-Air Releases*; UCRL-MA-l05607; Lawrence Livermore National Laboratory: Livermore, CA, USA, 1990.
4. Hankin, R.K.S. Heavy Gas Dispersion over Complex Terrain. Ph.D. Thesis, University of Cambridge, Cambridge, UK, 1997.
5. Hank, S.; Saurel, R.; LeMétayer, O.; Lapébie, E. Modeling blast waves, gas and particles dispersion in urban and hilly ground areas. *J. Hazard. Mater.* **2014**, *280*, 436–449. [CrossRef] [PubMed]
6. Hank, S. Modélisation et Simulation de la Dispersion de Fluide en Milieu Fortement Hétérogène. Ph.D. Thesis, Aix Marseille Université, Marseille, France, 2012.
7. Hanna, S.; Dharmavaram, S.; Zhang, J.; Sykes, I.; Witlox, H.; Khajehnajafi, S.; Koslan, K. Comparison of six widely-used dense gas dispersion models for three recent chlorine railcar accidents. *Process Saf. Prog.* **2008**, *27*, 248–259. [CrossRef]
8. Chiapolino, A.; Saurel, R. Models and methods for two-layer shallow water flows. *J. Comput. Phys.* **2018**, *371*, 1043–1066. [CrossRef]
9. Teshukov, V.M. Gas-Dynamic analogy for vortex free-boundary flows. *J. Appl. Mech. Tech. Phys.* **2007**, *48*, 303–309. [CrossRef]
10. Richard, G.; Gavrilyuk, S. A new model of roll waves: Comparison with Brock's experiments. *J. Fluid Mech.* **2012**, *698*, 374–405. [CrossRef]
11. Richard, G. Elaboration D'un Modèle D'écoulements Turbulents en Faible Profondeur. Application au Ressaut Hydraulique et aux Trains de Rouleaux. Ph.D. Thesis, Aix-Marseille Université, Marseille, France, 2013.
12. Richard, G.; Gavrilyuk, S. The classical hydraulic jump in a model of shear shallow-water flows. *J. Fluid Mech.* **2013**, *725*, 492–521. [CrossRef]
13. Richard, G.; Gavrilyuk, S. Modelling turbulence generation in solitary waves on shear shallow water flows. *J. Fluid Mech.* **2015**, *773*, 49–74. [CrossRef]
14. Gavrilyuk, S.; Liapidevskii, V.; Chesnokov, A. Spilling breakers in shallow water: Applications to Favre waves and to the shoaling and breaking of solitary waves. *J. Fluid Mech.* **2016**, *808*, 441–468. [CrossRef]
15. Saurel, R.; Pantano, C. Diffuse interface capturing methods for compressible two-phase flows. *Annu. Rev. Fluid Mech.* **2018**, *50*, 105–130. [CrossRef]
16. Marble, F. Dynamics of a gas containing small solid particles. In *Combustion and Propulsion (5th AGARD Colloquium)*; Pergamon Press: Oxford, UK, 1963; p. 175.
17. Baer, M.; Nunziato, J. A two-phase mixture theory for the deflagration-to-detonation transition (DDT) in reactive granular materials. *Int. J. Multiph. Flow* **1986**, *12*, 861–889. [CrossRef]
18. Saurel, R.; Chinnayya, A.; Carmouze, Q. Modelling compressible dense and dilute two-phase flows. *Phys. Fluids* **2017**, *29*, 063301. [CrossRef]
19. Lallemand, M.; Saurel, R. Pressure relaxation procedures for multiphase compressible flows. *Tech. Rep. INRIA Rep.* **2005**. [CrossRef]
20. Forestier, A.; Hérard, J.M.; Louis, X. Solveur de type Godunov pour simuler les écoulements turbulents compressibles. *Comptes Rendus l'Acad. Sci. Paris Série Math.* **1997**, *324*, 919–926. [CrossRef]
21. Saurel, R.; Gavrilyuk, S.; Renaud, F. A multiphase model with internal degrees of freedom: Application to shock–bubble interaction. *J. Fluid Mech.* **2003**, *495*, 283–321. [CrossRef]
22. Lhuillier, D.; Chang, C.; Theofanous, T. On the quest for a hyperbolic effective-field model of disperse flows. *J. Fluid Mech.* **2013**, *731*, 184–194. [CrossRef]
23. Abgrall, R.; Karni, S. Two-Layer shallow water system: A relaxation approach. *SIAM J. Sci. Comput.* **2009**, *31*, 1603–1627. [CrossRef]
24. Gallouet, T.; Masella, J. Un schéma de Godunov approché. *Comptes Rendus l'Acad. Sci. Paris Série Math.* **1996**, *323*, 77–84.

25. Saurel, R.; Petitpas, F.; Berry, R. Simple and efficient relaxation methods for interfaces separating compressible fluids, cavitating flows and shocks in multiphase mixtures. *J. Comput. Phys.* **2009**, *228*, 1678–1712. [CrossRef]
26. Kapila, A.; Menikoff, R.; Bdzil, J.; Son, S.; Stewart, D. Two-Phase modeling of deflagration-to-detonation transition in granular materials: Reduced equations. *Phys. Fluids* **2001**, *13*, 3002–3024. [CrossRef]
27. Chiapolino, A.; Saurel, R.; Nkonga, B. Sharpening diffuse interfaces with compressible fluids on unstructured meshes. *J. Comput. Phys.* **2017**, *340*, 389–417. [CrossRef]
28. Ovsyannikov, L. Two-layer "shallow water" model. *J. Appl. Mech. Tech. Phys.* **1979**, *20*, 127–135. [CrossRef]
29. Kurganov, A.; Petrova, G. Central-Upwind schemes for two-layer shallow water equations. *SIAM J. Sci. Comput.* **2009**, *31*, 1742–1773. [CrossRef]
30. Monjarret, R. Local well-posedness of the two-layer shallow water model with free surface. *SIAM J. Appl. Math.* **2015**, *75*, 2311–2332. [CrossRef]
31. Chinnayya, A.; Daniel, E.; Saurel, R. Modelling detonation waves in heterogeneous energetic materials. *J. Comput. Phys.* **2004**, *196*, 490–538. [CrossRef]
32. Harten, A.; Lax, P.; van Leer, B. On upstream differencing and godunov-type schemes for hyperbolic conservation laws. *SIAM Rev.* **1983**, *25*, 35–61. [CrossRef]
33. Davis, S. Simplified second-order Godunov-type methods. *SIAM J. Sci. Stat. Comput.* **1988**, *9*, 445–473. [CrossRef]
34. Adduce, C.; Sciortino, G.; Proietti, S. Gravity currents produced by lock exchanges: Experiments and simulations with a two-layer shallow-water model with entrainment. *J. Hydraul. Eng.* **2012**, *198*, 111–121. [CrossRef]
35. McQuaid, J.; Roebuck, B. Large scale field trials in dense vapour dispersion, final report to sponsors on the heavy gas dispersion trials at thorney island 1982–84. *Tech. Rep. Health Saf. Exec.* **1985**. [CrossRef]
36. Edgerton, H.E. Shock wave photography of large subjects in daylight. *Rev. Sci. Instrum.* **1958**, *29*, 171–172. [CrossRef]
37. Van der Walt, S.; Schönberger, J.L.; Nunez-Iglesias, J.; Boulogne, F.; Warner, J.D.; Yager, N.; Gouillart, E.; Yu, T. Scikit-Image: Image processing in python. *Peer J.* **2014**, *2*, e453. [CrossRef] [PubMed]
38. Frangi, A.F.; Niessen, W.J.; Vincken, K.L.; Viergever, M.A. Multiscale vessel enhancement filtering. *Int. Conf. Med Image Comput. Comput. Assist. Interv.* **1998**, *1496*, 130–137.
39. Canny, J. A computational approach to edge detection. *IEEE Trans. Pattern Anal. Mach. Intell.* **1986**, *8*, 679–698. [CrossRef] [PubMed]
40. Nielsen, M.; Søren, O. *A Collection of Data from Dense Gas Experiments*; Technical Report Risø-R-845; Risø National Laboratory, Risoe-R, Forskningscenter Risoe: Roskilde, Denmark, 1995.
41. Lord Kelvin Hydrokinetic solutions and observations. *Philos. Mag.* **1871**, *42*, 362–377. [CrossRef]
42. Helmholtz, H. Űber discontinuirliche Flüssigkeitsbewegungen. *Wiss. Abh.* **1882**, *154*, 146–157.
43. Lord Rayleigh Investigation of the character of the equilibrium of an incompressible heavy fluid of variable density. *Sci. Pap.* **1900**, *2*, 200–207.
44. Taylor, G.I. The instability of liquid surfaces when accelerated in a direction perpendicular to their planes. I. *Proc. R. Soc. Lond. Ser.* **1950**, *201*, 192–196.
45. van Leer, B. Towards the ultimate conservative difference scheme. II. Monotonicity and conservation combined in a second-order scheme. *J. Comput. Phys.* **1974**, *14*, 361–370. [CrossRef]

fluids

Article

Stokes Equation in a Semi-Infinite Region: Generalization of the Lamb Solution and Applications to Marangoni Flows

Goce Koleski and Thomas Bickel *

Laboratoire Ondes et Matière d'Aquitaine (UMR 5798), CNRS, University of Bordeaux, F-33400 Talence, France; gocek01@hotmail.fr
* Correspondence: thomas.bickel@u-bordeaux.fr

Received: 1 December 2020; Accepted: 15 December 2020; Published: 18 December 2020

Abstract: We consider the creeping flow of a Newtonian fluid in a hemispherical region. In a domain with spherical or nearly spherical geometry, the solution of the Stokes equation can be expressed as a series of spherical harmonics. However, the original Lamb solution is not complete when the flow is restricted to a semi-infinite space. The general solution in hemispherical geometry is then constructed explicitly. As an application, we discuss the solutions of Marangoni flows due to a local source at the liquid–air interface.

Keywords: Stokes flow; Lamb solution; spherical harmonics; hemispheric Legendre functions; Marangoni and thermocapillary flows

---

1. Introduction

At small length scales, the creeping flow of a Newtonian fluid is described by the linear Stokes equation. Since the latter is directly related to the Laplace equation, it admits a wide variety of analytical solutions that are well documented and constitute the subject of classical textbooks [1,2]. Applications are found in everyday life, ranging from the actuation of micro-organisms [3] to the draining of liquid foams [4] or the wetting dynamics of thin films [5], to name only a few.

Despite these facts, there are still numerous flow problems involving the Stokes equation that remain unresolved. In particular, flows driven by interfacial stresses, such as Marangoni flows, can be especially tenacious [6,7]. The first reason for that comes from the presence of the interface itself, which breaks the symmetry in the direction perpendicular to it. The second reason lies in the fact that Marangoni flows are usually coupled to transport phenomena, leading to intricate relations even in the linear regime [8,9]. It was also suggested in recent experimental studies that the presence of surface-active impurities at the interface might induce hydrodynamic instabilities at vanishing Reynolds numbers [10,11]. There is thus a strong need for a more thorough description of Marangoni flows.

Here, we focus more specifically on the Stokes equation in spherical geometry. The general solution, which was first derived by Lamb [12], can be written as a series of Legendre functions. The situation gets more involved when the flow is restricted to a semi-infinite region. In this case, the solution of Lamb is not complete anymore, and several authors have pointed out that additional terms have to be considered [13,14]. The aim of this work was thus to derive in a systematic manner the solution of the Stokes equation in hemispherical geometry. The paper is organized as follows. In Section 2, we first remind the reader of the main properties of the Lamb solution. We then discuss in Section 3 the thermocapillary flow due to a point-like heat source at the interface. This simple example shows unambiguously that the Lamb solution happens to be incomplete when considering a hemispherical domain. The general solution is then constructed in Section 4, and some applications to thermocapillary flows are given in Section 5. The main results are finally summarized in Section 6.

2. The Stokes Equation in Spherical Coordinates

2.1. Lamb Solution

We consider the viscous flow of an incompressible fluid in a domain with spherical, or nearly spherical, geometry. We note r the radial coordinate, θ the polar angle ($0 \leq \theta \leq \pi$) and φ the azimuthal angle ($0 \leq \varphi < 2\pi$). In the limit of the vanishing Reynolds number, the velocity and pressure fields are governed by the Stokes equation

$$\eta \nabla^2 \mathbf{v} = \boldsymbol{\nabla} p \,, \tag{1}$$

together with the continuity equation

$$\boldsymbol{\nabla} \cdot \mathbf{v} = 0 \,. \tag{2}$$

Due to the linearity of Equations (1) and (2), the general solution can be written as the sum of a homogeneous and a particular solution, $\mathbf{v} = \mathbf{v}_H + \mathbf{v}_P$.

- The homogeneous solution $\mathbf{v}_H$ satisfies the equations $\nabla^2 \mathbf{v}_H = \mathbf{0}$ and $\boldsymbol{\nabla} \cdot \mathbf{v}_H = 0$. It can thus be expressed as the linear combination of a potential and a toroidal field:

  $$\mathbf{v}_H = \boldsymbol{\nabla} \Phi + \boldsymbol{\nabla} \times (\mathbf{r} \chi) \ , \tag{3}$$

  where Φ and χ are both harmonic functions, $\nabla^2 \Phi = \nabla^2 \chi = 0$.
- The particular solution $\mathbf{v}_P$ is related to the theory of harmonic functions as well. By taking the divergence of the equation $\nabla^2 \mathbf{v}_p = \boldsymbol{\nabla} p$ together with $\boldsymbol{\nabla} \cdot \mathbf{v}_p = 0$, it is straightforward to show that the pressure field satisfies the Laplace equation, $\nabla^2 p = 0$.

In spherical coordinates, the solution of the Laplace equation $\nabla^2 \psi = 0$ can be expressed as a series of spherical harmonics. It can be written quite generally as $\psi(r, \theta, \varphi) = \sum_{l=-\infty}^{\infty} \psi_l(r, \theta, \varphi)$, with

$$\psi_l(r, \theta, \varphi) = \sum_{m=-l}^{l} A_{(lm)} r^l Y_l^m(\theta, \varphi) \,. \tag{4}$$

The spherical harmonics of degree l and order m are defined (up to a numerical prefactor) by

$$Y_l^m(\theta, \varphi) = P_l^m(\cos\theta) e^{im\varphi} \,, \tag{5}$$

where the associated Legendre polynomials can be expressed, for instance, by Rodrigues formula:

$$P_l^m(x) = \frac{(-1)^{l+m}}{2^l l!} \left(1 - x^2\right)^{|m|/2} \frac{\mathrm{d}^{l+|m|}}{\mathrm{d}x^{l+|m|}} \left(1 - x^2\right)^l \quad \text{for} \quad l \geq 0 \,. \tag{6}$$

The latter relation states in particular that $Y_l^m = 0$ if $|m| > l$. The definition of Y_l^m can be extended to negative degrees thanks to the equality $Y_l^m = Y_{-l-1}^m$. An essential property of spherical harmonics is that they form an orthogonal basis for scalar functions on the sphere surface.

Coming back to the Stokes equation, we can implement the same decomposition as in Equation (4) for the potential, toroidal and pressure fields, respectively. It is then possible to show that

$$\mathbf{v}(\mathbf{r}) = \sum_{l=-\infty}^{\infty} \left[\frac{(l+3) r^2 \boldsymbol{\nabla} p_l}{2\eta(l+1)(2l+3)} - \frac{\mathbf{r} l p_l}{\eta(l+1)(2l+3)} + \boldsymbol{\nabla} \Phi_l + \boldsymbol{\nabla} \times (\mathbf{r} \chi_l) \right] \,. \tag{7}$$

This expression is usually named after Lamb [12]. It is therefore a series in powers (for $l > 0$) or inverse powers (for $l < 0$) of the distance r. As a matter of fact, the convention $l \leftrightarrow -l-1$ is often assumed for the exterior flows in order to avoid negative indices. The components of the velocity $\mathbf{v} = v_r \boldsymbol{e}_r + v_\theta \boldsymbol{e}_\theta + v_\varphi \boldsymbol{e}_\varphi$ are finally obtained by applying the differential operators in Equation (7).

2.2. Explicit Expression for Exterior Flows

The Lamb solution is relevant to describe the motion of the fluid inside or outside a region with spherical symmetry. In this work, we focus specifically on exterior flows and assume that all fields vanish when $r \to \infty$. The pressure can then be conveniently expressed as

$$p = \eta \sum_{l\geq 1} \sum_m \frac{\pi_{(lm)}}{r^{l+1}} \frac{2(2l-1)}{(l+1)} Y_l^m \,, \tag{8}$$

with $-l \leq m \leq l$. The components of the velocity $\mathbf{v} = v_r \mathbf{e}_r + v_\theta \mathbf{e}_\theta + v_\varphi \mathbf{e}_\varphi$ are given by [1,2]

$$v_r = \sum_{l\geq 1} \sum_m \frac{\pi_{(lm)}}{r^l} Y_l^m + \sum_{l\geq 3} \sum_m \frac{\rho_{(l-2,m)}}{r^l} Y_{l-2}^m \,, \tag{9}$$

$$v_\theta = \sum_{l\geq 1} \sum_m \frac{\pi_{(lm)}}{r^l} \frac{(l-2)}{l(l+1)} s\partial_c Y_l^m + \sum_{l\geq 3} \sum_m \frac{\rho_{(l-2,m)}}{r^l} \frac{1}{(l-1)} s\partial_c Y_{l-2}^m + \sum_{l\geq 2} \sum_m \frac{\sigma_{(l-1,m)}}{r^l} \frac{im}{s} Y_{l-1}^m \,, \tag{10}$$

$$v_\varphi = -\sum_{l\geq 1} \sum_m \frac{\pi_{(lm)}}{r^l} \frac{(l-2)}{l(l+1)} \frac{im}{s} Y_l^m - \sum_{l\geq 3} \sum_m \frac{\rho_{(l-2,m)}}{r^l} \frac{1}{(l-1)} \frac{im}{s} Y_{l-2}^m + \sum_{l\geq 2} \sum_m \frac{\sigma_{(l-1,m)}}{r^l} s\partial_c \mathcal{Y}_{l-1}^m \,, \tag{11}$$

where we have introduced $c = \cos\theta$ and $s = \sin\theta$. Note that our notation differs slightly from that usually found in the literature, since we anticipate the generalization to a semi-infinite region.

As an illustration, let us consider the axisymmetric solutions that decay from the origin as the inverse of the distance. The radial and polar components of velocity field then read $v_r(r,\theta) = \Phi_r^{(0)}(\theta)/r$ and $v_\theta(r,\theta) = \Phi_\theta^{(0)}(\theta)/r$, where the functions $\Phi_r^{(0)}$ and $\Phi_\theta^{(0)}$ are given by

$$\Phi_r^{(0)}(\theta) = \pi_{(10)} P_1^0 \,, \quad \text{and} \quad \Phi_\theta^{(0)}(\theta) = -\frac{\pi_{(10)}}{2} s\partial_c P_1^0 \,, \tag{12}$$

with $P_1^0 = \cos\theta$ and $s\partial_c P_1^0 = \sin\theta$. The integration constant $\pi_{(10)}$ has then to be set by enforcing the relevant boundary conditions.

3. A First Encounter with Hemispheric Legendre Functions

So far, we have made no restriction regarding the polar angle θ. The issue gets more involved, however, when it is limited to part of the interval $[0, \pi]$. Such a situation typically occurs when the fluid is bounded by a flat surface or interface. This encompasses a large number of physical realizations, ranging from a droplet placed on a solid surface to the motion of a camphor scrap at the water–air interface. In a semi-infinite domain, Lamb's solution is not complete anymore, and several authors have recently derived additional terms to complement Equation (7). To illustrate our point, we first discuss a classic problem of fluid mechanics: the steady-state Marangoni flow due to a local heat source at the liquid–air interface [13].

3.1. Thermocapillary Flow Due to a Point Source

We study the stationary heat flow induced by a source located at $z = 0$. This can be achieved, for instance, with a colloidal particle heated by a laser beam [15]. Assuming that the size of the source is small compared to the other relevant length-scales, heat may be regarded as emerging from a point source $q(\mathbf{r}) = Q\delta(\mathbf{r})$, with Q the injected power ($[Q] = W$), in a semi-infinite liquid bounded by a flat interface. The z-axis is perpendicular to the interface and oriented downward; the liquid phase corresponds to $z > 0$. The system is schematically shown in Figure 1. We assume that the temperature variations are small enough so that both the viscosity and the fluid density can be regarded as constant.

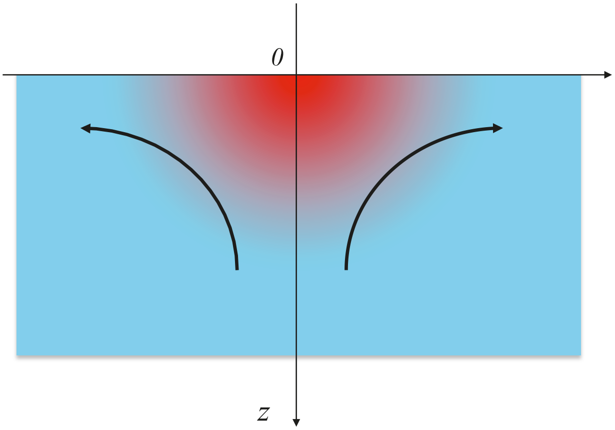

Figure 1. Schematic representation of the system. The temperature gradient induces horizontal stresses that drive the fluid from the hot to the cold areas of the interface. The z-axis is oriented downward.

The discussion is restricted to the linearized version of the transport equations; i.e., we focus on the limits of vanishing Reynolds and Péclet numbers. The temperature field is then solution of the heat equation

$$\rho c \partial_t T = \kappa \nabla^2 T + Q\delta(\mathbf{r}) \,, \tag{13}$$

with κ being the thermal conductivity ($[\kappa] = \mathrm{W} \cdot \mathrm{m}^{-1} \cdot \mathrm{K}^{-1}$), ρ the mass density ($[\rho] = \mathrm{kg} \cdot \mathrm{m}^{-3}$) and c the specific heat capacity ($[c] = \mathrm{J} \cdot \mathrm{K}^{-1} \cdot \mathrm{kg}^{-1}$) of the fluid. Here, δ is the Dirac delta function ($[\delta(\mathbf{r})] = \mathrm{m}^{-3}$ in 3D). We focus in this work on the stationary version of the heat equation

$$\nabla^2 T = -\frac{Q}{\kappa}\delta(\mathbf{r}) \,. \tag{14}$$

The results presented hereafter are thus valid in the long time limit $r \ll \sqrt{Dt}$, with $D = \kappa/(\rho c)$ being the thermal diffusion coefficient. The velocity field satisfies the incompressible Stokes equation (Equations (1) and (2)). Regarding the boundary conditions, it is assumed that there is neither mass nor heat flux across the interface

$$\mathbf{v} \cdot \boldsymbol{e}_z = 0 \quad \text{and} \quad \boldsymbol{\nabla} T \cdot \boldsymbol{e}_z = 0 \quad \text{at} \quad z = 0 \,, \tag{15}$$

whereas both the velocity and the temperature return to their equilibrium values far away from the disturbance

$$\lim_{r\to\infty} \mathbf{v}(\mathbf{r}) = \mathbf{0} \quad \text{and} \quad \lim_{r\to\infty} T(\mathbf{r}) = T_0 \,. \tag{16}$$

Finally, since the surface tension is usually a decreasing function of the temperature, the actuation of the fluid arises from stresses at the interface. This is expressed by the Marangoni boundary condition, which relates the shear stress and the gradient of interfacial tension

$$(\mathbf{1} - \mathbf{e}_z\mathbf{e}_z) \cdot (\boldsymbol{\sigma} \cdot \mathbf{e}_z - \boldsymbol{\nabla}\gamma)\Big|_{z=0} = 0 \,, \tag{17}$$

with σ the hydrodynamic stress tensor (whose Cartesian components are $\sigma_{ij} = -p\delta_{ij} + \eta\left(\partial_i v_j + \partial_j v_i\right)$). For moderate deviations with respect to the equilibrium temperature, one can assume a linearized relationship for the surface tension: $\gamma(T) = \gamma_0 - \gamma_T(T - T_0)$, with $\gamma_0 = \gamma(T_0)$. The coefficient $\gamma_T = |\partial\gamma/\partial T|$ characterizes the rate of change of surface tension with respect to temperature.

3.2. Solution of the Transport Equations

The mathematical problem defined by Equations (14)–(17) is solved in the semi-infinite region $z > 0$. First, the temperature field can be derived by analogy with electrostatics. Indeed, Equation (14) is equivalent to the Poisson equation for the electrostatic potential due to a point charge. One therefore gets

$$T(\mathbf{r}) = T_0 + \frac{Q}{2\pi\kappa r} \,. \tag{18}$$

Note that the numerical coefficient differs from the usual value (2π vs. 4π) since heat diffusion is restricted to a half-space. Note also that this solution is only valid down to a cut-off distance set by the size of the physical heat source.

Next, Equation (17) suggests that the velocity fields follows the same power law as the temperature. We can therefore search for solutions of the Stokes equations (Equations (1) and (2)) in the form $v_r(r,\theta) = \Phi_r(\theta)/r$ and $v_\theta(r,\theta) = \Phi_\theta(\theta)/r$. After some algebra, one obtains

$$\Phi_r(\theta) = \frac{Q\gamma_T}{4\pi\kappa\eta}(1 - 2\cos\theta)\,, \quad \text{and} \quad \Phi_\theta(\theta) = \frac{Q\gamma_T}{4\pi\kappa\eta}\frac{\cos\theta\sin\theta}{1+\cos\theta}\,. \tag{19}$$

At first sight, the connection between the θ-dependence in Equation (19) and the generic Lamb solution (Equation (12)) is not striking. Still, it can be noticed that the function $\Phi_r(\theta)$ can also be written as

$$\Phi_r(\theta) = \alpha P_1^0(c) - \frac{\alpha}{2}\,, \tag{20}$$

with $P_1^0(c) = c = \cos\theta$ and $\alpha = -Q\gamma_T/(2\pi\kappa\eta)$. Similarly, $\Phi_\theta(\theta)$ can be re-expressed as

$$\Phi_\theta(\theta) = -\frac{\alpha}{2}s\partial_c P_1^0 + \frac{\alpha}{2}\sqrt{\frac{1-c}{1+c}}\,, \tag{21}$$

with $s\partial_c P_1^0 = s = \sin\theta$. In both expressions, the first term involves an associated Legendre function (or its derivative) with $l = 1$ and $m = 0$, as expected from Lamb's solution (12). The second term, which is not present in Equation (12), is more puzzling. Let us focus, for instance, on the expression (21) for Φ_θ: although the second term is well defined in the upper half-space $0 \leq c \leq 1$, it is obviously singular in the limit $c \to -1$. Since the original Lamb solution only involves functions that are regular in the full range $-1 \leq c \leq 1$, this contribution is necessarily missing from the general solution. As we shall see in the following, the additional terms in Equations (20) and (21) can actually be defined as hemispheric Legendre functions.

4. Laplace and Stokes Equations in a Semi-Infinite Region

As argued in Section 2, the solution of the Stokes equation is closely related to the theory of harmonic functions. In this section, we first focus on Laplace equation in order to introduce generalized spherical harmonics. The derivation follows closely that of reference [16]. We then discuss how to extend Lamb's solution in a semi-infinite domain.

4.1. Method of Separation of Variables Applied to Laplace Equation

Let us consider the Laplace equation $\nabla^2\psi(\mathbf{r}) = 0$ satisfied by a real scalar function ψ. The position vector $\mathbf{r} = (r, \theta, \varphi)$ is restricted to the upper half-space $z \geq 0$, which corresponds to the interval $0 \leq \theta \leq \pi/2$. Results pertaining to the lower half-space $z \leq 0$ can be deduced in a straightforward manner thanks to the symmetry $\theta \leftrightarrow \pi - \theta$.

In spherical polar coordinates, the Laplace equation reads

$$\nabla^2\psi = \frac{1}{r^2}\frac{\partial}{\partial r}\left(r^2\frac{\partial\psi}{\partial r}\right) + \frac{1}{r^2\sin\theta}\frac{\partial}{\partial\theta}\left(\sin\theta\frac{\partial\psi}{\partial\theta}\right) + \frac{1}{r^2\sin^2\theta}\frac{\partial^2\psi}{\partial\varphi^2} = 0\,. \tag{22}$$

This equation can be solved using the method of separation of variables. To that end, we seek a general solution of the form $\psi(r,\theta,\varphi) = f(r)g(\theta)h(\varphi)$, where f, g and h are functions of a single variable. Equation (22) then leads to a set of ordinary differential equations

$$\frac{\mathrm{d}}{\mathrm{d}r}\left(r^2\frac{\mathrm{d}f}{\mathrm{d}r}\right) - \lambda f = 0\,, \tag{23}$$

$$\frac{1}{\sin\theta}\frac{\mathrm{d}}{\mathrm{d}\theta}\left(\sin\theta\frac{\mathrm{d}g}{\mathrm{d}\theta}\right) + \left(\lambda - \frac{\mu}{\sin^2\theta}\right)g = 0\,, \tag{24}$$

$$\frac{\mathrm{d}^2h}{\mathrm{d}\varphi^2} + \mu h = 0\,, \tag{25}$$

where λ and μ are two (yet unknown) constants.

We first consider the radial Equation (23). Without loss of generality, we can set $\lambda = l(l+1)$. Searching for power-law solutions, one readily gets

$$f(r) = Ar^l + Br^{-l-1}\,, \tag{26}$$

where A and B are two integration constants. In the particular case $l = -1/2$, the general solution (26) has to be replaced by $f(r) = Ar^{-1/2} + Br^{-1/2}\ln r$.

We next focus on the azimuthal Equation (25). On physical grounds, one requires the function h to be single-valued. Since (r,θ,φ) and $(r,\theta,\varphi+2\pi)$ represent the same location in space, the condition $h(\varphi+2\pi) = h(\varphi)$ demands that $\mu = m^2$, with m being an integer. We write the solution of Equation (25) as

$$h(\varphi) = e^{im\varphi}\,, \quad \text{with} \quad m \in \mathbb{Z}\,. \tag{27}$$

4.2. Hemispheric Legendre Functions

Regarding Equation (24), it can be recast in a more usual form by setting $c = \cos\theta$. Since we focus on the semi-infinite region $0 \le \theta \le \pi/2$, the variable c is always positive: $0 \le c \le 1$. Equation (24) is then equivalent to Legendre differential equation

$$(1-c^2)\frac{\mathrm{d}^2g}{\mathrm{d}c^2} - 2c\frac{\mathrm{d}g}{\mathrm{d}c} + \left[l(l+1) - \frac{m^2}{1-c^2}\right]g(c) = 0\,. \tag{28}$$

In the situations commonly encountered in physics, e.g., in quantum mechanics or in fluid mechanics, one is interested in solutions of Equation (28) that are regular over the entire interval $c \in [-1,1]$. These standard solutions are the well-known associated Legendre functions $P_l^m(c)$ defined in Section 2. In this work, however, the regularity condition is only required in the semi-infinite region $\mathcal{I}^+ = [0,1]$. Additional solutions, which can be singular on the complementary interval $\mathcal{I}^- = [-1,0]$, are therefore permitted. The essential point is that the extra singularities that may exist in $\mathcal{I}^-$ are physically irrelevant, since we exclusively focus on the interval $\mathcal{I}^+$. Although this issue is fairly well established in classical physics, e.g., in the context of the sharp point effect in electrostatics [17], we consider it worth it to remind the reader of the main steps of the derivation—see Appendix A. The general solution of Equation (28) is therefore $g(c) = \mathcal{P}_l^m(c)$, where the hemispheric Legendre functions are defined as

$$\mathcal{P}_l^m(c) = \left(\frac{1-c}{1+c}\right)^{|m|/2} F\left(-l, l+1; 1+|m|; \frac{1-c}{2}\right)\,, \quad c \in [0,1]\,, \tag{29}$$

where the hypergeometric function F is given by the series

$$F(\alpha, \beta; \gamma; x) = \sum_{n=0}^{\infty} \frac{(\alpha)_n (\beta)_n}{(\gamma)_n} \frac{x^n}{n!} , \tag{30}$$

with $(q)_n$ being the Pochhammer symbol: $(q)_n = q(q+1)\ldots(q+n-1)$ for $n > 0$, and $(q)_0 = 1$. The main properties of the hypergeometric function are listed in Appendix A.

In Equation (29), the degree l can assume any real value. Working in a semi-infinite region thus implies a rather unconventional definition of the associated Legendre functions. For $0 \leq |m| \leq l$, they coincide (up to a numerical prefactor) with the "usual" functions $P_l^m(c)$ defined in (6)—see Table 1. However, since the series (30) actually converges for all $c \in [0, 1]$, there is no restriction regarding the order m anymore. Solutions with $l < |m|$ do exist as well, although this is normally forbidden in $\mathbb{R}^3$. This assertion is of paramount importance, since these additional terms play a central role in accounting for interfacial phenomena such as the Marangoni effect. It can be noticed that the generalized Legendre functions with $|m| > l$ are proportional to $(1+c)^{-|m|/2}$. These functions are indeed regular in the semi-infinite region $0 \leq c \leq 1$, but would be otherwise singular over the whole interval $-1 \leq c \leq 1$. To illustrate our point, the first hemispheric Legendre functions are listed in Table 1.

Table 1. Expressions of the first hemispheric Legendre functions $\mathcal{P}_l^m(c)$ for $c > 0$.

	$m = 0$	$m = 1$	$m = 2$	$m = 3$
$l = 0$	1	$\left(\frac{1-c}{1+c}\right)^{1/2}$	$\frac{1-c}{1+c}$	$\left(\frac{1-c}{1+c}\right)^{3/2}$
$l = 1$	c	$\frac{1}{2}\left(1-c^2\right)^{1/2}$	$\frac{1}{3}(2+c)\left(\frac{1-c}{1+c}\right)$	$\frac{1}{4}(3+c)\left(\frac{1-c}{1+c}\right)^{3/2}$
$l = 2$	$\frac{1}{2}(3c^2-1)$	$\frac{1}{2}c\left(1-c^2\right)^{1/2}$	$\frac{1}{4}(1-c^2)$	$\frac{1}{20}(8+9c+3c^2)\left(\frac{1-c}{1+c}\right)^{3/2}$

Finally, the general solution of Laplace equation $\nabla^2\psi(\mathbf{r}) = 0$ can be written in spherical coordinates as

$$\psi(r, \theta, \varphi) = \int_{-\infty}^{\infty} \mathrm{d}l \sum_{m=-\infty}^{\infty} A_{(lm)} r^l \mathcal{Y}_l^m(\theta, \varphi) . \tag{31}$$

Here, we define the hemispheric spherical harmonics

$$\mathcal{Y}_l^m(\theta, \varphi) = \mathcal{P}_l^m(c) e^{im\varphi} , \tag{32}$$

with $\mathcal{P}_l^m(c)$ being given in Equation (29). The first difference between the solution (4) in $\mathbb{R}^3$ and Equation (31) in the semi-infinite region $0 \leq c \leq 1$ is that the sum now extends to any value of m, be it smaller or larger than the degree l. The second difference is that the degree l varies continuously, the sum being replaced by an integral. Note also that the functions $\mathcal{Y}_l^m$ (or $\mathcal{P}_l^m$) are in general not orthogonal on the half-sphere $0 \leq c \leq 1$ (although orthogonality is preserved regarding the azimuthal angle φ).

4.3. Generalized Solution for Exterior Flows

We now have all the elements to extend the Lamb solution to a hemispheric region. Two strategies are possible. The first is to directly transpose the solution given by Equations (8)–(11), provided the correspondence with $Y_l^m \Leftrightarrow \mathcal{Y}_l^m$ and

$$\sum_{l \geq l_0} \sum_{m=-l}^{l} \cdots \quad \Leftrightarrow \quad \int_0^{\infty} \mathrm{d}l \sum_{m=-\infty}^{\infty} \cdots , \tag{33}$$

with $l_0 = 1, 2$ or 3. As we shall see, this approach works for all but a few terms of the series. The second strategy consists of solving explicitly the Stokes equation. This gives of course the same results, but with the advantage that singular contributions can be handled consistently. Details regarding the algebra are given in Appendix B. Focusing as previously on the exterior solution, we find that the pressure and the components of the velocity can be written as

$$p(r,\theta,\varphi) = \int_0^\infty \mathrm{d}l \sum_{m=-\infty}^{\infty} \frac{1}{r^{l+1}} p_{lm}(c) e^{im\varphi} \, , \tag{34}$$

$$v_r(r,\theta,\varphi) = \int_0^\infty \mathrm{d}l \sum_{m=-\infty}^{\infty} \frac{1}{r^{l}} u_{lm}(c) e^{im\varphi} \, , \tag{35}$$

$$v_\theta(r,\theta,\varphi) = \int_0^\infty \mathrm{d}l \sum_{m=-\infty}^{\infty} \frac{1}{r^{l}} v_{lm}(c) e^{im\varphi} \, , \tag{36}$$

$$v_\varphi(r,\theta,\varphi) = \int_0^\infty \mathrm{d}l \sum_{m=-\infty}^{\infty} \frac{1}{r^{l}} w_{lm}(c) e^{im\varphi} \, , \tag{37}$$

where we get

$$p_{lm}(c) = \pi_{(lm)} \frac{2(2l-1)}{(l+1)} \mathcal{P}_l^m \, . \tag{38}$$

$$u_{lm}(c) = \pi_{(lm)} \mathcal{P}_l^m + \rho_{(l-2,m)} \mathcal{P}_{l-2}^m \, , \tag{39}$$

$$v_{lm}(c) = \pi_{(lm)} \frac{(l-2)}{l(l+1)} s\partial_c \mathcal{P}_l^m + \rho_{(l-2,m)} \frac{1}{(l-1)} s\partial_c \mathcal{P}_{l-2}^m + \sigma_{(l-1,m)} \frac{im}{s} \mathcal{P}_{l-1}^m \, , \tag{40}$$

$$w_{lm}(c) = -\pi_{(lm)} \frac{(l-2)}{l(l+1)} \frac{im}{s} \mathcal{P}_l^m - \rho_{(l-2,m)} \frac{1}{(l-1)} \frac{im}{s} \mathcal{P}_{l-2}^m + \sigma_{(l-1,m)} s\partial_c \mathcal{P}_{l-1}^m \, , \tag{41}$$

Equations (34)–(41) are the main outcomes of this work. They express the exterior solution of a Stokes flow as a straightforward generalization of the original Lamb solution. Still, there are a few terms in the series that are singular and should therefore be handled separately.

4.3.1. Polar and Azimuthal Components of the Velocity for $l = 1$ and $m \neq 0$.

It can be noticed in Equations (40) and (41) that both the polar and azimuthal components of the velocity are not properly defined for $l = 1$. To regularize the expressions, we need to solve explicitly the incompressible Stokes equations. This can be achieved by appealing the recurrence relations of Legendre functions. The main steps of the derivation are given in Appendix B, so that we directly get the results

$$v_{1m}(c) = -\frac{\pi_{(1m)}}{2} s\partial_c \mathcal{P}_1^m + (1+|m|)\rho_{(-1,m)} \frac{\mathcal{P}_1^m}{s} + \sigma_{(0,m)} \frac{im}{s} \mathcal{P}_0^m \, , \tag{42}$$

$$w_{1m}(c) = \frac{\pi_{(1m)}}{2} \frac{\partial_\varphi \mathcal{P}_l^m}{s} + \frac{is}{m} \rho_{(-1,m)} \left[\mathcal{P}_0^m - (1+|m|)\partial_c \mathcal{P}_1^m\right] + \sigma_{(0,m)} s\partial_c \mathcal{P}_0^m \, . \tag{43}$$

4.3.2. Polar Component of the Velocity for $l = 1$ and $m = 0$.

As a matter of fact, Equation (42) is still singular when the order m is equal to zero. To remove this very last singularity, we proceed as previously and solve directly the differential equations—see Appendix B. We obtain the explicit expression

$$v_{10}(c) = -\frac{\pi_{(10)}}{2} s - \rho_{(-1,0)} \sqrt{\frac{1-c}{1+c}} \, , \tag{44}$$

Regarding the azimuthal component for $m = 0$, one can deduce from Equation (41) that $w_{l0}(\theta,\varphi) = \sigma_{(l-1,0)} s\partial_c \mathcal{Y}_{l-1}^0$, so that finally $w_{10}(\theta,\varphi) = 0$.

5. Application of the Generalized Lamb Solution to Marangoni Flows

Bringing everything together, we finally reach the conclusion that the generalized exterior solution for the Stokes flow is given by Equations (34)–(41), supplemented with Equations (42)–(44) for $l = 1$. We now apply these results to thermocapillary flows.

5.1. Back to the First Encounter

In Section 3, we discussed the thermocapillary flow due to a point source at the liquid–air interface. At the vanishing Péclet number, the temperature field is found to decay as r^{-1}; see Equation (18). The Marangoni boundary condition then suggests that the velocity field assumes the same functional form: $v_r(r, \theta) = \Phi_r(\theta)/r$ and $v_\theta(r, \theta) = \Phi_\theta(\theta)/r$. Keeping only the terms proportional to r^{-1} in the generalized exterior solution, we can directly write

$$\Phi_r(\theta) = \pi_{(10)} c + \rho_{(-1,0)} \,, \tag{45}$$

$$\Phi_\theta(\theta) = -\frac{\pi_{(10)}}{2} s - \rho_{(-1,0)} \sqrt{\frac{1-c}{1+c}} \,. \tag{46}$$

If we enforce the condition of vanishing normal velocity at the interface, i.e., $v_\theta(r, \frac{\pi}{2}) = 0$, then the integration constants are related through $\pi_{(10)} = -2\rho_{(-1,0)}$. The solution then reads

$$\Phi_r(\theta) = \rho_{(-1,0)} (1 - 2c) \,, \tag{47}$$

$$\Phi_\theta(\theta) = \rho_{(-1,0)} \frac{cs}{1+c} \,, \tag{48}$$

which is precisely the result given in Equation (19). The remaining constant can be set by enforcing the stress continuity condition (17). We get $\rho_{(-1,0)} = Q\gamma_T/(4\pi\kappa\eta)$, as expected.

5.2. Thermocapillary Flow with Dipolar Symmetry

As a second example, we consider the self-propulsion of a heated particle at the water–air interface. This question has recently attracted much attention, both theoretically and experimentally [14,15,18]. The particle acts as a point-like heat source. It is assumed that the temperature profile in the liquid phase has a dipolar symmetry

$$T(\mathbf{r}) = T_0 + \frac{Q}{2\pi\kappa} \left(\frac{1}{r} + \frac{\mathbf{b} \cdot \mathbf{r}}{r^3} \right) \,, \tag{49}$$

with $\mathbf{b} = b\mathbf{e}_x$. The resulting thermocapillary flow is solution of the Stokes equations (Equations (1) and (2)) together with the Marangoni boundary condition (17). The explicit expression for the velocity field was obtained in reference [14] after tedious calculations. Here, we can get it directly from the generalized Lamb solution. According to the superposition principle, the velocity field can be written as

$$\mathbf{v}(\mathbf{r}) = \mathbf{v}_{10}(\mathbf{r}) + b\mathbf{v}_{21}(\mathbf{r}); \tag{50}$$

the axisymmetric term $\mathbf{v}_{10}$ has been discussed in the previous paragraph. It is then straightforward to get the dipolar contribution

$$u_{2,1}(c) = \pi_{(2,1)} \mathcal{P}_2^1(c) + \rho_{(0,1)} \mathcal{P}_0^1(c) = \frac{1}{2s} \left[2\rho_{(0,1)} + \left(\pi_{(2,1)} - 2\rho_{(0,1)} \right) c - \pi_{(2,1)} c^3 \right] \,, \tag{51}$$

$$v_{2,1}(c) = s\rho_{(0,1)} \partial_c \mathcal{P}_0^1 + \frac{i}{s} \sigma_{(1,1)} \mathcal{P}_1^1(c) = \frac{i\sigma_{(1,1)}}{2} - \rho_{(0,1)} \frac{1}{1+c} \,, \tag{52}$$

$$w_{2,1}(c) = -\frac{i}{s} \rho_{(0,1)} \mathcal{P}_0^1(c) + s\sigma_{(1,1)} \partial_c \mathcal{P}_1^1 = -i \left[\rho_{(0,1)} \frac{1}{1+c} - \frac{i\sigma_{(1,1)}}{2} c \right] \,. \tag{53}$$

This solution matches exactly with the one that was calculated previously, see Equation (4.6) in reference [14].

6. Conclusions

To summarize, we have derived a generalization of Lamb's solution for the Stokes flow in a semi-infinite domain. Equations (38)–(44) are the main results of this work. This new solution is relevant, for instance, when the liquid phase is bounded by a flat interface, or in the case of a hemispherical liquid drop moving on an inhomogeneous surface. The range of applications is therefore relatively wide.

We emphasize that, although our results look quite similar to the original Lamb solution, they present several features that are rather unconventional. First of all, the degree l is not limited to integers but is in general a real number. Second, the order m is not limited to the interval $-l \leq m \leq l$ but can take values larger than the degree l. These peculiarities are directly related to the fact that the flow is restricted to a semi-infinite region.

The expression of the velocity components (38)–(44) can be used directly for any problem with hemispherical geometry, exactly as one would proceed with Lamb's solution. As shown in Section 5, it is especially well suited for interfacial phenomena involving the Marangoni effect. We thus expect that this formalism might shed a new light on several important issues in interfacial science, including the spreading of surfactant from a point source or the actuation of Marangoni surfers.

Author Contributions: Conceptualization, methodology, validation, writing—original draft preparation, writing—review and editing, project administration and funding acquisition: T.B. Investigation and formal analysis: G.K. and T.B. All authors have read and agreed to the published version of the manuscript.

Funding: We gratefully acknowledge the University of Bordeaux and its "Initiative d'Excellence" program for financial support.

Acknowledgments: The authors wish to thank S. Michelin, F. Nadal and A. Würger for many useful and fruitful discussions.

Conflicts of Interest: The authors declare no conflict of interest.

Appendix A. From Legendre to Gauss Hypergeometric Equation

In this appendix, we follow reference [16] to construct the general solutions of the associated Legendre equation in a semi-infinite region

$$(1-c^2)\frac{\mathrm{d}^2 g}{\mathrm{d}c^2} - 2c\frac{\mathrm{d}g}{\mathrm{d}c} + \left[l(l+1) - \frac{m^2}{1-c^2}\right] g(c) = 0\,. \tag{A1}$$

First, it should be noticed that Equation (A1) admits three regular singular points at $c = 1$, $c = -1$ and $c = +\infty$, respectively. As a consequence, it is always possible to recast Equation (A1) into Gauss hypergeometric equation [16]

$$x(1-x)y''(x) + [\gamma - (\alpha+\beta+1)x]\,y'(x) - \alpha\beta y(x) = 0\,, \tag{A2}$$

where α, β and γ are three real (yet unknown) parameters. A fundamental solution of Equation (A2) is given by the hypergeometric function $F(\alpha,\beta;\gamma;x)$, which is defined as

$$F(\alpha,\beta;\gamma;x) = \sum_{n=0}^{\infty} \frac{(\alpha)_n(\beta)_n}{(\gamma)_n}\frac{x^n}{n!} = \frac{\Gamma(\gamma)}{\Gamma(\alpha)\Gamma(\beta)} \sum_{n=0}^{\infty} \frac{\Gamma(\alpha+n)\Gamma(\beta+n)}{\Gamma(\gamma+n)}\frac{x^n}{n!}\,, \tag{A3}$$

with $(q)_n = q(q+1)\ldots(q+n-1)$ the Pochhammer symbol [$(q)_0 = 1$], and $\Gamma(x) = \int_0^\infty t^{x-1}e^{-t}dt$ the gamma function. The hypergeometric function verifies the symmetry relation:

$$F(\alpha,\beta;\gamma;x) = F(\beta,\alpha;\gamma;x)\,. \tag{A4}$$

The radius of convergence of the series is $R = 1$. The series reduces to a polynomial of degree $l \in \mathbb{N}$ when either α or β is equal to $-l$.

The solution of Equation (A2) being known, the issue is to find the mathematical transformation that relates Equations (A1) and (A2). To this end, we make the substitution $g(c) = \chi(x)y(x)$, with $\chi(x)$ being an auxiliary function such that $y(x)$ is solution of Equation (A2). We also define the new variable $x = (1-c)/2$. Inserting in Equation (A1), one gets an intermediate differential equation for y

$$x(1-x)\chi y'' + \Big[2x(1-x)\chi' + (1-2x)\chi\Big]y' \\ + \left\{x(1-x)\chi'' + (1-2x)\chi' + \left(l(l+1) - \frac{m^2}{4x(1-x)}\right)\chi\right\} y = 0\,. \tag{A5}$$

On comparing the second and first-order terms with those in Equation (A2), one can infer that the term in square brackets must be proportional to χ. Without loss of generality, one can always absorb any overall constant factor in the definition of y. We thus obtain a first equation for χ

$$2x(1-x)\chi' + (1-2x)\chi = [\gamma - (\alpha+\beta+1)x]\,\chi\,, \tag{A6}$$

whose solution reads

$$\chi(x) = x^{(\gamma-1)/2}(1-x)^{(\alpha+\beta-\gamma)/2}\,. \tag{A7}$$

Then, comparison of the zeroth-order terms in Equations (A2) and (A5) imposes that the term in curly brackets must be proportional to χ as well

$$x(1-x)\chi'' + (1-2x)\chi' + \left\{l(l+1) - \frac{m^2}{4x(1-x)}\right\}\chi = -\alpha\beta\chi\,. \tag{A8}$$

Inserting the solution (A7) into Equation (A8), we can deduce that

$$\gamma - 1 = \epsilon_1|m|\,, \quad \alpha+\beta-\gamma = \epsilon_2|m|\,, \quad \text{and} \quad \alpha\beta = -l(l+1)\,. \tag{A9}$$

Here we define $\epsilon_i = \pm 1$. The problem therefore admits four independent solutions. For the discussion, it is convenient to switch back to the original variable c.

- If $\epsilon_1 = \epsilon_2 = +1$, then the auxiliary function reads $\chi(c) = \frac{1}{4}(1-c^2)^{|m|/2}$. This is the canonical definition usually adopted in the literature (see, e.g., reference [16]) in order to account for the regularity condition over the whole interval $c \in [-1, 1]$.
- If $\epsilon_1 = +1$ and $\epsilon_2 = -1$, then we get

  $$\chi(c) = \left(\frac{1-c}{1+c}\right)^{|m|/2}\,. \tag{A10}$$

  This function has a singularity at the south pole $c = -1$, but is regular otherwise. It is thus relevant in the upper half-space.
- If $\epsilon_1 = -1$ and $\epsilon_2 = +1$, we obtain $\chi(c) = [(1+c)/(1-c)]^{|m|/2}$. The singularity is now located at the north pole $c = 1$. This configuration being complementary to the previous one, it is suitable in the lower half-space.
- If $\epsilon_1 = \epsilon_2 = -1$, the auxiliary function $\chi(c) = 4(1-c^2)^{-|m|/2}$ is singular at both poles. It is therefore inappropriate with regard to the semi-infinite domains discussed in this work.

In the upper half-space, the relevant choice is then $\epsilon_1 = +1$ and $\epsilon_2 = -1$. It follows from Equation (A9) that the three Gauss parameters are

$$\alpha = -l\,, \quad \beta = l+1\,, \quad \text{and} \quad \gamma = |m|+1\,. \tag{A11}$$

Finally, the solutions of Equation (A1) are the generalized Legendre functions, defined for $c \in [0,1]$ by

$$\mathcal{P}_l^m(c) = \left(\frac{1-c}{1+c}\right)^{|m|/2} F\left(-l, l+1; |m|+1; \frac{1-c}{2}\right) . \tag{A12}$$

In the complementary interval $c \in [-1,0]$, the solutions are obtained thanks to the substitution $c \leftrightarrow -c$. It can be noted that the generalized Legendre functions satisfy the condition

$$\mathcal{P}_{-(l+1)}^m(c) = \mathcal{P}_l^m(c) . \tag{A13}$$

They also verify the following properties: (i) they are eigenfunctions of the differential operator $\mathcal{L}$

$$\mathcal{L}\mathcal{P}_l^m(c) \doteq \left[(1-c^2)\partial_c^2 - 2c\partial_c - \frac{m^2}{(1-c^2)}\right]\mathcal{P}_l^m(c) = -l(l+1)\mathcal{P}_l^m(c) . \tag{A14}$$

Note that one also has

$$\mathcal{L}\left[c\mathcal{P}_l^m\right] = -(l^2+l+2)c\mathcal{P}_l^m + 2(1-c^2)\frac{\mathrm{d}\mathcal{P}_l^m}{\mathrm{d}c} . \tag{A15}$$

They follow the recurrence relations

$$\left(1-c^2\right)\frac{\mathrm{d}\mathcal{P}_l^m}{\mathrm{d}c} = (l-|m|)\,\mathcal{P}_{l-1}^m(c) - lc\mathcal{P}_l^m(c) , \tag{A16}$$

$$\left(1-c^2\right)\frac{\mathrm{d}\mathcal{P}_l^m}{\mathrm{d}c} = -\left(l+|m|+1\right)\mathcal{P}_{l+1}^m(c) + (l+1)c\mathcal{P}_l^m(c) . \tag{A17}$$

Appendix B. Solutions of the Stokes Problem in a Semi-Infinite Region

The aim of this second appendix is to derive explicitly the solution of the Stokes equations (Equations (1) and (2)) in the semi-infinite region defined by $c = \cos\theta \geq 0$. The parameter $s = \sin\theta = \sqrt{1-c^2}$ is always positive since $\theta \in [0,\pi]$. Note also that $\partial_\theta = -s\partial_c$ and $\mathrm{d}s/\mathrm{d}c = -c/s$. In this representation, Equation (2) reads

$$\frac{1}{r^2}\partial_r\left(r^2 v_r\right) - \frac{1}{r}\partial_c(s v_\theta) + \frac{1}{sr}\partial_\varphi v_\varphi = 0 . \tag{A18}$$

The projection of the Stokes equations on the spherical basis $\left(\mathbf{e}_r, \mathbf{e}_\theta, \mathbf{e}_\varphi\right)$ leads to a set of partial differential equations that are listed, for instance, in [19]. We then look for solutions using the Anzats suggested in Equations (34)–(37).

Appendix B.1. Pressure Field

The pressure $p(\mathbf{r})$ satisfies Laplace equation $\Delta p = 0$, where we define the scalar Laplacian

$$\Delta\psi = r^{-1}\partial_r^2(r\psi) + r^{-2}\partial_c\left(s^2\partial_c\psi\right) + (rs)^{-2}\partial_\varphi^2\psi . \tag{A19}$$

By inserting the Ansatz $p(r,\theta,\varphi) = r^{-(l+1)}p_{lm}(c)e^{im\varphi}$, one obtains the Legendre differential equation for each mode $p_{lm}(c)$

$$(1-c^2)\frac{\mathrm{d}^2 p_{lm}}{\mathrm{d}c^2} - 2c\frac{\mathrm{d}p_{lm}}{\mathrm{d}c} + \left[l(l+1) - \frac{m^2}{1-c^2}\right]p_{lm}(c) = 0 . \tag{A20}$$

Following the discussion of Appendix A, it is straightforward to conclude that

$$p_{lm}(c) = \frac{2(2l-1)}{l+1}\pi_{(l,m)}\mathcal{P}_l^m(c) , \tag{A21}$$

with $\pi_{(lm)}$ being the integration constant. Here, the prefactor $2(2l-1)/(l+1)$ is introduced for later convenience.

Appendix B.2. Radial Component of the Velocity

The radial projection of the Stokes Equation (1) reads

$$\Delta v_r - \frac{2}{r^2} v_r + \frac{2}{r^2} \partial_c \left(s v_\theta\right) - \frac{2}{s r^2} \partial_\varphi v_\varphi = \frac{1}{\eta} \partial_r p \, . \tag{A22}$$

Then, eliminating v_θ and v_φ thanks to Equation (A18), one gets

$$\Delta v_r - \frac{2}{r^2} v_r + \frac{2}{r^3} \partial_r \left(r^2 v_r\right) = \frac{1}{\eta} \partial_r p \, . \tag{A23}$$

We then assume the functional form $v_r(r,\theta,\varphi) = r^{-l} u_{lm}(c) e^{im\varphi}$, so that each mode satisfies the following equation

$$(1-c^2)\frac{\mathrm{d}^2 u_{lm}}{\mathrm{d}c^2} - 2c\frac{\mathrm{d}u_{lm}}{\mathrm{d}c} + \left[(l-2)(l-1) - \frac{m^2}{1-c^2}\right] u_{lm}(c) = -2(2l-1)p_{lm}(c) \, . \tag{A24}$$

One recognizes on the left-hand side the Legendre equation of degree $l-2$: the homogeneous solution is thus $u_{lm}^{(h)}(c) \propto \mathcal{P}_{l-2}^m(c)$. Moreover, since $p_{lm}(c) \propto \mathcal{P}_l^m(c)$, a particular solution can be searched under the form $u_{lm}^{(p)}(c) = \alpha \mathcal{P}_{lm}(c)$, with α a constant. It is then straightforward to get $\alpha = \pi_{(lm)}$, so that finally

$$u_{lm}(c) = \pi_{(l,m)} \mathcal{P}_l^m(c) + \rho_{(l-2,m)} \mathcal{P}_{l-2}^m(c) \, . \tag{A25}$$

Appendix B.3. Polar Component of the Velocity

The projection of the Stokes Equation (1) on the polar direction leads to

$$\Delta v_\theta - \frac{1}{s^2 r^2} v_\theta - \frac{2s}{r^2} \partial_c v_r - \frac{2c}{s^2 r^2} \partial_\varphi v_\varphi = -\frac{s}{\eta r} \partial_c p \, . \tag{A26}$$

Defining $\tilde{v}_\theta = s v_\theta$ and eliminating v_φ thanks to Equation (A18), it can be rewritten as

$$s^2 \partial_c^2 \tilde{v}_\theta - 2c \partial_c \tilde{v}_\theta + \frac{1}{s^2} \partial_\varphi^2 \tilde{v}_\theta + r \partial_r^2 \left(r \tilde{v}_\theta\right) = -\frac{s^2 r}{\eta} \partial_c p + 2s^2 \partial_c v_r - \frac{2c}{r} \partial_r \left(r^2 v_r\right) \, . \tag{A27}$$

We then proceed along the same lines and look for solutions of the form $v_\theta = r^{-l} v_{lm}(c) e^{im\varphi}$. Setting $\tilde{v}_{lm} = s v_{lm}$ yields

$$\begin{aligned}(1-c^2)\frac{\mathrm{d}^2 \tilde{v}_{lm}}{\mathrm{d}c^2} - 2c\frac{\mathrm{d}\tilde{v}_{lm}}{\mathrm{d}c} &+ \left[l(l-1) - \frac{m^2}{1-c^2}\right] \tilde{v}_{lm}(c) \\ &= -(1-c^2)\frac{\mathrm{d}p_{lm}}{\mathrm{d}c} + 2(1-c^2)\frac{\mathrm{d}u_{lm}}{\mathrm{d}c} + 2(l-2)c u_{lm}(c) \, .\end{aligned} \tag{A28}$$

The left-hand side (LHS) corresponds to Legendre equation of degree $l-1$, so that the homogeneous solution is $\tilde{v}_{lm}^{(h)}(c) \propto \mathcal{P}_{l-1}^m(c)$. Coming back to the original function we get $v_{lm}^{(h)}(c) \propto \mathcal{P}_{l-1}^m(c)/s$, which happens to be singular at $c=1$ when $m=0$. However, since one can always search for a particular solution that is regular at this point (except for the case $l=1$; see below), the homogeneous solution has to be regular as well. To remove the singularity, one is naturally led to set

$$v_{lm}^{(h)}(c) = im\sigma_{(l-1,m)} \mathcal{P}_{l-1}^m(c)/s \, . \tag{A29}$$

Note that the homogeneous term can also be written as $v_{lm}^{(h)}(c)e^{im\varphi} = \sigma_{(l-1,m)}\partial_\varphi \mathcal{Y}_{l-1}^m/s$, with $\mathcal{Y}_l^m(c,\varphi) = \mathcal{P}_l^m(c)e^{im\varphi}$, which is the form generally used in Lamb's solution.

We next focus on the inhomogeneous equation. According to the previous results, the right-hand side (RHS) is a linear combination of $\mathcal{P}_l^m$ and $\mathcal{P}_{l-2}^m$. Due to the linearity of Equation (A28), the particular solution can be searched under the form $\tilde{v}_{lm}^{(p)} = \tilde{v}_{lm}^{(p1)} + \tilde{v}_{lm}^{(p2)}$, with

$$\tilde{v}_{lm}^{(p1)} = K_1(1-c^2)\frac{\mathrm{d}\mathcal{P}_l^m}{\mathrm{d}c}\,, \quad \text{and} \quad \tilde{v}_{lm}^{(p2)} = K_2(1-c^2)\frac{\mathrm{d}\mathcal{P}_{l-2}^m}{\mathrm{d}c}\,. \tag{A30}$$

The two constants $K_1 \propto \pi_{(lm)}$ and $K_2 \propto \rho_{(lm)}$ have yet to be determined. Thanks to the recurrence relations of the Legendre functions Equation (A16), we can write

$$\tilde{v}_{lm}^{(p1)} = K_1\left[(l-|m|)\mathcal{P}_{l-1}^m - lc\mathcal{P}_l^m\right]\,, \tag{A31}$$

and

$$\tilde{v}_{lm}^{(p2)} = K_2\left[(l-1)c\mathcal{P}_{l-2}^m - (l+m-1)\mathcal{P}_{l-1}^m\right]\,. \tag{A32}$$

Inserting into the LHS of Equation (A28), one finds LHS = LHS$_1$ + LHS$_2$, with

$$\mathrm{LHS}_1 = -2lK_1\left[(1-c^2)\frac{\mathrm{d}\mathcal{P}_l^m}{\mathrm{d}c} - (l+1)c\mathcal{P}_l^m\right]\,, \tag{A33}$$

$$\mathrm{LHS}_2 = 2(l-1)K_2\left[(1-c^2)\frac{\mathrm{d}\mathcal{P}_{l-2}^m}{\mathrm{d}c} + (l-2)c\mathcal{P}_{l-2}^m\right]\,. \tag{A34}$$

From the solution (A21) for p_{lm} and (A25) for u_{lm}, the RHS of Equation (A28) can also be written as RHS = RHS$_1$ + RHS$_2$, with

$$\mathrm{RHS}_1 = -2\frac{l-2}{l+1}\pi_{(lm)}\left[(1-c^2)\frac{\mathrm{d}\mathcal{P}_l^m}{\mathrm{d}c} - (l+1)c\mathcal{P}_l^m\right]\,, \tag{A35}$$

$$\mathrm{RHS}_2 = 2\rho_{(l-2,m)}\left[(1-c^2)\frac{\mathrm{d}\mathcal{P}_{l-2}^m}{\mathrm{d}c} + (l-2)c\mathcal{P}_{l-2}^m\right]\,. \tag{A36}$$

Comparing (A33) and (A35) on the one hand, and (A34) and (A36) on the other hand, one finally obtains

$$K_1 = \frac{l-2}{l(l+1)}\pi_{(lm)}\,, \quad \text{and} \quad K_2 = \frac{1}{l-1}\rho_{(l-2,m)}\,. \tag{A37}$$

We can then draw the conclusion that

$$v_{lm}(c) = s\left[\frac{l-2}{l(l+1)}\pi_{(lm)}\frac{\mathrm{d}\mathcal{P}_l^m}{\mathrm{d}c} + \frac{\rho_{(l-2,m)}}{l-1}\frac{\mathrm{d}\mathcal{P}_{l-2}^m}{\mathrm{d}c}\right] + \frac{im}{s}\sigma_{(l-1,m)}\mathcal{P}_{l-1}^m(c)\,. \tag{A38}$$

Appendix B.4. Azimuthal Component of the Velocity

Although one can proceed in the same way for the azimuthal projection, it is more convenient to deduce the component v_φ directly from Equation (A18). Defining $v_\varphi = r^{-l}w_{lm}(c)e^{im\varphi}$, the modes w_{lm} are given by

$$w_{lm}(c) = -\frac{is}{m}\left[\frac{\mathrm{d}\left(sv_{lm}\right)}{\mathrm{d}c} + (l-2)u_{lm}(c)\right]\,. \tag{A39}$$

Using (A25), (A38) and the definition of Legendre equation, we get after some algebra

$$w_{lm}(c) = -\frac{im}{s}\left[\frac{(l-2)}{l(l+1)}\pi_{(lm)}\mathcal{P}_l^m(c) + \frac{\rho_{(l-2,m)}}{l-1}\mathcal{P}_{l-2}^m(c)\right] + s\sigma_{(l-1,m)}\frac{\mathrm{d}\mathcal{P}_{l-1}^m}{\mathrm{d}c}\,. \tag{A40}$$

Appendix B.5. Singular Cases

It can be noticed that the expressions of v_{lm} and w_{lm} are not defined for $l = 1$; see Equations (A38) and (A40). These singular cases can be handled as follows. Using the recurrence relation (A17), Equation (A36) can be rewritten as

$$\mathrm{RHS}_2 = 2\rho_{(l-2,m)}(l-|m|-2)\mathcal{P}_{l-3}^m \,, \tag{A41}$$

so that the corresponding particular solution can be searched under the form $\tilde{v}_{lm}^{(p2)} = K_2' \mathcal{P}_{l-3}^m$. After some algebra one gets

$$K_2' = \left(\frac{l-|m|-2}{2l-3}\right)\rho_{(l-2,m)} \,. \tag{A42}$$

This expression is now regular for $l = 1$. We can thus write

$$v_{1m}(c) = -\frac{\pi_{(1m)}}{2} s\partial_c \mathcal{P}_1^m + (1+|m|)\rho_{(-1,m)}\frac{\mathcal{P}_1^m}{s} + \sigma_{(0,m)}\frac{im}{s}\mathcal{P}_0^m \,, \quad m \neq 0 \,. \tag{A43}$$

However, the latter relation has still to be regularized for $m = 0$. To do so, we set $\tilde{\sigma}_{(00)} = \left[im\sigma_{(0,m)}\right]_{m=0}$ and replace in Equation (A43) the generalized Legendre functions by their explicit expression

$$v_{10}(c) = \frac{\pi_{(10)}}{2s}\left[c^2 + 2\frac{\rho_{(-1,0)}}{\pi_{(10)}}c + \left(2\frac{\tilde{\sigma}_{(0,0)}}{\pi_{(10)}} - 1\right)\right] \tag{A44}$$

For this expression to be regular, $c = 1$ must be a root of the term in squared brackets; i.e.,

$$[\ldots] = (c-1)\left[c + \left(\frac{2\rho_{(-1,0)}}{\pi_{(10)}} + 1\right)\right] \,. \tag{A45}$$

This finally sets the value $\tilde{\sigma}_{(0,0)} = -\rho_{(-1,0)}$, so that

$$v_{10}(c) = -\frac{1}{2}\pi_{(10)}\sqrt{1-c^2} - \rho_{(-1,0)}\sqrt{\frac{1-c}{1+c}} \,. \tag{A46}$$

References

1. Happel, J.; Brenner, H. *Low Reynolds Number Hydrodynamics, with Special Applications to Particulate Media*; Kluver Academic Publishers: The Hague, The Netherlands, 1983.
2. Kim, S.; Karrila, S.J. *Microhydrodynamics: Principles and Selected Applications*; Dover: New York, NY, USA, 2005.
3. Lauga, E.; Powers, T.R. The hydrodynamics of swimming microorganisms. *Rep. Prog. Phys.* **2009**, *72*, 096601. [CrossRef]
4. Cantat, I. Liquid meniscus friction on a wet plate: Bubbles, lamellae, and foams. *Phys. Fluids* **2013**, *25*, 031303. [CrossRef]
5. Bertin, V.; Niven, J.; Stone, H.A.; Salez, T.; Raphaël, E.; Dalnoki-Veress, K. Symmetrization of Thin Freestanding Liquid Films via a Capillary-Driven Flow. *Phys. Rev. Lett.* **2020**, *124*, 184502. [CrossRef] [PubMed]
6. Scriven, L.E. The Marangoni effects. *Nature* **1960**, *187*, 186. [CrossRef]
7. Manikantan, H.; Squires, T.M. Surfactant dynamics: Hidden variables controlling fluid flows. *J. Fluid Mech.* **2020**, *892*, P1. [CrossRef]
8. Bickel, T.; Loudet, J.-C.; Koleski, G.; Pouligny, B. Hydrodynamic response of a surfactant-laden interface to a radial flow. *Phys. Rev. Fluids* **2019**, *4*, 124002. [CrossRef]
9. Bickel, T. Effect of surface-active contaminants on radial thermocapillary flows. *Eur. Phys. J. E* **2019**, *42*, 131. [CrossRef] [PubMed]
10. Mizev, A. Influence of an adsorption layer on the structure and stability of surface tension driven flows. *Phys. Fluids* **2005**, *17*, 122107. [CrossRef]

11. Koleski, G.; Vilquin, A.; Loudet, J.-C.; Bickel, T.; Pouligny, B. Azimuthal instability of the radial thermocapillary flow around a hot bead trapped at the water–air interface. *Phys. Fluids* **2020**, *32*, 092108. [CrossRef]
12. Lamb, H. *Hydrodynamics*, 6th ed.; Dover: New York, NY, USA, 1932.
13. Bratukhin, Y.K.; Maurin, L.N. Thermocapillary convection in a fluid filling a half-space. *J. Appl. Math. Mech.* **1967**, *31*, 577. [CrossRef]
14. Würger, A. Thermally driven Marangoni surfers. *J. Fluid Mech.* **2014**, *752*, 589. [CrossRef]
15. Girot, A.; Danné, N.; Würger, A.; Bickel, T.; Ren, F.; Loudet, J.-C.; Pouligny, B. Motion of optically heated spheres at the water-air interface. *Langmuir* **2016**, *32*, 2687. [CrossRef] [PubMed]
16. Seaborn, J.B. *Hypergeometric Functions and Their Applications*; Springer: New York, NY, USA, 1991.
17. Jackson, J.D. *Classical Electrodynamics*, 3rd ed.; Wiley: New York, NY, USA, 1999.
18. Masoud, H.; Stone, H.A. A reciprocal theorem for Marangoni propulsion. *J. Fluid Mech.* **2014**, *741*, R4. [CrossRef]
19. Landau, L.D.; Lifshitz, E.M. *Fluid Mechanics*, 2nd ed.; Pergamon Press: Oxford, UK, 1987.

fluids

MDPI

Article

Lightning Solvers for Potential Flows

Peter J. Baddoo

Department of Mathematics, Imperial College London, South Kensington Campus, London SW7 2AZ, UK;
p.baddoo@imperial.ac.uk

Received: 9 October 2020; Accepted: 20 November 2020; Published: 30 November 2020

Abstract: We present a method for computing potential flows in planar domains. Our approach is based on a new class of techniques, known as "lightning solvers", which exploit rational function approximation theory in order to achieve excellent convergence rates. The method is particularly suitable for flows in domains with corners where traditional numerical methods fail. We outline the mathematical basis for the method and establish the connection with potential flow theory. In particular, we apply the new solver to a range of classical problems including steady potential flows, vortex dynamics, and free-streamline flows. The solution method is extremely rapid and usually takes just a fraction of a second to converge to a high degree of accuracy. Numerical evaluations of the solutions are performed in a matter of microseconds and can be compressed further with novel algorithms.

Keywords: potential flows; vortex dynamics; free streamlines; numerical methods

---

1. Introduction

This paper is concerned with the numerical solution of the planar Laplace equation

$$\nabla^2 f(z) = 0, \qquad z \in D, \tag{1}$$

in contexts relevant to fluid dynamics. The domain D is assumed to be unbounded and simply connected (or periodic) and $z = x + \mathrm{i}y$ is the spatial co-ordinate. Laplace's equation is sometimes considered the simplest two-dimensional (2-D) partial differential equation but, nevertheless, its numerical solution is challenging in many scenarios of practical interest. In particular, typical numerical methods struggle when the boundary of the flow domain ∂D is not smooth; for example, the solution of (1) admits a singularity where the boundary has sharp corners [1], which hinders traditional techniques such as finite element methods [2,3] and boundary element methods [4]. Although these approaches have been successfully adapted to account for corners (e.g., [5]), their implementation is complex and requires expert knowledge. Recently, a new method that makes use of rational function approximation theory has been proposed for solving Laplace's equation in domains with corners [6,7]. Dubbed the "lightning solver" (due to the analogy of lightning striking a corner because of a singular electric potential there), this new solution technique is extremely fast, accurate, and straightforward to implement. Herein, we use the lightning method to devise new strategies for solving potential flow problems in domains with corners.

Potential flows are foundational to fluid mechanics. In the fluid mechanics pedagogy, the first problem that students encounter is often incompressible and irrotational flow past a cylinder. Equipped with the solution to this simple flow, students progress to more complicated geometries via conformal mappings such as the Joukowski map [8]. The ensuing solutions can usually be expressed in closed form and are, thus, highly interpretable. Much of classical aerodynamics was built on this approach [9–11] and the associated solutions continue to be relevant to modern aerodynamics studies today [12,13]. Idealised flow also commonly arises as an outer region problem in asymptotic analyses, and can then be matched to an inner boundary layer [14]. Another way to improve the physical fidelity of potential flows is by incorporating the effects of flow separation. The Brown–Michael equation [15] is a popular method for modelling point vortices shed from sharp corners [16–18] whereas contour dynamics models the shedding and roll-up of vortex sheets [19,20]. In Section 3.4, we shall see that the lightning approach of the present work can be used to rapidly compute point vortex trajectories in complicated domains. Free-streamline theory [21,22] provides an alternative approach to modelling flow separation; in Section 3.5, we shall use the lightning solver to calculate the idealised, separated flow past a flat plate.

The mathematically tractable structure of potential flows has inspired a rich mathematical theory rooted predominantly in complex analysis. The theory of conformal mappings [23–25] has enabled the study of potential flows in complicated domains beyond the aforementioned Joukowski map. Moreover, a theory for multiply connected flow domains has recently been expounded by Crowdy [26,27], and the present author adapted these studies to periodic domains [28]. Both of these approaches make use of the transcendental Schottky–Klein prime function [29]. The prime function also provides a closed-form expression for the Kirchhoff–Routh path function [30], which governs the trajectories of point vortices [31]. Riemann–Hilbert problems and singular integral equations are also relevant, and have previously been used to study flows through cascades [32], porous aerofoils [33], and dissolution and erosion [34].

Corners are obviously ubiquitous in real-life engineering applications and are often responsible for important physical behaviour; the local behaviour of flow past a sharp corner can have a significant impact on the global properties of the flow. For example, the Kutta condition implies that the flow at the sharp trailing edge of an aerofoil should depart the wing smoothly [35]. This specification determines the circulation around the wing and, thus, its lift [36]. At the leading edge of a wing, the leading-edge suction is critical in determining the thrust on unsteady bodies and has recently been proposed as a tool for modelling the onset of vortex shedding [37]. This approach has been coupled with real measurement data in order to account for absent physics via data assimilation to obtain a model that is simultaneously fast and physically faithful [38]. In summary, the flow behaviour at corners must be accurately modelled for physically relevant results.

The remainder of this article is arranged as follows. In Section 2, we explain the lightning solver framework and outline the mathematical details. We then apply this framework to a range of scenarios including potential flows, vortex dynamics, and free-streamline problems in Section 3. Finally, we present a discussion of the results in Section 4. Most of the results that are produced in this paper are computed using straightforward adaptations of the MATLAB code `laplace.m` available at [39]. The reported solve times are based on computations performed on a 2015 MacBook Pro with a 2.9 GHz processor.

2. Method

We now present the main mathematical ideas behind the lightning method.

2.1. The Lightning Method

We are interested in solving Laplace's equation in an unbounded 2-D domain D with corners on the boundary ∂D. Solutions of Laplace's equation typically exhibit singularities with behaviour z^α near corners; for example, z^α represents the complex potential for flow around an infinite wedge with a corner of interior angle $\pi(2-1/\alpha)$. The absence of viscosity and the infinite curvature of the boundary at the corner imply that the flow there either has infinite velocity or is stagnant. The presence of these singularities suggests that the recently developed lightning solvers can be an efficient and accurate method for computing potential flows.

The ideas behind the lightning method are based in rational approximation theory. A rational function is simply a ratio of two polynomials; we say that a rational function is type (m,n) if the numerator is a polynomial of degree at most m and the denominator is a polynomial of degree at most n. A detailed discussion of rational approximation can be found in chapters 22 to 27 of [40]. A principal result of rational approximation is due to Newman [41], who showed that the absolute value function $|x|$ can be approximated on the interval $x \in [-1, 1]$ with root-exponential accuracy. In mathematical language, there exist constants A, $C > 0$ and type (n, n) rational approximants r_n such that

$$\max_{-1 \le x \le 1} ||x| - r_n(x)| \le A\mathrm{e}^{-C\sqrt{n}}. \tag{2}$$

In contrast, a polynomial approximant can achieve, at best, algebraic convergence (i.e., the error decays in proportion to n^{-1}). Motivated by this result, Gopal and Trefethen [6] proved that similar approximants exist for more general types of singularities of the form z^α. Again, it is possible to attain root-exponential convergence when approximating with rational functions; there exist constants A, $C > 0$ and type (n, n) rational approximants r_n, such that

$$\max_{z \in H} |z^\alpha - r_n(z)| \le A\mathrm{e}^{-C\sqrt{n}} \tag{3}$$

where H represents the closed upper half of the unit disc. Theorem 2.3 of [6] extended this result to prove that solutions of Laplace's equation in convex polygons can be represented as rational functions with root-exponential accuracy. Although the theoretical results of [6] were valid when the domain is the interior of a convex polygon, the numerical results of the present paper indicate that they also hold when the domain is the exterior of some bounded domain.

Crucially, the rational approximants r_n in both (2) and (3) possess poles that are exponentially clustered near zero with exponentially decreasing residues. This observation, as well as the above theoretical results, inform a numerical scheme for Laplace's equation by considering an ansatz with poles clustered exponentially close to the corners of the domain. Gopal and Trefethen [6] suggest an ansatz of the form

$$f(z) = \underbrace{\sum_{j=0}^{n_1} \frac{a_j}{(z - z_*)^j}}_{\text{Runge part}} + \underbrace{\sum_{j=1}^{n_2} \frac{b_j}{z - z_j}}_{\text{Newman part}} \tag{4}$$

where z_* is a point near the center of ∂D, $\{z_j \,|\, j = 1, \ldots, n_2\}$ is a prescribed set of poles and $\{a_j \,|\, j = 0, \ldots, n_1\}$ and $\{b_j \,|\, j = 1, \ldots, n_2\}$ are sets of unknown, complex constants. Equation (4) is simply a rational function in partial fraction form. Because rational functions are analytic away from the poles, if all of the poles $\{z_j\}$ are outside D then (4) is a solution to Laplace's equation. The Runge part in (4) corresponds to the smooth part of the solution: it is a polynomial in $1/(z - z_*)$. If ∂D is smooth then the Runge part is all that is necessary in the ansatz. Conversely, the Newman part takes the singularities on the corners into account.

A key feature of the lightning method is that the poles in the Newman part $\{z_j\}$ are clustered exponentially close to the corners in order to exploit the root-exponential convergence guaranteed by (3). In particular, there is evidence to suggest that the poles should follow a "tapered" distribution near the corners [42]. In this case, the poles that are clustered around a given corner should be of distance

$$\mathrm{e}^{-\sigma(\sqrt{n} - \sqrt{j})}, \qquad 1 \le j \le n \tag{5}$$

from that corner. In our numerical results we use $\sigma = 3$ although $\sigma = 4$ is also a good choice.

By the linearity of Laplace's equation, the coefficients $\{a_j\}$ and $\{b_j\}$ can be determined by fitting f to satisfy some prescribed linear boundary conditions. This is achieved by sampling the ansatz (4) at a number of points on the boundary and solving for $\{a_j\}$ and $\{b_j\}$ in the least-squares sense. The sample points should also be exponentially clustered near the corners in order to ensure that the poles exponentially near the corners are properly resolved. For example, if the boundary condition is collocated at m points then the coefficients are given by

$$\arg\min_{\boldsymbol{c}} \|\boldsymbol{A}\boldsymbol{c} - \boldsymbol{d}\|_2 \tag{6}$$

where $\boldsymbol{c} \in \mathbb{R}^{2n_1+2n_2+2}$ is the stacked vector of the real and imaginary parts of the unknown coefficients, $\boldsymbol{d} \in \mathbb{R}^m$ represents the sampled boundary condition, and $\boldsymbol{A} \in \mathbb{R}^{m\times(2n_1+2n_2+2)}$ represents the sampled basis functions in (4). For example, suppose that the boundary condition is $\mathbb{I}\mathrm{m}[f(z)] = d(z)$ for some function d. Subsequently, for an $M \times 1$ vector of sample points $\boldsymbol{Z}$, we have

$$\boldsymbol{d} = d(\boldsymbol{Z}), \qquad \boldsymbol{c} = \begin{bmatrix} \mathbb{R}\mathrm{e}[\boldsymbol{a}] \\ \mathbb{I}\mathrm{m}[\boldsymbol{a}] \\ \mathbb{R}\mathrm{e}[\boldsymbol{b}] \\ \mathbb{I}\mathrm{m}[\boldsymbol{b}] \end{bmatrix}, \qquad \boldsymbol{A} = \begin{bmatrix} \boldsymbol{R} & \boldsymbol{N} \end{bmatrix} \tag{7}$$

where the blocks $\boldsymbol{R}$ and $\boldsymbol{N}$ correspond to the Runge and Newman parts respectively:

$$\boldsymbol{R} = \left[0 \quad \mathbb{I}\mathrm{m}\left(\frac{1}{\boldsymbol{Z}-z_*}\right) \quad \cdots \quad \mathbb{I}\mathrm{m}\left(\frac{1}{(\boldsymbol{Z}-z_*)^{n_1}}\right) \quad 1 \quad \mathbb{R}\mathrm{e}\left(\frac{1}{\boldsymbol{Z}-z_*}\right) \quad \cdots \quad \mathbb{R}\mathrm{e}\left(\frac{1}{(\boldsymbol{Z}-z_*)^{n_1}}\right)\right], \tag{8}$$

$$\boldsymbol{N} = \left[\mathbb{I}\mathrm{m}\left(\frac{1}{\boldsymbol{Z}-z_1}\right) \quad \cdots \quad \mathbb{I}\mathrm{m}\left(\frac{1}{\boldsymbol{Z}-z_{n_2}}\right) \quad \mathbb{R}\mathrm{e}\left(\frac{1}{\boldsymbol{Z}-z_1}\right) \quad \cdots \quad \mathbb{R}\mathrm{e}\left(\frac{1}{\boldsymbol{Z}-z_{n_2}}\right)\right]. \tag{9}$$

Thus, $\mathbb{I}\mathrm{m}[f(\boldsymbol{Z})] = \boldsymbol{A}\boldsymbol{c}$. It is important to note that the matrix $\boldsymbol{R}$ is exponentially ill-conditioned since its columns are the real and imaginary parts of the columns of a Vandermonde matrix. To address this issue, the Vandermonde matrix is not formed explicitly: instead, we form an equivalent matrix with orthogonal columns via the Vandermonde with Arnoldi algorithm [43]. Using these matrix constructions, the least-squares problem (6) can be easily solved using, for example, the backslash operator in MATLAB. Having obtained the coefficients $\{a_j\}$ and $\{b_j\}$, the rational approximant f can be computed via (4). This completes the description of the lightning solver. Pseudocode describing the main steps is included in Algorithm 1 and we refer the reader to [6] for further details.

Algorithm 1: Laplace lightning solver (Gopal and Trefethen, 2019 [6]).

```
Input: A domain boundary $\partial D$, boundary data $d(z)$ and a tolerance $\epsilon$
Output: A function handle $f$ that is harmonic and satisfies the boundary conditions.
begin
    Identify the $m$ corners of the boundary and define the interior point $z_*$
    for $n$ increasing (with $\sqrt{n}$ approximately evenly spaced) do
        Fix $n_1 = \mathcal{O}(mn)$ poles $\{z_j\}$ clustered inside the corners according to (5)
        Fix the order $n_2 = \mathcal{O}(n)$ inverse monomials $1, \ldots, (z - z_*)^{-n_2}$
        Define $\mathcal{O}(n_1 + n_2)$ sample points on the boundary
        Form an orthogonalised version of $\boldsymbol{R}$ using Vandermonde with Arnoldi [43]
        Construct the data matrix $\boldsymbol{A}$ and vector $\boldsymbol{d}$
        Solve the least squares problem $\arg\min_c \|\boldsymbol{A}\boldsymbol{c} - \boldsymbol{d}\|_2$
        Exit if $\|\boldsymbol{A}\boldsymbol{c} - \boldsymbol{d}\|_\infty < \epsilon$, $n$ becomes too large, or the error is increasing
    end
    Construct the function handle $f$ according to (4)
end
```

The lightning solver belongs to a broader class of techniques known as Methods of Fundamental Solutions (MFS) [44–46]. In these methods, the solution is expanded as a distribution of free-space solutions whose coefficients are tuned to satisfy a given boundary condition. However, the lightning solver differs from typical MFS in two important ways. Firstly, the singularities are exponentially clustered near the corners, which is a new idea in MFS. Secondly, the fundamental solutions that are used here are dipoles ($1/(z - z_j)$), whereas traditional MFS typically use point sources ($\log(z - z_j)$). These two qualities are essential to the root-exponential convergence of solutions that we observe herein.

The main idea of this paper is to use the lightning solver to solve potential flow problems. We will apply this approach to a plethora of scenarios to showcase its versatility, but as a first example, consider uniform flow past a stationary boundary ∂D. If w represents the complex potential then the no-flux condition states that $\mathbb{I}\text{m}[w(z)] = 0$ for $z \in \partial D$ and the far-field condition is $w \sim z$ as $|z| \to \infty$. Thus, we may write $w(z) = z + f(z)$ where f is the ansatz expressed in (4). After arranging the poles to cluster near the corners, the coefficients a_j and b_j are chosen in order to satisfy the no-flux condition. The resulting streamlines are plotted in Figure 1a for a square with a circular sector removed. The background color represents the horizontal perturbation velocity, which can be obtained by differentiating f. In Figure 1b, we plot the convergence of the solution as the number of degrees of freedom ($N = 2(n_1 + n_2 + 1)$) is increased. The problem is solved to six digits of accuracy in 0.5 s. Evaluating the solution takes 20 microseconds for each point. The root-exponential convergence is clear, and the approximation is accurate throughout the entire boundary, including the corners.

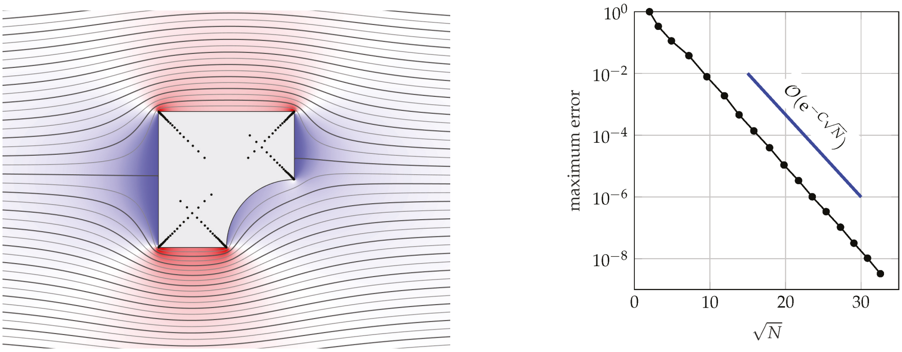

(**a**) Potential flow solution (**b**) Solution convergence

Figure 1. Incompressible, irrotational (i.e., potential) flow past a square circular sector removed. The problem takes 0.5 s to solve to six digits of accuracy and 5 s for eight digits. In (**a**) the black dots represent the poles. The background colour in (**a**) represents the horizontal velocity of the perturbation to the flow from uniformity. Note that in (**b**) the y-axis is on a log scale whereas the x-axis is $\sqrt{N}$, so that a straight line indicates root-exponential convergence.

2.2. *Compression of Solutions*

While the rational function representation (4) is very fast to evaluate, even faster evaluations are possible. In certain applications—such as the vortex dynamics example we shall encounter later—the solution f will be evaluated a large number of times and thus an inexpensive evaluation of f is desirable.

Recently, the AAA (adaptive Antoulas–Anderson) algorithm has emerged as a robust, flexible, and accurate tool for rational approximation and compression [47,48]. Given sets of sample points Z and function values $F = \{f(z)\,|\,z \in Z\}$, the AAA algorithm returns a rational function r that approximates f to some specified tolerance. One important feature of the AAA algorithm is that the rational function is expressed in barycentric form, i.e.,

$$r(z) = \sum_{j=1}^{m} \frac{f_j w_j}{z - t_j} \Bigg/ \sum_{j=1}^{m} \frac{w_j}{z - t_j}\ . \tag{10}$$

The set of support points $\{t_j\} \subseteq Z$ is a subset of the sample points and w_j are known as the weights. Note that $r(t_j) = f_j$ so r interpolates f at the support points. The AAA algorithm selects support points and weights by iteratively reducing the residual error. At each iteration, the next support point is chosen "greedily" as the one with the largest residual error between the approximant and function value. Subsequently, the weight w_j is updated by solving a minimisation problem via a singular value decomposition (SVD). When a desired accuracy is reached then the algorithm terminates—(10) consists of m support points and thus m iterations. These features—the barycentric form, greedy selection of support points and least-squares minimisation via SVD—are all central to the success of the AAA algorithm. The algorithm is straightforward to implement and use: the original article [47] contained an implementation in 40 lines of MATLAB code and a full implementation is available in Chebfun [49] (www.chebfun.org). The author has also developed a periodic version of the AAA algorithm, called AAAtrig [50]. The algorithm is built on the same principals as the original AAA algorithm, except the barycentric form (10) is replaced with its periodic analogue.

Let us return to the relevance of AAA to our compression problem. Suppose that we have computed a solution f of the form (4) to Laplace's equation satisfying some boundary conditions. If we evaluate f at a number of points on the boundary and run these points through the AAA/AAAtrig algorithm then we obtain a new function r that approximates f on the boundary. If r contains no poles in D, then r also solves Laplace's Equation (1). Moreover, AAA/AAAtrig usually selects an approximation that uses fewer poles than the original function and is, thus, faster to evaluate. Moreover, by the maximum value principle, $|r - f|$ is maximised on the boundary, so the error in D is guaranteed to be no larger than the approximation error on the boundary.

We illustrate the effects of compression in Figure 2. The problem is uniform flow around a rectangle with a reentrant corner. The lightning solver uses 617 poles to achieve eight digits of accuracy. Figure 2c indicates that the algorithm attains root-exponential convergence. After a sample of the boundary points have been passed through AAA, we obtain a rational approximant using only 412 poles. Thus, the new approximant r is faster to evaluate than the original solution f. Note that AAA has chosen a slightly different set of poles with which to represent the function; we believe that this alternative choice of poles is responsible for the enhanced compression. The idea of compressing harmonic functions using AAA originated in [51].

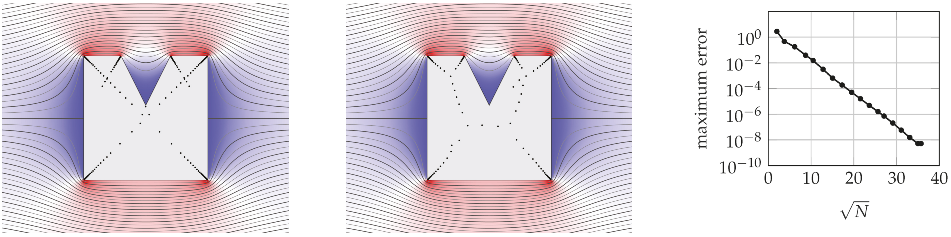

(**a**) Full solution (617 poles)

(**b**) Compressed solution (412 poles)

(**c**) Solution convergence

Figure 2. An example of AAA compression for the flow past a rectangle with a reentrant corner. The black dots in (**a**) and (**b**) indicate the poles used to represent the full and compressed solutions respectively.

3. Results and Discussion

Having outlined the mathematical preliminaries of the lightning solver, we now consider a number of fluid dynamics problems.

3.1. Potential Flows

The examples presented in the previous section were for simple uniform flows. The inclusion of more complicated flows follows in an analogous manner. Suppose that a given flow—which may consist of a background flow and a distribution of singularities in D—has a free-space solution $g(z)$. Subsequently, we represent the complex potential as $w(z) = f(z) + g(z)$. Thus, $f(z)$ is the correction term that is induced by the boundaries and can be found using the methods of Section 2. In order for the boundary to be a streamline, we enforce the boundary condition

$$\mathbb{I}\mathrm{m}[f(z) + g(z)] = 0, \qquad \text{for } z \in \partial D. \tag{11}$$

For example, suppose that we wish to calculate the potential flow that is generated by a uniform flow of magnitude U at an angle α with a distribution of N vortices of circulations $\{\Gamma_j\}$ at locations $\{v_j\}$. The free-space solution for the complex potential is

$$g(z) = \frac{1}{2\pi \mathrm{i}} \sum_{j=1}^{N} \Gamma_j \log\left(z - v_j\right) + Uze^{-\mathrm{i}\alpha}. \tag{12}$$

The lightning method presented in Section 2 can used to find a harmonic function that satisfies the boundary condition (11). In Figure 3, we visualise the flow past a curved boundary embedded in a uniform flow with two point vortices by plotting a set of streamlines and the horizontal velocity perturbation.

The method is also valid when the boundary is not a streamline. For example, when the boundary is rotating about the point c with angular velocity ω, (11) is replaced by

$$\mathbb{I}\mathrm{m}[f(z) + g(z)] = \mathbb{I}\mathrm{m}\left[\frac{\mathrm{d}\bar{c}}{\mathrm{d}t}\,(z - c)\right] - \frac{\omega}{2}|z - c|^2, \qquad \text{for } z \in \partial D. \tag{13}$$

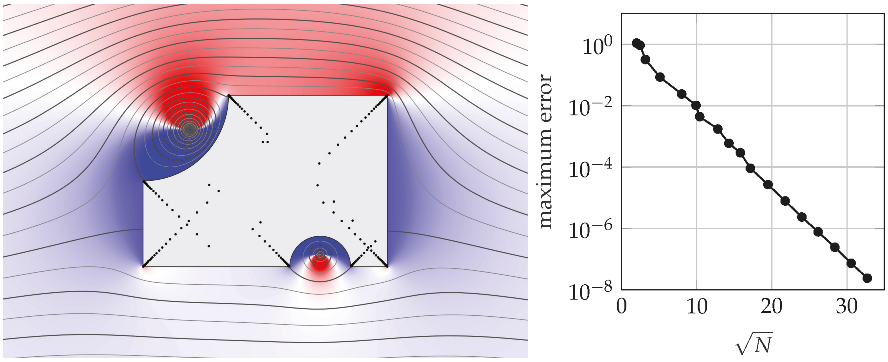

(**a**) Solution (**b**) Error convergence

Figure 3. Uniform flow past the polycircular domain from [52] with embedded point vortices. The lines are the streamlines and background color is the horizontal perturbation velocity. The black dots represent the prescribed poles of the rational function. The solution converges to five digits of accuracy in 0.8 s and 8 digits in 6 s.

3.2. Periodic Domains

Potential flows through periodic domains arise in a number of practical scenarios including turbomachinery flows [32], super-hydrophobic surfaces [53], and geological flows [54]. Recently, the author proposed a "calculus" for the analytical treatment of potential flows in general periodic domains with multiply connected period windows [28] thus extending the calculus of vortex dynamics proposed by Crowdy [27]. The analytical solutions in that work were based on the Schottky–Klein prime function [29]. The present lightning approach may be viewed as a complementary approach to those analytical solutions.

We now seek solutions of Laplace's equation that are periodic so that $f(z) = f(z + 2\pi k)$ for $k \in \mathbb{Z}$ (solutions of different periods can easily be constructed by rescaling the domain). An analogous approach to that of Section 2 can be employed with the ansatz (4) replaced by

$$f(z) = \sum_{j=0}^{n_1} a_j \cot\left(\frac{z - z_*}{2}\right)^j + \sum_{j=1}^{n_2} b_j \cot\left(\frac{z - z_j}{2}\right). \tag{14}$$

The connection between the periodic ansatz (14) and the original ansatz (4) is clarified by noting the partial fraction expansion of cotangent:

$$\cot(z) = \sum_{k=-\infty}^{\infty} \frac{1}{z - k\pi}. \tag{15}$$

Thus, (14) is analogous to (4) when the poles in (4) are repeated with period 2π. Similarly to the non-periodic case, the coefficients $\{a_j\}$ and $\{b_j\}$ are found by solving the least-squares problem.

In Figure 4 we plot the streamlines and horizontal velocity perturbation for uniform flow at angle $-\pi/4$ past a periodic array of curved boundaries with embedded point vortices. The periodicity has a significant effect on the flow field and the vortices can be seen to deflect the flow angle. At present, this problem cannot be solved with conformal maps, because the form of the required (polycircular) maps has not yet been found. Indeed, the general form of periodic polygonal maps has only been found recently [55]. Accordingly, the lightning approach provides a new method for tackling flows in periodic domains that were previously inaccessible.

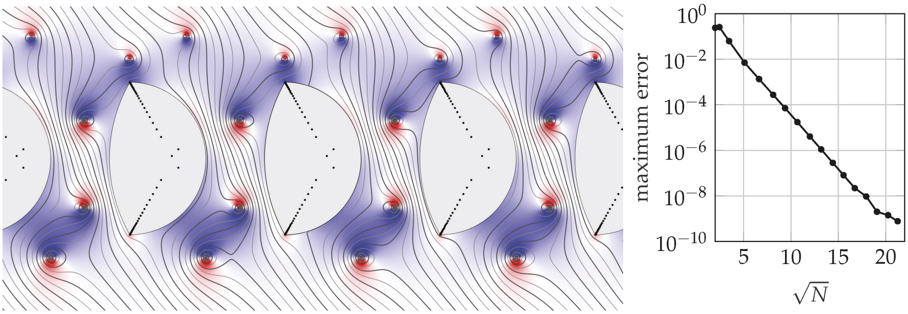

(**a**) Solution (**b**) Error convergence

Figure 4. Uniform flow past a periodic array of boundaries with embedded point vortices. The black dots represent the prescribed poles of the rational function. The solution converges to 9 digits of accuracy in 0.8 s.

3.3. The Kutta Condition

In the lightning ansatz (4), the circulation around ∂D is necessarily zero. It is possible to give ∂D arbitrary circulation Γ by replacing the ansatz (4) with

$$f(z) = \sum_{j=0}^{n_1} \frac{a_j}{(z - z_*)^j} + \sum_{j=1}^{n_2} \frac{b_j}{z - z_j} + \frac{\Gamma}{2\pi \mathrm{i}} \log(z - z_*), \tag{16}$$

and solving for $\{a_j\}$ and $\{b_j\}$ subject to the relevant boundary condition. However, in most applications, the circulation is not prescribed, but must be found as part of the problem. One method for selecting the circulation is to apply the Kutta condition [35,36]. On ∂D, a corner $\hat{z}$ is nominated as the downstream corner and the Kutta condition states that the fluid should leave $\hat{z}$ smoothly. In our potential flow framework (for a stationary boundary), this is equivalent to specifying that the corner represents a stagnation point. In other words, the circulation must be such that the velocity vanishes at the nominated corner, i.e.,

$$f'(\hat{z}) + g'(\hat{z}) = 0, \tag{17}$$

where g is the free-space solution and the prime $'$ indicates differentiation with respect to z. Practically, enforcing the Kutta condition simply involves supplementing the least-squares problem (6) with an extra row corresponding to the vectorised form of (17). Note that only one extra row is required as (17) is already satisfied in one direction by the no-flux condition.

In Figure 5, we illustrate the effect of the Kutta condition by computing the uniform flow past a bullet-shaped object with and without the Kutta condition applied. Applying the Kutta condition to the bottom right corner drastically increases the flow velocity in the vicinity of the boundary. It can be seen that the flow departs the selected corner smoothly, thus indicating that the Kutta condition is indeed satisfied.

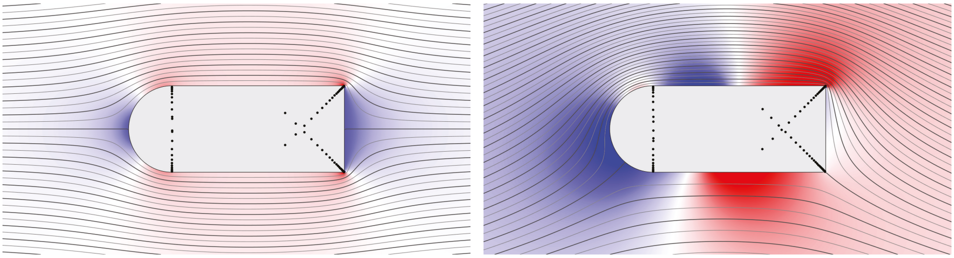

(**a**) Kutta condition not applied (**b**) Kutta condition applied

Figure 5. An illustration of the effects of the Kutta condition on the flow past a bullet-shaped object. The solutions are computed to 6 digits of accuracy; in (**a**) the solver takes 0.3 s and in (**b**) the solver takes 0.8 s. The color scale is the same in both figures.

3.4. Vortex Dynamics

The transport of vortical structures is an important phenomenon in fluid mechanics and is relevant to flow control, turbulence modelling, vortex shedding, and flow separation. A point vortex may be used in order to represent a discretised quantity of vorticity as an approximation to more complicated structures [56]. The dynamics of these point vortices—which has been described as "a classical mathematics playground" [57]—is another area that is amenable to these lightning methods.

The point vortex equation states that the velocity of a vortex is equal to the de-singularised velocity field at the vortex center [58]. Mathematically, if z is the position of a vortex of circulation Γ, then the motion of the vortex is governed by

$$\frac{\mathrm{d}z}{\mathrm{d}t} = \overline{\tilde{w}'(z)}, \tag{18}$$

where w is the complex potential and w' is the complex velocity. In (18), the tilde indicates that the velocity field has been de-singularised, i.e.,

$$\tilde{w}'(z) = \lim_{\hat{z}\to z}\left(\frac{\mathrm{d}w}{\mathrm{d}\hat{z}}(\hat{z}) - \frac{\Gamma}{2\pi\mathrm{i}}\,\frac{1}{\hat{z}-z}\right). \tag{19}$$

Accordingly, if we know the velocity field w when the vortex is at z then we can calculate the trajectory of the vortex. We could, in principle, use the lightning method of Section 3.1 to directly calculate w at each time step, but, since the vortices are moving, this approach would require solving a different Laplace problem at each time step, which would become prohibitively expensive. Nevertheless, we can still use the lightning framework to attack this problem.

Our approach is to use the lightning solver to conformally map the physical domain to a simple domain and then analytically construct w with the method of images. There are a number of techniques available that can be used to compute conformal mappings. The pre-eminent method is the Schwarz–Christoffel transformation [23,55,59] which provides analytical formulae for conformal maps to polygonal domains in terms of a number of accessory parameters that must generally be determined numerically. To circumvent this "parameter problem", an approach for numerically computing conformal maps was suggested in [60]; we briefly review the approach here.

In the simply connected case, the natural domain to map into is the interior of the unit disc. We denote the unit disc coordinate as ζ and the conformal map f, so that $z = f(\zeta)$. Figure 6 illustrates an example of a mapping. The inverse map (from the physical domain to the circular domain) is written as f^{-1}, so that $\zeta = f^{-1}(z)$.

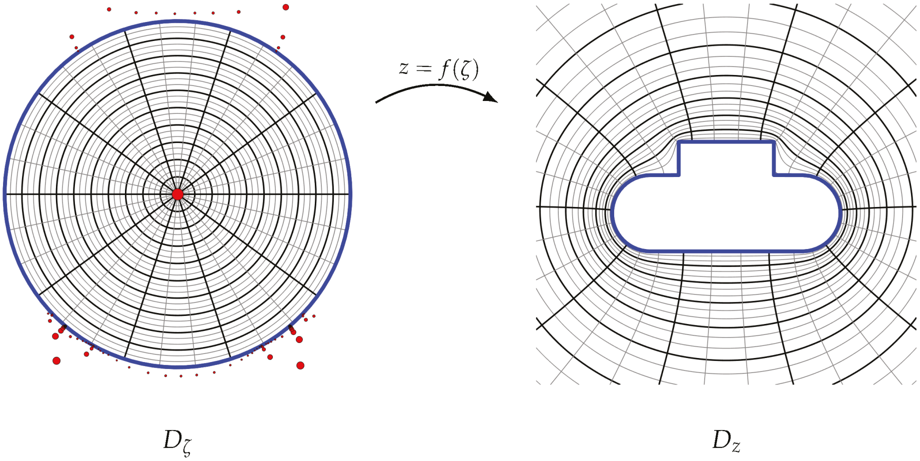

Figure 6. An example of a conformal map computed using the method of [60]. The red dots indicate the poles of the map and their size is proportional to their residue.

To compute the mappings we express the inverse map as

$$f^{-1}(z) = \frac{\mathrm{e}^{h(z)}}{z} \tag{20}$$

for analytic h. Taking the logarithm of both sides and evaluating on the boundary yields

$$\log(f^{-1}(z)) = h(z) - \log(z) = \mathrm{i}\arg(\zeta), \qquad \text{for } z \in \partial D_z, \tag{21}$$

where we have used the fact that the boundary ∂D_z maps to $|\zeta| = 1$. Note that the logarithm on the left side is pure imaginary since we are evaluating it on the unit circle. This imaginary function is unknown as we do not know the image of each boundary point a priori; we only know that the boundary is mapped to the unit circle. Accordingly, to determine f^{-1}, we must find an analytic function who's real part satisfies (21). In other words, we want to solve the Laplace problem

$$\nabla^2 h(z) = 0, \qquad \text{for } z \in D_z, \tag{22}$$

$$\mathbb{R}\mathrm{e}[h(z)] = \log(|z|), \qquad \text{for } z \in \partial D_z, \tag{23}$$

$$\mathbb{I}\mathrm{m}[h(z)] \to 0, \qquad \text{as } |z| \to \infty. \tag{24}$$

The last equation specifies a degree of freedom in the map and simplifies some of the ensuing formulae. This type of Laplace problem is amenable to the method that is presented in Section 2: we consider an ansatz in the form of a rational function (4) with poles clustered near the corners and then solve for the coefficients in the least-squares sense by collocating (23) on the boundary. Given h, we obtain f^{-1} by (20).

Now, we may compute the forward mapping f using the approach of [51]. By sampling $f^{-1}(z)$ at a number of points on the boundary $z \in \partial D_z$, we are equipped with a set of sample points $\{z_j\}$ and a set of function values $\{\zeta_j\}$ where $\zeta_j = f^{-1}(z_j)$. Subsequently we construct an approximant with the AAA algorithm using $\{z_j\}$ as function values and $\{\zeta_j\}$ as sample points. Thus, provided a rich enough sample set is selected, the approximant produced by AAA maps the boundary ∂D_ζ to ∂D_z; in other words, the new approximant computed by AAA approximates the forward mapping f. Moreover, by the maximum value principle, the accuracy of the approximation to the conformal map is bounded by the error on the boundary. Accordingly, we are now free to accurately and quickly map between the circular and physical domains using f and f^{-1}.

Armed with these numerical representations of the mappings, we now transform the point vortex Equation (18) into the circular domain D_ζ. Carefully applying L'Hôpital's rule to (18) yields

$$\frac{\mathrm{d}\zeta}{\mathrm{d}t} = \frac{1}{|f'(\zeta)|^2} \left(\overline{\tilde{W}'(\zeta) - \frac{\Gamma}{4\pi\mathrm{i}} \frac{f''(\zeta)}{f'(\zeta)}} \right), \tag{25}$$

where $W(\zeta) = w(z)$ is the complex potential in D_ζ and $\tilde{W}'(\zeta)$ is the de-singularised velocity field in D_ζ:

$$\tilde{W}'(z) = \lim_{\hat{\zeta} \to \zeta} \left(\frac{\mathrm{d}W}{\mathrm{d}\hat{\zeta}}(\hat{\zeta}) - \frac{\Gamma}{2\pi\mathrm{i}} \frac{1}{\hat{\zeta} - \zeta} \right). \tag{26}$$

The advantage of our approach is that the complex potential in the ζ-plane can be constructed analytically. For example, the complex potential that is induced by an arrangement of N vortices of strengths $\{\Gamma_j | j = 1, \ldots, N\}$ located at positions $\{\zeta_j | j = 1, \ldots, N\}$ embedded in a background uniform flow of strength U at angle of attack α is given by

$$W(\zeta) = \sum_{j=1}^{N} \frac{\Gamma_j}{2\pi\mathrm{i}} \log \left(\frac{\zeta - \zeta_j}{|\zeta_j|(\zeta - 1/\overline{\zeta_j})} \right) + aU \left(\frac{\mathrm{e}^{-\mathrm{i}\alpha}}{\zeta} + \mathrm{e}^{\mathrm{i}\alpha}\zeta \right). \tag{27}$$

where $a = \mathrm{e}^{h(\infty)}$ is the residue of the simple pole of the map. In this case, the de-singularised velocity at ζ_k is

$$\tilde{W}'(\zeta_k) = \sum_{\substack{j=1 \\ j \neq k}}^{N} \frac{\Gamma_j}{2\pi\mathrm{i}} \frac{1}{\zeta_k - \zeta_j} - \sum_{j=1}^{N} \frac{\Gamma_j}{2\pi\mathrm{i}} \frac{1}{\zeta_k - 1/\overline{\zeta_j}} + aU \left(-\frac{\mathrm{e}^{-\mathrm{i}\alpha}}{\zeta_k^2} + \mathrm{e}^{\mathrm{i}\alpha} \right). \tag{28}$$

Substituting (28) into the transformed point vortex equation (25) results in an autonomous dynamical system that can be integrated with standard numerical techniques such as the Euler method or

Runge–Kutta methods. In Figure 7, the resulting trajectories are plotted for 30 vortices outside a curved domain. The vortices have strengths that are randomly distributed in the interval $[-1, 1]$ and there is no background flow. A number of vortices are shot out to infinity, but a distinct structure emerges that traces out the boundary ∂D_z. This model could be used as, for example, an approximation for the motion of oceanic eddies [17] around a boundary. Alternatively, on use of the Blasius theorem, this model could provide estimates for the forces exerted on ∂D_z due to the transport of vorticity. The sound produced by such interactions could be also analysed with the vortex sound model of Howe [61].

This approach also applies to multiply connected domains—the analogous complex potential (27) can be constructed in a multiply connected circular domain using the formulae of Crowdy [26,27]. Additionally, this conformal mapping method can be applied to Kirchhoff–Routh theory to study the Hamiltonian dynamics of point vortices [58,62]. Again, analytic formulae for the multiply connected Kirchhoff–Routh path function are readily available [31]. A further consideration is that, in reality, a number of vortices will be shed from the sharp corners of the domain. The trajectories of these shed vortices could be modelled using the Brown–Michael equation [15] or the other approaches discussed in the introduction.

3.5. Free-Streamline Flows

Incompressible flow past a bluff body usually results in flow separation. This separation can generate a downstream wake or a cavity flow and can have a significant effect on estimates of the drag and lift coefficients. Free-streamline theory attempts to reconcile the physical reality of flow separation with the mathematical tractability of potential flows. In these problems, the boundaries of the domain are not known a priori—the boundary incorporates a "free streamline" whose shape must be found as part of the problem. Thus, we cannot use a direct conformal mapping approach as in Section 3.4. The typical approach for solving these problems is to construct mappings between auxiliary domains and then find the shape of the streamlines by considering the relationships between the auxiliary domains. Previous authors have presented numerical conformal mapping approaches in order to solve these problems [22,63,64]; we now demonstrate that the lightning approach can be leveraged in order to solve free-streamline problems.

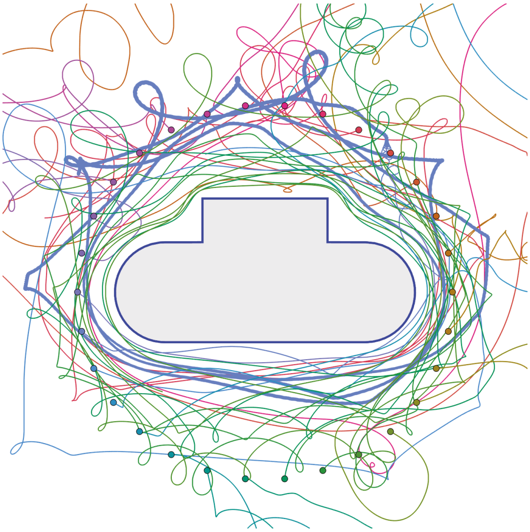

Figure 7. The trajectories of 30 vortices computed with the lightning method. The circulations of the vortices are randomly distributed in the interval $[-1, 1]$. The initial positions of the vortices are equispaced on a circle, as indicated by the coloured dots. The background flow is set to $U = 0$.

We consider a rigid body immersed in a separated flow that is uniform in the far-field. The goal is to calculate the velocity field induced by the boundary and the shape of the separation region behind the body. As before, we define the complex potential as $w(z) = \phi(z) + \mathrm{i}\psi(z)$ and the complex velocity as $w'(z) = u(z) - \mathrm{i}v(z)$. In this situation, enforcing the Kutta condition specifies that the flow detaches from the solid body at the edges. We assume that the fluid inside the separation region is stagnant and it is therefore of constant pressure. The free streamlines are the curves that divide the moving fluid from the stagnant fluid; therefore, they represent an infinitesimal shear layer. Because there can be no pressure jump either side of shear layer, the pressure along the free streamline must be constant. Accordingly, Bernoulli's theorem implies that (subject to a suitable scaling) the speed of fluid along the boundary of the wake is unity:

$$|w'(z)| = 1 \qquad \text{when } z \text{ is on a free streamline.} \tag{29}$$

Furthermore, the no-flux condition specifies that, on the surface of the solid body, the fluid velocity must be tangent to the boundary:

$$\angle w'(z(s)) = \angle \frac{\mathrm{d}\bar{z}}{\mathrm{d}s}(s) \quad \text{when } z \text{ is on solid body,} \tag{30}$$

where s is the arc length of the boundary.

The streamfunction is piecewise constant on both the rigid boundary and the free streamlines. We say 'piecewise constant' here, because there may be multiple free streamlines that correspond to different values of the streamfunction. Since both w and w' are analytic functions in simply connected domains, and assuming that they have a 1-to-1 relation, there exists a conformal map f between them:

$$w = f(w'). \tag{31}$$

We can now connect the physical coordinate z to the complex potential w and complex velocity w' by

$$z = \int^{w'} \frac{\mathrm{d}w}{\mathrm{d}w'_1}\frac{\mathrm{d}w'_1}{w'_1}. \tag{32}$$

The above maps a complex velocity value (w') to a physical coordinate (z). Thus, if f can be determined, then we know z and the corresponding velocity value there. The boundary conditions on f follow from (29) and (30), as

$$\mathbb{Im}[f(w')] = \text{constants} \qquad \text{for} \begin{cases} |w'| = 1, \\ \angle w'(z) = \angle \dfrac{\partial \bar{z}}{\mathrm{d}s}. \end{cases} \tag{33}$$

The precise constants that $\mathbb{Im}[f]$ attains on the boundaries are application dependent.

The problem of finding an analytic function f subject to the boundary conditions (33) may be solved using the lightning method introduced in Section 2. The lightning method is very appropriate to this problem, because the w' domain typically contains corners even though the physical z domain does not. While conventional methods struggle to resolve the singularities at the corners, the lightning method achieves root-exponential convergence.

In Figure 8, we illustrate the procedure for the separated flow past a flat plate. The incoming flow is inclined at an angle of $-\pi/8$. Along the free streamline, the velocity has magnitude 1 and along the plate the flow has zero normal velocity. Accordingly, the flow domain in the w' domain is a semicircle. We use the lightning method to compute the mapping from the complex velocity (w') domain to the complex potential domain (w), such that the semicircle is a streamline and the point $w' = \mathrm{e}^{-\mathrm{i}\pi/8}$ maps to infinity. Poles are clustered exponentially close to the corners of the semicircle in order to exploit the root-exponential convergence afforded by rational function approximation. In the complex potential domain, the boundaries are the upper and lower parts of the positive real axis. Having computed f, we may then use (32) to establish the relationship between the velocity and the spatial position z, which is plotted at the bottom of Figure 8. This problem can actually be solved analytically by appropriately placing image doublets in the w' domain, but the example is included here in order to illustrate the applicability of the lightning solver to free-streamline flows.

There are several methods available for improving the physical fidelity of free-streamline theory, the most conspicuous of which is the approach of Wu [21]. By allowing the pressure on the free streamline to increase monotonically, Wu [21] ensures that the free streamlines become asymptotically parallel to the background flow at infinity. This yields favourable comparisons for the lift and drag coefficients against experimental results. The simple example that we have presented does not allow the pressure on the free streamline to vary, but this effect could be incorporated to improve the realism of the model.

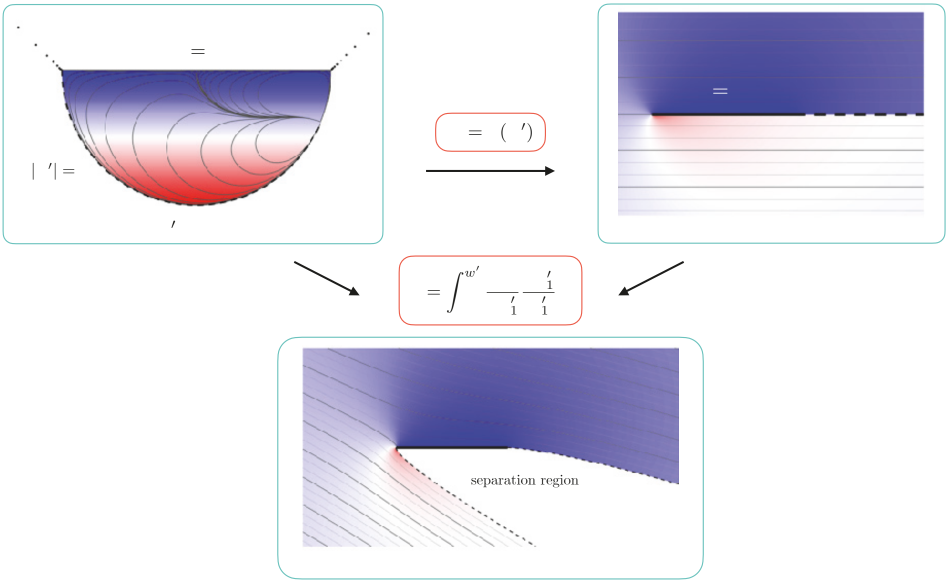

Figure 8. The separated flow past a flat plate at angle of attack $-\pi/8$. The lines are the streamlines and the colour represents the vertical velocity component.

4. Conclusions

In this paper we have presented a new method for numerically solving potential flow problems. Our method is based on the lightning method introduced by Gopal and Trefethen [6,7], and exploits the approximation power of rational functions. We believe that the technique will be useful to researchers in fluid mechanics who wish to quickly compute solutions to potential flows with modest accuracy in domains that prohibit fully analytical solutions and traditional numerical methods. The technique is comparatively simple and does not require specialised knowledge of finite element methods or boundary element methods. We have demonstrated that the method is valuable for several physical problems, including steady potential flows, unsteady vortex dynamics, and free streamline flows. Periodic domains are not an issue and are handled with a slightly different ansatz. The solutions converge extremely fast (with root-exponential convergence) and are themselves very fast to evaluate. When the solution is to be evaluated a large number of times, such as in the vortex dynamics simulations presented in Section 3.4, the solutions can be compressed using the AAA or AAAtrig algorithms.

Potential flows are mathematically elegant but neglect important physical phenomena. We have suggested two approaches to ameliorate these effects by incorporating vortex dynamics (Section 3.4) and flow separation (Section 3.5). The approach has also been demonstrated to apply to the Helmholtz equation [7], which could prove useful for acoustics and aeroacoustics problems. Additionally, there is the exciting possibility of extending the lightning solver to 3-D; apart from the conformal mapping of Section 3.4, our approach did not use complex variables except as a convenient coordinate system. This is a topic to be pursued in future studies.

Funding: This research was supported by an EPSRC Doctoral Prize from Imperial College London.

Acknowledgments: The author acknowledges the 2019 *Fluids* Travel Award from MDPI that supported attendance at the 2019 APS DFD meeting where some of the ideas in this paper were generated.

Conflicts of Interest: The author declares no conflict of interest.

References

1. Lehman, R. Developments at an analytic corner of solutions of elliptic partial differential equations. *Indiana Univ. Math. J.* **1959**, *8*, 727–760. [CrossRef]
2. Arndt, D.; Bangerth, W.; Blais, B.; Clevenger, T.C.; Fehling, M.; Grayver, A.V.; Heister, T.; Heltai, L.; Kronbichler, M.; Maier, M.; et al. The deal.II library, Version 9.2. *J. Numer. Math.* **2020**, *28*, 131–146. [CrossRef]
3. Logg, A.; Mardal, K.A.; Wells, G.N. *Automated Solution of Differential Equations by the Finite Element Method*; Lecture Notes in Computational Science and Engineering; Springer: Berlin/Heidelberg, Germany, 2012; Volume 84 LNCSE, pp. 1–736. [CrossRef]
4. Aliabadi, M.H.; Wen, P.H. Boundary element methods in engineering course. *Eng. Anal.* **1984**, *1*, 61–62. [CrossRef]
5. Serkh, K.; Rokhlin, V. On the solution of elliptic partial differential equations on regions with corners. *J. Comput. Phys.* **2016**, *305*, 150–171. [CrossRef]
6. Gopal, A.; Trefethen, L.N. Solving Laplace problems with corner singularities via rational functions. *SIAM J. Numer. Anal.* **2019**, *57*, 2074–2094. [CrossRef]
7. Gopal, A.; Trefethen, L.N. New Laplace and Helmholtz solvers. *Proc. Natl. Acad. Sci. USA* **2019**, *116*, 10223–10225. [CrossRef] [PubMed]
8. Joukowski, N. Über die Konturen der Tragflächen der Drachenflieger. *Z. Flugtech. Mot.* **1910**, *1*, 281–284.
9. Theodorsen, T. *General Theory of Aerodynamic Instability and the Mechanism of Flutter*; National Aeronautics and Space Administration: Washington, DC, USA, 1979; pp. 291–311.
10. Sears, W.R. Some Aspects of Non-Stationary Airfoil Theory and Its Practical Application. *J. Aeronaut. Sci.* **1941**, *8*, 104–108. [CrossRef]
11. Wu, T.Y.T. Swimming of a waving plate. *J. Fluid Mech.* **1961**, *10*, 321–344. [CrossRef]
12. Cordes, U.; Kampers, G.; Meiner, T.; Tropea, C.; Peinke, J.; Hölling, M. Note on the limitations of the Theodorsen and Sears functions. *J. Fluid Mech.* **2017**, *811*, R11–R111. [CrossRef]
13. Wei, N.J.; Kissing, J.; Wester, T.T.; Wegt, S.; Schiffmann, K.; Jakirlic, S.; Hölling, M.; Peinke, J.; Tropea, C. Insights into the periodic gust responseA ofA airfoils. *J. Fluid Mech.* **2019**, *876*, 237–263. [CrossRef]
14. Van Dyke, M. *Perturbation Methods in Fluid Mechanics*; Academic Press: New York, NY, USA, 1964.
15. Brown, C.E.; Michael, W.H. Effect of leading-edge separation on the lift of a delta wing. *J. Aeronaut. Sci.* **1954**, *21*, 690–694. [CrossRef]
16. Michelin, S.; Llewellyn Smith, S.G. An unsteady point vortex method for coupled fluid-solid problems. *Theor. Comput. Fluid Dyn.* **2009**, *23*, 127–153. [CrossRef]
17. Southwick, O.R.; Johnson, E.R.; McDonald, N.R. A point vortex model for the formation of ocean eddies by flow separation. *Phys. Fluids* **2015**, *27*, 16604. [CrossRef]
18. Manela, A.; Halachmi, M. Mechanisms of sound amplification and sound reduction in the flapping flight of side-by-side airfoils. *J. Sound. Vib.* **2015**, *346*, 216–228. [CrossRef]
19. Pullin, D. Contour Dynamics Methods. *Annu. Rev. Fluid Mech.* **1992**, *24*, 89–115. [CrossRef]
20. Krasny, R. Desingularization of periodic vortex sheet roll-up. *J. Comput. Phys.* **1986**, *65*, 292–313. [CrossRef]

21. Wu, T.Y.T. A wake model for free-streamline flow theory: Part 1. Fully and partially developed wake flows past an oblique flat plate. *J. Fluid Mech.* **1962**, *13*, 161–181. [CrossRef]
22. Hassenpflug, W.C. Free-streamlines. *Comput. Math. Appl.* **1998**, *36*, 69–129. [CrossRef]
23. Driscoll, T.A.; Trefethen, L.N. *Schwarz-Christoffel Mapping*; Cambridge University Press: Cambridge, UK, 2002.
24. Crowdy, D.G.; Marshall, J. Conformal mappings between canonical multiply connected domains. *Comput. Methods Funct. Theory* **2006**, *6*, 59–76. [CrossRef]
25. Nehari, Z. *Conformal Mapping*; McGraw-Hill: New York, NY, USA, 1952.
26. Crowdy, D.G. Solving problems in multiply connected domains. In *SIAM CBMS-NSF Regional Conference Series in Applied Mathematics*; SIAM: Philadelphia, PA, USA, 2020.
27. Crowdy, D.G. A new calculus for two-dimensional vortex dynamics. *Theor. Comput. Fluid Dyn.* **2010**, *24*, 9–24. [CrossRef]
28. Baddoo, P.J.; Ayton, L.J. A calculus for flows in periodic domains. *Theor. Comput. Fluid Dyn.* **2020**, arXiv:2001.00859.
29. Crowdy, D.G.; Kropf, E.H.; Green, C.C.; Nasser, M.M.S. The Schottky-Klein prime function: A theoretical and computational tool for applications. *IMA J. Appl. Math.* **2016**, *81*, 589–628. [CrossRef]
30. Lin, C.C. On the motion of vortices in two dimensions: I. Existence of the Kirchhoff–Routh function. *Proc. Natl. Acad. Sci. USA* **1941**, *27*, 575–577. [CrossRef] [PubMed]
31. Crowdy, D.G.; Marshall, J. Analytical formulae for the Kirchhoff-Routh path function in multiply connected domains. *Proc. R. Soc. A Math. Phys. Eng. Sci.* **2005**, *461*, 2477–2501. [CrossRef]
32. Baddoo, P.J.; Ayton, L.J. Potential flow through a cascade of aerofoils: Direct and inverse problems. *Proc. R. Soc. A Math. Phys. Eng. Sci.* **2018**, *474*, 20180065. [CrossRef]
33. Hajian, R.; Jaworski, J.W. The steady aerodynamics of aerofoils with porosity gradients. *Proc. R. Soc. A Math. Phys. Eng. Sci.* **2017**, *473*, 20170266. [CrossRef]
34. Moore, M.N.J. Riemann–Hilbert problems for the shapes formed by bodies dissolving, melting, and eroding in fluid flows. *Commun. Pure Appl. Math.* **2017**, *70*, 1810–1831. [CrossRef]
35. Crighton, D.G. The Kutta condition in unsteady flow. *Annu. Rev. Fluid Mech.* **1985**, *17*, 411–445. [CrossRef]
36. Eldredge, J.D. *Mathematical Modeling of Unsteady Inviscid Flows*; Interdisciplinary Applied Mathematics; Springer International Publishing: New York, NY, USA, 2019; Volume 50, p. 461. [CrossRef]
37. Ramesh, K.; Gopalarathnam, A.; Granlund, K.; Ol, M.V.; Edwards, J.R. Discrete-vortex method with novel shedding criterion for unsteady aerofoil flows with intermittent leading-edge vortex shedding. *J. Fluid Mech.* **2014**, *751*, 500–538. [CrossRef]
38. Darakananda, D.; da Silva, A.F.d.C.; Colonius, T.; Eldredge, J.D. Data-assimilated low-order vortex modeling of separated flows. *Phys. Rev. Fluids* **2018**, *3*, 124701. [CrossRef]
39. Trefethen, L.N. Lightning Laplace Software. 2020. Available online: https://people.maths.ox.ac.uk/trefethen/lightning (accessed on 21 November 2020).
40. Trefethen, L.N. *Approximation Theory and Approximation Practice, Extended Edition*; SIAM: Philadelphia, PA, USA, 2019.
41. Newman, D.J. Rational approximation to $|x|$. *Mich. Math. J.* **1964**, *11*, 11–14. [CrossRef]
42. Trefethen, L.N.; Nakatsukasa, Y.; Weideman, J.A.C. Exponential Node Clustering at Singularities for Rational Approximation, Quadrature, and PDEs. *Numer. Math.* **2020**, in press.
43. Brubeck, P.D.; Nakatsukasa, Y.; Trefethen, L.N. Vandermonde with Arnoldi. *SIAM Rev.* **2020**, in press.
44. Fairweather, G.; Karageorghis, A. The method of fundamental solutions for elliptic boundary value problems. *Adv. Comput. Math.* **1998**, *9*, 69–95. [CrossRef]
45. Mathon, R.; Johnston, R.L. The approximate solution of elliptic boundary-value problems by fundamental solutions. *SIAM J. Numer. Anal.* **1977**, *14*, 638–650. [CrossRef]
46. Kupradze, V.D.; Aleksidze, M.A. The method of functional equations for the approximate solution of certain boundary value problems. *USSR Comput. Math. Math. Phys.* **1964**, *4*, 82–126. [CrossRef]
47. Nakatsukasa, Y.; Sète, O.; Trefethen, L.N. The AAA algorithm for rational approximation. *SIAM J. Sci. Comput.* **2018**, *40*, A1494–A1522. [CrossRef]
48. Nakatsukasa, Y.; Trefethen, L.N. An algorithm for real and complex rational minimax approximation. *SIAM J. Sci. Comput.* **2020**, *42*, A3157–A3179. [CrossRef]
49. Driscoll, T.A.; Hale, N.; Trefethen, L.N. *Chebfun Guide*; Pafnuty Publications: Oxford, UK, 2014.

50. Baddoo, P.J. The AAAtrig algorithm for rational approximation of periodic functions. *arXiv* **2020**, arXiv:2008.05446.
51. Gopal, A.; Trefethen, L.N. Representation of conformal maps by rational functions. *Numer. Math.* **2019**, *142*, 359–382. [CrossRef]
52. Howell, L.H. Numerical conformal mapping of circular arc polygons. *J. Comput. Appl. Math.* **1993**, *46*, 7–28. [CrossRef]
53. Crowdy, D.G. Effective slip lengths for immobilized superhydrophobic surfaces. *J. Fluid Mech.* **2017**, *825*, R2. [CrossRef]
54. Vasconcelos, G.L. Multiple bubbles and fingers in a Hele-Shaw channel: Complete set of steady solutions. *J. Fluid Mech.* **2015**, *780*, 299–326. [CrossRef]
55. Baddoo, P.J.; Crowdy, D.G. Periodic Schwarz–Christoffel mappings with multiple boundaries per period. *Proc. R. Soc. A* **2019**, *475*. [CrossRef]
56. Llewellyn Smith, S.G. How do singularities move in potential flow? *Phys. D Nonlinear Phenom.* **2011**, *240*, 1644–1651. [CrossRef]
57. Aref, H. Point vortex dynamics: A classical mathematics playground. *J. Math. Phys.* **2007**, *48*, 065401. [CrossRef]
58. Saffman, P.G. *Vortex Dynamics*; Cambridge University Press: Cambridge, UK, 1993.
59. Crowdy, D.G. The Schwarz–Christoffel mapping to bounded multiply connected polygonal domains. *Proc. R. Soc. A Math. Phys. Eng. Sci.* **2005**, *461*, 2653–2678. [CrossRef]
60. Trefethen, L.N. Numerical conformal mapping with rational functions. *Comput. Methods Funct. Theory* **2020**, *20*, 369–387. [CrossRef]
61. Howe, M.S. *Theory of Vortex Sound*; Cambridge University Press, Cambridge, UK, 2003; p. 216.
62. Lin, C.C. On the Motion of Vortices in Two Dimensions: II. Some Further Investigations on the Kirchhoff-Routh Function. *Proc. Natl. Acad. Sci. USA* **1941**, *27*, 575–577. [CrossRef] [PubMed]
63. Elcrat, A.R.; Trefethen, L.N. Classical free-streamline flow over a polygonal obstacle. *J. Comput. Appl. Math.* **1986**, *14*, 251–265. [CrossRef]
64. Hureau, J.; Brunon, E.; Legallais, P. Ideal free streamline flow over a curved obstacle. *J. Comput. Appl. Math.* **1996**, *72*, 193–214. [CrossRef]

fluids

Communication

Polymers and Plastrons in Parallel Yield Enhanced Turbulent Drag Reduction

Anoop Rajappan and Gareth H. McKinley *

Hatsopoulos Microfluids Laboratory, Department of Mechanical Engineering, Massachusetts Institute of Technology, Cambridge, MA 02139, USA; anoopr@mit.edu
* Correspondence: gareth@mit.edu

Received: 13 October 2020; Accepted: 29 October 2020; Published: 1 November 2020

Abstract: Despite polymer additives and superhydrophobic walls being well known as stand-alone methods for frictional drag reduction in turbulent flows, the possibility of employing them simultaneously in an additive fashion has remained essentially unexplored. Through experimental friction measurements in turbulent Taylor–Couette flow, we show that the two techniques may indeed be combined favorably to generate enhanced levels of frictional drag reduction in wall-bounded turbulence. We further propose an additive expression in Prandtl–von Kármán variables that enables us to quantitatively estimate the magnitude of this cooperative drag reduction effect for small concentrations of dissolved polymer.

Keywords: drag reduction; polymers; superhydrophobic surfaces; Taylor–Couette turbulence

---

1. Introduction

Wall-bounded turbulent flows play a ubiquitous role in modern engineering and industry, in applications ranging from the internal flow of liquids in pipelines, to the external boundary layer flow around the hulls of ships and submarines [1,2]. The mitigation of frictional losses in turbulent flows is thus of considerable practical interest, with the potential to confer significant economic and environmental benefits. The systematic modification of turbulence dynamics through the introduction of either dissolved polymer chains [3–7] or boundary slip [8–10], leading to drag reduction, remains an active area of research and has witnessed resurgent interest in recent years [11–13]. The addition of soluble, high molar mass polymers has long been known to be an effective strategy for reducing frictional drag in turbulent flows [14–16]. Even at dilute concentrations as low as 10 ppm, dissolved long-chain polymers can interact with and alter near-wall coherent flow structures, yielding concomitant reductions in the frictional wall shear stress of 20–40 % [12–16]. A wide range of synthetic as well as naturally occurring high polymers have been successfully employed as drag reducing agents in a variety of turbulent flow configurations [17,18].

In recent years, superhydrophobic texturing of submerged solid surfaces has also emerged as a viable method of drag reduction in wall-bounded aqueous flows [19–22]. Superhydrophobic walls incorporate hydrophobic micro-textural features capable of thermodynamically stabilizing a thin layer of air—called the *plastron*—that remains pinned to the texture asperities in the Cassie–Baxter state, even when fully submerged underwater [19,20]. This intervening gas layer, in turn, shields the liquid from direct contact with the underlying solid substrate over large areal fractions of the flow boundary. Even as the usual no-slip condition continues to apply in regions of solid–liquid contact, the liquid–air interface atop the plastron layer serves as a nearly shear-free boundary over which the flow slips with minimal friction. The effect of this composite boundary on the outer flow is often modeled as an equivalent uniform slip velocity V_s at the wall, given by the Navier slip condition $V_s = b\,\tau_w/\eta$; here η is the dynamic viscosity of the liquid, τ_w the shear stress at the wall, and b represents an average "effective" slip length characterizing the superhydrophobic texture [20]. Despite early successes in laminar drag reduction as far back as 1996 [23], progress towards the use of superhydrophobic surfaces in turbulent flows has been slow, due in part to challenges in fabricating robust textures capable of sustaining an intact plastron layer even under the intense pressure fluctuations typically encountered in turbulence [22,24]. Several robust surfaces have, nevertheless, been developed in recent years, and turbulent drag reductions of up to 50 % on periodically micropatterned surfaces, and up to 30 % on scalable, randomly textured surfaces, have been reported in the open literature [22,25,26].

Consequently, we now have available two independent physical mechanisms for realizing practicable levels of drag reduction in turbulent flows: (i) dissolved polymer chains, which alter near-wall flow dynamics and disrupt turbulence production in the boundary layer, and (ii) plastron-supporting superhydrophobic surfaces, which enable diminished wetted contact of the fluid with the solid boundary, effectively inducing a slip velocity at the wall. Insofar as these physical mechanisms operate via fundamentally distinct pathways, a natural question arises as to whether the two approaches may be employed concurrently to yield enhanced reductions in frictional drag. Rather surprisingly, this possibility has remained largely unexplored in the extant literature. The only prior instance of polymers being used in conjunction with superhydrophobic textures for drag reduction seems to be an early experimental study by Watanabe and Udagawa [23], who measured the frictional pressure drop of aqueous polyethylene oxide (PEO) solutions in a circular pipe treated with a water-repellent coating. Although they separately observed wall slip in the laminar regime and polymer drag reduction in the turbulent regime, no combined effect arising from the two mechanisms operating in concert was reported, presumably due to the loss of entrapped gas from their superhydrophobic texture leading to plastron collapse in the turbulent regime. Recently, Davis and Park [27] presented direct numerical simulations of viscoelastic turbulent channel flow in the presence of wall slip; their preliminary results, however, indicated a slip-induced increase in the apparent drag.

In this paper, we answer the above question in the affirmative, and show that polymers and superhydrophobic textures can indeed be combined additively to yield enhanced drag reduction in turbulent flows. To this end, we perform experimental measurements of frictional drag in turbulent Taylor–Couette (TC) flow, using a superhydrophobic rotor comprising a periodic array of streamwise grooves, in parallel with a drag-reducing polymer (polyacrylamide) added to the working fluid (water) in the cell gap. Finally, we derive an additive expression to quantitatively estimate this combined drag reduction effect, which yields accurate predictions for low concentrations of the dissolved polymer.

2. Materials and Methods

2.1. Experimental Skin Friction Measurements

Experimental measurements of frictional drag in turbulent flow were performed using a bespoke TC apparatus with an improved design based on the wide-gap TC geometry introduced by Srinivasan et al. [28]. Since the construction and operational features of the TC apparatus are fully detailed elsewhere [26,29], we include here only a brief description of its key components: the rotating inner cylinder (rotor) of radius R_i and length L is housed concentrically inside the stationary outer cylinder (stator) of radius R_o, creating an annular gap of width $d = R_o - R_i$ to which the flow is confined; the radius ratio of our TC geometry is $R_i/R_o = 0.75$, and the gap aspect ratio is $L/d = 6.0$. The rotor is coupled to a commercial rotational rheometer (AR-G2, TA Instruments), enabling precise measurement of the steady-state frictional torque $\mathcal{T}$ exerted on the rotor as a function of its angular speed Ω.

As per the usual convention for TC flows, we define the Reynolds number $\mathrm{Re} = \rho V d/\eta$ based on the gap width d, the azimuthal speed $V = R_i\Omega$ of the rotor wall, and the density ρ and viscosity η of the working fluid. As the angular speed Ω of the rotor is increased, the flow inside the TC gap progresses through a sequence of intermediate vortical states, and eventually transitions to featureless (Newtonian) turbulence when a critical Reynolds number, Re_c, is reached. For our TC geometry, this latter transition to turbulent wall-driven shear flow occurs near $\mathrm{Re}_c = 11{,}000$, as determined from the power-law scaling of the baseline torque $\mathcal{T}_N$ with the Reynolds number Re when measured on a smooth no-slip rotor in deionized water (additional details are provided in the Supplementary Materials). Flow measurements employing polymers or superhydrophobic surfaces were subsequently performed at $\mathrm{Re} \geqslant 15{,}000$, well into the turbulent flow regime; a typical experiment consists of varying the angular speed Ω of the rotor in discrete steps, and recording the mean steady-state frictional torque $\mathcal{T}$. The average shear stress $\tau_w = \mathcal{T}/2\pi R_i^2 L$ at the rotor wall, and the friction velocity $u_\tau = \sqrt{\tau_w/\rho}$ in the near-wall layer, were then obtained from the experimental data. Finally, we computed the shear Reynolds number based on the gap width as $\mathrm{Re}_\tau = \rho u_\tau d/\eta$, with the reference viscosity η set equal to either the viscosity of water η_w, or—in tests involving drag-reducing polymers—the zero shear viscosity η_0 of the dilute solution employed as the working fluid; the latter was determined independently using an Ubbelöhde type glass capillary viscometer. Tests were conducted at room temperature, (23.0 ± 0.5) °C, and multiple replicates were obtained for each flow curve and averaged.

2.2. Fabrication of the Superhydrophobic Grooved Surface

To fabricate the superhydrophobic grooved surface, rectangular microgrooves were machined into the surface of the aluminum 6061-T6 rotor using a CNC lathe; the grooves were aligned in the circumferential direction, and spaced evenly along the rotor axis. The rotor was subsequently dip-coated in a $\simeq$0.1 % solution of a fluoropolymer resin (Teflon AF 2400, Chemours), and then cured on a laboratory hot plate at 240 °C. The dip-coating and baking steps were repeated at least five times to produce a mechanically durable coating firmly attached to the underlying grooves. Scanning electron microscope (SEM) images of the grooves were recorded at multiple spots on the rotor surface, and analyzed to determine the spatial periodicity (and thereby the wetted solid fraction) for the groove pattern. Water droplets were observed to be highly mobile over the final groove pattern, with roll-off occurring at very small (<5°) angles.

2.3. Preparation of Polyacrylamide Solutions

Polyacrylamide (PAM) was procured in powder form from Sigma-Aldrich, Inc., and used without further purification. A 0.4 % stock solution was first prepared by dispersing the powder in deionized water, and allowing it to hydrate and dissolve gradually on a laboratory bench-roller over several days to ensure homogeneous laminar mixing. Solutions of different concentrations in the range $10\,\mathrm{ppm} \leqslant c \leqslant 200\,\mathrm{ppm}$, for use in flow tests, were then prepared by diluting this stock solution with an appropriate volume of deionized water. Our dilute solutions have elasticity numbers of the order of $\mathrm{El} = \lambda\eta/\rho d^2 \simeq 4 \times 10^{-6}$, where λ is the (Zimm) relaxation time of the polymer; the Weissenberg number $\mathrm{Wi} = \mathrm{El} \cdot \mathrm{Re}$ in our experiments therefore ranges from $\mathrm{Wi} \simeq 6 \times 10^{-2}$ at $\mathrm{Re} = 15{,}000$, to $\mathrm{Wi} \simeq 0.2$ at $\mathrm{Re} = 52{,}000$.

3. Results

Below, we discuss and compare turbulent drag measurements in Newtonian and viscoelastic TC flows, with and without a superhydrophobic texture present at the inner wall. For clarity, results are organized into four sections based on the working fluid inside the gap (i.e., water or polymer solution), and the flow boundary condition (no-slip or superhydrophobic) at the rotor surface.

3.1. Water + No-Slip Rotor

In fully turbulent TC flow of a Newtonian fluid, Panton [30] used matched asymptotic expansions for the azimuthal angular momentum to derive a logarithmic friction law of the form

$$V_N^+ = M \ln \mathrm{Re}_\tau + N, \tag{1}$$

where $V^+ = V/u_\tau$ is the rotor wall speed in inner units, the subscript 'N' denotes Newtonian flow, and M and N are constants determined by the radius ratio of the TC geometry (for an alternative derivation of the logarithmic friction law, see Refs. [31,32]). In Figure 1a, data from flow measurements are presented in Prandtl–von Kármán coordinates, as a plot of V^+ against Re_τ on semi-logarithmic axes. The friction data for a smooth no-slip rotor in deionized water (empty black circles in Figure 1a) in the fully turbulent regime show good conformance to the functional form predicted by Equation (1), and we used a linear least squares regression of the baseline data to obtain the constants $M = 4.76$ and $N = -10.0$ for our bespoke TC geometry.

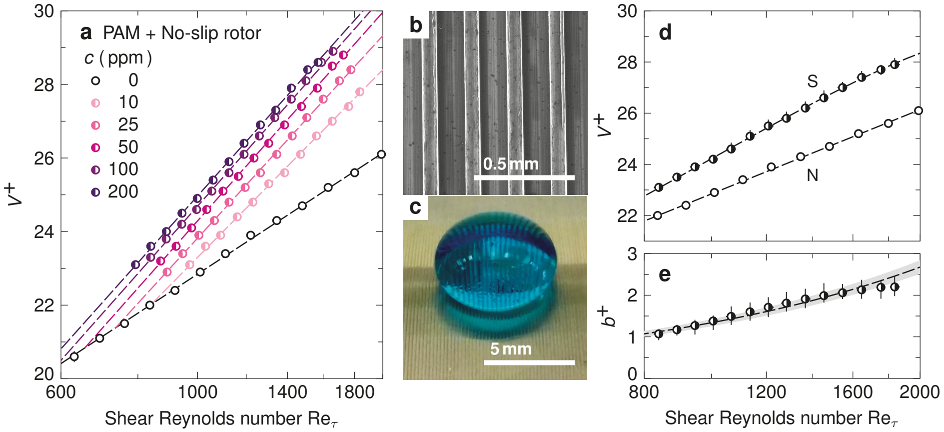

Figure 1. (**a**) Polymeric drag reduction curves for the no-slip rotor in aqueous polyacrylamide (PAM) solutions (concentration labeled in ppm). The hollow circles denote baseline friction in pure water. (**b**) SEM image of the grooved rotor surface. (**c**) Water drop, dyed blue, placed on the grooved rotor. The plastron within the groove troughs appears enlarged due to refraction through the drop. (**d**) Superhydrophobic drag reduction curve (S) for the grooved rotor in deionized water; the baseline no-slip data (N) from (**a**) is also included for comparison. (**e**) The dimensionless effective slip length b^+ measured on the grooved rotor. The dashed curve and the gray band denote the expected variation of b^+ for a constant dimensional slip length of $b = (17 \pm 1)\,\mu\mathrm{m}$. Error bars represent the full range of observations over 10 replicates.

3.2. Polymer Solution + No-Slip Rotor

As a model drag-reducing polymer system, we employed dilute solutions of aqueous polyacrylamide or PAM, composed of flexible, non-ionic, linear chains of large ($\gtrsim 10^6\,\mathrm{g\,mol^{-1}}$) molar mass. The intrinsic viscosity of this PAM solution, which we determined experimentally using capillary viscometry and Huggins–Kraemer extrapolation, was $[\eta] = 7.26\,\mathrm{dL\,g^{-1}}$ at 20 °C; using the Mark–Houwink–Sakurada expressions for PAM available in the literature [33], we inferred a viscosity-averaged molar mass of approximately $M_v \approx 2.54 \times 10^6\,\mathrm{g\,mol^{-1}}$ for our polymer sample (see Supplementary Materials for details). The critical chain overlap concentration for aqueous PAM may be evaluated [34] as $c^* = 0.77/[\eta] = 1.06\,\mathrm{g\,L^{-1}}$; the solutions used in our flow tests were considerably more dilute, with concentrations c in the range of 10–200 ppm, corresponding to normalized concentrations of $0.009 \leqslant c/c^* \leqslant 0.2$.

Figure 1a shows turbulent friction measurements on a smooth rotor in dilute PAM solutions of different concentrations. As in the Newtonian case, the data are again well described by straight line fits on the Prandtl–von Kármán plot of the form

$$V_P^+ = M_P \ln \mathrm{Re}_\tau + N_P, \tag{2}$$

where the subscript 'P' denotes polymeric turbulence, and the constants M_P and N_P obtained from the fit now depend also on the polymer used and its concentration c in solution. The drag-reducing effect of the dissolved polymer appears as a higher slope and an upward divergence of the polymeric friction curves from the Newtonian baseline in the turbulent regime. This becomes more evident if we consider the non-dimensional skin friction coefficient $C_f = 2\tau_w/\rho V^2$, which may equivalently be expressed as $C_f = 2/(V^+)^2$; a larger V^+ therefore implies a smaller value of C_f, and by extension, a reduced wall shear stress τ_w, at the same imposed speed V at the rotor wall. As expected, the extent of drag reduction increases with increasing Reynolds number, and at higher concentrations of the dissolved polymer; the PAM solution with the highest polymer concentration ($c = 200\,\text{ppm}$, $c/c^* = 0.2$) approaches the maximum drag reduction limit for our TC geometry at large Reynolds numbers, as discussed in the Supplementary Materials.

3.3. Water + Superhydrophobic Rotor

To obtain a robust plastron-bearing texture with repeatable wall slip characteristics, the surface of the aluminum rotor was machined to produce a regular array of parallel rectangular microgrooves aligned in the circumferential (streamwise) direction, similar to the grooved profile used by Van Buren and Smits [35]. The surface was then coated with a water-repellent fluoropolymer resin, yielding a superhydrophobic grooved texture (Figure 1b) with an average spatial periodicity of $l = 204\,\mu\text{m}$ and a gas fraction of $\phi = 0.66$ (see Section 2.2 under 'Materials and Methods' for details). Figure 1c shows a sessile water drop atop the superhydrophobic rotor surface, and the individual plastrons bridging the groove crests are clearly discernible.

Figure 1d shows experimental drag measurements on the grooved superhydrophobic rotor in deionized, air-saturated water; unlike the polymeric case, the friction curve does not approach the Newtonian, no-slip baseline at Reynolds numbers approaching Re_c, reflecting the fact that superhydrophobic drag reduction is effective in both the turbulent and laminar flow regimes. The skin friction law for fully turbulent TC flow of a Newtonian fluid with a slip boundary at the inner wall may be expressed as [28]

$$V_S^+ = M \ln \text{Re}_\tau + N + b^+, \tag{3}$$

where the subscript 'S' denotes a superhydrophobic wall, $b^+ = b\,\text{Re}_\tau/d$ is the effective slip length expressed in wall units, and the constants M and N are identical to those in Equation (1). In Figure 1e, the non-dimensional slip length b^+ computed from the friction curve using Equation (3) is shown for shear Reynolds numbers $\text{Re}_\tau \geqslant 800$; the data is seen to be well described by a constant slip length of $b = 17\,\mu\text{m}$, over the finite range of Reynolds numbers investigated in our study. Except for localized plastron depletion observed in a few grooves and isolated spots at large rotor speeds (leading to the slight decrease in measured slip length at large Re_τ seen in Figure 1e), the maintenance of the plastron layer on the grooved surface was visually confirmed at the end of each experiment.

In the limit of viscosity-dominated creeping flows, the slip length due to an alternating pattern of no-slip and shear-free stripes is given by $b_\parallel = (l/\pi)\ln[\sec(\pi\phi/2)]$ parallel to the stripe direction, and $b_\perp = b_\parallel/2$ perpendicular to it [36]. The situation is more complex in turbulent flows, wherein spanwise slip serves to strengthen near-wall vortices, and partly offsets the drag reduction due to displacement of the mean velocity profile induced by streamwise slip [37]. The effective slip length b^+ thus depends non-trivially on the local slip distribution as well as the viscous length scale of the inner flow, and an exact prediction usually warrants computational methods [37,38]. Moreover, the slip length at increasing flow speeds may also be influenced adversely by the curvature of the air–water interface spanning the groove troughs [39,40], occasional defects in the groove geometry, or the flow-induced collapse of the plastron in a small number of grooves [35]. Nevertheless, an estimate of the effective slip length—neglecting the complexities above—may be obtained [38] as $b \approx b_\parallel - b_\perp = (l/2\pi)\ln[\sec(\pi\phi/2)] = 22\,\mu\text{m}$, which is quite consistent with the average slip length of $b = 17\,\mu\text{m}$ observed in our experiments.

3.4. Polymer + Superhydrophobic Rotor

Lastly, we performed drag measurements on the superhydrophobic grooved rotor in aqueous PAM solutions of various concentrations; a representative friction curve for $c = 50\,\text{ppm}$ is shown in Figure 2a. The individual friction curves for the no-slip rotor in 50 ppm PAM solution and for the superhydrophobic rotor in water—cases (*B*) and (*C*) above—are also included for comparison. As evident from the plot, the combined drag reduction resulting from the dissolved polymer and the plastron is larger than that attainable by either technique employed alone at all values of Re_τ (and in fact exceeds the MDR limit estimated for our TC geometry, as described in the Supplementary Materials), signifying that the two mechanisms can indeed operate additively to yield enhanced overall drag reduction in turbulent flows. From an engineering perspective, the quantity that is often of immediate interest is the net decrease in fluid friction—the wall shear stress in external flows, or the head loss per unit length in internal flows—compared to the flow of pure solvent (water) with no-slip flow boundaries under identical conditions of wall speed or flow rate. Accordingly, we define the percentage drag reduction $\mathcal{D} = (1 - \tau_w/\tau_{w,N}) \cdot 100\,\%$, where τ_w is the actual shear stress measured at the rotor wall, and $\tau_{w,N}$ is the reference wall shear stress on the no-slip rotor in deionized water at the same speed V (or equivalently, at the same solvent-based Reynolds number $\mathrm{Re}_s = \rho V d/\eta_w$ computed using the viscosity η_w of water). In Figure 2b, the data from Figure 2a have been replotted as the percentage drag reduction $\mathcal{D}$ versus the Reynolds number Re_s, and the enhancement in drag reduction from combining polymer additives and superhydrophobic surfaces is again apparent.

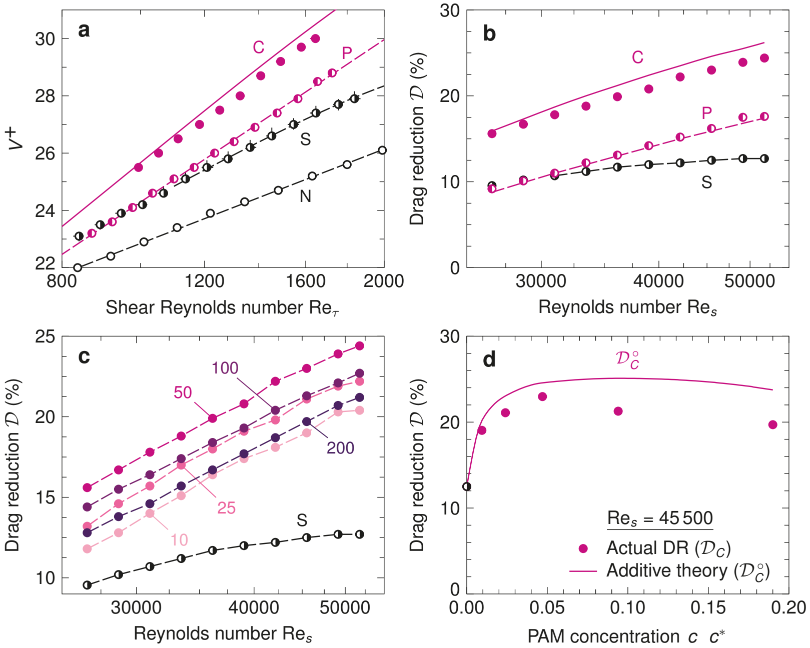

Figure 2. (**a**) Experimental friction curves and (**b**) the percentage drag reduction for the no-slip rotor in water (*N*) and in 50 ppm aqueous PAM (*P*), as well as for the superhydrophobic grooved rotor in water (*S*) and in 50 ppm aqueous PAM (*C*). The solid curves denote the ideal estimates $\left(V_C^+\right)^\circ$ and $\mathcal{D}_C^\circ$ predicted by our additive model. (**c**) Combined percentage drag reduction for the superhydrophobic rotor in PAM solutions of various concentrations (labeled in ppm). (**d**) The actual percentage drag reduction $\mathcal{D}_C$, and the ideal estimate $\mathcal{D}_C^\circ$, as a function of c/c^* at $\mathrm{Re}_s = 45{,}500$.

4. Discussion

We next proceed to formulate an empirical law to predict the combined drag reduction expected from a given polymer–wall pair, if their individual drag reduction efficacies are known beforehand. Insofar as both polymeric and superhydrophobic drag reduction results from complex modifications of the near-wall dynamics—induced respectively by dissolved macromolecules and interfacial slip—it is to be expected that their concurrent action will elicit mutual interactions that are amenable to quantitative prediction only through numerical methods [27]. Notwithstanding these complexities, we envision a simple two-layer model (see Figure 3) in which we assume that: (*i*) viscoelastic effects, which operate predominantly in the buffer layer and beyond [12,13], are largely oblivious to the influence of wall slip, which is confined mostly to the viscous sublayer [8–10]; and (*ii*) the average flux of streamwise momentum to the wall (i.e., the frictional shear stress) constitutes the principal mode of information exchange between the viscous sublayer and the outer flow. In this simple additive framework, we superimpose the velocity defects from Equations (2) and (3) to obtain the composite friction law:

$$\left(V_C^+\right)^\circ = V_P^+ + b^+ = V_P^+ + \left(V_S^+ - V_N^+\right), \tag{4}$$

representing the parallel action of the two drag-reducing mechanisms via a linear addition of the corresponding velocity increments expressed in wall units. Here, the subscript '*C*' denotes 'combined' drag reduction, and the superscript ° indicates an ideal estimate derived from the additive theory described above.

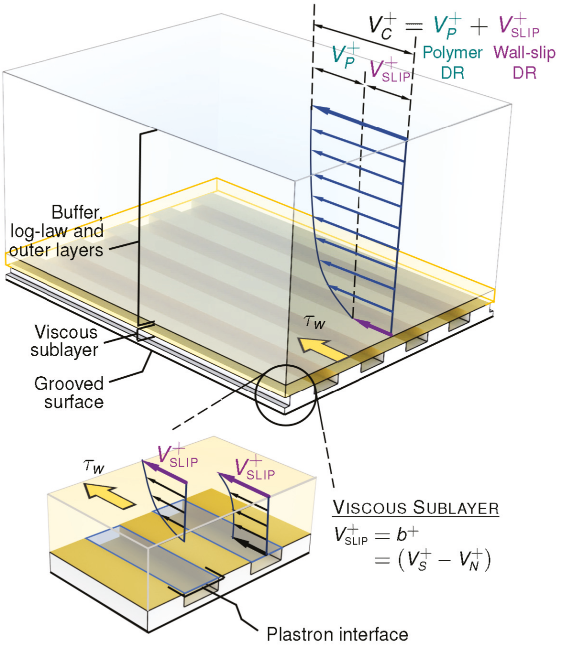

Figure 3. Schematic depiction of the additive two-layer model for combined drag reduction. The inset shows the thin near-wall viscous sublayer within which the composite boundary conditions are assumed to homogenize, yielding a uniform effective slip velocity V_{SLIP}^+ perceived by the outer layers. Dimensions are merely illustrative and are not to scale.

In Figure 2a,b, the solid curves represent the wall friction predicted by Equation (4), and the corresponding ideal estimate for the percentage drag reduction $\mathcal{D}_C^\circ$; while there is fair agreement with experimental data especially at moderate Reynolds numbers ($\mathrm{Re}_s \leqslant 30{,}000$), the actual drag reduction levels are seen to be somewhat smaller than that obtained from our two-layer model. This, in turn, suggests that 'non-linear' interactions between the two drag reduction mechanisms serve to counteract rather than reinforce one another, and the additive expression in Equation (4) consequently represents an upper bound for the combined drag reduction levels that are actually realizable in practice. In Figure 2c, we show the variation of the combined drag reduction $\mathcal{D}_C$ with the Reynolds number Re_s for different concentrations c of the dissolved polymer. Drag reduction initially increases with rising polymer concentration, plateaus, and subsequently falls off at concentrations exceeding 50 ppm; this latter decline arises from the increasing shear viscosity η_0 of the solution, which progressively offsets the drag reduction produced by polymeric suppression of turbulence. The effect of polymer concentration can also be seen in Figure 2d, in which the model predictions and measured drag reduction levels are shown as a function of c/c^* at a fixed value of the Reynolds number $\text{Re}_s = 45{,}500$. Evidently, the additive law provides a good estimate of the friction reduction attainable in dilute solutions, but slightly overpredicts the combined effect as the polymer concentration is raised.

In closing, we note that although periodically patterned textures—exemplified by the streamwise groove array employed in our study—serve as useful canonical surfaces with tunable slip properties, high fabrication cost and limited scalability render them impracticable in large-scale engineering applications. There is thus a practical imperative to explore combined drag reduction strategies that use scalable surfaces possessing irregular textural roughnesss. Furthermore, a number of common drag-reducing polymers, including PEO [41], are known to depress the surface tension of aqueous solutions, and their use may entail interfacial effects that adversely influence the overall slip at the wall [42]; our choice of PAM was prompted, in fact, by its notable lack of adsorption at the air–water interface [43]. Such practical considerations clearly merit further investigation, and we address some of these questions in a forthcoming article.

Supplementary Materials: Further details on experimental flow measurements using the TC apparatus, the viscometric characterization of PAM solutions, and the fabrication of the grooved superhydrophobic surface, as well as a discussion on polymer-mediated drag reduction in Taylor–Couette turbulence, are included in the Supplementary Material available online at http://www.mdpi.com/2311-5521/5/4/197/s1. Additionally, raw datasets from experimental friction measurements in the TC apparatus are provided separately as a Microsoft Excel spreadsheet.

Author Contributions: Conceptualization, A.R. and G.H.M.; methodology, A.R.; investigation, A.R.; supervision, G.H.M.; writing—original draft preparation, A.R.; writing—review and editing, G.H.M. All authors have read and agreed to the published version of the manuscript.

Funding: Financial support for this work was provided in part by the MRSEC program of the National Science Foundation (NSF) under award number DMR-1419807, and by the Office of Naval Research (ONR) under the MURI program through contract number 3002453814.

Acknowledgments: The authors would like to thank T. Van Buren and A. J. Smits at Princeton University for providing the grooved rotor used in this study.

Conflicts of Interest: The authors declare no conflict of interest. The funding sources had no role in the design of the study; in the collection, analyses, or interpretation of data; in the writing of the manuscript, or in the decision to publish the results.

References

1. Tennekes, H.; Lumley, J.L. *A First Course in Turbulence*; The MIT Press: Cambridge, MA, USA, 1972.
2. Pope, S.B. *Turbulent Flows*; Cambridge University Press: Cambridge, UK, 2000.
3. Stone, P.A.; Waleffe, F.; Graham, M.D. Toward a structural understanding of turbulent drag reduction: nonlinear coherent states in viscoelastic shear flows. *Phys. Rev. Lett.* **2002**, *89*, 208301. [CrossRef] [PubMed]
4. Roy, A.; Morozov, A.; van Saarloos, W.; Larson, R.G. Mechanism of polymer drag reduction using a low-dimensional model. *Phys. Rev. Lett.* **2006**, *97*, 234501. [CrossRef] [PubMed]
5. Kim, K.; Adrian, R.J.; Balachandar, S.; Sureshkumar, R. Dynamics of hairpin vortices and polymer-induced turbulent drag reduction. *Phys. Rev. Lett.* **2008**, *100*, 134504. [CrossRef] [PubMed]
6. Xi, L.; Graham, M.D. Active and hibernating turbulence in minimal channel flow of Newtonian and polymeric fluids. *Phys. Rev. Lett.* **2010**, *104*, 218301. [CrossRef] [PubMed]

7. Xi, L.; Graham, M.D. Dynamics on the laminar-turbulent boundary and the origin of the maximum drag reduction asymptote. *Phys. Rev. Lett.* **2012**, *108*, 028301. [CrossRef]
8. Martell, M.B.; Rothstein, J.P.; Perot, J.B. An analysis of superhydrophobic turbulent drag reduction mechanisms using direct numerical simulation. *Phys. Fluids* **2010**, *22*, 065102. [CrossRef]
9. Park, H.; Park, H.; Kim, J. A numerical study of the effects of superhydrophobic surface on skin-friction drag in turbulent channel flow. *Phys. Fluids* **2013**, *25*, 110815. [CrossRef]
10. Rastegari, A.; Akhavan, R. On the mechanism of turbulent drag reduction with super-hydrophobic surfaces. *J. Fluid Mech.* **2015**, *773*, R4. [CrossRef]
11. Perlin, M.; Dowling, D.R.; Ceccio, S.L. Freeman scholar review: Passive and active skin-friction drag reduction in turbulent boundary layers. *J. Fluids Eng.* **2016**, *138*, 091104. [CrossRef]
12. Graham, M.D. Drag reduction and the dynamics of turbulence in simple and complex fluids. *Phys. Fluids* **2014**, *26*, 101301. [CrossRef]
13. Xi, L. Turbulent drag reduction by polymer additives: Fundamentals and recent advances. *Phys. Fluids* **2019**, *31*, 121302.
14. Hoyt, J.W. The effect of additives on fluid friction. *J. Basic Eng.* **1972**, *94*, 258–285. [CrossRef]
15. Virk, P.S. Drag reduction fundamentals. *AIChE J.* **1975**, *21*, 625–656. [CrossRef]
16. White, C.M.; Mungal, M.G. Mechanics and prediction of turbulent drag reduction with polymer additives. *Annu. Rev. Fluid Mech.* **2008**, *40*, 235–256. [CrossRef]
17. Han, W.J.; Choi, H.J. Role of bio-based polymers on improving turbulent flow characteristics: Materials and applications. *Polymers* **2017**, *9*, 209. [CrossRef] [PubMed]
18. Han, W.J.; Dong, Y.Z.; Choi, H.J. Applications of water-soluble polymers in turbulent drag reduction. *Processes* **2017**, *5*, 24. [CrossRef]
19. McHale, G.; Newton, M.I.; Shirtcliffe, N.J. Immersed superhydrophobic surfaces: Gas exchange, slip and drag reduction properties. *Soft Matter* **2010**, *6*, 714–719. [CrossRef]
20. Rothstein, J.P. Slip on superhydrophobic surfaces. *Annu. Rev. Fluid Mech.* **2010**, *42*, 89–109. [CrossRef]
21. Bhushan, B.; Jung, Y.C. Natural and biomimetic artificial surfaces for superhydrophobicity, self-cleaning, low adhesion, and drag reduction. *Prog. Mater. Sci.* **2011**, *56*, 1–108. [CrossRef]
22. Golovin, K.B.; Gose, J.W.; Perlin, M.; Ceccio, S.L.; Tuteja, A. Bioinspired surfaces for turbulent drag reduction. *Phil. Trans. R. Soc. A* **2016**, *374*, 20160189. [CrossRef]
23. Watanabe, K.; Udagawa, H. Drag reduction of Non-Newtonian fluids in a circular pipe with a highly water-repellent wall. *AIChE J.* **2001**, *47*, 256–262. [CrossRef]
24. Seo, J.; García-Mayoral, R.; Mani, A. Pressure fluctuations and interfacial robustness in turbulent flows over superhydrophobic surfaces. *J. Fluid Mech.* **2015**, *783*, 448–473. [CrossRef]
25. Park, H.; Sun, G.; Kim, C.J. Superhydrophobic turbulent drag reduction as a function of surface grating parameters. *J. Fluid Mech.* **2014**, *747*, 722–734. [CrossRef]
26. Rajappan, A.; Golovin, K.; Tobelmann, B.; Pillutla, V.; Abhijeet.; Choi, W.; Tuteja, A.; McKinley, G.H. Influence of textural statistics on drag reduction by scalable, randomly rough superhydrophobic surfaces in turbulent flow. *Phys. Fluids* **2019**, *31*, 042107. [CrossRef]
27. Davis, E.A.; Park, J.S. Turbulence dynamics of dilute polymer solutions: Apparent slip and the effect of slip-inducing surfaces. In Proceedings of the 91st Annual Meeting of the Society of Rheology, Raleigh, NC, USA, 20–24 October 2019.
28. Srinivasan, S.; Kleingartner, J.A.; Gilbert, J.B.; Cohen, R.E.; Milne, A.J.B.; McKinley, G.H. Sustainable drag reduction in turbulent Taylor-Couette flows by depositing scalable superhydrophobic surfaces. *Phys. Rev. Lett.* **2015**, *114*, 014501. [CrossRef]
29. Rajappan, A.; McKinley, G.H. Epidermal biopolysaccharides from plant seeds enable biodegradable turbulent drag reduction. *Sci. Rep.* **2019**, *9*, 18263. [CrossRef]
30. Panton, R.L. Scaling laws for the angular momentum of a completely turbulent Couette flow. *C. R. Acad. Sci. Paris Ser. II* **1992**, *315*, 1467–1473.
31. Lathrop, D.P.; Fineberg, J.; Swinney, H.L. Transition to shear-driven turbulence in Couette-Taylor flow. *Phys. Rev. A* **1992**, *46*, 6390–6405. [CrossRef]
32. Lewis, G.S.; Swinney, H.L. Velocity structure functions, scaling and transitions in high Reynolds number Couette-Taylor flow. *Phys. Rev. E* **1999**, *59*, 5457–5467. [CrossRef]

33. McCarthy, K.J.; Burkhardt, C.W.; Parazak, D.P. Mark-Houwink-Sakurada constants and dilute solution behavior of heterodisperse poly(acrylamide-co-sodium acrylate) in 0.5 M and 1 M NaCl. *J. Appl. Polym. Sci.* **1987**, *33*, 1699–1714. [CrossRef]
34. Rubinstein, M.; Colby, R.H. *Polymer Physics*; Oxford University Press: Oxford, UK, 2003.
35. Buren, T.V.; Smits, A.J. Substantial drag reduction in turbulent flow using liquid-infused surfaces. *J. Fluid Mech.* **2017**, *827*, 448–456. [CrossRef]
36. Philip, J.R. Flows satisfying mixed no-slip and no-shear conditions. *Z. Angew. Math. Phys.* **1972**, *23*, 353–372. [CrossRef]
37. Min, T.; Kim, J. Effects of hydrophobic surface on skin-friction drag. *Phys. Fluids* **2004**, *16*, L55. [CrossRef]
38. Fairhall, C.T.; García-Mayoral, R. Spectral analysis of the slip-length model for turbulence over textured superhydrophobic surfaces. *Flow Turbul. Combust.* **2018**, *100*, 961–978. [CrossRef]
39. Sbragaglia, M.; Prosperetti, A. A note on the effective slip properties for microchannel flows with ultrahydrophobic surfaces. *Phys. Fluids* **2007**, *19*, 043603. [CrossRef]
40. Steinberger, A.; Cottin-Bizonne, C.; Kleimann, P.; Charlaix, E. High friction on a bubble mattress. *Nat. Mater.* **2007**, *6*, 665–668. [CrossRef] [PubMed]
41. Kim, M.W.; Cao, B.H. Additional reduction of surface tension of aqueous polyethylene oxide (PEO) solution at high polymer concentration. *Europhys. Lett.* **1993**, *24*, 229–234. [CrossRef]
42. Peaudecerf, F.J.; Landel, J.R.; Goldstein, R.E.; Luzzatto-Fegiz, P. Traces of surfactants can severely limit the drag reduction of superhydrophobic surfaces. *Proc. Natl. Acad. Sci. USA* **2017**, *114*, 7254–7259. [CrossRef]
43. Hu, R.Y.Z.; Wang, A.T.A.; Hartnett, J.P. Surface tension measurement of aqueous polymer solutions. *Exp. Therm. Fluid Sci.* **1991**, *4*, 723–729. [CrossRef]

fluids

Article

On the Foundations of Eddy Viscosity Models of Turbulence

Nan Jiang [1], William Layton [2,*], Michael McLaughlin [2], Yao Rong [3] and Haiyun Zhao [2]

[1] Department of Mathematics, University of Florida, Gainesville, FL 32611, USA; jiangn@ufl.edu
[2] Department of Mathematics, University of Pittsburgh, Pittsburgh, PA 15260, USA; mem266@pitt.edu (M.M.); haz50@pitt.edu (H.Z.)
[3] School of Mechanical Engineering and Automation, Harbin Institute of Technology, Shenzhen 518055, China; yr926@hit.edu.cn
* Correspondence: wjl@pitt.edu

Received: 26 August 2020; Accepted: 26 September 2020; Published: 29 September 2020

Abstract: This report gives a summary of some recent developments in the mathematical foundations of eddy viscosity models of turbulence.

Keywords: Boussinesq assumption; eddy viscosity hypothesis

---

1. Introduction

Predicting turbulent flows in practical settings means solving models intended to predict averages of turbulent velocities. In practical simulations, the most common turbulence models of averages of the Navier-Stokes equations (NSE)

$$u_t + u \cdot \nabla u - \nu \triangle u + \nabla p = f(x,t), \text{ and } \nabla \cdot u = 0, \tag{1}$$

are eddy viscosity models. Yet in evaluations and assessments of models, eddy viscosity models are also the most criticized. This report will give a survey of some recent work, aiming to bridge at least partially this gap, on the foundations of eddy viscosity models. The work is based on the papers [1–6]. From these we present the most interesting cases rather than the most general ones.

The mean velocities, herein denoted $\langle u \rangle$ are defined in various ways including

$$\begin{aligned} \text{Ensemble average:} \quad & \langle u \rangle_J (x,t) = \tfrac{1}{J}\textstyle\sum_{j=1}^{J} u(x,t;\omega_j), \\ \text{Time Average:} \quad & \langle u \rangle_\tau (x,t) = \tfrac{1}{\tau}\textstyle\int_{t-\tau}^{t} u(x,t')dt'. \end{aligned}$$

In addition to the view that turbulence is fundamentally a stochastic phenomena, the parameter ω and its sampled values ω_j can incorporate variation in flow parameters not represented by the model (e.g., variation of viscosity with temperature in an isothermal model) or measurement imprecision in input data (e.g., inflow or initial velocities). In such cases parameters can serve to extend predictability horizons or quantify uncertainty. The model of these most common in practical computations is an eddy viscosity (EV) model, [7], consisting of replacing the kinematic viscosity ν by $\nu + \nu_T$, where ν_T is the eddy viscosity coefficient that must be determined. Simulations of EV models produce results for averaged quantities with reasonable accuracy in many cases. Durbin and Pettersson Reif [8] (p. 195) write

> “Virtually all practical engineering computations are done with some variation of eddy viscosity ...”.

Eddy viscosity models also fail in other cases, such as turbulent flow not at statistical equilibrium so there is a robust effort to develop improved models, e.g., [9–12]. We present herein a review of some recent ideas in the mathematical foundations of these eddy viscosity models.

Aside from the problem of choosing, calibrating or calculating the eddy viscosity ν_T, EV produces a model for the mean velocity that requires a simple modification of laminar flow codes. For example, consider the most basic linearly implicit timestepping method for the (above) NSE (suppressing the space discretization, letting $\triangle t$ be the time step and u^n denote the approximation at $t_n = n\triangle t$)

$$\frac{u^{n+1}-u^n}{\triangle t} + u^n \cdot \nabla u^{n+1} + \nabla p^{n+1} - \nu \triangle u^{n+1} = f^{n+1} \,\&\, \nabla \cdot u^{n+1} = 0.$$

Implementing an eddy viscosity term in a well understood code can be done by lagging its dependence on flow quantities by $\nu_T(u^n, p^n, \cdots)$. Then ν_T can be treated as a know distribution $\nu_T(x) = \nu_T(u^n, p^n, \cdots)$ (varying from one step to the next). With $\nabla^s u$ the symmetric part of ∇u and $\nu_T(x)$ the lagged value, the timestepping becomes

$$\frac{u^{n+1}-u^n}{\triangle t} + u^n \cdot \nabla u^{n+1} + \nabla p^{n+1} - \nabla \cdot \left(2[\nu + \nu_T(x)]\nabla^s u^{n+1}\right) = f^{n+1}.$$

In the more typical case of a complex code possibly legacy or team developed, a modular eddy viscosity, introduced in [13,14], can be used. In this approach a step can be added to the above linearly implicit NSE step to induce the eddy viscosity model

$$\begin{array}{ll} \text{Step 1: NSE} & \begin{array}{c} \frac{u^{n+1}-u^n}{\triangle t} + u^n \cdot \nabla u^{n+1} + \nabla p^{n+1} - \nu \triangle u^{n+1} = f^{n+1}, \\ \nabla \cdot u^{n+1} = 0. \end{array} \\ \text{Step 2: EV} & \begin{array}{c} \text{solve: } -\nabla \cdot (2\nu_T(x)\nabla^s w) + \frac{1}{\triangle t} w = \frac{1}{\triangle t} u^{n+1}, \\ \text{then: } u^{n+1} \Leftarrow w. \end{array} \end{array}$$

Modularity generally refers to the use of distinct functional units. Step 2 represents a distinct step or functional unit implementing the eddy viscosity model. Modular eddy viscosity has advantages in cognitive complexity and for legacy codes. Additionally it can be used to ameliorate the typical EV failure model of over diffusion as follows. Given a collection of eddy viscosity parameterizations, scale them so that

$$0 \le \nu_{i,T}(u^n, p^n, \cdots) \le 1, \quad i = 1, \cdots, I.$$

Then $\nu_T(x)$ used in the modular step is the geometric average of the collection

$$\nu_T(x) := \left(\Pi_{i=1}^{I} \nu_{i,T}\right)^{1/I}.$$

Geometric averaging means that, where the models agree that turbulent dissipation is active, it will be switched on, and where one model recognizes a laminar region, a persistent eddy or other local activities where eddy breakdown does not occur, turbulent dissipation is switched off. Specifically, if all eddy viscosities have $\nu_{i,T}(x) = \mathcal{O}(1)$ then $\nu_T(x) = \mathcal{O}(1)$ and if one eddy viscosity has $\nu_{i,T}(x) = 0$ then $\nu_T(x) = 0$. Models are thereafter refined by adding function subroutines defining a new eddy viscosity based on a new insight into the physics of turbulent energy transfer. As a concrete example, it is known that helicity is large during strong rotation and increases with depletion of nonlinearity. Thus, one way to decrease EV locally where helicity is large is to choose one of the $\nu_{i,T}$ to be:

$$\nu_{helicity}(x,t) := \frac{|u \cdot \nabla \times u|^2}{|u|^2 |\nabla \times u|^2}(x,t).$$

See [13,14] for other examples of $\nu_{i,T}$.

Eddy viscosity models are based on the early work of Saint-Venant [15] and Boussinesq [7,16] and developed to their current state by Prandtl, Kolmogorov and von Karman, e.g., [17]. Eddy viscosity models are based on two conjectures:

Boussinesq:	Turbulent fluctuations have a dissipative effect on the mean flow.
EV hypothesis:	This dissipation can be modelled by an eddy viscosity term $\nabla \cdot (\nu_T \nabla^s \langle u \rangle)$.

The eddy viscosity coefficient ν_T must depend only on quantities computable from the mean flow and express the physical idea of Saint-Venant that ν_T increases "the intensity of the whirling agitation", [16] (p. 235). The Kolmogorov-Prandtl relation expresses this in a dimensionally consistent way as

$$\begin{aligned} \nu_T &= \mu l \sqrt{k'}, \text{ where} \\ \mu &= \text{ calibration constant (typically 0.2 to 0.6)}, \\ l(x) &= \text{mixing length / turbulence length scale}, \\ k' &= \frac{1}{2}\left\langle |u - \langle u \rangle|^2 \right\rangle \text{ the turbulent kinetic energy.} \end{aligned}$$

Then l and k' are specified to determine the model. Current ideas involve determining the eddy viscosity coefficient using machine learning tools, [18].

Aside from eddy viscosity, turbulence models increasingly use a variety of mechanisms for dissipativity such as tensor diffusion, hyper viscosity, variational multi-scale diffusion, time relaxation and so on, e.g., [1,2,19–28].

2. Ensemble Averages and the Boussinesq Conjecture

The conjecture that turbulent fluctuations have a dissipative effect on the mean flow was proven in a widely circulated report [4] and developed further extensively, [2,3,29]. In this section we develop it mathematically and give a proof (that motivates further model development). The effect of the fluctuations on the mean flow occurs through the Reynolds stresses.

Definition 1 (Reynolds stresses)**.** *The Reynolds stresses are*

$$R(u,u) := \langle u \rangle \otimes \langle u \rangle - \langle u \otimes u \rangle = -\left\langle u' \otimes u' \right\rangle .$$

The main result is the following theorem.

Theorem 1. *Suppose that each realization is a strong solution of the NSE, the ensemble is generated by different initial data (and not different body forces or physical parameters) and that* $u^0(x;\omega_j) \in L^2(\Omega)$, $f(x,t) \in L^\infty(0,\infty;L^2(\Omega))$. *Then, for any sequence* $T_j \to \infty$ *for which the limits exist*

$$\lim_{T_j \to \infty} \frac{1}{T_j} \int_0^{T_j} \int_\Omega R(u,u) : \nabla \langle u \rangle \, dxdt = \lim_{T_j \to \infty} \frac{1}{T_j} \int_0^{T_j} \int_\Omega \left\langle \nu |\nabla u'|^2 \right\rangle dxdt \geq 0.$$

The meaning of the terms in the theorem is developed precisely in the next subsection. Loosely, the left hand side represents the (time averaged) effects of fluctuations on the kinetic energy of the mean flow. The right hand side being non-negative means that (time averaged) effect is dissipative. The next subsection sets notation and shows why this is precisely the Boussinesq conjecture. We note that the proof for dissipative weak solutions is not naturally expressed in the standard terms of turbulence modelling. It is technical but even simpler than for strong solutions. The case of weak solutions is presented in the referenced papers. For recent developments see [30,31].

2.1. Preliminaries

Ω denotes the $2d$ or $3d$ flow domain, ν the kinematic viscosity, $f(x,t)$ the body force, $u(x,t;\omega_j)$, $p(x,t;\omega_j)$, $j=1,\cdots,J$, a collection of velocities and pressures that depend on a parameter ω_j. We let $||\cdot||, (\cdot,\cdot)$ denote the usual L^2 norm and inner product. We assume $f = f(x,t) \in L^{\infty}(0,\infty;L^2(\Omega))$, i.e., the body force can be persistent (including $f = f(x)$) with

$$ess\ sup_{0<t<\infty}||f(\cdot,t)|| < \infty.$$

If v, w are two vectors in $\mathbb{R}^d$ then $v \otimes w$ is the tensor ($d \times d$ array) with (r,s) component $v_r w_s$.

Let the ensemble of initial conditions determining the ensemble of velocities (for motivation of this choice see [32]) be denoted by

$$u(x,0;\omega_j) = u^0(x;\omega_j), \ \ j = 1,\cdots,J, \text{ in } \Omega. \tag{2}$$

The subscript $j =$ ensemble realization number and does not denote a component or derivative. The velocities and pressures u, p satisfy no slip boundary conditions $u = 0$ on $\partial\Omega$ and the NSE

$$u_t + u\cdot\nabla u - \nu\triangle u + \nabla p = f(x,t), \text{ and } \nabla\cdot u = 0 \ \text{ in } \Omega\,. \tag{3}$$

Definition 2 (Mean, Fluctuation and Variance)**.** *For an ensemble $\phi(x,t;\omega_j)$, $j = 1,\cdots,J$, the mean $\langle\phi\rangle$ and fluctuation ϕ' are*

$$\langle\phi\rangle(x,t) = \frac{1}{J}\sum_{j=1}^{J}\phi(x,t;\omega_j), \ \ \phi'(x,t;\omega_j) = \phi - \langle\phi\rangle\,.$$

The variance of u and ∇u are, respectively,

$$V(u) := \int_{\Omega}\left\langle|u|^2\right\rangle - |\langle u\rangle|^2 dx \quad \textit{and} \quad V(\nabla u) := \int_{\Omega}\left\langle|\nabla u|^2\right\rangle - |\nabla\langle u\rangle|^2 dx.$$

The average $\langle v\rangle$ is independent of ω_j. Ensemble averaging satisfies well known properties, e.g., [25,33,34],

$$\begin{array}{cc}
\langle\langle v\rangle\rangle = \langle v\rangle\,, & \frac{\partial}{\partial t}\langle v\rangle = \left\langle\frac{\partial}{\partial t}v\right\rangle, \\
\langle v'\rangle = 0, & \frac{\partial}{\partial x}\langle v\rangle = \left\langle\frac{\partial}{\partial x}v\right\rangle, \\
\langle\langle w\rangle\otimes v\rangle = \langle w\rangle\otimes\langle v\rangle\,, & \langle\langle w\rangle\cdot v\rangle = \langle w\rangle\cdot\langle v\rangle\,, \\
\langle\langle w\rangle\otimes v'\rangle = \langle w\rangle\otimes\langle v'\rangle = 0, & \langle\langle w\rangle\cdot v'\rangle = \langle w\rangle\cdot\langle v'\rangle = 0.
\end{array}$$

Variance is nonnegative and measures the size of fluctuations according to the following well known identity.

Lemma 1. *We have*

$$V(u) = \left\langle\int_{\Omega}|u'|^2 dx\right\rangle \geq 0 \quad \textit{and} \quad V(\nabla u) = \left\langle\int_{\Omega}|\nabla u'|^2 dx\right\rangle \geq 0.$$

Proof. Expand $V(u) = \int\langle(\langle u\rangle + u')\cdot(\langle u\rangle + u')\rangle\,dx - \int\langle u\rangle\cdot\langle u\rangle\,dx$ and cancel (similarly for $V(\nabla u)$):

$$V(u) = \int_{\Omega}\langle u'\rangle\cdot\langle u\rangle\,dx + \int_{\Omega}\langle u\rangle\cdot\langle u'\rangle\,dx + \left\langle\int_{\Omega}u'\cdot u' dx\right\rangle = \left\langle\int_{\Omega}|u'|^2 dx\right\rangle.$$

□

2.2. *Mathematical Formulation*

The Boussinesq conjecture is about the kinetic energy balance of the mean velocity, derived next. Ensemble averaging the NSE gives

$$\langle u\rangle_t + \langle u\rangle \cdot \nabla \langle u\rangle - \nu \triangle \langle u\rangle - \nabla \cdot R(u,u) + \nabla \langle p\rangle = f(x) \text{ and } \nabla \cdot \langle u\rangle = 0 \text{ in } \Omega.$$

Taking the dot product with $\langle u\rangle$, integrating over the flow domain Ω and integrating by parts gives the energy equation for the mean flow

$$\frac{d}{dt}\frac{1}{2}\int_\Omega |\langle u\rangle|^2 dx + \int_\Omega \nu |\nabla \langle u\rangle|^2 dx + \int_\Omega R(u,u) : \nabla \langle u\rangle\, dx = \int_\Omega f \cdot \langle u\rangle\, dx. \tag{4}$$

These terms carry the meaning:

$\frac{d}{dt}\frac{1}{2}\int_\Omega |\langle u\rangle|^2 dx$: rate of change of kinetic energy of mean flow,
$\int_\Omega \nu |\nabla \langle u\rangle|^2 dx$: rate of viscous energy dissipation of mean flow,
$\int_\Omega f(x,t) \cdot \langle u\rangle\, dx$: rate of energy input to mean flow by body forces,
$\int_\Omega R(u,u) : \nabla \langle u\rangle\, dx$: effect of fluctuations upon mean flow's energy.

Thus fluctuations dissipating energy in the mean flow in a space-time averaged sense (Theorem 1) is equivalent to

$$\limsup_{T\to\infty} \frac{1}{T}\int_0^T \left(\int_\Omega R(u,u) : \nabla \langle u\rangle\, dx \right) dt \geq 0.$$

2.3. *Proof of Theorem 1*

The proof outline is as follows. We calculate the energy equality for $\left\langle \frac{1}{2}||u||^2 \right\rangle$ (and use (4) for $\frac{1}{2}||\langle u\rangle||^2$). By subtracting, we obtain an equation for variance evolution. The variance evolution equation contains one inconvenient term which is eliminated by time averaging.

The standard energy equality for strong solutions of the NSE is

$$\frac{d}{dt}\frac{1}{2}||u||^2 + \nu ||\nabla u||^2 = \int_\Omega f(x,t) \cdot u dx. \tag{5}$$

The terms above have an analogous interpretation to those of Equation (4).

$\frac{d}{dt}||u||^2$: rate of change of total kinetic energy,
$\nu||\nabla u||^2$: rate of total viscous energy dissipation,
$\int_\Omega f(x,t) \cdot u dx$: rate of total energy input to flow by body forces.

Using the Poincaré - Friedrichs inequality $||\nabla u||^2 \geq \lambda_0 ||u||^2$ (where $\lambda_0 > 0$) and $(f,u) \leq \frac{\nu\lambda_0}{2}||u||^2 + C||f||^2$ on the RHS we have

$$\frac{d}{dt}\frac{1}{2}||u||^2 + \frac{\nu\lambda_0}{2}||u||^2 \leq C||f||^2. \tag{6}$$

An integrating factor and a calculation then implies $||u(T)||^2$ is uniformly bounded in T (a well known result). Integrating the energy equality over $[0,T]$ gives, for $j = 1, \cdots, J$,

$$\frac{1}{2T}||u(T)||^2 - \frac{1}{2T}||u^0||^2 + \frac{1}{T}\int_0^T \nu ||\nabla u||^2 dt = \frac{1}{T}\int_0^T \int_\Omega f(x,t) \cdot u dx dt \leq C. \tag{7}$$

Since $u(x,0;\omega_j) \in L^{\infty}(0,\infty;L^2(\Omega))$, $f(x,t) \in L^{\infty}(0,\infty;L^2(\Omega))$, this implies the uniformly in T bounds for each realization and thus also for their averages:

$$\begin{aligned} ||u(T)|| &\leq C < \infty \quad \text{and} \quad \frac{1}{T}\int_0^T ||\nabla u||^2 dt \leq C < \infty, \\ ||\left\langle u \right\rangle (\cdot,T)|| &\leq \left\langle ||u(\cdot,T;\omega_j)|| \right\rangle \leq C < \infty, \\ \frac{1}{T}\int_0^T ||\nabla \left\langle u \right\rangle ||^2 dt &\leq \frac{1}{T}\int_0^T \left\langle ||\nabla u||^2 \right\rangle dt \leq C < \infty, \end{aligned}$$

since $|| \left\langle u \right\rangle || \leq \left\langle ||u|| \right\rangle$ and $||\nabla \left\langle u \right\rangle ||^2 = || \left\langle \nabla u \right\rangle ||^2 \leq \left\langle ||\nabla u||^2 \right\rangle$. The first estimate means that bounded energy input does not lead to unbounded total kinetic energy and that the time average of total energy dissipation is also bounded.

Next, ensemble and time average the realization's energy equality. This yields

$$\frac{1}{T}\left\{ \left\langle \frac{1}{2}||u(T)||^2 \right\rangle - \left\langle \frac{1}{2}||u^0||^2 \right\rangle \right\} + \frac{1}{T}\int_0^T \left\langle \nu||\nabla u(t)||^2 \right\rangle dt = \frac{1}{T}\int_0^T \int_\Omega f(x,t)\cdot \left\langle u \right\rangle dxdt. \tag{8}$$

Next, integrate

$$\frac{d}{dt}\frac{1}{2}\int_\Omega |\left\langle u \right\rangle|^2 dx + \int_\Omega \nu|\nabla \left\langle u \right\rangle|^2 dx + \int_\Omega R(u,u) : \nabla \left\langle u \right\rangle dx = \int_\Omega f(x,t)\cdot \left\langle u \right\rangle dx. \tag{9}$$

over $[0,T]$ and divide by T:

$$\begin{aligned} &\frac{1}{T}\left\{ \frac{1}{2}||\left\langle u \right\rangle (T)||^2 - \frac{1}{2}||\left\langle u^0 \right\rangle ||^2 \right\} + \frac{1}{T}\int_0^T \nu||\nabla \left\langle u \right\rangle (t)||^2 dt \\ &\qquad + \frac{1}{T}\int_0^T \left(\int_\Omega R(u,u) : \nabla \left\langle u \right\rangle dx \right) dt = \frac{1}{T}\int_0^T \left(\int_\Omega f(x,t)\cdot \left\langle u \right\rangle dx \right) dt. \end{aligned} \tag{10}$$

Subtracting (10) from (8) gives

$$\begin{aligned} &\frac{1}{T}\left\{ \left\langle \frac{1}{2}||u(T)||^2 \right\rangle - \left\langle \frac{1}{2}||u^0||^2 \right\rangle - \frac{1}{2}\int_\Omega |\left\langle u \right\rangle (T)|^2 dx + \frac{1}{2}\int_\Omega |\left\langle u \right\rangle (0)|^2 dx \right\} \\ &\qquad + \frac{\nu}{T}\int_0^T \left(\left\langle ||\nabla u(t)||^2 \right\rangle - ||\nabla \left\langle u \right\rangle (t)||^2 \right) dt = \frac{1}{T}\int_0^T \int_\Omega R(u,u) : \nabla \left\langle u \right\rangle dxdt. \end{aligned} \tag{11}$$

The first term (in braces) $\to 0$ as $T \to \infty$. The second term is uniformly bounded in T thus so is the RHS, the Reynolds stress term. Thus, subsequence limits of this term exist as $T_j \to \infty$. Since $\left\langle ||\nabla u(t)||^2 \right\rangle - ||\nabla \left\langle u \right\rangle (t)||^2 = \left\langle ||\nabla u'(t)||^2 \right\rangle$ this completes the proof:

$$\lim_{T_j\to\infty} \frac{1}{T_j}\int_0^{T_j} \int_\Omega R(u,u) : \nabla \left\langle u \right\rangle dxdt = \lim_{T_j\to\infty} \frac{1}{T_j}\int_0^{T_j} \int_\Omega \left\langle \nu|\nabla u'|^2 \right\rangle dxdt \geq 0.$$

Within the proof the following result from [2] was established.

Corollary 1 (Variance evolution)**.** *The variance of strong solutions of the NSE satisfies*

$$\frac{1}{2}\frac{d}{dt}V(u(t)) + \nu V(\nabla u(t)) = \int_\Omega R(u,u) : \nabla \left\langle u \right\rangle dx.$$

Thus the means and fluctuations satisfy respectively

$$\frac{d}{dt}\frac{1}{2}||\langle u\rangle||^2+\nu||\nabla\langle u\rangle||^2+\int_\Omega R(u,u):\nabla\langle u\rangle\,dx=\int_\Omega f(x,t)\cdot\langle u\rangle\,dx,$$
$$\frac{1}{2}\frac{d}{dt}\left\langle||u'(t)||^2\right\rangle+\nu\left\langle||\nabla u'||^2\right\rangle=\int_\Omega R(u,u):\nabla\langle u\rangle\,dx.$$

Since the time average of the Reynolds stress term is non-negative, it follows that the Reynolds stresses act (on average) as an energy source for the fluctuations and sink for the means, an observation developed for turbulence models in [2].

2.4. The Connection to $\frac{\mathcal{P}}{\varepsilon}\simeq 1$

In the space-time-average, fluctuations dissipate energy. Eddy viscosity models this process by dissipating energy at every instant of time. From Corollary 1, the additional assumption that fluctuations dissipate energy in the mean flow at every instance in time is connected to

$$\frac{d}{dt}\left\langle||u'(t)||^2\right\rangle\simeq 0.$$

The condition $\frac{d}{dt}\left\langle||u'(t)||^2\right\rangle\simeq 0$ is also connected to the hypothesis that turbulent flows forget initial conditions as well as being equivalent to the assumption that the flow is statistically stationary. We develop these connections and their implications in this sub-section.

The assumption of statistically steady turbulence is fundamental to the statistical theory of turbulence but is as murky as the whole field. While some averages of turbulent flows converge to approximately steady values in numerical simulations, $\frac{d}{dt}\left\langle||u'(T)||^2\right\rangle\simeq 0$ cannot easily be checked (because fluctuations are not computed) and there is no proof that such convergence occurs. There are also simple flows which never become statistically steady [8]. If a flow does become statistically steady, the term $\frac{d}{dt}\left\langle||u'(t)||^2\right\rangle\simeq 0$ drops out in the variance evolution equation. Thus, statistically steady is equivalent to

$$\nu\left\langle||\nabla u'||^2\right\rangle=\int_\Omega R(u,u):\nabla\langle u\rangle\,dx.$$

Statistical steady state is often expressed as $\mathcal{P}/\varepsilon\simeq 1$ where

$$\varepsilon=\text{ dissipation of turbulent kinetic energy (TKE)}=\nu\left\langle||\nabla u'||^2\right\rangle,$$
$$\mathcal{P}=\text{production of TKE}=\int_\Omega R(u,u):\nabla\langle u\rangle\,dx.$$

When $\mathcal{P}/\varepsilon\simeq 1$, the models that are dissipative pointwise in time, such as simple eddy viscosity models, have the correct aggregate effect.

The EV approximation formally replaces $R(u,u)$ by $2\nu_T\nabla^s\langle u\rangle$ plus terms incorporated into the pressure. The effect this replacement must have at statistical steady state is the balance

$$\int_\Omega R(u,u):\nabla\langle u\rangle\,dx=\int_\Omega\nu\left\langle|\nabla u'|^2\right\rangle dx\simeq\int_\Omega\nu_T(\cdot)|\nabla\langle u\rangle|^2dx.$$

The two integrands in the above relation suggest that EV models $-\nu\triangle u'\simeq-\nabla\cdot(\nu_T(\cdot)\nabla\langle u\rangle)$ (+ terms incorporated into the pressure). Thus, the EV approximation can arise from two separate assumptions:

A1. (Statistical steady state) What holds in a time averaged sense holds pointwise in time

$$\frac{\mathcal{P}}{\varepsilon}\simeq 1\Leftrightarrow\int R(u,u):\nabla\langle u\rangle\,dx\simeq\int\nu\left\langle|\nabla u'|^2\right\rangle dx\Leftrightarrow\frac{d}{dt}\left\langle||u'(T)||^2\right\rangle\simeq 0.$$

A2: (A fluctuation model) The action of the fluctuating velocity can be represented in terms of the means

$$action(\nabla u') \simeq a(\cdot)\nabla \langle u \rangle ,$$

where $a(\cdot)$ is a function that depends on the mean flow (and is found by calibration of the model).

With these two assumptions we then have the EV. Indeed, by assumptions A1 and A2

$$\int_\Omega R(u,u) : \nabla \langle u \rangle \, dx = \int_\Omega \nu \left\langle \nabla u' : \nabla u' \right\rangle dx$$
$$= \int_\Omega \nu a(\cdot)^2 \nabla \langle u \rangle : \nabla \langle u \rangle \, dx = \int_\Omega -\nabla \cdot \left(\nu a(\cdot)^2 \nabla \langle u \rangle \right) : \langle u \rangle \, dx.$$

This arises from an eddy viscosity term with

$$\nu_T(\cdot) = \nu a(\cdot)^2.$$

3. Extending Models to Non-Stationary Turbulence

Extending models to turbulence not at statistical equilibrium is important because most turbulent flows in engineering applications are seldom at statistical equilibrium. Simply calibrating EV models to these flows leads to negative viscosities and numerical instabilities. (titled *Physics of Negative Viscosity Phenomena*, contains a collection of flows which correspond to a negative eddy viscosity [35]). The resulting negative viscosities explain many of the criticisms of eddy viscosity models such as:

Monographs:

> " ... the physics of turbulence is vastly different than the physics of the molecular processes that lead to the viscous stress law ...", Pope [36] (p. 359),
>
> " ... significant defects when compared with experiment ... important effects are missed...", Mathieu and Scott [37] (p. 81),
>
> " ... eddy viscosity is frequently negative and thus leads to instabilities.", Frisch [38] (p. 233),
>
> " ... this makes the whole concept of an eddy viscosity more than a little strange ...", Monin & Yaglom [33] (p. 373).

Papers:

> " ... The results using numerical ... or experimental data are very consistent in pointing the non-validity of the Boussinesq hypothesis...", Schmitt [39].

The papers [40,41] also give important criticisms. Omitting kinetic energy flow from fluctuations back to the mean velocity (as in EV models) is equivalent to omitting a model for the term $\frac{1}{2}\frac{d}{dt}\left\langle ||u'(t)||^2 \right\rangle$ in

$$\frac{1}{2}\frac{d}{dt}\left\langle ||u'(t)||^2 \right\rangle + \nu \left\langle ||\nabla u'||^2 \right\rangle = \int_\Omega R(u,u) : \nabla \langle u \rangle \, dx.$$

An eddy viscosity model selects the turbulent viscosity $\nu_T(\cdot)$ consistent with the Prandtl-Kolmogorov relation

$$\nu_T(\cdot) = \mu l \sqrt{k'}, \mu = \text{ calibration constant.}$$

Then, at statistical equilibrium,

$$\int_\Omega R(u,u) : \nabla \langle u \rangle \, dx = \nu \left\langle ||\nabla u'||^2 \right\rangle \simeq \int_\Omega \nu_T(\cdot) |\nabla \langle u \rangle|^2 dx.$$

The modelling question is therefore to use the EV's fluctuation model to add a term representing $\frac{1}{2}\frac{d}{dt}\left\langle ||u'(t)||^2 \right\rangle$ (a different physical process from viscosity) in a way consistent with the EV term.

Two examples of consistent models of this term have been developed in [3,6]. An example that captures this idea is as follows. Consider the (simplified) Baldwin-Lomax eddy viscosity parameterization

$$\nu_T(\cdot) = \mu l(x)^2 |\nabla \times \langle u \rangle|, \ \mu = \text{ calibration constant.}$$

Comparing $l(x)^2|\nabla \times \langle u\rangle|$ with $l(x)\sqrt{k'}$ we see that this means $action(u') \simeq l(x)\nabla \times \langle u\rangle$. This suggests modelling

$$\begin{aligned} \frac{1}{2}\frac{d}{dt}\left\langle ||u'(t)||^2 \right\rangle &= \left\langle \int_\Omega u'_t \cdot u' dx \right\rangle \simeq \int_\Omega l(x)\nabla \times \langle u\rangle_t \cdot l(x)\nabla \times \langle u \rangle \, dx \\ & \quad or \\ & \quad \int_\Omega \nabla \times \left(l^2(x)\nabla \times \langle u\rangle_t \right) \cdot v dx|_{v=\langle u\rangle}. \end{aligned}$$

This yields a model for the term responsible for intermittence that is consistent with the chosen eddy viscosity model for time averaged dissipativity. Let the model's (approximate) velocity and pressure be denoted w, q then, in this combination, the intermittence corrected Baldwin-Lomax model is

$$\left\{ \begin{array}{c} \frac{\partial}{\partial t}\left(w + \nabla \times \left(l^2(x)\nabla \times w\right)\right) + w \cdot \nabla w - \nu \triangle w \\ -\nabla \cdot \left(\mu l(x)^2 |\nabla \times w| \nabla w\right) + \nabla q = f(x,t), \\ \text{and } \nabla \cdot w = 0 \ . \end{array} \right. \tag{12}$$

In [6] this model was derived and analyzed and it was shown how to adapt a NSE code to the new model in a modular fashion. Numerical tests therein confirmed that the new term $\frac{\partial}{\partial t}\nabla \times \left(l^2(x)\nabla \times w\right)$ allowed time averaged-zero backscatter. Existence was proven for a (further simplified) equilibrium model in [42] and for time dependent model in [43]. The most recent advance in analysis of this model was a proof of Pakzad [44] that the model produces time averaged energy dissipation rates consistent with the K41 phenomenology.

4. New Ideas for a Classical 1–Equation EV Model

Recent work in [5] by Layton and McLaughlin presented some new ideas in a classic 1-equation model due to Prandtl [45] and contained within a 2 equation model of Kolmogorov [46–48], summarized in this section. The model is

$$\begin{aligned} v_t + v \cdot \nabla v - \nabla \cdot \left(\left[2\nu + \mu l\sqrt{k}\right] \nabla^s v \right) + \nabla p = f(x), \\ \nabla \cdot v = 0, \\ k_t + v \cdot \nabla k - \nabla \cdot \left(\left[\nu + \mu l \sqrt{k}\right] \nabla k \right) + \frac{1}{l} k\sqrt{k} = \mu l \sqrt{k} |\nabla^s v|^2. \end{aligned} \tag{13}$$

Briefly, $f(x)$ is a smooth, divergence free ($\nabla \cdot f = 0$) body force, μ (typically between 0.27 and 0.55, [36] and [49] (p. 114)) is a calibration parameter, and $k(x,t)$ is the model approximation to the fluctuations' kinetic energy distribution, $\frac{1}{2}|(u - \overline{u})(x,t)|^2$. The third equation describes the turbulent kinetic energy evolution; see [50] (p. 99, Section 4.4), [49], [25] (p. 60, Section 5.3) or [36] (p. 369, Section 10.3). The above 1-equation model holds in Ω with initial conditions, $v(x,0)$ and $k(x,0)$, and (here no-slip) v, k boundary conditions on the boundary $\partial\Omega$. The variable $l(x,t)$ is the turbulence length scale that must be specified.

To derive the model's energy balance, multiply the $v-$equation by v and integrate over Ω. Add to this the integrated $k-$ equation. This yields

$$\frac{d}{dt}\int_{\Omega}\left(\frac{1}{2}|v|^2+k\right)dx+\int_{\Omega}\left(2\nu|\nabla^s v|^2+\frac{1}{l(x)}k^{3/2}\right)dx=\int_{\Omega}f\cdot v dx\,, \tag{14}$$

$$\text{Kinetic energy} = \frac{1}{|\Omega|}\int_{\Omega}\frac{1}{2}|v(x,t)|^2+k(x,t)dx, \tag{15}$$

$$\text{Dissipation rate }\varepsilon_{\text{model}}(t) = \frac{1}{|\Omega|}\int_{\Omega}2\nu|\nabla^s v(x,t)|^2+\frac{1}{l(x)}k^{3/2}(x,t)dx. \tag{16}$$

This is a URANS (unsteady Reynolds averaged Navier-Stokes) model. Thus the question arises as to what exactly its solution approximates. There is no clear separation line between URANS models and time-filtered LES models. There are also other interpretations of what a URANS model solution should approximate. In [5] we begin with the assumption that the model velocity, $v(x,t)\simeq\overline{u}(x,t)$, a finite time window average of the Navier-Stokes velocity $u(x,t)$

$$\overline{u}(x,t)=\frac{1}{\tau}\int_{t-\tau}^{t}u(x,t')dt'. \tag{17}$$

From this basic assumption 5 model conditions follow:

Condition 1: The filter window τ should appear as a model parameter. As $\tau\downarrow 0$ the model $\rightarrow$ NSE. As $\tau\uparrow$, the eddy viscosity $\nu_T(\cdot)\uparrow$.

Condition 2: The turbulence length-scale $l(x)$ must $l(x)\rightarrow 0$ as $x\rightarrow walls$.

Condition 3: (Finite kinetic energy) The model's representation of the total kinetic energy in the fluid must be uniformly bounded in time:

$$\int_{\Omega}\frac{1}{2}|v(x,t)|^2+k(x,t)dx\leq Const.<\infty\text{ uniformly in time.}$$

Condition 4: (Time-averaged statistical equilibrium) The time average of the model's total energy dissipation rate,

$$\varepsilon_{\text{model}}(t)=\frac{1}{|\Omega|}\int_{\Omega}2\nu|\nabla^s v(x,t)|^2+\frac{1}{l(x)}k^{3/2}(x,t)dx$$

is at most the time average energy input rate:

$$\limsup_{T\rightarrow\infty}\frac{1}{T}\int_0^T\varepsilon_{\text{model}}(t)dt\leq Const.\frac{U^3}{L},\text{ uniformly in }\mathcal{R}e.$$

Condition 5: The model allows flow of energy from fluctuations back to means without negative eddy viscosities. This energy flow has space time average zero.

The only undetermined model parameter is the mixing length / turbulence length-scale $l=l(x,t)$, introduced by Taylor [51]. For channel flow a common choice, Wilcox [52] (Ch. 3, eqn. (3.99), p. 76), is

$$l_0(x)=\min\{0.41y,0.082\mathcal{R}e^{-1/2}\},\ y=\text{wall normal distance.}$$

With a specification of $l_0(x)$ as above, Conditions 1 and 5 are violated. The condition $l(x)\downarrow 0$ at walls, is not easily enforced for complex boundaries and, in current models, e.g., Spalart [53], Wilcox [52], requires input of (unknown) subregions where different formulas for $l(x)$ apply. Conditions 3 and 4 also do not follow from energy estimates due to the mismatch of the powers of k in the energy term and the dissipation term.

The correction proposed in [5] was a kinematic $l(x,t)$ that simplifies and enforces Conditions 1,2,3 and 4. This choice also occurs in [1] and may be related to an ambiguous possibility mentioned by Prandtl [54] for $l(x,t)$

> "... the distance traversed by a mass of this type before it becomes blended in with neighboring masses...".

This suggestion can be interpreted as the distance a fluctuating eddy travels in one time unit

$$l = |u'(x,t)|\tau.$$

As $|u'| \simeq \sqrt{2}k(x,t)^{1/2}$, define $l(x,t)$ kinematically by

$$l(x,t) = \sqrt{2}k(x,t)^{1/2}\tau. \tag{18}$$

In the above $k^{1/2}$ is well defined because the weak maximum principle implies $k(x,t) \geq 0$, e.g., [55,56]. Then τ enters into the model, modified to be

$$\begin{aligned} v_t + v \cdot \nabla v - \nabla \cdot \left(\left[2\nu + \sqrt{2}\mu k \tau \right] \nabla^s v \right) + \nabla p &= f(x), \\ \nabla \cdot v &= 0, \\ k_t + v \cdot \nabla k - \nabla \cdot \left(\left[\nu + \sqrt{2}\mu k \tau \right] \nabla k \right) + \frac{\sqrt{2}}{2}\tau^{-1}k &= \sqrt{2}\mu k \tau |\nabla^s v|^2. \end{aligned} \tag{19}$$

Let L, U denote large length and velocity scales

$$\left.\begin{aligned} L &= \min\left[L_\Omega, \frac{F}{\sup_{x\in\Omega}|\nabla^s f(x)|}, \frac{F}{\left(\frac{1}{|\Omega|}\int_\Omega |\nabla^s f(x)|^2 dx\right)^{1/2}} \right] \\ U &= \left(\limsup_{T\to\infty} \frac{1}{T}\int_0^T \frac{1}{|\Omega|}\int_\Omega |v(x,t)|^2 dx dt \right)^{1/2}. \end{aligned}\right\} \tag{20}$$

Let $\mathcal{R}e = LU/\nu$ denote usual Reynolds number and let $T^* = L/U$ the large scale turnover time. In [5] it was proven that the modified model satisfies Conditions 1–4.

Theorem 2. *Let μ, τ be positive and Ω a bounded regular domain. Let*

$$l(x,t) = \sqrt{2}k(x,t)^{1/2}\tau.$$

Then, Condition 1 holds.

Suppose the boundary conditions are no-slip ($v = 0, k = 0$ on $\partial\Omega$). Then, Condition 2 is satisfied. At walls

$$l(x) \to 0 \text{ as } x \to \text{walls}.$$

Suppose the model's energy balance (14) holds for $l = \sqrt{2}k^{1/2}\tau$. Then Condition 3 also holds:

$$\int_\Omega \frac{1}{2}|v(x,t)|^2 + k(x,t)dx \leq Const. < \infty \text{ uniformly in time.}$$

The model's energy dissipation rate is

$$\varepsilon_{model}(t) = \frac{1}{|\Omega|}\int_\Omega 2\nu|\nabla^s v(x,t)|^2 + \frac{\sqrt{2}}{2}\tau^{-1}k(x,t)dx.$$

Time averages of the model's energy dissipation rate are finite:

$$\limsup_{T\to\infty} \frac{1}{T}\int_0^T \varepsilon_{model}(t)dt < \infty.$$

Suppose in addition the body force satisfies $f(x) = 0$ on the boundary. If the selected time averaging window satisfies

$$\frac{\tau}{T^*} \leq \frac{1}{\sqrt{\mu}} \quad (\simeq 1.35 \, \textit{for} \; \mu = 0.55)\,,$$

then Condition 4 holds uniformly in the Reynolds number

$$\limsup_{T\to\infty} \frac{1}{T}\int_0^T \varepsilon_{model}(t)dt \leq 4\left(1+\mathcal{R}e^{-1}\right)\frac{U^3}{L}.$$

The proof of Condition 4 builds on previous work on Navier-Stokes equations in [57–59].

5. Discussion

Practical needs for predictive flow simulations drive development of turbulence models to greater complexity. Often this occurs by introducing more calibration parameters or different formulations in different flow regions to extend predictive ability of a known model.

Model calibration will likely always be necessary. However, we believe that the more carefully models adhere to the physics of fluid flows as expressed in averages of solutions of the NSE, the simpler models will become and the need for calibration reduced. We have reviewed some recent work aiming at model simplification herein. A proof of the Boussinesq conjecture was reviewed. This proof led to ideas about how to adapt EV models to non-statistically stationary turbulence without "absurdities" (leading to numerical instabilities) like negative eddy viscosities. This idea was worked out for one zero-equation model. Next a classical 1-equation model was considered. A reinterpretation of the turbulence length scale led again to a significant model simplification and a stronger connection between properties of the model and the NSE. These are small steps but hopefully useful ones.

6. Materials and Methods

No proprietary materials were used in this research. The methods used were rigorous mathematical analysis. Full details about each step are available in the published literature in the cited papers. No animal or human subjects were used in the reported research.

Author Contributions: Section 2: Conceptualization, methodology, formal analysis, validation, Writing—Review and editing, N.J. and W.L.; software, data curation, visualization, N.J.; Writing—Original draft preparation, supervision, project administration, and funding acquisition, W.L.; Section 3: Conceptualization, methodology, formal analysis, validation, writing-review and editing, Y.R., H.Z. and W.L.; software, data curation, visualization, Y.R. and H.Z.; writing-original draft preparation, supervision, project administration, and funding acquisition, W.L.; Section 4: Conceptualization, methodology, formal analysis, validation, writing-review and editing, M.M. and W.L.; software, data curation, visualization, M.M.; Writing—Original draft preparation, supervision, project administration, and funding acquisition, W.L. All authors have read and agreed to the published version of the manuscript.

Funding: The research of WL reported herein was partially supported by the National Science Foundation under NSF grant DMS 1817542.

Conflicts of Interest: The author declare no conflict of interest. The funders had no role in the design of the study; in the collection, analyses, or interpretation of data; in the writing of the manuscript, or in the decision to publish the results.

Abbreviations

The following abbreviations are used in this manuscript:

NSE	Navier-Stokes Equations
EV	Eddy Viscosity
URANS	Unsteady Reynolds Averaged Navier Stokes
LD	linear dichroism

References

1. Jiang, N.; Layton, W. Numerical analysis of two ensemble eddy viscosity numerical regularizations of fluid motion. *Numer. Methods Partial Differ. Equ.* **2014**, *31*, 630–651. [CrossRef]
2. Jiang, N.; Kaya, S.; Layton, W. Analysis of Model Variance for Ensemble Based Turbulence Modeling. *Comput. Methods Appl. Math.* **2015**, *15*, 173–188. [CrossRef]
3. Jiang, N.; Layton, W. Algorithms and models for turbulence not at statistical equilibrium. *Comput. Math. Appl.* **2016**, *71*, 2352–2372. [CrossRef]
4. Layton, W. The 1877 Boussinesq Conjecture: Turbulent Fluctuations are Dissipative on the Mean Flow, TR 14-07. 2014. Available online: yearwww.mathematics.pitt.edu/research/technical-reports (accessed on 28 September 2020).
5. Layton, W.; McLaughlin, M. On URANS Congruity with Time Averaging: Analytical laws suggest improved models. In Proceedings of the International conference in honor of the 90th Birthday of Constantin Corduneanu, Ekaterinburg, Russia, 26–31 July 2018; Springer: Berlin/Heidelberg, Germany, 2018; pp. 85–108.
6. Rong, Y.; Layton, W.; Zhao, H. Extension of a simplified Baldwin-Lomax model to non-equilibrium turbulence: Model, analysis and algorithms. *Numer. Methods Partial Differ. Equ.* **2.019**, *35*, 1821–1846. [CrossRef]
7. Boussinesq, J. Essai sur la théorie des eaux courantes. *Mémoires Présentés Par Divers Savants à l'Académie Sci.* **1877**, *23*, 1–680.
8. Durbin, P.A.; Pettersson Reif, B.A. *Statistical Theory and Modeling for Turbulent Flows*, 2nd ed.; Wiley: Chichester, UK, 2011.
9. Iliescu, T.; Layton, W. Approximating the larger eddies in fluid motion III: The Boussinesq model for turbulent fluctuations. *Analele Stinfice ale Universitatii Al. I. Cuza Iasi* **1998**, *XLIV*, 245–261.
10. Layton, W.; Lewandowski, R. Analysis of an Eddy Viscosity Model for Large Eddy Simulation of Turbulent Flows. *J. Math. Fluid Mech.* **2002**, *4*, 374–399. [CrossRef]
11. Jiang, N. A Higher Order Ensemble Simulation Algorithm for Fluid Flows. *J. Sci. Comput.* **2014**, *64*, 264–288. [CrossRef]
12. Layton, W.; Takhirov, A. Numerical analysis of wall adapted nonlinear filter models of turbulent flows. *Contemp. Math.* **2013**, *586*, 219–229.
13. Layton, W.; Rebholz, L.G.; Trenchea, C. Modular Nonlinear Filter Stabilization of Methods for Higher Reynolds Numbers Flow. *J. Math. Fluid Mech.* **2011**, *14*, 325–354. [CrossRef]
14. Layton, W.; Mays, N.; Neda, M.; Trenchea, C. Numerical analysis of modular regularization methods for the BDF2 time discretization of the Navier-Stokes equations. *ESAIM Math. Model. Numer. Anal.* **2014**, *48*, 765–793. [CrossRef]
15. Saint-Venant (Barré), A.J.C. Note à joindre au Mémoire sur la dynamique des fluides. *CRAS* **1843**, *17*, 1240–1243.
16. Darrigol, O. *Worlds of Flow*; Oxford University Press: Oxford, UK, 2005.
17. Eckert, M. *The Dawn of Fluid Dynamics*; Wiley-VCH: Weinheim, Germany, 2006.
18. Layton, W.; Schneier, M. Diagnostics for eddy viscosity models of turbulence including data-driven/neural network based parameterizations. *Results Appl. Math.* **2020**, *8*, 100099. [CrossRef]
19. Guermond, J.-L. Subgrid stabilization of Galerkin approximations of monotone operators. *C. R. Acad. Sci. Paris Série I* **1999**, *328*, 617–622. [CrossRef]
20. Germano, M.; Piomelli, U.; Moin, P.; Cabot, W.H. A dynamic subgrid-scale eddy viscosity model. *Phys. Fluids A Fluid Dyn.* **1991**, *3*, 1760–1765. [CrossRef]
21. Berselli, L.C.; Iliescu, T.; Layton, W. *Mathematics of Large Eddy Simulation of Turbulent Flows*; Springer: Berlin, Germany, 2006.

22. Hughes, T.J.; Mazzei, L.; Jansen, K.E. Large Eddy Simulation and the variational multiscale method. *Comput. Vis. Sci.* **2000**, *3*, 47–59. [CrossRef]
23. Layton, W. A connection between subgrid scale eddy viscosity and mixed methods. *Appl. Math. Comput.* **2002**, *133*, 147–157. [CrossRef]
24. Lund, T.S.; Novikov, E.A. Parametrization of subgrid-scale stress by the velocity gradient tensor. *Annu. Res. Briefs* **1992**, *CTR*, 27–43.
25. Mohammadi, B.; Pironneau, O. *Analysis of the K-Epsilon Turbulence Model*; Masson: Paris, France, 1994.
26. Sagaut, P. *Large Eddy Simulation for Incompressible Flows*; Springer: Berlin, Germany, 2001.
27. Takhirov, A.; Neda, M.; Waters, J. Time relaxation algorithm for flow ensembles. *Numer. Methods Partial Differ. Equ.* **2015**, *32*, 757–777. [CrossRef]
28. Vreman, A.W. An eddy-viscosity subgrid-scale model for turbulent shear flow: Algebraic theory and applications. *Phys. Fluids* **2004**, *16*, 3670. [CrossRef]
29. Labovsky, A.; Layton, W. Magnetohydrodynamic flows: Boussinesq conjecture. *J. Math. Anal. Appl.* **2016**, *434*, 1665–1675. [CrossRef]
30. Chow, Y.T.; Pakzad, A. On the zeroth law of turbulence for the stochastically forced Navier-Stokes equations. *arXiv* **2020**, arXiv:2004.08655.
31. Pakzad, A. Damping Functions correct over-dissipation of the Smagorinsky Model. *Math. Methods Appl. Sci.* **2017**, *40*, 5933–5945. [CrossRef]
32. Kalnay, E. *Atmospheric Modelling, Data Assimilation and Predictability*; Cambridge University Press: Cambridge, UK, 2003.
33. Monin, A.S.; Yaglom, A.M. *Statistical Fluid Mechanics, Mechanics of Turbulence*; Dover publications: Mineola, NY, USA, 2007; Volume 1.
34. Panchev, S. *Random Functions and Turbulence*; Pergammon Press: Oxford, UK, 1971.
35. Starr, V.P. *Physics of Negative Viscosity Phenomena*; McGraw Hill: New York, NY, USA, 1968.
36. Pope, S. *Turbulent Flows*; Cambridge University Press: Cambridge, UK, 2000.
37. Mathieu, J.; Scott, J. *An Introduction to Turbulent Flows*; Cambridge University Press: Cambridge, UK, 2000.
38. Frisch, U. *Turbulence*; Cambridge University Press: Cambridge, UK, 1995.
39. Schmitt, F.G. About Boussinesq's turbulent viscosity hypothesis: Historical remarks and a direct evaluation of its validity. *Comptes Rendus Mécanique* **2007**, *335*, 617–627. [CrossRef]
40. Frahnert, H.; Dallmann, U.C. Examination of the eddy viscosity concept regarding its physical justification. *Notes Numer. Fluid Mech.* **2002**, *77*, 255–262.
41. Vergassola, M.; Gama, S.; Frisch, U. Proving the Existence of Negative, Isotropic Eddy Viscosity. In *Solar and Planetary Dynamics*; Proctor, M., Mattheus, D., Rucklidge, A., Eds.; Cambridge U. Press: Cambridge, UK,1994; pp. 321–328.
42. Berselli, L.C.; Breit, D. On the existence of weak solutions for the steady Baldwin-Lomax model and generalizations. *arXiv* **2020**, arXiv:2003.00691x.
43. Berselli, L.C.; Lewandowski, R.; Nguyen, D. Rotational forms of Large Eddy Simulation Turbulence Models: Modeling and Mathematical Theory. Technical Report. 2020. Available online: https://hal.archives-ouvertes.fr/hal-02569244/document (accessed on 28 September 2020).
44. Pakzad, A. A study of energy dissipation in a corrected eddy viscosity model. *Prelim. Rep.* **2020**, in prep.
45. Prandtl, L. Über ein nenes Formelsystem für die ausgebildete Turbulenz. *Nacr. Akad. Wiss. Göttingen Math Phys. Kl.* **1945**, 6–16.
46. Bulicek, M.; Malek, J. Large data analysis for Kolmogorov's two-equation model of turbulence. *Nonlinear Anal.* **2019**, *50*, 104–143. [CrossRef]
47. Spalding, D.B. Kolmogorov's two-equation model of turbulence. *Proc. R. Soc. Lond. Ser. A* **1991**, *434*, 211–216.
48. Kolmogorov, A.N. Equations of turbulent motion in an incompressible fluid. *Izv. Akad. Nauk SSSR* **1942**, *6*, 56–58.
49. Davidson, P. *Turbulence: An Introduction for Scientists and Engineers*; Oxford University Press: Oxford, UK, 2015.
50. Chacon-Rebollo, T.; Lewandowski, R. *Mathematical and Numerical Foundations of Turbulence Models and Applications*; Springer: New York, NY, USA, 2014.
51. Taylor, G.I. Eddy motion in the atmosphere. *Philos. Trans. R. Soc. Ser. A* **1915**, *215*, 1–26. [CrossRef]
52. Wilcox, D.C. *Turbulence Modeling for CFD*, DCW Industries: La Canada, CA, USA, 2006.
53. Spalart, P.R. Philosophies and fallacies in turbulence modeling. *Prog. Aerosp. Sci.* **2015**, *74*, 1–15. [CrossRef]

54. Prandtl, L. On fully developed turbulence. In Proceedings of the 2nd International Congress of Applied Mechanics, Zürich, Switzerland, 12–17 September 1926; pp. 62–74.
55. Lewandowski, R.; Mohammadi, B. Existence and positivity results for the $\phi - \theta$ model and a modified $k - \varepsilon$ model. *Math. Model Methods Appl. Sci.* **1993**, *3*, 195–215. [CrossRef]
56. Wu, Z.-N.; Fu, S. Positivity of k-epsilon turbulence models for incompressible flow. *Math. Model. Methods Appl. Sci.* **2002**, *12*, 393–406. [CrossRef]
57. Doering, C.R.; Foias, C. Energy dissipation in body-forced turbulence. *J. Fluid Mech.* **2002**, *467*, 289–306. [CrossRef]
58. Doering, C.R.; Constantin, P. Energy dissipation in shear driven turbulence. *Phys. Rev. Lett.* **1992**, *69*, 1648. [CrossRef]
59. Wang, X. Time averaged energy dissipation rate for shear driven flows in R^n. *Phys. D Nonlinear Phenom.* **1997**, *99*, 555–563. [CrossRef]

fluids

Article

Influence of Wind Buffers on the Aero-Thermal Performance of Skygardens

Murtaza Mohammadi *, Paige Wenbin Tien and John Kaiser Calautit *

Department of Architecture and Built Environment, University of Nottingham, University Park, Nottingham NG7 2RD, UK; engineeringpgr@nottingham.ac.uk

* Correspondence: murtaza.mohammadi1@nottingham.ac.uk (M.M.); john.calautit1@nottingham.ac.uk (J.K.C.); Tel.: +44-778-035-3163 (M.M.); +44-780-268-5370 (J.K.C.)

Received: 17 August 2020; Accepted: 15 September 2020; Published: 18 September 2020

Abstract: Many high-rise buildings have semi-enclosed landscaped spaces, which act as design elements to improve the social and environmental aspects of the building. Designs such as skygardens are open to outdoor airflow and allow occupants to observe the city skyline from a height. Due to their often high location, they are subjected to strong wind speeds and extreme environmental conditions. The current study investigates the effects of three common wind buffers (railing, hedges, and trees) located at a height of 92 m on the performance of a skygarden, in terms of occupants' wind comfort. Computational fluid dynamics (CFD) simulations were carried out using the realisable k-epsilon method, where the vegetation was modelled as a porous zone with cooling capacity. The computational modelling of the high-rise building and vegetation were validated using previous works. The quality class (QC) of the Lawson comfort criteria was used for the evaluation of the wind comfort across the skygarden. The results indicate that, although the three wind buffers offer varying levels of wind reduction in the skygarden, the overall wind conditions generated are suitable for occupancy. Furthermore, vegetation is also able to offer slight temperature reductions in its wake. The right combination and dimension of these elements can greatly assist in generating aero-thermal comfort across skygardens.

Keywords: CFD; buildings; outdoor platform; skygarden; skycourts; wind comfort

---

1. Introduction and Literature Review

Rapid urbanisation, along with the transformation of the built environment results in the intensification of the urban heat island (UHI) effect [1] and consequently an increase in global energy demand [2,3]. High-rise buildings and skyscrapers are one of the products of such a transformation, which have emerged as a result of urban growth and development [4]. The number of high-rise buildings is projected to increase, growing with the increasing demand for office spaces and housing within cities [5]. This increasing urbanisation also results in an imbalance between the indoor and outdoor space, which can affect the occupants' well-being. Hence, novel concepts and approaches for the sustainable design and planning of urban spaces [6] are increasingly being explored by researchers to allow buildings and cities to cope with future challenges, such as the increasing building energy demand and a shortage of green spaces [7,8].

The presence of green spaces can improve the quality of life in urban areas by influencing the health and well-being of the local populations [9]. Green spaces are large spatial areas of vegetation which can improve the local thermal conditions by enabling shading and evaporative cooling to lower air temperatures [10,11]. It also acts as a filter which reduces pollutants, dust, and other harmful particles within highly polluted dense city areas to improve outdoor air quality. Vegetation, including trees, hedges, and green walls located along open roads and street canyons, can provide aid as a barrier between traffic emissions and adjacent areas [12].

Vegetation has been increasingly used in various aspects of cities to provide extensive benefits towards local and global energy balances [13]. The use of vegetation in and around buildings can be an effective strategy to enhance the thermal comfort and energy performance of buildings [14]. Aflaki et al. [15] highlighted that the presence of vegetation could decrease local air temperature and aid in the mitigation of the UHI effect. Hirano et al. [16] and Gomes et al. [17] suggested that urban vegetation and vertical greenery can also aid in the reduction of global CO2 emissions.

Previous works have shown that various forms of vegetation provide benefits towards occupants' aero-thermal comfort conditions [18–20] and can enable people to stay in outdoor areas for an extended duration, while also improving outdoor air quality. Kang et al. [18] used numerical modelling to evaluate the wind flow around trees and its effect on pedestrian's wind comfort in urban areas. Meanwhile, Lin et al. [19] performed a thermal comfort assessment of urban parks under various climatic conditions using field tests and observations. They investigated the influence of thermal conditions on the thermal perception of visitors in an outdoor urban space.

Solutions such as the addition of semi-outdoor spaces within and around buildings are explored in the literature. This includes balconies, rooftop gardens, courtyards, and semi-outdoor interbuilding communal spaces [21]. Montazeri et al. [22] performed a wind comfort analysis on balconies of high-rise buildings, which suggests that the balcony parapet can significantly improve wind comfort. The implementation of a new façade concept showed its ability to control wind flow in semi-outdoor spaces.

Another example of a semi-outdoor green space which is incorporated into the design of high-rise buildings is a skygarden or skycourt. Skygardens or "courtyards in the sky" have been increasingly utilised within densely populated areas, such as in Singapore and Hong Kong. They are semi-outdoor spaces consisting of various forms of vegetation integrated within the intermediate levels of a high-rise building [23]. The Bosco Verticale in Milan [24] and the Park Royal Collection Pickering in Singapore [25] are examples of buildings with skygardens. Skygardens can provide additional space for occupants residing inside, or in the proximity of, a building. It is designed for mixed-use purposes and as a transitional, social, and environmental space benefitting the occupants and the inhabitants [26]. Greenery can be added to the horizontal and vertical surfaces of the skygarden. Hence, it can also be an effective solution to reduce the UHI effect in densely built urban areas which have limited space for private and public green spaces on the ground [27].

However, despite the advantages of skygardens detailed above, the number of skygarden-integrated buildings remains relatively low [28]. Furthermore, limited studies exist which evaluate the wind and thermal comfort conditions in skygardens. Previous works by Tien and Calautit [29] and Mohammadi and Calautit [30] used Computational Fluid Dynamics (CFD) modelling to understand the influence of the design of the skygarden on the wind and thermal comfort.

Literature Gap and Novelty

The study of Tien and Calautit [29] evaluated the aerothermal conditions and characteristics of wind flow around skygardens at intermediate levels of a high-rise building. The work highlighted the importance of the geometry and shape of the skygarden, which can have a significant influence on wind comfort. The work also showed that the airflow distribution in the skygarden can lead to variations in the thermal comfort levels and could potentially create uncomfortable and even dangerous conditions for occupants. Mohammadi and Calautit [30] evaluated the attenuation and cooling effect of vegetation in skygardens. The authors highlighted the positive influence of the addition of vegetation on the conditions in the skygarden and suggested that future studies should focus on other elements apart from trees which could modify the airflow (as shown in Figure 1). The addition of/combination with other attenuating elements can provide better control of the wind flow, especially in locations with very strong winds. Furthermore, the influence of the integration of different types of attenuating elements on the wind distribution and thermal conditions should be evaluated.

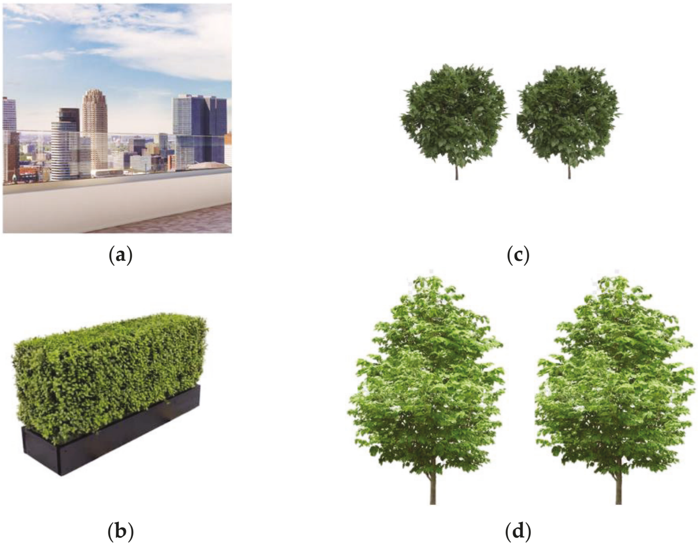

(**a**) (**c**)

(**b**) (**d**)

Figure 1. Wind barrier elements used in skygarden design; (**a**) railing or windscreen, (**b**) hedge, and (**c**) small and (**d**) large trees.

To address the research gaps, this study will build on the previous works to investigate the impact of different types of wind-attenuating elements such as hedges, railings, and plants, which are typically present in skygardens, on the aero-thermal comfort characteristics of the semi-outdoor space. The present study uses one of the cases, identified previously, to analyse the attenuation effect of vegetation in skygardens. A benchmark high-rise building model was developed and validated with the experimental data of the Commonwealth Advisory Aeronautical Council (CAARC) standard tall building model [31]. Various wind barrier configurations will be incorporated across the boundary regions of the skygarden model.

2. Method

The present work will employ numerical modelling to assess the effect of vegetation configurations on the wind and thermal conditions within a skygarden. The evapotranspiration cooling effect of the vegetation will be considered for the assessment of the thermal conditions. The numerical investigation will use the CFD software FLUENT (Ansys® Academic Research Fluent, Release 18.1, Canonsburg, PA, USA).

2.1. CFD Governing Equation

In the present study, the Reynolds averaged Navier–Stokes (RANS) equation approach, and the k-ε equations are applied, which are common and well established in the field of urban flow simulations. The simulation was conducted at steady state and with a three-dimensional computational domain. The semi-implicit method for a pressure-linked equations segregated pressure-based algorithm solver is employed [32]. The Reynolds averaged Navier-Stokes (RANS) equation is implemented using the realisable k-ε turbulence model, following the study conducted by Gromke et al. [33]. The Boussinesq approximation is employed to account for thermal effects and buoyancy. The governing equations for continuity, mean strain rate tensor, turbulence kinetic energy (k), dissipation rate (ε), turbulent viscosity, and energy are used (not shown here, but fully available in the FLUENT theory guide).

To account for the vegetation cooling effect, the present study adopted a simplified approach based on the works of Rahman et al. [34] and Gromke et al. [35] and a volumetric cooling potential of

350 W/m^3 per LAD was assigned as a source term in the energy equation. Leaf Area Density, or LAD, is defined as the leaf area per unit volume of the vegetation. While the actual shape of the vegetation can vary from species to species and can be quite spatially complex, it was decided to model the geometry following [36] with a constant LAD of 2.3 m^2/m^3, as shown in Figure 2a. To account for the effect of vegetation on air flow, the Ergun equation was utilised to determine the viscous resistance factor ($1/\alpha$) and the inertial resistance factor (C_2). The FLUENT theory guide provides these formulae as:

$$\alpha = \frac{d^2}{150}\frac{\varnothing^3}{(1-\varnothing)^2} \tag{1}$$

$$C_2 = \frac{3.5}{d}\frac{(1-\varnothing)}{\varnothing^3} \tag{2}$$

where d is the particle diameter and $\varnothing$ is the void fraction, set to 0.02 m and 0.96, respectively, in the present work.

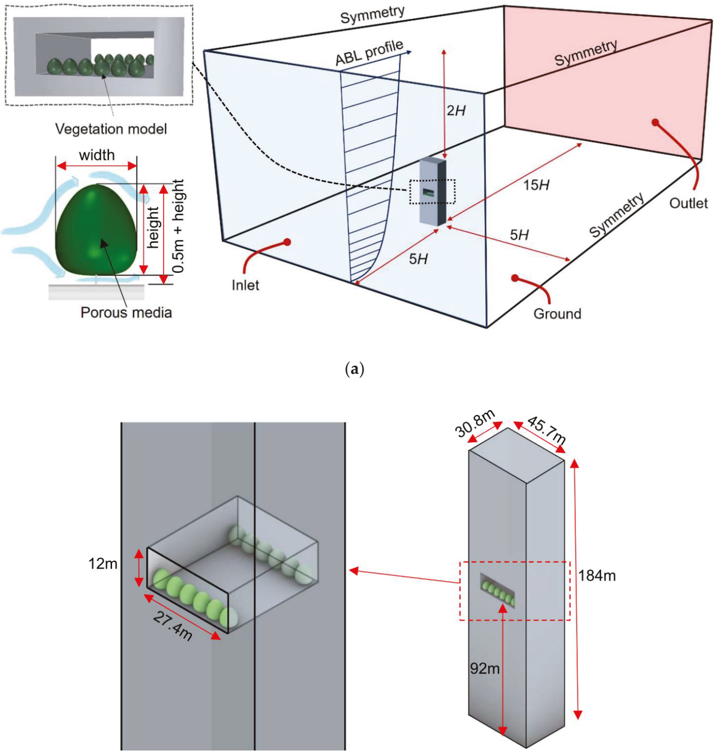

(**a**)

(**b**)

Figure 2. (**a**) Example of the computational domain and boundary conditions (large trees); (**b**) skygarden model and schematic showing dimensions.

2.2. Computational Geometry and Domain

For pre-processing, the solid geometry is modelled in CAD and imported into ANSYS for meshing and flow analysis. The present study requires the modelling of separate components that are assembled into an integrated model which can be done in the CAD software. The CAD geometry is imported to

ANSYS Design Modeler, which requires further modification to define the computational fluid domain required for the CFD simulations, as shown in Figure 2a. The present work adopts a domain size based on [37]. The upstream and side domain lengths are 5H or five times the height of the building, 920 m. The downstream domain length is 15H, while the total height of the domain is 3H. The building has a height, width, and depth of 184 m, 45.7 m, and 30.8 m, respectively, with the width to depth in the ratio of 3:2. The validation model consists of a rectangular building, without the skygarden.

The present work adopts the hollowed-out configuration of the skygarden, as shown in Figure 2b, characterised by a void going through the depths of the building [26]. Buildings, such as the Abeno Harukas (Osaka) and Post Tower (Bonn), have integrated such skygarden designs. The modelled high-rise building is 46 storeys high, with each storey being 4 m. In total, the height reaches 184 m, and the skygarden covers three storeys, i.e., 12 m. Additionally, the skygarden is placed centrally at 92 m above the ground.

The railing, hedges and trees are placed in the zones of high wind speeds, which are near the edge of the skygarden. Table 1 lists some of studies which have modelled these elements. As observed in previous works [30,38], this arrangement functions as an attenuator or barrier for the oncoming wind. Figure 2b shows an example of the arrangement of trees in the skygarden. The railing is modelled as a thin solid wall with a width of 0.05 m and height of 1.5 m and 2 m, generating a blockage of 13% and 17%. The hedge is modelled as a rectangular-shaped porous fluid volume (air) to set it as a porous medium, detailed in Section 2.1. The hedge has a width of 1.5 m and height of 1.5 m and 2 m, generating a blockage of 13% and 17%. Both the railing and hedge are placed at the edge of the skygarden. An oval-shaped tree with maximum diameter of 2.5 m (small tree) and a 4.5 m diameter (large tree) is used to represent a generic tree shape and is placed 0.5 m above the floor, following the study by [34]. To account for structural and architectural reasons, the trees are placed 2.5 m from the edge and equally spaced out. Table 2 summarises the specifications of the different wind barrier solutions considered in this study. While the hedge and railing are continuous in nature, trees are discretely placed along the skygarden edge, and the maximum number of trees is placed to ensure full coverage. Thus, 12 small trees (c1) and six large trees (c2) are placed at either edge.

Table 1. Studies which modelled railings, hedges, and trees.

Type	Dimension		Reference
	Height (m)	Width (m)	
Railing	1.2 m	-	[22]
	1.1 m (minimum)	-	[39]
	~2 m	-	Typical skygarden baluster height (e.g., 20 Fenchurch Street, Marina Bay Sands, etc.)
Hedge	1.5 m, 2.5 m	1.5 m	[38]
	0.5~4 m	1.5 m	[40]
	1~4 m	1 m	[41]
	1.5 m	-	[42]
Trees (Small)	1.5~4 m	1~7.5 m	[43]
	1.7 m~2.4 m	1.6~3.2 m	[44]
	2.2 m	1.6 m	[45]
	2~4 m	1~2 m	[46]
Trees (Large)	3.4 m	2.2 m	[47]
	4~8 m	2~6 m	[48]
	6.1–7.2 m	3.6–4.5 m	[49]
	6 m, 9 m	6, 12, 18 m	[50]

Table 2. Specifications of the railing, hedges, and trees incorporated into the skygarden model (present study).

Configuration	Element Type	Element Width (m)	Element Height (m)	Center-to-Center Tree Distance (m)	Blockage Ratio
a1	Railing	0.050	1.5	-	13%
a2	Railing	0.050	2.0	-	17%
b1	Hedge	1.5	1.5	-	13%
b2	Hedge	1.5	2.0	-	17%
c1	Trees	2.5	2.5	2.3	16%
c2	Trees	4.5	5.0	4.6	33%

Figure 3 shows the seven skygarden models simulated in the present study. Four main configurations were simulated: no wind barriers (reference), glass railing, hedge, and trees. From previous works [29,30], it was observed that wind speeds are higher near the edges of the skygarden and, consequently, the wind barriers are placed along the edges for an effective windbreak. Moreover, in practice, each skygarden is uniquely designed considering the contextual nature of the site, making it difficult to simulate any particular type. Both the windward and leeward edges are lined with wind barriers to account for the dynamic nature of the wind direction. The centre line marked in Figure 3 was used for comparing the values across the different configurations of the skygardens.

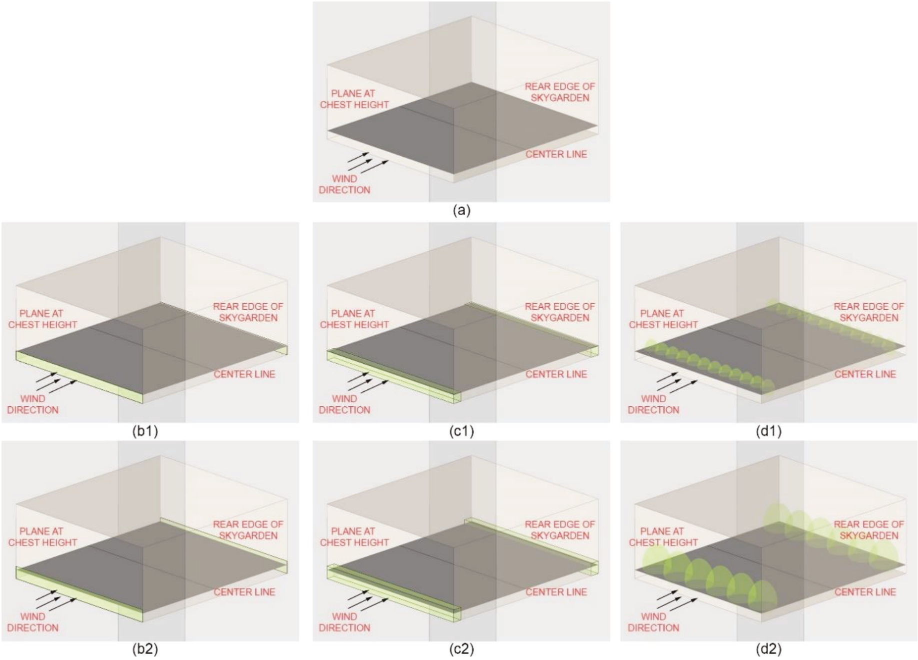

Figure 3. Arrangements within the skygarden model, with the centre line marked on the reference plane; (**a**) base skygarden configuration, skygarden with (**b1**) 1.5 m glass railing, (**b2**) 2 m glass railing, (**c1**) 1.5 m hedge, (**c2**) 2 m hedge, (**d1**) trees of height 2.5 m, and (**d2**) trees of height 4.5 m.

2.3. Boundary Conditions

The domain was created as an enclosure which allows for the simulation of airflow around the high-rise building model [51], as shown in Figure 2a. A velocity flow field is generated by setting one side of the enclosure as the velocity inlet and the other side as the pressure outlet.

Following the works of Dagnew [52] and Huang et al. [53], the power-law wind profile was created to account for the wind speed modifications due to presence of urban surroundings, shown in Figure 4 and given by:

$$u(z) = u(z_1)\cdot\left(\frac{z}{z_1}\right)^{\alpha} \tag{3}$$

where $u(z)$ is the calculated wind velocity (m/s) at the desired height z and $u(z_1)$ is the reference wind speed at the height z_1. In this case, the reference height was the height of the building, 184 m, and the reference speed was 12 m/s. α is the power-law exponent, which was set to 0.33 to represent towns and cities. Since the region of interest was located high up on the building, a fully turbulent flow was considered with turbulent kinetic energy (k) and a turbulent dissipation rate (ε) set to 0.8 m^2/s^2 and 1 m^2/s^3, respectively, at the inlet. The wind speed was modelled at a higher side to investigate the effectiveness of buffer attenuation.

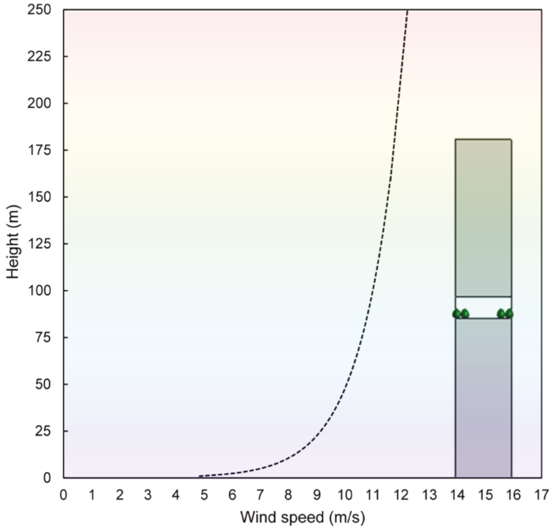

Figure 4. Atmospheric boundary layer wind velocity profile.

The pressure outlet was set as 0 Pa. The air temperature for the inlet was kept constant at 303 K (30 °C). The boundary condition for the outlet was set to a pressure outlet with 0 pa. Gravity of -9.8 m/s^2 was set for the simulation domain to account for buoyancy. Symmetry for top and sidewalls and a no-slip condition for the ground were implemented as a standard roughness model. The simulation was considered converged when the area of interest (skygarden centre line) recorded a constant value.

2.4. Mesh Design

Figure 5 shows the generated computational mesh around the surfaces of the 3D model of the high-rise building and skygarden. Since the FLUENT tool is based on the FVM method, it has a variety of mesh generation flexibilities and the capacity to deal with unstructured and structure mesh in its solver. An unstructured mesh was generated for the domain, except in the area of the building surface, where a structured mesh was generated to allow for the flow fields near the critical areas of interest to be captured in the simulation. Sizing functions were applied in the inner domain. The mesh element size was refined in areas with a high gradient to improve the accuracy of the velocity and temperature field results. The size ensured that every building edge was resolved by at least 10 cells. The 3D mesh consisted of 2.7 million elements.

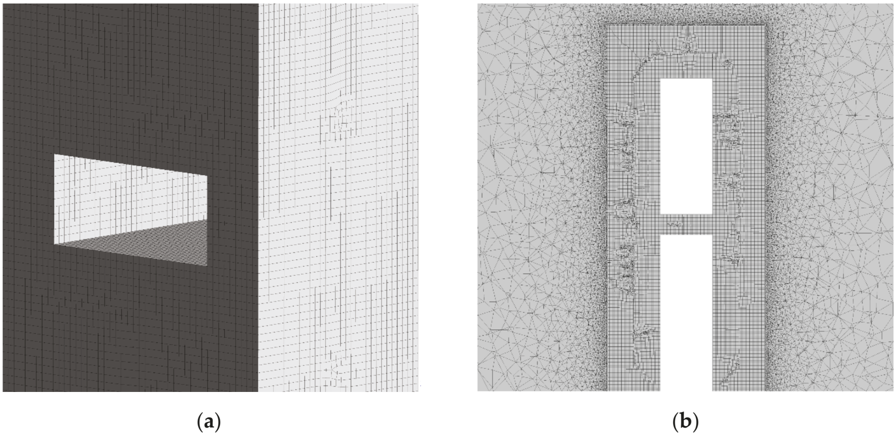

Figure 5. Computational mesh around the surfaces of the skygarden model (**a**) at the building face and (**b**) along the central plane.

Grid sensitivity analysis was also carried out to assess the independence of the CFD solution from the mesh size. The set boundary conditions remained fixed throughout the simulation process to ascertain a precise comparison of the results. Various mesh sizes ranging from 3 m to 1 m near the building and skygarden area were generated, and simulated with similar boundary conditions (detailed in the next section).

2.5. Outdoor Comfort Criteria

The Lawson (1978) [54] criterion (Table 3) was selected as the wind comfort requirement for this investigation. It enables the identification of wind velocity achieved across the skygarden in relation to occupancy activities.

Table 3. Wind speed classification based on pedestrian comfort after Lawson [54].

Threshold of Wind Speed	Quality Class	Original Description	Reference Activity
U > 1.8 m/s	A	Covered area	Sitting long
U > 3.6 m/s	B	Pedestrians standing around	Sitting short
U > 5.3 m/s	C	Pedestrian walkthrough	Strolling
U > 7.6 m/s	D	Roads and car parks	Walking fast
U > 15 m/s	E	Dangerous	Unacceptable

3. Method Verification and Validation

To verify the benchmark high-rise building model, a grid sensitivity analysis was carried out, and the results were validated with experimental and numerical data from previous studies. For this purpose, the pressure coefficient (Cp) along the front, side, and back face of the building at two-thirds of the height, following Huang et al. [53], was extracted. This enabled comparison with studies which previously employed the CAARC building with similar dimensions.

3.1. Verification of the Base High-Rise Building

A sensitivity analysis was performed to determine the most suitable mesh size and configuration. Table 4 presents the details of the various forms of mesh applied to the base building model. All mesh configurations of the base high-rise building was simulated to verify the benchmark model and select the mesh setup that provided a balance between the mesh size, computational time, rate of convergence, solution quality, and grid independence.

Table 4. Mesh setup for verification.

Mesh Config.	Mesh Settings	Number of	
	Building Vicinity Sizing	**Nodes**	**Elements**
A	0.25 m	667,228	2,603,555
B	0.2 m	552,357	2,466,524
C	0.1 m	1,049,698	3,029,468
D	0.1 m	697,824	2,714,337

Simulations of the base high-rise building with the k-ε turbulence model were performed using the mesh configurations detailed Table 4. Using the assigned wind velocity profile (Figure 4) and the initial CFD setup conditions, the pressure coefficients along the windward, side, and leeward surfaces at two-thirds (2/3 h) of the building height (123 m above ground) were evaluated. The pressure coefficients were comparable as it showed that mesh configuration and sizes had a high impact on the results of the pressure coefficient (Figure 6).

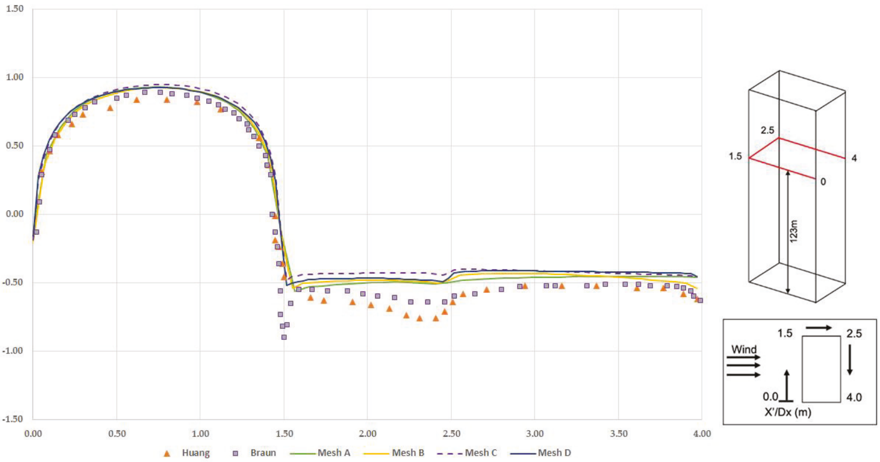

Figure 6. Mesh sensitivity results in terms of pressure coefficient around the windward, side, and leeward surfaces of the benchmark building model at the height of 2/3 h, 123 m above ground using various meshing configurations indicated in Table 4 and compared with the study by Huang et al. [53] and Braun and Awruch [55].

The pressure coefficient results are also comparable with the results of Huang et al. [53] and Braun and Awruch [55] in the same plot. Comparing the results of the different mesh arrangements, the predicted pressure values from Mesh A were closer to those from the available data. Meanwhile, the pattern of Mesh D is much closer to the available data. On the windward surface, the overall agreement between the present numerical results and previous work is quite good. The present model slightly overpredicted the pressure values on the side and leeward surfaces. This can be attributed to the difference in the experimental test, simulated boundary layer, turbulence model, and characteristics.

3.2. Validation of Vegetation and Trees

The vegetation model was validated against the study by Manickathan et al. [56], where the domain size of the reference case was 35 m in length and 11.5 m in height (Figure 7). Within the 2D domain, vegetation was represented by a 1 m square placed 8.5 m from the inlet and 0.5 m above the ground. Inlet velocity was modelled after Richard and Norris [57], where the von Karman number and roughness height were set to 0.41 and 0.0217 m, respectively. The inlet air temperature was set to 32 °C.

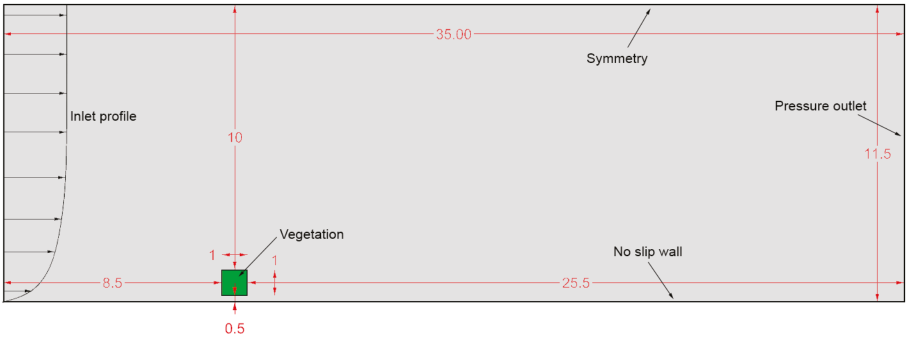

Figure 7. Simulation domain of the validation model, with the porous vegetation indicated by the green square and centred along the *x*-axis.

The velocity and temperature distribution of the area around the vegetation ($-2 < X < 6$; $0 <$ Height < 3) is shown in Figure 8. The vegetation zone offers resistance to the flow of air, with reduced speeds in the wake of the zone. The velocity distribution is in good agreement with the reference study [55]. A plot of velocity along the analysis line (marked in the figure, which runs through the centre of the vegetation patch) is shown in Figure 9. Vegetation is represented by the green patch, extending from −0.5 to 0.5 on the *x*-axis. The trend closely follows the numerical model of [55], with a slight underprediction towards the back of the vegetation patch. A deviation of about 0.04 m/s^2 is observed towards the far end. The model performs well given the low modelling complexity of the vegetation zone. A temperature drop of about 1 °C is observed in the wake of the vegetation, similar to the decrease estimated by the reference case.

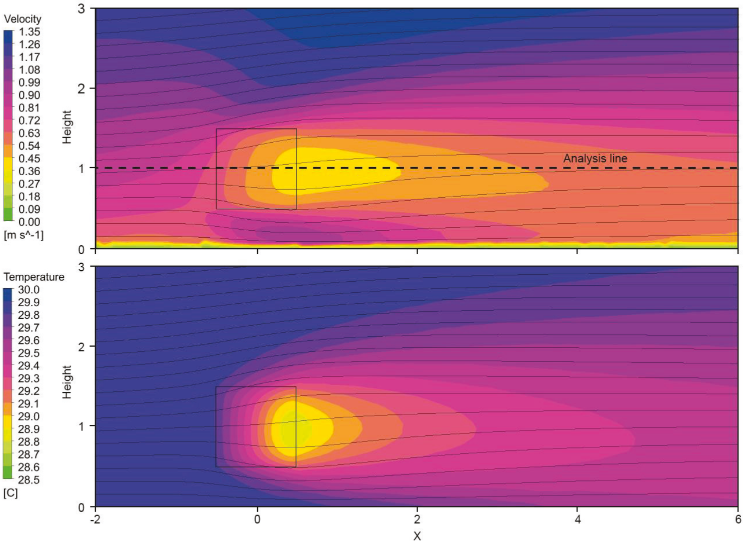

Figure 8. Contours of velocity and temperature around the vegetation (black square) from the validation model.

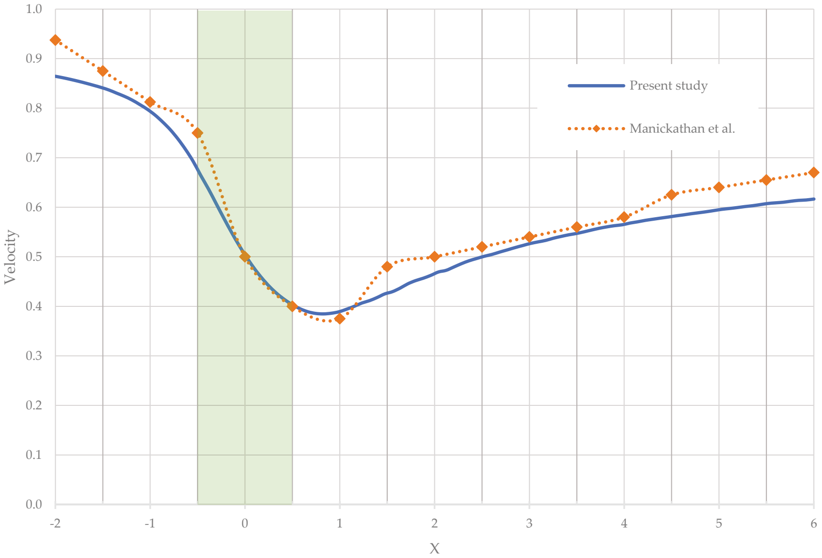

Figure 9. Comparison of wind speed along the analysis line, with the vegetation zone indicated by the green patch from −0.5 to 0.5 on the *x*-axis.

The slight variations in temperature and velocity could be due to the complex approach by Manickathan [55], wherein the authors inserted source/sink terms to account for modifications in air humidity, temperature, momentum, and turbulence. However, in the present case, a simplified vegetation model was adopted here without taking into account the detailed energy fluxes at the leaf surface. Furthermore, the numerical simulation was carried out in ANSYS, as opposed to OpenFOAM, which was utilised for the reference case. Given the objective of the present study to determine the attenuation effect of vegetation in a skygarden and of the observed wind pattern on the building platform, the deviations were considered quite small, and the observed contour was sufficiently accurate for further analysis.

4. Results and Discussion

The location and configuration of the skygarden have a major impact on the local wind speeds within the building [29,30] and the wind speeds are usually higher at the central location of the skygarden. The analysis is carried out at occupants' chest height, on a plane at a height of 1.4 m. Typically, wind speeds within the skygarden are amplified due to pressure short circuiting, and the air is drawn from around the opening into the void. Recirculation zones are observed in the wake of the building, while airflow, from the skygarden, is seen to move upwards after exiting in the rear (Figure 10).

A closer observation within the skygarden (Figure 11) indicates that wind speeds are highest near the front, in the range of 10 m/s to 13 m/s. Speeds are generally lower along the middle of the skygarden and increase towards the sides. On average, the velocity at the occupants' level is 12 m/s, which is significantly higher than the human comfort range. Thus, people will always experience discomfort within the skygarden. Even for intense physical activity, like running, such high wind speeds will be a cause of distress.

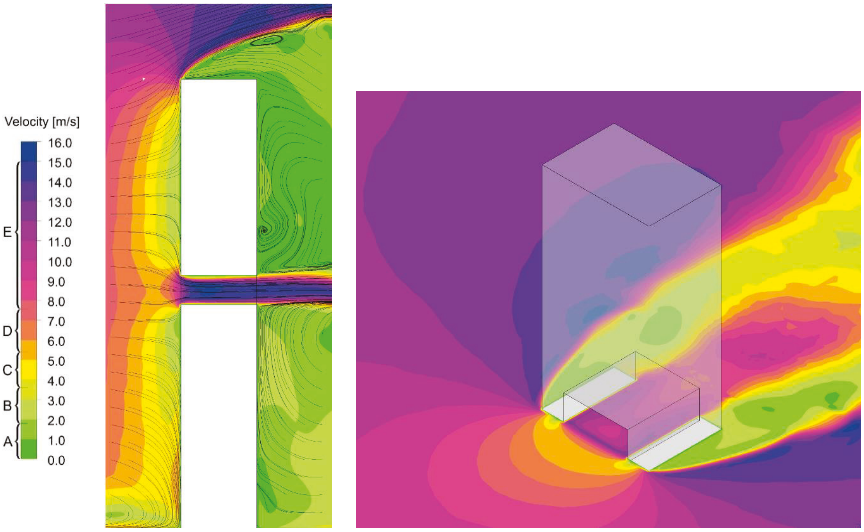

(**a**) (**b**)

Figure 10. Wind velocity contour around the base skygarden model on (**a**) a central vertical plane through the centre of the skygarden, (**b**) a horizontal plane at occupants' chest height (1.4 m).

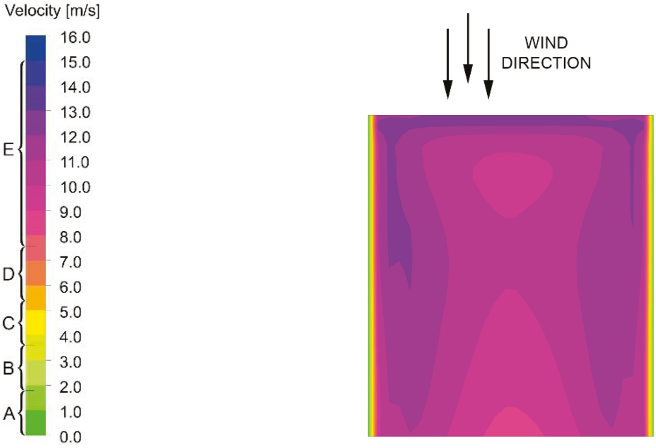

Figure 11. Wind velocity contour in the skygarden at occupants' height.

4.1. Impact of Buffer Elements on Wind Speed

In reality, most skygardens have a parapet or a railing for security purposes which also serves to deflect the wind away from occupants. With the introduction of such buffers, the wind speed is attenuated in the skygarden to create a more conducive environment for occupants. Three cases are simulated here, wherein the buffer elements are erected at the open edge of the skygarden. Case a (1 and 2) are integrated with a solid railing, case b (1 and 2) with 1.5 m thick hedges, and case c (1 and 2) with trees. A comparative analysis of the three elements is discussed below.

From Figure 12, it can be inferred that the wind speeds are generally reduced for all cases when compared with the base case. The buffer elements significantly reduce the wind velocity across the skygardens, as more areas achieve a wind velocity of less than 5 m/s. Specifically, the buffers along the windward side provide a barrier to the direct wind flow. In the case of railings and hedges, it is observed that the larger elements provide better attenuation. The high railing provides the highest attenuation, with an average velocity of about 2 m/s, while the configuration with low-level hedges is the least effective for wind reduction, with an average velocity of about 4.2 m/s. Each configuration has a distinct airflow pattern, specific to the interaction between the buffer elements and wind. Correspondingly, Table 5 presents the average wind speed across the skygarden at occupants' height for each of the configuration cases. However, in terms of wind comfort, most configurations generate a Lawson quality class (QC) of C and below near the centre of the skygarden (Figure 13). This suggests that although the various elements have varying potential to attenuate the wind speed, they generally create a conducive environment for the skygarden occupants. However, the short railing and hedge are not able to reduce the winds speeds to comfortable levels near the sides.

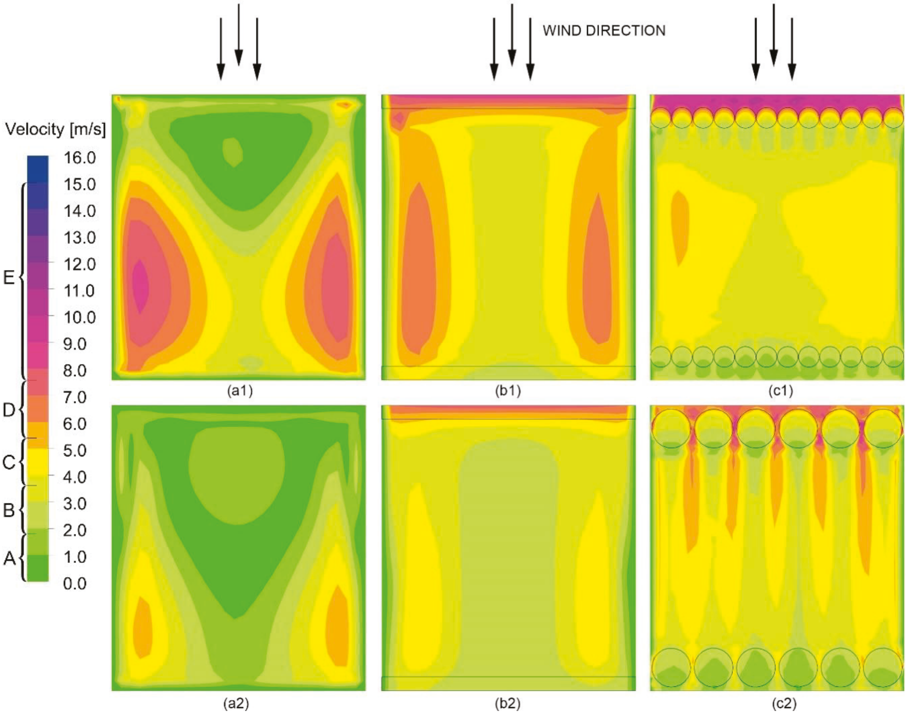

Figure 12. Wind velocity contour in the skygarden captured at 1.4 m above the skygarden plane, corresponding to occupants' height with (**a1**) 1.5 m railing, (**a2**) 2 m railing, (**b1**) 1.5 m hedge, (**b2**) 2 m hedge, (**c1**) 2.5 m trees, and (**c2**) 5 m trees.

Table 5. Average wind speed in the skygarden at occupants' height, (base) base configuration, (a1) 1.5 m railing, (a2) 2 m railing, (b1) 1.5 m hedge, (b2) 2 m hedge, (c1) 2.5 m trees, and (c2) 5 m trees.

Case	Base	A1	A2	B1	B2	C1	C2
Average wind speeds (m/s)	11.99	4.07	2.24	4.20	2.91	3.93	4.00

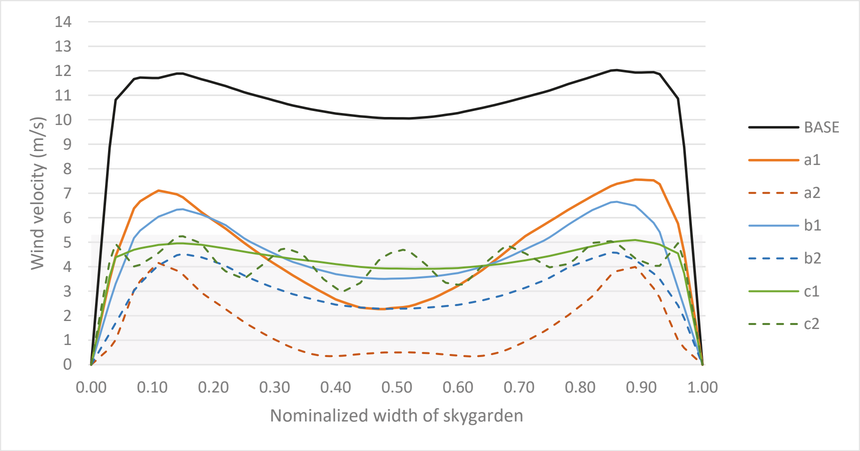

Figure 13. Velocity profile along the middle of the skygarden, the grey patch indicates wind speeds of quality class C and below; (**a1**) railing 1.5 m, (**a2**) railing 2 m, (**b1**) hedge 1.5 m, (**b2**) hedge 2 m, (**c1**) tree 2.5 m, and (**c2**) tree 5 m.

4.2. Wind Comfort within the Skygarden

In the base configuration, without any buffer element, it was observed that wind speeds are generally of QC-E. In fact, in some places near the front edge, the speeds are dangerously high and unsafe for occupancy. With the addition of a 1.5 m high railing, QCs of A and B are generated near the anterior of the skygarden. This gradually shifts to QC-C near the rear, while some areas on the sides experience QC-D. The QC is further improved by increasing the height of the railing to 2 m. Similarly, the hedges create better QCs near the centre of the skygarden. In the case of a 1.5 m hedge, QC-D is observed near the walls, which is not preferable for sedentary activity. However, it can support activities like running and jogging. In the case of trees, the entire region between the front and rear row is seen to experience a QC of C and below. Alternate bands are created due to the funnelling effect, but on average, the zone is comfortable for occupants.

Table 6 lists the percentage of the skygarden area with a QC of C and below. A higher number indicates a larger area where occupants will be comfortable. It can be observed that the addition of buffer elements significantly improves the wind comfort in the region. Even the worst performing setup, i.e., the 1.5 m hedge configuration, still has 69% of the area within comfort limits. The 2 m railing can achieve comfort criteria for the entire skygarden, followed by a 2 m high hedge and then by the tree configurations.

Table 6. Percentage area of skygarden within quality class of C; (a1) railing 1.5 m, (a2) railing 2 m, (b1) hedge 1.5 m, (b2) hedge 2 m, (c1) tree 2.5 m, and (c2) tree 5 m.

Case	Base	A1	A2	B1	B2	C1	C2
Percentage area of skygarden with Quality Class of C or below	3.68%	71.84%	98.60%	69.02%	96.01%	93.10%	91.09%

A sectional view of the skygarden configuration is shown in Figure 14. In the base case, wind speeds are quite high, of the class E, throughout the height of the skygarden, except near the floor and the ceiling. The addition of buffer elements significantly stalls the airflow near the floor, while generally reducing the speed in the entire volume. The height of the element determines the relative height of a calm region which can be discerned for all three configurations. A higher railing generates larger depths of QC-C in the skygarden, compared to the lower railing. A similar pattern is observed for the hedge as well as the trees. This indicates that based on the occupancy and activity envisaged in the skygarden, the height of the buffer element can be determined to ensure sufficient attenuation is achieved. The large trees, due to their sheer size, generate comfortable wind flow in the entire depth and to a significant height for the skygarden. However, there is a slight increase in wind speeds near the floor due to the raised tree crown.

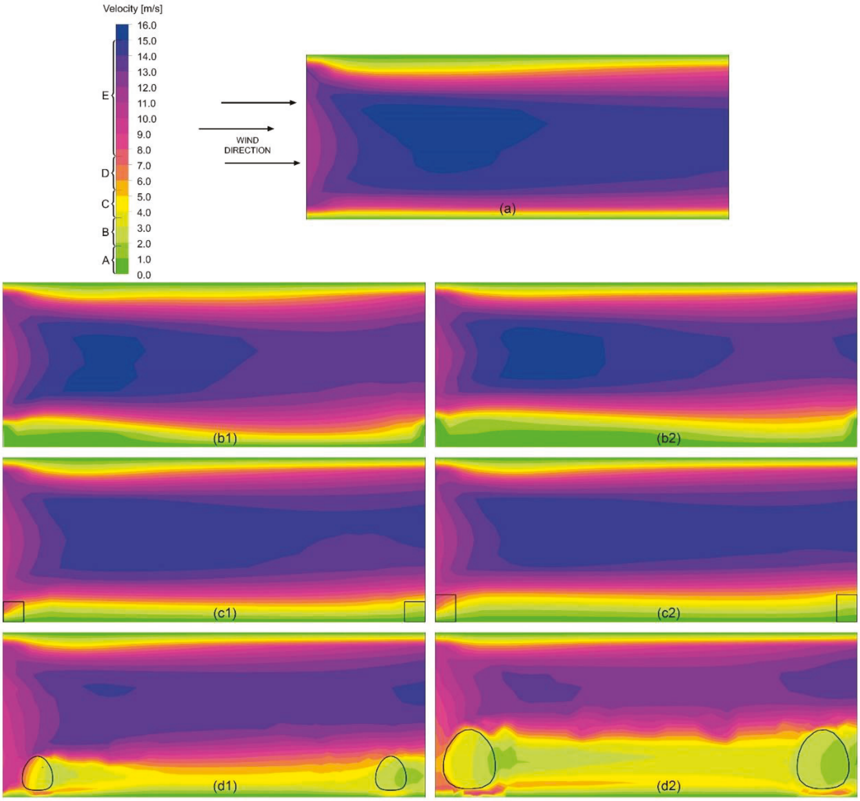

Figure 14. Plot of wind speed in the skygarden along a vertical plane; (**a**) base configuration without any buffer, (**b1**) railing 1.5 m, (**b2**) railing 2 m, (**c1**) hedge 1.5 m, (**c2**) hedge 2 m, (**d1**) tree 2.5 m, and (**d2**) tree 5 m.

4.3. Impact of Buffer Elements on Air Temperature

Vegetation is known to provide evapotranspirational cooling, which can be harnessed to improve the microclimate of the skygarden. Figure 15 shows the temperature distribution across the skygarden for the hedge and tree configuration. Configurations with railings are not considered for this effect, and the temperature is assumed to be constant, similar to the base case. In the case of the skygarden with hedges, there is slight cooling near the foliage. Reductions ranging from 0.3 °C to 0.5 °C can be seen in the vicinity of the hedges, however, the drop in temperature is negligible towards the rear. In the case of small trees, the reduction in temperature is similar but is spread across the skygarden. The larger trees are, however, able to produce cooling, ranging from 0.5 °C to 1 °C in their wake. Furthermore, the contours are fairly spread out across the depth and occupiable height of the skygarden. The leeward trees can extract more heat from the air and reduce temperatures further by a degree.

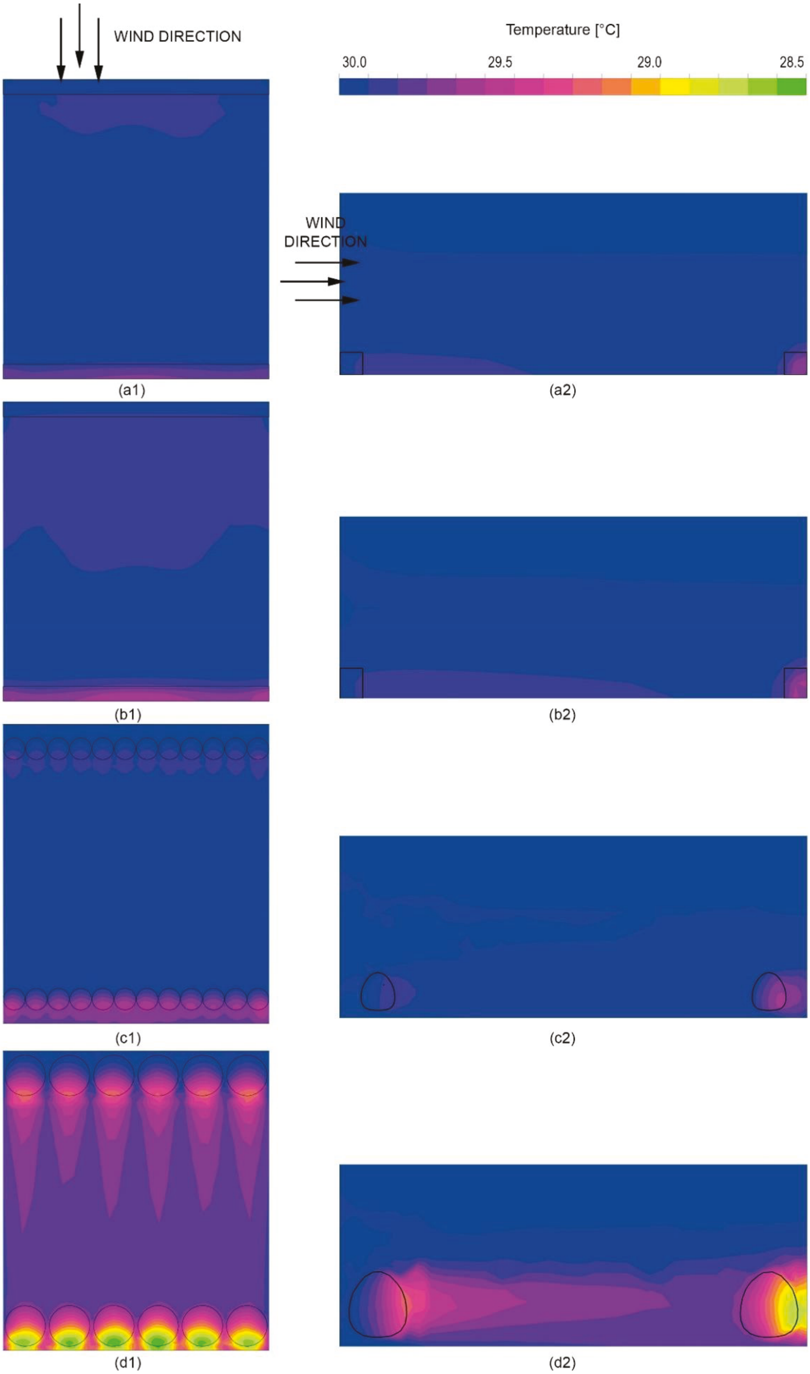

Figure 15. Temperature profile along the (1) horizontal and (2) vertical plane of the skygarden; (**a**) hedge 1.5 m, (**b**) hedge 2 m, (**c**) tree 2.5 m, and (**d**) tree 5 m.

The study by Mohammadi and Calautit [30] suggests that increasing the number of trees would produce more cooling in the skygarden. In the current scenario, the total foliage volumes for 2.5 m trees and 5 m trees are 162.26 m^3 and 649 m^3, respectively. Consequently, the area average temperature reduction in the skygarden for case c2 is about 3.8 times higher than for case c1 (average temperature reductions being 0.35 °C and 0.09 °C, respectively). Overall, the foliage can induce both cooling and attenuation in wind speeds for the comfort of occupants. It also has the potential for blocking solar radiation and improving air quality, although the effects have not been considered in this study.

5. Conclusions

The main aim of the study was to identify the effects of various buffer elements on the general air quality of the skygarden. Such buffers are primarily installed as a security feature in skygardens but can also assist in modifying the airflow. The right combination and dimension of these elements can greatly assist in generating aero-thermal comfort across the skygarden. This is an important indicator of the performance of a skygarden-integrated building design and the achievement of comfortable environments for occupants. A quality class (QC) of C of the Lawson comfort criteria was assumed as the desired maximum condition to enable skygardens to have a suitable wind comfort level for the performance of any type of occupancy activities. The hollowed-out skygarden design, located centrally in the building with no parapet, was found to be dangerous for occupancy as it produced high wind speeds in the region.

The addition of buffer elements, like railings or hedges and trees, greatly stalled the air. However, the aero-thermal quality of air greatly differed in each case. While railings are solid barriers, hedges and trees, modelled as a porous zone, provide momentum sinks for reducing wind speeds. Railings are most effective in deflecting wind flow and generate QC-C at occupant height. Higher railings ensure a better spread of wind for improved comfort quality across the skygarden. Although hedges can stall airflow, their relative performance is lower than railings. Trees, on the other hand, can generate QC-C at a sufficient height and depth of the skygarden. They also provide cooling up to 1 °C, which can be increased depending on the variety of species planted.

While railings are easy to install and maintain, foliage requires careful planning and regular maintenance. Trees can be relatively expensive and pose structural challenges, but can provide added benefits like providing shade, better cooling, fresh air, carbon sinks, and psychological benefits. Further study can investigate the impact towards various tree geometries, volumetric cooling potential and planting location to optimise the design. Other factors like lighting, view factors, solar radiation, pollutants, and noise abatement can also be investigated. These studies have been carried out for roadside vegetation and vertical greenery; however, their impact is relatively unknown in the context of a skygarden. Moreover, skygardens appear in various forms and geometries dictated by building designs across the globe, and further studies could assess the aero-thermal comfort characteristics with these buffer elements for various other shapes and configurations as well varying meteorological conditions.

Author Contributions: Conceptualisation, J.K.C.; methodology, J.K.C., P.W.T., and M.M.; software, M.M.; validation, J.K.C. and M.M.; formal analysis, P.W.T. and M.M.; investigation, M.M.; resources, J.K.C.; data curation, J.K.C.; writing—original draft preparation, P.W.T. and M.M.; writing—review and editing, J.K.C.; visualisation, M.M.; supervision, J.K.C.; project administration, J.K.C. All authors have read and agreed to the published version of the manuscript.

Funding: This research received no external funding.

Conflicts of Interest: The authors declare no conflict of interest.

References

1. Heat Island Impacts. EPA United States Environmental Protection Agency. Available online: https://www.epa.gov/heat-islands/heat-island-impacts (accessed on 23 June 2020).
2. World Energy Outlook 2018. Available online: https://www.iea.org/reports/world-energy-outlook-2018 (accessed on 23 June 2020).
3. Krefis, A.C.; Augustin, M.; Schlünzen, K.H.; Oßenbrügge, J.; Augustin, J. How Does the Urban Environment Affect Health and Well-Being? A Systematic Review. *Urban Sci.* **2018**, *2*, 21. [CrossRef]
4. Cities in Numbers: How Patterns of Urban Growth Change the World. Available online: https://www.theguardian.com/cities/2015/nov/23/cities-in-numbers-how-patterns-of-urban-growth-change-the-world (accessed on 23 June 2020).
5. High Demand for High-Rise: Where will the City Put Its New Skyscrapers? Available online: https://www.architectsjournal.co.uk/news/high-demand-for-high-rise-where-will-the-city-put-its-new-skyscrapers/8691245.article (accessed on 23 June 2020).
6. Akristiniy, V.A.; Boriskina, Y.I. Vertical cities-the new form of high-rise construction evolution. In *E3S Web of Conferences*; 2018; Volume 33. [CrossRef]
7. Jim, C.Y.; Chan, M.W.H. Urban greenspace delivery in Hong Kong: Spatial-institutional limitations and solutions. *Urban For. Urban Green.* **2016**, *18*, 65–85. [CrossRef]
8. Lo, A.; Byrne, J.A.; Jim, C.Y. How climate change perception is reshaping attitudes towards the functional benefits of urban trees and green space: Lessons from Hong Kong. *Urban For. Urban Green.* **2016**, *23*, 74–83. [CrossRef]
9. Haaland, C.; van den Bosch, C.K. Challenges and strategies for urban green-space planning in cities undergoing densification: A review. *Urban For. Urban Green.* **2015**, *14*, 760–771. [CrossRef]
10. Moss, J.L.; Doick, K.J.; Smith, S.; Shahrestani, M. Influence of evaporative cooling by urban forests on cooling demand in cities. *Urban For. Urban Green.* **2019**, *37*, 65–73. [CrossRef]
11. Ow, L.F.; Ghosh, S.; Yusof, M.L.M. Growth of Samanea saman: Estimated cooling potential of this tree in an urban environment. *Urban For. Urban Green.* **2019**, *41*, 264–271. [CrossRef]
12. Abhijith, K.V.; Kumar, P.; Gallagher, J.; McNabola, A.; Baldauf, R.; Pilla, F.; Broderick, B.; Di Sabatino, S.; Pulvirenti, B. Air pollution abatement performances of green infrastructure in open road and built-up street canyon environments-A review. *Atmos. Environ.* **2017**, *162*, 71–86. [CrossRef]
13. Wellmann, T.; Schug, F.; Haase, D.; Pflugmacher, D.; van der Linden, S. Green growth? On the relation between population density, land use and vegetation cover fractions in a city using a 30-years Landsat time series. *Landsc. Urban Plan.* **2020**, *202*, 103857. [CrossRef]
14. Malys, L.; Musy, M.; Inard, C. Direct and Indirect Impacts of Vegetation on Building Comfort: A Comparative Study of Lawns, Green Walls and Green Roofs. *Energies* **2016**, *9*, 32. [CrossRef]
15. Aflaki, A.; Mirnezhad, M.; Ghaffarianhoseini, A.; Ghaffarianhoseini, A.; Omrany, H.; Wang, Z.H.; Akbari, H. Urban heat island mitigation strategies: A state-of-the-art review on Kuala Lumpur, Singapore and Hong Kong. *Cities* **2017**, *62*, 131–145. [CrossRef]
16. Hirano, Y.; Ihara, T.; Gomi, K.; Fujita, T. Simulation-Based Evaluation of the Effect of Green Roofs in Office Building Districts on Mitigating the Urban Heat Island Effect and Reducing CO_2 Emissions. *Sustainability* **2019**, *11*, 2055. [CrossRef]
17. Gomes, M.G.M.; Silva, C.; Valadas, A.S.; Silva, M. Impact of Vegetation, Substrate, and Irrigation on the Energy Performance of Green Roofs in a Mediterranean Climate. *Water* **2019**, *11*, 2016. [CrossRef]
18. Kang, G.; Kim, J.-J.; Kim, D.-J.; Choi, W.; Park, S.-J. Development of a computational fluid dynamics model with tree drag parameterizations: Application to pedestrian wind comfort in an urban area. *Build. Environ.* **2017**, *124*, 209–218. [CrossRef]
19. Lin, C.-H.; Lin, T.-P.; Hwang, R.-L. Thermal comfort for urban parks in subtropics: Understanding visitor's perceptions, behavior and attendance. *Adv. Meteorol.* **2013**, *2013*. [CrossRef]
20. Gatto, E.; Buccolieri, R.; Aarrevaara, E.; Ippolito, F.; Emmanuel, R.; Perronace, L.; Santiago, J.L. Impact of Urban Vegetation on Outdoor Thermal Comfort: Comparison between a Mediterranean City (Lecce, Italy) and a Northern European City (Lahti, Finland). *Forests* **2020**, *11*, 228. [CrossRef]
21. Ochodo, C.; Ndetei, D.M.; Moturi, W.N.; Otieno, J.O. External Built Residential Environment Characteristics that Affect Mental Health of Adults. *J. Urban Health* **2014**, *91*, 908–927. [CrossRef]

22. Montazeri, H.; Blocken, B.; Janssen, W.D.; van Hooff, T. CFD analysis of wind comfort on high-rise building balconies: Validation and application. In Proceedings of the 7th International Colloquium on Bluff Body Aerodynamics and Applications (BBAA7), Shanghai, China, 2–6 September 2012; Volume 2012, pp. 1–10.
23. Tian, Y.; Jim, C.Y. Factors influencing the spatial pattern of sky gardens in the compact city of Hong Kong. *Landsc. Urban Plan.* **2011**, *101*, 299–309. [CrossRef]
24. Giacomello, E.; Valagussa, M. *Vertical Greenery: Evaluating the High-Rise Vegetation of the Bosco Verticale, Milan*; Council on Tall Buildings and Urban Habitat: Chicago, IL, USA, 2015. Available online: https://store.ctbuh.org/index.php?controller=attachment&id_attachment=32 (accessed on 23 June 2020).
25. Terrapin Bright Green. ParkRoyal on Pickering Hotel and Spa. 2017. Available online: https://www.terrapinbrightgreen.com/wp-content/uploads/2015/11/Parkroyal_Case-Study.pdf (accessed on 23 June 2020).
26. Pomeroy, J. *The Skycourt and Skygarden, Greening the Urban Habitat*, 1st ed.; Routledge: Abingdon, UK, 2014; ISBN 978-0-415-63698-8.
27. WHO—World Health Organization. Health and Sustainable Development: Urban Green Spaces 2020. Available online: https://www.who.int/sustainable-development/cities/health-risks/urban-green-space/en// (accessed on 23 June 2020).
28. Tian, Y.; Jim, C.Y.; Tao, Y. Challenges and Strategies for Greening the Compact City of Hong Kong. *J. Urban Plan. Dev.* **2012**, *138*, 101–109. [CrossRef]
29. Tien, P.W.; Calautit, J.K. Numerical analysis of the wind and thermal comfort in courtyards "skycourts" in high rise buildings. *J. Build. Eng.* **2019**, *24*, 100735. [CrossRef]
30. Mohammadi, M.; Calautit, J.K. Numerical investigation of the wind and thermal conditions in sky gardens in high-rise buildings. *Energies* **2019**, *12*, 1380. [CrossRef]
31. Melbourne, W.H. Comparison of measurements on the CAARC standard tall building model in simulated model wind flows. *J. Wind Eng. Ind. Aerodyn.* **1980**, *6*, 73–88. [CrossRef]
32. Kichah, A.; Bournet, P.-E.; Migeon, C.; Boulard, T. Measurement and CFD simulation of microclimate characteristics and transpiration of an Impatiens pot plant crop in a greenhouse. *Biosyst. Eng.* **2012**, *112*, 22–34. [CrossRef]
33. Gromke, C.; Blocken, B.; Janssen, W.; Merema, B.; van Hooff, T.; Timmermans, H. CFD analysis of transpirational cooling by vegetation: Case study for specific meteorological conditions during a heat wave in Arnhem, Netherlands. *Build. Environ.* **2015**, *83*, 11–26. [CrossRef]
34. Rahman, M.A.; Smith, J.G.; Stringer, P.; Ennos, A.R. Effect of rooting conditions on the growth and cooling ability of Pyrus calleryana. *Urban. For. Urban. Green.* **2011**, *10*, 185–192. [CrossRef]
35. Gromke, C.; Ruck, B. Pollutant Concentrations in Street Canyons of Different Aspect Ratio with Avenues of Trees for Various Wind Directions. *Bound. Layer Meteorol.* **2012**, *144*, 41–64. [CrossRef]
36. Bitog, J.P.; Lee, I.-B.; Hwang, H.-S.; Shin, M.-H.; Hong, S.-W.; Seo, I.-H.; Mostafa, E.; Pang, Z. A wind tunnel study on aerodynamic porosity and windbreak drag. *For. Sci. Technol.* **2011**, *7*, 8–16. [CrossRef]
37. Tominaga, Y.; Mochida, A.; Murakami, S.; Sawaki, S. Comparison of various revised k-ε models and LES applied to flow around a high-rise building model with 1:1:2 shape placed within the surface boundary layer. *J. Wind Eng. Ind. Aerodyn.* **2008**, *96*, 389–411. [CrossRef]
38. Gromke, C.; Jamarkattel, N.; Ruck, B. Influence of roadside hedgerows on air quality in urban street canyons. *Atmos. Environ.* **2016**, *139*, 75–86. [CrossRef]
39. British Standards Institution. *BS 6180:2011 Barriers in and about Buildings-Code of Practice*; British Standards Institution: London, UK, 2011; p. 46.
40. Li, X.B.; Lu, Q.C.; Lu, S.J.; He, H.D.; Peng, Z.R.; Gao, Y.; Wang, Z.Y. The impacts of roadside vegetation barriers on the dispersion of gaseous traffic pollution in urban street canyons. *Urban. For. Urban. Green.* **2016**, *17*, 80–91. [CrossRef]
41. Vos, P.E.J.; Maiheu, B.; Vankerkom, J.; Janssen, S. Improving local air quality in cities: To tree or not to tree? *Environ. Pollut.* **2013**, *183*, 113–122. [CrossRef]
42. Wania, A.; Bruse, M.; Blond, N.; Weber, C. Analysing the influence of different street vegetation on traffic-induced particle dispersion using microscale simulations. *J. Environ. Manage.* **2012**, *94*, 91–101. [CrossRef] [PubMed]
43. Morakinyo, T.E.; Lam, Y.F. Simulation study of dispersion and removal of particulate matter from traffic by road-side vegetation barrier. *Environ. Sci. Pollut. Res.* **2016**, *23*, 6709–6722. [CrossRef] [PubMed]

44. Tiwary, A.; Morvan, H.P.; Colls, J.J. Modelling the size-dependent collection efficiency of hedgerows for ambient aerosols. *J. Aerosol. Sci.* **2006**, *37*, 990–1015. [CrossRef]
45. Tiwary, A.; Reff, A.; Colls, J.J. Collection of ambient particulate matter by porous vegetation barriers: Sampling and characterization methods. *J. Aerosol. Sci.* **2008**, *39*, 40–47. [CrossRef]
46. Morakinyo, T.E.; Lam, Y.F.; Hao, S. Evaluating the role of green infrastructures on near-road pollutant dispersion and removal: Modelling and measurement. *J. Environ. Manag.* **2016**, *182*, 595–605. [CrossRef]
47. Al-Dabbous, A.N.; Kumar, P. The influence of roadside vegetation barriers on airborne nanoparticles and pedestrians exposure under varying wind conditions. *Atmos. Environ.* **2014**, *90*, 113–124. [CrossRef]
48. Lin, M.Y.; Hagler, G.; Baldauf, R.; Isakov, V.; Lin, H.Y.; Khlystov, A. The effects of vegetation barriers on near-road ultrafine particle number and carbon monoxide concentrations. *Sci. Total Environ.* **2016**, *553*, 372–379. [CrossRef]
49. Hagler, G.S.; Lin, M.Y.; Khlystov, A.; Baldauf, R.W.; Isakov, V.; Faircloth, J.; Jackson, L.E. Field investigation of roadside vegetative and structural barrier impact on near-road ultrafine particle concentrations under a variety of wind conditions. *Sci. Total Environ.* **2012**, *419*, 7–15. [CrossRef]
50. Tong, Z.; Baldauf, R.W.; Isakov, V.; Deshmukh, P.; Zhang, K.M. Roadside vegetation barrier designs to mitigate near-road air pollution impacts. *Sci. Total Environ.* **2016**, *541*, 920–927. [CrossRef]
51. Franke, J. Recommendations of the COST action C14 on the use of CFD in predicting pedestrian wind environment. In Proceedings of the Fourth International Symposium on Computational Wind Engineering (CWE2006), Yokohama, Japan, 16–19 July 2006.
52. Dagnew, A.K.; Bitsuamalk, G.T.; Merrick, R. Computational evaluation of wind pressures on tall buildings. In Proceedings of the 11th Americas Conference on Wind Engineering, San Juan, Puerto Rico, 20–26 June 2009.
53. Huang, S.; Li, Q.S.; Xu, S. Numerical evaluation of wind effects on a tall steel building by CFD. *J. Constr. Steel. Res.* **2007**, *63*, 612–627. [CrossRef]
54. Lawson, T.V. The wind content of the built environment. *J. Wind Eng. Ind. Aerodyn.* **1978**, *3*, 93–105. [CrossRef]
55. Braun, A.L.; Awruch, A.M. Aerodynamic and aeroelastic analyses on the CAARC standard tall building model using numerical simulation. *Comput. Struct.* **2009**, *87*, 564–581. [CrossRef]
56. Manickathan, L.; Defraeye, T.; Allegrini, J.; Derome, D.; Carmeliet, J. Parametric study of the influence of environmental factors and tree properties on the transpirative cooling effect of trees. *Agric. For. Meteorol.* **2018**, *248*, 259–274. [CrossRef]
57. Richards, P.J.; Norris, S.E. Appropriate boundary conditions for computational wind engineering models revisited. *J. Wind Eng. Ind. Aerodyn.* **2011**, *99*, 257–266. [CrossRef]

fluids

MDPI

Article

A Simple Construction of a Thermodynamically Consistent Mathematical Model for Non-Isothermal Flows of Dilute Compressible Polymeric Fluids

Mark Dostalík [1], Josef Málek [1,*], Vít Průša [1] and Endre Süli [2]

[1] Faculty of Mathematics and Physics, Charles University, Sokolovská 83, CZ 186 75 Praha 8–Karlín, Czech Republic; dostalik@karlin.mff.cuni.cz (M.D.); prusv@karlin.mff.cuni.cz (V.P.)

[2] Mathematical Institute, University of Oxford, Radcliffe Observatory Quarter, Woodstock Road, Oxford OX2 6GG, UK; suli@maths.ox.ac.uk

* Correspondence: malek@karlin.mff.cuni.cz

Received: 13 July 2020; Accepted: 6 August 2020; Published: 11 August 2020

Abstract: We revisit some classical models for dilute polymeric fluids, and we show that thermodynamically consistent models for non-isothermal flows of these fluids can be derived in a very elementary manner. Our approach is based on the identification of energy storage mechanisms and entropy production mechanisms in the fluid of interest, which, in turn, leads to explicit formulae for the Cauchy stress tensor and for all of the fluxes involved. Having identified these mechanisms and derived the governing equations, we document the potential use of the thermodynamic basis of the model in a rudimentary stability analysis. In particular, we focus on finite amplitude (nonlinear) stability of a stationary spatially homogeneous state in a thermodynamically isolated system.

Keywords: thermodynamics; compressible dilute polymeric fluids; stability

MSC: 76A05; 35Q79; 37L15

1. Introduction

Starting from the seminal work by Kramers [1] kinetic-type models have been widely used in the mathematical modelling of polymeric fluids, see the monographs by Bird et al. [2], Beris and Edwards [3], Öttinger [4], Huilgol and Phan-Thien [5], Dressler et al. [6], Öttinger [7] Kröger [8], and the review paper by Lozinski et al. [9] to name a few (a mathematically inclined reader—a specialist in theory of partial differential equations—is also referred to the concise presentation in Le Bris and Lelièvre [10]). The overwhelming majority of the works, especially in the field of numerical simulations, see, for example Lozinski and Chauvière [11], Knezevic and Süli [12] or Mizerová and She [13], are however restricted to isothermal flows. In particular, the temperature field is often tacitly assumed to be homogeneous in space, and an evolution equation describing the temporal and spatial variations of the temperature field is rarely formulated, albeit some approaches, such as the GENERIC formalism, see Öttinger [7], or Pavelka et al. [14], allow one to do so. (regarding the classical macroscopic models, temperature evolution equations have been formulated for example in Peters and Baaijens [15], Wapperom and Hulsen [16] and Dressler et al. [6], see also Hron et al. [17] for further discussion). In the present contribution, we provide a straightforward self-contained derivation of a simple kinetic-type model for non-isothermal flows of compressible dilute polymeric fluids. The model is essentially the same as the model discussed in Öttinger and Grmela [18], but the approach to the derivation of a thermodynamically consistent model is substantially different.

We only use elementary arguments easily accessible to everyone familiar with basic principles of continuum mechanics such as the general form of balance equations. It turns out that, once one correctly specifies the energy storage mechanisms and the entropy production mechanisms in the fluid of interest, then some formulae, in particular the Kramers formula for the stress tensor, are natural consequences of the basic principles (there is no need to assume these formulae *a priori*). The same holds true in the derivation proposed by Öttinger and Grmela [18], where the authors claim that this fact is a "quite remarkable" consequence of the GENERIC structure. While the GENERIC framework has definitely its merits, we show that much more elementary arguments lead—regarding this issue—to the same conclusion. Furthermore, having obtained a thermodynamically consistent model, we exploit thermodynamic considerations in a rudimentary stability analysis in the spirit of Coleman [19], see also Bulíček et al. [20] for a discussion.

The paper is organised, as follows. First we recall basic principles of continuum mechanics, see Section 2, with particular attention placed on the basic tenets of the classical kinetic-type theory for dilute polymeric fluids. The key assumption regarding dilute polymeric fluids is that the polymeric chains do not effectively contribute to the mass of the solvent/polymer mixture, which means that the density of the mixture coincides with the density of the solvent. Furthermore, the kinetic energy of the polymeric chains is also neglected, the only mechanical energy contribution of the polymeric chains being via the energy stored in the stretched polymeric chains.

In Section 3, we focus on the dynamics of polymeric chains. Regarding the chains, we do not model them individually, but we again follow a kinetic-type theory, and we instead formulate a general form of the Fokker–Planck equation for the configurational distribution function of the polymeric chains. In our setting, the Fokker–Planck equation contains two unknown flux terms, namely the flux in configurational space and the flux in physical space. The latter is essential if we want to model the so-called centre-of-mass diffusion. Furthermore, we also comment on possible stationary solutions of the Fokker–Planck equation, and we carefully discuss the interplay between boundary conditions in the configurational space and asymptotic behaviour of the spring potential.

In Section 4, we give a formula for the specific Helmholtz free energy for the given fluid, which is we specify possible energy storage mechanisms. Subsequently, we proceed in Section 5 with the derivation of the constitutive relations, that is with the derivation of the equations relating the Cauchy stress tensor, the energy flux, the fluxes in the Fokker–Planck equation, and the kinematical quantities. The basic idea is that we look for closure relations that guarantee the nonnegativity of the entropy production. In this sense, the identification of the entropy production mechanisms and energy storage mechanisms provides a complete characterisation of the fluid of interest. A summary of the resulting model is given in Section 5.4.

Once we obtain the constitutive relations we discuss, see Section 6, the implications of the thermodynamic basis regarding the investigation of the stability of container flows (from the thermodynamic point of view, the flow in a thermally and mechanically isolated container constitutes an example of a thermodynamically isolated system). We show that the system of governing equations has a “trivial” stationary solution, and using thermodynamic arguments, we explicitly construct a nonnegative functional that decays in time and vanishes if and only if the system reaches the spatially homogeneous stationary state. The construction of such a functional is clearly a precursor for a rigorous stability analysis, which is, however, beyond the scope of the present contribution.

2. Preliminaries

The classical balance equations for the mass and momentum and the evolution equation for the internal energy of a continuous medium are

$$\frac{\mathrm{d}\rho}{\mathrm{d}t} + \rho \operatorname{div}_{\boldsymbol{x}} \boldsymbol{v} = 0, \tag{1a}$$

$$\rho \frac{\mathrm{d}\boldsymbol{v}}{\mathrm{d}t} = \operatorname{div}_{\boldsymbol{x}} \mathbb{T} + \rho \boldsymbol{b}, \tag{1b}$$

$$\rho \frac{\mathrm{d}e}{\mathrm{d}t} = \mathbb{T} : \mathbb{D} - \operatorname{div}_{\boldsymbol{x}} \boldsymbol{j}_e. \tag{1c}$$

The symbol ρ denotes the density of the medium, $\boldsymbol{v}$ denotes the Eulerian velocity field, $\mathbb{D} =_{\mathrm{def}} \frac{1}{2}\left(\nabla_{\boldsymbol{x}} \boldsymbol{v} + (\nabla_{\boldsymbol{x}} \boldsymbol{v})^{\top}\right)$ denotes the symmetric velocity gradient, $\mathbb{T}$ denotes the Cauchy stress tensor, e denotes the specific internal energy, $\boldsymbol{j}_e$ denotes the energy flux, and $\boldsymbol{b}$ denotes the external body force. The symbol

$$\frac{\mathrm{d}}{\mathrm{d}t} =_{\mathrm{def}} \frac{\partial}{\partial t} + \boldsymbol{v} \cdot \nabla_{\boldsymbol{x}}, \tag{2}$$

denotes the material derivative, and the symbol $\mathbb{A} : \mathbb{B} =_{\mathrm{def}} \operatorname{Tr}\left(\mathbb{A}\mathbb{B}^{\top}\right)$ denotes the Frobenius norm. The subscript $\boldsymbol{x}$ reminds us that the differential operator concerned is applied with respect to the spatial variable $\boldsymbol{x}$. Regarding the derivation of the balance equations, see, for example, Málek and Průša [21] or any standard textbook on continuum mechanics, such as Müller [22] or Gurtin et al. [23].

The basic idea in a kinetic-type theory of dilute polymeric fluids is that the mass contribution of the polymer chains is assumed to be negligible, hence we can replace the total density ρ in (1) by the solvent density ρ_{s}. Moreover, the barycentric velocity of the solvent/polymer mixture coincides with the velocity of the solvent, hence $\boldsymbol{v}$ in (1) can be interpreted as the velocity of the solvent only. The only place where the polymeric chains enter the balance equations is the formula for the internal energy e, the Cauchy stress tensor $\mathbb{T}$ and the energy flux $\boldsymbol{j}_e$. All of these assumptions/simplifications are common in kinetic-type theories of dilute polymeric fluids, and we also adopt them in the current contribution.

For further reference, we can therefore write the balance equations as

$$\frac{\mathrm{d}\rho_{\mathrm{s}}}{\mathrm{d}t} + \rho_{\mathrm{s}} \operatorname{div}_{\boldsymbol{x}} \boldsymbol{v} = 0, \tag{3a}$$

$$\rho_{\mathrm{s}} \frac{\mathrm{d}\boldsymbol{v}}{\mathrm{d}t} = \operatorname{div}_{\boldsymbol{x}} \mathbb{T} + \rho_{\mathrm{s}} \boldsymbol{b}, \tag{3b}$$

$$\rho_{\mathrm{s}} \frac{\mathrm{d}e}{\mathrm{d}t} = \mathbb{T} : \mathbb{D} - \operatorname{div}_{\boldsymbol{x}} \boldsymbol{j}_e, \tag{3c}$$

and we recall that the unknown fields ρ_{s} and $\boldsymbol{v}$ are functions of the spatial position $\boldsymbol{x}$ and time t.

We note that, if one wanted to develop a model wherein the mass of the polymeric chains is not negligible, then one would need to use a variant of mixture theory, see, for example, Rajagopal and Tao [24] or Hutter and Jöhnk [25], and also Souček et al. [26] for a careful discussion.

3. Fokker–Planck Equation

We are in a position to describe the dynamics of the polymeric chains dispersed in the solvent. In what follows, we deal with a very simple setting, and we assume that the whole polymeric chain can be modelled as a single dumbbell (two beads connected with a spring), while more sophisticated models are typically necessary in order to obtain quantitative agreement between the model predictions and the experimental data (see the aforementioned monographs for a list of such models. Additional references regarding viscoelastic models can be also found in Vinogradov and Malkin [27], Larson [28] or Leonov and Prokunin [29]. A historical perspective is given in Tanner and Walters [30]). Note however that a generalisation to more complex polymeric chains/more sophisticated models is straightforward.

The dynamics of the individual polymeric chain are governed by a stochastic differential equation, which has the associated Fokker–Planck equation, see, for example, Le Bris and Lelièvre [10] or Barrett and Süli [31] for details. If we consider dumbbells, their configuration is fully determined by the end-to-end vector $\boldsymbol{q}$, and the Fokker–Planck equation governs the evolution of the configurational distribution function $\varphi(t, \boldsymbol{x}, \boldsymbol{q})$ in the configurational space D of all admissible end-to-end vectors. The physical meaning of the configurational distribution function is clear, the integral

$$\int_{D' \subset D} \varphi(t, \boldsymbol{x}, \boldsymbol{q}) \, \mathrm{d}\boldsymbol{q} \tag{4}$$

gives the number of polymer chains at time t and spatial location $\boldsymbol{x}$ whose configuration vector lies in the domain D'. The integral over the whole D gives the particle number density $n_{\mathrm{p}}(t, \boldsymbol{x})$,

$$n_{\mathrm{p}}(t, \boldsymbol{x}) =_{\mathrm{def}} \int_{D} \varphi(t, \boldsymbol{x}, \boldsymbol{q}) \, \mathrm{d}\boldsymbol{q}, \tag{5}$$

and the integral over a spatial domain

$$\int_{\Omega'} \int_{D} \varphi(t, \boldsymbol{x}, \boldsymbol{q}) \, \mathrm{d}\boldsymbol{q} \, \mathrm{d}\boldsymbol{x}, \tag{6}$$

gives one the number of polymeric chains in the spatial domain Ω'.

In the case of Hookean dumbbells, the configurational space D is the whole $\mathbb{R}^3$, since the stretch of the spring is not limited. In the case of the FENE dumbbell model (finitely extensible nonlinear elastic spring) the configurational space D is a ball in $\mathbb{R}^3$ centred at the origin with a given radius, and the radius determines the maximum stretch of the spring.

3.1. Fokker–Planck Equation in the Case of Velocity Field with Nonzero Divergence

The Fokker–Planck equation has, in our case, the form

$$\frac{\partial \varphi}{\partial t} + \mathrm{div}_{\boldsymbol{x}}(\boldsymbol{v}\varphi + \boldsymbol{j}_{\varphi,\boldsymbol{x}}) + \mathrm{div}_{\boldsymbol{q}}((\nabla_{\boldsymbol{x}}\boldsymbol{v})\boldsymbol{q}\varphi + \boldsymbol{j}_{\varphi,\boldsymbol{q}}) = 0, \tag{7}$$

where $\boldsymbol{j}_{\varphi,\boldsymbol{x}}$ and $\boldsymbol{j}_{\varphi,\boldsymbol{q}}$ are unknown flux terms. Our task will be to identify these flux terms using the known energy storage mechanisms and entropy production mechanisms. We note that the spatially dependent term reads $\mathrm{div}_{\boldsymbol{x}}(\boldsymbol{v}\varphi)$ and not $\boldsymbol{v}\mathrm{div}_{\boldsymbol{x}}\varphi$ (this subtle difference does not matter in the case of incompressible fluids, but it is critical provided that we are working with a compressible fluid. See. for example, Degond and Liu [32] for a careful discussion of the Fokker–Planck equation). For further reference we also record that (7) can be rewritten as

$$\frac{\mathrm{d}\varphi}{\mathrm{d}t} + \varphi \mathrm{div}_{\boldsymbol{x}}\boldsymbol{v} + \mathrm{div}_{\boldsymbol{x}}\boldsymbol{j}_{\varphi,\boldsymbol{x}} + \mathrm{div}_{\boldsymbol{q}}\left((\nabla_{\boldsymbol{x}}\boldsymbol{v})\boldsymbol{q}\varphi + \boldsymbol{j}_{\varphi,\boldsymbol{q}}\right) = 0. \tag{8}$$

3.2. Boundary Condition in the Configurational Space

The boundary condition on ∂D is the no-flux boundary condition

$$\left((\nabla_{\boldsymbol{x}}\boldsymbol{v})\,\boldsymbol{q}\varphi + \boldsymbol{j}_{\varphi,\boldsymbol{q}}\right) \bullet \boldsymbol{n}_{\boldsymbol{q}}\big|_{\partial D} = 0, \tag{9}$$

where $\boldsymbol{n}_{\boldsymbol{q}}$ denotes the unit outward normal to the set of admissible end-to-end vectors $D \subset \mathbb{R}^3$ (in the case of Hookean dumbbells where $D = \mathbb{R}^3$ the boundary condition is interpreted as a decay of the corresponding function at infinity). This choice of boundary condition has several implications regarding the evolution equation for polymer number density, see below, and regarding the behaviour of the configurational distribution function on the boundary of D, see Section 3.4.

3.3. Evolution Equation for Polymer Number Density

The evolution of the polymer number density n_{p} introduced in (5) is governed by the partial differential equation

$$\frac{\partial n_{\mathrm{p}}}{\partial t} + \operatorname{div}_{\boldsymbol{x}} \left(\boldsymbol{v} n_{\mathrm{p}} + \int_D \boldsymbol{j}_{\varphi,\boldsymbol{x}} \, \mathrm{d}\boldsymbol{q} \right) = 0. \tag{10}$$

This equation is straightforward to obtain via integration of the Fokker–Plank equation with respect to the configurational variable $\boldsymbol{q}$. The boundary term in the configurational space vanishes by virtue of (9). The last equation can be rewritten as

$$\frac{\mathrm{d}n_{\mathrm{p}}}{\mathrm{d}t} + n_{\mathrm{p}} \operatorname{div}_{\boldsymbol{x}} \boldsymbol{v} = -\operatorname{div}_{\boldsymbol{x}} \left(\int_D \boldsymbol{j}_{\varphi,\boldsymbol{x}} \, \mathrm{d}\boldsymbol{q} \right), \tag{11}$$

where $\frac{\mathrm{d}}{\mathrm{d}t}$ denotes the standard material time derivative. Equation (11) shows that if $\boldsymbol{j}_{\varphi,\boldsymbol{x}} \neq \boldsymbol{0}$ and if the velocity field does not identically satisfy $\operatorname{div}_{\boldsymbol{x}} \boldsymbol{v} = 0$, then, in general, we cannot expect that the polymer number density n_{p} at the given material point is preserved. This makes the study of the dynamics of a compressible fluid with polymeric centre-of-mass diffusion substantially different from the simpler case of an incompressible fluid without polymeric centre-of-mass diffusion, see, for example, Barrett and Süli [33] and Feireisl et al. [34].

3.4. Force Potential

The force $\boldsymbol{F}$ in the spring connecting the beads is determined by a spherically symmetric potential

$$\boldsymbol{F} =_{\mathrm{def}} \nabla_{\boldsymbol{q}} U \left(\frac{1}{2} \left| \frac{\boldsymbol{q}}{q_{\mathrm{ref}}} \right|^2 \right), \tag{12}$$

where q_{ref} is a characteristic length scale for the spring. (Note the sign convention in (12) and the sign convention used later in (15).) For example, a popular choice for the force potential is the potential that is introduced by Warner [35] for the FENE dumbbell model. The potential is given by the formula

$$U_{\mathrm{FENE}}(s) =_{\mathrm{def}} -\frac{b}{2} \log \left(1 - \frac{2s}{b} \right). \tag{13}$$

We note that the choice (13) predicts infinite force as $s \to \frac{b}{2}-$. This means that an infinite force is necessary to maximally stretch the spring, which is the expected behaviour in view of the fact that we are dealing with a finitely extensible spring. The spring can not be extended beyond a certain length no matter what force is applied.

In what follows, we will not work with a specific force potential, we will only assume that the force potential U is composed of two parts $U = U_e + U_{\eta,\theta}$, where

$$U_e = U_e \left(\frac{1}{2} \left| \frac{\boldsymbol{q}}{q_{\mathrm{ref}}} \right|^2 \right), \tag{14a}$$

$$U_{\eta,\theta} = \frac{\theta_{\mathrm{s}}}{\theta_{\mathrm{ref}}} U_\eta \left(\frac{1}{2} \left| \frac{\boldsymbol{q}}{q_{\mathrm{ref}}} \right|^2 \right), \tag{14b}$$

and where θ_{ref} is a reference temperature, and q_{ref} is a characteristic length scale. The potential $U_{\eta,\theta}$ is the "entropic" part of the spring potential, and it is proportional to the ambient temperature θ_{s}, while the potential U_e is independent of the temperature (see, for example, Ericksen [36] for the rationale of the nomenclature, and the fact that it makes sense to consider the potential proportional to the temperature). If we are dealing with a finitely extensible spring, then the force tends to infinity as the spring reaches its maximum length (see for example the FENE potential introduced in (13)).

This suggests that the value of the configurational distribution function φ on the boundary of D should be zero. We informally show that this property is in fact encoded in the no-flux boundary condition (9).

If we for a moment suppose that the Fokker–Planck Equation (7) reads

$$\frac{\partial \varphi}{\partial t} + \operatorname{div}_{\boldsymbol{x}} \left(\boldsymbol{v}\varphi - \frac{k_{\mathrm{B}}\theta_{\mathrm{s}}}{2\zeta} \nabla_{\boldsymbol{x}} \varphi \right) + \operatorname{div}_{\boldsymbol{q}} \left((\nabla_{\boldsymbol{x}} \boldsymbol{v}) \boldsymbol{q} \varphi - \frac{2\boldsymbol{F}}{\zeta} \varphi - \frac{2k_{\mathrm{B}}\theta_{\mathrm{s}}}{\zeta} \nabla_{\boldsymbol{q}} \varphi \right) = 0, \tag{15}$$

that is if we consider specific formulae for the fluxes $\boldsymbol{j}_{\varphi,\boldsymbol{q}}$ and $\boldsymbol{j}_{\varphi,\boldsymbol{x}}$, then (9) reduces to

$$\left((\nabla_{\boldsymbol{x}} \boldsymbol{v}) \boldsymbol{q} \varphi - \frac{2\boldsymbol{F}}{\zeta} \varphi - \frac{2k_{\mathrm{B}}\theta_{\mathrm{s}}}{\zeta} \nabla_{\boldsymbol{q}} \varphi \right) \bullet \boldsymbol{n}_{\boldsymbol{q}} \Big|_{\partial D} = 0. \tag{16}$$

Here, θ_{s} denotes the solvent temperature, ζ denotes the hydrodynamic drag coefficient and k_{B} denotes the Boltzmann constant. If D is a ball in $\mathbb{R}^3$, then $\boldsymbol{q}|_{\partial D} = q_{\max} \boldsymbol{n}_{\boldsymbol{q}}$, and (16) reduces to

$$\left((\nabla_{\boldsymbol{x}} \boldsymbol{v}) q_{\max} \boldsymbol{n}_{\boldsymbol{q}} \varphi - \frac{2\boldsymbol{F}}{\zeta} \varphi - \frac{2k_{\mathrm{B}}\theta_{\mathrm{s}}}{\zeta} \nabla_{\boldsymbol{q}} \varphi \right) \bullet \boldsymbol{n}_{\boldsymbol{q}} \Big|_{\partial D} = 0. \tag{17}$$

Furthermore, in the case of spherically symmetric potential, the force $\boldsymbol{F}$ is parallel to $\boldsymbol{q}$, and if we are dealing with a finitely extensible spring, then the potential is chosen in such a way that the magnitude of $\boldsymbol{F}$ approaches infinity as the vector $\boldsymbol{q}$ approaches the boundary of D. Having this piece of information in hand we inspect (17), and we see that if (17) holds, then the middle term $\frac{2\boldsymbol{F}}{\zeta} \varphi \bullet \boldsymbol{n}_{\boldsymbol{q}}$ constrains the configurational distribution function φ to decay to zero faster than the growth of the force $\boldsymbol{F}$ as one approaches the boundary of D. Consequently, we can claim that (17) implies $\varphi|_{\partial D} = 0$.

3.5. Stationary Solution of the Fokker–Planck Equation in a Spatially Homogeneous State at a Given Temperature

If we assume for a moment that the fluxes in the general Fokker–Planck equation have been successfully identified, and have the form discussed in (15), then we can explicitly identify the stationary solution to the Fokker–Planck equation in the case of a spatially homogeneous temperature field and configurational distribution function field (partial derivatives with respect to time and the spatial variable $\boldsymbol{x}$ vanish). Under these assumptions, we see that the Fokker–Planck Equation (15) reduces to

$$\operatorname{div}_{\boldsymbol{q}} \left(\frac{2\boldsymbol{F}}{\zeta} \varphi + \frac{2k_{\mathrm{B}}\theta_{\mathrm{s}}}{\zeta} \nabla_{\boldsymbol{q}} \varphi \right) = 0. \tag{18}$$

If we assume that the force in the spring is given in terms of a potential, see (12), and if we substitute (12) into (18), then we get

$$\operatorname{div}_{\boldsymbol{q}} \left(\left[\nabla_{\boldsymbol{q}} U \left(\frac{1}{2} \left| \frac{\boldsymbol{q}}{q_{\mathrm{ref}}} \right|^2 \right) \right] \varphi + k_{\mathrm{B}}\theta_{\mathrm{s}} \nabla_{\boldsymbol{q}} \varphi \right) = 0. \tag{19}$$

Using the formulae for the differential operators in a spherical coordinate system, we see that (19) reduces to a single ordinary differential equation

$$\frac{1}{q^2} \frac{\mathrm{d}}{\mathrm{d}q} \left[q^2 \left(\frac{\mathrm{d}}{\mathrm{d}q} U \left(\frac{1}{2} \left| \frac{\boldsymbol{q}}{q_{\mathrm{ref}}} \right|^2 \right) \varphi + k_{\mathrm{B}}\theta_{\mathrm{s}} \frac{\mathrm{d}\varphi}{\mathrm{d}q} \right) \right] = 0, \tag{20}$$

where we have used the notation $q =_{\mathrm{def}} |\boldsymbol{q}|$. We immediately see that the solution to (20) reads

$$\varphi = \mathrm{C} \mathrm{e}^{-\frac{U\left(\frac{1}{2} \left| \frac{\boldsymbol{q}}{q_{\mathrm{ref}}} \right|^2 \right)}{k_{\mathrm{B}}\theta_{\mathrm{s}}}}, \tag{21}$$

where C is a constant. The constant is fixed by the condition $n_{\mathrm{p}}(t, \boldsymbol{x}) = \int_D \varphi(t, \boldsymbol{x}, \boldsymbol{q})\, \mathrm{d}\boldsymbol{q}$, with φ now independent of t and x here, and hence the configurational distribution function that solves the stationary Fokker–Planck in the case of spatially homogeneous fields is given by the formula $\varphi = M_{n_{\mathrm{p}}, \theta_{\mathrm{s}}}$, where

$$M_{n_{\mathrm{p}}, \theta_{\mathrm{s}}} =_{\mathrm{def}} n_{\mathrm{p}} \frac{\mathrm{e}^{-\frac{U\left(\frac{1}{2}\left|\frac{\boldsymbol{q}}{q_{\mathrm{ref}}}\right|^2\right)}{k_{\mathrm{B}}\theta_{\mathrm{s}}}}}{\int_D \mathrm{e}^{-\frac{U\left(\frac{1}{2}\left|\frac{\boldsymbol{q}}{q_{\mathrm{ref}}}\right|^2\right)}{k_{\mathrm{B}}\theta_{\mathrm{s}}}}\, \mathrm{d}\boldsymbol{q}}, \tag{22}$$

and n_{p} is a positive constant. This configurational distribution function is the expected "equilibrium" configurational distribution function in the case when the dilute polymeric fluid occupies a thermodynamically isolated vessel. We return to this issue in Section 6.

4. Helmholtz Free Energy

Having discussed the Fokker–Planck equation that governs the evolution of the configurational distribution function, we have completed the system of equations for the unknown fields ρ_{s}, $\boldsymbol{v}$, θ_{s} and φ. It remains to identify the fluxes, which are quantities that are unique for the given fluid (they provide a unique characterisation of the given material or given class of materials). The first step in this direction is the identification of energy storage mechanism, which is done by means of specific Helmholtz free energy.

We assume that the Helmholtz free energy ψ, $[\psi] = {}^{\mathrm{J}}/_{\mathrm{kg}}$, is given by the formula

$$\psi(\theta_{\mathrm{s}}, \rho_{\mathrm{s}}, \varphi) =_{\mathrm{def}} \psi_{\mathrm{s}}(\theta_{\mathrm{s}}, \rho_{\mathrm{s}}) + \frac{1}{\rho_{\mathrm{s}}} \int_D U_e\left(\frac{1}{2}\left|\frac{\boldsymbol{q}}{q_{\mathrm{ref}}}\right|^2\right) \varphi\, \mathrm{d}\boldsymbol{q} + \frac{k_{\mathrm{B}}\theta_{\mathrm{s}}}{\rho_{\mathrm{s}}} \int_D \left(\frac{U_\eta\left(\frac{1}{2}\left|\frac{\boldsymbol{q}}{q_{\mathrm{ref}}}\right|^2\right)}{k_{\mathrm{B}}\theta_{\mathrm{ref}}} \varphi + \varphi \ln \frac{\varphi}{K} \right) \mathrm{d}\boldsymbol{q}, \tag{23}$$

where K is a constant to be specified later (so far its only purpose is to provide a normalisation factor in the argument of the logarithm function, since we must have a dimensionless quantity under the logarithm. We also recall the physical units of the configurational distribution function φ, $[\varphi] = {}^{1}/_{\mathrm{m}^6}$, particle number density n_{p}, $[n_{\mathrm{p}}] = {}^{1}/_{\mathrm{m}^3}$, potentials U_e, $[U_e] = J$, and U_η, $[U_\eta] = J$, and the Boltzmann constant k_{B}, $[k_{\mathrm{B}}] = {}^{\mathrm{J}}/_{\mathrm{K}}$). The inclusion of the potentials U_e and U_η into the formula for the Helmholtz free energy is a standard one known from elasticity theory, while the term $\varphi \ln \varphi$ is a well known contribution due to configurational entropy of the dumbbells. The solvent contribution $\psi_{\mathrm{s}}(\theta_{\mathrm{s}}, \rho_{\mathrm{s}})$ to the specific Helmholtz free energy is left unspecified, since its particular form is not important for the ongoing discussion. We however give a particular formula for $\psi_{\mathrm{s}}(\theta_{\mathrm{s}}, \rho_{\mathrm{s}})$ in Section 6, where it plays a fundamental role.

Having introduced the formula for the Helmholtz free energy, we can find other thermodynamic quantities of interest via differentiation. Namely, the formula for the specific entropy η reads

$$\eta(\theta_{\mathrm{s}}, \rho_{\mathrm{s}}, \varphi) = -\frac{\partial \psi}{\partial \theta_{\mathrm{s}}} = -\frac{\partial \psi_{\mathrm{s}}(\theta_{\mathrm{s}}, \rho_{\mathrm{s}})}{\partial \theta_{\mathrm{s}}} - \frac{k_{\mathrm{B}}}{\rho_{\mathrm{s}}} \int_D \left(\frac{U_\eta\left(\frac{1}{2}\left|\frac{\boldsymbol{q}}{q_{\mathrm{ref}}}\right|^2\right)}{k_{\mathrm{B}}\theta_{\mathrm{ref}}} \varphi + \varphi \ln \frac{\varphi}{K} \right) \mathrm{d}\boldsymbol{q}, \tag{24}$$

and the specific internal energy e is given by the formula

$$e(\theta_{\mathrm{s}}, \rho_{\mathrm{s}}, \varphi) = \psi + \theta_{\mathrm{s}}\eta = \psi_{\mathrm{s}}(\theta_{\mathrm{s}}, \rho_{\mathrm{s}}) - \theta_{\mathrm{s}} \frac{\partial \psi_{\mathrm{s}}(\theta_{\mathrm{s}}, \rho_{\mathrm{s}})}{\partial \theta_{\mathrm{s}}} + \frac{1}{\rho_{\mathrm{s}}} \int_D U_e\left(\frac{1}{2}\left|\frac{\boldsymbol{q}}{q_{\mathrm{ref}}}\right|^2\right) \varphi\, \mathrm{d}\boldsymbol{q}. \tag{25}$$

5. Constitutive Relations

Once we have specified the Helmholtz free energy we can proceed with the derivation of constitutive relations for the fluxes $\boldsymbol{j}_e$, $\boldsymbol{j}_\eta$, $\boldsymbol{j}_{\varphi,\boldsymbol{x}}$, $\boldsymbol{j}_{\varphi,\boldsymbol{q}}$, and the Cauchy stress tensor $\mathbb{T}$. Our first objective is to identify the entropy flux $\boldsymbol{j}_\eta$ and the entropy production ξ, such that the evolution equation for the specific entropy has the form

$$\rho_{\mathrm{s}} \frac{\mathrm{d}\eta}{\mathrm{d}t} + \operatorname{div}_{\boldsymbol{x}} \boldsymbol{j}_\eta = \xi. \tag{26}$$

The requirement on the nonnegativity of the entropy production then gives us a hint regarding the choice of constitutive relations for the fluxes $\boldsymbol{j}_e$, $\boldsymbol{j}_\eta$, $\boldsymbol{j}_{\varphi,\boldsymbol{x}}$, $\boldsymbol{j}_{\varphi,\boldsymbol{q}}$.

So far, we have identified an evolution equation for the internal energy (3c),

$$\rho_{\mathrm{s}} \frac{\mathrm{d}e}{\mathrm{d}t} = \mathbb{T} : \mathbb{D} - \operatorname{div}_{\boldsymbol{x}} \boldsymbol{j}_e, \tag{27}$$

and we know that the relation between the Helmholtz free energy and the internal energy and the entropy reads $\psi(\theta_{\mathrm{s}}, \rho_{\mathrm{s}}, \varphi) = e - \theta_{\mathrm{s}}\eta$. Differentiation of this relation yields

$$\frac{\partial \psi}{\partial \theta_{\mathrm{s}}} \frac{\mathrm{d}\theta_{\mathrm{s}}}{\mathrm{d}t} + \frac{\partial \psi}{\partial \rho_{\mathrm{s}}} \frac{\mathrm{d}\rho_{\mathrm{s}}}{\mathrm{d}t} + \frac{\partial \psi}{\partial \varphi} \frac{\mathrm{d}\varphi}{\mathrm{d}t} = \frac{\mathrm{d}e}{\mathrm{d}t} - \eta \frac{\mathrm{d}\theta_{\mathrm{s}}}{\mathrm{d}t} - \theta_{\mathrm{s}} \frac{\mathrm{d}\eta}{\mathrm{d}t}. \tag{28}$$

Making use of (27) and the fact that $\eta = -\frac{\partial \psi}{\partial \theta_{\mathrm{s}}}$, we then see that (28) reduces to

$$\rho_{\mathrm{s}}\theta_{\mathrm{s}} \frac{\mathrm{d}\eta}{\mathrm{d}t} = \mathbb{T} : \mathbb{D} - \operatorname{div}_{\boldsymbol{x}} \boldsymbol{j}_e - \rho_{\mathrm{s}} \frac{\partial \psi}{\partial \rho_{\mathrm{s}}} \frac{\mathrm{d}\rho_{\mathrm{s}}}{\mathrm{d}t} - \rho_{\mathrm{s}} \frac{\partial \psi}{\partial \varphi} \frac{\mathrm{d}\varphi}{\mathrm{d}t}. \tag{29}$$

Now we need to manipulate (29) into the form (26). The lengthy but essential algebraic manipulations that allow us to achieve this objective are described in the following section, see Section 5.1. In particular, the desired final form of the entropy evolution equation is given in (51). The reader who is at the moment not interested in the necessary algebraic manipulations can go directly to Section 5.2, where we discuss the implications of the entropy evolution Equation (51) with respect to the choice of constitutive relations.

5.1. Evolution Equation for the Specific Entropy

Let us for a moment denote

$$\mathcal{F}(\theta_{\mathrm{s}}, \varphi) =_{\mathrm{def}} \int_D \left[U_e \left(\frac{1}{2} \left| \frac{\boldsymbol{q}}{q_{\mathrm{ref}}} \right|^2 \right) \varphi + \frac{\theta_{\mathrm{s}}}{\theta_{\mathrm{ref}}} U_\eta \left(\frac{1}{2} \left| \frac{\boldsymbol{q}}{q_{\mathrm{ref}}} \right|^2 \right) \varphi + k_{\mathrm{B}} \theta_{\mathrm{s}} \varphi \ln \frac{\varphi}{K} \right] \mathrm{d}\boldsymbol{q}. \tag{30}$$

Using this notation the formula for the Helmholtz free energy reads

$$\psi(\theta_{\mathrm{s}}, \rho_{\mathrm{s}}, \varphi) = \psi_{\mathrm{s}}(\theta_{\mathrm{s}}, \rho_{\mathrm{s}}) + \frac{1}{\rho_{\mathrm{s}}} \mathcal{F}(\theta_{\mathrm{s}}, \varphi), \tag{31}$$

and the evolution equation for the entropy (29) can be—with a slight abuse of notation—rewritten as

$$\rho_{\mathrm{s}}\theta_{\mathrm{s}} \frac{\mathrm{d}\eta}{\mathrm{d}t} = \mathbb{T} : \mathbb{D} - \operatorname{div}_{\boldsymbol{x}} \boldsymbol{j}_e - \rho_{\mathrm{s}} \frac{\partial \psi_{\mathrm{s}}}{\partial \rho_{\mathrm{s}}} \frac{\mathrm{d}\rho_{\mathrm{s}}}{\mathrm{d}t} + \frac{\mathcal{F}}{\rho_{\mathrm{s}}} \frac{\mathrm{d}\rho_{\mathrm{s}}}{\mathrm{d}t} - \frac{\partial \mathcal{F}}{\partial \varphi} \frac{\mathrm{d}\varphi}{\mathrm{d}t}. \tag{32}$$

Let us first consider the term $\frac{\partial \mathcal{F}}{\partial \varphi}\frac{\mathrm{d}\varphi}{\mathrm{d}t}$. Making use of the Fokker–Planck Equation (8), we see that

$$\begin{aligned}
\frac{\partial \mathcal{F}}{\partial \varphi}\frac{\mathrm{d}\varphi}{\mathrm{d}t} &= \int_D \left[U_e\left(\frac{1}{2}\left|\frac{\boldsymbol{q}}{q_{\mathrm{ref}}}\right|^2\right)+\frac{\theta_{\mathrm{s}}}{\theta_{\mathrm{ref}}}U_\eta\left(\frac{1}{2}\left|\frac{\boldsymbol{q}}{q_{\mathrm{ref}}}\right|^2\right)+k_{\mathrm{B}}\theta_{\mathrm{s}}\left(\ln\frac{\varphi}{K}+1\right)\right]\frac{\mathrm{d}\varphi}{\mathrm{d}t}\,\mathrm{d}\boldsymbol{q} \\
&= -\int_D \left[U_e\left(\frac{1}{2}\left|\frac{\boldsymbol{q}}{q_{\mathrm{ref}}}\right|^2\right)+\frac{\theta_{\mathrm{s}}}{\theta_{\mathrm{ref}}}U_\eta\left(\frac{1}{2}\left|\frac{\boldsymbol{q}}{q_{\mathrm{ref}}}\right|^2\right)+k_{\mathrm{B}}\theta_{\mathrm{s}}\left(\ln\frac{\varphi}{K}+1\right)\right]\left[\varphi\mathrm{div}_{\boldsymbol{x}}\boldsymbol{v}+\mathrm{div}_{\boldsymbol{x}}\boldsymbol{j}_{\varphi,\boldsymbol{x}}+\mathrm{div}_{\boldsymbol{q}}\left((\nabla_{\boldsymbol{x}}\boldsymbol{v})\boldsymbol{q}\varphi+\boldsymbol{j}_{\varphi,\boldsymbol{q}}\right)\right]\mathrm{d}\boldsymbol{q} \\
&= \underbrace{-\int_D \left[U_e\left(\frac{1}{2}\left|\frac{\boldsymbol{q}}{q_{\mathrm{ref}}}\right|^2\right)+\frac{\theta_{\mathrm{s}}}{\theta_{\mathrm{ref}}}U_\eta\left(\frac{1}{2}\left|\frac{\boldsymbol{q}}{q_{\mathrm{ref}}}\right|^2\right)+k_{\mathrm{B}}\theta_{\mathrm{s}}\left(\ln\frac{\varphi}{K}+1\right)\right]\left[\varphi\mathrm{div}_{\boldsymbol{x}}\boldsymbol{v}+\mathrm{div}_{\boldsymbol{x}}\boldsymbol{j}_{\varphi,\boldsymbol{x}}\right]\mathrm{d}\boldsymbol{q}}_{A} \\
&\quad \underbrace{-\int_D \left[U_e\left(\frac{1}{2}\left|\frac{\boldsymbol{q}}{q_{\mathrm{ref}}}\right|^2\right)+\frac{\theta_{\mathrm{s}}}{\theta_{\mathrm{ref}}}U_\eta\left(\frac{1}{2}\left|\frac{\boldsymbol{q}}{q_{\mathrm{ref}}}\right|^2\right)+k_{\mathrm{B}}\theta_{\mathrm{s}}\left(\ln\frac{\varphi}{K}+1\right)\right]\mathrm{div}_{\boldsymbol{q}}\left((\nabla_{\boldsymbol{x}}\boldsymbol{v})\boldsymbol{q}\varphi+\boldsymbol{j}_{\varphi,\boldsymbol{q}}\right)\mathrm{d}\boldsymbol{q}}_{B}\,. \qquad (33)
\end{aligned}$$

We will first focus on the term B that contains the divergence operator with respect to the $\boldsymbol{q}$ variable. We see that

$$\begin{aligned}
&\int_D \left[U_e\left(\frac{1}{2}\left|\frac{\boldsymbol{q}}{q_{\mathrm{ref}}}\right|^2\right)+\frac{\theta_{\mathrm{s}}}{\theta_{\mathrm{ref}}}U_\eta\left(\frac{1}{2}\left|\frac{\boldsymbol{q}}{q_{\mathrm{ref}}}\right|^2\right)+k_{\mathrm{B}}\theta_{\mathrm{s}}\left(\ln\frac{\varphi}{n_{\mathrm{p}}K}+1\right)\right]\left[\mathrm{div}_{\boldsymbol{q}}\left((\nabla_{\boldsymbol{x}}\boldsymbol{v})\boldsymbol{q}\varphi+\boldsymbol{j}_{\varphi,\boldsymbol{q}}\right)\right]\mathrm{d}\boldsymbol{q} \\
&\quad = \int_D \mathrm{div}_{\boldsymbol{q}}\left\{\left[U_e\left(\frac{1}{2}\left|\frac{\boldsymbol{q}}{q_{\mathrm{ref}}}\right|^2\right)+\frac{\theta_{\mathrm{s}}}{\theta_{\mathrm{ref}}}U_\eta\left(\frac{1}{2}\left|\frac{\boldsymbol{q}}{q_{\mathrm{ref}}}\right|^2\right)+k_{\mathrm{B}}\theta_{\mathrm{s}}\left(\ln\frac{\varphi}{K}+1\right)\right]\left((\nabla_{\boldsymbol{x}}\boldsymbol{v})\boldsymbol{q}\varphi+\boldsymbol{j}_{\varphi,\boldsymbol{q}}\right)\right\}\mathrm{d}\boldsymbol{q} \\
&\qquad - \int_D \nabla_{\boldsymbol{q}}\left[U_e\left(\frac{1}{2}\left|\frac{\boldsymbol{q}}{q_{\mathrm{ref}}}\right|^2\right)+\frac{\theta_{\mathrm{s}}}{\theta_{\mathrm{ref}}}U_\eta\left(\frac{1}{2}\left|\frac{\boldsymbol{q}}{q_{\mathrm{ref}}}\right|^2\right)+k_{\mathrm{B}}\theta_{\mathrm{s}}\left(\ln\frac{\varphi}{K}+1\right)\right]\bullet\left[(\nabla_{\boldsymbol{x}}\boldsymbol{v})\boldsymbol{q}\varphi+\boldsymbol{j}_{\varphi,\boldsymbol{q}}\right]\mathrm{d}\boldsymbol{q}. \qquad (34)
\end{aligned}$$

The first integral vanishes by virtue of the Stokes theorem and the boundary condition (9) on ∂D. In the second term we first evaluate the gradient, and then we proceed, as follows

$$\begin{aligned}
&\int_D \nabla_{\boldsymbol{q}}\left[U_e\left(\frac{1}{2}\left|\frac{\boldsymbol{q}}{q_{\mathrm{ref}}}\right|^2\right)+\frac{\theta_{\mathrm{s}}}{\theta_{\mathrm{ref}}}U_\eta\left(\frac{1}{2}\left|\frac{\boldsymbol{q}}{q_{\mathrm{ref}}}\right|^2\right)+k_{\mathrm{B}}\theta_{\mathrm{s}}\left(\ln\frac{\varphi}{K}+1\right)\right]\bullet\left[(\nabla_{\boldsymbol{x}}\boldsymbol{v})\boldsymbol{q}\varphi+\boldsymbol{j}_{\varphi,\boldsymbol{q}}\right]\mathrm{d}\boldsymbol{q} \\
&\quad = \int_D \left[\left(\left.\frac{\mathrm{d}U_e}{\mathrm{d}s}\right|_{s=\frac{1}{2}\left|\frac{\boldsymbol{q}}{q_{\mathrm{ref}}}\right|^2}+\frac{\theta_{\mathrm{s}}}{\theta_{\mathrm{ref}}}\left.\frac{\mathrm{d}U_\eta}{\mathrm{d}s}\right|_{s=\frac{1}{2}\left|\frac{\boldsymbol{q}}{q_{\mathrm{ref}}}\right|^2}\right)\frac{\boldsymbol{q}}{q_{\mathrm{ref}}^2}+k_{\mathrm{B}}\theta_{\mathrm{s}}\frac{\nabla_{\boldsymbol{q}}\varphi}{\varphi}\right]\bullet\left[(\nabla_{\boldsymbol{x}}\boldsymbol{v})\boldsymbol{q}\varphi+\boldsymbol{j}_{\varphi,\boldsymbol{q}}\right]\mathrm{d}\boldsymbol{q} \\
&= \int_D \left[\left(\left.\frac{\mathrm{d}U_e}{\mathrm{d}s}\right|_{s=\frac{1}{2}\left|\frac{\boldsymbol{q}}{q_{\mathrm{ref}}}\right|^2}+\frac{\theta_{\mathrm{s}}}{\theta_{\mathrm{ref}}}\left.\frac{\mathrm{d}U_\eta}{\mathrm{d}s}\right|_{s=\frac{1}{2}\left|\frac{\boldsymbol{q}}{q_{\mathrm{ref}}}\right|^2}\right)\frac{\boldsymbol{q}}{q_{\mathrm{ref}}}\otimes\frac{\boldsymbol{q}}{q_{\mathrm{ref}}}\varphi\right]:(\nabla_{\boldsymbol{x}}\boldsymbol{v})\,\mathrm{d}\boldsymbol{q}+\int_D\left[k_{\mathrm{B}}\theta_{\mathrm{s}}\nabla_{\boldsymbol{q}}\varphi\right]\bullet\left[(\nabla_{\boldsymbol{x}}\boldsymbol{v})\boldsymbol{q}\right]\mathrm{d}\boldsymbol{q} \\
&\qquad + \int_D \frac{1}{\varphi}\left[\left(\left.\frac{\mathrm{d}U_e}{\mathrm{d}s}\right|_{s=\frac{1}{2}\left|\frac{\boldsymbol{q}}{q_{\mathrm{ref}}}\right|^2}+\frac{\theta_{\mathrm{s}}}{\theta_{\mathrm{ref}}}\left.\frac{\mathrm{d}U_\eta}{\mathrm{d}s}\right|_{s=\frac{1}{2}\left|\frac{\boldsymbol{q}}{q_{\mathrm{ref}}}\right|^2}\right)\frac{\boldsymbol{q}}{q_{\mathrm{ref}}^2}\varphi+k_{\mathrm{B}}\theta_{\mathrm{s}}\nabla_{\boldsymbol{q}}\varphi\right]\bullet\boldsymbol{j}_{\varphi,\boldsymbol{q}}\,\mathrm{d}\boldsymbol{q} \\
&= \int_D \left[\left(\left.\frac{\mathrm{d}U_e}{\mathrm{d}s}\right|_{s=\frac{1}{2}\left|\frac{\boldsymbol{q}}{q_{\mathrm{ref}}}\right|^2}+\frac{\theta_{\mathrm{s}}}{\theta_{\mathrm{ref}}}\left.\frac{\mathrm{d}U_\eta}{\mathrm{d}s}\right|_{s=\frac{1}{2}\left|\frac{\boldsymbol{q}}{q_{\mathrm{ref}}}\right|^2}\right)\frac{\boldsymbol{q}}{q_{\mathrm{ref}}}\otimes\frac{\boldsymbol{q}}{q_{\mathrm{ref}}}\varphi\right]:\mathbb{D}\,\mathrm{d}\boldsymbol{q}+\int_D\left[k_{\mathrm{B}}\theta_{\mathrm{s}}\nabla_{\boldsymbol{q}}\varphi\right]\bullet\left[(\nabla_{\boldsymbol{x}}\boldsymbol{v})\boldsymbol{q}\right]\mathrm{d}\boldsymbol{q} \\
&\qquad + \int_D \frac{1}{\varphi}\left[\left(\left.\frac{\mathrm{d}U_e}{\mathrm{d}s}\right|_{s=\frac{1}{2}\left|\frac{\boldsymbol{q}}{q_{\mathrm{ref}}}\right|^2}+\frac{\theta_{\mathrm{s}}}{\theta_{\mathrm{ref}}}\left.\frac{\mathrm{d}U_\eta}{\mathrm{d}s}\right|_{s=\frac{1}{2}\left|\frac{\boldsymbol{q}}{q_{\mathrm{ref}}}\right|^2}\right)\frac{\boldsymbol{q}}{q_{\mathrm{ref}}^2}\varphi+k_{\mathrm{B}}\theta_{\mathrm{s}}\nabla_{\boldsymbol{q}}\varphi\right]\bullet\boldsymbol{j}_{\varphi,\boldsymbol{q}}\,\mathrm{d}\boldsymbol{q}. \qquad (35)
\end{aligned}$$

Furthermore, the second term on the right-hand side can be manipulated, as follows

$$\begin{aligned}
\int_D\left[k_{\mathrm{B}}\theta_{\mathrm{s}}\nabla_{\boldsymbol{q}}\varphi\right]\bullet\left[(\nabla_{\boldsymbol{x}}\boldsymbol{v})\boldsymbol{q}\right]\mathrm{d}\boldsymbol{q} &= \int_D \mathrm{div}_{\boldsymbol{q}}\left[k_{\mathrm{B}}\theta_{\mathrm{s}}\varphi(\nabla_{\boldsymbol{x}}\boldsymbol{v})\boldsymbol{q}\right]\mathrm{d}\boldsymbol{q}-\int_D k_{\mathrm{B}}\theta_{\mathrm{s}}\varphi\nabla_{\boldsymbol{x}}\boldsymbol{v}:\nabla_{\boldsymbol{q}}\boldsymbol{q}\,\mathrm{d}\boldsymbol{q} \\
&= -\int_D k_{\mathrm{B}}\theta_{\mathrm{s}}\varphi\mathrm{div}_{\boldsymbol{x}}\boldsymbol{v}\,\mathrm{d}\boldsymbol{q} = -k_{\mathrm{B}}\theta_{\mathrm{s}}n_{\mathrm{p}}\mathrm{div}_{\boldsymbol{x}}\boldsymbol{v}, \qquad (36)
\end{aligned}$$

where we have again used the fact that the Stokes theorem and the boundary condition in configurational space (9) imply that the first term vanishes. As a matter of fact, we have used that $\varphi|_{\partial D} = 0$, which is a consequence of the particular choice of the flux $\boldsymbol{j}_{\varphi,\boldsymbol{q}}$, see Section 3.4 for details. So far, we do not, however, have a formula for the flux $\boldsymbol{j}_{\varphi,\boldsymbol{q}}$, and therefore we can not decide whether the term really vanishes. We will simply assume that the term vanishes, derive the formula for the flux $\boldsymbol{j}_{\varphi,\boldsymbol{q}}$, and then we retrospectively check, that the derived formula for the flux $\boldsymbol{j}_{\varphi,\boldsymbol{q}}$ and boundary condition (9) are consistent with this assumption (this is indeed the case). We also note that the critical term can also be rewritten as

$$\begin{aligned}\int_D \mathrm{div}_{\boldsymbol{q}} \left[k_{\mathrm{B}} \theta_{\mathrm{s}} \varphi (\nabla_{\boldsymbol{x}} \boldsymbol{v}) \boldsymbol{q} \right] \mathrm{d}\boldsymbol{q} = \int_{\partial D} k_{\mathrm{B}} \theta_{\mathrm{s}} \varphi (\nabla_{\boldsymbol{x}} \boldsymbol{v}) \boldsymbol{q} \bullet \boldsymbol{n}_{\boldsymbol{q}} \, \mathrm{d}\boldsymbol{q} &= \int_{\partial D} k_{\mathrm{B}} \theta_{\mathrm{s}} q_{\max} \varphi (\nabla_{\boldsymbol{x}} \boldsymbol{v}) \boldsymbol{n}_{\boldsymbol{q}} \bullet \boldsymbol{n}_{\boldsymbol{q}} \, \mathrm{d}\boldsymbol{q} \\ &= \left[\int_{\partial D} k_{\mathrm{B}} \theta_{\mathrm{s}} q_{\max} \varphi \boldsymbol{n}_{\boldsymbol{q}} \otimes \boldsymbol{n}_{\boldsymbol{q}} \, \mathrm{d}\boldsymbol{q} \right] : \mathbb{D}, \end{aligned} \tag{37}$$

hence, if we wanted to keep it in the equations, we could easily do so. If we summarise the partial results, we therefore see that

$$\begin{aligned} B = &- \int_D \left[\left(\left. \frac{\mathrm{d}U_e}{\mathrm{d}s} \right|_{s=\frac{1}{2}\left|\frac{\boldsymbol{q}}{q_{\mathrm{ref}}}\right|^2} + \frac{\theta_{\mathrm{s}}}{\theta_{\mathrm{ref}}} \left. \frac{\mathrm{d}U_\eta}{\mathrm{d}s} \right|_{s=\frac{1}{2}\left|\frac{\boldsymbol{q}}{q_{\mathrm{ref}}}\right|^2} \right) \frac{\boldsymbol{q}}{q_{\mathrm{ref}}} \otimes \frac{\boldsymbol{q}}{q_{\mathrm{ref}}} \varphi \right] : \mathbb{D} \, \mathrm{d}\boldsymbol{q} + k_{\mathrm{B}} \theta_{\mathrm{s}} n_{\mathrm{p}} \mathrm{div}_{\boldsymbol{x}} \boldsymbol{v} \\ &- \int_D \frac{1}{\varphi} \left[\left(\left. \frac{\mathrm{d}U_e}{\mathrm{d}s} \right|_{s=\frac{1}{2}\left|\frac{\boldsymbol{q}}{q_{\mathrm{ref}}}\right|^2} + \frac{\theta_{\mathrm{s}}}{\theta_{\mathrm{ref}}} \left. \frac{\mathrm{d}U_\eta}{\mathrm{d}s} \right|_{s=\frac{1}{2}\left|\frac{\boldsymbol{q}}{q_{\mathrm{ref}}}\right|^2} \right) \frac{\boldsymbol{q}}{q_{\mathrm{ref}}^2} \varphi + k_{\mathrm{B}} \theta_{\mathrm{s}} \nabla_{\boldsymbol{q}} \varphi \right] \bullet \boldsymbol{j}_{\varphi,\boldsymbol{q}} \, \mathrm{d}\boldsymbol{q}. \end{aligned} \tag{38}$$

Next we focus on the term A in (33). We see that

$$\begin{aligned} &\int_D \left[U_e \left(\frac{1}{2} \left| \frac{\boldsymbol{q}}{q_{\mathrm{ref}}} \right|^2 \right) + \frac{\theta_{\mathrm{s}}}{\theta_{\mathrm{ref}}} U_\eta \left(\frac{1}{2} \left| \frac{\boldsymbol{q}}{q_{\mathrm{ref}}} \right|^2 \right) + k_{\mathrm{B}} \theta_{\mathrm{s}} \left(\ln \frac{\varphi}{K} + 1 \right) \right] \left[\varphi \mathrm{div}_{\boldsymbol{x}} \boldsymbol{v} + \mathrm{div}_{\boldsymbol{x}} \boldsymbol{j}_{\varphi,\boldsymbol{x}} \right] \mathrm{d}\boldsymbol{q} \\ &\quad = \int_D \left[U_e \left(\frac{1}{2} \left| \frac{\boldsymbol{q}}{q_{\mathrm{ref}}} \right|^2 \right) \varphi + \frac{\theta_{\mathrm{s}}}{\theta_{\mathrm{ref}}} U_\eta \left(\frac{1}{2} \left| \frac{\boldsymbol{q}}{q_{\mathrm{ref}}} \right|^2 \right) \varphi + k_{\mathrm{B}} \theta_{\mathrm{s}} \varphi \ln \frac{\varphi}{K} + k_{\mathrm{B}} \theta_{\mathrm{s}} \varphi \right] \mathrm{div}_{\boldsymbol{x}} \boldsymbol{v} \, \mathrm{d}\boldsymbol{q} \\ &\qquad + \int_D \left[U_e \left(\frac{1}{2} \left| \frac{\boldsymbol{q}}{q_{\mathrm{ref}}} \right|^2 \right) + \frac{\theta_{\mathrm{s}}}{\theta_{\mathrm{ref}}} U_\eta \left(\frac{1}{2} \left| \frac{\boldsymbol{q}}{q_{\mathrm{ref}}} \right|^2 \right) + k_{\mathrm{B}} \theta_{\mathrm{s}} \left(\ln \frac{\varphi}{K} + 1 \right) \right] \mathrm{div}_{\boldsymbol{x}} \boldsymbol{j}_{\varphi,\boldsymbol{x}} \, \mathrm{d}\boldsymbol{q} \\ &= \mathcal{F} \mathrm{div}_{\boldsymbol{x}} \boldsymbol{v} + k_{\mathrm{B}} \theta_{\mathrm{s}} n_{\mathrm{p}} \mathrm{div}_{\boldsymbol{x}} \boldsymbol{v} + \int_D \left[U_e \left(\frac{1}{2} \left| \frac{\boldsymbol{q}}{q_{\mathrm{ref}}} \right|^2 \right) + \frac{\theta_{\mathrm{s}}}{\theta_{\mathrm{ref}}} U_\eta \left(\frac{1}{2} \left| \frac{\boldsymbol{q}}{q_{\mathrm{ref}}} \right|^2 \right) + k_{\mathrm{B}} \theta_{\mathrm{s}} \left(\ln \frac{\varphi}{K} + 1 \right) \right] \mathrm{div}_{\boldsymbol{x}} \boldsymbol{j}_{\varphi,\boldsymbol{x}} \, \mathrm{d}\boldsymbol{q}, \end{aligned} \tag{39}$$

and, hence

$$A = \mathcal{F} \mathrm{div}_{\boldsymbol{x}} \boldsymbol{v} + k_{\mathrm{B}} \theta_{\mathrm{s}} n_{\mathrm{p}} \mathrm{div}_{\boldsymbol{x}} \boldsymbol{v} + \int_D \left[U_e \left(\tfrac{1}{2} \left| \tfrac{\boldsymbol{q}}{q_{\mathrm{ref}}} \right|^2 \right) + \tfrac{\theta_{\mathrm{s}}}{\theta_{\mathrm{ref}}} U_\eta \left(\tfrac{1}{2} \left| \tfrac{\boldsymbol{q}}{q_{\mathrm{ref}}} \right|^2 \right) + k_{\mathrm{B}} \theta_{\mathrm{s}} \left(\ln \tfrac{\varphi}{K} + 1 \right) \right] \mathrm{div}_{\boldsymbol{x}} \boldsymbol{j}_{\varphi,\boldsymbol{x}} \, \mathrm{d}\boldsymbol{q}. \tag{40}$$

Now, we can finally return to the formula (32) for the material time derivative of entropy, and we find that

$$\rho_{\mathrm{s}} \theta_{\mathrm{s}} \frac{\mathrm{d}\eta}{\mathrm{d}t} = \mathbb{T} : \mathbb{D} - \mathrm{div}_{\boldsymbol{x}} \boldsymbol{j}_e - \rho_{\mathrm{s}} \frac{\partial \psi_{\mathrm{s}}}{\partial \rho_{\mathrm{s}}} \frac{\mathrm{d}\rho_{\mathrm{s}}}{\mathrm{d}t} + \frac{\mathcal{F}}{\rho_{\mathrm{s}}} \frac{\mathrm{d}\rho_{\mathrm{s}}}{\mathrm{d}t} - \frac{\partial \mathcal{F}}{\partial \varphi} \frac{\mathrm{d}\varphi}{\mathrm{d}t} = \mathbb{T} : \mathbb{D} - \mathrm{div}_{\boldsymbol{x}} \boldsymbol{j}_e + \rho_{\mathrm{s}}^2 \frac{\partial \psi_{\mathrm{s}}}{\partial \rho_{\mathrm{s}}} \mathrm{div}_{\boldsymbol{x}} \boldsymbol{v} - \mathcal{F} \mathrm{div}_{\boldsymbol{x}} \boldsymbol{v} + A + B, \tag{41}$$

which reduces to

$$
\begin{aligned}
\rho_{\mathrm{s}}\theta_{\mathrm{s}}\frac{\mathrm{d}\eta}{\mathrm{d}t} &= \mathbb{T}:\mathbb{D} - \mathrm{div}_{\boldsymbol{x}}\boldsymbol{j}_e + \rho_{\mathrm{s}}^2\frac{\partial\psi_{\mathrm{s}}}{\partial\rho_{\mathrm{s}}}\mathrm{div}_{\boldsymbol{x}}\boldsymbol{v} + 2k_{\mathrm{B}}\theta_{\mathrm{s}}n_{\mathrm{p}}\mathrm{div}_{\boldsymbol{x}}\boldsymbol{v} \\
&\quad - \int_D \left[\left(\left.\frac{\mathrm{d}U_e}{\mathrm{d}s}\right|_{s=\frac{1}{2}\left|\frac{\boldsymbol{q}}{q_{\mathrm{ref}}}\right|^2} + \frac{\theta_{\mathrm{s}}}{\theta_{\mathrm{ref}}}\left.\frac{\mathrm{d}U_\eta}{\mathrm{d}s}\right|_{s=\frac{1}{2}\left|\frac{\boldsymbol{q}}{q_{\mathrm{ref}}}\right|^2}\right)\frac{\boldsymbol{q}}{q_{\mathrm{ref}}}\otimes\frac{\boldsymbol{q}}{q_{\mathrm{ref}}}\varphi\right]:\mathbb{D}\,\mathrm{d}\boldsymbol{q} \\
&\quad - \int_D \frac{1}{\varphi}\left[\left(\left.\frac{\mathrm{d}U_e}{\mathrm{d}s}\right|_{s=\frac{1}{2}\left|\frac{\boldsymbol{q}}{q_{\mathrm{ref}}}\right|^2} + \frac{\theta_{\mathrm{s}}}{\theta_{\mathrm{ref}}}\left.\frac{\mathrm{d}U_\eta}{\mathrm{d}s}\right|_{s=\frac{1}{2}\left|\frac{\boldsymbol{q}}{q_{\mathrm{ref}}}\right|^2}\right)\frac{\boldsymbol{q}}{q_{\mathrm{ref}}^2}\varphi + k_{\mathrm{B}}\theta_{\mathrm{s}}\nabla_{\boldsymbol{q}}\varphi\right]\bullet\boldsymbol{j}_{\varphi,\boldsymbol{q}}\,\mathrm{d}\boldsymbol{q} \\
&\quad + \int_D \left[U_e\left(\frac{1}{2}\left|\frac{\boldsymbol{q}}{q_{\mathrm{ref}}}\right|^2\right) + \frac{\theta_{\mathrm{s}}}{\theta_{\mathrm{ref}}}U_\eta\left(\frac{1}{2}\left|\frac{\boldsymbol{q}}{q_{\mathrm{ref}}}\right|^2\right) + k_{\mathrm{B}}\theta_{\mathrm{s}}\left(\ln\frac{\varphi}{K}+1\right)\right]\mathrm{div}_{\boldsymbol{x}}\boldsymbol{j}_{\varphi,\boldsymbol{x}}\,\mathrm{d}\boldsymbol{q},
\end{aligned}
\tag{42}
$$

where we have used the evolution equation for the solvent density (3a). We divide (42) by the solvent temperature, and manipulate the energy flux term $\mathrm{div}_{\boldsymbol{x}}\boldsymbol{j}_e$ in the usual manner. We also split the term containing $\mathrm{div}_{\boldsymbol{x}}\boldsymbol{j}_{\varphi,\boldsymbol{x}}$ into a part with a temperature-independent coefficient and a part with a temperature-dependent coefficient, and after some manipulations we get

$$
\begin{aligned}
\rho_{\mathrm{s}}\frac{\mathrm{d}\eta}{\mathrm{d}t} &= \frac{1}{\theta_{\mathrm{s}}}\left\{\mathbb{T} - \int_D\left[\left(\left.\frac{\mathrm{d}U_e}{\mathrm{d}s}\right|_{s=\frac{1}{2}\left|\frac{\boldsymbol{q}}{q_{\mathrm{ref}}}\right|^2} + \frac{\theta_{\mathrm{s}}}{\theta_{\mathrm{ref}}}\left.\frac{\mathrm{d}U_\eta}{\mathrm{d}s}\right|_{s=\frac{1}{2}\left|\frac{\boldsymbol{q}}{q_{\mathrm{ref}}}\right|^2}\right)\frac{\boldsymbol{q}}{q_{\mathrm{ref}}}\otimes\frac{\boldsymbol{q}}{q_{\mathrm{ref}}}\varphi\right]\right\}:\mathbb{D} \\
&\quad + \frac{1}{\theta_{\mathrm{s}}}\left[\rho_{\mathrm{s}}^2\frac{\partial\psi_{\mathrm{s}}}{\partial\rho_{\mathrm{s}}} + 2k_{\mathrm{B}}\theta_{\mathrm{s}}n_{\mathrm{p}}\right]\mathrm{div}_{\boldsymbol{x}}\boldsymbol{v} \\
&\quad - \frac{1}{\theta_{\mathrm{s}}}\int_D\frac{1}{\varphi}\left[\left(\left.\frac{\mathrm{d}U_e}{\mathrm{d}s}\right|_{s=\frac{1}{2}\left|\frac{\boldsymbol{q}}{q_{\mathrm{ref}}}\right|^2} + \frac{\theta_{\mathrm{s}}}{\theta_{\mathrm{ref}}}\left.\frac{\mathrm{d}U_\eta}{\mathrm{d}s}\right|_{s=\frac{1}{2}\left|\frac{\boldsymbol{q}}{q_{\mathrm{ref}}}\right|^2}\right)\frac{\boldsymbol{q}}{q_{\mathrm{ref}}^2}\varphi + k_{\mathrm{B}}\theta_{\mathrm{s}}\nabla_{\boldsymbol{q}}\varphi\right]\bullet\boldsymbol{j}_{\varphi,\boldsymbol{q}}\,\mathrm{d}\boldsymbol{q} \\
&\quad + \int_D\frac{U_e\left(\frac{1}{2}\left|\frac{\boldsymbol{q}}{q_{\mathrm{ref}}}\right|^2\right)}{\theta_{\mathrm{s}}}\mathrm{div}_{\boldsymbol{x}}\boldsymbol{j}_{\varphi,\boldsymbol{x}}\,\mathrm{d}\boldsymbol{q} + \int_D\left[\frac{U_\eta\left(\frac{1}{2}\left|\frac{\boldsymbol{q}}{q_{\mathrm{ref}}}\right|^2\right)}{\theta_{\mathrm{ref}}} + k_{\mathrm{B}}\left(\ln\frac{\varphi}{K}+1\right)\right]\mathrm{div}_{\boldsymbol{x}}\boldsymbol{j}_{\varphi,\boldsymbol{x}}\,\mathrm{d}\boldsymbol{q} - \mathrm{div}_{\boldsymbol{x}}\left(\frac{\boldsymbol{j}_e}{\theta_{\mathrm{s}}}\right) - \frac{\boldsymbol{j}_e\bullet\nabla_{\boldsymbol{x}}\theta_{\mathrm{s}}}{\theta_{\mathrm{s}}^2}.
\end{aligned}
\tag{43}
$$

We introduce the notation

$$
\mathbb{P} =_{\mathrm{def}} \int_D\left[\left(\left.\frac{\mathrm{d}U_e}{\mathrm{d}s}\right|_{s=\frac{1}{2}\left|\frac{\boldsymbol{q}}{q_{\mathrm{ref}}}\right|^2} + \frac{\theta_{\mathrm{s}}}{\theta_{\mathrm{ref}}}\left.\frac{\mathrm{d}U_\eta}{\mathrm{d}s}\right|_{s=\frac{1}{2}\left|\frac{\boldsymbol{q}}{q_{\mathrm{ref}}}\right|^2}\right)\frac{\boldsymbol{q}}{q_{\mathrm{ref}}}\otimes\frac{\boldsymbol{q}}{q_{\mathrm{ref}}}\varphi\right]\mathrm{d}\boldsymbol{q},
\tag{44}
$$

and we split the Cauchy stress tensor $\mathbb{T}$ into the mean normal stress m and the traceless part $\mathbb{T}_\delta$,

$$
\mathbb{T} = m\mathbb{I} + \mathbb{T}_\delta,
\tag{45}
$$

where $m =_{\mathrm{def}} \frac{1}{3}\mathrm{Tr}\,\mathbb{T}$ and $\mathbb{T}_\delta =_{\mathrm{def}} \mathbb{T} - \frac{1}{3}(\mathrm{Tr}\,\mathbb{T})\,\mathbb{I}$ (this standard manipulation allows us to treat the volume-changing and volume-preserving deformations separately, see for example Málek and Průša [21] for details). We also do the same for the tensor $\mathbb{P}$, and we rewrite (43) as

$$
\begin{aligned}
\rho_{\mathrm{s}}\frac{\mathrm{d}\eta}{\mathrm{d}t} &= \frac{1}{\theta_{\mathrm{s}}}\left\{[\mathbb{T}_\delta - \mathbb{P}_\delta]:\mathbb{D}_\delta + \left[m - \frac{1}{3}\mathrm{Tr}\,\mathbb{P} + \rho_{\mathrm{s}}^2\frac{\partial\psi_{\mathrm{s}}}{\partial\rho_{\mathrm{s}}} + 2k_{\mathrm{B}}\theta_{\mathrm{s}}n_{\mathrm{p}}\right]\mathrm{div}_{\boldsymbol{x}}\boldsymbol{v}\right\} \\
&\quad - \frac{1}{\theta_{\mathrm{s}}}\int_D\frac{1}{\varphi}\left[\left(\left.\frac{\mathrm{d}U_e}{\mathrm{d}s}\right|_{s=\frac{1}{2}\left|\frac{\boldsymbol{q}}{q_{\mathrm{ref}}}\right|^2} + \frac{\theta_{\mathrm{s}}}{\theta_{\mathrm{ref}}}\left.\frac{\mathrm{d}U_\eta}{\mathrm{d}s}\right|_{s=\frac{1}{2}\left|\frac{\boldsymbol{q}}{q_{\mathrm{ref}}}\right|^2}\right)\frac{\boldsymbol{q}}{q_{\mathrm{ref}}^2}\varphi + k_{\mathrm{B}}\theta_{\mathrm{s}}\nabla_{\boldsymbol{q}}\varphi\right]\bullet\boldsymbol{j}_{\varphi,\boldsymbol{q}}\,\mathrm{d}\boldsymbol{q} \\
&\quad + \int_D\frac{U_e\left(\frac{1}{2}\left|\frac{\boldsymbol{q}}{q_{\mathrm{ref}}}\right|^2\right)}{\theta_{\mathrm{s}}}\mathrm{div}_{\boldsymbol{x}}\boldsymbol{j}_{\varphi,\boldsymbol{x}}\,\mathrm{d}\boldsymbol{q} + \int_D\left[\frac{U_\eta\left(\frac{1}{2}\left|\frac{\boldsymbol{q}}{q_{\mathrm{ref}}}\right|^2\right)}{\theta_{\mathrm{ref}}} + k_{\mathrm{B}}\left(\ln\frac{\varphi}{K}+1\right)\right]\mathrm{div}_{\boldsymbol{x}}\boldsymbol{j}_{\varphi,\boldsymbol{x}}\,\mathrm{d}\boldsymbol{q} - \mathrm{div}_{\boldsymbol{x}}\left(\frac{\boldsymbol{j}_e}{\theta_{\mathrm{s}}}\right) - \frac{\boldsymbol{j}_e\bullet\nabla_{\boldsymbol{x}}\theta_{\mathrm{s}}}{\theta_{\mathrm{s}}^2}.
\end{aligned}
\tag{46}
$$

Now, we are ready to manipulate the part with the temperature independent coefficient

$$\int_D \left[\frac{U_\eta\left(\frac{1}{2}\left|\frac{q}{q_{\mathrm{ref}}}\right|^2\right)}{\theta_{\mathrm{ref}}} + k_{\mathrm{B}}\left(\ln\frac{\varphi}{K}+1\right)\right] \mathrm{div}_{\boldsymbol{x}} \boldsymbol{j}_{\varphi,\boldsymbol{x}}\,\mathrm{d}\boldsymbol{q} = \mathrm{div}_{\boldsymbol{x}}\left[\int_D \left[\frac{U_\eta\left(\frac{1}{2}\left|\frac{q}{q_{\mathrm{ref}}}\right|^2\right)}{\theta_{\mathrm{ref}}} + k_{\mathrm{B}}\left(\ln\frac{\varphi}{K}+1\right)\right] \boldsymbol{j}_{\varphi,\boldsymbol{x}}\,\mathrm{d}\boldsymbol{q}\right]$$
$$- \int_D \nabla_{\boldsymbol{x}}\left[\frac{U_\eta\left(\frac{1}{2}\left|\frac{q}{q_{\mathrm{ref}}}\right|^2\right)}{\theta_{\mathrm{ref}}} + k_{\mathrm{B}}\left(\ln\frac{\varphi}{K}+1\right)\right] \bullet \boldsymbol{j}_{\varphi,\boldsymbol{x}}\,\mathrm{d}\boldsymbol{q}. \tag{47}$$

Substituting (47) back into (43) yields

$$\rho_{\mathrm{s}}\frac{\mathrm{d}\eta}{\mathrm{d}t} = \frac{1}{\theta_{\mathrm{s}}}\left\{\left[\mathbb{T}_\delta - \mathbb{P}_\delta\right] : \mathbb{D}_\delta + \left[m - \frac{1}{3}\operatorname{Tr}\mathbb{P} + \rho_{\mathrm{s}}^2\frac{\partial\psi_{\mathrm{s}}}{\partial\rho_{\mathrm{s}}} + 2k_{\mathrm{B}}\theta_{\mathrm{s}}n_{\mathrm{p}}\right]\mathrm{div}_{\boldsymbol{x}}\boldsymbol{v}\right\}$$
$$- \frac{1}{\theta_{\mathrm{s}}}\int_D \frac{1}{\varphi}\left[\left(\left.\frac{\mathrm{d}U_e}{\mathrm{d}s}\right|_{s=\frac{1}{2}\left|\frac{q}{q_{\mathrm{ref}}}\right|^2} + \frac{\theta_{\mathrm{s}}}{\theta_{\mathrm{ref}}}\left.\frac{\mathrm{d}U_\eta}{\mathrm{d}s}\right|_{s=\frac{1}{2}\left|\frac{q}{q_{\mathrm{ref}}}\right|^2}\right)\frac{\boldsymbol{q}}{q_{\mathrm{ref}}^2}\varphi + k_{\mathrm{B}}\theta_{\mathrm{s}}\nabla_{\boldsymbol{q}}\varphi\right] \bullet \boldsymbol{j}_{\varphi,\boldsymbol{q}}\,\mathrm{d}\boldsymbol{q}$$
$$+ \int_D \frac{U_e\left(\frac{1}{2}\left|\frac{q}{q_{\mathrm{ref}}}\right|^2\right)}{\theta_{\mathrm{s}}}\mathrm{div}_{\boldsymbol{x}}\boldsymbol{j}_{\varphi,\boldsymbol{x}}\,\mathrm{d}\boldsymbol{q} - \int_D \frac{k_{\mathrm{B}}}{\varphi}\nabla_{\boldsymbol{x}}\varphi \bullet \boldsymbol{j}_{\varphi,\boldsymbol{x}}\,\mathrm{d}\boldsymbol{q}$$
$$- \mathrm{div}_{\boldsymbol{x}}\left(\frac{\boldsymbol{j}_e}{\theta_{\mathrm{s}}} - \int_D \left[\frac{U_\eta\left(\frac{1}{2}\left|\frac{q}{q_{\mathrm{ref}}}\right|^2\right)}{\theta_{\mathrm{ref}}} + k_{\mathrm{B}}\left(\ln\frac{\varphi}{K}+1\right)\right] \boldsymbol{j}_{\varphi,\boldsymbol{x}}\,\mathrm{d}\boldsymbol{q}\right) - \frac{\boldsymbol{j}_e \bullet \nabla_{\boldsymbol{x}}\theta_{\mathrm{s}}}{\theta_{\mathrm{s}}^2}. \tag{48}$$

We rewrite the last equation as

$$\rho_{\mathrm{s}}\frac{\mathrm{d}\eta}{\mathrm{d}t} + \mathrm{div}_{\boldsymbol{x}}\left(\frac{\boldsymbol{j}_e}{\theta_{\mathrm{s}}} - \int_D \left[\frac{U_\eta\left(\frac{1}{2}\left|\frac{q}{q_{\mathrm{ref}}}\right|^2\right)}{\theta_{\mathrm{ref}}} + k_{\mathrm{B}}\left(\ln\frac{\varphi}{K}+1\right)\right] \boldsymbol{j}_{\varphi,\boldsymbol{x}}\,\mathrm{d}\boldsymbol{q}\right)$$
$$= \frac{1}{\theta_{\mathrm{s}}}\left\{\left[\mathbb{T}_\delta - \mathbb{P}_\delta\right] : \mathbb{D}_\delta + \left[m - \frac{1}{3}\operatorname{Tr}\mathbb{P} + \rho_{\mathrm{s}}^2\frac{\partial\psi_{\mathrm{s}}}{\partial\rho_{\mathrm{s}}} + 2k_{\mathrm{B}}\theta_{\mathrm{s}}n_{\mathrm{p}}\right]\mathrm{div}_{\boldsymbol{x}}\boldsymbol{v}\right\}$$
$$- \frac{1}{\theta_{\mathrm{s}}}\int_D \frac{1}{\varphi}\left[\left(\left.\frac{\mathrm{d}U_e}{\mathrm{d}s}\right|_{s=\frac{1}{2}\left|\frac{q}{q_{\mathrm{ref}}}\right|^2} + \frac{\theta_{\mathrm{s}}}{\theta_{\mathrm{ref}}}\left.\frac{\mathrm{d}U_\eta}{\mathrm{d}s}\right|_{s=\frac{1}{2}\left|\frac{q}{q_{\mathrm{ref}}}\right|^2}\right)\frac{\boldsymbol{q}}{q_{\mathrm{ref}}^2}\varphi + k_{\mathrm{B}}\theta_{\mathrm{s}}\nabla_{\boldsymbol{q}}\varphi\right] \bullet \boldsymbol{j}_{\varphi,\boldsymbol{q}}\,\mathrm{d}\boldsymbol{q}$$
$$+ \int_D \frac{U_e\left(\frac{1}{2}\left|\frac{q}{q_{\mathrm{ref}}}\right|^2\right)}{\theta_{\mathrm{s}}}\mathrm{div}_{\boldsymbol{x}}\boldsymbol{j}_{\varphi,\boldsymbol{x}}\,\mathrm{d}\boldsymbol{q} - \int_D \frac{k_{\mathrm{B}}}{\varphi}\nabla_{\boldsymbol{x}}\varphi \bullet \boldsymbol{j}_{\varphi,\boldsymbol{x}}\,\mathrm{d}\boldsymbol{q} - \frac{\boldsymbol{j}_e \bullet \nabla_{\boldsymbol{x}}\theta_{\mathrm{s}}}{\theta_{\mathrm{s}}^2}, \tag{49}$$

which helps us to identify the fluxes and entropy production terms. It remains to manipulate the term with the potential U_e. We see that

$$\int_D \frac{U_e\left(\frac{1}{2}\left|\frac{q}{q_{\mathrm{ref}}}\right|^2\right)}{\theta_{\mathrm{s}}}\mathrm{div}_{\boldsymbol{x}}\boldsymbol{j}_{\varphi,\boldsymbol{x}}\,\mathrm{d}\boldsymbol{q} = \mathrm{div}_{\boldsymbol{x}}\left(\int_D \frac{U_e\left(\frac{1}{2}\left|\frac{q}{q_{\mathrm{ref}}}\right|^2\right)}{\theta_{\mathrm{s}}}\boldsymbol{j}_{\varphi,\boldsymbol{x}}\,\mathrm{d}\boldsymbol{q}\right) + \frac{\nabla_{\boldsymbol{x}}\theta_{\mathrm{s}} \bullet \int_D U_e\left(\frac{1}{2}\left|\frac{q}{q_{\mathrm{ref}}}\right|^2\right)\boldsymbol{j}_{\varphi,\boldsymbol{x}}\,\mathrm{d}\boldsymbol{q}}{\theta_{\mathrm{s}}^2}. \tag{50}$$

This manipulation implies that we can rewrite (49) in the final form as

$$
\begin{aligned}
\rho_{\mathrm{s}}\frac{\mathrm{d}\eta}{\mathrm{d}t} + \operatorname{div}_{\boldsymbol{x}}&\left(\frac{\boldsymbol{j}_e}{\theta_{\mathrm{s}}} - \int_D \left[\frac{U_\eta\left(\frac{1}{2}\left|\frac{\boldsymbol{q}}{q_{\mathrm{ref}}}\right|^2\right)}{\theta_{\mathrm{ref}}} + k_{\mathrm{B}}\left(\ln\frac{\varphi}{K}+1\right) + \frac{U_e\left(\frac{1}{2}\left|\frac{\boldsymbol{q}}{q_{\mathrm{ref}}}\right|^2\right)}{\theta_{\mathrm{s}}}\right]\boldsymbol{j}_{\varphi,\boldsymbol{x}}\,\mathrm{d}\boldsymbol{q}\right) \\
&= \frac{1}{\theta_{\mathrm{s}}}\left\{[\mathbb{T}_\delta - \mathbb{P}_\delta]:\mathbb{D}_\delta + \left[m - \frac{1}{3}\operatorname{Tr}\mathbb{P} + \rho_{\mathrm{s}}^2\frac{\partial\psi_{\mathrm{s}}}{\partial\rho_{\mathrm{s}}} + 2k_{\mathrm{B}}\theta_{\mathrm{s}}n_{\mathrm{p}}\right]\operatorname{div}_{\boldsymbol{x}}\boldsymbol{v}\right\} \\
&\quad - \frac{1}{\theta_{\mathrm{s}}}\int_D \frac{1}{\varphi}\left[\left(\left.\frac{\mathrm{d}U_e}{\mathrm{d}s}\right|_{s=\frac{1}{2}\left|\frac{\boldsymbol{q}}{q_{\mathrm{ref}}}\right|^2} + \frac{\theta_{\mathrm{s}}}{\theta_{\mathrm{ref}}}\left.\frac{\mathrm{d}U_\eta}{\mathrm{d}s}\right|_{s=\frac{1}{2}\left|\frac{\boldsymbol{q}}{q_{\mathrm{ref}}}\right|^2}\right)\frac{\boldsymbol{q}}{q_{\mathrm{ref}}^2}\varphi + k_{\mathrm{B}}\theta_{\mathrm{s}}\nabla_{\boldsymbol{q}}\varphi\right]\bullet\boldsymbol{j}_{\varphi,\boldsymbol{q}}\,\mathrm{d}\boldsymbol{q} \\
&\quad - \int_D \frac{k_{\mathrm{B}}}{\varphi}\nabla_{\boldsymbol{x}}\varphi\bullet\boldsymbol{j}_{\varphi,\boldsymbol{x}}\,\mathrm{d}\boldsymbol{q} - \frac{\left[\boldsymbol{j}_e - \int_D U_e\left(\frac{1}{2}\left|\frac{\boldsymbol{q}}{q_{\mathrm{ref}}}\right|^2\right)\boldsymbol{j}_{\varphi,\boldsymbol{x}}\,\mathrm{d}\boldsymbol{q}\right]\bullet\nabla_{\boldsymbol{x}}\theta_{\mathrm{s}}}{\theta_{\mathrm{s}}^2}. \qquad (51)
\end{aligned}
$$

5.2. Entropy Production and Constitutive Relations

Now, we are in a position to choose $\boldsymbol{j}_\eta$, $\boldsymbol{j}_e$, $\boldsymbol{j}_{\varphi,\boldsymbol{x}}$, $\boldsymbol{j}_{\varphi,\boldsymbol{q}}$, m and $\mathbb{T}_\delta$ in such a way that the right-hand side is nonnegative. We start with the flux $\boldsymbol{j}_{\varphi,\boldsymbol{x}}$ in physical space, the nonnegativity of the term $-\int_D \frac{k_{\mathrm{B}}}{\varphi}\nabla_{\boldsymbol{x}}\varphi\bullet\boldsymbol{j}_{\varphi,\boldsymbol{x}}\,\mathrm{d}\boldsymbol{q}$ is granted if we make, for example, the simple choice

$$
\boldsymbol{j}_{\varphi,\boldsymbol{x}} =_{\mathrm{def}} -\frac{k_{\mathrm{B}}\theta_{\mathrm{s}}}{2\zeta}\nabla_{\boldsymbol{x}}\varphi, \qquad (52)
$$

where ζ denotes the hydrodynamic drag coefficient, $[\zeta] = \frac{\mathrm{N}}{\frac{\mathrm{m}}{\mathrm{s}}}$ (the presence of the hydrodynamic drag coefficient is motivated by the insight into the microscopic dynamics of the polymeric chains, see for example Barrett and Süli [31] for details). The choice (52) in turn implies that we have to fix the energy flux as

$$
\boldsymbol{j}_e =_{\mathrm{def}} -\kappa\nabla_{\boldsymbol{x}}\theta_{\mathrm{s}} + \int_D U_e\left(\frac{1}{2}\left|\frac{\boldsymbol{q}}{q_{\mathrm{ref}}}\right|^2\right)\boldsymbol{j}_{\varphi,\boldsymbol{x}}\,\mathrm{d}\boldsymbol{q} = -\kappa\nabla_{\boldsymbol{x}}\theta_{\mathrm{s}} - \frac{k_{\mathrm{B}}\theta_{\mathrm{s}}}{2\zeta}\int_D U_e\left(\frac{1}{2}\left|\frac{\boldsymbol{q}}{q_{\mathrm{ref}}}\right|^2\right)\nabla_{\boldsymbol{x}}\varphi\,\mathrm{d}\boldsymbol{q}. \qquad (53)
$$

We note that (53) is the same energy flux as in Öttinger and Grmela [18]. We also note that only the "energetic" part U_e of the potential U enters the formula for the energy flux $\boldsymbol{j}_e$, which is an expected result.

Next, we fix the constitutive relation for the flux $\boldsymbol{j}_{\varphi,\boldsymbol{q}}$ in the configurational space; we set

$$
\boldsymbol{j}_{\varphi,\boldsymbol{q}} =_{\mathrm{def}} -\frac{2}{\zeta}\left[\left(\left.\frac{\mathrm{d}U_e}{\mathrm{d}s}\right|_{s=\frac{1}{2}\left|\frac{\boldsymbol{q}}{q_{\mathrm{ref}}}\right|^2} + \frac{\theta_{\mathrm{s}}}{\theta_{\mathrm{ref}}}\left.\frac{\mathrm{d}U_\eta}{\mathrm{d}s}\right|_{s=\frac{1}{2}\left|\frac{\boldsymbol{q}}{q_{\mathrm{ref}}}\right|^2}\right)\frac{\boldsymbol{q}}{q_{\mathrm{ref}}^2}\varphi + k_{\mathrm{B}}\theta_{\mathrm{s}}\nabla_{\boldsymbol{q}}\varphi\right], \qquad (54)
$$

where the coefficient $\frac{2}{\zeta}$ is again motivated by the microscopic dynamics of the polymeric chains. In particular, we want to keep the link between the Fokker–Planck equation and the associated stochastic process, see, for example, Barrett and Süli [31] for details. If we recall the relation between the force and the corresponding potential (12), we see that (54), in fact, reads

$$
\boldsymbol{j}_{\varphi,\boldsymbol{q}} = -\frac{2}{\zeta}\left[\boldsymbol{F}\varphi + k_{\mathrm{B}}\theta_{\mathrm{s}}\nabla_{\boldsymbol{q}}\varphi\right], \qquad (55)
$$

where

$$
\boldsymbol{F} =_{\mathrm{def}} \nabla_{\boldsymbol{q}}\left(U_e\left(\frac{1}{2}\left|\frac{\boldsymbol{q}}{q_{\mathrm{ref}}}\right|^2\right) + \frac{\theta_{\mathrm{s}}}{\theta_{\mathrm{ref}}}U_\eta\left(\frac{1}{2}\left|\frac{\boldsymbol{q}}{q_{\mathrm{ref}}}\right|^2\right)\right), \qquad (56)
$$

which, together with (52), gives upon substitution into (7) the Fokker–Planck equation in the form

$$\frac{\partial \varphi}{\partial t} + \operatorname{div}_{\boldsymbol{x}} \left(\boldsymbol{v} \varphi - \frac{k_{\mathrm{B}} \theta_{\mathrm{s}}}{2\zeta} \nabla_{\boldsymbol{x}} \varphi \right) + \operatorname{div}_{\boldsymbol{q}} \left((\nabla_{\boldsymbol{x}} \boldsymbol{v}) \boldsymbol{q} \varphi - \frac{2\boldsymbol{F}}{\zeta} \varphi - \frac{2 k_{\mathrm{B}} \theta_{\mathrm{s}}}{\zeta} \nabla_{\boldsymbol{q}} \varphi \right) = 0. \tag{57}$$

This is the specific Fokker–Planck equation that we have used in Section 3.

From the left-hand side of (51) we can infer the entropy flux $\boldsymbol{j}_\eta$. If we use the formula for $\boldsymbol{j}_e$, we see that the term under the $\operatorname{div}_{\boldsymbol{x}}$ operator reads

$$\boldsymbol{j}_\eta =_{\mathrm{def}} -\frac{\kappa \nabla_{\boldsymbol{x}} \theta_{\mathrm{s}}}{\theta_{\mathrm{s}}} - \int_D \left[\frac{U_\eta \left(\frac{1}{2} \left| \frac{\boldsymbol{q}}{q_{\mathrm{ref}}} \right|^2 \right)}{\theta_{\mathrm{ref}}} + k_{\mathrm{B}} \left(\ln \frac{\varphi}{K} + 1 \right) \right] \boldsymbol{j}_{\varphi,\boldsymbol{x}} \, \mathrm{d}\boldsymbol{q}, \tag{58}$$

where $\boldsymbol{j}_{\varphi,\boldsymbol{x}}$ is given by (52). We note that the term with the "energetic" part U_e of the potential U has cancelled, and only the entropic part U_η enters the entropic flux, which is an expected result.

Finally, we fix the constitutive relation for the Cauchy stress tensor, namely for the mean normal stress m and the deviatoric part $\mathbb{T}_\delta$. We need a choice that makes the term $[\mathbb{T}_\delta - \mathbb{P}_\delta] : \mathbb{D}_\delta + \left[m - \frac{1}{3} \operatorname{Tr} \mathbb{P} + \rho_{\mathrm{s}}^2 \frac{\partial \psi_{\mathrm{s}}}{\partial \rho_{\mathrm{s}}} + 2 k_{\mathrm{B}} \theta_{\mathrm{s}} n_{\mathrm{p}} \right] \operatorname{div}_{\boldsymbol{x}} \boldsymbol{v}$ on the right-hand side of (51) nonnegative. If we want to model the solvent as a classical compressible Navier–Stokes fluid, then we set

$$\mathbb{T}_\delta =_{\mathrm{def}} 2\nu \mathbb{D}_\delta + \mathbb{P}_\delta, \tag{59a}$$

$$m =_{\mathrm{def}} \frac{1}{3} \operatorname{Tr} \mathbb{P} - \rho_{\mathrm{s}}^2 \frac{\partial \psi_{\mathrm{s}}}{\partial \rho_{\mathrm{s}}} - 2 k_{\mathrm{B}} \theta_{\mathrm{s}} n_{\mathrm{p}} + \tilde{\lambda} \operatorname{div}_{\boldsymbol{x}} \boldsymbol{v}, \tag{59b}$$

where ν and $\tilde{\lambda}$ are the positive constants referred to as the shear viscosity and bulk viscosity. If we use (59), then the full formula for the Cauchy stress tensor reads

$$\mathbb{T} = -\rho_{\mathrm{s}}^2 \frac{\partial \psi_{\mathrm{s}}}{\partial \rho_{\mathrm{s}}} \mathbb{I} + \lambda \left(\operatorname{div}_{\boldsymbol{x}} \boldsymbol{v} \right) \mathbb{I} + 2\nu \mathbb{D} - 2 k_{\mathrm{B}} \theta_{\mathrm{s}} n_{\mathrm{p}} \mathbb{I} + \mathbb{P}, \tag{60}$$

where $\tilde{\lambda} = \frac{3\lambda + 2\nu}{3}$. The first three terms on the right-hand side of (60) are the familiar ones. In particular, we recognise the formula for the thermodynamic pressure

$$p_{\mathrm{th,s}}(\theta_{\mathrm{s}}, \rho_{\mathrm{s}}) =_{\mathrm{def}} \rho_{\mathrm{s}}^2 \frac{\partial \psi_{\mathrm{s}}}{\partial \rho_{\mathrm{s}}}; \tag{61}$$

hence, we can rewrite (60) as

$$\mathbb{T} = -p_{\mathrm{th,s}} \mathbb{I} + \lambda \left(\operatorname{div}_{\boldsymbol{x}} \boldsymbol{v} \right) \mathbb{I} + 2\nu \mathbb{D} - 2 k_{\mathrm{B}} \theta_{\mathrm{s}} n_{\mathrm{p}} \mathbb{I} + \mathbb{P}. \tag{62}$$

The polymeric contribution $\mathbb{T}_{\mathrm{polymer}}$ to the Cauchy stress tensor $\mathbb{T}$ is given by the last two terms in (62). If we recall the definition of the tensor $\mathbb{P}$, see (44), we see that

$$\mathbb{T}_{\mathrm{polymer}} = -2 k_{\mathrm{B}} \theta_{\mathrm{s}} n_{\mathrm{p}} \mathbb{I} + \int_D \left[\left(\left. \frac{\mathrm{d} U_e}{\mathrm{d}s} \right|_{s = \frac{1}{2} \left| \frac{\boldsymbol{q}}{q_{\mathrm{ref}}} \right|^2} + \frac{\theta_{\mathrm{s}}}{\theta_{\mathrm{ref}}} \left. \frac{\mathrm{d} U_\eta}{\mathrm{d}s} \right|_{s = \frac{1}{2} \left| \frac{\boldsymbol{q}}{q_{\mathrm{ref}}} \right|^2} \right) \frac{\boldsymbol{q}}{q_{\mathrm{ref}}} \otimes \frac{\boldsymbol{q}}{q_{\mathrm{ref}}} \varphi \right] \mathrm{d}\boldsymbol{q}. \tag{63}$$

This is the Kramers expression for the polymeric contribution to the Cauchy stress tensor. We note that the Kramers expression has not been assumed *a priori*: it is a consequence of the choice of energy storage and entropy production mechanisms. The same formula also follows from the GENERIC formalism, see Öttinger and Grmela [18], where it is also a consequence of the proposed modelling approach and it is not assumed *a priori*.

5.3. Temperature Evolution Equation

A cautious reader might notice that the energy flux $\boldsymbol{j}_e$ and the entropy flux $\boldsymbol{j}_\eta$ depend on the potentials U_e and U_η and on the normalisation constant K. However, if one shifts the value of a potential by a constant, then this operation should have no impact on the dynamics of the system. The same should hold for the constant K. Its particular choice should have no impact on the dynamics.

We show that this is indeed true. First, we observe that the shift of the value of the potentials and the choice of K have no impact on the balance of mass (3a) (evolution equation for the solvent density ρ_s) and on the balance of linear momentum (78b) (evolution equation for the velocity field $\boldsymbol{v}$). Indeed, the Cauchy stress tensor, see (60), depends on the gradients of the potentials. Next we observe that the Fokker–Planck equation (evolution equation for φ) in the form (57) also contains only gradients of the potentials. It remains to check the evolution equation for the last quantity of interest, namely for the temperature.

In order to do so, we first need to explicitly formulate the evolution equation for the temperature. We start with the evolution equation for the entropy in the form (29), which is

$$\rho_\mathrm{s}\theta_\mathrm{s}\frac{\mathrm{d}\eta}{\mathrm{d}t} = \mathbb{T}:\mathbb{D} - \mathrm{div}_{\boldsymbol{x}}\boldsymbol{j}_e - \rho_\mathrm{s}\frac{\partial\psi}{\partial\rho_\mathrm{s}}\frac{\mathrm{d}\rho_\mathrm{s}}{\mathrm{d}t} - \rho_\mathrm{s}\frac{\partial\psi}{\partial\varphi}\frac{\mathrm{d}\varphi}{\mathrm{d}t}. \tag{64}$$

Because the entropy is given as the derivative of the Helmholtz free energy with respect to the temperature, $\eta = -\frac{\partial\psi}{\partial\theta_\mathrm{s}}$, we can use the chain rule on the left-hand side of (64), and with a slight abuse of notation we get

$$\rho_\mathrm{s}\theta_\mathrm{s}\frac{\mathrm{d}\eta}{\mathrm{d}t} = \rho_\mathrm{s}\theta_\mathrm{s}\left(-\frac{\partial^2\psi}{\partial\theta_\mathrm{s}^2}\frac{\mathrm{d}\theta_\mathrm{s}}{\mathrm{d}t} - \frac{\partial^2\psi}{\partial\theta_\mathrm{s}\partial\rho_\mathrm{s}}\frac{\mathrm{d}\rho_\mathrm{s}}{\mathrm{d}t} - \frac{\partial^2\psi}{\partial\theta_\mathrm{s}\partial\varphi}\frac{\mathrm{d}\varphi}{\mathrm{d}t}\right). \tag{65}$$

Making use of (65) in (64) yields

$$-\rho_\mathrm{s}\theta_\mathrm{s}\frac{\partial^2\psi}{\partial\theta_\mathrm{s}^2}\frac{\mathrm{d}\theta_\mathrm{s}}{\mathrm{d}t} = \rho_\mathrm{s}\theta_\mathrm{s}\frac{\partial^2\psi}{\partial\theta_\mathrm{s}\partial\rho_\mathrm{s}}\frac{\mathrm{d}\rho_\mathrm{s}}{\mathrm{d}t} + \rho_\mathrm{s}\theta_\mathrm{s}\frac{\partial^2\psi}{\partial\theta_\mathrm{s}\partial\varphi}\frac{\mathrm{d}\varphi}{\mathrm{d}t} + \mathbb{T}:\mathbb{D} - \mathrm{div}_{\boldsymbol{x}}\boldsymbol{j}_e - \rho_\mathrm{s}\frac{\partial\psi}{\partial\rho_\mathrm{s}}\frac{\mathrm{d}\rho_\mathrm{s}}{\mathrm{d}t} - \rho_\mathrm{s}\frac{\partial\psi}{\partial\varphi}\frac{\mathrm{d}\varphi}{\mathrm{d}t}. \tag{66}$$

On the left-hand side, we have obtained the material time derivative of the temperature field θ_s, and we can explicitly evaluate all terms on the right-hand side. We take into account the particular structure of the Helmholtz free energy (23), which is

$$\psi(\theta_\mathrm{s},\rho_\mathrm{s},\varphi) =_{\mathrm{def}} \psi_\mathrm{s}(\theta_\mathrm{s},\rho_\mathrm{s}) + \underbrace{\frac{1}{\rho_\mathrm{s}}\int_D U_e\left(\frac{1}{2}\left|\frac{\boldsymbol{q}}{q_{\mathrm{ref}}}\right|^2\right)\varphi\,\mathrm{d}\boldsymbol{q} + \frac{k_\mathrm{B}\theta_\mathrm{s}}{\rho_\mathrm{s}}\int_D\left(\frac{U_\eta\left(\frac{1}{2}\left|\frac{\boldsymbol{q}}{q_{\mathrm{ref}}}\right|^2\right)}{k_\mathrm{B}\theta_{\mathrm{ref}}}\varphi + \varphi\ln\frac{\varphi}{K}\right)\mathrm{d}\boldsymbol{q}}_{\psi_\mathrm{p}} \tag{67}$$

and we arrive at

$$\begin{aligned}-\rho_\mathrm{s}\theta_\mathrm{s}\frac{\partial^2\psi_\mathrm{s}}{\partial\theta_\mathrm{s}^2}\frac{\mathrm{d}\theta_\mathrm{s}}{\mathrm{d}t} &= \rho_\mathrm{s}\left(\theta_\mathrm{s}\frac{\partial^2\psi_\mathrm{s}}{\partial\theta_\mathrm{s}\partial\rho_\mathrm{s}} - \frac{\partial\psi_\mathrm{s}}{\partial\rho_\mathrm{s}}\right)\frac{\mathrm{d}\rho_\mathrm{s}}{\mathrm{d}t} + \mathbb{T}:\mathbb{D} - \mathrm{div}_{\boldsymbol{x}}\boldsymbol{j}_e \\ &\quad + \rho_\mathrm{s}\theta_\mathrm{s}\frac{\partial^2\psi_\mathrm{p}}{\partial\theta_\mathrm{s}\partial\rho_\mathrm{s}}\frac{\mathrm{d}\rho_\mathrm{s}}{\mathrm{d}t} + \rho_\mathrm{s}\theta_\mathrm{s}\frac{\partial^2\psi_\mathrm{p}}{\partial\theta_\mathrm{s}\partial\varphi}\frac{\mathrm{d}\varphi}{\mathrm{d}t} - \rho_\mathrm{s}\frac{\partial\psi_\mathrm{p}}{\partial\rho_\mathrm{s}}\frac{\mathrm{d}\rho_\mathrm{s}}{\mathrm{d}t} - \rho_\mathrm{s}\frac{\partial\psi_\mathrm{p}}{\partial\varphi}\frac{\mathrm{d}\varphi}{\mathrm{d}t}.\end{aligned} \tag{68}$$

By virtue of the linearity of the polymeric part ψ_p with respect to temperature, we get

$$\begin{aligned}-\rho_\mathrm{s}\theta_\mathrm{s}\frac{\partial^2\psi_\mathrm{s}}{\partial\theta_\mathrm{s}^2}\frac{\mathrm{d}\theta_\mathrm{s}}{\mathrm{d}t} &= \rho_\mathrm{s}\left(\theta_\mathrm{s}\frac{\partial^2\psi_\mathrm{s}}{\partial\theta_\mathrm{s}\partial\rho_\mathrm{s}} - \frac{\partial\psi_\mathrm{s}}{\partial\rho_\mathrm{s}}\right)\frac{\mathrm{d}\rho_\mathrm{s}}{\mathrm{d}t} + \mathbb{T}:\mathbb{D} - \mathrm{div}_{\boldsymbol{x}}\boldsymbol{j}_e \\ &\quad + \frac{1}{\rho_\mathrm{s}}\left(\int_D U_e\left(\frac{1}{2}\left|\frac{\boldsymbol{q}}{q_{\mathrm{ref}}}\right|^2\right)\varphi\,\mathrm{d}\boldsymbol{q}\right)\frac{\mathrm{d}\rho_\mathrm{s}}{\mathrm{d}t} - \int_D U_e\left(\frac{1}{2}\left|\frac{\boldsymbol{q}}{q_{\mathrm{ref}}}\right|^2\right)\frac{\mathrm{d}\varphi}{\mathrm{d}t}\,\mathrm{d}\boldsymbol{q}.\end{aligned} \tag{69}$$

Next, we recall that the expression on the left-hand side of (69) is the classical definition of the specific heat at constant volume $c_{\mathrm{V,s}}$ for the solvent only,

$$c_{\mathrm{V,s}}(\theta_{\mathrm{s}}, \rho_{\mathrm{s}}) =_{\mathrm{def}} -\theta_{\mathrm{s}} \frac{\partial^2 \psi_{\mathrm{s}}}{\partial \theta_{\mathrm{s}}^2}, \tag{70}$$

we use the definition of the thermodynamic pressure $p_{\mathrm{th,s}}$ for the solvent, see (61), the balance of mass (3a), and we get

$$\begin{aligned}\rho_{\mathrm{s}} c_{\mathrm{V,s}} \frac{\mathrm{d}\theta_{\mathrm{s}}}{\mathrm{d}t} &= -\theta_{\mathrm{s}} \frac{\partial p_{\mathrm{th,s}}}{\partial \theta_{\mathrm{s}}} \operatorname{div}_{\boldsymbol{x}} \boldsymbol{v} + p_{\mathrm{th,s}} \operatorname{div}_{\boldsymbol{x}} \boldsymbol{v} + \mathbb{T} : \mathbb{D} - \operatorname{div}_{\boldsymbol{x}} \boldsymbol{j}_e \\ &\quad - \left(\int_D U_e \left(\frac{1}{2} \left| \frac{\boldsymbol{q}}{q_{\mathrm{ref}}} \right|^2 \right) \varphi \, \mathrm{d}\boldsymbol{q} \right) \operatorname{div}_{\boldsymbol{x}} \boldsymbol{v} - \int_D U_e \left(\frac{1}{2} \left| \frac{\boldsymbol{q}}{q_{\mathrm{ref}}} \right|^2 \right) \frac{\mathrm{d}\varphi}{\mathrm{d}t} \, \mathrm{d}\boldsymbol{q}. \end{aligned} \tag{71}$$

Now, we are in a position to use the formula for the energy flux $\boldsymbol{j}_e$, see (53), and the Fokker–Planck Equation (8) for the configurational distribution function φ, which yields

$$\begin{aligned}\rho_{\mathrm{s}} c_{\mathrm{V,s}} \frac{\mathrm{d}\theta_{\mathrm{s}}}{\mathrm{d}t} &= -\theta_{\mathrm{s}} \frac{\partial p_{\mathrm{th,s}}}{\partial \theta_{\mathrm{s}}} \operatorname{div}_{\boldsymbol{x}} \boldsymbol{v} + p_{\mathrm{th,s}} \operatorname{div}_{\boldsymbol{x}} \boldsymbol{v} + \mathbb{T} : \mathbb{D} + \operatorname{div}_{\boldsymbol{x}} \left(\kappa \nabla_{\boldsymbol{x}} \theta_{\mathrm{s}} \right) \\ &\quad + \int_D U_e \left(\frac{1}{2} \left| \frac{\boldsymbol{q}}{q_{\mathrm{ref}}} \right|^2 \right) \operatorname{div}_{\boldsymbol{q}} \left((\nabla_{\boldsymbol{x}} \boldsymbol{v}) \boldsymbol{q} \varphi + \boldsymbol{j}_{\varphi,\boldsymbol{q}} \right) \mathrm{d}\boldsymbol{q}. \end{aligned} \tag{72}$$

Let us now focus on the last term. Integration by parts in the last term together with the boundary condition (9) and the constitutive relation (54) for $\boldsymbol{j}_{\varphi,\boldsymbol{q}}$ then gives us

$$\begin{aligned}
\int_D U_e \left(\frac{1}{2} \left| \frac{\boldsymbol{q}}{q_{\mathrm{ref}}} \right|^2 \right) \operatorname{div}_{\boldsymbol{q}} \left((\nabla_{\boldsymbol{x}} \boldsymbol{v}) \boldsymbol{q} \varphi + \boldsymbol{j}_{\varphi,\boldsymbol{q}} \right) \mathrm{d}\boldsymbol{q} &= \int_D \operatorname{div}_{\boldsymbol{q}} \left[U_e \left(\frac{1}{2} \left| \frac{\boldsymbol{q}}{q_{\mathrm{ref}}} \right|^2 \right) \left((\nabla_{\boldsymbol{x}} \boldsymbol{v}) \boldsymbol{q} \varphi + \boldsymbol{j}_{\varphi,\boldsymbol{q}} \right) \right] \mathrm{d}\boldsymbol{q} \\
&\quad - \int_D \left. \frac{\mathrm{d}U_e}{\mathrm{d}s} \right|_{s = \frac{1}{2} \left| \frac{\boldsymbol{q}}{q_{\mathrm{ref}}} \right|^2} \frac{\boldsymbol{q}}{q_{\mathrm{ref}}^2} \bullet \left((\nabla_{\boldsymbol{x}} \boldsymbol{v}) \boldsymbol{q} \varphi + \boldsymbol{j}_{\varphi,\boldsymbol{q}} \right) \mathrm{d}\boldsymbol{q} \\
&= - \int_D \left. \frac{\mathrm{d}U_e}{\mathrm{d}s} \right|_{s = \frac{1}{2} \left| \frac{\boldsymbol{q}}{q_{\mathrm{ref}}} \right|^2} \frac{\boldsymbol{q}}{q_{\mathrm{ref}}^2} \bullet \left((\nabla_{\boldsymbol{x}} \boldsymbol{v}) \boldsymbol{q} \varphi + \boldsymbol{j}_{\varphi,\boldsymbol{q}} \right) \mathrm{d}\boldsymbol{q} \\
&= - \left[\int_D \left. \frac{\mathrm{d}U_e}{\mathrm{d}s} \right|_{s = \frac{1}{2} \left| \frac{\boldsymbol{q}}{q_{\mathrm{ref}}} \right|^2} \frac{\boldsymbol{q}}{q_{\mathrm{ref}}} \otimes \frac{\boldsymbol{q}}{q_{\mathrm{ref}}} \varphi \, \mathrm{d}\boldsymbol{q} \right] : \mathbb{D} - \int_D \left. \frac{\mathrm{d}U_e}{\mathrm{d}s} \right|_{s = \frac{1}{2} \left| \frac{\boldsymbol{q}}{q_{\mathrm{ref}}} \right|^2} \frac{\boldsymbol{q}}{q_{\mathrm{ref}}^2} \bullet \boldsymbol{j}_{\varphi,\boldsymbol{q}} \, \mathrm{d}\boldsymbol{q} \\
&= - \left[\int_D \left. \frac{\mathrm{d}U_e}{\mathrm{d}s} \right|_{s = \frac{1}{2} \left| \frac{\boldsymbol{q}}{q_{\mathrm{ref}}} \right|^2} \frac{\boldsymbol{q}}{q_{\mathrm{ref}}} \otimes \frac{\boldsymbol{q}}{q_{\mathrm{ref}}} \varphi \, \mathrm{d}\boldsymbol{q} \right] : \mathbb{D} \\
&\quad + \frac{2}{\zeta} \int_D \left. \frac{\mathrm{d}U_e}{\mathrm{d}s} \right|_{s = \frac{1}{2} \left| \frac{\boldsymbol{q}}{q_{\mathrm{ref}}} \right|^2} \frac{\boldsymbol{q}}{q_{\mathrm{ref}}^2} \bullet \left[\left(\left. \frac{\mathrm{d}U_e}{\mathrm{d}s} \right|_{s = \frac{1}{2} \left| \frac{\boldsymbol{q}}{q_{\mathrm{ref}}} \right|^2} + \frac{\theta_{\mathrm{s}}}{\theta_{\mathrm{ref}}} \left. \frac{\mathrm{d}U_\eta}{\mathrm{d}s} \right|_{s = \frac{1}{2} \left| \frac{\boldsymbol{q}}{q_{\mathrm{ref}}} \right|^2} \right) \frac{\boldsymbol{q}}{q_{\mathrm{ref}}^2} \varphi + k_{\mathrm{B}} \theta_{\mathrm{s}} \nabla_{\boldsymbol{q}} \varphi \right] \mathrm{d}\boldsymbol{q} \\
&= - \left[\int_D \left. \frac{\mathrm{d}U_e}{\mathrm{d}s} \right|_{s = \frac{1}{2} \left| \frac{\boldsymbol{q}}{q_{\mathrm{ref}}} \right|^2} \frac{\boldsymbol{q}}{q_{\mathrm{ref}}} \otimes \frac{\boldsymbol{q}}{q_{\mathrm{ref}}} \varphi \, \mathrm{d}\boldsymbol{q} \right] : \mathbb{D} \\
&\quad + \frac{2}{\zeta} \int_D \left. \frac{\mathrm{d}U_e}{\mathrm{d}s} \right|_{s = \frac{1}{2} \left| \frac{\boldsymbol{q}}{q_{\mathrm{ref}}} \right|^2} \frac{\boldsymbol{q}}{q_{\mathrm{ref}}^2} \bullet \left(\left. \frac{\mathrm{d}U_e}{\mathrm{d}s} \right|_{s = \frac{1}{2} \left| \frac{\boldsymbol{q}}{q_{\mathrm{ref}}} \right|^2} + \frac{\theta_{\mathrm{s}}}{\theta_{\mathrm{ref}}} \left. \frac{\mathrm{d}U_\eta}{\mathrm{d}s} \right|_{s = \frac{1}{2} \left| \frac{\boldsymbol{q}}{q_{\mathrm{ref}}} \right|^2} \right) \frac{\boldsymbol{q}}{q_{\mathrm{ref}}^2} \varphi \, \mathrm{d}\boldsymbol{q} \\
&\quad + \frac{2 k_{\mathrm{B}} \theta_{\mathrm{s}}}{\zeta} \int_D \left. \frac{\mathrm{d}U_e}{\mathrm{d}s} \right|_{s = \frac{1}{2} \left| \frac{\boldsymbol{q}}{q_{\mathrm{ref}}} \right|^2} \frac{\boldsymbol{q}}{q_{\mathrm{ref}}^2} \bullet \nabla_{\boldsymbol{q}} \varphi \, \mathrm{d}\boldsymbol{q}.
\end{aligned} \tag{73}$$

If we want to, we can also integrate by parts in the last term on the right-hand side, and we get

$$
\begin{aligned}
&\frac{2k_{\mathrm{B}}\theta_{\mathrm{s}}}{\zeta}\int_D \left.\frac{\mathrm{d}U_e}{\mathrm{d}s}\right|_{s=\frac{1}{2}\left|\frac{\boldsymbol{q}}{q_{\mathrm{ref}}}\right|^2}\frac{\boldsymbol{q}}{q_{\mathrm{ref}}^2}\bullet\nabla_{\boldsymbol{q}}\varphi\,\mathrm{d}\boldsymbol{q}\\
&\quad=\frac{2k_{\mathrm{B}}\theta_{\mathrm{s}}}{\zeta}\int_D \mathrm{div}_{\boldsymbol{q}}\left(\left.\frac{\mathrm{d}U_e}{\mathrm{d}s}\right|_{s=\frac{1}{2}\left|\frac{\boldsymbol{q}}{q_{\mathrm{ref}}}\right|^2}\frac{\boldsymbol{q}}{q_{\mathrm{ref}}^2}\varphi\right)\mathrm{d}\boldsymbol{q}-\frac{2k_{\mathrm{B}}\theta_{\mathrm{s}}}{\zeta}\int_D \mathrm{div}_{\boldsymbol{q}}\left(\left.\frac{\mathrm{d}U_e}{\mathrm{d}s}\right|_{s=\frac{1}{2}\left|\frac{\boldsymbol{q}}{q_{\mathrm{ref}}}\right|^2}\frac{\boldsymbol{q}}{q_{\mathrm{ref}}^2}\right)\varphi\,\mathrm{d}\boldsymbol{q}\\
&\quad=-\frac{2k_{\mathrm{B}}\theta_{\mathrm{s}}}{\zeta}\int_D \mathrm{div}_{\boldsymbol{q}}\left(\nabla_{\boldsymbol{q}}U_e\left(\frac{1}{2}\left|\frac{\boldsymbol{q}}{q_{\mathrm{ref}}}\right|^2\right)\right)\varphi\,\mathrm{d}\boldsymbol{q}=-\frac{2k_{\mathrm{B}}\theta_{\mathrm{s}}}{\zeta}\int_D\left(\Delta_{\boldsymbol{q}}U_e\left(\frac{1}{2}\left|\frac{\boldsymbol{q}}{q_{\mathrm{ref}}}\right|^2\right)\right)\varphi\,\mathrm{d}\boldsymbol{q},
\end{aligned}
\tag{74}
$$

where we have again exploited the fact that $\varphi|_{\partial D}=0$. Now, we substitute back into (72), and we arrive at

$$
\begin{aligned}
\rho_{\mathrm{s}}c_{\mathrm{V,s}}\frac{\mathrm{d}\theta_{\mathrm{s}}}{\mathrm{d}t}&=-\theta_{\mathrm{s}}\frac{\partial p_{\mathrm{th,s}}}{\partial\theta_{\mathrm{s}}}\mathrm{div}_{\boldsymbol{x}}\boldsymbol{v}+p_{\mathrm{th,s}}\mathrm{div}_{\boldsymbol{x}}\boldsymbol{v}+\mathbb{T}:\mathbb{D}+\mathrm{div}_{\boldsymbol{x}}\left(\kappa\nabla_{\boldsymbol{x}}\theta_{\mathrm{s}}\right)\\
&\qquad-\left[\int_D\left.\frac{\mathrm{d}U_e}{\mathrm{d}s}\right|_{s=\frac{1}{2}\left|\frac{\boldsymbol{q}}{q_{\mathrm{ref}}}\right|^2}\frac{\boldsymbol{q}}{q_{\mathrm{ref}}}\otimes\frac{\boldsymbol{q}}{q_{\mathrm{ref}}}\varphi\,\mathrm{d}\boldsymbol{q}\right]:\mathbb{D}\\
&\qquad+\frac{2}{\zeta}\int_D\left.\frac{\mathrm{d}U_e}{\mathrm{d}s}\right|_{s=\frac{1}{2}\left|\frac{\boldsymbol{q}}{q_{\mathrm{ref}}}\right|^2}\frac{\boldsymbol{q}}{q_{\mathrm{ref}}^2}\bullet\left(\left.\frac{\mathrm{d}U_e}{\mathrm{d}s}\right|_{s=\frac{1}{2}\left|\frac{\boldsymbol{q}}{q_{\mathrm{ref}}}\right|^2}+\frac{\theta_{\mathrm{s}}}{\theta_{\mathrm{ref}}}\left.\frac{\mathrm{d}U_\eta}{\mathrm{d}s}\right|_{s=\frac{1}{2}\left|\frac{\boldsymbol{q}}{q_{\mathrm{ref}}}\right|^2}\right)\frac{\boldsymbol{q}}{q_{\mathrm{ref}}^2}\varphi\,\mathrm{d}\boldsymbol{q}\\
&\qquad-\frac{2k_{\mathrm{B}}\theta_{\mathrm{s}}}{\zeta}\int_D\left(\Delta_{\boldsymbol{q}}U_e\left(\frac{1}{2}\left|\frac{\boldsymbol{q}}{q_{\mathrm{ref}}}\right|^2\right)\right)\varphi\,\mathrm{d}\boldsymbol{q}.
\end{aligned}
\tag{75}
$$

Finally, we use the formula for the Cauchy stress tensor (62), which is

$$
\mathbb{T}=-p_{\mathrm{th,s}}\mathbb{I}+\lambda\left(\mathrm{div}_{\boldsymbol{x}}\boldsymbol{v}\right)\mathbb{I}+2\nu\mathbb{D}-2k_{\mathrm{B}}\theta_{\mathrm{s}}n_{\mathrm{p}}\mathbb{I}+\int_D\left[\left(\left.\frac{\mathrm{d}U_e}{\mathrm{d}s}\right|_{s=\frac{1}{2}\left|\frac{\boldsymbol{q}}{q_{\mathrm{ref}}}\right|^2}+\frac{\theta_{\mathrm{s}}}{\theta_{\mathrm{ref}}}\left.\frac{\mathrm{d}U_\eta}{\mathrm{d}s}\right|_{s=\frac{1}{2}\left|\frac{\boldsymbol{q}}{q_{\mathrm{ref}}}\right|^2}\right)\frac{\boldsymbol{q}}{q_{\mathrm{ref}}}\otimes\frac{\boldsymbol{q}}{q_{\mathrm{ref}}}\varphi\right]\mathrm{d}\boldsymbol{q},
\tag{76}
$$

which, upon substitution into (75), yields

$$
\begin{aligned}
\rho_{\mathrm{s}}c_{\mathrm{V,s}}\frac{\mathrm{d}\theta_{\mathrm{s}}}{\mathrm{d}t}&=-\theta_{\mathrm{s}}\frac{\partial p_{\mathrm{th,s}}}{\partial\theta_{\mathrm{s}}}\mathrm{div}_{\boldsymbol{x}}\boldsymbol{v}+\mathrm{div}_{\boldsymbol{x}}\left(\kappa\nabla_{\boldsymbol{x}}\theta_{\mathrm{s}}\right)+\lambda\left(\mathrm{div}_{\boldsymbol{x}}\boldsymbol{v}\right)^2+2\nu\mathbb{D}:\mathbb{D}\\
&\qquad-2k_{\mathrm{B}}\theta_{\mathrm{s}}n_{\mathrm{p}}\mathrm{div}_{\boldsymbol{x}}\boldsymbol{v}+\left[\int_D\frac{\theta_{\mathrm{s}}}{\theta_{\mathrm{ref}}}\left.\frac{\mathrm{d}U_\eta}{\mathrm{d}s}\right|_{s=\frac{1}{2}\left|\frac{\boldsymbol{q}}{q_{\mathrm{ref}}}\right|^2}\frac{\boldsymbol{q}}{q_{\mathrm{ref}}}\otimes\frac{\boldsymbol{q}}{q_{\mathrm{ref}}}\varphi\,\mathrm{d}\boldsymbol{q}\right]:\mathbb{D}\\
&\qquad+\frac{2}{\zeta}\int_D\left.\frac{\mathrm{d}U_e}{\mathrm{d}s}\right|_{s=\frac{1}{2}\left|\frac{\boldsymbol{q}}{q_{\mathrm{ref}}}\right|^2}\frac{\boldsymbol{q}}{q_{\mathrm{ref}}^2}\bullet\left(\left.\frac{\mathrm{d}U_e}{\mathrm{d}s}\right|_{s=\frac{1}{2}\left|\frac{\boldsymbol{q}}{q_{\mathrm{ref}}}\right|^2}+\frac{\theta_{\mathrm{s}}}{\theta_{\mathrm{ref}}}\left.\frac{\mathrm{d}U_\eta}{\mathrm{d}s}\right|_{s=\frac{1}{2}\left|\frac{\boldsymbol{q}}{q_{\mathrm{ref}}}\right|^2}\right)\frac{\boldsymbol{q}}{q_{\mathrm{ref}}^2}\varphi\,\mathrm{d}\boldsymbol{q}\\
&\qquad-\frac{2k_{\mathrm{B}}\theta_{\mathrm{s}}}{\zeta}\int_D\left(\Delta_{\boldsymbol{q}}U_e\left(\frac{1}{2}\left|\frac{\boldsymbol{q}}{q_{\mathrm{ref}}}\right|^2\right)\right)\varphi\,\mathrm{d}\boldsymbol{q}.
\end{aligned}
\tag{77}
$$

This is the sought evolution equation for the temperature field. A brief inspection of (77) reveals that the evolution equation for the temperature is not affected by shifts of the values of the potentials U_e and U_η and the value of scaling constant K.

5.4. Summary

The system of governing equations for the solvent density $\rho_{\mathrm{s}}(t, \boldsymbol{x})$, velocity $\boldsymbol{v}(t, \boldsymbol{x})$, solvent temperature $\theta_{\mathrm{s}}(t, \boldsymbol{x})$, and configurational distribution function $\varphi(t, \boldsymbol{x}, \boldsymbol{q})$ read, as follows:

$$\frac{\mathrm{d}\rho_{\mathrm{s}}}{\mathrm{d}t} + \rho_{\mathrm{s}} \mathrm{div}_{\boldsymbol{x}} \boldsymbol{v} = 0, \tag{78a}$$

$$\rho_{\mathrm{s}} \frac{\mathrm{d}\boldsymbol{v}}{\mathrm{d}t} = \mathrm{div}_{\boldsymbol{x}} \mathbb{T} + \rho_{\mathrm{s}} \boldsymbol{b}, \tag{78b}$$

$$\frac{\partial \varphi}{\partial t} + \mathrm{div}_{\boldsymbol{x}} \left(\boldsymbol{v}\varphi - \frac{k_{\mathrm{B}}\theta_{\mathrm{s}}}{2\zeta} \nabla_{\boldsymbol{x}} \varphi \right) + \mathrm{div}_{\boldsymbol{q}} \left((\nabla_{\boldsymbol{x}} \boldsymbol{v}) \boldsymbol{q} \varphi - \frac{2\boldsymbol{F}}{\zeta} \varphi - \frac{2 k_{\mathrm{B}} \theta_{\mathrm{s}}}{\zeta} \nabla_{\boldsymbol{q}} \varphi \right) = 0, \tag{78c}$$

where the spring force $\boldsymbol{F}$ is given via the potentials U_e and U_η by the formula

$$\boldsymbol{F} = \nabla_{\boldsymbol{q}} \left[U_e \left(\frac{1}{2} \left| \frac{\boldsymbol{q}}{q_{\mathrm{ref}}} \right|^2 \right) + \frac{\theta_{\mathrm{s}}}{\theta_{\mathrm{ref}}} U_\eta \left(\frac{1}{2} \left| \frac{\boldsymbol{q}}{q_{\mathrm{ref}}} \right|^2 \right) \right] = \left(\left. \frac{\mathrm{d}U_e}{\mathrm{d}s} \right|_{s=\frac{1}{2}\left|\frac{\boldsymbol{q}}{q_{\mathrm{ref}}}\right|^2} + \frac{\theta_{\mathrm{s}}}{\theta_{\mathrm{ref}}} \left. \frac{\mathrm{d}U_\eta}{\mathrm{d}s} \right|_{s=\frac{1}{2}\left|\frac{\boldsymbol{q}}{q_{\mathrm{ref}}}\right|^2} \right) \frac{\boldsymbol{q}}{q_{\mathrm{ref}}^2}, \tag{78d}$$

and the Cauchy stress tensor $\mathbb{T}$ is given by the formula

$$\mathbb{T} = -p_{\mathrm{th,s}} \mathbb{I} + \lambda \left(\mathrm{div}_{\boldsymbol{x}} \boldsymbol{v} \right) \mathbb{I} + 2\nu \mathbb{D} - 2 k_{\mathrm{B}} \theta_{\mathrm{s}} n_{\mathrm{p}} \mathbb{I} + \int_D \boldsymbol{F} \otimes \boldsymbol{q} \varphi \, \mathrm{d}\boldsymbol{q}. \tag{78e}$$

The temperature evolution equation reads

$$\begin{aligned} \rho_{\mathrm{s}} c_{\mathrm{V,s}} \frac{\mathrm{d}\theta_{\mathrm{s}}}{\mathrm{d}t} = &-\theta_{\mathrm{s}} \frac{\partial p_{\mathrm{th,s}}}{\partial \theta_{\mathrm{s}}} \mathrm{div}_{\boldsymbol{x}} \boldsymbol{v} + \mathrm{div}_{\boldsymbol{x}} \left(\kappa \nabla_{\boldsymbol{x}} \theta_{\mathrm{s}} \right) + \lambda \left(\mathrm{div}_{\boldsymbol{x}} \boldsymbol{v} \right)^2 + 2\nu \mathbb{D} : \mathbb{D} - 2 k_{\mathrm{B}} \theta_{\mathrm{s}} n_{\mathrm{p}} \mathrm{div}_{\boldsymbol{x}} \boldsymbol{v} \\ &+ \left[\int_D \left(\nabla_{\boldsymbol{q}} \frac{\theta_{\mathrm{s}}}{\theta_{\mathrm{ref}}} U_\eta \right) \otimes \boldsymbol{q} \varphi \, \mathrm{d}\boldsymbol{q} \right] : \mathbb{D} + \frac{2}{\zeta} \int_D \left(\nabla_{\boldsymbol{q}} U_e \right) \bullet \nabla_{\boldsymbol{q}} \left(U_e + \frac{\theta_{\mathrm{s}}}{\theta_{\mathrm{ref}}} U_\eta \right) \mathrm{d}\boldsymbol{q} \\ &- \frac{2 k_{\mathrm{B}} \theta_{\mathrm{s}}}{\zeta} \int_D \left[\Delta_{\boldsymbol{q}} U_e \right] \varphi \, \mathrm{d}\boldsymbol{q}, \end{aligned} \tag{78f}$$

and the thermodynamic pressure $p_{\mathrm{th,s}}$ and the specific heat at constant volume $c_{\mathrm{V,s}}$ are given in terms of the derivative of the solvent specific Helmholtz free energy ψ_{s}, as follows:

$$p_{\mathrm{th,s}}(\theta_{\mathrm{s}}, \rho_{\mathrm{s}}) = \rho_{\mathrm{s}}^2 \frac{\partial \psi_{\mathrm{s}}}{\partial \rho_{\mathrm{s}}}, \tag{78g}$$

$$c_{\mathrm{V,s}}(\theta_{\mathrm{s}}, \rho_{\mathrm{s}}) = -\theta_{\mathrm{s}} \frac{\partial^2 \psi_{\mathrm{s}}}{\partial \theta_{\mathrm{s}}^2}, \tag{78h}$$

We recall that the solvent density ρ_{s} is in the given model identified with the density of the whole solvent-polymeric chains mixture. We note that if the spring potential only contains the entropic part, that is if $U_e = 0$, then the governing equations simplify considerably. This system of governing equations is essentially the same as that reported by Öttinger and Grmela [18], albeit the model has been derived in a different manner. In fact our approach is similar to that used in the derivation of macroscopic viscoelastic rate-type models, see especially Rajagopal and Srinivasa [37], Málek et al. [38], Hron et al. [17], Málek et al. [39], Málek et al. [40], and Dostalík et al. [41]. For a coupling between microscopic and macroscopic models, see also Souček et al. [42].

The boundary condition in the configurational space D reads

$$\left. \left[(\nabla_{\boldsymbol{x}} \boldsymbol{v}) \boldsymbol{q} \varphi - \frac{2\boldsymbol{F}}{\zeta} \varphi - \frac{2 k_{\mathrm{B}} \theta_{\mathrm{s}}}{\zeta} \nabla_{\boldsymbol{q}} \varphi \right] \bullet \boldsymbol{n}_{\boldsymbol{q}} \right|_{\partial D} = 0, \tag{79}$$

see discussion in Section 3.2. Because we are working with a model with centre-of-mass diffusion, we also need a boundary condition for the configurational distribution function in the physical space. If we consider a vessel Ω with an impermeable rigid wall, we set

$$\left.\boldsymbol{j}_{\varphi,\boldsymbol{x}} \bullet \boldsymbol{n}_{\boldsymbol{x}}\right|_{\partial\Omega} = 0, \tag{80}$$

which, by virtue of (52), means that $\left.\nabla_{\boldsymbol{x}}\varphi \bullet \boldsymbol{n}_{\boldsymbol{x}}\right|_{\partial\Omega} = 0$. Regarding the remaining boundary conditions in physical space, we can opt for any standard boundary conditions. Because we have access to the velocity field $\boldsymbol{v}$ as well as to the Cauchy stress tensor $\mathbb{T}$, we can choose from plethora of boundary conditions used for flows of polymeric fluids, see, for example, Hatzikiriakos [43] or Málek and Průša [21].

6. Stability

Following Coleman and Greenberg [44] and Coleman [19], see also Gurtin [45,46], Grmela and Öttinger [47] and Bulíček et al. [20] for further discussion, we can exploit the thermodynamic basis of the derived model in a rudimentary stability analysis of thermo-mechanical processes described by the corresponding governing equations. In particular, it is straightforward to investigate the finite amplitude (nonlinear) stability of the spatially homogeneous stationary states in a thermodynamically isolated container.

The spatially homogeneous equilibrium stationary state $\theta_{\mathrm{s,eq}}$, $\rho_{\mathrm{s,eq}}$, φ_{eq} and $\boldsymbol{v}_{\mathrm{eq}}$ is, in our case, given as

$$\theta_{\mathrm{s,eq}} = \widehat{\theta_{\mathrm{s}}}, \tag{81a}$$

$$\rho_{\mathrm{s,eq}} = \widehat{\rho_{\mathrm{s}}}, \tag{81b}$$

$$\varphi_{\mathrm{eq}} = M_{\widehat{n_{\mathrm{p}}},\widehat{\theta_{\mathrm{s}}}}, \tag{81c}$$

$$\boldsymbol{v}_{\mathrm{eq}} = \boldsymbol{0}. \tag{81d}$$

The symbol $\widehat{n_{\mathrm{p}}}$ is the spatially homogeneous polymer number density, which is $\widehat{n_{\mathrm{p}}} = \frac{N}{|\Omega|}$, where N is the total number of polymeric chains in the container and $|\Omega|$ is the volume of the container, the solvent density $\widehat{\rho_{\mathrm{s}}}$ is the spatially homogeneous density, which is $\widehat{\rho_{\mathrm{s}}} = \frac{M}{|\Omega|}$, where M is the total mass of the solvent in the container. The symbol $\widehat{\theta_{\mathrm{s}}}$ denotes a spatially homogeneous temperature field, and $M_{\widehat{n_{\mathrm{p}}},\widehat{\theta_{\mathrm{s}}}}$ stands for the equilibrium configurational distribution function (22) discussed in Section 3.5. Clearly, the quadruple (81) is a solution to the governing equations subject to boundary conditions

$$\left.\boldsymbol{v}\right|_{\partial\Omega} = \boldsymbol{0}, \tag{82a}$$

$$\left.\nabla_{\boldsymbol{x}}\varphi \bullet \boldsymbol{n}_{\boldsymbol{x}}\right|_{\partial\Omega} = 0, \tag{82b}$$

$$\left.\nabla_{\boldsymbol{x}}\theta_{\mathrm{s}} \bullet \boldsymbol{n}_{\boldsymbol{x}}\right|_{\partial\Omega} = 0, \tag{82c}$$

that guarantee that the energy flux $\boldsymbol{j}_e$, $\boldsymbol{j}_\eta$, and $\boldsymbol{j}_{\varphi,\boldsymbol{x}}$, see (53), (58), and (52), vanish on the container wall. We also have the standard boundary condition in the configurational space (9), which is

$$\left.\left(\left(\nabla_{\boldsymbol{x}}\boldsymbol{v}\right)\boldsymbol{q}\varphi + \boldsymbol{j}_{\varphi,\boldsymbol{q}}\right) \bullet \boldsymbol{n}_{\boldsymbol{q}}\right|_{\partial D} = 0, \tag{82d}$$

where $\boldsymbol{j}_{\varphi,\boldsymbol{q}}$ is given by (54). If we denote

$$S_{\widehat{\theta}} =_{\mathrm{def}} \int_{\Omega} \rho_{\mathrm{s}} \widehat{\theta_{\mathrm{s}}} \eta \, \mathrm{dv}, \tag{83a}$$

$$S =_{\mathrm{def}} \int_{\Omega} \rho_{\mathrm{s}} \eta \, \mathrm{dv}, \tag{83b}$$

$$E_{\mathrm{tot}} =_{\mathrm{def}} \int_{\Omega} \left(\rho_{\mathrm{s}} e + \frac{1}{2} \rho_{\mathrm{s}} \left| \boldsymbol{v} \right|^2 \right) \mathrm{dv}, \tag{83c}$$

then using the governing equations it is straightforward to see that, since all of the fluxes through the vessel wall vanish, the net total energy E_{tot} is constant and the net total entropy S is a nondecreasing function in time. Moreover, the total mass of the solvent and the number of polymeric chains are also preserved in time.

Consequently, the following functional is a reasonable candidate for a Lyapunov type functional for the analysis of the stability of the stationary spatially homogeneous state with temperature $\widehat{\theta_{\mathrm{s}}}$,

$$\mathcal{V}_{\mathrm{meq}} = - \left\{ S_{\widehat{\theta_{\mathrm{s}}}} - \left(E_{\mathrm{tot}} - \widehat{E_{\mathrm{tot}}} \right) \right\}, \tag{84}$$

see, for example, Bulíček et al. [20] for details, where $\widehat{E_{\mathrm{tot}}}$ denotes the net total energy at the spatially homogeneous stationary state (we use the nomenclature Lyapunov type functional, since we will only show the decay along trajectories and non-negativity of the functional everywhere except at the equilibrium. We will not investigate the link between the proposed functional and a suitable norm in the given state space, as this is beyond the scope of the current contribution). The rationale for the choice of such a functional is apparent from the following manipulation

$$\frac{\mathrm{d}\mathcal{V}_{\mathrm{meq}}}{\mathrm{d}t} = - \frac{\mathrm{d}}{\mathrm{d}t} \left\{ S_{\widehat{\theta}} - \left(E_{\mathrm{tot}} - \widehat{E_{\mathrm{tot}}} \right) \right\} = -\widehat{\theta} \frac{\mathrm{d}S}{\mathrm{d}t} = -\widehat{\theta} \int_{\Omega} \xi \, \mathrm{dv}, \tag{85}$$

where ξ denotes the entropy production, which is a nonnegative quantity that vanishes at the spatially homogeneous stationary state (81). In the current case, we are forced however to modify the functional by explicitly adding zero terms

$$\mathcal{V}_{\mathrm{meq}} = - \left\{ S_{\widehat{\theta_{\mathrm{s}}}} - \left(E_{\mathrm{tot}} - \widehat{E_{\mathrm{tot}}} \right) \right\} + \lambda_2 \int_{\Omega} \left(\rho_{\mathrm{s}} - \widehat{\rho_{\mathrm{s}}} \right) \mathrm{dv} + \lambda_3 \int_{\Omega} \left(n_{\mathrm{p}} - \widehat{n_{\mathrm{p}}} \right) \mathrm{dv}, \tag{86}$$

which help us to articulate the constraints of mass conservation and the conservation of total number of polymeric chains. While the values of Lagrange multipliers can be found *a priori*, see, for example, Coleman [19] for a discussion in the case of a compressible fluid, we shall not proceed in that direction (in fact we have already tacitly identified one of the multipliers: the equilibrium temperature $\widehat{\theta_{\mathrm{s}}}$ is the multiplier that enforces the conservation of net total energy). We shall find instead the multipliers on-the-fly. Indeed, from the pragmatic point of view, we will need the additional zero terms (after the integration) to show the nonnegativity of the integrands in $\mathcal{V}_{\mathrm{meq}}$.

Finally, we note that, in order to ensure that the functional vanishes at the equilibrium, we need to shift the functional by a constant value. We will denote the shifted functional by the same symbol, since this shift has no impact on the time evolution of the functional: it is just a matter of normalisation.

6.1. Outline of the Construction of the Lyapunov Like Functional

We see that the explicit formula for $\mathcal{V}_{\mathrm{meq}}$ reads

$$\mathcal{V}_{\mathrm{meq}} = \int_{\Omega} \left(g \left(\theta_{\mathrm{s}}, \rho_{\mathrm{s}}, \varphi \| \widehat{\theta_{\mathrm{s}}}, \widehat{\rho_{\mathrm{s}}}, \widehat{\varphi} \right) + \frac{1}{2} \rho_{\mathrm{s}} \left| \boldsymbol{v} \right|^2 \right) \mathrm{dv} \tag{87}$$

where

$$g \left(\theta_{\mathrm{s}}, \rho_{\mathrm{s}}, \varphi \| \widehat{\theta_{\mathrm{s}}}, \widehat{\rho_{\mathrm{s}}}, \widehat{\varphi} \right) =_{\mathrm{def}} - \left[\rho_{\mathrm{s}} \widehat{\theta_{\mathrm{s}}} \eta(\theta_{\mathrm{s}}, \rho_{\mathrm{s}}, \varphi) - \rho_{\mathrm{s}} \left(e(\theta_{\mathrm{s}}, \rho_{\mathrm{s}}, \varphi) - e(\widehat{\theta_{\mathrm{s}}}, \widehat{\rho_{\mathrm{s}}}, \widehat{\varphi}) \right) \right]. \tag{88}$$

By virtue of (24) and (25), we can further split the internal energy and the entropy into their respective solvent part and polymeric part:

$$e\left(\theta_{\mathrm{s}}, \rho_{\mathrm{s}}, \varphi\right) = e_{\mathrm{s}}\left(\theta_{\mathrm{s}}, \rho_{\mathrm{s}}\right) + e_{\mathrm{p}}\left(\theta_{\mathrm{s}}, \rho_{\mathrm{s}}, \varphi\right), \tag{89a}$$

$$\eta\left(\theta_{\mathrm{s}}, \rho_{\mathrm{s}}, \varphi\right) = \eta_{\mathrm{s}}\left(\theta_{\mathrm{s}}, \rho_{\mathrm{s}}\right) + \eta_{\mathrm{p}}\left(\theta_{\mathrm{s}}, \rho_{\mathrm{s}}, \varphi\right), \tag{89b}$$

where

$$e_{\mathrm{p}}\left(\theta_{\mathrm{s}}, \rho_{\mathrm{s}}, \varphi\right) =_{\mathrm{def}} \frac{1}{\rho_{\mathrm{s}}} \int_{D} U_{e}\left(\frac{1}{2}\left|\frac{\boldsymbol{q}}{q_{\mathrm{ref}}}\right|^{2}\right) \varphi \,\mathrm{d}\boldsymbol{q}, \tag{90a}$$

$$\eta_{\mathrm{p}}\left(\theta_{\mathrm{s}}, \rho_{\mathrm{s}}, \varphi\right) =_{\mathrm{def}} -\frac{k_{\mathrm{B}}}{\rho_{\mathrm{s}}} \int_{D}\left(\frac{U_{\eta}\left(\frac{1}{2}\left|\frac{\boldsymbol{q}}{q_{\mathrm{ref}}}\right|^{2}\right)}{k_{\mathrm{B}} \theta_{\mathrm{ref}}} \varphi + \varphi \ln \frac{\varphi}{K}\right) \mathrm{d}\boldsymbol{q}. \tag{90b}$$

Next, we split the function g into a solvent and a polymeric part as well

$$g\left(\theta_{\mathrm{s}}, \rho_{\mathrm{s}}, \varphi \,\middle\|\, \widehat{\theta}_{\mathrm{s}}, \widehat{\rho}_{\mathrm{s}}, \widehat{\varphi}\right) = g_{\mathrm{s}}\left(\theta_{\mathrm{s}}, \rho_{\mathrm{s}} \,\middle\|\, \widehat{\theta}_{\mathrm{s}}, \widehat{\rho}_{\mathrm{s}},\right) + g_{\mathrm{p}}\left(\theta_{\mathrm{s}}, \rho_{\mathrm{s}}, \varphi \,\middle\|\, \widehat{\theta}_{\mathrm{s}}, \widehat{\rho}_{\mathrm{s}}, \widehat{\varphi}\right), \tag{91}$$

where

$$g_{\mathrm{s}}\left(\theta_{\mathrm{s}}, \rho_{\mathrm{s}} \,\middle\|\, \widehat{\theta}_{\mathrm{s}}, \widehat{\rho}_{\mathrm{s}}\right) =_{\mathrm{def}} -\left[\rho_{\mathrm{s}} \widehat{\theta}_{\mathrm{s}} \eta_{\mathrm{s}}(\theta_{\mathrm{s}}, \rho_{\mathrm{s}}) - \rho_{\mathrm{s}}\left(e_{\mathrm{s}}(\theta_{\mathrm{s}}, \rho_{\mathrm{s}}) - e_{\mathrm{s}}(\widehat{\theta}_{\mathrm{s}}, \widehat{\rho}_{\mathrm{s}})\right)\right], \tag{92a}$$

$$g_{\mathrm{p}}\left(\theta_{\mathrm{s}}, \rho_{\mathrm{s}}, \varphi \,\middle\|\, \widehat{\theta}_{\mathrm{s}}, \widehat{\rho}_{\mathrm{s}}, \widehat{\varphi}\right) =_{\mathrm{def}} -\left[\rho_{\mathrm{s}} \widehat{\theta}_{\mathrm{s}} \eta_{\mathrm{p}}(\theta_{\mathrm{s}}, \rho_{\mathrm{s}}, \varphi) - \rho_{\mathrm{s}}\left(e_{\mathrm{p}}(\theta_{\mathrm{s}}, \rho_{\mathrm{s}}, \varphi) - e_{\mathrm{p}}(\widehat{\theta}_{\mathrm{s}}, \widehat{\rho}_{\mathrm{s}}, \widehat{\varphi})\right)\right], \tag{92b}$$

and, finally, we also split the whole functional, which is we write

$$\mathcal{V}_{\mathrm{meq}} = \int_{\Omega} \frac{1}{2} \rho_{\mathrm{s}} |\boldsymbol{v}|^{2} \,\mathrm{dv} + \underbrace{\int_{\Omega} g_{\mathrm{s}}\left(\theta_{\mathrm{s}}, \rho_{\mathrm{s}} \,\middle\|\, \widehat{\theta}_{\mathrm{s}}, \widehat{\rho}_{\mathrm{s}}\right) \mathrm{dv}}_{\mathcal{V}_{\mathrm{meq,s}}} + \underbrace{\int_{\Omega} g_{\mathrm{p}}\left(\theta_{\mathrm{s}}, \rho_{\mathrm{s}}, \varphi \,\middle\|\, \widehat{\theta}_{\mathrm{s}}, \widehat{\rho}_{\mathrm{s}}, \widehat{\varphi}\right) \mathrm{dv}}_{\mathcal{V}_{\mathrm{meq,p}}}. \tag{93}$$

We shall first find an explicit formula for the polymeric contribution, see Section 6.2, and then we introduce an explicit equation of state for the solvent, and we find the formula for the solvent contribution, see Section 6.3.

6.2. Polymeric Part

First, we choose the characteristic temperature θ_{ref} in the polymeric part of the Helmholtz free energy (23) as $\widehat{\theta}_{\mathrm{s}}$, which is we set

$$\theta_{\mathrm{ref}} =_{\mathrm{def}} \widehat{\theta}_{\mathrm{s}}. \tag{94}$$

We are using the fact that the temperature field $\widehat{\theta}_{\mathrm{s}}$ at equilibrium is constant in space and time. Straightforward substitution of (90) into (92b) then yields

$$g_{\mathrm{p}}\left(\theta_{\mathrm{s}}, \rho_{\mathrm{s}}, \varphi \,\middle\|\, \widehat{\theta}_{\mathrm{s}}, \widehat{\rho}_{\mathrm{s}}, \widehat{\varphi}\right) = k_{\mathrm{B}} \widehat{\theta}_{\mathrm{s}} \int_{D}\left(\frac{U_{\eta}\left(\frac{1}{2}\left|\frac{\boldsymbol{q}}{q_{\mathrm{ref}}}\right|^{2}\right)}{k_{\mathrm{B}} \widehat{\theta}_{\mathrm{s}}} \varphi + \varphi \ln \frac{\varphi}{K}\right) \mathrm{d}\boldsymbol{q} + \int_{D} U_{e}\left(\frac{1}{2}\left|\frac{\boldsymbol{q}}{q_{\mathrm{ref}}}\right|^{2}\right) \varphi \,\mathrm{d}\boldsymbol{q} - \int_{D} U_{e}\left(\frac{1}{2}\left|\frac{\boldsymbol{q}}{q_{\mathrm{ref}}}\right|^{2}\right) \widehat{\varphi} \,\mathrm{d}\boldsymbol{q}. \tag{95}$$

Now, we can combine the terms with the potentials to deduce that

$$g_{\mathrm{p}}\left(\theta_{\mathrm{s}},\rho_{\mathrm{s}},\varphi \,\middle\|\, \widehat{\theta_{\mathrm{s}}},\widehat{\rho_{\mathrm{s}}},\widehat{\varphi}\right) = k_{\mathrm{B}}\widehat{\theta_{\mathrm{s}}}\int_D \varphi \ln\left(\frac{\varphi}{K\mathrm{e}^{-\frac{U_\eta\left(\frac{1}{2}\left|\frac{\boldsymbol{q}}{q_{\mathrm{ref}}}\right|^2\right)+U_e\left(\frac{1}{2}\left|\frac{\boldsymbol{q}}{q_{\mathrm{ref}}}\right|^2\right)}{k_{\mathrm{B}}\widehat{\theta_{\mathrm{s}}}}}}\right)\mathrm{d}\boldsymbol{q} - \int_D U_e\left(\frac{1}{2}\left|\frac{\boldsymbol{q}}{q_{\mathrm{ref}}}\right|^2\right)\widehat{\varphi}\,\mathrm{d}\boldsymbol{q}. \tag{96}$$

Because the choice of the normalisation factor K has no impact on the dynamics of the system, we choose it to serve our objective. We fix the normalisation factor K as

$$K =_{\mathrm{def}} \frac{\widehat{n_{\mathrm{p}}}}{\int_D \mathrm{e}^{-\frac{U_\eta\left(\frac{1}{2}\left|\frac{\boldsymbol{q}}{q_{\mathrm{ref}}}\right|^2\right)+U_e\left(\frac{1}{2}\left|\frac{\boldsymbol{q}}{q_{\mathrm{ref}}}\right|^2\right)}{k_{\mathrm{B}}\widehat{\theta_{\mathrm{s}}}}}\,\mathrm{d}\boldsymbol{q}}, \tag{97}$$

Using the notation introduced in (22), we see that (96) with the constant K chosen as in (97) reduces to

$$g_{\mathrm{p}}\left(\theta_{\mathrm{s}},\rho_{\mathrm{s}},\varphi \,\middle\|\, \widehat{\theta_{\mathrm{s}}},\widehat{\rho_{\mathrm{s}}},\widehat{\varphi}\right) = k_{\mathrm{B}}\widehat{\theta_{\mathrm{s}}}\int_D \varphi \ln\left(\frac{\varphi}{M_{\widehat{n_{\mathrm{p}}},\widehat{\theta_{\mathrm{s}}}}}\right)\mathrm{d}\boldsymbol{q} - \int_D U_e\left(\frac{1}{2}\left|\frac{\boldsymbol{q}}{q_{\mathrm{ref}}}\right|^2\right)\widehat{\varphi}\,\mathrm{d}\boldsymbol{q}. \tag{98}$$

The last term is a constant in time and space, hence we can safely ignore it. It only shifts the value of g_{p} and consequently of the functional $\mathcal{V}_{\mathrm{meq}}$. If we ignore it, we get in the end a functional that vanishes at equilibrium, which is a desired property. We see that

$$\frac{1}{M_{\widehat{n_{\mathrm{p}}},\widehat{\theta_{\mathrm{s}}}}} = \frac{1}{M_{n_{\mathrm{p}},\widehat{\theta_{\mathrm{s}}}}}\frac{n_{\mathrm{p}}}{\widehat{n_{\mathrm{p}}}}, \tag{99}$$

and by virtue of the normalisation constraint (5), it follows that

$$\begin{aligned} k_{\mathrm{B}}\widehat{\theta_{\mathrm{s}}}\int_D \varphi \ln\left(\frac{\varphi}{M_{\widehat{n_{\mathrm{p}}},\widehat{\theta_{\mathrm{s}}}}}\right)\mathrm{d}\boldsymbol{q} &= k_{\mathrm{B}}\widehat{\theta_{\mathrm{s}}}\int_D \varphi \ln\left(\frac{\varphi}{M_{n_{\mathrm{p}},\widehat{\theta_{\mathrm{s}}}}}\frac{n_{\mathrm{p}}}{\widehat{n_{\mathrm{p}}}}\right)\mathrm{d}\boldsymbol{q} \\ &= k_{\mathrm{B}}\widehat{\theta_{\mathrm{s}}}\int_D \varphi \ln\left(\frac{\varphi}{M_{n_{\mathrm{p}},\widehat{\theta_{\mathrm{s}}}}}\right)\mathrm{d}\boldsymbol{q} + k_{\mathrm{B}}\widehat{\theta_{\mathrm{s}}}\int_D \varphi \ln\left(\frac{n_{\mathrm{p}}}{\widehat{n_{\mathrm{p}}}}\right)\mathrm{d}\boldsymbol{q} \\ &= k_{\mathrm{B}}\widehat{\theta_{\mathrm{s}}}\int_D M_{n_{\mathrm{p}},\widehat{\theta_{\mathrm{s}}}}\left[\frac{\varphi}{M_{n_{\mathrm{p}},\widehat{\theta_{\mathrm{s}}}}}\ln\left(\frac{\varphi}{M_{n_{\mathrm{p}},\widehat{\theta_{\mathrm{s}}}}}\right) - \frac{\varphi}{M_{n_{\mathrm{p}},\widehat{\theta_{\mathrm{s}}}}} + 1\right]\mathrm{d}\boldsymbol{q} + k_{\mathrm{B}}\widehat{\theta_{\mathrm{s}}}n_{\mathrm{p}}\ln\left(\frac{n_{\mathrm{p}}}{\widehat{n_{\mathrm{p}}}}\right). \end{aligned} \tag{100}$$

It is straightforward to check that the function in the square bracket, $f(x) =_{\mathrm{def}} x\ln x - x + 1$, is for $x \in (0,+\infty)$ nonnegative and vanishes if and only if $x = 1$, which is if

$$\frac{\varphi}{M_{n_{\mathrm{p}},\widehat{\theta_{\mathrm{s}}}}} = 1. \tag{101}$$

Therefore, the corresponding term is related to the equilibration of the configurational distribution function φ to $M_{n_{\mathrm{p}},\widehat{\theta_{\mathrm{s}}}}$. We note that $M_{n_{\mathrm{p}},\widehat{\theta_{\mathrm{s}}}}$ depends on the local particle number density n_{p} and not on the equilibrium particle number density $\widehat{n_{\mathrm{p}}}$. Consequently, from this term only, we cannot monitor the progress of n_{p} to $\widehat{n_{\mathrm{p}}}$. This piece of information must be inferred from elsewhere.

Now, we are in a position to construct the functional $\mathcal{V}_{\mathrm{meq,p}}$. In order to guarantee the nonnegativity of the functional we need to add a term that reflects the additional constraints imposed on the closed system, namely, the constraint on the constant total number of polymeric chains. See the discussion in the introductory part of this section. We set

$$\mathcal{V}_{\mathrm{meq,p}} = \int_{\Omega} g_{\mathrm{p}} \left(\theta_{\mathrm{s}}, \rho_{\mathrm{s}}, \varphi \| \widehat{\theta_{\mathrm{s}}}, \widehat{\rho_{\mathrm{s}}}, \widehat{\varphi} \right) \, \mathrm{d}v - k_{\mathrm{B}} \widehat{\theta_{\mathrm{s}}} \int_{\Omega} \left(n_{\mathrm{p}} - \widehat{n_{\mathrm{p}}} \right) \, \mathrm{d}v, \tag{102}$$

which, by virtue of (98) and (100), yields

$$\begin{aligned} \mathcal{V}_{\mathrm{meq,p}} = k_{\mathrm{B}} \widehat{\theta_{\mathrm{s}}} \int_{\Omega} \left(\int_{D} M_{n_{\mathrm{p}}, \widehat{\theta_{\mathrm{s}}}} \left[\frac{\varphi}{M_{n_{\mathrm{p}}, \widehat{\theta_{\mathrm{s}}}}} \ln \left(\frac{\varphi}{M_{n_{\mathrm{p}}, \widehat{\theta_{\mathrm{s}}}}} \right) - \frac{\varphi}{M_{n_{\mathrm{p}}, \widehat{\theta_{\mathrm{s}}}}} + 1 \right] \mathrm{d}\boldsymbol{q} \right) \mathrm{d}v \\ + k_{\mathrm{B}} \widehat{\theta_{\mathrm{s}}} \int_{\Omega} \widehat{n_{\mathrm{p}}} \left[\frac{n_{\mathrm{p}}}{\widehat{n_{\mathrm{p}}}} \ln \left(\frac{n_{\mathrm{p}}}{\widehat{n_{\mathrm{p}}}} \right) - \frac{n_{\mathrm{p}}}{\widehat{n_{\mathrm{p}}}} + 1 \right] \mathrm{d}v. \end{aligned} \tag{103}$$

A brief inspection of the last term reveals that the term is nonnegative, and that it vanishes if and only if

$$\frac{n_{\mathrm{p}}}{\widehat{n_{\mathrm{p}}}} = 1 \tag{104}$$

everywhere in the domain Ω. Consequently, we are done with the polymeric contribution to the functional $\mathcal{V}_{\mathrm{meq,p}}$ and we can proceed to the solvent contribution.

6.3. Solvent Part: Noble–Abel Stiffened-Gas Equation Of State

Regarding the solvent part, we need to choose an equation of state. In the current contribution, we opt for the Noble–Abel stiffened-gas equation of state (NASG), see Le Métayer and Saurel [48], which is a recently formulated equation of state that is easy to deal with analytically, and that can describe, by a suitable choice of parameters, both gaseous and liquid substances (see also Chiapolino and Saurel [49] for further elaboration of NASG). Let us follow Le Métayer and Saurel [48], and let us first recall various formulae of the Noble–Abel stiffened-gas equations of state. The quantities of interest in engineering practice are given by the formulae

$$p_{\mathrm{th,s}}(\theta_{\mathrm{s}}, \rho_{\mathrm{s}}) = \frac{c_{\mathrm{V,s}} \left(\gamma - 1 \right) \rho_{\mathrm{s}} \theta_{\mathrm{s}}}{1 - b \rho_{\mathrm{s}}} - p_{\infty}, \tag{105a}$$

$$e_{\mathrm{s}}(p_{\mathrm{th,s}}, \rho_{\mathrm{s}}) = \frac{p_{\mathrm{th,s}} + \gamma p_{\infty}}{p_{\mathrm{th,s}} + p_{\infty}} c_{\mathrm{V,s}} \theta_{\mathrm{s}} + q, \tag{105b}$$

$$\eta_{\mathrm{s}}(p_{\mathrm{th,s}}, \rho_{\mathrm{s}}) = c_{\mathrm{V,s}} \ln \left[\left(\frac{\theta_{\mathrm{s}}}{\theta_{\mathrm{s,ref}}} \right)^{\gamma} \left(\frac{p_{\mathrm{th,s}} + p_{\infty}}{p_{\mathrm{ref}}} \right)^{1-\gamma} \right] + q', \tag{105c}$$

where $p_{\mathrm{th,s}}$, θ_{s}, ρ_{s}, e_{s}, and η_{s} are, respectively, the thermodynamic pressure, the temperature, the density, the specific internal energy, and the specific entropy. The symbols $c_{\mathrm{V,s}}$, γ, b, p_{∞}, q, and q' denote constant material parameters that are specific for the given fluid. The symbols $\theta_{\mathrm{s,ref}}$ and p_{ref} denote constant reference temperature and constant reference pressure. These quantities can be chosen at will, as they serve only for normalisation purposes. Combining the Formulae (105), we obtain

$$e_{\mathrm{s}} \left(\theta_{\mathrm{s}}, \rho_{\mathrm{s}} \right) = c_{\mathrm{V,s}} \theta_{\mathrm{s}} + \left(\frac{1}{\rho_{\mathrm{s}}} - b \right) p_{\infty} + q, \tag{106a}$$

$$\eta_{\mathrm{s}} \left(\theta_{\mathrm{s}}, \rho_{\mathrm{s}} \right) = c_{\mathrm{V,s}} \ln \left(\frac{\theta_{\mathrm{s}}}{\theta_{\mathrm{s,ref}}} \right) + c_{\mathrm{V,s}} \left(1 - \gamma \right) \ln \left[\frac{c_{\mathrm{V,s}} \left(\gamma - 1 \right) \rho_{\mathrm{s}}}{1 - b \rho_{\mathrm{s}}} \frac{\theta_{\mathrm{s,ref}}}{p_{\mathrm{ref}}} \right] + q'. \tag{106b}$$

Finally, using (106), we obtain the specific Helmholtz free energy ψ_{s} defined by the thermodynamic relation $\psi_{\mathrm{s}}(\theta_{\mathrm{s}}, \rho_{\mathrm{s}}) = e_{\mathrm{s}}(\theta_{\mathrm{s}}, \rho_{\mathrm{s}}) - \theta_{\mathrm{s}} \eta_{\mathrm{s}}(\theta_{\mathrm{s}}, \rho_{\mathrm{s}})$. The explicit formula for the specific Helmholtz free energy as a function of its natural variables reads

$$\psi_{\mathrm{s}}(\theta_{\mathrm{s}}, \rho_{\mathrm{s}}) = -c_{\mathrm{V,s}} \theta_{\mathrm{s}} \left[\ln\left(\tfrac{\theta_{\mathrm{s}}}{\theta_{\mathrm{s,ref}}} \right) - 1 \right] - c_{\mathrm{V,s}} \theta_{\mathrm{s}} \left(1 - \gamma \right) \ln\left[\tfrac{c_{\mathrm{V,s}} (\gamma - 1) \rho_{\mathrm{s}}}{1 - b\rho_{\mathrm{s}}} \tfrac{\theta_{\mathrm{s,ref}}}{p_{\mathrm{ref}}} \right] - q' \theta_{\mathrm{s}} + \left(\tfrac{1}{\rho_{\mathrm{s}}} - b \right) p_{\infty} + q, \tag{107}$$

and using this formula in (23) gives us a complete thermodynamic characterisation of the given fluid.

We are now in a position to construct the functional $\mathcal{V}_{\mathrm{meq,s}}$, see (93). As in the previous section, we first choose the characteristic temperature of the solvent $\theta_{\mathrm{s,ref}}$ as $\widehat{\theta}_{\mathrm{s}}$, which is we set

$$\theta_{\mathrm{s,ref}} =_{\mathrm{def}} \widehat{\theta}_{\mathrm{s}}. \tag{108}$$

We are using the fact that the temperature field $\widehat{\theta}_{\mathrm{s}}$ at equilibrium is constant in space and time. With this choice of the reference temperature field $\theta_{\mathrm{s,ref}}$, we use the formulae for the specific internal energy e_{s}, and the specific entropy η_{s}, see (106), and we get

$$\begin{aligned} \mathcal{V}_{\mathrm{meq,s}} = &- \int_{\Omega} \left(\rho_{\mathrm{s}} c_{\mathrm{V,s}} \widehat{\theta}_{\mathrm{s}} \ln\left(\frac{\theta_{\mathrm{s}}}{\widehat{\theta}_{\mathrm{s}}} \right) + \rho_{\mathrm{s}} c_{\mathrm{V,s}} \left(1 - \gamma \right) \widehat{\theta}_{\mathrm{s}} \ln\left[\frac{c_{\mathrm{V,s}} \left(\gamma - 1 \right) \rho_{\mathrm{s}}}{1 - b\rho_{\mathrm{s}}} \frac{\widehat{\theta}_{\mathrm{s}}}{p_{\mathrm{ref}}} \right] + \rho_{\mathrm{s}} q' \widehat{\theta}_{\mathrm{s}} \right) \mathrm{dv} \\ &+ \int_{\Omega} \left(\rho_{\mathrm{s}} c_{\mathrm{V,s}} \theta_{\mathrm{s}} + \left(1 - b\rho_{\mathrm{s}} \right) p_{\infty} + \rho_{\mathrm{s}} q \right) \mathrm{dv} - \int_{\Omega} \left(\widehat{\rho}_{\mathrm{s}} c_{\mathrm{V,s}} \widehat{\theta}_{\mathrm{s}} + \left(1 - b\widehat{\rho}_{\mathrm{s}} \right) p_{\infty} + \widehat{\rho}_{\mathrm{s}} q \right) \mathrm{dv}. \end{aligned} \tag{109}$$

Now, we need to manipulate the right-hand side of (109), and we need to show that it is nonnegative. This can be done, as follows. First, we exploit conservation of mass, which implies that $\int_{\Omega} \left(\rho_{\mathrm{s}} - \widehat{\rho}_{\mathrm{s}} \right) \mathrm{dv} = 0$. See also the discussion in the introductory part, in particular the discussion following (86). This observation allows for us to write $\int_{\Omega} \rho_{\mathrm{s}} c_{\mathrm{V,s}} \widehat{\theta}_{\mathrm{s}} \, \mathrm{dv} = \int_{\Omega} \widehat{\rho}_{\mathrm{s}} c_{\mathrm{V,s}} \widehat{\theta}_{\mathrm{s}} \, \mathrm{dv}$. Second, we fix the reference pressure as

$$p_{\mathrm{ref}} =_{\mathrm{def}} \frac{\widehat{\rho}_{\mathrm{s}} \left(\gamma - 1 \right) c_{\mathrm{V,s}} \widehat{\theta}_{\mathrm{s}}}{1 - b\widehat{\rho}_{\mathrm{s}}} \mathrm{e}^{-\frac{q'}{c_{\mathrm{V,s}}(\gamma - 1)}}, \tag{110}$$

and regroup the terms of (109) arriving at

$$\begin{aligned} \mathcal{V}_{\mathrm{meq,s}} = &\int_{\Omega} \rho_{\mathrm{s}} c_{\mathrm{V,s}} \widehat{\theta}_{\mathrm{s}} \left[\frac{\theta_{\mathrm{s}}}{\widehat{\theta}_{\mathrm{s}}} - 1 - \ln\left(\frac{\theta_{\mathrm{s}}}{\widehat{\theta}_{\mathrm{s}}} \right) \right] \mathrm{dv} + \int_{\Omega} \rho_{\mathrm{s}} c_{\mathrm{V,s}} \left(\gamma - 1 \right) \widehat{\theta}_{\mathrm{s}} \ln\left(\frac{\rho_{\mathrm{s}}}{\widehat{\rho}_{\mathrm{s}}} \frac{1 - b\widehat{\rho}_{\mathrm{s}}}{1 - b\rho_{\mathrm{s}}} \right) \mathrm{dv} \\ &+ \int_{\Omega} \left(\rho_{\mathrm{s}} - \widehat{\rho}_{\mathrm{s}} \right) \left(q - bp_{\infty} \right) \mathrm{dv}. \end{aligned} \tag{111}$$

We note that the choice (110) leads to vanishing entropy at the equilibrium state. In this sense, the choice (110) is tantamount to the convenient fix of the entropy value at the equilibrium. Next we again exploit conservation of mass, which allows us to eliminate the last term on the right-hand side of (111), and yields

$$\mathcal{V}_{\mathrm{meq,s}} = \int_{\Omega} \rho_{\mathrm{s}} c_{\mathrm{V,s}} \widehat{\theta}_{\mathrm{s}} \left[\frac{\theta_{\mathrm{s}}}{\widehat{\theta}_{\mathrm{s}}} - 1 - \ln\left(\frac{\theta_{\mathrm{s}}}{\widehat{\theta}_{\mathrm{s}}} \right) \right] \mathrm{dv} + \int_{\Omega} \rho_{\mathrm{s}} c_{\mathrm{V,s}} \left(\gamma - 1 \right) \widehat{\theta}_{\mathrm{s}} \ln\left(\frac{\rho_{\mathrm{s}}}{\widehat{\rho}_{\mathrm{s}}} \frac{1 - b\widehat{\rho}_{\mathrm{s}}}{1 - b\rho_{\mathrm{s}}} \right) \mathrm{dv}. \tag{112}$$

Moreover, by adding the zero term

$$- \int_{\Omega} \frac{c_{\mathrm{V,s}} \left(\gamma - 1 \right) \widehat{\theta}_{\mathrm{s}}}{1 - b\widehat{\rho}_{\mathrm{s}}} \left(\rho_{\mathrm{s}} - \widehat{\rho}_{\mathrm{s}} \right) \mathrm{dv}, \tag{113}$$

to the right-hand side of (112), we arrive at

$$\mathcal{V}_{\mathrm{meq,s}} = \int_{\Omega} \rho_{\mathrm{s}} c_{\mathrm{V,s}} \widehat{\theta}_{\mathrm{s}} \left[\frac{\theta_{\mathrm{s}}}{\widehat{\theta}_{\mathrm{s}}} - 1 - \ln\left(\frac{\theta_{\mathrm{s}}}{\widehat{\theta}_{\mathrm{s}}} \right) \right] \mathrm{dv} + \int_{\Omega} c_{\mathrm{V,s}} (\gamma - 1) \widehat{\theta}_{\mathrm{s}} \left[\rho_{\mathrm{s}} \ln\left(\frac{\rho_{\mathrm{s}}}{\widehat{\rho}_{\mathrm{s}}} \frac{1 - b\widehat{\rho}_{\mathrm{s}}}{1 - b\rho_{\mathrm{s}}} \right) - \frac{\rho_{\mathrm{s}} - \widehat{\rho}_{\mathrm{s}}}{1 - b\widehat{\rho}_{\mathrm{s}}} \right] \mathrm{dv}. \tag{114}$$

Because the function $f(x) =_{\mathrm{def}} x - 1 - \ln x$, is nonnegative for $x \in (0, \infty)$ and vanishes if and only if $x = 1$, we obtain the desired nonnegativity of the first term on the right-hand side of (114).

Finally, we denote

$$g_{\widehat{\rho_{\mathrm{s}}},b}(\rho_{\mathrm{s}}) =_{\mathrm{def}} \rho_{\mathrm{s}} \ln\left(\frac{\rho_{\mathrm{s}}}{\widehat{\rho_{\mathrm{s}}}}\frac{1 - b\widehat{\rho_{\mathrm{s}}}}{1 - b\rho_{\mathrm{s}}}\right) - \frac{\rho_{\mathrm{s}} - \widehat{\rho_{\mathrm{s}}}}{1 - b\widehat{\rho_{\mathrm{s}}}}, \tag{115}$$

where $\rho_{\mathrm{s}} \in \left(0, \frac{1}{b}\right)$. Clearly, $g_{\widehat{\rho_{\mathrm{s}}},b}(\widehat{\rho_{\mathrm{s}}}) = 0$. Moreover, by calculating the first and the second derivatives of the function $g_{\widehat{\rho_{\mathrm{s}}},b}$ one obtains that, irrespective of the values of $b > 0$ and $\widehat{\rho_{\mathrm{s}}} \in \left(0, \frac{1}{b}\right)$, the function $g_{\widehat{\rho_{\mathrm{s}}},b}$ is nonnegative and vanishes if and only if $\rho_{\mathrm{s}} = \widehat{\rho_{\mathrm{s}}}$. The second term on the right-hand side of (114) is thus nonnegative as well. We also note that the function $g_{\widehat{\rho_{\mathrm{s}}},b}(\rho_{\mathrm{s}})$ blows-up as $\rho_{\mathrm{s}} \to \frac{1}{b}-$.

Consequently, we have shown that the functional $\mathcal{V}_{\mathrm{meq,s}}$ is nonnegative and vanishes if and only if $\theta_{\mathrm{s}} = \widehat{\theta_{\mathrm{s}}}$ and $\rho_{\mathrm{s}} = \widehat{\rho_{\mathrm{s}}}$, which is in the case when the temperature and density fields reach their respective equilibrium values. The final formula for the solvent contribution reads

$$\mathcal{V}_{\mathrm{meq,s}} = \int_\Omega \rho_{\mathrm{s}} c_{\mathrm{V,s}} \widehat{\theta_{\mathrm{s}}} \left[\frac{\theta_{\mathrm{s}}}{\widehat{\theta_{\mathrm{s}}}} - 1 - \ln\left(\frac{\theta_{\mathrm{s}}}{\widehat{\theta_{\mathrm{s}}}}\right)\right] \mathrm{d}\mathrm{v} + \int_\Omega c_{\mathrm{V,s}}(\gamma - 1)\widehat{\theta_{\mathrm{s}}} \left[\rho_{\mathrm{s}} \ln\left(\frac{\rho_{\mathrm{s}}}{\widehat{\rho_{\mathrm{s}}}}\frac{1 - b\widehat{\rho_{\mathrm{s}}}}{1 - b\rho_{\mathrm{s}}}\right) - \frac{\rho_{\mathrm{s}} - \widehat{\rho_{\mathrm{s}}}}{1 - b\widehat{\rho_{\mathrm{s}}}}\right] \mathrm{d}\mathrm{v}. \tag{116}$$

6.4. Summary

We are now in a position to collect all partial results. The explicit formula for the functional (87) reads

$$\begin{aligned}
\mathcal{V}_{\mathrm{meq}} &= \int_\Omega \frac{1}{2}\rho_{\mathrm{s}} |\boldsymbol{v}|^2 \,\mathrm{d}\mathrm{v} + \mathcal{V}_{\mathrm{meq,p}} + \mathcal{V}_{\mathrm{meq,s}} \\
&= \int_\Omega \frac{1}{2}\rho_{\mathrm{s}} |\boldsymbol{v}|^2 \,\mathrm{d}\mathrm{v} + k_{\mathrm{B}}\widehat{\theta_{\mathrm{s}}} \int_\Omega \left(\int_D M_{n_{\mathrm{p}},\widehat{\theta_{\mathrm{s}}}} \left[\frac{\varphi}{M_{n_{\mathrm{p}},\widehat{\theta_{\mathrm{s}}}}} \ln\left(\frac{\varphi}{M_{n_{\mathrm{p}},\widehat{\theta_{\mathrm{s}}}}}\right) - \frac{\varphi}{M_{n_{\mathrm{p}},\widehat{\theta_{\mathrm{s}}}}} + 1 \right] \mathrm{d}\boldsymbol{q} \right) \mathrm{d}\mathrm{v} \\
&\quad + k_{\mathrm{B}}\widehat{\theta_{\mathrm{s}}} \int_\Omega \widehat{n_{\mathrm{p}}} \left[\frac{n_{\mathrm{p}}}{\widehat{n_{\mathrm{p}}}} \ln\left(\frac{n_{\mathrm{p}}}{\widehat{n_{\mathrm{p}}}}\right) - \frac{n_{\mathrm{p}}}{\widehat{n_{\mathrm{p}}}} + 1 \right] \mathrm{d}\mathrm{v} + \int_\Omega \rho_{\mathrm{s}} c_{\mathrm{V,s}} \widehat{\theta_{\mathrm{s}}} \left[\frac{\theta_{\mathrm{s}}}{\widehat{\theta_{\mathrm{s}}}} - 1 - \ln\left(\frac{\theta_{\mathrm{s}}}{\widehat{\theta_{\mathrm{s}}}}\right)\right] \mathrm{d}\mathrm{v} \\
&\quad + \int_\Omega c_{\mathrm{V,s}}(\gamma - 1)\widehat{\theta_{\mathrm{s}}} \left[\rho_{\mathrm{s}} \ln\left(\frac{\rho_{\mathrm{s}}}{\widehat{\rho_{\mathrm{s}}}}\frac{1 - b\widehat{\rho_{\mathrm{s}}}}{1 - b\rho_{\mathrm{s}}}\right) - \frac{\rho_{\mathrm{s}} - \widehat{\rho_{\mathrm{s}}}}{1 - b\widehat{\rho_{\mathrm{s}}}}\right] \mathrm{d}\mathrm{v}
\end{aligned} \tag{117}$$

From the construction of the functional, it is clear that it decreases in time and that it is zero at equilibrium. In fact, we have an explicit formula for the time derivative of the functional:

$$\frac{\mathrm{d}\mathcal{V}_{\mathrm{meq}}}{\mathrm{d}t} = -\widehat{\theta} \int_\Omega \xi \,\mathrm{d}\mathrm{v}. \tag{118}$$

The entropy production ξ can be identified from the right-hand side of (51), provided that we substitute for the fluxes $\boldsymbol{j}_{\varphi,\boldsymbol{x}}$, $\boldsymbol{j}_{\varphi,\boldsymbol{q}}$, $\boldsymbol{j}_e$ and the Cauchy stress tensor $\mathbb{T}$ while using the formulae (52)–(54) and (62), which yields

$$\begin{aligned}
\xi &= \frac{1}{\theta_{\mathrm{s}}} \left(2\nu \mathbb{D}_\delta : \mathbb{D}_\delta + \tilde{\lambda} \left(\mathrm{div}_{\boldsymbol{x}} \boldsymbol{v}\right)^2\right) \\
&\quad + \frac{2}{\theta_{\mathrm{s}}\zeta} \int_D \frac{1}{\varphi} \left| \left(\left.\frac{\mathrm{d}U_e}{\mathrm{d}s}\right|_{s = \frac{1}{2}\left|\frac{\boldsymbol{q}}{q_{\mathrm{ref}}}\right|^2} + \frac{\theta_{\mathrm{s}}}{\theta_{\mathrm{ref}}} \left.\frac{\mathrm{d}U_\eta}{\mathrm{d}s}\right|_{s = \frac{1}{2}\left|\frac{\boldsymbol{q}}{q_{\mathrm{ref}}}\right|^2} \right) \frac{\boldsymbol{q}}{q_{\mathrm{ref}}^2} \varphi + k_{\mathrm{B}}\theta_{\mathrm{s}} \nabla_{\boldsymbol{q}} \varphi \right|^2 \mathrm{d}\boldsymbol{q} \\
&\quad + \frac{k_{\mathrm{B}}^2 \theta_{\mathrm{s}}}{2\zeta} \int_D \frac{1}{\varphi} \left|\nabla_{\boldsymbol{x}} \varphi\right|^2 \mathrm{d}\boldsymbol{q} + \kappa \frac{\left|\nabla_{\boldsymbol{x}} \theta_{\mathrm{s}}\right|^2}{\theta_{\mathrm{s}}^2}.
\end{aligned} \tag{119}$$

The first term in (117) monitors the approach of the velocity field to its equilibrium value (zero), the second term does the same regarding the configurational distribution function, the third term takes care of the polymer number density, the fourth term deals with the temperature field, and the last term monitors the approach of the density to the equilibrium density. However, we recall that we have not discussed the relation between the functional and a metric structure on the state space; hence, the functional does not, at the moment, deserve to be referred to as the Lyapunov functional. See also Dostalík et al. [50,51] for a similar application in the case of macroscopic viscoelastic rate-type models, where the authors have actually found a relation between the proposed Lyapunov type functionals and a metric on the state space.

Inspecting (119) and (118), we also note that the time derivative of $\mathcal{V}_{\mathrm{meq}}$ is proportional to the net entropy production that vanishes at the stationary spatially homogeneous equilibrium state (81). These observations conclude our rudimentary stability analysis.

Finally, we note that, on the right-hand side of (119), we explicitly see all entropy production mechanisms that are active in the given fluid. Because the entropy production terms, in fact, determine the fluxes in the sense of the discussion in Section 5.2, we see that the identification of the entropy production and the identification of the Helmholtz free energy indeed provide a complete characterisation of the fluid of interest.

7. Conclusions

We have provided a simple derivation of a model for non-isothermal flows of dilute polymeric fluids. The analysis outlined above shows that if the microscopic dynamics of the polymeric chains is governed by the Fokker–Planck equation with a centre-of-mass diffusion term, then it is possible to find a corresponding evolution equation for the temperature field in such a way that the whole system of governing equations is compatible with the first and second law of thermodynamics.

However, we note that, although the derivation outlined above seems to be completely self-consistent, some of the steps require insight into the microscopic dynamics of the polymeric chains. In particular, the interpretation of the coefficient ζ as hydrodynamic drag, see especially Formula (55) for the flux $\boldsymbol{j}_{\varphi,\boldsymbol{q}}$, would be impossible without the insight into the microscopic nature of the model (this is however true also for the derivation proposed by Öttinger and Grmela [18]). Without such an insight, one could easily misidentify the flux $\boldsymbol{j}_{\varphi,\boldsymbol{q}}$ and lose the connection between the Fokker–Planck type equation and the underlying stochastic process at the level of individual polymeric chains.

While the presence of the centre-of-mass diffusion term is motivated by physical considerations, see for example El-Kareh and Leal [52], Bhave et al. [53], Schieber [54] and Degond and Liu [32], it turns out that its presence can be gainfully exploited in the mathematical analysis of the corresponding governing equations in the purely mechanical setting as well, see especially Barrett and Süli [31,33,55,56,57] or Feireisl et al. [34]. (See also Bulíček et al. [58], Bulíček et al. [59] and Bathory et al. [60] in the context of macroscopic models with a stress diffusion term.) One might hope that once thermodynamically consistent models for the full thermo-mechanical coupling are derived, similar rigorous mathematical results might also be obtained for the corresponding full system of governing equations, that is including the governing equation for the temperature.

In particular, the knowledge of the thermodynamic background leads to natural *a priori* estimates, and to the design of natural functionals that might be used to monitor the stability of steady equilibrium or non-equilibrium states or to analyse weak-strong uniqueness. (See for example Feireisl and Novotný [61], Feireisl et al. [62] and Feireisl and Pražák [63] for the discussion in the case of a compressible Navier–Stokes–Fourier fluid. In the context of purely mechanical models of dilute polymeric fluids and stability of the corresponding flows, see especially Jourdain et al. [64].) Indeed, we *formally*—that is under the assumption that the governing equations posses a strong solution—identify such a functional, which might be of use in such analyses.

Author Contributions: All four authors were equally involved in the formulation of the problem. The calculations were carried out by M.D. and V.P. The discussion of the results and the presentation of the material were carried out by all four authors. All authors have read and agreed to the published version of the manuscript.

Funding: J.M. thanks the Czech Science Foundation for the support through the project 18-12719S. M.D. and V.P. thank the Czech Science Foundation for the support through the project 20-11027X. M.D. has been also supported by Charles University Research program No. UNCE/SCI/023.

Acknowledgments: J.M. and V.P. acknowledge the membership of the Nečas Center for Mathematical Modeling (NCMM).

Conflicts of Interest: The authors declare no conflict of interest.

References

1. Kramers, H.A. The behavior of macromolecules in inhomogeneous flow. *J. Chem. Phys.* **1946**, *14*, 415–424. [CrossRef]
2. Bird, R.B.; Armstrong, R.C.; Hassager, O. *Dynamics of Polymeric Liquids*, 2nd ed.; Kinetic Theory; John Wiley & Sons: Hoboken, NJ, USA, 1987; Volume 2.
3. Beris, A.N.; Edwards, B.J. *Thermodynamics of Flowing Systems: With Internal Microstructure*; Number 36 in Oxford Engineering Science Series; Oxford University Press: Oxford, UK, 1994.
4. Öttinger, H.C. *Stochastic Processes in Polymeric Fluids: Tools and Examples for Developing Simulation Algorithms*; Springer: Berlin, Germay, 1996.
5. Huilgol, R.R.; Phan-Thien, N. *Fluid Mechanics of Viscoelasticity: General Principles, Constitutive Modelling, Analytical and Numerical Techniques*; Rheology Series; Elsevier: Amsterdam, The Netherlands, 1997; Volume 6. [CrossRef]
6. Dressler, M.; Edwards, B.J.; Öttinger, H.C. Macroscopic thermodynamics of flowing polymeric liquids. *Rheol. Acta* **1999**, *38*, 117–136. [CrossRef]
7. Öttinger, H.C. *Beyond Equilibrium Thermodynamics*; John Wiley & Sons: Hoboken, NJ, USA, 2005.
8. Kröger, M. *Models for Polymeric and Anisotropic Liquids*; Lecture Notes in Physics; Springer: Berlin, Germany, 2005; Volume 675.
9. Lozinski, A.; Owens, R.G.; Phillips, T.N. The Langevin and Fokker–Planck equations in polymer rheology. In *Numerical Methods for Non-Newtonian Fluids*; Glowinski, R., Xu, J., Eds.; Handbook of Numerical Analysis; Elsevier: Amsterdam, The Netherlands, 2011; Volume 16, pp. 211–303. [CrossRef]
10. Le Bris, C.; Lelièvre, T. Multiscale modelling of complex fluids: A mathematical initiation. In *Multiscale Modeling and Simulation in Science*; Engquist, B., Lötstedt, P., Runborg, O., Eds.; Lecture Notes in Computational Science and Engineering; Springer: Berlin/Heidelberg, Germany, 2009; Volume 66, pp. 49–137. [CrossRef]
11. Lozinski, A.; Chauvière, C. A fast solver for Fokker-Planck equation applied to viscoelastic flows calculations: 2D FENE model. *J. Comput. Phys.* **2003**, *189*, 607–625. [CrossRef]
12. Knezevic, D.J.; Süli, E. A heterogeneous alternating-direction method for a micro-macro dilute polymeric fluid model. *M2AN Math. Model. Numer. Anal.* **2009**, *43*, 1117–1156. [CrossRef]
13. Mizerová, H.; She, B. A conservative scheme for the Fokker-Planck equation with applications to viscoelastic polymeric fluids. *J. Comput. Phys.* **2018**, *374*, 941–953. [CrossRef]
14. Pavelka, M.; Klika, V.; Grmela, M. *Multiscale Thermo-Dynamics*; de Gruyter: Berlin, Germany, 2018.
15. Peters, G.W.M.; Baaijens, F.P.T. Modelling of non-isothermal viscoelastic flows. *J. Non-Newton. Fluid Mech.* **1997**, *68*, 205–224. [CrossRef]
16. Wapperom, P.; Hulsen, M.A. Thermodynamics of viscoelastic fluids: The temperature equation. *J. Rheol.* **1998**, *42*, 999–1019. [CrossRef]
17. Hron, J.; Miloš, V.; Průša, V.; Souček, O.; Tůma, K. On thermodynamics of viscoelastic rate type fluids with temperature dependent material coefficients. *Int. J. Non-Linear Mech.* **2017**, *95*, 193–208. [CrossRef]
18. Öttinger, H.C.; Grmela, M. Dynamics and thermodynamics of complex fluids. II. Illustrations of a general formalism. *Phys. Rev. E* **1997**, *56*, 6633–6655. [CrossRef]
19. Coleman, B.D. On the stability of equilibrium states of general fluids. *Arch. Ration. Mech. Anal.* **1970**, *36*, 1–32. [CrossRef]
20. Bulíček, M.; Málek, J.; Průša, V. Thermodynamics and stability of non-equilibrium steady states in open systems. *Entropy* **2019**, *21*, 704. [CrossRef]

21. Málek, J.; Průša, V. Derivation of equations for continuum mechanics and thermodynamics of fluids. In *Handbook of Mathematical Analysis in Mechanics of Viscous Fluids*; Giga, Y., Novotný, A., Eds.; Springer: Berlin/Heidelberg, Germany, 2018; pp. 3–72. [CrossRef]
22. Müller, I. *Thermodynamics*; Interaction of Mechanics and Mathematics; Pitman: London, UK, 1985.
23. Gurtin, M.E.; Fried, E.; Anand, L. *The Mechanics and Thermodynamics of Continua*; Cambridge University Press: Cambridge, UK, 2010; p. xxii+694.
24. Rajagopal, K.R.; Tao, L. *Mechanics of Mixtures*; Series on Advances in Mathematics for Applied Sciences; World Scientific Publishing Co. Inc.: River Edge, NJ, USA, 1995; Volume 35, p. xii+195.
25. Hutter, K.; Jöhnk, K. *Continuum Methods of Physical Modeling*; Springer: Berlin, Germany, 2004.
26. Souček, O.; Průša, V.; Málek, J.; Rajagopal, K.R. On the natural structure of thermodynamic potentials and fluxes in the theory of chemically non-reacting binary mixtures. *Acta Mech.* **2014**, *225*, 3157–3186. [CrossRef]
27. Vinogradov, G.V.; Malkin, A.Y. *Rheology of Polymers: Viscoelasticity and Flow of Polymers*; Springer: Berlin/Heidelberg, Germany, 1980.
28. Larson, R.G. *Constitutive Equations for Polymer Melts and Solutions*; Butterworths Series in Chemical Engineering; Butterworth-Heinemann: Oxford, UK, 1988. [CrossRef]
29. Leonov, A.I.; Prokunin, A.N. *Nonlinear Phenomena in Flows of Viscoelastic Polymer Fluids*; Springer: Berlin/Heidelberg, Germany, 1994. [CrossRef]
30. Tanner, R.; Walters, K. *Rheology: An Historical Perspective*; Rheology Series; Elsevier: Amsterdam, The Netherlands, 1998; Volume 7.
31. Barrett, J.W.; Süli, E. Existence of global weak solutions to finitely extensible nonlinear bead-spring chain models for dilute polymers with variable density and viscosity. *J. Diff. Equ.* **2012**, *253*, 3610–3677. [CrossRef]
32. Degond, P.; Liu, H. Kinetic models for polymers with inertial effects. *Netw. Heterog. Media* **2009**, *4*, 625–647. [CrossRef]
33. Barrett, J.W.; Süli, E. Existence of global weak solutions to compressible isentropic finitely extensible bead-spring chain models for dilute polymers. *Math. Model. Methods Appl. Sci.* **2016**, *26*, 469–568. [CrossRef]
34. Feireisl, E.; Lu, Y.; Süli, E. Dissipative weak solutions to compressible Navier–Stokes–Fokker–Planck systems with variable viscosity coefficients. *J. Math. Anal. Appl.* **2016**, *443*, 322–351. [CrossRef]
35. Warner, H.R. Kinetic theory and rheology of dilute suspensions of finitely extendible dumbbells. *Ind. Eng. Chem. Fundam.* **1972**, *11*, 379–387. [CrossRef]
36. Ericksen, J.L. *Introduction to the Thermodynamics of Solids*, revised ed.; Applied Mathematical Sciences; Springer: New York, NY, USA, 1998; Volume 131, p. xii+189. [CrossRef]
37. Rajagopal, K.R.; Srinivasa, A.R. A thermodynamic frame work for rate type fluid models. *J. Non-Newton. Fluid Mech.* **2000**, *88*, 207–227. [CrossRef]
38. Málek, J.; Rajagopal, K.R.; Tůma, K. On a variant of the Maxwell and Oldroyd-B models within the context of a thermodynamic basis. *Int. J. Non-Linear Mech.* **2015**, *76*, 42–47. [CrossRef]
39. Málek, J.; Rajagopal, K.R.; Tůma, K. Derivation of the variants of the Burgers model using a thermodynamic approach and appealing to the concept of evolving natural configurations. *Fluids* **2018**, *3*, 69. [CrossRef]
40. Málek, J.; Průša, V.; Skřivan, T.; Süli, E. Thermodynamics of viscoelastic rate-type fluids with stress diffusion. *Phys. Fluids* **2018**, *30*, 023101. [CrossRef]
41. Dostalík, M.; Průša, V.; Skřivan, T. On diffusive variants of some classical viscoelastic rate-type models. *AIP Conf. Proc.* **2019**, *2107*, 020002. [CrossRef]
42. Souček, O.; Orava, V.; Málek, J.; Bothe, D. A continuum model of heterogeneous catalysis: Thermodynamic framework for multicomponent bulk and surface phenomena coupled by sorption. *Int. J. Eng. Sci.* **2019**, *138*, 82–117. [CrossRef]
43. Hatzikiriakos, S.G. Wall slip of molten polymers. *Prog. Polym. Sci.* **2012**, *37*, 624–643. [CrossRef]
44. Coleman, B.D.; Greenberg, J.M. Thermodynamics and the stability of fluid motion. *Arch. Ration. Mech. Anal.* **1967**, *25*, 321–341. [CrossRef]
45. Gurtin, M.E. Thermodynamics and the energy criterion for stability. *Arch. Ration. Mech. Anal.* **1973**, *52*, 93–103. [CrossRef]
46. Gurtin, M.E. Thermodynamics and stability. *Arch. Ration. Mech. Anal.* **1975**, *59*, 63–96. [CrossRef]
47. Grmela, M.; Öttinger, H.C. Dynamics and thermodynamics of complex fluids. I. Development of a general formalism. *Phys. Rev. E* **1997**, *56*, 6620–6632. [CrossRef]

48. Le Métayer, O.; Saurel, R. The Noble–Abel stiffened-gas equation of state. *Phys. Fluids* **2016**, *28*, 046102. [CrossRef]
49. Chiapolino, A.; Saurel, R. Extended Noble–Abel stiffened-gas equation of state for sub-and-supercritical liquid-gas systems far from the critical point. *Fluids* **2018**, *3*, 48. [CrossRef]
50. Dostalík, M.; Průša, V.; Tůma, K. Finite amplitude stability of internal steady flows of the Giesekus viscoelastic rate-type fluid. *Entropy* **2019**, *21*, 1219. [CrossRef]
51. Dostalík, M.; Průša, V.; Stein, J. Unconditional finite amplitude stability of a viscoelastic fluid in a mechanically isolated vessel with spatially non-uniform wall temperature. *Math. Comput. Simul.* **2020**. [CrossRef]
52. El-Kareh, A.W.; Leal, L.G. Existence of solutions for all Deborah numbers for a non-Newtonian model modified to include diffusion. *J. Non-Newton. Fluid Mech.* **1989**, *33*, 257–287. [CrossRef]
53. Bhave, A.V.; Armstrong, R.C.; Brown, R.A. Kinetic theory and rheology of dilute, nonhomogeneous polymer solutions. *J. Chem. Phys.* **1991**, *95*, 2988–3000. [CrossRef]
54. Schieber, J.D. Generalized Brownian configuration fields for Fokker–Planck equations including center-of-mass diffusion. *J. Non-Newton. Fluid Mech.* **2006**, *135*, 179–181. [CrossRef]
55. Barrett, J.W.; Süli, E. Existence of global weak solutions to some regularized kinetic models for dilute polymers. *Multiscale Model. Simul.* **2007**, *6*, 506–546. [CrossRef]
56. Barrett, J.W.; Süli, E. Existence and equilibration of global weak solutions to kinetic models for dilute polymers I: Finitely extensible nonlinear bead-spring chains. *Math. Model. Methods Appl. Sci.* **2011**, *21*, 1211–1289. [CrossRef]
57. Barrett, J.W.; Süli, E. Existence and equilibration of global weak solutions to kinetic models for dilute polymers II: Hookean-type models. *Math. Model. Methods Appl. Sci.* **2012**, *22*, 1150024. [CrossRef]
58. Bulíček, M.; Málek, J.; Průša, V.; Süli, E. A PDE-analysis for a class of thermodynamically compatible viscoelastic rate type fluids with stress diffusion. In *Mathematical Analysis in Fluid Mechanics: Selected Recent Results*; Danchin, R., Farwig, R., Neustupa, J., Penel, P., Eds.; Contemporary Mathematics; American Mathematical Society: Providence, RI, USA, 2018; Volume 710, pp. 25–53. [CrossRef]
59. Bulíček, M.; Feireisl, E.; Málek, J. On a class of compressible viscoelastic rate-type fluids with stress-diffusion. *Nonlinearity* **2019**, *32*, 4665. [CrossRef]
60. Bathory, M.; Bulíček, M.; Málek, J. Large Data Existence Theory for Three-Dimensional Unsteady Flows of Rate-Type Viscoelastic Fluids with Stress Diffusion. *arXiv* **2020**, arXiv:2002.11224. [CrossRef]
61. Feireisl, E.; Novotný, A. Weak–strong uniqueness property for the full Navier–Stokes–Fourier system. *Arch. Ration. Mech. Anal.* **2012**, *204*, 683–706. [CrossRef]
62. Feireisl, E.; Jin, B.J.; Novotný, A. Relative entropies, suitable weak solutions, and weak-strong uniqueness for the compressible Navier-Stokes system. *J. Math. Fluid Mech.* **2012**, *14*, 717–730. [CrossRef]
63. Feireisl, E.; Pražák, D. *Asymptotic Behavior of Dynamical Systems in Fluid Mechanics*; AIMS Series on Applied Mathematics; American Institute of Mathematical Sciences (AIMS): Springfield, MO, USA, 2010; Volume 4, p. xii+298.
64. Jourdain, B.; Le Bris, C.; Lelièvre, T.; Otto, F. Long-time asymptotics of a multiscale model for polymeric fluid flows. *Arch. Ration. Mech. Anal.* **2006**, *181*, 97–148. [CrossRef]

fluids

MDPI

Article

Numerical Simulation of Fountain Formation due to Normal and Inclined Twin-Jet Impingement on Ground

Xiang Zhang and Ramesh K. Agarwal *

Department of Mechanical Engineering and Materials Science, Washington University in St. Louis, St. Louis, MO 63131, USA; xzhang53@wustl.edu
* Correspondence: rka@wustl.edu

Received: 29 June 2020; Accepted: 6 August 2020; Published: 8 August 2020

Abstract: The goal of this paper is to study numerically the flow physics of a fountain formed by twin-jet impingement on ground. The incompressible Reynolds-Averaged Navier-Stokes (RANS) equations with realizable k-ε and WA (Wray-Agarwal) turbulence model are employed in the numerical simulations with ANSYS Fluent. A series of numerical simulations for straight and inclined fountain formations are conducted by changing the geometric and flow parameters of twin jets and distance between them. The changes in parameters include variations in the jet Reynolds number from 2×10^4 to 8×10^4, impingement height, distance between the centerlines of the two jets from 1.4*D* to 16*D* where *D* is the jet diameter, and ratio of the Reynolds number of the two jets from 1 to 4. It is shown that different Reynolds numbers of the two jets can result in a fountain that inclines towards the jet with smaller Reynolds number. Detailed flow field simulations for a large number of cases are presented, and the flow physics of fountain formation is analyzed for the first time in the literature.

Keywords: jet impingement; fountain formation; turbulence models

---

1. Introduction

Impinging jets have been widely studied because of their significance in many fluid mechanics and engineering applications. For example, impinging jets are applied for industrial cleaning, metal cutting and cooling systems of high pressure turbine blades that face extremely high temperatures in gas turbine engine [1–3]. In another important fighter aircraft application related to the propulsion system of a Short-Takeoff and Vertical Landing (STOVL) or Vertical Take-off and Landing (VTOL) aircraft, multiple jets from the jet engine can impinge in the close vicinity of the ground during landing and take-off.

Several numerical and experimental studies have been conducted for twinjet impingement on ground resulting in fountain formation. Saripalli [4] conducted a flow visualization experiment of twin-jet impingement and studied the basic flow patterns near the stagnation lines and the effect of the ratio of jet momentum on the flow field. Ozmen [5] carried out the experimental investigation of flow characteristics of confined twin air jets at high Reynolds number where downwash fountain was formed. The Reynolds number of the air jet ranged from 30,000 to 50,000, nozzle to plate spacing was in the range 0.5*D*–4*D*, and the spacing between the jets was in the range 0.5*D*–2*D*. Barata et al. [6] measured the velocities in the flow field resulting from single and twin jets impingement against a wall in the presence of cross-flow by laser-dropper velocimetry. They also performed the RANS computations using a two-equation turbulence model and compared the computed results against the experimental data. Greco et al. [7] investigated the flow features in the near field region of single and twin synthetic jets to evaluate influence of the jet interactions by varying the distance between the axis of two jets by 1.1, 3 and 5 times the nozzle diameters. Abdel-Fattah [8] studied the impinging twin-jet flow without cross flow by both the experimental and numerical methods. The parameters in his study considered jet Reynolds number from 9.5×10^4 to 22.4×10^4; nozzles to plate spacing of 3*D* to 12*D*; nozzle to nozzle spacing of 3*D*, 5*D* and 8*D*; and jet angles from 0 to 20 degrees. Wang et al. [9] conducted an experimental investigation of a single water jet impingement at various impingement angles and Reynolds numbers. Taghinia et al. [10] investigated twin-jet impingement numerically with Reynolds-Averaged Navier–Stokes (RANS)—Large Eddy Simulation (LES) hybrid turbulence model and showed that Shear Stress Transport (SST)—Scale Adaptive Simulation (SAS) model can produce more accurate predictions. Attalla et al. [11] performed an experiment with a pair of inclined circular air jets and studied their impact on heat transfer characteristics of the impingement plate. Sharif [12] investigated inclined twin slot-jet impingement numerically and studied the influence of impingement angle on heat transfer distribution on the impingement surface. Faris et al. [13] conducted both an experimental and numerical study of twin jet impingement and studied the mechanism of heat transfer enhancement.

Although several numerical simulations have been reported in the literature, twin jet impingement has been studied only for a very small range of parameters. Also, there is paucity of results for parameters that result in inclined fountain flow in contrast to symmetrical fountain flow. Inclined fountain flow has more engineering importance since impinging jets are difficult to be controlled as completely identical.

In this study, RANS equations with realizable k-ε [14] and Wray-Agarwal (WA) [15] turbulence models are used to conduct numerical simulations of twin impinging jets. The range of parameters considered include the inlet jet Reynolds number from 2×10^4 to 8×10^4, distance between centerlines of twinjet from 1.4*D* to 16*D*, and ratio of Reynolds number between the two jets from 1 to 4. Velocity and pressure fields are computed and analyzed.

2. Numerical Method and Validation

2.1. Physical Model

The computational domain is a cuboid with length × width × height = 5000 mm × 1000 mm × 400 mm as shown in Figure 1a. The physical model is very similar in all cases computed, except there are changes in some parameters. In most cases, *D*, diameter of the jet, is fixed at 0.02 m and impingement height *H* from jets exit to the ground is fixed at a distance of 3*D*. The distance between the centerline of jets, *S* is changed between various cases.

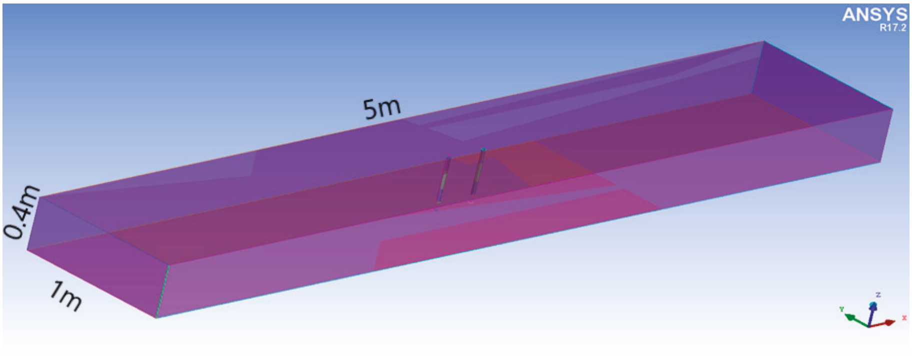

(**a**)

Figure 1. *Cont.*

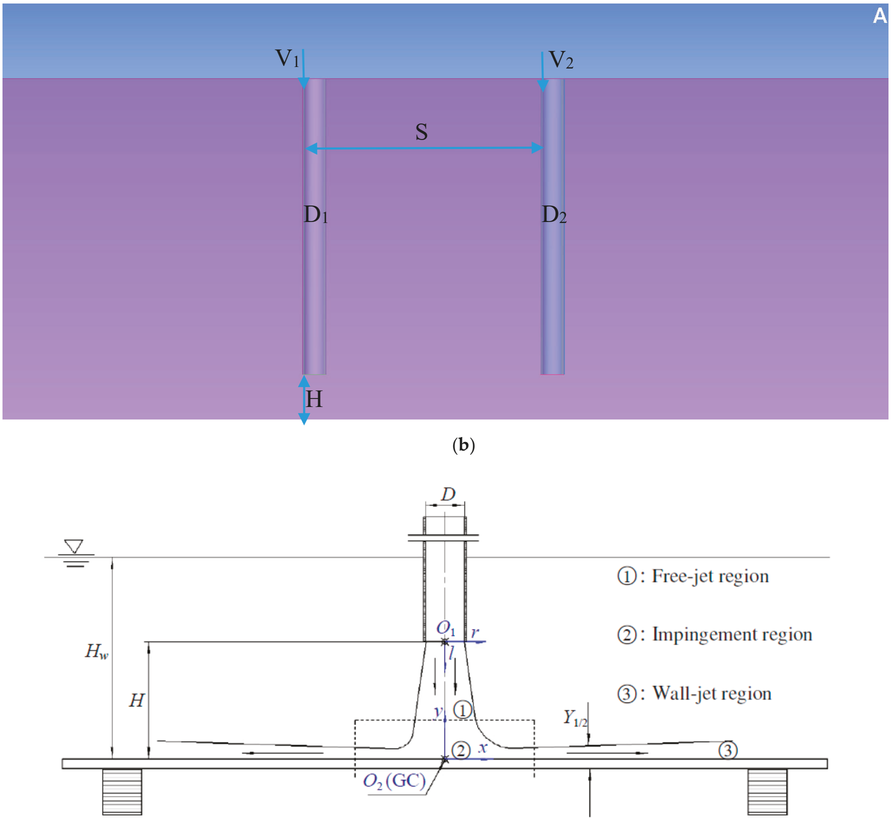

(**b**)

(**c**)

Figure 1. (**a**) Physical model and 3*D* computational domain, (**b**) Cross section of physical model, (**c**) Schematic of submerged impinging jet.

Since the physical model is not complex, a structured grid was generated by ICEM CFD, which is part of ANSYS 18.2 software, Canonsburg, PA, USA. The mesh was refined in regions with large velocity gradients including the areas near the impingement plane, near the interior surface of the pipe from which the jet exits, and in the fountain region resulting from the twin-jet interaction. The size of the first mesh layer is 1×10^{-4} m from the interior surface of the pipe and is 1×10^{-5} m from the impingement plane in order to ensure that $y+ < 1$. Around a pipe, a cuboid block with square cross-section is created. In this block, three layers of O-grid are generated: The edge of the first layer of O-grid is associated with the exterior surface of the pipe; the second layer of O-grid is associated with the interior surface of the pipe; and the grids inside the third O-grid are adapted to the flow in the pipe. Figure 2 shows the grid refinement regions when the distance between the jets is 16*D*. Figure 3 shows the grid quality distribution. The mesh independence of the solution study was performed for 90 degree single jet impingement case and a fountain formation case with twin-jet impingement at 90 degree by computing the solution on a coarse, medium and fine mesh. Medium mesh was found to be accurate and efficient and was selected in all single and twin-jet computations reported in this paper.

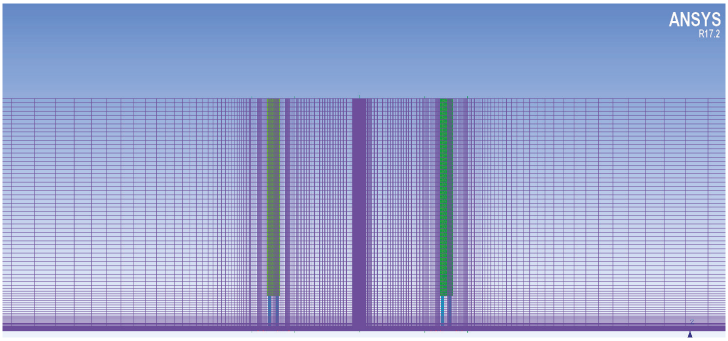

(**a**) Vertical Cross-section in symmetry plane.

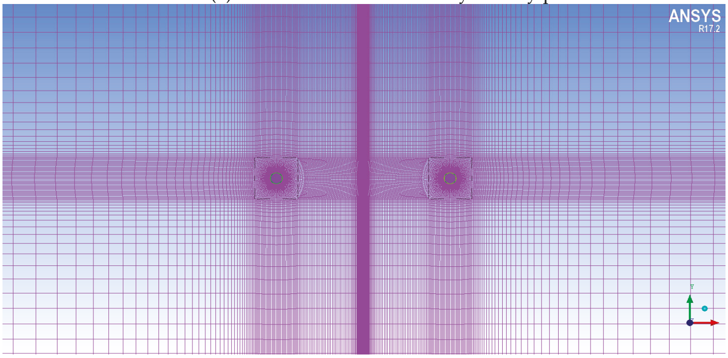

(**b**) Plan-view.

Figure 2. Structured grid in the computational domain.

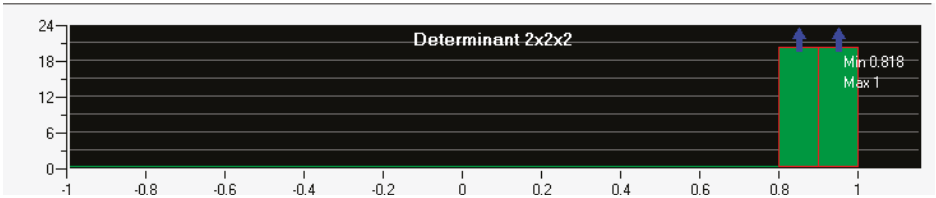

Figure 3. Pre-mesh grid quality distribution.

2.2. Governing Equations and Numerical Method

Since the fluid medium is water, the governing equations are incompressible Navier–Stokes (NS) equations including continuity and momentum Equations as shown below:

$$\frac{\partial \rho}{\partial t} + \nabla \cdot \left(\rho \vec{u}\right) = 0 \tag{1}$$

$$\frac{\partial}{\partial t}\left(\rho \vec{u}\right) + \nabla \cdot \left(\rho \vec{u}\,\vec{u}\right) = -\nabla P + \mu \nabla \cdot \left(\nabla \vec{u} + \nabla \vec{u}^{T}\right) \tag{2}$$

where density ρ = constant, $\vec{u}$ is the velocity vector, P is pressure, and μ is dynamic viscosity. However, it is not possible to solve NS equations by Direct Numerical Simulation (DNS) or even by Large Eddy Simulation (LES) for 3D flows because of current unavailability of computational resources required. Currently, Reynolds-Averaged Navier-Stokes (RANS) equations are widely used in majority of industrial applications. RANS equations are time-averaged NS equations and produce an extra term in momentum equation called the Reynolds Stress tensor, which leads to the closure problem for RANS equations. The closure is achieved by modeling the Reynolds stresses by employing a turbulence model. In this paper, we employ the two-equation realizable k-ε and one-equation Wray-Agarwal (WA) turbulence models, which are eddy/turbulent viscosity models based on Boussinesq assumption. With Boussinesq assumption, the momentum equations in RANS Equations can be written as:

$$\frac{\partial}{\partial t}\left(\rho\vec{u}\right)+\nabla\cdot\left(\rho\vec{u}\,\vec{u}\right)=-\nabla P+(\mu+\mu_t)\nabla\cdot\left(\nabla\vec{u}+\nabla\vec{u}^{T}\right) \tag{3}$$

where μ_t is the turbulent eddy viscosity obtained by the turbulence model.

Realizable k-ε model consists of a transport equation for turbulent kinetic energy k and its dissipation rate ε, which can be expressed as follows; the details are provided in Ref. [14].

$$\frac{\partial}{\partial t}(\rho k)+\frac{\partial}{\partial x_j}\left(\rho k u_j\right)=\frac{\partial}{\partial x_j}\left[\left(\mu+\frac{\mu_t}{\sigma_\varepsilon}\right)\frac{\partial k}{\partial x_j}\right]+G_\kappa+G_b-\rho\varepsilon-Y_M+S_k \tag{4}$$

$$\frac{\partial}{\partial t}(\rho\varepsilon)+\frac{\partial}{\partial x_j}\left(\rho\varepsilon u_j\right)=\frac{\partial}{\partial x_j}\left[\left(\mu+\frac{\mu_t}{\sigma_\varepsilon}\right)\frac{\partial\varepsilon}{\partial x_j}\right]+\rho C_1 S\varepsilon-\rho C_2\frac{\epsilon^2}{k+\sqrt{\epsilon\nu}}+C_{1\epsilon}\frac{\epsilon}{\kappa}C_{3\epsilon}+S_\varepsilon \tag{5}$$

$$\mu_t=\rho C_\mu\frac{k^2}{\epsilon} \tag{6}$$

One-equation WA model is also used in this study and is governed by the transport equation for $R = k/\omega$, the details are provided in Refs. [15,16]:

$$\begin{aligned}&\tfrac{\partial}{\partial t}(R)+\tfrac{\partial}{\partial x_j}\left(Ru_j\right)\\ &\qquad=\tfrac{\partial}{\partial x_j}\left[(\sigma_R R+\nu)\tfrac{\partial R}{\partial x_j}\right]+C_1RS+f_1C_{2\kappa\omega}\tfrac{R}{S}\tfrac{\partial R}{\partial x_j}\tfrac{\partial S}{\partial x_j}\\ &\qquad-(1-f_1)C_{2\kappa\epsilon}R^2\left(\frac{\frac{\partial S}{\partial x_j}\frac{\partial S}{\partial x_j}}{S^2}\right)\end{aligned} \tag{7}$$

The eddy viscosity is given by:

$$\mu_t=\rho f_\mu R \tag{8}$$

Realizable k-ε model can be selected directly from the viscosity model page in ANSYS Fluent, while Wray-Agarwal (WA) model is loaded in Fluent as UDF [17]. SIMPLE algorithm is used for pressure-velocity coupling. Second order scheme is used for discretization of pressure equation in SIMPLE and second order upwind discretization scheme is used for the momentum and turbulence model equations. The material for the entire domain is water, whose density is 998.2 kg/m^3 and dynamic viscosity is 0.001003 kg/(m·s). The solution is considered as converged when residuals of monitored equations and parameters are $<10^{-5}$.

For boundary conditions, the upper surfaces of pipes are set as velocity inlets where the velocity is normal to the surface. The lower surfaces of the pipes are set is pressure outlet where the gauge pressure is 0. All other surfaces are set as static walls without slip. In the validation case of a single jet impingement, inlet velocity at the pipe is 1.16 m/s with Reynolds number of ~23,400. In the fountain cases, inlet velocity varies from 1 m/s to 4 m/s with Reynolds number varying from 20,000 to 80,000.

2.3. Validation with Experiment of Single Jet Impingement

This part compares the results from numerical simulation using k-ε and WA turbulence models and experiment conducted by Wang et al. [9]. A mesh independence of the solution study was conducted by performing the computations on coarse, medium and fine mesh. Figure 4a shows the definition of average velocity, v_b, and maximum velocity, v_m, in the jet flow. In this study, v_b and v_m

are used to normalize the velocity profiles, and the diameter of jet D is used to normalize the length parameters, e.g., axial distance l, radial distance r, etc. The average velocity v_b in this case is 1.28 m/s, corresponding to Re (= $v_b\ D/v$, v is the kinematic viscosity of water = 1×10^{-6}) = 25,600. Figure 4b shows the velocity profile near the exit of the jet flow (l/D = 0.5) from both CFD and experimental results. There is an excellent agreement between the two.

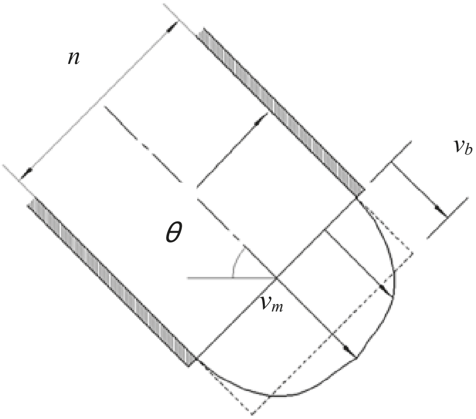

(**a**) Definitions of average velocity v_b and maximum velocity v_m in jet flow.

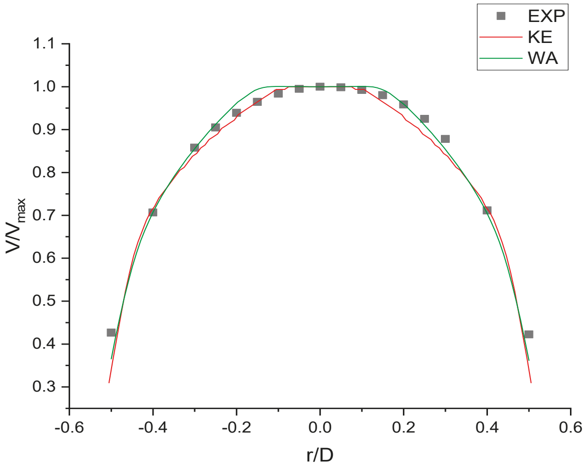

(**b**) Normalized velocity near jet exit (l/D = 0.5).

Figure 4. Velocity profile after exit from pipe.

Figure 5 shows the normalized computed and experimental velocity profiles v/v_b at various l/D for normal impingement at Re = 25,600 and H/D = 3. The magnitude of velocity decreases rapidly as $|r/D|$ becomes greater than 0.5, especially in the region near the impingement plane.

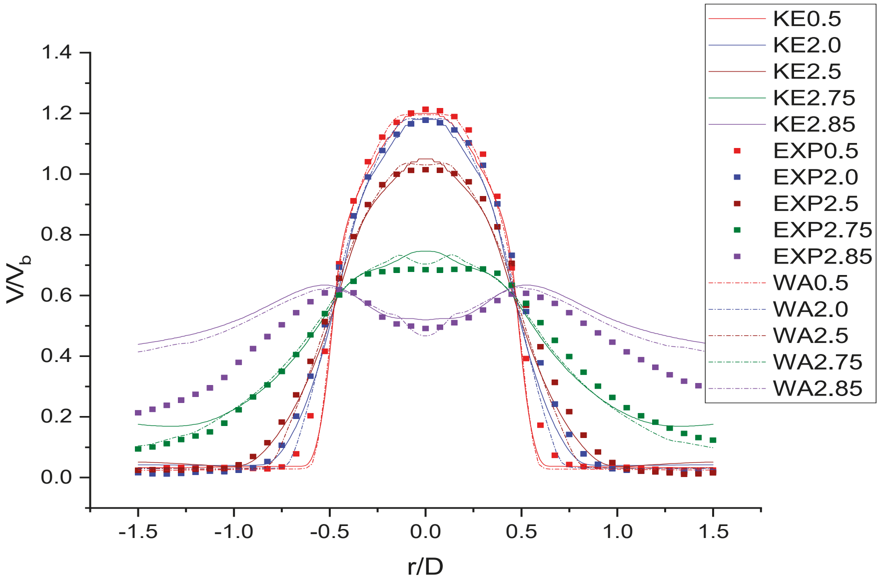

Figure 5. Velocity profiles along the centerline after jet exit.

Figure 6 shows the normalized velocity along the centerline of the jet from jet exit to impingement plane when impingement angle is 90 degree. The velocity decreases significantly after l/*D* = 2.5, where the flow transitions from free jet region to impingement region. CFD results from both k-ε and WA turbulence model, show excellent agreement with experiment results.

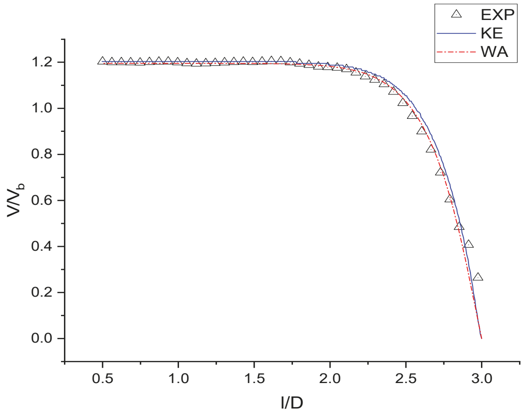

Figure 6. Velocity along the jet centerline.

Figure 7 shows the normalized velocity profiles along the centerline of the jet at different locations parallel to the centerline. The peak velocity occurs where *r*/*D* is +/− 0.5 at l/*D* = 2.91 when v/v_b reaches 0.62 approximately. The agreement between the CFD using both k-ε and WA model, and experimental results, is overall very good. There is some asymmetry in the experimentally measured velocity profiles. As a result, there are small differences in the CFD results and the experimental results on two sides of the centerline.

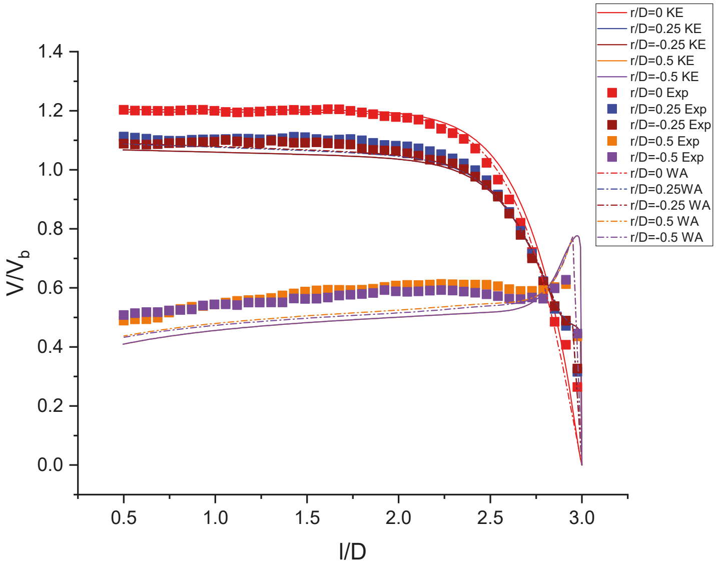

Figure 7. Normalized velocities along lines parallel to centerline at different radial distances from jet.

Figure 8 shows the normalized maximum velocity in the wall jet region and a series of velocity ratios for different scaling along x-direction in the wall jet region. It can be seen that CFD results match with experimental data well.

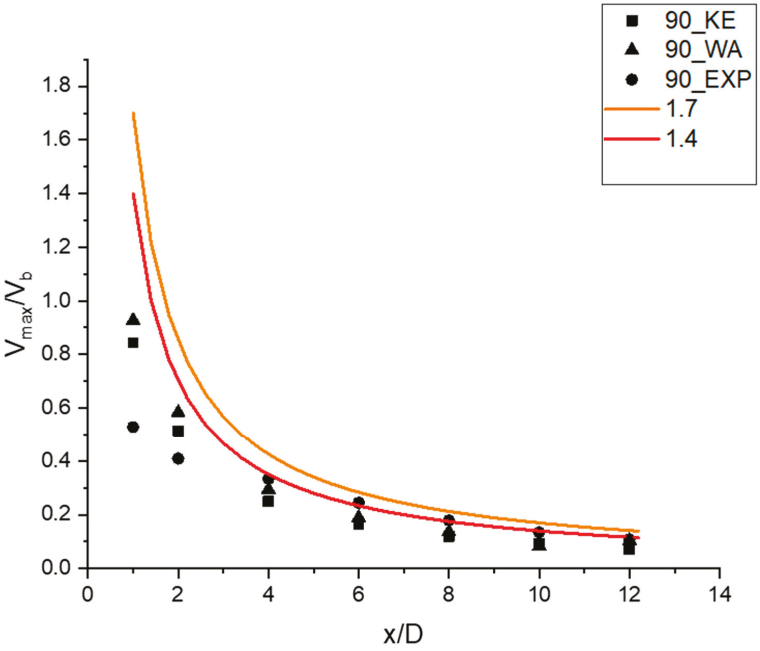

Figure 8. Normalized maximum velocity at various radical distances.

The velocity contours from numerical simulation and experiment are shown in Figure 9. The entrainment of surrounding water due to jet is obvious. The stagnation point is located at the centerline of the jet as expected.

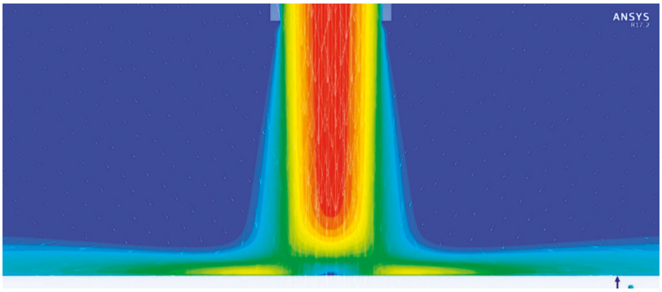

(**a**) Computed velocity contours.

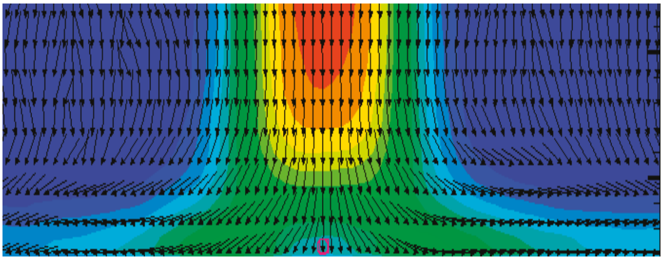

(**b**) Experimental velocity contours.

Figure 9. Velocity contours and velocity vectors.

The pressure coefficient in the impingement plane is defined as $C_p = \frac{P-P_{ref}}{\frac{1}{2}\rho V_b^2}$ where $P_{ref} = \rho g H$. The small difference between the CFD result and experiment result could be due to a difference in boundary conditions in the experiment and CFD. In the experiment, v_b = 1.17 m/s is calculated based on velocity measured near the jet exit. In simulation, the boundary condition at velocity inlet was set at 1.17 m/s. Due to viscosity of the fluid, velocity at the pipe surface is zero. The velocity of the jet at centerline gets larger and velocity distribution becomes more uneven as fluid flows through the pipe due to gravity. Figure 10 shows the pressure coefficient at different impingement angles. Results from both k-ε and WA models show good agreement at 90 degree impingement angle.

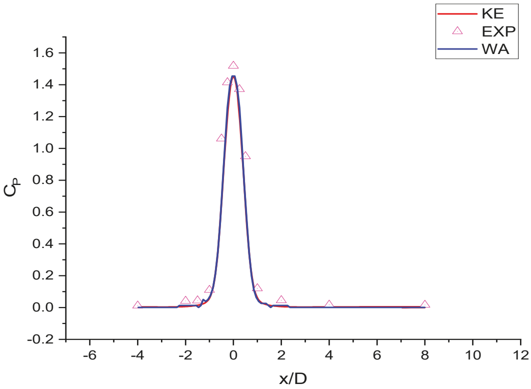

Figure 10. Pressure coefficient distribution on ground surface.

It can be noted from Figure 11 that y^+ near the impingement region on the plate is less than 1, attesting to the proper implementation of CFD methodology in ANSYS Fluent.

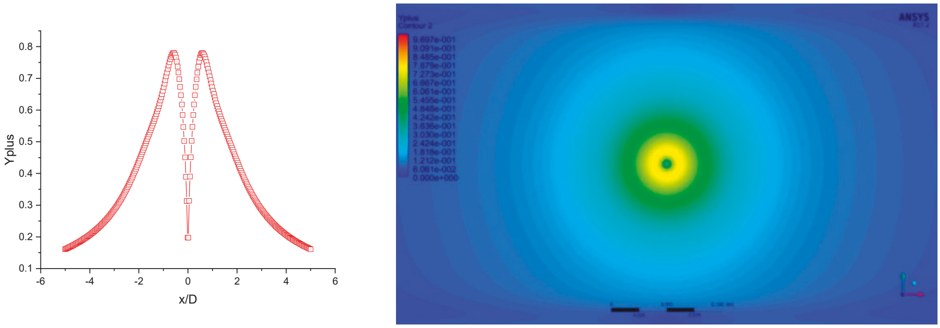

Figure 11. y^+ distribution (**a**) at different radial distances from stagnation point (**b**) in the impingement plane.

3. Results and Discussion

3.1. Flow Conditions to Form a Straight Fountain

When the wall jets produced by jet impingement are of identical strength, they can produce a fountain normal to impingement surface. Therefore, it is critical to find the parameters that form a normal fountain. In this section, the fountain formation is considered by jets of different diameters: $D_1 = 0.02$ m and $D_2 = 0.03$ m. To determine the factors that influence the character of the fountain, three cases are conducted. Two cases have twin-jet with different diameters ($D_1 = 0.02$ m, $D_2 = 0.03$ m), in which the difference is that in the first case, twin-jets are controlled to have identical mass flow rate while in the second case twin-jets are controlled to have identical Reynolds number. The third case is performed under the condition that $D_1 = D_2 = 0.02$ m and $V_1 = V_2 = 1.5$ m/s. In all three cases, inlet velocity of the left jet is fixed at $V_1 = 1.5$ m/s, distance between the two jets is fixed such that $S/D = 5$ where $D = \sqrt{D_1 * D_2}$. Figures 12–14 show the velocity contours of the fountain in the three cases. It can be easily observed from Figure 12 that when the mass flow rates of two jets of different diameters are the same, the fountain has asymmetry inclining toward the jet of larger diameter; however, when the Reynolds numbers of the two jets of different diameter are the same, the fountain formed is straight upward as shown in Figure 13, like the reference case when the diameters and velocities of the two jets are the same as shown in Figure 14. The difference between Figures 13 and 14 could be due to minor differences in the physical model. Diameter of jet D, which is used to create the physical model, is $D = \sqrt{D_1 * D_2}$ ($D_1 = 0.02$ m, $D_2 = 0.03$ m) in Figures 12 and 13, which is larger than $D = \sqrt{D_1 * D_2}$ ($D_1 = D_2 = 0.02$ m) in Figure 14. This leads to larger impingement height as well as larger distance between the two jets, which can decrease the strength of fountain when Reynolds number is identical for both cases.

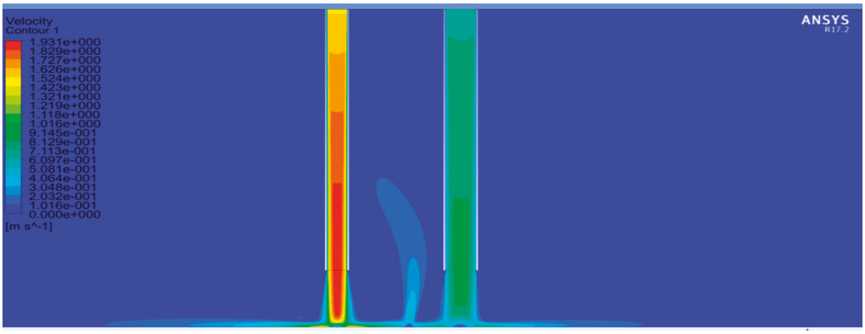

Figure 12. Fountain formed by twin jets with identical mass flow rate.

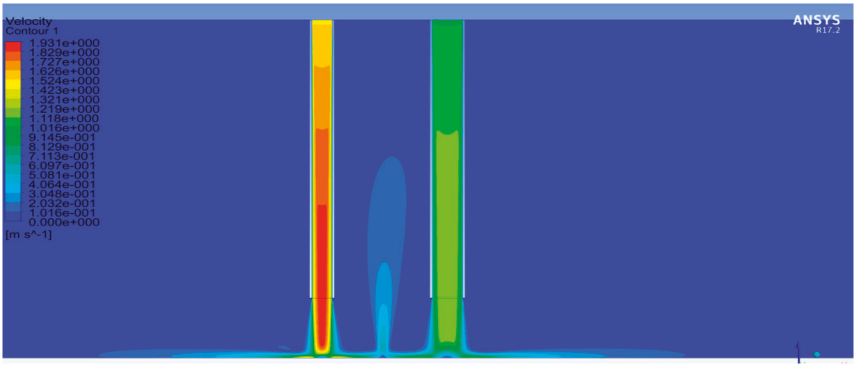

Figure 13. Fountain formed by two jets with identical inlet Reynolds number.

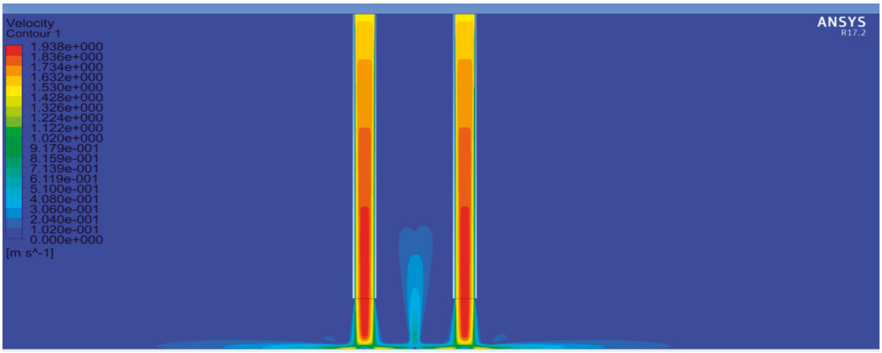

Figure 14. Fountain formed by two identical jets.

3.2. Straight Up-Wash Fountain

Figure 15 shows the velocity streamlines in a fountain formed by two jets where S/D = 16, H/D = 3 and V_1 = V_2 = 2.5 m/s. In the region away from the bottom plane, two upstream vortices are formed on two sides of the fountain as shown in Figure 15a. In the region close to the bottom plane, two ground vortices are formed on two sides of the fountain as shown in Figure 15b. Although an up-wash fountain is formed in the middle of two jets, the flow is down-wash in the region very close to ground.

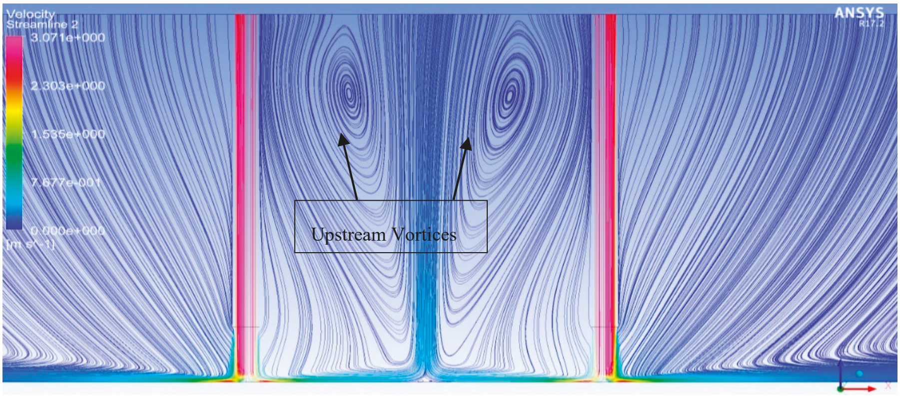

(**a**) Up-stream vortices on two sides of fountain.

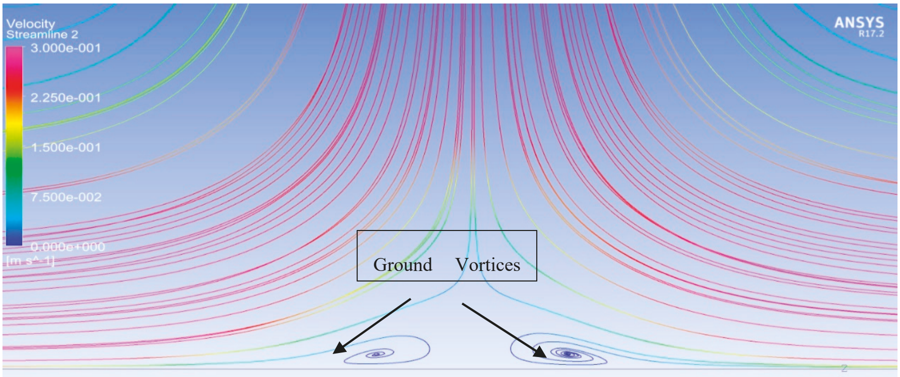

(**b**) Vortices near ground on two sides of the fountain.

Figure 15. Velocity streamlines in a fountain formed by two jets.

For the same simulation, Figure 16a,b shows the velocity distribution at different radial distances from the centerline of the fountain, ranging from 0*D* to 4*D*. The velocity distributions show different characteristics before and after $x/D = 0.5$. Velocity increases at a smaller rate when x/D is less than 0.5 compared to when it is larger than 0.5. Peak velocity decreases as x/D increases when x/D is less than 0.5; on the other hand, if x/D is larger than 0.5, peak velocity increases as x/D becomes larger.

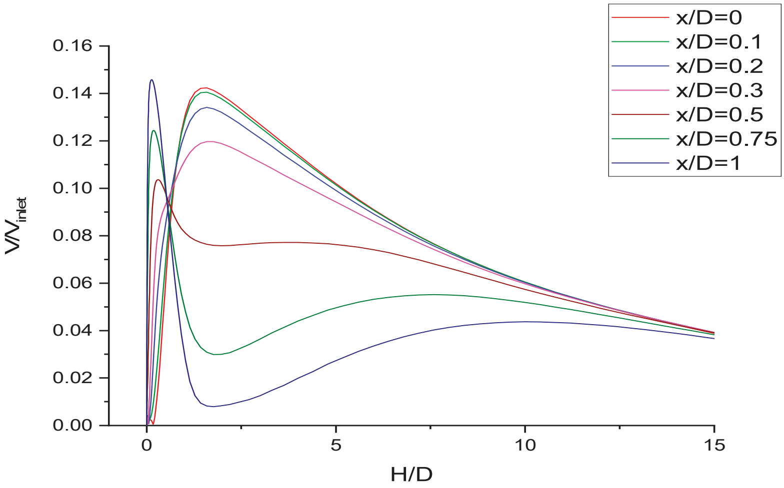

(**a**) 0 < x/D <1

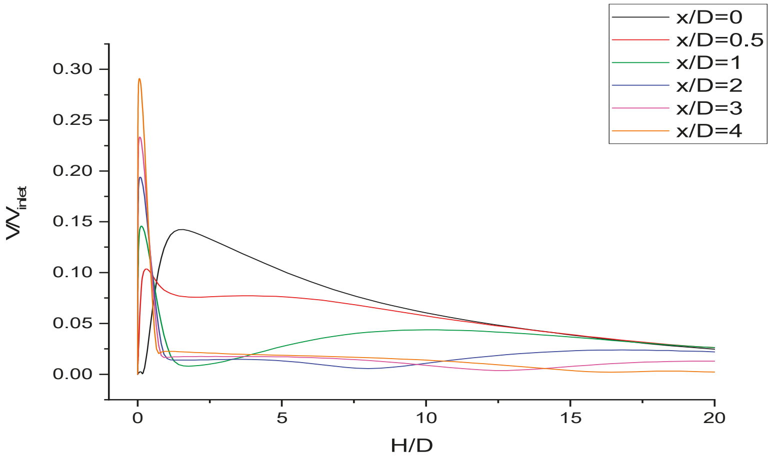

(**b**) 0 < x/D <4

Figure 16. Normalized vertical velocity distribution for various radial distances, x/D.

Figure 17a,b shows the location and magnitude of maximum velocity respectively at different radial distances from the centerline of the fountain; they are normalized by the diameter of the jet and inlet velocity respectively. Location and magnitude of maximum velocity are used to describe the strength and shape of the fountain, which is due to multiple factors. Fountain shows different flow characteristics when $x/D < 0.5$ and when $x/D > 0.5$. Maximum velocity occurs significantly close to ground when $x/D > 0.5$. Maximum velocity increases gradually as x/D gets larger than 0.5.

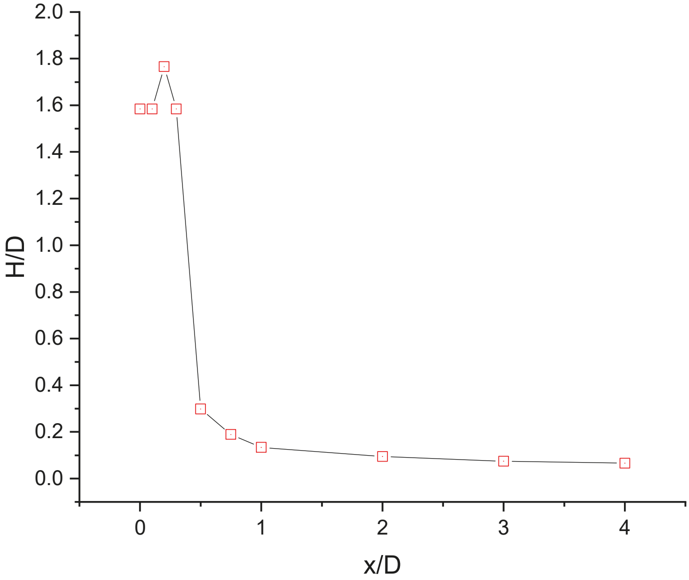

(**a**) Location of maximum velocity

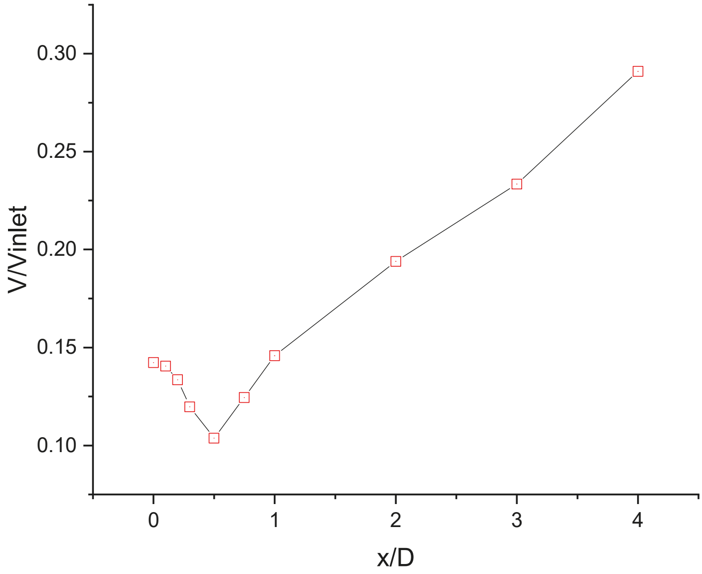

(**b**) Normalized maximum velocity

Figure 17. Location and magnitude of maximum velocity at various radial distances, x/D.

3.3. Straight Fountain Formation under Various Flow Conditions

A series of simulations is performed when Reynolds numbers at two velocity inlets of the two jets are the same. Diameters of the two jets are set identical at 0.02 m. Inlet velocity is set at 1 m/s, 1.5 m/s, 2 m/s, and 2.5 m/s, and corresponding Reynolds numbers are 20,000, 29,900, 39,900, and 49,900 respectively. Figure 18 shows the logarithm of stagnation pressure coefficient, defined as $C_p = \frac{P - \rho g h}{0.5\rho v_{inlet}^2}$, versus logarithm of inlet Reynolds number at different conditions when parameters including the distance between twin jets, *S*/*D* and impingement height *H*/*D* are changed. For fixed S/D, logarithm of pressure coefficient and logarithm of inlet Reynolds number show a linear relationship. Furthermore, change in impingent height leads to a greater change in pressure coefficient for small *S*/*D*, such as 1.4, while the pressure coefficient for *S*/*D* = 16 changes slightly.

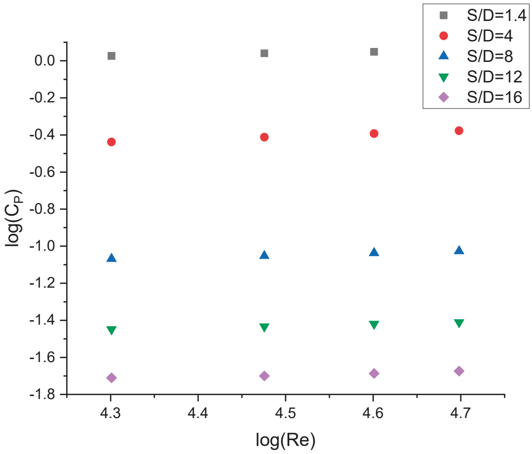

(**a**) Impingement height = 3*D*

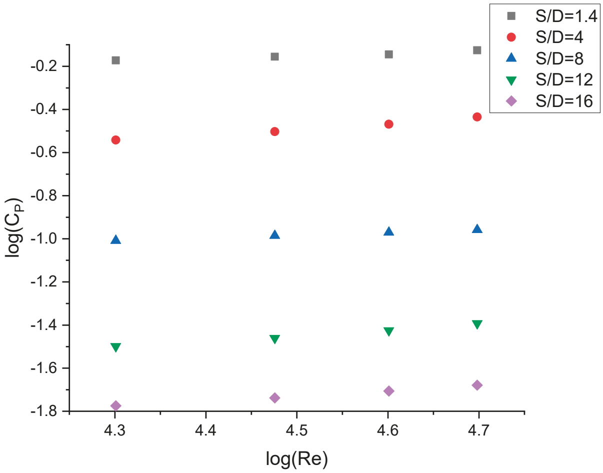

(**b**) Impingement height = 6*D*

Figure 18. Variation in pressure coefficient at stagnation point of the fountain with jet inlet Reynolds numbers for various cases.

Figures 19 and 20 show the location and magnitude of maximum velocity at the centerline of the fountain under various conditions. For fixed twin-jet distance and impingement height, location of maximum velocity at centerline of the fountain does not change with inlet Reynolds number. Maximum velocities for *S*/*D* = 1.4 and 4 at the centerline are very close especially when impingement height is 3*D*. In addition, change in impingement height has a greater influence on maximum velocity of the centerline for *S*/*D* = 1.4 and 4 than on that for *S*/*D* = 8, 12 and 16. The larger the *S*/*D*, the less is the influence of change in impingement height on maximum velocity of the centerline of the fountain.

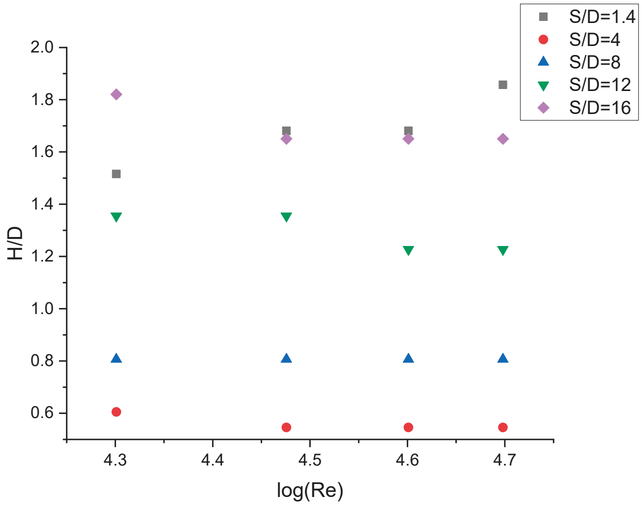

(**a**) Impingement height = 3*D*

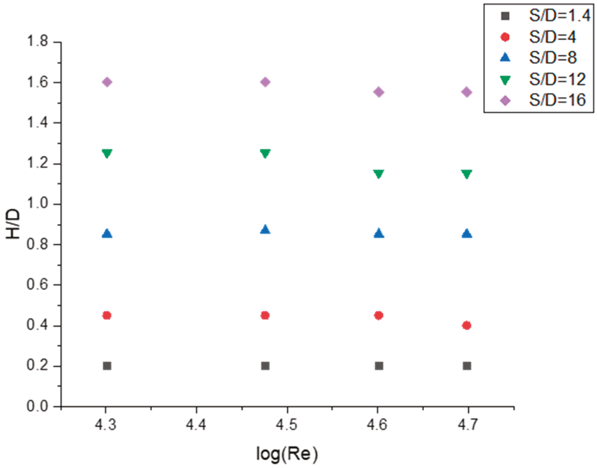

(**b**) Impingement height = 6*D*

Figure 19. Location of maximum velocity at centerline of the fountain for various flow conditions.

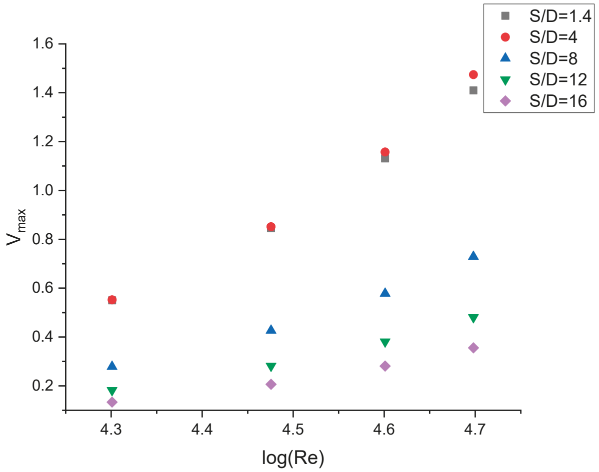

(**a**) Impingement height = 3*D*

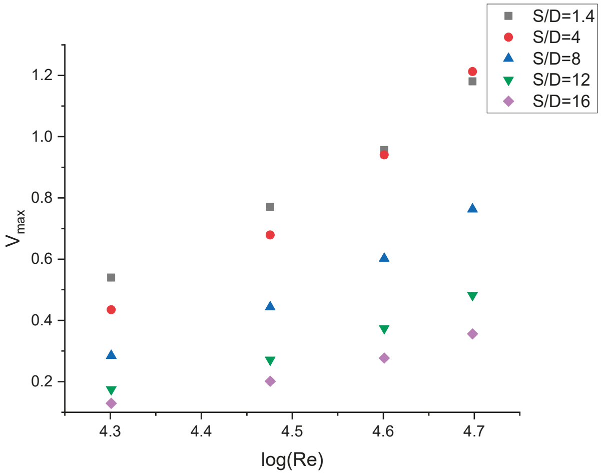

(**b**) Impingement height = 6*D*

Figure 20. Magnitude of maximum velocity at centerline of the fountain at various flow conditions.

3.4. Inclined Fountain Formation

From part A above, it can be seen that differences in Reynolds numbers of the two jets lead to the formation of a fountain that moves and curves towards the jet with smaller Reynolds number. In this case, the character of the fountain is highly influenced by the ratio of the Reynolds numbers, R_{Re}, at jet inlets. The inlet velocity of the right jet is changed to achieve different ratios of Reynolds numbers, while the inlet velocity of left jet is fixed at 1 m/s ($Re = 2 \times 10^4$). Distance between the two jets is fixed at 5*D*. Figures 21–29 show velocity contours of inclined fountain for various ratios of Reynolds numbers for velocities between 0 and 1 m/s. By connecting the upper and lower boundary of the velocity contour, the formed lines display similar velocity distribution at the centerline of the straight fountain. Therefore, these lines can be treated as centerlines of the inclined fountain. Location and velocity distribution of the centerline of the inclined fountain are also included in Figures 22–26.

When the ratio of Reynolds numbers becomes larger than 3.3, it becomes very hard to identify the centerline of the inclined fountain. As the ratio of Reynolds numbers increases, the stagnation point of the fountain moves towards the left jet that has smaller Reynolds number than the right jet. As ratio of Reynolds number reaches 3.8, the stagnation point of fountain almost overlaps with that of the left jet impingement. Furthermore, the fountain is also inclined to the same side. However, when the ratio of Reynolds numbers is larger than 2.5, as can be observed in Figure 25, the fountain reflects from the left jet and moves back towards the right jet.

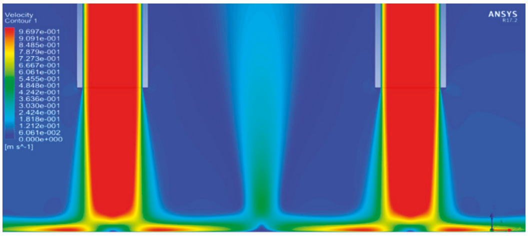

Figure 21. Straight Fountain when R_{Re} = 1.

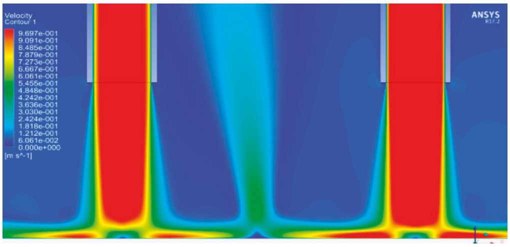

(**a**) Velocity contours

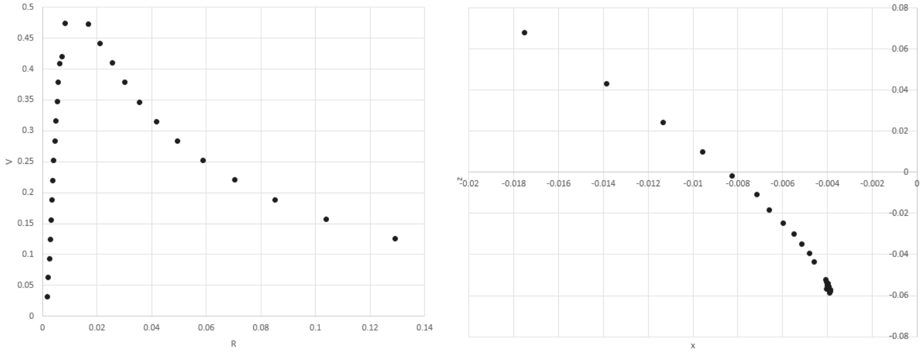

(**b**) Velocity distribution and location of centerline of the fountain.

Figure 22. Inclined fountain when R_{Re} = 1.2.

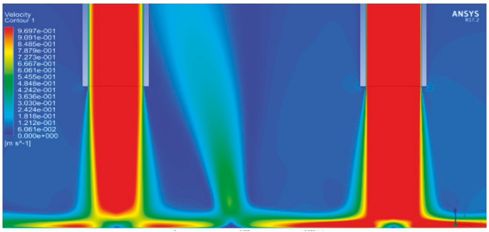

(**a**) Velocity contours

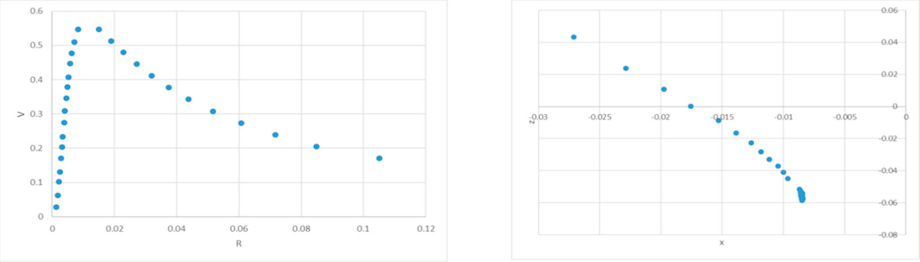

(**b**) Velocity distribution and location of centerline of the fountain.

Figure 23. Inclined fountain when R_{Re} = 1.5.

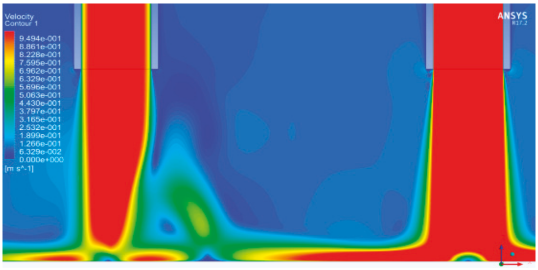

(**a**) Velocity contours

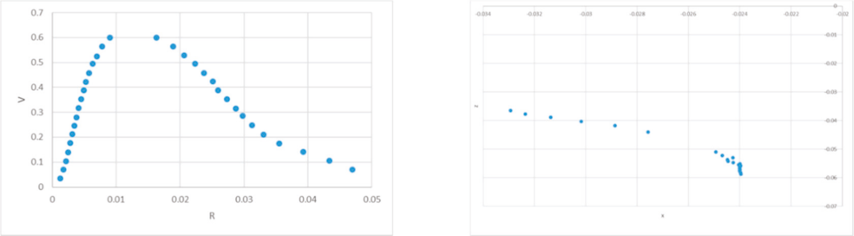

(**b**) Velocity distribution and location of centerline of the fountain.

Figure 24. Inclined fountain when R_{Re} = 2.

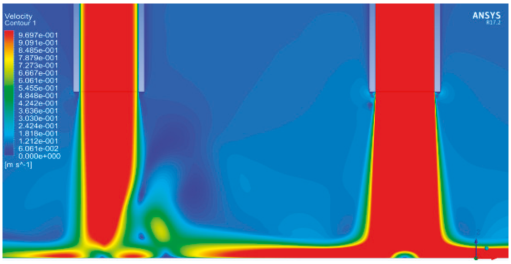

(**a**) Velocity contours

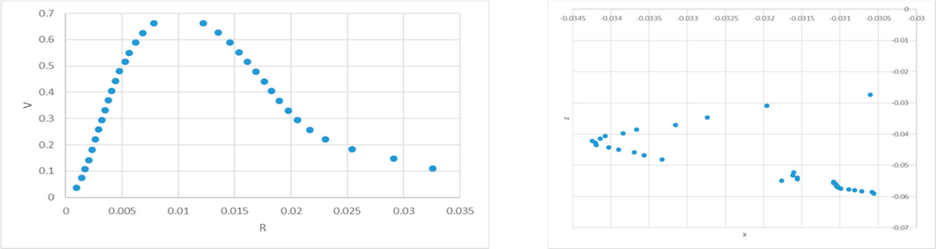

(**b**) Velocity distribution and location of centerline of the fountain.

Figure 25. Inclined fountain when R_{Re} = 2.5.

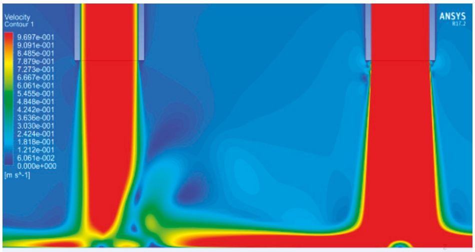

(**a**) Velocity contours

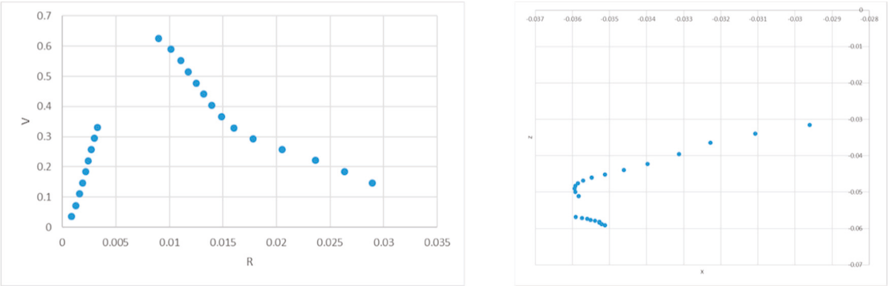

(**b**) Velocity distribution and location of centerline of the fountain.

Figure 26. Inclined fountain when R_{Re} = 3.

Pressure distribution at the bottom plane when R_{Re} is 3.3 is shown in Figure 30a. Two peak values in the pressure can be seen; the left one corresponds to the stagnation point of the left jet while the right one is the stagnation point of the formed fountain. However, for cases where R_{Re} is 3.8 and 4, the second peak cannot be observed as distinctly as shown in Figure 30b,c.

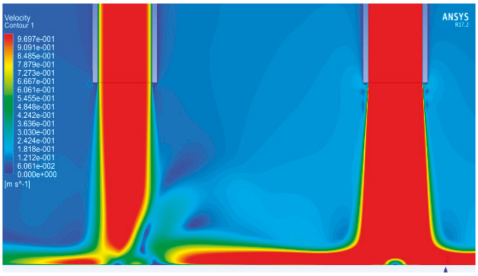

Figure 27. Inclined fountain when R_{Re} = 3.3.

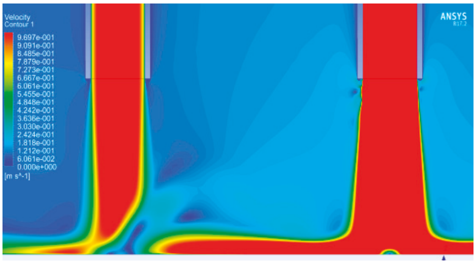

Figure 28. Inclined fountain when R_{Re} = 3.8.

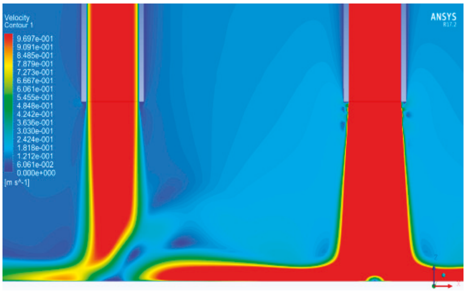

Figure 29. Inclined fountain when R_{Re} = 4.

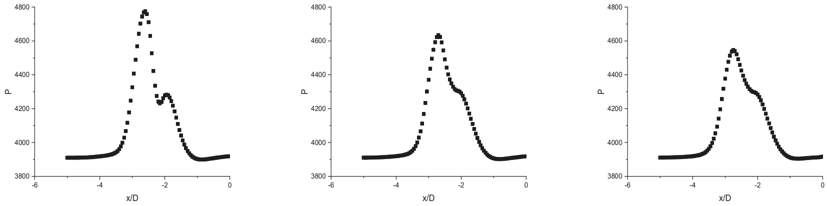

(**a**) R_{Re} = 3.3 (**b**) R_{Re} = 3.8 (**c**) R_{Re} = 4

Figure 30. Pressure distribution at the bottom plane for different R_{Re}.

Figure 31 shows the location of stagnation point of the fountain normalized by diameter of jet for various ratios of Reynolds number. When R_{Re} is 1, the fountain is straight upward and the stagnation point is at $x/D = 0$, right in the middle of the two jets as expected. As R_{Re} increases, the stagnation point of the fountain approaches $x/D = -2.5$, which is the centerline of the left jet. In addition, for $R_{Re} > 3.3$, the movement of the stagnation point decreases greatly. Figure 32 shows the static pressure at stagnation points. Similarly, before R_{Re} reaches 3.3, pressure at the stagnation point increases more rapidly compared to that when R_{Re} increases beyond 3.3 when it changes more slowly, and pressure at the stagnation point approaches 4300Pa where 3916 Pa is generated by water due to gravity acceleration.

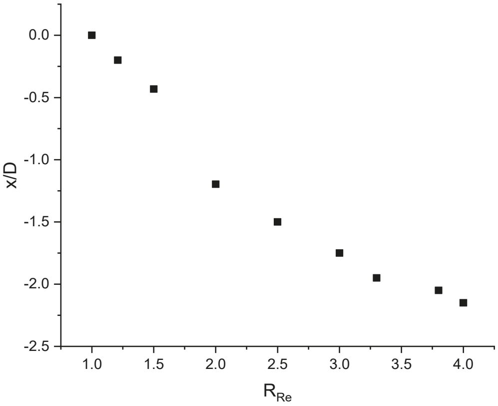

Figure 31. Variation in location of stagnation point of the fountain for various R_{Re}.

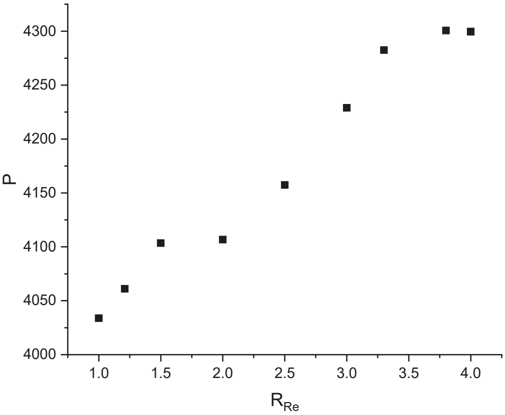

Figure 32. Variation in static pressure at stagnation point of fountain with R_{Re}.

Figure 33 shows the displacement of the stagnation point of the left jet for different values of R_{Re} Displacement of the stagnation point of left jet for $R_{Re} > 3.3$ is much faster than for $R_{Re} < 3.3$. Figure 34 shows the static pressure at the stagnation point. Similarly, for $R_{Re} > 3.3$, the pressure at the stagnation point of the left jet decreases significantly. This phenomenon could be the result of a strong wall jet produced by the right jet when $R_{Re} > 3.3$. The vertical velocity component of the wall jet from the right side prevents the left jet from impinging on the bottom plate. Therefore, delayed impingent of the left jet reduces pressure at the stagnation point of the left jet.

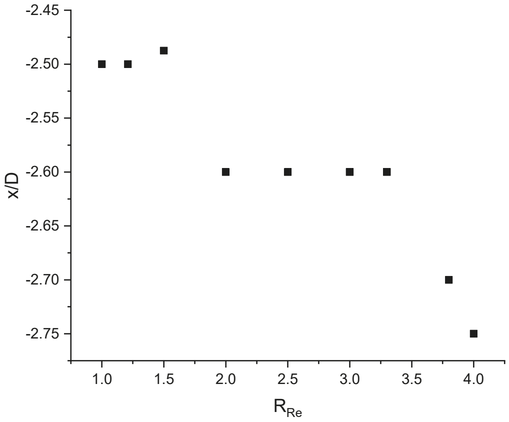

Figure 33. Variation in location of stagnation point of left jet with R_{Re}.

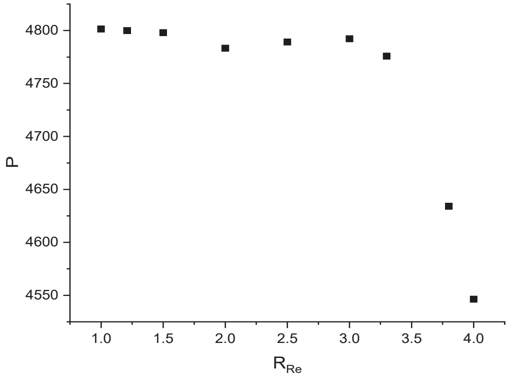

Figure 34. Variation in pressure at stagnation point of left jet with R_{Re}.

3.5. Fountain Formed by Inclined Jets

The discussion in the sections above has been for the fountain formed by twin-jets normal to impingement surface. However, in many applications, jets are inclined from the normal position. This section describes the simulations and analyzes how the flow properties of the fountain would be affected by impingement angles of the two jets. The two jets are symmetric about the centerline with identical diameter, inlet velocity and inclination angle. When building the geometry, both pipes are rotated towards the origin point while O_1 points (see Figure 1c) of two pipes are fixed, which means that the left pipe rotates counterclockwise and the right pipe rotates clockwise. The distance between the two jets, from O_1 point on left side to that on right side, is 5*D*. The impingement height is 3*D*. Inlet velocity is 1 m/s. Figure 35 shows the velocity contour when impinging angles are 60, 75 and 90 degrees.

Figure 36 shows the distribution of the pressure coefficient at various impingement angles in the region close to the fountain center. As the jets get inclined further from normal position, the pressure coefficient in this region becomes much higher. This phenomenon is mainly led by two factors. If the impinging jet is inclined from its normal position to the ground, the wall jet on two sides will be asymmetric. Wall jet of one side is stronger than that of the other side. Such a difference becomes larger when impingement angle becomes smaller since the jet is further away from normal or symmetric position. In these cases, fountains are formed by wall jets of stronger side and are thus of greater strength as impingement angle becomes smaller. Besides, rotation of pipe while fixing O_1 point leads to an impinging center of two jets or O_2 point (see Figure 1c) getting closer. Thus, the distance of the initial location of wall jets from two impinging jets is smaller than the distance of two jets, which increases the strength of the fountain.

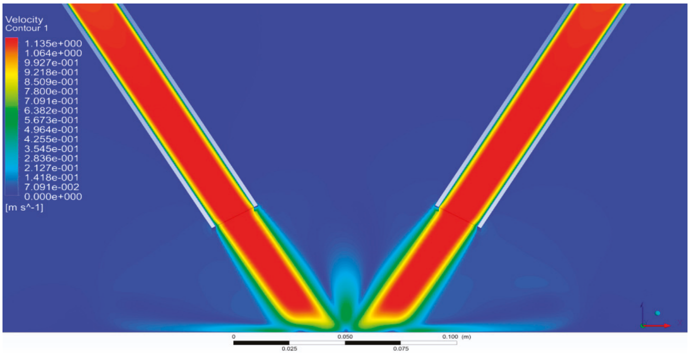

(**a**) 60 degree

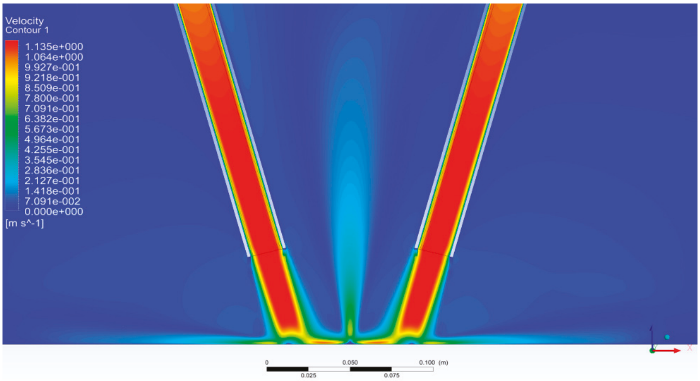

(**b**) 75 degree

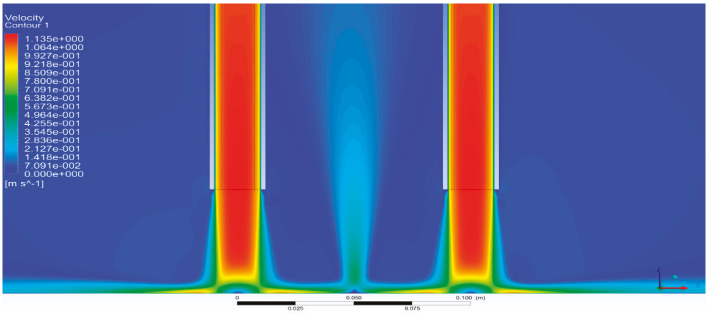

(**c**) 90 degree

Figure 35. Velocity contours at various impinging angles.

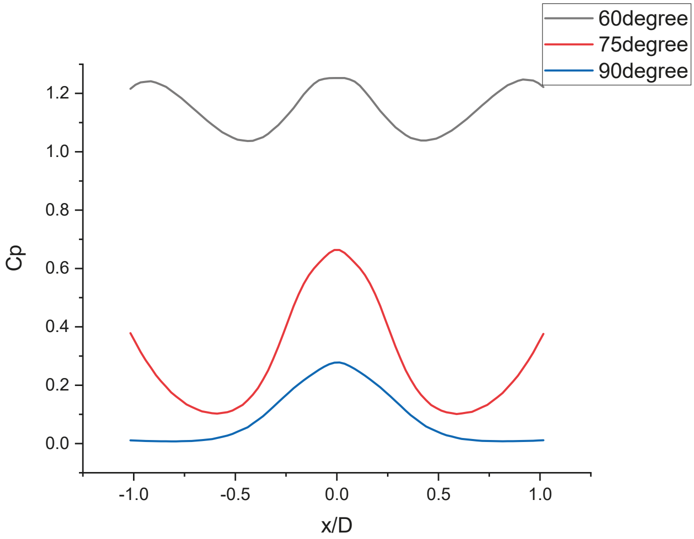

Figure 36. Pressure Coefficient on ground at different impingement angles.

Figure 37a–c shows velocity profiles at various heights above the ground when the impingement angles are 60, 75 and 90 degrees. There are significant differences in the velocity profiles due to inclination angle of the jets. All velocity profiles in the region near the formation of the fountain exhibit a similar behavior. Lines of h = 0.2*D* have a local minimum point at *x*/*D* = 0, while velocities at other heights have a local maximum point at *x*/*D* = 0. Besides, velocities at *h* = 0.5*D* have the largest local maximum at *x*/*D* = 0. As height becomes larger than 0.5*D*, the local maximum of velocity becomes smaller and plotted lines reach their local maximum point with a smaller slope.

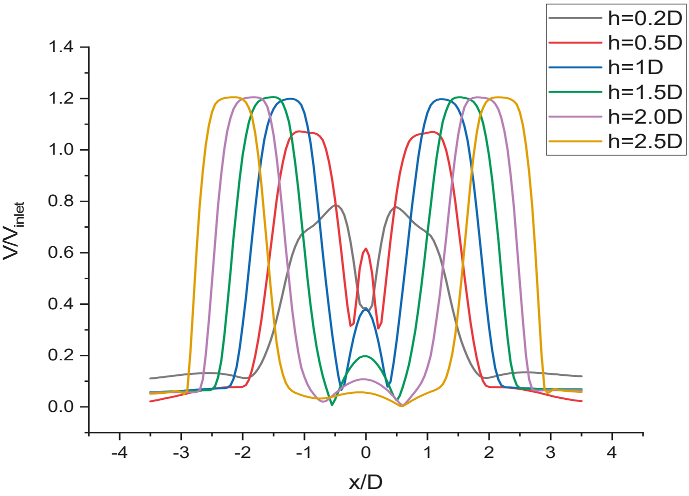

(**a**) 60 degrees

Figure 37. *Cont.*

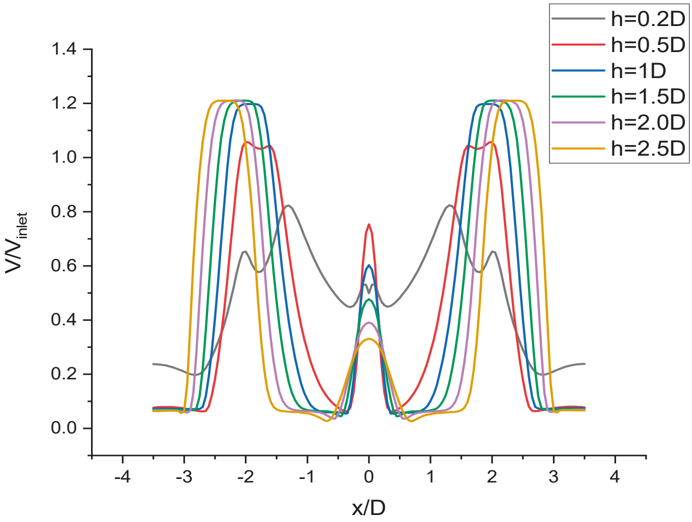

(**b**) 75 degrees

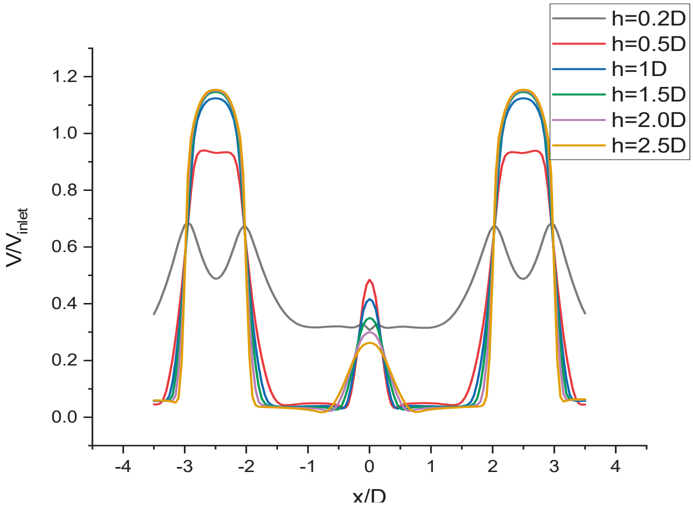

(**c**) 90 degrees

Figure 37. Velocity profiles at different heights from ground surface.

Figure 38a–c shows the velocity profiles at different radial distances from the centerline of the fountain. In all three figures, the velocity lines have a point of maximum velocity. When R is $0.1D$ or less, maximum velocity occurs at larger h/D, while when radial distance is larger than $0.1D$, maximum velocity occurs at smaller h/D very close to the ground. Also, when R is greater than $0.1D$, peak velocity increases as R becomes larger. However, there are some differences among the three cases. Looking at the velocity plot of $R = 0.1D$, there are two stages in slope before reaching the peak point. The slope of the first stage is always greater than that of the second stage. However, the slope of the first stage is largest at the impingement angle of 60 degree and is the smallest at normal impingement. Cases of 75 and 90 degree impingement angles show similar behavior. However, in the 60 degree impingement case, the velocity plot when R is greater than $0.1D$ is different from the cases of 75 and 90 degree impingement angle; the velocity plot of $R = 0.1D$ shows two stages of slope before the peak point. The peak velocities in cases of 75 and 90 degree impingement angles are at similar positions and are very close to the ground, while in the case of the 60 degree impingement angle, peak occurs at different h/D.

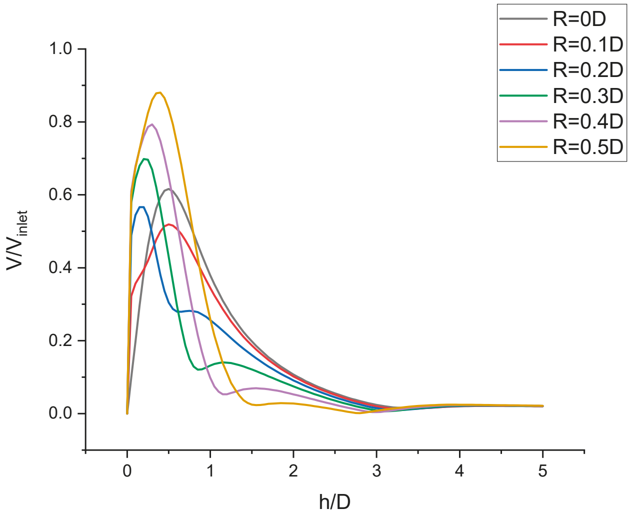

(**a**) 60 degrees

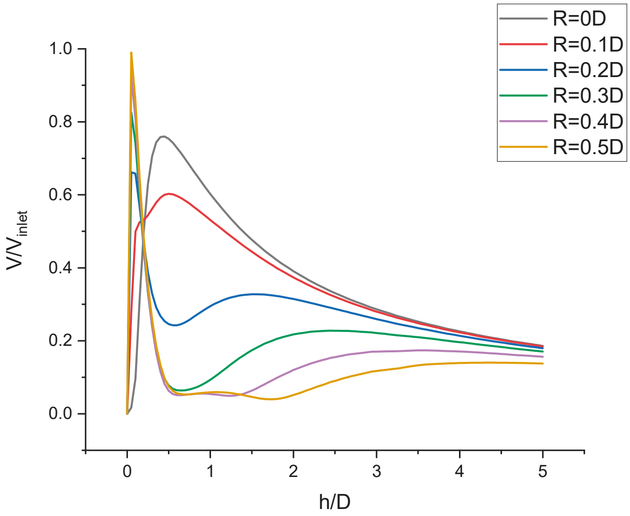

(**b**) 75 degrees

Figure 38. *Cont*.

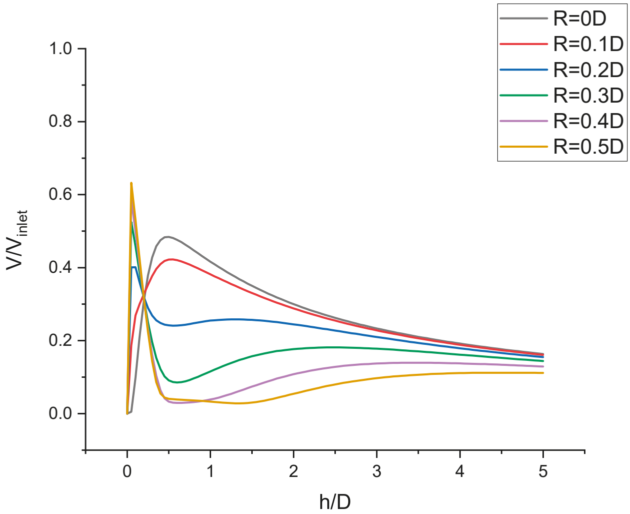

(**c**) 90degree

Figure 38. Velocity profiles at different radial distances from the fountain center.

4. Conclusions

Based on the results presented in this paper, the following conclusions can be drawn:

1 Numerical results from both k-ε and Wray-Agarwal turbulence model show good agreement with experimental data for single jet impingement.

2 For the fountain formed by two round jets, if Reynolds number of the two jets at the inlet is identical and exits of jets are located at same horizontal level, the fountain formed in this condition is straight and upwards.

3 Pressure at the fountain center is highly sensitive to the inlet Reynolds number of the jets when distance between the jets S, is small. However, the pressure coefficient is much less sensitive to inlet Reynolds number than pressure in Pascal.

4 Straight fountain exhibits different velocity profiles in regions at different radial distances. Fountain flow has larger acceleration near the bottom plane when radial distance $x/D > 0.5$ compared to when $x/D < 0.5$.

5 When inlet Reynolds number of jets are different, the fountain formed by the two jets moves to the side of the jet with smaller inlet Reynolds number and stagnation point of the fountain also moving along the same direction. As the ratio of Reynolds number increases, the fountain reflects back to the jet with larger inlet Reynolds number and the stagnation point of the fountain tends to merge with the stagnation point of the left jet that has smaller inlet Reynolds number. Meanwhile, strong wall jet from the right side has a negative influence on impingement of the left jet.

6 Change in impinging angle of the jets significantly changes the behavior of the fountain because of the change in strength and location of the wall jets.

Author Contributions: R.K.A. conceived, formulated, provided technical guidance and administered the project. X.Z. performed the computations and wrote the paper which was reviewed and edited by R.K.A. All authors have read and agreed to the published version of the manuscript.

Funding: This research received no external funding.

Conflicts of Interest: The authors declare no conflict of interest.

Nomenclature

C_p	Pressure coefficient
D	diameter of water jet
H	vertical distance from impingement plane
S	Distance between the centerlines of two jets
Re	Reynolds number based on the diameter of the pipe
y^+	dimensionless wall distance of first grid layer
P	static pressure
P_{ref}	reference pressure
ρ	density of water
V_{inlet}	velocity at jet inlet

References

1. Weigand, B.; Spring, S. Multiple jet impingement—A review. *Heat Transf. Res.* **2011**, *42*, 101–142. [CrossRef]
2. Dewan, A.; Dutta, R.; Srinivasan, B. Recent trends in computation of turbulent jet impingement heat transfer. *Heat Transf. Eng.* **2012**, *33*, 447–460. [CrossRef]
3. Ostheimer, D.; Yang, Z. A CFD Study of Twin Impinging Jets in a Cross-Flow. *Open Numer. Methods J.* **2012**, *4*, 24–34. [CrossRef]
4. Saripalli, K.R. Visualization of Multi-Jet Impingement Flow. *AIAA J.* **1983**, *21*, 483–484. [CrossRef]
5. Ozmen, Y. Confined impinging twin air jets at high reynolds numbers. *Exp. Therm. Fluid Sci.* **2011**, *35*, 355–363. [CrossRef]
6. Barata, J.M.; Durao, D.F.G.; Heitor, M.V.; McGuirk, J. Impingement of single and twin turbulent jets through a crossflow. *AIAA J.* **1991**, *29*, 595–602. [CrossRef]
7. Greco, C.S.; Ianiro, A.; Astarita, T.; Cardone, G. On the near field of single and twin circular synthetic air jets. *Int. J. Heat Fluid Flow* **2013**, *44*, 41–52. [CrossRef]
8. Abdel–Fattah, A. Numerical and experimental study of turbulent impinging twin-jet flow. *Exp. Therm. Fluid Sci.* **2007**, *31*, 1061–1072. [CrossRef]
9. Wang, C.; Wang, X.; Shi, W.; Lu, W.; Tan, S.K.; Zhou, L. Experimental investigation on impingement of a submerged circular water jet at varying impinging angles and Reynolds numbers. *Exp. Therm. Fluid Sci.* **2017**, *89*, 189–198. [CrossRef]
10. Taghinia, J.; Rahman, M.M.; Siikonen, T. Numerical investigation of twin–Jet impingement with hybrid–type turbulence modeling. *Appl. Therm. Eng.* **2014**, *73*, 648–657. [CrossRef]
11. Attalla, M.; Maghrabie, H.M.; Specht, E. Effect of inclination angle of a pair of air jets on heat transfer into the flat surface. *Exp. Therm. Fluid Sci.* **2017**, *85*, 85–94. [CrossRef]
12. Sharif, M.A.R. Heat transfer from an isothermally heated flat surface due to twin oblique slot-jet impingement. *Procedia Eng.* **2013**, *56*, 544–550. [CrossRef]
13. Faris, A.M.; Zulkifli, R.; Harun, Z.; Abdullah, S.; Wan Ghopa, W.A. Experimental and numerical simulation of the heat transfer enhancement on the twin impingement jet mechanism. *Energies* **2018**, *11*, 927. [CrossRef]
14. Shih, T.-H.; Liou, W.W.; Shabbir, A.; Yang, Z.; Zhu, J. A new k-ϵ eddy viscosity model for high Reynolds number turbulent flows. *Comput. Fluids* **1995**, *24*, 227–238. [CrossRef]
15. Han, X.; Wray, T.J.; Agarwal, R.K. Application of a new DES model based on Wray-Agarwal turbulence model for simulation of wall-bounded flows with separation. In Proceedings of the 47th AIAA Fluid Dynamics Conference, Denver, CO, USA, 5–9 June 2017; AAIA: Reston, VA, USA, 2017; p. AIAA2017-3966.
16. Turbulence Modeling Resource. Available online: https://www.turbmodels.larc.nasa.gov/wray_agarwal.html (accessed on 22 September 2019).
17. Wray Agarwal Models. Available online: https://www.github.com/xuhanwustl/WrayAgarwalModels (accessed on 14 August 2019).

fluids

MDPI

Article

Controlled Synthetic Freestream Turbulence Intensity Introduced by a Local Volume Force

Eike Tangermann * and Markus Klein

Numerical Methods in Aerospace Engineering, Bundeswehr University Munich, 85577 Neubiberg, Germany; markus.klein@unibw.de

* Correspondence: eike.tangermann@unibw.de

Received: 24 June 2020; Accepted: 1 August 2020; Published: 7 August 2020

Abstract: Generating freestream turbulence within the computational domain instead of applying it as a boundary condition requires a method to introduce the turbulent fluctuations at a specific location. A method based on applying local volume forces has been adapted and supplemented with a control loop in order to compensate for alterations of the turbulence structure resulting from the numerical treatment and physical reasons. The criteria for the tuning of the controller have been developed and the performance of the approach has been assessed. The capabilities of the method are demonstrated for the flow around an airfoil at high angle of attack and with massive flow separation.

Keywords: freestream turbulence; resolved turbulence; synthetic turbulence; control loop

---

1. Introduction

Freestream turbulence is a feature to be found very commonly in flows of many kinds. It occurs in ducted flows as well as in unbounded flows and represents disturbances situated in the upstream history of the flow. It might, for example, result from the wake turbulence of objects, thermal bubbles or free shear layers. The freestream turbulence can have a significant effect on the flow along surfaces, where it affects boundary flow phenomena like transition and separation. Depending on its length scale it, either changes the magnitude and direction of momentum locally or even in larger regions.

In computational fluid dynamics (CFD) simulations with fully or partially resolved turbulence, the freestream turbulence needs to be accounted for. However, generally it does not appear feasible to resolve its formation, which often occurs far upstream of the focus region. Instead synthetic turbulence is applied. Several methods have been proposed using different mechanisms for the generation of synthetic turbulent fluctuations based on filtered random fields [1,2], vortex spot distributions [3], reconstruction of measured spectra [4–6] or reconstruction using proper orthogonal decomposition (POD) of measured time series [7]. Often they are introduced into the computational domain as a boundary condition.

However, in applications from the field of external aerodynamics it is common to use boundaries of farfield type for the outer edge of the computational domain in order to investigate the flow around a free flying object with the boundary being as unaffected as possible by the object in focus. Most of the computational domain is not of interest in the investigation and therefore usually is resolved very coarsely, which also filters out disturbances approaching the boundary. Introducing synthetic turbulence in a farfield boundary condition would then require a grid resolution fine enough to fully resolve the turbulent structures in order to transport them convectively up to the focus region. Furthermore a long time span would have to be simulated until the turbulence arrives at the investigated object. Besides the high computational effort, the decay of the turbulence during this time would also have to be considered in prescribing the boundary condition.

Since this appears unfeasible, different approaches have been proposed to introduce turbulence closer to the focus region. It is, for example, possible to introduce turbulence by superposition from an overlapping mesh as proposed in [8]. This requires the solver software being capable of handling mesh overlays. Alternatively, volumetric force fields can be applied to manipulate the flow field. Numerical simulations of volume forced turbulence are most often formulated in Fourier space, where forcing [9,10] or stochastic forcing [11] is typically applied to low wave number modes. A comprehensive overview for such spectral forcing schemes can be found in Rosales and Meneveau [12]. It is generally accepted that forcing the Navier–Stokes equation at low wave number does not influence the small-scale statistics of the flow, provided that there is a wide separation between the largest and smallest scales [13]. Similarly, the spectral nudging method developed by Waldron et al. [14] imposes time-variable large-scale flow states on a local model and is often used for regional climate modeling [15].

However, many engineering problems do not admit periodic boundary conditions and the solution cannot be expanded in a Fourier series. They are often simulated using numerical codes formulated in physical space such as finite volume methods and consequently spectral forcing is difficult to implement [12]. In the linear physical space forcing proposed by Lundgren [13], the force is proportional to the velocity fluctuation. While this is an attractive approach, which has been well characterized in [12], it has been also demonstrated that the length scale converges to an average scale near 35% of the domain size (based on the estimate $l = k^{3/2}/\epsilon$) independently of the initial conditions and the situation becomes even worse on non-cubic domains [16]. In order to control the length scales it has been suggested in Klein et al. [16] to make the forcing proportional to a high pass filtered velocity fluctuation. However, implementation of a high pass filter on an arbitrary unstructured grid is not straightforward. Recently, Schmidt and Breuer [17] have proposed a method based on applying a local volume force to superimpose synthetic turbulence at arbitrary locations of the computational domain, which can relatively easy be integrated into a Navier–Stokes solver by adding a source term.

The present work introduces an approach based on the latter method. Treatment of the source term in the pressure correction algorithm is addressed, as well as monitoring and scaling the resulting turbulence by supplementing it with a controller mechanism. The approach then is calibrated using a simple channel setup with free slip walls, validated using a farfield configuration and further assessed with respect to performance with the flow around a cylinder with an alternating vortex street pattern. Finally, results of the flow around a NACA0012 airfoil at high angle of attack with and without freestream turbulence will be presented and discussed. Applying the method in all these cases demonstrates the generality of the method.

2. Numerical Method

For the flow simulation an incompressible flow solver from OpenFOAM has been used. It solves the Navier–Stokes equations in an incompressible formulation. Pressure and velocity are coupled using a dual time stepping pressure correction method combining PISO time steps with outer iterations of the SIMPLE algorithm.

According to Schmidt and Breuer [17] a locally acting force is introduced to the momentum equation, which then, in the commonly used incompressible form of OpenFOAM with the pressure normalized by the constant density, becomes

$$\frac{\partial \vec{u}}{\partial t} + \nabla \cdot (\vec{u}\vec{u}) - \nabla \cdot (\nu \nabla \vec{u}) = -\nabla p + \vec{F}^{syn}. \tag{1}$$

The force F^{syn} needs to be set appropriately in order to achieve the desired velocity fluctuations. Typically, the force is only acting in a certain zone upstream of the focus region. The volume force represents the force which is necessary to accelerate the fluid to the desired fluctuation velocity. It depends primarily on the transition time T a fluid element spends traveling across the influence region and the fluctuation velocity vector.

To stabilize the numerical solution, the force should not introduce sudden jumps into the momentum equation. Therefore a Gaussian bell-shaped function G is introduced to soften the force field towards its boundaries. To preserve the total force effect, G is normalized by its mean value $\overline{G}$. Assuming that the undisturbed flow primarily is pointing in the x-direction, the transition time can be calculated from the width of the forcing zone L_x and the x-wise bulk velocity u_0. The force term superimposing a fluctuation velocity $(u')^{syn}$ then is expressed by

$$F_{syn} = \frac{(u')^{syn}}{T} \cdot G(x,y,z)/\overline{G} = \frac{(u')^{syn}}{L_x/u_0} \cdot G(x,y,z) \cdot \left(\frac{1}{L_x} \int_{-L_x/2}^{L_x/2} G(x)\,dx \right)^{-1} . \tag{2}$$

At very low levels of turbulence intensity the bell function primarily is acting to smooth steps in the stream-wise direction. For stronger turbulence it is necessary to also smooth the force field towards the sides of the forcing region unless they reach the boundary of the computational domain. Thus, depending on the specific setup, a two- or three-dimensional function is applied.

$$G = \exp\left(-\frac{\pi}{2} \left(\frac{(x-x_0)^2}{(L_x/2)^2} + \frac{(y-y_0)^2}{(L_y/2)^2} + \frac{(z-z_0)^2}{(L_z/2)^2} \right) \right) \tag{3}$$

The additional force term in the momentum equation needs to be taken into account in the pressure correction. An additional term arises in the pressure equation representing the divergence of the force field. The semi discretized form according to Jasak [18] then becomes

$$\nabla \left(\frac{1}{a_p} \nabla p \right) = \nabla \left(\frac{H(\vec{u})}{a_p} \right) + \nabla \vec{F}^{syn} \tag{4}$$

where a_p denotes the matrix coefficient for the central cell and $H(\vec{u})$ represents the neighbor cells and the temporal derivative. It needs to be mentioned that, if the forcing term is implemented correctly in OpenFOAM, $H(\vec{u})$ will also incorporate it as a source term. However, in an intermediate step this has been prevented here for the sake of demonstration.

For an ideal transfer of the fluctuations into the fluid flow it would be necessary to move the force field along with the flow across the forcing zone. In order to facilitate the implementation of the method and its computational overhead just one slice of the force field is taken at a time and spread across the forcing zone. That means, that the local force changes, while a fluid element is passing. This changes the amount of force applied depending on the ratio of the length scale of each fluctuation to the forcing region length. The wider the forcing zone is selected the lower the fluctuation magnitude will become. On the other hand it is desirable to have a wider forcing zone for a smoother transition into and out of the force field.

The effect of forcing zone width on the resulting fluctuation field is illustrated in Figure 1. In order to give a clearer view to the fluctuations, they are in this context applied to a passive scalar field. The scalar is transported only convectively with a constant bulk velocity. The upper image of Figure 1 shows the original field of synthetic fluctuations. Below the resulting fields from calculations with different settings for the width of the forcing zone are shown. The length scale L_t of the fluctuations generally is produced well. Some structures, where two or more spots are very close to each other become blurred and the individual spots form one larger spot in the resulting field. This happens regardless of the forcing zone width.

The effect of the width is most obvious in the lower image where the width is four times the fluctuation length scale, which for practical use definitively is too big. The primary consequence is, that the resulting spots are much less intense, which results from the mechanism described above. This also appears for the other cases with different length scale ratios shown in Figure 1. It is less obvious but still measurable and significant since it changes the resulting mean fluctuation intensity.

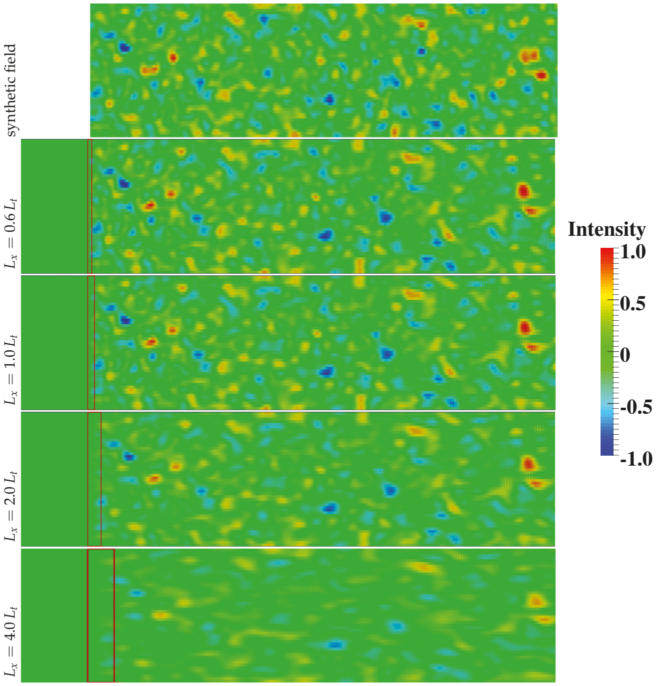

Figure 1. Original fluctuation field (top) and transport as a passive scalar with variations of L_x. Decreasing intensity of small scale fluctuations with increasing width.

Another effect which modifies the introduced fluctuation velocity is, that the pressure correction algorithm reacts to a positive acceleration with a positive pressure gradient unless the acceleration field is free of divergence. Thus the accelerating force is partly balanced by a counteracting pressure gradient. This effect is relatively small in weak turbulence and only relevant for intense turbulence at larger scales. Finally, besides these effects, which arise from the numerical treatment, the viscous decay of turbulence also alters the turbulence intensity between its introduction until it reaches the focus zone.

To overcome all of these effects a control loop has been introduced. Applying a mechanism to control the generated turbulence has been proposed previously [16,19,20] with proportional correction terms. In the present work a full PID controller has been applied. An amplification factor is applied in Equation (2), which scales the force field globally. Downstream of the forcing region a control region needs to be placed, in which the resulting fluctuation intensity or the turbulent kinetic energy is measured. In order to reduce local variations of turbulence intensity as the fluctuations are passing by, the control region should be selected sufficiently wide. At each time step, the mean value of u'_{rms} is calculated inside.

The difference between the actual and desired fluctuation velocity, the error variable $e = u'_{target} - u'_{rms}$, is determined. The calculated error is then processed in a common PID control function, which thereby determines the control variable.

$$u(t) = K_p \cdot e(t) + K_i \int_0^t e(\tau)\, d\tau + K_d \frac{d\,e(t)}{dt} \tag{5}$$

Here, $u(t)$ denotes the control output and K the gain coefficients for the individual controller terms.

The controller is implemented in a discrete formulation, where the integral is replaced by a sum of all measured error terms and the derivative is approximated by finite differences.

$$u_n = K_p \cdot e_n + K_i \sum_{0}^{n} e_n \Delta t_n + K_d \frac{e_n - e_{n-1}}{\Delta t_n}. \tag{6}$$

The controller output u is then added to the force amplification factor, which results in another integral effect. It has proven beneficial to limit the amplification to positive values since negative scaling is not appropriate.

For the performance of the controller it is essential to select an appropriate set of gain coefficients. They depend strongly on the individual setup, namely the delay times, which arise from the propagation of fluctuations from the formation within the forcing zone until they reach the measurement zone and further until they have completely passed and filled the measurement zone. The first part can be considered as dead time T_d since the scaling effect is not being measured, yet. In the present work it is defined as the time needed to come from the middle of the forcing zone to the beginning of the measurement zone at bulk velocity. The second part, the passage through the measurement zone at bulk velocity, can be considered as the rise time T_r of the measurement. From simulations of a two-dimensional slip-wall channel with synthetic fluctuations the following correlations have been developed inspired by the criteria according to Chien, Hrones and Reswick [21]. The setup for calibrating the controller parameters has been selected two-dimensional, because not the development of actual turbulence but only the presence of fluctuations is of importance in this context. Thus a two-dimensional case decreases the computational effort significantly.

$$\begin{aligned} K_p &= k_p \cdot \frac{T_r}{3 \cdot T_d} \\ K_i &= k_i \cdot \frac{K_p}{2 \cdot T_d} \\ K_d &= k_d \cdot K_p \cdot T_d / 2 \end{aligned} \tag{7}$$

Three different tunings are presented in Table 1. The baseline setting generally showed good results in keeping the measured error low as well as not allowing too much variation of the scaling factor. The smooth setting allows for slightly more measurement error variations and makes the controller reacting slower. This leads to a smoother behavior of the scaling factor. In the agile setting the controller allows quicker adaption of the scaling and reduces the measured error. It also tends to produce an overshoot in the initial phase. The evolution of the amplification factor for these three tunings is shown in Figure 2 for a channel flow with 10% fluctuation intensity. The width of forcing and measurement zones is varied, which leads to different delay and rise times, respectively. Setting the width of the forcing zone to approximately the fluctuation length scale appears reasonable. With the measurement zone being two to three times as wide as the forcing zone the rise time can be kept low while still taking advantage of the smoothing effect by its size.

One might expect, that the coefficients should be dependent on the target fluctuation intensity. Taking such a dependency into account, indeed leads to a very quick response of the controller and the desired intensity level is reached soon. However, afterwards the scaling factor will show too strong variations. Instead it is advisable to estimate an initial setting for the scaling and delay the controller activation by $T_d + T_r$, which will ease the initial adaptation.

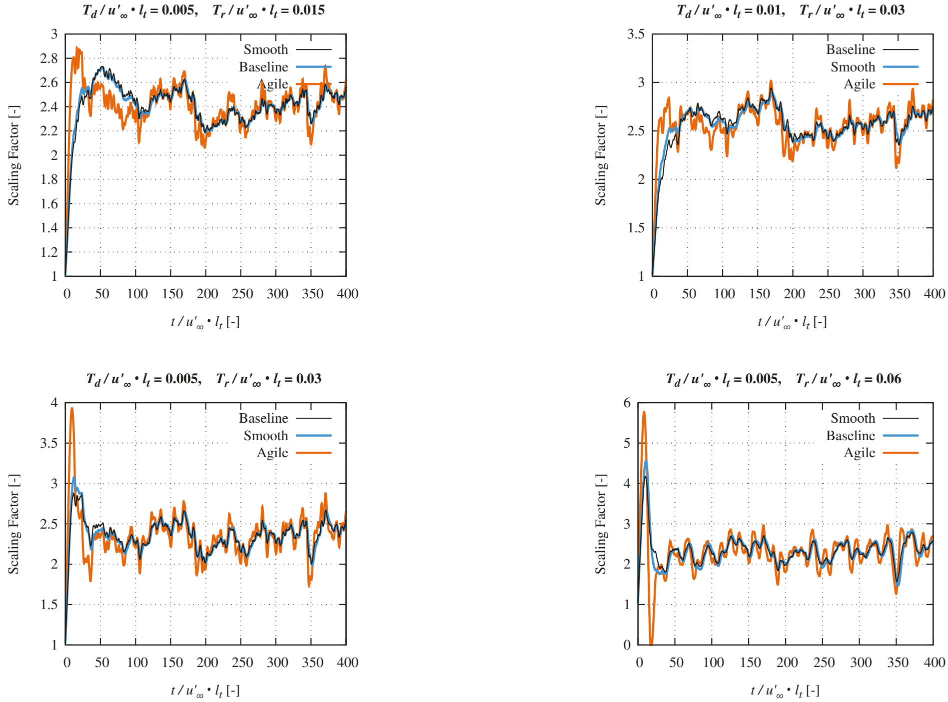

Figure 2. Evolution of the amplification factor from smooth, baseline and agile controller coefficient settings for several pairs of delay and rise time.

Table 1. Tuning constants for the controller coefficient setting.

	Baseline	Smooth	Agile
k_p	0.1	0.1	0.2
k_i	0.02	0.02	0.02
k_d	5.0	1.0	5.0

The schematic sketch for a practical application, an airfoil flow, is shown in Figure 3. One slice of the synthetic fluctuation field is applied in the red forcing region. The result is measured in the yellow control region and fed back through the controller. The resulting turbulence field is indicated by blue iso-surfaces of Q criterion.

In all cases presented here the synthetic fluctuations have been generated using a method proposed by Kempf et al. [2] based on diffusive filtering of a random field. Depending on the amount of diffusion applied, the length scale can be controlled. Finally, the field is normalized and transformed to fulfill the prescribed intensity or, if the specific applications requires this, even the full Reynolds stress tensor using the transformation by Lund [22].

It is worth noting that the forcing method is completely independent of the generation method and it can be combined with synthetic or real turbulence from an arbitrary source. It is not necessary, that the fluctuation field is free of divergence. Unlike in a synthetic turbulence boundary condition as proposed by [23] the volume force will not generate divergence of the velocity field beyond the limits of the pressure correction algorithm after the solution of a time step is converged.

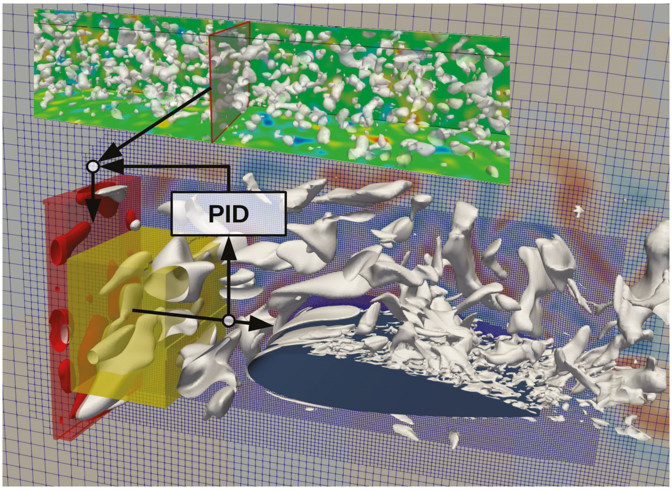

Figure 3. Sketch of forcing and controller. The synthetic fluctuations are taken from a slice of the separate fluctuation field and then introduced in the red forcing region (instantaneous force is indicated by red iso-surfaces), the resulting fluctuation velocity is then determined in the yellow control region and looped back via the PID controller.

3. Results and Discussion

3.1. Validation in Empty Domain with Farfield Boundary

The first step in the validation process is to verify that the fluctuations induced into the simulation domain agree with the prescribed statistical properties. To ensure that the turbulence does not interfere with geometry an empty farfield domain has been simulated. The setup is based on the flow around an obstacle like an airfoil. The entire domain extends 20 units of length in stream-wise and vertical direction with a farfield condition along the outer boundary. Its span-wise extension is 0.5 units with periodic boundaries. The unstructured hexahedra-based mesh features 4×10^6 cells with hierarchical refinement towards the central region. Between the stages of refinement polyhedral cells are introduced to avoid hanging nodes. The fluctuations are introduced in the range of $x = -0.75$ to -0.67 immediately followed downstream by the controller measurement region up to $x = -0.3$. If an airfoil was present it could be expected within $x = 0.0$ and 1.0 and the refinement is kept further up to $x = 1.2$. In perpendicular direction the refined area extends between $y = -0.4$ and 0.5. This is equivalent to the extension of the forcing region with the forcing being smoothed out towards top and bottom as described above.

The prescribed turbulence is set to a relatively low value of $Tu = 0.51\%$ and an integral length scale of $L_t = 0.0327$ units of length. Even though the method would allow to specify individual components of the Reynolds stress tensor, in the present case only a homogeneous turbulence intensity has been prescribed using the diagonal tensor components. The Reynolds number based on one unit of length is 80,000.

With this setup, after sufficient initial relaxation time, data have been collected for 10 convective time units, from which the achieved mean fluctuation intensity as well as the actual integral length scale, calculated from autocorrelation, have been determined. The development of both values is shown in Figures 4 and 5, respectively, along lines ranging from the forcing zone through the fine mesh region in six vertical locations. Each of these is covered by two lines in periodic direction, which mostly coincide in the plots therefore showing only one line. An airfoil shape, which not has been present in the computations, is indicted in the figures by dashed lines to show a possible application setup.

It can be seen that after passing the forcing zone both quantities reach the prescribed values. In the topmost and lowermost lines the intensity stays slightly below the target value since the damping function towards the edges starts acting. During the downstream propagation, the fluctuation intensity shows a very slight decay as it can be expected. Accordingly, the value of the integral length scale rises slightly as the fluctuations decay. These results give confidence that the entire setup of forcing and controlling reliably produces the prescribed fluctuation properties and can be applied to more complex applications.

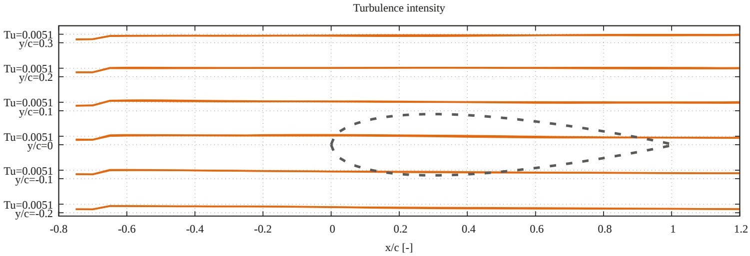

Figure 4. Development of fluctuation intensity along an empty domain. The dashed lines indicate where an object like an airfoil could have been placed.

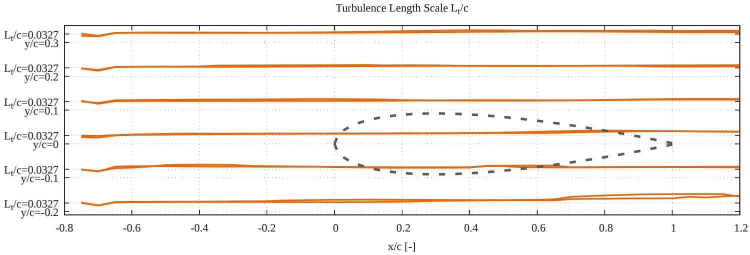

Figure 5. Development of integral turbulence length scale along an empty domain. The dashed lines indicate where an object like an airfoil could have been placed.

3.2. Performance Assessment

By introducing the controller mechanism the magnitude of the original input fluctuation field becomes irrelevant. Only the length scale and, if required, the cross correlations of the Reynolds stresses need to be prescribed correctly in advance. The magnitude of the fluctuations can then be amplified to an arbitrary value. Thus, series of simulations with variation of the turbulence intensity are possible with only a single set of synthetic fluctuations.

To demonstrate and validate this capability the two-dimensional flow around a cylinder with synthetic fluctuations in the approaching flow has been calculated with different settings for the turbulence intensity. Here, again, two-dimensionality has been chosen to reduce the computational effort. The demonstrative purpose is to show the behavior of the controller and not that of the turbulence field.

The setup is shown in Figure 6, the forcing zone is located one diameter upstream of the cylinder and 1.5 times the diameter downstream of the inlet boundary. It extends up to five cells in stream-wise direction, which appears to be sufficient for stable operation. The measuring region of the controller is located immediately downstream of the forcing. For the controller it would be favorable to increase the width of the measurement zone. However, since the cylinder is affecting the flow upstream it is not suitable to further increase the measurement zone in this case.

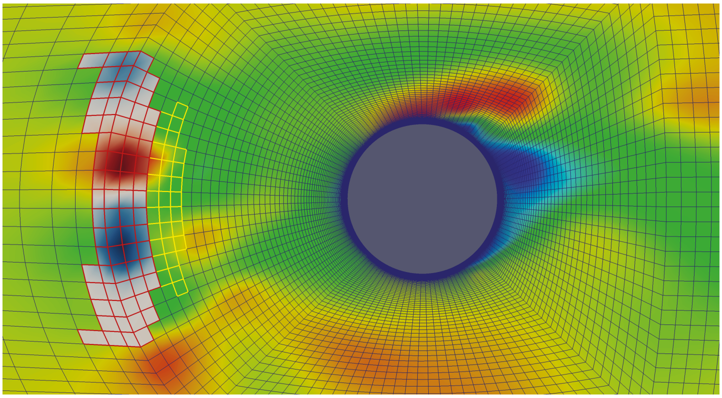

Figure 6. Stream-wise velocity u_x field around the cylinder and volume force F_x^{syn} in the forcing region marked red. Controller measurement region marked yellow.

From one field of synthetic fluctuations four different simulations have been performed with different levels of u'_{rms}. They range from from almost undisturbed flow ($u'_{rms}/u_\infty = 0.01$) to high turbulence ($u'_{rms}/u_\infty = 1$). At a Reynolds-number of 2×10^5, based on bulk flow velocity and diameter, the cylinder wake flow forms a characteristic von Karman vortex street, which is disturbed by the approaching fluctuations. An instantaneous view to the flow field is given by Figure 7 for the highest setting of turbulence intensity after sufficient computed time to achieve a relaxed quasi-steady state. The smaller scale eddies become dissipated very quickly downstream of the cylinder because the mesh is getting coarser.

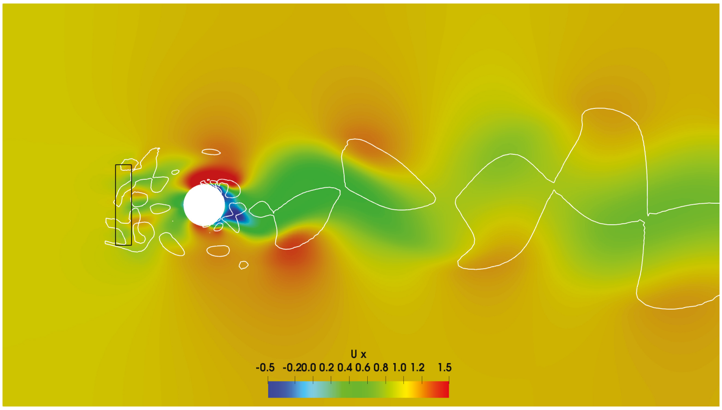

Figure 7. Cylinder flow with synthetic fluctuations.

The controller reaches the prescribed turbulence level approximately within one to five characteristic time units (CTU $= D_{\text{cyl}}/u_\infty$) depending on the intensity level as illustrated in Figure 8. In the case with lowest turbulence intensity the amplification factor drops close to zero (where it is bounded) remains zero after about twelve CTU, when the vortex street has fully developed. The reason is, that the vortex street induces very small variations of the velocity upstream of the cylinder. These are recorded by the controller and in this case they are sufficient to pretend the presence of enough synthetic fluctuations. To overcome this, the mechanism would have to be placed further upstream of the cylinder, where no upstream influence of the vortex street is measurable. Consequently, this case is almost identical with a case without freestream fluctuations.

In the case with highest turbulence intensity a drop of the scaling factor at twelve CTU appears in the plot. This is a combined effect of one particular event in the synthetic turbulence field and the integral error term vanishing at the end of a slight controller overshoot. Hence afterwards the scaling coefficient remains at a slightly lower value.

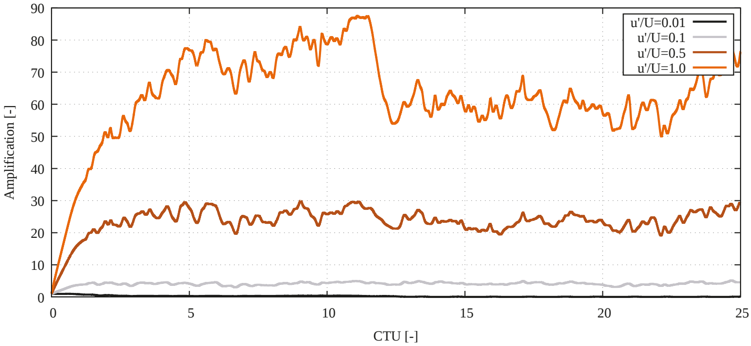

Figure 8. Amplification factor from the controller for different turbulence intensities.

The effect of turbulence in the approaching flow is, that the vortex street forms sooner. The fluctuations help breaking up the shear layer and form instabilities. Figure 9 shows the temporal evolution of the lift coefficient. In the case with the lowest turbulence the longest time is needed to achieve the final amplitude of the alternating vortex separation. In the second case the development of the vortex street happens slightly sooner and it then reaches its final amplitude after a shorter time. The appearance of the lift curve still is regular with only slight disturbances.

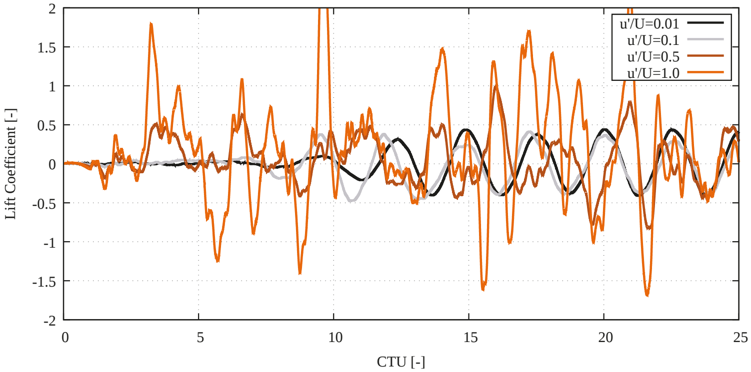

Figure 9. Temporal evolution of the cylinder lift coefficient.

In the third case the separation starts almost immediately compared to the previous two cases. The influence of the fluctuations is clearly visible but also the characteristic of the alternating separation remains visible in the lift plot. In the case of highest turbulence intensity the alternating pattern almost vanishes while the force is dominated by the fluctuations. The coefficient reaches values far higher than those seen purely from the vortex street. The events indicated by the drop of the amplification factor around twelve CTU also are visible in the lift coefficient as the pattern changes in the same interval. As also visible from the velocity field in Figure 7 the vortex street is still present but it is deformed by the fluctuations.

In order to determine the significance of modifying the pressure equation by introducing the force term the same set of cases has been calculated again with the original pressure equation and the forcing term only being present in the momentum equation. As long as the iterative procedure of the PIMPLE algorithm converges, this is supposed to reach the same converged state for each time step as in the previous setup but might need more corrective iteration steps for the pressure equation. The result of the comparison is presented in Table 2.

For all four cases the computing time and the number of iterations performed to achieve the convergence of the pressure correction algorithm are compared. The data is taken from a calculation at quasi-steady state simulating a range of five CTU starting after the first twenty CTU. In the first case it needs to be reminded, that the controller mechanism has faded out the turbulent forcing for most of the time. This still produces overhead to handle the zero-forcing in the pressure equation and leads to an increase of computing time. However, the number of pressure correction iterations decreases during the short phases, at which the amplification becomes greater than zero. This results in a slight decrease of the total number of pressure correction iterations.

For the three cases with significant fluctuation level the result changes considerably. The number of pressure iterations decreases by more than ten percent and up to thirteen percent. The reduction of computing time is not as big as the decrease of pressure iterations but still significant. It ranges from six to almost eight percent. It appears to be independent of the fluctuation magnitude. However, the difference for each case certainly has a strong dependence on the solver settings and can vary for different applications.

Table 2. Relative change in computational effort with corrected pressure equation.

u'_{rms}/u_∞	Computing Time	Pressure Iterations
0.01	+3.5%	–0.63%
0.1	–6.0%	–13.3%
0.5	–7.8%	–11.5%
1.0	–7.0%	–10.4%

3.3. Airfoil in Freestream Turbulence

As mentioned before the two-dimensional cases presented here have been selected in order to reduce computational effort for validation and demonstration. Actual turbulence needs to be studied in three-dimensional applications to resolve the three-dimensional aspect of turbulent motion correctly. Such turbulence-resolving computations require parallelization to achieve results within reasonable computing wall time. It should be noted, that in a parallel computation the controller requires intercommunication between the parallel processes, which are involved in measurement and forcing, to produce one uniform amplification factor.

The flow around a wing is known to be very sensitive to freestream turbulence. Particularly at low Reynolds numbers, when the flow tends to separate easily, freestream turbulence changes the separation process significantly. While large scale turbulent eddies in the order of the chord length change the angle of attack globally, smaller eddies affect the momentum in the boundary layer and thus have an impact on transition and on separation of the flow.

In the present case a NACA0012 wing has been investigated in freestream turbulence. The case is quasi two-dimensional with periodic conditions in span-wise direction. The computational domain size in periodic direction is 50% of the chord length. The outer boundary is of farfield type and located 20 times the chord length from the wing. The mesh is of structured C-type topology even though it is treated in an unstructured way by the flow solver. The total number of cells results in 2.5×10^6. Gradients of the boundary layer are resolved in wall-normal direction with a y^+ of the first cell layer well below unity. x^+ and z^+ are selected higher using values of 30 and 50, respectively. The mesh is designed to be used with a k-ω-SST-DDES turbulence model, which resolves large eddies in the separated flow region and models the immediate wall boundary layer turbulence using the k-ω-SST two-equation model.

At an angle of attack of 12° and a Reynolds number of 50,000 based on freestream velocity and chord length the flow is separated along almost all the upper side of the wing. Therefore a very unsteady behavior with vortex shedding in the shear layer above the separation zone can be observed.

Freestream turbulence is applied with 10% fluctuation intensity based on the freestream velocity. The length scale is 10% of the chord length. This has primarily an effect on the boundary layer and shear layer momentum balance. It affects the vortex shedding and enhances the turbulent breakup of shear layer vortices, which then can reach the wing surface. Local variation of the angle of attack plays only a minor role.

Figure 10 gives an instantaneous view to the flow in laminar and turbulent freestream conditions. The separated regions are marked by the green iso-surfaces of zero stream-wise velocity. It is obvious, that in turbulent freestream the flow reattaches quickly. Only some patches of reverse flow remain after about one third of the chord length, which are induced by larger vortices passing along the surface.

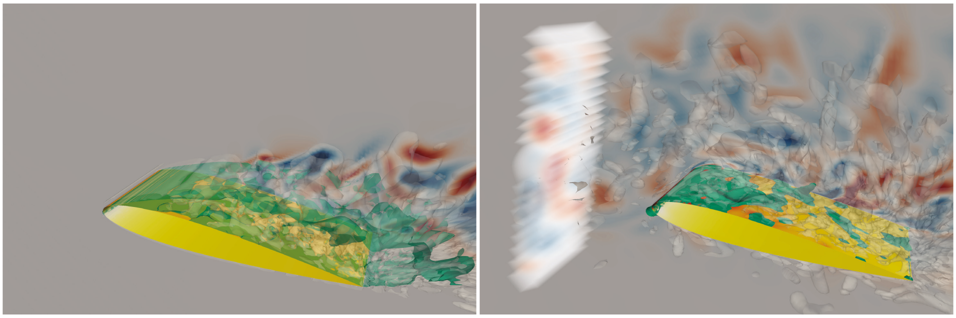

Figure 10. Instantaneous view of the NACA0012 airfoil flow in laminar (**left**) and turbulent (**right**) freestream. Reverse flow in separation is marked by green iso-surfaces. Fluctuations are indicated by red/blue color and by gray iso-surfaces of Q-criterion. The forcing zone is located upstream of the airfoil.

Conversely, in laminar freestream as mentioned above the flow is separated along almost the entire upper side of the wing. Within the reverse flow zone the flow also is not completely attached to the surface. Spots with secondary recirculation are embedded along the wing surface.

These mechanisms also appear in the averaged flow fields. Figure 11 shows the mean turbulent kinetic energy. In the laminar freestream case the fluctuations increase along the shear layer and reach the maximum at the end of the reverse flow region above the trailing edge, whereas the turbulence reaches high intensity immediately after separation in turbulent freestream conditions. This turbulence develops close enough to the surface that it causes the flow to reattach soon.

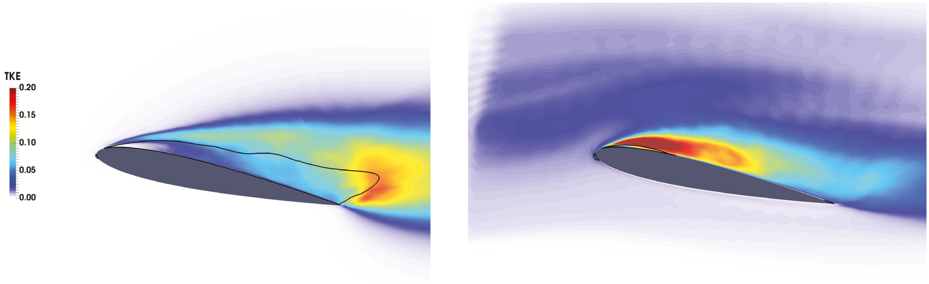

Figure 11. Contours of mean turbulent kinetic energy (TKE) in laminar (**left**) and turbulent (**right**) freestream conditions. The reverse flow zone is indicated by a black line.

The streamlines in Figure 12 clearly indicate the locations of separation and reattachment. In the laminar freestream case the secondary recirculation, which has been seen instantaneously, also appears here. Inside the separated region a small system of recirculating vortices appears.

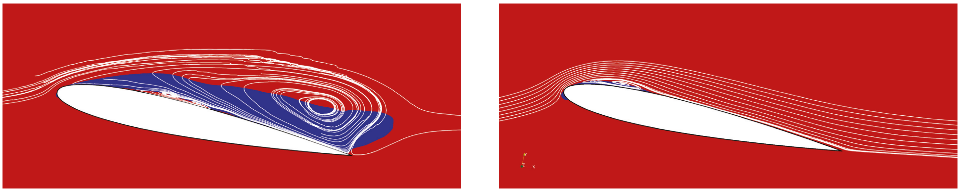

Figure 12. Streamlines over the wing in laminar (**left**) and turbulent (**right**) freestream conditions. The reverse flow is marked by a blue zone.

In order to validate the simulation setup results from a DNS of the flow in laminar freestream by Rodriguez et al. [24] have been used. Figure 13 shows the averaged pressure coefficient on both and the friction coefficient on the upper side of the wing. The curves of c_p for laminar freestream are in very good agreement. On the lower side the curves are almost identical. Some differences appear along the front half of the upper side. They result from slightly different systems of the secondary recirculation between DNS and DDES. In the turbulent freestream case, the presence of a separation bubble in the front is obvious as a plateau forms in the c_p curve.

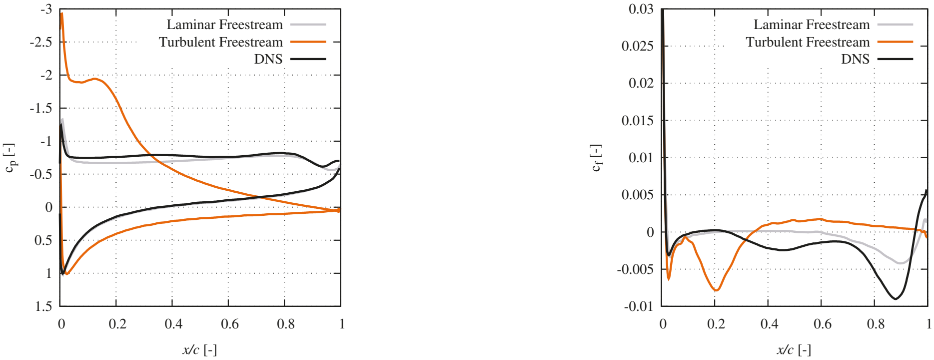

Figure 13. Averaged pressure friction coefficients along the wing surface. DNS data [24] with laminar freestream for comparison and validation.

In the skin friction plot the locations of the first separation are very similar for all three cases, since this cannot be prevented or delayed by the approaching turbulence at such a high angle of attack. Then both the DDES and the DNS show a secondary recirculation region with positive pointing friction. However, in the DNS only a short range appears whereas in the DDES it is predicted further downstream and lasting for a longer range. The following part of the curves shows the same characteristic with a minimum close to the trailing edge indicating proximity to the recirculation vortex core with higher velocities. The flow reattaches shortly before the trailing edge. This occurs slightly further upstream in the DNS than predicted by the DDES, which is certainly connected with the slight differences in the recirculating flow structure. At turbulent freestream conditions the flow clearly reattaches soon and remains attached until very close to the trailing edge. A very slight separation is indicated around the trailing edge.

The flow process around the wing in these conditions is a highly unsteady system. Unsteadiness arises not only from the approaching freestream turbulence. The separation process involves vortex shedding and its turbulent breakup into smaller scales. The temporal evolution of the lift coefficient is shown in Figure 14 for both cases. A quasi steady state is achieved after approximately ten characteristic time units based on chord length and bulk velocity. At laminar freestream one dominant frequency can be seen. It is the frequency of vortex shedding, which causes a periodic oscillation of the lifting force. The Strouhal number based on chord length and bulk velocity ($Sr = f \cdot c/U$) is $Sr = 0.70$. Rodriguez et al. state a value of $Sr = 0.613$ from their DNS data.

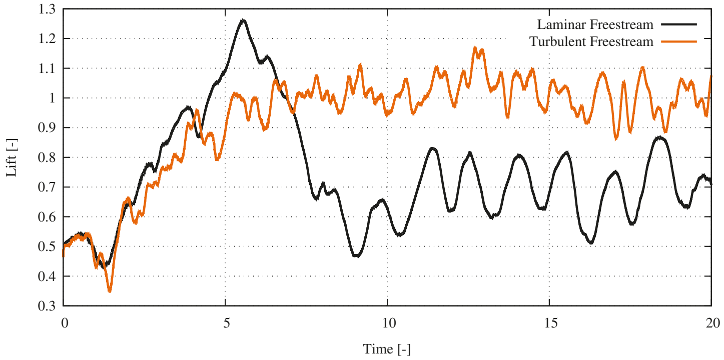

Figure 14. Temporal evolution of the lift coefficient.

In turbulent conditions the evolution of the lift is determined by several modes. Two of them are dominant, namely $Sr = 0.80$ and $Sr = 1.82$. The latter one is connected with the shear layer vortex shedding, which leads to an oscillation of the separation zone length. The origin of the former one cannot definitively be found based on the available data. It is suspected to arise from the interaction between vortices from the upper and the lower side and requires further investigation.

4. Conclusions and Outlook

A method to introduce turbulence at arbitrary locations within the computational domain by applying volume forces has been supplemented with a mechanism to control the turbulence intensity. The control loop becomes necessary since the turbulence is affected by several phenomena during this process. A set of gain coefficients for the controller terms has been proposed based on simulations of a plain channel to ensure stability of the control loop as well as reasonable response time to achieve a quasi steady state. In order to validate the method synthetic turbulence has been introduced within a farfield-bounded domain without any geometry present. In the resulting fluctuating flow, both turbulence length scale as well as intensity agree with the prescribed target values.

Modifying the momentum equation with a spatially varying volume force implies modifications in the pressure correction equation. The significance of those has been assessed in simulations of a cylinder in freestream turbulence. The cylinder setup also demonstrates, that the controller is capable of scaling the desired fluctuations to an arbitrary intensity. This allows to use one set of fluctuations for a series of simulations with different freestream turbulence intensities.

Finally, the method has been applied to a fully three-dimensional setup of the flow around a NACA0012 airfoil including parallel computing, which requires intercommunication between the processes to exchange the in- and output of the controller. In laminar freestream the flow features full separation, which has been compared and validated with DNS data. The freestream turbulence enhances the formation of shear layer turbulence and thereby causes the flow to reattach. This changes the flow structure above the airfoil entirely. As determined from the oscillations of the lifting force also the dominating frequencies are changed.

The application in separated airfoil and wing flows will be subject to further investigations and was a significant part of the motivation for this work. Laminar separation, particularly at lower angles of attack, is known to be very sensitive to freestream turbulence as shown in other work of the authors [25,26]. Further work is required to understand the ongoing phenomena.

Another aspect, which has not been taken into account here, is, that the length scale also is slightly modified in the process. This mainly occurs due to the width of the forcing region, which causes smaller fluctuation spots to be blurred. An approach as proposed in [20] allows to adapt the length scale dynamically and hence will be followed in the context of controlled freestream turbulence in future work.

Author Contributions: Conceptualization, E.T. and M.K.; Data curation, E.T.; Formal analysis, E.T.; Investigation, E.T.; Methodology, E.T.; Resources, M.K.; Software, E.T.; Visualization, E.T.; Writing—original draft, E.T.; Writing—review & editing, E.T. and M.K. All authors have read and agreed to the published version of the manuscript.

Funding: This research received no external funding.

Conflicts of Interest: The authors declare no conflict of interest.

References

1. Klein, M.; Sadiki, A.; Janicka, J. A digital filter based generation of inflow data for spatially developing direct numerical or large eddy simulations. *J. Comput. Phys.* **2003**, *186*, 652–665, doi:10.1016/S0021-9991(03)00090-1. [CrossRef]
2. Kempf, A.; Klein, M.; Janicka, J. Efficient generation of initial-and inflow-conditions for transient turbulent flows in arbitrary geometries. *Flow Turbul. Combust.* **2005**, *74*, 67–84, doi:10.1007/s10494-005-3140-8. [CrossRef]
3. Kornev, N.; Kröger, H.; Hassel, E. Synthesis of homogeneous anisotropic turbulent fields with prescribed second-order statistics by the random spots method. *Commun. Numer. Methods Eng.* **2008**, *24*, 875–877, doi:10.1002/cnm.1009. [CrossRef]
4. Kraichnan, R.H. Diffusion by a random velocity field. *Phys. Fluids* **1970**, *13*, 22–31, doi:10.1063/1.1692799. [CrossRef]
5. Fung, J.C.H.; Vassilicos, J.C. Two-particle dispersion in turbulentlike flows. *Phys. Rev. E* **1998**, *57*, 1677, doi:10.1103/PhysRevE.57.1677. [CrossRef]
6. Smirnov, A.; Shi, S.; Celik, I. Random flow generation technique for large eddy simulations and particle-dynamics modeling. *J. Fluids Eng.* **2001**, *123*, 359–371, doi:10.1115/1.1369598. [CrossRef]
7. Druault, P.; Lardeau, S.; Bonnet, J.P.; Coiffet, F.; Delville, J.; Lamballais, E.; Largeau, J.F.; Perret, L. Generation of three-dimensional turbulent inlet conditions for large-eddy simulation. *AIAA J.* **2004**, *42*, 447–456, doi:10.2514/1.3946. [CrossRef]
8. Auerswald, T.; Bange, J.; Knopp, T.; Weinman, K.; Radespiel, R. Large-Eddy Simulations of realistic atmospheric turbulence with the DLR-TAU-code initialized by in situ airborne measurements. *Comput. Fluids* **2012**, *66*, 121–129, doi:10.1016/j.compfluid.2012.06.013. [CrossRef]
9. Jiménez, J.; Wray, A.A.; Saffman, P.G.; Rogallo, R.S. The structure of intense vorticity in isotropic turbulence. *J. Fluid Mech.* **1993**, *255*, 65, doi:10.1017/s0022112093002393. [CrossRef]
10. Ghosal, S.; Lund, T.S.; Moin, P.; Akselvoll, K. A dynamic localization model for large-eddy simulation of turbulent flows. *J. Fluid Mech.* **1995**, *297*, 402–402, doi:10.1017/s0022112095003156. [CrossRef]
11. Eswaran, V.; Pope, S. An examination of forcing in direct numerical simulations of turbulence. *Comput. Fluids* **1988**, *16*, 257–278, doi:10.1016/0045-7930(88)90013-8. [CrossRef]
12. Rosales, C.; Meneveau, C. Linear forcing in numerical simulations of isotropic turbulence: Physical space implementations and convergence properties. *Phys. Fluids* **2005**, *17*, 095106, doi:10.1063/1.2047568. [CrossRef]
13. Lundgren, T. *Linearly Forced Isotropic Turbulence, Annual Research Briefs*; Technical Report; Center for Turbulence Research, Stanford, CA, SUA, 2003. Available online: https://web.stanford.edu/group/ctr/ResBriefs03/lundgren.pdf (accessed on 5 August 2020).
14. Waldron, K.M.; Paegle, J.; Horel, J.D. Sensitivity of a Spectrally Filtered and Nudged Limited-Area Model to Outer Model Options. *Mon. Weather Rev.* **1996**, *124*, 529–547, doi:10.1175/1520-0493(1996)124<0529:soasfa>2.0.co;2. [CrossRef]

15. von Storch, H.; Langenberg, H.; Feser, F. A Spectral Nudging Technique for Dynamical Downscaling Purposes. *Mon. Weather Rev.* **2000**, *128*, 3664–3673, doi:10.1175/1520-0493(2000)128<3664:asntfd>2.0.co;2. [CrossRef]
16. Klein, M.; Chakraborty, N.; Ketterl, S. A Comparison of Strategies for Direct Numerical Simulation of Turbulence Chemistry Interaction in Generic Planar Turbulent Premixed Flames. *Flow Turbul. Combust.* **2017**, *99*, 955–971, doi:10.1007/s10494-017-9843-9. [CrossRef]
17. Schmidt, S.; Breuer, M. Source term based synthetic turbulence inflow generator for eddy-resolving predictions of an airfoil flow including a laminar separation bubble. *Comput. Fluids* **2017**, *146*, 1–22, doi:10.1016/j.compfluid.2016.12.023. [CrossRef]
18. Jasak, H. Error Analysis and Estimation for Finite Volume Method with Applications to Fluid Flow. Ph.D. Thesis, Imperial College London, London, UK, 1996.
19. Mallouppas, G.; George, W.; van Wachem, B. New forcing scheme to sustain particle-laden homogeneous and isotropic turbulence. *Phys. Fluids* **2013**, *25*, 083304, doi:10.1063/1.4818553. [CrossRef]
20. Ketterl, S.; Klein, M. A Band-Width Filtered Forcing Based Generation of Turbulent Inflow Data for Direct Numerical or Large Eddy Simulations and its Application to Primary Breakup of Liquid Jets. *Flow Turbul. Combust.* **2018**, 1–20, doi:10.1007/s10494-018-9897-3. [CrossRef]
21. Chien, K.L.; Hrones, J.A.; Reswick, J.B. On the automatic control of the generalized passive systems. *Trans. Assoc. Soc. Mech. Eng* **1952**, *74*, 175–185.
22. Lund, T.S.; Wu, X.; Squires, K.D. Generation of turbulent inflow data for spatially-developing boundary layer simulations. *J. Comput. Phys.* **1998**, *140*, 233–258, doi:10.1006/jcph.1998.5882. [CrossRef]
23. Xie, Z.T.; Castro, I.P. Efficient generation of inflow conditions for large eddy simulation of street-scale flows. *Flow Turbul. Combust.* **2008**, *81*, 449–470, doi:10.1007/s10494-008-9151-5. [CrossRef]
24. Rodríguez, I.; Lehmkuhl, O.; Borrell, R.; Oliva, A. Direct numerical simulation of a NACA0012 in full stall. *Int. J. Heat Fluid Flow* **2013**, *43*, 194–203, doi:10.1016/j.ijheatfluidflow.2013.05.002. [CrossRef]
25. Tangermann, E.; Klein, M. Numerical Simulation of Laminar Separation on an Airfoil in Small-Scale Freestream Turbulence. In *Notes on Numerical Fluid Mechanics and Multidisciplinary Design*; Dillmann, A., Heller, G., Krämer, E., Wagner, C., Tropea, C., Jakirlić, S., Eds.; Springer International Publishing: Cham, Switzerland, 2020; pp. 619–629, doi:10.1007/978-3-030-25253-3_59. [CrossRef]
26. Tangermann, E.; Klein, M. Simulation of a Three-Dimensional Wing with Laminar Separation in Large-Scale Freestream Turbulence. In *Progress in Hybrid RANS-LES Modelling*; Hoarau, Y., Peng, S., Schwamborn, D., Revell, A., Mockett, C., Eds.; Springer International Publishing: Cham, Switzerland, 2020; pp. 215–225, doi:10.1007/978-3-030-27607-2_17. [CrossRef]

fluids

MDPI

Article

NARMAX Identification Based Closed-Loop Control of Flow Separation over NACA 0015 Airfoil

Sohaib Obeid [1,*], Goodarz Ahmadi [1,*] and Ratneshwar Jha [2,*]

[1] MAE Department, Clarkson University, Potsdam, NY 13699, USA
[2] Department of Mechanical Engineering, Rowan University, Glassboro, NJ 08028, USA
* Correspondence: sobied@clarkson.edu (S.O.); ahmadi@clarkson.edu (G.A.); jhar@rowan.edu (R.J.); Tel.: +1-315-212-4474 (S.O.); +1-315-268-2322 (G.A.); +1-856-256-5370 (R.J.)

Received: 1 April 2020; Accepted: 22 June 2020; Published: 29 June 2020

Abstract: A closed-loop control algorithm for the reduction of turbulent flow separation over NACA 0015 airfoil equipped with leading-edge synthetic jet actuators (*SJAs*) is presented. A system identification approach based on Nonlinear Auto-Regressive Moving Average with eXogenous inputs (*NARMAX*) technique was used to predict nonlinear dynamics of the fluid flow and for the design of the controller system. Numerical simulations based on URANS equations are performed at Reynolds number of 10^6 for various airfoil incidences with and without closed-loop control. The *NARMAX* model for flow over an airfoil is based on the static pressure data, and the synthetic jet actuator is developed using an incompressible flow model. The corresponding *NARMAX* identification model developed for the pressure data is nonlinear; therefore, the describing function technique is used to linearize the system within its frequency range. Low-pass filtering is used to obtain quasi-linear state values, which assist in the application of linear control techniques. The reference signal signifies the condition of a fully re-attached flow, and it is determined based on the linearization of the original signal during open-loop control. The controller design follows the standard proportional-integral (*PI*) technique for the single-input single-output system. The resulting closed-loop response tracks the reference value and leads to significant improvements in the transient response over the open-loop system. The *NARMAX* controller enhances the lift coefficient from 0.787 for the uncontrolled case to 1.315 for the controlled case with an increase of 67.1%.

Keywords: *NARMAX*; control; lift; drag; NACA 0015; k-ε model

1. Introduction

Efficient and safe design of aircraft, missiles, propellers, turbines, compressors, automobiles, ships, trains, and civil engineering structures depend to a far extent on an understanding of the nature of flow around bodies (Gad-el-Hak [1]). Aircraft wings are typically evaluated according to their aerodynamic performance, mainly measured in terms of lift to drag ratio. At high angles of attack, airfoils suffer from flow separations and significant loss of aerodynamic performance.

Separation is defined as the detachment of the fluid flow from a solid surface. Whether caused by an adverse pressure gradient, a geometric disruption, or by any other means, separation is generally associated with significant thickening of a rotational flow region adjacent to the airfoil surface and by an increase in the velocity component normal to the surface (Simpson [2]). Flow separation always causes adverse effects on airfoil performance, such as reduced lift, increased drag, noise emissions, and airfoil buffeting. This decrease in airfoil performance, which could lead to the stall regime, can be avoided or delayed with the use of flow control techniques (Benard et al. [3]).

When the flow separation flow cannot be avoided, it is important to understand the effects of separation on a specific design (Mable et al. [4]). In particular, aerospace researchers are continually searching for efficient methods to improve the aerodynamic efficiency of flight vehicles. The main goals of flow control are to improve performance characteristics by avoiding a stall, reducing drag, enhancing lift, and abating noise. The specific objectives of flow control are usually achieved through one of the following: (1) delay or eliminate flow separation; (2) delay boundary layer transition; or (3) reduce skin friction drag (Huebsch et al. [5]).

From an aerodynamic perspective, proper flow control schemes have the ability to manipulate the flow and improve the performance features by reducing skin friction and form drag, increasing lift, improving flight controllability and maneuverability, and providing significant savings in overall fuel consumption. For example, maintaining laminar flow over the entire wing surface can reduce total aircraft drag by as much as 15% (Schrauf [6]). In the commercial aircraft industry, overall drag reduction of just 1% can lead to millions of dollars of saving in annual fuel costs (Huebsch et al. [5]).

The capability to actively or passively control the flow around an object to achieve an enhanced performance is of great value (Joslin and Miller [7]). Various passive and active separation control approaches have been tested with different degrees of success. Passive control techniques encompass approaches that lead to geometric modifications to change the flow features, while active control techniques utilize actuators to modify the flow and therefore require external energy (Cattafesta et al. [8]). Passive flow control for aircraft wings includes leading-edge slats, trailing edge slotted flaps, or a combination of the two. Another passive flow control device is the vortex generators, which are relatively small rigid fixtures that are placed on the top surface of an airfoil. However, vortex generators increase drag, and due to their nature of being fixed on the surface of the airfoil, they decrease the efficiency of flight when they are not needed. Passive actuation also includes such devices as riblets, spoilers, strakes, and steady suction or blowing.

Passive flow control methods have been a field of considerable interest since long ago and found abundantly in the aerospace industry. The main merit of passive control over an active control is its simplicity to implement, tendency to be lighter, less expensive to design and manufacture, and easier to maintain. Hence passive control techniques are more likely to be used in real-world applications (Williams et al. [9]). The passive control methods, however, may only be effective over a restricted range of operating conditions. The system performance may even be deteriorated under certain conditions with the use of passive control. The disadvantages of current designs are that they add mechanical complexity to the wing design, take up the volume when not in use, add weight, and generate vibration and noise. Likewise, since most engineering flows contain complex unsteady motions (instabilities, turbulence), the ability of a passive device to control these unsteady motions is inherently limited. Examples of passive flow control applications can be found in (Bechert et al. [10]; Fisher et al. [11]; Kaplanski et al. [12,13]; Hussainov et al. [14,15]).

Active flow control (*AFC*) is an enabling technology as fluid dynamics, controllers, actuators, and sensors merge to form advanced control systems capable of modifying flow behavior under challenging aerospace applications (Joslin and Miller [7]). Actuators and sensors become increasingly more powerful, cheaper, and more reliable to be considered for practical applications (Noack et al. [16]). *AFC* provides numerous advantages over passive methods. When not needed, active control devices may be turned off, and they could also adjust to the changes in the flow conditions (Williams et al. [9]). *AFC* technology typically used small, localized energy input to alter the flow. Active control can be utilized to control dynamical flow patterns such as turbulence to reduce skin friction drag.

In boundary layers, the turbulence production mechanism is a complex series of dynamical events associated with organized, near-wall streaks and their instabilities. This process results in sudden bursts of low-momentum fluid away from the wall. Bushnell [17] reported that the correct phasing of the control inputs with respect to the organized flow patterns could be the cause for the success of a control algorithm. In this respect, Lumley and Blossey [18] described the applications of active control of turbulent flow by modifying the production of turbulence.

Flow sensors need to be robust and not significantly alter the flow field that is measured. Flow sensors should possess sufficient spatial and temporal resolution to accurately capture the relevant flow physics to be controlled (Cattafesta et al. [19]). For practical reasons, most flow sensors for *AFC* are flush-mounted on a solid surface. Typically, at the solid surface, the wall pressure and/or skin friction can be measured. For cases in which the wall pressure is important, there are many devices for measuring pressure changes, which are essentially small microphones. Many flow sensors fall under the categories of classical, optical, and Micro Electro Mechanical Systems (*MEMS*). Some examples of sensors for measuring wall shear stress include floating element sensors, hot films, and shear stress crystals.

There are various ways to classify flow control actuators, including type (e.g., fluidic, thermal, acoustic, and plasma), transduction scheme (piezoelectric, electromagnetic, electrodynamic, and electrostatic), output form (constant blowing, constant suction, periodic excitation, and synthetic jets) and structural design (shape memory alloys, *MEMS*, Nano-elements). The input to an actuator is an electrical quantity that produces an output flow perturbation. The most critical design parameters for active flow actuators are the control authority (or stroke) and the bandwidth. Unfortunately, these two parameters conflict with one another. A rise in stroke usually led to decreased bandwidth (Mathew et al. [20]). The design objective usually requires that the actuator generates sufficient stroke over a range of frequencies to generate the appropriate control effects. Low power consumption, rapid response, reliability, and low cost are appropriate characteristics of actuators.

Active control may be categorized as predetermined (open loop) or reactive (closed-loop). Predetermined control includes the application of steady or unsteady energy input regardless of the particular state of the flow with no need for sensors. Most cases of *AFC* require parameter adjustments for flow conditions and occasionally real-time response using flow sensors. Closed-loop flow control offers a promising alternative to passive (no power) and active open-loop (no sensing) flow control approaches. It relies on small-scale powered actuators, forcing the flow dynamically in response to a sensor signal transformed by control law. The key advantage of feedback control lies in the ability of the controller to adapt to changes in exogenous parameters and to modify the dynamics of the flow system.

Examples of steady jet control techniques can be found in the works of Wong and Kontis [21], and Eldredge and Bons [22]. For the case of unsteady jet actuation, readers are referred to Shan et al. [23], Seifert et al. [24], and Amitay and Glezer [25]. The steady or quasi-steady-state of increasing lift enhancement and reducing drag at relatively low chord Reynolds number (typically <0.5 million) were considered in these studies. Using periodic excitation that making use of natural flow instability has the ability to overcome the efficiency barrier. Seifert et al. [26] reported that separation control excitation, at frequencies somewhat higher than the vortex shedding frequencies, leads to 90–99% saving of the momentum needed to achieve results in performance with steady blowing. Closed-loop separation control has not yet received significant attention in experimental studies. In addition, the characteristics of hardware needed (sensors, actuators, and real-time control systems) impose significant limits on the complexity of the closed-loop control system (Billings and Leontaritis [27]).

Recently a variety of closed-loop separation control techniques have been developed for a wide range of applications and geometries.

Nishizawa et al. [28] successfully conducted experiments on the NACA 0015 airfoil wing model to control leading-edge separation using a closed-loop system composed of a flow-direction discriminator, a simple control algorithm, and disturbance actuators. Later in 2005, Nishizawa et al. [29], designed PID closed-loop controllers for both NACA 0015 and MEL001 airfoils flow separation control using Micro Jet Vortex Generators (*MJVG*). Applications of *MJVG* on a *MEL001* airfoil at $Re = 10^4$ to 10^5 gave an appreciable increase in the lift coefficient (Abe et al. [30]). An alternative suction/blowing jet (*ASBJ*) was developed, and in a preliminary experiment, its drag reduction effect was observed (Segawa et al. [31]).

Tian et al. [32] implemented an adaptive closed-loop to control flow over NACA 0025 airfoil utilizing zero-net-mass flux (*ZNMF*) actuators. In another work, Tian et al. [33] also implemented an adaptive disturbance rejection control algorithm with system identification using synthetic jet actuators and two dynamic pressure sensors. The objective was to minimize the unsteady pressure fluctuations over the airfoil, which results in up to ~5 dB of power reduction and ~5× improvements in the lift/drag ratio. Song et al. [34] used the same set-up with *MIMO* generalized predictive control algorithm. The results showed 7× improvements in the lift/drag ratio with less computational cost compared to Tian et al. [32].

Pinier et al. [35] used a proportional controller based on a low order model to control separation on NACA 4412 airfoil using piezoelectric synthetic jet actuators. The unsteady pressure measurements were used to estimate the proper orthogonal decomposition (*POD*) coefficients for the model. Later on, Ausseur et al. [36] used the same set-up with different techniques of reduced-order modeling based on a combined technique of Proper Orthogonal Decomposition and Linear Stochastic Estimations (*POD/LSE*) and taking the estimated temporal coefficient of first *POD* mode as control candidate.

Becker et al. [37] conducted an experimental investigation on NACA 4412 airfoil using Single-Input Single-Output *SISO* extremum seeking control using pulsed jet actuator over a two elements high lift configuration. They extended it to the *SISO* slope seeking control to avoid saturation of the control input. Finally, for more realistic 3-D flight configurations, span-wise *MIMO* slope seeking control was used. The pressure gradient on the flap was used as the criterion for reattachment. For non-model based adaptive control, slope seeking approach was developed as a new concept which involves driving the output of a plant to a value corresponding to a guided slope of its reference-to-output chart. The extremum seeking scheme is a special case of slope seeking in which the guided slope is zero. Examples of closed-loop control algorithms for flow separation control can be found in the works done by Allan et al. [38], Becker et al. [39], Henning and King [40], Becker and King [41], Duvigneau and Visonneau [42], Bourgois [43], Cattafesta et al. [44], Cho et al. [45], Taira et al. [46], Benard et al. [47], Luchtenburg et al. [48], Colonius et al. [49].

Most experiments on flow control have used a backward-facing step or different NACA airfoils. A variety of actuators has been used, while sensors were mostly pressure transducers. Also, a large variety of controllers were used. Most of the studies were at relatively low Reynolds (4×10^3 to 5×10^5) except that by Allan et al. [38], where the chord Reynolds number was 16 million.

Over the last few years, much attention from the fluid dynamic research community has been given to the development of synthetic jet actuators (*SJA*) or "zero mass flux" devices. Also, *SJAs* are preferable as they characterized by a small, low- energy, typically high-frequency actuators, in which the operation is based on the concentrated input of energy at high receptivity regions of the flow field. A variety of promising flow control applications based on synthetic jet actuators have been presented. Numerous investigations on synthetic jet have shown that flow separation can be diminished or even eliminated entirely (Tuck and Soria [50] Amitay and Glezer [51]; He et al. [52]; Amitay et al. [53]; Crook et al. [54]; Seifert and Pack [55]; Amitay et al. [56]; Smith et al. [57]; and Seifert et al. [26]). Synthetic jets have also been used for separation control in inlet ducts (Amitay et al. [58]). *SJAs* were also utilized on an unmanned aerial vehicle (Parekh et al. [59]), flight control on scaled models (Ciuryla et al. [60]), as well as jet vectoring (Smith and Glezer [61]). Maldonado et al. [62] used *SJA* for control of wind turbines' vibrations. Chatlynne et al. [63] and Amitay et al. [64]) used the synthetic jets for flow control over a 2-D airfoil at low angles of attack, where the flow is fully attached. Application to 3-D configurations was reported by Farnsworth et al. [65].

Timor et al. [66] reported that in some cases using synthetic jets, considerable control forces were exerted by cropping the trailing edge of an airfoil. These suggest the potential for replacing the classical control surfaces (flaps, aileron, rudder) with *AFC* or at least improve their performance in terms of control authority as well as frequency response. Darabi and Wygnanski [67,68] described their investigations dealing with the transient flow attachment and separation in response to a synthetic jet actuator.

And Amitay and Glezer [25,69]. More recently, Mathis et al. [70] performed a similar study using a steady jet to provoke separation for enhancement of mixing. In the current research, we utilize *SJA* as an actuator and investigate the performance of the control system to modify the lift and drag of 2-D airfoils.

The ability to simulate aerodynamic flows utilizing Computational Fluid Dynamics (*CFD*) has advanced rapidly during the last several decades and has fundamentally changed the aerospace design process. Recently, the increasingly crucial role of the *CFD* in the fields of analysis, design, certification, and support of aerospace products has been described by many researchers. The utilization of *CFD* codes has become standard engineering practice to examine flow physics around geometrically complicated shapes (Jones and Clarke [71]). Advanced simulation capabilities of *CFD* codes do not only enable reductions in ground-based and in-flight testing requirements, but also provide added physical insight, enabling superior designs at reduced cost and risk, and open new frontiers in aerospace performance (Slotnick et al. [72]). *CFD* codes provide numerical approaches for solving the governing equations of the fluid motion, which are mainly the Navier-Stokes (N–S) or the Reynolds averaged Navier-Stokes (RANS) equations.

An additional element stimulating new developments in AFC occurred in the 1990s when *CFD* was used as a tool to explore new concepts in AFC. The *CFD*, coupled with the control theory, proved to be a powerful combination leading to improved understanding of the flow physics. Not only were numerical simulations useful in providing details about the flow, but they were more amenable than experiments to the integration with modern control theory (Choi et al. [73], Kim [74]). Application-oriented simulations for flow control was found to be useful for determining locations for high receptivity to actuator and sensor placement, and for obtaining scaling information needed for full-scale application.

Given the extensive computing requirements, it has been known that real-time solutions of the Reynolds averaged Navier-Stokes (RANS) equations for control applications would not be feasible in practical situations. The development of reduced-order models has enabled closed-loop flow control to be implemented for many cases. Some non-model based control algorithms have attracted attention as they alleviate the difficulties of modeling separated flow while achieving the control goals. Methods used in the works reported by Banaszuk et al. [75], Becker et al. [40], Becker et al. [37], Tian et al. [31], Tian et al. [32] and Benard et al. [47] are capable of "training" the excitation signals to be most effective in terms of objective functions (i.e., pressure recovery, and lift-to-drag ratio). The main drawback of these methods is that they work on the time-averaged objective functions as they operate on a time scale that is much larger than that of the flow dynamics. For non-model based flow control, the well-known system identification (ID) schemes are utilized to model the system dynamics, including the actuator and unsteady surface pressure sensors. The system to be identified includes the dynamics of the actuators, flow structures excited by *SJA*, and dynamics of the sensors. Information contained in this system information is then utilized to predict the subsequent evolution of the pressure fluctuations around the airfoil. An attractive scheme for discrete systems employed in control applications is the *NARMAX* model, where the system output can be forecasted utilizing the past input and output lags of the system. Chen and Billings [76] proposed the *NARMAX* approach to represent the discrete nonlinear systems.

The *NARMAX* is a nonlinear autoregressive moving average model that can represent a broad class of nonlinear systems. The approach provides the ability to construct the model sequentially by determining the most critical term and then determining and adding the next important term, and so on. Therefore, the model is constructed step by step until the desired accuracy is achieved (Billings [77]). The *NARMAX* power-form polynomial identification of nonlinear systems offers many advantages over other nonlinear difference equation structures (Liu [78]). The model has an explicit recursion in the present output $y(t)$, and it is suitable for modeling both the stochastic and deterministic systems and is capable of describing a wide variety of nonlinear systems (Leontaritis and Billings [79]). The resulting model is linear, which enables the application of well-established parameter estimation techniques developed for linear system identification. Although *NARMAX* is capable of describing a wide variety of nonlinear systems, it has been mainly used for control problems. The *NARMAX* representation provides an alternative to block-structured models (Liu [78]). Several successful applications of polynomial *NARMAX* models were reported in the literature demonstrating its application in system identification (Thomson et al. [80]; Swain et al. [81,82]; and Kukreja and Brenner [83]).

In the current study, the *NARMAX* approach is utilized to construct a feedback control subroutine for flow separation on NACA 0015 airfoil with leading-edge *SJA* mounted at 10% chord length. The purpose is to obstruct flow separation or stall by maintaining the flow attached to the surface of the airfoil. Here, the flow model is built by using the synthetic jet velocity as input and pressure as an output. Hence, it is suitable to construct a *SISO* system identification dynamic model directly via parameter estimation of input-output data relationships.

With the *NARMAX* method, the Airfoil-*SJA* system is modeled in terms of the difference equations relating the current output to combinations of inputs and past outputs.

The flow around the NACA 0015 airfoil was first modeled using the ANSYS-FLUENT code in a series of studies. The airfoil geometry was constructed, and the computational domain was identified and meshed. The boundary conditions were set, and the Reynolds Averaged Navier Stokes (RANS) equations were solved. The mesh independence studies were performed, and then the RANS simulations were conducted, and the flow patterns around the airfoil at various incidence angles were evaluated. Fluent simulation results were validated using experimental data obtained from wind tunnel testing of flow over a model of 30 cm chord length and 40 cm span at $Re = 10^6$. Simulation results provided core information for the baseline case (no control) at AoA = 16° that used for control purposes. In addition, the flows around the airfoil with synthetic jet actuators (*SJAs*) were considered, and the RANS simulations were performed for the control-on cases when the synthetic jet actuator was active. Information obtained from open-loop control was used to develop a closed-loop control algorithm.

For implementing linear control, a *NARMAX* model for flow over airfoil based on the static pressure data and the synthetic jet actuator was developed using the data from the incompressible flow simulations results for cases with and without *SJAs.* The describing function technique was used for linearization of the identified pressure signal within its frequency range, and then a low pass filtering was used to provide quasi-linear state values (linear in plant/nonlinear in instrumentation), which was used in the application of the quasi-linear control techniques. Quasi-linear control techniques are similar to the linear control techniques and used in cases where the plant can be viewed as linear, but the instrumentation, i.e., the actuators and sensors, cannot (Ching et al. [84]). The desired pressure signal that signifies the condition of fully re-attached flow over the airfoil surface was selected based on the linearized original pressure signal reported by the sensor during open-loop control.

The closed-loop control algorithm was designed and inspected in the MATLAB Simulink environment. The controller design followed the standard proportional-integral (PI) approach for single-input single-output systems. The results showed that the closed-loop response tracks the reference value reasonably well and leads to significant improvements in the transient response over the open-loop system. The *NARMAX* based controller enhanced the lift coefficient of the NACA 0015 airfoil at AoA = 16° from 0.787 for the uncontrolled case to 1.315 for the controlled case with an increase of 67.1%.

2. Numerical Simulation of Flow over the NACA 0015 Airfoil

Flow over airfoils at high angles of attack and its control is quite complicated due to the flow separation that leads to vortex shedding from both the leading and trailing edges of the airfoil (Wu et al. [85]). Secondary and tertiary separations from the middle part of the airfoil upper surface may also be induced, which makes the airflow field inherently unsteady. Therefore, understanding the mechanisms of post-stall lift enhancement by unsteady controls, which requires careful numerical simulations and detailed experimental studies, has attracted considerable attention.

Motivated by these needs, in this study, a series of two-dimensional URANS simulations of airflow around NACA 0015 airfoil are performed to study the separation control capabilities of synthetic jet actuators. The effect of the actuators on the lift characteristics of the airfoil is investigated. A close examination of the controlled and uncontrolled flow fields reveals the features of the airflow that are difficult to observe via experimentation. The ANSYS-FLUENT software is used for the flow simulations, while the MATLAB package is used for the analysis and design of the controller.

A MATLAB script is constructed to simulate the geometry of NACA 0015 airfoil (Abbott, and Von Doenhoff [86]). The dataset for the NACA 0015 airfoil geometry (with 602 points around the airfoil contour) together with the computational domain that was constructed surrounding the airfoil is preprocessed by using the design modeler platform. Finally, the mesh generating tool complementing the software package was used to generate the mesh around the NACA 0015 airfoil.

A structured 2-D C-grid topology of a semi-elliptical shape is used in the present work. In order to attain a fully developed flow, the computational domain with semi-major diameter 43.5 c and semi-minor diameter 10 c, where c is the chord length, is selected and utilized. The semi-elliptical shape of the computational domain provides major advantages over the conventional rectangular and semicircle upstream and rectangular downstream configurations. Dolle [87] recommended this mesh configuration as it leads a considerable reduction in the needed number of cells in the mesh in the far-field, thus allowing for the majority of the cells in the mesh to be concentrated around the airfoil.

The main benefit of this class of mesh is its easy adaptation. The same mesh can also be utilized for different angles of attack by only shifting the tail part of the mesh at the airfoil trailing edge in accordance with the specific angle of attack. To achieve this objective, it was made sure that the straight segment of the elliptic domain has sufficient length to include the incoming flow for all inspected angles of attack (Duvigneau and Visonneau [88]). The distance from the airfoil trailing edge to the downstream pressure far-field boundary is 30 c. The majority of the mesh cells are clustered around the airfoil surface. The domain with these adequately large dimensions was chosen to contain flow disturbances created by the airfoil and to avoid unphysical reflections from the outer boundaries of the mesh. Based on the 4-node quadrilateral elements structure, the grids constructed for this study has about 107,000 cells and 109,000 nodes. Refined quadrilateral cells were placed on top of the boundary layer grid on the upper side and the lower side of the airfoil outline. In addition to this and in order to capture flow features properly in the wake region, Dolle [87] recommended the utilization of a fine grid with quadrilateral cells in these areas rather than other types of cells. The pressure far-field at the fluid domain periphery, velocity-inlet at the *SJA* location, and wall at the airfoil surface were chosen as boundary conditions during this simulation. Additionally, a velocity boundary condition modeled by a sinusoidal function (in space and time) is developed to fulfill the perturbation effect of periodic jets in the vicinity of the actuator. The schematic of the computational domain and location of the airfoil with boundary conditions is shown in Figure 1.

In this paper, the realizable k-ε turbulence model is used for solving the Unsteady Reynolds Average Navier–Stokes (URANS) equations for the simulation of flow around the NACA 0015 airfoil with and without synthetic actuators. The ANSYS-FLUENT code solves the equations of conservation of mass and balance of momentum together with the transport equations of the realizable k-ε turbulence model. In some cases, the mesh is adapted based on the static pressure gradient, so the solver periodically refines the mesh in the vicinity of regions with substantial pressure variations. A time-dependent pressure-based solver is used in the analysis. Air is treated as an ideal gas with Sutherland Law for viscosity variation. A simple scheme with a Green-Gauss cell-based gradient implicit formulation of pressure velocity coupling is used.

For a free stream velocity of 50 m/s, the flow Reynolds number based on the airfoil cord is $Re = 10^6$. Here the free stream ambient temperature is 300 K, the air density is $\rho = 1.225$ kg/m^{3,} and the air viscosity is $\mu = 1.7894 \times 10^{-5}$ kg/ms. For these conditions, the airflow is treated as being incompressible. A segregated, implicit solver is utilized to simulate the flow. The second-order upwind differencing scheme is utilized for spatial discretization. For computing viscous flows, the second-order upwind differencing formulation offers several advantages over a central-differencing scheme (Anderson and Bonhaus [89]). The temporal resolution with a fixed time-stepping method with a time step size (Δt) is set at 0.000125 (s) was utilized. To secure a fully converged solution based on chosen spatial and temporal resolutions of the mesh, a convergence criterion of 1×10^{-8} is used for the continuity equation, x-velocity, and y-velocity, and maximum iterations of 120 are used per time step. The code solves the coupled governing equations of fluid motion simultaneously and provides updating correction for the pressure values in iteration (Bakker [90]).

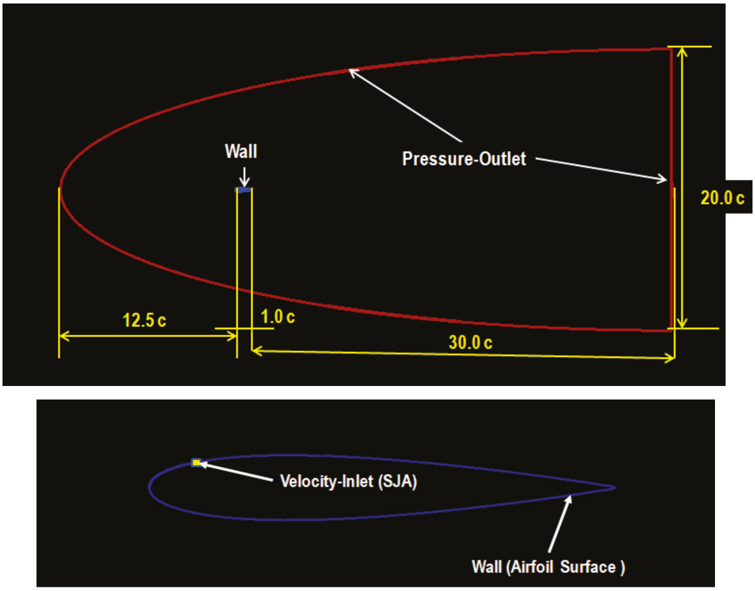

Figure 1. URANS Simulation, schematic of the computational domain, airfoil location, and boundary conditions.

For reducing errors and uncertainties during the numerical solutions, the location of the airfoil with respect to the computational domain boundaries was inspected using the potential flow theory. For capturing the flow physics over the surface of the airfoil, the mesh density was sufficiently high for evaluating the vortex shedding and boundary layer and separation.

For making sure that the computed aerodynamic results are independent of the grid size, the density of the grid was increased until the negligible difference in solution is seen. Six different grid resolutions were tested. At first, a coarse mesh with 415 nodes on the airfoil surface was constructed and inspected for lift and drag values at an angle of attack of 12° and two Reynolds numbers of 10^5 and 10^6 using the Realizable k-ε and the Spalart Allmaras turbulence models. The results obtained for steady-state simulation were compared with the experimental data, and an error of 15% in the lift coefficient at Reynolds number of 10^5 was found. Then refined meshes with 484, 496, 584, 664, and 725 nodes on the airfoil surface were constructed, and the grid independence study was conducted for the same conditions stated for the coarse grid.

Results obtained from the six meshes show that the mesh with 584 nodes around the airfoil surface is quite sufficient to simulate the airflow around the airfoil with both values of lift coefficient and drag coefficient not changing with a further increase of the number of nodes. The wall y^+ values of the first grid used in the simulations of the flow around the NACA0015 airfoil vary in the range of 9.2–0.8 (size of the first cell height from the wall is in the range of 2.11×10^{-4} c–1.83×10^{-5}c). More details about the approach followed for the grid independence study with the use of six different meshes, and the results obtained were reported by Obeid et al. [91].

Figure 2 explores the results of mesh intensity inspection on the model prediction. In this figure, the predicted lift coefficients for different numbers of grid points on the surface of the airfoil are plotted and compared with the experimental data. Figure 2 shows the lift coefficient values obtained by using both the Spalart-Allmaras model and the Realizable *k*-ε model at AoA = 12° and for two different cases of Reynolds numbers, (a) $Re = 10^5$ and (b) $Re = 10^6$ as compared with the experimental results of Rethmel [92]. It is seen that for the mesh with 584 nodes around the airfoil surface, the simulation results predicted by the Realizable *k*-ε model for the lift coefficient are much closed to the experimental data for both Reynolds numbers. The predictions of the Spalart-Allmaras model, however, generally overestimate the lift coefficient. Therefore, the Realizable *k*-ε model and this mesh were selected for the subsequent simulations.

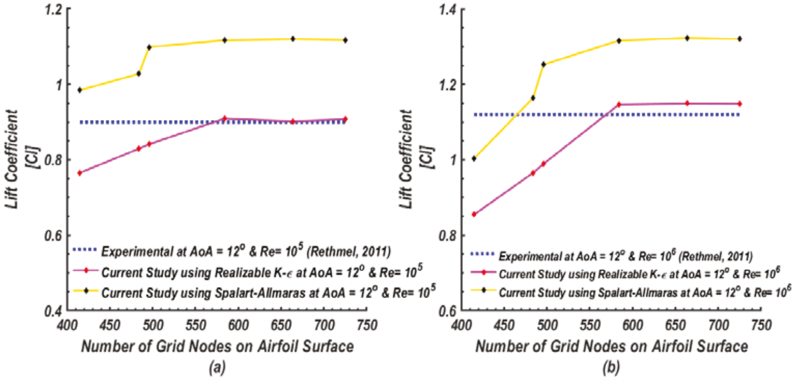

Figure 2. Results of mesh intensity inspection for lift coefficient as predicted by the Spalart-Allmaras and the Realizable *k*-ε models at AoA = 12° for (**a**) $Re = 10^5$ and (**b**) $Re = 10^6$.

Figure 3 shows the grid structure with 584 nodes around the airfoil surface. The mesh is densely clustered toward the airfoil surface, and in cases with *SJA*, it is very fine in the vicinity of the synthetic jet.

In the numerical simulations, the jet velocity U_j was modeled by a User_Defined_Function (UDF). The influences of the jet velocity and frequency are discussed in Section 5 of this paper.

For verifying that the selected time step is appropriate for simulating the transient airflow around the airfoil and also assuring that the mesh cells are not too small compared with the time step, Δt was selected at least one order of magnitude smaller than the time taken by the flow to pass the smallest mesh element in the system. The values of the Courant number within the domain were inspected to make sure that they do not exceed a value of 20–40 in most sensitive transient regions of the domain for obtaining stable and efficient simulations (Fluent lecture notes, 2010).

Simulations were conducted to determine the effects of pressure distribution on lift, drag, and pitching moment and the behavior of stall for laminar and turbulent boundary layers. The airfoil was tested at angles of attack ranging from 0° to 20°. Figure 4 presents the variation of the average lift coefficient with the incidence angle for the case without control at free stream conditions corresponding to a chord Reynolds number of 10^6. Here the unsteady Reynolds averaged Navier-Stokes (URANS) simulations were performed. This figure shows that the average value of the lift coefficient increases with the incidence angle up to about 13° and then decreases sharply. The lift coefficient obtained from 2-D potential flow analysis using the panel method, the Large Eddy Simulation (LES) results of You and Moin [93] at Reynolds number of 10^6 in addition to experimental data of Rethmel [92] are also shown in this figure for comparison. The potential flow solution treats the flow around the airfoil as inviscid and irrotational, and it represents an idealized case for extremely high Reynolds number flows (Joseph and Liao [94]). The present URANS-realizable k-ε turbulence model simulation results for the lift coefficient are quite close to the LES results of You and Moin [93], as well as the experimental data of Rethmel [92]. It should be mentioned that the slope of the lift curve for the idealized potential flow case is $\frac{\partial C_l}{\partial \alpha} = 0.110$ while the slope of the lift curve obtained from the current study, as well as those for the earlier numerical results and experimental data, is $\frac{\partial C_l}{\partial \alpha} = 0.101$ for low angles of attack, which remains constant for incidence angles up to about 11°. The maximum lift coefficient obtained by the present *CFD* works is 1.15 obtained at the angle of attack of $\alpha = 13°$.

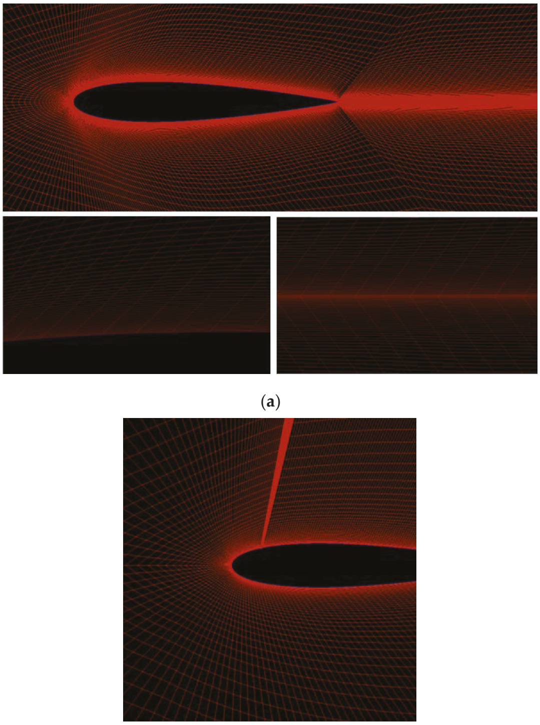

(**a**)

(**b**)

Figure 3. Mesh structure for cases without *SJA* and with *SJA*, (**a**) Mesh clustering around airfoil surfaces, and (**b**) dense in the vicinity of the synthetic jet actuator.

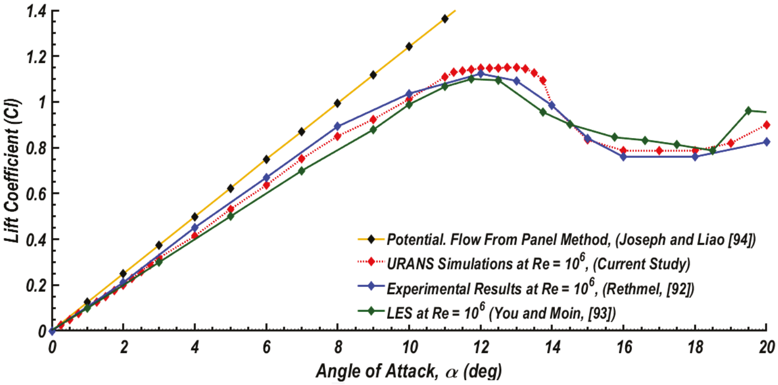

Figure 4. Airfoil average lift coefficient as a function of angle of attack at chord $Re = 10^6$ (No-control case).

The slope of the lift curve for the idealized potential flow case is $\frac{\partial C_l}{\partial \alpha} = 0.110$. Figure 5 shows the predicted variation of average drag coefficients with the angle of attack and gives a comparison with the earlier RANS simulations and the experimental data. As expected, the drag coefficient increases with the increase of angle of attack. The RANS simulation results with the Spalart-Allmaras model of Schroeder [95] for the NACA 0012 airfoil at $Re = 10^6$ and the RANS simulation results with the k-ω SST of Manni et al. [96] for the NACA 0012 airfoil at $Re = 10^6$. In addition, the experimental drag coefficient reported by Sharma [97] for the NACA 0015 at $Re = 0.7 \times 10^6$ and the measured drag coefficient data of Rediniotis [98] for the NACA 0015 at $Re = 10^6$, as well as the numerical simulations of Shroeder [95] are also shown in this figure for comparison. For angles of attack less than 13°, it is seen that the drag coefficients predicted by the Realizable k-ε model are in satisfactory agreement with the experimental data and earlier numerical results.

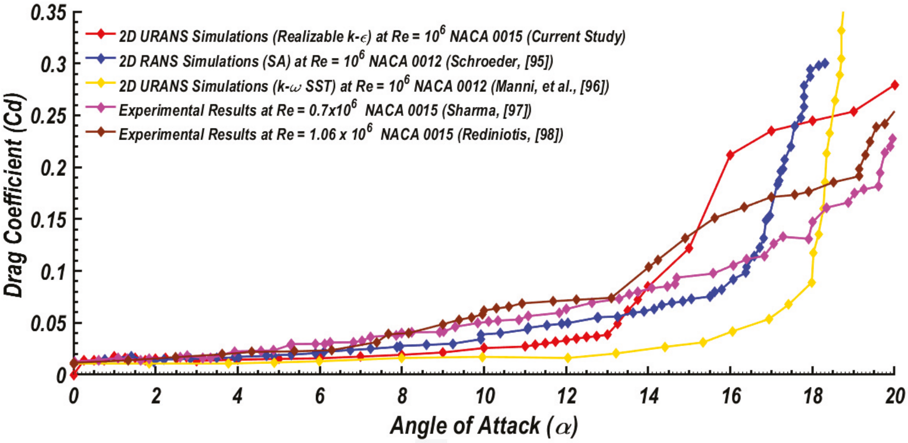

Figure 5. Comparison of airfoil average drag coefficient against the angle of attack at chord $Re = 10^6$ (No-control case) with the experimental data and earlier numerical results.

The minimum drag coefficient is obtained when the angle of attack zero. The drag coefficient then increases gradually with the incidence angle to the value of 0.038 at the stall condition. The slope of the drag coefficient with respect to the angle of attack $(\partial C_d\ )/\partial\alpha$, remains approximately constant at around 0.003. At angles of attack beyond the stall, the drag coefficient enhances expeditiously with the incidence angle and reaches a value of 0.28 at $\alpha = 20°$. At incidence angle $\alpha = 20°$, the predicted drag coefficient is found more than seven-times the drag coefficient at the stall condition. After the stall condition, the slope of the drag coefficient with respect to the attack angle $(\partial C_d\ )/\partial\alpha$ increases to a value of 0.040.

It is also noticed that the value of the drag coefficient obtained from the URANS simulations is in general agreement with the earlier numerical of Schroeder [95] and experimental data of Sharma [97] and Rediniotis [98] for angles of attack lower than the stall angle of 13°. For angles of attack beyond separation in the range of 14–17°, the present URANS-realizable k-ε turbulence model simulation overestimates the experimental data and some of the earlier simulations for the drag coefficient.

3. NARMAX Identification of Flow over an Airfoil

In addition to providing basic physical features of the flow around the NACA 0015 airfoil at various flight scenarios, *CFD* offers row data for various input-output relationships of the system. The objective in this section is to develop a simple model that is capable of reproducing the dynamic characteristics of the flow over an airfoil with the synthetic jet actuators. The system identification technique aims to develop models that approximate the dataset collected from input-output relationships with the least mean-squared errors such that good predictions can be made (Billings [77]). In this work, the synthetic jets produce a series of unsteady moment injection into the flow that alters the flow dynamics. Therefore, the flow system identification model aims to have synthetic jet velocity as input and static pressure as an output. As a result, it is possible to build a Single-Input Single-Output (*SISO*) dynamical model via parameter estimation of input-output data relationships. In this section, a SISO discrete-time *NARMAX* model for the flow dynamics using URANS simulation data of flow around NACA 0015 is developed.

The *NARMAX* model describes the variable pressure output at a chosen downstream sensor location under the influence of the synthetic jet actuators on the airfoil upper surface in terms of difference equations. This model relates the current output to combinations of inputs and past outputs. A *NARMAX* power-form polynomial model is fitted to *SJA* velocity and sensor pressure data at the selected point and is used for predicting the pressure as a function of *SJA* velocity. Construction of the *NARMAX* identification model contains the following steps: The first step is identifying the model structure and which independent statistical variables (regressors) are to be used, followed by the determination of the model coefficients associated with those model regressors (parameter estimation). A combination of these two steps sometimes is referred to as the structure selection. The third step in the process of the *NARMAX* construction is to inspect the accuracy of the model using the model validation methods. The model validation indicates whether the model is unbiased and correct or not. The fourth and the last step consist of the use of the validated model for prediction of the output at some future times and verifying that the prediction is correct. One challenge associated with this modeling process is to avoid over-fitting that might result from using either excessive time lags or excessive nonlinear function approximations.

By following the steps mentioned above, the *NARMAX* modeling process will involve feedback in the model-fitting approach. For instance, if the initial collection of the regressor terms of the model is not large enough, then the algorithms will be unable to find the appropriate model. As a result, the model validation process does not provide reasonable accuracy. In some cases, the validation process can suggest what type of terms is missing. For improving the model accuracy, the estimation process can then be repeated by including a wider range of independent statistical variables. Only when the structure detection and all validation procedures are satisfied, then the model provides a good representation of the system (Billings [77]).

The method of Orthogonal Least Squares (OLS) is used for parameter selection in this study. In the OLS method, the contributions of each term in the model are measured based on an error reduction ratio (ERR). The value of the ERR depends on the order of the terms in the regression equation, and there is a possibility of leading to inaccurate estimated values. To resolve this issue, the forward regression OLS is used, which is computationally more expensive. Also, users need to decide the ERR value, but there are no specific criteria for this value. The number of terms to include in the final model is determined through the implementation of information theory criteria such as Bayesian information criterion (*BIC*), Akaike information criterion (*AIC*), and final prediction error (*FPE*) (Billing and Leontaritis [99]).

The general formulation of The *NARMAX* model as introduced by Leontaritis and Billings [100] is defined as:

$$\begin{aligned} p(k) \;=\; F[p(k-1),\; p(k-2),\; \cdots\cdots\cdots\; p\big(k-n_p\big), \\ v(k-d),\; v(k-d-1),\; \cdots\cdots\cdots\; v(k-d-n_v), e(k-1), \\ e(k-2),\; \cdots\cdots\cdots\; e(k-n_e) \end{aligned} \tag{1}$$

where $p(k)$, $v(k)$, and $e(k)$ are the system output, input, and noise series, respectively; n_p, n_v and n_e are the maximum lags for the system output, input, and noise; F[ ] is a nonlinear function, and d is a time delay that can take any integer value, d ≥ 1, but d typically set to 1 and d = 1 is used. The model essentially provides a correlation of the present predictions with past inputs, outputs, and noise terms. In this paper, a polynomial-form for the nonlinear function in Equation (1) is implemented, neglecting the noise terms.

In the current study, the sampling time is selected in a way to hold all the frequency contents of the input variable $v(k)$. Since the Navier-Stokes equation governing the motion of airflow over the airfoil contains terms of second-degree nonlinearity, the assumption made regarding the mapping function exists on the model structure is to be a polynomial (difference equations) of second degree of non-linearity as well. Second-degree polynomials represent the minimum nonlinearity and are sufficient to approximate numerous dynamical systems. The pressure response is assumed to depend on past pressure values and to have second-order dynamics so that the maximum time lags for p are given by $p(k-2)$, and the time delays are also included in the input terms. All terms forming the model are chosen by minimizing the error.

Taking these factors into account, the following discrete *NARMAX* equation is assumed,

$$\begin{aligned} p(k) \;=\; & \sum_{i=1}^{m^{v1}} C_i^{v1} v\left(k-n_i^{v1}\right) + \sum_{i=1}^{m^{p1}} C_i^{p1} p\left(k-n_i^{p1}\right) + \sum_{i=1}^{m^{v2}} C_i^{v2} v\left(k-n_i^{v2}\right) v\left(k-n_i^{v2}\right) \\ & + \sum_{i=1}^{m^{p2}} C_i^{p2} p\left(k-n_i^{p2}\right) p\left(k-n_i^{p2}\right) + \sum_{i=1}^{m^{vp}} C_i^{vp} v\left(k-n_i^{vp}\right) p\left(k-n_i^{vp}\right) \end{aligned} \tag{2}$$

where $v(k)$ and $p(k)$ are system input and output, respectively; m^{v1} and m^{p1} are the number of first order input and output regressor terms ($v(k-1)$, $v(k-2)$ …, and $p(k-1)$, $p(k-2)$, …), respectively; n_i^{v1} and n_i^{p1} are, respectively, the maximum lags for the system first-order input and first-order output regressor terms; n_i^{v2} and n_i^{p2} are, respectively, the maximum lags for the system second-order input and second-order output regressor terms; m^{v2} and m^{p2} stand for the number of second order input and output regressor terms, respectively; m^{vp} represents the number of coupled regressor terms; n_i^{vp} stand for the maximum lags for the system coupled regressors, and the C's in all terms in Equation (2) stand for the individual regressor coefficients.

Examples for the notations describing the regressor coefficients used in Equation (2) are as follows: C_4^{v1} stands for the coefficient associated with the 4th term of first-order regressors of the system input variable, C_4^{v2} the coefficient associated with the 4th term of second-order regressors of the system input variable, C_4^{p1} the coefficient associated with the 4th term of first-order regressors of the system output variable, C_4^{p2} the coefficient associated with the 4th term of second-order regressors of the system output variable, and C_4^{vp} the coefficient associated with the 4th term of combined regressors of (first-order input and first-order output) of system variables.

A summary of the procedure utilized in estimating the parameters of function F of Equation (1) is given by Leontaritis and Billings [100], Chiras et al. [101], Billings and Chen [102], Aguirre and Billing [103], and Billings and Aguirre [104]. The model selection criteria are useful tools for determining the number of terms to include in the final model. Several criteria have been proposed in the identification community for selecting the parameter estimation procedure and for evaluating the efficiency of the final model. These criteria count for estimating the amount of information lost when adding new parameters. In this study, the Akaike Information Criterion (*AIC*) (Akaike [105]), as well as the Bayesian Information Criterion (*BIC*) (Akaike [105]) are used for the parameter estimation process while the Nash-Sutcliffe Efficiency (*NSE*) criterion (Nash and Sutcliffe [106]) is used for evaluating the efficiency of the final model.

When fitting models, it is possible to increase the likelihood by adding parameters, but doing so may result in over-fitting. Both the Akaike Information Criterion (*AIC*) and Bayesian Information Criterion (*BIC*) are logarithmic-based criteria that are concerned in part, with the likelihood function and the trade-off between the goodness of fit of the model and its simplicity. The *AIC* is mainly dealing with the risk of over-fitting, as well as the threats of under-fitting problems. *BIC* is another criterion that attempts to resolve over-fitting problems by introducing a penalty term for the number of parameters in the model as the *AIC* does, but the penalty term is larger in *BIC* than in *AIC*. The model with the lowest *BIC* and the lowest *AIC* is considered the best model. Mathematically, *AIC* and *BIC* are defined, respectively, as:

$$AIC \;=\; \log\left(\frac{SSE_k}{n}\right) + \frac{2(k+1)}{n} \tag{3}$$

$$BIC = \log\left(\frac{SSE_k}{n}\right) + \frac{log(n)k}{n} \tag{4}$$

where k stands for the number of parameters used in the model, n is the number of observations (sample size) and SSE_k is the sum of squared residuals.

The efficiency criterion *NSE* proposed by Nash and Sutcliffe for model evaluation is defined as one minus the sum of the absolute squared differences between the predicted and observed values normalized by the variance of the observed values during the period under investigation. That is *NSE* is calculated using,

$$NSE = 1 - \frac{\sum_{i\,=\,1}^{n}[y_i(k) - \widetilde{y}_i(k)]^2}{\sum_{i\,=\,1}^{n}[y_i(k) - \overline{y}(k)]^2} \tag{5}$$

where $y_i(k)$ is the i-th observation for the data being evaluated, $\widetilde{y}_i(k)$ is the i-th predicted value for the data being evaluated, $\overline{y}(k)$ is the mean value of observed data for the data being evaluated, and n is the total number of observations. The range of *NSE* lies between $-\infty \leq NSE \leq 1$ with $NSE = 1$ corresponding to the perfect fit. The *NSE* values between 0.0 and 1.0 are generally viewed as acceptable levels of performance, whereas negative values indicate that the mean observed value is a better predictor than the predicted value, which indicates the unacceptable performance of the model.

For providing additional information on the *NARMAX* model construction and model features, two examples are discussed here. The first example is concerned with the cornerstones of the *NARMAX* construction and explains some performance features of the model. In particular, this example discusses the effects of synthetic jet excitations on model construction. The second example focuses mainly on the *NARMAX* model performance due to changes in main flow parameters.

In the first example, the observed static pressure time series on the airfoil upper surface at a point at 30% chord length from the leading edge was recorded at the sensor location for 120,000 time steps duration. Here the free stream velocity, $U_\infty = 50$ m/s, the mean jet velocity measured at mid-point in slot width, $U_j = 35$ m/s, the velocity ratio, $V_r = U_j/U_\infty = 0.7$, and the synthetic jet was operating at 250 Hz. The jet driving frequency is constant at 250 Hz, and the jet velocity used as an input in the *NARMAX* construction was a sinusoidal signal. A sample output static pressure signal at the senor point used in the model construction is shown in Figure 6.

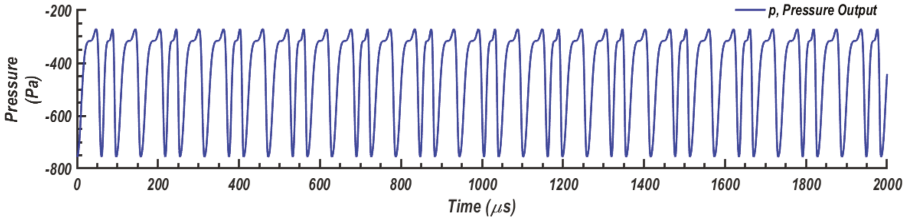

Figure 6. The output static pressure signal as obtained from numerical simulations and used in the *NARMAX* construction.

The pressure data were obtained using a (non-dimensional) time step of $\Delta t = 0.000125$, and the sampling rate for the recording was $\Delta ts = \Delta t = 0.000125$. The pressure recording started at $t_o = 2.4 \times 10^6\ \Delta t$ and ended at $t_{\text{final}} = 2.52{\times}10^6\ \Delta t$. Overall, 120,000 pressure data were collected. The starting time t_o, the sampling rate Δts and recoded data simulation period are all chosen to reach a steady-state pressure pattern. Typically, 60% of the pressure time series was used for training, while 40% are used for validation purposes. The model structure was chosen following the procedure explained in Leontaritis and Billings [100] and the information criteria discussed above.

Figure 7 shows how the model parameters are selected, part (a) of the figure depicts values of *AIC* and *BIC* for both estimation series and validation series against the number of parameters included in the model. As noted before, *AIC* and *BIC* indicate the amount of information lost between observed data and the predicted one. Therefore, Figure 7a is used to select the best (optimum) model in each model class (with the same structure). For each class, the best model is the one with minimum *AIC* or *BIC* for the validation series. This figure shows that the criterion *AIC* index decreasing with increasing the number of parameters until it reaches its minimum value and then starts to increase when additional parameters are added. That means adding more parameters decreases the amount of information lost between the observed and the predicted data initially. After adding a certain number of parameters up to an optimal number, the amount of information loss will tend to increase. That is, an increase in the number of terms beyond the optimal number results in model overestimation and an increase in the *AIC* (*BIC*) index.

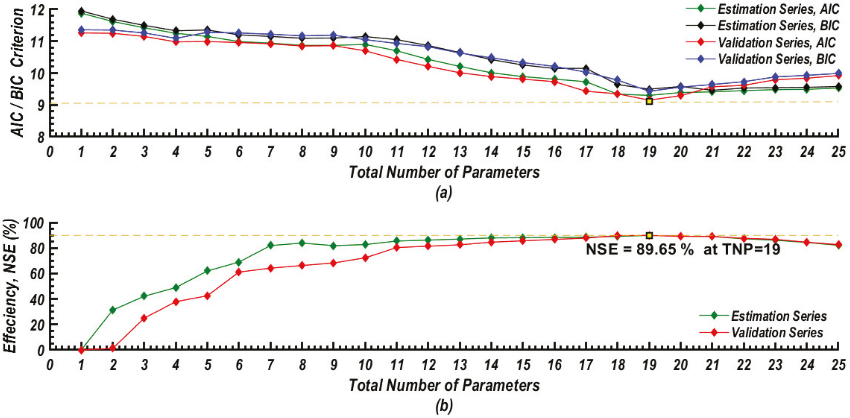

Figure 7. (**a**) Variation of *AIC* and *BIC* with the *NARMAX* total number of parameters. (**b**) Variation of *NSE* efficiency with the *NARMAX* total number of parameters.

The applications of the *AIC* on validation data are useful in determining when to stop adding parameters to a model. However, the use of this criterion alone would not always result in an optimal model (Wu et al. [85]). Figure 7a shows those *BIC* indices for both estimation and validation series are of higher values than *AIC* indices. The minimum index value is 9.151 found by the *AIC* criterion for the validation series when the total number of parameters *TNP* = 19.

Part (b) of Figure 7 presents the variation of the *NSE* efficiency with the *NARMAX* total number of parameters for both estimation and validation series. The values of the *NSE* shown in this figure express the efficiency in percentage (i.e., *NSE* = 100% means *NSE* = 1). It is seen that there is a continuous rise in *NSE* for both estimation and validation series, with increasing the number of parameters until the optimum number of parameters is reached; after that, the *NSE* efficiency starts to decrease. The maximum *NSE* efficiency reported is 89.65% for both the estimation and validation series when the total number of parameters *TNP* = 19.

Figure 7 also shows the trend of variation of *NSE* with the increasing number of parameters is opposite to the variation of the *AIC* (*BIC*) index, which shows a continuous decrease until the optimal number of parameters is reached and then increases. Since the estimation series is the fitting series, an increment in the number of parameters consistently results in a better fit for the series.

Not so for the validation series. The validations of NSEs indicate fairly good fits and predictions from the selected models.

It is seen from Figure 7 that the optimum number of parameters is 19, including a constant term (an intercept). It is important to note that while the full regressor terms number 35, only 19 were found to be significant for the full *NARMAX* case for this model structure. The resulting model consists of an intercept term, 3 first-order regressors, 8 *s*-order regressors, and 7 coupled regressors with two backward time steps in pressure, current and 4 backward terms in velocity.

The time-domain response of the observed and predicted pressure signals for the case with 250 Hz of synthetic jet actuation is shown in Figure 8. The Figure also presents the absolute difference reported between the observed and estimated pressure signals $|P_{CFD} - P_{NARMAX}|$ versus time for the best model of pressure identification. In part (a), the pressure outputs of the simulation (blue), and the identified model (red) for the pressure signal recorded at the sensor location were plotted against time. It is clearly seen that both the observed and predicted pressure signals have roughly identical periodic features. Each fluctuates between a minimum value and a maximum peak value and the time domain responses show that the *NARMAX* model matches the URANS simulation results successfully in the steady-state with small differences appear in the proximity of the peaks. Part (b) of Figure 8 indicates that the absolute difference in the pressure series is also periodic and fluctuates with a very small amplitude.

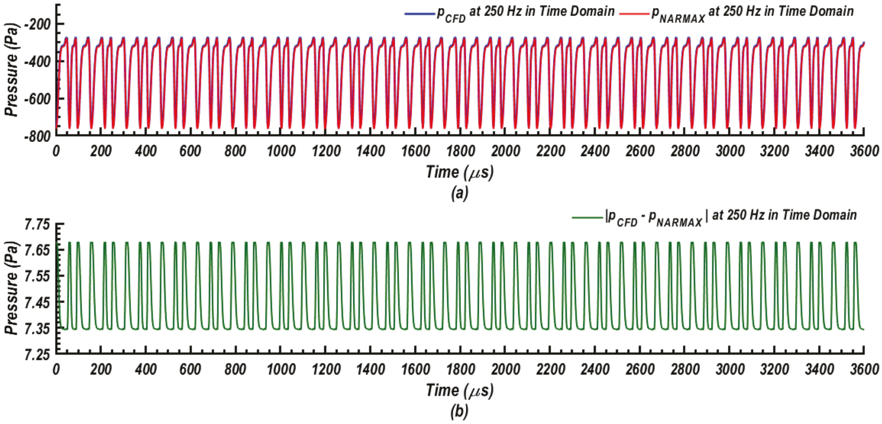

Figure 8. (**a**) Time variations of the observed and predicted pressure signals at 250Hz. (**b**) Time variation of the absolute difference between the observed and estimated pressure signals $|P_{CFD} - P_{NARMAX}|$.

The behavior of the average pressure obtained from the *CFD* calculations and the comparison with the behavior of the average pressure predicted by the *NARMAX* model is performed in this section. A moving-average-type filter using N data points was used to extract the mean pressure of the two signals. That is,

$$\overline{p}(k) = \frac{1}{N}\sum_{i=0}^{N-1} p(k-i) \tag{6}$$

Figure 9 compares the moving averages of the pressure response as obtained from the *CFD* with that evaluated from *NATMAX* prediction for an *SJA* frequency of 250 Hz. The difference in the mean pressure is of the order of 1.3% during the transition and about 0.7% when the steady-state is reached. The moving average in each case uses 200 data points for evaluating the mean value.

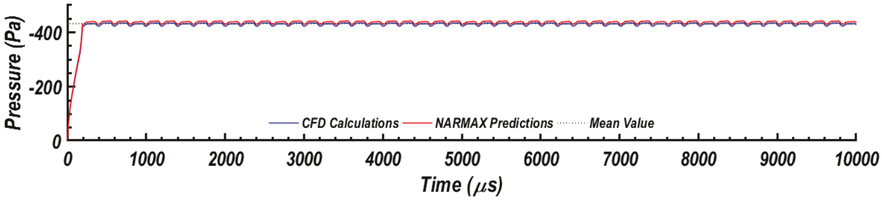

Figure 9. Comparison of moving average of the pressure response as obtained from *CFD* calculations and NARMAX predictions for constant input.

For investigating the frequencies associated with both observed (*CFD*) and estimated (*NARMAX*) pressure signals shown in Figure 8a and their relationship to the jet driving frequency (250 Hz), the power spectrum analysis was conducted using the fast-Fourier-transform functions in MATLAB. The corresponding results are as shown in Figure 10. For identifying the frequencies of the original baseline flow and those of the controlled flow with the synthetic jet actuation, the power spectrum of the pressure signal for the baseline case (without actuation) is also added to Figure 10. This figure has two horizontal axes; one is a frequency in (Hz), and the other is the Strouhal number (normalized frequency), $Sr = \left(\frac{fc}{U_\infty}\right)$, where U_∞ is the free stream flow velocity, and c is the chord length.

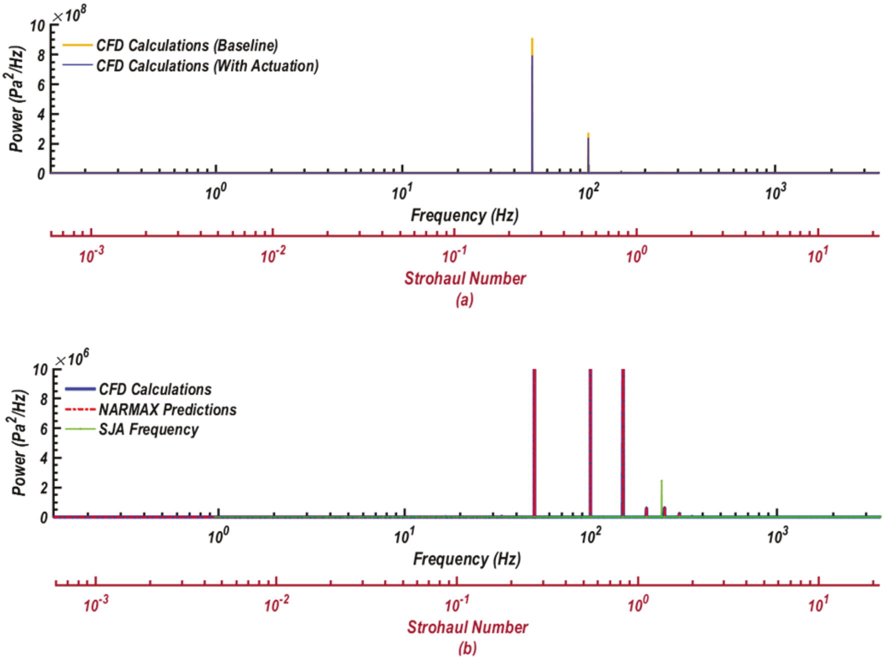

Figure 10. Comparison of the power spectra of pressure signals. (**a**) Baseline flow (uncontrolled) and controlled flow with jet actuation at the frequency of 250 Hz. (**b**) CFD pressure signal and NARMAX estimated pressure signals with the jet driving frequency at 250Hz.

Figure 10a compares the power spectrum of *CFD* signals for the baseline case and the controlled case with constant actuation at 250 Hz. The spectra of the two signals indicate that both the baseline case and the case with actuation have dominant frequencies at 49 Hz (St = 0.294) and 98 Hz (St = 0.588) with power intensity higher than 10^8 Pa^2/Hz. It is also seen that the baseline pressure signal has higher strength compared with the case for the controlled flow. Examination of these power spectra at a lower intensity (not shown in this figure) indicates that there are other frequencies associated with these two signals at 150 Hz (St = 0.9), 198 Hz (St =1.188), 299 Hz (St =1.794), and 327 Hz (St = 1.962) that are in the range of (10^6–10^7) Pa^2/Hz. Again the baseline flow frequencies are typically stronger than those associated with the controlled case. There is also a dominant frequency at 253 Hz (St = 1.518) associated with the synthetic jet signal for the controlled flow that does not appear in the baseline signal. There are other frequencies associated with the baseline signal with much weaker strength at 18 Hz (St = 0.108), and 127 Hz (St = 0.762) with power in the range (10^5–10^6) Pa^2/Hz, which were found to be suppressed due to actuation.

According to Mittal and Kotapati [107], there are at least three natural frequencies in a separated airfoil flow. These are the well-known wake frequency, f_{wake}, due to the flow global instability and caused by Kármán vortex shedding, a shear frequency, f_{shear}, due to the Kelvin-Helmholtz-type instability of the separated boundary layer, and if the flow does reattach before the airfoil trailing edge, a third frequency scale f_{sep}, corresponding to the separation bubble. Colonius et al. [48] showed that for a fully separated flow over the entire suction surface, the airfoil behaves as a bluff body, the vortex shedding occurs at $St \approx 0.15$–0.2. Instabilities in shear layers were reviewed by Ho and Huerre [108] who reported a shear Strouhal number of $St_{shear} \cong 0.032$ for laminar flows, and $St_{shear} \cong 0.044$–0.048 for turbulent flows. The shear Strouhal number is defined using the momentum thickness as the length scale. Addition discussion of post-stall flows was reported by Wu et al. [109]. It is seen that the frequencies provided by the power spectrum analysis of the baseline flow in the current study are in the range of the wake vortex shedding and shear frequencies.

There have also been many studies on the uncontrolled flow characteristics of the NACA 0015 airfoil, including identification of the key flow frequency content. Synthetic jet actuators are then used at the identified frequencies of the shear layer and wake for flow separation control. Earlier results reported in the literature revealed that for the NACA 0015 airfoil at $Re = 10^6$, the optimum non-dimensional jet driving frequency is in the range of $0.3 \le F^+ \le 4$ (Seifert et al. [24], Sharma [97], and Tuck and Soria [50]). Here the non-dimensional jet frequency is defined as,

$$F^+ = \frac{f_j\, c}{U_\infty} \tag{7}$$

where f_j is the jet actuation frequency (Hz), c is the chord length, and U_∞ is the free stream velocity (Kim [110]). Note that the non-dimensional jet frequency is the same as the Strouhal number for jet frequency.

Figure 10b compares the power spectra of the observed (*CFD*) and predicted (*NARMAX*) pressure signals shown in Figure 8a with the *SJA* activated at a frequency of 250 Hz. Here the maximum power level in the graph was reduced by two orders of magnitude so that additional frequencies, including the actuation frequency, can be seen. It is seen that the power spectrum of the predicted signal matches with the power spectrum of the observed signal. Figure 10 shows that both *CFD* and *NARMAX* signals have dominant frequencies at 49 Hz ($St = 0.294$), 98 Hz ($St = 0.588$), 150 Hz ($St = 0.9$), 198 Hz ($St = 1.188$) and 253 Hz ($St = 1.518$). The first four frequencies are related to the vortex shedding associated with the baseline flow, while the last frequency is related to the jet actuation at 250 Hz. It is also concluded that the *NARAMAX* model is capable of capturing the frequency contents of the static pressure signal. Further discussions on the effects of the excitation frequency on the magnitude of response frequencies of the shear layer and wake are provided in Section 6.2 of this paper.

The influence of variations of the synthetic jet excitation frequency on the model parameters and the controlled flow structures was also studied. The same procedure of *NARMAX* construction is repeated for flow with synthetic jet frequencies of 850 Hz and 1200 Hz. The regressor terms are kept the same as those for flow excitation with a frequency of 250 Hz. In the case with 850 Hz excitation, it is found that the model coefficients changed, and the *NSE* efficiency dropped by 2%. For the same flow with 1200 Hz excitation, it is found that for an optimal model structure, the total number of the model regressors should be increased to 21 parameters with the addition of one first-order regressor and one second-order regressor, and the efficiency also drops by 2%.

The second interesting example is for the case in which the effects of variations in basic flow parameters on the *NARMAX* structure are investigated. Impacts of both the external flow conditions and the flow forcing variations on the *NARMAX* structure are examined. The airfoil-*SJA* system is set at a fixed incidence angle while the jet frequency is fixed at 850 Hz. More precisely, the influences of changes in the free stream velocity and, consequently, the effects of momentum coefficient (velocity ratios) changes on the model parameters and estimation error with the fixed model structure are discussed. In order to compare the results, a reference model structure is constructed. Here the “reference model” refers to the case that the same model regressor terms (model predictors) are used in identifying other flows.

Three different free stream velocities at U_∞ = 35 m/s, 50 m/s and 65 m/s were used. The mean synthetic jet velocity was kept a constant at 50 m/s. The variation in the flow forcing amplitude is quantified either by using the velocity ratio, V_r or the momentum coefficient C_μ (Lavoie [111]). The jet momentum coefficient, C_μ has been defined in several ways in the literature. In this work, the jet momentum coefficient is defined as introduced by Gressick in Maldonado et al. [112]. That is,

$$C_\mu \ = \ 2\rho_j U_j^2 b / \rho_o U_\infty^2 c \tag{8}$$

where ρ_j is the jet fluid density, ρ_o is the free stream fluid density, U_∞ is the free stream velocity, U_j is the average jet velocity measured at mid-point in slot width, b is the *SJA* slot width, and c is the airfoil chord length. (In the present study $\rho_j = \rho_o$ as the air is assumed incompressible.) The available literature indicates that the momentum coefficient ratios C_μ of at least 0.002 are required to affect the flow.

The external flow conditions used are equivalent to the Reynolds numbers of $Re = 7 \times 10^5$, $Re = 10^6$ and $Re = 1.3 \times 10^6$. The *SJA* actuator used has a slot width b = 2.7 mm extended into the left and right sides of the slot center. The jet fluid density ρ_j and the free stream fluid density is assumed identical in all cases. Therefore, the values of the jet momentum coefficient corresponding to these conditions are $C_\mu \ = \ 0.0367$, 0.0180, and 0.0125, and the values for the velocity ratio are, respectively, V_r = 0.7, 1.0, and 1.30.

The reference *NARMAX* model taken in this study is the one that was constructed to identify the pressure signal recorded at the airfoil upper surface point at a 30% chord length position measured from the leading edge and at free stream velocity of 50 m/s ($Re = 10^6$). This model was constructed using 8 first-order regressors, 24 *s*-order regressors, and 12 coupled regressors with two backward time steps in pressure, and 6 backward time steps in velocity. Therefore, the reference model consists of 44 total number of regressors, excluding an intercept.

When these 44 regressors utilized as basic constituent regressors to construct *NARMAX* models for the identification pressure series at U_∞ = 35 m/s and U_∞ = 65 m/s respectively, each of the model coefficients found changes monotonically as the free stream velocity increases, while the Nash-Sutcliffe NSE varies slightly. The model coefficients were found changing for different free stream velocities. The physical interpretation of this is that the physical behavior of the fluid system is at least consistent within the range of given free stream velocities such that each parameter may be described as simple functions of free stream velocity.

The jet frequency is changed to cover a wide range of frequencies from 50 Hz to 1000 Hz with a 50 Hz step. The mean pressure corresponding to each actuation frequency was reported. The variations of the mean pressure at the sensor location as a function of the jet frequency for different free stream velocities are shown in Figure 11 (thick lines). This figure also shows a comparison between the identified static pressure signals (thin lines) and URANS simulation results (thick lines) for the same operating conditions. It is seen that the responses of this *NARMAX* model for different free stream velocities and various synthetic jet frequencies are in good agreement with the corresponding simulation results.

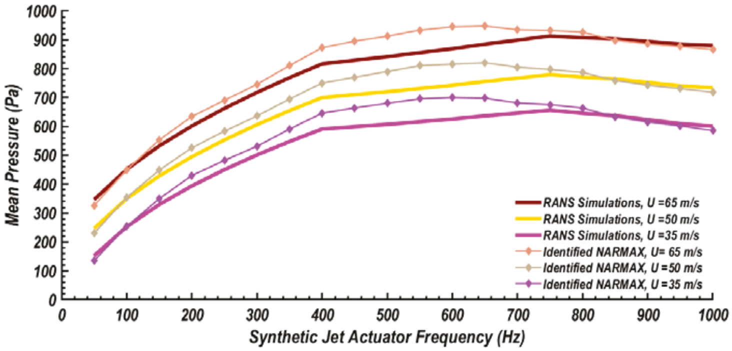

Figure 11. Comparison between *NARMAX* model and *CFD* results for the mean pressure and *SJA* frequency at AoA = 16°

It should also be pointed out that regardless of the free stream velocity, the maximum pressure recovery is achieved consistently at the same dimensionless frequency F^+ of synthetic jets. Therefore concerning the pressure recovery, the optimal dimensional frequency of the jet actuation should be increased proportionally to the free stream velocity. The difference between plots widens as the jet frequency increases, whereas the overall features are not changed despite different free stream velocities. This consistency is beneficial to a feedback control synthesis as will be shown in the next sections, since it implies that regarding a flow model, the effects of free-stream velocity varying within a certain range can be incorporated into model coefficients, with the model structure retained.

4. Flow Control Problem

Given the airfoil-*SJA* system, as shown in Figure 12, a feedback control system for flow separation over the airfoil is developed. While numerous parameters are affecting the aerodynamic performance of such a fluidic system, the parameters involved in such a control problem can be divided into main flow parameters, geometric parameters, and actuation parameters. From the control point of view, these variables can be classified into three groups of variables, namely, independent, dependent, and controlled variables. The control variables are those that are varied by the actuator to reach the desired outcome.

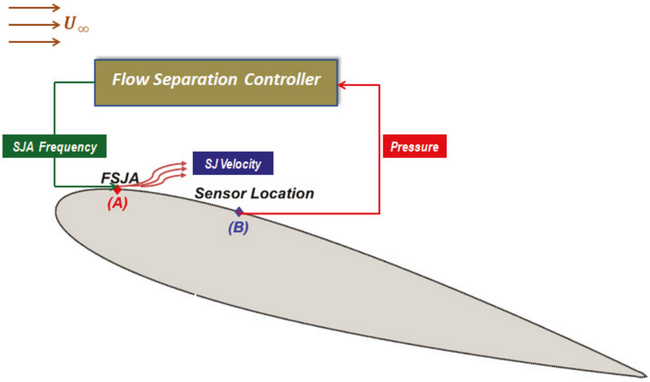

Figure 12. Schematic diagram for the flow separation control.

The independent variables in the control problem are those imposed independently. This set includes but not limited to the free stream velocity, U_∞, the airfoil incidence angle, α, the size of the *SJA* slot width, b, the chord-wise location of the slit of the synthetic jet, x_j/c, and the inclination angle of synthetic jets with the horizontal direction, ψ The dependent variables are all parameters of the flow and thermal field that depend on the independent variables and many of which can be measured. This set may include one (or more) of the following properties: pressure, velocity, density, temperature, turbulence intensities, wall fluxes, lift and drag forces. In the present problem, the control variables are the amplitude of the synthetic jet velocity and the actuation frequency of synthetic jets.

Considerable amount of information on the synthetic (zero-net-mass flux) jets, their formation, evolution, and the mechanisms of their interaction with different flows were reported in the literature. The mechanism by which synthetic jets restrain the flow separation over an airfoil can be briefly explained as follows: Synthetic jets actuators introduces vortices into the boundary layer over the airfoil. These vortices cause the high momentum from the outer edge of the boundary layer to transfer to the near-wall region producing favorable pressure gradients and preventing the boundary layer flow from being detached from the surface. Motivated by the wide range of benefits offered by synthetic jets in controlling the flow separation, a synthetic jet actuator is selected for the active flow control in this study.

The synthetic jet actuator has the advantage of generating zero-net-mass flux, which facilitates both the fabrication and installation of the actuator. The jet velocity, however, produces periodic velocity configuration. Therefore, the control variables are the amplitude and frequency of the synthetic jet. The possible ways to modify the excitation signal is by introducing amplitude or frequency modulations or by operating the actuator in burst mode, i.e., switching on and off the actuator for prescribed periods (Benard & Moreau [113]). Frequency modulation of synthetic jet excitation signal on flow control problems is found more beneficial when targeting flow structures of high frequencies. In order to widen the range of effective flow control to include flow structures with low frequencies, the use of a synthetic jet actuator operating at a high resonant frequency with the amplitude modulation is recommended. In the case of bursting mode, the ratio of time the actuator is turned "on" to the total time between consecutive turnings "on" instants defines the duty cycle and effectively acts as the excitation frequency of the actuator.

In this study, the control objective is to maintain the maximum mean surface pressure at the sensor location (Point B in Figure 12) by the synthetic jet actuators despite the variation of the free stream velocity. At the constant incidence angle of the airfoil, α, the size of the *SJA* slot width, b, the chord-wise location of the slit of the synthetic jet, x_j/c and the inclination angle of synthetic jets with respect to the horizontal, ψ, the free-stream velocity is found to be a key parameter that affects the synthetic jet actuation. The surface static pressure at the sensor location on the airfoil is given as,

$$p(t) \;=\; f\Big(f_j(t),\; U_j(t),\; U_\infty\Big) \tag{9}$$

where f_j is the *SJA* frequency, U_j is the synthetic jet velocity and U_∞ is the free-stream velocity. The controller's objective is to get the maximum (absolute) mean pressure for varying the free stream velocity variations for a fixed *SJA* velocity. Thus, the average pressure value $\overline{p}$ becomes the controlled variable. In this study, the jet velocity is assumed to be constant, and only the jet frequency is varied.

For generating variable jet frequency, the actuator operates in frequency modulation mode and the jet frequency f_j is a function of time. More information about frequency modulation by the actuator was reported by (Kim [110]).

5. Modeling of Synthetic Jet Actuators

The synthetic jet actuators (*SJA*) have been used extensively for active flow control. The synthetic jet flow is generated by the vibration of a membrane or a diaphragm that sucks and ejects air through a narrow nozzle. *SJAs* can be developed with an electromagnetic driver, a piezoelectric driver, or even a mechanical driver such as a piston. The unique feature distinguishing *SJAs* from other devices is that the jets provided by these devices are created by the periodic suction and blowing of air so that momentum is transferred to the flow no net mass addition. In that sense, synthetic jets are widely known as "zero-net-mass flux flow" devices. An *SJA* operates in a stand-alone manner without any extra piping or fluidic packages and thus can be simply fabricated and easily integrated into fluid systems (Glezer and Amitay [114]).

To simulate the oscillatory momentum fluxes generated by the *SJA* to energize the boundary layer flow, an *SJA* with a slot width of 2.7 mm flush-mounted with the airfoil upper surface at 10% chord length from the leading edge is selected in this study. The actuator is placed in a way that its injection line is at 30° with the airfoil tangent line. A wall-normal velocity condition with a spatial waveform $F(s)$ is given to the jet velocity. The corresponding velocity components are given by:

$$u_j(x, y = 0, t) = 0, 0 < x/(b) < 1 v_j(x, y = 0, t) = U_j\, F(s) sin\left(2\pi f_j t\right) \tag{10}$$

where x denotes the stream-wise direction tangential to a surface measured from the left edge of a jet slot, y the cross-stream direction normal to a surface and u_j and v_j are the velocities for x and y directions, respectively. Here b is the synthetic jet slot width. The temporal configuration, $sin\left(2\pi f_j t\right)$), which represents the periodic excitation of synthetic jets, leads to the zero net mass flux in the time-average sense.

Although there are various forms of spatial *SJA* velocity profiles (along slot width) that were discussed in the literature, four forms are considered most popular. These are the top hat, parabolic, sinusoidal, and sine squared profiles. In this work, the half-sine spatial velocity profile of *SJA* is considered, while the temporal part is given by sinusoidal periodic motions with frequencies in the range of $0.5 \leq F^+ \leq 1.5$, where the reduced jet actuation frequency is as defined in Equation (7).

The resultant wall-normal velocity component for synthetic jets is

$$v_j(x, y = 0, t) = U_j\, sin\left[\frac{\pi x}{b}\right] sin\left(2\pi f_j t\right) \text{ for } 0 < x/(b) < 1 \tag{11}$$

where U_j is the average jet velocity measured at mid-point in slot width, which is taken as 50 m/s in this study, b is the *SJA* slot width which is taken 2.7 mm, ψ is the angle formed by jet flow line and the horizontal direction which is taken as 30°.

An incompressible flow model for *SJA* in quiescent flow was suggested by Tang et al. [115] and verified experimentally by Sharma [116]. This model relates the motion of the synthetic jet actuator diaphragm to the power supply driving the actuator. According to this model, the instantaneous space averaged velocity at the orifice exit can be described as a function in the jet amplitude, U_j and the jet frequency, f_j. Mathematically, this velocity can be expressed as

$$v = U_j sin\left[\int_0^t 2\pi f_j(\tau) d\tau\right] \tag{12}$$

This approximate model valid for values of $f_j(t) > 0$ at all times.

6. Feedback Controller Design and Performance

The main objective of the current work is to develop a control algorithm aiming for improving the aerodynamic performance of the airfoil. At relatively high incidence angles, the airfoil's natural behavior leads to a separated flow. Generally, to ensure that separated flow is reattached to the airfoil surface, an "actuator" is used to perturb the airflow that works as a "controller." The objective here is to design a control system that analyzes the errors between measured pressure values and the desired pressure value and then actuate to minimize these errors.

To design a closed-loop controller to suppress flow separation over NACA 0015 airfoil at AoA = 16°, a reference (desired) average pressure signal is taken from the airfoil upper surface based on open-loop control performance of the system at the state corresponding to a fully re-attached flow. The closed-loop control algorithm works on minimizing the differences in the sensor average pressure signal and the reference value. The control objective is to maintain the maximum mean surface pressure at sensor location (B) in Figure 11 using the synthetic jets (actuator) despite the variation of free stream velocity. This objective would be fulfilled by minimizing the error between the measured pressure and the desired one. The controller has the authority over the synthetic jet actuation frequency at point (A), with the downstream pressure at point (B) is utilized as a feedback signal for the controller. The difficulties of this control problem arise from the sinusoidal nature of the actuator pulsations as well as the nonlinear flow dynamics. As mentioned before, to secure the basic feature of synthetic jets (zero-net-mass flux), the actuator cannot produce an arbitrary waveform of the jet velocity. The velocity profile is restricted to a periodic waveform; therefore, possible control variables are the *SJA* airflow amplitude and frequency. In this study, the *SJA* airflow amplitude is a constant, and the frequency is treated as the control variable.

The *SJA* pulsation generates and oscillatory flow. Therefore, the pressure output at the sensor location (over the airfoil surface) also oscillates periodically. To avoid the challenge of dealing with the high-frequency signal, the mean pressure $\overline{p}$, instead of the instantaneous pressure, p is used for the control. A moving-average-type filter using N data points, as given by Equation (6), was first applied to extract the mean pressure. Although the moving average is a method to smooth data with a small number of data points, the results in this study revealed that a larger number of data is necessary to effectively suppress the oscillatory components. It was also found that the moving average has a slow transition until the steady-state is reached.

In this study, an infinite impulse response (IIR) low-pass filter (fourth-order Butterworth low-pass filter) is used to obtain the *DC* component of pressure at zero frequency (which is equivalent to the average of the signal). Such low-pass filtering requires only a small number of data points and provides a fast transient response. The stop frequency of the low-pass filter is maintained to be less than or equal to the lower bound of the synthetic jet frequency, following suggestions of Kugelstadt [117].

The controller design requires a frequency response analysis of the Airfoil-*SJA* system; however, the nonlinear features of the system prevent a direct frequency analysis. Instead, the describing function approach is proposed here to analyze the *DC* component (quasi-linear) frequency response of the Airfoil-*SJA* system (*NARMAX* model) to the sinusoidal inputs. In addition, the describing function is used to predict a limit cycle oscillation (Taylor [118,119], Schwartz and Gran [120]). Since the describing function provides a quasi-linear model for the nonlinear system whose linearity extent depends on the type of input, the sinusoidal input describing function (SIDF) is used in this work.

As the name implies, the SIDF represents an approximate mathematical technique of linearization used in limit cycle analysis for nonlinear systems subjected to a sinusoidal input. The basic idea behind SIDF is that given the sinusoidal input to the nonlinear system, all high frequencies associated with the output of that nonlinear system can be ignored (filtered out) compared with only one fundamental (low) frequency component. Slotine and Li [121] proposed this type of low-pass filtering. Results obtained from the frequency response analysis for the pressure signal before and after the low-pass filtering play an important role in the controller design. The describing function allows predicting a limit cycle performance for the identified signal within a certain frequency range. Thereby the low-pass filter works to preserve a DC component of the pressure signal, which is then used as a feedback signal (Kim [122]).

6.1. Open-Loop Control

The primary purpose of the open-loop analysis is to explore the effect of the SJ actuation. Here the case of the airfoil-*SJA* system for the following condition is investigated: fixed incidence angle of 16°, free stream velocity $U_\infty = 50$ m/s and synthetic jet velocity $U_j = 50$ m/s (which corresponds to a momentum coefficient of $C_\mu = 0.0180$). In this case, the *SJA* works as a controller whose action is independent of the "process output," which is being controlled. For the open-loop case, the synthetic jet actuator does not use feedback to determine if its output has achieved the desired goal and only operates in on/off modes.

This type of control is used to examine the capability of the *SJA* to perturb the separated flow over the airfoil surface and to determine at which operating conditions the synthetic jet actuator can provide a fully re-attached flow over the airfoil surface. This mode of operation of the *SJA* is recommended when the control result is known to be adequate without the need for feedback. Figure 13 illustrates the open-loop scheme of the control system.

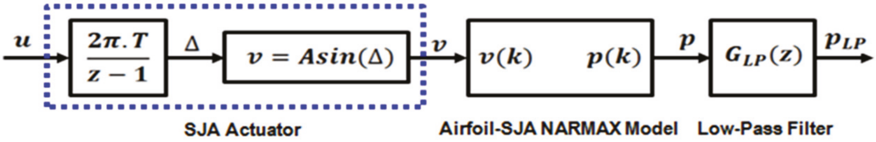

Figure 13. Schematic of an open-loop control system.

The Airfoil-*SJA* system response to various frequencies was examined for aerodynamics performance in addition to the synthetic jet velocity variation and the corresponding pressure signal at the sensor location. The frequency response of the open-loop system is analyzed using step inputs for the jet frequency f_j. The quasi-linear characteristics of the system incorporating the low pass filter are discussed. The system response for three different step inputs, namely 375, 775, and 1050 Hz, is illustrated in Figure 14.

Figure 14a shows the time variation of the synthetic jet frequency, and Figure 14b gives the corresponding synthetic jet velocity $v_j(t)$. Figure 14c presents the static pressure signals $p(t)$ resulting from the synthetic jet actuation and Figure 14d shows the set of filtered pressure signals p_{LP} as the output of the low pass filter. At 375 Hz, the filtered output shows the disturbances coming internally from high-frequency components. By increasing *SJA* frequency to 775 Hz, the disturbances disappear, and the filter is more effective since the filter stop frequency is 415 Hz in this study. With the jet frequency stepped to 1050 Hz, the filtered pressure drops due to the non-linear relation of *SJA* frequency and the mean wall pressure.

Open-loop responses show that at *SJA* frequency of 629 Hz, the flow at sensor location (point B in Figure 12) tends to reattach with the airfoil. At that condition, the lift coefficient of the airfoil attains its maximum value (L/D = 6.84), and the average static pressure value is 83.54 Pa. This pressure value is used as a set point in the closed-loop controller design.

6.2. Closed Loop Control

For the closed-loop control, the *SJA* works as a component of the overall control system to execute the control action. The *SJA* responds according to the feedback signal with the aim to manipulate the process variable to be the same as the "reference input" or "set point."

Proportional-Integral (*PI*) controller is one of the most popular control loop feedback mechanisms for linear time-invariant systems (Vukic and Kuljaca [123]). The Proportional-Integral (*PI*) controller calculates an error value as the difference between a measured process variable and the desired set point. The controller attempts to minimize the error by adjusting the process inputs. The algorithm of *PI* control involves two separate constant parameters, namely proportional and integral gain values. The proportional action depends on the present error, and the integral action depends on the accumulation of past errors. The weighted sum of these two actions is used to adjust the process via a control element.

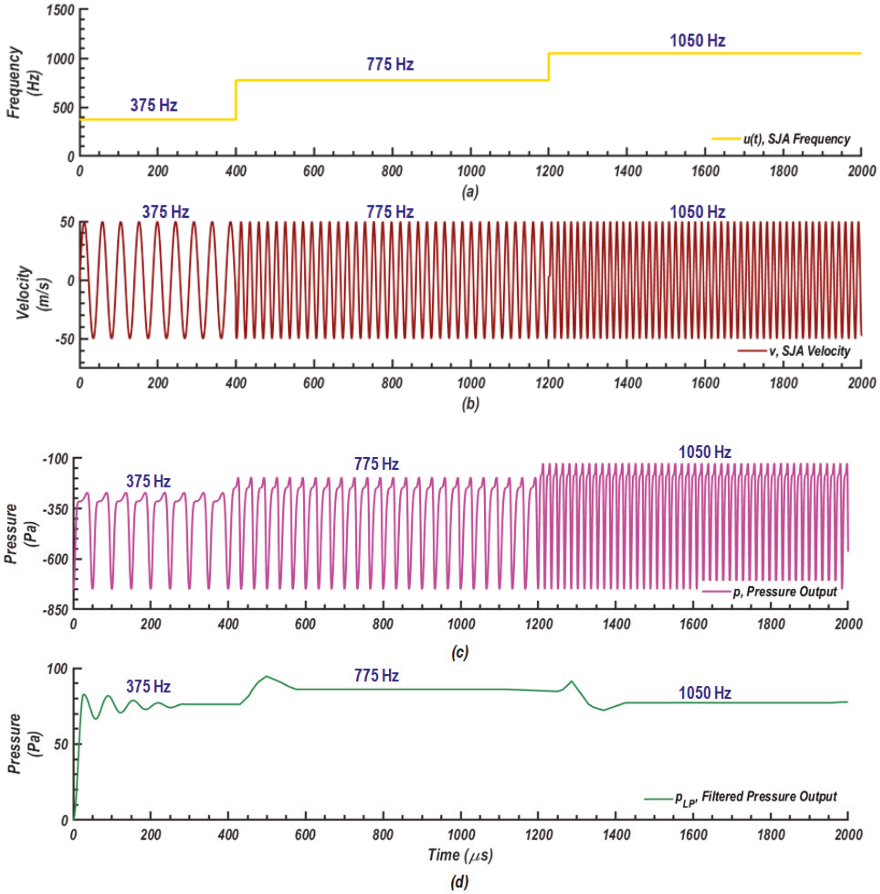

Figure 14. Open-loop responses for the step inputs at 375 Hz, 775 Hz, and 1050 Hz. Time variations of (**a**) the synthetic jet frequency (f_j), (**b**) synthetic jet velocity, $v_j(t)$, (**c**) static pressure signals as a result of synthetic jet actuation, and (**d**) filtered pressure signals from the low-pressure filter, p_{LP}.

Taylor et al. [124,125] introduced the describing function as a powerful mathematical approach for analyzing and improving the behavior of nonlinear systems. In this work, the sinusoidal input describing function (*SIDF*) is used to perform an approximate frequency response analysis and predict the limit cycle oscillation of the system for different synthetic jet frequencies. The low-pass filtering adds further to the linearization of the pressure signal and enables employing linear control theories. Figure 15 shows a Simulink diagram for the *PI* feedback control system used in this study. The block corresponding to the linearized plant includes fluidic system blocks where the describing function analysis is applied in addition to the low pass filtering process. The saturation block interposed between the controller and the plant is used to impose the upper and the lower limits on the input signal. When the input signal is within the range specified by the Lower limit and Upper limit parameters, the input signal passes through unchanged. When the input signal is outside these bounds, the signal is clipped to the upper or lower bound. For achieving the desired control action, our analysis indicates that the saturation limits should be set as follows: lower bound at $f_{\min} = 375$ Hz and upper bound at $f_{\max} = 775$ Hz.

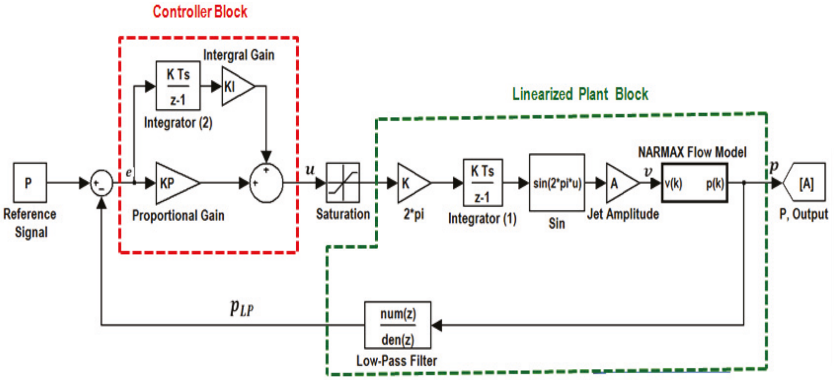

Figure 15. Simulink diagram for *PI* feedback control.

Figure 16 compares the power spectrum of the identified output pressure signal at a constant jet driving frequency of $f_j = 629$ Hz with the power spectra of the identified baseline signal and the identified controlled signal with a jet frequency at 250 Hz. Figure 16a shows that all these signals have dominant frequencies at 49 Hz (*St* = 0.294) and 98 Hz (*St* = 0.588) with power intensity higher than 10^8 Pa^2/Hz. It is also seen that the identified baseline pressure signal has higher strength compared with the cases for the controlled flow. The jet actuation with frequency 250 Hz reduces the strength of the baseline frequency at 49 Hz (*St* = 0.294) by 1.1×10^8 while the actuation at 629 Hz results in 4.38×10^8 reductions. The strength of the baseline frequency at 98 Hz (*St* = 0.588) is also affected by actuation. The controlled signal with jet frequency at 250 Hz has a lower strength by 0.35×10^8, while the controlled signal with jet frequency at 629 Hz shows a reduction of 1.55×10^8.

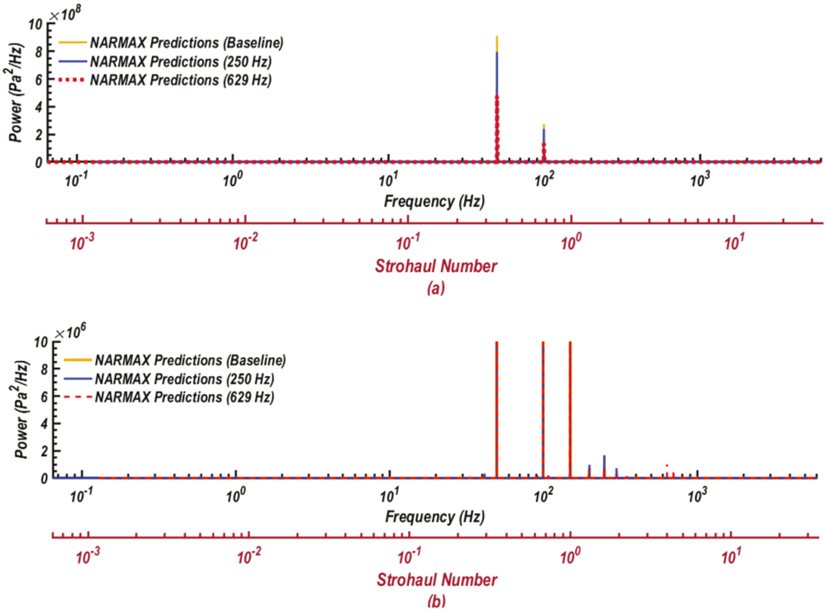

Figure 16. Comparison of the power spectra of the predicted output pressure signals for the baseline and controlled flows with the synthetic jet actuation at 250 Hz and 629 Hz. (**a**) Higher than 10^8 power order and (**b**) in the range (10^6–10^7).

Examination of these power spectra at a lower intensity range of (10^6–10^7) Pa^2/Hz, as shown in Figure 16b, indicates that there are other frequencies with lower power that are associated with these three signals. These three spectra have a sharp peak of 10^7 Pa^2/Hz at a frequency of 150 Hz (St = 0.9). However, the spectral peak at 198 Hz (St = 1.188), which is seen in both the baseline signal as well as the controlled flow signal with the jet frequency of 250 Hz, is replaced by a peak at 199 Hz (St = 1.194) for the jet actuation frequency at 629 Hz. There are two other lower amplitude frequencies in the range of (10^6–10^7) Pa^2/Hz at 299 Hz (St = 1.794), and 327 Hz (St = 1.962) that are associated, respectively, with the baseline signal and the signal with jet actuated at 250 Hz do not appear in the spectra of the controlled flow pressure with jet actuation at 629 Hz. However, new lower amplitude peaks at frequencies of 638 Hz (St = 3.828) and 702 Hz (St = 4.212) with power in the range (10^6–10^7) Pa^2/Hz are seen in spectra when the jet is actuated at 629 Hz. Figure 16b also shows that the spectral peaks associated with the pressure signal for the jet actuation at 629 Hz are of lower strength than those with jet actuation at 250 Hz.

Careful examinations of the power spectra show that there are smaller peaks at 18 Hz (St = 0.108) and 127 Hz (St = 0.762) with power in the range (10^5–10^6) Pa^2/Hz in the baseline (uncontrolled) flow that are eliminated due to jet actuation at both frequencies with 250 Hz and 629 Hz. In addition, low power peaks in the range (10^4–10^5) Pa^2/Hz at 41 Hz (St = 0.246), 91 Hz (St = 0.546), and 121 Hz (St = 0.726) are generated due to the jet actuation at 629 Hz. These low energy peaks are not shown here for brevity.

The presented results show that jet actuation significantly affects the frequency contents of the baseline flow. The frequency content of the baseline shear layer(s) may be different from those of the controlled cases. The dominant flow frequencies for actuation at 250 Hz also may be different from those with the jet actuation at 629 Hz, as well as their strength is also different. Wu et al. [109] and Kotapati et al. [126] reported that the shear layer rolls up into discrete vortices, which then merges into larger ones. Thus, when the nature of the flow changes due to the synthetic jet actuation, the corresponding frequency content would be affected.

When the quasi-linear model of a nonlinear system for a range of operating points is available, the frequency response is obtained readily from its Fourier transform. However, due to the complexity of the airfoil controlled by *SJA* in this study, the simplified linearization is not feasible. Thus, the approximate frequency response is obtained using the describing function method by assuming a small perturbation around a constant jet frequency.

The describing function method is an approximate technique used in the analysis of certain nonlinear control problems. The method is based on quasi-linearization, which approximates a non-linear system by a linear time-invariant (LTI) transfer function that depends on the amplitude of the input signal. The dependence on amplitude generates a family of linear systems that are combined to capture the features of the non-linear system behavior (Slotine and Li [121]).

In this study, to compute the describing function for a *NARMAX* system, a method combining the low-pass filtering introduced by Slotine and Li [121] and the harmonic balance method developed by Glass and Franchek [127] was developed. Then, a MATLAB script was constructed and utilized to find the approximate frequency responses for different jet frequencies using a small perturbation approach.

The controller design is based on the resulting quantification of the output response. This approach linearizes plant dynamics about each input frequency. Figure 17 shows a set of frequency responses for the linearized plant at different input frequencies f_o while Figure 18 presents a set of frequency responses for the system open-loop transfer function Gp Gc, where Gp is the transfer function of the plant, and Gc is the transfer function of the controller (Appendix A).

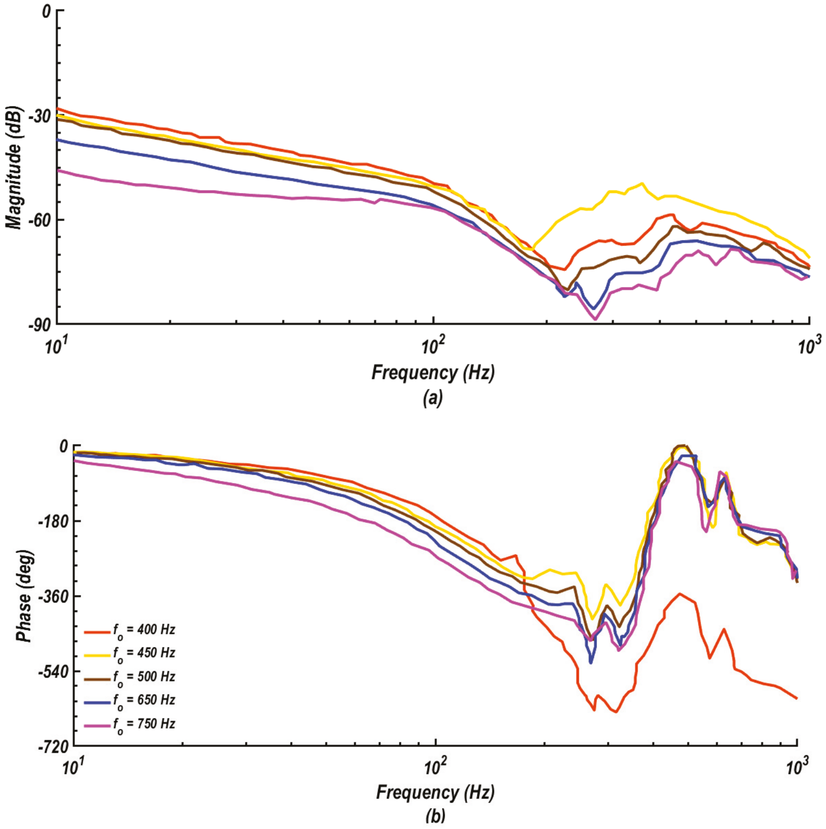

Figure 17. A set of frequency responses of the linearized plant. (**a**) Magnitude in decibel versus frequency in Hz. (**b**) Phase in deg versus frequency in Hz.

The frequency response of a system refers to the steady-state response of the system when subjected to a sinusoidal input signal. When a linear system reaches its steady-state, it differs from the input signal only in amplitude/gain (A) and phase/lag (φ). Moreover, the Bode diagram is used for plotting frequency response of Linear Time-Invariant (LTI) systems, which is used to study the stability of the control system. The Bode diagram maps the frequency response of the system through two graphs- the Bode magnitude plot (expressing the magnitude in decibels) and the Bode phase plot (expressing the phase shift in degrees).

To accurately construct Bode Graphs, it is required to collect gain and phase responses of the system for a large range of frequencies. Then the Gain Bode Plot (amplitude response vs. frequency) and Phase Bode Plot (phase response vs. frequency) are displayed on a single diagram (John [128]). Different criterion relevant to drawing Bode plots (and calculating control system stability) is described in the literature. Three measures found important for the stability analysis of control systems are system bandwidth, *BW*, gain margin, *GM*, and phase margin, *PM*.

"Bandwidth" is used to describe the "efficiency" of a control system. The stability of control systems is commonly described by using the "Gain Margin" and "Phase Margin." Gain margins and phase margins are measured using the open-loop frequency response of the system. Note that the gain and phase margins cannot be developed directly from a closed-loop frequency response (Shahzad [129]). Therefore, by definition, for a closed-loop system to be stable, the frequency response of its open-loop components must have a positive phase margin and the gain margin must be greater than 1 (0 dB). More detailed definitions for system bandwidth, *BW*, gain margin, *GM*, and phase margin, *PM*, are provided in Appendix A.

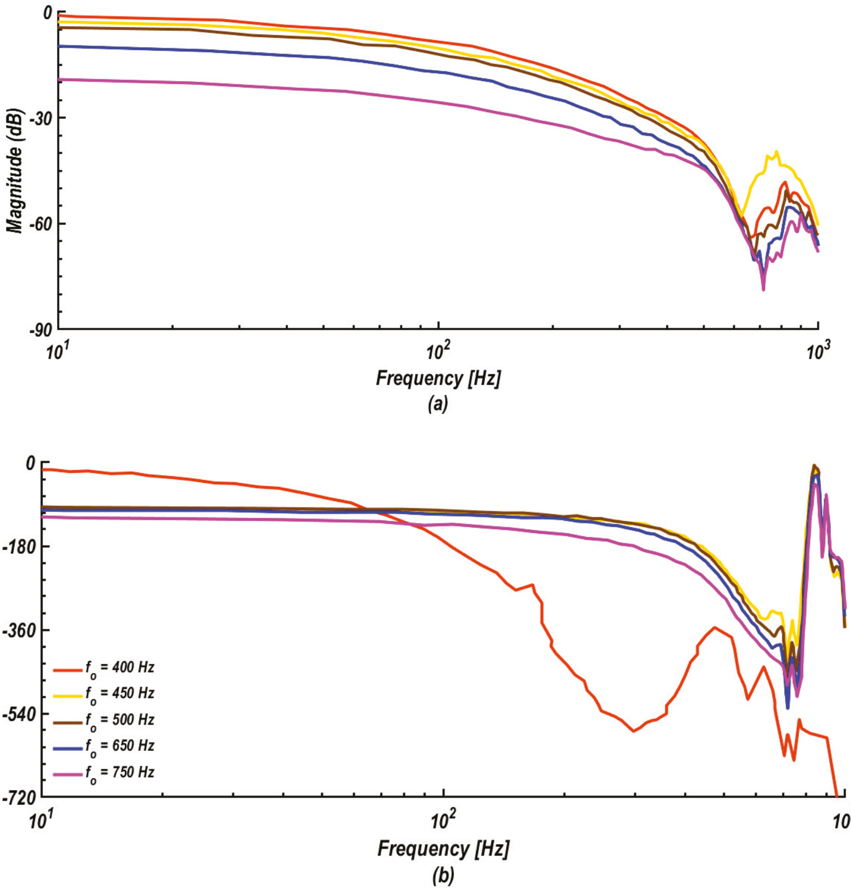

Figure 18. A set of frequency responses of the open-loop transfer function of the controller-plant system, *GpGc*. (**a**) Magnitude in decibel versus frequency in Hz. (**b**) Phase in deg versus frequency in Hz.

The designed controller is first tested for the influence of proportional gains only. Proportional gain (*KP*) up to *KP* = 21 is found inadequate for the control output *u* to overcome the lower bound of the jet frequency. As a result, the jet frequency was set continuously to the lower limit of the actuator frequency, but a significant steady-state error was reported. Meanwhile, at proportional gains *KP* > 21, the control output u, would be able to overcome the lower bound of the jet frequency but reaches the upper bound as well and oscillates between lower and upper bounds in a sense similar to a limit cycle oscillation caused by saturation (Patino et al. [130]). Therefore, a saturation of the jet frequency represents a crucial condition for the linear controller design as it limits the proportional gain and has a negative effect on the bandwidth of the controller.

The algorithm defining the proportional controller can be expressed as:

$$u(t) \;=\; KP * e(t) \tag{13}$$

where $u(t)$ is the controller output (control action), $e(t)$ is the control error signal, and *KP* is the proportional gain (factor of proportionality between output control signal and control error). The proportional gain determines how fast the system responds to the control signal (Kim [110]). The error signal $e(t)$ is defined as $e(t) = r(t) - y(t)$, here $r(t)$ is the reference signal (setpoint), and $y(t)$ is the current measured process value. Proportional control serves to eliminate the oscillation associated with on-off controllers. Let us express the transfer function of the process, and the controller by *P(s)* and *C(s)*, the Laplace form of the transfer function from reference to output is then given by:

$$G_{yr} = \frac{P(s)C(s)}{1 + P(s)C(s)} \tag{14}$$

The steady-state response of the proportional controller, which corresponds to the zero frequency gain is achieved when *C(s)* = *KP*. The transfer function in Equation (14) may then be expressed as $G_{yr}(0) = P(0)KP/1 + P(0)KP$ and the corresponding steady-state error for a unit step is given by $1 - G_{yr}(0) = 1/1 + P(0)KP$. This indicates that in the absence of a correction action, the output never reaches the reference, and hence the process would be left with a non-zero steady-state error.

Figure 19 exhibits responses of the output to a unit step in the command signal for the system with simple proportional control at different gain settings in Simulink. The steady-state errors associated with these responses for the set of proportional gains *KP* = 1.636, 2.455, 3.273, 4.427, 5.581, and 6.735 are found to be 37.93%, 28.94%, 23.40%, 18.43%, 15.18% and 12,93% respectively. It is noticed that the steady-state error decreases with increasing the gain, but the system also becomes oscillatory.

In order to avoid having a steady-state error from using the proportional gain control, a corrective action term is added to the design of the controller. The proportional control algorithm in Equation (13) then changes to

$$m(t) = KP * e(t) + M \tag{15}$$

where $m(t)$ is the magnitude of the correction signal, the constant M is known as the controller bias because it represents the magnitude of the correction signal when no correction is needed (i.e., *e(t)* = 0). The magnitude of the corrective action is reduced as the controlled variable approaches the reference value.

In proportional control systems, when the controlled variable becomes close to the reference value, the magnitude of the required corrective action becomes small. In some cases, the actuator operates in on-off mode, and the proportionality is reached by adjusting the ratio of on-time/off-time periods.

The ratio of on-time/off-time equals to 1 when the desired value is achieved. The proportional gain *KP* is usually a fixed property of the controller, but in some proportional controllers, *KP* is manually adjusted. If *KP* is increased, the sensitivity of the controller to error increases, but the stability is deteriorated. The system approaches the behavior of on-off controlled systems, and its response becomes oscillatory. Therefore, the bias M in Equation (15) should be adjusted to stabilize the system at a state slightly different from the reference value (Berk [131]). The offset is defined as the difference between the measured value y and the reference value r at a stable (steady) state. Reset is used by adjusting the bias to eliminate the offset. Reaching a zero offset under for a controller needs readjusting for every change in the process conditions.

The term that is adjusted to provide the desired steady-state value is known as a feed-forward term and shown by u_d. If the feed-forward term is selected as $u_d = r(t)/P(0) = k_r r(t)$, then the output exactly equals the reference value. However, this requires exact knowledge of the process dynamics, which is usually not available.

The *PI* controller design could be done starting from the mathematical formulation algorithm of *PI* control which is expressed as:

$$u(t) = KP * e(t) + \frac{KP}{T_i} \int_0^t e(\tau)d\tau = KP * e(t) + KI \int_0^t e(\tau)d\tau \tag{16}$$

where T_i is the integral time constant, and KI is the integral gain. The Laplace transform expresses the transfer function of the PI controller as:

$$C_{PI}(s) = \frac{u(s)}{e(s)} = KP + KP/(T_i s) = KP(T_i s + 1)/(T_i s) \tag{17}$$

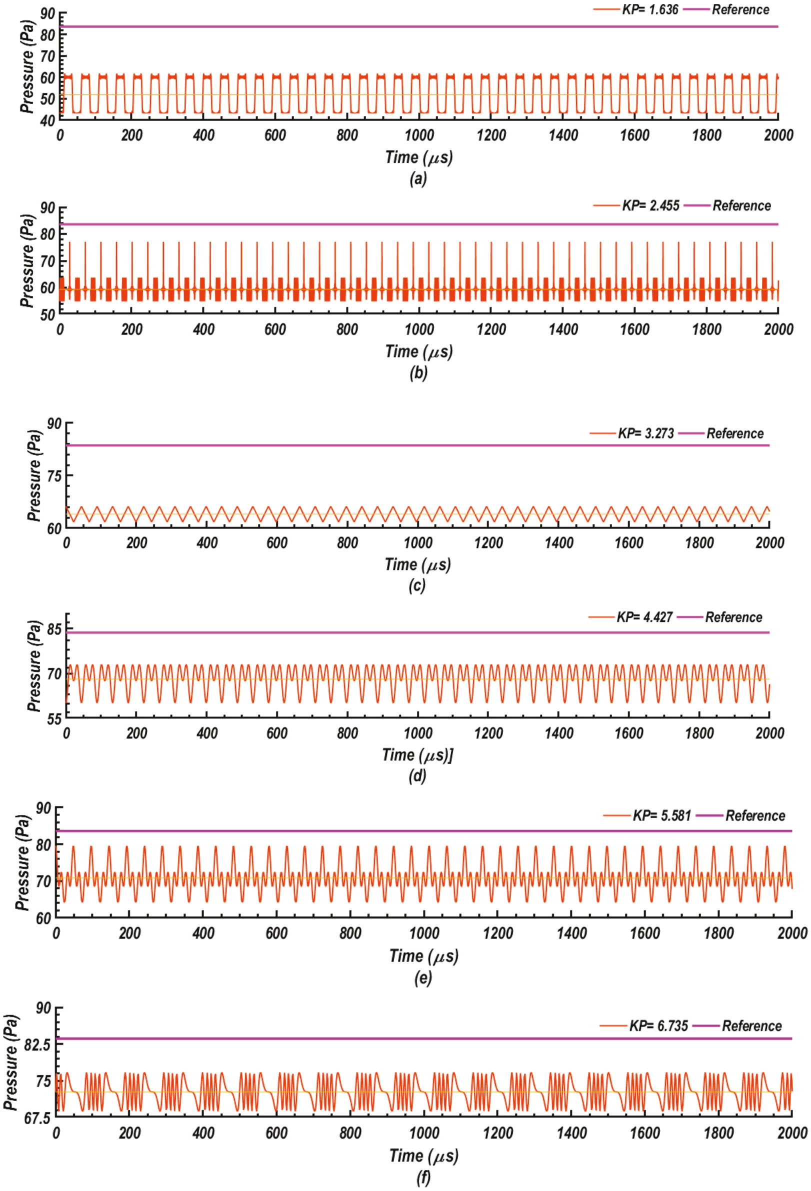

Figure 19. System responses to step changes in the command signal for a proportional controller at various gain settings. (**a**) KP =1.636, (**b**) KP = 2.455, (**c**) KP = 3.273, (**d**) KP = 4.427, (**e**) KP = 5.581, and (**f**) KP = 6.735.

This equation indicates that the *PI* controller has an infinite zero frequency gain ($C_{PI}(0) = \infty$) and it then follows from Equation (15) that $G_{yr}(0) = 1$, which implies that there is no steady-state error.

In the design of the controller, it is found that adding an integral element to the proportional gain leads to improved performance. Simulations are performed for a controller with a proportional gain of *KP* = 3.27 and different values of integral gain ranging from 0 to 0.330.

Figure 20 illustrates the closed-loop responses of the proposed *PI* controller subject to a step input. By definition, the step response of a system is the time evolution of the system output when it is subjected to a unit step input (Shahzad [129]). Figure 20a presents responses for cases with constant proportional gain *KP* = 3.27 and different values of integral gain (*KI)* ranging from *KI* = 0.0 to 0.0330. Figure 20b shows responses for cases with different values of proportional gain ranging from *KP* = 0.0 to 13.080 and constant integral gain *KI* = 0.083. This figure shows that the addition of the integral gain eliminates the steady-state error.

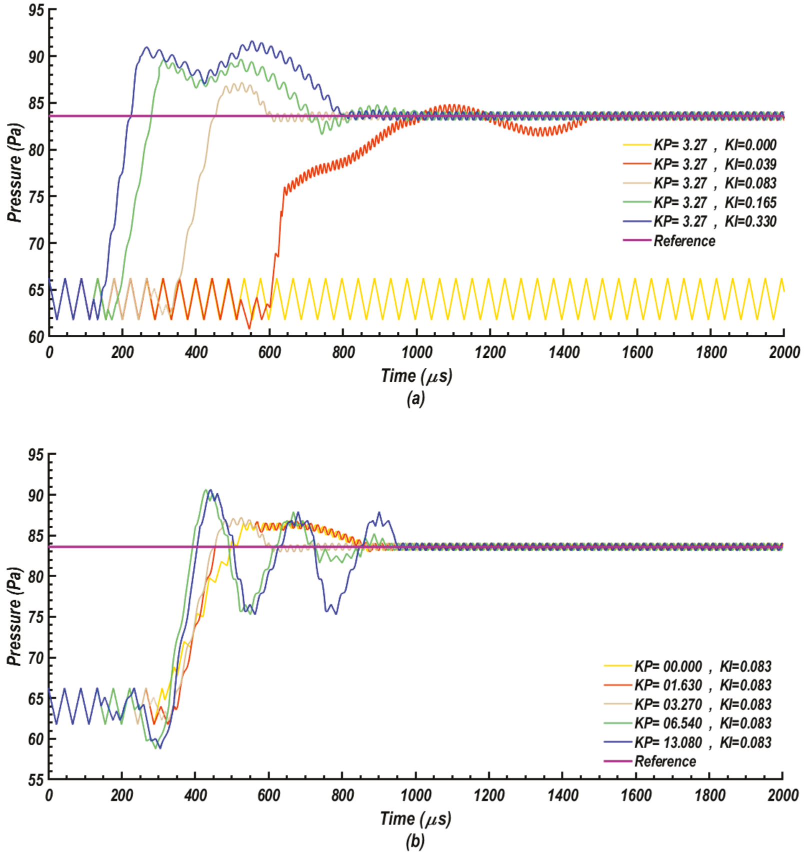

Figure 20. Closed-loop step responses for *PI* controller for cases with (**a**) *KP* = 3.27 & various values of *KI* [0–0.330], and (**b**) *KI* = 0.083 and various values of *KP* [0–13.080].

Furthermore, the transient response improves as the integral gain increases. However, beyond a certain value of the integral gain, there is a significant overshoot of the plant response. It is also observed that the combination of *KP* = 3.27 and *KI* = 0.083 produces the best performance.

When the controller is turned on at $t = 0$, the control results with *KP* = 3.27 and *KI* = 0.083 are presented in Figure 21. The response P_{LP} converges successfully to the reference pressure $P_{ref} = 83.54$, as shown in Figure 21. The time response of the saturated *SJA* frequency, f_{js}, to a step input is as shown in Figure 21a. Initially, the jet frequency is saturated at the lower bound, and it takes about 200 µs to compensate for the feedback errors. The saturated jet frequency will then increase with time to reach its peak value of 731 Hz within only 150 µs, making an overshoot of about 100 Hz in the response. Within another 150 µs, the jet saturated frequency reaches it's steady-state and takes the value of f_j = 629 Hz.

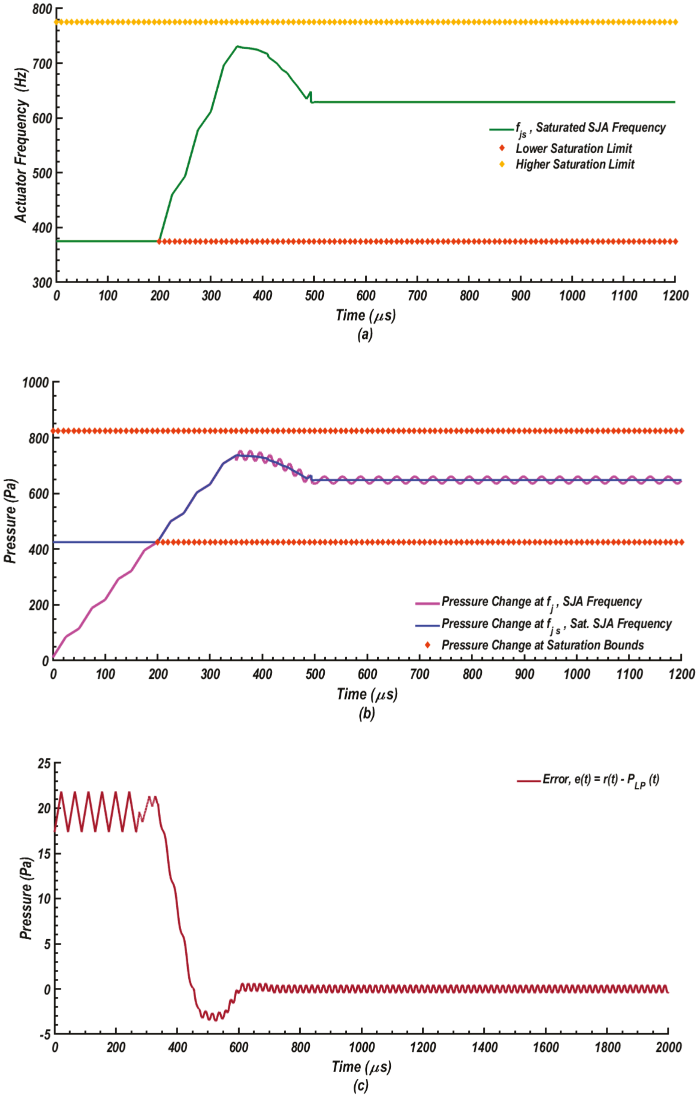

Figure 21. Closed-loop responses using a *PI* controller with *KP* = 3.27 and *KI* = 0.083. (**a**) Time response of saturated *SJA* frequency, f_{js}, to step input (200 µs required by integral efforts to compensate feedback errors.) (**b**) Time response of pressure signal at 30% chord location to step input of 20 Pa. (200 µs required by integral efforts to compensate feedback errors.) and (**c**) Time response of pressure error signal to step input of 20 Pa. (Error signal reduces rapidly).

Changes in the static pressure at the sensor location associated with the saturated jet frequency response are shown in Figure 21b. Other pressure changes, as shown in Figure 21b, illustrate the amount of pressure change at sensor location when the jet frequency is operating at lower bound, higher bound, and in the open-loop, respectively. Figure 21c presents the time response of the pressure error signal $[e(t) = r(t) - P_{LP}(t)]$ to step input of 20 Pa. It is observable that the error signal reduces rapidly.

The physical interpretation behind why the gains of KP = 3.27 and KI = 0.083 leads to the optimal choice for the proposed control system is described in this section. Initially, the jet frequency is set at its lower saturation bound (775 Hz), the proportional gain up to KP = 3.27 is found insufficient to have the control output to overcome the lower bound of the jet frequency. As a result, the jet frequency is continuously set at this lower limit. As mentioned previously, a proportional controller with proportional gain up to KP = 21 is found inadequate for the control output u, to overcome the lower bound of the jet frequency, and a significant steady-state error is reported. In proportional controller with $KP > 21$, the control output u would be able to overcome the lower bound of the jet frequency but reaches the upper bound as well and oscillates between lower and upper bounds in a sense similar to a limit cycle oscillation caused by saturation.

The addition of an integral element with integral gain KI = 0.083 to the proportional controller with a relatively small proportional gain KP = 3.27 improves the controller performance effectively and eliminates the steady-state bias errors. Only a fraction of the second is needed for the system to reach the steady-state condition.

The proposed control system was investigated for closed-loop stability, good disturbance rejection (without excessive control action), fast reference tracking (without excessive control action), low sensitivity to measurement noise, and a satisfactory degree of robustness to process variations and model uncertainty. The system closed-loop stability analysis in this study was done base on the Bode stability criterion, which provides a necessary and sufficient condition for closed-loop stability based on the properties of the open-loop transfer function (Horowitz [132]). Bode plots provide relative stability in terms of gain margin, *GM,* and phase margin, *PM*. For a closed-loop system to be stable, both margins should be positive or phase margin, *PM* should be greater than the gain margin, *GM.* If both the margins are zero or phase margin is equal to the gain margin, the closed-loop system is classified as a marginally stable. If any of the gain margin or phase margin is negative or phase margin is less than gain margin, then the closed-loop system is unstable.

The Bode diagram in Figure 22a provides the relationship between the magnitude (in dB) and phase shift versus frequency (in rad/s) for the transfer function of the *PI* controller, $Gc = C_{PI}(s)$. At low frequencies, magnitude equals 39 dB, the controller output is around ninety times greater than the input, and the phase between input-output is close to −90 degrees. The magnitude decreases linearly with an increase in frequency until it reaches a value in which the output is three times greater than the input at 9.5 dB. The phase between the input-output of the controller diminishes with the increase of frequency as well until they become in-phase. This figure also shows that the magnitude of the frequency response never reaches a value of I dB, which means the system output never becomes equal to the system input. Moreover, both the Bode plots shown in Figure 22a indicate that the proposed controller as a standalone unit has an infinite gain margin as well as an infinite phase margin, which means that the controller will never become unstable.

The Bode diagram in Figure 22b,c depict, respectively, the magnitude plot and the phase plots of the open-loop transfer function $G_P(s)G_C(s)$. It can be seen that the gain margin provided by the Bode stability criterion is GM = 22 dB, while the phase margin PM = 68°. Based upon this stability analysis and taking into consideration the error of the *NARMAX* model (compared to URANS results), the gain margin, *GM*, should be greater than 22 dB, and the phase margin, *PM*, should be greater than 68 degrees in order to get a stable feedback loop.

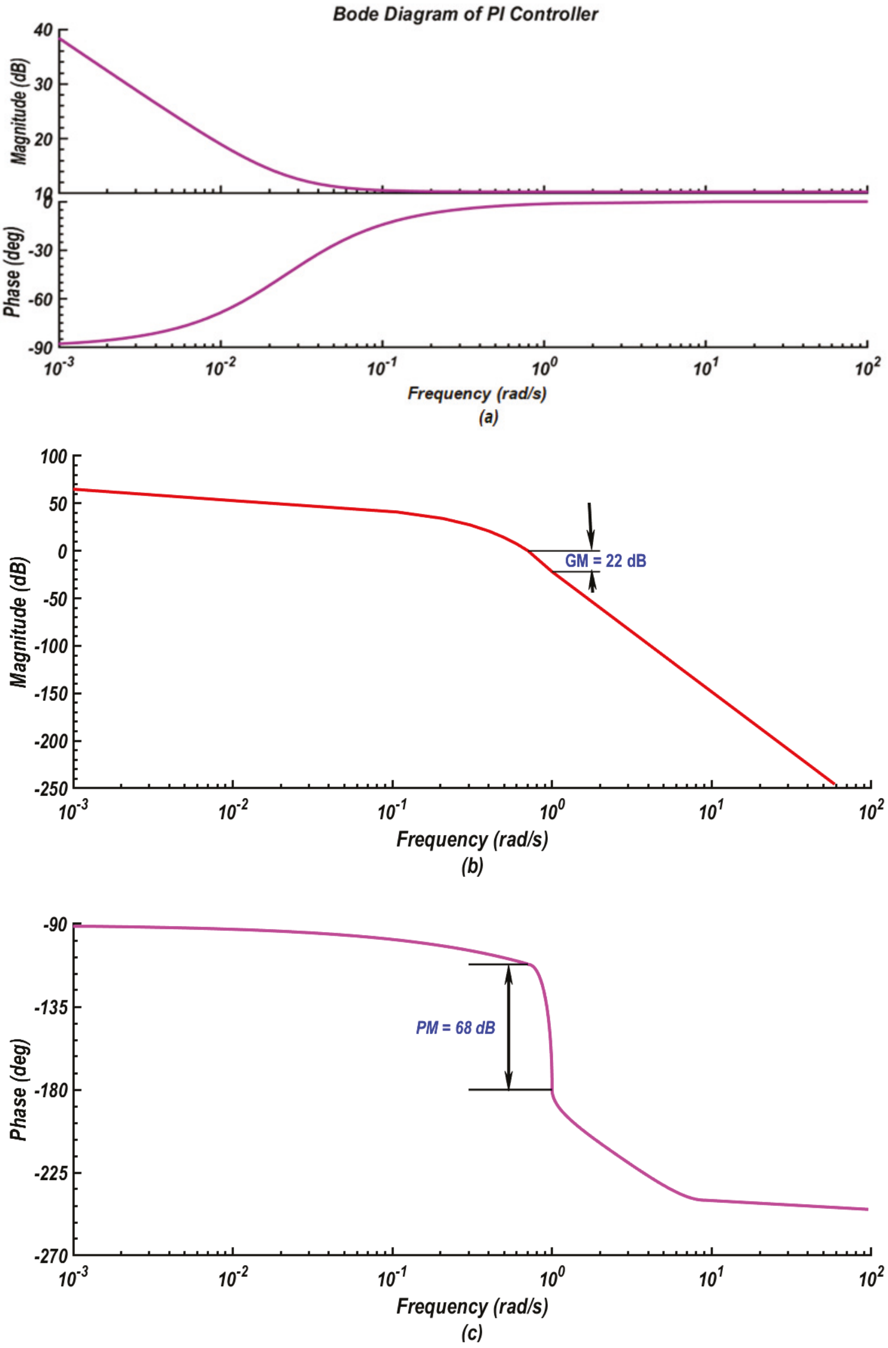

Figure 22. Bode diagrams of the system. (**a**) Magnitude and phase plots of the *PI* Controller with *KP* = 3.27 and *KI* = 0.083. (**b**) Magnitude plot of the open-loop transfer function of the controller-plant system, *GpGc*, and (**c**) Phase plot of the open-loop transfer function of the controller-plant system, *GpGc*.

At this point, the *PI* controller is examined either as a standalone unit or integrated with the fluidic system (Airfoil + *SJA* plant) for reference tracking and disturbance rejection. A feedback controller is mainly designed either to reject disturbances that take place in the process and/or to track a reference value (set-point) in the process (Vandoren [133]). The controller needs to take action to force the process variable back toward the desired reference whenever a disturbance or variation on the process causes a deviation. The reference tracking ability is needed and appropriate when the reference is expected to change frequently, and the controller is required to raise or lower the process variable accordingly. In this study, the Control System Toolbox of Matlab R2019b is used for the design of the *PI* controller, step input signals were used as the prototype for load disturbances, and the results are discussed in this section.

The *PI* feedback controller described in Figure 15 could now be simplified for a case of a single degree of freedom controller (1-DOF PI) by the block diagram A1 shown in Appendix A. Furthermore, the control system feedback is assumed for simplicity to be restricted to operate on the error signal only. This includes the ability to follow reference signals, effects of load disturbances, and the effects of measurement noise (Åström [134]). Investigation of the effects of process variations is left for future studies. It turns out that the properties to be studied can be captured by a set of four transfer functions in addition to the system open-loop transfer function, which is needed in control system analysis. The set of transfer functions used in this analysis is as described in Appendix A.

Plots in Figure 23 show the step response of the proposed controller-plant system subject to unit step inputs. The abscissa in plots stands for the time while the ordinate shows the amplitude of oscillation about a final value of steady-state. Figure 23a,b present step responses of the controller-plant system for reference tracking (to reduce overshoot) and input disturbance rejection (to improve rejection of a disturbance at the plant input) when the controller works, respectively, in open-loop mode and closed-loop mode. The physical interpretation of reference tracking is that the controlled output should track the reference input, and this is ideally achieved when $y(t) = r(t)$. The disturbance rejection occurs when the controller keeps the controlled output at its desired value in the presence of a disturbance $d(t) \neq 0$. This means the transfer function ideally from d to y would be zero.

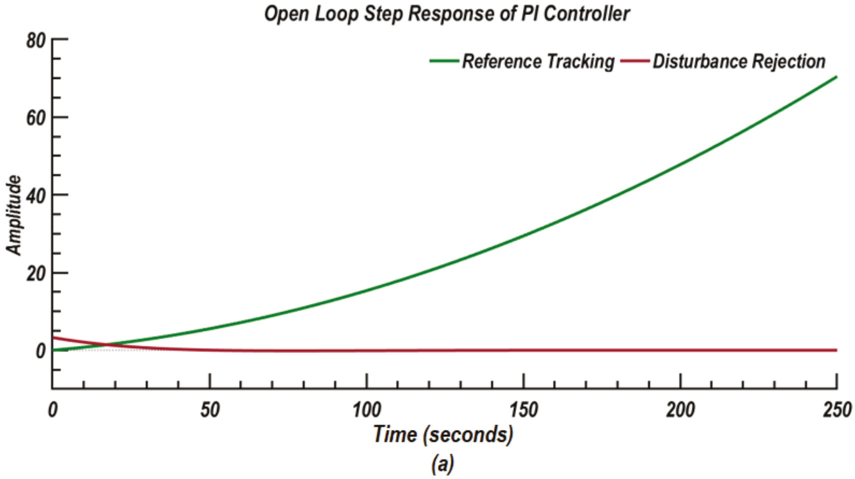

Figure 23. *Cont.*

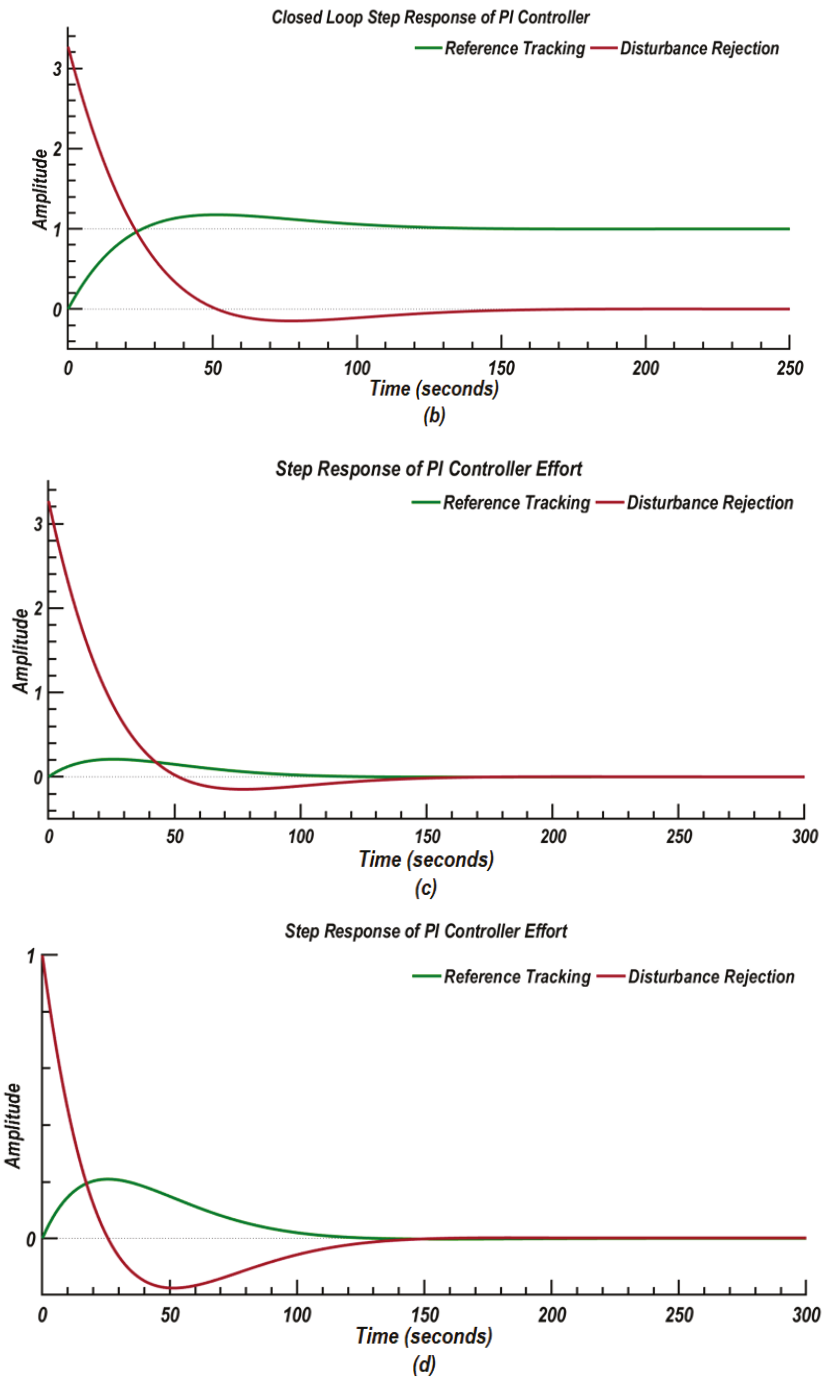

Figure 23. Step responses of the *PI* controller with *KP* = 3.27 and *KI* = 0.083 for reference tracking and disturbance rejection. (**a**) Open-loop step response of *PI* controller. (**b**) Closed-loop step response of *PI* controller. (**c**) Closed-loop step response in case of input disturbance (d_1). (**d**) Closed-loop step response in case of output disturbance (d_2).

In Figure 23, the ordinate amplitude stands for the ratio of the response to the steady-state response. Figure 23a shows that when a change in the reference occurs, the open-loop *PI* controller cannot track reference changes, and the error between the new reference signal and the controller output diverges with time (increased overshoots in reference tracking). Figure 23b shows that the closed-loop control, however, provides a significant improvement in the *PI* performance, and the controller is capable of tracking the reference. The transfer function inspected in Figure 23b is called the complementary sensitivity function of the system. It is the closed-loop transfer function from r to y, and it is also the transfer function from measurement noise to controlled output (Åström [134]). Moreover, Figure 23a,b show that the controllers reject input disturbances (d_1) in both open-loop and closed-loop modes, but in the closed-loop configuration, the disturbances rejection action is quicker.

It is important to examine the proposed controller design against limitations in the control effort (due to practical constraints from controller saturation). Saturation effects occur when any part of the feedback control system reaches its physical limit. The phenomenon of saturation in the *PI* controller is called reset windup (integral upwind). The definition of the term integral upwind is provided in Appendix A. Saturation is a physical limitation of the system, which is actually the point where the system reaches safe limits of operation. The specific problem is the excess overshooting (Åström [134]). On the other side, noise sensitivity is an important subject for most control systems. Noise from sensors and other sources can distort the control system output, introducing unwanted perturbations on the control variable, and generating unacceptable levels of acoustic noise. Knowledge of noise is essential in the design of observer-based control systems.

Observer-based control is often more sensitive to sensor noise than are traditional control systems. The system noise sensitivity function expressed in Equation (A3), which is sometimes called the output sensitivity function (Horowitz [132]), was used to inspect the step response for the controller action to track reference changes. This equation also represents the model between the control output, $U(S)$ and the reference $R(S)$, where $U(S)$ and $R(S)$ are the Laplace transform of the control output *u*(*t*) and reference signal *r(t)* respectively. Figure 23c shows the closed-loop response of controller output $u(t)$ to a step-change in the reference signal $r(t)$ (controller effort for reference tracking) as well as the closed-loop system response to a load disturbance (controller effort against disturbance rejection for step disturbance at the plant input, d_1).

The controller effort measures how much effort (power) is needed by the controller to respond to a step-change in the reference point (Vandoren [133], Matlab R2019b Manual [135]). Again, the abscissa in Figure 23c stands for the time while the ordinate is the amplitude variation of the controller output *u(t)* from its final value of steady-state as a result of a step-change in the reference signal. When step-changes in the reference point occur, Figure 23c shows a good closed-loop output response with reduced overshoot characteristics in the reference tracking. It can also be seen that the controller exhibit an acceptable response against a step disturbances at the plant input d_1. The system capability for reference tracking to a change in the desired value is faster than the system ability to reject step disturbance at the plant input, d_1.

The output noise sensitivity is another property of interest in this study. Output noise sensitivity measures reference tracking with taking into consideration disturbances at the plant input, d_1 The transfer function which governs this case is as expressed in the appendix by Equation (A2) but proceeded by a negative sign. This equation also represents the model between the control output, $Y(S)$ and the reference $R(S)$ with a negative sign, where $Y(S)$ and $R(S)$ are the Laplace transform of the control output *y(t)* and reference signal *r(t)* respectively (Horowitz [132]). This is equivalent to the control effort paid in reference tracking in the presence of disturbances at the plant input, d_1.

Figure 23d illustrates the closed-loop control system output response to a step-change in the reference value in the presence of disturbances at the plant input, d_1, which is equivalent to the controller effort to track the reference change. Figure 23d also shows the closed-loop system response to a load disturbance (step disturbance at the plant output d_2). The abscissa in Figure 23d represents the time while the ordinate is the amplitude variation of the control output $y(t)$ from its final value of steady-state as a result of a step-change in the reference signal. When compared with the case with a step disturbance at the input. d_1 presented in Figure 23c, the case with step disturbance at the output, d_2 in Figure 23d shows lower overshoot behavior in tracking new references and approximately the same ability to reject disturbances.

The set of plots in Figure 23 indicates that the closed-loop performance of the proposed control system is more powerful from the point of reference tracking than its open-loop performance. The designed closed-loop control system has the ability to fulfill the basic requirements of the design. The controlled output can track the reference input easily, and only short time periods needed for the controlled output, $y(t)$ to equate the reference signal $r(t)$. This is in addition to the controller has the ability to keep the controlled output at its desired value in the presence of a disturbance, $d_1(t) \neq 0$. Ideally the transfer function from d_1 to y would tend quickly to zero. Moreover, reasonable control effort is required, as shown in the analysis, to track changes in the reference signal and reject disturbances. Finally, the controller showed an acceptable response to suppress effects of measurement noise that takes place in plant output, d_2, on the control input.

6.3. Closed-Loop Control Results

The application of the designed control algorithm yields significant improvements in terms of lift enhancement and drag reduction. As the proposed control law is based on information taken from the airfoil performance at the incidence angle of 16° The discussion below focuses on comparing the flow features around the airfoil with control-off and control-on cases for the same incidence angle.

Figure 24 shows the chord-wise distributions of the pressure coefficient (C_p) profile along the airfoil upper and lower surfaces for two different cases, the base-line case (control-off) and the case with the synthetic jet control-on. This figure shows significant changes in the distributions of the pressure coefficient along the top and bottom surfaces of the airfoil due to synthetic jet excitation. The baseline case is characterized by a negative pressure peak of approximately −2 situated at 0.03 c from the leading edge on the suction side followed by another negative pressure peak of −1.4 at nearly 0.22 c from the leading edge on the suction side. The C_p distribution for the case with SJA control-on is characterized by a negative pressure peak of −6.4 near the leading edge (at 0.001 c from leading edge) on the suction side followed by another negative pressure peak of −1.5 at 0.68 c. Beyond this point, the C_p value gradually increases along the chord of the airfoil. On the pressure side of the airfoil, the C_p value reaches a maximum of $C_p = 1$ at the stagnation point. This stagnation point is shifted toward the leading edge due to the application of synthetic jets. Further down the chord length of the airfoil, the pressure side C_p value increases gradually until it equals the suction side value at the trailing edge. The delay of flow separation due to the application of synthetic jet leads to an increase in the velocity and a decrease in pressure on the suction side. The result is the suppression of large pressure fluctuations and the introduction of more organized flow patterns. Alternations in the pressure coefficient distributions that can be seen from pressure peak values and their locations on pressure and suction sides due to control application influence the lift and drag forces that are acting on the airfoil.

Contours of the x-velocity component of the airflow around the airfoil for both control-off and control-on cases are shown in Figure 25. The velocity contours for the control-off case are shown on the left-hand side, while contours for the control-on case are shown on the right-hand side of the figure. Regions of re-circulating flow are observed over the upper surface of the airfoil for the control-off case. That is, the airfoil at the angle of attack of 16° experiences a large adverse pressure gradient that results in flow separation on the upper surface of the airfoil. As a result, a low-pressure area immediately downstream is created, which sucks fluid into this region from the main flow, creating vortices that are shed from the airfoil.

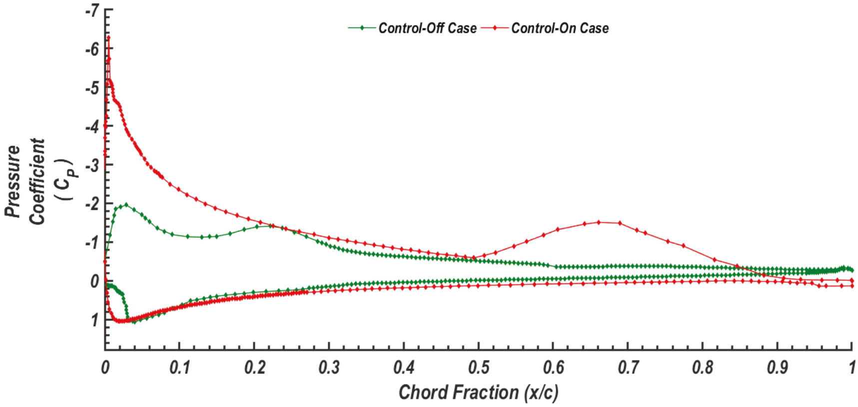

Figure 24. Comparison of chord-wise average pressure coefficient curves along the sides of the airfoil at AoA = 16° for the control-off case and control-on cases.

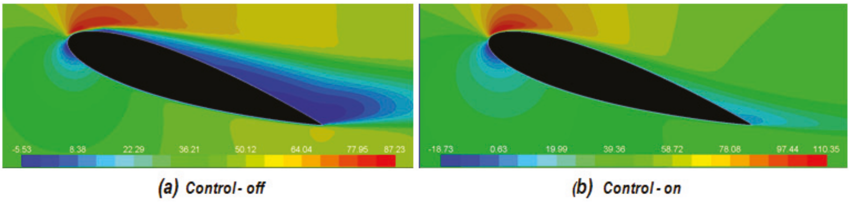

(**a**) Control- off (**b**) Control - on

Figure 25. Contours of the x-velocity component around the NACA 0015 airfoil at AoA = 16° for (**a**) control-off and (**b**) control-on case.

Flow separation creates a marked increase in drag and a considerable decrease in lift compared to situations where the flow remains attached to the surface. Increased separation is a condition in which the airfoil is stalled.

Figure 25 presents a typical example of how unsteady forcing (excitation) of synthetic jets affects the flow around the airfoil surface. The application of the *SJA* controller leads to the elimination of the re-circulation flow regions on the airfoil upper surface. With control-on, the separation region vanishes or becomes quite small, and it is shifted towards the trailing edge of the airfoil as the flow is forced to reattach.

For providing information on the level of velocity fluctuation in the fluid flow around airfoils, the level of the flow turbulence for control-off and control-on cases is examined. The main objective here is to study the variation of turbulence kinetic energy (TKE) and the associated turbulence intensity in the flow. The unit for the turbulence kinetic energy k, is the kinetic energy per unit mass [J/Kg], which is equal to [m^2/s^2].

Figure 26 shows the contours of turbulence kinetic energy around the NACA 0015 airfoil at an angle of attack of 16° in the range of $k \leq 150\ m^2/s^2$ for the control-off and control-on cases. For the control-off case, it is seen that the flow is fully separated from the top surface of the airfoil and is in the turbulent regime. The large region with high turbulence kinetic energy (TKE) is seen from this figure. Region of high turbulence intensity enhances turbulence diffusivity and increase mass and momentum transport.

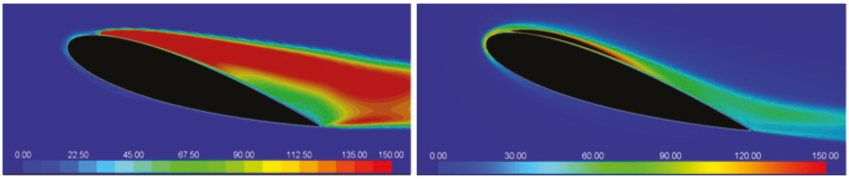

(a) Control- off

(b) Control- on

Figure 26. Contours of turbulence kinetic energy around the NACA 0015 airfoil at AoA = 16° for (**a**) control-off and (**b**) control-on case.

Figure 26 shows that by activating the synthetic jets, the turbulence kinetic energy around the airfoil is reduced significantly. That is, the application of closed-loop control markedly reduces the separation region and substantially lowers the turbulence kinetic energy compared to the uncontrolled flow. The corresponding effects on the lift and drag acting on the airfoil are described in the subsequent sections.

Contours used in flow analysis for the state control-on above are all taken from open-loop simulations. The proposed *NARMAX* based controller is designed to arrive at these flow patterns in closed-loop control configuration.

Another important result of the present study is the variation in the lift and drag coefficients due to the application of the closed-loop control. Figure 27 shows the variation of the lift coefficient as a function of the angle of the attack (as obtained from the URANS-realizable k-ε) for control-off and control-on cases. For the control–on case of the study, the synthetic jet actuator oscillates at a constant frequency of 629 Hz while the airfoil angle of attack is varied. The LES simulation results of Duvigneau and Visonneau [88] for the NACA 0015 at $Re = 10^6$ with *SJA* oscillating at relatively high frequency are shown in this figure for comparison. In addition, the experimental data of Rediniotis [98] for the NACA 0015 at $Re = 0.895 \times 10^6$ with *SJA* oscillating at three different low frequencies are also reproduced in Figure 27. It is seen that in the absence of control, the lift coefficient increases linearly with the angle of attack for small values of α. The lift coefficient levels off at angles of attack of about 11° to 13°, and then drops rapidly after the stall angle of about 13°.

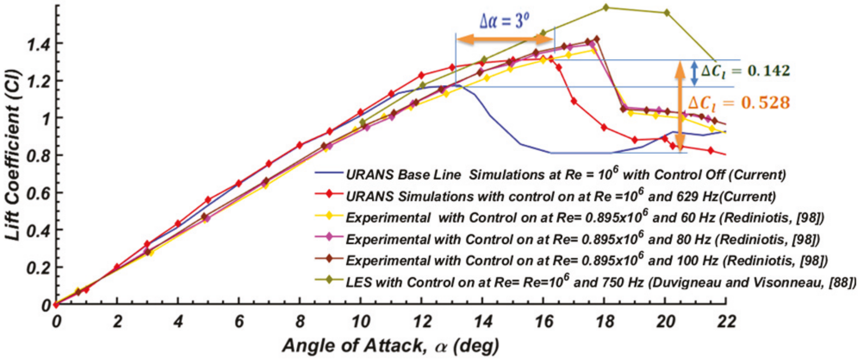

Figure 27. Airfoil lift coefficient as a function of angle of attack at chord $Re = 10^6$ for control-off and control-on cases. Comparison with the earlier numerical results and experimental data.

It is observed that, with the application of closed-loop control, no changes in the lift coefficient are seen for a low angle of attack up to 12°. At incidence angles greater than AoA = 13° and up to about AoA = 16.25°, the airfoil aerodynamic performance improves significantly, and considerable enhancement in the lift coefficient is achieved. Lift coefficient decreases for the attack angle beyond AoA = 16.25°. It is interesting to note that at AoA = 16° with the control on, the airfoil provides a lift coefficient of $C_l = 1.315$ compared to $C_l = 0.78678$ for the uncontrolled case (with lift increment reaching 67.1%). In addition, the application of control has a significant influence on the shape of the lift curve at high angles of attack. The controller enhances the maximum lift coefficient $C_{l,\ max}$ of the NACA 0015 from $C_l = 1.173$ at AoA = 13.25° to 1.315 at AoA = 16.25° resulting in $\Delta C_{l,\ max} = 0.142$ and the increase of stall angle of attack from 13.25° to 16.25°.

Figure 27 also shows that the present URANS simulation results for the control-on case are in agreement with both the LES results of Duvigneau and Visonneau [88] and the experimental data of Rediniotis [98] up to AoA = 16°. At angles higher than AoA = 16°, the URANS simulations predict lower lift coefficients than those of LES results and experimental data. The discrepancies are perhaps in part due to the differences in actuation frequency and Reynolds number.

Figure 28 shows the predicted variation of drag coefficients for both control-on and control-off cases at $Re = 10^6$. As expected, the drag coefficient increases with the increase of angle of attack. The LES simulation results of Duvigneau and Visonneau [88] for the NACA 0015 at $Re = 10^6$ with *SJA* oscillating at relatively high frequency are shown in this figure for comparison. In addition, the experimental data of Rediniotis [98] for the NACA 0015 at $Re = 0.895 \times 10^6$ with *SJA* oscillating at three different low frequencies are also reproduced in Figure 28. It is noticed that the application of the controller does not affect the values of the drag coefficient up to AoA = 14°. Beyond the angle of attack of 14°, the controller mildly decreases the drag coefficient compared to the control-off case.

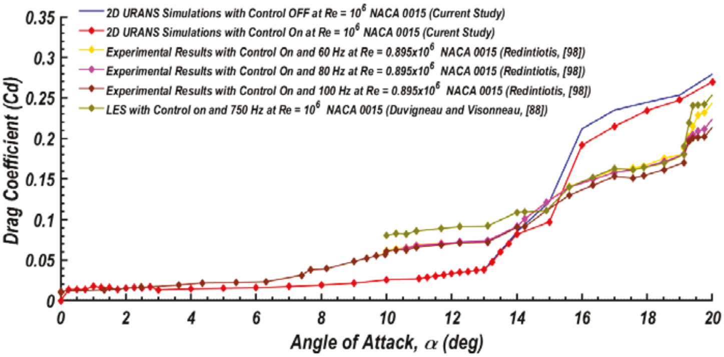

Figure 28. Airfoil drag coefficient as a function of angle of attack at chord *Re* = 1 Million for control-off and control-on cases. Published numerical results and experimental data are also shown for comparison.

The present URANS simulations for the control-on case is found to be in general agreement with both the LES simulation results of Duvigneau and Visonneau [88] and the experimental data of Rediniotis [98] up to AoA = 15°. The current URANS simulations for the control-on case deviate from the earlier simulation results as well as the experimental data at higher angles of attack for $15° \leq \alpha \leq 19°$. That is, the present realizable k-ε turbulence model over-predicts the LES and experimental data for the drag coefficient. At this point, the discrepancy in drag coefficient results may also be attributed to the differences in the actuation frequencies and the Reynolds number, as well as the limitation of the RANS turbulence model. Further investigation of the factors affecting this discrepancy is left for a future study.

Figure 29 shows the predicted drag polar for both control-on and control-off cases at $Re = 10^6$. Here the drag coefficient $\mathrm{C_d}$ is plotted versus lift coefficient $\mathrm{C_l}$ and for a range of angles of attack, α. It should be emphasized that the lift coefficient is not an independent variable, but both lift and drag coefficients are functions of the angle of attack, α, Reynolds number, and Mach number. For low drag coefficient values up to $\mathrm{C_d} = 0.033$, (angle of attack up to 12°), it is seen that the drag polar curve for the control-on case matches well with that of the control-off case. For drag coefficient values in the range $0.033 < \mathrm{C_d} < 0.275$, $(12° < \alpha < 20°)$, the drag polar curve for the control-on case shows considerable differences with the polar curve for the control-off case. In this range, the synthetic jet actuation results in a significant increase in the values of the lift coefficient for roughly the same drag coefficients. The largest difference is seen at for $C_d = 0.211$, which corresponds to a lift coefficient $Cl = 0.78678$ for the uncontrolled case and $Cl = 1.315$ for the controlled case. This indicates that the application of synthetic jets at AoA = 16° increases the lift-to-drag ratio from 3.71 for the uncontrolled case to 6.85 for the controlled case.

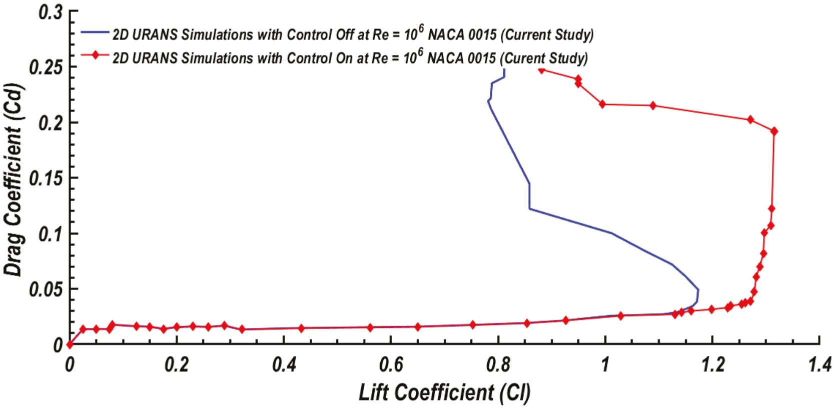

Figure 29. Airfoil drag coefficient as a function of angle of attack at chord *Re* = 1 Million for control-off and control-on cases. Published numerical results and experimental data are also shown for comparison.

7. Conclusions

Extensive simulations using the URANS in conjunction with the realizable *k*-ε turbulence model were performed, and the flow characteristics over the NACA 0015 airfoil at different angles of attack were evaluated. A semi-elliptical computational domain with 107,000 structured cells along with 10% turbulence intensity at the far-pressure field at its boundaries was used in these analyses. The dimensions of the computational domain were tested, and the grid sensitivity was performed to satisfy the mesh independence condition. The selected time step was also tested to confirm the proper simulation of the transient flow conditions. For different configurations, flows over the airfoil were simulated and predicted lift and drag coefficients were validated by comparison with earlier experimental data and numerical simulation results. The generated data sets were used to model the nonlinear flow behaviors over the airfoil using the *NARMAX* identification methodology. At an angle of attack of 16° and Reynold's number of 10^6, where the flow is separated, a closed-loop controller was designed based on the open-loop control results and the *NARMAX* identification procedure. Based on the presented results, the following conclusions are drawn:

- The *k*-ε model was found to be an acceptable turbulence model for predicting the airflow around an airfoil at different angles of attack.
- An increase in the angle of attack led to the increase of the lift coefficient until the maximum of 1.15 at $\alpha = 13°$ is reached. The lift coefficient then sharply dropped for further increase in the angle of attack. Before stall, The slope of the lift versus incidence angle, $\frac{\partial C_l}{\partial \alpha}$, was approximately a constant at about 0.101 before the stall. After the stall incident angle, C_l decreased significantly, leading to a lift coefficient of 0.79 at $\alpha = 17°$.
- At zero angles of attack, the drag coefficient was small but increased gradually with α to 0.038 at the stall condition. The slope of the drag variation with the angle of attack, $\frac{\partial C_d}{\partial \alpha}$, was approximately constant at about 0.003. After the stall condition, the drag increased sharply with the increase

of the incident angle of attack to attain a value of 0.28 at $\alpha = 20°$. The slope of the drag against the angle of attack, $\frac{\partial C_d}{\partial \alpha}$, increases to 0.04 after the stall condition.

- The simulation results showed that synthetic jets are a suitable means to suppress flow separation.
- At an attack angle of 16° and the flow Reynolds number of 10^6, the *NARMAX* identification found as a powerful tool for modeling the mean static pressure signal. Identified static pressure matches well with the URANS simulation results. The associated differences were found to be within 9%.
- The Low-pass filtering approach utilized in the controller design facilitated treat the system as a quasi-linear in the frequency domain. The sinusoidal input describing function applied in the frequency domain analysis assisted in applying the linear control theories.
- A standard proportional-integral (PI) algorithm for the single-input single-output system was designed based on a reference signal that was determined during the open-loop performance of the plant at the conditions corresponding to a fully re-attached flow.
- When inspected for different values of proportional gain (*KP*) and integral gain (*KI*), the proposed closed-loop controller with $KP = 3.27$ and $KI = 0.083$ is found to be efficient for both reference tracking and disturbance rejection for open-loop and closed-loop modes.
- Flow features around the NACA 0015 airfoil were significantly improved for the control-on state. This is clearly seen by comparing contours of static pressure, x-velocity, and turbulence kinetic energy around the airfoil at AoA = 16° for the control-off state with those of control-on state. For the control-on case, the flow separation regions over the airfoil upper surface were found to reduce significantly. The turbulence kinetic energy was also much reduced by the activation of the synthetic jet actuators. At AoA = 16°, the lift coefficient increased by about 67% and the stall angle of attack increase by 3°.

The designed controller was for an angle of attack of 16° and at a constant free stream velocity of $U_\infty = 50$ m/s. For the design of the controller for other airfoil incident angles and free stream velocities, the same procedure could be used. Further investigation in this regard was left for a future effort.

Author Contributions: This study was a part of the Ph.D. research work of S.O., who was responsible for developing the computational model and for performing the simulations and data analysis. G.A. and R.J. contributed to the interpretation of the results and to the critical revision of the article. All authors have read and agreed to the published version of the manuscript.

Funding: This research was funded by the U.S. Air Force Office of Scientific Research grant No. FA9550-09-1-005.

Acknowledgments: The authors gratefully acknowledge the financial support of the U.S. Air Force Office of Scientific Research through Grant No. FA9550-09-1-0051. The authors would like to thank Robert Schilling Department of Electrical and Computer Engineering at Clarkson University for his valuable suggestions on different approaches to control design.

Conflicts of Interest: The authors declare no conflict of interest.

Appendix A

In this Appendix, the terminology used in the control applications are summarized, and the single degree of freedom *PI* controller is described.

Appendix A.1 Control Terminology

While there are different definitions reported in the literature, here, the most commonly used terminologies are listed (Horowitz [132], Åström [134], and Seborg et al. [136]).

Time-domain characteristic is the time trace of control system response due to testing in the signal, such as using step input, impulse input, and ramp input, to name a few.

Frequency Response is the measure of magnitude and phase of the control system output as a function of frequency in response to a sinusoidal input.

Transient characteristics are the time response of the control system due to a change from equilibrium or a steady-state that will decay with time.

Transient response parameters are parameters such as peak time, settling time, rise time, maximum overshoot, which are determined by evaluating the step response of the system.

Peak time is the time at which the peak value of amplitude occurs in step response of the system.

Settling time is the time it takes for the error $\left|y(t) - y_{\text{final}}\right|$ between the response $y(t)$ and the steady-state y_{final} response to fall to within 2% of y_{final} in the step response of the system.

Rise time refers to the time it takes for the response to rise from 10% to 90% of the steady-state response in step response of the system.

Settling$_{\mathbf{Min}}$ is the minimum value of response *y(t)* in the step response of the system.

Settling$_{\mathbf{Max}}$ refers to the maximum value of response *y(t)* in the step response of the system.

Degree of freedom of a control system, DOF is defined as the number of closed-loop transfer functions that can be adjusted independently. In the 1 DOF system, there is only one closed-loop transfer function, which can be adjusted independently (Horowitz [132]).

Bandwidth, *BW* of a control loop is defined as the frequency at which the open-loop amplitude response reaches −3 dB. At this point, the output gain (ratio of output to input) equals approximately 70.7% of its maximum, and the output power (power delivered to the load) equals 50% of the input power (Seborg et al. [136]).

Gain Margin, *GM* is the amount of gain in open-loop, which can be increased or decreased without making the system unstable. The gain margin is usually expressed in dB. Larger gain margin implies greater stability of the system. In other words, gain margin is the difference (in dB) between unity (0 dB) and the actual system open-loop gain at the point where a 180° phase shift occurs.

Phase margin, *PM* is the phase in open-loop, which can be increased or decreased without making the system unstable. The phase margin is the difference (in°) between the system phase at 180° and the actual system open-loop phase at the point where the open-loop gain of unity (i.e., 0 dB) occurs.

Integral windup is the state of a feedback *PI* controller at which a large change in reference value occurs (say a positive change), and the integral terms accumulate a significant error during the rise (windup), thus overshooting and continuing to increase as this accumulated error is unwound (offset by errors in the other direction). Integral windup is also known as integrator windup or reset windup.

Appendix A.2 Single Degree of Freedom PI *Controller (1-DOF PI) Analysis*

The block diagram of a simplified single degree of freedom *PI* controller (1-DOF PI) is shown in Figure A1. The system loop shown in this figure is composed of two components, the controller G_C and the plant G_P. The controller has two inputs blocks, the feedback block *C*, and the feed-forward summing point. There are two disturbances acting on the plant, the load disturbance d_1 and the measurement noise d_2. The load disturbance represents disturbances that drive the process away from its desired behavior. The plant variable x is the real physical variable that needed to be controlled. Control is based on the measured signal y, where the measurements are corrupted by measurement noise d_2. Information about the plant variable x is thus distorted by the measurement noise. The plant is influenced by the controller via the control variable u.

The plant is thus a system with three inputs and one output. The inputs are: the control variable u, the load disturbance d_1 and the measurement noise d_2. The output is the measured signal y. The controller is a system with two inputs and one output. The inputs are the measured signal y and the reference signal r and the output is the control signal u. Note that the control signal u is an input to the plant and the output of the controller and that the measured signal y is the output of the plant and input to the controller.

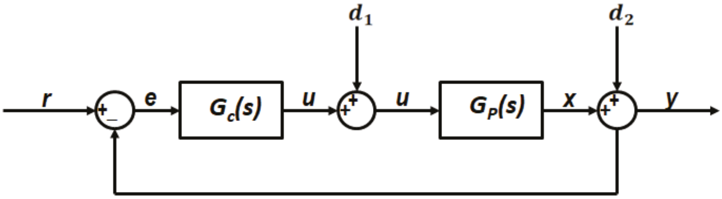

Figure A1. Block diagram of a single degree of freedom (1-DOF) *PI* controller.

Moreover, for simplicity, the control system feedback is assumed to be restricted to operate on the error signal only. This includes the ability to follow reference signals, effects of load disturbances, and measurement noise (Åström [134]). The effects of process variations are not discussed here. For linear systems, the properties are captured by a set of four transfer functions. This is in addition to the system open-loop transfer function, which is needed in control system analysis. The transfer functions can be inspected in different ways, by their step responses or frequency responses. The following set of transfer functions was used in the present analysis:

- Open-loop transfer function which defined by

$$G_P(s)G_C(s) \tag{A1}$$

- Closed-loop system reference tracking (from r to y), which is called the complementary sensitivity function:

$$G_P(s)G_C(s)/(1+G_P(s)G_C(s)) \tag{A2}$$

- Closed-loop system noise sensitivity function used for controller action (effort) calculations due to limitations caused by practical constraints, such as controller saturation (from r to y),

$$G_C(s)/(1+G_P(s)G_C(s)) \tag{A3}$$

- Closed-loop system response to a load disturbance (for a step disturbance at the plant input, d_1) (from d_1 to y), which is called the load disturbance sensitivity function

$$G_P(s)/(1+G_P(s)G_C(s)) \tag{A4}$$

  and

- Closed-loop system response to a step disturbance at plant output, d_2.which is called the sensitivity function (from d_2 to y)

$$(1+G_P(s)G_C(s)) \tag{A5}$$

The basic difference between input and output disturbances is that the input disturbance is generated in actuator while the output disturbance is generated in the sensor. For obtaining the time-domain characteristics of the control systems, frequently the step response, impulse response, and ramp response are evaluated. Transient characteristics such as peak time, settling time, rise time, maximum overshoot can be determined by evaluating the step response of the system.

References

1. Gad-El-Hak, M. Flow Control: The Future. *J. Aircr.* **2001**, *38*, 402–418. [CrossRef]
2. Simpson, R.L. Turbulent Boundary-Layer Separation. *Annu. Rev. Fluid Mech.* **1998**, *21*, 205–232. [CrossRef]
3. Benard, N.; Cattafesta, L.N.; Moreau, E.; Griffin, J.; Bonnet, J.-P. On the benefits of hysteresis effects for closed-loop separation control using plasma actuation. *Phys. Fluids* **2011**, *23*, 083601. [CrossRef]

4. Mabe, J.H.; Calkins, F.T.; Wesley, B.; Woszidlo, R.; Taubert, L.; Wygnanski, I. Single Dielectric Barrier Discharge Plasma Actuators for Improved Airfoil Performance. *J. Aircr.* **2009**, *46*, 847–855. [CrossRef]
5. Huebsch, W.W.; Gall, P.D.; Hamburg, S.; Rothmayer, A.P. Dynamic Roughness as a Means of Leading-Edge Separation Flow Control. *J. Aircr.* **2012**, *49*, 108–115. [CrossRef]
6. Schrauf, G. Application of Laminar Flow Technology on Transport Aircraft. In Proceedings of the CEAS Drag Reduction Conference, Potsdam, Germany, 3–5 June 2000; pp. 19–21. Available online: https://ntrs.nasa.gov/search.jsp?R=19780019127-2020-01-26T01:38:49+00:00Z (accessed on 17 May 2019).
7. Joslin, R.D.; Miller, D.N. (Eds.) *Fundamentals and Applications of Modern Flow Control*; American Institute of Aeronautics and Astronautics (AIAA): Reston, VA, USA, 2009; Volume 231, pp. 1–20. [CrossRef]
8. Cattafesta, L.; Song, Q.; Williams, D.R.; Rowley, C.W.; Alvi, F.S. Active control of flow-induced cavity oscillations. *Prog. Aerosp. Sci.* **2008**, *44*, 479–502. [CrossRef]
9. Williams, D.R.; MacMynowski, D. *Brief History of Flow Control Fundamentals and Applications of Modern Flow Control*; AIAA: Reston, VA, USA, 2008; Chapter 1; pp. 1–20. [CrossRef]
10. Bechert, D.W.; Bruse, M.; Hage, W.; Van Der Hoeven, J.T.; Hoppe, G. Experiments on drag-reducing surfaces and their optimization with an adjustable geometry. *J. Fluid Mech.* **1997**, *338*, 59–87. [CrossRef]
11. Fisher, D.; Cobleigh, B.; Banks, D.; Hall, R.; Wahls, R. Reynolds number effects at high angles of attack. In Proceedings of the 20th AIAA Advanced Measurement and Ground Testing Technology Conference, Albuquerque, NM, USA, 15–18 June 1998. [CrossRef]
12. Kaplanski, F.; Kartushinsky, A.; Hussainov, M.; Rudi, U.; Konhen, G.; Rüger, M. Some Experimental and Numerical Investigations of Flow near the Riblet Surfaces. In Proceedings of the 9th Workshop on Two-phase Flow Predictions, Merseburg, Germany, 13–16 April 1999; pp. 226–231. Available online: https://wwwresearchgate.net/publication/278242403 (accessed on 12 August 2019).
13. Kaplanski, F.; Hussainov, M.; Kartushinsky, A.; Rudi, Ü. Flow near the Hemispherical Depressions. *J. Mech. Behav. Mater.* **2000**, *11*, 407–417. [CrossRef]
14. Hussainov, M.; Kartushinsky, A.; Rudi, Ü.; Shcheglov, I.; Kohnen, G.; Sommerfeld, M. Experimental investigation of turbulence modulation by solid particles in a grid-generated vertical flow. *Int. J. Heat Fluid Flow* **2000**, *21*, 365–373. [CrossRef]
15. Hussainov, M.; Kartushinsky, A.; Rudi, U.; Shcheglov, I.; Tisler, S. Experimental Study of the Effect of Velocity Slip and Mass Loading on the Modification of Grid-Generated Turbulence in Gas-Solid Particles Flows. *Proc. Estonian Acad. Sci. Eng.* **2005**, *11*, 169–180.
16. Noack, B.; Morzyński, M.; Tadmor, G. *Reduced Order Modeling for Flow Control*; Springer Wien New York: Udine, Italy, 2011; Available online: https://www.springerprofessional.de/en/reduced-order-modelling-for-flow-control/4427676 (accessed on 8 February 2019).
17. Bushnell, D.M. Turbulence Sensitivity and Control in Wall Flows. In *Theoretical Approaches to Turbulence*; Springer: New York, NY, USA, 1985. [CrossRef]
18. Lumley, J.; Blossey, P. Control of Turbulence. *Annu. Rev. Fluid Mech.* **1998**, *30*, 311–327. [CrossRef]
19. Cattafesta, L.; Sheplack, M. Actuators and Sensors. In *Fundamentals and Applications of Modern Flow Control*; AIAA: Reston, VA, USA, 2008; Chapter 6; pp. 149–176. [CrossRef]
20. Mathew, J.; Song, Q.; Sankar, B.; Sheplak, M.; Cattafesta, L.N., III. Optimized Design of Piezoelectric Flap Actuators for Active Flow Control. *AIAA J.* **2006**, *44*, 2919–2928. [CrossRef]
21. Wong, C.; Kontis, K. Flow Control by Spanwise Blowing on a NACA 0012. *J. Aircr.* **2007**, *44*, 337–340. [CrossRef]
22. Eldredge, R.; Bons, J. Active Control of a Separating Boundary Layer with Steady Vortex Generating Jets–Detailed Flow Measurements. In Proceedings of the 42nd AIAA Aerospace Sciences Meeting and Exhibit, Reno, NV, USA, 5–8 January 2004. [CrossRef]
23. Shan, H.; Jiang, L.; Liu, C.; Love, M.; Maines, B. Numerical study of passive and active flow separation control over a NACA0012 airfoil. *Comput. Fluids* **2008**, *37*, 975–992. [CrossRef]
24. Seifert, A.; Greenblatt, D.; Wygnanski, I.J. Active separation control: An overview of Reynolds and Mach numbers effects. *Aerosp. Sci. Technol.* **2004**, *8*, 569–582. [CrossRef]
25. Amitay, M.; Glezer, A. Controlled transients of flow reattachment over stalled airfoils. *Int. J. Heat Fluid Flow* **2002**, *23*, 690–699. [CrossRef]
26. Seifert, A.; Darabi, A.; Wyganski, I. Delay of airfoil stall by periodic excitation. *J. Aircr.* **1996**, *33*, 691–698. [CrossRef]

27. Billings, S.A.; Leontaritis, I.J. Parameter Estimation Techniques for Non-linear Systems. In Proceedings of the 6th IFAC Symposium on System Identification and Parameter Estimation, Washington, DC, USA, 7–11 June 1982; pp. 505–510. [CrossRef]
28. Nishizawa, A.; Takagi, S.; Abe, H.; Kikushima, Y.; Maeda, R.; Yoshida, H. Toward Smart Control of Separation around Wing-part 1. In Proceedings of the 5th Symposium of Smart Control of Turbulence, Tokyo, Japan, 2–5 March 2005. [CrossRef]
29. Nishizawa, A.; Takagi, S.; Abe, H.; Segawa, T.; Yoshida, H. Smart Control of Separation around a Wing–Control System. In Proceedings of the 6th Symposium of Smart Control of Turbulence, Tokyo, Japan, 6–9 March 2005; pp. 1–8. Available online: https://www.nmri.go.jp/oldpages/turbulence/PDF/symposium/FY2003/Nishizawa.pdf (accessed on 15 January 2020).
30. Abe, H.; Segawa, T.; Kikushima, Y.; Pang, J.; Yoshida, H.; Nishizawa, A.; Takagi, S. Smart Control of Separation around a Wing—Control Device. In Proceedings of the 6th Symposium, Smart Control of Turbulence, Tokyo, Japan, 2–5 March 2005; Available online: https://www.nmri.go.Jp/oldpages2/turbulence/PDF/symposium/FY2004/Abe.pdf (accessed on 15 January 2020).
31. Segawa, T.; Yoshida, H.; Nishizawa, A.; Murakami, K.; Mizunuma, H. Sensors and Actuators for Smart Control of Separation. In Proceedings of the Theoretical and Applied Mechanics, Tokyo Japan, 12–17 March 2003; Volume 52, pp. 117–125. Available online: https://www.jstage.jst.go.jp/article/nctam/52/0/52_0_117/_article/-char/ja (accessed on 2 January 2020).
32. Tian, Y.; Cattafesta, L.; Mittal, R. Adaptive Control of Separated Flow. In Proceedings of the 44th AIAA Aerospace Sciences Meeting and Exhibit, Reno, NV, USA, 9–12 January 2006; pp. 1401–1411. [CrossRef]
33. Tian, Y.; Song, Q.; Cattafesta, L. Adaptive Feedback Control of Flow Separation. In Proceedings of the 3rd AIAA Flow Control Conference, San Francisco, CA, USA, 5–8 June 2006. [CrossRef]
34. Song, Q.; Tian, Y.; Cattafesta, L. MIMO Feedback Control of Flow Separation. In Proceedings of the 45th AIAA Aerospace Sciences Meeting and Exhibit, Reno, NV, USA, 8–11 January 2007. [CrossRef]
35. Pinier, J.; Ausseur, J.M.; Glauser, M.N.; Higuchi, H. Proportional Closed-Loop Feedback Control of Flow Separation. *AIAA J.* **2007**, *45*, 181–190. [CrossRef]
36. Ausseur, J.; Pinier, J.; Glauser, M. Estimation Techniques in a Turbulent Flow Field. In Proceedings of the 37th AIAA Fluid Dynamics Conference and Exhibit, Miami, FL, USA, 25–28 June 2007; Available online: https://www.researchgate.net/publication/259676298 (accessed on 19 December 2019).
37. Becker, R.; King, R.; Petz, R.; Nitsche, W. Adaptive Closed-Loop Separation Control on a High-Lift Configuration Using Extremum Seeking. *AIAA J.* **2007**, *45*, 1382–1392. [CrossRef]
38. Allan, B.; Juang, J.; Raney, D.; Seifert, A.; Pack, L.; Brown, D. *Closed-Loop Separation Control Using Oscillatory Flow Excitation*; NACA/CR, Technical Report; NACA Langley Research Center: Hampton, VA, USA, 2000; pp. 1–24. Available online: https://www.researchgate.net/publication/24301862 (accessed on 2 January 2020).
39. Becker, R.; Garwon, M.; Gutknecht, C.; Bärwolff, G.; King, R. Robust control of separated shear flows in simulation and experiment. *J. Process. Control.* **2005**, *15*, 691–700. [CrossRef]
40. Henning, L.; King, R. Multivariable Closed-Loop Control of the Reattachment Length Downstream of a Backward-Facing Step. In Proceedings of the 16th International IFAC World Congress, Praha, Czech Republic, 4–8 July 2005. [CrossRef]
41. Becker, R.; King, R. Comparison of a robust and a flatness based control for a separated shear flow. In Proceedings of the 16th International IFAC World Congress, Praha, Czech Republic, 4–8 July 2005. [CrossRef]
42. Duvigneau, R.; Visonneau, M. Optimization of a synthetic jet actuator for aerodynamic stall control. *Comput. Fluids* **2006**, *35*, 624–638. [CrossRef]
43. Bourgois, P.R. *Closed-Loop Proportional Controller for Flow Separation on ONERA Airfoil*; CNRS UMR 7128; ONERA Publications: Toulouse, France, 2009; pp. 1–34. Available online: https://www.imft.fr/IMG/pdf/liste_des_publications_2005_2009_imft.pdf (accessed on 2 March 2019).
44. Cattafesta, L.; Tian, Y.; Mittal, R. Adaptive Control of Post-Stall Separated Flow Application to Heavy Vehicles. In *The Aerodynamics of Heavy Vehicles II: Trucks, Buses, and Trains, Lecture Notes in Applied and Computational Mechanics Fracture Mechanics*; Springer: Berlin/Heidelberg, Germany, 2009; Volume 41, pp. 151–160. Available online: https://www.researchgate.net/publication/227108242 (accessed on 2 March 2019).

45. Cho, Y.C.; Fledderjohn, M.; Holzel, M.; Jayaraman, B.; Santillo, M.; Bernstein, D.S.; Shyy, W. Adaptive Flow Control of Low Reynolds Number Aerodynamics Using a Dielectric Barrier Discharge Actuator. In Proceedings of the 47th AIAA Aerospace Sciences Meeting Including The New Horizons Forum and Aerospace Exposition, Orlando, FL, USA, 5–8 January 2009. [CrossRef]
46. Taira, K.; Rowley, C.W.; Colonius, T. Feedback Control of High-Lift State for a Low-Aspect-Ratio Wing. In Proceedings of the 48th AIAA Aerospace Sciences Meeting Including the New Horizons Forum and Aerospace Exposition, Orlando, FL, USA, 4–7 January 2010. [CrossRef]
47. Benard, N.; Moreau, E.; Griffin, J.; Iii, L.N.C. Slope seeking for autonomous lift improvement by plasma surface discharge. *Exp. Fluids* **2009**, *48*, 791–808. [CrossRef]
48. Luchtenburg, D.M.; Aleksić, K.; Schlegel, M.; Noack, B.R.; King, R.; Tadmor, G.; Günther, B.; Thiele, F. Turbulence Control Based on Reduced-Order Models and Nonlinear Control Design. In *Active Flow Control II*; King, R., Ed.; Springer: Berlin/Heidelberg, Germany, 2010; pp. 341–356. [CrossRef]
49. Colonius, T.; Williams, D.R. Control of vortex shedding on two-and three-dimensional aerofoils. *Philos. Trans. R. Soc. Math. Phys. Eng. Sci.* **2011**, *369*, 1525–1539. [CrossRef] [PubMed]
50. Tuck, A.; Soria, J. Separation control on a NACA 0015 airfoil using a 2D micro ZNMF jet. *Aircr. Eng. Aerosp. Technol.* **2008**, *80*, 175–180. [CrossRef]
51. Amitay, M.; Glezer, A. Role of Actuation Frequency in Controlled Flow Reattachment over a Stalled Airfoil. *AIAA J.* **2002**, *40*, 209–216. [CrossRef]
52. He, Y.; Cary, A.; Peters, D. Parametric and dynamic modeling for synthetic jet control of a post-stall airfoil. In Proceedings of the 39th Aerospace Sciences Meeting and Exhibit, Reno, NV, USA, 8–11 January 2001. [CrossRef]
53. Amitay, M.; Kibens, V.; Parekh, D.; Glezer, A. The dynamics of flow reattachment over a thick airfoil controlled by synthetic jet actuators. In Proceedings of the 37th Aerospace Sciences Meeting and Exhibit, Reno, NV, USA, 11–14 January 1999. [CrossRef]
54. Crook, A.; Sadri, A.; Wood, N. The development and implementation of synthetic jets for the control of separated flow. In Proceedings of the 17th Applied Aerodynamics Conference, Norfolk, VA, USA, 28 June–1 July 1999. [CrossRef]
55. Seifert, A.; Pack, L. Oscillatory excitation of unsteady compressible flows over airfoils at flight Reynolds numbers. In Proceedings of the 37th Aerospace Sciences Meeting and Exhibit, Reno, NV, USA, 11–14 January 1999. [CrossRef]
56. Amitay, M.; Smith, D.; Kibens, V.; Parekh, D.; Glezer, A. Aerodynamic Flow Control of Bluff Bodies Using Synthetic Jet Actuators. In Proceedings of the IUTAM Symposium on Mechanics of Passive and Active Control, Gottingen, Germany, 7–11 September 1998; Available online: https://link.springer.com/chapter/10.1007/978-94-011-4199444 (accessed on 19 December 2019).
57. Smith, D.; Amitay, M.; Kibens, V.; Parekh, D.; Glezer, A. Modification of lifting body aerodynamics using synthetic jet actuators. In Proceedings of the 36th AIAA Aerospace Sciences Meeting and Exhibit, Reno, NV, USA, 12–15 January 1998. [CrossRef]
58. Amitay, M.; Pitt, D.; Glezer, A. Separation Control in Duct Flows. *J. Aircr.* **2002**, *39*, 616–620. [CrossRef]
59. Parekh, D.; Williams, S.; Amitay, M.; Glezer, A.; Washburn, T.; Gregory, I.; Scott, R. Synthetic Jet Aerodynamic Control on a Full Scale UAV. In Proceedings of the 33rd AIAA Fluid Dynamics Conference and Exhibit, Orlando, FL, USA, 23–26 June 2003. [CrossRef]
60. Ciuryla, M.; Liu, Y.; Farnsworth, J.; Kwan, C.; Amitay, M. Flight Control Using Synthetic Jets on a Cessna 182 Model. *J. Aircr.* **2007**, *44*, 642–653. [CrossRef]
61. Smith, B.L.; Glezer, A. Jet vectoring using synthetic jets. *J. Fluid Mech.* **2002**, *458*, 1–34. [CrossRef]
62. Maldonado, V.; Farnsworth, J.; Gressick, W.; Amitay, M. Active control of flow separation and structural vibrations of wind turbine blades. *Wind. Energy* **2010**, *13*, 221–237. [CrossRef]
63. Chatlynne, E.; Rumigny, N.; Amitay, M.; Glezer, A. Virtual aero-shaping of a Clark-Y airfoil using synthetic jet actuators. In Proceedings of the 39th Aerospace Sciences Meeting and Exhibit, Reno, NV, USA, 8–11 January 2001. [CrossRef]
64. Amitay, M.; Horvath, M.; Michaux, M.; Glezer, A. Virtual aerodynamic shape modification at low angles of attack using synthetic jet actuators. In Proceedings of the 15th AIAA Computational Fluid Dynamics Conference, Anaheim, CA, USA, 11–14 June 2001. [CrossRef]

65. Farnsworth, J.A.N.; Vaccaro, J.C.; Amitay, M. Active Flow Control at Low Angles of Attack: Stingray Unmanned Aerial Vehicle. *AIAA J.* **2008**, *46*, 2530–2544. [CrossRef]
66. Timor, I.; Ben-Hamou, E.; Guy, Y.; Seifert, A. Maneuvering Aspects and 3D Effects of Active Airfoil Flow Control. *Flow Turbul. Combust.* **2007**, *78*, 429–443. [CrossRef]
67. Darabi, A.; Wygnanski, I. Active Management of Naturally Separated Flow over a Solid Surface. Part 1: The forced reattachment process. *J. Fluid Mech.* **2004**, *510*, 105–129. [CrossRef]
68. Darabi, A.; Wygnanski, I. Active Management of Naturally Separated Flow over a Solid Surface. Part 2: The Separation Process. *J. Fluid Mech.* **2004**, *510*, 131–144. [CrossRef]
69. Amitay, M.; Glezer, A. Flow transients induced on a 2D airfoil by pulse-modulated actuation. *Exp. Fluids* **2005**, *40*, 329–331. [CrossRef]
70. Mathis, R.; Lebedev, A.; Collin, E.; Delville, J.; Bonnet, J.-P. Experimental study of transient forced turbulent separation and reattachment on a bevelled trailing edge. *Exp. Fluids* **2008**, *46*, 131–146. [CrossRef]
71. Jones, D.A.; Clarke, D.B. *Simulation of Flow Past a Sphere Using the Fluent Code*; Maritime Platforms Division: Fishermans Bend, Australia, 2008; pp. 1–35. Available online: https://pdfs.Semanticscholar.org/34cf/df61323f0c871e3c97e7cbce1e1f7dbef00e.pdf (accessed on 2 March 2019).
72. Slotnick, J.; Khodadoust, A.; Alonso, J.; Darmofal, D.; Gropp, W.; Lurie, E.; Mavriplis, D. *CFD Vision 2030 Study: A Path to Revolutionary Computational Aerosciences*; NASA Langley Research Center: Hampton, VA, USA, 2014; pp. 1–58. Available online: https://ntrs.nasa.gov/search.jsp?R=20140003093 (accessed on 2 March 2019).
73. Choi, H.; Moin, P.; Kim, J. Active turbulence control for drag reduction in wall-bounded flows. *J. Fluid Mech.* **1994**, *262*, 75. [CrossRef]
74. Kim, J. Control of turbulent boundary layers. *Phys. Fluids* **2003**, *15*, 1093–1105. [CrossRef]
75. Banaszuk, A.; Naraynan, S.; Zhang, Y. Adaptive Control of Flow Separation in a Planar Diffuser. In Proceedings of the 41st Aerospace Sciences Meeting and Exhibit, Reno, Nevada, 6–9 January 2003. [CrossRef]
76. Chen, S.; Billings, S.A. Representation of Non-linear Systems: The NARMAX Model. *Int. J. Control* **1989**, *49*, 1013–1032. Available online: http://eprints.soton.ac.uk/id/eprint/251145 (accessed on 27 December 2019).
77. Billings, S.A. *Nonlinear System Identification, NARMAX Methods in the Time, Frequency, and Spatio-Temporal Domains*; John Wiley & Sons: Hoboken, NJ, USA, 2013; ISBN 978-1-119-94359-4. Available online: https://www.wiley.com/en-us/exportProduct/pdf/9781119943594 (accessed on 4 January 2019).
78. Liu, Y.P. Identification of Nonlinear Systems: The NARMAX Polynomial Model Approach. Ph.D. Thesis, University of Sheffield, Sheffield, UK, 1988. Available online: https://sheffield.libguides.com/guideacse/communicating (accessed on 4 January 2019).
79. Leontaritis, I.J.; Billings, S.A. Input-output parametric models for non-linear systems Part II: Stochastic non-linear systems. *Int. J. Control* **1985**, *41*, 329–344. [CrossRef]
80. Thomson, M.; Schooling, S.; Soufian, M. The practical application of a nonlinear identification methodology. *Control. Eng. Pr.* **1996**, *4*, 295–306. [CrossRef]
81. Swain, A.; Billings, S.; Stansby, P.; Baker, M. Accurate prediction of non-linear wave forces: Part I (fixed cylinder). *Mech. Syst. Signal Process.* **1998**, *12*, 449–485. [CrossRef]
82. Billings, S.; Stansby, P.; Swain, A.; Baker, M. Accurate Prediction of Non-Linear Wave Forces: Part II (Responding Cylinder). *Mech. Syst. Signal Process.* **1998**, *12*, 487–498. [CrossRef]
83. Kukreja, S.L.; Brenner, M.J. Nonlinear System Identification of Aero-elastic Systems: A Structure-detection Approach. In *Identification and Control*; Part II; Springer: London, UK, 2007; pp. 117–145. [CrossRef]
84. Ching, S.; Eun, Y.; Kabamba, P.T.; Meerkov, S.M. Quasilinear Control Theory: An Overview. In Proceedings of the 18th IFAC World Congress, Milano, Italy, 28 August–2 September 2011. [CrossRef]
85. Wu, J.M.; Lu, X.Y.; Denney, A.G.; Fan, M.; Wu, J.Z. Post-stall Lift Enhancement on an Airfoil by Local Unsteady Control Part I, Lift, Drag and Pressure Characteristics. In Proceedings of the 4th Shear Flow Control Conference, Snowmass Village, CO, USA, 29 June–2 July 1997; Available online: http://staff.ustc.edu.cn/~{}xlu/download/JFM_1998.pdf (accessed on 27 December 2019).
86. Abbott Ira, H.; Von Doenhoff, A.E. *Theory of Wing Sections: Including a Summary of Airfoil Data (Dover Books on Aeronautical Engineering)*; Courier Corporation: North Chelmsford, MA, USA, March 1959; pp. 324–390. ISBN 978-0486605869. Available online: https://aeroknowledge77.files.wordpress.com/2011/09/589-86488-theory-of-wing-sections-including-a-summary-of-airfoil-data.pdf (accessed on 1 February 2020).

87. Dolle, T.J.A. Flap Performance Improvement by Surface Excitation. Master's Thesis, Aerospace Engineering at Delft University of Technology, Mekelweg, The Netherlands, 2009; pp. 1–144. Available online: http://resolver.tudelft.nl/uuid:985ea160-f12c-472f-9670-fd8ad333ee64 (accessed on 27 December 2019).
88. Duvigneau, R.; Visonneau, M. Simulation and optimization of stall control for an airfoil with a synthetic jet. *Aerosp. Sci. Technol.* **2006**, *10*, 279–287. [CrossRef]
89. Anderson, W.; Bonhaus, D.L. An implicit upwind algorithm for computing turbulent flows on unstructured grids. *Comput. Fluids* **1994**, *23*, 1–21. [CrossRef]
90. Bakker, A. Solution Methods Applied Computational Fluid Dynamics. In *Lectures of Fluent Instructor*; Lecture 5Fluent Inc.: New York, NY, USA, 2002; pp. 1–45. Available online: http://www.bakker.org/dartmouth06/engs150/05-solv.pdf (accessed on 7 January 2020).
91. Obeid, S.; Jha, R.; Ahmadi, G. RANS Simulations of Aerodynamic Performance of NACA 0015 Flapped Airfoil. *Fluids* **2017**, *2*, 2. [CrossRef]
92. Rethmel, C.C. Airfoil Leading Edge Flow Separation Control Using Nano-second Pulse DBD Plasma Actuators. Master's Thesis, The Ohio State University, Columbus, OH, USA, May 2011; pp. 1–80. Available online: http://rave.ohiolink.edu/etdc/view?acc_num=osu1306348260 (accessed on 27 December 2019).
93. You, D.; Moin, P. Active control of flow separation over an airfoil using synthetic jets. *J. Fluids Struct.* **2008**, *24*, 1349–1357. [CrossRef]
94. Joseph, D.D.; Liao, T.Y. Potential flows of viscous and viscoelastic fluids. *J. Fluid Mech.* **1994**, *265*, 1–23. [CrossRef]
95. Schroeder, E.J. Low Reynolds Number Flow Validation Using Computational Fluid Dynamics with Application to Micro Air Vehicles. Master's Thesis, University of Maryland, College Park, MD, USA, 2005; pp. 20–23. Available online: https://drum.lib.umd.edu/handle/1903/3349 (accessed on 2 March 2019).
96. Manni, L.; Nishino, T.; Delafin, P.-L. Numerical study of airfoil stall cells using a very wide computational domain. *Comput. Fluids* **2016**, *140*, 260–269. [CrossRef]
97. Sharma, D.M. Experimental Investigations of Dynamic Stall for an Oscillating Airfoil. Ph.D. Thesis, Aeronautical Engineering, Indian Institute of Technology Kanpur, Kanpur, India, 2010; pp. 90–102. [CrossRef]
98. Rediniotis, O.K. *Synthetic Jet Actuation—Modeling, Actuator Development and Application to Separation Control*; Texas Engineering Experiment College Station, Texas A&M University: College Station, TX, USA, 2004. Available online: https://apps.dticmil/dtic/tr/fulltext/u2/a424008.pdf (accessed on 4 February 2020).
99. Billings, S.A.; Leontaritis, I.J. Identification of Non-Linear System Using Parameter Estimation. In Proceedings of the 6th IFAC Symposium on Identification and System Parameter Estimation, Washington, DC, USA, 7–11 June 1982; Volumes 15, pp. 505–510. Available online: https://www.sciencedirect.com/journal/ifac-proceedings-volumes/vol/15/issue/4 (accessed on 10 October 2019).
100. Leontaritis, I.J.; Billings, S.A. Input-output parametric models for non-linear systems Part I: Deterministic non-linear systems. *Int. J. Control* **1985**, *41*, 303–328. [CrossRef]
101. Chiras, N.; Evans, C.; Rees, D. Nonlinear gas turbine computer modelling using NARMAX structures. In Proceedings of the 17th IEEE Instrumentation and Measurement Technology Conference, Baltimore, MD, USA, 1–4 May 2000; pp. 1278–1284. [CrossRef]
102. Billings, S.A.; Chen, S. Extended model set, global data and threshold model identification of severely non-linear systems. *Int. J. Control* **1989**, *50*, 1897–1923. [CrossRef]
103. Aguirre, L.A.; Billings, S.A. Improved structure selection for nonlinear models based on term clustering. *Int. J. Control* **1995**, *62*, 569–587. [CrossRef]
104. Billings, S.A.; Aguirre, L.A. Effects of the Sampling Time on the Dynamics and Identification of Nonlinear Models. *Int. J. Bifurc. Chaos* **1995**, *5*, 1541–1556. [CrossRef]
105. Akaike, H. A new look at the statistical model identification. *IEEE Trans. Autom. Control* **1974**, *19*, 716–723. [CrossRef]
106. Nash, J.E.; Sutcliffe, J.V. River Flow Forecasting through Conceptual Models. *J. Hydraul.* **1970**, *10*, 282–290. [CrossRef]
107. Mittal, R.; Kotapati, R.B. Resonant Mode Interaction in a Canonical Separated Flow. In Proceedings of the Sixth IUTAM Symposium on Laminar-Turbulent Transitions, Bangalore, India, 11–15 June 2006; Volume 78, pp. 341–348. [CrossRef]
108. Ho, C.; Huerre, P. Perturbed Free Shear Layers. *Annu. Rev. Fluid Mech.* **1984**, *16*, 365–422. [CrossRef]

109. Wu, J.-Z.; Lu, X.-Y.; Denny, A.G.; Fan, M.; Wu, J.-M. Post-stall flow control on an airfoil by local unsteady forcing. *J. Fluid Mech.* **1998**, *371*, 21–58. [CrossRef]
110. Kim, K. Feedback Control of FlowFlow Separation Using Synthetic Jets. Ph.D. Thesis, Texas A&M University, Bizzell St, TX, USA, December 2005; pp. 1–187. Available online: https//etd-tamu-2005C-MEEN-Kim.pdf (accessed on 27 December 2019).
111. Lavoie, P. Control of Separated Flows. Available online: http://arrow.utias.utoronto.ca/crsa/sssa/2016/lavoie.phil-UTIAS-separation.control-2016sssa.pdf (accessed on 14 February 2020).
112. Maldonado, V.; Farnsworth, J.; Gressick, W.; Amitay, M. Active Enhancement of Wind Turbine Blades Performance. In Proceedings of the 46th AIAA Aerospace Sciences Meeting and Exhibit, Reno, NV, USA, 7–10 January 2008. [CrossRef]
113. Benard, N.; Moreau, E. Capabilities of the dielectric barrier discharge plasma actuator for multi-frequency excitations. *J. Phys. D Appl. Phys.* **2010**, *43*, 145201. [CrossRef]
114. Glezer, A.; Amitay, M. Syntheticjets. *Annu. Rev. Fluid Mech.* **2002**, *34*, 503–529. [CrossRef]
115. Tang, H.; Zhong, S.; Jabbal, M.; Garcillan, L.; Guo, F.; Wood, N.; Warsop, C. Towards the Design of Synthetic-jet Actuators for Full-scale Flight Conditions. *Flow Turbul. Combust.* **2007**, *78*, 309–329. [CrossRef]
116. Sharma, R.N. Some Insights into Synthetic Jet Actuation from Analytical Modelling. In Proceedings of the 16th Australasian Flu. Mechanics Conference, Gold Coast, Australia, 2–7 December 2007; pp. 1242–1248. Available online: https://people.eng.unimelb.edu.au/imarusic/proceedings/16/Sharma2.pdf (accessed on 11 August 2019).
117. Kugelstadt, T. Active Filter Design Techniques. In *Fundamentals of Low-Pass Filters Book*; Texas Instruments: Dallas, TX, USA, March 2002; Chapter 16; pp. 1–66. Available online: https://www2.seas.gwu.edu/~{}ece121/Spring-11/filterdesign.pdf (accessed on 2 March 2019).
118. Taylor, J.H.; Strobel, K.L. Applications of a Nonlinear Controller Design Approach based on Quasilinear System Models. In Proceedings of the 1984 American Control Conference, San Diego, CA, USA, 7–10 June 1984; pp. 817–824. [CrossRef]
119. Taylor, J.H. Sinusoidal-Input Describing Function (SIDF). Available online: https://ocw.mit.edu/courses/aeronautics-and-astronautics/16-30-estimation-and-control-of-aerospace-systems-spring-2004/readings/gelb_ch2_ocr.pdf (accessed on 19 December 2019).
120. Schwartz, C.; Gran, R. Describing function analysis using MATLAB and Simulink. *IEEE Control. Syst.* **2001**, *21*, 19–26. [CrossRef]
121. Slotine, J.J.E.; Li, W. *Applied Nonlinear Control*; Prentice-Hall: Englewood Cliffs, NJ, USA, 1991; pp. 191–433. ISBN 0-13-040890-5. Available online: http://www.ioe.nchu.edu.tw/Pic/CourseItem/4497APPLIED%20NONLINEAR%20CONTROLslotine_Part1.pdf (accessed on 27 December 2019).
122. Kim, K.; Kerr, M.; Beskok, A.; Jayasuriya, S. Frequency-domain based feedback control of flow separation using synthetic jets. In Proceedings of the American Control Conference, Minneapolis, MN, USA, 14–16 June 2006. [CrossRef]
123. Vukic, Z.; Kuljaca, O. *Lectures on PID Controllers*; University of Texas: Arlington, TX, USA, 2002; pp. 5–41. Available online: http://www.uta.edu/utari/acs/jyotirmay/EE4343/Labs_Projects/pidcontrollers.pdf (accessed on 27 December 2019).
124. Taylor, J.H. A General Limit Cycle Analysis Method for Multivariable Systems. In *New Approaches to Nonlinear Problems in Dynamics*; Holmes, P.J., Ed.; SIAM (Society of Industrial and Applied Mathematics): Philadelphia, PA, USA, 1980; ISBN 978-0898711677. Available online: https://trove.nla.gov.au/version/11860584 (accessed on 2 July 2019).
125. Taylor, J.H. Describing Functions. In *Electrical Engineering Encyclopedia*; John Wiley & Sons, Inc.: New York, NY, USA, 1999. [CrossRef]
126. Kotapati, R.B.; Mittal, R.; Marxen, O.; Ham, F.; You, D.; Cattafesta, L.N. Nonlinear dynamics and synthetic-jet-based control of a canonical separated flow. *J. Fluid Mech.* **2010**, *654*, 65–97. [CrossRef]
127. Glass, J.W.; Franchek, M.A. Frequency-based nonlinear controller design for regulating systems subjected to time-domain constraints. *Int. J. Robust Nonlinear Control* **2000**, *10*, 39–57. [CrossRef]
128. John, A. *Understanding Bode Plots*; Motion Engineering Inc. Notes: Santa Barbara, CA, USA, 2019; pp. 1–99. Available online: http://support.Motioneng.com/utilities/bode/bode_16.html (accessed on 2 January 2020).

129. Shahzad, U. Design and Analysis of a Control System Using Root Locus and Frequency Response Methods. *ITEE J.* **2017**, *6*, 14–19. Available online: https://www.researchgate.net/publication/319653031 (accessed on 12 January 2020).
130. Patino, D.; Riedinger, P.; Iung, C. Practical Optimal State Feedback Control Law for Continuous-Time Switched Affine Systems with Cyclic Steady State. *Int. J. Control* **2010**, *82*, 1251–1276. [CrossRef]
131. Berk, Z. Elements of Process Control. In *Food Process Engineering Technology*; Science Dirt Elvester Book; Springer: New York, NY, USA, 2009; Chapter 5; pp. 129–151. Available online: https://www.sciencedirect.com/book/9780123736604/food-process-engineering-and-technology (accessed on 8 February 2020).
132. Horowitz, I.M. *Synthesis of Feedback Systems*, 1st ed.; Elsevier: Amsterdam, The Netherlands, 1963; ISBN 9781 4 83267708. Available online: https://www.elsevier.com/books/synthesis-of-feedback-systems/horowitz/978-1-4832-3282-9 (accessed on 19 January 2020).
133. Vandoren, V. Designing a Feedback Control Loop Starts with Understanding its Objective as well as the Process's Behavior. *Control Engineering Magazine*. 7 March 2011, pp. 1–13. Available online: https://www.controleng.com/articles/disturbance-rejection-vs-setpoint-tracking-controllers (accessed on 23 December 2019).
134. Åström, K.J. Control System Design. In *Lecture Notes for ME 155A on Department of Mechanical Environmental Engineering*; University of California: Santa Barbara, CA, USA, 2002; Available online: http://clux.x-pec.com/files/fronter/ENE103%20-%20Reguleringsteknikk/fagstoffsuplement%20Reg%20tek%20engelsk%20.pdf (accessed on 19 December 2019).
135. MATLAB. *Control System Tool Box, User's Guide*; The Math Works, Inc.: Natick, MA, USA, 2019; pp. 1–1815. Available online: https://www.mathworks.com/help/pdf_doc/control/index.html?s.cid=doc.ftr (accessed on 3 June 2019).
136. Seborg, D.E.; Edgar, T.F.; Mellichamp, D.A.; Doyle, F.I., III. *Process Dynamics and Control*, 4th ed.; Johns Wiley & Sons: Hoboken, NJ, USA, 2017; Available online: https://www.wiley.com/en-us/Process.Dynamics.and.Control.4th.Edition-p-9781119285915 (accessed on 7 January 2020).

fluids

Article

Experiments on Flexible Filaments in Air Flow for Aeroelasticity and Fluid-Structure Interaction Models Validation

Jorge Silva-Leon [1] and Andrea Cioncolini [2,*]

[1] Escuela Superior Politécnica del Litoral, ESPOL, Facultad de Ingeniería en Mecánica y Ciencias de la Producción, Campus Gustavo Galindo Km 30.5 Vía Perimetral, Guayaquil P.O. Box 09-01-5863, Ecuador; jfsilva@espol.edu.ec

[2] Department of Mechanical, Aerospace and Civil Engineering, University of Manchester, George Begg Building, Sackville Street, Manchester M1 3BB, UK

* Correspondence: andrea.cioncolini@manchester.ac.uk

Received: 27 April 2020; Accepted: 3 June 2020; Published: 5 June 2020

Abstract: Several problems in science and engineering are characterized by the interaction between fluid flows and deformable structures. Due to their complex and multidisciplinary nature, these problems cannot normally be solved analytically and experiments are frequently of limited scope, so that numerical simulations represent the main analysis tool. Key to the advancement of numerical methods is the availability of experimental test cases for validation. This paper presents results of an experiment specifically designed for the validation of numerical methods for aeroelasticity and fluid-structure interaction problems. Flexible filaments of rectangular cross-section and various lengths were exposed to air flow of moderate Reynolds number, corresponding to laminar and mildly turbulent flow conditions. Experiments were conducted in a wind tunnel, and the flexible filaments dynamics was recorded via fast video imaging. The structural response of the filaments included static reconfiguration, small-amplitude vibration, large-amplitude limit-cycle periodic oscillation, and large-amplitude non-periodic motion. The present experimental setup was designed to incorporate a rich fluid-structure interaction physics within a relatively simple configuration without mimicking any specific structure, so that the results presented herein can be valuable for models validation in aeroelasticity and also fluid-structure interaction applications.

Keywords: experiment; benchmark; validation; aeroelasticity; fluid-structure interaction; flexible; filament; ribbon; string

---

1. Introduction

Fluid-structure interaction (FSI) problems, where a fluid flow and a movable or deformable structure dynamically interact, are relevant in several fields of engineering including aeroelasticity, biomechanics, flow control, and energy harvesting. Examples include aircraft wing design [1,2], flapping wing propulsion [3–5], flexible turbomachinery [6,7], cardiovascular medicine [8–11], swimming micro-organisms [12,13], piezoelectric wind energy harvesting [14,15], and several more. A flexible structure exposed to fluid flow deforms owing to the fluid force acting along its surface. When the deformation of the structure is large enough to affect the flow field, the resulting FSI problem is a coupled, non-linear multi-physics problem where the flow and the structure dynamically interact and modulate each other.

Despite their practical relevance, a comprehensive treatment of FSI problems remains a challenge due to their intrinsic complexity and multidisciplinary nature. FSI problems are typically too complex to solve analytically, and are therefore analyzed by means of experiments and numerical simulations.

Frequently, conducting experiments at operating conditions representative of actual applications may be challenging or impractical. In these cases, numerical modelling may be used as the main design and analysis tool to investigate the fundamental physics of FSI problems. The development of numerical methods for FSI problems has been an active area of research over the last decades, and several numerical procedures have been proposed to account for large structural deformations and faithfully reproduce the coupling between the structure and the fluid [16–19]. The effectiveness of numerical FSI methods is normally assessed via verification and validation. Whilst the verification is carried out by comparing the simulations with synthetic data generated with numerical experiments (see, e.g., [20–24]), the validation relies on comparing the simulations with experimental test cases, i.e., data originated from physical experiments. In order to be informative and, at the same time, minimize the computational burden, the experimental test cases used to validate numerical FSI methods do not normally mimic any realistic structure. Instead, these experimental test cases are typically designed to incorporate a rich fluid-structure interaction physics within a relatively simple configuration. For illustrative purposes, a non-exhaustive selection of popular experimental FSI test cases is provided in Table 1.

Table 1. Experimental FSI validation test cases.

Reference	Fluid	Structure	Motion
Pereira Gomez et al. [25]	Polyethylene glycol syrup in laminar flow	Flexible metal plate with rear mass at the trailing edge, clamped behind a rigid circular cylinder free to rotate around its axis, oriented in cross-flow	2D
Pereira Gomes and Lienhart [26]	Water and polyethylene glycol syrup in laminar and turbulent flow	Flexible metal plate with rear mass at the trailing edge, clamped behind a rigid cylindrical body (circular or rectangular cross section) oriented in cross-flow	2D
Kalmbach and Breuer [27]	Water in turbulent flow	Flexible rubber membrane with rear mass at the trailing edge, clamped behind a rigid and fixed circular cylinder oriented in cross-flow	2D
De Nayer et al. [28]	Water in turbulent flow	Flexible rubber membrane clamped behind fixed rigid circular cylinder oriented in cross-flow	2D/3D
Hessenthaler et al. [29]	Aqueous glycerol solution in laminar flow	Flexible cantilever-beam plate in merging flow from two inlets	3D
This study	Air in laminar and turbulent flow	Flexible cantilever-beam filaments of variable length in uniform flow	3D

As can be noted in Table 1, the experimental setups comprise an elastic structure of simple geometry, such as a plate or a membrane, which undergoes large deformations with moderate motion frequency whilst interacting with a flow of moderate Reynolds number, so that the complication of simulating highly turbulent flows is avoided. Sometimes, the structure dynamics is restricted to two-dimensional, so that the validation can be achieved by means of two-dimensional numerical simulations, which are less demanding than three-dimensional simulations in terms of run-time and computational resources. In addition to the structural dynamics, which is always resolved in validation experiments, when practical also the flow field is measured. Faithfully resolving this latter is not always feasible, however, particularly when the structural deformation is three-dimensional, so that flow field measurements, when provided, are frequently of low resolution and of limited scope.

With the rapid development of numerical FSI methods, the demand for validation test cases increases. The objective of this work is to contribute one such case. In particular, we tested six flexible filaments of rectangular cross-section and varying length, which were exposed to air flow of moderate Reynolds number corresponding to laminar and mildly turbulent flow conditions. In order to explore a wider range of structural responses during the tests, besides varying the air flow velocity we also varied the length of the elastic filaments. This was instrumental to observing structural responses as diverse as: (1) static reconfiguration, (2) small-amplitude vibration, (3) limit-cycle periodic oscillations, and (4) non-periodic oscillations. The dynamics of the flexible filaments was generally three-dimensional, though a two-dimensional structural response was sometimes observed during limit-cycle periodic oscillations. Even though the focus here is clearly on three-dimensional large deformations of flexible structures in air flow, the practical relevance of the work goes beyond aeroelasticity applications, and the present results can be of interest for FSI applications in general.

The rest of this paper is organized as follows: the test set-up, the flexible filaments characterization, the flow characterization and the experimental methodology are presented in Section 2, whilst the measured results are presented and discussed in Section 3.

2. Materials and Methods

2.1. Flexible Filament Manufacturing and Characterization

The flexible filament was manufactured with commercial silicone rubber (density 1.00 ± 0.05 g/cm^3) using an additive manufacturing system (3D-Bioplotter by EnvisionTEC, https://envisiontec.com) following a rectilinear path during printing to avoid any curvature or deformation, and therefore produce a straight filament of uniform cross section and smooth surface finishing. The filament had rectangular cross section with width w of 2.00 ± 0.05 mm and height h of 0.40 ± 0.05 mm (measured with a digital caliper), and a linear mass density of 0.80 ± 0.16 g/m. Note that, in order to avoid the large error that would have arisen from measuring directly the mass of the filament (which was on the order of 0.1 g), the density of the silicon rubber provided above was deduced from measuring the mass of a bigger chunk of silicon rubber. The linear mass density of the filament provided above was therefore calculated as the product of the silicon rubber density times the width and height of the filament cross-section. One portion of the filament was used for the mechanical characterization described below, whilst another portion was used to realize the test piece for the FSI experiments (described in Section 2.2).

The mechanical behavior of the filament was characterized with uniaxial tensile tests. The results are provided in raw format in Figure 1a as filament elongation (measurement accuracy ± 0.5 mm) versus applied force (measurement accuracy ± 1%), whilst the corresponding stress-strain curve is provided in Figure 1b. The tensile strain ϵ and the tensile stress σ are calculated as indicated in Equations (1) and (2), respectively:

$$\epsilon = \frac{\Delta L}{L_0} = \frac{L - L_0}{L_0} \tag{1}$$

$$\sigma = \frac{F}{A} = \frac{FL}{A_0 L_0} \tag{2}$$

where ΔL is the filament elongation, L is the length of the filament when loaded, L_0 is the initial length of the filament (note that the filament used for the tensile test had an initial length of 52.0 ± 0.5 mm), F is the applied force, and A is the area of the cross-section of the filament. As can be noted in Equation (2), the tensile stress was calculated by assuming incompressible deformation, which is an acceptable approximation for silicone rubber [29]. No permanent deformation was observed after loading and the data in Figure 1b are linearly correlated, therefore indicating a linear-elastic behavior of the flexible filament during the tensile tests. The experimental uncertainties, estimated with standard single-sample error propagation [30], were on the order of ± 2% for the tensile strain, and ± 10% for the tensile stress. The corresponding Young modulus of the filament, deduced from the slope of the fitting line in Figure 1b, is E = 757 ± 91 kPa.

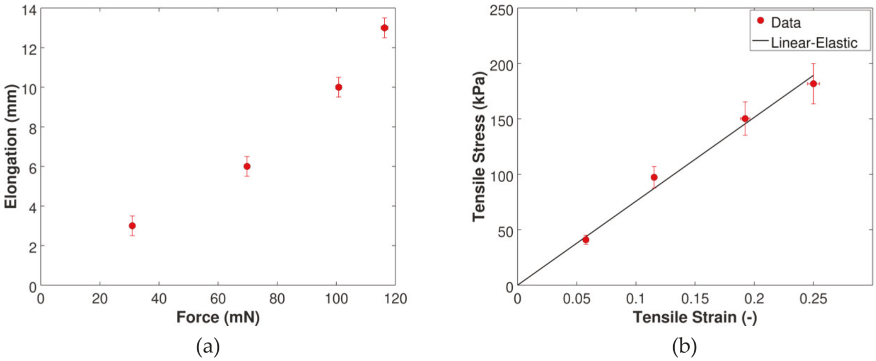

Figure 1. Mechanical characterization of the flexible filaments. (**a**) Uniaxial tensile tests results; (**b**) Stress-strain curve.

2.2. Test Piece Description and Preliminary Characterization

As schematically shown in Figure 2a, the test piece for the FSI experiments comprises the flexible filament, a support tube, and a support plate. The support tube, a rigid stainless-steel circular tube with external diameter of 2.40 ± 0.05 mm and length of 140 ± 0.5 mm, was rigidly connected to the support plate so that the test piece could be introduced from the top inside the wind tunnel for testing, as shown in Figure 2c. The filament extremity was introduced inside the support tube and then glued, so as to realize a cantilever boundary condition at the connection between the filament and the tube. The length of the support tube was selected to place the filament in the middle of the wind tunnel cross-section. During the tests, the filament was always oriented with the longer side of the rectangular cross section facing the flow, as schematically shown in Figure 2b. The flexible filament protruding from the support tube had an initial length L of 60 mm. The filament was progressively shortened during the experiments, and tests were carried out for six different lengths: 60 mm, 50 mm, 40 mm, 30 mm, 20 mm, and 10 mm. These are referred to, in the following, as Filament 1 (60 mm) through Filament 6 (10 mm), as indicated in Table 2.

Table 2. Flexible filaments used in the present FSI experiments.

Filament No.	L (mm)	f_1 (Hz)	ζ_1 (-)
1	60.0 ± 0.5	2.5 ± 0.1	0.012 ± 0.002
2	50.0 ± 0.5	2.8 ± 0.1	0.015 ± 0.002
3	40.0 ± 0.5	3.3 ± 0.2	0.017 ± 0.002
4	30.0 ± 0.5	3.9 ± 0.3	0.021 ± 0.003
5	20.0 ± 0.5	6.3 ± 1.0	0.028 ± 0.004
6	10.0 ± 0.5	16 ± 3	0.035 ± 0.005

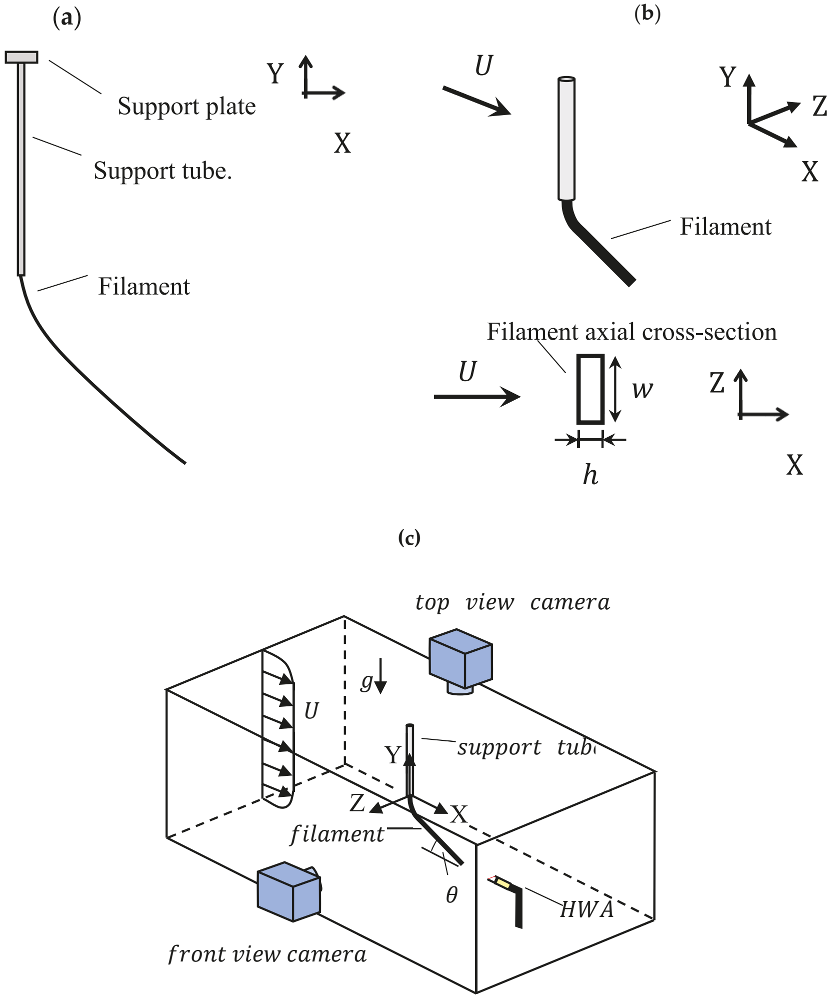

Figure 2. (**a**) Schematic representation of the test piece; (**b**) Filament orientation during the tests in the wind tunnel; (**c**) Schematic representation of the experimental wind tunnel setup.

Before running the FSI tests in the wind tunnel, the filaments were preliminary characterized by measuring their natural vibration frequencies and damping ratios. The results are provided in Table 2. In particular, first-mode natural vibration frequencies f_1 were measured in forced vibration shaker tests under single-frequency excitation. The test setup included an electromagnetic shaker (of in-house design and construction) with control signal provided by a signal generator operated in sine wave mode with frequency resolution of 0.1 Hz. During the tests, the filaments hang vertically with the top extreme fixed to the shaker. Following common practice, the amplitude of response of the filament was recorded (using a Panasonic Lumix DMC-FZ200 digital camera) as a function of the excitation frequency, and the natural vibration frequency was identified as the peak in the response (experimental uncertainty deduced from the full-width at half maximum of the peak in the amplitude response). On the other hand, first-mode damping ratios ζ_1 were deduced from free vibration tests in stagnant air. Starting with the filament hanging vertically in equilibrium with the top extreme fixed, the filament free-end was manually displaced (displacement small enough to trigger a mode-1 response). The filament free-end was then released, and the free vibration of the filament was recorded (using a Panasonic Lumix DMC-FZ200 digital camera). Following common practice, the damping ratio was evaluated from the logarithmic decrement of the envelope of the displacement time-series (experimental uncertainty deduced as standard deviation from repeated measurements). Natural vibration frequencies of the filaments are presented in Figure 3a together with the predictions of Equations (3) and (4):

$$f_{Beam} = \frac{1.875^2}{2\pi} \sqrt{\frac{E\,I}{m\,L^4}} \tag{3}$$

$$f_{String} = \frac{2.4048}{4\pi} \sqrt{\frac{g}{L}} \tag{4}$$

where E is the Young modulus of the filament, m is the total linear mass density of the filament (since the density of the filament is 3 orders of magnitude larger than the density of air, the added mass is negligible in the present case), g is the acceleration of gravity, and I is the second area moment of the cross-section of the filament with respect to the axis aligned with the longer side (z-axis in Figure 2b):

$$I = \frac{wh^3}{12} \tag{5}$$

In particular, Equation (3) predicts the first-mode natural vibration frequency of a cantilevered elastic beam according to standard Euler-Bernoulli beam theory, whereas Equation (4) predicts the first-mode natural vibration frequency of a one-dimensional elastic and inextensible hanging string [31]. As can be noted in Figure 3a, whilst the natural vibration frequencies of the shorter filaments (Filaments 5 and 6) agree with Equation (3), those of the longer filaments (Filaments 1 through 4) agree with Equation (4). This indicates that, from a structural point of view, the shorter filaments behave as elastic beams, whereas the longer ones behave as elastic strings. Even though this conclusion, strictly speaking, is only valid for the forced vibration tests discussed here, the FSI tests discussed later provide similar results: the structural response of the filaments is modulated by their length. This highlights the usefulness of using the filament length as control parameter during the experiments to explore different structural responses. As can be noted in Figure 3b, the damping ratio decreases when increasing the filament length, confirming previous observations with flexible filaments of circular cross section [32,33].

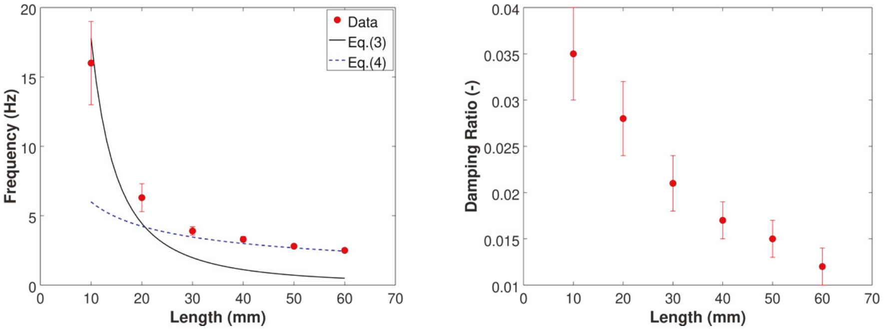

(a) (b)

Figure 3. Preliminary characterization of the flexible filaments. (**a**) First-mode natural vibration frequency; (**b**) First-mode damping ratio in stagnant air.

2.3. Wind Tunnel Flow Characterization

The experiments were performed in a horizontal-axis commercial wind tunnel (by Armfield Limited, Ringwood, UK (armfieldonline.com)) of octagonal cross-section with height and width of

300 mm, operated with air at ambient conditions (air pressure and temperature during the experiments were 101 ± 1 kPa and 293 ± 2 K, respectively). The blockage ratio associated with the present test piece was on the order of 0.5%, so that wind tunnel flow confinement effects can be ignored. The free-stream flow velocity was measured (to within ± 2% accuracy) with a hot-wire anemometer (by Dantec Dynamics, Bristol, UK (www.dantecdynamics.com); probe type 55P15: 5 μm diameter tungsten wire of 2 mm length), calibrated prior to the tests and operated in constant temperature mode with a sampling frequency of 10 kHz. As shown schematically in Figure 2c, the hot-wire anemometer (HWA) was located downstream of the test piece in the same vertical plane of the filament but at a lower vertical elevation, so as to avoid any interference between the anemometer and the wake of the filament.

The uniformity of the free-stream velocity profile and the extension of the boundary layer in the wind tunnel were assessed before introducing the flexible filaments in the tunnel for testing. The boundary layer thickness was of about 5 mm at the lowest wind speed considered, whilst the velocity profile (excluding the boundary layer) was uniform to within ± 2%, i.e., velocity variations were within the present experimental resolution. This assures that the flexible filaments were always exposed to a fully-developed velocity profile during the tests. The free-stream wind tunnel flow was further characterized by estimating the streamwise component of the turbulence intensity Tu and the streamwise macro Λ and micro λ turbulence length scales [34]:

$$Tu = \frac{\sqrt{\overline{u^2}}}{U} \tag{6}$$

$$\Lambda = \left[\frac{E(f)U}{4\overline{u^2}}\right]_{f\to 0} \tag{7}$$

$$\lambda = \left[\frac{2\pi^2}{U^2\overline{u^2}}\int_0^\infty f^2 E(f)df\right]^{-2} \tag{8}$$

where $\overline{u^2}$ is the mean square fluctuating velocity, U is the mean flow velocity, and $E(f)$ is the energy spectrum of the velocity signal as function of the frequency f. Equations (7) and (8), in particular, are valid under the assumption of homogeneous and isotropic turbulence, which is normally acceptable for wind tunnel flow experiments [34]. As is well known, the turbulence intensity measures the relative intensity of the velocity fluctuation. On the other hand, the turbulence macroscale can be considered as a measure of the largest eddy size in the flow, whilst the turbulence microscale can be considered a measure of the smallest eddies in the flow, which are responsible for the dissipation of turbulence energy. Turbulence intensity and length scales estimates are presented as functions of the wind speed in Figure 4. As can be noted, the turbulence intensity is mild and ranges between 1% and 2.5%, whilst the macro and micro length scales range between 1−30 mm and 0.02−0.38 mm, respectively. The estimates provided in Figure 4 were generated from five-seconds long hot-wire velocity measurements of the flow, sampled at 10 kHz. The free-stream flow is not further characterized at this stage, but raw free-stream flow data are included as Supplementary Materials for future reference and further analysis.

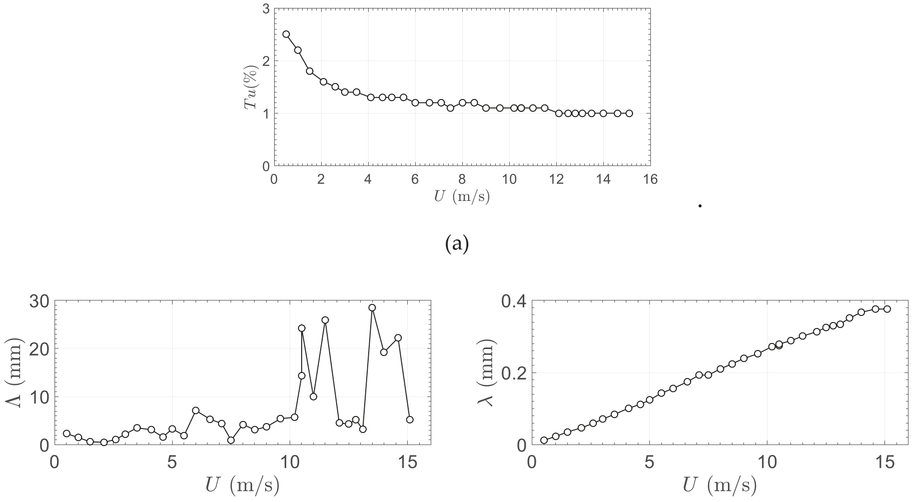

(b) (c)

Figure 4. Preliminary characterization of the free-stream wind tunnel flow. (**a**) Streamwise turbulence intensity; (**b**) Streamwise turbulence macroscale; (**c**) Streamwise turbulence microscale.

2.4. Experimental Procedure

During the FSI tests, the free-stream flow velocity was gradually and stepwise varied between 1 m/s and 15 m/s, corresponding to a Reynolds number in the range of 133−2027. The Reynolds number, in particular, is based on the filament width w:

$$Re = \frac{\rho U w}{\mu} \tag{9}$$

where ρ and μ are the air density and viscosity. With cylinders in cross-flow, the vortex street becomes turbulent for Reynolds numbers above about $Re \approx 200 - 300$ [35]. The Reynolds number range explored here, therefore, covers laminar (flow velocity up to ~1.5 m/s), transitional (flow velocity from ~1.5 m/s up to ~2.5 m/s), and mildly turbulent (flow velocity above ~2.5 m/s) flow conditions. Measurements were taken for both increasing and decreasing flow velocity, observing no hysteresis in the response of the filaments.

The motion of the filaments was recorded simultaneously in the horizontal and vertical planes using two synchronized digital cameras (Panasonic Lumix DMC-FZ200, recording frequency: 200 frames per second, image resolution: 480 × 640 pixels), located at the front and at the top of the wind tunnel as shown in Figure 2c. The digital cameras provided a spatial resolution of 0.20 mm/pixel, which is appropriate to resolve the large displacements of interest here. The videos (15 s recording) were synchronized and post-processed with the Image Processing Toolbox of MATLAB (version R2015a), using a tracking methodology previously developed for flexible fluid-structure interaction and flow-induced vibration applications [32,33,36–38].

Representative envelopes of motion for Filament 1 at three different Reynolds numbers ($Re = 202$, $Re = 410$, and $Re = 804$) are presented in Figure 5. Except at the lowest Reynolds number value ($Re = 202$), when the motion of the filament is two-dimensional and confined to the vertical plane, the motion of the filament is clearly three-dimensional, with significant displacements in both the vertical and horizontal planes. Not surprisingly, the free-end is the point along the filament that experiences the largest displacement. As shown in previous research on flexible filaments in cross-flow [32,33], the dynamics of the filament free-end is representative of the dynamics of any point along the flexible filament, meaning that the dynamics of any point along the flexible filament is qualitatively similar to the dynamics of the filament free-end, despite the different amplitude of motion. In the present study, therefore, the response of the filaments was characterized by analyzing the dynamics of the filament free-end, which experiences the largest displacement and therefore maximizes the signal-to-noise ratio. On account of the filament motion being mostly three-dimensional, the filament free-end dynamics was characterized by analyzing the displacement time-series $A_y(t)$ and $A_z(t)$ recorded in the vertical plane (front view in Figure 2c) and horizontal plane (top view in Figure 2c), and by analyzing the filament free-end total displacement time-series $A_{tot}(t)$:

$$A_{tot}(t) = \sqrt{A_y(t)^2 + A_z(t)^2} \tag{10}$$

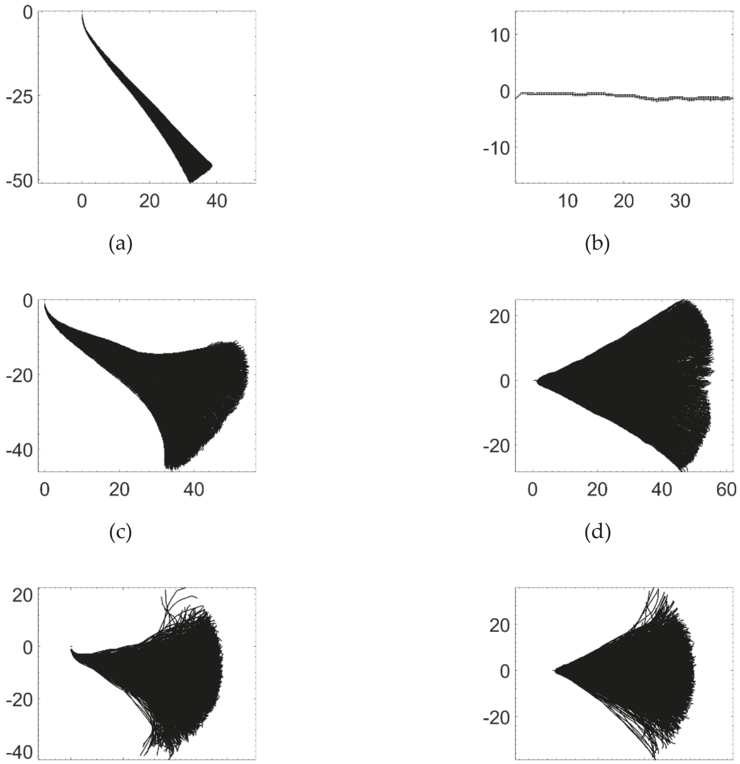

(a) (b)

(c) (d)

(e) (f)

Figure 5. Representative envelopes of motion for Filament 1 in the vertical plane (left) and horizontal plane (right) at three Reynolds numbers (top, middle and bottom). (**a**) Vertical plane, $Re = 202$; (**b**) Horizontal plane, $Re = 202$; (**c**) Vertical plane, $Re = 410$; (**d**) Horizontal plane, $Re = 410$; (**e**) Vertical plane, $Re = 804$; (**f**) Horizontal plane, $Re = 804$ (x-axis and y-axis scales are in mm).

The total displacement combines the vertical and horizontal motions of the filament free-end, and can therefore be used to characterize both planar and three-dimensional dynamics. In particular, the recorded time-series were not filtered prior to the analysis. Flapping frequencies in the vertical and horizontal planes were identified as the dominant frequencies in the power spectral densities (computed using the Welch method [39] and MATLAB built-in functions) of the corresponding displacement time-series.

The total displacement time-series was used to compute the autocorrelation function and to reconstruct the system trajectory in phase-space, which together provide a thorough characterization of the filament free-end dynamics. Whilst the autocorrelation function was computed using MATLAB built-in functions, the trajectory of the system in phase-space (i.e., the system attractor) was reconstructed using the delayed vector method [40]: a methodology developed for nonlinear time-series analysis that is particularly useful for fluid-structure interaction problems. The topology of the reconstructed attractor of the filament free-end, in fact, gives a useful qualitative characterization of the filament dynamics, which completes and corroborates the quantitative information provided by the displacements and flapping frequency. The concept of phase-space representation, rather than a classic analysis in time or frequency domain, is the key point in nonlinear time-series analysis. The topology of the trajectory in phase-space of a nonlinear system, in fact, provides important qualitative information regarding the fundamental dynamics of the systems being investigated. The problem is that, in experimental studies, one normally observes a time-series of scalar measurements of some quantity that depends on the current state of the system, and not the trajectory of the system in phase-space. The delayed vectors method [40] allows reconstructing the trajectory of the system in phase-space from a time-series of scalar measurements, and can therefore be used in experimental studies such as the present one where only time-series of scalar measurements of some quantity (the instantaneous total displacement in the present case) are available. In the present case, the trajectory in phase-space was reconstructed by plotting the time-delayed instantaneous total displacement $A_{tot}(t + \tau)$ versus $A_{tot}(t)$. If the delay τ is chosen properly (on the order of 5-30 ms in the present case, the lower the delay the higher the flow velocity and Reynolds number), then the topology of the reconstructed attractor is representative of the underlying system dynamics [40].

As noted previously, experimental FSI test cases should always include the structural dynamics and, when feasible, also the measurement of the flow field. Measuring the flow field in the present case would require a three-dimensional flow visualization with sub-millimeter space resolution and high-frequency (on the order of several kHz) time resolution. Even for the simplest test case documented here, which corresponds to Filament 6 statically reconfigured at a flow velocity of 1 m/s (corresponding to a Reynolds number of $Re = 133$), measuring the flow field would require the resolution of a vortex street where vortices of sub-millimetric size are shed at a frequency of about 100 Hz [41]. As previously noted, in FSI test cases it is normally preferred to have flexible structures which undergo large deformations with moderate motion frequency whilst interacting with a flow of moderate Reynolds number, thereby avoiding the complications of simulating highly turbulent flows. The small size and high flexibility of the present filaments were instrumental in achieving large displacements and relatively small oscillation frequencies and, at the same time, keep the Reynolds number small. Unfortunately, the details of the flow field scale with the size of the structure, so that the smaller the structure the smaller the space resolution that is needed to faithfully resolve the flow field. In the present case, the requirements for a faithful flow field visualization were beyond our experimental capabilities, and the flow field was therefore not measured.

3. Results and Discussion

The results for Filament 1 are presented in Figures 6–9. In particular, displacements and flapping frequencies in the horizontal and vertical planes are presented in Figure 6 as functions of the Reynolds number, whilst the trajectory of the filament free-end (as seen by an observed located downstream of the filament and facing the flow), the autocorrelation function and the reconstructed attractor (computed from the total displacement of the filament free-end) are provided, for all Reynolds number values tested, in Figures 7–9. Each data point presented in the paper has been generated from averaging one video recording of 15 seconds, corresponding to 3000 frames. Selected data points were repeated, showing good repeatability.

It is evident that the filament response gradually changes as the Reynolds number is progressively increased. For low values of the Reynolds number ($Re \lesssim 333$) the filament motion is small-amplitude and mostly confined to the vertical plane, with a rapidly decaying autocorrelation function and a blob-like attractor. These are typical features of a small-amplitude vibration: a random and not self-sustained motion confined around the equilibrium position corresponding to the statically reconfigured filament.

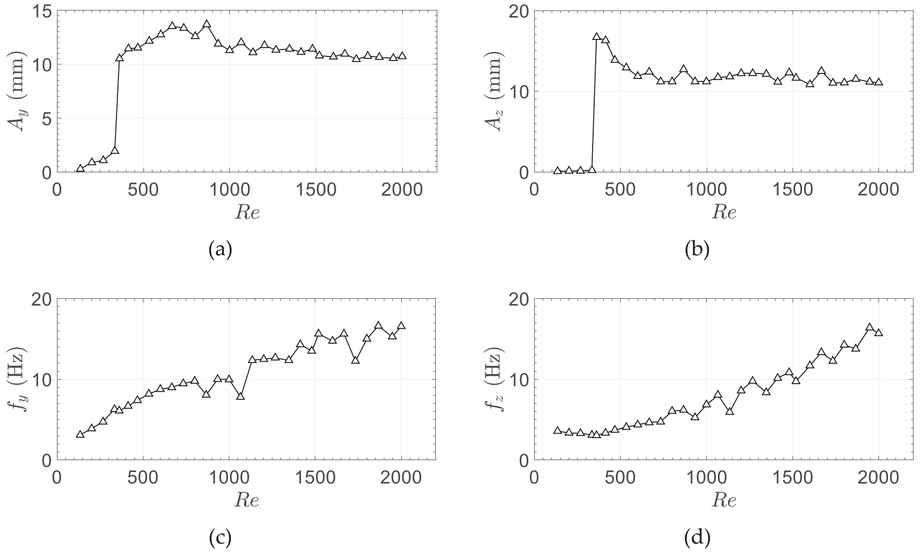

(a) (b)

(c) (d)

Figure 6. Displacements and flapping frequencies measured for Filament 1. (**a**) Displacement in the vertical plane; (**b**) Displacement in the horizontal plane; (**c**) Frequency in the vertical plane; (**d**) Frequency in the horizontal plane.

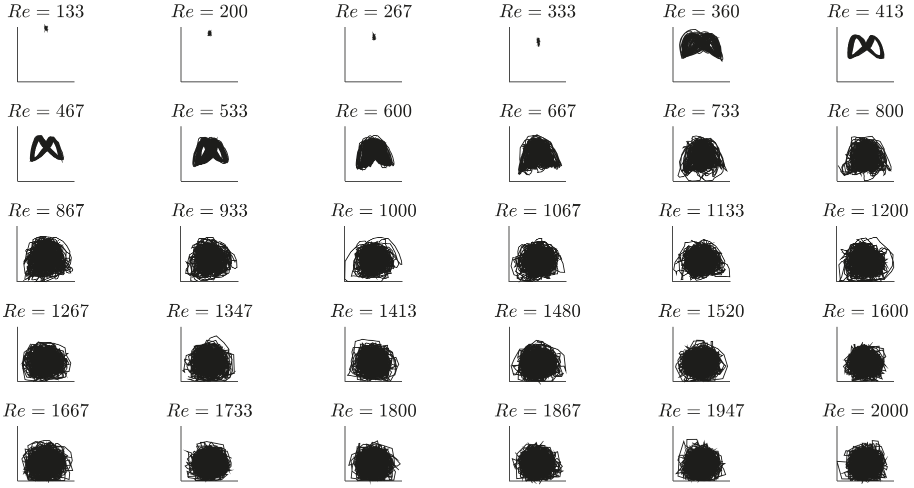

Figure 7. Trajectory of the free-end of Filament 1 as seen by an observer located downstream of the filament and facing the flow (Y-Z plane in Figure 2c).

For Reynolds numbers beyond about $Re = 360$, the filament motion becomes large-amplitude and three-dimensional, with displacements in the horizonal and vertical planes of comparable magnitude. For Reynolds numbers in the range of $413 - 533$, in particular, the autocorrelation function becomes periodic and slowly decaying and the attractor is ring-like, indicating that the filament motion is a large-amplitude limit-cycle oscillation where the filament free-end describes a figure-eight shaped (or ∞-shaped) trajectory.

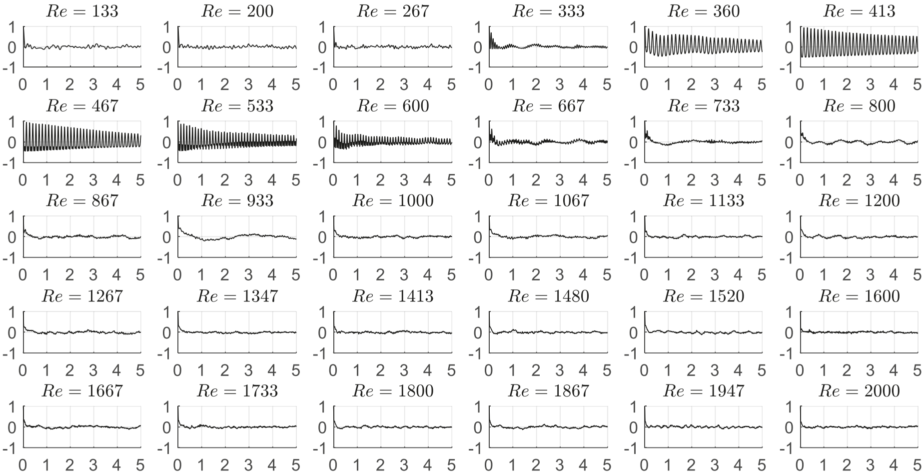

Figure 8. Autocorrelation function of the total displacement of the free-end of Filament 1 at different Reynolds number values (the x-axis scale is in seconds).

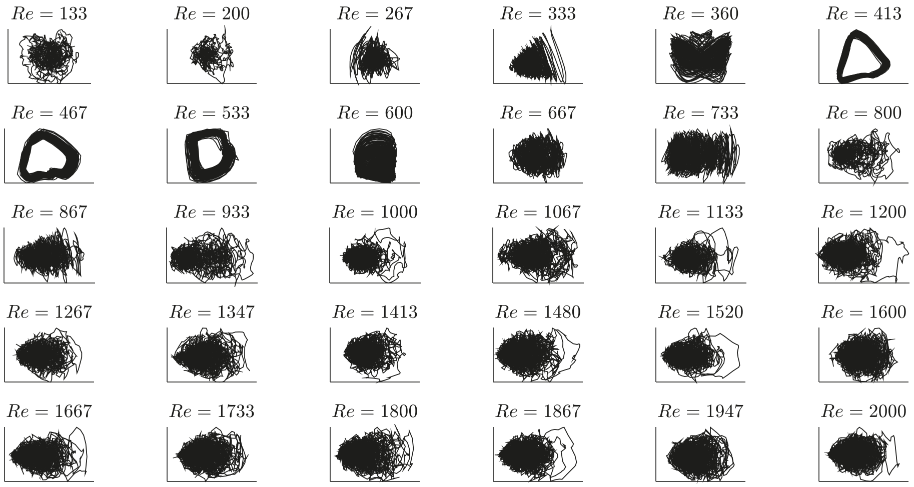

Figure 9. Reconstructed attractor in phase-space for the total displacement of the free-end of Filament 1 at different Reynolds number values.

Notably, the transition from the small-amplitude vibration to the large-amplitude limit-cycle oscillation is gradual and not abrupt: at $Re = 360$ the filament motion is large-amplitude, the autocorrelation function is already periodic and slowly decaying, though the attractor is still blob-like, thus indicating a dynamic intermediate between a small-amplitude vibration and a large-amplitude limit-cycle oscillation. For Reynolds number beyond about $Re = 667$, the filament motion is large-amplitude, the autocorrelation function decays rapidly and the attractor becomes blob-like, indicating a large-amplitude non-periodic oscillation. Again, the transition from large-amplitude limit-cycle oscillation to large-amplitude non-periodic oscillation is gradual, as can be noticed at $Re = 600$ where the autocorrelation function is still periodic and rather slowly decaying, though the attractor is already blob-like. Finally, the dominant frequency of oscillation gradually increases with increasing Reynolds number.

Plots for Filaments 2, 3, 4, and 5 analogous to those for Filament 1 included in Figures 6–9 are provided in the Appendix A. As can be noted, the dynamics of Filaments 2−3 is qualitatively similar to that observed with Filament 1: as the flow velocity gradually increases, the structural response gradually evolves from a small-amplitude vibration to a large-amplitude limit cycle oscillation, and then into a large-amplitude non-periodic motion. With Filaments 4−5, on the other hand, the small-amplitude vibration evolves directly into a large-amplitude non-periodic motion. Whilst with Filament 4 there is a range of Reynolds number values where the large-amplitude oscillation becomes periodic, limit-cycle oscillations are no longer observed with Filament 5. In general, the Reynolds number values where the filament response changes gradually increase with decreasing filament length, indicating that higher flow velocities are required to trigger a change in structural response as the filament gradually shortens.

The Reynolds number range where limit-cycle oscillations are sustained widens when moving from Filament 1 (413–533) to Filament 2 (533–733) and then to Filament 3 (587-960), then contracts with Filament 4 (1053–1333). As previously noted, during limit-cycle oscillation with Filament 1 the filament free-end describes a figure-eight shaped trajectory. This is also the case with Filaments 2 and 3 but only for low Reynolds number values: for high Reynolds numbers the filament motion during limit-cycle oscillation tends to become two-dimensional and confined to the vertical plane. Notably, this is always the case with Filament 4, where the figure-eight shaped trajectory is not observed and limit-cycle oscillations are always two-dimensional.

Finally, the structural response of Filament 6 was reduced to a static deflection, i.e., the Filament 6 deflected, as the flow velocity was gradually increased, always maintaining a static equilibrium configuration. Static deflection angles of Filament 6 are provided in Figure 10 as function of the Reynolds number (the static deflection angle is defined as indicated in the insert in Figure 10).

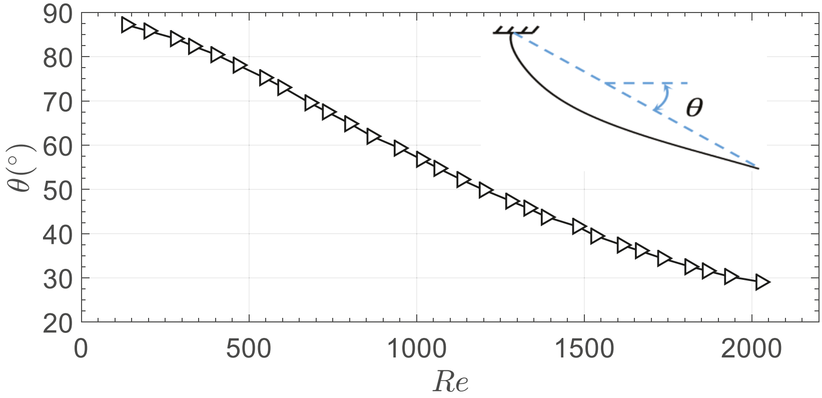

Figure 10. Static deflection angle θ for Filament 6 vs. Reynolds number.

As can be noted in Figure 10, the static deflection angle decreases with increasing Reynolds number following a sigmoidal trend, similarly to previous observations with circular cross-section filaments [42]. The sigmoidal trend of the static deflection angle indicates that the incremental change in inclination gradually decreases, as the flow velocity gradually increases. This trend can be explained by considering that, as the deflection gradually increases, the filament exposes a gradually smaller frontal area to the flow, and consequently becomes gradually more streamlined. A qualitatively similar behavior has been observed with flexible plates [43,44] and flexible vegetation [45].

In order to better compare the structural responses of Filaments 1–5, the measurements are provided in aggregated form in Figure 11, where the displacements and frequencies are presented in dimensionless form as functions of the Reynolds number. The dimensionless displacement, in particular, is defined as follows:

$$A^* = \frac{A}{L} \tag{11}$$

where A is the displacement (in either the horizontal or the vertical plane) and L is the length of the filament (from Table 2). The dimensionless frequency, on the other hand, is defined as follows:

$$f^* = \frac{f}{f_1} \tag{12}$$

where f is the flapping frequency (in either the horizontal or the vertical plane) and f_1 is the mode-1 fundamental frequency of vibration for each filament (from Table 2). As can be seen from the plot of the dimensionless displacement in the vertical direction (A_y^* in Figure 11a), the onset of large-amplitude motion progressively occurs at higher Reynolds numbers as the length of the filament is decreased. The dimensionless displacement then increases as function of Reynolds number and levels off at a certain maximum. This maximum dimensionless displacement is progressively higher as the filament length is decreased. Moreover, it can be noted that, regardless of the Reynolds number for the onset of large-amplitude motion or the amplitude of motion, the dimensionless frequency in the vertical direction (f_y^* in Figure 11c) exhibits a linearly increasing trend as function of the Reynolds number, indicating that at a higher wind speed corresponds a stronger fluid forcing and, therefore, a faster dynamic. As highlighted in Figure 11c, the onset of vibration in the vertical plane occurs at around $f_y/f_1 = 1$, therefore indicating that the filaments start vibrating (in the vertical plane) with a frequency that is comparable with their mode-1 natural vibration frequency. As can be seen from the plot of the dimensionless displacement in the horizontal direction (A_z^* in Figure 11b), the Reynolds number ranges where the filaments motion tends to become two-dimensional and confined to the vertical plane are clearly recognizable. Other than this, the trends in Figure 11b are similar to those observed in Figure 11a, particularly so for Filament 1 whose dynamics is always three-dimensional. Dimensionless frequencies in the horizontal plane (f_z^* in Figure 11d) grow approximately linearly with increasing Reynolds number, similarly to what observed in the vertical plane (Figure 11c). The spikes in dimensionless frequency observed in Figure 11d correspond to harmonics of the lowest peak frequency from the power spectral density, approximately corresponding to double of the lowest peak frequency. Similar to the case of vertical motion, the onset of large-amplitude motion for Filaments 1–3 occur at around $f_z/f_1 = 1$, indicating that these filaments start vibrating also in the horizontal plane with a frequency that is comparable with their mode-1 natural vibration frequency. Notably, for Filaments 4 and 5 the onset of motion is close to $f_z/f_1 = 2$, so that these filaments start vibrating in the horizontal plane with a frequency that is approximately twice their mode-1 natural vibration frequency.

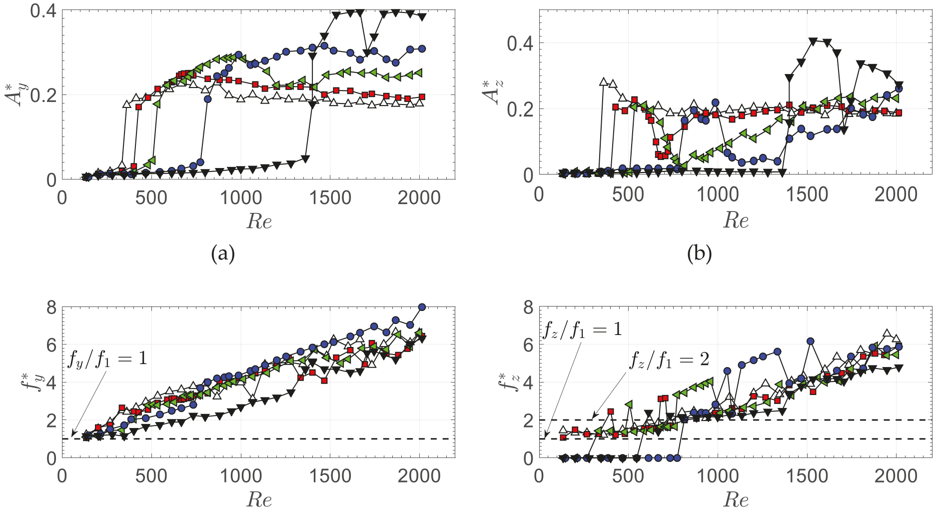

(a) (b) (c) (d)

Figure 11. Dimensionless displacements and frequencies for Filaments 1–5 vs. Reynolds number. (**a**) Dimensionless displacement in the vertical plane; (**b)** Dimensionless displacement in the horizontal plane; (**c**) Dimensionless frequency in the vertical plane; (**d**) Dimensionless frequency in the horizontal plane. Legend: Filament 1 (white △); Filament 2 (red □); Filament 3 (green ◁); Filament 4 (blue ○); Filament 5 (black ▽).

A condensed representation of the observed filaments response is presented in the dynamics map provided in Figure 12a, where the observed filament dynamics is displayed as function of the filament length and Reynolds number, and in the stability map in Figure 12b, where the observed filament dynamics is displayed as function of the Scruton number Sc and reduced velocity U^*:

$$Sc = \frac{2m\zeta_1}{\rho L^2} \tag{13}$$

$$U^* = \frac{U}{f_1 L} \tag{14}$$

where f_1 and ζ_1 are the first-mode natural vibration frequency and damping ratio of the filament (values provided in Table 2). Whilst the Scruton number can be regarded as a dimensionless representation of the filament damping, the reduced velocity be regarded as the ratio of the time-scale of the structural movement to the time-scale of the flow. As noted previously, the natural vibration frequency and the damping ratio of the filaments depend on the filament length. Accordingly, the filament length is used here as the representative linear dimension in place of the filament diameter, which is normally used with cross-flow-induced vibration. Even though the information conveyed by the dynamic map and the stability map in Figure 12 is essentially the same, the former is of more direct use for numerical methods validation, whereas the latter is more frequently used in the fluid-structure interaction literature.

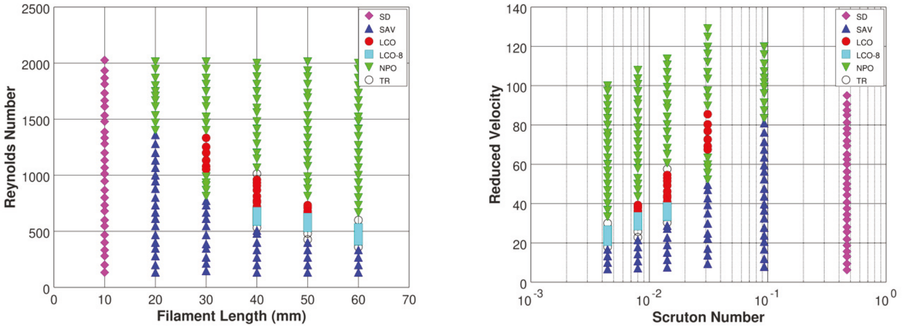

(a) (b)

Figure 12. Condensed representation of the observed structural response of the flexible filaments. (**a**) Dynamic map; (**b**) Stability map. Legend: SD = static deflection; SAV = small-amplitude vibration; LCO = large-amplitude limit-cycle oscillation with two-dimensional trajectory; LCO-8 = large-amplitude limit-cycle oscillation with three-dimensional figure-eight-shaped trajectory; NPO = large-amplitude non-periodic oscillation; TR = transition.

It is evident that the observed filament responses are well separated and clustered in the dynamic and stability maps in Figure 12, thereby indicating that the structural response of the filaments is controlled by the Reynolds number (i.e., by the air flow velocity) and by the length of the filament or, equivalently, by the reduced velocity and Scruton number. The filament length clearly plays a central role in the structural response: as the filament length decreases the damping increases and so does the Scruton number, so that the excitation needed to trigger a transition or sustain a large-amplitude response increases, as it is evident in the corresponding increase of the Reynolds number and reduced velocity. For the shortest Filament 6, in particular, the damping is large enough to suppress any dynamic response within the flow velocity range explored, so that the structural response is reduced to a static deflection. The results highlight the importance of the filament damping ratio, which is modulated by the filament length, as a controlling parameter for the structural response. The importance of the filament length was already noted previously, when discussing the mode-1 natural vibration frequency and damping which also depend on the filament length. Finally, as it is evident from the reduced velocity values in Figure 12b (from about 5 up to about 130), the time-scale of the structure is much bigger than that of the flow, thereby indicating that the flow changes faster than the movement of the filaments. The interaction between the flow and the structure is not one-way, however, because the structural movement is large enough to significantly modify the flow field. The present results are in qualitative agreement with documented observations of flexible filaments of circular cross-section in air flow [32,33]. A notable difference is that the large-amplitude limit-cycle oscillation where the filament free-end describes a figure-eight-shaped trajectory documented here was not observed with circular cross-section filaments, which suggests that reducing the symmetry of the filament cross-section may yield a richer dynamic.

4. Conclusions

We presented results of an experiment specifically designed for the validation of numerical methods for aeroelasticity and FSI problems, and intended to complement and extend available benchmark validation test cases. The experiments were conducted in a wind tunnel, using flexible filaments of rectangular cross-section and varying length whose dynamics was recorded via fast-video imaging. The Reynolds number range covered corresponds to laminar and mildly turbulent flow conditions. The structural response of the filaments is modulated by the Reynolds number (i.e., by the air flow velocity) and by the filament length, and includes: (1) static reconfiguration, (2) small-amplitude vibration, (3) large-amplitude limit-cycle periodic oscillation, and (4) large-amplitude non-periodic motion. The damping of the flexible filaments, which is controlled by the filament length, plays a central role in the structural response. The experimental results presented herein are valuable for the validation of numerical methods for aeroelasticity and, more generally, for fluid-structure interaction applications.

Supplementary Materials: The following are available online at http://www.mdpi.com/2311-5521/5/2/90/s1, Raw wind speed time series (unit m/s) from flow characterization stored in comma-separated value file 'free_stream_raw_data.dat'. Each column of csv file 'free_stream_raw_data.dat' corresponds to a fixed wind speed setting (in m/s). Sampling time: 5 seconds; sampling frequency: 20 kHz.

Author Contributions: Conceptualization, J.S.-L. and A.C.; experiments, J.S.-L.; formal analysis, J.S.-L. and A.C.; writing—original draft preparation, J.S.-L. and A.C.; writing—review and editing, J.S.-L. and A.C. All authors have read and agreed to the published version of the manuscript.

Funding: This research received no external funding.

Acknowledgments: Andrew Kennaugh from the Department of Mechanical, Aerospace and Civil Engineering of the University of Manchester (UK) is gratefully acknowledged for his technical support.

Conflicts of Interest: The authors declare no conflict of interest.

Appendix A

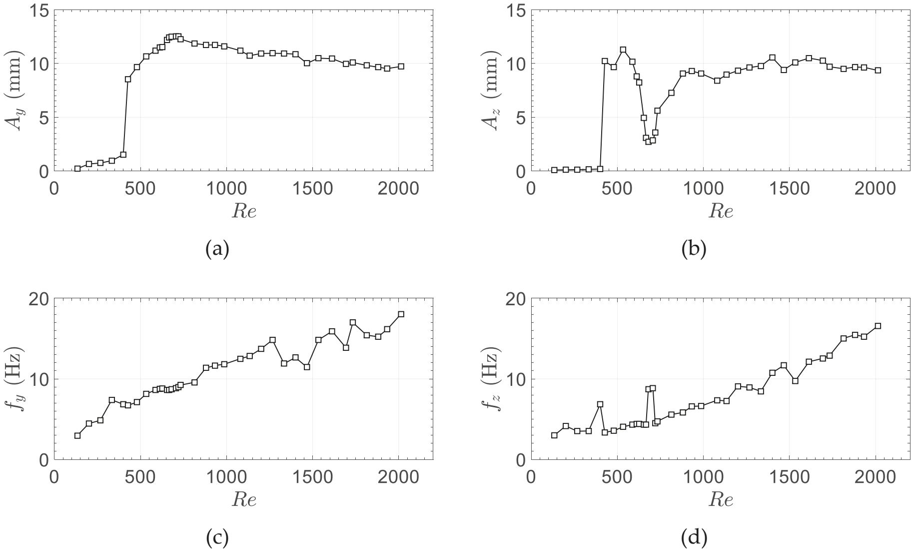

(a) (b)

(c) (d)

Figure A1. Displacements and flapping frequencies measured for Filament 2. (**a**) Displacement in the vertical plane; (**b**) Displacement in the horizontal plane; (**c**) Frequency in the vertical plane; (**d**) Frequency in the horizontal plane.

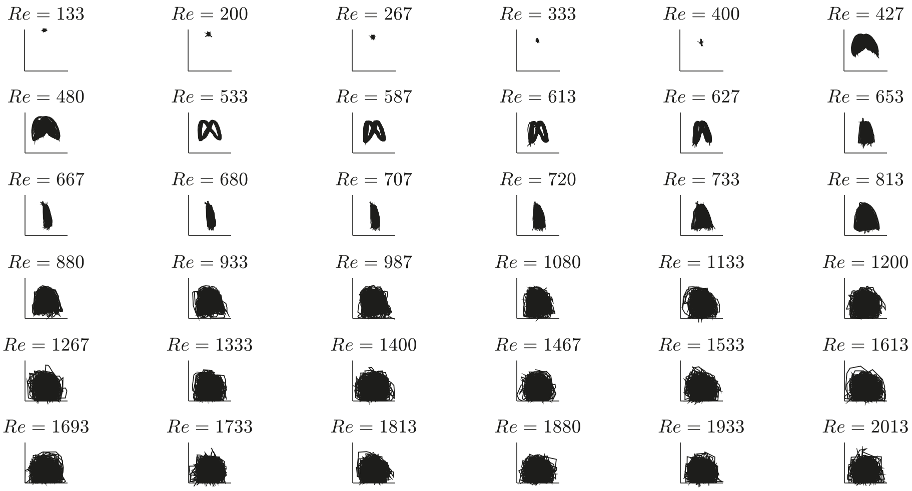

Figure A2. Trajectory of the free-end of Filament 2 as seen by an observer located downstream of the filament and facing the flow (Y-Z plane in Figure 2c).

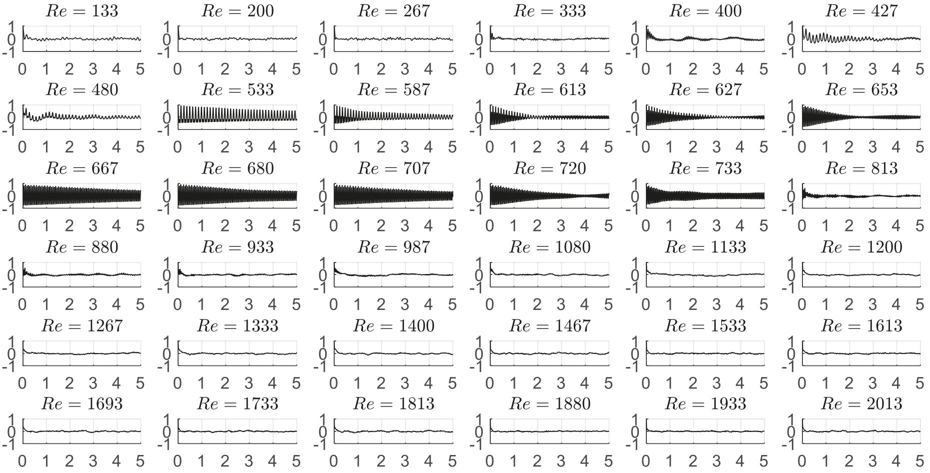

Figure A3. Autocorrelation function of the total displacement of the free-end of Filament 2 at different Reynolds number values (the x-axis scale is in seconds).

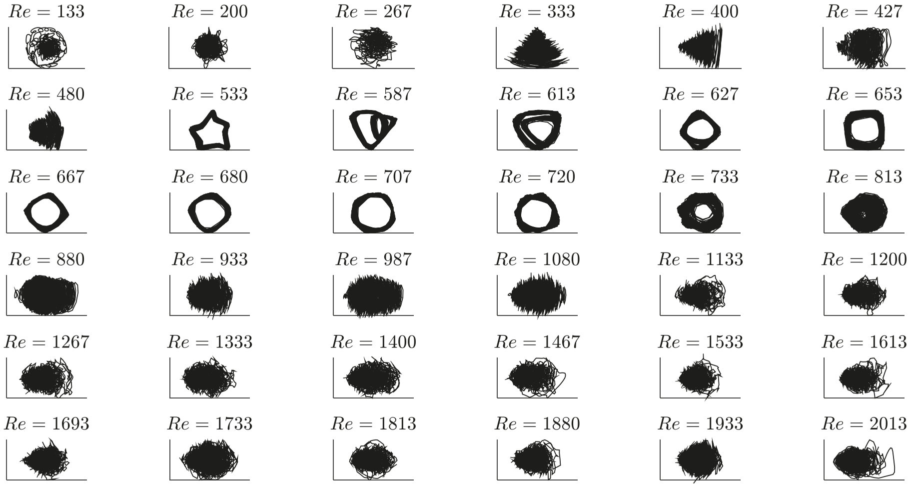

Figure A4. Reconstructed attractor in phase-space for the total displacement of the free-end of Filament 2 at different Reynolds number values.

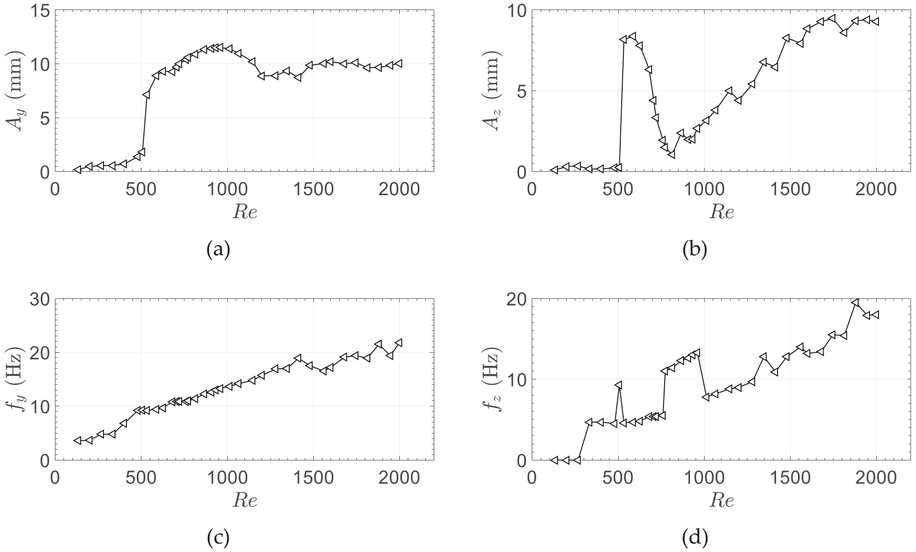

(a) (b)

(c) (d)

Figure A5. Displacements and flapping frequencies measured for Filament 3. (**a**) Displacement in the vertical plane; (**b)** Displacement in the horizontal plane; (**c**) Frequency in the vertical plane; (**d**) Frequency in the horizontal plane.

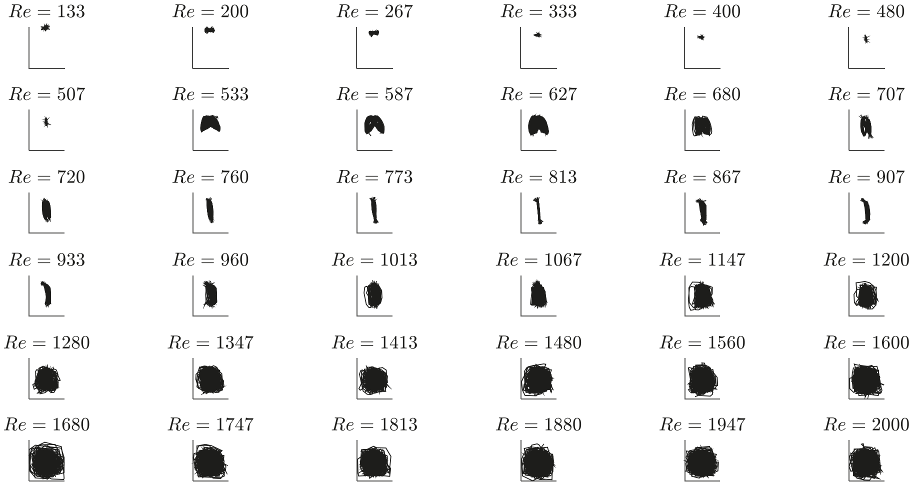

Figure A6. Trajectory of the free-end of Filament 3 as seen by an observer located downstream of the filament and facing the flow (Y-Z plane in Figure 2c).

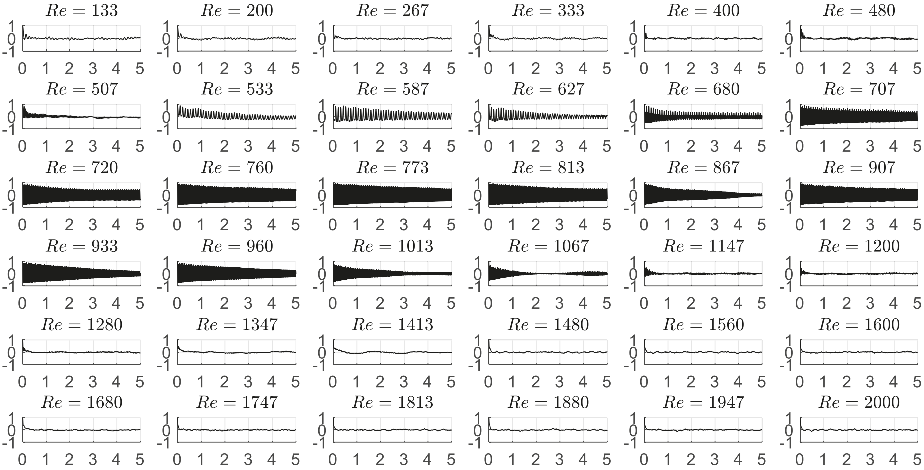

Figure A7. Autocorrelation function of the total displacement of the free-end of Filament 3 at different Reynolds number values (the x-axis scale is in seconds).

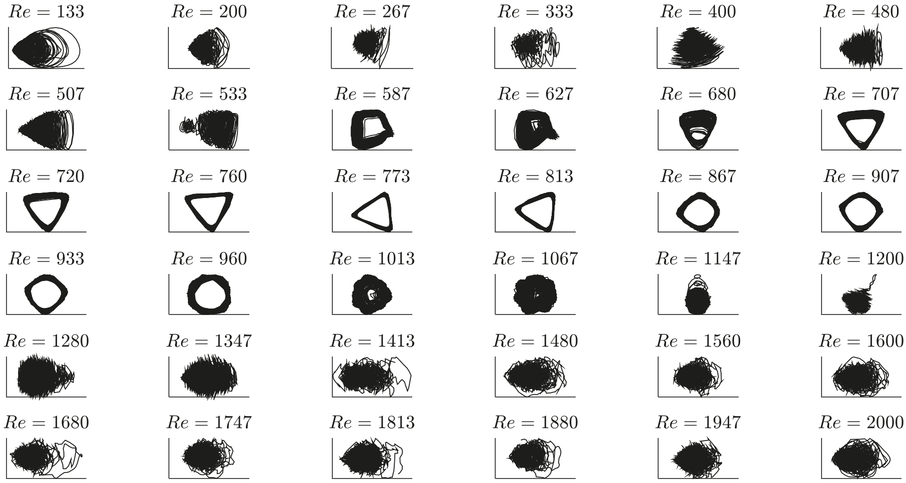

Figure A8. Reconstructed attractor in phase-space for the total displacement of the free-end of Filament 3 at different Reynolds number values.

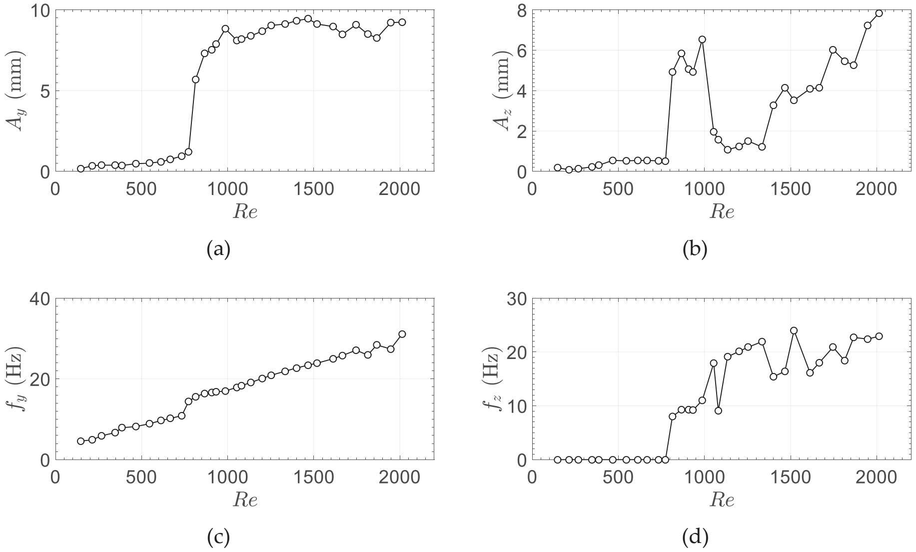

(a) (b)

(c) (d)

Figure A9. Displacements and flapping frequencies measured for Filament 4. (**a**) Displacement in the vertical plane; (**b)** Displacement in the horizontal plane; (**c**) Frequency in the vertical plane; (**d**) Frequency in the horizontal plane.

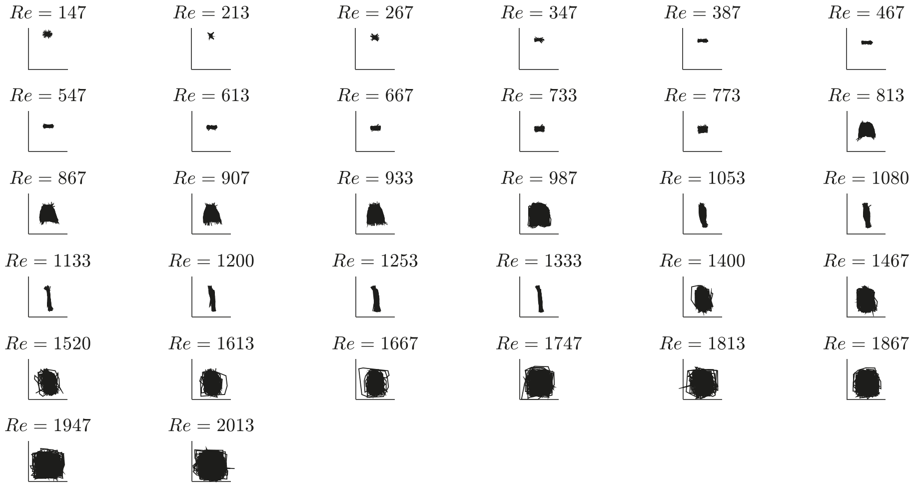

Figure A10. Trajectory of the free-end of Filament 4 as seen by an observer located downstream of the filament and facing the flow (Y-Z plane in Figure 2c).

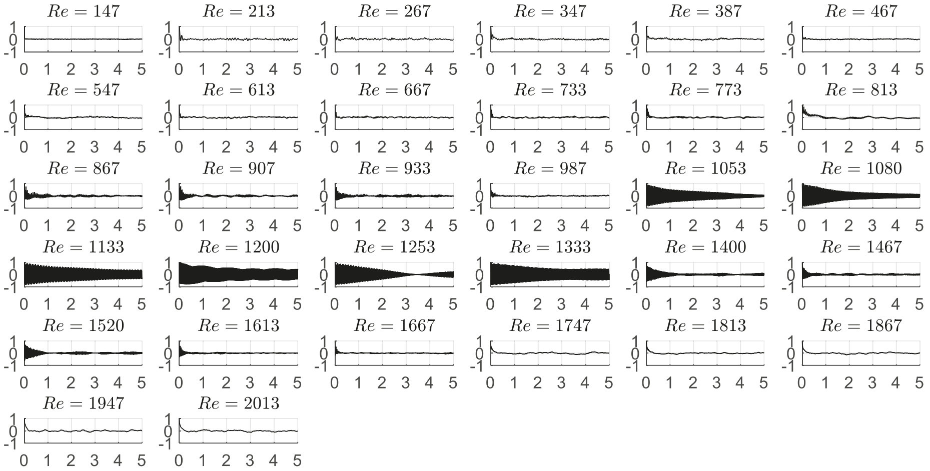

Figure A11. Autocorrelation function of the total displacement of the free-end of Filament 4 at different Reynolds number values (the x-axis scale is in seconds).

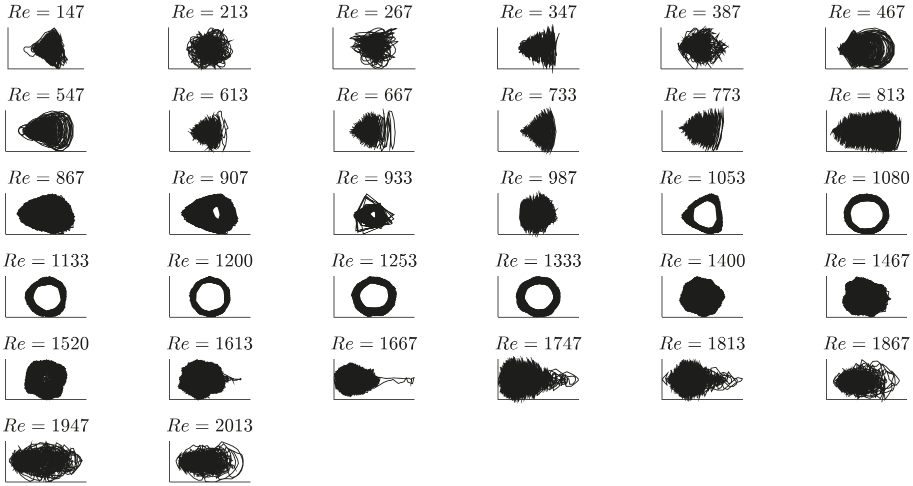

Figure A12. Reconstructed attractor in phase-space for the total displacement of the free-end of Filament 4 at different Reynolds number values.

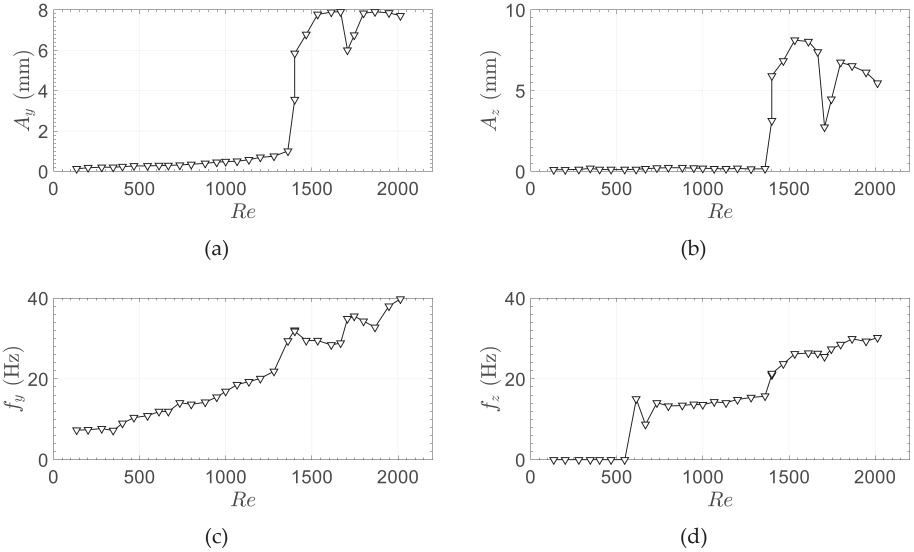

(a) (b)

(c) (d)

Figure A13. Displacements and flapping frequencies measured for Filament 5. (**a**) Displacement in the vertical plane; (**b)** Displacement in the horizontal plane; (**c**) Frequency in the vertical plane; (**d**) Frequency in the horizontal plane.

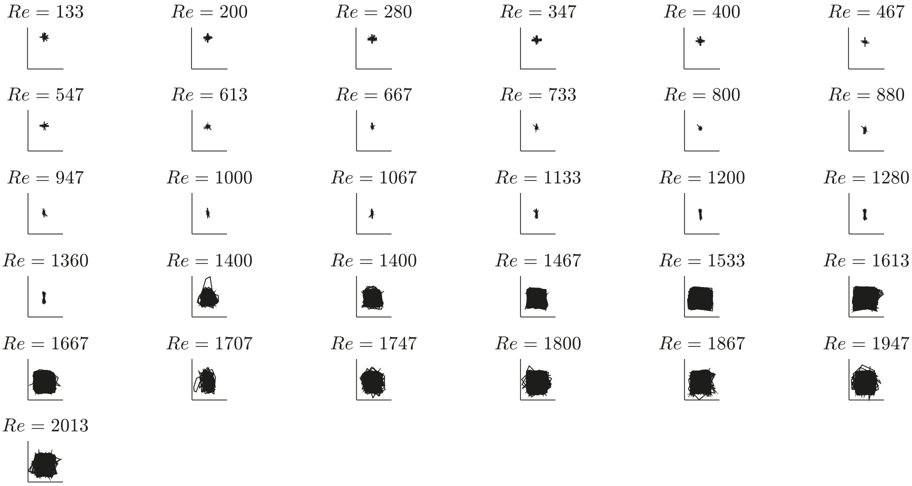

Figure A14. Trajectory of the free-end of Filament 5 as seen by an observer located downstream of the filament and facing the flow (Y-Z plane in Figure 2c).

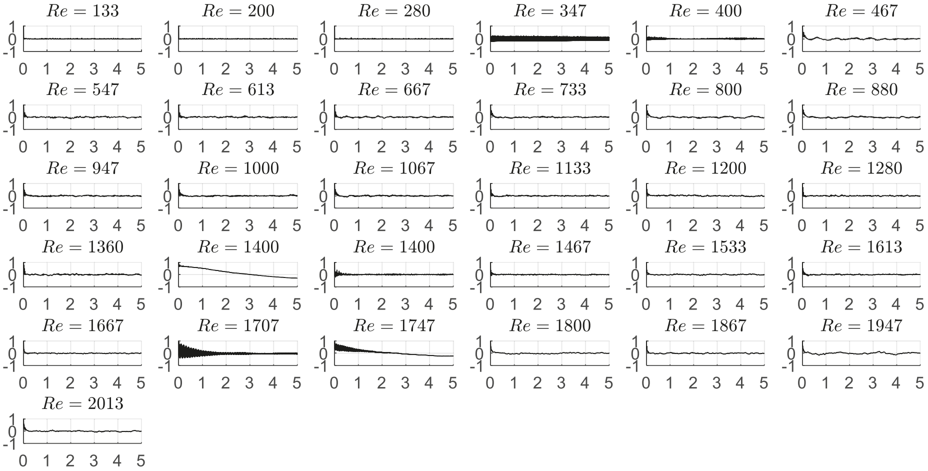

Figure A15. Autocorrelation function of the total displacement of the free-end of Filament 5 at different Reynolds number values (the x-axis scale is in seconds).

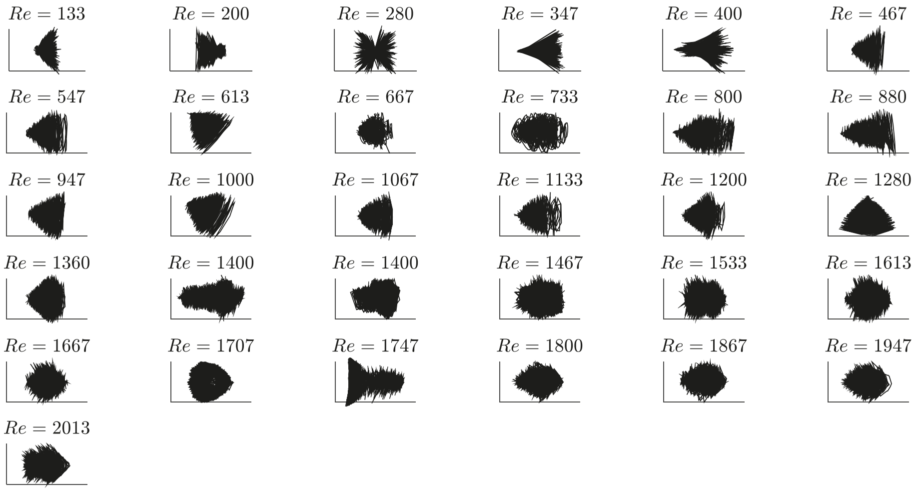

Figure A16. Reconstructed attractor in phase-space for the total displacement of the free-end of Filament 5 at different Reynolds number values.

References

1. Afonso, F.; Vale, J.; Oliveira, É.; Lau, F.; Suleman, A. A review on non-linear aeroelasticity of high aspect-ratio wings. *Prog. Aerosp. Sci.* **2017**, *89*, 40–57. [CrossRef]
2. Jonsson, E.; Riso, C.; Lupp, C.A.; Cesnik, C.E.S.; Martins, J.R.R.A.; Epureanu, B.I. Flutter and post-flutter constraints in aircraft design optimization. *Prog. Aerosp. Sci.* **2019**, *109*, 100537. [CrossRef]
3. Helbling, E.F.; Wood, R.J. A review of propulsion, power, and control architectures for insect-scale flapping-wing vehicles. *Appl. Mech. Rev.* **2018**, *70*, 010801. [CrossRef]
4. Chen, C.; Zhang, T. A review of design and fabrication of the bionic flapping wing micro air vehicle. *Micromachines* **2019**, *10*, 144. [CrossRef] [PubMed]
5. Wu, X.; Shang, X.; Tian, X.; Li, X.; Lu, W. A review on fluid dynamics of flapping foils. *Ocean Eng.* **2020**, *195*, 106712. [CrossRef]
6. Young, Y.L. Fluid-structure interaction analysis of flexible composite marine propellers. *J. Fluid Struct.* **2008**, *24*, 799–818. [CrossRef]
7. Campbell, R.L.; Paterson, E.G. Fluid-structure interaction analysis of flexible turbomachinery. *J. Fluid Struct.* **2011**, *27*, 1376–1391. [CrossRef]
8. Kallekar, L.; Viswanath, C.; Anand, M. Effect of wall flexibility on the deformation during flow in a stenosed coronary artery. *Fluids* **2017**, *2*, 16. [CrossRef]
9. Gilmanov, A.; Barker, A.; Stolarski, H.; Sotiropoulos, F. Image-guided fluid-structure interaction simulation of transvalvular hemodynamics: Quantifying the effects of varying aortic valve leaflet thickness. *Fluids* **2019**, *4*, 119. [CrossRef]
10. Stergiou, Y.G.; Kanaris, A.G.; Mouza, A.A.; Paras, S.V. Fluid-structure interaction in abdominal aortic aneurysms: Effect of haematocrit. *Fluids* **2019**, *4*, 11. [CrossRef]
11. Hirschhorn, M.; Tchatchaleishvili, V.; Stevens, R.; Rossano, J.; Throckmorton, A. Fluid-structure interaction modelling in cardiovascular medicine—A systematic review 2017–2019. *Med. Eng. Phys.* **2020**, *78*, 1–13. [CrossRef] [PubMed]
12. Elgeti, J.; Winkler, R.G.; Gompper, G. Physics of microswimmers—Single particle motion and collective behaviour: A review. *Rep. Prog. Phys.* **2015**, *78*, 056601. [CrossRef] [PubMed]
13. Jeznach, C.; Olson, S.D. Dynamics of swimmers in fluids with resistance. *Fluids* **2020**, *5*, 14. [CrossRef]
14. McCarty, J.M.; Watkins, S.; Deivasigamani, A.; John, S.J. Fluttering energy harvesters in the wind: A review. *J. Sound Vib.* **2016**, *361*, 355–377. [CrossRef]

15. Nabavi, S.; Zhang, L. Portable wind energy harvesters for low-power applications: A survey. *Sensors* **2016**, *16*, 1101. [CrossRef]
16. Hou, G.; Wang, J.; Layton, A. Numerical methods for fluid-structure interaction—A review. *Commun. Comput. Phys.* **2012**, *12*, 337–377. [CrossRef]
17. Borazjani, I. A review of fluid-structure interaction simulations of prosthetic heart valves. *J. Long Term Eff. Med. Implants* **2015**, *25*, 75–93. [CrossRef]
18. Chiang, C.-Y.; Pironneau, O.; Sheu, T.W.H.; Thiriet, M. Numerical study of a 3D Eulerian monolithic formulation for incompressible fluid-structures systems. *Fluids* **2017**, *2*, 34. [CrossRef]
19. Murea, C.M. Three-dimensional simulation of fluid-structure interaction problems using monolithic semi-implicit algorithm. *Fluids* **2019**, *4*, 94. [CrossRef]
20. Bathe, K.J.; Ledezma, G.A. Benchmark problems for incompressible fluid flows with structural interactions. *Comput. Struct.* **2007**, *85*, 628–644. [CrossRef]
21. Küttler, U.; Gee, M.W.; Förster, C.; Comerford, A.; Wall, W.A. Coupling strategies for biomedical fluid-structure interaction problems. *Int. J. Numer. Meth. Eng.* **2009**, *26*, 305–321. [CrossRef]
22. Turek, S.; Hron, J.; Razzaq, M.; Wobker, H.; Schäfer, M. Numerical benchmarking of fluid-structure interaction: A comparison of different discretization and solution approaches. In *Fluid Structure Interaction II, The First International Workshop on Computational Engineering, Herrsching, Germany, October 2009*; Bungartz, H.J., Mehl, M., Schäfer, M., Eds.; Springer: Berlin/Heidelberg, Germany, 2010; pp. 413–424.
23. Fernández, M.A. Coupling schemes for incompressible fluid-structure interaction: Implicit, semi-implicit and explicit. *SeMA J.* **2011**, *55*, 59–108. [CrossRef]
24. Degroote, J. Partitioned simulation of fluid-structure interaction. *Arch. Comput. Methods Eng.* **2013**, *20*, 185–238. [CrossRef]
25. Pereira Gomes, J.; Yigit, S.; Lienhart, H.; Schäfer, M. Experimental and numerical study on a laminar fluid-structure interaction reference test case. *J. Fluids Struct.* **2011**, *27*, 43–61. [CrossRef]
26. Pereira Gomes, J.; Lienhart, H. Fluid-structure interaction-induced oscillations of flexible structures in laminar and turbulent flows. *J. Fluid Mech.* **2013**, *715*, 537–572. [CrossRef]
27. Kalmbach, A.; Breuer, M. Experimental PIV/V3V measurements of vortex-induced fluid-structure interaction in turbulent flow-A new benchmark FSI-PfS-2a. *J. Fluids Struct.* **2013**, *42*, 369–387. [CrossRef]
28. De Nayer, G.; Kalmbach, A.; Breuer, M.; Sicklinger, S.; Wüchner, R. Flow past a cylinder with a flexible splitter plate: A complementary experimental-numerical investigation and a new FSI test case (FSI-PfS-1a). *Comput. Fluids* **2014**, *99*, 18–43. [CrossRef]
29. Hessenthaler, A.; Gaddum, N.R.; Holub, O.; Sinkus, R.; Röhrle, O.; Nordsletten, D. Experiment for validation of fluid-structure interaction models and algorithms. *Int. J. Numer. Meth. Biomed. Eng.* **2017**, *33*, e2848. [CrossRef]
30. Taylor, J.R. *An Introduction to Error Analysis*; University Science Books: Sausalito, CA, USA, 1997.
31. Yong, D. Strings, chains, and ropes. *SIAM Rev.* **2006**, *48*, 771–781. [CrossRef]
32. Silva-Leon, J.; Cioncolini, A.; Filippone, A.; Domingos, M. Flow-induced motions of flexible filaments hanging in cross-flow. *Exp. Therm. Fluid Sci.* **2018**, *97*, 254–269. [CrossRef]
33. Silva-Leon, J.; Cioncolini, A. Modulation of flexible filaments dynamics due to attachment angle relative to the flow. *Exp. Therm. Fluid Sci.* **2019**, *102*, 232–244. [CrossRef]
34. Roach, P.E. The generation of nearly isotropic turbulence by means of grids. *Int. J. Heat Fluid Flow* **1987**, *8*, 82–92. [CrossRef]
35. Blevins, R.D. *Flow-Induced Vibrations*, 2nd ed.; Krieger Publishing Company: Malabar, FL, USA, 2001.
36. Cioncolini, A.; Silva-Leon, J.; Cooper, D.; Quinn, M.K.; Iacovides, H. Axial-flow-induced vibration experiments on cantilevered rods for nuclear reactor applications. *Nucl. Eng. Des.* **2018**, *338*, 102–118. [CrossRef]
37. Cioncolini, A.; Nabawy, M.R.A.; Silva-Leon, J.; O'Connor, J.; Revell, A. An experimental and computational study on inverted flag dynamics for simultaneous wind-solar energy harvesting. *Fluids* **2019**, *4*, 87. [CrossRef]
38. Silva-Leon, J.; Cioncolini, A.; Nabawy, M.R.A.; Revell, A.; Kennaugh, A. Simultaneous wind and solar energy harvesting with inverted flags. *Appl. Energy* **2019**, *239*, 846–858. [CrossRef]
39. Welch, P.D. The use of Fast Fourier Transform for the estimation of power spectra: A method based on time averaging over short, modified periodograms. *IEEE Trans. Audio Electroacoustics* **1967**, *15*, 70–73. [CrossRef]
40. Bradley, E.; Kantz, H. Non-linear time-series analysis revisited. *Chaos* **2015**, *25*, 097610. [CrossRef]

41. Silva-Leon, J.; Cioncolini, A. Effect of inclination on vortex shedding frequency behind a bent cylinder: An experimental study. *Fluids* **2019**, *4*, 100. [CrossRef]
42. Silva-Leon, J.; Cioncolini, A.; Filippone, A. Determination of the normal fluid load on inclined cylinders from optical measurements of the reconfiguration of flexible filaments in flow. *J. Fluid Struct.* **2018**, *76*, 488–505. [CrossRef]
43. Alben, S.; Shelley, M. How flexibility induces streamlining in a two-dimensional flow. *Phys. Fluids* **2004**, *16*, 1694–1713. [CrossRef]
44. Gosselin, F.; De Langre, E.; Machado-Almeida, B.A. Drag reduction of flexible plates by reconfiguration. *J. Fluid Mech.* **2010**, *650*, 319–341. [CrossRef]
45. De Langre, E.; Gutierrez, A.; Cossé, J. On the scaling of drag reduction by reconfiguration in plants. *Comp. Rend. Mech.* **2012**, *340*, 35–40. [CrossRef]

fluids

Article

Scaling of Second-Order Structure Functions in Turbulent Premixed Flames in the Flamelet Combustion Regime

Peter Brearley [1], Umair Ahmed [1], Nilanjan Chakraborty [1] and Markus Klein [2,*]

[1] School of Engineering, Newcastle University, Newcastle-upon-Tyne NE1 7RU, UK;
p.brearley@newcastle.ac.uk (P.B.); umair.ahmed@newcastle.ac.uk (U.A.);
nilanjan.chakraborty@newcastle.ac.uk (N.C.)
[2] Bundeswehr University Munich, Department of Aerospace Engineering, LRT1, Werner-Heisenberg-Weg 39, 85577 Neubiberg, Germany
* Correspondence: markus.klein@unibw.de

Received: 27 April 2020; Accepted: 28 May 2020; Published: 2 June 2020

Abstract: The second-order velocity structure function statistics have been analysed using a DNS database of statistically planar turbulent premixed flames subjected to unburned gas forcing. The flames considered here represent combustion for moderate values of Karlovitz number from the wrinkled flamelets to the thin reaction zones regimes of turbulent premixed combustion. It has been found that the second-order structure functions exhibit the theoretical asymptotic scalings in the dissipative and (relatively short) inertial ranges. However, the constant of proportionality for the theoretical asymptotic variation for the inertial range changes from one case to another, and this value also changes with structure function orientation. The variation of the structure functions for small length scale separation remains proportional to the square of the separation distance. However, the constant of proportionality for the limiting behaviour according to the separation distance square remains significantly different from the theoretical value obtained in isotropic turbulence. The disagreement increases with increasing turbulence intensity. It has been found that turbulent velocity fluctuations within the flame brush remain anisotropic for all cases considered here and this tendency strengthens towards the trailing edge of the flame brush. It indicates that the turbulence models derived based on the assumptions of homogeneous isotropic turbulence may not be fully valid for turbulent premixed flames.

Keywords: structure function; Kolmogorov scaling; premixed turbulent flames; direct numerical simulations

---

1. Introduction

Velocity structure functions (SFs) take a central role in turbulence theory [1–6], where they are mostly used to analyse the scale invariance of fully developed turbulence, characterized by a sequence of scaling exponents [7]. They have been measured up to the eighteenth order [4], primarily to establish the dependence on the order of the inertial range power-law exponent and to deduce information about the energy transfer distribution in the inertial range. Velocity (and scalar) SFs have been considered in a laboratory environment (see [8] for a summary of experimental results in various flow configurations) for a range of Reynolds numbers [8,9], but also for atmospheric shear flows [9] or in astrophysics [10]. Kolmogorov [1] developed his theory of locally homogeneous, isotropic turbulence by analyzing the second-order velocity SFs which forms the basis of many models used to close turbulence, thus second-order SFs play a fundamentally important role in understanding turbulence. Although SFs are widely used in the turbulence community to analyse experimental or numerical data, its application has been limited mostly to the analysis of non-reacting turbulent fluid flows.

The heat release rate due to combustion gives rise to flame normal acceleration and a significant magnitude of mostly positive dilatation rate due to thermal expansion. These effects lead to an augmentation of turbulence intensity within the turbulent premixed flame brush under some conditions, whereas turbulence decays across the flame brush under some other conditions. Furthermore, the flow field in turbulent premixed flames cannot be considered homogeneous and isotropic because of thermal expansion and preferential flow acceleration locally normal to the flame. The theoretical relations derived for homogeneous isotropic non-reacting turbulence are expected to be rendered invalid in premixed turbulent combustion. This suggests that the second-order SF behaviours in turbulent premixed flames can be significantly different from non-reacting flows.

SFs are commonly studied in conjunction with the correlation functions and their energy spectra [2]. Kolmogorov's famous $-5/3$ scaling law for the turbulent kinetic energy spectrum in the inertial range ($E(\kappa) \propto \kappa^{-5/3}$ with $E(\kappa)$ and κ being the turbulent kinetic energy spectrum and wavenumber, respectively) is equivalent to the $2/3$ scaling law for second-order structure functions (i.e., SF $\propto r^{2/3}$ with r being the separation distance) in physical space [1]. Since the turbulence is inherently inhomogeneous in turbulent premixed flames due to density change and preferred directionality associated with flame normal acceleration, the energy spectrum evaluation can be a challenging task. Although density-weighted correlation functions have been proposed [11], there are remaining questions regarding the differences in the turbulent kinetic energy spectrum between turbulent premixed flames and non-reacting flows [11]. As SFs depend only on velocity differences separated by spatial distances and do not rely upon Fourier transform to present the information in the spectral space, they have the potential to be more accessible than energy spectra to analyse turbulent flow structures in premixed turbulent combustion [12–15].

To date, the structure function behaviors in premixed flames have received relatively limited attention [12–15]. Sabelnikov et al. [12,14] analysed second-order SFs for weakly turbulent premixed flames in the corrugated flamelets regime [16] and analysed the SFs conditional upon different events (e.g., two points in reactants, two points in products, two points in the flame, one point in reactants and the other point in products). Recently, Brearley et al. [15] extended the analysis of Sabelnikov et al. [12,14] for flames belonging to the thin reaction zones regime [16] and revealed that the effects of heat release, which play key roles in the wrinkled flamelets regime, survive even for high Karlovitz number conditions in the thin reaction zones regime. In another study, Whitman et al. [13] analysed SFs conditioned on the flame normal and tangential directions for high turbulence intensities representative of high Karlovitz number, thin reaction zones regime combustion and indicated that Kolmogorov-type SF scaling laws might retain some validity in turbulent premixed flames. However, the scaling of the second-order velocity SFs within the flame brush belonging to different regimes of combustion are yet to be analysed in detail, and thus are investigated in this paper. Furthermore, the SF scaling constants for small and moderate separations associated with the inertial range according to Kolmogorov's theory [1] for homogeneous, isotropic turbulence have not yet been evaluated in turbulent premixed flames. Therefore, the differences in statistical behaviours of the second-order SFs in a turbulent premixed flame brush in comparison to the well-known asymptotic behaviours for non-reacting homogeneous isotropic turbulence are of fundamental importance from a modelling perspective, which motivates the current analysis.

A Direct Numerical Simulation (DNS) database [15,17,18] of statistically planar flames ranging from the wrinkled flamelet to thin reaction zone regimes of premixed combustion has been considered for this analysis. The unburned gas turbulence is subject to isotropic forcing, which ensures desired values of both turbulence intensity and integral length scale upstream of the flame.

2. Mathematical Background and Numerical Implementation

The second-order SFs are defined as [2,3]:

$$D_{ij}(\mathbf{x},\mathbf{r},t) = \langle [u_i(\mathbf{x}+\mathbf{r},t) - u_i(\mathbf{x},t)][u_j(\mathbf{x}+\mathbf{r},t) - u_j(\mathbf{x},t)]\rangle \tag{1}$$

where $\mathbf{r}$ is the vector separating the points $\mathbf{x}$ and $\mathbf{x}+\mathbf{r}$ with magnitude $r = |\mathbf{r}|$, t is time and $\langle \dots \rangle$ refers to a suitable averaging operation. Equation (1) signifies the second moment of the velocity difference corresponding with eddies of size r. Numerous expressions can be derived from Eq. (1) for different flow configurations. For example, $D_{ij}(\mathbf{x},\mathbf{r},t)$ is independent of $\mathbf{x}$ in homogeneous turbulence, therefore $D_{ij}(\mathbf{r},t) = 2\langle u'_i u'_j \rangle - R_{ij}(\mathbf{r},t) - R_{ji}(\mathbf{r},t)$ where $u'_i = u_i - \langle u_i \rangle$ is the velocity fluctuation in direction i and $R_{ij}(\mathbf{r},t) = \langle u'_i(\mathbf{x}+\mathbf{r},t) u'_j(\mathbf{x},t) \rangle$ is the two-point correlation tensor. $R_{ij}(\mathbf{r},t)$ approaches zero for $r \gg \ell$, with ℓ being the integral length scale. Consequently, when $r \gg \ell$, $D_{ij} = 2\langle u'_i u'_j \rangle$ in homogeneous turbulence which can be simplified further to $D_{ij} = 2u'^2 \delta_{ij}$ in isotropic turbulence, where $u' = \sqrt{\langle u'_i u'_i \rangle / 3}$. Under homogeneous, incompressible turbulence, $D_{ij}(r,t)$ can be expressed completely in terms of the longitudinal SF $D_{LL}(r,t) = \langle [\mathbf{u}_L(\mathbf{x}+\mathbf{r},t) - \mathbf{u}_L(\mathbf{x},t)]^2 \rangle$ as $D_{ij}(r,t) = D_{TT}(r,t)\delta_{ij} + [D_{LL}(r,t) - D_{TT}(r,t)] r_i r_j / r^2$, where the transverse SF $D_{TT}(r,t) = \langle [\mathbf{u}_T(\mathbf{x} + \mathbf{r},t) - \mathbf{u}_T(\mathbf{x},t)]^2 \rangle$ for homogeneous, incompressible turbulence is given by $D_{TT}(r,t) = D_{LL}(r,t) + 0.5r[\partial D_{LL}(r,t)/\partial r]$, where $\mathbf{u}_L = (\mathbf{u} \cdot \mathbf{r})\mathbf{r}/r^2$ is the component of the velocity in the direction of $\mathbf{r}$, and $\mathbf{u}_T = \mathbf{u} - \mathbf{u}_L$ is the velocity vector normal to $\mathbf{r}$. According to Kolmogorov's inertial range theory [1], one obtains $D_{LL}(r,t) = C_L \langle \varepsilon r \rangle^{2/3}$ and $D_{TT}(\mathbf{r},t) = 4D_{LL}(\mathbf{r},t)/3$ for $\eta < r < \ell$, with the universal constant $C_L \approx 2.0$ [2]. The kinetic energy dissipation rate is $\varepsilon = \mu(\partial u_i/\partial x_j)(\partial u_i/\partial x_j)/\rho$, with μ and ρ being dynamic viscosity and density, respectively.

In premixed flames, the velocity field cannot be regarded as statistically homogeneous or isotropic and the assumption of incompressibility is invalid. Thus, it is not straightforward to have one-to-one correspondence between the correlation functions and second-order SFs in premixed flames. However, it is worthwhile to consider the relations based on non-reacting homogeneous isotropic turbulence so that it can be ascertained if $D_{LL}(\mathbf{r},t)/\langle \varepsilon r \rangle^{2/3}$ and $D_{TT}(\mathbf{r},t)/\langle \varepsilon r \rangle^{2/3}$ remain independent of r for $\eta < r < \ell$ where $\eta = [\mu^3/\rho^3 \langle \varepsilon \rangle]^{1/4}$ is the Kolmogorov length scale. Furthermore, it is important to evaluate if the ratios $D_{LL}(\mathbf{r},t)/\langle \varepsilon r \rangle^{2/3}$ and $D_{TT}(\mathbf{r},t)/\langle \varepsilon r \rangle^{2/3}$ are equal to C_L and $4C_L/3$ according to Kolmogorov's theory [1] in turbulent reacting flows. For small separation distances (i.e., $r < \eta$), one obtains $D_{ij} \propto (\partial u_i/\partial x_k)(\partial u_j/\partial x_l) r_k r_l$, which implies that $D_{LL} = C'_L[\rho\langle \varepsilon \rangle/\mu] r^2$ and $D_{TT} = 2C'_L[\rho\langle \varepsilon \rangle/\mu] r^2$ with $C'_L = 1/15$ for homogeneous isotropic turbulence [1,2].

The simulations comprising the current DNS database have been carried out using the well-known DNS code SENGA+ [19]. The simulation configuration consists of inlet and outlet boundaries in the direction of mean flame propagation, with the transverse boundaries being periodic. A tenth-order finite difference scheme has been used to calculate the spatial derivatives for the internal grid points. The scheme gradually reduces to second-order and one-sided at the non-periodic boundaries. An explicit, third-order Runge-Kutta scheme has been used for time advancement. The mean inlet velocity U_{mean} has been gradually adjusted to match the turbulent flame speed for each case so the flame remains statistically stationary within the computational domain. The turbulent flame speed values are provided elsewhere [17] for this database and thus are not repeated here. The outflow boundary is assumed to be partially non-reflecting. Table 1 shows, from left to right, the root-mean-square turbulent velocity fluctuation in the unburned mixture normalised by the unperturbed laminar flame speed u'/S_L, the integral length scale normalised by thermal flame thickness ℓ/δ_{th}, the Damköhler number $Da = \ell S_L/u'\delta_{th}$, the Karlovitz number $Ka = (u'/S_L)^{3/2}(\ell/\delta_{th})^{-1/2}$, the heat release parameter $\tau = (T_{ad} - T_0)/T_0$, the physical size of the domain in terms of the flame thickness, the equidistant Cartesian grid used for discretization and finally, the corresponding regime of premixed combustion. In these equations, $\delta_{th} = (T_{ad} - T_0)/\max|\nabla T|_L$ is the thermal flame thickness with T_{ad}, T_0 and T being the adiabatic flame temperature, the unburned gas temperature and dimensional temperature respectively. The Cartesian grid provides at least 10 grid points within δ_{th} and 1.5 grid points within the Kolmogorov length scale η for all cases. The turbulence intensity u'/S_L and integral length scale ℓ/δ_{th} are maintained upstream of the flame using a modified bandwidth filtered physical space forcing method [20]. The cases considered in this analysis range from the wrinkled flamelet regime to the thin reaction zones regime, as shown in the Borghi-Peters diagram in Figure 1 [16]. In the present analysis, the chemical reaction is simplified by a single-step

Arrhenius type reaction for the purpose of computational economy. As the analysis focuses on the velocity statistics, the simplification related to the chemical reaction is not expected to play a major role. This follows from the fact that the fluid velocity is affected by thermal expansion arising from heat release, and not by the intermediate steps of a chemical reaction. For example, the enstrophy transport characteristics obtained from simplified chemistry DNS [21,22] of turbulent premixed flames have been found to be qualitatively consistent with detailed chemistry results [23,24]. Thus, the findings regarding the SF statistics are likely to be qualitatively valid in the presence of detailed chemistry and transport. The Lewis number of all the species is taken to be unity and the specific heat of all the species is considered to be identical for the purpose of simplicity. These assumptions do not alter the qualitative nature of the heat release characteristics in turbulent premixed flames [25,26] and the SF statistics are unlikely to be affected by these assumptions. The reaction progress variable is defined using the suitably normalised reactant mass fraction Y_R by $c = (Y_{R0} - Y_R)/(Y_{R0} - Y_{R\infty})$, where the subscripts 0 and ∞ refer to the quantity in the unburned and burned mixture, respectively. The simulations were continued until the turbulent kinetic energy k, integral length scale ℓ, turbulent flame speed S_T and flame surface area A_T reach statistically stationary values. This duration was found to be longer than the throughpass time (i.e., $t_{\text{sim}} > L_x/U_{\text{mean}}$) and 10 eddy turn over times (i.e., $t_{\text{sim}} > 10\ell/u'$) for each case. The contours of c for the DNS database considered have been provided elsewhere [17,18] and are not repeated here.

Table 1. The properties of the DNS database considered in this analysis.

Case	u'/S_L	ℓ/δ_{th}	Da	Ka	τ	Domain	Grid	Regime
A	1.0	3.0	3.00	0.577	4.5	$79.5\delta_{th} \times (39.8\delta_{th})^2$	800×400^2	wrinkled flamelets
B	2.5	3.0	1.20	2.28	4.5	$79.5\delta_{th} \times (39.8\delta_{th})^2$	800×400^2	corrugated flamelets
C	5.0	3.0	0.600	6.45	4.5	$79.5\delta_{th} \times (39.8\delta_{th})^2$	800×400^2	thin reaction zones
D	7.5	3.0	0.400	11.9	4.5	$79.5\delta_{th} \times (39.8\delta_{th})^2$	800×400^2	thin reaction zones
E	10	3.0	0.300	18.3	4.5	$79.5\delta_{th} \times (39.8\delta_{th})^2$	800×400^2	thin reaction zones

In the case of statistically planar flames, the mean direction of propagation is parallel with the x_1-direction (right to left). This results in the x_2–x_3 plane at a given x_1 location to be statistically homogeneous. Thus, the analysis of the SFs has been limited to two sets of two points $\mathbf{x}_A = \{x_{AB}, y_A, z_A\}$ and $\mathbf{x}_B = \{x_{AB}, y_A+r_y, z_A+r_z\}$. These points are located on the same transverse plane with coordinate x_{AB} separated by the distance vector $\mathbf{r} = \{0, r_y, r_z\}$. The transverse SF $D_{11,T}(r)$ is calculated by considering $(u_{B,1} - u_{A,1})^2$ and for two set of points given by $\mathbf{x}_A = \{x, y, z\}$; $\mathbf{x}_B = \{x, y+r, z\}$ and by $\mathbf{x}_A = \{x, y, z\}$; $\mathbf{x}_B = \{x, y, z+r\}$. The transverse SFs $D_{22,T}(r)$ and $D_{33,T}(r)$ are evaluated by considering $(u_{B,2} - u_{A,2})^2$ and $(u_{B',3} - u_{A',3})^2$ respectively based on points $\mathbf{x}_A = \{x, y, z\}$; $\mathbf{x}_B = \{x, y, z+r\}$ and $\mathbf{x}_{A'} = \{x, y, z\}$; $\mathbf{x}_{B'} = \{x, y+r, z\}$, respectively. Here, the notation $u_{B,1}$ signifies the velocity component u_1 at point $\mathbf{x}_B$. Finally, the longitudinal SFs $D_{22,L}(r)$ and $D_{33,L}(r)$ are calculated by evaluating $(u_{B,2} - u_{A,2})^2$ and $(u_{B',3} - u_{A',3})^2$ respectively based on points $\mathbf{x}_A = \{x, y, z\}$; $\mathbf{x}_B = \{x, y+r, z\}$ and $\mathbf{x}_{A'} = \{x, y, z\}$; $\mathbf{x}_{B'} = \{x, y, z+r\}$. This analysis considers $D_{23,T}(r) = 0.5[D_{22,T}(r) + D_{33,T}(r)]$ and $D_{23,L}(r) = 0.5[D_{22,L}(r) + D_{33,L}(r)]$ to account for the small departure from isotropy in the homogeneous directions (not to be confused with the cross-SF based on u_2 and u_3).

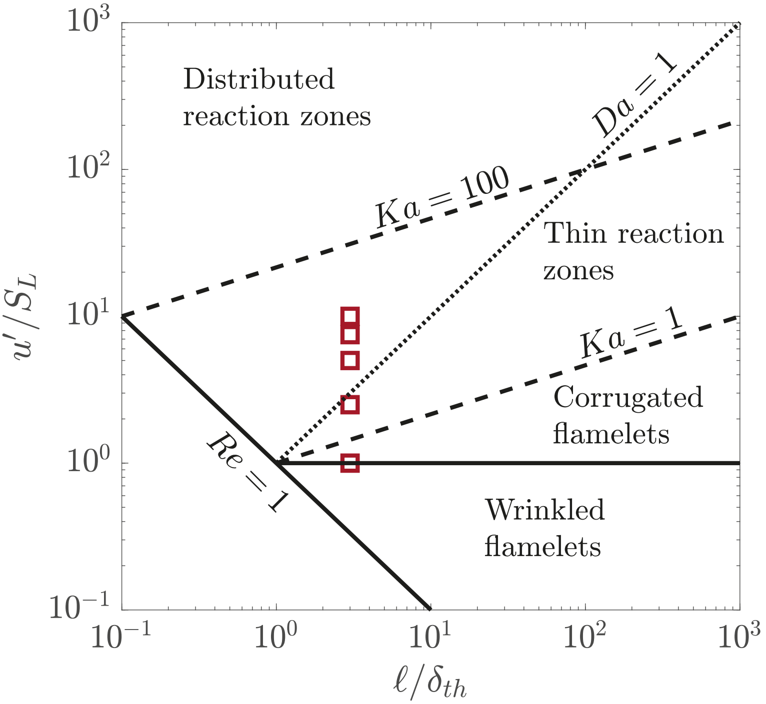

Figure 1. The cases considered in this analysis on a Borghi-Peters diagram.

3. Results and Discussion

The variations of $\{D_{11,T}/(\tau S_L)^2\}(r/\delta_{th})^{-2/3}$, $\{D_{23,T}/(\tau S_L)^2\}(r/\delta_{th})^{-2/3}$ and $\{D_{23,L}/(\tau S_L)^2\}(r/\delta_{th})^{-2/3}$ for all cases at the spatial location corresponding to the Reynolds averaged reaction progress variable $\overline{c} = 0.5$ (where the overbar suggests a Reynolds averaging operation) are exemplarily shown in Figure 2a–c respectively, where the SFs are conditionally averaged on bins of reaction progress variable c for one of the points (i.e., $\mathbf{x}_B$ or $\mathbf{x}_{B'}$) in question. This suggests that the samples associated with small values of c in Figure 2 correspond to the events where $\mathbf{x}_B$ or $\mathbf{x}_{B'}$ is in reactants (e.g., $c \leq 0.05$) and $\mathbf{x}_A$ or $\mathbf{x}_{A'}$ might be either in reactants or in products (e.g., $c \geq 0.95$) or in the flame (e.g., $0.05 < c < 0.95$). Similarly, large values of c in Figure 2a–c include samples from the events where $\mathbf{x}_B$ or $\mathbf{x}_{B'}$ is in the products and $\mathbf{x}_A$ or $\mathbf{x}_{A'}$ might be either in reactants or in products or within the flame.

The lines corresponding to the Kolmogorov scaling (i.e., $\{D_{11,T}/(\tau S_L)^2\}(r/\delta_{th})^{-2/3} = (4C_L/3)\widetilde{\varepsilon}^{2/3}\delta_{th}^{2/3}/(\tau S_L)^2$, $\{D_{23,T}/(\tau S_L)^2\}(r/\delta_{th})^{-2/3} = (4C_L/3)\widetilde{\varepsilon}^{2/3}\delta_{th}^{2/3}/(\tau S_L)^2$ and $\{D_{23,L}/(\tau S_L)^2\}(r/\delta_{th})^{-2/3} = C_L\widetilde{\varepsilon}^{2/3}\delta_{th}^{2/3}/(\tau S_L)^2$ and the limiting condition for small separation distances (i.e., $\{D_{11,T}/(\tau S_L)^2\}(r/\delta_{th})^{-2/3} = (2C_L')\overline{\rho}\widetilde{\varepsilon}\delta_{th}^{2/3}r^{4/3}/\mu(\tau S_L)^2$, $\{D_{23,T}/(\tau S_L)^2\}(r/\delta_{th})^{-2/3} = (2C_L')\overline{\rho}\widetilde{\varepsilon}\delta_{th}^{2/3}r^{4/3}/\mu(\tau S_L)^2$ and $\{D_{23,L}/(\tau S_L)^2\}(r/\delta_{th})^{-2/3} = C_L'\overline{\rho}\widetilde{\varepsilon}\delta_{th}^{2/3}r^{4/3}/\mu(\tau S_L)^2$ are shown by black dash and grey dash-dot lines, respectively. The qualitative behaviours of the SFs for other $\overline{c}$ values remain similar and thus are not shown for the sake of brevity.

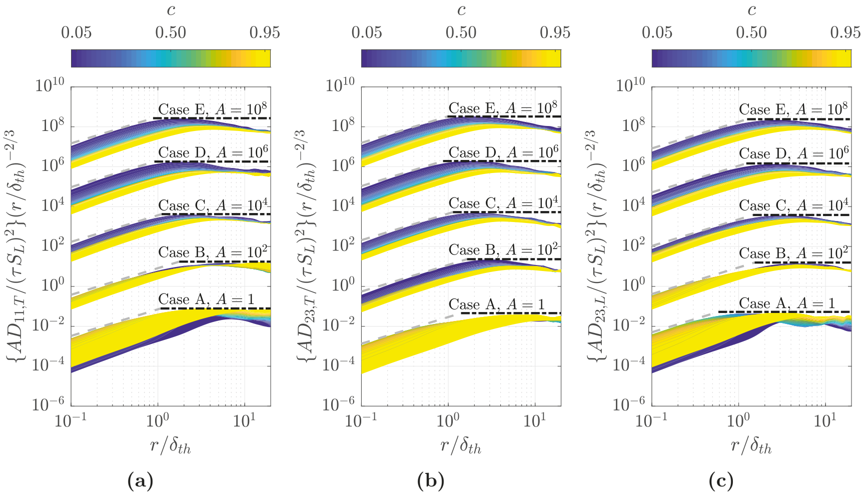

Figure 2. Variations of $\{AD_{11,T}/(\tau S_L)^2\}(r/\delta_{th})^{-2/3}$, $\{AD_{23,T}/(\tau S_L)^2\}(r/\delta_{th})^{-2/3}$ and $\{AD_{23,L}/(\tau S_L)^2\}(r/\delta_{th})^{-2/3}$ (**a**–**c**) with r/δ_{th} for cases A–E (from bottom to top) at $\bar{c} = 0.5$ where $A = 1$, 10^2, 10^4, 10^6 and 10^8 for cases A–E respectively. The analytic r^2 scaling and the Kolmogorov scaling $r^{2/3}$ are shown by grey dashed lines and black dash-dot lines respectively and the constants of proportionality used for these lines are shown in Figure 5. The colour bar indicates the values of c for one of the points (i.e., $\mathbf{x}_B$ or $\mathbf{x}_{B'}$) in question for the given value of $\bar{c}$. The coefficient A is introduced for the convenience of presentation.

Figure 2 shows that the peak value of the SFs $\{D_{ij}/(\tau S_L)^2\}(r/\delta_{th})^{-2/3}$ is obtained around $r/\delta_{th} \approx 2.0$–$4.0$ for all cases considered here. As expected, $\{D_{11,T}/(\tau S_L)^2\}(r/\delta_{th})^{-2/3}$, $\{D_{23,T}/(\tau S_L)^2\}(r/\delta_{th})^{-2/3}$ and $\{D_{23,L}/(\tau S_L)^2\}(r/\delta_{th})^{-2/3}$ all deviate from the Kolmogorov scaling, indicated by a plateau, for separation distances $r/\delta_{th} > \ell/\delta_{th}$, whereas for small separation distances these SFs exhibit reasonable agreement with a $D_{ij} \propto r^2$ scaling. The departure of the structure functions from the Kolmogorov scaling for the inertial range is not clearly visible in the previous results by Whitman et al. [13] due to a limited range of r/δ_{th} values. Note that Whitman et al. [13] considered the SF behaviours in the local normal and tangential directions of flamelets, whereas this analysis focuses on the SFs in the normal and tangential directions of the mean flame brush. It has been demonstrated elsewhere [23,27] that the relative strength of thermal expansion due to chemical heat release diminishes with increasing Karlovitz number, especially for high Karlovitz number within the thin reaction zones and the distributed reaction zones regimes of turbulent premixed combustion. Furthermore, turbulence forcing was used for the whole of the domain in Ref. [13], whereas in this analysis the forcing term is proportional to $(1 - c)$ [20] to allow for the evolution of turbulence across the flame without the interference of numerical forcing. Despite these differences, the SFs, in particular, for cases C–E are in good agreement with the results presented in [13].

Note that substantial departures from the Kolmogorov scaling have been found previously even for non-reacting flows due to internal intermittency especially for low turbulent Reynolds numbers [5,28–30]. In order to better understand the observations made from Figure 2, the variations of Favre-averaged turbulent kinetic energy $\widetilde{k} = \overline{\rho u_i'' u_i''}/2\bar{\rho}$ normalised by its value at $\bar{c} = 0.001$ (representing the leading edge of the flame brush) are shown for cases A–E as functions of Reynolds-averaged reaction progress variable $\bar{c}$ in Figure 3. The values of $\widetilde{k}_{\bar{c}=0.001}/S_L^2$ are provided in Table 2 for the purpose of quantitative comparison between the different cases. Figure 3 shows that $\widetilde{k}$ increases significantly from the leading edge and decays only close to the trailing edge of the flame brush in case A, whereas the augmentation of $\widetilde{k}$ from the leading edge of the flame brush in cases B and C is followed by a decay before another increasing trend is observed in the region of the flame brush where the effects of chemical reaction and heat release are significant (i.e., where the probability of finding $0.5 \leq c \leq 0.9$ remains significant) before turbulence decays towards the product side of the flame brush. The augmentation of $\widetilde{k}$ in the region of the flame brush where the effects of heat release are significant weakens progressively from case B to case C. The turbulent kinetic energy decays monotonically from the leading edge to the trailing edge of the flame brush in cases D and E. The observations from Figure 3 indicate that turbulence is sustained for the major part of the flame brush and it gets locally augmented within some parts of the flame brush in cases A, B and C in decreasing order, whereas turbulence decays across the flame brush in cases D and E. Moreover, Figure 2a–c reveal that the mean values of the SFs attain high levels for high values of c for cases A and B, whereas cases C–E show the greatest value is attained at low values of c. These results agree with those by Whitman et al. [13]. While the SFs seem to be ordered according to the value of c for cases C–E, some SFs with different c value cross each other for case A. This general behaviour can be deduced from the longitudinal SF $D_{11,L}$ of a laminar 1D flame, as shown in Figure 4, and by noting that the local flame normal is not aligned with the mean direction of flame propagation in Figure 2a–c, such that for example $D_{11,T}$ contains samples of the longitudinal 1D SF. Figure 4 shows that for small separation distances, the magnitude of $D_{11,L}$ increases with increasing c before attaining a maximum around $c \approx 0.5$. Moreover, some of the SFs starting from a higher value of c intercept the SFs starting from a lower value of c. Finally, it is noted that case A with a low u'/S_L belongs to the wrinkled flamelet regime and case B shows a behaviour in-between case A and cases C–E. For $r/\delta_{th} \gg \ell/\delta_{th}$, the ordering of all SF magnitudes for all cases is in agreement with the approximation $D_{ij} = 2\langle u_i' u_j' \rangle$ [15] together with the increasing, respectively decreasing, trends of $\widetilde{k}$ as reported in Figure 3. The inertial range plateau in cases A and B extends to higher values of r/δ_{th}, presumably caused by the relatively strong effects of heat release and the associated elongation of flow structures.

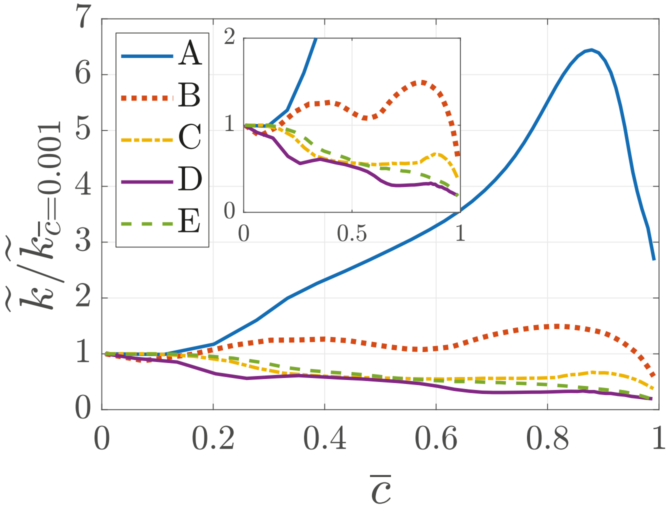

Figure 3. Variations of $\widetilde{k}$ normalised by its value at $\bar{c} = 0.001$ with $\bar{c}$ for cases A–E.

Table 2. Values of $\widetilde{k}_{\bar{c}=0.001}/S_L^2$ and $\widetilde{\varepsilon}_{\bar{c}=0.001}\delta_{th}/S_L^3$ for cases A–E.

Case	$\widetilde{k}_{\bar{c}=0.001}/S_L^2$	$\widetilde{\varepsilon}_{\bar{c}=0.001}\delta_{th}/S_L^3$
A	0.727	0.132
B	6.31	4.18
C	20.0	54.5
D	87.0	209
E	124	356

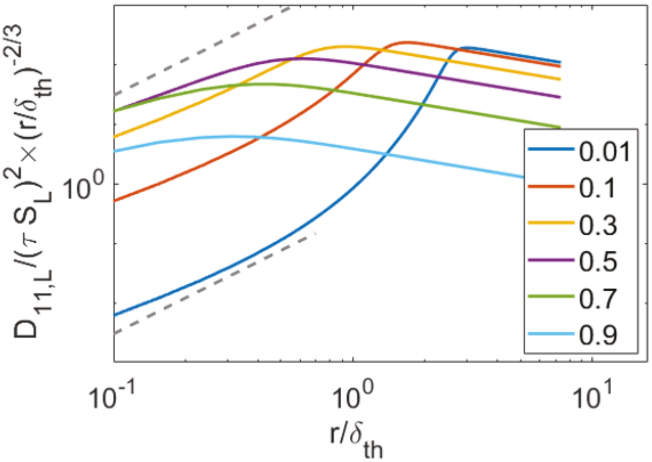

Figure 4. Variations $\{D_{11,L}/(\tau S_L)^2\}(r/\delta_{th})^{-2/3}$ with r/δ_{th} for a laminar 1D flame for SFs starting from different c values. The analytic r^2 scaling is shown by grey dashed lines.

The variation of the proportionality parameters (i.e., $C_L = \{3D_{11,T}/4\}(\tilde{\varepsilon}r)^{-2/3}, C'_L = \{D_{11,T}\mu/2\overline{\rho}\tilde{\varepsilon}\}(r)^{-2}$; $C_L = \{3D_{23,T}/4\}(\tilde{\varepsilon}r)^{-2/3}$, $C'_L = \{D_{23,T}\mu/2\overline{\rho}\tilde{\varepsilon}\}(r)^{-2}$ and $C_L = \{D_{23,L}\}(\tilde{\varepsilon}r)^{-2/3}$, $C'_L = \{D_{23,L}\mu/\overline{\rho}\tilde{\varepsilon}\}(r)^{-2}$) corresponding to the dash and dash-dot lines showing the limiting behaviours in Figure 2 for cases A–E are shown in Figure 5, which indicates that both C_L and C'_L values are different for $D_{11,T}$, $D_{23,T}$ and $D_{23,L}$, and these values change from one case to another. However, for all cases C_L remains of the order of 1.5 (which is close to the theoretical value of 2.0), whereas C'_L remains significantly smaller than $1/15$ for all cases considered here and C'_L decreases from case A to case E. The departures from Kolmogorov scaling can be explained in the following manner. The Kolmogorov scaling is applicable for homogeneous isotropic turbulence in the inertial range. However, the inertial range possibly is not fully observed for these cases because of the moderate values of turbulent Reynolds number and the isotropy is disturbed by the flow acceleration within the flame. In addition to that, the dissipation rate $\tilde{\varepsilon}$ variation within these flames is significantly affected by the heat release, which can be substantiated from Figure 6 where the variations of $\tilde{\varepsilon}$ normalised by its value at $\overline{c} = 0.001$ representing the leading edge of the flame brush are shown for cases A–E as functions of $\overline{c}$. The values of $\tilde{\varepsilon}_{\overline{c}=0.001}\delta_{th}/S_L^3$ are also provided in Table 2 for the purpose of quantitative comparison. A comparison between Figures 3 and 6 reveals that the variation of $\tilde{\varepsilon}$ within the flame brush is qualitatively similar to that of $\tilde{k}$. This suggests that the thermal expansion within the flame brush has a significant influence on $\tilde{\varepsilon}$, which is absent in the classical turbulence theory by Kolmogrorov [1]. Furthermore, the nature of the underlying flow within the flame brush can be characterised with the help of the Lumley triangle [2]. The Lumley triangles for the limiting cases A and E are exemplarily shown in Figure 7 where ξ and η are given by

$$6\xi^3 = b_{ij}b_{jk}b_{ki}; \quad 6\eta^2 = b_{ij}b_{ji} \tag{2}$$

where $b_{ij} = \widetilde{u''_i u''_j}/2\tilde{k} - \delta_{ij}/3$ is the normalised Reynolds stress anisotropy tensor. Figure 7 shows that the underlying turbulence within the flame brush is anisotropic for cases A and E, with cases B, C and D following the same trend. Though, the extent of anisotropy in the unburned gas side of the flame brush decreases with increasing u'/S_L. However, turbulence becomes anisotropic for all cases within the flame brush, and this tendency strengthens with increasing $\overline{c}$ within the flame brush. This indicates that the limiting conditions based on homogeneous isotropic turbulence may not be applicable for the second-order SFs within the flame brush for moderate values of Ka. This also indicates that the assumption of isotropy is rendered invalid in the modelling for turbulent premixed flames for moderate values of Karlovitz number. This is consistent with recent findings in the context of the closures of sub-grid scalar flux [31] and stresses [18,32] in turbulent premixed combustion.

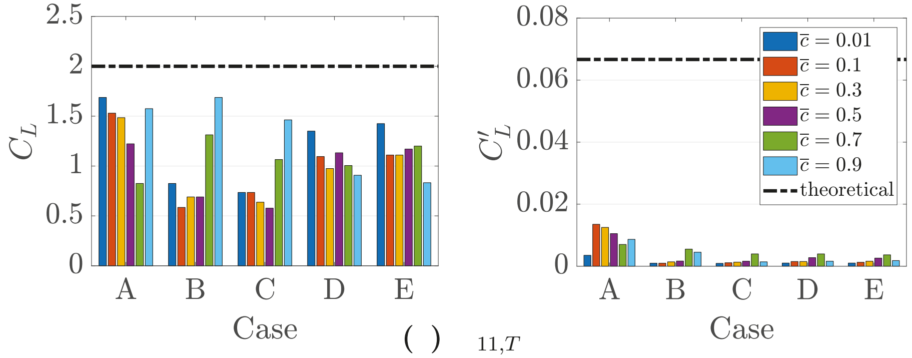

( ) $_{11,T}$

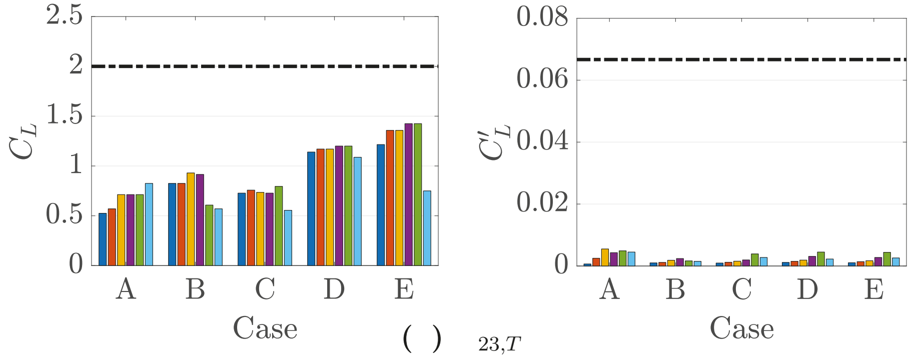

( ) $_{23,T}$

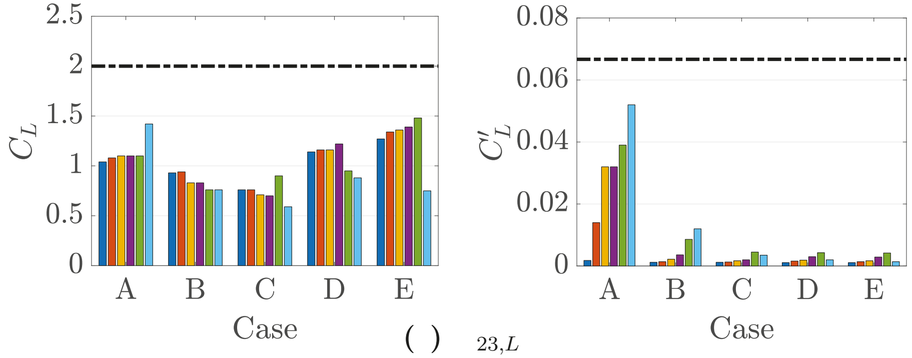

( ) $_{23,L}$

Figure 5. Variations of the proportionality parameters (i.e., $C_L = \{3D_{11,T}/4\}(\widetilde{\varepsilon}r)^{-2/3}$,$C'_L = \{D_{11,T}\mu/2\overline{\rho}\widetilde{\varepsilon}\}(r)^{-2}$; $C_L = \{3D_{23,T}/4\}(\widetilde{\varepsilon}r)^{-2/3}$, $C'_L = \{D_{23,T}\mu/2\overline{\rho}\widetilde{\varepsilon}\}(r)^{-2}$ and $C_L = \{D_{23,L}\}(\widetilde{\varepsilon}r)^{-2/3}$, $C'_L = \{D_{23,L}\mu/\overline{\rho}\widetilde{\varepsilon}\}(r)^{-2}$) for cases A–E for (a) $D_{11,T}$, (b) $D_{23,T}$, (c) $D_{23,L}$, respectively. The horizontal lines show the asymptotic values based on Kolmogorov scaling (i.e., $C_L = 2.0$) and homogeneous isotropic turbulence (i.e., $C'_L = 1/15$) assumption for C_L and C'_L, respectively.

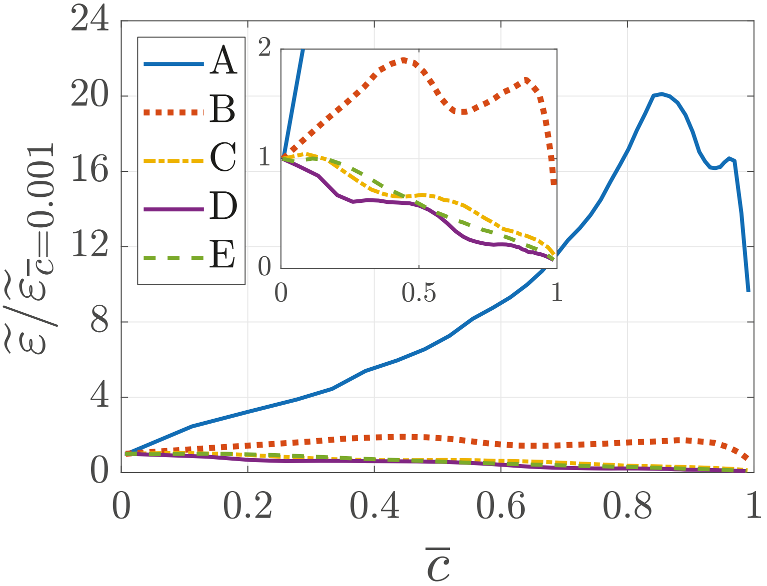

Figure 6. Variations of normalised $\widetilde{\varepsilon}$ normalised by its value at $\bar{c}\ = 0.001$ with $\bar{c}$ for cases A–E.

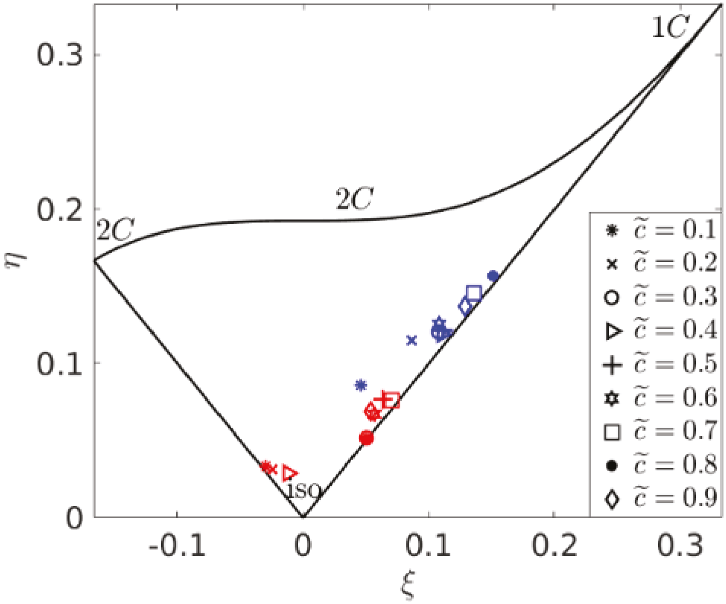

Figure 7. Lumley triangle on the plane of the invariants ξ and η of the Reynolds stress anisotropy tensor for case A (blue) and E (red) for different values of $\bar{c}$. $1C$, $2C$ and iso are the one component limit, two component limit and isotropic respectively.

4. Conclusions

The statistical behaviours of second-order velocity SFs have been analysed based on a DNS database of statistically planar turbulent premixed flames. The simulation parameters have been chosen such that the cases considered here span from the wrinkled flamelets to the thin reaction zones regimes of turbulent premixed combustion. The second-order SFs for these flames show, especially for high values of turbulence, the theoretical scalings but considerable departures from the expected constants of proportionality. These departures of the constants are more prominent in the flames with higher values of u'/S_L among the cases considered here. Moreover, the constant of proportionality $C_L = D_{ij}\langle\widetilde{\varepsilon}r\rangle^{-2/3}$ for the theoretical asymptotic (i.e., $D_{ij} \propto \langle\widetilde{\varepsilon}r\rangle^{2/3}$) variation changes from one case to another although it has roughly the correct order of magnitude. For short separation distances, the second-order velocity SFs have been found to be proportional to r^2 (i.e. $D_{ij}\propto r^2$) but the constants of proportionality $C_L' = \{D_{ij}\mu/\overline{\rho}\widetilde{\varepsilon}\}(r)^{-2}$ are significantly smaller than $1/15$, which is obtained based on the assumption of homogeneous isotropic turbulence. It has been demonstrated based on the Lumley triangle that the underlying turbulent flow within the flame brush is highly anisotropic for all cases within the flame brush and this tendency strengthens with increasing $\bar{c}$ within the flame brush. This indicates that the assumptions of homogeneous isotropic turbulence may not be accurate for turbulent combustion modelling for moderate values of Karlovitz number.

The present analysis has been carried out with simple chemistry and molecular transport. Although these assumptions are unlikely to alter the qualitative nature of the findings, further investigations in the presence of detailed chemistry and transport will be necessary for a more comprehensive understanding of the SF statistics in turbulent premixed flames.

Author Contributions: Conceptualization, P.B., U.A., N.C. and M.K.; methodology, P.B., U.A. and N.C.; formal analysis, P.B., U.A. and N.C.; writing—original draft preparation, N.C., P.B. and M.K.; writing—review and editing, U.A. and N.C.; supervision, N.C.; funding acquisition, N.C. All authors have read and agreed to the published version of the manuscript.

Funding: This research was funded by the Engineering and Physical Sciences Research Council, grant number EP/R029369/1.

Acknowledgments: The authors are grateful to the Archer and Rocket HPC services for computational support

Conflicts of Interest: The authors declare no conflict of interest.

References

1. Kolmogorov, A.N. The local structure of turbulence in incompressible viscous fluid for very large Reynolds number. *Dokl. Akad. Nauk SSSR* **1941**, *30*, 299–303.
2. Pope, S.B. *Turbulent Flows*; Cambridge University Press: Cambridge, UK, 2000.
3. Frisch, U. *The Legacy of A. N. Kolmogorov*; Cambridge University Press: Cambridge, UK, 1995.
4. Anselmet, F.; Gagne, Y.; Hopfinger, E.J.; Antonia, R.A. High-order velocity structure functions in turbulent shear flows. *J. Fluid Mech.* **1984**, *140*, 63–89. [CrossRef]
5. Sreenivasan, K.R.; Antonia, R. The phenomenology of small scale turbulence. *Annu. Rev. Fluid Mech.* **1997**, *29*, 435–472. [CrossRef]
6. Lohse, D.; Xia, K.-Q. Small-Scale Properties of Turbulent Rayleigh-Bénard Convection. *Annu. Rev. Fluid Mech.* **2010**, *42*, 335–364. [CrossRef]
7. Huang, Y.X.; Schmitt; F.G.; Lu, Z.M.; Fougairolles, P.; Gagne, Y.; Liu, Y.L. Second-order structure function in fully developed turbulence. *Phys. Rev. E* **2010**, *82*, 026319. [CrossRef]
8. Arneodo, A.; Baudet, C.; Belin, F.; Benzi, R.; Castaing, B.; Chabaud, B.; Chavarria, R.; Ciliberto, S.; Camussi, R.; Chillà, F.; et al. Structure functions in turbulence, in various flow configurations, at Reynolds number between 30 and 5000, using extended self-similarity. *Europhys. Lett.* **1996**, *34*, 411–416. [CrossRef]
9. Antonia, R.A.; Satyaprakash, B.R.; Chambers, A.J. Reynolds number dependence of velocity structure functions in turbulent shear flows *Phys. Fluids* **1982**, *25*, 29–37.
10. Heyer, M.H.; Brunt, C.M. The Universality of Turbulence in Galactic Molecular Clouds. *Astrophys. J.* **2004**, *615*, L45–L48. [CrossRef]
11. Kolla, H.; Hawkes, E. R.; Kerstein, A.R.; Swaminathan, N; Chen, J.H. On velocity and reactive scalar spectra in turbulent premixed flames. *J. Fluid Mech.* **2014**, *754*, 456–487. [CrossRef]

12. Sabelnikov, V.A.; Lipatnikov, A.N.; Nishiki, S.; Hasegawa, T. Application of conditioned structure functions to exploring influence of premixed combustion on two-point turbulence statistics. *Proc. Combust. Inst.* **2019**, *37*, 2433–2441. [CrossRef]
13. Whitman, S.H.R.; Towery, C.A.Z.; Poludnenko, A.Y.; Hamlington, P.E. Scaling and collapse of conditional velocity structure functions in turbulent premixed flames. *Proc. Combust. Inst.* **2019**, *37*, 2427–2435. [CrossRef]
14. Sabelnikov, V.A.; Lipatnikov, A.N.; Nishiki, S.; Hasegawa, T. Investigation of the influence of combustion-induced thermal expansion on two-point turbulence statistics using conditioned structure functions. *J. Fluid. Mech.* **2019**, *867*, 45–76. [CrossRef]
15. Brearley, P.; Ahmed, U.; Chakraborty, N.; Lipatnikov, A. N. Statistical behaviours of conditioned two-point second-order structure functions in turbulent premixed flames in different combustion regimes. *Phys. Fluids* **2019**, *31*, 115109. [CrossRef]
16. Peters, N. *Turbulent Combustion*; Cambridge University Press: Cambridge, UK, 2000.
17. Ahmed, U.; Chakraborty, N.; Klein, M. Insights into the bending effect in premixed turbulent combustion using the Flame Surface Density transport. *Combust. Sci. Technol.* **2019**, *191*, 898–920. [CrossRef]
18. Ahmed, U.; Chakraborty, N.; Klein, M. On the stress-strain alignment in premixed turbulent flames. *Sci. Rep.* **2019**, *9*, 5092. [CrossRef] [PubMed]
19. Jenkins, K. W.; Cant, R. S. Direct numerical simulation of turbulent flame kernels. In *Recent Advances in DNS and LES: Proceedings of the Second AFOSR Conference, Rutgers, New Brunswick, NJ, USA, 7–9 June 1999*; Springer: Berlin/Heidelberg, Germany, 1999; pp. 191–202.
20. Klein, M.; Chakraborty, N.; Ketterl, S. A comparison of strategies for direct numerical simulation of turbulence chemistry interaction in generic planar turbulent premixed flames. *Flow Turbul. Combust.* **2017**, *99*, 955–971. [CrossRef]
21. Chakraborty, N.; Konstantinou, I.; Lipatnikov, A. Effects of Lewis number on vorticity and enstrophy transport in turbulent premixed flames. *Phys. Fluids* **2016**, *28*, 015109. [CrossRef]
22. Doan, N.A.K.; Swaminathan, N.; Chakraborty, N. Multiscale analysis of turbulence-flame interaction in premixed flames. *Proc. Combust. Inst.* **2017**, *36*, 1929–1935. [CrossRef]
23. Papapostolou, V.; Wacks, D.H.; Klein, M.; Chakraborty, N.; Im, H.G. Enstrophy transport conditional on local flow topologies in different regimes of premixed turbulent combustion. *Sci. Rep.* **2017**, *7*, 11545. [CrossRef]
24. Ahmed, U.; Doan, N.A.K.; Lai., J.; Klein, M.; Chakraborty, N.; Swaminathan, N. Multiscale analysis of head-on quenching premixed turbulent flames. *Phys. Fluids* **2018**, *30*, 105102. [CrossRef]
25. Poinsot, T.; Echekki, T.; Mungal, M.G. A study of the laminar flame tip and implications for premixed turbulent combustion. *Combust. Sci. Technol.* **1992**, *81*, 45–73. [CrossRef]
26. Louch, D.S.; Bray, K.N.C. Vorticity in unsteady premixed flames: Vortex pair–premixed flame interactions under imposed body forces and various degrees of heat release and laminar flame thickness. *Combust. Flame* **2001**, *125*, 1279–1309. [CrossRef]
27. Wacks, D.H.; Chakraborty, N.; Klein, M.; Arias, P.G; Im, H.G. Flow topologies in different regimes of premixed turbulent combustion: A direct numerical simulation analysis. *Phys. Rev. Fluids* **2016**, *1*, 083401. [CrossRef]
28. Kolmogorov, A.N. A refinement of previous hypotheses concerning the local structure of turbulence in a viscous incompressible fluid at high Reynolds number. *J. Fluid Mech.* **1962**, *13*, 82–85. [CrossRef]
29. Cao, N.; Chen, S.; Sreenivasan, K. R. Scaling of low-order structure functions in homogeneous turbulence. *Phys. Rev. Lett.* **1996**, *77*, 3799–3802. [CrossRef]
30. Antonia, R.A.; Djenidi, L.; Danaila, L.; Tang, S.L. Small scale turbulence and the finite Reynolds number effect. *Phys. Fluids* **2017**, *29*, 020715. [CrossRef]
31. Klein, M.; Kasten, C.; Chakraborty, N.; Gao, Y.; A-priori Direct Numerical Simulation assessment of sub-grid scale stress tensor closures for turbulent premixed combustion. *Comp. Fluids* **2015**, *122*, 1–11. [CrossRef]
32. Klein, M.; Kasten, C.; Chakraborty, N.; Mukhadivev, N.; Im, H.G. Turbulent scalar fluxes in Hydrogen-Air premixed flames at low and high Karlovitz numbers. *Combust. Theor. Model.* **2018**, *22*, 1–16. [CrossRef]

fluids

Article

Numerical Study of the Magnetic Damping Effect on the Sloshing of Liquid Oxygen in a Propellant Tank

Yutaro Furuichi *,† and Toshio Tagawa

Department of Aeronautics and Astronautics, Tokyo Metropolitan University, Hino, Tokyo 191-0065, Japan; tagawa-toshio@tmu.ac.jp
* Correspondence: furuichi@aero.t.u-tokyo.ac.jp; Tel.: +81-90-3735-4211
† Current address: Department of Aeronautics and Astronautics, The University of Tokyo, Bunkyo-ku, Tokyo 113-8656, Japan.

Received: 27 April 2020; Accepted: 28 May 2020; Published: 1 June 2020

Abstract: Nowadays, the use of baffle plates is anticipated to be one of potential devices used to dampen the sloshing of propellant in rocket tanks. However, some of previous studies reported that the use of a baffle plate may cause larger pressure fluctuations in the tank. In this study, aiming at damping the sloshing without a baffle plate, we paid attention to the characteristic that liquid oxygen is paramagnetic and numerically investigated damping effect of a magnetic field when liquid oxygen sloshing occurs. An incompressible gas–liquid two-phase flow of gaseous oxygen and liquid oxygen was assumed in a spherical spacecraft tank with a diameter of 1 m in a non-gravitational field, and a triangular impact force was assumed to be imposed as the excitation force. In addition, an electric circular coil was placed outside the spherical tank to generate a static magnetic field. For the sake of simplicity, the effect of heat was not taken into consideration. As a result of computation, the sloshing was damped to a certain extent when the magnetic flux density at the coil center was 1.0 T, and a sufficient damping effect was obtained by setting it to 3.0 T. In fact, it is anticipated that less than 3.0 T is sufficient if the coil is placed on the tank surface. This may contribute to damping of the movement of the center of gravity of a spacecraft and prevention of mixing of ullage gas into the piping.

Keywords: sloshing; magnetizing force; liquid oxygen; fuel tank; computation

---

1. Introduction

In a dynamic acceleration environment caused by changes in the thrust and attitude of a spacecraft, the liquid with a free surface in the propellant tank oscillates violently. This phenomenon is called sloshing. Besides, the pressure inside the tank and the center of gravity of the spacecraft fluctuate. Because the propellant occupies most of the weight of the spacecraft, the fluctuation of the center of gravity due to the sloshing adversely affects the attitude control, and there is a risk of misfiring or malfunction [1,2]. Furthermore, when very low temperature liquid and relatively high temperature gas coexist inside of the tank, heat exchange and phase change between gas and liquid are promoted by the sloshing, and the tank pressure drops quickly, resulting in a unstable supply of propellant and in a cavitation at an entry of a turbopump [3–5]. There is another risk that the thrust control becomes difficult. One of the potential tools to prevent the sloshing is to use a device called baffle plate, which is installed inside the tank. Research on baffle plates has been carried out since the 1960s [6], and the optimal shape of the baffle plate is still being studied vigorously [7–9]. However, according to several previous studies, the baffle plate can suppress the kinematic fluctuation of the liquid surface during the sloshing in a tank, but it cannot necessarily suppress the thermal fluctuation occurring between the gas and the liquid phases. The pressure fluctuation in the tank with a baffle plate may be greater than that without a baffle plate [10]. The other previous study reports that the reason for this is that the liquid phase becomes turbulent due to the inner edge of the baffle plate and the temperature stratification is disrupted. It was found that the temperature exchange between the gas and the liquid phases was promoted by cold liquid exposure to the interface [11]. This may have a serious impact on flight feasibility for a spacecraft currently equipped with baffle plates. If the sloshing can be suppressed without a baffle plate, the thermal stratification will not be destroyed and the dynamic and thermal behaviors with sloshing may be well controlled simultaneously. However, at present there is little accumulation of knowledge about the propellant control without a baffle plate.

In this study, we paid attention to the fact that liquid oxygen, which is one of the propellants widely used in rockets, is a paramagnetic substance. We numerically investigated the damping effect of the magnetic field when liquid oxygen sloshing in a tank occurred.

2. Numerical Method

2.1. Computational Model

A computational model in this study is shown in Figure 1. We assume an incompressible gas–liquid two-phase flow of gaseous oxygen and liquid oxygen in a spherical spacecraft tank with a diameter of 1 m under zero gravity. A triangle acceleration force whose maximum value is 0.40 G ($0.40 \times 9.8\ \mathrm{m/s^2}$) is imposed in the x direction, as shown in Figure 2. In this computation, the effects of heat and wettability are not considered. The computation area is a cube containing a spherical tank. It is assumed that the magnetic field is a static magnetic field generated by a circular coil placed outside the spherical tank. Each computational case is performed by varying the position of the coil and the magnetic field strength gauged at the center of the coil. Computational conditions of the coil are shown in Table 1.

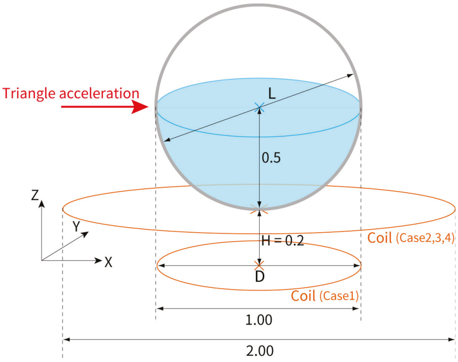

Figure 1. Computational model.

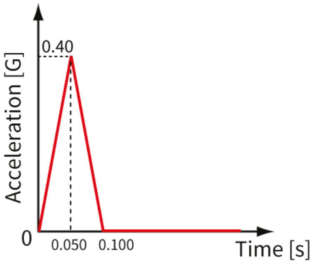

Figure 2. Acceleration as a function of time for the model of lateral impact force.

Table 1. Computational conditions for coils.

Case No. of Computational Conditions	Case 0	Case 1	Case 2	Case 3	Case 4
Dimensionless height of the coils (H) [-]	No coil	−0.2	0.0	0.0	0.0
Ratio of coil diameter to characteristic length (D/L) [-]		1.0	2.0	2.0	2.0
Magnetic flux density at the center of coils (b_c) [T]		1.0	0.1	1.0	3.0

2.2. Initial Condition

Considering the most dangerous situation on the attitude of the spacecraft, we focused on the case that the initial liquid phase was located in the lower half of the tank under the impact force excited from the lateral direction. The liquid surface is assumed to be flat to make it easier to capture the tendencies of liquid level fluctuations. In fact, it should be noted that in zero gravity the liquid surface would not be flat due to surface tension and wettability. At the initial condition, the excitation force is zero at $t = 0$ (Figure 2) and the static magnetic field generated by the coil has been already imposed.

2.3. Computational Grid

For the discretization of the computational domain, a regular staggered grid is used in the Cartesian coordinate system. As shown in Figure 3, scalar quantities such as pressure p, density ρ, Level set function ϕ and VOF function C are defined at the center of the cell (i, j), and vector quantities such as velocity u, v, w and magnetic flux density B_x, B_y, B_z are defined at the interface of the cells $(i + 1/2, j)$, $(i, j + 1/2)$.

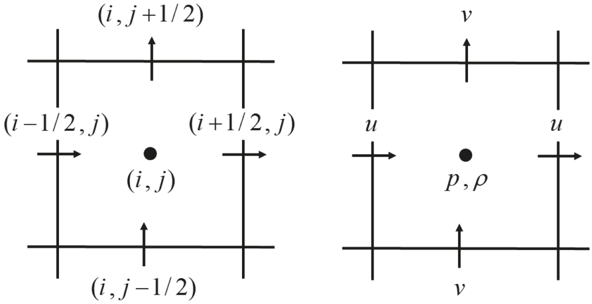

Figure 3. Staggered grid.

2.4. Model of Two-Phase Flow

Since the gas–liquid interface is inherently discontinuous, such computation, including the discontinuous interface, tends to be unstable, especially when the density ratio of gas and liquid is very large. Therefore, it is necessary to provide a transitional region with a certain thickness for the discontinuous gas–liquid interface in physical properties, such as density, viscosity and susceptibility. For the estimation of the surface normal force, the continuum surface force (CSF) model [12] was employed in this study. The following shows the equations expressing the physical properties (density ρ, viscosity μ, magnetic susceptibility χ) of gas–liquid two-phase flow with a transitional region.

$$\rho = \rho_G + (\rho_L - \rho_G)H_\alpha(\phi) \tag{1}$$

$$\mu = \mu_G + (\mu_L - \mu_G)H_\alpha(\phi) \tag{2}$$

$$\chi = \chi_G + (\chi_L - \chi_G)H_\alpha(\phi) \tag{3}$$

Here, the subscript L represents the liquid phase, G represents the gas phase and ϕ is the level set function measured from the interface. $H_\alpha(\phi)$ is the smoothed Heaviside function expressing the transitional region, and α is the interface thickness. In this computation, $\alpha = 1.75\Delta x$, where Δx is the grid interval.

$$H_\alpha(\phi) = \begin{cases} 0 & (\phi < -\alpha) \\ \frac{1}{2}\left[1 + \frac{\phi}{\alpha} + \frac{1}{\pi}\sin\left(\frac{\pi\phi}{\alpha}\right)\right] & (-\alpha \le \phi \le \alpha) \\ 1 & (\alpha < \phi) \end{cases} \tag{4}$$

However, in this study, the density difference between gas and liquid is large, so the calculation of the surface tension was stabilized by using the density-scaled balanced CSF model proposed by Yokoi [13]. $H_\alpha^{scaled}(\phi)$ represents the density-scaled Heaviside function.

$$H_\alpha^{scaled}(\phi) = \begin{cases} 0 & (\phi < -\alpha) \\ \frac{1}{2}\left[\frac{1}{2} + \frac{\phi}{\alpha} + \frac{\phi^2}{2\alpha^2} - \frac{1}{4\pi^2}\left\{\cos\left(\frac{2\pi\phi}{\alpha}\right) - 1\right\} + \frac{\alpha+\phi}{\alpha\pi}\sin\left(\frac{2\pi\phi}{\alpha}\right)\right] & (-\alpha \le \phi \le \alpha) \\ 1 & (\alpha < \phi) \end{cases} \tag{5}$$

Figure 4 shows the Heaviside function and the density-scaled Heaviside function. The density-scaled Heaviside function is deviated to the liquid phase compared to the simple smoothed Heaviside function. By reducing the surface normal force acting on the gas phase, gas velocities near the interface can be suppressed even for the case of high density ratios.

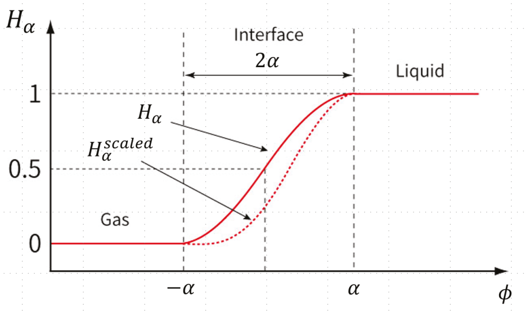

Figure 4. Smoothed Heaviside function and density-scaled Heaviside function.

2.5. Method to Capture the Dynamic Surface

The coupled level set and volume of fluid (CLSVOF) method possesses an advantage of surface force estimation and volume preservation, since it is a method coupled between the level set method and the Volume Of Fluid (VOF) method [14]. In the present CLSVOF method, the level set function is used for estimation of the surface force, whereas the VOF method is used for calculation of the advection equation. In this study, the phenomena are assumed to be occurred in a zero-gravity environment where the interface shape is greatly deformed and the influence of surface tension is significant. Therefore, the CLSVOF method was used to capture the surface deformation accurately in this study, and the Tangent of Hyperbola for INterface Capturing/Weighed Line Interface Calculation (THINC/WLIC) method [15] was used for advection of the VOF function. The coupling formula between the level set function and the VOF function was defined as shown in Equation (6), where α is the width of the transitional interface of the CSF (continuum surface force) model and ϕ is the level set function. It should be noted that the VOF function, especially in the case of severe breaking of surface waves, significantly increases or decreases the liquid phase volume due to numerical diffusion and the expansion of the interfacial transitional region. To circumvent this problem, we employed a volume correction method proposed by Sakuraba et al. [16].

$$\phi = \begin{cases} -\alpha & (C = 0) \\ \alpha(2C-1) & (0 < C < 1) \\ \alpha & (C = 1) \end{cases} \tag{6}$$

2.6. Governing Equation

The following shows the dimensional governing equations used in this study.

Continuity equation

$$\nabla \cdot \boldsymbol{u} = 0 \tag{7}$$

Navier–Stokes equation

$$\frac{\partial \boldsymbol{u}}{\partial t} = -\left(\boldsymbol{u} \cdot \nabla\right)\boldsymbol{u} - \frac{1}{\rho}\nabla p + \frac{1}{\rho}\nabla \cdot (\mu \nabla \boldsymbol{u}) + a(t)\boldsymbol{e_{exc}} + \frac{1}{\rho}\boldsymbol{f_{surf}} + \frac{1}{\rho}\boldsymbol{f_{mag}} \tag{8}$$

$$\boldsymbol{f_{surf}} = \gamma\kappa\nabla H_{\alpha}^{scaled}(\phi)\,, \quad \kappa = \nabla \cdot \frac{\nabla\phi}{|\nabla\phi|} \tag{9}$$

$$\boldsymbol{f_{mag}} = \frac{\rho\chi}{\mu_m}\left(\boldsymbol{b} \cdot \nabla\right)\boldsymbol{b} \tag{10}$$

Advection equation (density conservation)

$$\frac{\partial \rho}{\partial t} + \left(\boldsymbol{u} \cdot \nabla\right)\rho = 0 \tag{11}$$

Biot–Savart law

$$\boldsymbol{b}(\boldsymbol{x}) = \frac{\mu_m i_c}{4\pi}\int_{coil}\frac{(\boldsymbol{r}-\boldsymbol{x}) \times d\boldsymbol{r}}{|\boldsymbol{r}-\boldsymbol{x}|^3} \tag{12}$$

Gauss's law for magnetic field

$$\nabla \cdot \boldsymbol{b} = 0 \tag{13}$$

The notation $\boldsymbol{e_{exc}}$ in Equation (8) is the unit vector in the direction of excitation force, and the notation $a(t)$ is acceleration and varies over time according to Figure 2. Equation (9) is the surface normal force in the density-scaled balanced CSF model, and Equation (10) is the magnetizing force [17].

The above dimensional governing equation was made dimensionless using the dimensionless variables and dimensionless numbers defined below, where subscript ϕ represents physical property depending on the level set function.

- Dimensionless variables

$$\begin{gathered} \boldsymbol{X} = \frac{\boldsymbol{x}}{l}, \quad \boldsymbol{R} = \frac{\boldsymbol{r}}{l}, \quad \boldsymbol{U} = \frac{\boldsymbol{u}}{\frac{\mu_G}{\rho_G l}}, \quad P = \frac{p}{\frac{\mu_G{}^2}{\rho_G l^2}}, \quad \tau = \frac{t}{\frac{\rho_G l^2}{\mu_G}}, \quad \boldsymbol{B} = \frac{\boldsymbol{b}}{\frac{\mu_m i_c}{l}}, \quad A(\tau) = \frac{a(t)}{g} \\ \bar{\rho} = \frac{\rho_L}{\rho_G}, \quad \bar{\mu} = \frac{\mu_L}{\mu_G}, \quad \bar{\chi} = \frac{\chi_L}{\chi_G}, \quad \hat{\kappa} = \kappa l, \quad \hat{\alpha} = \frac{\alpha}{l}, \quad \Phi = \frac{\phi}{l}, \quad \boldsymbol{\nabla} = \nabla l \end{gathered} \tag{14}$$

- Dimensionless numbers

$$Ga = \frac{g\rho_G{}^2 l^3}{\mu_G{}^2}, \;\; \Gamma = \frac{\gamma\rho_G l}{\mu_G{}^2}, \;\; M = \frac{\rho_G{}^2\chi_G{}^2 i_c^2 \mu_m}{\mu_G{}^2} \tag{15}$$

The dimensionless numbers are the Galilei number Ga representing the strength of gravity; the Laplace number Γ represents the strength of surface tension; and the dimensionless number M represents the strength of the magnetic field. Note that i_c was calculated from the magnetic flux density at the center of the single-turn coil $b_c = \mu_m i_c / 2r$. The following shows the dimensionless governing equations.

Definition of physical properties

$$\begin{aligned} \rho_\phi &= 1 + (\bar{\rho} - 1)\, H_{\hat{\alpha}}^{scaled}(\Phi) \\ \mu_\phi &= 1 + (\bar{\mu} - 1)\, H_{\hat{\alpha}}^{scaled}(\Phi) \\ \chi_\phi &= 1 + (\bar{\chi} - 1)\, H_{\hat{\alpha}}^{scaled}(\Phi) \end{aligned} \tag{16}$$

Continuity equation

$$\boldsymbol{\nabla} \cdot \boldsymbol{U} = 0 \tag{17}$$

Navier–Stokes equation

$$\frac{\partial \boldsymbol{U}}{\partial \tau} = -\left(\boldsymbol{U} \cdot \boldsymbol{\nabla}\right) \boldsymbol{U} - \frac{1}{\rho_\phi} \boldsymbol{\nabla} P + \frac{1}{\rho_\phi} \boldsymbol{\nabla} \cdot \left(\mu_\phi \boldsymbol{\nabla} \boldsymbol{U}\right) + Ga A(\tau) \boldsymbol{e_{exc}} + \boldsymbol{F_{surf}} + \boldsymbol{F_{mag}} \tag{18}$$

$$\boldsymbol{F_{surf}} = \frac{\Gamma}{\rho_\phi} \hat{\kappa} \boldsymbol{\nabla} H_{\alpha}^{scaled}(\Phi)\,, \quad \hat{\kappa} = \boldsymbol{\nabla} \cdot \frac{\boldsymbol{\nabla} \Phi}{|\boldsymbol{\nabla} \Phi|} \tag{19}$$

$$\boldsymbol{F_{mag}} = M \chi_\phi \left(\boldsymbol{B} \cdot \boldsymbol{\nabla}\right) \boldsymbol{B} \tag{20}$$

Advection equation

$$\frac{\partial C}{\partial \tau} + \boldsymbol{\nabla} \cdot (C\boldsymbol{U}) - C\left(\boldsymbol{\nabla} \cdot \boldsymbol{U}\right) = 0 \tag{21}$$

Biot–Savart law

$$\boldsymbol{B_{Biot}}(\boldsymbol{X}) = \frac{1}{4\pi} \int_{coil} \frac{(\boldsymbol{R} - \boldsymbol{X}) \times d\boldsymbol{R}}{|\boldsymbol{R} - \boldsymbol{X}|^3} \tag{22}$$

Gauss's law for magnetic field

$$\boldsymbol{\nabla} \cdot \boldsymbol{B} = 0 \tag{23}$$

Figure 5 shows the acceleration as a function of dimensionless time for the model of lateral impact force. At $\tau = 0.079 \times 10^{-6}$, the acceleration takes its peak, and at $\tau = 0.158 \times 10^{-6}$, the excitation force reaches zero. The entire computational time is $\tau = 5.0 \times 10^{-6}$ (stated later), and the acceleration can be regarded as an impact force.

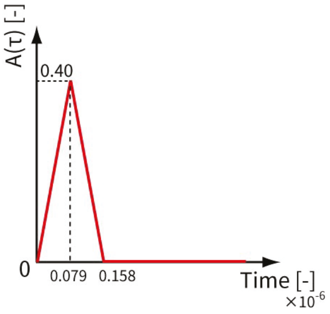

Figure 5. Acceleration as a function of dimensionless time for the model of lateral impact force.

For discretization, the Euler explicit method was used for the time derivative term, the third-order upwind difference (UTOPIA) [18] was used for the advection term in the Navier–Stokes equation, and the second-order center difference was used for the others.

As a method of obtaining an approximate solution of the line integral in Equation (12), the composite Simpson's rule was used. In fact, magnetic flux density obtained from the Biot–Savart law $\boldsymbol{B}_{\boldsymbol{Biot}}(\boldsymbol{X})$ does not necessarily satisfy the Gauss's law for magnetic field (Equation (23)), so it is necessary to correct $\boldsymbol{B}_{\boldsymbol{Biot}}(\boldsymbol{X})$. In order to satisfy Equation (23), a scalar potential ϕ_p was introduced as shown in Equation (24).

$$\boldsymbol{B} = \boldsymbol{B}_{\boldsymbol{Biot}} - \boldsymbol{\nabla}\phi_p \tag{24}$$

Taking the divergence of both sides,

$$\boldsymbol{\nabla} \cdot \boldsymbol{B} = \boldsymbol{\nabla} \cdot \boldsymbol{B}_{\boldsymbol{Biot}} - \boldsymbol{\nabla}^2\phi_p \tag{25}$$

Because of the Gauss's law for magnetic field ($\boldsymbol{\nabla} \cdot \boldsymbol{B} = 0$),

$$\therefore\ \boldsymbol{\nabla} \cdot \boldsymbol{B}_{\boldsymbol{Biot}} - \boldsymbol{\nabla}^2\phi_p = 0 \simeq \mathrm{Err}\ (\text{numerical error}) \tag{26}$$

This is the Poisson equation about ϕ_p, and iterative correction was repeated until this numerical error became below a certain value. The HSMAC method was used to repeat iterative correction in this study.

2.7. IB (Immersed Boundary) Method

The tank shape in the square grid in the Cartesian coordinate system was represented using a immersed boundary (IB) method with linear interpolations of velocity, as shown in Figure 6 and the following equations from (27) to (30).

$$\boldsymbol{U}_{IB} = \frac{\psi \boldsymbol{U}_{IP} + (\delta_{IP} - \psi)\boldsymbol{U}_B}{\delta_{IP}} \tag{27}$$

$\boldsymbol{U}_{IP}$ is calculated by linear interpolations with nearest eight IPs (image points).

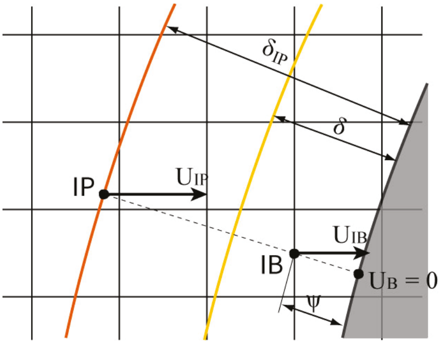

Figure 6. Schematic of IB method.

The way to find U_{IP} in the two-dimensional case is described below. Figure 7 shows a schematic of the grid around the IP point. Defining the velocity components in the X direction above and below the IP point are U_{up} and U_{low}, the linear interpolations of Equations (28) and (29) can be used to calculate U_{up} and U_{low}.

$$U_{up} = \frac{\Delta X_{IP} U_{I+1,J+1} + (\Delta X - \Delta X_{IP}) U_{I,J+1}}{\Delta X} \tag{28}$$

$$U_{low} = \frac{\Delta X_{IP} U_{I+1,J} + (\Delta X - \Delta X_{IP}) U_{I,J}}{\Delta X} \tag{29}$$

with U_{up}, U_{low} from the above equations and a linear interpolation below, U_{IP} can be calculated.

$$U_{IP} = \frac{\Delta Y_{IP} U_{up} + (\Delta Y - \Delta Y_{IP}) U_{low}}{\Delta Y} \tag{30}$$

V_{IP} can be calculated likewise.

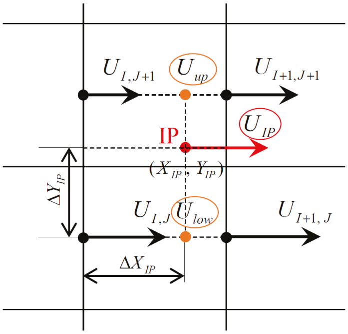

Figure 7. Schematic of how to calculate U_{IP}.

2.8. Boundary Condition

On the surface of the spherical tank, the no-slip condition and the no inflow/outflow condition were applied. In other words, all the velocity components are zero on the boundary, and the pressure gradient is also zero. In addition, the effect of wettability is not taken into account in this computation because the velocity vector near the tank wall is circumvented by the IB method to represent the wall surface. In fact, since the effect of wettability should be significant in zero gravity [19,20], the method for expressing wettability together with the IB method is required as one of the future issues.

2.9. Pressure Correction

In general CFD computation, iterative calculation of pressure correction occupies most of the whole computational time. Therefore, reduction of this iterative corrections greatly contributes to reduce the consumed time. Especially in the multiphase flow problem, since a fluid with a large density ratio is handled, the coefficient matrix of the pressure Poisson equation becomes bad condition, and enormous time is required for convergence. As a countermeasure, the pressure correction was performed by using the Projection method compatible with the IB method. In addition, the multigrid method was applied to reduce the number of corrections together with using C++AMP as a programming language and parallel computation on GPU.

2.10. Parameters for Computation

Of the parameters for the present computation, the physical property values are shown in Table 2, and the dimensionless parameters are shown in Table 3. Physical properties refer to the values of gaseous oxygen and liquid oxygen at 90 K under atmospheric pressure [21,22].

Table 2. Physical property values.

Parameter	Symbol	Value	Unit
Characteristic length (diameter of spherical tank)	l	1.00	[m]
Density of gaseous oxygen	ρ_G	4.4509	[kg/m^3]
Density of LOX	ρ_L	1141.4	[kg/m^3]
Viscosity of gaseous oxygen	μ_G	7.0112×10^{-6}	[Pa · s]
Viscosity of LOX	μ_L	1.9602×10^{-4}	[Pa · s]
Mass magnetic susceptibility of gaseous oxygen	χ_G	1.355×10^{-6}	[m^3/kg]
Mass magnetic susceptibility of LOX	χ_L	3.023×10^{-6}	[m^3/kg]
gravitational acceleration	g	9.80665	[m/s^2]
Surface tension	γ	1.3183×10^{-2}	[N/m]

Table 3. Dimensionless computational conditions.

Parameter	Symbol	Value (Dimensionless)
Number of grids	X_n, Y_n, Z_n	80, 80, 80
Number of grids per tank diameter	(None)	64
Computation time	τ_{MAX}	5.0×10^{-6}
Time step	$\Delta\tau$	1.0×10^{-10}
Density ratio	$\bar{\rho}$	256
Viscosity ratio	$\bar{\mu}$	28.0
Magnetic susceptibility ratio	$\bar{\chi}$	2.23
Galilei number	Ga	3.95×10^{12}
Laplace number	Γ	1.19×10^{9}
Dimensionless number about magnetic field	M	Case1: 4.35×10^{11} Case 2: 4.35×10^{9} Case 3: 4.35×10^{11} Case 4: 3.91×10^{12}

3. Validation of the Numerical Method

In order to verify the validity of this computational code, we computed the oscillation of a droplet in zero gravity. Since the validity of the magnetic field calculation method and the gas–liquid two-phase flow calculation method has been verified by previous studies [14,23], in this section we confirm whether the program could be implemented correctly and the number of grids be sufficient.

We assumed that the case where a cubic droplet at the initial state was gently ejected into a weightless field, and the subsequent change was obtained by numerical calculation. The calculation parameters are shown in Table 4.

Table 4. Dimensionless computational conditions for droplet oscillation.

Parameter	Symbol	Value (Dimensionless)
Number of grids	X_n, Y_n, Z_n	64, 64, 64
Number of grids per characteristic length	(None)	32
Computation time	τ_{MAX}	2.0×10^{-3}
Time step	$\Delta\tau$	1.0×10^{-7}
Density ratio	$\bar{\rho}$	100
Viscosity ratio	$\bar{\mu}$	10.0
Magnetic susceptibility ratio	$\bar{\chi}$	0.0
Galilei number	Ga	0.0
Laplace number	Γ	2.0×10^{6}
Dimensionless number about magnetic force	M	0.0

The results are shown in Figure 8. Due to the surface normal force acting at the surface of the droplet, the part with a large curvature entered inside and the interface deformed from the cubic shape to the octahedral shape. The advection of the interfacial shape was successfully performed while keeping its symmetry with respect to the X, Y and Z directions. No results contradicted the physics, and we were convinced that the implementation was completed correctly and the number of grids was sufficient.

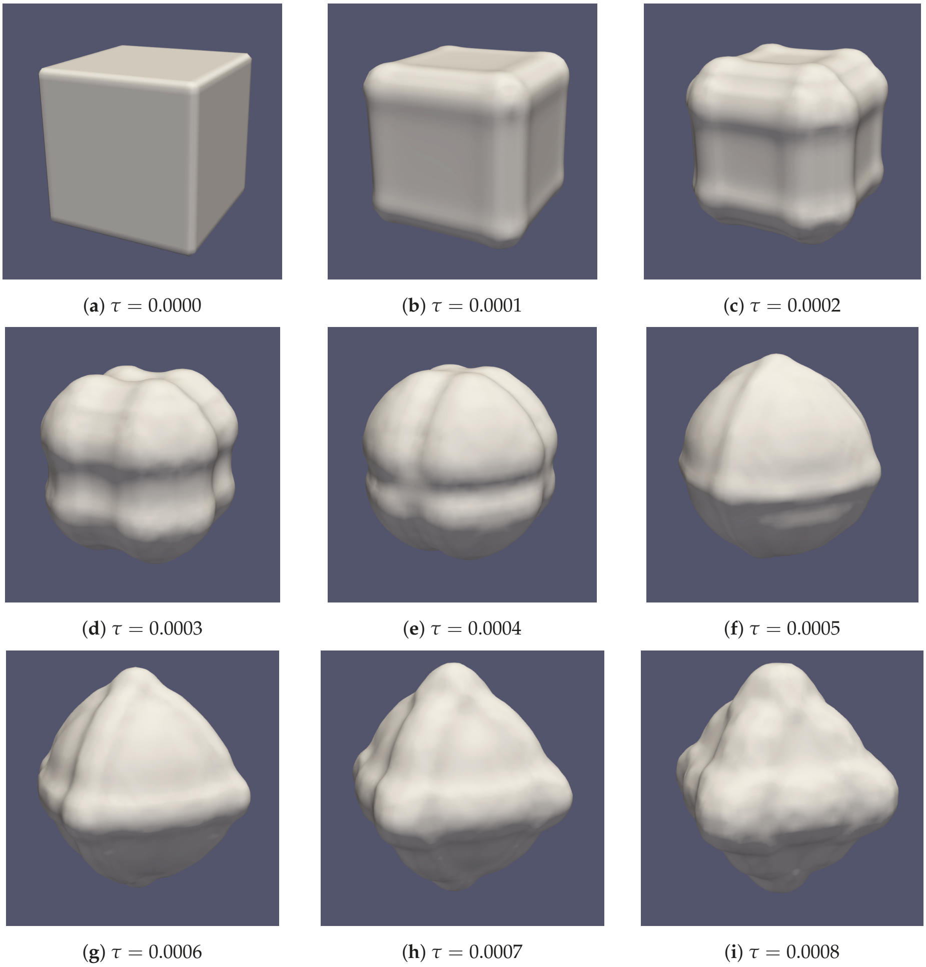
(**a**) $\tau = 0.0000$ (**b**) $\tau = 0.0001$ (**c**) $\tau = 0.0002$
(**d**) $\tau = 0.0003$ (**e**) $\tau = 0.0004$ (**f**) $\tau = 0.0005$
(**g**) $\tau = 0.0006$ (**h**) $\tau = 0.0007$ (**i**) $\tau = 0.0008$

Figure 8. A series of an oscillating droplet in zero gravity field.

4. Results and Discussion

The computational results of Case 0, 1, 2, 3, 4 are shown in Figures 9–13 respectively. In the visualizations of Cases 1, 2, 3 and 4, the visualization of Case 0 is additionally shown in translucent red for comparison. The translucent sphere represents a spherical tank, and the liquid phase is visualized for the value of the VOF function $C \geq 0.5$. The vector represents the magnetic flux density vector.

In Case 0 (no coil), the liquid phase moved along the wall due to the lateral excitation force, and the interface was greatly deformed. Additionally, a small amount of liquid phase remained on the left wall of the tank due to the influence of the IB method. In Case 1 ($D/L = 1.0, H = -0.2, b_c = 1.0$ T), the amount of liquid phase moving along the tank was smaller and the moving speed was slower than that in Case 0, but the interface was not settled. This must be probably because the position of the coil was far from the tank location, and the magnetizing force intensity in the tank was not sufficient. In Case 2 ($D/L = 2.0, H = 0.0, b_c = 0.1$ T), the results were similar to those of Case 0, and no significant difference was observed. It is considered that the magnetizing force exerted in the tank was weak and the effect of damping of the sloshing was insufficient when the magnetic flux density at the center of the coil was 0.1 T. On the other hand, in Case 3 ($D/L = 2.0, H = 0.0, b_c = 1.0$ T), the liquid level fluctuated and droplets appeared from the liquid surface near the center of the tank, but the most liquid phase remained in the lower part of the tank. Under the computational conditions in this study, if the magnetic flux density at the center of the coil was about 1.0 T, the sloshing was suppressed to a certain extent, which might contribute to the damping of the movement of the center of gravity of the spacecraft and the prevention of mixing of ullage gas into piping. Additionally, comparing between Case 1 and Case 3, a tendency was suggested that when the magnetic flux density at the center of the coil was the same, the effect of suppressing the sloshing was higher when the coil location was closer to the tank than when the coil diameter was equal to the tank. In Case 4 ($D/L = 2.0, H = 0.0, b_c = 3.0$ T), the movement of the liquid phase was mostly suppressed, and the liquid surface near the center of the tank only remained wavy. In this computation, considering that the coil was not placed near the tank, at least 3.0 T at the coil center was required for sufficient damping of the sloshing for the tank with a diameter of about 1 m. But it is anticipated that the magnetic field less than 3.0 T is even effective, if the coil actually can be attached on the tank surface.

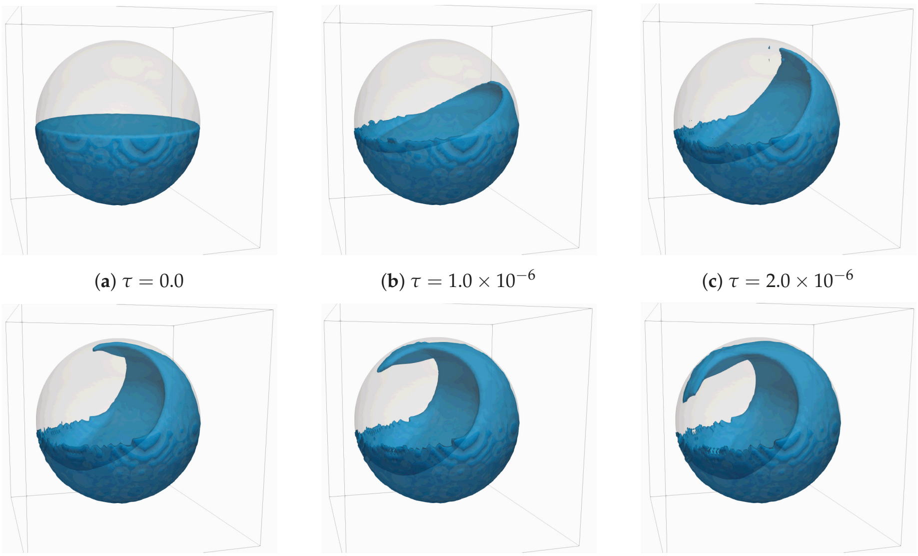

(**a**) $\tau = 0.0$ (**b**) $\tau = 1.0 \times 10^{-6}$ (**c**) $\tau = 2.0 \times 10^{-6}$

(**d**) $\tau = 3.0 \times 10^{-6}$ (**e**) $\tau = 4.0 \times 10^{-6}$ (**f**) $\tau = 5.0 \times 10^{-6}$

Figure 9. Computational results of Case 0 (no coil). The color indicates liquid phase in the spherical tank.

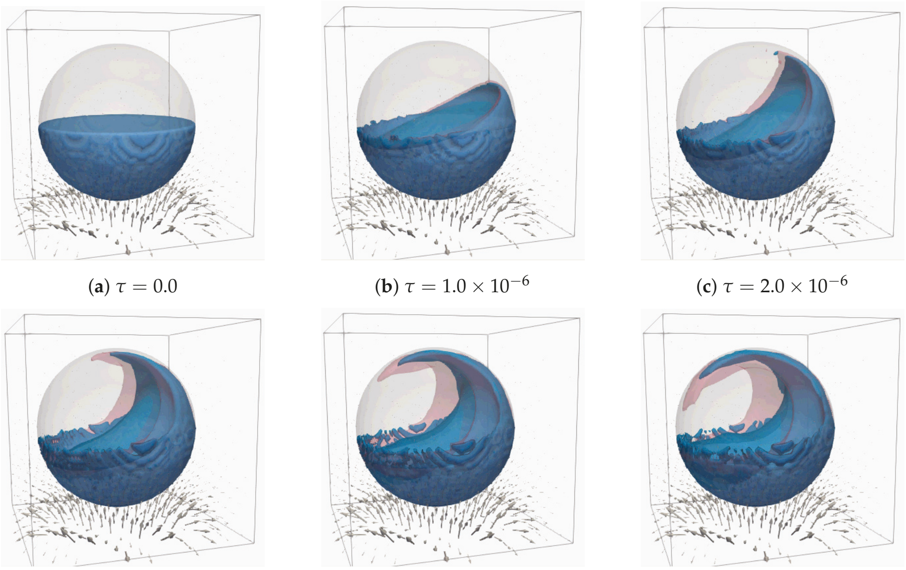

(**a**) $\tau = 0.0$ (**b**) $\tau = 1.0 \times 10^{-6}$ (**c**) $\tau = 2.0 \times 10^{-6}$

(**d**) $\tau = 3.0 \times 10^{-6}$ (**e**) $\tau = 4.0 \times 10^{-6}$ (**f**) $\tau = 5.0 \times 10^{-6}$

Figure 10. Computational results of Case 1 ($D/L = 1.0,\ H = -0.2,\ b_c = 1.0$ [T]; i.e., coil is smaller and farther from the tank, and magnetic flux density is medium). The blue color indicates the movement of liquid phase damped by the magnetic force, whereas the pink color indicates that in Case 0 (no magnetic force). The black vectors represent the magnetic field generated by the coil current.

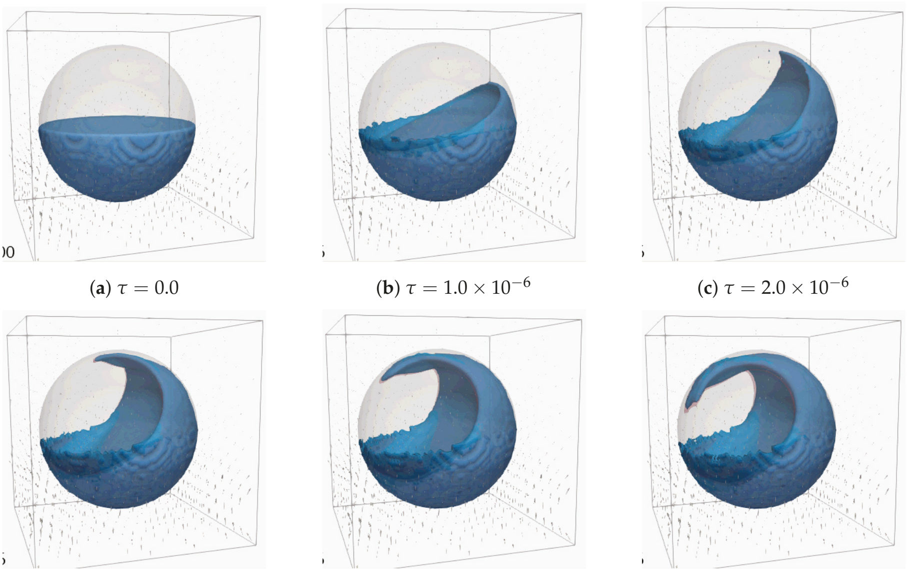

(**a**) $\tau = 0.0$ (**b**) $\tau = 1.0 \times 10^{-6}$ (**c**) $\tau = 2.0 \times 10^{-6}$

(**d**) $\tau = 3.0 \times 10^{-6}$ (**e**) $\tau = 4.0 \times 10^{-6}$ (**f**) $\tau = 5.0 \times 10^{-6}$

Figure 11. Computational results of Case 2 ($D/L = 2.0,\ H = 0.0,\ b_c = 0.1$ [T]; i.e., coil is larger, closer to the tank and magnetic flux density is weak). The blue color indicates the movement of liquid phase damped by the magnetic force, whereas the pink color indicates that in Case 0 (no magnetic force). The black vectors represent the magnetic field generated by the coil current.

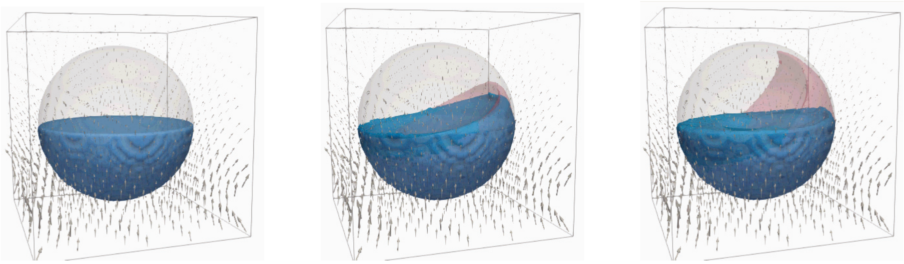

(**a**) $\tau = 0.0$ (**b**) $\tau = 1.0 \times 10^{-6}$ (**c**) $\tau = 2.0 \times 10^{-6}$

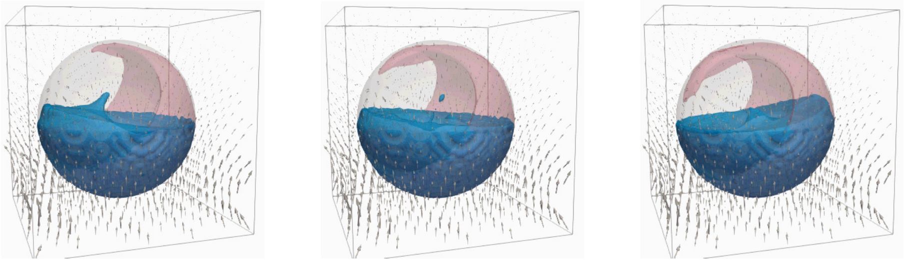

(**d**) $\tau = 3.0 \times 10^{-6}$ (**e**) $\tau = 4.0 \times 10^{-6}$ (**f**) $\tau = 5.0 \times 10^{-6}$

Figure 12. Computational results of Case 3 ($D/L = 2.0,\ H = 0.0,\ b_c = 1.0$ [T]; i.e., coil is larger, closer to the tank and magnetic flux density is medium). The blue color indicates the movement of liquid phase damped by the magnetic force, whereas the pink color indicates that in Case 0 (no magnetic force). The black vectors represent the magnetic field generated by the coil current.

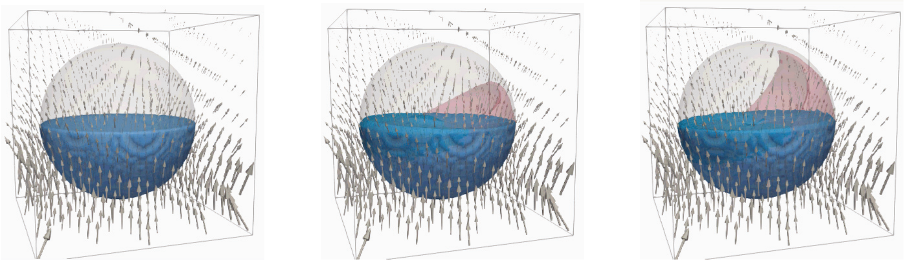

(**a**) $\tau = 0.0$ (**b**) $\tau = 1.0 \times 10^{-6}$ (**c**) $\tau = 2.0 \times 10^{-6}$

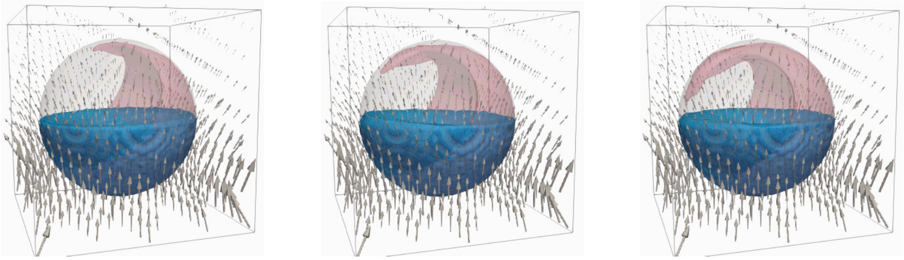

(**d**) $\tau = 3.0 \times 10^{-6}$ (**e**) $\tau = 4.0 \times 10^{-6}$ (**f**) $\tau = 5.0 \times 10^{-6}$

Figure 13. Computational results of Case 4 ($D/L = 2.0,\ H = 0.0,\ b_c = 3.0$ [T], i.e., coil is larger, closer to the tank and magnetic flux density is strong). The blue color indicates the movement of liquid phase damped by the magnetic force, whereas the pink color indicates that in Case 0 (no magnetic force). The black vectors represent the magnetic field generated by the coil current.

In these computational results, the tendency of damping effect of the sloshing due to differences in the coil position and the magnetic field strength at the coil center was shown, but these computations were performed when the coil was set outside the fluid domain and the coil was not near the tank. This is because if the coil is placed in the fluid domain, the denominator ($|\boldsymbol{R} - \boldsymbol{X}|^3$) diverges to infinity when calculating the magnetic field according to the Biot–Savart law, and the calculation does not converge. Furthermore, the unwanted behavior that a small amount of liquid phase remained on the wall was observed. Since the accuracy of the IB method is restricted by the grid width, the undesirable behavior can be reduced by increasing the number of grids, but the computational time becomes longer. In order to construct a model that can predict more real phenomena, there is room for improvement in the speed of computation and the representation of arbitrary wall shape by the IB method. In addition, we did not introduce wettability in this study, so we need to construct a useful method that can apply wettability to arbitrary wall shape.

On the subject of feasibility of 3 T, since most of superconducting magnets can produce up to 10 T, it is easy to produce 3 T. However, considering the current resistance of the coils, it is highly possible that the coil needs to be superconducting in order to produce 3 T, and therefore it is neither efficient nor economical to install a superconducting system on a spacecraft. Since the sloshing in the present case can be dampened to some extent at 1 T, a superconducting system is not necessarily required, but the details of the tank size, coil shape design, and electric current value should be designed carefully as the future issues.

As other future tasks, it is necessary to demonstrate the magnetic damping effect when the coil comes into contact with the tank, and quantitatively to evaluate not only the movement and deformation of the liquid surface but also the movement of the center of gravity in the tank. In addition, the pressure field and the thermal behavior in the tank have to be predicted by introducing a beneficial model of phase change.

5. Conclusions

In this paper, damping effect by the magnetizing force for the sloshing of liquid oxygen was discussed by using numerical computations. The following conclusions were obtained.

- When the magnetic flux density at the center of the coil was the same, the sloshing damping effect tended to be higher when the coil surface was closer to the tank than when the coil diameter was equal to the tank.
- When the magnetic flux density at the center of the coil was 1.0 T, the sloshing was dampened to a certain extent, and by setting the magnetic flux density at the center of the coil to 3.0 T, a sufficient sloshing damping effect was obtained. Actually, it is anticipated that even if less than 3.0 T, the damping effect is sufficient by placing the coil closer to the tank. This has the potential to contribute to the damping of the center of gravity movement of spacecrafts and the prevention of mixing of ullage gas into the piping.
- Future tasks include speeding up the computation, improving the IB method, and introducing wettability to an arbitrary shaped wall. Besides, it is necessary to evaluate quantitatively the shift of the center of gravity in the tank and the thermal behavior when the sloshing is dampened by a magnetic field.

Author Contributions: Conceptualization, Y.F.; methodology, Y.F.; software, Y.F.; validation, Y.F. and T.T.; formal analysis, Y.F.; investigation, Y.F.; resources, T.T.; data curation, Y.F.; writing—original draft preparation, Y.F.; writing—review and editing, T.T.; visualization, Y.F.; supervision, T.T.; project administration, Y.F. and T.T.; funding acquisition, T.T. All authors have read and agreed to the published version of the manuscript.

Funding: This research received no external funding.

Conflicts of Interest: The authors declare no conflict of interest.

Nomenclature

$a(t)$	Acceleration as a function of time	$[\mathrm{m/s^2}]$
$A(\tau)$	Acceleration as a function of dimensionless time	[-]
b_c	Magnetic flux dencity at the center of the coil	[T]
$\boldsymbol{b}$	Corrected magnetic flux density vector	[T]
$\boldsymbol{b_{Biot}}$	Magnetic flux density vector by Biot–Savart law	[T]
$\boldsymbol{B}$	Corrected dimensionless magnetic flux density vector	[-]
$\boldsymbol{B_{Biot}}$	Dimensionless magnetic flux density vector by Biot-Savart law	[-]
C	VOF function	[-]
D	Dimensionless coil diameter	[-]
$\boldsymbol{e_{exc}}$	Unit vector in the direction of excitation force	[-]
$\boldsymbol{f_{mag}}$	Magnetizing force vector	$[\mathrm{N/m^3}]$
$\boldsymbol{F_{mag}}$	Dimensionless magnetizing force vector	[-]
$\boldsymbol{f_{surf}}$	Surface normal force vector	$[\mathrm{N/m^3}]$
$\boldsymbol{F_{surf}}$	Dimensionless surface normal force vector	[-]
g	Gravitational acceleration	$[\mathrm{m/s^2}]$
Ga	Galilei number	[-]
$H_{\alpha}^{scaled}(\phi)$	Density-scaled Heaviside function	[-]
i_c	Coil current	[A]
l	Characteristic length (Tank diameter)	[m]
L	Dimensionless characteristic length (Tank diameter)	[-]
M	Dimensionless number representing the strength of the magnetic field	[-]
p	Pressure	[Pa]
P	Dimensionless pressure	[-]
$\boldsymbol{r}$	Position vector of the coil	[m]
$\boldsymbol{R}$	Dimensionless position vector of the coil	[-]
t	Time	[s]
$\boldsymbol{u}$	Velocity vector	[m/s]
$\boldsymbol{U}$	Dimensionless velocity vector	[-]
$\boldsymbol{U_B}$	Dimensionless velocity vector on the wall	[-]
$\boldsymbol{U_{IB}}$	Dimensionless velocity vector at IB point	[-]
$\boldsymbol{U_{IP}}$	Dimensionless velocity vector at IP	[-]
U_{IP}	X-direction component of $\boldsymbol{U_{IP}}$	[-]
V_{IP}	Y-direction component of $\boldsymbol{U_{IP}}$	[-]
$\boldsymbol{x}$	Position vector in the calculation area	[m]
$\boldsymbol{X}$	Dimensionless position vector in the calculation area	[-]
X_n, Y_n, Z_n	Number of grids in the X, Y, Z direction	[-]
$\Delta X, \Delta Y, \Delta Z$	Grid width in the X, Y, Z direction	[-]
Greek letters		
α	Interface thickness	[m]
$\hat{\alpha}$	Dimensionless interface thickness	[-]
γ	Surface tension	[N/m]
$\mathit{\Gamma}$	Laplace number	[-]
δ_{IP}	Distance to IP	[-]
κ	Local mean curvature at interface	[1/m]
$\hat{\kappa}$	Dimensionless interface curvature	[-]
μ_G	Viscosity of gas phase	$[\mathrm{Pa \cdot s}]$
μ_L	Viscosity of liquid phase	$[\mathrm{Pa \cdot s}]$
$\bar{\mu}$	Viscosity ratio	[-]

μ_ϕ	Dimensionless viscosity	[-]
μ_m	Magnetic permeability in vacuum	[H/m]
π	Circle ratio	[-]
ρ_G	Density of gas phase	[kg/m^3]
ρ_L	Density of liquid phase	[kg/m^3]
$\bar{\rho}$	Density ratio	[-]
ρ_ϕ	Dimensionless density	[-]
τ	Dimensionless time	[-]
τ_{MAX}	Dimensionless calculation time	[-]
ϕ	Level set function	[m]
ϕ_p	Scalar potential	[-]
Φ	Dimensionless level set function	[-]
χ_G	Mass magnetic susceptibility of gas phase	[m^3/kg]
χ_L	Mass magnetic susceptibility of liquid phase	[m^3/kg]
$\bar{\chi}$	Mass magnetic susceptibility ratio	[-]
χ_ϕ	Dimensionless magnetic susceptibility	[-]
ψ	Distance function from wall surface	[-]

References

1. Himeno, T. Propellant Management in Liquid Rockets and Space Vehicles. *J. Jpn. Soc. Multiph. Flow* **2013**, *27*, 385–392. [CrossRef]
2. Himeno, T. Liquid Motion in the Propellant Tanks of Space Vehicles. *J. Jpn. Soc. Fluid Mech. Nagare* **2013**, *32, 239–244*.
3. Maemura, T.; Gotou, T.; Akiyama, K.; Nimura, K.; Watanabe, A. New H-IIA Launce Vehicle Technology and Maiden Flight Results. *Mitsubishi Heavy Ind. Tech. Rev.* **2002**, *39*, 43–50.
4. Gen, M.; Ogasawara, K.; Kitayama, O.; Ochiai, T. Conceptual Study of Space Environmental Experiment Platform using H-IIA 2nd Stage. *Int. Symp. Space Technol. Sci.* **2008**. Unpublished work.
5. Kitayama, O.; Tokunaga, T.; Igarashi, I.; Okita, K.; Fujita, M. Cryogenic Propellant Management of H-IIA Upper Stage. *Int. Symp. Space Technol. Sci.* **2006**. Unpublished work.
6. Abramson, H.N. (Ed.) The Dynamic Behavior of Liquids in Moving Containers. In *NASA SP-106*; National Technical Information Service: Springfield, VA, USA, 1966.
7. Demirel, E.; Aral, M.M. Liquid Sloshing Damping in an Accelerated Tank Using a Novel Slot-Baffle Design. *Water* **2018**, *10*, 1565. [CrossRef]
8. Jamalabadi, M.Y.A.; Ho-Huu, V.; Nguyen, T.K. Optimal Design of Circular Baffles on Sloshing in a Rectangular Tank Horizontally Coupled by Structure. *Water* **2018**, *10*, 1504. [CrossRef]
9. Zheng, X.; You, Y.; Ma, Q.; Khayyer, A.; Shao, S. A Comparative Study on Violent Sloshing with Complex Baffles Using the ISPH Method. *Appl. Sci.* **2018**, *8*, 904. [CrossRef]
10. Ohashi, A. Effects of Baffle Plate on Cryogenic Fluid Sloshing and Pressure Fluctuation. Bachelor's Thesis, The University of Tokyo, Tokyo, Japan, 2015.
11. Furuichi, Y.; Ohashi, A.; Kameyama, S.; Haba, D.; Sakuma, Y.; Uzawa, S.; Himeno, T.; Watanabe, T. Effects of Thermal Stratification Thickness on Cryogenic Fluid Sloshing and Pressure Fluctuation. In Proceedings of the 57th Aeronautics and Astronautics Propulsion Conference, Okinawa, Japan, 9 March 2017.
12. Brackbill, J.U.; Kothe, D.B.; Zemach, C. A Continuum Method for Modeling Surface Tension. *J. Comput. Phys.* **1992**, *100*, 335–354. [CrossRef]
13. Yokoi, K. A density-scaled continuum surface force model within a balanced force formulation. *J. Comput. Phys.* **2014**, *278*, 221–228. [CrossRef]
14. Yokoi, K. A practice numerical framework for free surface flows based on CLSVOF method, multi moment meth od and density scaled CSF model: Numerical simulation of droplet splashing. *J. Comput. Phys.* **2013**, *232*, 252–271. [CrossRef]
15. Yokoi, K. Efficient implementation of THINC scheme: A simple and practical smoothed VOF algorithm. *J. Comput. Phys.* **2007**, *226*, 1985–2002. [CrossRef]

16. Sakuraba, M.; Hirosaki, S.; Kashiyama, K. Development of Accurate Interface-Capturing method for Free Surface Flow Analysis based on CIVA/VOF method. *J. Appl. Mech.* **2003**, *6*, 215–222. [CrossRef]
17. Bednarz, T.; Tagawa, T.; Kaneda, M.; Ozoe, H.; Szmyd, J.S. Magnetic and gravitational convection of air with a coil inclined around the X axis. *Numer. Heat Transf. Part A Appl.* **2004**, *46*, 99–113. [CrossRef]
18. Tagawa, T.; Ozoe, H. Effect of Prandtl number and computational schemes on the oscillatory natural convection in an enclosure. *Numer. Heat Transf. Part A Appl.* **1996**, *30*, 271–282. [CrossRef]
19. Neu, J.T.; Good, R.J. Equilibrium behavior of fluids in containers at zero gravity. *AIAA J.* **1963**, *1*, 814–819. [CrossRef]
20. Utsumi, M. Low-Gravity Sloshing in an Axisymmetrical Container Excited in the Axial Direction. *J. Appl. Mech.* **2000**, *67*, 344–354. [CrossRef]
21. National Institute of Standards and Technology Material Measurement Laboratory. Thermophysical Properties of Fluid Systems. Available online: http://webbook.nist.gov/chemistry/fluid/ (accessed on 5 December 2019).
22. National Astronomical Observatory of Japan. Magnetic susceptibility of paramagnetic and diamagnetic substance. In *Chronological Scientific Tables Premium*; Maruzen Publishing: Tokyo, Japan, 2019. Available online: http://www.rikanenpyo.jp/member/?module=Member&action=Login (accessed on 21 April 2020).
23. Tagawa, T.; Ozoe, H. Effect of external magnetic fields on various free-surface flows. *Prog. Comput. Fluid Dyn.* **2008**, *8*, 461–468. [CrossRef]

fluids

MDPI

Article

Hydrodynamic Dispersion in Porous Media and the Significance of Lagrangian Time and Space Scales

Vi Nguyen and Dimitrios V. Papavassiliou *

School of Chemical Biological and Materials Engineering, The University of Oklahoma,
Norman, OK 73019, USA; nguyen.kimvi@ou.edu
* Correspondence: dvpapava@ou.edu; Tel.: +1-405-546-6526

Received: 15 April 2020; Accepted: 18 May 2020; Published: 21 May 2020

Abstract: Transport in porous media is critical for many applications in the environment and in the chemical process industry. A key parameter for modeling this transport is the hydrodynamic dispersion coefficient for particles and scalars in a porous medium, which has been found to depend on properties of the medium structure, on the dispersing compound, and on the flow field characteristics. Previous studies have resulted in suggestions of different equation forms, showing the relationship between the hydrodynamic dispersion coefficient for various types of porous media in various flow regimes and the Peclet number. The Peclet number is calculated based on a Eulerian length scale, such as the diameter of the spheres in packed beds, or the pore diameter. However, the nature of hydrodynamic dispersion is Lagrangian, and it should take the molecular diffusion effects, as well as the convection effects, into account. This work shifts attention to the Lagrangian time and length scales for the definition of the Peclet number. It is focused on the dependence of the longitudinal hydrodynamic dispersion coefficient on the effective Lagrangian Peclet number by using a Lagrangian length scale and the effective molecular diffusivity. The lattice Boltzmann method (LBM) was employed to simulate flow in porous media that were constituted by packed spheres, and Lagrangian particle tracking (LPT) was used to track the movement of individual dispersing particles. It was found that the hydrodynamic dispersion coefficient linearly depends on the effective Lagrangian Peclet number for packed beds with different types of packing. This linear equation describing the dependence of the dispersion coefficient on the effective Lagrangian Peclet number is both simpler and more accurate than the one formed using the effective Eulerian Peclet number. In addition, the slope of the line is a characteristic coefficient for a given medium.

Keywords: hydrodynamic dispersion; porous media; Lagrangian length scale; Lagrangian time scale; lattice Boltzmann method; Lagrangian Peclet number

1. Introduction

Hydrodynamic dispersion through porous media has long been of great importance in many engineering fields. For instance, in the field of petroleum engineering, chemicals such as surfactants are injected into hydrocarbon reservoirs to enhance oil recovery [1]. The theory of hydrodynamic dispersion can assist engineers to estimate how far the chemicals reach, thereby designing appropriate injection points to cover the targeted zone. In environmental applications, dispersion in porous media has helped to predict how pollutants spread in the ground water and contaminate aquifers [2–4].

What is hydrodynamic dispersion? In general, substances or particles that disperse in a porous medium do so because of two effects: molecular diffusion and convective dispersion (or mechanical dispersion). The transport that combines both mechanisms of dispersion is known as hydrodynamic dispersion [3,5,6]. The effectiveness of solute transport is based on the hydrodynamic dispersion coefficient, and many researchers have worked to determine this coefficient for various porous geometries at different flow regions by using both experimental and numerical methods. All studies have agreed that the hydrodynamic dispersion coefficient is the sum of an effective molecular diffusivity coefficient and a mechanical dispersion coefficient. Furthermore, the coefficient for effective molecular diffusion in porous media D'_m is always smaller than that for molecular diffusion in a pure solvent D_m [3–8].

There have been several suggestions for calculating the effective molecular diffusion coefficient in a porous medium. Several researchers have proposed to estimate this parameter based on the diffusive tortuosity, which is defined by the squared ratio of the average length of the path traveled by a substance as it diffuses through the porous medium over the straight-line length $\tau_d = \left(\frac{L_d}{L_s}\right)^2$ [9]. The diffusive tortuosity is often defined as the molecular diffusion coefficient of a species in a free fluid relative to that in a porous medium $\tau_d = \frac{D_m}{D'_m}$ [9–14]. However, others have argued that the porosity ε should be present in the equation of tortuosity as $\tau_d = \varepsilon \frac{D_m}{D'_m}$ [15–17]. From another perspective, other researchers have found that there is a link between the diffusion in a porous medium and its electrical conductivity, proposing a correlation such as $\frac{1}{F\varepsilon} = \frac{D_m}{D'_m}$, where F is the formation electrical resistivity factor [6,18,19]. At the end of the day, it appears that the most accurate method is to experimentally measure the diffusive tortuosity of a porous medium by measuring the diffusion coefficient, both in the bulk fluid and in the porous medium [20].

Regarding the hydrodynamic dispersion coefficient, a vast amount of studies for different types of porous media have ended up with different equation forms. In some studies, the longitudinal and transverse dispersion coefficient have been expressed in the general form:

$$D_L = D'_m + \alpha_L u^n \tag{1}$$

$$D_T = D'_m + \alpha_T u^n \tag{2}$$

where n is an empirical constant, varying from 1 to 2; u is the pore velocity; and α_L and α_T represent the effects of geometry in the longitudinal and transverse dispersion, respectively. Other researchers have worked with beds packed with spheres and found different results for different flow regimes; these are briefly summarized in Table 1 [5,7,21,22]. The longitudinal hydrodynamic dispersion coefficient has been found to depend on the Eulerian Peclet number Pe_m^E determined by the diameter of the spheres d_p and molecular diffusion in the bulk fluid D_m [5,6], as follows:

$$Pe_m^E = ud_p/D_m. \tag{3}$$

Koch and Brady suggested equations for both the longitudinal and transverse dispersion coefficient as a function of an effective Eulerian Peclet number defined with the use of the effective diffusivity, Pe'^E_m,

$$Pe'^E_m = ud_p/D'_m \tag{4}$$

by analytically solving the Stokes flow equations in packed beds consisting of randomly packed spheres [7].

Delgado et al. collected their own data and combined them with experimental data available in the literature to characterize the dispersion in packed beds based on the effective Eulerian Peclet number at different flow regimes [5].

It is commonly accepted that the Peclet number is estimated based on the diameter of the spheres that constitute the porous media packing, d_p. The sphere diameter is an Eulerian length scale. It has the advantage of being known a priori. However, the nature of dispersion is Lagrangian, so the hypothesis here is that a Lagrangian length scale should be used in order to combine the molecular diffusion effects and the convection effects in dispersion. In the present study, we set up model equations for the dispersion coefficient with the effective Peclet number based on either the Eulerian or the Lagrangian length scale and examine their predictive ability. The porous media that were investigated in this study included the face-centered cubic (FCC) packing of spheres and randomly packed spheres (RPS), and we then extended to the body-centered cubic (BCC) sphere arrangement for validation purposes. The images of these three packing types are shown in Figure 1. The lattice Boltzmann method (LBM) was used to simulate the flow of water at room temperature through the given porous media, and then Lagrangian particle tracking (LPT) was applied to follow particle trajectories in space and time. The transport of nanoparticles (NPs) of different sizes, corresponding to different dimensionless Schmidt numbers, was investigated. Since all prior studies have confirmed that the dispersion in the streamwise direction (flow direction) is far larger than the one in spanwise direction [3,5], this paper mainly focused on longitudinal dispersion. The contributions of the present work are (a) a comparison of Eulerian and Lagrangian scales for dispersion in porous media; (b) the introduction of a Lagrangian effective Peclet number that is found to be more appropriate for the description of dispersivity, thus unifying hydrodynamic dispersion across porous media types; and (c) the development of model equations that relate longitudinal dispersivity to the Peclet number.

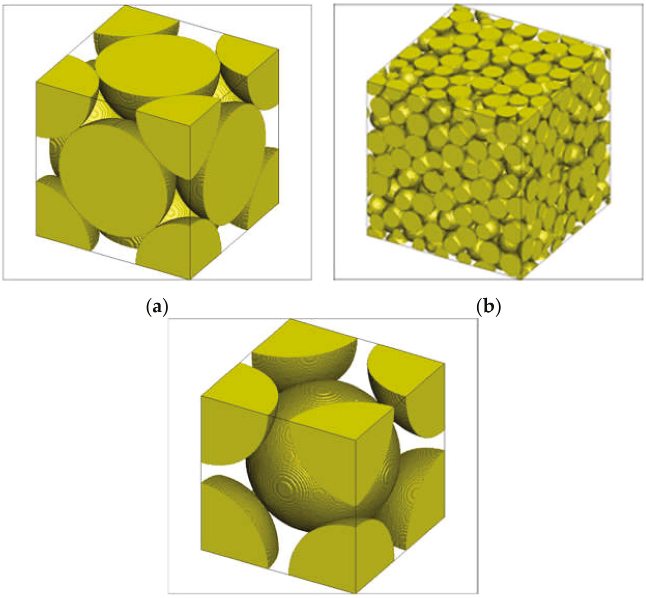

(**a**) (**b**)

(**c**)

Figure 1. The packing types that were examined in this study: (**a**) face-centered cubic (FCC), (**b**) randomly packed spheres (RPS), and (**c**) body-centered cubic (BCC).

Table 1. Summary of studies on hydrodynamic dispersion through packed beds in the randomly packed spheres (RPS) configuration.

Reference	Conditions	Equations of Hydrodynamic Dispersion Coefficient
Fried-Combranous [21]	$Pe_m^E < 300$ $Pe_m^E < 10^5$	$\frac{D_L}{D_m} = \frac{1}{\tau_d} + 0.5 Pe_m^{E\,1.2}$ $\frac{D_L}{D_m} = \frac{1}{\tau_d} + (1.8 \pm 0.4) Pe_m^E$
Hiby [5,22]	$Re < 100$	$\frac{D_L}{D_m} = \frac{1}{\tau_d} + \frac{0.65 Pe_m^E}{1+7 Pe_m^{E\,-0.5}}$
Harleman et al. [22]	$20 < Pe_m^E < 4000$	$\frac{D_L}{D_m} = 0.67 + 0.66 {Pe_m}^{1.2}$
Koch and Brady [7]	Impermeable packed bed $(1-\varepsilon)^2 < Pe_m'^E/2 < 1$ $Pe_m'^E/2 > 1$	 $\frac{D_L}{D_m'} = 1 + \frac{3}{4}\frac{Pe_m'^E}{2}$ $\frac{D_L}{D_m'} = 1 + \frac{3}{4}\frac{Pe_m'^E}{2} + \frac{\pi^2}{6}(1-\varepsilon)\frac{Pe_m'^E}{2}\ln\left(\frac{Pe_m'^E}{2}\right)$

Table 1. *Cont.*

Reference	Conditions	Equations of Hydrodynamic Dispersion Coefficient
Delgado et al. [5]	Longitudinal dispersion	
	Diffusion regime ($Pe^E_m < 0.1$)	$\frac{D_L}{D'_m} = 1$
	Predominant diffusional regime ($0.1 < Pe^E_m < 4$)	$\frac{D_L}{D'_m} = \frac{Pe'^E_m}{0.8/Pe'^E_m + 0.4}$
	Predominant mechanical dispersion ($4 < Pe^E_m$ and $Re < 10$)	$\frac{D_L}{D'_m} = \frac{Pe'^E_m}{\sqrt{18 Pe'^{E\,-1.2}_m + 2.35 Sc^{-0.38}}}$
	Pure mechanical dispersion ($10 < Re$ and $Pe^E_m < 10^6$)	$\frac{D_L}{D'_m} = \frac{Pe'^E_m}{25 Sc^{1.14}/Pe'^E_m + 0.5}$
	Dispersion out of Darcy domain ($Pe^E_m > 10^6$)	$\frac{D_L}{D'_m} = \frac{Pe'^E_m}{2}$
	Transverse dispersion	
	Diffusion regime ($Pe^E_m < 1$)	$\frac{D_T}{D'_m} = 1$
	Predominant mechanical dispersion ($1 < Pe^E_m < 1600$)	$\frac{D_T}{D'_m} = 1 + \frac{1}{2.7\times10^{-5} Sc + 12/Pe'^E_m}$
	Pure mechanical dispersion ($1600 < Pe^E_m < 10^6$)	$\frac{D_T}{D'_m} = \frac{Pe'^E_m}{(0.058 Sc + 14) - (0.058 Sc + 2)\exp(-500 Sc^{0.5} Pe'^E_m)}$
	Dispersion out of Darcy domain ($Pe^E_m > 10^6$)	$\frac{D_T}{D'_m} = \frac{Pe'^E_m}{12}$

2. Materials and Methods

2.1. Lattice Boltzmann Method

In order to simulate the flow through different types of porous media, we used an in-house code based on the LBM. In the LBM, one applies the discretized Boltzmann equation to calculate the probability of fluid particles to move and distribute in different pre-determined directions. The method is mesoscopic, where the macroscopic properties of the flow and the fluid, such as velocity and density, are accurately recovered [23–25]. It is important to highlight that the fluid particles in the LBM can move only in certain directions on a lattice, and these directions are defined by the selected lattice velocity model. In general, an LBM lattice is specified as *DmQn*, where m indicates the dimensionality (2 or 3 for a two-dimensional or a three-dimensional space, respectively) and *n* indicates the number of lattice directions that particles are permitted to travel. Hence, the first step in applying the LBM is to divide the computational domain geometry into structured cartesian meshes, and each node in the lattice is represented by a binary value; for instance, the nodes inside the solid phase of a porous medium are described as 'TRUE,' whereas the ones in the pore space are designated as 'FALSE' [26]. By adopting this discretization of the porous medium space, one may lose fidelity close to the solid boundaries. On the other hand, Cartesian meshing with the LBM is very convenient when simulating the flow field in complicated geometries, like the pore space in digital rock images, where the generation of unstructured grids is required for each porous medium realization without using LBM. Other techniques for simulating flow fields have been recently developed, which demonstrate high order of accuracy and can resolve flow velocities at points very close to the solid grains [27,28]. In Appendix A, we present details of the grid resolution analysis for the LBM to justify the use of the method, in addition to its other computational advantages.

The LBM is relatively simple to implement computationally, and LBM algorithms are parallelizable due to the application of the discrete Boltzmann equation to each single fluid node. Each node needs information from its neighboring nodes in order to calculate particle distribution functions, making the algorithm a good candidate for Message Passing Interface (MPI) [23,25,29]. The key term in this method is the particle distribution function *f*, which represents the fraction of particles at a fluid node position at a certain time. Basically, there are three main steps for solving the discretized Boltzmann equation, i.e., the streaming, the collision, and the forcing steps, as follows:

$$\underbrace{f_i\left(\vec{x}+\vec{e}_i\Delta t, t+\Delta t\right)=f_i\left(\vec{x},t\right)}_{Streaming}+\underbrace{\Omega_i\left(\vec{x},t\right)}_{Collision}\pm\underbrace{ff_i}_{Forcing}. \tag{5}$$

In the streaming step, the particle distribution function f_i at the position $\vec{x}$ at time t moves along the direction i with velocity $\vec{e}_i$ to the new position $(\vec{x}+\vec{e}_i\Delta t)$ during one time step Δt. The collisions occurring during streaming steps are demonstrated by the collision operator Ω_i [2] that represents the change of f_i due to the collision among particles. In the present work, the Bhatnagar, Gross, and Krook (BGK) approximation for the single-relaxation time was used to estimate the collision operator. The BGK has been a simple and reliable relaxation time approximation, and it is given by:

$$\Omega_i\left(\vec{x},t\right)=-\frac{1}{\tau_r}\left(f_i-f_i^{eq}\right). \tag{6}$$

The term τ_r is the relaxation time towards the equilibrium distribution function f_i^{eq}, and it relates to the fluid viscosity ν as follows:

$$\nu=\frac{1}{3}\left(\tau_r-\frac{1}{2}\right). \tag{7}$$

The particle equilibrium distribution function f_i^{eq} is calculated by:

$$f_i^{eq}\left(\vec{x}\right)=w_i\rho\left[1+\frac{\vec{e}_i.\vec{U}}{c^2}+\frac{\left(\vec{e}_i.\vec{U}\right)^2}{2c^4}-\frac{\vec{U}^2}{2c^2}\right] \tag{8}$$

where w_i is the lattice specific weighting factor for the lattice direction i, ρ is the density, $\vec{U}$ is the macroscopic velocity, and c is the speed of sound. The last component added in the Boltzmann equation is the forcing factor to account for the pressure drop during streaming steps [23,25,29].

As mentioned above, the main purpose of using the LBM is to calculate the macroscopic properties such as the fluid density ρ and macroscopic velocity $\vec{U}$; this requirement can be achieved by applying the conservation equations of mass and momentum, as follows:

$$\rho=\sum_{i=0}^{n} f_i \tag{9}$$

$$\rho\vec{U}=\sum_{i=0}^{n} f_i\vec{e}_i \tag{10}$$

where n is the number of lattice directions that particles are permitted to move, including the rest position. In our work, D3Q15 was selected as the lattice velocity model with 15 allowable lattice directions. Moreover, the periodic boundary condition was used in three directions x, y, and z; and at the solid–fluid interfaces, the no-slip boundary condition with the bounce-back technique was applied [24,30].

2.2. LBM Code Validation and Verification

In order to verify the LBM code, we calculated the permeability of periodic simple cubic (SC), FCC, or BCC porous medium and then compared our results with those of two other groups. The size of the simulation box used for each geometry was 100 × 100 × 100 µm, and the domain consisted of 201 nodes in each x, y, and z direction. The LBM was used to run for different values of the forcing factor (the pressure drop over the domain length), resulting in different velocity fields. Next, Darcy's empirical law, showing the relation between the pressure drop $\frac{\Delta P}{L}$ through the flow and the superficial fluid velocity U_s was applied to determine the permeability k of different packing arrays [31]. Darcy's law is expressed as:

$$U_s = -\frac{k}{\mu}\frac{\Delta P}{L} \tag{11}$$

where k is the medium permeability and μ is the dynamic viscosity of the fluid. The k value was then divided by the sphere diameter squared to obtain a dimensionless permeability. Our results for the dimensionless permeability of different geometries, including SC, FCC, and BCC, compared well to the ones of Chapman and Higdon [32] that were obtained by solving the unsteady Stokes equations for the microscopic flow. Moreover, Eshghinejadfard et al. [33] used their own LBM code to calculate the permeability of FCC and BCC and showed similar results to ours. The details of the comparison are shown in Table 2.

Table 2. Comparison of the results for dimensionless permeability with prior results. The reported error is the relative absolute error compared to references.

Geometry	Porosity	Dimensionless Permeability ($k/{d_p}^2$)			Relative Error (%) Compared to	
		Present Results	Reference (1) [32]	Reference (2) [33]	Reference (1) [32]	Reference (2) [33]
FCC	0.26	1.75×10^{-4}	1.74×10^{-4}	1.70×10^{-4}	0.76%	2.96%
BCC	0.32	5.10×10^{-4}	5.02×10^{-4}	5.10×10^{-4}	1.49%	0.10%
SC	0.48	2.61×10^{-3}	2.53×10^{-3}		3.10%	

Moreover, the LBM code was verified for laminar flow through different sphere packing types (SC, BCC, and FCC) of fixed-bed columns. This flow is usually modeled by the Blake–Kozeny (BK) equation [31], which shows the correlation between the pressure drop over the length with superficial velocity:

$$U_s = \frac{\Delta P}{L}\frac{d_p^2}{150\mu}\frac{\varepsilon^3}{(1-\varepsilon)^2}. \tag{12}$$

The results are presented in Table 3, revealing that SC followed the BK correlation with a less than 1% error, while other types of packing deviated from the BK equation with errors of 8.08% and 17.7% for BCC and FCC, respectively. In prior work out of our laboratory, this code was also validated against flow cases with known analytical solutions, such as flow in a slit, in a pipe, and flow around an infinite array of spheres [29].

Table 3. The lattice Boltzmann method (LBM) code verification by Blake–Kozeny equation. The reported error is the relative absolute error for the calculated superficial velocity.

Parameter	SC	BCC	FCC	RPS
Porosity, ε	0.48	0.32	0.26	0.37
Spheres' diameter, d_p (cm)	1.00×10^{-3}	8.66×10^{-3}	7.07×10^{-3}	1.41×10^{-3}
Pressure drop, $\Delta P/L$ (g/cm^2 s^2)	3.66×10^{3}	1.67×10^{4}	5.93×10^{4}	5.33×10^{5}
Pore velocity (cm/s)	2.00×10^{-1}	2.00×10^{-1}	2.00×10^{-1}	2.00×10^{-1}
Superficial velocity, U_s (cm/s)	9.53×10^{-2}	6.40×10^{-2}	5.19×10^{-2}	7.42×10^{-2}
Blake–Kozeny velocity (cm/s)	9.62×10^{-2}	5.92×10^{-2}	6.31×10^{-2}	9.08×10^{-2}
Relative error	0.91%	8.08%	17.70%	18.26%

2.3. Lagrangian Particle Tracking

LPT is an effective method to track the trajectories of particles in a Lagrangian framework while they move in a flow field. However, there are several assumptions when this method is applied. Firstly, the nanoparticles (NPs) are considered as passive, so the presence of NPs does not modify the flow field. Secondly, the NP concentration is low, so the particle–particle interactions are not taken into consideration. Thirdly, the NP–wall interactions and the adsorption of NPs on the wall of the packing spheres are neglected. In short, there are just two kinds of transport contributing to the motion of the NPs—the convection by the flow field and the molecular diffusion of NPs. Therefore, the equation of motion of the NPs can be expressed by:

$$\overrightarrow{X}_{t+\Delta t} = \overrightarrow{X}_t + \Delta t.\overrightarrow{U}_t + \Delta \overrightarrow{X}_m \tag{13}$$

where $\overrightarrow{X}_t$ is the position of a NP at time t and $\overrightarrow{X}_{t+\Delta t}$ is the new position of that NP in the next time step $(t + \Delta t)$ [24,26]. The velocity of the nanoparticle $\overrightarrow{U}_t$, which leads to the convective transport, can be obtained from the LBM flow field using a trilinear interpolation scheme to calculate the velocity of the NPs, $\overrightarrow{U}_t$, at its position between the grid nodes [2,24,30]. The second motion $\Delta\overrightarrow{X}_m$, the molecular diffusion, of the particles is estimated by Einstein's theory for Brownian motion. After moving because of convection, each particle undertakes a Brownian motion jump that is calculated according to a random number drawn from a normal distribution with a zero mean (because the Brownian motion is equally probable to be in the positive or the negative direction) and a standard deviation σ determined by the NP diffusivity D_m. The standard deviation in each space direction is found as follows:

$$\sigma = \sqrt{2D_m\Delta t} = \sqrt{\frac{2\nu\Delta t}{Sc}} \tag{14}$$

where the Schmidt number Sc is the ratio of the fluid kinematic viscosity ν and the NP molecular diffusivity [31]. At this point, by estimating the travelling distance of all NPs caused by convection and Brownian motion, the position of each particle can be tracked at every single time step. In the case that the NPs move into the solid packing after a time step, they are bounced back to their current position in the fluid phase. To be more specific, the new position of each particle in every single time step was checked, and if it was inside the grains, the new position was not updated. The time step in LPT was chosen so that NPs never moved more than one-half of the LBM mesh unit. We determined the timestep by ensuring that any LPT particle that moved with the maximum fluid velocity in every time step plus the maximum Brownian motion in the same direction did not move more than half of the lattice unit. This algorithm has been validated with Taylor–Aris diffusion theory and has shown excellent results [24].

2.4. Velocity Autocorrelation Function

A Lagrangian length scale is determined based on the relevant Lagrangian time scale and the average velocity of all NPs, which is equal to the average pore velocity of $l^L = \tau^L u_p$. Taylor defined the Lagrangian time scale as [34]:

$$\tau^L = \int_0^\infty R^L(\tau)d\tau \tag{15}$$

where $R^L(\tau)$ is the velocity autocorrelation function (VACF). While Taylor's work was focused on turbulent velocity fluctuations along the trajectories of fluid particles, the analogous VACF for porous media would be based on the velocity fluctuations of the NP velocities relative to the average NP velocity at each time step. Furthermore, since the NPs move with both Brownian motion and convection, the VACF should be the material autocorrelation function, as proposed by Saffman [35]. In that work, it was recognized that a scalar marker does not follow the same path as a fluid particle, since it can move off a streamline because of Brownian diffusion. The VACF would need to be defined with the velocity of a diffusing particle, instead of the velocity of a fluid particle, as follows:

$$R^L(t, t_0) = \frac{\overline{V'_j(t)V'_j(t_0)}}{\overline{V'^2_j(t)}^{1/2}\overline{V'^2_j(t_0)}^{1/2}} \tag{16}$$

where t_0 is the initial time, and $V'_j(t)$ is the velocity fluctuation of NP j, $V'_j(t) = V_j(t) - \overline{V}_j(t)$. This equation has been used for dispersion in turbulent flow to estimate the Lagrangian time scale [36–40]. At small times after the NP release, the VACF is almost equal to unity, because the initial velocity is correlated with itself; however, over time, the VACF drops to zero. This happens because the random molecular movement of the particles takes them away from their original velocity streamlines, and the velocity of NPs as time advances has no correlation with the initial velocity of the NPs [34,36,37]. Hence, the Lagrangian time scale represents the time that the particles need to "forget" the velocity of the location from where they came, and it is appropriate to be used to cover the effect of molecular diffusion in the dispersion.

2.5. Scope of Work

Numerical experiments were conducted for two types of porous media, with infinite arrays of spheres packed in the FCC and RPS configurations. The computational domain size was the same for both types of porous media (100 × 100 × 100 µm), but the diameter of the spheres was different. The FCC domain was the minimum periodic cell for the FCC configuration, which contained four spheres with a diameter of 70.76 µm, whereas the simulation box for randomly packed spheres consisted of 432 spheres of a 14.06 µm diameter each. In the RPS configuration, 432 spheres were packed in a cubic domain by the Lubachevsky–Stillinger simulation algorithm [30,41,42]. The images of two packing types are shown in Figure 1.

The number and the size of the spheres in RPS were chosen to ensure that the simulation domain was representative of the porous medium (i.e., that the domain was at least as large as a representative elementary volume for the packed bed). This means that if the size of the RPS simulation box was larger and contained more spheres, the porous media properties (e.g., porosity, tortuosity, and permeability) would remain unchanged. The method used to determine the number of spheres needed to obtain a representative RPS volume included the generation of domains with more spheres keeping the same porosity. After completing flow runs, the average fluid velocity was calculated within a small cube in the center of the domain, and this calculation was repeated by increasing the calculations from the center to the full domain. In Figure 2, we plot the average fluid velocity obtained with the LBM in the streamwise (x direction) and spanwise directions (y and z directions) as a function of increasing the size of the cube from the center to the full length of the cubic domain. With the selected simulation box for RPS configuration, the average velocities in all directions were stable with the increment in the domain size. Since the pressure drop was the same, this means that the permeability of the porous medium did not change with domain size, as seen from Darcy's law. Similar results were achieved when we changed the direction of the flow in the same RPS configuration, setting the flow direction as the y direction and then the z direction. Therefore, the created RPS computational domain was representative of an isotropic medium with RPS packing.

The simulation boxes for FCC and RPS were discretized into LBM lattice nodes. The number of lattice nodes greatly affected the accuracy of the results, as did the computational time. Details of the grid independence analysis that was conducted are presented in Appendix A. Finally, the number of nodes was chosen to balance accuracy with computational resources so that the FCC domain was meshed with a 201 × 201 × 201 mesh, while a 401 × 401 × 401 mesh was applied for the RPS domain. Next, the LBM code in conjunction with a D3Q15 lattice velocity model was implemented to obtain the flow field of water at room temperature through porous media, with the pore velocities 0, 50, 100, 200, 500, 1000, 2000, 3000, and 4000 µm/s. Next, 50,000 NPs were released in the flow domain at randomly and uniformly selected positions in the pore space, and the velocity and trajectory of each of these particles were tracked using the LPT algorithm, as already discussed. For each velocity field, different LPT runs with different values of the particle Schmidt number (*Sc* = 100, 1000, 7080, and 10,000) were performed, providing data for *Sc* covering two orders of magnitude. Moreover, the range of the Schmidt number was chosen to cover particles with diameters from 0.22 to 5 nm, and *Sc* = 7080 was the Schmidt number of Janus particles (d_p = 3.6 nm) in water, which has been investigated in prior work to lower oil–water interfacial tension [1]. Thus, thirty-six LBM/LPT simulations were conducted for each one of the two porous media configurations.

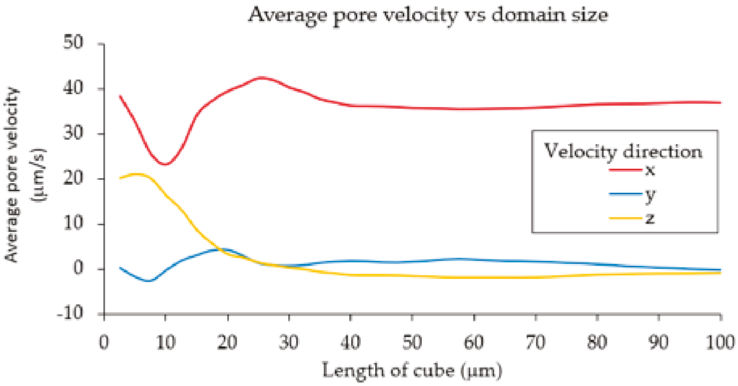

Figure 2. Pore velocity calculated by averaging over an increasing part of the domain volume. The average pore velocity changed with the domain size when water at room temperature flows through the RPS-packed bed in x direction.

The resulting data were used to estimate the VACF and the Lagrangian timescale, as mentioned previously, with initial velocity obtained at the beginning of the LPT run ($t_o = 0$). After that, the hydrodynamic dispersion coefficient was determined based on the positional variance method [24,43]:

$$D = \lim_{t\to\infty}\frac{1}{2}\cdot\frac{d\sigma^2}{dt} \tag{17}$$

where the position variance σ^2 is calculated in each direction as:

$$\sigma^2 = \overline{\left(X_j - \overline{X_j}\right)^2}. \tag{18}$$

The dispersion coefficient, calculated for the flow velocity equal to 0 was considered as the effective molecular dispersion D'_m.

3. Results

3.1. Velocity Autocorrelation Function

Figure 3 is a presentation of the VACF of the streamwise velocity in different cases, when water at room temperature flowed through a porous bed packed with an infinite array of spheres arranged in the FCC geometry. The VACF was calculated based on the initial velocity at the beginning of the LPT run (t_o = 0), which started once the flow field had reached a steady state. Figure 3 consists of four graphs—Figure 3a–d—that represent the VACF of four different types of diffusion NPs with Schmidt numbers of 100, 1000, 7080, and 10,000, respectively. For each value of *Sc*, the velocity autocorrelation functions for various values of average pore velocity, ranging from 50 to 4000 µm/s, are illustrated.

Similarly, Figure 4 is a demonstration of the results for the geometry of randomly packed spheres and at the same simulation conditions as Figure 3. In Figure 5 the effect of molecular diffusion on the Lagrangian timescale is highlighted. In other words, the dependence of the VACF on *Sc*, for both the FCC Figure 5a and RPS geometries Figure 5b, at the same average pore velocity of 1000 μm/s, is highlighted.

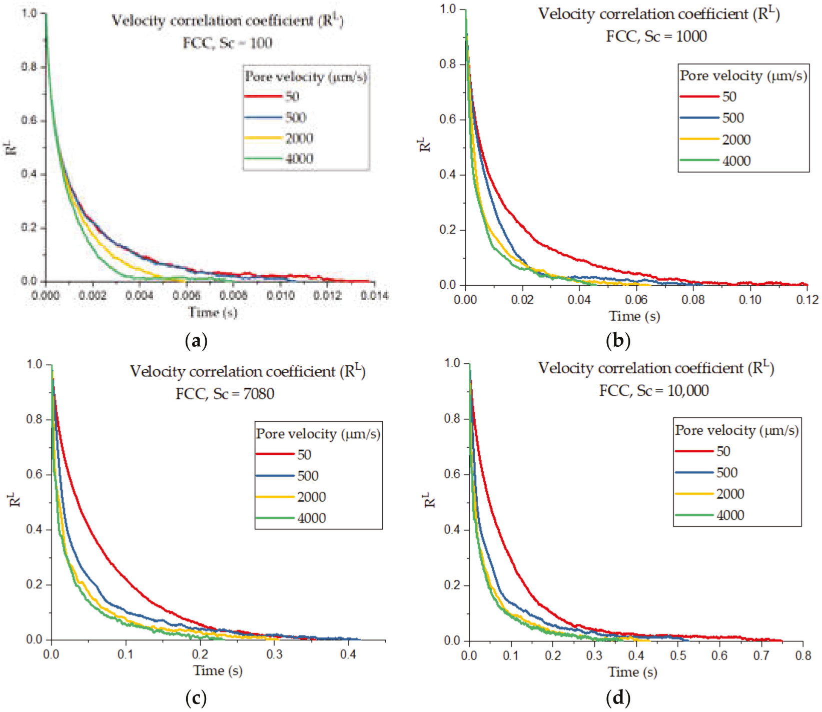

Figure 3. The velocity correlation coefficient for the packed bed with an FCC geometry with time for (**a**) Schmidt number (*Sc*) = 100, (**b**) *Sc* = 1000, (**c**) *Sc* = 7080, and (**d**) *Sc* = 10,000. Each graph contains a velocity autocorrelation coefficient for different average pore velocities.

3.2. Hydrodynamic Dispersion Coefficient

All the data from numerical experiments related to the hydrodynamic dispersion coefficient and Lagrangian timescale for flow of NPs through FCC- and RPS-packed beds are summarized in Appendix B. There were, in total, thirty-six experiments carried out for each porous bed configuration. Four types of NPs with *Sc* = 100, 1000, 7080, and 1000 were released in the flow field with an average pore velocity of 0, 50, 100, 200, 500, 1000, 2000, 3000, and 4000 μm/s. The value of the dispersion coefficient in the static flow field (u = 0) was used as the effective diffusivity D'_m in order to estimate the ratio of dispersion over diffusion (D_L/D'_m). In addition, the effective Peclet number was obtained from the Eulerian length scale (diameter of the packed spheres, see Equation (4)) or the Lagrangian length scale ($l^L = u\tau^L$), as follows:

$$Pe'^L_m = \frac{ul^L}{D'_m} = \frac{u^2\tau^L}{D'_m}. \tag{19}$$

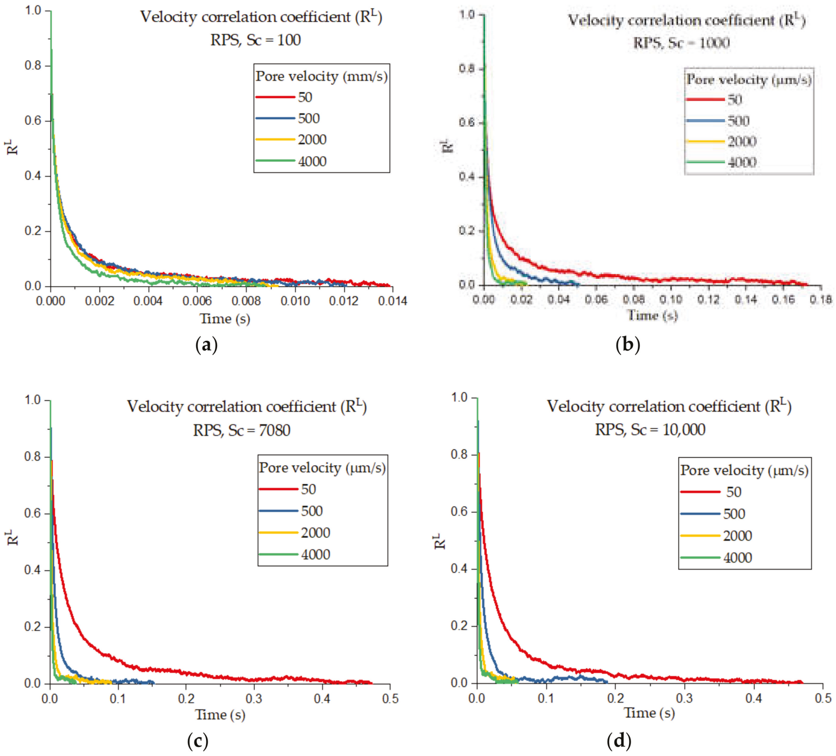

(**a**) (**b**)

(**c**) (**d**)

Figure 4. The velocity correlation coefficients for the packed bed with an RPS geometry with time for (**a**) *Sc* = 100, (**b**) *Sc* = 1000, (**c**) *Sc* = 7080, and (**d**) *Sc* = 10,000. Each graph contains velocity autocorrelation coefficients for different average pore velocities.

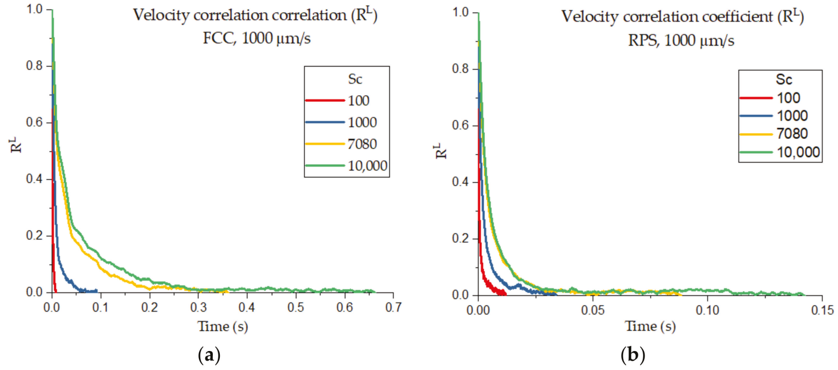

(**a**) (**b**)

Figure 5. The effect of the Schmidt number on the velocity correlation coefficient, as well as Lagrangian timescales for both cases including the FCC (**a**) and RPS (**b**) configurations at the same average pore velocity of 1000 µm/s.

Figure 6 is a plot of the ratio of the hydrodynamic dispersion coefficient over the effective molecular diffusion coefficient for particles in the FCC-packed bed as a function of the effective Peclet number. Figure 6a, b displays the dependence of the coefficient ratio on the effective Eulerian Peclet number and the effective Lagrangian Peclet number, respectively. The examined ratio is linearly correlated with the effective Lagrangian Peclet number. The same analysis was done for the randomly-packed bed; the results are reported in Figure 7.

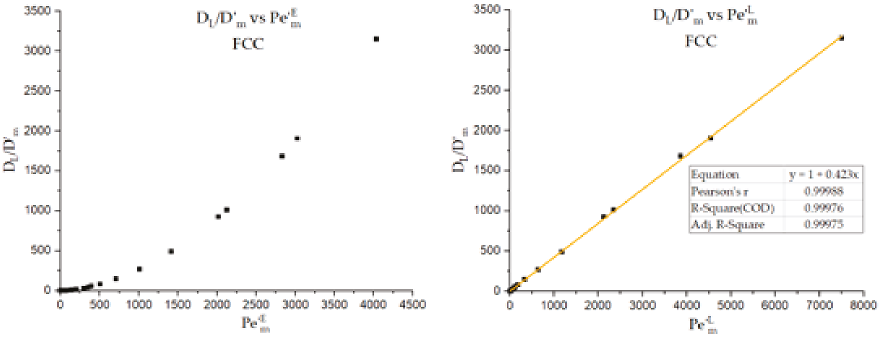

(**a**) (**b**)

Figure 6. The ratio of the hydrodynamic dispersion coefficient over the effective molecular diffusion coefficient in an FCC-packed bed as a function of the Peclet number: (**a**) the dependence of that ratio on the effective Eulerian Peclet number calculated based on the diameter of the packed spheres and (**b**) the dependence of that ratio on the effective Peclet number determined from the Lagrangian length scale.

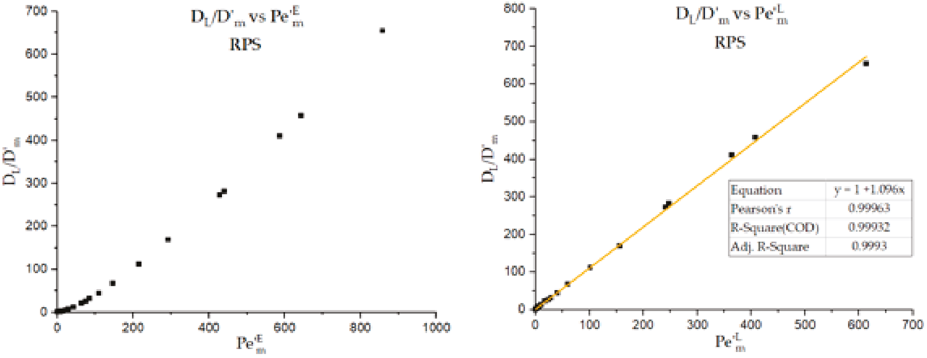

(**a**) (**b**)

Figure 7. The ratio of the hydrodynamic dispersion coefficient over the effective molecular diffusion coefficient in an RPS-packed bed as a function of the Peclet number: (**a**) the dependence of that ratio on the Eulerian Peclet number calculated based on the diameter of the packed spheres and (**b**) the dependence of that ratio on the effective Peclet number determined from the Lagrangian length scale.

4. Discussion

4.1. Velocity Autocorrelation Function and Lagrangian Timescale

Figures 3–5 show that the velocity autocorrelation coefficients started from unity and dropped to zero in different patterns. The VACF dropped depending on the Schmidt number, average velocity, and geometry. Therefore, the Lagrangian timescale also changed with these parameters because it was calculated as the area formed by the velocity correlation and the two coordinate axes x and y (see Equations (15) and (16)). Figures 3 and 4 demonstrate that the Lagrangian timescale decreased when the velocity increased. This means that particles in high pore velocity cases tend to drop off the flow lines quicker at a constant molecular diffusion coefficient. At the same time after the NP release, the NPs in high pore velocity simulations traveled farther in the streamwise direction and had the opportunity to experience a longer tortuous path than NPs in lower pore velocity cases. Moreover, from Figure 5, it is firmly seen that the higher the Schmidt number was, the larger the Lagrangian timescale was. This observation can be explained considering that, when the Schmidt number was high, the random movement because of molecular diffusion was small relative to the movement due to convection. Hence, it took a longer time for the NPs to completely stop following the flow streamlines and for the velocity autocorrelation coefficient to drop to zero. In addition, when the same type of fluid and NPs flowed through the porous media with the same average velocity, the characteristic time scale in the case of the FCC-packed bed was much larger than that in the RPS bed. The reason for this is that the FCC configuration was less tortuous than the RPS configuration. When the particles traveled in the porous media, not only random jumps of particles by diffusion but also their movement due to interaction with the spheres in the packed bed, made them move away from their streamline trajectories. Hence, the particles, moving in more tortuous paths, interacted with the wall more often. This could explain why they quickly decorrelated with their initial velocity.

There are two important messages about the Lagrangian scale that should be highlighted. First, Figures 3 and 4 show that with the same geometry, the Lagrangian timescale changed with molecular diffusivity (or Schmidt number) and flow velocity. Hence, the relevant length scale also varied with Schmidt number and flow velocity. In contrast, for the same geometry, the Eulerian length scale was unchanged, because it only related to the geometrical configuration of the porous medium. Second, by comparing the change of Lagrangian timescale in Figures 3 and 4 with that in Figure 5, it can be seen that the effects of the Schmidt number (molecular diffusion) were more prominent than the effects of flow velocity and geometry.

4.2. Hydrodynamic Dispersion Coefficient

By examining Figures 6 and 7, it is seen that the ratio of the dispersion coefficient and the diffusion coefficient is a function of *Pe*. Figures 6a and 7a indicate that the ratio does not linearly depend on the Eulerian Peclet number Pe'^{E}_{m}. A linear equation is a good fit to the correlation of the dispersion and diffusion ratio with Lagrangian Peclet number Pe'^{L}_{m} for both types of packing (as seen in Figures 6b and 7b). This finding is applicable for an Eulerian Peclet number below 4035 for FCC and 860 for RPS, as well as a Lagrangian Peclet number up to 7500 for FCC and 613 for RPS.

As the relationship between the dispersion coefficient and Eulerian Peclet number is not clear, to correlate the dispersion and diffusion ratio with the Eulerian Peclet number, we suggested two equations that give a minimum value for the mean relative error for this case. Following Taylor–Aris dispersion through a tube [44,45], in the first correlation scheme, a quadratic equation was applied. However, a quadratic equation could not represent well the whole data set for both types of packing. Hence, two equations, including one for low *Pe* and one for high *Pe*, were used for each type of packing. In the second correlation scheme, the form of Equation (1) was utilized, which also showed a good fit in this situation. While there was uncertainty in selecting the appropriate equation in the case of Eulerian *Pe*, only the linear equation was found to be suitable to correlate the dispersion and diffusion ratio with the Lagrangian Peclet number. This was named "Correlation Scheme 3". The three schemes are well-presented in Table 4 for FCC and Table 5 for RPS.

Table 4. Three correlation schemes for hydrodynamic dispersion of particle transport in an FCC-packed bed.

Correlation Scheme	Correlation Equation	Mean Relative Error
1	$Pe'^{E}_{m} < 700 \quad \frac{D_L}{D'_m} = 0.000343\left(Pe'^{E}_{m}\right)^2 + 1$ $Pe'^{E}_{m} > 700 \quad \frac{D_L}{D'_m} = 0.000168\ (Pe'^{E}_{m})^2 + 0.112Pe'^{E}_{m} + 1$	6.3%
2	$\frac{D_L}{D'_m} = 1 + 0.00126\left(Pe'^{E}_{m}\right)^{1.774}$	3.3%
3	$\frac{D_L}{D'_m} = 1 + 0.423Pe'^{L}_{m}$	3.3%

Table 5. Three correlation schemes for hydrodynamic dispersion of particles transport in RPS-packed bed.

Correlation Scheme	Correlation Equation	Mean Relative Error
1	$Pe'^E_m < 50$ $\frac{D_L}{D'_m} = 0.00853(Pe'^E_m)^2 + 1$ $Pe'^E_m > 50$ $\frac{D_L}{D'_m} = 0.000365\ (Pe'^E_m)^2 + 0.462Pe'^E_m + 1$	13.5%
2	$\frac{D_L}{D'_m} = 1 + 0.114(Pe'^E_m)^{1.283}$	15.5%
3	$\frac{D_L}{D'_m} = 1 + 1.096Pe'^L_m$	3.1%

Among these three correlation schemes, the third correlation with effective the Lagrangian Peclet number appeared to be superior for three reasons. It had a higher accuracy in comparison with the first and second schemes, based on an effective Eulerian Peclet number, as seen by the smaller mean relative error of Scheme 3, especially for the case of RPS. Moreover, while there was uncertainty in selecting the form of the correlation equation with effective Eulerian *Pe*, the form of the equation with effective Lagrangian *Pe* was uniform no matter what mode of particle transport was dominant (molecular diffusion or convection). There were at least two unknown parameters in the correlation equation with Eulerian *Pe*, and it was difficult to determine to which properties they related. On the contrary, the equation of the effective Lagrangian *Pe* contained only one unknown coefficient, *A*, as given by:

$$\frac{D_L}{D'_m} = 1 + A\ Pe'^L_m \tag{20}$$

or

$$D_L = D'_m + Au_p l^L = D'_m + A\ \frac{l^{L2}}{\tau^L}. \tag{21}$$

Though this is a simple equation, it still can express the nature of hydrodynamic dispersion. According to this equation, the coefficient D_L is the sum of two terms. The first term is the effective molecular diffusion coefficient D'_m, and the second term $A\ l^{L2}/\tau^L$ is proportional to the characteristic length scale squared over the characteristic timescale. Importantly, with this kind of form, the second term represents the coefficient of mechanical dispersion. Therefore, this correlation equation matches with the theory that hydrodynamic dispersion is a combination of molecular diffusion and convective transport. This confirmed that the Lagrangian scale is a proper approach to represent the theory of hydrodynamic dispersion. This correlation type was further confirmed with the BCC-packed bed, as shown in Figure 8, in order to conclude that it is valid for different packing types. In this equation, only the parameter *A* changes with various geometry structures; therefore, it is reasonable to argue that *A* represents the properties of porous media. The values of *A* for three porous media are briefly summarized in Table 6, together with their properties such as porosity, permeability, and Darcy number.

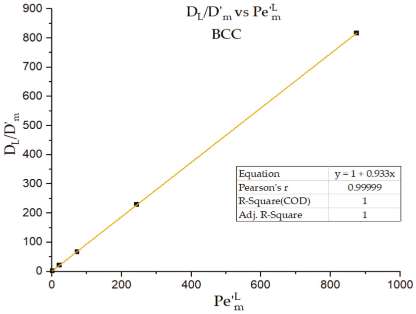

Figure 8. The ratio of hydrodynamic dispersion coefficient over the effective molecular diffusion coefficient in BCC-packed bed dependence on an effective Lagrangian Peclet number.

Table 6. Summary of properties of different packing types of porous media together with the *A* value.

Geometry	Porosity	Permeability k (cm^2)	Diameter of Spheres d_p (cm)	Darcy Number $Da = k/d_p^2$	*A*
FCC	0.26	8.75×10^{-9}	7.07×10^{-3}	1.75×10^{-4}	0.423
BCC	0.32	3.82×10^{-8}	8.66×10^{-3}	5.10×10^{-4}	0.933
RPS-432 spheres	0.37	1.39×10^{-9}	1.41×10^{-3}	7.04×10^{-4}	1.096

The linear connection between dispersion, the diffusion ratio, and the effective Lagrangian *Pe* in this study was only confirmed for packed beds. Further work should focus on the question of whether this finding holds for other types of real porous media found in the subsurface for environmental or oil recovery applications, such as sandstones or limestones. Moreover, the link between *A* and the properties of a porous medium should be further investigated.

5. Conclusions

This work examined the physics of hydrodynamic dispersion in porous media through a Lagrangian point of view. Hydrodynamic dispersion is one of those porous media-related topics that are typically associated with a lot of uncertainty and a lack of fundamental understanding, even though several applications are critically dependent on predicting dispersion in porous media. The conventional approach has been the Eulerian approach, often through macroscopic tools of analysis. Dispersion, however, is an effect that is driven by particle transport phenomena that are below the scale of consideration for macro-scale models. The present study was focused on providing a fresh approach and on identifying the relevant parameters, dimensionless numbers, and quantities. Given the currently available computational techniques that allow for in-depth calculations devoid of empiricisms, such as the use a lattice Boltzmann models and specialized particle tracking algorithms that provide paths of individual particles from a Lagrangian perspective, it is possible to analyze hydrodynamic dispersion in a physically sound framework and to probe its relationship to the effective Peclet number from both the Eulerian and Lagrangian viewpoints.

The results led to the definition of a Peclet number that is based on more naturally relevant scales rather than using Eulerian macroscopic quantities. The length scale used in defining an effective Eulerian Peclet number was the diameter of the spheres making up the porous media and was constant for a certain porous medium configuration. In contrast, the effective Lagrangian Peclet number was calculated from the Lagrangian length and time scales, which varied with molecular diffusion (i.e., the Schmidt number), the fluid velocity, and the pore geometry. This new definition has a strong impact on simplifying and unifying the correlation between the ratio of dispersion over diffusion with the Peclet number in packed beds, as seen in Equation (20). This unified correlation reveals a linear dependence on the effective Lagrangian Peclet number for different packing types, with the clear appearance of a geometrical coefficient *A* as the slope of the line. We conclude that the Lagrangian scales are the appropriate scales for studying hydrodynamic dispersion, as one might have predicted because both molecular diffusion effects and flow are taken into consideration

Author Contributions: Both D.V.P. and V.N. designed the numerical experiments, V.N. performed the simulations, and both D.V.P. and V.N. analyzed the data and wrote the paper. All authors have read and agreed to the published version of the manuscript.

Funding: This research was partially funded by the donors of The American Chemical Society Petroleum Research Fund through grant PRF # 58518-ND9.

Acknowledgments: The use of computing facilities at the University of Oklahoma Supercomputing Center for Education and Research (OSCER) and at XSEDE (under allocation CTS-090025) is gratefully acknowledged.

Conflicts of Interest: The authors declare no conflict of interest. The funders had no role in the design of the study; in the collection, analyses, or interpretation of data; in the writing of the manuscript, and in the decision to publish the results.

Nomenclature

A	geometrical coefficient
c	speed of sound
d_p	sphere diameter
D_m	diffusion coefficient in the pure solvent
D'_m	effective diffusion coefficient in porous media
$\vec{e}$	microscopic velocity
f	particle distribution function
f^{eq}	particle equilibrium distribution function
ff	forcing factor
F	formation electrical resistivity factor
k	permeability of the porous media
L_d	length of the path traveled by a substance
L_s	straight-line length
L	length of porous media in x direction
m	dimensionality indication (m=1, 2, 3)
n	number of allowable directions
$Pe\prime^E_m$	effective Eulerian Peclet number
Pe^E_m	Eulerian Peclet number
$Pe\prime^L_m$	effective Lagrangian Peclet number
Pe^L_m	Lagrangian Peclet number
Re	Reynolds number
R^L	velocity correlation coefficient
Sc	Schmidt number
t	Time
t_0	initial time ($t = 0$)
u	pore velocity
U_s	superficial velocity
$\vec{U}$	macroscopic velocity
V	velocity of a particle
V'	velocity fluctuation
w	lattice specific weighing factor
$\vec{x}$	Position
x	location in the flow direction
X	location of a particle
Greek symbols	
Δt	time interval of each time step
Δx	lattice constant
ΔP	pressure drop
$\Delta\vec{X}_m$	movement due to diffusion
ε	Porosity
μ	fluid dynamic viscosity
ν	fluid kinematic viscosity
ρ	fluid density
σ	standard deviation
σ^2	position variance
τ	Timescale
τ_r	relaxion time
τ_d	diffusive tortuosity
τ^L	Lagrangian timescale
Ω	collision operator
Subscripts and superscripts	
i	lattice direction index
j	nano-particle index
$\overline{(\ )}$	average value

Appendix A. The Grid Independence Analysis for FCC and RPS

In order to conduct grid independence analyses, numerical experiments to simulate the flow of water at room temperature in FCC and RPS were conducted. They all had the same domain size and pressure drop, but they had different resolutions varying from 101 × 101 × 101 to 501 × 501 × 501. The mean velocity was calculated for each run and is shown in Table A1 and Figure A1. Convergence was obtained at the resolution 201 × 201 × 201 for FCC and 401 × 401 × 401 for RPS, with a convergence tolerance of less than 0.53%. In addition to the average velocity, the full fluid velocity distribution was calculated. The range of velocities of the NPs was divided into 20 bins; then, the number of fluid nodes and the percent in each bin was calculated. It was found that there was no significant difference in the velocity distribution of the two LBM runs in the FCC that had the same average pore velocity (1000 μm/s) but different resolutions (201 × 201 × 201 and 501 × 501 × 501), as shown in Figure A2a. Similarly, the velocity distribution profiles for the two LBM runs in the RPS that had the resolutions 201 × 201 × 201 and 501 × 501 × 501 were almost identical, as demonstrated in Figure A2b. Hence, we accept that the chosen resolutions for FCC (201 × 201 × 201) and RPS (401 × 401 × 401) could provide results with an acceptable accuracy.

Table A1. The effect of the number of mesh resolution on the mean velocity of the LBM flow field for FCC and RPS. Bold highlights the values discussed in the text.

Domain Resolution	Number of Grid Points	FCC_Mean Velocity (μm/s)	Error (%) Compared to (501 × 501 × 501)	RS Mean Velocity (μm/s)	Error (%) Compared to (501 × 501 × 501)
101 × 101 × 101	1,030,301	502.340	0.972%	478.762	6.376%
201 × 201 × 201	**8,120,601**	**500.130**	**0.528%**	500.174	2.189%
301 × 301 × 301	27,270,901	497.880	0.075%	505.520	1.143%
401 × 401 × 401	64,481,201	497.540	0.007%	**508.920**	**0.478%**
501 × 501 × 501	125,751,501	497.505	0.000	511.367	0.000

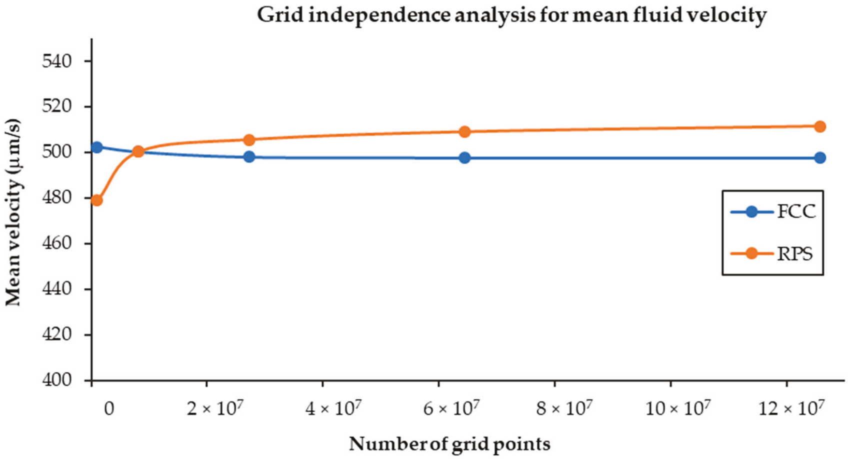

Figure A1. The effect of the number of mesh points on the accuracy of the mean fluid velocity of the LBM flow field for FCC and RPS.

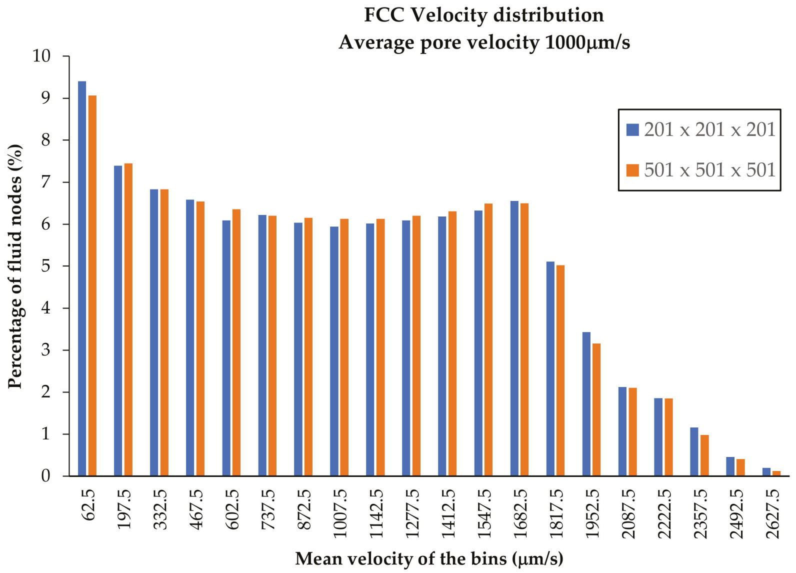

(**a**)

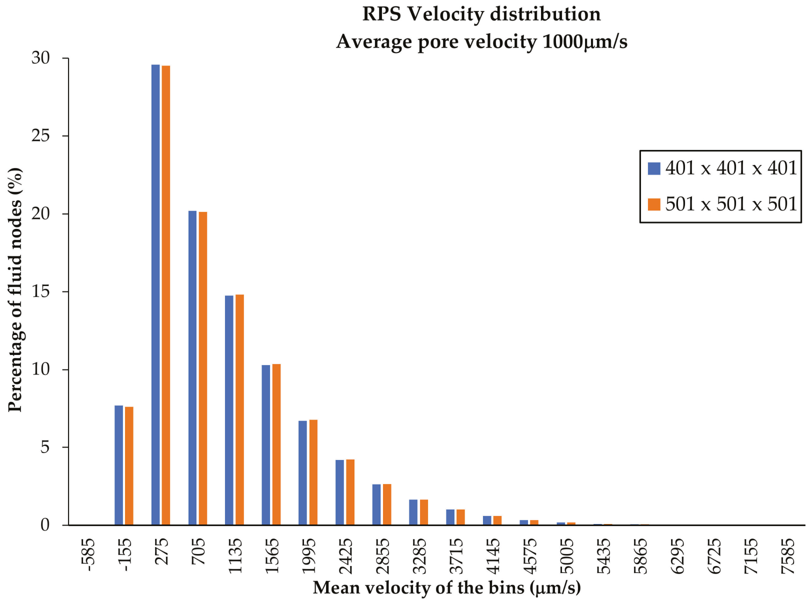

(**b**)

Figure A2. The velocity distribution profiles for the flow fields in (**a**) FCC domains with resolutions of 201 × 201 × 201 and 501 × 501 × 501 and (**b**) RPS domains with resolutions of 401 × 401 × 401 and 501 × 501 × 501. The x-axis shows the mean velocity of the bins, while the y-axis shows the percent of the fluid nodes with the velocity in the range of the corresponding bin.

Appendix B

Table A2. Summary of the Results Related to the ratio of the Hydrodynamic Dispersion Coefficient over the Effective Molecular Diffusion Coefficient together with Eulerian and Lagrangian Peclet Numbers

Sc	Pore velocity, u (cm/s)	FCC				RPS			
		Pe'^{L}_{m}	Pe'^{E}_{m}	$\frac{D_L}{D'_m}$	τ^L(s)	Pe'^{L}_{m}	Pe'^{E}_{m}	$\frac{D_L}{D'_m}$	τ^L(s)
100	5.00×10^{-3}	1.00×10^{-3}	4.94×10^{-1}	9.83×10^{-1}	1.50×10^{-3}	3.00×10^{-4}	1.10×10^{-1}	9.60×10^{-1}	8.20×10^{-4}
	1.00×10^{-2}	2.00×10^{-3}	9.88×10^{-1}	9.99×10^{-1}	1.40×10^{-3}	1.30×10^{-3}	2.10×10^{-1}	1.02	8.70×10^{-4}
	2.00×10^{-2}	8.00×10^{-3}	1.98	9.85×10^{-1}	1.40×10^{-3}	5.50×10^{-3}	4.30×10^{-1}	1.01	9.10×10^{-4}
	5.00×10^{-2}	4.80×10^{-2}	4.94	1.01	1.40×10^{-3}	3.08×10^{-2}	1.09	1.03	7.80×10^{-4}
	1.00×10^{-1}	1.68×10^{-1}	9.88	1.00	1.20×10^{-3}	1.10×10^{-1}	2.13	1.14	7.30×10^{-4}
	2.00×10^{-1}	5.77×10^{-1}	1.98×10	1.12	1.00×10^{-3}	3.95×10^{-1}	4.27	1.37	6.50×10^{-4}
	3.00×10^{-1}	1.15	2.96×10	1.39	9.10×10^{-4}	7.29×10^{-1}	6.40	1.74	5.30×10^{-4}
	4.00×10^{-1}	2.00	3.95×10	1.71	8.90×10^{-4}	1.13	8.53	2.11	4.70×10^{-4}
1000	5.00×10^{-3}	4.70×10^{-2}	4.96	9.90×10^{-1}	1.30×10^{-2}	3.70×10^{-2}	1.08	1.02	9.40×10^{-3}
	1.00×10^{-2}	1.68×10^{-1}	9.93	1.01	1.20×10^{-2}	1.18×10^{-1}	2.13	1.12	7.80×10^{-3}
	2.00×10^{-2}	5.88×10^{-1}	1.99×10	1.14	1.00×10^{-2}	3.92×10^{-1}	4.26	1.40	6.50×10^{-3}
	5.00×10^{-2}	3.01	4.96×10	2.16	8.60×10^{-3}	1.54	1.09×10	2.55	3.90×10^{-3}
	1.00×10^{-1}	1.07×10	9.93×10	5.24	7.60×10^{-3}	3.94	2.13×10	5.15	2.60×10^{-3}
	2.00×10^{-1}	3.59×10	1.99×10^{2}	1.65×10	6.40×10^{-3}	1.04×10	4.26×10	1.23×10	1.70×10^{-3}
	3.00×10^{-1}	7.78×10	2.98×10^{2}	3.29×10	6.20×10^{-3}	1.71×10	6.39×10	2.17×10	1.30×10^{-3}
	4.00×10^{-1}	1.19×10^{2}	3.97×10^{2}	5.35×10	5.30×10^{-3}	2.87×10	8.53×10	3.18×10	1.20×10^{-3}
7080	5.00×10^{-3}	1.56	3.55×10	1.63	6.20×10^{-2}	9.04×10^{-1}	7.47	1.91	3.30×10^{-2}
	1.00×10^{-2}	5.59	7.09×10	3.28	5.60×10^{-2}	2.38	1.47×10	3.39	2.30×10^{-2}
	2.00×10^{-2}	1.97×10	1.42×10^{2}	9.19	4.90×10^{-2}	5.98	2.94×10	7.77	1.40×10^{-2}
	5.00×10^{-2}	1.02×10^{2}	3.55×10^{2}	4.37×10	4.10×10^{-2}	2.33×10	7.47×10	2.62×10	8.60×10^{-3}
	1.00×10^{-1}	3.32×10^{2}	7.09×10^{2}	1.45×10^{2}	3.30×10^{-2}	5.95×10	1.47×10^{2}	6.73×10	5.70×10^{-3}
	2.00×10^{-1}	1.18×10^{3}	1.42×10^{3}	4.86×10^{2}	2.90×10^{-2}	1.56×10^{2}	2.93×10^{2}	1.69×10^{2}	3.70×10^{-3}
	3.00×10^{-1}	2.35×10^{3}	2.13×10^{3}	1.01×10^{3}	2.60×10^{-2}	2.48×10^{2}	4.40×10^{2}	2.82×10^{2}	2.60×10^{-3}
	4.00×10^{-1}	3.86×10^{3}	2.84×10^{3}	1.68×10^{3}	2.40×10^{-2}	3.64×10^{2}	5.87×10^{2}	4.11×10^{2}	2.20×10^{-3}
10000	5.00×10^{-3}	3.07	5.04×10	2.17	8.60×10^{-2}	1.26	1.09×10	2.55	3.20×10^{-2}
	1.00×10^{-2}	1.04×10	1.01×10^{2}	5.26	7.30×10^{-2}	3.69	2.15×10	5.20	2.40×10^{-2}
	2.00×10^{-2}	3.75×10	2.02×10^{2}	1.65×10	6.60×10^{-2}	9.86	4.29×10	1.25×10	1.60×10^{-2}
	5.00×10^{-2}	1.86×10^{2}	5.04×10^{2}	8.03×10	5.20×10^{-2}	4.06×10	1.09×10^{2}	4.41×10	1.00×10^{-2}
	1.00×10^{-1}	6.38×10^{2}	1.01×10^{3}	2.68×10^{2}	4.50×10^{-2}	1.02×10^{2}	2.15×10^{2}	1.11×10^{2}	6.70×10^{-3}
	2.00×10^{-1}	2.13×10^{3}	2.02×10^{3}	9.24×10^{2}	3.70×10^{-2}	2.41×10^{2}	4.29×10^{2}	2.72×10^{2}	4.00×10^{-3}
	3.00×10^{-1}	4.54×10^{3}	3.03×10^{3}	1.91×10^{3}	3.50×10^{-2}	4.08×10^{2}	6.44×10^{2}	4.58×10^{2}	3.00×10^{-3}
	4.00×10^{-1}	7.50×10^{3}	4.03×10^{3}	3.15×10^{3}	3.30×10^{-2}	6.13×10^{2}	8.58×10^{2}	6.55×10^{2}	2.50×10^{-3}

References

1. Vu, T.V.; Papavassiliou, D.V. Synergistic effects of surfactants and heterogeneous nanoparticles at oil-water interface: Insights from computations. *J. Colloid Interface Sci.* **2019**, *553*, 50–58. [CrossRef] [PubMed]
2. Pham, N.H.; Voronov, R.S.; Tummala, N.R.; Papavassiliou, D.V. Bulk stress distributions in the pore space of sphere-packed beds under Darcy flow conditions. *Phys. Rev. E Stat. Nonlinear Soft Matter Phys.* **2014**, *89*, 1–13. [CrossRef] [PubMed]
3. Lowe, C.P.; Frenkel, D. Do hydrodynamic dispersion coefficients exist? *Phys. Rev. Lett.* **1996**, *77*, 4552–4555. [CrossRef] [PubMed]
4. Dutta, D. Hydrodynamic Dispersion. In *Encyclopedia of Microfluidics and Nanofluidics*; Springer: Boston, MA, USA, 2013; pp. 1–14.
5. Delgado, J.M.P.Q. Longitudinal and transverse dispersion in porous media. *Chem. Eng. Res. Des.* **2007**, *85*, 1245–1252. [CrossRef]

6. Perkins, T.K.; Johnston, O.C. A Review of Diffusion and Dispersion in Porous Media. *Soc. Pet. Eng. J.* **1963**, *3*, 70–84. [CrossRef]
7. Koch, D.L.; Brady, J.F. Dispersion in fixed beds. *J. Fluid Mech.* **1985**, *154*, 399–427. [CrossRef]
8. Zhu, Y.; Fox, P.J. Simulation of pore-scale dispersion in periodic porous media using smoothed particle hydrodynamics. *J. Comput. Phys.* **2002**, *182*, 622–645. [CrossRef]
9. Hunt, A.G.; Ewing, R.P.; Sahimi, M. Tortuosity in Porous Media: A Critical Review. *Soil Sci. Soc. Am. J.* **2013**, *77*, 1461–1477. [CrossRef]
10. Sahimi, M. *Flow and Transport in Porous Media and Fractured Rock: From Classical Methods to Modern Approaches*, 2nd ed.; Wiley-VCH: Weinheim, Germany, 2011.
11. Sahimi, M. Flow phenomena in rocks: From continuum models to fractals, percolation, cellular automata, and simulated annealing. *Rev. Mod. Phys.* **1993**, *65*, 1393–1534. [CrossRef]
12. Kim, A.S.; Chen, H. Diffusive tortuosity factor of solid and soft cake layers: A random walk simulation approach. *J. Memb. Sci.* **2006**, *279*, 129–139. [CrossRef]
13. Satterfield, C.N.; Sherwood, T.K. *The Role of Diffusion in Catalysis*; Addison-Wesley: Boston, MA, USA, 1963.
14. Ben Clennell, M. Tortuosity: A guide through the maze. *Geol. Soc. Spec. Publ.* **1997**, *122*, 299–344. [CrossRef]
15. Moldrup, P.; Olesen, T.; Komatsu, T.; Schjønning, P.; Rolston, D.E. Tortuosity, Diffusivity, and Permeability in the Soil Liquid and Gaseous Phases. *Soil Sci. Soc. Am. J.* **2001**, *65*, 613–623. [CrossRef]
16. Epstein, N. On tortuosity and the tortuosity factor in flow and diffusion through porous media. *Chem. Eng. Sci.* **1989**, *44*, 777–779. [CrossRef]
17. Currie, J.A. Gaseous diffusion in porous media. Part 2.—Dry granular materials. *Br. J. Appl. Phys.* **1960**, *11*, 318–324. [CrossRef]
18. Klinkenberg, L.J. Analog Between Diffusion and Electrical Conductivity in Porous Rocks. *Geol. Soc. Am. Bull.* **1951**, *62*, 559–564. [CrossRef]
19. Grane, F.E.; Gardner, G.H.F. Measurements of Transverse Dispersion in Granular Media. *J. Chem. Eng. Data* **1961**, *6*, 283–287. [CrossRef]
20. Li, Z.; Dong, M. Experimental study of diffusive tortuosity of liquid-saturated consolidated porous media. *Ind. Eng. Chem. Res.* **2010**, *49*, 6231–6237. [CrossRef]
21. Fried, J.J.; Combarnous, M.A. *Dispersion in Porous Media*; Academic Press: New York, NY, USA, 1971; Volume 7.
22. Rose, D.A. Some aspects of the hydrodynamic dispersion of solutes in porous materials. *J. Soil Sci.* **1973**, *24*, 284–295. [CrossRef]
23. Mohamad, A.A. *Lattice Boltzmann Method*; Springer: London, UK, 2011; Volume 20.
24. Voronov, R.S.; VanGordon, S.B.; Sikavitsas, V.I.; Papavassiliou, D.V. Efficient Lagrangian scalar tracking method for reactive local mass transport simulation through porous media. *Int. J. Numer. Methods Fluids* **2011**, *67*, 501–517. [CrossRef]
25. Chen, G.D.; Doolen, S. Lattice Boltzmann Method for fluid flows. *Annu. Rev. Fluid Mech. Palo Alto* **1998**, *30*, 329–364. [CrossRef]
26. Pham, N.H.; Swatske, D.P.; Harwell, J.H.; Shiau, B.J.; Papavassiliou, D.V. Transport of nanoparticles and kinetics in packed beds: A numerical approach with lattice Boltzmann simulations and particle tracking. *Int. J. Heat Mass Transf.* **2014**, *72*, 319–328. [CrossRef]
27. Massoudi, M. Boundary conditions in mixture theory and in CFD applications of higher order models. *Comput. Math. Appl.* **2007**, *53*, 156–167. [CrossRef]
28. Mofakham, A.A.; Stadelman, M.; Ahmadi, G.; Shanley, K.T.; Crandall, D. Computational modeling of hydraulic properties of a sheared single rock fracture. *Transp. Porous Media* **2018**, *124*, 1–30. [CrossRef]
29. Voronov, R.; VanGordon, S.; Sikavitsas, V.I.; Papavassiliou, D.V. Computational modeling of flow-induced shear stresses within 3D salt-leached porous scaffolds imaged via micro-CT. *J. Biomech.* **2010**, *43*, 1279–1286. [CrossRef]
30. Pham, N.H.; Papavassiliou, D.V. Nanoparticle transport in heterogeneous porous media with particle tracking numerical methods. *Comput. Part. Mech.* **2017**, *4*, 87–100. [CrossRef]
31. Bird, W.E.; Stewart, R.B. *Transport Phenomena*; Wiley: New York, NY, USA, 2002.
32. Chapman, A.M.; Higdon, J.J.L. Oscillatory Stokes flow in periodic porous media. *Phys. Fluids A* **1992**, *4*, 2099–2116. [CrossRef]

33. Eshghinejadfard, A.; Daróczy, L.; Janiga, G.; Thévenin, D. Calculation of the permeability in porous media using the lattice Boltzmann method. *Int. J. Heat Fluid Flow* **2016**, *62*, 93–103. [CrossRef]
34. Taylor, G.I. Diffusion by continuous movements. *Proc. Lond. Math. Soc.* **1992**, *2*, 196–212. [CrossRef]
35. Saffman, P.G. On the effect of the molecular diffusivity in turbulent diffusion. *J. Fluid Mech.* **1960**, *8*, 273–283. [CrossRef]
36. Srinivasan, C.; Papavassiliou, D.V. Backwards and forwards dispersion of a scalar in turbulent wall flows. *Int. J. Heat Mass Transf.* **2010**, *53*, 1023–1035. [CrossRef]
37. Le, P.M.; Papavassiliou, D.V. Turbulent dispersion from elevated line sources in channel and couette flow. *AIChE J.* **2005**, *51*, 2402–2414. [CrossRef]
38. Mito, Y.; Hanratty, T.J. Use of a modified Langevin equation to describe turbulent dispersion of fluid particles in a channel flow. *Flow Turbul. Combust. 2* **0002**, *68*, 1–26, 2002. [CrossRef]
39. Luo, J.P.; Lu, Z.M.; Liu, Y.L. Lagrangian time scales and its relationship to Eulerian equivalents in turbulent channel flow. *J. Shanghai Univ.* **2010**, *14*, 71–75. [CrossRef]
40. Luo, J.; Ushijima, T.; Kitoh, O.; Lu, Z.; Liu, Y. Lagrangian dispersion in turbulent channel flow and its relationship to Eulerian statistics. *Int. J. Heat Fluid Flow* **2007**, *28*, 871–881. [CrossRef]
41. Lubachevsky, B.D.; Stillinger, F.H. Geometric properties of random disk packings. *J. Stat. Phys.* **1990**, *60*, 561–583. [CrossRef]
42. Skoge, M.; Donev, A.; Stillinger, F.H.; Torquato, S. Packing hyperspheres in high-dimensional Euclidean spaces. *Phys. Rev. E Stat. Nonlinear Soft Matter Phys.* **2006**, *74*, 1–11. [CrossRef]
43. Manz, B.; Gladden, L.F.; Warren, P.B. Flow and dispersion in porous media: Lattice-Boltzmann and N M R studies. *AIChE J.* **1999**, *45*, 1845–1854. [CrossRef]
44. Taylor, G. Dispersion of soluble matter in solvent flowing slowly through a tube. *Proc. R. Soc. London. Ser. A Math. Phys. Sci.* **1953**, *219*, 186–203. [CrossRef]
45. Aris, R. On the dispersion of a solute in a fluid flowing through a tube. *Proc. R. Soc. Lond. Ser. A Math. Phys. Sci.* **1956**, *235*, 67–77.

fluids

MDPI

Article

The Heat Flux Vector(s) in a Two Component Fluid Mixture

A. D. Kirwan, Jr. [1,*,†] **and Mehrdad Massoudi** [2,†]

[1] School of Marine Science and Policy, University of Delaware, 103 Robinson Hall, Newark, DE 19716, USA
[2] U.S. Department of Energy, National Energy Technology Laboratory (NETL), 626 Cochrans Mill Road, P.O. Box 10940, Pittsburgh, PA 15236, USA; massoudi@netl.doe.gov
* Correspondence: adk@udel.edu; Tel.: +1-302-831-2977
† Both authors contributed equally to this work.

Received: 22 January 2020; Accepted: 12 May 2020; Published: 20 May 2020

Abstract: Bulk kinematic properties of mixtures such as velocity are known to be the density weighed averages of the constituent velocities. No such paradigm exists for the heat flux of mixtures when the constituents have different temperatures. Using standard principles such as frame indifference, we address this topic by developing linear constitutive equations for the constituent heat fluxes, the interaction force between constituents, and the stresses for a mixture of two fluids. Although these equations contain 18 phenomenological coefficients, we are able to use the Clausius-Duhem inequality to obtain inequalities involving the principal and cross flux coefficients. The theory is applied to some special cases and shown to reduce to standard results when the constituents have the same temperature.

Keywords: mixtures; Fourier's heat conduction; heat flux vector; continuum theory; Clausius-Duhem inequality

PACS: J0101

---

1. Introduction

Of general concern here are the heat fluxes of multicomponent materials where the temperatures of the components are not equal. A general theory for multi-temperature mixtures was proposed by Dunwoody and Müller [1], extended by Bowen and Garcia [2], and applied to a mixture of Navier Stokes fluids by Ahmadi [3]. Despite this theoretical framework, as well as many examples from both the environment and industry of multicomponent materials with distinct constituent temperatures, there is a paucity of research on the thermodynamic implications of characterizing the bulk properties of the heat fluxes of such materials. Perhaps this is due to the myth that such materials quickly come to thermal equilibrium. In reality, many processes such as radiative heat transfer, disparate thermal conductivities of constituent materials, and relative motion of the constituents may disrupt a rapid approach to overall thermal equilibrium.

Quantification of the heat flux has been a goal of researchers ever since the beginning of thermodynamics. Early theories were phenomenologically motivated, but in recent years considerable attention has been devoted to Maxwell-Cattaneo type models; see [4,5] and a more recent discussion in Jou et al. [6]. Typically this approach leads to some form of the telegraph equation, a special case of which is Fourier's law of heat conduction. As our concern here is not with the propagation of heat pulses but with constraints imposed on constitutive models by the second law, it is sufficient to focus here on Fourier's law. For an isotropic material this is given by the familiar expression:

$$\mathbf{q} = -k\nabla\theta. \tag{1}$$

Here $\mathbf{q}$ is the heat flux vector, θ is the temperature, ∇ denotes the gradient operator, and k is a material property known as thermal conductivity. The latter is readily obtained from standard measurements of $\nabla\theta$ and $\mathbf{q}$.

However, a substance composed of two components with different thermal conductivities is not so trivial. Consider two scenarios of a mixture of two constituents, one with temperature θ_a and thermal conductivity k_a and the other with temperature θ_b and thermal conductivity k_b. If both follow the Fourier's heat conduction relation and the two components are at thermal equilibrium, i.e., $\theta_a = \theta_b = \theta$, then

$$\begin{aligned} \mathbf{q}_a &= -k_a \nabla\theta \\ \mathbf{q}_b &= -k_b \nabla\theta. \end{aligned} \tag{2}$$

One is then tempted to take as the mixture heat flux

$$\mathbf{q}_{mix} = \mathbf{q}_a + \mathbf{q}_b = -(k_a + k_b)\nabla\theta = -k_{mix}\nabla\theta. \tag{3}$$

This is just like the single constituent case, and Fourier's law applies to the mixture. Standard methods can determine the conductivity of the mixture.

Now suppose the two constituents are at different temperatures. Allowing for cross-thermal gradient heat fluxes one has

$$\begin{aligned} \mathbf{q}_a &= -k_{aa}\nabla\theta_a - k_{ab}\nabla\theta_b \\ \mathbf{q}_b &= -k_{ba}\nabla\theta_b - k_{bb}\nabla\theta_b. \end{aligned} \tag{4}$$

Simply adding the fluxes as in the previous case gives

$$\mathbf{q}_{mix} = -(k_{aa} + k_{ba})\nabla\theta_a - (k_{ab} + k_{bb})\nabla\theta_b. \tag{5}$$

Although the definition of the mixture heat flux is the same, it is not possible to prescribe both a unique temperature and conductivity for the mixture if the constituents are not in thermal equilibrium.

These idealized examples raise the ontological question: *What flux laws are appropriate that ensure consistency with the primitive notion that the consequent flow of heat does not violate the second law?* In this regard Petroski [7] pointed out that for many non-homogenous and anisotropic materials the simple Fourier's assumption does not hold (see also [8]). For complex materials such as polymers, granular materials, and non-Newtonian fluids, the thermal conductivity of the material is assumed to depend on parameters such as volume fraction, particle size, shear rate, etc. [9–11]. Also see [12,13] for detailed reviews. These and other matters have spurred research on general theories such as Maxwell-Cattaneo models, as noted previously.

To address the ontological question noted above, we develop a unified theory for multicomponent materials with different temperatures. Previously, Massoudi [14] used a mixture theory approach to obtain an explicit constitutive relation for the heat flux vector(s) $\mathbf{q}$ of a two-phase mixture with a single temperature. We extend that study to allow for distinct temperatures θ_1 and θ_2 for the components.

We intend for this study to provide some theoretical guidance for experimenters attempting to establish the phenomenological parameters for mixtures. To achieve this we utilize the second law requirement that the rate of entropy production of the mixture as a whole is non-negative to establish inequality constraints on the phenomenological coefficients. In this regard some investigators have also imposed Onsager's reciprocal relations to reduce the number of cross flux coefficients. For example in (4) this constraint requires $k_{ab} = k_{ba}$, thus reducing the number of coefficients that are needed to be determined to three. By appealing to just the second law, we do not need to make this restriction. In this regard it should be noted that in addition to Onsager type constraints, Klika et al. [15] and Klika and Krause [16] have developed functional constraints for phenomenological coefficients. Although their theory does not necessarily reduce the number of coefficients, it should simplify experimental procedures necessary to establish their values.

Our report is organized as follows. Section 2 gives a succinct review of the conservation equations for mass, linear momentum, angular momentum, and energy, and the entropy tendency equation for the entropy for a two-component fluid mixture. The traditional approach introduces the Helmholtz free energy into the Clausius-Duhem inequality from which constraints on phenomenological coefficients can be developed from constitutive equations with explicit statements connecting the fluxes and thermodynamic forces, i.e., rate variables. Our observation is that thermodynamic constraints arising from the inequality sometimes are neglected in constitutive theories for nonlinear and complex materials such as polymers and second grade fluids. To address this and other more fundamental issues Rajagopal and Srinivasa [17–19] developed a consistent theory built around constitutive equations where the thermodynamic forces and fluxes are connected through implicit relations.

As there is a substantial body of literature on applications of the traditional framework to mixture theory we elect to follow that approach. However, we deviate slightly from that approach by relying on classical irreversible thermodynamics concepts [20] and utilize the Gibbs relation for the mixture to establish the non-negative entropy production. In Section 3 we develop linear constitutive relations for this two-component mixture. We extend previous work to allow for constituents with different temperatures. Section 4 addresses constraints imposed on the constitutive equations by the second law of thermodynamics. Section 5 analyzes some special cases and implications for characterizing the heat flux of multi-temperature mixtures. We conclude in section 6 with a discussion of the implications of this study.

2. Review of the Basic Equations of Mixture Theory

2.1. Background

Foundations of mixture theory, sometimes called the theory of interacting continua, are given in books by [21,22], and early review articles by [23–25]. A recent review article by Klika, [20], provides a critical assessment of standard approaches to multicomponent material. Here we appeal to the classical irreversible thermodynamics paradigm as advocated by [20]. The conceptual premise of this approach regards each component as a single continuum, denoted as S_α, and at each instant of time, every point in space is considered to be occupied by a particle belonging to each component of the mixture. Conservation laws are then written for each component accounting for interactions with other constituents. Constitutive relations for the fluxes of heat and momentum are used to close the governing equations.

Balance equations for the conservation of mass, linear momentum, angular momentum, and energy equations for each constituent are obtained by summing the appropriate constituent equations over all constituents; see for example [23,25]. Many early researchers attributed fundamental significance to the mixture equations, but more recent works simply regard these as statements that the mixture obeys the basic principles of physics. See [20,26,27] for additional discussion of this matter.

Our concern here is with the mixture of the two constituents that comprise a thermo-mechanical system in which electromagnetic and chemical reactions are ignored and material isotropy is assumed. Of course, the latter effects can be incorporated in mixture theory but are not essential here.

At each instant of time t, it is assumed that each point in space is occupied by particles belonging to both S_1 and S_2. Then the equations describing the motion of a two-component system are (see [20,23,24,28]):

$$\mathbf{x}_1 = \mathcal{X}_1(\mathbf{X}_1, t),\ \mathbf{x}_2 = \mathcal{X}_2(\mathbf{X_2}, t) \tag{6}$$

while the kinematical quantities associated with these motions are

$$\mathbf{v}_1 = \frac{d_1\mathbf{x}_1}{dt},\ \mathbf{v}_2 = \frac{d_2\mathbf{x}_2}{dt}, \tag{7}$$

$$\mathbf{D}_1 = \frac{1}{2}\left(\nabla\mathbf{v}_1 + (\nabla\mathbf{v}_1)^T\right),\ \mathbf{D}_2 = \frac{1}{2}\left(\nabla\mathbf{v}_2 + (\nabla\mathbf{v}_2)^T\right), \tag{8}$$

$$\mathbf{W}_1 = \frac{1}{2}\left(\nabla \mathbf{v}_1 - (\nabla \mathbf{v}_1)^T\right), \mathbf{W}_2 = \frac{1}{2}\left(\nabla \mathbf{v}_2 - (\nabla \mathbf{v}_2)^T\right). \tag{9}$$

In the above, $\mathbf{v}$ is the velocity field, $\mathbf{D}$ is the symmetric part of velocity gradient or deformation rate tensor, $\mathbf{W}$ is the skew-symmetric part of the velocity gradient or spin tensor, the superscript T indicates the matrix transpose, and $\frac{d_1}{dt}$ and $\frac{d_2}{dt}$ denote differentiation with respect to time holding $\mathbf{X}_1$ and $\mathbf{X}_2$ fixed, respectively.

The densities ρ_1 and ρ_2 for these two components are

$$\rho_1 = \phi\rho_{10}, \;\; \rho_2 = (1-\phi)\,\rho_{20} \tag{10}$$

where ρ_{10} and ρ_{20} are the pristine densities of the constituents in the reference configuration; ϕ is the volume fraction of constituent 1. In the case of a mixture of a fluid and solid, ϕ usually refers to the solid phase. Generally, $0 \leq \phi < \phi_{max} < 1$. The function ϕ is represented as a continuous function of position and time; in reality, ϕ is either one or zero at any position and at any time, depending upon whether one is pointing to a particle in constituent 1 or 2 at that position. In other words, the real volume distribution content has been averaged, in some sense, over a neighborhood of any given position. In practice, ϕ has a maximum value, especially for fluid-solid particle systems, generally designated as the maximum packing fraction, which depends on the shape, size, method of packing, etc.

The mixture density ρ is given by

$$\rho = \rho_1 + \rho_2 \tag{11}$$

and a mixture or average velocity $\mathbf{v}$ typically is defined by

$$\rho\mathbf{v} = \rho_1\mathbf{v}_1 + \rho_2\mathbf{v}_2. \tag{12}$$

Of course other weighting functions could be used in (12), but we prefer the partial densities since momentum density is fundamental in the equations of motion.

2.2. Conservation of Mass

Assuming no chemical reactions involving mass exchange between the constituents, the equations of conservation of mass for each constituent in the Eulerian form are (see [20,22–24]):

$$\begin{aligned} \frac{d_1\rho_1}{dt} + \rho_1 \nabla \cdot \mathbf{v}_1 &= \frac{\partial \rho_1}{\partial t} + \nabla \cdot (\rho_1 \mathbf{v}_1) = 0 \\ \frac{d_2\rho_2}{dt} + \rho_2 \nabla \cdot \mathbf{v}_2 &= \frac{\partial \rho_2}{\partial t} + \nabla \cdot (\rho_2 \mathbf{v}_2) = 0 \end{aligned} \tag{13}$$

where $\frac{\partial}{\partial t}$ is the partial derivative with respect to time holding the space dimensions fixed. Using (11) and (12) it is clear that

$$\frac{\partial \rho}{\partial t} + \nabla \cdot (\rho \mathbf{v}) = 0.$$

2.3. Conservation of Linear Momentum

Let $\mathbf{T}_1$ and $\mathbf{T}_2$ denote the respective partial stress tensors. We follow Eckart [29] and include hydrostatic or equilibrium components in these stresses. Then the balances of linear momentum for the two components are given by

$$\begin{aligned} \rho_1 \frac{d_1 \mathbf{v}_1}{dt} &= \nabla \cdot \mathbf{T}_1 + \rho_1 \mathbf{b}_1 + \mathbf{f}_I \\ \rho_1 \frac{d_2 \mathbf{v}_2}{dt} &= \nabla \cdot \mathbf{T}_2 + \rho_2 \mathbf{b}_2 - \mathbf{f}_I. \end{aligned} \tag{14}$$

Here $\mathbf{b}_\alpha$ are the external body forces and $\mathbf{f}_I$ is a frame invariant form of the interaction forces resulting in the exchange of momentum between the components. The importance of frame invariance in this context is discussed by Truesdell and Noll [30]. Note that in writing (14) we appealed to Newton's third law of motion to require that the latter exactly cancels in the conservation of total linear momentum of the mixture.

Once the partial stress tensors are specified, a mixture stress tensor can be defined as in [31,32].

$$\mathbf{T}_{mix} = \mathbf{T}_1 + \mathbf{T}_2 \tag{15}$$

where, as suggested by [33],

$$\begin{aligned}\mathbf{T}_1 &= (1-\phi)\,\mathbf{T}_{10}\\ \mathbf{T}_2 &= \phi\mathbf{T}_{20}.\end{aligned} \tag{16}$$

Here $\mathbf{T}_{10}$ and $\mathbf{T}_{20}$ are the pristine stress tensors for the respective material. Thus the mixture stress tensor reduces to that of substance 1 as $\phi \to 0$ and to that of substance 2 as $\phi \to 1$. We note that there are other ways to define $\mathbf{T}_{mix}$ in terms of $\mathbf{T}_1$ and $\mathbf{T}_2$, such as equation (2.13) in [34].

2.4. Conservation of Angular Momentum

The balance of moment of momentum for mixtures was analyzed in some detail by Bowen, [25]. It is sufficient here to write this as

$$\begin{aligned}&\mathbf{T}_\alpha = \mathbf{T}_\alpha^T + \mathbf{M}_\alpha,\ \alpha = 1,2\\ &\mathbf{M}_1 + \mathbf{M}_2 = 0.\end{aligned} \tag{17}$$

Bowen [25] refers to $\mathbf{M}_\alpha$ as the couple stress for constituent α. In the absence of couple stresses, i.e., when $\mathbf{M}_\alpha = 0$ then (17) states the total stress tensor is symmetric. Equation (17) states that the constituent couple stresses cancel each other.

2.5. Conservation of Energy

Each component of the mixture satisfies a balance of energy equation. This is expressed as

$$\begin{aligned}\rho_1\frac{d_1}{dt}\left(u_1 + \frac{\mathbf{v}_1\cdot\mathbf{v}_1}{2}\right) &= \nabla\cdot(\mathbf{T}_1\cdot\mathbf{v}_1 - \mathbf{q}_1) + \rho_1 r_1 + \mathbf{v}_1\cdot(\rho_1\mathbf{b}_1 + \mathbf{f}_I) + e_1\\ \rho_1\frac{d_2}{dt}\left(u_2 + \frac{\mathbf{v}_2\cdot\mathbf{v}_2}{2}\right) &= \nabla\cdot(\mathbf{T}_2\cdot\mathbf{v}_2 - \mathbf{q}_2) + \rho_2 r_2 + \mathbf{v}_2\cdot(\rho_2\mathbf{b}_2 - \mathbf{f}_I) + e_2.\end{aligned} \tag{18}$$

Here the u_α denote the specific internal energies of constituent α, $\mathbf{q}_\alpha$ is the partial heat flux of α, r_α accounts for the external heat supply of α, and e_α is the frame invariant energy supply to α.

For our purposes, it is more useful to focus on the internal energy balances for each constituent. This is obtained by subtracting the kinetic energy equations derived from (14). Thus

$$\begin{aligned}\rho_1\frac{d_1 u_1}{dt} &= \mathbf{T}_1 : \nabla\mathbf{v}_1 - \nabla\cdot\mathbf{q}_1 + \rho_1 r_1 + e_1\\ \rho_2\frac{d_2 u_2}{dt} &= \mathbf{T}_2 : \nabla\mathbf{v}_2 - \nabla\cdot\mathbf{q}_2 + \rho_2 r_2 + e_2.\end{aligned} \tag{19}$$

Following [25] we use (8), (9), and (17) to express (19) as

$$\begin{aligned}\rho_1\frac{d_1 u_1}{dt} &= \mathbf{T}_1^T : \mathbf{D}_1 - \nabla\cdot\mathbf{q}_1 + \rho_1 r_1 + e_1 - \left(\frac{1}{2}\right)\mathbf{M}_1 : \mathbf{W}_1\\ \rho_2\frac{d_2 u_2}{dt} &= \mathbf{T}_2^T : \mathbf{D}_2 - \nabla\cdot\mathbf{q}_2 + \rho_2 r_2 + e_2 - \left(\frac{1}{2}\right)\mathbf{M}_2 : \mathbf{W}_2.\end{aligned} \tag{20}$$

As shown in [25], Equation (20) is frame invariant if the internal energy sources e_α include the work performed by the $\mathbf{M}_\alpha$. There the energy sources are written as

$$e_\alpha - \left(\frac{1}{2}\right) \mathbf{M}_\alpha : \mathbf{W}_\alpha = e^*_\alpha \tag{21}$$

Of course there may be additional internal energy sources. One important supply relevant to the heat flux is the heat generated by the friction resulting from the relative motion of the constituents. In Appendix 5A of [21] Bowen writes this as

$$\mathcal{W} = (\mathbf{v}_1 - \mathbf{v}_2) \cdot \mathbf{f}_I. \tag{22}$$

Thus we specify objective internal energy supplies as

$$\begin{aligned} e^*_1 &= -\left[\left(\frac{1}{2}\right) \mathbf{M}_1 : \mathbf{W}_1 + \mathcal{W}\right] \\ e^*_2 &= -\left[\left(\frac{1}{2}\right) \mathbf{M}_2 : \mathbf{W}_2 + \mathcal{W}\right]. \end{aligned} \tag{23}$$

Equation (23) states that the rate of work done on constituents by the internal couples contributes to the constituent internal energy as does the contribution arising from the relative motions.

2.6. Entropy Tendency

Although the non-negative generation of entropy for mixtures is fundamental to any theory, there is no universal agreement on how it is achieved. Some workers treat this from the standpoint of small deviations from equilibrium as, for example, in [35]. Recently Grmela has proposed a general approach utilizing Hamiltonian mechanics that is less restrictive. See [36,37] and references cited therein.

For present purposes it is sufficient to start with generic partial entropy tendency equations for both constituents based on classical irreversible thermodynamics. In their equation (2.48) Rajagopal and Tao [22] state the sum of these equations, from which it is straightforward to obtain the individual equations in our notation as

$$\begin{aligned} \rho_1 \frac{d_1 s_1}{dt} + \nabla \cdot \mathbf{J}_1 - \rho_1 r_{s1} &= \sigma_1 \\ \rho_2 \frac{d_2 s_2}{dt} + \nabla \cdot \mathbf{J}_2 - \rho_2 r_{s2} &= \sigma_2. \end{aligned} \tag{24}$$

Here the $\mathbf{J}_\alpha$ are the transports of s_α by non-advective or diffusive processes, the $r_{s\alpha}$ terms account for external entropy supply, and σ_α are the internal productions of entropy. If thermally interacting materials equations of the form of (4) apply, it is possible that the temperature or velocity gradients of one constituent could be strong enough to produce a negative entropy production for the second constituent. Then $\sigma_\alpha < 0$ for that constituent. Nevertheless, for the mixture we require

$$\sigma_1 + \sigma_2 = \Gamma \geq 0. \tag{25}$$

The presence of disparate constituent temperatures complicates the analysis of the mixture entropy production terms since there is no consensus definition for the internal energy for a mixture when the components have distinct temperatures. We avoid this issue and follow Eckart [29], de Groot and Mazur [38], Jou et al. [6], and more recently Klika [20] and use the Gibbs relation for the mixture. This presupposes the existence of both entropy and temperature functions. Of course the downside of this approach is that the Gibbs relation applies to equilibrium conditions. This restriction is not critical here as our primary goal is to explore the consequences of the second law on phenomenological parameters.

Nevertheless the disparate temperatures of the constituents require special consideration. First we apply the Gibbs relation to each constituent of (19) and (24) so as to accommodate the temperatures. Then we sum the resulting equations to give the Gibbs equation for the mixture as

$$\rho_1 \frac{d_1 s_1}{dt} + \rho_2 \frac{d_2 s_2}{dt} = \theta_1^{-1} \left(\rho_1 \frac{d_1 u_1}{dt} - p_1 \frac{d_1 v_1}{dt} \right) + \theta_2^{-1} \left(\rho_2 \frac{d_2 u_2}{dt} - p_2 \frac{d_2 v_2}{dt} \right). \tag{26}$$

In (26) the p_α are thermodynamic partial pressures associated with reversible processes, i.e., the pressure each constituent would have if it occupied the mixture space. The sum of the partial pressures would be the mixture partial pressure. Also in (26) the $v_\alpha (= \rho_\alpha^{-1})$ are the partial volumes, and the θ_α are the temperatures of the respective constituents.

Using (23) for the internal energy sources and (13) to express the partial volume changes of the constituents in terms of the respective velocity divergences, (26) is rewritten as

$$\begin{aligned}
&\rho_1 \frac{d_1 s_1}{dt} + \rho_2 \frac{d_2 s_2}{dt} - \theta_1^{-1} \left[\rho_1 \frac{d_1 u_1}{dt} + p_1 \nabla \cdot \mathbf{v}_1 \right] - \theta_2^{-1} \left[\rho_2 \frac{d_2 u_2}{dt} + p_2 \nabla \cdot \mathbf{v}_2 \right] \\
&= \Gamma - \nabla \cdot (\mathbf{J}_1 + \mathbf{J}_2) + \nabla \cdot \left(\frac{\mathbf{q}_1}{\theta_1} + \frac{\mathbf{q}_2}{\theta_2} \right) + \rho_1 r_{s1} + \rho_2 r_{s2} + \theta_1^{-1} \rho_1 r_1 + \theta_2^{-1} \rho_2 r_2 \\
&- \theta_1^{-1} \left[\mathbf{T}_1^T : \mathbf{D}_1 + \mathbf{q}_1 \cdot \nabla \theta_1^{-1} - \left(\frac{1}{2} \right) \mathbf{M}_1 : \mathbf{W}_1 - \mathcal{W} \right] \\
&- \theta_2^{-1} \left[\mathbf{T}_2^T : \mathbf{D}_2 + \mathbf{q}_2 \cdot \nabla \theta_2^{-1} - \left(\frac{1}{2} \right) \mathbf{M}_2 : \mathbf{W}_2 - \mathcal{W} \right].
\end{aligned} \tag{27}$$

The Gibbs formulation given in (27) suggests the mixture entropy flux and mixture external entropy source is given by

$$\begin{aligned}
\mathbf{J}_1 + \mathbf{J}_2 &= \left(\frac{\mathbf{q}_1}{\theta_1} + \frac{\mathbf{q}_2}{\theta_2} \right) \\
\rho_1 r_{s1} + \rho_2 r_{s2} &= \left(\frac{\rho_1 r_1}{\theta_1} + \frac{\rho_2 r_2}{\theta_2} \right).
\end{aligned} \tag{28}$$

It then follows from (27) that

$$\begin{aligned}
\Gamma = &\left(\theta_1^{-1} p_1 \nabla \cdot \mathbf{v}_1 + \theta_2^{-1} p_2 \nabla \cdot \mathbf{v}_2 \right) \\
&+ \theta_1^{-1} \left[\mathbf{T}_1^T : \mathbf{D}_1 + \mathbf{q}_1 \cdot \nabla \theta_1^{-1} - \left(\frac{1}{2} \right) \mathbf{M}_1 : \mathbf{W}_1 - \mathcal{W} \right] \\
&+ \theta_2^{-1} \left[\mathbf{T}_2^T : \mathbf{D}_2 + \mathbf{q}_2 \cdot \nabla \theta_2^{-1} - \left(\frac{1}{2} \right) \mathbf{M}_2 : \mathbf{W}_2 - \mathcal{W} \right] \geq 0.
\end{aligned} \tag{29}$$

Equation (29) is the Clausius-Duhem equation for a two constituent mixture with different temperatures.

3. Constitutive Equations

3.1. Theory

The main objective of constitutive modeling is to supply connections between kinematical, mechanical, chemical, electro-magnetic, and thermal fields in such a way that when used along with the governing conservation equations the result is a well-posed theory for properly defined problems. Since the fluxes and the dependent variables of the governing equations constitute more unknowns than governing equations, it is necessary to develop constitutive relations between the fluxes and dependent variables so that the number of fundamental equations equals the number of unknowns. Here we employ an additional condition on the constitutive equations: the constitutive variables must also be constrained by the second law of thermodynamics. If they do not appear in the second law inequality then they should not be used in the constitutive equations. As noted below this is actually a constraint on the mathematical structure of the appropriate constitutive equations.

We speculate that for a two-constituent mixture of two fluids whose constituents have different temperatures, densities, velocities, etc., the constitutive relations for the stress tensors and the heat flux vectors should depend on the velocity difference, velocity gradient, temperatures, temperature gradient, densities, density gradient, etc. Then application of frame-indifference results in the following objective quantities:

$$\mathcal{G}^* = (\rho_1, \rho_2, \theta_1, \theta_2, \triangle, \nabla\rho_1, \nabla\rho_2, \nabla\theta_1, \nabla\theta_2, \mathbf{a}, \mathbf{D}_1, \mathbf{D}_2). \tag{30}$$

Here $\triangle = \theta_1 - \theta_2$ and $\mathbf{a} = \mathbf{v}_1 - \mathbf{v}_2$. There is an obvious redundancy in specifying both θ_1, θ_2 as well as their difference. We include both, as some workers use just the latter. Note also that the partial density dependencies can be replaced by the volume fractions ϕ_α.

Equations (13), (14), and (19) are the balance equations that govern the flow of a two-component mixture with different temperatures. To close this system of equations, it is necessary to prescribe constitutive relations for the stress tensors $\mathbf{T}_\alpha$, the momentum interaction force $\mathbf{f}_I$, and the heat fluxes $\mathbf{q}_\alpha$ in terms of objective variables that arise in the balance equations. Constitutive equations characterize the interactions between the constituents, thus different relations are used for various types of flows such as gas-solid, bubbly liquids, solid-liquid, fluid diffusing through an elastic layer, etc. Regardless of their specific forms, the latter equations are subject to the constraint imposed by (29).

3.2. Linear Constitutive Equations for a Mixture of Two Fluids

Here we develop constitutive relations to include heat fluxes for each constituent while neglecting density variations, as our analysis is restricted to linear constitutive equations. We take as the objective variable set a restricted version of $\mathcal{G}^*$:

$$\mathcal{G} = \left(\nabla\theta_1, \nabla\theta_2, \mathbf{a}, \mathbf{D}_1, \mathbf{D}_2\right). \tag{31}$$

Consider first constitutive equations for the heat fluxes and the momentum interaction force. The general linear representation for the former are assumed to be

$$\begin{aligned}\mathbf{q}_1 &= \alpha_1\nabla\theta_1 + \alpha_2\nabla\theta_2 + \alpha_3\mathbf{a}\\ \mathbf{q}_2 &= \beta_1\nabla\theta_1 + \beta_2\nabla\theta_2 + \beta_3\mathbf{a}.\end{aligned} \tag{32}$$

Onsager's reciprocal criteria provides some simplification to (32) by requiring $\alpha_2 = \beta_1$; however, it is not necessary to impose this condition here. Note further that $\alpha_3 \neq -\beta_3$ implies a mixture heat flux even in the absence of thermal gradients. The friction associated with the relative motions of the constituents heats both constituents. This process is not accounted for by the Fourier law.

The phenomenological coefficients in (32) are functions of the invariants $\mathcal{H}$ of $\mathcal{G}$. See [39] for details on invariants of vectors and tensors. Specifically

$$\begin{aligned}\alpha_i &= \alpha_i\left(\mathcal{H}\right)\\ \beta_i &= \beta_i\left(\mathcal{H}\right).\end{aligned} \tag{33}$$

Similar to (32) $\mathbf{f}_I$ is assumed to be given as

$$\mathbf{f}_I = \gamma_1\mathbf{a} + \gamma_2\nabla\theta_1 + \gamma_3\nabla\theta_2 \tag{34}$$

with γ_1, γ_2, and γ_3 also functions of $\mathcal{H}$. It is noteworthy that (34) allows for a transfer of momentum between the constituents due to the constituent temperature gradients even in the absence of relative motion of the constituents.

Müller [34] indicated that in order to get well-posed problems, the interaction forces due to density gradients, i.e., $\nabla\rho_1$ and $\nabla\rho_2$, should also be included among the interaction forces in (34). For a detailed review and discussion of various interaction forces such as lift forces, forces due to mixing, virtual mass, etc., see [40]. However, in the linear theory considered here there are no second laws constraint on these processes; consequently they are excluded in our analysis.

Now consider constitutive equations for the partial stresses. These are specified as

$$\begin{aligned}\mathbf{T}_1 &= \left(-p_1 + \lambda_1 tr\mathbf{D}_1 + \lambda_3 tr\mathbf{D}_2\right)\mathbf{I} + 2\mu_1\mathbf{D}_1 + 2\mu_3\mathbf{D}_2 + \lambda_5\left(\mathbf{W}_1 - \mathbf{W}_2\right)\\ \mathbf{T}_2 &= \left(-p_2 + \lambda_4 tr\mathbf{D}_1 + \lambda_2 tr\mathbf{D}_2\right)\mathbf{I} + 2\mu_4\mathbf{D}_1 + 2\mu_2\mathbf{D}_2 - \lambda_5\left(\mathbf{W}_1 - \mathbf{W}_2\right).\end{aligned} \tag{35}$$

Here $\mathbf{I}$ is the identity operator.Note also that these equations specify $\mathbf{M}_1 = -\mathbf{M}_2 = \lambda_5(\mathbf{W}_1 - \mathbf{W}_2)$. There are a total of 9 phenomenological coefficients in (35), which are functions of $\mathcal{H}$. Application of Onsager's reciprocal relation principle would reduce the number to 7 by setting $\lambda_3 = \lambda_4$ and $\mu_3 = \mu_4$.

4. Entropy Production Constraints on the Constitutive Equations

In this section we use the Clausius-Duhem inequality (29) to determine constraints on the phenomenological coefficients in the constitutive equations for a two-fluid mixture given by (32), (34), and (35). They are determined by inserting (32), (34), and (35) into (29). Our approach relies on establishing conditions on the phenomenological coefficients that insure non-negative quadratic forms for the Clausius-Duhem inequality. Since we regard this condition to be a property of the quadratic form, we employ symmetrized forms of the phenonemological matrices. This avoids evoking Onsager conditions on the cross gradient coefficients a-priori, but reduces to that case when these conditions are prescribed aposteriori.

The result can be broken down into entropy production by processes due to vectorial terms $\mathcal{V}$ and tensorial terms $\mathcal{T}$ as

$$\Gamma = \mathcal{V} + \mathcal{T} \geq 0. \tag{36}$$

Following [41], we expect $\mathcal{V}$ and $\mathcal{T}$ to be ≥ 0 independently.

Consider first the contribution to entropy production from the vector processes. After some calculation, using (32) and (34) one obtains $\mathcal{V}$ as

$$\mathcal{V} = \left[\nabla\theta_1, \nabla\theta_2, \mathbf{a}\right]^T \cdot \mathbf{\Lambda} \cdot \left[\nabla\theta_1, \nabla\theta_2, \mathbf{a}\right] \geq 0 \tag{37}$$

with

$$\mathbf{\Lambda} = \frac{-1}{2}\begin{bmatrix} 2\alpha_1\theta_1^{-3} & \left(\alpha_2\theta_1^{-3} + \beta_1\theta_2^{-3}\right) & \left[\alpha_3\theta_1^{-3} + \gamma_2\left(\theta_1+\theta_2\right)^{-1}\right] \\ \left(\alpha_2\theta_1^{-3} + \beta_1\theta_2^{-3}\right) & 2\beta_2\theta_2^{-3} & \left[\beta_3\theta_2^{-3} + \gamma_3\left(\theta_1+\theta_2\right)^{-1}\right] \\ \left[\alpha_3\theta_1^{-3} + \gamma_2\left(\theta_1+\theta_2\right)^{-1}\right] & \left[\beta_3\theta_2^{-3} + \gamma_3\left(\theta_1+\theta_2\right)^{-1}\right] & 2\gamma_1\left(\theta_1+\theta_2\right)^{-1} \end{bmatrix}. \tag{38}$$

Equation (38) differs from an earlier result given in [26] where the energy source terms were not frame invariant.

The requirement for non-negative entropy production is that $\mathbf{\Lambda}$ be non-negative definite. This requires the 6 determinants of the principal submatrices and the determinate of $\mathbf{\Lambda}$ to be non-negative definate. Thus

$$\alpha_1,\ \beta_2,\ \gamma_1\ \leq 0 \tag{39}$$

since θ_1, $\theta_2 > 0$. The inequality constraints arising from the second order principal minors are

$$\begin{aligned}
&\frac{\alpha_1\beta_2}{\theta_1^3\theta_2^3} - \left(\frac{1}{4}\right)\left(\frac{\alpha_2}{\theta_1^3} + \frac{\beta_1}{\theta_2^3}\right)^2 \leq 0 \\
&\left(\frac{\alpha_1}{\theta_1^2}\right)\left(\frac{\gamma_1}{\theta_1+\theta_2}\right) - \left(\frac{1}{4}\right)\left(-\frac{\beta_3}{\theta_2^3} + \frac{\gamma_3}{\theta_1+\theta_2}\right)^2 \leq 0 \\
&\left(\frac{\beta_2}{\theta_2^3}\right)\left(\frac{\gamma_1}{\theta_1+\theta_2}\right) - \left(\frac{1}{4}\right)\left(-\frac{\beta_3}{\theta_2^3} + \frac{\gamma_3}{\theta_1+\theta_2}\right)^2 \leq 0.
\end{aligned} \tag{40}$$

The determinate of $\mathbf{\Lambda}$ provides a cubic constraint, but it is not recorded here.

Now consider the second law constraints on the tensor processes. Here

$$\begin{aligned}
\mathcal{T} = &\left[\lambda_1 (tr\mathbf{D}_1)^2 + \lambda_3 (tr\mathbf{D}_2)(tr\mathbf{D}_1) + 2\mu_1 tr\mathbf{D}_1^2 + 2\mu_3 tr(\mathbf{D}_2\mathbf{D}_1) + \lambda_5 tr\left[(\mathbf{W}_1 - \mathbf{W}_2)\mathbf{W}_1\right]\right]\theta_1^{-1} \\
&+ \left[\lambda_4 (tr\mathbf{D}_1)(tr\mathbf{D}_2) + \lambda_2 (tr\mathbf{D}_2)^2 + 2\mu_4 tr(\mathbf{D}_1\mathbf{D}_2) + 2\mu_2 tr\mathbf{D}_2^2 - \lambda_5 tr\left[(\mathbf{W}_1 - \mathbf{W}_2)\mathbf{W}_2\right]\right]\theta_2^{-1}.
\end{aligned} \tag{41}$$

Using (29) in (35) it is found the partial pressures p_α cancel in obtaining (41). Thus they do not play any role in the generation of entropy for the mixture, [6,29], consequently they are not considered further. Such processes are elegantly treated by Hamiltonian mechanics methods as described in [36,37].

Rendering (41) in matrix form gives

$$\begin{aligned}
\mathcal{T} \quad = \quad & \left[tr(\mathbf{D}_1), tr(\mathbf{D}_2)\right]\begin{bmatrix} \frac{\lambda_1}{\theta_1} & \left(\frac{1}{2}\right)\left(\frac{\lambda_3}{\theta_1} + \frac{\lambda_4}{\theta_2}\right) \\ \left(\frac{1}{2}\right)\left(\frac{\lambda_3}{\theta_1} + \frac{\lambda_4}{\theta_2}\right) & \frac{\lambda_2}{\theta_2} \end{bmatrix}\begin{bmatrix} tr(\mathbf{D}_1) \\ tr(\mathbf{D}_2) \end{bmatrix} \\
+ \quad & tr\left\{\left[\mathbf{D}_1, \mathbf{D}_2\right]\begin{bmatrix} \frac{2\mu_1}{\theta_1} & \left(\frac{1}{2}\right)\left(\frac{2\mu_3}{\theta_1} + \frac{2\mu_4}{\theta_2}\right) \\ \left(\frac{1}{2}\right)\left(\frac{2\mu_3}{\theta_1} + \frac{2\mu_4}{\theta_2}\right) & \frac{2\mu_2}{\theta_2} \end{bmatrix}\begin{bmatrix} \mathbf{D}_1 \\ \mathbf{D}_2 \end{bmatrix}\right\} \\
+ \quad & \lambda_5\, tr\left\{\left[\mathbf{W}_1, \mathbf{W}_2\right]\begin{bmatrix} \frac{1}{\theta_1} & -\left(\frac{1}{2}\right)\left(\frac{1}{\theta_1} + \frac{1}{\theta_2}\right) \\ -\left(\frac{1}{2}\right)\left(\frac{1}{\theta_1} + \frac{1}{\theta_2}\right) & \frac{1}{\theta_2} \end{bmatrix}\begin{bmatrix} \mathbf{W}_1 \\ \mathbf{W}_2 \end{bmatrix}\right\}.
\end{aligned} \tag{42}$$

Consider the first term on the right-hand side of (42). Note that this is a quadratic form of $tr\mathbf{D}_1, tr\mathbf{D}_2$. The requirement that this form be non-negative is

$$\begin{aligned}
&\frac{\lambda_1}{\theta_1} \geq 0 \\
&\frac{\lambda_2}{\theta_2} \geq 0 \\
&\frac{\lambda_1\lambda_2}{\theta_1\theta_2} - \left(\frac{\lambda_3}{\theta_1} + \frac{\lambda_4}{\theta_2}\right)^2 \geq 0.
\end{aligned} \tag{43}$$

Similarly, the second term in (42) is a quadratic form of $tr(\mathbf{D}_1^2, \mathbf{D}_2^2) \geq 0$. From this it is concluded that

$$\begin{aligned}
&\frac{\mu_1}{\theta_1} \geq 0 \\
&\frac{\mu_2}{\theta_2} \geq 0 \\
&\frac{\mu_1\mu_2}{\theta_1\theta_2} - \left(\frac{1}{4}\right)\left(\frac{2\mu_3}{\theta_1} + \frac{2\mu_4}{\theta_2}\right)^2 \geq 0.
\end{aligned} \tag{44}$$

The third line of (42) is a quadratic form in $\mathbf{W}_1$ and $\mathbf{W}_2$. Since the matrix determinate is non-positive the relevant constraint requiring non-negative entropy production is

$$\lambda_5 \leq 0. \tag{45}$$

These inequalities reduce to the standard condition for a linear Navier-Stokes fluid when the temperatures of the two constituents are the same.

The main results of this section are the constraints imposed by the second law on the coefficients in the constitutive equations. These are equations (39), (40), (43), (44) and (45). After adjusting for notation, these results are the same as reported by those earlier in [26]. Note that if $\theta_1 = \theta_2$ these constraints reduce to well-established conditions. The interesting aspect is the role the constituent temperatures play in the second order principal minor constraints. These could be relevant to experimentalists and to the stability of solutions of specific problems.

5. Special Cases

5.1. Heat Flux

We are now in a position to study several special cases of the constitutive equations for heat flux vectors and the interaction force $\mathbf{f}_I$ that are relevant to the issues raised in Section 1. First, recall (32)

$$\begin{aligned} \mathbf{q}_1 &= \alpha_1 \nabla\theta_1 + \alpha_2 \nabla\theta_2 + \alpha_3 \mathbf{a} \\ \mathbf{q}_2 &= \beta_1 \nabla\theta_1 + \beta_2 \nabla\theta_2 + \beta_3 \mathbf{a}. \end{aligned} \tag{46}$$

The first two terms are a generalization of the Fourier law of heat conduction that accounts for constituent heat fluxes that depend on the temperature gradients in both constituents. The third term predicts a contribution to the constituent heat fluxes from friction arising from the different motions of the constituents. However, if $\alpha_3 = -\beta_3$ this term cancels in $\mathbf{q}_{mix}$ and so the result is (5). If further $\theta_1 = \theta_2$, then

$$\mathbf{q}_{mix} = (\alpha_1 + \alpha_2 + \beta_1 + \beta_2)\nabla\theta. \tag{47}$$

Hence $\alpha_1 + \alpha_2 + \beta_1 + \beta_2 = k$ is the effective thermal conductivity of a mixture as noted in (3). Moreover, $\mathbf{q}$ obtained from (46) is the same form as equation (6.39) in [31], who wrote this as

$$\mathbf{q} = \alpha\nabla\theta + \alpha_{ik}\left(\mathbf{v}_i - \mathbf{v}_k\right).$$

Note also that the momentum transfer between constituents simplifies to

$$\mathbf{f}_I = \gamma_1 \mathbf{a} + (\gamma_2 + \gamma_3)\nabla\theta. \tag{48}$$

5.2. Green Adkins Massoudi Theory

In response to the ontological question "How does mixture know it is a mixture?" Truesdell [21] proposed three metaphysical principles to govern mixture dynamics. Although widely accepted, they apparently do not account for all mixture behavior. Consequently several additional metaphysical principles have been proposed. A recent review is given in [26]. Here we investigate the Green Adkins Massoudi principle. Simply stated, this principle requires the governing equations and the constitutive relations for mixtures to reduce to the appropriate form for a single constituent if the concentrations of the other constituents vanish. This can be achieved by a number of weighting functions. Here we elect to follow Massoudi, [33], by requiring the phenomenological coefficients to be functions of the volume fractions of the constituents. That choice is also consistent with the analysis given in [27,42]. See also a recent discussion of volume fractions in [20].

Application to a fluid–fluid mixture with the phenomenological coefficients in (32), (34), and (35) taken as linear functions of the volume fraction ϕ of constituent 2 gives

$$\begin{aligned}
\mathbf{q}_1 &= (1-\phi)[\alpha_{30}\nabla\theta_1 + \phi\alpha_{40}\nabla\theta_2 + \phi\alpha_{50}\mathbf{a}] \\
\mathbf{q}_2 &= \phi[(1-\phi)\beta_{30}\nabla\theta_1 + \beta_{40}\nabla\theta_2 - (1-\phi)\alpha_{50}\mathbf{a}] \\
\mathbf{f}_I &= \phi(1-\phi)\,(\gamma_{10}\mathbf{a} + \gamma_{20}\nabla\theta_1 + \gamma_{30}\nabla\theta_2) \\
\mathbf{T}_1 &= (1-\phi)[(\lambda_{10} tr\mathbf{D}_1 + \phi\lambda_{30} tr\mathbf{D}_2)\mathbf{I} + 2(\mu_{10}\mathbf{D}_1 + \phi\mu_{30}\mathbf{D}_2) + \phi\lambda_{50}(\mathbf{W}_1 - \mathbf{W}_2)] \\
\mathbf{T}_2 &= \phi\,\{[(1-\phi)\lambda_4 tr\mathbf{D}_1 + \lambda_2 tr\mathbf{D}_2]\,\mathbf{I} + 2[(1-\phi)\mu_{40})\mathbf{D}_1 + \mu_2\mathbf{D}_2]\} \\
&- \phi(1-\phi)\lambda_{50}(\mathbf{W}_1 - \mathbf{W}_2).
\end{aligned} \tag{49}$$

It is stressed that (49) reduces to the standard constitutive equations for a Navier-Stokes fluid in the extreme cases of $\phi = 1, 0$. Moreover, the inclusion of the volume fraction in the phenomenological coefficients in (49) does not impact the thermodynamic constraints given by equations (39), (40), (43), (44) and (45); see [26].

The mixture heat flux implied by (49) is

$$\mathbf{q}_{mix} = (1-\phi)(\alpha_{30} + \phi\beta_{30})\nabla\theta_1 + \phi[(1-\phi)\alpha_{40} + \beta_{40}]\nabla\theta_2. \tag{50}$$

The heat flux generated by the differential movement of the two constituents does not contribute to $\mathbf{q}_{mix}$, and the conductivities are weighted by the respective volume fractions. Moreover, when $\nabla\theta_1 = \nabla\theta_2$ the effective conductivity includes contributions from the cross flux terms α_{40} and β_{30}. These, however, are weighted by $\phi(1-\phi)$ and further constrained by (40).

From (49) a mixture stress can be defined as

$$\mathbf{T}_{mix} = \mathbf{T}_1 + \mathbf{T}_2. \tag{51}$$

The weighting system in (51) is similar to that proposed in [31,32] for the mixture stress, except that it includes the cross viscous terms μ_{30} and μ_{40} weighted by the respective volume fractions.

6. Conclusions

Several new results have emerged from this effort. First, we extended mixture theory for two Navier-Stokes fluids to include temperature differences between the constituents. The general theory has 18 phenomenological coefficients. This number can be reduced to 15 if Onsager's reciprocal principle is evoked. Despite this rather large number, constraints on the constitutive equations were established by the requirement of non-negative entropy production and shown to be consistent with previous results.

Secondly, consider the constitutive model given by (49). As suggested by Hansen et al., [27] volume fraction serves as a weighting function for the constituent stresses and heat fluxes in the same fashion Truesdell [21] proposed using constituent densities to define the mixture velocity. That paper also provides a succinct argument for using volume fraction for these fluxes.

Thirdly, the heat flux laws proposed here will require new phenomenological parameters and thus pose significant challenges to experimentalists. Weighting the constitutive equations by the constituent volume fractions or other suitable weighting function could be an important attribute in this regard since some of the coefficients can be determined from experiments with pristine substances. The cross gradient fluxes, of course, will remain a challenge for experimentalists. However, the second law inequalities established here put useful constraints on their values.

Although the constitutive models considered here are for two fluids, it has some applicability to the mixture of a fluid and a solid. As an example, consider the two limiting cases of (49). In the first case, suppose $\phi \to 0$, i.e., the particle component vanishes. Then $\alpha_1 = k_1$, indicating that we have a case of pure fluid. In the second case, $\phi \to 1$, i.e., the fluid component vanishes and we have a solid matrix, $\beta_1 = k_2$, where k_2 is the pure thermal conductivity of the solid material.

This study calls attention to other areas for further investigation. First is the energy equation for mixtures with different constituent temperatures. The case of equal constituent temperatures is straightforward and well established in the literature, whereas the two-temperature scenario considered here is not. A second area involves extending the theory to include density effects such as in suspensions of granular materials in fluids as studied by [43–45]. Here the constitutive equations will include second order effects such as density gradients in the stress constitutive equations. This means the entropy inequality will no longer be of quadratic form. Nevertheless, as shown in [44,46], second law constraints on the phenomenological coefficients can still be obtained.

Author Contributions: Conceptualization, A.D.K.J. and M.M.; Formal analysis, A.D.K.J. and M.M.; Investigation, A.D.K.J. and M.M.; Methodology, A.D.K.J. and M.M.; Validation, A.D.K. and M.M.; Writing: original draft, A.D.K.J. and M.M.; Writing: review & editing, A.D.K.J. and M.M. Both authors contributed equally to the analysis and writing of the manuscript. All authors have read and agreed to the published version of the manuscript.

Funding: This research received no external funding.

Acknowledgments: The authors gratefully acknowledge a reviewer's suggestions for making the constituent energy and entropy equations frame invariant. Karal Gregory supplied outstanding technical support in preparation of the manuscript.

Conflicts of Interest: The authors declare no conflict of interest.

References

1. Dunwoody, N.T.; Müller, I.A. A thermodynamic theory of two chemically reacting ideal gases with different temperatures. *Arch. Ration. Mech. Anal.* **1968**, *29*, 344–369. [CrossRef]
2. Bowen, R.M.; Garcia, D.J. On the thermodynamics of mixtures with several temperatures. *Int. J. Eng. Sci.* **1970**, *8*, 63–83. [CrossRef]
3. Ahmadi, G. Thermodynamics of multi-temperature fluids with applications to turbulence modelling. *Appl. Math. Model.* **1985**, *9*, 271–274. [CrossRef]
4. Maxwell, J.C. On the dynamic theory of gases. *Philos. Trans. R. Soc. Lond.* **1867**, *147*, 49–88.
5. Cattaneo, C. Sulla Conduzione Del Calore. *Atti Semin. Mat. Fis. Univ. Modena* **1948**, *3*, 83–101.
6. Jou, D.; Casas-Vazquez, J.; Lebon, G. Extended Irreversible Thermodynamics. In *Extended Irreversible Thermodynamics*; Springer: Berlin, Germany, 1996; pp. 41–74.
7. Petroski, H.J. Departures from Fourier's law. *ZAMP* **1975**, *26*, 119–124. [CrossRef]
8. Mitchell, J.K. Conduction phenomena: From theory to geotechnical practice. *Geotechnique* **1991**, *41*, 299–340. [CrossRef]
9. Bashir, Y.M.; Goddard, J.D. Experiments on the conductivity of suspensions of ionically conductive spheres. *AlChE J.* **1990**, *36*, 387–396. [CrossRef]
10. Prasher, R.S.; Koning, P.; Shipley, J.; Devpura, A. Dependence of thermal conductivity and mechanical rigidity of particle-laden polymeric thermal interface material on particle volume fraction. *ASME J. Electron. Packag.* **2003**, *125*, 386–391. [CrossRef]
11. Lee, D.L.; Irvine, T.F., Jr. Shear rate dependent thermal conductivity measurements of non-Newtonian fluids. *Exp. Therm. Fluid Sci.* **1997**, *15*, 16–24. [CrossRef]
12. Massoudi, M. On the heat flux vector for flowing granular materials, Part 1: Effective thermal conductivity and background. *Math. Methods Appl. Sci.* **2006**, *29*, 1585–1598. [CrossRef]
13. Massoudi, M. On the heat flux vector for flowing granular materials, Part 2: Derivation and special cases. *Math. Methods Appl. Sci.* **2006**, *29*, 1599–1613. [CrossRef]
14. Massoudi, M. On the heat flux vector in mixtures. *Int. Commun. Heat Mass Transf.* **2005**, *32*, 1111–1266. [CrossRef]
15. Klika, V.; Pavelka, M.; Benziger, J.B. Functional constraints on phenomenological coefficients. *Phys. Rev. E* **2017**, *95*, 022125. [CrossRef]
16. Klika, V.; Krause, A.L. Beyond Onsager-Casimir relations: Shared dependence of phenomenological coefficients on state variables. *J. Phys. Chem. Lett.* **2018**, *9*. [CrossRef]

17. Rajagopal, K.R.; Srinivasa, A.R. A thermodynamic frame work for rate type fluid models. *J. Non-Newtonian Fluid Mech.* **2000**, *88*, 207–227. [CrossRef]
18. Rajagopal, K.R.; Srinivasa, A.R. Modeling anisotropic fluids within the framework of bodies with multiple natural configurations. *J. Non-Newtonian Fluid Mech.* **2001**, *99*, 109–124. [CrossRef]
19. Rajagopal, K.; Srinivasa, A. On the development of fluid models of the differential type within a new thermodynamical framework. *Mech. Res. Commun.* **2008**. doi:10.1016/j.mechrescom.2008.02.004. [CrossRef]
20. Klika, V. A guide through available mixture theories for applications. *Crit. Rev. Solid State Mater. Sci.* **2014**, *39*, 154–174. [CrossRef]
21. Truesdell, C. *Rational Thermodynamics*, 2nd ed.; Springer: New York, NY, USA, 1984.
22. Rajagopal, K.R.; Tao, L. *Mechanics of Mixtures*; World Scientific: Singapore, 1995.
23. Atkin, R.J.; Craine, R.E. Continuum theories of mixtures: Applications. *IMA J. Appl. Math* **1976**, *17*, 153–207. [CrossRef]
24. Atkin, R.J.; Craine, R.E. Continuum theories of mixtures: Basic theory and historical development. *Q. J. Mech. Appl. Math.* **1976**, *29*, 209–244. [CrossRef]
25. Bowen, R.M. Theory of Mixtures. In *Continuum Physics*; Eringen, A.C., Ed.; Academic Press: New York, NY, USA, 1976; Volume 3, pp. 1–127.
26. Kirwan, A.D., Jr. Second Law constraints on the dynamics of a mixture of two fluids at different temperatures. *Entropy* **2012**, *14*, 880–891. [CrossRef]
27. Hansen, A.C.; Crane, R.L.; Damson, M.H.; Donovan, M.H.; Horning, R.P.; Walker, J.L. Some notes on a volume fraction mixture theory and a comparison with the kinetic theory of gases. *Int. J. Eng. Sci.* **1991**, *29*, 561–573. [CrossRef]
28. Beevers, C.E.; Craine, R.E. On the determination of response functions for a binary mixture of incompressible Newtonian fluids. *Int. J. Eng. Sci.* **1982**, *20*, 737–745. [CrossRef]
29. Eckart, C. The thermodynamics of irreversible processes, II Fluid mixtures. *Phys. Rev. E* **1940**, *58*, 269–275. [CrossRef]
30. Truesdell, C.; Noll, W. *The Classical Field Theories*; Springer: Berlin, Germany, 1965; Volume 3.
31. Green, A.E.; Naghdi, P.M. A theory of mixtures. *Arch. Ration. Mech. Anal.* **1967**, *24*, 243–263. [CrossRef]
32. Green, A.E.; Naghdi, P.M. A note on mixtures. *Int. J. Eng. Sci.* **1968**, *6*, 631–635. [CrossRef]
33. Massoudi, M. A note on the meaning of mixture viscosity using the classical continuum theories of mixtures. *Int. J. Eng. Sci.* **2008**, *46*, 677–689. [CrossRef]
34. Müller, I.A. A thermodynamic theory of mixtures of fluids. *Arch. Ration. Mech. Anal.* **1968**, *28*, 1–39. [CrossRef]
35. Dunn, J.E.; Serrin, J. On thermodynamics of interstitial working. *Arch. Ration. Mech. Anal.* **1985**, *88*, 95–133. [CrossRef]
36. Grmela, M. Externally driven macroscopic systems: Dynamics versus thermodynamics. *J. Stat. Phys.* **2017**, *166*, 282–316. [CrossRef]
37. Grmela, M. Generic guide to the multiscale dynamics and thermodynamics. *J. Phys. Commun.* **2018**, *2*, 032001. [CrossRef]
38. de Groot, S.; Mazur, P. *Non-Equilibrium Thermodynamics*; Dover Publications, Inc.: New York, NY, USA, 1984.
39. Zheng, Q.S. Theory of representations for tensor functions—A unified invariant approach to constitutive equations. *Appl. Mech. Rev.* **1994**, *47*, 545–587. [CrossRef]
40. Massoudi, M. Constitutive relations for the interaction force in multicomponent particulate flows. *Int. J. Non-Linear Mech.* **2003**, *38*, 313–336. [CrossRef]
41. Kuiken, G.D.C. *Thermodynamics of Irreversible Processes*; Wiley: New York, NY, USA, 1994.
42. Klika, V.; Whiteley, J.P.; Brown, C.P.; Gaffney, E.A. The combined impact of tissue heterogeneity and fixed charge for models of cartilage: The one-dimensional biphasic swelling model revisited. *Biomech. Model. Mechanobiol.* **2019**, *18*, 953–968. [CrossRef]
43. Yang, H.; Massoudi, M. Conduction and convection heat transfer in a dense granular suspension. *Appl. Math. Comput.* **2018**, *332*, 351–362. [CrossRef]
44. Yang, H.; Massoudi, M.; Kirwan, A. D., Jr. Entropy analysis for a nonlinear fluid with a nonlinear heat flux vector. *Entropy* **2017**, *19*, 689. [CrossRef]

45. Massoudi, M. On the flow of granular materials with variable material properties. *Int. J. Non-Linear Mech.* **2001**, *36*, 25–37. [CrossRef]
46. Massoudi, M.; Kirwan, A. D., Jr. On the thermodynamics of a nonlinear heat conducting suspension. *Fluids* **2016**, *1*, 19. [CrossRef]

fluids

MDPI

Article

Investigation of High Lift Force Generation of Dragonfly Wing by a Novel Advanced Mode in Hover

Xiaohui Su [1,*], Kaixuan Zhang [1], Juan Zheng [1], Yong Zhao [2,*], Ruiqi Han [3] and Jiantao Zhang [1]

[1] School of Hydraulic Engineering, Dalian University of Technology, Dalian 116024, China; zkx@mail.dlut.edu.cn (K.Z.); Zhengjuan@mail.dlut.edu.cn (J.Z.); zhangjt@dlut.edu.cn (J.Z.)

[2] College of Engineering, Nazarbayev University, 53 Kabanbaybatyr Ave., Astana 010000, Kazakhstan

[3] Department of Mechanical & Industrial Engineering, University of Toronto, 5 King's College Rd, Toronto, ON M5S 3G8, Canada; ruiqi.han@mail.utoronto.ca

* Correspondence: sxh@dlut.edu.cn (S.X.); yong.zhao@nu.edu.kz (Z.Y.)

Received: 30 March 2020; Accepted: 22 April 2020; Published: 24 April 2020

Abstract: In the paper, a novel flapping mode is presented that can generate high lift force by a dragonfly wing in hover. The new mode, named partial advanced mode (PAM), starts pitching earlier than symmetric rotation during the downstroke cycle of the hovering motion. As a result, high lift force can be generated due to rapid pitching coupling with high flapping velocity in the stroke plane. Aerodynamic performance of the new mode is investigated thoroughly using numerical simulation. The results obtained show that the period-averaged lift coefficient, C_L, increases up to 16% compared with that of the traditional symmetrical mode when an earlier pitching time is set to 8% of the flapping period. The reason for the high lift force generation mechanism is explained in detail using not only force investigation, but also by analyzing vortices produced around the wing. The proposed PAM is believed to lengthen the dynamic stall mechanism and enhance the LEV generated during the downstroke. The improvement of lift force could be considered as a result of a combination of the dynamic stall mechanism and rapid pitch mechanism. Finally, the energy expenditure of the new mode is also analyzed.

Keywords: dragonfly wing; high lift force generation; partial advanced motion; vortex dynamics; hovering motion

---

1. Introduction

In the last two decades, attention has increasingly been paid to the aerodynamic performance of insect wings [1–5] due to the rising popularity of micro air vehicles (MAVs) [6,7]. Insects were the first creatures to develop flapping flight capability and remain in many ways unsurpassed in aerodynamic performance and maneuverability. Among insects, super flying capabilities, such as taking off backwards, flying sideways and landing upside-down et al. have been already discovered and reported [2]. People are very interested in the high-lift generation mechanisms and the corresponding energy expenditure in insect flight, mainly for the following two reasons. One is that biologists want to understand the effects of aerodynamic force production and energy expenditure from the point of view of physiology, ecology, evolution and other aspects of insects. The other is that engineers, who wish to develop small autonomous flying machines, want to understand the novel aerodynamics of flying insects and are eager to find inspiration from them [5].

Since the conventional aerodynamic theory of flapping wings has not been successful [3], much effort and progress has been made in revealing the dynamic mechanisms of insect flights. By using unsteady aerodynamic theory, lift force generation mechanisms have been identified and studied continually, such as clapping and fling [8], dynamic stall (delayed stall) [1], rapid pitch [2], wake capture [2] and tip vortex (TipV) [9] as well as induced jet [10] for rigid wings. As for deformable wings, the effect of deformation has been investigated and it was concluded that deformation enhances lift force during both wake capture and delayed stall mechanisms [11]. The deformation of wings, including camber and angle of incidence, changes leading edge vortex (LEV) and trailing edge vortex (TEV) generation and development processes [11,12]. Among the above research works, most studies are carried out focusing on hovering motion. Hovering flight is a kind of flight mode where the body is assumed to be fixed in space and the freestream velocity is zero [11]. It is the most energetically expensive form of flight [8] and exceptionally fine control is also needed to remain stationary [13]. The power produced by the flapping of insect wings should sustain the insect itself in the air. To design and build MAVs with the capability of hovering flight, the mechanism of aerodynamic lift force generation of hovering flight is important to consider and worthy of detailed investigation.

In the numerical investigation of the flapping motion of insect wings, hovering action is generally simplified as a combination of two motions, translation and rotation. Normally, harmonic function is used to mimic rotation for all insect species, while there are two kinds of functions, trapezoidal function [2] and harmonic function [3], used to mimic translation depending on different insect species. Compared to simple harmonic function, trapezoidal function exaggerates the acceleration at the beginning and the deceleration near the end of a half-stroke and also makes the deceleration start at a later time (Figure 1). This pattern of wing translation, combined with proper wing rotation timing, can create aerodynamic forces by all the mechanisms currently known on wings. Different timings of wing rotation for the wings can be employed to provide control of forces on the wings during maneuver [1,2,5].

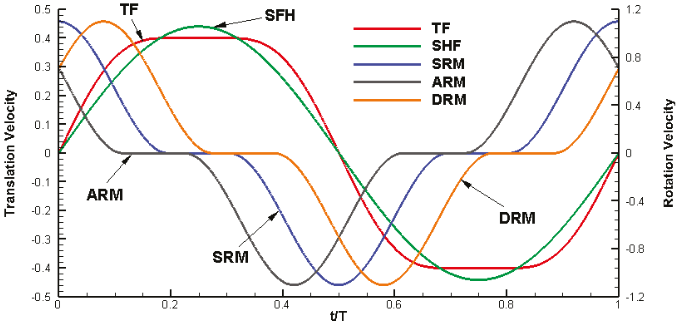

Figure 1. Non-dimensional translation (azimuthal rotation) velocity (left axis) and rotation velocity (right axis) in one cycle. (SHF: simple harmonic function; TF, trapezoidal function [5]; SRM: symmetrical rotation mode; ARM: advanced rotation mode; DRM: delayed rotation mode).

Currently, there are three combination modes appearing in the vast research works based on translation and rotation. When half of the wing rotation duration is completed at the end of a half-stroke and the other half in the beginning of the next half-stroke (Figure 1), the wing rotation is called symmetrical rotation mode (SRM); when the major part of rotation is finished before the stroke reversal, it is called advanced rotation mode (ARM); when the major part of rotation is only completed after the stroke reversal, it is called delayed rotation mode (DRM). The timing of the wing rotation can change the time history and the mean value of the aerodynamic forces significantly, especially in the case of translational velocity varying as a trapezoidal function [2,5].

Inspired by Dickinson's work [2], investigation of the high lift force generation of dragonfly wings by changing rotation timing are carried out in this study. During the investigation of the ARM coupling with harmonic translation function, good improvement of lift force during downstroke is found, but with poor performance of lift force during upstroke if ARM is also adopted near the end of the upstroke. The negative performance of lift force during upstroke action is even worse compared with the results of SRM. As a result, the period-averaged lift force does not improve much or even worse. Therefore, it is proposed that the ARM be adopted for the downstroke only for its advantage, while the SRM is used for the upstroke, which can be named as partial advanced mode (PAM). Hereby, in this paper, we carry out numerical investigations on the aerodynamic performance of dragonfly wings using the proposed PAM. An unstructured mesh unsteady incompressible 3D flow solver, named TetraALEFSI, which was originally developed by Zhao's group [14–16] and was recently enhanced by Su et al. with an arbitrary Lagrangian-Eulerian (ALE) function [12,17], is used for the numerical simulations.

The structure of this paper is as follows: the governing equations of the unsteady incompressible 3D ALE flow solver are briefly introduced in Section 2. In Section 3, the geometry and kinematics of the dragonfly wing during hovering motion is described. In Section 4, high lift force generation mechanisms due to the proposed partial advanced mode are investigated and discussed. Conclusions are made in the last section.

2. Mathematical and Numerical Formulation

The three-dimensional incompressible unsteady Navier-Stokes governing equations, modified by the artificial compressibility method (ACM) with dual time steps and arbitrary Langrangian-Eulerian (ALE) method in non-dimensional vector form, are as follows:

$$\mathbf{C}\frac{\partial \mathbf{W}}{\partial \tau} + \mathbf{K}\frac{\partial \mathbf{W}}{\partial t} + \nabla \cdot \mathbf{F_c} = \nabla \cdot \mathbf{F_v} \tag{1}$$

where,

$$\mathbf{W} = \begin{bmatrix} p \\ u \\ v \\ w \end{bmatrix} \mathbf{F}_c = \begin{bmatrix} \mathbf{U} \\ u\mathbf{U} + p\delta_{ij} \\ v\mathbf{U} + p\delta_{ij} \\ w\mathbf{U} + p\delta_{ij} \end{bmatrix} \mathbf{F_v} = \begin{bmatrix} 0 \\ (1/\mathrm{Re}) \cdot \nabla \cdot u \\ (1/\mathrm{Re}) \cdot \nabla \cdot v \\ (1/\mathrm{Re}) \cdot \nabla \cdot w \end{bmatrix}$$

$$\mathbf{K} = \begin{bmatrix} 0 & 0 & 0 & 0 \\ 0 & 1 & 0 & 0 \\ 0 & 0 & 1 & 0 \\ 0 & 0 & 0 & 1 \end{bmatrix} C = \begin{bmatrix} \frac{1}{\beta} & 0 & 0 & 0 \\ 0 & 1 & 0 & 0 \\ 0 & 0 & 1 & 0 \\ 0 & 0 & 0 & 1 \end{bmatrix}$$

where $\mathbf{W}$ is the vector of dependent variables and $\mathbf{F}_c$ and $\mathbf{F_v}$ are the convective flux and viscous flux vectors, respectively. β is a constant called artificial compressibility whose value affects the solution convergence to steady state. $\mathbf{K}$ is the unit matrix with first element equal to zero and $\mathbf{C}$ a preconditioning matrix. $\mathbf{U} = \mathbf{U}_f - \mathbf{U}_m$ is the velocity vector, $\mathbf{U}_f$ and $\mathbf{U}_m$ are the fluid velocity and grid velocity, respectively; Re is the Reynolds number.

The governing equation, Equation (1) is discretized on an unstructured tetrahedral grid using the control volume method. The details of discretization of the governing equation, numerical validations of the proposed solver, as well as the moving mesh algorithm can be found in reference [12,14–17].

3. Geometry and Kinematics of Dragonfly Wing

3.1. Geometry of Dragonfly Wing

The hindwing of a dragonfly, as used in this research, is described as a rigid plate with a span length of R, 4.6 cm, average chord length of c = 1.12 cm, and a thickness of 1% of average chord length, about 0.0112 cm. The symmetric plane is located on the left 0.61 cm away from the root of wing, and the rotation axis of the wing is 0.28 cm, about $c/4$ from the leading edge. The simplified geometric model of the hindwing of a dragonfly is plotted in Figure 2.

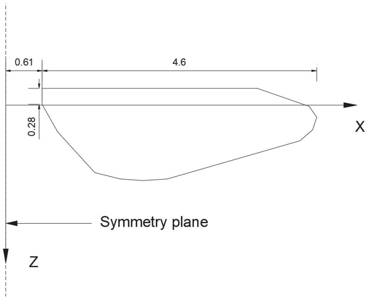

Figure 2. Simplified geometric model of the dragonfly hindwing.

3.2. The Traditional Kinematics of Hovering Motion

The traditional kinematics of hovering motion are described using formulas presented by Norberg [18] and Sun [19], and the sketch of the flapping motion is defined and presented in Figure 3. It assumes that the stroke plane, also named the flapping plane, has an inclined angle, β, about 52° to the horizontal plane. Thus, only two parameters, the flapping angle, Φ, which is relative to the Y-Z plane, and the angle of attack (AOA), α, which is relative to the flapping plane, will be used together to control the movement of the wing. The flapping frequency is set to 36 Hz.

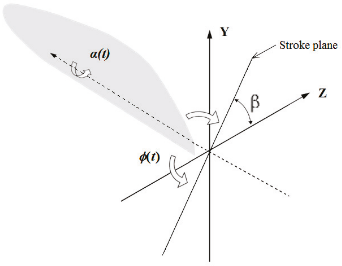

Figure 3. Sketch of the flapping motion of the wing.

The instantaneous flapping angle, $\Phi(t)$, and relative AOA angle, $\alpha(t)$, are described in Equations (2) and (3), respectively:

$$\varphi(t) = \varphi_0[\cos(2\pi f t) - 1] \tag{2}$$

$$\alpha(t) = \alpha_d - \frac{(\alpha_d - \alpha_u)}{\Delta t_r}\left[(\mathrm{mod}(t,T) + T - t_{ru}) - \frac{\Delta t_r}{2\pi}\sin(2\pi\frac{\mathrm{mod}(t,T) + T - t_{ru}}{\Delta t_r})\right]$$

$$0 \le \mathrm{mod}(t,T) < \frac{\Delta t_r}{2}$$

$$\alpha(t) = \alpha_u$$

$$\frac{\Delta t_r}{2} \le \mathrm{mod}(t,T) < t_{rd}$$

$$\alpha(t) = \alpha_u + \frac{(\alpha_d - \alpha_u)}{\Delta t_r}\left[(\mathrm{mod}(t,T) - t_{rd}) - \frac{\Delta t_r}{2\pi}\sin(2\pi\frac{\mathrm{mod}(t,T) - t_{rd}}{\Delta t_r})\right]$$

$$t_{rd} \le \mathrm{mod}(t,T) < t_{rd} + \Delta t_r$$

$$\alpha(t) = \alpha_d$$

$$t_{rd} + \Delta t_r \le \mathrm{mod}(t,T) < t_{ru}$$

$$\alpha(t) = \alpha_d - \frac{(\alpha_d - \alpha_u)}{\Delta t_r}\left[(\mathrm{mod}(t,T) - t_{ru}) - \frac{\Delta t_r}{2\pi}\sin(2\pi\frac{\mathrm{mod}(t,T) - t_{ru}}{\Delta t_r})\right]$$

$$t_{ru} \le \mathrm{mod}(t,T) < t_{ru} + \frac{\Delta t_r}{2} \tag{3}$$

where Φ_0 is the amplitude of the flapping angle and $\varphi_0 = 0.602$, according to reference [19]. $\alpha_d = 66°$ and $\alpha_u = 14°$, Δt_r is the duration of the wing flip and t_{ru} and t_{rd} are time moments that the wing starts to rotate in the upstroke and downstroke actions. According to reference [19], $\Delta t_r = 0.39T$ is the same for both the downstroke and upstroke in SRM, and $t_{rd} = 0.305T$ and $t_{ru} = 0.805T$, where T is the time period of AOA movement. Besides SRM, there are another two unsymmetrical modes, called ARM and DRM, respectively. These two unsymmetrical modes are obtained by shifting $\alpha(t)$ with a negative angle for the ARM and with a positive angle for the DRM. Both ARM and DRM can be expressed by Equation (4).

$$\alpha(t) = \alpha(t)_s \mp \alpha_0 \tag{4}$$

where subscript s denotes AOA in SRM. In fact, the physical meaning of two unsymmetrical modes is to shift wing rotation timing in downstroke and upstroke. The time histories of the flapping angle and angle of attack in two cycles for the above mentioned three modes are shown in Figure 4. It is noted that when the relative AOA is zero, the wing is actually 40° relative to the flapping plane.

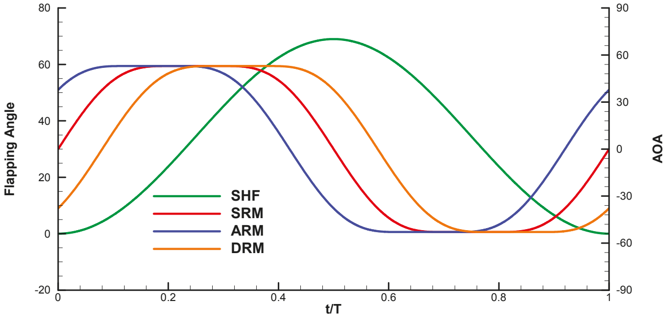

Figure 4. The time histories of flapping (green) and relative AOA angles in one period during hovering motion. (SHF: simple harmonic function; AOA: angle of attack; SRM: symmetrical rotation mode; ARM: advanced rotation mode; DRM: delayed rotation mode. Units of flapping angle and relative AOA are degree).

3.3. The New Kinematics of Flapping Motion

In this paper, a partial advanced mode (PAM) is proposed by shifting the wing rotation timing for near the end of the downstroke while keeping the wing rotation in upstroke motion intact, as that of the symmetrical mode. The wing downstroke rotation is now given as $t_{rd} = (0.305 \mp t_0)T$, where t_0 is the ratio of shifted start time to time period. A new rotation kinematics of wing flapping motion is generated, meanwhile the time histories of the flapping angle and the angle of attack in two cycles are shown in Figure 5.

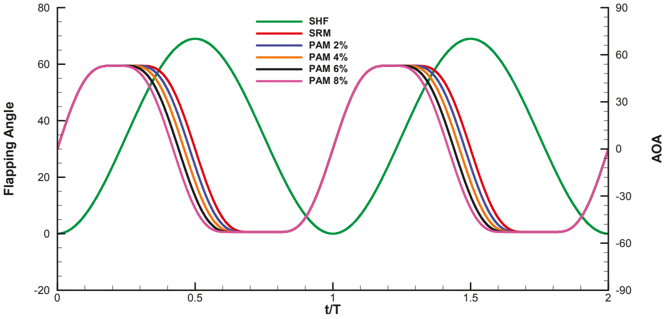

(**a**)

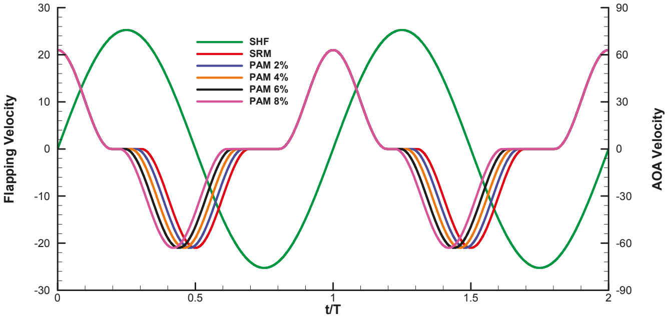

(b)

Figure 5. The time histories of flapping and attack angles (**a**) and flapping and AOA angular velocities (**b**) in two periods during hovering motion. (SHF: simple harmonic function; AOA: angle of attack; SRM: symmetrical rotation mode; PAM: partial advanced mode). (**a**) The time histories of flapping (green) and AOA angles; (**b**) The time histories of flapping (green) and AOA angular velocities.

3.4. Model Setup

In the model, air density, $\rho = 1.185\ \mathrm{kg/m^3}$, and dynamic viscosity, $\mu = 1.831 \times 10^{-5}\ \mathrm{kg \cdot m^{-1} \cdot s^{-1}}$, are set in a still air. Transient analysis calculates 30 cycles to ensure the final solution in one period to attain convergence status. The time step is set to 5×10^{-6} s. The computational domain is chosen as a sphere with a radius of 30 cm, which is more than six times the wingspan of 4.6 cm. The center of the sphere is located at the point of origin of the coordinate system X, Y and Z, which can be seen in Figures 2 and 3. There are two types of boundaries in the above computational domain, wing surface and sphere surface. In the paper, the wing surface is a moving boundary, while the sphere surface is the far field boundary. The far field and moving boundary conditions are selected as opening and non-slip wall boundary conditions respectively.

4. Results and Discussions

4.1. Mesh Convergence Test

There are four meshes used to verify mesh convergence. The total mesh cells of the model are 35,566, 68,497, 11,3614 and 23,3150, which are summarized in Table 1.

Table 1. Mesh information.

Mesh Model	Wing Surface Mesh	Total Mesh	Node Point
Coarse	1024	35,566	6566
Medium	1024	68,497	12,058
Fine	2786	113,614	19,995
Finer	6084	233,150	40,746

As an example, the mesh of the whole computational domain (a) and the cross section and zoom-out view of the mesh around the wing (b and c) are presented in Figure 6. The instantaneous pressure values of those monitoring points are shown in Figure 7.

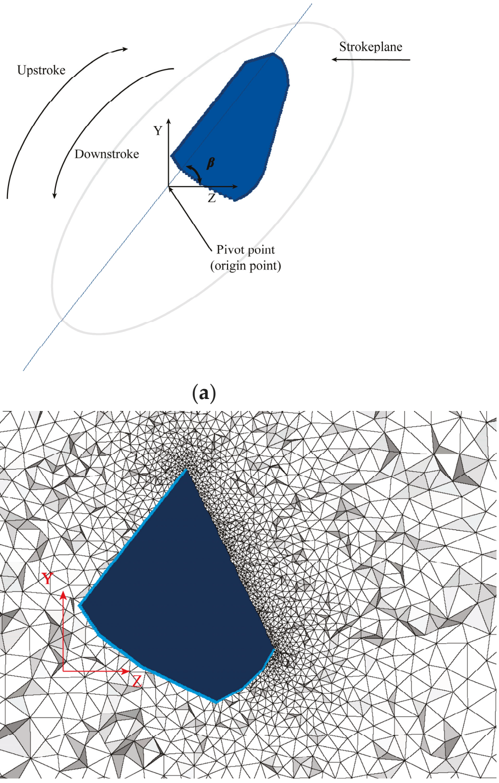

(**a**)

(**b**)

Figure 6. Mesh grid (fine) and motion parameters for the simulation of a dragonfly hindwing during hovering motion in the initial time step. (**a**) Flapping motion parameters in the initial time step; (**b**) grid of computational flow field in the initial time step.

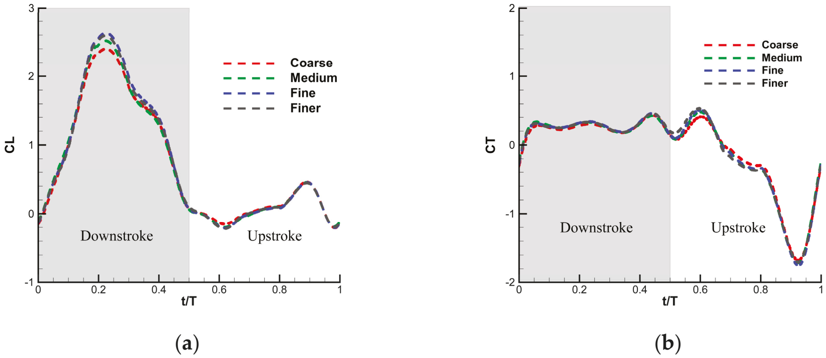

(**a**) (**b**)

Figure 7. A comparison of the instantaneous lift and thrust coefficients of the wing in the hovering motion between coarse, medium, fine and finer grids (**a**) four kinds of lift force coefficient curves, C_L, in comparison; (**b**) four kinds of thrust coefficient curves, C_T, in comparison.

Figure 7 shows that with the increasing of mesh density, the instantaneous lift and thrust coefficients gradually converge to stable and mesh independent values. When the mesh used is the fine grid, the relative error of the instantaneous values is below 1%. Therefore, the solution with the fine mesh could be considered as reaching mesh convergence. Taking into account the requirements of computational accuracy and time cost, the fine mesh is used as the optimal computational mesh for subsequent studies.

4.2. Aerodynamic Performance of Symmetrical Model and Validation of Results

In the study of insect flapping flight, aerodynamic factors, including the lift force coefficient, C_L, and thrust coefficient, C_T, are the most important in order to characterize the aerodynamic forces. In this study, C_L denotes the aerodynamic component perpendicular to the horizontal plane pointing to the y-axis for lifting the weight of the dragonfly, while the C_T represents the aerodynamic component orthogonal to the C_L directed to the z-axis. The C_L and C_T are obtained by Equation (5) and (6) as follows.

$$C_L = \frac{F_Y}{0.5\rho U^2 S_h} \tag{5}$$

$$C_T = \frac{F_Z}{0.5\rho U^2 S_h} \tag{6}$$

where U = 4.0724 m/s is the dimensionless speed, and S_h is the hindwing area of 5.152 cm^2.

The C_L and C_T obtained by the current model are presented in Figure 8, where the results obtained by Sun [19] are also plotted for comparison and validation purposes. The period-averaged C_L of the present model is 0.736, while the value using Sun's model [19] is 0.675, which shows a relative error of about 9%. The lift force generation mechanisms including wake capture and dynamic stall, as well as rapid pitch, are clearly captured, which serves to validate the capability of the current numerical model.

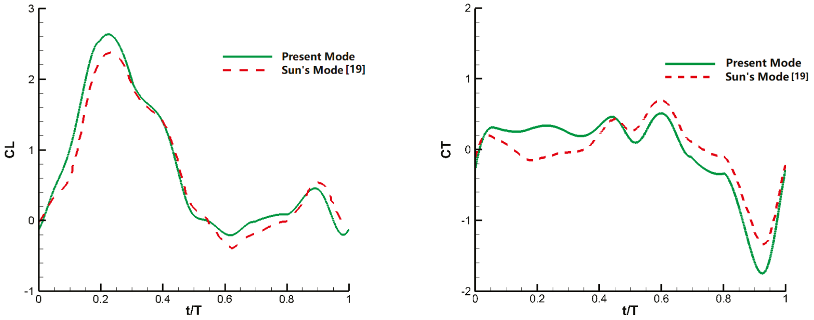

(**a**) (**b**)

Figure 8. The comparison of the profiles of C_L and C_T in one hovering motion cycle. (**a**) The time history of C_L; (**b**) the time history of C_T.

4.3. Aerodynamic Performance of PAM

In this section, aerodynamic performance of the proposed PAM is investigated. The numerical investigations are conducted in the following three steps. Firstly, the shift time, t_0, effects of PAM are investigated. Secondly, with the typical shift time value, t_0, from the first step, the results of the SRM, ARM and PAM are compared. Thirdly, analyses and discussions of the vortex formations and energy consumption are carried out in order to provide a proper aerodynamic explanation for the results obtained and to further evaluate the performance of the proposed PAM.

4.3.1. The Shift Time Effects of PAM and PDM

As described in Figure 5, the PAM cases, with a set of shift times, t_0, such as 2%T, 4%T, 6%T and 8%T, are implemented. Aerodynamic performances of the above cases are simulated using our inhouse solver TetraALEFSI [12,14,17], and the results are plotted in Figure 9.

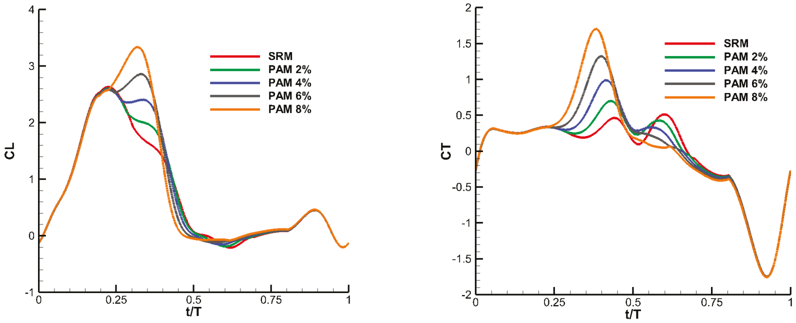

(**a**) the profile of C_L (**b**) the profile of C_T

Figure 9. Time histories of C_L and C_T for PAM with different shift time values.

Figure 9 reveals that aerodynamic forces are improved dramatically by using the PAM in the hovering motion. Compared with the results of the SRM, significant improvement of lift force appeared during the partial advanced shifting phase, 0.22T~0.41T. According to the results, the higher the shift time value, the larger the lift force that could be obtained. When the shift time reaches 8%T in PAM, the maximum lift force is about 3.4, nearly 1.36 times larger than the maximum value of the SRM, 2.5. At the same time, different from C_L distribution in SRM, lift force resulting from the PAM continues increasing in the cases of 6%T and 8%T. The time moment for the maximum lift force appearing is shifted later for the 6%T and 8%T cases, for example, 0.32T for the 8%T case, almost 0.07T delayed from the time moment in the SRM case. Together with the increase of the lift force, the thrust force is higher during the partial shifting phase. The maximum value of the thrust force is about 1.78 for the 8%T case. The aerodynamic force during upstroke actually has no change since the same flapping action as the one in SRM is used.

4.3.2. The Comparisons of PAM and ARM Modes

To further understand the effects of the proposed PAM on lift force generation, systematical comparisons with PAM and ARM modes are carried out. The shift time value, 8%T, is chosen for the PAM and ARM due to the outstanding performance obtained in the previous section.

Figure 10 shows the time histories of C_L and C_T during one cycle of hovering motion using the above-mentioned three modes. The comparison is mainly focused on aerodynamic forces from the PAM and ARM. Significant difference has been found in the upstroke. Rapid pitch in the first half of the upstroke in ARM does not play any positive effect on lift force generation. On the contrary, both the ARM lift and thrust forces decrease rapidly in the upstroke due to the orientation of the wing at the ends of both strokes of 40° relative to the flapping plane in the downward direction. Only during the second half of the upstroke, the lift force in ARM increases slightly, also due to the rapid pitch, but being much less effective than the corresponding downstroke because of the above-mentioned wing orientation relative to the flapping plane. Therefore, one can conclude that the overall lift force could only be improved by using PAM alone.

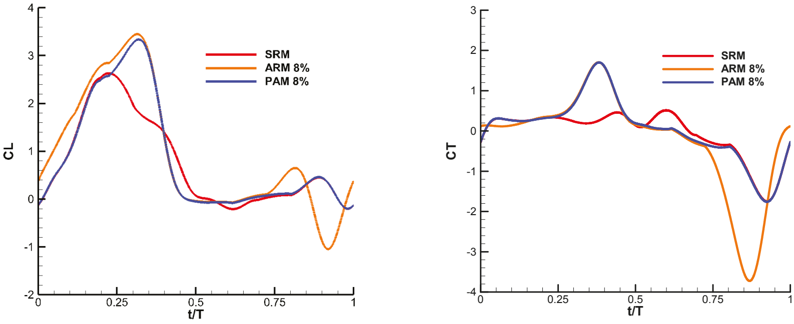

(**a**) (**b**)

Figure 10. Time histories of C_L and C_T during one cycle of hovering motion for three flapping modes. (**a**) The profile of C_L; (**b**) the profile of C_T.

4.4. Vortex Analyses in Lift Force Generation by PAM

In Section 4.3, aerodynamic forces from PAM are described and the significant points of the proposed mode have been obtained mainly based on the C_L and C_T profiles and the comparisons between SRM and ARM. In this section, further investigation on the lift force generation mechanism in PAM is to be carried out with focus on vortex analyses.

Figure 11 shows snapshots of typical fluid structures, in the form of pressure contours, streamlines and iso-vorticity surfaces in one cycle of hovering motion with the PAM. The cross-sectional plane is chosen with 0.65R for pressure contours and streamlines, while the contour values of the iso-vorticity surface are set to $-18{,}400s^{-2}$. The background color (lilac) of the vorticity contour is the cross-sectional plane which intersects with the iso-vorticity surfaces (grey) in Figure 11. Figure 12 plots the lift force time history for the case in Figure 11 with the same time instants marked by solid points and their corresponding iso-vorticity surfaces.

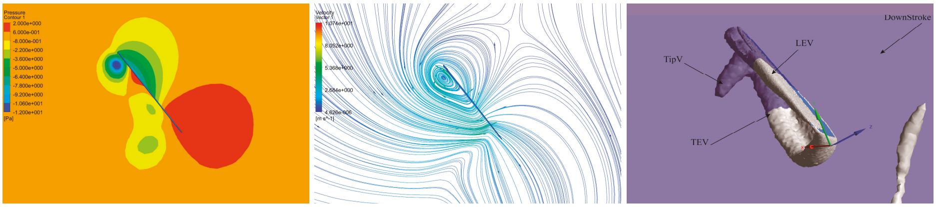

(**a**) t/T = 0

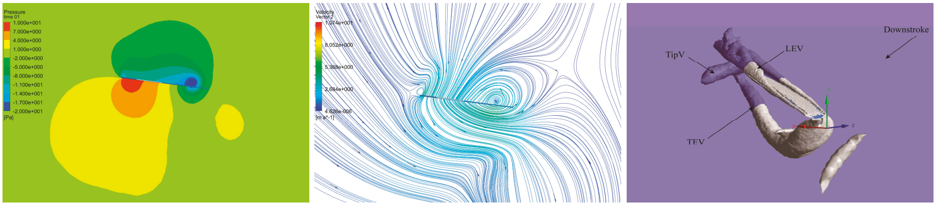

(**b**) t/T = 0.1

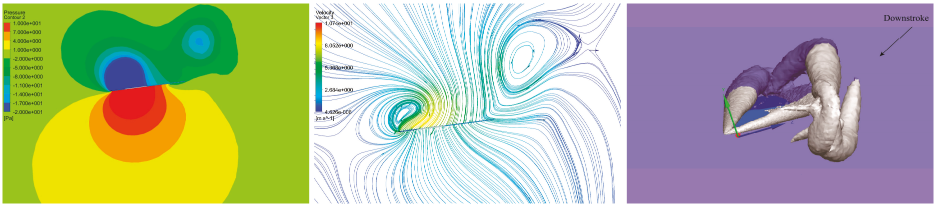

(**c**) t/T = 0.22

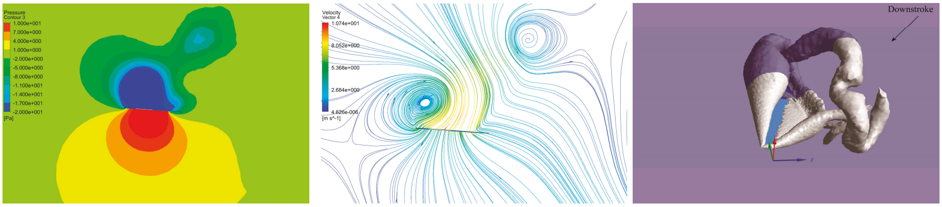

(**d**) t/T = 0.34

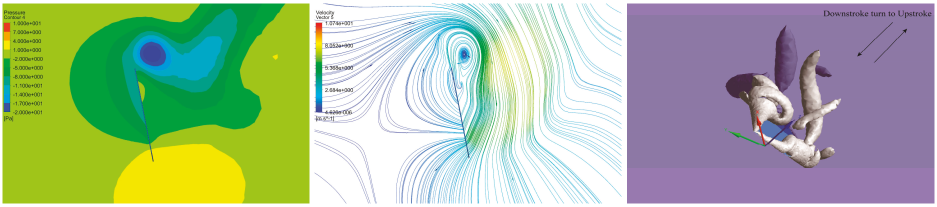

(**e**) t/T=0.5

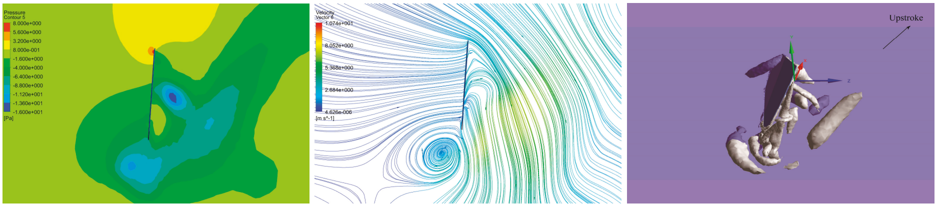

(**f**) t/T = 0.62

Figure 11. *Cont.*

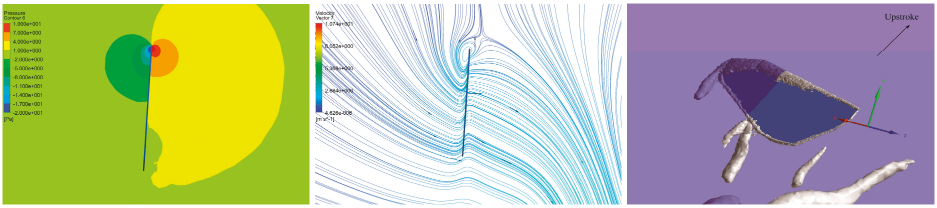

(**g**) t/T = 0.80

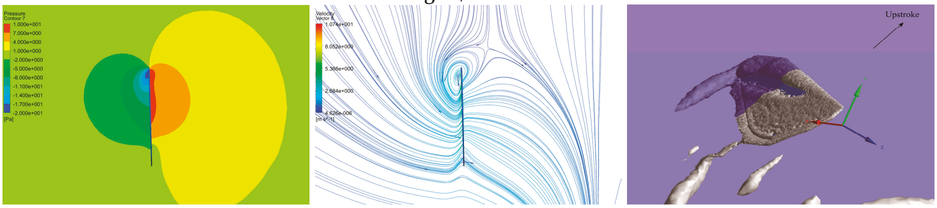

(**h**) t/T = 0.88

Figure 11. Pressure contours (left), streamlines (middle) and iso-vorticity surfaces (right). At different time instants with PAM 8%T in one cycle of hovering motion (**a**–**h** corresponds to t/T = 0, 0.1, 0.22, 0.34, 0.5, 0.62, 0.80 and 0.88, respectively).

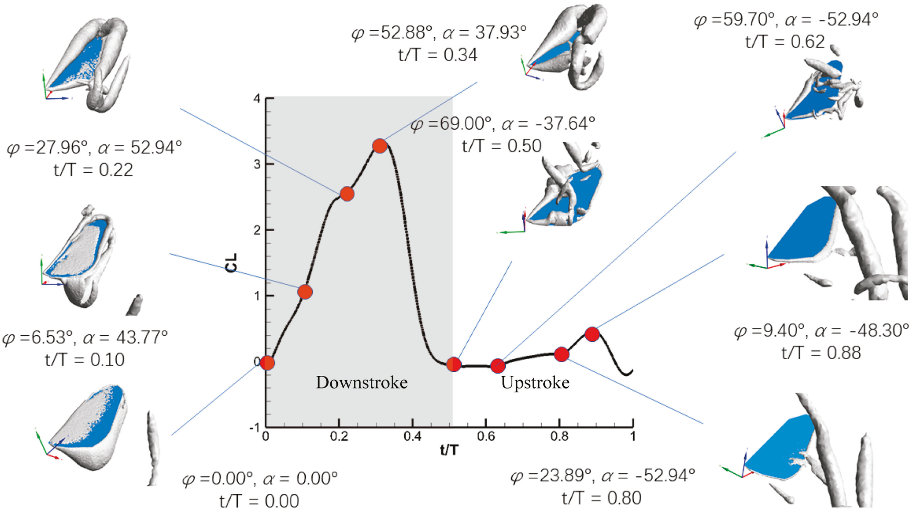

Figure 12. The lift force and iso-vorticity surface plots for 8%T PAM.

At time instant t/T = 0, unshed vortices in the previous cycle still exist at the edge of the wing. At this moment, the wing is starting to accelerate downward, accompanied by a counterclockwise rotation.

When t/T = 0.1, air moves around the wing from the leading edge to the trailing edge and around the wing tip, and a new vortex system around the wing is generated which is composed of a leading edge vortex (LEV), a trailing edge vortex (TEV) and a tip vortex (TipV). In fact, the new vortex system has been found as a whole at the beginning, as the vortices, such as LEV, TEV and TipV, are well established from the beginning. It is noted that the LEV is a clockwise vortex while the TEV is counterclockwise. At the same time, air impacts the lower surface of the wing and goes though the wing, which enhances the LEV, TEV and TipV. A large negative pressure area is formed on the upper surface of the wing, while a positive pressure area is formed on the lower surface. The pressure difference between the upper and lower surfaces generates a vertical upward lift. It can be seen from the iso-vortex surfaces that the vortex on the edge of the wing in the previous cycle gradually falls off, which shows that the mechanism of wake capture is almost over and the dynamic stall mechanism will start to work.

When t/T = 0.22, lift force on the wing reaches an instantaneous peak due to the dynamic stall mechanism. From the diagrams shown in Figure 11c, it can be seen that the clockwise vortex at the leading edge is still attached to the upper surface of the wing, but the counterclockwise vortex at the trailing edge starts to fall off, causing the pressure difference between the upper and lower surfaces to decrease. Thus, the lift force will decrease if there is no more other action. However, the PAM can now be activated and play a role at this moment, which will start rapid pitch in the second half of the downstroke.

When t/T = 0.34, the increasing lift force due to PAM reaches its peak, which is also the maximum lift force generated in the whole cycle. From 0.22T to 0.34T, the wing partial advanced rotation in a clockwise direction leads to the LEV continuing development and keeps it attached to the leading edge. The action of the proposed PAM indeed lengthens the dynamic stall and enhances the lift force.

At t/T = 0.5, the LEV rotates clockwise to the right and falls off the wing eventually, which means that the wing cannot produce lift from this LEV anymore. At this point, the wing starts to accelerate up on the right.

From t/T = 0.62 to t/T = 0.88, the wing moves upward along the stroke plane with a small AOA angle, and the air flow around the wing is almost unimpeded, thus no lift force is generated. The vortex ring is basically completely detached from the wing.

In conclusion, at the beginning of the downstroke, the wing accelerates downward and the LEV starts to take shape, which leads to an increase in lift force. In the intermediate translational stage, the LEV is further enhanced resulting in instantaneous lift peak due to the dynamic stall mechanism. Both PAM and SRM share the same motions, therefore their mechanisms of lift generation are basically the same up to a quarter of the cycles. After this, the wing starts to flap with greater rotational speed using the PAM, thus the lift can continue to increase. However, the rotational speed of the wing has been reduced to a very small value for the SRM, thus the lift force cannot be increased. This is a new way to generate lift force using a combination of dynamic stall and rapid pitch mechanisms. Moreover, PAM follows the same motion as SRM during upstroke since lift force cannot be enhanced significantly using ARM (Figure 10). In fact, this is the reason that the partial advanced mode is proposed because the lift force generated during the upstroke in the ARM is very poor.

4.5. Energy Consumption Analyses Using PAM

The aerodynamic parameters, including time period-averaged C_L, C_T and power coefficient C_P, as well as figure-of-merit M, are calculated and summarized in Table 2 and plotted in Figure 13. Figure 14 shows the time-averaged aerodynamic parameters using the PAM.

Table 2. Time-averaged aerodynamic parameters for partial advanced mode.

Model	$\overline{C_L}$	$\overline{C_T}$	$\overline{C_P}$	η
Symmetry	0.7374	−0.0593	0.196	3.7622
2%	0.7642	−0.0368	0.214	3.5710
4%	0.7946	−0.0124	0.242	3.2835
6%	0.8240	0.0134	0.275	2.9964
8%	0.8522	0.0401	0.312	2.7314

Energy consumption of the wing during one flapping period is calculated using the following formulations:

$$P = \int_0^T \oint_A (\vec{U}(t) \cdot \vec{n}(t))p(t)dA(t)d(t) \tag{7}$$

where P is the power supporting wing movement during one hovering motion cycle. The efficiency of power, C_P, is calculated by

$$C_P = \frac{P}{0.5\rho U^3 S_{\mathrm{h}}} \tag{8}$$

where ρ is the density of air, $\rho = 1.185\ \mathrm{kg/m^3}$, S_h is the area of the hindwing, $S_h = cR = 1.12 \times 4.6 = 5.152\ \mathrm{cm}^2$, and U is the reference velocity, calculated at the location of 0.65R, $U = 4.0724\ \mathrm{m/s}$.

The wing efficiency is evaluated by a parameter, η, the lift-to-power ratio [20], which is defined as follows:

$$\eta = \frac{\overline{C_L}}{\overline{C_p}} \tag{9}$$

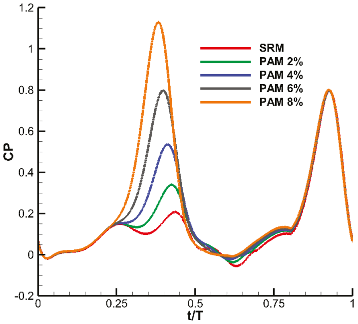

Figure 13. The time histories of power coefficient C_P for partial advanced mode.

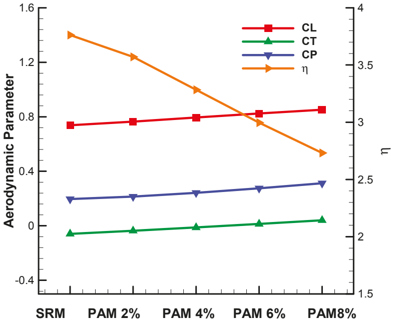

Figure 14. Time-averaged aerodynamic parameters for different start times of stroke reversal.

Table 2 shows the time-averaged C_L, C_T, C_P and η in PAM with different shift times. Compared with C_L = 0.7374 using ARM, PAM has a time-averaged C_L = 0.8522, about a 16% increase in lift force in the 8%T PAM case. Lift force is dramatically improved by the PAM. The time-averaged C_T also increases with increasing shift time in PAM. The time-averaged C_P reaches 0.312 in the 8%T PAM case, 0.116 larger than that of the SRM case, which means that although the proposed partial advanced mode could improve lift force, energy consumption has also increased and the corresponding wing efficiency parameter has decreased significantly.

5. Conclusions

In the paper, a numerical method is presented, validated and then applied to numerically investigate life force generation mechanisms of a dragonfly wing during hovering motions. High lift force is generated by implementing the partial advanced flapping mode during hovering motion, namely PAM. The aerodynamic performance of the proposed PAM is numerically investigated and compared with those of the traditional SRM, as well as the ARM. The results show that lift forces, not only the peak value but also the period-averaged values, are dramatically improved by using PAM. Peak lift force increases by 1.36 times, while period-averaged Cl increases by 16% in the 8%T PAM case, compared with those of the SRM. The high lift force generation mechanism is analyzed and investigated by studying flow structures, including pressures and streamlines as well as iso-vorticty surfaces, around the wing. The proposed PAM is believed to lengthen the dynamic stall mechanism and enhance the LEV generated during downstroke. The improvement of lift force could be considered as a result of a combination of the dynamic stall mechanism and rapid pitch mechanism. However, it should be noted that although the PAM mode could improve lift force, the increase of energy consumption and corresponding decrease in wing efficiency parameter have to be considered as byproducts of this mode.

Author Contributions: Conceptualization, X.S. and K.Z.; methodology, K.Z., J.Z. (Juan Zheng) and J.Z. (Jiantao Zhang); software, K.Z. and R.H.; validation, K.Z., J.Z. (Juan Zheng) and R.H.; formal analysis, J.Z. (Jiantao Zhang); investigation, K.Z. and J.Z. (Juan Zheng); resources, J.Z. (Jiantao Zhang); data curation, K.Z. and J.Z. (Juan Zheng); writing—original draft preparation, X.S., K.Z.; writing—review and editing, X.S., K.Z. and Y.Z.; visualization, K.Z. and J.Z. (Juan Zheng); supervision, X.S.; project administration, X.S.; funding acquisition, X.S. All authors have read and agreed to the published version of the manuscript.

Funding: This research is supported by The National Natural Science Foundation, project No: 11672059. The financial support is gratefully acknowledged.

Conflicts of Interest: The authors declare no conflict of interest.

Nomenclature

symbol	**meaning**	**unit**
c	average chord length	cm
C	preconditioning matrix	-
$\mathrm{C_L}$	lift force coefficient	-
$\mathrm{C_T}$	thrust coefficient	-
$\mathbf{F}_\mathrm{c}$	convective flux	-
$\mathbf{F}_\mathrm{v}$	viscous flux	-
$\mathbf{K}$	unit matrix with first element equal to zero	-
R	wing length	cm
Re	Reynolds number	-
t	time	s
t_0	ratio of shifted start time to time period	s
t_{rd}	divided point from translate to rotate in downstroke	s
t_{ud}	divided point from translate to rotate in upstroke	s
Δt_r	duration of wing flip	s
T	flapping period	s
X,Y,Z	rectangular coordinate system	-
α	angle of attack	^{0}
α_d	midstroke geometric angle of attack of downstroke	^{0}
α_u	midstroke geometric angle of attack of upstroke	^{0}
α_0	phase angle of flapping motion	^{0}
α_s	angle of attack in symmetrical rotation mode	^{0}
β	artificial compressibility coefficient	-
β	inclined angle	^{0}
η	wing efficiency parameter	-
μ	dynamic viscosity	kg/m/s
ρ	air density	kg/m^3
φ	flapping angle	^{0}
φ_0	amplitude of flapping angle	^{0}

References

1. Dickinson, M.H.; Gotz, K.G. Unsteady aerodynamic performance of model wings at low Reynolds numbers. *J. Exp. Biol.* **1993**, *174*, 45–64.
2. Dickinson, M.H.; Lehman, F.O.; Sane, S.P. Wing rotation and the aerodynamic basis of insect flight. *Science* **1999**, *284*, 1954–1960. [CrossRef] [PubMed]
3. Ellington, C.P. The aerodynamics of hovering insect flight. VI. Lift and power requirements. *Philos. Trans. R. Soc. London B* **1984**, *305*, 145–181.
4. Sun, M.; Du, G. Lift and power requirements of hovering insect flight. *Acta Mech. Sinica* **2003**, *19*, 24–31.
5. Sun, M. High-lift generation and power requirements of insect flight. *Fluid Dyn. Res.* **2005**, *37*, 21. [CrossRef]
6. Whitney, J.P.; Wood, R.J. Conceptual design of flapping-wing micro air vehicles. *Bioinspir. Biomim* **2012**, *7*, 036001. [CrossRef] [PubMed]
7. Zhang, C.; Rossi, C. A review of compliant transmission mechanisms for bio-inspired flapping-wing micro air vehicles. *Bioinspir. Biomim* **2017**, *12*, 025005. [CrossRef] [PubMed]
8. Weis-Fogh, T. Energetics of hovering flight in hummingbirds and in Drosophila. *J. Exp. Biol* **1972**, *56*, 79–104.
9. Shyy, W.; Trizila, P.; Kang, C.K.; Aono, H. Can tip vortices enhance lift of a flapping wing? *AIAA J.* **2009**, *47*, 289–293. [CrossRef]
10. Trizila, P.; Kang, C.; Visbal, M.; Shyy, W. Unsteady Fluid Physics and Surrogate Modeling of Low Reynolds Number, Flapping Airfoils. In Proceedings of the 38th Fluid Dynamics Conference and Exhibit, Seattle, WA, USA, 23–26 June 2008.
11. Du, G.; Sun, M. Effects of wing deformation on aerodynamic forces in hovering hoverflies. *J. Exp. Biol.* **2010**, *213*, 2273–2283. [CrossRef] [PubMed]
12. Su, X.H.; Zhen, Y.; Cao, Y.W.; Zhao, Y. 2017. Numerical investigations on aerodynamic forces of deformable foils in hovering motions. *Phys. Fluids* **2017**, *29*, 041902. [CrossRef]
13. Walker, S.M.; Thomas, A.L.R.; Taylor, G.K. Deformable wing kinematics in free-flying hoverflies. *J. R. Soc. Interface* **2009**. [CrossRef] [PubMed]
14. Zhao, Y.; Tai, C.H. Higher-order characteristics-based method for incompressible flow computation on unstructured grids. *AIAA J* **2001**, *39*, 1280–1287. [CrossRef]
15. Tai, C.H.; Zhao, Y. Parallel unsteady incompressible viscous flow simulation using an unstructured multigrid method. *J. Comput. Phys.* **2003**, *192*, 277–311. [CrossRef]
16. Su, X.H.; Zhao, Y.; Huang, X.H. On the characteristics-based ACM for incompressible flows. *J. Comput. Phys.* **2007**, *227*, 1–11. [CrossRef]
17. Su, X.H.; Cao, Y.W.; Zhao, Y. An unstructured mesh arbitrary Lagrangian-Eulerian unsteady incompressible flow solver and its application to insect flight aerodynamics. *Phys. Fluid* **2016**, *28*, 061901. [CrossRef]
18. Norberg, R.A. Hovering flight of the dragonfly Aeschna juncea L., kinematics and aerodynamics. In *Swimming and Flying in Nature*; Wu, T.Y.-T., Brokaw, C.J., Brennen, C., Eds.; Springer: Boston, MA, USA, 1975; pp. 763–781.
19. Sun, M.; Lan, S.L. A computational study of the aerodynamic forces and power requirements of dragonfly (Aeschna juncea) hovering. *J. Exp. Biol* **2004**, *207*, 1887–1901. [CrossRef] [PubMed]
20. Masoud, H.; Alexeev, A. Resonance of flexible flapping wings at low Reynolds number. *Phys. Rev. E* **2010**, *81*, 056304. [CrossRef] [PubMed]

fluids MDPI

Article

Flow in Fractured Porous Media Modeled in Closed-Form: Augmentation of Prior Solution and Side-Stepping Inconvenient Branch Cut Locations

Ruud Weijermars * and Aadi Khanal

Harold Vance Department of Petroleum Engineering, Texas A&M University, College Station, TX 77843-3116, USA; akhanal@tamu.edu
* Correspondence: r.weijermars@tamu.edu

Received: 12 February 2020; Accepted: 13 April 2020; Published: 16 April 2020

Abstract: Carefully chosen complex variable formulations can solve flow in fractured porous media. Such a calculus approach is attractive, because the gridless method allows for fast, high-resolution model results. Previously developed complex potentials to describe flow in porous media with discrete heterogeneities such as natural fractures can be modified to expand the accuracy of the solution range. The prior solution became increasingly inaccurate for flows with fractures oriented at larger angles with respect to the far-field flow. The modified solution, presented here, based on complex analysis methods (CAM), removes the limitation of the earlier solution. Benefits of the CAM model are (1) infinite resolution, and (2) speed of use, as no gridding is required. Being gridless and meshless, the CAM model is computationally faster than integration methods based on solutions across discrete volumes. However, branch cut effects may occur in impractical locations due to mathematical singularities. This paper demonstrates how the augmented formulation corrects physically unfeasible refraction of streamlines across high-permeability bands (natural fractures) oriented at high angles with respect to a far-field flow. The current solution is an important repair. An application shows how a drained rock volume in hydraulically fractured hydrocarbon wells will be affected by the presence of natural fractures.

Keywords: complex potential; stream function; potential function; flow in porous media; flow in natural fracture systems

---

1. Introduction

Fast and accurate solutions for flow in fractured porous media are sought after in the petroleum industry, which increasingly extracts oil and gas from hydraulically and naturally fractured shale formations. Practical applications for flow models of fractured porous media are ubiquitous and not limited to the petroleum industry. For example, medical applications involving flow across fractured bone structures, and magmatic melts moving from the Earth's mantle to the crust via pore space and fractures also are governed by equations for flow in fractured porous media. Of particular interest to the current study is the modeling of the flow of hydrocarbon fluids in fractured reservoirs, for which our models can provide detailed solutions. However, the formulation provided here may also be applied to subsurface flow studies for geothermal energy extraction from naturally fractured rocks.

Modeling flow in fractured porous media with discrete fractures using explicit numerical methods is computationally intensive and requires excessive meshing and gridding adjustments near fracture intersections [1–4]. An alternative model approach, advocated here, uses a gridless and meshless analytical modeling technique based on complex analysis methods (CAM), and has been stepwise developed in two key, earlier papers. The first paper [5] presented a solution using areal doublets, which is accurate for flow through fractures aligned with a far-field flow and can account for an unlimited (but finite) number of fractures and any permeability contrast between the fractures and matrix. The second paper [6] resolved branch cut choices arising in solutions of the real part (potential function) of the complex potential for areal doublets, which is relevant when plotting the pressure fields involving flow near natural fractures.

We revisit the superposition process used to derive the expressions for an areal doublet and an areal dipole, developed in the two prior studies [5,6] to model flow in fractured porous media. In these prior studies, instantaneous stream function solutions were used to visualize streamlines in porous media with randomly oriented fractures [5]. The potential function, with appropriate scaling, was used to plot the pressure field [6]. The velocity field can also be solved in every location and, combined with an Eulerian particle tracking method, enables the construction of fluid particle paths for time-dependent flows and allows for the insertion of time-of-flight (TOF) contours to show the flow advance at specific time increments after the onset of flow [7].

This study augments the prior solutions [5,6] by removing certain limitations when the method is applied to fractures oriented at high angles to the far-field flow. Although the code used in previous studies is accurate for flow near fractures at low angles to the ambient (far-field) flow direction, the earlier solution does not adequately account for flow through natural fractures at a high angle to the far-field flow direction. The augmentation proposed in the present study provides a comprehensive solution, valid for any orientation of the natural fractures and does not require (manual) adjustments for high-angle fractures, as was the case in the prior code.

This article proceeds as follows. Section 2 first explains the functionality of the existing closed-form algorithms to describe flow in fractured porous media. Section 3 presents the augmented solution, which can account for flow near the fractures at any angle with the far-field flow. Section 4 presents a field case application of the augmented algorithms. A discussion follows in Section 5, and conclusions are given in Section 6.

2. Complex Potential Solutions

In this section, we revisit some fundamental closed-form solutions required to ultimately adjust complex potentials used to describe flow through discrete fracture systems. Redirection of streamlines can be effectuated when an existing flow, described by a set of single-valued complex potentials is superposed by a complex potential that represents the desired disturbance. For example, Figure 1a shows an undisturbed flow between a direct line drive with streamlines connecting a series of injectors and producer wells. The basic flow pattern will be altered when a rectangular domain of high permeability is placed in the flow path between the injector and producers; the streamlines converge (with a faster time-of-flight) toward the producer wells (Figure 1b). The opposite occurs (i.e., a slower time-of-flight) when the rectangular domain instead has a lower permeability than the surrounding matrix, which will result in streamline divergence (Figure 1c). Both the flow convergence and divergence (in Figure 1b,c) were modeled by superposing a series of line doublets [7].

Section 2 moves through three systematic steps that highlight how the line doublets and related line dipoles are transformed into areal doublets and line dipoles that are suitable for modeling flow through discrete natural fractures in a reservoir. First, Section 2.1 explains the difference between the line doublet and a line dipole, which are two end members of a continuous series of line doublet/line dipole intermediates. Next, Section 2.2 reviews the prior complex potential used for closed-form flow models of fractured porous media and gives a comprehensive complex potential which can describe both the areal doublet and areal dipole. Section 2.3 highlights the limitations to the practical use of the derived solution due to branch cut effects. The results of Section 2 are necessary for an amended solution given in Section 3 that avoids the branch cut effects.

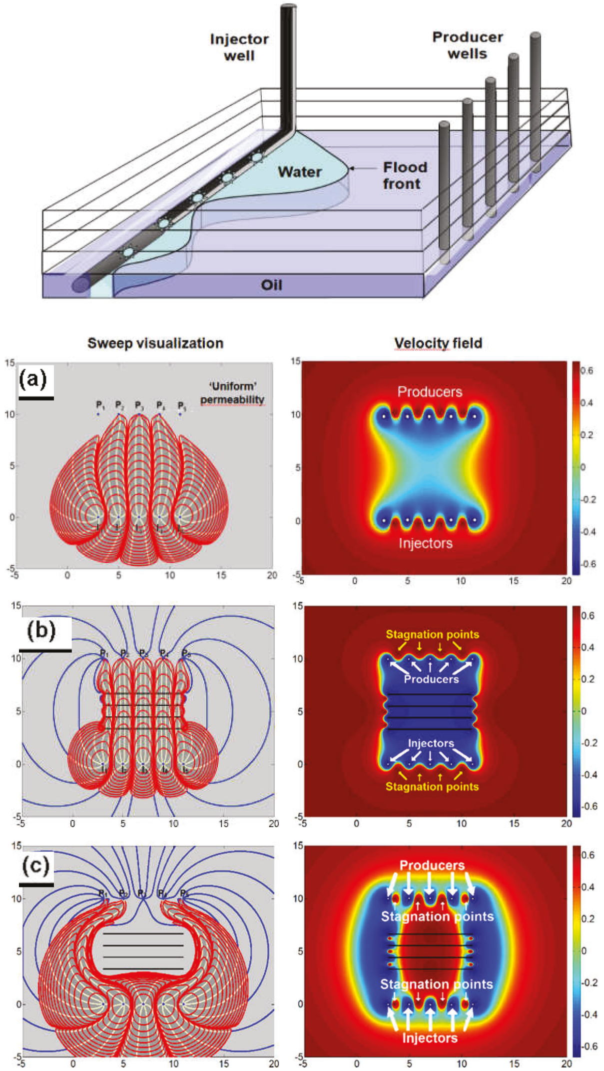

Figure 1. (**a**–**c**) Waterfront advance between a series of injector outlets and producer wells in streamline visualizations (left column; yellow flow paths inside grey injection water body; blue curves beyond injection water body). Time-of-flight contours (TOFCs, red curves). Velocity field magnitude (right), scaled by a Bernoulli pressure proxy using the natural logarithm and inverse tangent, outlines the regions (blue) where the fastest flow occurs. Reproduced with permission from [7].

2.1. Line Doublets and Line Dipoles

The distinction between doublets and dipoles was originally proposed by Strack [8], and was required for constructing line arrays called, respectively, line doublets and line dipoles. The line doublet is composed of a linear array of superposed singularity doublets (Figure 2a). The polarity of each singularity doublet [defined by its source (+) and sink (−) sides] remains perpendicular to the line array at all times (Figure 2a). Similarly, the line dipole is a linear array of superposed singularity dipoles

(Figure 2b). In the line dipole, the source and sink sides of the singularity are rotated 90° clockwise, and thus the polarity of each dipole remains aligned with the line array at all times (Figure 2b).

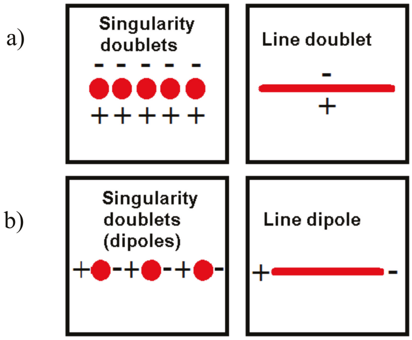

Figure 2. Conceptual models of: (**a**) line doublet obtained by superposing an infinite number of singularity doublets; (**b**) line dipole obtained by superposing an infinite number of singularity dipoles. Reproduced with permission from [5].

The complex potential for a line doublet and a line dipole are invariant [6], which means these potentials represent two physically distinct flows. The comprehensive solution presented below shows that the invariant nature of the respective complex potentials does not preclude the formulation of a concise complex potential that covers a broader spectrum of physical flows, including the line doublet and line dipole as end-members. The comprehensive solution is given by the following complex potential (Ω) [5]:

$$\Omega_1(z,t) = \frac{m(t)e^{i\theta} \cdot e^{i\beta}}{2\pi n H} \frac{[Log(z-z_a) - Log(z-z_b)]}{(z_a - z_b)} \tag{1}$$

with strength *m(t)* [$\mathrm{m}^4\ \mathrm{s}^{-1}$], unit depth H [m], and porosity n. A practical way to rewrite Equation (1) is to introduce $z_a = z_c - 0.5We^{i\beta}$ and $z_b = z_c + 0.5We^{i\beta}$[9], where W, z_c and β are the width, center coordinates and tilt angle of the line doublet/dipole element. The need to have two complex coordinates (z_a and z_b) is removed, and instead the mid-point (z_c) between the two ends of the region occupied by the flow element is given by specifying a width W. The polarity of the singularity doublet/dipole can be controlled by θ. For $\theta = 90°$, we obtain the line doublet solution given in Weijermars and Van Harmelen [9]. However, when $\beta = 0°$, the angle θ of the doublet singularities in the line element does not need to be 90°. For $\theta = 0°$ we have the line dipole solution. Intermediate flow types occur for $90° < \theta < 0°$ (see below).

There are two separate methods to obtain the streamlines for flows described by the complex potential of Equation (1). The first method separates the real and imaginary parts of the complex potential to obtain, respectively, the potential function and the stream function. The solutions for the stream function and the potential function can then be obtained (for any steady-state flow moment at time t) as an integral solution with standard software packages (like MATLAB, Python, Mathematica or others), as follows:

$$\psi(z) = \Im[\Omega(z)] \tag{2a}$$

$$\phi(z) = \Re[\Omega(z)] \tag{2b}$$

Figure 3a–d are solutions for ψ and ϕ using Equations (1) and (2a,b), with the input data of Table 1, and various angles for doublet polarity given by θ. Figure 3a–d confirm that the complex potential of Equation (1) gives a continuous solution series for physically viable flows ranging from the line doublet (Figure 3a) to the line dipole (Figure 3d), via intermediate flow types (Figure 3b,c). The stream function solutions are in the left column. The corresponding potential function solutions appear in the right column.

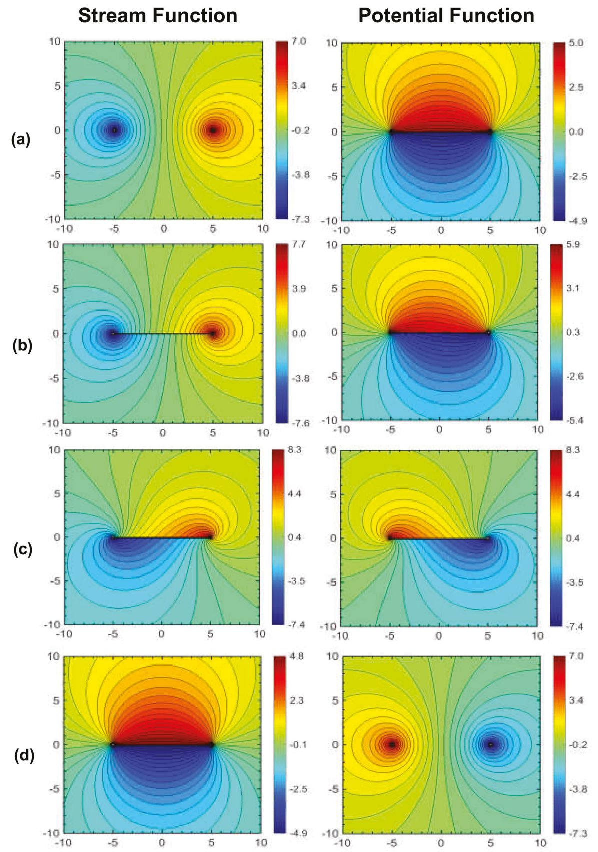

Figure 3. Stream function solutions (in left column) with streamlines for line doublets/line dipoles, based on Equation (1), for a range of polarity angles: (**a**) $\theta = 90°$, (**b**) $\theta = 45°$, (**c**) $\theta = 10°$, and (**d**) $\theta = 0°$. The tilt angle $\beta = 0°$ for all cases. Stream function values (ψ) given by rainbow colors ($m^2 \cdot s^{-1}$) relative to line $y = 0$. Potential function solutions are shown in the right column.

Table 1. Inputs data for line doublet/dipole element in Figure 3.

Quantity	Value	Units	Symbol
Matrix Porosity	0.1		n
Center of the line element	0	m	z_c
Length	10	m	L
Tilt angle	0	°	β
Strength	0.01	$m^4\ s^{-1}$	$m(t)$
Height	1	m	H
Polarity	(a) 90°, (b) 45°, (c) 10°, (d) 0°	°	θ

The second method to plot the streamlines for the flow of Equation (1) is to trace individual particles with an Eulerian particle tracking method. The particle tracking for any particular flow is made possible by first deriving the velocity field from the complex potential specific to the flow of concern, using:

$$V(z,t) = \overline{\frac{d\Omega(z,t)}{dt}} = v_x + iv_y; V(z,t) = \frac{d\Omega(z,t)}{dt} = v_x - iv_y \tag{3a}$$

Application of the derivative of Equation (3a) to the complex potential of Equation (1), using $z = x + iy = |z|(\cos\theta + i\sin\theta) = r(\cos\theta + i\sin\theta) = re^{i\theta}$, gives:

$$V(z) = \frac{m \cdot e^{i\theta} \cdot e^{i\beta}}{2\pi nH} \frac{1}{(z - z_b)(z - z_a)} = \frac{m \cdot e^{i\theta} \cdot e^{i\beta}}{2\pi nH} \frac{1}{(z - (z_c + 0.5W \cdot e^{i\beta}))(z - (z_c - 0.5W \cdot e^{i\beta}))} \tag{3b}$$

Equation (3b) is the generalized line doublet/dipole equation, which can be used to generate the velocity field for any line doublet/dipole analytical element with an angle of β to the real axis measured in an anti-clockwise direction. Additionally, θ can be used to change the angle of the polarity of the singularities, which collectively makes the line element. As before, for a special case when $\theta = 90°$, $e^{i\theta} = i$, this equation becomes identical to Equation (C9) for the line doublet in Weijermars and van Harmelen [9] and Equation (B2) in van Harmelen and Weijermars [5]. Note that the complex conjugate $\overline{z} = re^{-i\theta}$, and Euler's formula $e^{i\theta} = \cos\theta + i\sin\theta$ gives for $\theta = 0°$ $e^{i\theta} = 1$, and for $\theta = 90°$ it follows that $e^{i\theta} = i$.

Equation (3b) gives (v_x, v_y) for fluid particles in each location of the flow field. The particle tracking method uses a time-step, Δt, and initial particle position z_0 at time $t_0 = 0$ to track the streamlines followed by the particles. The position $z_1(t_1)$ of the tracer at time $t_1 = t_0 + \Delta t$ is:

$$z_1(t_1) \approx z_0(t_0) + v(z_0(t_0)) \cdot \Delta t \tag{4a}$$

The position $z_j(t_j)$ of the tracer particles at any other future time t_j is:

$$z_j(t_j) \approx z_{j-1}(t_{j-1}) + v(z_{j-1}(t_{j-1})) \cdot \Delta t \tag{4b}$$

Figure 4a–d show the streamlines for the complex potential of Equation (1), based on the particle tracking method of Equations (3b) and (4a,b) using selected angles θ and tilt angle of the line element $\beta = 0°$. Streamline solutions of Equations (3b) using the Eulerian particle tracking method of Equations (4a,b) offer the advantage that so-called time-of-flight contours (TOFCs) can be constructed [7]. Additionally, the flow is integrated over time and the particle paths represent the true flow path of time-dependent flows. The TOFCs show the advancement of an infinite number of tracers for periodic (constant) time-steps.

Comparison of Figures 3a–d and 4a–d reveals that the two methods provide the same streamline solutions. The first approach (stream function approach; Figure 3a–d) gives additional information on the fluid fluxes (stream function values relative to the origin). The alternative particle tracking method (Figure 4a–d) gives additional information on the time-of-flight, which is useful for studies of hydrocarbon drainage and reservoir depletion [7], studies of geothermal reservoirs that require monitoring of the advancement of injected fluids [9], and for studies of subsurface flow including the tracking of pollution plumes.

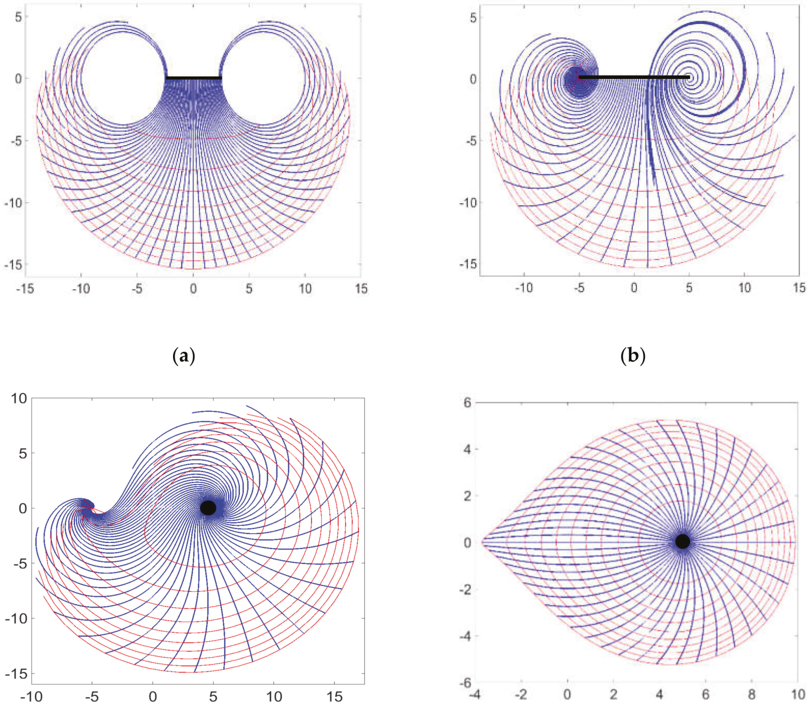

(**a**) (**b**)

(**c**) (**d**)

Figure 4. Streamlines (blue) and time-of-flight contours (red) for the line doublet of Equation (1), for a range of polarity angles: (**a**) $\theta = 90°$, (**b**) $\theta = 45°$, (**c**) $\theta = 10°$, and (**d**) $\theta = 0°$, and a tilt angle $\beta = 0°$ based on particle tracking method of Equations (3a,b) and (4a,b). The initial position of the tracked particles is shown in black color. For case (**a**) and (**b**) straight lines of length 5 (from -2.5 to 2.5 in x-axis) and 10 m (from -5 to 5 in x-axis) are tracked. For case (**c**) and (**d**), particles initially arranged on a minuscule circle with a radius of 0.01 m (located at 5 m from origin in x-axis) are tracked. Cases a-c are simulated for a period of 100 s whereas case d is simulated for 10 s both with a step-size of 0.0001 s.

2.2. *Areal Doublets and Areal Dipoles*

Section 2.1 has shown that a comprehensive complex potential exists for a suite of flows ranging from the line doublet (Figure 3a) to the line dipole (Figure 3d), via intermediate flow types (with arbitrary oblique orientations of the singularity doublets/dipoles in the respective line array (Figure 3b,c).

A prior study has integrated an infinite number of line doublets to formulate a complex potential for an areal doublet (Figure 5). The flow field of an areal doublet can be interpreted as an infinite number of doublet singularities with poles aligned with the direction of flow as schematically shown in Figure 5a. The complex potential $\Omega_1(z,t)$ for the areal doublet, scaled by a flow strength $v(t)$ [$\mathrm{m}^4\mathrm{s}^{-1}$] is [5]:

$$\Omega_2(z,t) = \frac{v(t)}{2\pi nHLW}\left[\Re[A-B+C-D] + i\cdot\Im[A-B+C-D]\right] \tag{5}$$

with dimensions of the areal doublet given by reservoir depth, H, doublet length, L, and aperture (or width), W, with porosity, n. The dummy terms $A - D$ in the real and imaginary parts $\Re[A-B+C-D]$ and $\Im[A-B+C-D]$, for an areal doublet with corner points located at z_{a1}, z_{a2}, z_{b1}, and z_{b2}, and tilt angle γ with the real axis (Figure 6), are as follows:

$$A = -i \cdot e^{-i\gamma}[(z+z_{a2})(\log(-e^{-i\gamma}(z-z_{a2}))] \tag{6a}$$

$$B = -i \cdot e^{-i\gamma}[(z+z_{a1})(\log(-e^{-i\gamma}(z-z_{a1}))] \tag{6b}$$

$$C = -i \cdot e^{-i\gamma}[(z+z_{b1})(\log(-e^{-i\gamma}(z-z_{b1}))] \tag{6c}$$

$$D = -i \cdot e^{-i\gamma}[(z+z_{b2})(\log(-e^{-i\gamma}(z-z_{b2}))] \tag{6d}$$

With corner point co-ordinates given by:

$$\begin{aligned} z_{a1} &= z_c - \mathrm{e}^{i\gamma} \cdot (0.5L + 0.5W \cdot e^{i\beta}) \\ z_{a2} &= z_c - \mathrm{e}^{i\gamma} \cdot (0.5L - 0.5W \cdot e^{i\beta}) \\ z_{b1} &= z_c - \mathrm{e}^{i\gamma} \cdot (-0.5L + 0.5W \cdot e^{i\beta}) \\ z_{b2} &= z_c - \mathrm{e}^{i\gamma} \cdot (-0.5L - 0.5W \cdot e^{i\beta}) \end{aligned} \tag{7}$$

A generic, comprehensive complex potential can be formulated for both areal doublets/areal dipoles (Figure 5a,b), and areal flow elements with singularity doublets/dipoles oriented oblique to the boundaries of the areal flow element. In analogy to Equation (1), the prior solution of an areal doublet [5,6] given here in Equation (5), can be modified into a general complex potential for areal doublets/dipoles (Figure 5a), as follows:

$$\Omega_3(z,t) = \frac{v(t) \cdot e^{i(\theta+\beta-\gamma)}}{2\pi nHL} \left[\frac{[(z-z_{a2})\log(-e^{-i\gamma}(z-z_{a2}))-(z-z_{a1})\log(-e^{-i\gamma}(z-z_{a1}))+(z-z_{b1})\log(-e^{-i\gamma}(z-z_{b1}))-(z-z_{b2})\log(-e^{-i\gamma}(z-z_{b2}))]}{W \cdot e^{i\beta}} \right] \tag{8}$$

With the corner-point coordinates again given by Equation (7). The solution of Equation (8) differs from the prior solution of Equation (5) in that the doublet/dipole polarity is separately parameterized, by not necessarily letting $\theta = \beta$. The velocity potential corresponding to Equation (8) is given by:

$$V(z,t) = \frac{v(t) \cdot e^{i(\theta+\beta-\gamma)}}{2\pi nHL} \left[\frac{[\log(-e^{-i\gamma}(z-z_{a2}))-\log(-e^{-i\gamma}(z-z_{a1}))+\log(-e^{-i\gamma}(z-z_{b1}))-\log(-e^{-i\gamma}(z-z_{b2}))]}{W \cdot e^{i\beta}} \right] \tag{9}$$

This is the general equation that allows for setting the angle of all the analytical elements (point dipole/doublet (θ) to line dipole/doublet (β) to areal dipole/doublet (γ)). In Equations (6) and (7), we have the imaginary i in the equation and we have $e^{i\beta}$ in the denominator, which will cancel each other out for all the cases, and is kept only to maintain analogy with the previous Equations (1) and (5).

The streamlines can again be obtained from Equation (8) applying the stream function and the potential function solutions of Equations (2a,b). First, only θ is varied for an areal doublet/dipole that has $\gamma = 0°$ and $\beta = 90°$ (Figure 7a–f), for angles θ similar to those used for the line doublet/dipole in Figure 3a–d. The solution of Equation (9) correctly shows the morphing transitions of a pure areal doublet (Figure 5a) to a pure areal dipole (Figure 5b).

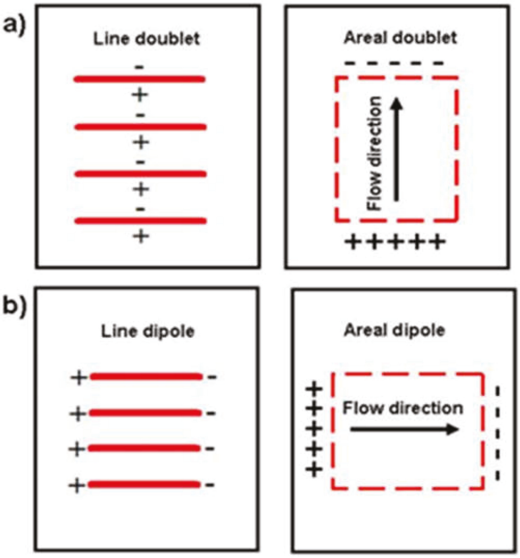

Figure 5. Conceptual models of: (**a**) areal doublet obtained by superposing an infinite number of line doublets; (**b**) areal dipoles obtained by superposing an infinite number of line dipoles. Reproduced with permission from [6].

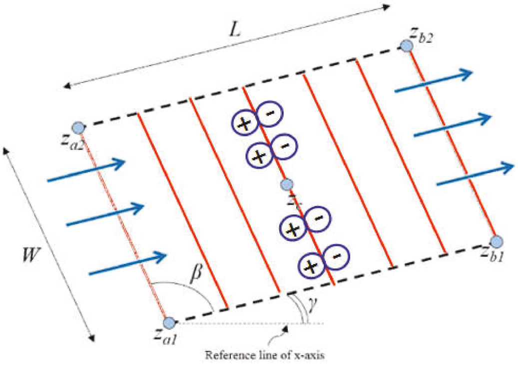

Figure 6. Conceptual model of areal doublet obtained by superposing an infinite number of line doublets. Reproduced with permission from [6]. The angles of tilt angle of γ, corner point angle of β, and polarity angle θ of doublet/dipole singularity in line arrays, located at center z_c, and with width W (m), and length of L (m), and z_{a1}, z_{a2}, z_{a3}, and z_{b2} are the corners of the flow element. The ∞-shaped circulation pattern shows the orientation of the doublet singularities in the line array. Angles are all measured anticlockwise.

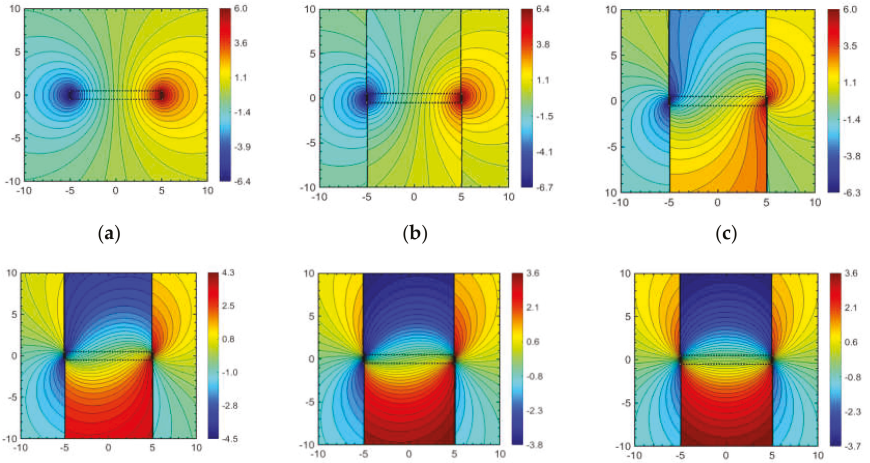

(**a**) (**b**) (**c**)

(**d**) (**e**) (**f**)

Figure 7. Stream function solution and streamlines for line doublet/line dipole of Equation (9), for a range of polarity angles: (**a**) $\theta = 90°$, (**b**) $\theta = 80°$, (**c**) $\theta = 70°$, (**d**) $\theta = 45°$, (**e**) $\theta = 30°$, and (**f**) = $\theta = 10°$, with a tilt angle for the line doublet element $\beta = 90°$. Stream function values (ψ) given by rainbow colors ($m^2 \cdot s^{-1}$) relative to line $y = 0$. Branch cuts appear at the fracture tips. Solved using the imaginary part of Equation (8).

2.3. Branch Cut Effects

Equation (8) correctly solves the streamlines for a generic areal doublet/dipole element and can be used to represent the streamline deflections occurring near high permeability fractures in fractured porous media. The solutions of Figure 8 show the progressive rotation of a fracture element and the stationary far-field flow (superposed on the doublet-dipole flow) by selecting θ such that $\theta + \gamma = 180°$, for a variety of angles γ. The composite complex potential, $\Omega_{Comp}(z,t)$, including the complex potential for the uniform far-field flow, $\Omega_4(z,t) = e^{i\theta}u_\infty(t)z$ (with $u_\infty(t)$ already being the effective velocity, accounting for porosity) is:

$$\Omega_{Comp}(z,t) = \Omega_3(z,t) + \Omega_4(z,t) \tag{10}$$

The streamline solutions given in Figures 7 and 8 are perturbed by the branch cuts emanating from the singularities, which cause "apparent" jumps in the stream function values from positive to negative, and vice versa. For the areal doublet (Figure 5a), the branch cut seems not to occur, but these are present as a row of singularities in the high and low streamline values. The corresponding potential function solutions also exhibit branch cuts jumps, which we discussed in considerable detail in a prior study [6].

The issue we now face is to move the branch cuts for the general solution to a place where they would not render the use of the Equations (8) and (9) impractical. For the pure areal doublet (Figure 5a), we have earlier succeeded to find a practical branch cut placement solution [6]. However, as pointed out by Holzbecher [10], available procedures for removing branch cut effects from analytical solutions remain limited.

In spite of numerous efforts in our present research program to move the branch cuts from the general solutions of Equations (8) and (9) to a practical location, we did not succeed, which meant that we could not apply Equations (8) and (9) in practical situations that required continuous Eulerian particle tracking. The next section discusses an alternative, augmented solution for areal doublet representation of flow deflections by discrete natural fractures of arbitrary orientation, which solves the prior limitation.

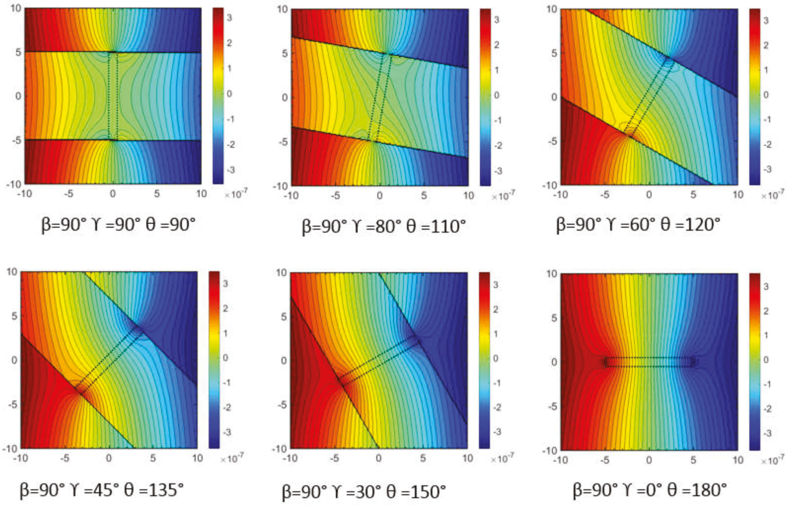

$\beta=90^\circ$ $\Upsilon=90^\circ$ $\theta=90^\circ$ $\beta=90^\circ$ $\Upsilon=80^\circ$ $\theta=110^\circ$ $\beta=90^\circ$ $\Upsilon=60^\circ$ $\theta=120^\circ$

$\beta=90^\circ$ $\Upsilon=45^\circ$ $\theta=135^\circ$ $\beta=90^\circ$ $\Upsilon=30^\circ$ $\theta=150^\circ$ $\beta=90^\circ$ $\Upsilon=0^\circ$ $\theta=180^\circ$

Figure 8. Stream function solutions for the areal doublet/line dipole of Equation (9), based on the integral method.

3. Augmented Solution

A new flow element used to model flow in fractured porous media was generated by the integration of line doublets [5]. The derived flow element was initially termed a natural fracture element [5], but later renamed as an areal doublet [6]. The reason for the re-examination of the earlier approach is that the existing formulation is accurate for fractures aligned with a far-field flow, and works well for fractures oriented moderately obliquely with respect to the far-field flow, but becomes increasingly inaccurate when the fractures are perpendicular to or at a large angle to the far-field flow.

3.1. Shortcomings of the Prior Solution

Figure 9 illustrates the problem arising when the simple area doublet formulation of Equation (5) is used to progressively increase the angle of the natural fracture (represented by a narrow areal doublet) relative to a steady far-field flow. A long and narrow fracture aligned with the far-field flow direction can be modeled accurately with an areal doublet (Figure 9a). However, for the larger incidence angles, the flow solution is no longer accurate. Figure 9f shows the solution for a fracture at a large angle to the far-field. The areal doublet would require reorientation of the polarities in the fracture to align with the far-field flow. If we try to implement such polarity changes using Equation (9), the branch cut effects do not allow continuous particle tracking across the fracture region.

To develop an augmented solution, while avoiding the branch cut effects, we first discuss the two end-members, areal doublet and areal dipoles, in some detail (Sections 3.2 and 3.3) paying specific attention to the orientation of corner point co-ordinates given in Equation (7). Ultimately, the branch cut issues that rendered Equation (9) impractical for use in real world problems were sidestepped by superposing the two end-members of the areal doublet/dipole family of solutions.

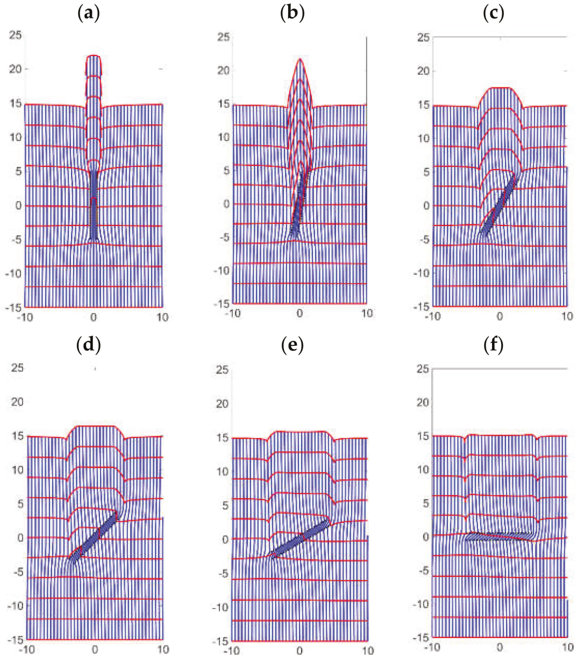

Figure 9. Particle path solutions showing streamlines (blue) and time of flight contours (red) for a range of inclination angles, based on the Eulerian particle path tracking method: (**a**) $\gamma = 90^\circ$, (**b**) $\gamma = 80^\circ$, (**c**) $\gamma = 60^\circ$, (**d**) $\gamma = 45^\circ$, (**e**) $\gamma = 30^\circ$, and (**f**) = $\gamma = 0^\circ$; keeping $\beta = \theta = 90^\circ$. The far-field velocity and the strength of the areal doublet/dipole element (adjusted for a porosity of 0.1) is 3.12×10^{-8} m/s and 3.12×10^{-7} m^2/s respectively.

3.2. Areal Doublet Solution

The stream function solutions of the areal doublet of Equation (5) with the integral method are given in Figure 10a,b for the two extreme orientations of the natural fracture prototype (vertical and horizontal, as in Figure 9a,f), *with a superposed far-field flow*. Figure 10c,d show the areal doublet flow *without the superposed far-field flow*. The solutions given in Figure 10 are possible with Equation (5) while avoiding undue branch cuts by changing the corner point co-ordinates given in Equation (7), according to the respective *L*/*W* pairs of the fracture slots (as indicated in the sketches next to the respective solutions). When applied to Eulerian particle tracking, Equation (5) gives continuous solutions, as illustrated in the example of Figure 9. However, for the larger inclinations of the natural fracture element with respect to the far-field flow direction (e.g., Figure 9e,f) the solutions for the flow paths become unrealistic. The initial repair of the natural fracture algorithm occurred via the steps in Section 2.2. However, the proposed algorithms of Equation (8) resulted in multiple branch cuts, which make the continuous Eulerian tracking of particle movement impossible to use. We investigated numerous avenues to move branch cuts to locations where they would not cause multivalued functions along the particle paths, using our experience of a prior study [6]. All efforts failed, except for one approach via the steps explained in Sections 3.3 and 3.4.

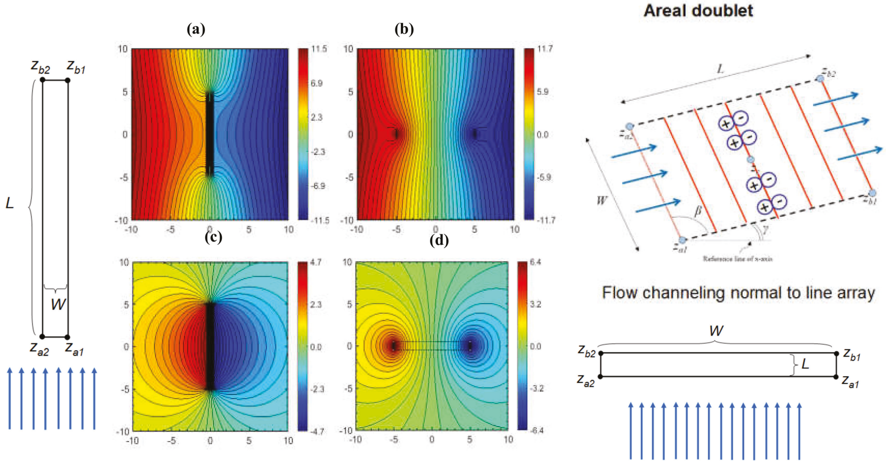

Figure 10. Stream function and streamlines solution for areal doublet representation for vertical and horizontal fracture elements. (**a**) Vertical fracture element, with a far-field flow, and (**c**) without a far-field flow superposed. (**b**) Horizontal fracture element, with a far-field flow, and (**d**) without a far-field flow superposed. Stream function values (ψ) given by rainbow colors ($m^2 \cdot s^{-1}$) relative to line $y = 0$. Solved using Equation (5).

3.3. Areal Dipole Solution

The alternative model for the long fracture aligned with the far-field flow is given by the complex potential for the areal dipole [6]:

$$\Omega_5(z,t) = \frac{iv(t)}{2\pi nHLW}[\Re[A - B + C - D] + i \cdot \Im[A - B + C - D]] \tag{11}$$

Equations (5) and (11) differ in that their real and imaginary axes are switched, which is achieved by multiplying the complex potential of Equation (5) with the imaginary number *i*. The dummy terms $A - D$ remain unchanged and are given by Equations (6a)–(6d). Figure 11a–d are solutions for the areal dipole for the same orientations as in Figure 10a–d, *with and without a superposed far-field flow.* The solutions given in Figure 11 are possible with Equation (11) while avoiding undue branch cuts by changing the corner point co-ordinates given in Equation (7), according to the respective *L/W* pairs of the fracture slots (as indicated in the sketches next to the respective solutions). Although the solutions of Figures 10 and 11 appear the same, the important difference lies in the coordinate transformation, due to which the orientations of the examples shown in each set of Figures are swapped 90°. This is a simple but essential step to correctly model the flow across natural fracture elements at a high angle to the far-field flow (see Section 3.4). The branch-cut effects that impeded continuous particle tracking across the natural fracture element with the solution of Equations (8) and (9) do not occur with the solution enabled by the superposition of Equations (5) and (11), given in Section 3.4.

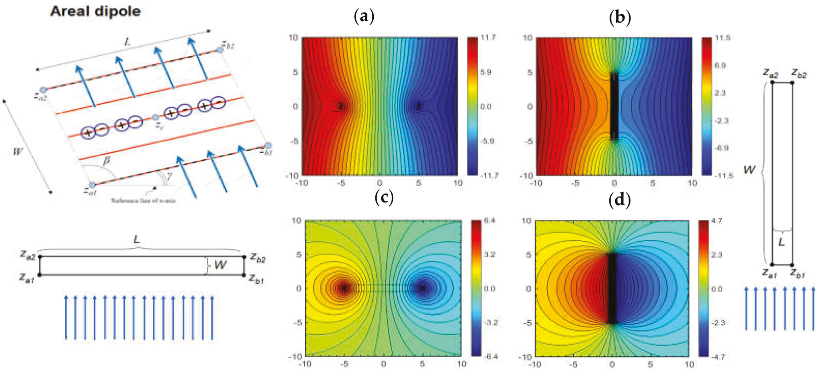

Figure 11. Stream function and streamlines solution for areal dipole of Figure 5c,d. (**a**,**b**) With a far-field flow, and (**c**,**d**) without a far-field flow superposed. Stream function values (ψ) given by rainbow colors ($m^2 \cdot s^{-1}$) relative to line $y = 0$. Solved using Equation (11).

3.4. Superpositions

Changing the corner point co-ordinates according to the respective *L/W* pairs of the fracture slots as applied in Figures 10 and 11 will avoid the occurrence of branch cuts in impractical places, but is not very user-friendly when superposing multiple fracture elements in practical applications. Thus, the velocity fields for two areal doublets are superposed with the velocity field of the far field flow, such that the two end angles (0° and 90°) result in the correct particle-path solutions based on the conceptual model of Figure 12.

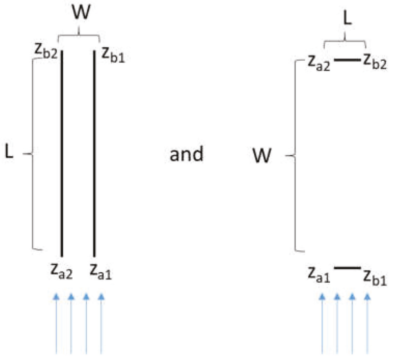

Figure 12. Areal doublet oriented in two extreme directions [parallel (left) and normal (right) to the far-field flow] are combined to generate the superposed augmented solution. When the element is parallel to flow (such as the first set of vertices in the left image), only the vertical element contributes. When the element is normal to the flow (right image), only the horizontal element contributes. For intermediate elements, sine angles are used to "mix" the appropriate "contribution" of each element. For the first case $L = 10$, $W = 1$ and $\theta = 90°$, for the second case $L = 1$ m, $W = 10$ m, and $\theta = 0°$.

For the intermediate cases, where the tilt angle is between the two end angles, the contribution of each element (0° and 90°) is proportioned by using the *sine* function. The vertical solution has a more dominant effect when the natural fractures oriented at an angle lower than 45° (more parallel to the fluid flow) and vice versa. The superposed complex potential (with the augmented solution in the second term on the right-hand side) is:

$$\Omega(z) = \Omega_f(z) + \sum_{n=1}^{2} (-1)^{n+1} \sin \gamma_n \cdot \Omega_n(z) \tag{12}$$

$\Omega_f(z)$ is complex potential for the far-field flow given by:

$$\Omega_f(z) = u_\infty(t) z \tag{13}$$

$\Omega_n(z)$ is the complex potential for the areal doublet/dipole element given by:

$$\begin{aligned} \Omega_n(z) = {} & \frac{-v(t)}{2\pi h n \cdot L_n \cdot W_n} \cdot e^{-i(\gamma-\theta_n)} \cdot [(z+z_{a2n})(\log(-e^{-i\gamma}(z-z_{a2n})) - (z+z_{a1n})(\log(-e^{-i\gamma}(z-z_{a1n})) \\ & +(z+z_{b1n})(\log(-e^{-i\gamma}(z-z_{b1n})) - (z+z_{b2n})(\log(-e^{-i\gamma}(z-z_{b2n}))] \end{aligned} \tag{14}$$

The vertices z_{a1n}, z_{a2n}, z_{b1n}, and z_{b2n} are the vertices for the areal doublet/dipole element given by:

$$\begin{aligned} z_{a1n} &= z_c - \mathrm{e}^{i\gamma} \cdot (0.5L_n + 0.5W_n \cdot e^{i\beta}) \\ z_{a2n} &= z_c - \mathrm{e}^{i\gamma} \cdot (0.5L_n - 0.5W_n \cdot e^{i\beta}) \\ z_{b1n} &= z_c - \mathrm{e}^{i\gamma} \cdot (-0.5L_n + 0.5W_n \cdot e^{i\beta}) \\ z_{b2n} &= z_c - \mathrm{e}^{i\gamma} \cdot (-0.5L_n - 0.5W_n \cdot e^{i\beta}) \end{aligned} \tag{15}$$

The transformations and inputs needed to calculate the vertices given in Equation (15) are given below:

$$\begin{aligned} \theta_1 &= (\pi/2) \\ \theta_2 &= -\theta_1 \\ \gamma_2 &= \gamma_1 - (\pi/2) \\ L_2 &= W_1 \\ W_2 &= L_1 \end{aligned} \tag{16}$$

Figure 13 shows the particle path across a single, highly conductive fracture at different orientations with respect to a far-field flow incoming from below generated by using the velocity potential derived from Equation (12). The length (L_1) and the width (W_1) were assumed to be 10 m and 1 m respectively. The results in Figure 13 show more plausible flow paths compared to the results in Figure 9 for the cases where the fracture is tilted at an angle of more than 45° with respect to the direction of the far-field flow.

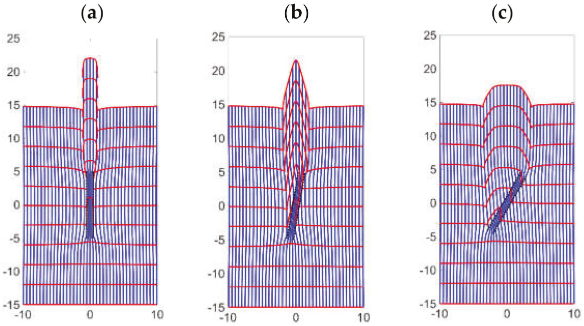

Figure 13. *Cont.*

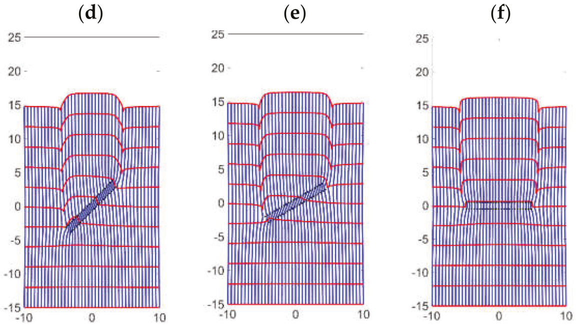

Figure 13. Particle path solutions showing streamlines (blue) and time of flight contours (red) for the line doublet/line dipole of Equation (12), for a range of inclination angles, based on the Eulerian particle path tracking method: (**a**) $\gamma = 90°$, (**b**) $\gamma = 80°$, (**c**) $\gamma = 60°$, (**d**) $\gamma = 45°$, (**e**) $\gamma = 30°$, and (**f**) $\gamma = 0°$. The length and the width of the areal doublet/dipole element are 10 m and 1 m respectively. The far-field velocity and the strength of the areal doublet/dipole element adjusted for a porosity of 0.1 is 3.12×10^{-8} m/s and 3.12×10^{-7} m^2/s respectively.

4. Application

In this section, the augmented solution for flow across discrete fractures will be applied to a practical situation. Natural fractures may have a significant impact on the performance and flow of hydraulically fractured wells tapping into hydrocarbon reservoirs [11]. The interaction of hydraulic and natural fractures makes forecasting the performance of wells in such reservoirs a major challenge [12,13]. Alternatively, conductive natural fractures may promote pressure communication between the adjoining hydraulic fractures and wells, which increase the well/fracture interference [14]. The nonconductive natural fractures may affect the sweep pattern due to waterflood between the injector and the producer wells [15]. Hence, the estimation of a reservoir's flow performance and overall production depends on accurate description of the flow diversion due to the presence of natural fractures and natural fracture networks. Section 4.1 provides a brief background on different modeling methods for naturally fractured reservoirs.

Natural fractures distort the drained rock volume (DRV) around hydraulic fractures and may result in pressure communication with fractures of the adjoining stages and wells. The DRV is defined as the reservoir volume that contributes to oil and gas production through the movement of fluid particles to the wellbore after a particular specified production period. Although there is movement of fluid particles throughout the reservoir, only a limited fraction of those particles reaches the wellbore in a reasonable time period, which is shown by the DRV. Unusual refractions of streamlines near the well system occurred in our prior model code (compare Figures 9f and 13f) when natural fractures were oriented at a high angle to the far-field flow direction. We revisit the examples presented in an earlier study (in Section 4.2), where the effect of natural fractures on the DRV was investigated by using the algorithm presented in Equation (5) [16]. In Section 4.3, the DRV is regenerated using the modified solution of Equation (12). Finally, in Section 4.4, we compare results obtained earlier [16] with the results from the modified algorithm presented in this paper. The DRV for the reservoirs where natural fractures are oriented in the direction of flow remains unchanged. However, the DRV for the reservoirs where the natural fractures are oriented at a high angle to the far-field flow direction show a drastic change. A brief validation of the augmented solution is given in Section 4.5.

4.1. Flow in Fractured Reservoirs

Oil and gas reservoirs may contain vast networks of natural fractures, which interact with the hydraulic fractures, and therefore the most accurate flow simulation and production forecasting models must strive to account for the impact of natural fractures, based on their orientation, distribution, connectivity, strength and interaction with the hydraulic fractures [17,18]. Previously, naturally fractured reservoirs were mainly modeled by using dual porosity and modifications of the dual porosity model [19,20]. These models consider natural fractures as a secondary continuum with up-scaled flow properties, but have limited accuracy, and cannot be used to model discrete fracture networks [21]. Another widely used technique uses discrete fracture network (DFN) models [22] and embedded discrete fracture network models (EDFM) [23]. Such discrete models have some benefits over dual porosity models, such as flexibility and give more accurate representations of the fracture network, but they are computationally very demanding and expensive for complex reservoirs with numerous natural fractures. Both the continuum model (dual porosity) and the discrete model (DFN, EDFM) have been thoroughly reviewed in our prior study [16].

Hence, there is a need for new fast and gridless methods (such as the one presented in this study), which allow for efficient modeling of fluid flow in naturally fractured reservoirs. The present study builds forward on the earlier studies where closed-form analytical solutions based on complex analysis methods (CAM) were applied to single-phase flow reservoirs, assuming either hydraulic fractures only [24] or hydraulic fractures intersecting with natural fractures [6]. The natural fracture algorithms have been used in fundamental studies of the equivalent tensor concept [25]. An advantage of CAM models over numerical models is the ability to visualize the drained rock volume (DRV) with infinite resolution.

Unlike discretized numerical simulators, the CAM simulator offers enhanced visual resolution of the DRV around the hydraulic and natural fractures. Flow visualization at high resolution can be especially important to optimize fracture and well spacing in already crowded shale fields with several horizontal wells and hydraulic fractures. The prior studies [24,25] used an algorithm developed earlier [5], which works well when the natural fractures are oriented in the direction of the fluid flow. However, the algorithm needs to be modified when the natural fractures occur at larger angles to the direction of the fluid flow, as illustrated in the following section.

4.2. Field Application: Flow Near Hydraulic Fractures

In this section, we revisit some results of our previous study [16], which presented an extensive collection of results where natural fractures of varying orientations were introduced to a base case (Figure 14), and were simulated using Equation (5).

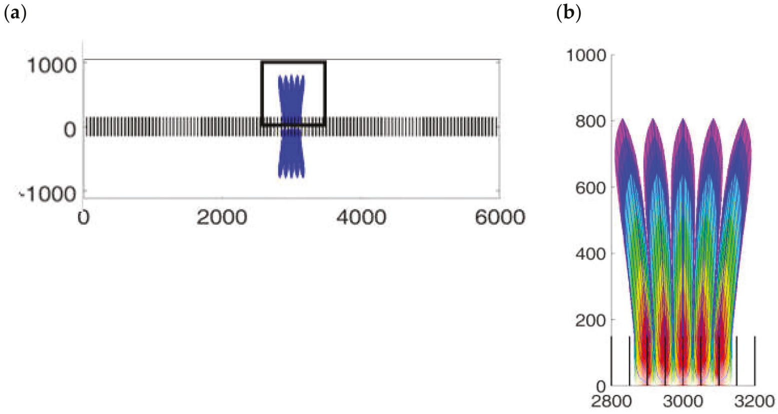

Figure 14. (**a**). Top view of the full-scale model (horizontal map view) of a well with 119 transverse hydraulic fractures with a fracture half-length of 150 ft (45.7 m). Each hydraulic fracture is assumed to be identical and producing at a constant rate of 13.6 ft^3/day (0.39 m^3/day) for 30 years. (**b**). Time of flight contours, represented by the rainbow colors, showing the drainage at each three-year interval of around five hydraulic fractures in the central portion of the well. Reproduced with permission from [16].

Figure 14a shows the streamlines (blue color) for a full-scale model of a hydraulically fractured well. The particle paths are generated only for the middle five hydraulic fractures for computational efficiency. However, the flow toward all the hydraulic fractures in the complex plane (119 fractures) is accounted for in the model simulation and were simulated for a period of 30 years. The identical hydraulic fractures, each of which has a fracture half-length of 150 ft (45.7 m) and height of 60 ft (18.3 m), are assumed to have a constant flux of 13.6 ft^3/day (0.39 m^3/day) per fracture, which is equivalent to the hydraulic fracture (line sink) strength of 8.47 ft^2/day (0.79 m^2/day). The rainbow colors in Figure 14b show the time of flight contours (TOFC), where each different color represents the DRV expansion for three-year increments from five hydraulic fractures (one stage) in the center of the well.

When natural fractures are present in the reservoir, the DRV shape around the hydraulic fractures will be progressively distorted when natural fractures (oriented oblique—at 45°—to the horizontal well) occur in the proximity of the hydraulic fractures. The permeability contrast between the matrix and the fractures is increasing from the left to the right (Table 2). Figure 15c,d shows the DRV distortion due to highly conductive natural fractures oriented at a high angle with respect to the far-field flow (10°) to the horizontal well). The natural fracture permeability contrast with the matrix (and corresponding strengths) and other properties for each of the cases are presented in Table 2. The DRV, for each case (Figure 15a–d), is distorted. However, where natural fractures have steep angles with respect to the far-field flow, the resulting sideward deflection of the particle paths appeared physically unrealistic (Figure 15c,d). As shown earlier (in Figure 9), the application of Equation (5) leads to such unrealistic particle paths for steep natural fractures. For higher angles to the far-field flow direction, the results of Figure 15c,d present an improved solution (Section 4.3).

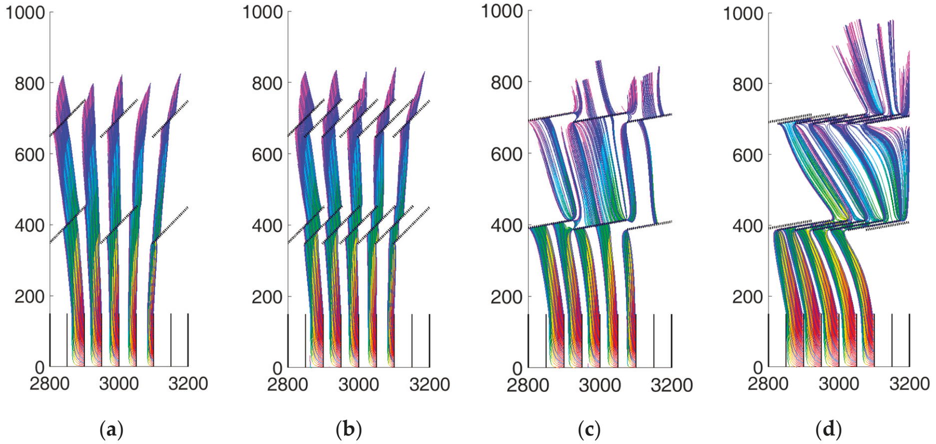

(**a**) (**b**) (**c**) (**d**)

Figure 15. Top view of central five hydraulic fractures for central stage in the well of Figure 14a, with DRV distortion due to (**a**) six nearby natural fractures, with a strength of 6×10^3 ft^4/day (51.8 m^4/day) each, at an angle of 45°. (**b**) As (**a**), but with 14 natural fractures. (**c**) Six natural fractures, with a strength of 60×10^3 ft^4/day (518 m^4/day) each, at an angle of 10°. (**d**) As (**c**), but with 14 natural fractures. Time of flight contours (multicolored) show the drainage at each three-year interval. Reproduced with permission from [8].

4.3. Augmented Solution for Flow Near Hydraulic Fractures with Natural Fractures

Next, we implement the augmented solution of Equation (12) and rerun the results, aimed at removing any unrealistic particle paths seen in Figure 15. Figure 16a–d shows the DRV generated from the augmented solutions corresponding to the cases shown in Figure 15a–d. Comparison of the DRVs for the first two cases (Figure 15a,b and Figure 16a,b) show minimal effect due to the change in algorithms because the natural fractures are oriented at a moderate angle of 45° to the direction of the particle paths. However, the DRV distortion intensifies for highly conductive natural fractures oriented at a large angle to the far-field flow direction (Figure 15c,d), as can be calculated from the augmented equation (Equation (12)).

Table 2. Input summary for reservoir and natural fractures simulated in Figures 14 and 15. Modified from [8].

Attributes of Reservoir and Hydraulic Fractures	
Reservoir height	60 ft (18.3 m)
Porosity	4.4%
Hydraulic fracture half-length	150 ft (45.7 m)
Residual oil saturation	0.25
Initial Strength (m_0)	8.47 ft^2/day (0.79 m^2/day)
Formation volume factor (B)	1.05 RB/STB

Attributes of Areal Doublets (Natural Fractures)

Figure	Length	Width	Height (ft)	No. of natural fractures	Orientation (with respect to wellbore)	Strength (ft^4/day)	Permeability Contrast Ratio
15a	150 ft (45.7 m)	3 ft (0.91 m)	60 ft (18.3 m)	6	45°	6×10^3 ft^4/day 51.8 m^4/day	7.87
15b	150 ft (45.7 m)	3 ft (0.91 m)	60 ft (18.3 m)	14	45°	6×10^3 ft^4/day 51.8 m^4/day	7.87
15c	150 ft (45.7 m)	3 ft (0.91 m)	60 ft (18.3 m)	6	10°	60×10^3 ft^4/day 518 m^4/day	78.68
15d	150 ft (45.7 m)	3 ft (0.91 m)	60 ft (18.3 m)	14	10°	60×10^3 ft^4/day 51.8 m^4/day	78.68

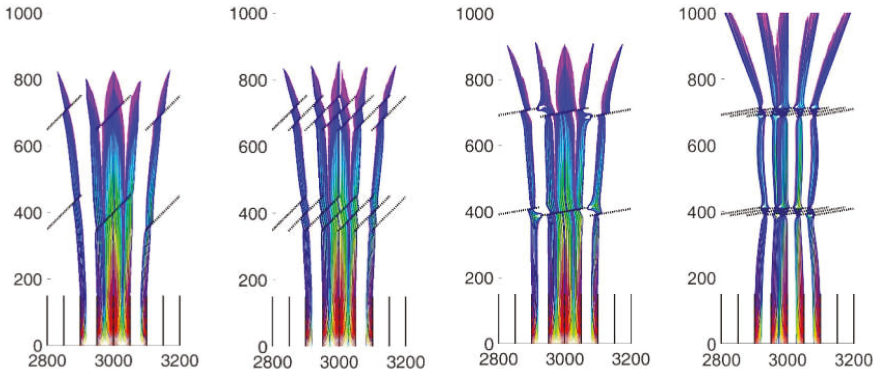

Figure 16. Same as Figure 15a–d, but generated with the augmented solution of Equations (12)–(18).

4.4. Comparison of Results Augmented and Earlier Solution

The DRV shapes of Figure 15c,d and Figure 16c,d differ significantly. The extreme deflection of particle paths seen in Figure 15c,d does not occur in Figure 16c,d, due to the application of the augmented code based on Equation (12). The extent of the fluid plume drained from the reservoir reaches farther into the reservoir (up to 1000 ft or 305 m, with natural fractures) for all cases (even after the application of the augmented solution), as compared to only 800 ft (244 m) in a reservoir without natural fractures (Figure 14b) or with few natural fractures oriented at moderate angles to the far-field flow (Figure 15a,b and Figure 16a,b).

4.5. Verification

Finally, the augmented solution is verified here in a straightforward experiment, which compares the prior solution of Equation (5) with the augmented solution of Equation (12). Consider a square domain with a higher permeability than the ambient matrix. The flow through the domain can be simulated by superposing an areal doublet of a certain strength on the far-field flow (Table 3), similar to what is shown in Figure 1b. The left column in Figure 17 gives the prior solution for three angles using Equation (5). The right column gives the flow behavior according to the augmented solution. The left bottom image in Figure 17 shows the problem arising when the prior solution is at a large angle with respect to the far-field flow: fluid appears to be deflected in a horizontal direction, which is physically unrealistic. The problem does not occur for the 90° rotated square [bottom right; using Equation (12)], which shows the same flow behavior as for the topmost right image, henceforth the solution for the large incidence angle may be assumed to be correct.

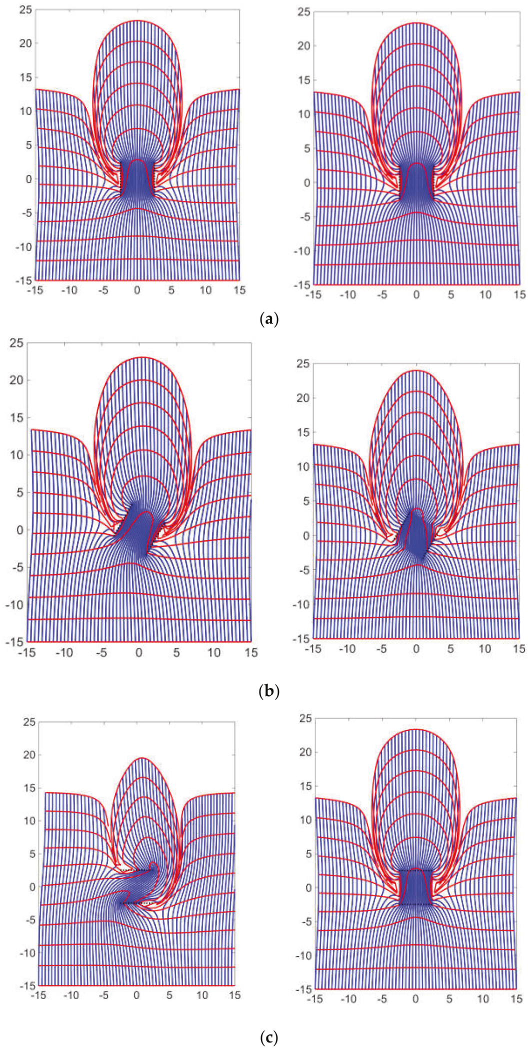

Figure 17. Particle path solutions showing streamlines (blue) and time of flight contours (red) for the line doublet/line dipole of Equation (5) (left column) and Equation (12) (right column), for a range of inclination angles, based on the Eulerian particle path tracking method: (**a**) $\gamma = 90°$, (**b**) $\gamma = 60°$, (**c**) $\gamma = 0°$. The length and width of the areal doublet/dipole elements are 5 m × 5 m, respectively. The far-field velocity and the strength of the areal doublet/dipole element adjusted for a porosity of 0.1 are 3.12×10^{-8} m/s and 2.97×10^{-6} m^2/s, respectively.

Table 3. Natural fracture attributes for fractures oriented at different angles.

Natural Fracture Attributes	Symbol	Value
Natural fracture width (m)	W	5
Natural fracture length (m)	L	5
Natural fracture height (m)	H	1
Natural fracture angle to far-field flow	α	(a) 90° (b) 60° (c) 0°
Porosity	n	0.1
Effective far-field flow rate (m/s)	u_x/n	3.12×10^{-8}
Effective natural fracture strength (m^4/s)	υ/n	2.97×10^{-6}

5. Discussion

The areal doublet is an analytical element formed by superposing an infinite number of line doublets. The mathematical function can be used to model the physical flow of fluids in highly conductive, narrow flow-channels such as natural fractures [5,6]. The areal doublet locally accelerates the flow of fluids due to the enhanced permeability contrast with the matrix and can be superposed with other flow elements such as nearby hydraulic fractures to model the fluid withdrawal patterns (drained rock volume—DRV) in hydraulically fractured hydrocarbon and geothermal reservoirs [8,23]. The work presented here provides a modification of the algorithm for an areal doublet, which corrects the high deviation of streamlines, when the areal doublet is not parallel to the direction of the fluid flow. The original equation (Equation (5)) results in the same solution as the augmented algorithm (Equation (12)) when the flow direction is parallel to the natural fractures as shown by Figures 9a and 13a. However, the DRV becomes progressively unrealistic when the inclination of the areal doublet increases with respect to the far-field flow (Figure 9b–f). The augmented algorithm superposes two doublet solutions with different vertices based on the tilt angle to generate realistic results for doublets oriented at any angle with respect to the far-field flow. The superposition was needed to avoid the occurrence of branch cuts in inconvenient locations, while still providing corrections to the prior solution. Some key observations from the current study are briefly discussed below.

5.1. Effect of Permeability Contrast

The augmented solution corrects the high deviation of streamlines that occurs when the natural fractures are not oriented parallel to the direction of the flow. The augmented solution has a significant impact on results when the permeability contrast is high, as shown by the comparisons of Figures 15 and 16. The permeability contrast for Figure 15c,d is 10 times higher than the permeability contrast of Figure 15a,b (Table 2). The augmented solution (Figure 16a–d), shows that the DRV reaches slightly further into the reservoir than before (Figure 15a,d), which may increase interference between adjoining wells. The high permeability contrast with the matrix results in larger distortion of the DRV and the impact increases when natural fractures occur at oblique angles with respect to the far-field flow. The DRV is significantly shifted from the original location, whereas the effect of natural fractures that are either parallel or perpendicular to the far-field flow is much more muted. The orientation of the natural fractures, the permeability contrast of the individual natural fractures with the matrix rock, and the natural fracture density, will control the final shape of the DRV.

5.2. Model Strengths and Weaknesses

Discrete finite volume methods are widely used to model flow in porous media. Models based on CAM have several strengths, which overcome some of the drawbacks of grid-based methods. The most significant strength of the CAM method is the high resolution, which allows for a closer examination of flow patterns near tightly spaced hydraulic fractures. Another benefit is the high computational speed due to the avoidance of arduous gridding thanks to the closed-form formulation of algorithms. Models based on CAM have been validated with commercial numerical reservoir simulators to verify the accuracy of the results [25,26]. CAM studies allow differentiation between the tracer front (calculated from the outer boundary of the DRV) and pressure front (calculated from the diffusivity equation) [27,28]. Previously, it was assumed that the pressure front marks the drainage boundary around a horizontal well and a hydraulic fracture, but the results from the CAM model showed that pressure front highly exaggerates the actual DRV.

As with any new technology, CAM has some limitations and drawbacks. Current modeling is only limited to 2D single-phase flow. Although, some efforts have been made to expand the model to 3D [23], the additional complexity results in loss of computational efficiency.

6. Conclusions

A modification to an algorithm developed in earlier studies [5,6] is presented to account for the unusual deviation of the streamlines when natural fractures (represented by the areal doublets) are oriented at large angles with respect to the direction of a far-field flow. The algorithm presented earlier [5] had been validated by using an independent numerical simulator when the flow direction is parallel to the areal doublets or at a moderate angle [25,26].

Our earlier paper [6] was concerned with the evasion of branch cuts such that the flow across natural fractures could still be modeled by continuous Eulerian particle tracking, avoiding discontinuities by smart placement of the branch cuts. In the present paper, the solution of the previous paper [6] was augmented in several steps. We first derived Equation (8), which can give the correct instantaneous streamline solutions by the integral method, but not by the Eulerian particle tracking method. Solutions for the Eulerian method are needed because it allows (1) particle path solutions for both steady and time-dependent flows, and (2) time-of-flight contouring for fluid withdrawal studies of hydrocarbon resources. Subsequently, several additional steps resulted in the augmented solution of Equation (12), which sidesteps the branch cut issues and can be used with both the integral method for instantaneous streamline solutions and with the Eulerian particle tracking method. The augmented solution is an important achievement, because it can accurately model the flow paths across discrete natural fractures, regardless of their orientation with respect to the far-field flow. The prior solution in the earlier branch cut solution paper [6] would become progressively inaccurate for high-incidence angles of the far-field flow to the natural fractures.

The current augmented solution was validated by rotating a rectangular region into different alignment directions with the far-field flow direction (Section 4.5). Based on the results in the current study, the following conclusions can be drawn:

a. Areal dipole/doublet solutions suffer from branch cuts due to the multivalued nature of the algorithm. The branch cuts can be manually removed, but the procedure is cumbersome [6,10].
b. Areal doublets can be used to model the flow in high conductivity flow channels such as the natural fractures in porous media. The natural fractures (areal doublets) distort the DRV and locally increase the velocity while modeling the flow in porous media (Figure 16).
c. The modified areal doublet algorithm in Equation (12) yields a more realistic result for fractures oriented at a high angle with respect to the direction of fluid flow (Figure 16d).
d. The augmented solution in the present study avoids the branch cuts and therefore provides an efficient method to model the flow paths of fluids in naturally fractured porous media.

Author Contributions: Conceptualization, R.W.; Methodology, R.W. and A.K.; Investigation, R.W. and A.K.; writing—original draft preparation, R.W. and A.K.; review and editing, R.W.; supervision, R.W. All authors have read and agreed to the published version of the manuscript.

Funding: This project was sponsored by funds of the senior author (R.W.) from the Texas A&M Engineering Experiment Station (TEES) and funds from the Crisman Institute at the Harold Vance Department of Petroleum Engineering at Texas A&M University.

Conflicts of Interest: The authors declare no conflict of interest.

References

1. Karimi-Fard, M.; Durlofsky, L.J.; Aziz, K. An efficient discrete-fracture model applicable for general-purpose reservoir simulators. *Soc. Pet. Eng.* **2004**. [CrossRef]
2. Moridis, G.J.; Blasingame, T.A.; Freeman, C.M. Analysis of mechanisms of flow in fractured tight-gas and shale-gas reservoirs. In Proceedings of the SPE Latin American and Caribbean Petroleum Engineering Conference, Lima, Peru, 1–3 December 2010. [CrossRef]
3. Olorode, O.; Freeman, C.M.; Moridis, G.; Blasingame, T.A. High-resolution numerical modeling of complex and irregular fracture patterns in shale-gas reservoirs and tight gas reservoirs. *SPE Reserv. Eval. Eng.* **2013**, *16*. [CrossRef]
4. Sun, J.; Hu, K.; Wong, J.; Hall, B.; Schechter, D. Investigating the effect of improved fracture conductivity on production performance of hydraulic fractured wells through field case studies and numerical simulations. *Soc. Pet. Eng.* **2014**. [CrossRef]
5. Van Harmelen, A.; Weijermars, R. Complex analytical solutions for flow in hydraulically fractured hydrocarbon reservoirs with and without natural fractures. *Appl. Math. Model.* **2018**, *56*, 137–157. [CrossRef]
6. Khanal, A.; Weijermars, R. Modeling flow and pressure fields in porous media with high conductivity flow channels and smart placement of branch cuts for variant and invariant complex potentials. *Fluids* **2019**, *4*, 154. [CrossRef]
7. Weijermars, R.; van Harmelen, A.; Zuo, L. Controlling flood displacement fronts using a parallel analytical streamline simulator. *J. Pet. Sci. Eng.* **2016**, *139*, 23–42. [CrossRef]
8. Strack, O.D.L. *Groundwater Mechanics*; Prentice-Hall: Englewood Cliffs, NJ, USA, 1989.
9. Weijermars, R.; van Harmelen, A. Breakdown of doublet re-circulation and direct line drives by far-field flow: Implications for geothermal and hydrocarbon well placement. *Geophys. J. Int.* **2016**, *206*, 19–47. [CrossRef]
10. Holzbecher, E. Streamline visualization of potential flow with branch cuts, with applications to groundwater. *J. Flow Vis. Image Process.* **2018**, *25*, 119–144. [CrossRef]
11. Walton, I.; Mclennan, J. The role of natural fractures in shale gas production. *Eff. Sustain. Hydraul. Fract.* **2013**, 327–356. [CrossRef]
12. Aguilera, R. Effect of fracture compressibility on gas-in-place calculations of stress-sensitive naturally fractured reservoirs. *SPE Reserv. Eval. Eng.* **2008**, *11*, 307–310. [CrossRef]
13. Kolawole, O.; Ispas, I. Interaction between hydraulic fractures and natural fractures: Current status and prospective directions. *J. Petrol. Explor Prod. Technol.* **2019**. [CrossRef]
14. Yang, X.; Yu, W.; Wu, K.; Weijermars, R. Assessment of production interference level due to fracture hits using diagnostic charts. *Soc. Pet. Eng.* **2020**. [CrossRef]
15. Weijermars, R.; Van Harmelen, A. Advancement of sweep zones in waterflooding: Conceptual insight and flow visualizations of oil-withdrawal contours and waterflood time-of-flight contours using complex potentials. *J. Pet. Explor. Prod. Technol.* **2017**, *7*, 785–812. [CrossRef]
16. Khanal, A.; Weijermars, R. Visualization of drained rock volume (DRV) in hydraulically fractured reservoirs with and without natural fractures using complex analysis methods (CAMs). *Pet. Sci.* **2019**, *16*, 550–577. [CrossRef]
17. Olson, J.E. Multi-fracture propagation modeling: Applications to hydraulic fracturing in shales and tight gas sands. In Proceedings of the the 42nd U.S. Rock Mechanics Symposium (USRMS), San Francisco, CA, USA, 1 January 2008.
18. Cipolla, C.L.; Lewis, R.E.; Maxwell, S.C.; Mack, M.G. Appraising unconventional resource plays: Separating reservoir quality from completion effectiveness. In Proceedings of the International Petroleum Technology Conference, Bangkok, Thailand, 1 January 2011. [CrossRef]
19. Warren, J.E.; Root, P.J. The behavior of naturally fractured reservoirs. *Soc. Pet. Eng. J.* **1963**, *3*, 245–255. [CrossRef]
20. Kazemi, H.; Merrill, L.S., Jr.; Porterfield, K.L.; Zeman, P.R. Numerical simulation of water-oil flow in naturally fractured reservoirs. *SPE J.* **1976**, *6*, 317–326. [CrossRef]
21. March, R.; Elder, H.; Doster, F.; Geiger, S. Accurate dual-porosity modeling of co2 storage in fractured reservoirs. In Proceedings of the 2017 SPE Reservoir Simulation Conference, Montgomery, TX, USA, 20–22 February 2017. [CrossRef]

22. Geiger, S.; Matthai, S.K.; Niessner, J.; Helmig, R. Black-oil simulations for three-component, three-phase flow in fractured porous media. *SPE J.* **2009**. [CrossRef]
23. Moinfar, A.; Varavei, A.; Sepehrnoori, K.; Johns, R.T. Development of an efficient embedded discrete fracture model for 3D compositional reservoir simulation in fractured reservoirs. *SPE J.* **2014**, *19*, 289–303. [CrossRef]
24. Parsegov, S.G.; Nandlal, K.; Schechter, D.S.; Weijermars, R. Physics-driven optimization of drained rock volume for multistage fracturing: Field example from the Wolfcamp formation, Midland Basin. In Proceedings of the Unconventional Resources Technology Conference, Houston, TX, USA, 23–25 July 2018. [CrossRef]
25. Weijermars, R.; Khanal, A. High-resolution streamline models of flow in fractured porous media using discrete fractures: Implications for upscaling of permeability anisotropy. *Earth-Sci. Rev.* **2019**, *194*, 399–448. [CrossRef]
26. Weijermars, R.; Khanal, A.; Zuo, L. Fast models of hydrocarbon migration paths and pressure depletion based on complex analysis methods (CAM): Mini-review and verification. *Fluids* **2020**, *5*, 7. [CrossRef]
27. Zuo, L.; Weijermars, R. Rules for flight paths and time of flight for flows in heterogeneous isotropic and anisotropic porous media. *Geofluids* **2017**, *2017*, 5609571. [CrossRef]
28. Weijermars, R. Improving well productivity—Ways to reduce the lag between the diffusive and convective time of flight in shale wells. *J. Pet. Sci. Eng.* **2020**, in press.

fluids

Article

Modeling of Sedimentation and Creaming in Suspensions and Pickering Emulsions

Rajinder Pal

Department of Chemical Engineering, University of Waterloo, Waterloo, ON N2L 3G1, Canada;
rpal@uwaterloo.ca; Tel.: +1-519-888-4567 (ext. 32985)

Received: 20 September 2019; Accepted: 18 October 2019; Published: 22 October 2019

Abstract: Suspensions and emulsions are prone to kinetic instabilities of sedimentation and creaming, wherein the suspended particles and droplets fall or rise through a matrix fluid. It is important to understand and quantify sedimentation and creaming in such dispersed systems as they affect the shelf-life of products manufactured in the form of suspensions and emulsions. In this article, the unhindered and hindered settling/creaming behaviors of conventional emulsions and suspensions are first reviewed briefly. The available experimental data on settling/creaming of concentrated emulsions and suspensions are interpreted in terms of the drift flux theory. Modeling and simulation of nanoparticle-stabilized Pickering emulsions are carried out next. The presence of nanoparticles at the oil/water interface has a strong influence on the creaming/sedimentation behaviors of single droplets and swarm of droplets. Simulation results clearly demonstrate the strong influence of three-phase contact angle of nanoparticles present at the oil/water interface. This is the first definitive study dealing with modeling and simulation of unhindered and hindered creaming and sedimentation behaviors of nanoparticle-stabilized Pickering emulsions.

Keywords: Pickering; emulsion; suspension; droplet; nanoparticles; creaming; sedimentation; drift flux; Stokes law; contact angle

1. Introduction

Emulsions and suspensions form a large group of materials of industrial importance [1]. In suspensions, the dispersed phase consists of fine insoluble solid particles whereas in emulsions the dispersed phase consists of fine immiscible liquid droplets. In conventional emulsions, the dispersed droplets are stabilized against coalescence by the presence of surfactant at the oil-water interface. Pickering emulsions are a special class of emulsions where the dispersed droplets are stabilized against coalescence by solid nanoparticles which accumulate at the oil-water interface and provide steric barrier against intimate contact and coalescence between approaching droplets [2–11]. Thus Pickering emulsions are surfactant-free (see Figure 1). As Pickering emulsions are free of surfactants, they can replace conventional emulsions in household and personal care products where surfactants are known to exhibit adverse effects such as skin and eye irritation [5,12]. Due to outstanding properties of Pickering emulsions, there has been a rapid growth of interest in such systems recently [2–35]. In interfacial catalysis, the solid nanoparticles placed at the oil-water interface can be used to serve the dual purpose of catalyst and emulsion stabilizer [22–26]. Furthermore, chemical reactions can be carried out simultaneously in both aqueous and non-aqueous phases by placing solid catalyst nanoparticles at the oil-water interface [22–26]. Figure 2 shows a cryo-SEM image of an aqueous droplet of Pickering emulsion covered with silica nanoparticles [35]. The cryo-SEM image shows that the silica nanoparticles present at the interface are closely packed and they form a shell on the droplet.

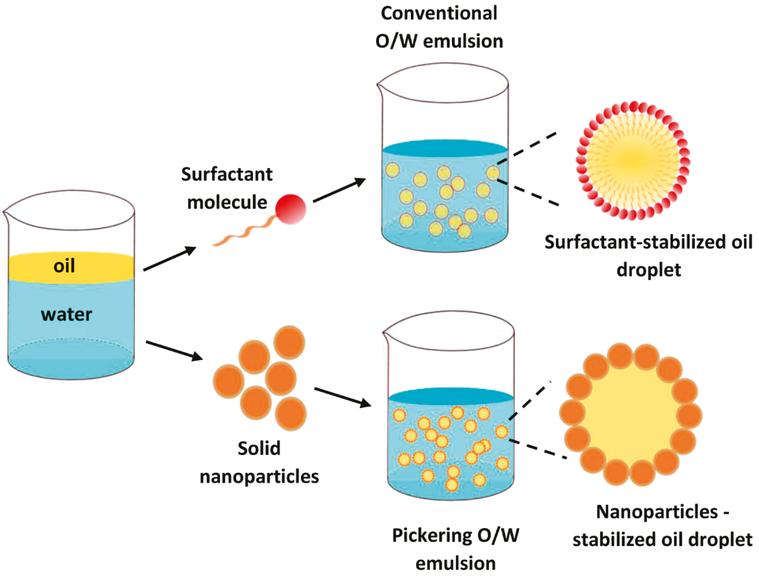

Figure 1. Schematic representation of conventional surfactant-stabilized and Pickering nanoparticle-stabilized oil-in-water (O/W) emulsions (Adapted with permission from [11]).

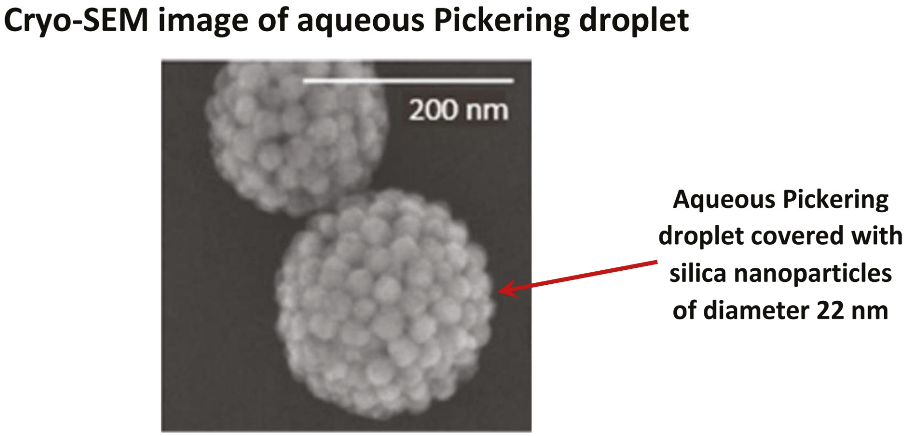

Figure 2. A cryo-scanning electron microscopy (cryo-SEM) image of droplet of W/O Pickering emulsion (Adapted with permission from [35]).

For nanoparticles to adsorb at the oil-water interface, it is necessary that the nanoparticles are partially wetted by both water and oil phases. Thus three-phase contact angle of nanoparticles is important [2–10]. If the contact angle measured through the aqueous phase is less than 90°, the nanoparticles are preferentially wetted by the aqueous phase. In such situations, oil-in-water (O/W) type of emulsions are favored. When the contact angle is greater than 90°, the nanoparticles are relatively more wetted by the oil phase [10]. In such situations, water-in-oil (W/O) emulsions are favored. A large variety of nanoparticles, inorganic and organic, exhibit partial wetting characteristics [3–8,18] and hence are suitable for stabilization of emulsions.

Sedimentation and creaming, wherein particles or droplets fall or rise through a fluid in which they are suspended under the influence of gravity, is a common occurrence in suspensions and emulsions [36,37]. Sedimentation and creaming are usually undesirable as they affect the shelf-life of the product. According to some estimates [37], nearly 40% of the cost of developing a new food emulsion product is incurred in testing of the shelf-life. Creaming and sedimentation are kinetic instabilities that not only affect the uniformity (uniform distribution of droplets) of the product, they are also precursors to thermodynamic instabilities [38]. For example, a creamed oil-in-water emulsion consisting of a concentrated layer of oil droplets at the top of the sample tends to coalesce (thermodynamic instability) faster due to close proximity of oil droplets in the creamed layer. Thus a good understanding of the sedimentation and creaming behaviors of emulsions and suspensions is important in the formulation, handling, processing, and storage of such dispersed systems.

The objectives of this work are as follows: (a) to briefly review the unhindered and hindered settling/creaming behaviors of conventional emulsions and suspensions; (b) to interpret the existing hindered settling/creaming experimental data on conventional emulsions and suspensions in terms of the drift flux theory; (c) to develop a new model for unhindered and hindered settling/creaming of nanoparticle-stabilized Pickering emulsions; and (d) to simulate the settling/creaming behavior of Pickering emulsions using the proposed model.

2. Theoretical Background

2.1. Settling of a Single Rigid Particle

Consider a rigid particle of mass m settling in a liquid matrix under the action of a gravitational force. The forces acting on the particle are: gravity force (F_G), drag force (F_D), and buoyancy force (F_B). Thus the net force acting on the particle in the downward direction is:

$$F_{net,downward} = m\frac{dU}{dt} = F_G - F_B - F_D \tag{1}$$

The gravitational force F_G on the particle is equal to mg, the drag force F_D on the particle is equal to $C_D A_p\left(\rho U^2/2\right)$, where C_D is the drag coefficient and A_p is the projected area of the particle measured in a plane normal to direction of motion of particle (for spherical particle, $A_p = \pi R^2$), and the buoyancy force F_B on the particle is equal to weight of the fluid displaced by the particle, that is, $F_B = m\rho g/\rho_p$ where ρ_p is particle density. Thus:

$$m\frac{dU}{dt} = mg - \frac{mg\rho}{\rho_p} - \frac{C_D A_p \rho U^2}{2} \tag{2}$$

or,

$$\frac{dU}{dt} = g\left(\frac{\rho_p - \rho}{\rho_p}\right) - \frac{C_D A_p \rho U^2}{2m} \tag{3}$$

Under steady state condition ($dU/dt = 0$), the particle settles at a constant velocity called the terminal velocity. Thus:

$$U_0 = \sqrt{\frac{2gm\left(\rho_p - \rho\right)}{A_p \rho_p C_D \rho}} \tag{4}$$

For spherical particles:

$$m = \frac{\pi D_p^3 \rho_p}{6} \quad \text{and} \quad A_p = \frac{\pi D_p^2}{4} \tag{5}$$

This leads to the following settling velocity of spherical particles:

$$U_0 = \sqrt{\frac{4g\left(\rho_p - \rho\right)D_p}{3C_D\rho}} \tag{6}$$

The drag coefficient is a function of the particle Reynolds number (Re_p), defined as:

$$\mathrm{Re}_p = \frac{\rho D_p U_0}{\mu} \tag{7}$$

For creeping flow around a spherical particle ($\mathrm{Re}_p < 0.1$), C_D is given by the Stokes Law as:

$$C_D = \frac{24}{\mathrm{Re}_p} \tag{8}$$

Upon substitution of the expression for C_D into Equation (6), the following expression for the terminal settling velocity of spherical rigid particles is obtained:

$$U_0 = \frac{gD_p^2\left(\rho_p - \rho\right)}{18\mu}\ \mathrm{Re}_p < 0.1 \tag{9}$$

2.2. *Settling of a Swarm of Particles (Hindered Settling)*

In the preceding section, the settling behavior of a single rigid particle in quiescent fluid is discussed. In practical applications, sedimentation of a swarm of particles is important. Due to hydrodynamic interactions between the neighboring particles, the settling velocity of a swarm of particles is hindered or slower. When a swarm of particles settle, the suspending medium fluid moves upward in order to compensate for the settling of particles (see Figure 3). Due to the backflow drag on the particles, the particles settle at a velocity lower than that of an isolated article.

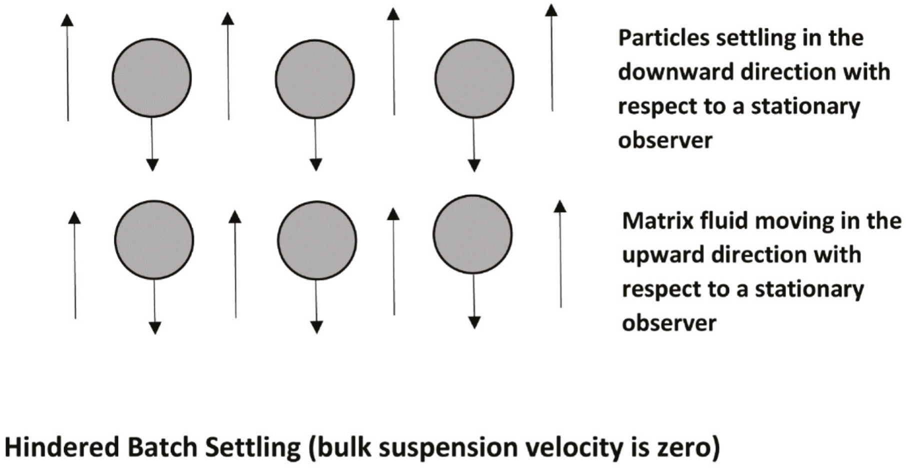

Figure 3. Hindered batch settling of particles.

The relative decrease in the settling velocity of particles in a dilute suspension is proportional to ϕ, the volume fraction of particles, and is given as:

$$\frac{U_p - U_0}{U_0} = -\alpha\phi \tag{10}$$

where U_p is the settling velocity of particles in a suspension of concentration ϕ. Equation (10) can be re-written as:

$$U_p = U_0(1 - \alpha\phi) \tag{11}$$

Assuming the spatial distribution of particles to be random, Batchelor [39] theoretically found the value of α to be 6.55.

The linear relationship, Equation (11), is valid only at low concentrations ($\phi < 0.05$). At high particle concentrations, the hindrance effect becomes more pronounced and the relationship becomes non-linear. A number of empirical and semi-empirical correlations have been proposed in the literature to describe hindered settling of particles at high particle concentrations. The most popular ones are due to Richardson and Zaki [40] and Garside and Al-Dibouni [41]. The Richardson and Zaki correlation is given as:

$$U_p = U_0(1 - \phi)^n \tag{12}$$

where n is a function of particle Reynolds number Re_p. For low $\mathrm{Re}_p(\mathrm{Re}_p < 0.2)$, $n = 4.65$. The Garside and Al-Dibouni correlation is given as:

$$\frac{U_R - A}{B - U_R} = 0.06(\mathrm{Re}_p)^{\varepsilon + 0.2} \tag{13}$$

where $A = \varepsilon^{4.14}$, $B = 0.8\varepsilon^{1.28}$ (when $\varepsilon \le 0.85$), $B = \varepsilon^{2.65}$ (when $\varepsilon > 0.85$), ε is volume fraction of fluid, and U_R is defined as:

$$U_R = \frac{U_p}{\varepsilon U_0} \tag{14}$$

In the limit $\mathrm{Re}_p \to 0$, Equation (13) reduces to:

$$U_p = U_0(1 - \phi)^{5.14} \tag{15}$$

This equation has the same form as that of the Richardson and Zaki equation, Equation (12), with a different value of n. Al-Naafa and Sami-Selim [42] proposed the following equation to describe their data on sedimentation of monodisperse suspensions:

$$U_p = U_0(1 - \phi)^{6.55} \tag{16}$$

In the limit $\phi \to 0$, Equation (16) reduces to Batchelor's equation, Equation (11) with $\alpha = 6.55$.

3. Drift Flux Theory and Re-Interpretation of Existing Hindered Settling Data

3.1. Drift Flux Theory

The drift flux theory is used widely in the analysis of two-phase flows when the two phases move with different velocities. For example, it can be used to predict the in-situ gas hold up in bubbly gas-liquid two-phase flows from the knowledge of superficial gas and liquid velocities, bubble size, and fluid properties. The drift flux theory can be readily applied to sedimentation of particles in non-dilute suspensions. The advantage of the drift flux theory is that it can applied to both batch sedimentation and continuous sedimentation of suspensions. Note that in batch sedimentation there is no net motion of suspension, that is, the particles and the matrix fluid move in opposite directions such that the net suspension velocity is zero with respect to a stationary observer. In continuous sedimentation, the suspension has a net motion with a non-zero net velocity with respect to a stationary observer.

Consider a suspension of solid particles in Newtonian liquid. The drift velocity of solid particles, denoted as $\vec{U}_{pm}$, is defined as:

$$\vec{U}_{pm} = \vec{U}_p - \vec{U}_m \tag{17}$$

where $\vec{U}_p$ is the particle velocity and $\vec{U}_m$ is the mixture (suspension) velocity with respect to a stationary observer. Thus the drift velocity of a particle is the velocity of a particle relative to an observer moving with the suspension velocity $\vec{U}_m$. The suspension velocity $\vec{U}_m$ can be expressed as:

$$\vec{U}_m = \vec{J}_p + \vec{J}_l \tag{18}$$

where $\vec{J}_p$ is the volumetric flux of particles and $\vec{J}_l$ is the volumetric flux of liquid phase. The volumetric fluxes are related to particle and liquid velocities as follows:

$$\vec{J}_p = \phi\, \vec{U}_p \tag{19}$$

$$\vec{J}_l = (1-\phi)\, \vec{U}_l \tag{20}$$

where $\vec{U}_l$ is the liquid phase velocity. From Equations (17) and (18), it follows that:

$$\vec{U}_{pm} = \vec{U}_p - \left(\vec{J}_p + \vec{J}_l\right) \tag{21}$$

Substituting the relations for $\vec{J}_p$ (Equation (19)) and $\vec{J}_l$ (Equation (20)) into Equation (21), we obtain:

$$\vec{U}_{pm} = (1-\phi)\left(\vec{U}_p - \vec{U}_l\right) = (1-\phi)\vec{U}_s \tag{22}$$

where $\vec{U}_s = \left(\vec{U}_p - \vec{U}_l\right)$ is the slip velocity between the particles and the fluid (liquid).

The drift flux of particles, denoted as $\vec{J}_{pm}$, is related to the drift velocity of particles $\vec{U}_{pm}$ as:

$$\vec{J}_{pm} = \phi\, \vec{U}_{pm} \tag{23}$$

Substitution of Equations (21) into (23) yields:

$$\vec{J}_{pm} = (1-\phi)\,\vec{J}_p - \phi\, \vec{J}_l \tag{24}$$

From the knowledge of volumetric fluxes $\vec{J}_p$, $\vec{J}_l$ and volume fraction of particles ϕ, one can calculate the drift flux using Equation (24). Once the drift flux is known, the drift velocity $\vec{U}_{pm}$ can be calculated from Equation (23) and the slip velocity $\vec{U}_s$ can be calculated from Equation (22).

The drift velocity can be expressed as:

$$\vec{U}_{pm} = \vec{U}_0 f(\phi) \tag{25}$$

where $\vec{U}_0$ is the settling velocity of a single isolated particle in quiescent liquid and $f(\phi)$ is the hindered settling function of the form of Richardson and Zaki correlation. Thus,

$$\vec{U}_{pm} = \vec{U}_0 (1-\phi)^n \tag{26}$$

$$\vec{J}_{pm} = \phi\,\vec{U}_{pm} = \vec{U}_0\phi(1-\phi)^n \tag{27}$$

In the absence of any relative motion or slip between the particles and fluid, we have:

$$\vec{U}_{pm} = 0\,;\,\vec{J}_{pm} = 0\,;\vec{U}_s = 0 \tag{28}$$

Under these conditions, the suspension flow can be treated as a homogeneous single-phase flow with average properties. In the present topic of discussion, that is, batch sedimentation of particles where there is no net flow of suspension, the following relations are applicable:

$$\vec{U}_m = 0 \tag{29}$$

$$\vec{U}_{pm} = \vec{U}_p \tag{30}$$

$$\vec{J}_{pm} = \phi\,\vec{U}_p \tag{31}$$

$$\vec{U}_p = \vec{U}_0(1-\phi)^n \tag{32}$$

3.2. *Re-interpretation of Existing Hindered Settling Data in Terms of Drift Flux Theory*

According to the drift flux model, the normalized drift velocity (see Equation (25)) is a function of the concentration of particles or droplets. The normalized drift velocity $U_{Drift,N}$ can be expressed in scalar form as:

$$U_{Drift,N} = U_{pm}/U_0 = (1-\phi)^n \tag{33}$$

where the value of the exponent n needs to be determined from experimental data. For low particle Reynolds number, the Richardson and Zaki correlation gives $n = 4.65$.

Two sets of experimental data on creaming (upward motion) of oil droplets in concentrated oil-in-water emulsions and four sets of experimental data on settling of particles in concentrated suspensions are considered to validate the drift flux model, Equation (33). Table 1 provides the details of the emulsion and suspension systems considered here. The experimental data covers both creaming in emulsions and sedimentation in suspensions over broad ranges of droplet/particle concentration and sizes.

Table 1. Six sets of creaming/sedimentation data taken from different sources.

Set No.	Dispersion Type	Creaming or Sedimentation	Particle Volume Fraction	Particle Mean Diameter	Reference
1	emulsion	creaming	0–0.40	1.72 µm	Chanamai & McClements [43]
2	emulsion	creaming	0–0.40	0.86 µm	Chanamai & McClements [43]
3	suspension	sedimentation	0–0.40	788 µm	Nicolai et al. [44]
4	suspension	sedimentation	0–0.48	3.1 µm	Buscall et al. [45]
5	suspension	sedimentation	0–0.15	136 µm	Davis & Birdsell [46]
6	suspension	sedimentation	0–0.53	0.27–0.31 µm	Davis et al. [47]

Figure 4 shows the experimental data for emulsions and suspensions plotted as normalized drift velocity versus droplet or particle concentration (vol. %). Interestingly the experimental data for very different dispersed systems such as emulsions undergoing creaming effect (upward motion of oil droplets) and suspensions undergoing sedimentation effect (downward motion of particles), with very different droplet or particle sizes (see Table 1), show the same trend. However, there is a significant scatter of experimental data from one set to another. The likely cause for this scatter is the solvation of particles and droplets. The particles and droplets of dispersions become coated with thin layers or films of matrix fluid due to strong attractive interactions between the particle/droplet surfaces and the matrix molecules. The attractive interactions between the particle surface and matrix molecules are particularly important when the particles/droplets are electrically charged or the droplets are stabilized by surfactant (see Figure 5).

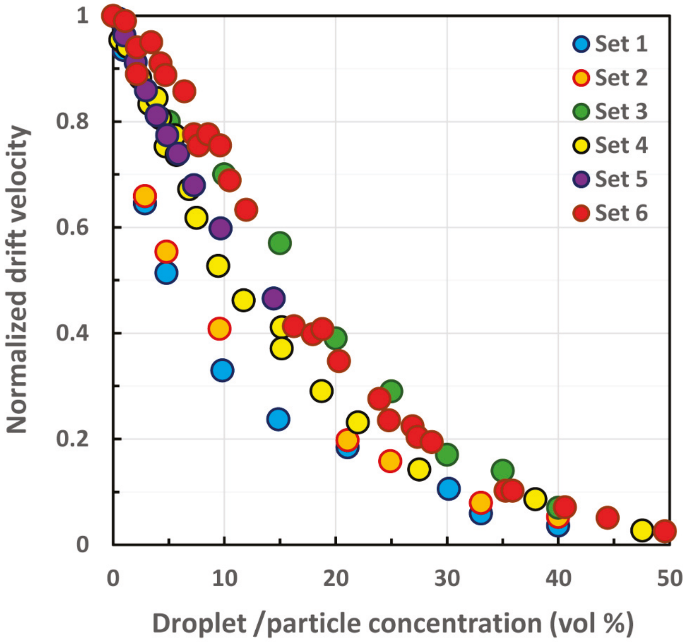

Figure 4. Experimental data for creaming/sedimentation of emulsions and suspensions plotted as normalized drift velocity versus droplet or particle concentration (vol. %).

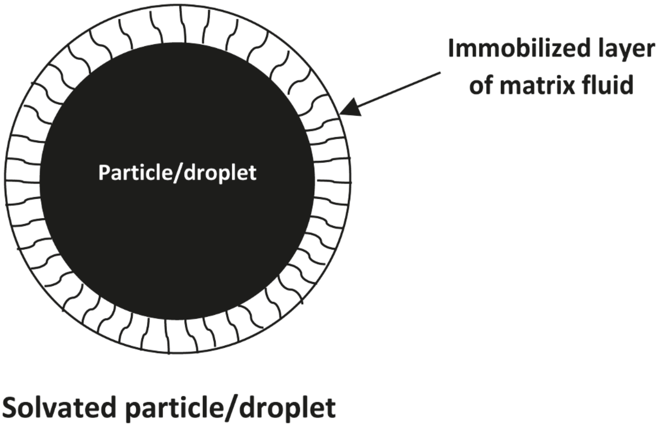

Figure 5. Particle/droplet coated with a thin film of immobilized matrix fluid.

The solvation films become part of the particles increasing their effective size and volume fraction. The effective volume fraction of solvated particles ϕ_{eff} can be expressed as:

$$\phi_{eff} = \phi\left[1 + \frac{\delta}{R}\right]^3 = k_s\phi \tag{34}$$

where δ is the solvation layer thickness, R is the particle/droplet radius, and k_s is the solvation coefficient. For a given solvation layer thickness δ, the solvation effect increases with the decrease in droplet/particle radius. Thus the solvation effect cannot be ignored in dispersions of small size particles.

In order to take into account the effect of solvation of particles on creaming and sedimentation of particles, the volume fraction of un-solvated particles is replaced by ϕ_{eff} in the expression for normalized drift velocity:

$$U_{Drift,N} = U_{pm}/U_0 = (1 - \phi_{eff})^n = (1 - k_s\phi)^n \tag{35}$$

Using the Richardson and Zaki n value of 4.65, one can estimate the solvation coefficient k_s by re-arranging Equation (35) as:

$$\left[U_{Drift,N}\right]^{1/4.65} = 1 - k_s\phi \tag{36}$$

According to Equation (36), the plot of $\left[U_{Drift,N}\right]^{1/4.65}$ versus ϕ data is a straight line with a slope of $-k_s$. Figure 6 shows the typical plots of $\left[U_{Drift,N}\right]^{1/4.65}$ versus ϕ data. The data exhibit a linear relationship passing through (0, 1) with a slope of $-k_s$. Table 2 summarizes the values of the solvation coefficient for different systems. The solvation coefficients are large in the case of electrostatically stabilized emulsions consisting of small size droplets.

Table 2. Summary of solvation coefficients for different dispersed systems.

Set No.	Dispersion Type	Creaming or Sedimentation	Solvation Coefficient, k_s	Particle Mean Radius, R	Solvation Layer Thickness, δ
1	emulsion	creaming	1.40	0.86 µm	0.102 µm
2	emulsion	creaming	1.30	0.43 µm	0.039 µm
3	suspension	sedimentation	1.0	394 µm	0 µm
4	suspension	sedimentation	1.14	1.55 µm	0.069 µm
5	suspension	sedimentation	1.11	68 µm	2.41 µm
6	suspension	sedimentation	1.0	0.13–0.155 µm	0 µm

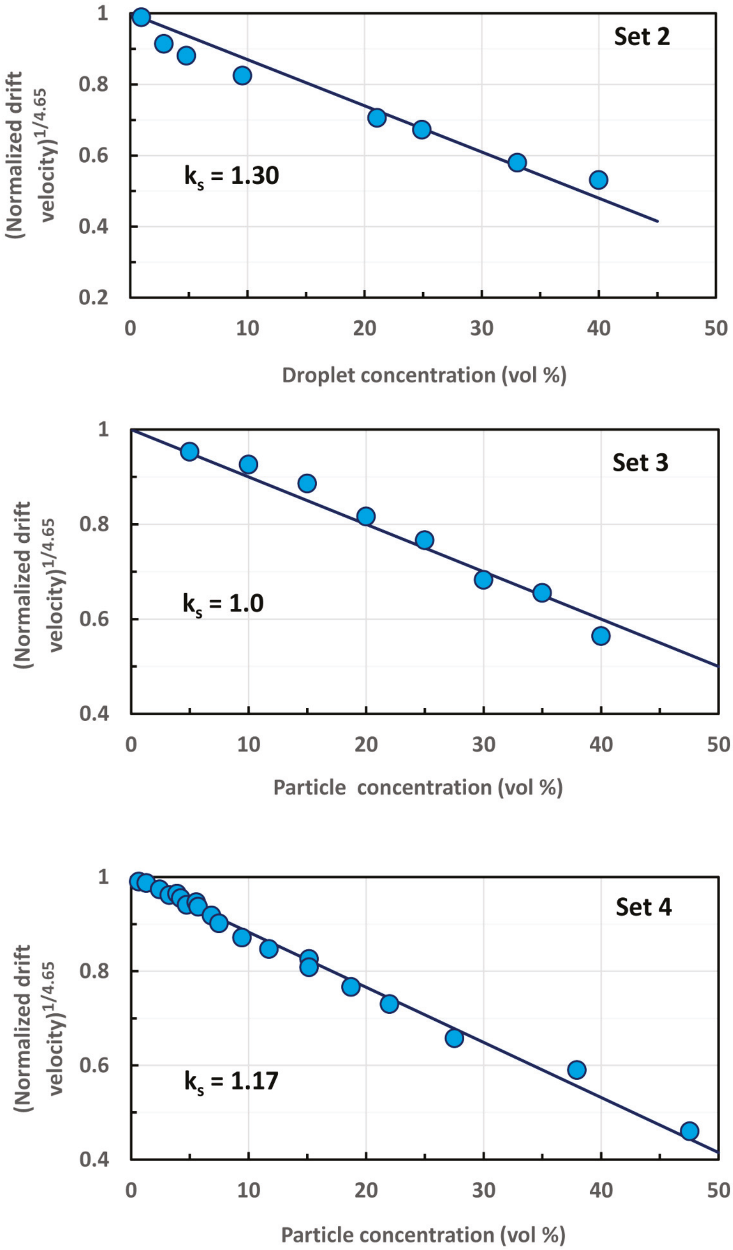

Figure 6. Typical plots of $\left[U_{Drift,N}\right]^{1/4.65}$ versus ϕ experimental data.

The experimental data for emulsions and suspensions are re-plotted in Figure 7 as normalized drift velocity versus effective volume fraction of particles/droplets ϕ_{eff} (vol. %). Now the scatter in experimental data is reduced significantly and the following model describes the data adequately:

$$U_{Drift,N} == (1-\phi_{eff})^{4.65} = (1-k_s\phi)^{4.65} \tag{37}$$

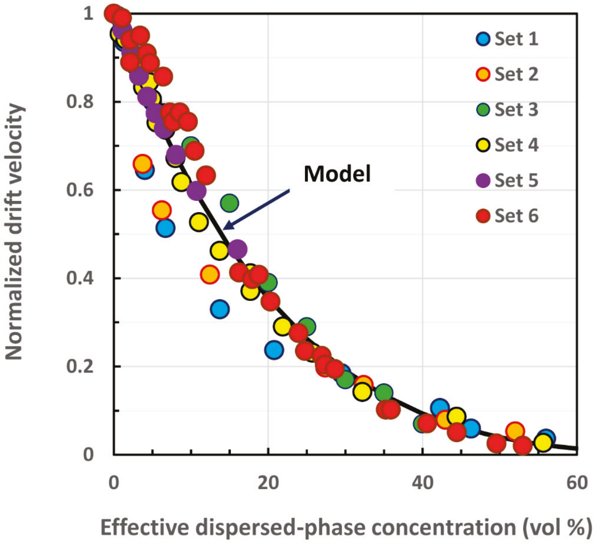

Figure 7. Normalized drift velocity versus effective volume fraction of particles/droplets ϕ_{eff}.

Figure 8 shows the plot of normalized drift flux $J_{drift,N}$ as a function of effective dispersed-phase concentration ϕ_{eff}. The experimental data are compared with the following model for normalized drift flux:

$$J_{drift,N} = J_{pm}/U_0 = \phi_{eff}\,(1 - \phi_{eff})^{4.65} \tag{38}$$

where $\phi_{eff} = k_s\phi$. The experimental data follow the drift flux model, Equation (38), reasonably well.

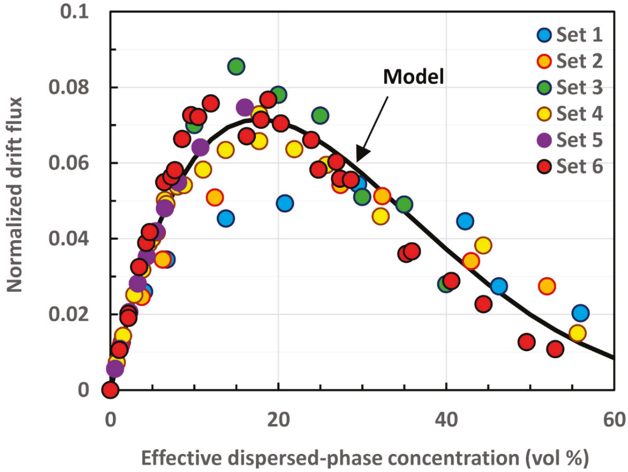

Figure 8. Normalized drift flux $J_{drift,N}$ as a function of effective dispersed-phase concentration ϕ_{eff} (vol %).

In summary, the creaming and sedimentation experimental data obtained for a variety of different systems covering a broad range of particle and droplet sizes can be described adequately by the drift flux model, Equations (37) and (38). In what follows, this drift flux approach is applied to modeling of creaming and sedimentation of Pickering emulsions.

4. Modeling and Simulation of Creaming and Sedimentation of Pickering Emulsions

4.1. Upward Rise and Downward Settling of a Single Pickering Emulsion Droplet

Consider a single Pickering emulsion droplet shown in Figure 9. The droplet has a core-shell morphology with liquid core and a monolayer of packed nanoparticles as a shell. The droplet may rise (cream) or settle (sediment) depending on the difference between the effective density of droplet and the density of matrix fluid.

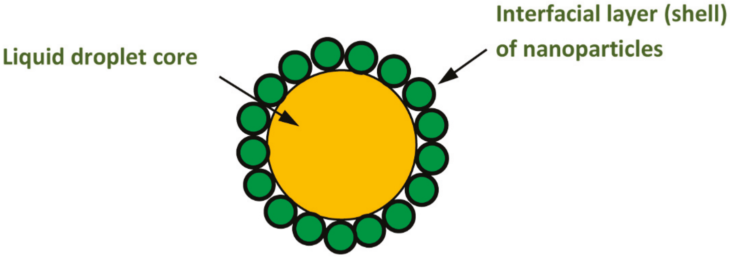

Figure 9. Core-shell Pickering emulsion droplet.

Figure 10 shows a schematic diagram of a Pickering emulsion droplet with relevant dimensions. The effective density of the Pickering core-shell droplet is different from that of the bare droplet due to loading of nanoparticles at the interface. The effective density of core-shell droplets can be calculated using the following approach assuming a monolayer of spherical nanoparticles present on the droplet surface. The number of particles loaded on the droplet is:

$$N = \frac{4\pi(R^*)^2}{\pi R_{np}^2}\beta = 4(R^*/R_{np})^2\beta \tag{39}$$

where R_{np} is the radius of the nanoparticle, R^* is the radius of spherical surface passing through the equator of nanoparticles (see Figure 10), β is the fraction of the surface area $4\pi(R^*)^2$ occupied by the nanoparticles. For square packing of nanoparticles shown in Figure 11, $\beta = 0.785$. For hexagonal packing (see Figure 12), $\beta = 0.907$.

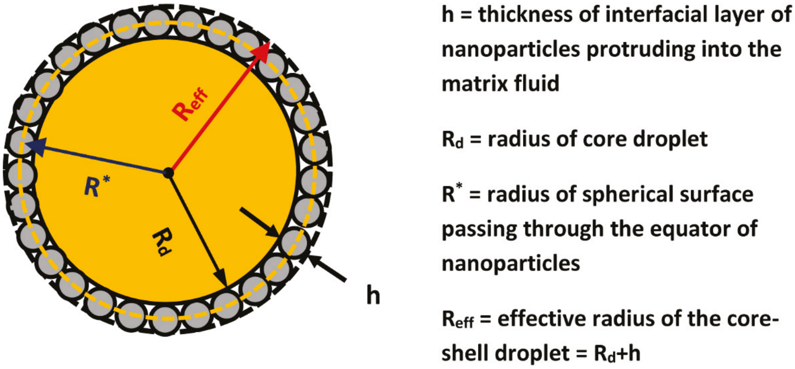

Figure 10. Schematic diagram of a Pickering emulsion droplet with relevant dimensions.

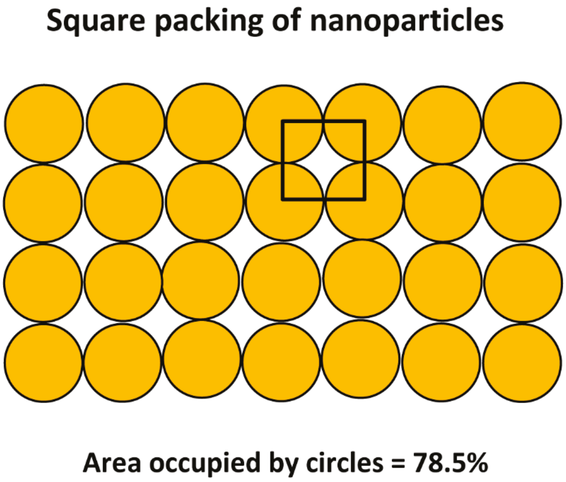

Figure 11. Square packing of nanoparticles.

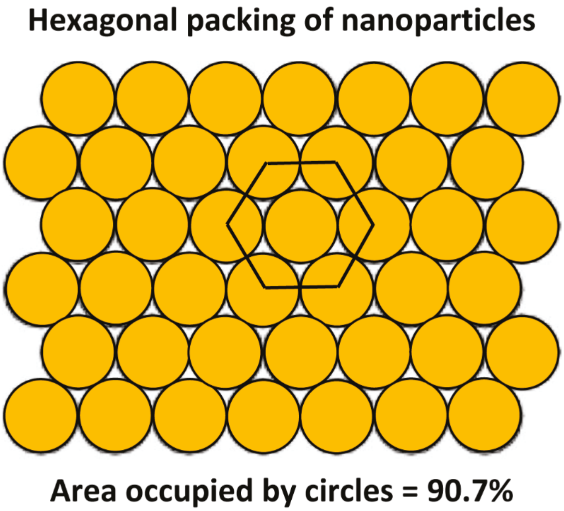

Figure 12. Hexagonal packing of nanoparticles.

4.2. Oil-in-water (O/W) Emulsions

For oil-in-water (O/W) emulsions, the thickness of the interfacial layer of nanoparticles protruding into the matrix aqueous fluid (see Figure 13) is given as follows [10]:

$$h = R_{np}(1 + \cos\theta) \tag{40}$$

where θ is the three-phase contact angle measured through the aqueous phase. The radius R^* can be expressed as:

$$R^* = R_d + h - R_{np} = R_d\left(1 + \frac{R_{np}}{R_d}\cos\theta\right) \tag{41}$$

where R_d is the radius of bare emulsion droplet (see Figure 10). The mass of nanoparticles present on the surface of a single oil droplet can be calculated as follows:

$$m_{nanoparticles} = N\rho_{np}\left(4\pi R_{np}^3/3\right) \tag{42}$$

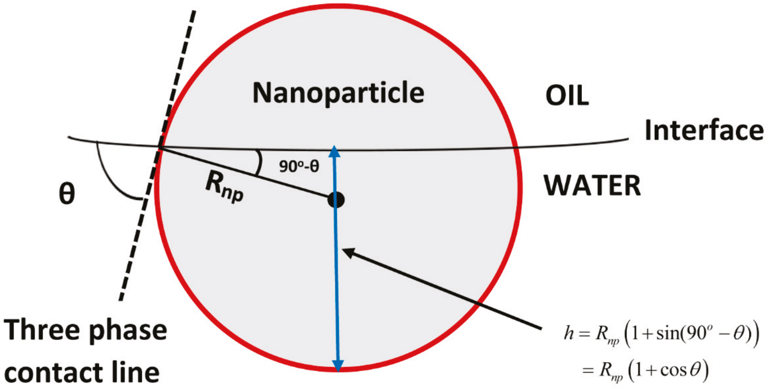

Figure 13. Thickness of interfacial layer of solid nanoparticles protruding into the continuous phase of an emulsion.

From Equations (39) and (42) it follows that:

$$m_{nanoparticles} = (16\pi/3)\left(R^*\right)^2 R_{np}\beta\rho_{np} \tag{43}$$

The mass of the matrix fluid attached to the interfacial layer of nanoparticles is as follows:

$$m_{matrix-fluid-immobilized} = N\left[4R_{np}^2 h - (\pi/3)h^2\left(3R_{np} - h\right)\right]\rho_w \tag{44}$$

Thus the effective density of an oil droplet of a Pickering O/W emulsion can be expressed as:

$$\rho_{d,eff} = \left(m_{bare-droplet} + m_{nanoparticles} + m_{matrix-fluid-immobilized}\right)/\left(4\pi R_{eff}^3/3\right) \tag{45}$$

where R_{eff} is the effective radius of the composite droplet ($R_{eff} = R_d + h$) and $m_{bare-droplet}$ is the mass of the bare oil droplet given as $\left(4\pi R_d^3/3\right)\rho_o$ where ρ_o is the oil density.

Using the effective density of a droplet given by Equation (45), the rise velocity of a single Pickering oil droplet suspended in water matrix can now be calculated from the following modified Stokes law:

$$U_0 = \frac{2gR_{eff}^2\left(\rho_w - \rho_{d,eff}\right)}{9\mu} \tag{46}$$

Figures 14 and 15 show the simulation results for two model Pickering O/W emulsions: PSNPMO-OW and SNPCO-OW, respectively. PSNPMO-OW refers to Pickering O/W emulsion consisting of polystyrene nanoparticles (PSNP) and mineral oil (MO) droplets. SNPCO-OW refers to Pickering O/W emulsion consisting of silica nanoparticles (SNP) and castor oil (CO) droplets. For the PSNPMO-OW Pickering emulsion, the values of the various parameters used in the simulation are: $R_d = 1$ μm, $R_{np} = 0.1$ μm, $\rho_o = 773\ \text{kg/m}^3$, $\rho_w = 997\ \text{kg/m}^3$, $\rho_{np} = 1054\ \text{kg/m}^3$, $\mu = 0.89$ mPa.s, and $g = 9.8\ \text{m/s}^2$. For the SNPCO-OW Pickering emulsion, the values of the various parameters used in the simulation are: $R_d = 1$ μm, $R_{np} = 0.1$ μm, $\rho_o = 960\ \text{kg/m}^3$, $\rho_w = 997\ \text{kg/m}^3$, $\rho_{np} = 2650\ \text{kg/m}^3$,

$\mu = 0.89$ mPa.s, and $g = 9.8\ \text{m/s}^2$. The Stokes (rise or fall) velocity U_o and relative density $\rho_{d,eff}/\rho_o$ of a single Pickering oil droplet are plotted as functions of contact angle. The solid curves are generated using $\beta = 0.785$ (square packing of nanoparticles at the interface) and the dashed curves are generated using $\beta = 0.907$ (hexagonal packing of nanoparticles at the interface).

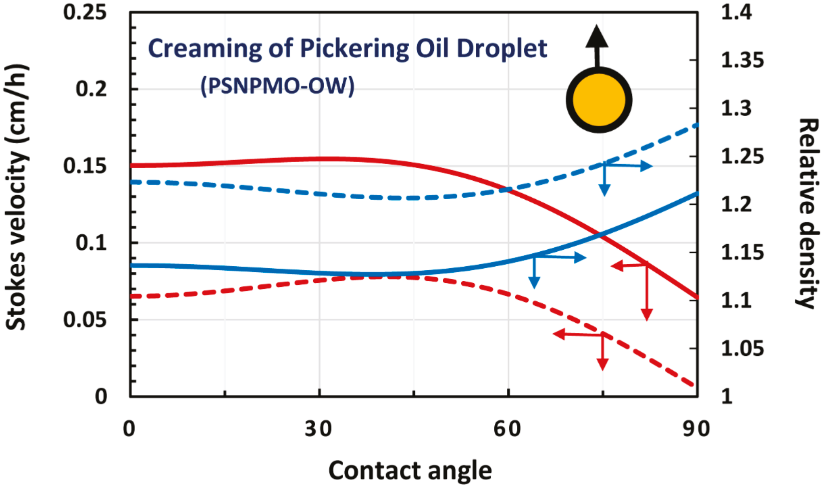

Figure 14. Variations of Stokes rise velocity and relative density of a single Pickering oil droplet with contact angle (PSNPMO-OW Pickering emulsion). The solid curves represent square packing and the dashed curves represent hexagonal packing of nanoparticles at the oil-water interface.

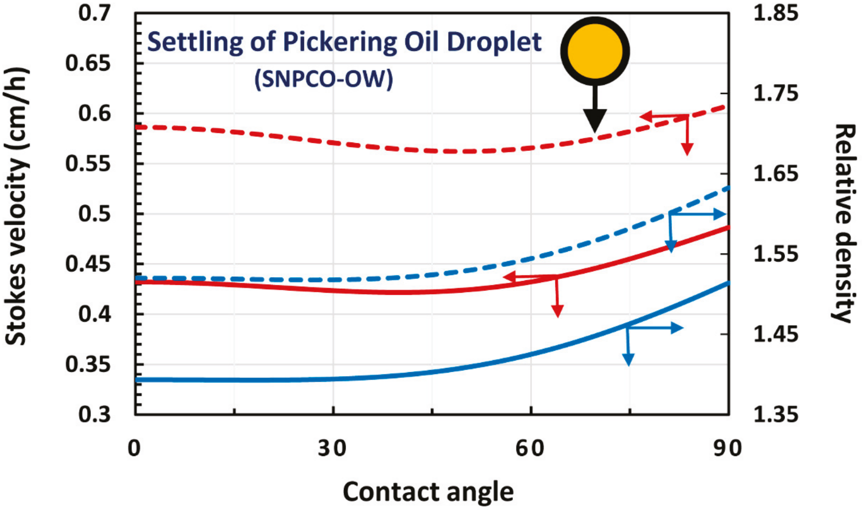

Figure 15. Variations of Stokes settling velocity and relative density of a single Pickering oil droplet with contact angle (SNPCO-OW Pickering emulsion). The solid curves represent square packing and the dashed curves represent hexagonal packing of nanoparticles at the oil-water interface.

For the PSNPMO-OW Pickering emulsion (Figure 14), the Stokes rise velocity of a Pickering oil droplet increases initially with the increase in contact angle, reaches a maximum value, and then falls off with further increase in the contact angle. The relative density of a single composite droplet shows the opposite behavior in that the density initially decreases, reaches a minimum, and then rises with further increase in the contact angle. With the increase in contact angle initially from a value of zero, the mass of the attached high-density matrix fluid to the droplet is decreased as the matrix fluid is displaced with the increase in contact angle. Consequently the density of the composite droplet decreases and there occurs a corresponding increase in the Stokes rise velocity due to an increase in the density difference between the composite droplet and matrix fluid. However, with further increase in the contact angle, the amount of the matrix fluid displaced is little but the effective radius of the composite droplet becomes smaller and smaller resulting in an increase in the effective density of a composite droplet and the corresponding decrease in the Stokes velocity. Upon increasing the packing density of nanoparticles from square packing to hexagonal packing, the relative density curve of Pickering oil droplet shifts upward to higher densities, as expected. The Stokes rise velocity curve shows the opposite behavior in that it shifts to lower velocities due to decrease in the density difference between the Pickering oil droplet and matrix fluid.

For the SNPCO-OW Pickering emulsion (Figure 15), the composite oil droplets are no longer able to cream or rise in the matrix fluid as the effective density of the Pickering oil droplets exceeds the density of the matrix fluid. Note that the oil density ($\rho_o = 960\ \ \text{kg/m}^3$) is now close to that of the matrix fluid density ($\rho_w = 997\ \ \text{kg/m}^3$) and that the silica nanoparticles have a high density ($\rho_{np} = 2650$ kg/m^3). The relative density and Stokes settling velocity of Pickering oil droplet increase with the increase in the contact angle. The relative density increases with the increase in the contact angle due to a decrease in the effective radius of the composite droplet. The Stokes settling velocity increases due to an increase in the density difference between the composite droplet and matrix fluid. With the increase in the packing density of nanoparticles from square packing to hexagonal packing, the relative density curve of Pickering oil droplet shifts upward to higher densities, as expected. The Stokes settling velocity curve also shifts upward to higher velocities due to an increase in the density difference between the Pickering oil droplet and matrix fluid.

4.3. Water-in-oil (W/O) Emulsions

For water-in-oil (W/O) emulsions, the thickness of the interfacial layer of nanoparticles protruding into the matrix fluid (oil) is given as follows [10]:

$$h = R_{np}(1 - \cos\theta) \tag{47}$$

where θ is the three-phase contact angle measured through the aqueous phase. The radius R^* can be expressed as:

$$R^* = R_d + h - R_{np} = R_d\left(1 - \frac{R_{np}}{R_d}\cos\theta\right) \tag{48}$$

The mass of nanoparticles present on the surface of a single water droplet can be calculated from Equation (43). The mass of the matrix fluid attached to the interfacial layer of nanoparticles is as follows:

$$m_{matrix-fluid-immobilized} = N\left[4R_{np}^2 h - (\pi/3)h^2\left(3R_{np} - h\right)\right]\rho_o \tag{49}$$

Thus the effective density of a water droplet of Pickering W/O emulsion can be expressed as:

$$\rho_{d,eff} = \left(m_{bare-droplet} + m_{nanoparticles} + m_{matrix-fluid-immobilized}\right)/\left(4\pi R_{eff}^3/3\right) \tag{50}$$

where R_{eff} is the effective radius of the composite droplet ($R_{eff} = R_d + h$) and $m_{bare-droplet}$ is the mass of the bare water droplet given as $\left(4\pi R_d^3/3\right)\rho_w$ where ρ_w is the water density.

Using the effective density of a droplet given by Equation (50), the sedimentation or settling velocity of a single Pickering water droplet suspended in oil matrix can now be calculated from the following modified Stokes law:

$$U_0 = \frac{2gR_{eff}^2\left(\rho_{d,eff} - \rho_o\right)}{9\mu} \tag{51}$$

Figures 16 and 17 show the simulation results for two model Pickering W/O emulsions: PSNPMO-WO and SNPCO-WO, respectively. PSNPMO-WO refers to Pickering W/O emulsion consisting of polystyrene nanoparticles (PSNP) and mineral oil (MO) matrix. SNPCO-WO refers to Pickering W/O emulsion consisting of silica nanoparticles (SNP) and castor oil (CO) matrix. The values of the parameters are the same as given earlier for the model Pickering O/W emulsions (PSNPMO-OW and SNPCO-OW) except for the matrix fluid viscosity μ. For the PSNPMO-WO Pickering emulsion, the viscosity of the matrix fluid (mineral oil) is 2.5 mPa.s and for the SNPCO-WO Pickering emulsion, the viscosity of the matrix fluid (castor oil) is 650 mPa.s. The Stokes settling velocity U_o and relative density $\rho_{d,eff}/\rho_w$ of a single Pickering water droplet are plotted as functions of contact angle. The solid curves are generated using $\beta = 0.785$ (square packing of nanoparticles at the interface) and the dashed curves are generated using $\beta = 0.907$ (hexagonal packing of nanoparticles at the interface).

For both PSNPMO-WO and SNPCO-WO Pickering W/O emulsions, the effective density of the composite water droplet decreases with the increase in the contact angle from 90° to 180° due to an increase in the effective radius of the composite droplet. The Stokes settling velocity of a Pickering water droplet decreases with the increase in contact angle due to a decrease in the density difference between the composite droplet and matrix fluid. Upon increasing the packing density of nanoparticles from square packing to hexagonal packing, the relative density curve of Pickering water droplet shifts upward to higher densities, as expected. The Stokes settling velocity curve also shifts to higher velocities due to an increase in the density difference between the Pickering water droplet and matrix fluid (oil).

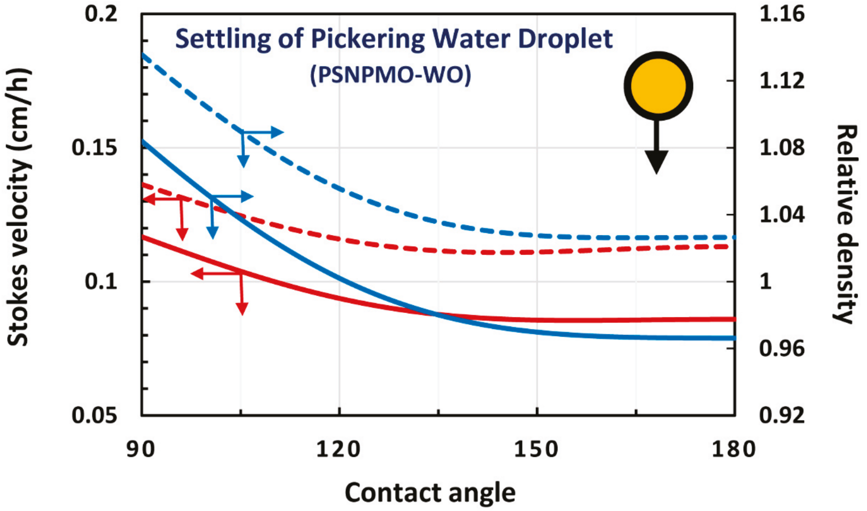

Figure 16. Variations of Stokes settling velocity and relative density of a single Pickering water droplet with contact angle (PSNPMO-WO Pickering emulsion). The solid curves represent square packing and the dashed curves represent hexagonal packing of nanoparticles at the oil-water interface.

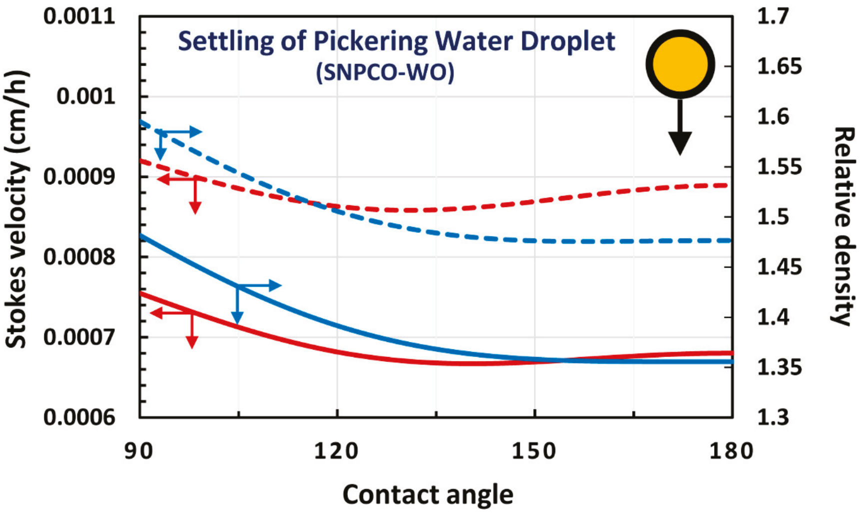

Figure 17. Variations of Stokes settling velocity and relative density of a single Pickering water droplet with contact angle (SNPCO-WO Pickering emulsion). The solid curves represent square packing and the dashed curves represent hexagonal packing of nanoparticles at the oil-water interface.

4.4. Drift Flux of Emulsions

As noted in Section 3.2, the normalized drift velocity $U_{Drift,N}$ and the normalized drift flux $J_{drift,N}$ for emulsions over a broad range of droplet concentration can be expressed as:

$$U_{Drift,N} = (1 - \phi_{eff})^{4.65} \tag{52}$$

$$J_{drift,N} = \phi_{eff}\,(1 - \phi_{eff})^{4.65} \tag{53}$$

where the effective volume fraction of Pickering droplets ϕ_{eff} is given as:

$$\phi_{eff} = \phi\left[1 + \frac{h}{R_d}\right]^3 \tag{54}$$

The thickness h of the interfacial layer of nanoparticles protruding into the matrix fluid is given by Equation (40) for O/W emulsions and Equation (47) for W/O emulsions.

Figure 18 shows the plots of normalized drift flux $J_{drift,N}$ versus ϕ for concentrated oil-in-water (O/W) emulsions for different values of contact angle. With the increase in contact angle, the normalized drift flux at high volume fractions of oil droplets increases due to a decrease in the effective volume fraction of the composite oil droplets.

Figure 19 shows the plots of normalized drift flux $J_{drift,N}$ versus ϕ for concentrated water-in-oil (W/O) emulsions for different values of contact angle. With the increase in contact angle from 90° to 150°, the normalized drift flux at high volume fractions of water droplets decreases due to an increase in the effective volume fraction of the composite water droplets.

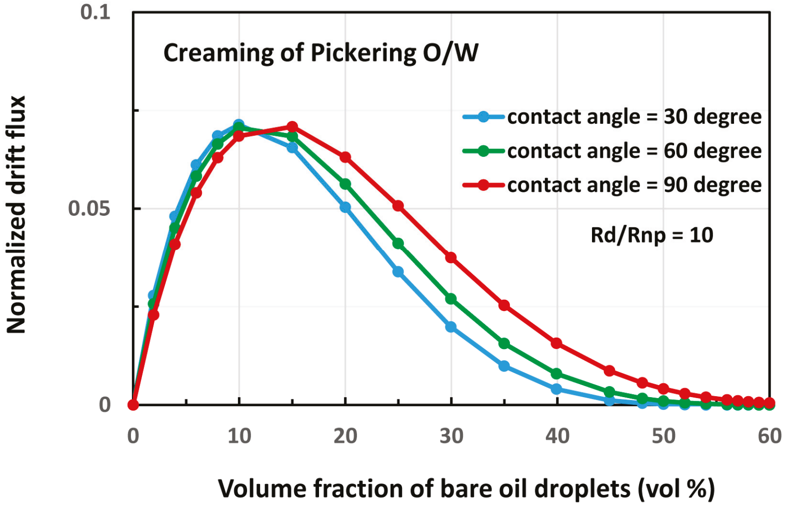

Figure 18. Effect of contact angle on normalized drift flux of Pickering O/W emulsions.

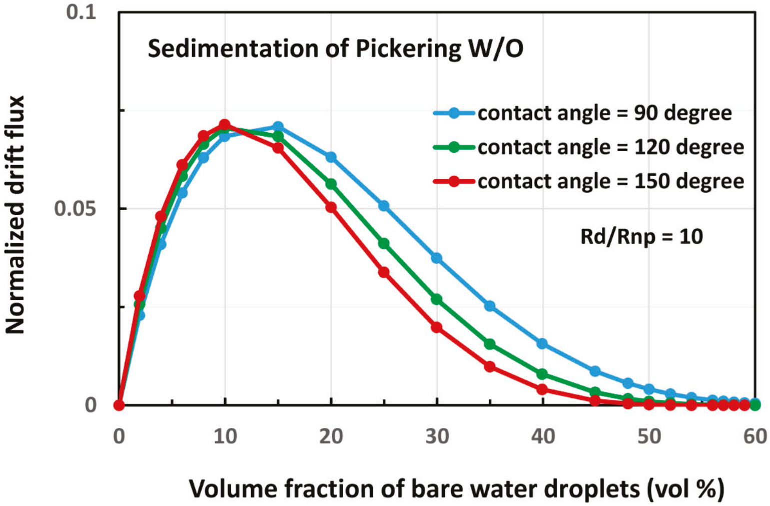

Figure 19. Effect of contact angle on normalized drift flux of Pickering W/O emulsions.

5. Conclusions

The creaming/settling behaviors of single droplet/particle and swarm of droplets/particles are reviewed briefly. The available experimental data on hindered creaming/settling of conventional emulsions and suspensions are interpreted in terms of a drift flux theory. The drift flux model describes the experimental data of creaming and sedimentation in conventional emulsions and suspensions adequately over a broad range of particle and droplet sizes provided that solvation of droplets/particles is taken into account. The unhindered and hindered creaming/settling behaviors of nanoparticle-stabilized Pickering emulsions are modelled. According to the proposed model, the key factors affecting the sedimentation and creaming of droplets in Pickering emulsions are: bare droplet size, size of nanoparticles, three-phase contact angle of the nanoparticles, and packing density of nanoparticles at the oil-water interface. The simulation results generated from the proposed model are presented and discussed. Experimental studies dealing with creaming/settling of single Pickering droplets and Pickering emulsions are lacking.

Funding: This research received no external funding.

Conflicts of Interest: The author declares no conflict of interest.

Notation

A	parameter in Equation (13)
A_p	projected area of particle
B	parameter in Equation (13)
C_D	drag coefficient
D_p	diameter of particle
F_B	buoyance force on the particle
F_D	drag force on the particle
F_G	gravity force (weight) on the particle
F_{net}	net force on the particle
g	acceleration due to gravity
h	thickness of interfacial layer of nanoparticles protruding into the matrix fluid
J_l	volumetric flux of liquid phase (units of velocity)
J_p	volumetric flux of particles (units of velocity)
J_{pm}	drift flux of particles (units of velocity)
$J_{drift,N}$	normalized drift flux of particles
k_s	solvation coefficient
m	mass
n	exponent in Richarson and Zaki correlation, Equation (12)
N	number of nanoparticles loaded on the Pickering droplet
O/W	oil-in-water
R	radius of particle
R_d	radius of core (bare) droplet
R_{eff}	effective radius of composite (Pickering) droplet
R_{np}	radius of nanoparticles
R^*	radius of spherical surface passing through the equator of nanoparticles (see Figure 10)
Re_p	particle Reynolds number
t	time
U	velocity
$U_{Drift,N}$	normalized drift velocity of particle
U_l	liquid phase velocity
U_m	mixture (suspension) velocity
U_0	unhindered terminal velocity of particle
U_p	settling velocity of particle in suspension (hindered settling)
U_{pm}	drift velocity of particle
U_R	dimensionless velocity defined in Equation (14)
U_s	slip velocity between particle and matrix fluid
W/O	water-in-oil
α	coefficient in Equation (11)
β	packing density of nanoparticles at the oil-water interface
δ	thickness of solvation layer
ε	volume fraction of fluid in a suspension
ϕ	actual volume fraction of particles/droplets
ϕ_{eff}	effective volume fraction of particles/droplets
μ	viscosity of matrix fluid
ρ	density of matrix fluid
$\rho_{d,eff}$	effective density of composite (Pickering) droplet
ρ_{np}	density of nanoparticle
ρ_o	density of oil

ρ_p density of particle
ρ_w density of water
θ contact angle

References

1. Pal, R. *Rheology of Particulate Dispersions and Composites*; CRC Press: Boca Raton, FL, USA, 2007.
2. Wu, J.; Ma, G.H. Recent studies of Pickering emulsions: Particles make the difference. *Small* **2006**, *12*, 4633–4648. [CrossRef] [PubMed]
3. Yang, Y.; Fang, Z.; Chen, X.; Zhang, W.; Xie, Y.; Chen, Y.; Liu, Z.; Yuan, W. An overview of Pickering emulsions: Solid-particle materials, classification, morphology, and applications. *Front. Pharmacol.* **2017**, *3*, 287. [CrossRef] [PubMed]
4. Berton-Carabin, C.C.; Schroen, K. Pickering emulsions for food applications: Background, trends, and challenges. *Ann. Rev. Food Sci. Technol.* **2015**, *6*, 263–297. [CrossRef] [PubMed]
5. Chevalier, Y.; Bolzinger, M.A. Emulsions stabilized with solid nanoparticles: Pickering emulsions. *Colloids Surf.* **2013**, *439*, 23–34. [CrossRef]
6. Dickinson, E. Use of nanoparticles and microparticles in the formation and stabilization of food emulsions. *Trends Food Sci. Technol.* **2012**, *24*, 4–12. [CrossRef]
7. Dickinson, E. Food emulsions and foams: Stabilization by particles. *Curr. Opin. Colloid Interface Sci.* **2010**, *15*, 40–49. [CrossRef]
8. Binks, B.P. Colloidal particles at a range of fluid-fluid interfaces. *Langmuir* **2017**, *33*, 6947–6963. [CrossRef]
9. Tarimala, S.; Wu, C.Y.; Dai, L.L. Pickering emulsions—A paradigm shift. In Proceedings of the AIChE Annual Meeting Conference Proceedings 2005, Cincinnati, OH, USA, 30 October–4 November 2005.
10. Pal, R. A simple model for the viscosity of Pickering emulsions. *Fluids* **2018**, *3*, 2. [CrossRef]
11. Bains, U.; Pal, R. In-situ continuous monitoring of the viscosity of surfactant-stabilized and nanoparticles-stabilized Pickering emulsions. *Appl. Sci.* **2019**, *9*, 4044. [CrossRef]
12. Rozynek, Z.; Bielas, R.; Jozefczak, A. Efficient formation of oil-in-oil Pickering emulsions with narrow size distributions by using electric fields. *Soft Matter* **2018**, *14*, 5140–5149. [CrossRef]
13. Timgren, A.; Rayner, M.; Dejmek, P.; Marku, D.; Sjoo, M. Emulsion stabilizing capacity of intact starch granules modified by heat treatment or octenyl succinic anhydride. *Food Sci. Nutr.* **2013**, *1*, 157–171. [CrossRef] [PubMed]
14. Zoppe, J.O.; Venditti, R.A.; Rojas, O.J. Pickering emulsions stabilized by cellulose nanocrystals grafted with thermos-responsive polymer brushes. *J. Colloid Interface Sci.* **2012**, *369*, 202–209. [CrossRef] [PubMed]
15. Chen, X.; Song, X.; Huang, J.; Wu, C.; Ma, D.; Tian, M.; Jiang, H.; Huang, P. Phase behavior of Pickering emulsions stabilized by graphene oxide sheets and resins. *Energy Fuels* **2017**, *31*, 13439–13447. [CrossRef]
16. Binks, B.P.; Fletcher, P.D.I.; Holt, B.L.; Beaussoubre, P. Phase inversion of particle-stabilized perfume oil-water emulsions: Experiment and theory. *Phys. Chem. Chem. Phys.* **2010**, *12*, 11954–11966. [CrossRef] [PubMed]
17. Fournier, C.O.; Fradette, L.; Tanguy, P.A. Effect of dispersed phase viscosity on solid-stabilized emulsions. *Chem. Eng. Res. Des.* **2009**, *87*, 499–506. [CrossRef]
18. Tsabet, E.; Fradette, L. Effect of the properties of oil, particles, and water on the production of Pickering emulsions. *Chem. Eng. Res. Des.* **2015**, *97*, 9–17. [CrossRef]
19. Simon, S.; Theiler, S.; Knudsen, A.; Oye, G.; Sjoblom, J. Rheological properties of particle-stabilized emulsions. *J. Dispers. Sci. Technol.* **2010**, *31*, 632–640. [CrossRef]
20. Li, C.; Liu, Q.; Mei, Z.; Wang, J.; Xu, J.; Sun, D. Pickering emulsions stabilized by paraffin wax and laponite clay particles. *J. Colloid Interface Sci.* **2009**, *336*, 314–321. [CrossRef]
21. Leclercq, L.; Nardello-Rataj, V. Pickering emulsions based on cyclodextrinx: A smart solution for antifungal azole derivatives topical delivery. *Eup. J. Pharm. Sci.* **2016**, *82*, 126–137. [CrossRef]
22. Crossley, S.; Faria, J.; Shen, M.; Resasco, D.E. Solid nanoparticles that catalyze biofuel upgrade reactions at the water/oil interface. *Science* **2010**, *327*, 68–72. [CrossRef]
23. Yang, B.; Leclercq, L.; Clacens, J.M.; Nardello-Rataj, V. Acidic/amphiphilic silica nanoparticles: New eco-friendly Pickering interfacial catalysis for biodiesel production. *Green Chem.* **2017**, *19*, 4552–4562. [CrossRef]

24. Pera-Titus, M.; Leclercq, L.; Clacens, J.M.; De Campo, F.; Nardello-Rataj, V. Pickering interfacial catalysis for biphasic systems: From emulsion design to green reactions. *Angew. Chem. Int. Ed.* **2015**, *54*, 2006–2021. [CrossRef]
25. Leclercq, L.; Company, R.; Muhlbauer, A.; Mouret, A.; Aubry, J.M.; Nardello-Rataj, V. Versatile eco-friendly Pickering emulsions based on substrate/native cyclodextrin complexes: A winning approach for solvent-free oxidations. *ChemSusChem* **2013**, *6*, 1533–1540. [CrossRef] [PubMed]
26. Leclercq, L.; Mouret, A.; Proust, A.; Schmitt, V.; Bauduin, P.; Aubry, J.M.; Nardello-Rataj, V. Pickering emulsions stabilized by catalytic polyoxometalate nanoparticles: A new effective medium for oxidation reactions. *Chem. Eur. J.* **2012**, *18*, 14352–14358. [CrossRef] [PubMed]
27. Kaptay, G. On the equation of the maximum capillary pressure induced by solid particles to stabilize emulsions and foams and on the emulsion stability diagrams. *Colloids Surf. A* **2006**, *282/283*, 387–401. [CrossRef]
28. Katepalli, H.; John, V.T.; Tripathi, A.; Bose, A. Microstructure and rheology of particle stabilized emulsions: Effects of particle shape and inter-particle interactions. *J. Colloid Interface Sci.* **2017**, *485*, 11–17. [CrossRef]
29. Braisch, B.; Kohler, K.; Schuchmann, H.P.; Wolf, B. Preparation and flow behavior of oil-in-water emulsions stabilized by hydrophilic silica particles. *Chem. Eng. Technol.* **2009**, *32*, 1107–1112. [CrossRef]
30. Ganley, W.J.; Van Duijneveldt, J.S. Controlling the rheology of montmorillonite stabilized oil-in-water emulsions. *Langmuir* **2017**, *33*, 1679–1686. [CrossRef]
31. Hermes, M.; Clegg, P.S. Yielding and flow of concentrated Pickering emulsions. *Soft Matter* **2013**, *9*, 7568–7575. [CrossRef]
32. Ogunlaja, S.B.; Pal, R.; Sarikhani, K. Effects of starch nanoparticles on phase inversion of Pickering emulsions. *Can. J. Chem. Eng.* **2018**, *96*, 1089–1097. [CrossRef]
33. Malhotra, V.; Pal, R.; Alhassan, S. Catastrophic phase inversion of emulsions stabilized by amphiphilic nanoparticles. *J. Nanofluids* **2018**, *7*, 30–36. [CrossRef]
34. Pal, R.; Malhotra, V. Influence of hybrid nanoparticle-surfactant stabilizers on catastrophic phase inversion of emulsions. *J. Nanofluids* **2018**, *7*, 300–308. [CrossRef]
35. Sihler, S.; Schrade, A.; Cao, Z.; Ziener, U. Inverse Pickering Emulsions with Droplet Sizes below 500 nm. *Langmuir* **2015**, *31*, 10392–10401. [CrossRef] [PubMed]
36. Becher, P. *Emulsions: Theory and Practice*; Reinhold Publishing Corp: New York, NY, USA, 1957.
37. Robins, M.M. Emulsions-creaming phenomena. *Curr. Opin. Colloid Interface Sci.* **2000**, *5*, 265–272. [CrossRef]
38. Becher, P. (Ed.) *Encyclopedia of Emulsion Technology: Basic Theory*; Marcel Dekker: New York, NY, USA, 1983.
39. Batchelor, G.K. Sedimentation in a dilute dispersion of spheres. *J. Fluid Mech.* **1972**, *52*, 245–268. [CrossRef]
40. Richardson, J.F.; Zaki, W.N. Sedimentation and fluidization. *Trans. Inst. Chem. Eng.* **1954**, *32*, 35–53.
41. Garside, J.; Al-Dibouni, M.R. Velocity-voidage relationships for fluidization and sedimentation in solid-liquid systems. *Ind. Eng. Chem. Process Des. Dev.* **1977**, *16*, 206–214. [CrossRef]
42. Al-Naafa, M.A.; Sami Selim, M. Sedimentation of monodisperse and bidisperse hard-sphere colloidal suspensions. *AIChE J.* **1992**, *38*, 1618–1630. [CrossRef]
43. Chanamai, R.; McClements, D.J. Dependence of creaming and rheology of monodisperse oil-in-water emulsions on droplet size and concentration. *Coll. Surf. A Physicochem. Eng. Asp.* **2000**, *172*, 79–86. [CrossRef]
44. Nicolai, H.; Herzhaft, B.; Hinch, E.J.; Oger, L.; Guazzelli, E. Particle velocity fluctuations and hydrodynamic self-diffusion of sedimenting non-Brownian spheres. *Phys. Fluids* **1995**, *7*, 12–23. [CrossRef]
45. Buscall, R.; Goodwin, J.W.; Ottewill, R.H.; Tadros, T.F. The settling of particles through Newtonian and non-Newtonian media. *J. Colloid Interface Sci.* **1982**, *85*, 78–86. [CrossRef]
46. Davis, R.H.; Birdsell, K.H. Hindered settling of semidilute monodisperse and polydisperse suspensions. *AIChE J.* **1988**, *34*, 123–129. [CrossRef]
47. Davis, K.E.; Russel, W.B.; Glantschnig, W.J. Settling suspensions of colloidal silica: Observations and x-ray measurements. *J. Chem. Soc. Faraday Trans.* **1991**, *87*, 411–424. [CrossRef]

fluids

Article

Turbulence Intensity Scaling: A Fugue

Nils T. Basse

Elsas väg 23, 423 38 Torslanda, Sweden; nils.basse@npb.dk

Received: 5 July 2019; Accepted: 30 September 2019; Published: 9 October 2019

Abstract: We study streamwise turbulence intensity definitions using smooth- and rough-wall pipe flow measurements made in the Princeton Superpipe. Scaling of turbulence intensity with the bulk (and friction) Reynolds number is provided for the definitions. The turbulence intensity scales with the friction factor for both smooth- and rough-wall pipe flow. Turbulence intensity definitions providing the best description of the measurements are identified. A procedure to calculate the turbulence intensity based on the bulk Reynolds number (and the sand-grain roughness for rough-wall pipe flow) is outlined.

Keywords: streamwise turbulence intensity definitions; Princeton Superpipe measurements; smooth- and rough-wall pipe flow; friction factor; computational fluid dynamics boundary conditions

1. Introduction

The turbulence intensity (TI) is of great importance in, e.g., industrial fluid mechanics, where it can be used for computational fluid dynamics (CFD) simulations as a boundary condition [1]. The TI is at the center of the fruitful junction between fundamental and industrial fluid mechanics.

This paper contains an extension of the TI scaling research in [2] (smooth-wall pipe flow) and [3] (smooth- and rough-wall pipe flow). As in those papers, we treat streamwise velocity measurements from the Princeton Superpipe [4,5]. The measurements were done at low speed in compressed air with a pipe radius of about 65 mm. Details on, e.g., the bulk Reynolds number range and uncertainty estimates can be found in [4]. Other published measurements including additional velocity components can be found in [6] (smooth-wall pipe flow) and [7,8] (smooth- and rough-wall pipe flow).

Our approach to streamwise TI scaling is global averaging; physical mechanisms include separate inner- and outer-region phenomena and interactions between those [9]. Here, the inner (outer) region is close to the pipe wall (axis), respectively.

The local TI definition (see, e.g., Figure 9 in [10]) is:

$$I(r) = \frac{v_{\mathrm{RMS}}(r)}{v(r)}, \tag{1}$$

where r is the radius ($r = 0$ is the pipe axis and $r = R$ is the pipe wall), $v(r)$ is the local mean streamwise flow velocity, and $v_{\mathrm{RMS}}(r)$ is the local root-mean-square (RMS) of the turbulent streamwise velocity fluctuations. Using the radial coordinate r means that outer scaling is employed for the position. As was done in [2,3], we use v as the streamwise velocity (in much of the literature, u is used for the streamwise velocity).

The measurements in [10] were on turbulent flow in a two-dimensional channel and similar work for pipe flow was published in [11].

In this paper, we study TI defined using a global (radial) averaging of the streamwise velocity fluctuations. The mean flow is either included in the global averaging or as a reference velocity. This covers the majority of the standard TI definitions.

There is a plethora of TI definitions, which is why we use the term fugue in the title. This is inspired by [12], where Frank Herbert's *Dune* novels [13] are interpreted as "an ecological fugue".

The ultimate purpose of our work is to be able to present a robust and well-researched formulation of the TI; an equivalent TI in the presence of shear flow. Our work is not adding significant knowledge of the fundamental processes [14–16], but we need to understand them in order to use them as a foundation for the scaling expressions.

The main contributions of this paper compared to [3] are:

- The introduction of additional definitions of the TI
- Log-law fits in addition to power-law fits
- New findings on the rough pipe friction factor behaviour of the Princeton Superpipe measurements.

Furthermore, we include a discussion on the link between the TI and the friction factor [3,17] in the light of the Fukagata–Iwamoto–Kasagi (FIK) identity [18].

Our paper is organised as follows: In Section 2, we introduce the velocity definitions. These are used in Section 3 to define various TI expressions. In Section 4 we present scaling laws using the presented definitions. We discuss our findings in Section 5 and conclude in Section 6.

2. Velocity Definitions

The friction velocity is:

$$v_\tau = \sqrt{\tau_w/\rho}, \tag{2}$$

where τ_w is the wall shear stress and ρ is the fluid density.

The area-averaged (AA) velocity of the turbulent fluctuations is:

$$\langle v_{\text{RMS}} \rangle_{\text{AA}} = \frac{2}{R^2} \times \int_0^R v_{\text{RMS}}(r) r \mathrm{d}r \tag{3}$$

The fit between v_τ and $\langle v_{\text{RMS}} \rangle_{\text{AA}}$ is shown in Figure 1:

$$\langle v_{\text{RMS}} \rangle_{\text{AA}} = 1.7277 \times v_\tau \tag{4}$$

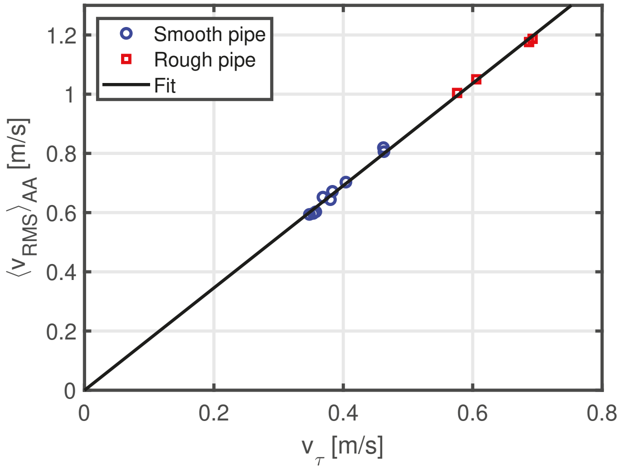

Figure 1. Relationship between v_τ and $\langle v_{\text{RMS}} \rangle_{\text{AA}}$.

The velocity on the pipe axis is the centerline (CL) velocity:

$$v_{\text{CL}} = v(r = 0) \tag{5}$$

The (area-averaged) mean velocity is given by:

$$v_m = \frac{2}{R^2} \times \int_0^R v(r) r \mathrm{d}r \tag{6}$$

The difference between the centerline and the mean velocity scales with the friction velocity. The corresponding fit is shown in Figure 2:

$$v_{\mathrm{CL}} - v_m = 4.4441 \times v_\tau, \tag{7}$$

where the fit constant is close to the value of 4.28 [19] found using earlier Princeton Superpipe measurements [20].

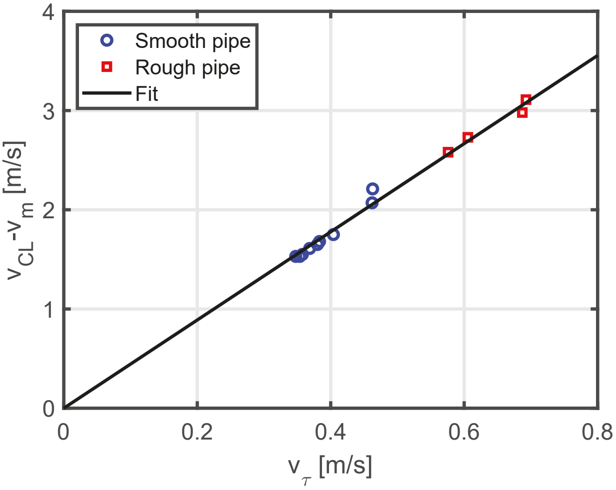

Figure 2. Relationship between v_τ and $v_{\mathrm{CL}} - v_m$.

3. Turbulence Intensity Definitions

3.1. Local Velocity Definitions

The arithmetic mean (AM) definition is:

$$I_{\text{Pipe area, AM}} = \frac{1}{R} \int_0^R \frac{v_{\mathrm{RMS}}(r)}{v(r)} \mathrm{d}r \tag{8}$$

The area-averaged definition is:

$$I_{\text{Pipe area, AA}} = \frac{2}{R^2} \int_0^R \frac{v_{\mathrm{RMS}}(r)}{v(r)} r \mathrm{d}r \tag{9}$$

In [3] (Equation (9)), $\langle v_{\mathrm{RMS}} \rangle$ was defined as the product of v_m and $I_{\text{Pipe area, AA}}$. Comparing the resulting Equations (11) and (12) in [3] to the current Equation (4), we find a difference of less than 5% (9/5 compared to 1.7277).

Finally, the volume-averaged (VA) definition (inspired by the FIK identity) is:

$$I_{\text{Pipe area, VA}} = \frac{3}{R^3} \int_0^R \frac{v_{\mathrm{RMS}}(r)}{v(r)} r^2 \mathrm{d}r \tag{10}$$

3.2. Reference Velocity Definitions

As mentioned in the Introduction, we use outer scaling for the radial position r. For the TI, we separate the treatment to inner and outer scaling below, see, e.g., [15].

3.2.1. Inner Scaling

For inner scaling, we define the TI using v_τ as the reference velocity:

$$I_\tau = \frac{\langle v_{\mathrm{RMS}} \rangle_{\mathrm{AA}}}{v_\tau} = 1.7277, \tag{11}$$

where the final equation is found using Equation (4).

The square of the local version of this, $I_\tau^2(r) = \frac{v_{\mathrm{RMS}}(r)^2}{v_\tau^2}$, is often used as the TI in the literature, see also Section 5.1 in [3]. This is the normal streamwise Reynolds stress normalised by the friction velocity squared.

I_τ is shown in Figure 3; no scaling is observed with Re_{D}, the bulk Reynolds number:

$$Re_{\mathrm{D}} = \frac{D v_m}{\nu_{\mathrm{kin}}}, \tag{12}$$

where $D = 2R$ is the pipe diameter and ν_{kin} is the kinematic viscosity.

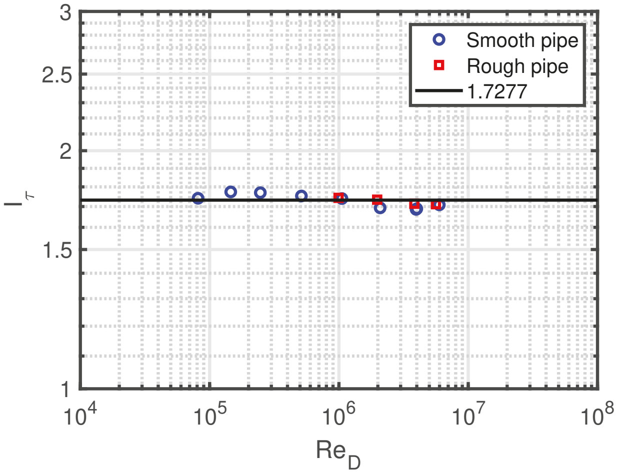

Figure 3. I_τ as a function of Re_{D}.

3.2.2. Outer Scaling

For outer scaling, we use either v_m or v_{CL} as the reference velocity.
The TI using v_m as the reference velocity is:

$$I_m = \frac{\langle v_{\mathrm{RMS}} \rangle_{\mathrm{AA}}}{v_m} \tag{13}$$

Finally, the TI using v_{CL} as the reference velocity [15] is:

$$I_{\mathrm{CL}} = \frac{\langle v_{\mathrm{RMS}} \rangle_{\mathrm{AA}}}{v_{\mathrm{CL}}} \tag{14}$$

4. Turbulence Intensity Scaling Laws

The Princeton Superpipe measurements and the TI definitions in Section 3 are used to create the TI data points. Thereafter we fit the points using the power-law fit:

$$Q_{\text{Power-law fit}}(x) = a \times x^b, \tag{15}$$

and the log-law fit:

$$Q_{\text{Log-law fit}}(x) = c \times \ln(x) + d \tag{16}$$

Here, a, b, c, and d are constants. Q is the quantity to fit and x is a corresponding variable. We first apply the two fits using $Q = I$ and $x = Re_{\text{D}}$.

The log-law fit is obtained by taking the (natural) logarithm of the power-law fit. The reason we use these two fits is that they have been discussed in the literature [21,22] as likely scaling candidates. We apply the two fits to the measurements and calculate the resulting root-mean-square deviations (RMSD) between the fits and the measurements. A small RMSD means that the fit is closer to the measurements.

Note that the smooth pipe Re_{D} measurement range is much larger than the rough pipe Re_{D} measurement range: a factor of 74 (9 points) compared to a factor of 6 (4 points). The consequence is a major uncertainty in the rough pipe results, e.g., (i) fits and (ii) extrapolation.

It is also important to be aware that we only have two sets of measurements with the following sand-grain roughnesses k_s:

- Smooth pipe: $k_s = 0.45$ µm [23]
- Rough pipe: $k_s = 8$ µm [24] (see the related discussion in Section 5.1)

The results are presented in Figures 4 and 5 and Tables 1–4.

We do not discuss the quality of fits to the rough pipe, since there are only 4 measurements for a single k_s. Thus, these values are provided as a reference.

For the smooth pipe, the power-law fits perform slightly better than the log-law fits, except for the CL definition. The best fit is using the power-law fit to the AA definition of the TI:

$$I_{\text{Pipe area, AA}} = 0.3173 \times Re_{\text{D}}^{-0.1095}, \tag{17}$$

which is the same as Equation (5) in [3].

Table 1. Power-law fit constants, smooth pipe.

TI Definition	a	b	RMSD
$I_{\text{Pipe area, AM}}$	0.2274	−0.1004	4.0563×10^{-4}
$I_{\text{Pipe area, AA}}$	0.3173	−0.1095	3.5932×10^{-4}
$I_{\text{Pipe area, VA}}$	0.3758	−0.1134	3.6210×10^{-4}
I_m	0.2657	−0.1000	5.2031×10^{-4}
I_{CL}	0.1811	−0.0837	6.9690×10^{-4}

Table 2. Log-law fit constants, smooth pipe.

TI Definition	c	d	RMSD
$I_{\text{Pipe area, AM}}$	−0.0059	0.1391	6.7748×10^{-4}
$I_{\text{Pipe area, AA}}$	−0.0080	0.1808	8.8173×10^{-4}
$I_{\text{Pipe area, VA}}$	−0.0093	0.2074	1.1018×10^{-3}
I_m	−0.0069	0.1634	5.8899×10^{-4}
I_{CL}	−0.0049	0.1257	5.4179×10^{-4}

Table 3. Power-law fit constants, rough pipe.

TI Definition	a	b	RMSD
$I_{\text{Pipe area, AM}}$	0.1172	-0.0522	4.0830×10^{-4}
$I_{\text{Pipe area, AA}}$	0.1702	-0.0638	3.5784×10^{-4}
$I_{\text{Pipe area, VA}}$	0.1989	-0.0667	3.7697×10^{-4}
I_m	0.1568	-0.0610	3.4902×10^{-4}
I_{CL}	0.1177	-0.0519	3.4317×10^{-4}

Table 4. Log-law fit constants, rough pipe.

TI Definition	c	d	RMSD
$I_{\text{Pipe area, AM}}$	-0.0028	0.0960	4.3111×10^{-4}
$I_{\text{Pipe area, AA}}$	-0.0042	0.1291	4.0028×10^{-4}
$I_{\text{Pipe area, VA}}$	-0.0050	0.1477	4.2938×10^{-4}
I_m	-0.0039	0.1213	3.8575×10^{-4}
I_{CL}	-0.0028	0.0967	3.6542×10^{-4}

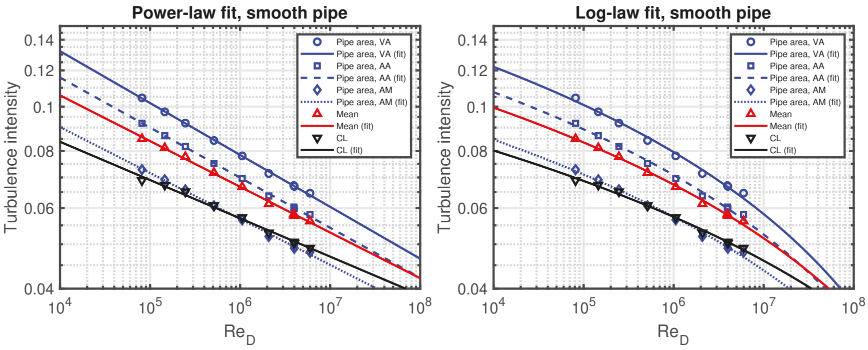
Power-law fit, smooth pipe

Log-law fit, smooth pipe

Figure 4. Smooth pipe turbulence intensity as a function of Re_D, left: Power-law fit, right: Log-law fit.

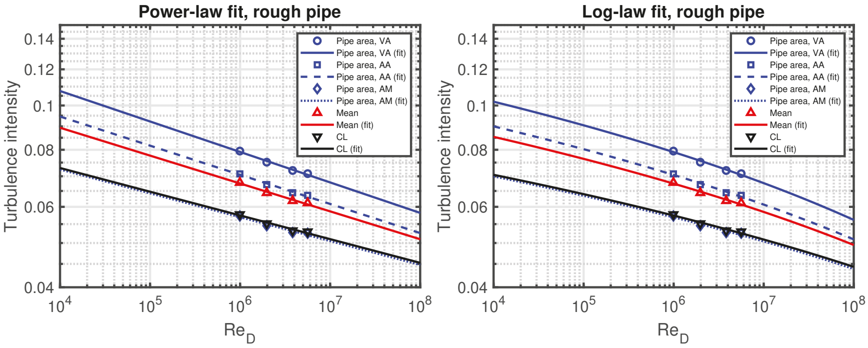
Power-law fit, rough pipe

Log-law fit, rough pipe

Figure 5. Rough pipe turbulence intensity as a function of Re_D, left: Power-law fit, right: Log-law fit.

Instead of Re_D, one can also express the TI fits using the friction Reynolds number [4]:

$$Re_\tau = \frac{R v_\tau}{\nu_{\text{kin}}} = \frac{v_\tau}{2 v_m} \times Re_\text{D} \tag{18}$$

The relationship between Re_D and Re_τ can fitted using Equation (15) where $Q = Re_\tau$ and $x = Re_\text{D}$, see Figure 6 and Table 5. A log-law fit was also performed but resulted in a bad fit, i.e., a RMSD which was between one and two orders of magnitude larger than for the power-law fit. As mentioned above, the rough pipe fit is only provided as a reference. For channel flow, it has been found that $a = 0.09$ and $b = 0.88$, see Figure 7.11 in [25] and associated text.

We choose to focus on the bulk Reynolds number since it is possible to determine for applications where the friction velocity is unknown.

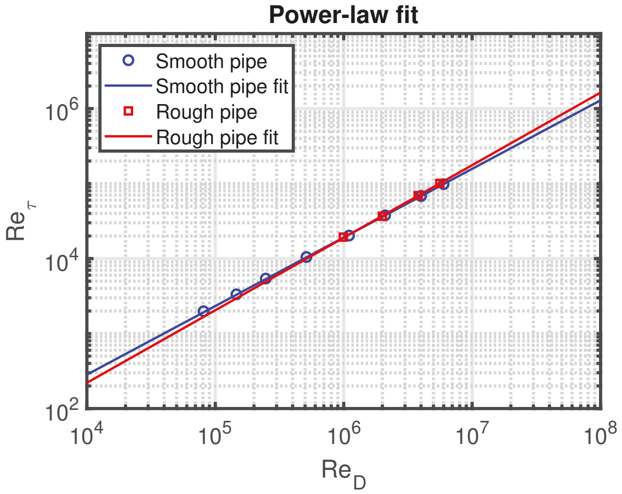

Figure 6. Relationship between Re_{D} and Re_{τ}.

Table 5. Bulk and friction Reynolds number fits.

Case	a	b
Smooth	0.0621	0.9148
Rough	0.0297	0.9675

5. Discussion

5.1. Friction Factor

In [26], the following expression for the smooth pipe friction factor has been derived based on Princeton Superpipe measurements:

$$\frac{1}{\sqrt{\lambda_{\mathrm{Smooth}}}} = 1.930 \log_{10}\left(Re_{\mathrm{D}}\sqrt{\lambda_{\mathrm{Smooth}}}\right) - 0.537 \tag{19}$$

A corresponding rough pipe friction factor has been proposed in [27]:

$$\frac{1}{\sqrt{\lambda_{\mathrm{Rough}}}} = -2 \log_{10}\left(\frac{k_s}{3.7D} + \frac{2.51}{Re_{\mathrm{D}}\sqrt{\lambda_{\mathrm{Rough}}}}\right) \tag{20}$$

The friction factor can also be expressed using the friction velocity and the mean velocity, see Equation (1.1) in [26]:

$$\lambda = 8 \times \frac{v_{\tau}^2}{v_m^2} \tag{21}$$

or:

$$\frac{v_{\tau}}{v_m} = \sqrt{\frac{\lambda}{8}} \tag{22}$$

The equations for the smooth- and rough-wall pipe flow friction factors are shown in Figure 7, along with Princeton Superpipe measurements.

We have included additional smooth pipe measurements [20,28]. Both sets agree with Equation (19).

Additional rough pipe measurements can be found in Table 2 (and Figure 3) in [24]. Here, it was found that $k_s = 8$ µm. For our main data set [4,5], $k_s = 8$ µm does not match the measurements; instead we get $k_s = 3$ µm for a fit to those measurements using Equation (20). It is the same pipe; the reason for the discrepancy is not clear [29]. However, the difference is within the experimental uncertainty of 5% stated in [24].

For the rough pipe friction factor, we use $k_s = 3$ µm in the remainder of this paper.

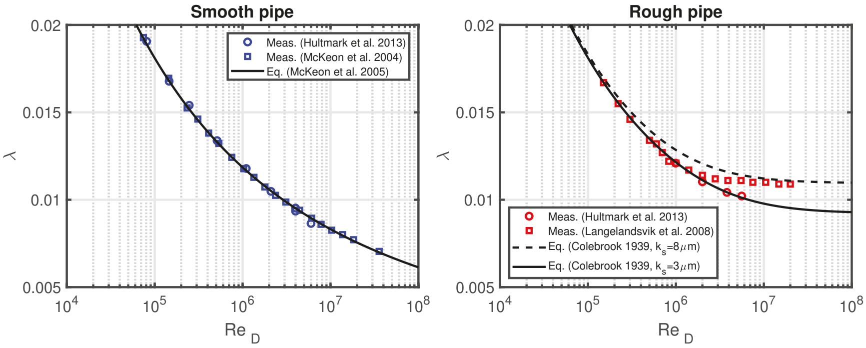

Figure 7. Friction factors, left: Smooth pipe, right: Rough pipe.

5.2. Turbulence Intensity Aspects

5.2.1. Importance for Flow

The TI is an important quantity for many physical phenomena [30], e.g.:

- The critical Reynolds number for the drag of a sphere [31]
- The laminar–turbulent transition [32]
- Development of the turbulent boundary layer [33]
- The position of flow separation [34]
- Heat transfer [35]
- Wind farms [36]
- Wind tunnels [37].

We mention these examples to illustrate the importance of the TI for real world applications.

5.2.2. Scaling with the Friction Factor

The wall-normal [17] and streamwise (this paper and [3]) Reynolds stress have both been shown to be linked to the friction factor $\lambda = 4C_f$, where C_f is the skin friction coefficient. These observations can be interpreted as manifestations of the FIK identity [18], where an equation for C_f is derived based on the streamwise momentum equation: C_f is proportional to the integral over the Reynolds shear stress weighted by the quadratic distance from the pipe axis.

An alternative formulation for C_f based on the streamwise kinetic energy is derived in [38]: here, C_f is proportional to the integral over the Reynolds shear stress multiplied by the streamwise mean velocity gradient weighted by the distance from the pipe axis. It is concluded that the logarithmic region dominates friction generation for high Reynolds number flow. The dominance of the logarithmic region has been confirmed in [39].

The seeming equivalence between Reynolds stress (shear or normal) and the friction factor leads us to propose that the TI scales with v_τ / v_m. Therefore we fit to Equations (15) and (16) using $Q = I$ and $x = v_\tau / v_m$, see Figure 8 and Tables 6 and 7.

In this case, the power-law fits are best for the local velocity definitions and the log-law fits are best for the reference velocity definitions. Overall, the best fit is the power-law fit using the AM definition of the TI:

$$I_{\text{Pipe area, AM}} = 0.6577 \times \lambda^{0.5531}, \tag{23}$$

which is a modification of Equation (14) in [3].

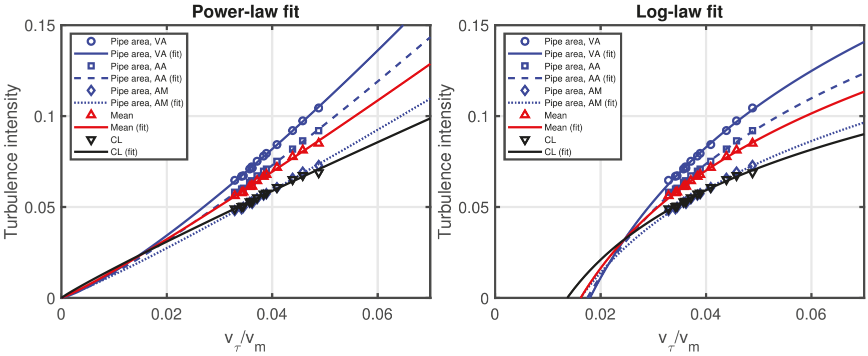

Figure 8. TI as a function of v_τ / v_m.

Table 6. Power-law fit constants.

TI Definition	a	b	RMSD
$I_{\text{Pipe area, AM}}$	2.0776	1.1062	4.7133×10^{-4}
$I_{\text{Pipe area, AA}}$	3.5702	1.2088	5.0224×10^{-4}
$I_{\text{Pipe area, VA}}$	4.6211	1.2530	4.9536×10^{-4}
I_m	2.4238	1.1039	6.8412×10^{-4}
I_{CL}	1.1586	0.9260	7.5876×10^{-4}

Table 7. Log-law fit constants.

TI Definition	c	d	RMSD
$I_{\text{Pipe area, AM}}$	0.0658	0.2715	5.5459×10^{-4}
$I_{\text{Pipe area, AA}}$	0.0890	0.3602	6.6955×10^{-4}
$I_{\text{Pipe area, VA}}$	0.1036	0.4162	8.0775×10^{-4}
I_m	0.0775	0.3195	5.5182×10^{-4}
I_{CL}	0.0551	0.2367	5.8536×10^{-4}

Combining Equation (22) with Equations (15) and (16) leads to:

$$I_{\text{Power-law fit}}(\lambda) = a \times \left(\frac{\lambda}{8}\right)^{b/2} \tag{24}$$

$$I_{\text{Log-law fit}}(\lambda) = \frac{c}{2} \times \ln\left(\frac{\lambda}{8}\right) + d \tag{25}$$

The predicted TI for the best case (power-law AM) is shown in Figure 9; one reason for the better match to measurements compared to Figure 9 in [3] is that we use $k_s = 3$ µm instead of $k_s = 8$ µm for the rough pipe. The correspondence between the TI and the friction factor means that the TI will approach a constant value for rough-wall pipe flow at large Re_D (fully rough regime). It also means that a larger k_s leads to a higher TI.

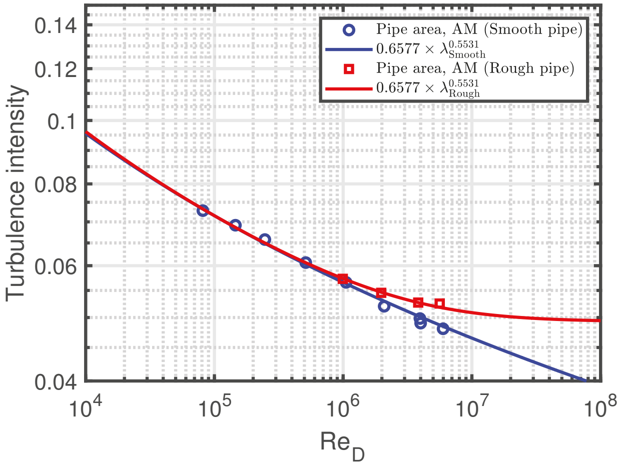

Figure 9. AM definition of TI as a function of Re_D for smooth- and rough-wall pipe flow.

5.2.3. CFD Definition

Let us now consider a typical CFD turbulence model, the standard $k - \varepsilon$ model [40]. Here, k is the turbulent kinetic energy (TKE) per unit mass and ε is the rate of dissipation of TKE per unit mass.

As an example of a boundary condition, the user provides the TI (I_{user}) and the turbulent viscosity ratio μ_t/μ, where μ_t is the dynamic turbulent viscosity and μ is the dynamic viscosity. For a defined reference velocity v_{ref}, k can then be calculated as:

$$k = \frac{3}{2}\left(v_{\text{ref}} I_{\text{user}}\right)^2 \tag{26}$$

As the next step, ε is defined as:

$$\varepsilon = \frac{\rho C_\mu k^2}{(\mu_t/\mu)\,\mu}, \tag{27}$$

where ρ is density and $C_\mu = 0.09$.

An example of default CFD settings is $I_{\text{user}} = 0.01$ (1%) and $\mu_t/\mu = 10$.

The output from a CFD simulation is the total TKE, not the individual components. If we assume that the turbulence is isotropic, the streamwise TI we are treating in this paper is proportional to the square root of the TKE:

$$v_{\text{RMS}} = \sqrt{\frac{2}{3}k} \tag{28}$$

5.2.4. Proposed Procedure for CFD and an Example

A standard definition of TI for CFD is to use the free-stream velocity as the reference velocity, i.e., I_{CL} for pipe flow. For I_{CL}, we use the log-law version since this has the smallest RMSD, see Tables 6 and 7:

$$I_{\text{CL}} = 0.0276 \times \ln(\lambda) + 0.1794 \tag{29}$$

We note that this scaling is based on the Princeton Superpipe measurements; for industrial applications, the TI may be much higher, so our scaling should be considered as a lower limit.

A procedure to calculate the TI, e.g., for use in CFD is:

1. Define Re_D (and k_s for a rough pipe)
2. Calculate the friction factor: Equation (19) for a smooth pipe and Equation (20) for a rough pipe
3. Use Equation (29) to calculate the TI.

As a concrete example, we consider incompressible (water) flow through a 130 mm diameter pipe. CFD boundary conditions can be velocity inlet and pressure outlet. The steps are:

1. Define the mean velocity, we use 10 m/s
2. Calculate $Re_D = 1.3 \times 10^6$
3. Use Equation (19) to calculate $\lambda_{\text{Smooth}} = 0.0114$
4. Use Equation (29) to calculate $I_{\text{CL}} = 0.0561$.

For this example, we conclude that the minimum TI is 5.6%. A code with this example is available as Supplementary Materials, a link is provided after the Conclusions.

5.2.5. Open Questions

It remains an open question to what extent the quality of the fits (RMSD) impacts the outcome of a CFD simulation. For the TI definitions used, the RMSD varies less than a factor of two for the fits of TI as a function of v_τ / v_m, see Tables 6 and 7. For CFD, a single TI definition is used, so it is not possible to switch TI models in CFD and compare simulations to measurements.

To continue our measurement-based research, we would need measurements of all velocity components, i.e., wall-normal and spanwise, in addition to the available streamwise measurements.

As mentioned earlier [2], it would also be interesting to have measurements for higher Mach numbers, where compressibility will play a larger role.

In addition to pipe flow, other canonical flows, such as zero-pressure gradient flows [14], might be suitable for analysis similar to what we have presented.

6. Conclusions

We have used Princeton Superpipe measurements of smooth- and rough-wall pipe flow [4,5] to study the properties of various TI definitions. The scaling of TI with Re_D is provided for the definitions. For scaling purposes, we recommend the AA definition and a power-law fit: Equation (17). The TI also scales with v_τ / v_m, where the best result is obtained with a power-law fit and the AM definition. This fit implies that the turbulence level scales with the friction factor: Equation (23).

Scaling of TI with Re_D and v_τ / v_m was done using both power-law and log-law fits.

A proposed procedure to calculate the TI, e.g., CFD is provided and exemplified in Section 5.2.4.

Supplementary Materials: The following is available online at https://www.researchgate.net/publication/336374461_Python_code_to_calculate_turbulence_intensity_based_on_Reynolds_number_and_surface_roughness, Supplementary Material: Python code to calculate turbulence intensity based on Reynolds number and surface roughness.

Funding: This research received no external funding.

Acknowledgments: We thank Alexander J. Smits for making the Princeton Superpipe data publicly available.

Conflicts of Interest: The authors declare no conflict of interest.

References

1. *ANSYS Fluent User's Guide, Release 19.0, Section 6.3.2.1.3*; ANSYS, Inc.: Canonsburg, PA, USA, 2018.
2. Russo, F.; Basse, N.T. Scaling of turbulence intensity for low-speed flow in smooth pipes. *Flow Meas. Instrum.* **2016**, *52*, 101–114. [CrossRef]
3. Basse, N.T. Turbulence intensity and the friction factor for smooth- and rough-wall pipe flow. *Fluids* **2017**, *2*, 30. [CrossRef]

4. Hultmark, M.; Vallikivi, M.; Bailey, S.C.C.; Smits, A.J. Logarithmic scaling of turbulence in smooth- and rough-wall pipe flow. *J. Fluid Mech.* **2013**, *728*, 376–395. [CrossRef]
5. Princeton Superpipe. Available online: https://smits.princeton.edu/superpipe-turbulence-data (accessed on 5 July 2019).
6. Willert, C.E.; Soria. J.; Stanislas, M.; Klinner, J.; Amili, O.; Eisfelder, M.; Cuvier. C.; Bellani, G.; Fiorini, T.; Talamelli, A. Near-wall statistics of a turbulent pipe flow at shear Reynolds numbers up to 40 000. *J. Fluid Mech.* **2017**, *826*, R5. [CrossRef]
7. Schultz, M.P.; Flack, K.A. The rough-wall turbulent boundary layer from the hydraulically smooth to the fully rough regime. *J. Fluid Mech.* **2007**, *580*, 381–405. [CrossRef]
8. Flack, K.A.; Schultz, M.P. Roughness effects on wall-bounded turbulent flows. *Phys. Fluids* **2014**, *26*, 101305. [CrossRef]
9. Marusic, I.; Baars, W.J.; Hutchins, N. Scaling of the streamwise turbulence intensity in the context of inner-outer interactions in wall turbulence. *Phys. Rev. Fluids* **2017**, *2*, 100502. [CrossRef]
10. Laufer, J. *Investigation of Turbulent Flow in a Two-Dimensional Channel*; NACA-TR-1053; National Advisory Committee for Aeronautics: Washington, DC, USA, 1951.
11. Laufer, J. *The Structure of Turbulence in Fully Developed Pipe Flow*; NACA-TR-1174; National Advisory Committee for Aeronautics: Washington, DC, USA, 1954.
12. Touponce, W.F. *Frank Herbert*; Twayne Publishers: Boston, MA, USA, 1988.
13. Frank Herbert's Classic Dune. Available online: http://www.dunenovels.com/frank-herbert-classic-dune (accessed on 5 July 2019).
14. Marusic, I.; Kunkel, G.J. Streamwise turbulence intensity formulation for flat-plate boundary layers. *Phys. Fluids* **2003**, *15*, 2461–2464. [CrossRef]
15. Alfredsson, P.H.; Örlü, R.; Segalini, A. A new formulation for the streamwise turbulence intensity distribution in wall-bounded turbulent flows. *Eur. J. Mech. B Fluids* **2012**, *36*, 167–175. [CrossRef]
16. Monkewitz, P.A.; Nagib, H.M. Large-Reynolds number asymptotics of the streamwise normal stress in zero-pressure-gradient turbulent boundary layers. *J. Fluid Mech.* **2015**, *783*, 474–503. [CrossRef]
17. Orlandi, P. The importance of wall-normal Reynolds stress in turbulent rough channel flows. *Phys. Fluids* **2013**, *25*, 110813. [CrossRef]
18. Fukagata, K.; Iwamoto, K.; Kasagi, N. Contribution of Reynolds stress distribution to the skin friction in wall-bounded flows. *Phys. Fluids.* **2002**, *14*, L73–L76. [CrossRef]
19. Gersten, K. Fully developed turbulent pipe flow. In *Fluid Mechanics of Flow Metering*; Merzkirch, W., Ed.; Springer: Berlin, Germany, 2005.
20. Princeton Superpipe. Available online: https://smits.princeton.edu/mckeon (accessed on 5 July 2019).
21. Barenblatt, G.I. Scaling laws for fully developed turbulent shear flows. Part 1. Basic hypotheses and analysis. *J. Fluid Mech.* **1993**, *248*, 513–520. [CrossRef]
22. Zagarola, M.V.; Perry, A.E.; Smits, A.J. Log laws or power laws: The scaling in the overlap region. *Phys. Fluids* **1997**, *9*, 2094–2100. [CrossRef]
23. Zagarola, M.V.; Smits, A.J. Mean-flow scaling of turbulent pipe flow. *J. Fluid Mech.* **1998**, *373*, 33–79. [CrossRef]
24. Langelandsvik, L.I.; Kunkel, G.J.; Smits, A.J. Flow in a commercial steel pipe. *J. Fluid Mech.* **2008**, *595*, 323–339. [CrossRef]
25. Pope, S.B. *Turbulent Flows*; Cambridge University Press: Cambridge, UK, 2000.
26. McKeon, B.J.; Zagarola, M.V.; Smits, A.J. A new friction factor relationship for fully developed pipe flow. *J. Fluid Mech.* **2005**, *538*, 429–443. [CrossRef]
27. Colebrook, C.F. Turbulent flow in pipes, with particular reference to the transition region between the smooth and rough pipe laws. *J. Inst. Civ. Eng.* **1939**, *11*, 133–156. [CrossRef]
28. McKeon, B.J.; Li, J.; Jiang, W.; Morrison, J.F; Smits, A.J. Further observations on the mean velocity distribution in fully developed pipe flow. *J. Fluid Mech.* **2004**, *501*, 135–147. [CrossRef]
29. Hultmark, M. (Princeton University, Princeton, New Jersey, USA). Personal communication, 2017.
30. Schlichting, H.; Gersten, K. *Boundary-Layer Theory*, 8th ed.; Springer: Berlin, Germany, 2000.
31. Zarin, N.A. *Measurement of Non-Continuum and Turbulence Effects on Subsonic Sphere Drag*; NASA CR-1585; National Aeronautics and Space Administration: Washington, DC, USA, 1970.

32. Fransson, J.H.M; Matsubara, M.; Alfredsson, P.H. Transition induced by free-stream turbulence. *J. Fluid Mech.* **2005**, *527*, 1—25. [CrossRef]
33. Hollingsworth, D.K.; Bourgogne, H.-A. The development of a turbulent boundary layer in high free-stream turbulence produced by a two-stream mixing layer. *Exp. Therm. Fluid Sci.* **1995**, *11*, 210–222. [CrossRef]
34. Scheichl, B.; Kluwicki, A.; Smith, F.T. Break-away separation for high turbulence intensity and large Reynolds number. *J. Fluid Mech.* **2011**, *670*, 260—300. [CrossRef]
35. Ahn, J.; Sparrow, E.M.; Gorman, J.M. Turbulence intensity effects on heat transfer and fluid-flow for a circular cylinder in crossflow. *Int. J. Heat Mass Trans.* **2017**, *113*, 613-621. [CrossRef]
36. Hansen, K.S.; Barthelmie, R.J.; Jensen, L.E.; Sommer, A. The impact of turbulence intensity and atmospheric stability on power deficits due to wind turbine wakes at Horns Rev wind farm. *Wind Energy* **2012**, *15*, 183–196. [CrossRef]
37. Calautita, J.K.; Chaudhrya, H.N.; Hughes, B.R.; Sim, L.F. A validated design methodology for a closed-loop subsonic wind tunnel. *J. Wind Eng. Ind. Aerodyn.* **2014**, *125*, 180–194. [CrossRef]
38. Renard, N.; Deck, S. A theoretical decomposition of mean skin friction generation into physical phenomena across the boundary layer. *J. Fluid Mech.* **2016**, *790*, 339–367. [CrossRef]
39. De Giovanetti, M.; Hwang, Y.; Choi, H. Skin-friction generation by attached eddies in turbulent channel flow. *J. Fluid Mech.* **2016**, *808*, 511–538. [CrossRef]
40. Versteeg, H.K.; Malalasekera, W. *An Introduction to Computational Fluid Dynamics: The Finite Volume Method*, 2nd ed.; Pearson Education Limited: Harlow, UK, 2007.

fluids

MDPI

Review

A Review of Vortex Methods and Their Applications: From Creation to Recent Advances

Chloé Mimeau * and Iraj Mortazavi

Laboratory M2N, CNAM, 75003 Paris, France; iraj.mortazavi@cnam.fr
* Correspondence: chloe.mimeau@cnam.fr; Tel.: +33-0140-272-283

Abstract: This review paper presents an overview of Vortex Methods for flow simulation and their different sub-approaches, from their creation to the present. Particle methods distinguish themselves by their intuitive and natural description of the fluid flow as well as their low numerical dissipation and their stability. Vortex methods belong to Lagrangian approaches and allow us to solve the incompressible Navier-Stokes equations in their velocity-vorticity formulation. In the last three decades, the wide range of research works performed on these methods allowed us to highlight their robustness and accuracy while providing efficient computational algorithms and a solid mathematical framework. On the other hand, many efforts have been devoted to overcoming their main intrinsic difficulties, mostly relying on the treatment of the boundary conditions and the distortion of particle distribution. The present review aims to describe the Vortex methods by following their chronological evolution and provides for each step of their development the mathematical framework, the strengths and limits as well as references to applications and numerical simulations. The paper ends with a presentation of some challenging and very recent works based on Vortex methods and successfully applied to problems such as hydrodynamics, turbulent wake dynamics, sediment or porous flows.

Keywords: hydrodynamics; incompressible flows; particle methods; remeshing; semi-Lagrangian vortex methods; vortex methods; Vortex-Particle-Mesh methods; vorticity; wake dynamics

check for updates

Citation: Mimeau, C.; Mortazavi, I. A Review of Vortex Methods and Their Applications: From Creation to Recent Advances. *Fluids* **2021**, *6*, 68. https://doi.org/10.3390/fluids6020068

Academic Editor: Markus Klein
Received: 24 December 2020
Accepted: 28 January 2021
Published: 4 February 2021

1. Introduction

Vortex methods (VM) belong to Lagrangian methods, also called particle methods, used to solve continuous systems of the form:

$$\frac{d}{dt}\int_{\Omega}\mathbf{Q}(\mathbf{x},t)\,d\mathbf{x}=\int_{\Omega}\mathbf{F}(\mathbf{x},t,\mathbf{Q},\nabla\mathbf{Q},\ldots)\,d\mathbf{x} \tag{1}$$

where $\mathbf{Q}$ denotes the unsteady solution vector evolving in space ($\mathbf{x}$) and time (t), composed of the physical quantities Q_i, and where $\mathbf{F}$ is the source term depending on space and time and on the solution $\mathbf{Q}$ and its partial derivatives. In a general point of view, Lagrangian methods differ from Eulerian ones by the way they discretize the problem. In an Eulerian approach, the computational domain is described as a mesh and the solution vector $\mathbf{Q}$ is approximated on each node according to a numerical scheme involving the solution at the neighboring mesh nodes. In the Lagrangian framework, the domain discretization is not realized on a mesh but on a set of particles that follow the dynamic of the system and are displaced with respect to the flow velocity $\mathbf{u}$. More precisely, in the Lagrangian approach, the solution $\mathbf{Q}$ is discretized on numerical particles and, given a location $\mathbf{x}$ in the domain, each quantity Q among the vector solution $\mathbf{Q}$ is thus approximated at this location $\mathbf{x}$ by:

$$Q(\mathbf{x})=\int_{\Omega}Q(\mathbf{y})\delta(\mathbf{x}-\mathbf{y})\,d\mathbf{y} \tag{2}$$

where δ denotes the Dirac distribution. To write this expression in a regularized and discrete form, the Lagrangian methods define a volume v_p for the particles as well as a smoothing function W, of compact support and radial symmetry of radius ε, which tends to the Dirac distribution when ε tends to 0. Therefore, the discrete approximation of the quantity Q at location $\mathbf{x}$ can be written as:

$$Q(\mathbf{x}) \simeq \sum_p Q_p W_\varepsilon(\mathbf{x} - \mathbf{x}_p) \tag{3}$$

In other words, the quantity Q at location $\mathbf{x}$ is evaluated as the sum of the quantity Q carried by the particles p located in the compact support of the smoothing radial function W of radius ε, centered at location $\mathbf{x}$. The Lagrangian discretization of the continuous system (1) is therefore obtained by solving the following system of ordinary differential equations (ODEs) in order to update the particle positions $\mathbf{x}_p$, their volume v_p and each quantity Q_p they carry according to the source term $\mathbf{F}$:

$$\begin{cases} \dfrac{d\mathbf{x}_p}{dt} = \mathbf{u}(\mathbf{x}_p, t) \\ \dfrac{dv_p}{dt} = v_p \mathrm{div}(\mathbf{u}(\mathbf{x}_p)) \\ \dfrac{dQ_p}{dt} = v_p \mathbf{F}_p \end{cases} \tag{4}$$

The key common thread of all particle methods used for continuum flow simulations therefore relies on the approximation in the Lagrangian form of the governing continuous Equation (1) where the derivative operators involved in $\mathbf{F}$ are replaced by equivalent integral operators that are then discretized on the particle locations. Among the most popular particle methods used to solve continuous equations, one can cite the Vortex Methods (VM) and the Smooth Particle Hydrodynamics (SPH). They differ from each other by the governing Equation (1) they aim to solve and by the way they handle the resolution of the third ODE of system (4). SPH methods [1–5] solve the weakly compressible Navier-Stokes equations in velocity-pressure formulation and the particles carry the pressure and the flow density variables. They need a coupling with an equation of state to close the governing system. Regarding Vortex Methods, they are used to solve the incompressible Navier-Stokes equations in their velocity-vorticity formulation and the particles only carry the vorticity field.

If one starts from a present observation, one admits that in the computational fluid dynamic community, Vortex Methods do not benefit from the same recognition or the same expanded scope than Eulerian methods (spectral methods, finite elements, finite volumes, finite differences, etc.). However, they early raised the interest of the CFD research community due to their capability to precisely and naturally simulate flows dominated by the advection phenomenon. They have been the subject of plentiful of research works, which allowed these last recent years to lead to challenging applications involving important issues in fluid dynamics, in particular in hydrodynamics [6–9], in flow mediated transport [10,11], in turbulent wake dynamics of rotorcrafts [12,13], aircrafts [13,14] and vertical axis wind turbines [15,16], in aeroacoustics [17], in free jet flows [18] or in active [19] and passive [20] flow control. One of the first thorough reviews of Vortex methods has been proposed in 1991 by Sethian and Gustafson [21]. In 2000, Cottet and Koumoutsakos [22] proposed a further detailed book, gathering all the theory and numerical practice related to these methods. In 2011, Yokota and Obi completed this overview with a review paper dedicated to the simulation of turbulent flows with Vortex methods [23].

The present paper, starting from preliminary survey carried out in [24], proposes a synthetic review of Vortex methods from their genesis in the 1930s until their very recent advances. In the context of incompressible flow simulations, one of the first goals of this work is to provide an insight of a particle approach based on a solid mathematical framework with convergence analysis and conservation features, which is able to provide accurate simulations and which could be considered as a complement or an alternative to purely Eulerian methods. Concerning the Vortex methods themselves, the literature survey of this review aims to give an overall landscape (although not exhaustive due to the finite format of a review paper) of the existing Vortex Methods, depicting the different sub-families of VMs with their own advantages, drawbacks and applications. It also aims to highlight the intrinsic advantages of Vortex Methods that explain their intensive and continuous development from the 1970s, and attempts at showing how they progressively evolved in time to meet the requirements involved by the CFD community, namely the capability of handling complex physics while ensuring convergence to solution, accuracy, efficiency, and performance. This review is addressed both to scientists specialized in numerical analysis and discretization schemes, and those dedicated to incompressible fluid dynamics using as well direct numerical simulations or large eddy simulations.

The present review paper follows the chronological advances of Vortex Methods and is structured this way: First, Section 2 gives the global description and formulation of Vortex Methods in the initial context they were used for, that is to say the resolution of the inviscid Euler equations. In Section 3, one will explain how they expand to solve the Navier-Stokes equations, including the diffusion effects. Section 4 will address the crucial issue of particle distortion in Lagrangian methods and their need to perform a spatial adaptation of the particle locations in order to ensure the numerical convergence; this section introduces the so-called hybrid Vortex Methods, which include in their discretization schemes the presence of an underlying grid in order to circumvent the particle distortion phenomenon. In Section 5, we will focus on the treatment of boundary conditions in VMs, and more precisely on the enforcement of no-slip boundary conditions at the surface of a solid and rigid immersed obstacle. Section 6 will describe the progresses made in VMs in terms of algorithmic issues, allowing them to handle complex or computationally costly problems. Finally, Section 7 will propose a finite list of relevant and challenging simulations performed with Vortex Methods.

2. Vortex Methods for Inviscid Incompressible Flows

2.1. General Description and Formulation

The first calculations based on vortex methods were performed, by hand, independently by Prager in 1928 [25] and Rosenhead in 1931 [26]. For that purpose, they discretized the flow into elements, namely the particles, characterized by their position and the local circulation they carry. One recall that the circulation Γ corresponds to the macroscopic rotation of the flow. It is a scalar field defined as the integral of the vorticity field $\boldsymbol{\omega}$ on patch of vorticity $\mathcal{A}$, bounded by a closed path:

$$\Gamma = \int_{\mathcal{A}} \boldsymbol{\omega} \, d\mathbf{x}, \tag{5}$$

where the vorticity $\boldsymbol{\omega}$ measures the local rotation of the fluid flow and is obtained by taking the curl of the velocity field:

$$\boldsymbol{\omega} \equiv \nabla \times \mathbf{u}. \tag{6}$$

In the case of a two dimensional flow, the vorticity is perpendicular to the flow plane and corresponds to a scalar field. We note it by ω in that case. In the Cartesian coordinates system, the vorticity respectively expresses in 2D and 3D as follows:

$$\omega = \omega_z = \frac{\partial u_y}{\partial x} - \frac{\partial u_x}{\partial y} \,, \qquad \boldsymbol{\omega} = (\omega_w, \omega_y, \omega_z) = \left(\frac{\partial u_z}{\partial y} - \frac{\partial u_y}{\partial z} \,, \frac{\partial u_x}{\partial z} - \frac{\partial u_z}{\partial x} \,, \frac{\partial u_y}{\partial x} - \frac{\partial u_x}{\partial y} \right). \tag{7}$$

Based on the pioneer works [25,26], the method described in the sequel corresponds to the general definition of vortex methods, first introduced in the 1970s for the two-dimensional formulation [27] and in the late 1980s for the three-dimensional formulation [28,29].

The design of vortex methods for inviscid incompressible flows is based on vorticity-velocity formulation of the Euler equations. The latter represent hyperbolic equations of conservation of mass (continuity), and balance of momentum and energy. They correspond to particular Navier–Stokes equations for inviscid (zero viscosity) flows, without thermal conductivity. In vorticity-velocity formulation and in the case of incompressible flows, they can be written as follows:

$$\frac{\partial \boldsymbol{\omega}}{\partial t} + (\mathbf{u} \cdot \nabla)\boldsymbol{\omega} - (\boldsymbol{\omega} \cdot \nabla)\mathbf{u} = 0 \tag{8}$$

$$\text{div } \mathbf{u} = 0 \tag{9}$$

$$\boldsymbol{\omega}(\cdot, 0) = \boldsymbol{\omega}_0 \tag{10}$$

$$|\mathbf{u}| \to \mathbf{u}_\infty \tag{11}$$

where $(\mathbf{u} \cdot \nabla)\boldsymbol{\omega}$ denotes the advection term, $(\boldsymbol{\omega} \cdot \nabla)\mathbf{u} = [\nabla \mathbf{u}][\boldsymbol{\omega}]$ corresponds to the stretching term (which vanishes in two-dimensions) and where Equation (9) corresponds to the incompressibility condition, resulting from the continuity equation. In fact, the Euler equations were originally formulated in the Lagrangian form which involves $D\boldsymbol{\omega}/dt$, the material derivative in time of the vorticity $\boldsymbol{\omega}$ with respect to the advective field $\mathbf{u}$. The discretization of these equations with a vortex method, that is to say with a particle method, is therefore natural and straightforward. It goes as follows: Let a regular approximation $\boldsymbol{\omega}^h$ of $\boldsymbol{\omega}$, and let $\mathbf{x}_p^h$ the trajectories of the particles transported by the flow, the approximated vorticity $\boldsymbol{\omega}^h$ may be numerically expressed at time t by:

$$\boldsymbol{\omega}^h(\mathbf{x}, t) = \sum_p \boldsymbol{\alpha}_p^h \delta(\mathbf{x} - \mathbf{x}_p^h(t)), \tag{12}$$

where the numerical particles locations $\mathbf{x}_p^h(t)$ are obtained by solving the following ODEs:

$$\frac{d\mathbf{x}_p^h(t)}{dt} = \mathbf{u}^h(\mathbf{x}_p^h(t), t) \tag{13}$$

and where $\boldsymbol{\alpha}_p^h$ corresponds to the local circulation around $\mathbf{x}_p^h$, defined as the product of the vorticity by the volume of the particle $\boldsymbol{\alpha}_p^h = \mathbf{v}_p \boldsymbol{\omega}_p^h$. According to the Kelvin's theorem, which states that in an inviscid flow the circulation around a closed curve remains constant in time when moving with the fluid, the local circulation $\boldsymbol{\alpha}_p^h$ satisfies the following ODEs in 2D and 3D respectively:

$$\frac{d\alpha_p^h}{dt} = 0 \ \text{(2D)}, \qquad \frac{d\boldsymbol{\alpha}_p^h}{dt} = \boldsymbol{\alpha}_p^h \cdot \nabla \mathbf{u}^h(\mathbf{x}_p^h, t) \ \text{(3D)}. \tag{14}$$

From the Kelvin's and Helmholtz theorems, the vorticity is advected at the local fluid velocity $\mathbf{u}^h$ in the potential flow (one refers the reader to section 1.3 of Cottet and Koumoutsakos' book [22] for a detailed presentation of the first and second Helmholtz theorems that drive the motions of fluid particles carrying vorticity in inviscid flows and their further extension by Kelvin to include the effects of viscosity). The velocity can be recovered at all times from the vorticity through the following Poisson equation, based on the incompressibility condition:

$$\Delta \mathbf{u}^h = -\nabla \times \boldsymbol{\omega}^h, \tag{15}$$

which can be solved through an integral representation:

$$\mathbf{u}^h(\mathbf{x}) = \text{curl}(\mathbf{G}(\mathbf{x}, \mathbf{x}') \star \boldsymbol{\omega}^h(\mathbf{x})) + \mathbf{u}_\infty^h(\mathbf{x}), \tag{16}$$

where $\mathbf{G}$ is the Green's function for the Laplacian operator, $\nabla^2 \mathbf{G}(\mathbf{x}, \mathbf{x}') = \delta(\mathbf{x} - \mathbf{x}')$ and where $\star$ denotes the convolution product. Then, from Equation (16) and denoting $\mathbf{K} = \nabla \mathbf{G}$, one finally obtains the velocity field through the following Biot–Savart equation:

$$\mathbf{u}^h = \mathbf{K} \star \boldsymbol{\omega}^h + \mathbf{u}_\infty^h, \tag{17}$$

with

$$\text{in 2D}: \qquad \mathbf{G}(\mathbf{x}) = \frac{1}{2\pi}\ln(|\mathbf{x}|), \qquad \mathbf{K}(\mathbf{x},\mathbf{x}') = \nabla\mathbf{G}(\mathbf{x},\mathbf{x}') = \frac{1}{2\pi}\frac{\mathbf{x}-\mathbf{x}'}{|\mathbf{x}-\mathbf{x}'|^2} \tag{18}$$

$$\text{in 3D}: \qquad \mathbf{G}(\mathbf{x}) = (4\pi|\mathbf{x}|)^{-1}, \qquad \mathbf{K}(\mathbf{x},\mathbf{x}') = \nabla\mathbf{G}(\mathbf{x},\mathbf{x}') = -\frac{1}{4\pi}\frac{\mathbf{x}-\mathbf{x}'}{|\mathbf{x}-\mathbf{x}'|^3} \tag{19}$$

To summarize, in vortex method, each vortex element is made to move at a single velocity according to the Biot–Savart law and Equations (12)–(14) and (17) model the transport of the vorticity in inviscid incompressible flow. However, the Dirac distribution involved in the vorticity definition (12) makes unaffordable the numerical discretization and approximation of the vorticity field in practice. Faced with this problem arose the idea of the vortex blob method, originally introduced by Chorin and Bernard [27]. In this numerical approach, the vorticity of each particle is distributed on a blob, that is to say on a disk of finite radius ε. This vorticity blob-distribution is defined by a smooth cutoff function ζ.

If the blob radius ε is small enough, one denotes ζ_ε the mollified function defined in 2D and 3D by:

$$\zeta_\varepsilon = \frac{1}{\varepsilon^n}\,\zeta\left(\frac{\mathbf{x}}{\varepsilon}\right), \quad n = 2,3. \tag{20}$$

Among the possible cutoff functions, the Gaussian-based ones are often favored because of their smoothness property, their radial symmetry and their fast decay.
In vortex blob method, the vorticity $\boldsymbol{\omega}_\varepsilon^h$ of the mollified particles is then given by the following expression (one refers to Figure 1 for a graphical support):

$$\boldsymbol{\omega}_\varepsilon^h(\mathbf{x}) = \sum_p \boldsymbol{\alpha}_{p_\varepsilon}^h \zeta_\varepsilon(\mathbf{x}-\mathbf{x}_p^h), \tag{21}$$

with

$$\frac{d\alpha_{p_\varepsilon}^h}{dt} = 0 \;\; (2\text{D}), \quad / \quad \frac{d\boldsymbol{\alpha}_{p_\varepsilon}^h}{dt} = \boldsymbol{\alpha}_{p_\varepsilon}^h \cdot \nabla \mathbf{u}_\varepsilon{}^h(\mathbf{x}_p^h, t) \;\; (3\text{D}) \tag{22}$$

$$\frac{d\mathbf{x}_p^h(t)}{dt} = \mathbf{u}_\varepsilon^h(\mathbf{x}_p^h(t), t) \tag{23}$$

$$\mathbf{u}_\varepsilon^h = \mathbf{K}_\varepsilon \star \boldsymbol{\omega}_\varepsilon^h = (\mathbf{K} \star \zeta_\varepsilon) \star \boldsymbol{\omega}_\varepsilon^h. \tag{24}$$

Concerning the resolution of three dimensional inviscid flows using vortex method, most works mainly rely on the 3D formulation exposed here, which is a direct extension of the 2D method, but it has to be noticed that the very first proposition of 3D vortex method was based on a different approach, called the vortex filament method. The latter was introduced by Leonard [30–32] and leans on the theorems of Helmholtz and Kelvin, stating that tubes of vorticity retain their identity and move as material elements in an inviscid flow. In this approach, the quantity carried by the Lagrangian elements is a scalar, as in two dimensions, and the elements are now deformable lines (or filaments) instead of discrete points. Also, as for two-dimensional vortex schemes, the circulation of the particles remains constant in time. In practice, vortex filament methods were used to perform one of the first 3D simulations in CFD by Leonard [31] and were also used more recently by Angelidis and Neyret [33] with smoke simulations in graphic works. However, despite their very natural approach from a physical point of view, they suffer from several weaknesses: first of all, they are most of the time quite difficult to initialize for a given flow. Only specific problems like vorticity rings and jets are spared from this trouble. Also, some filament "surgeries" might become necessary in order to avoid tiny loops or to reconnect neighboring filaments, which make the method complex to use. Eventually, there is no straightforward way to include the physical diffusion effects in the model with filament method.

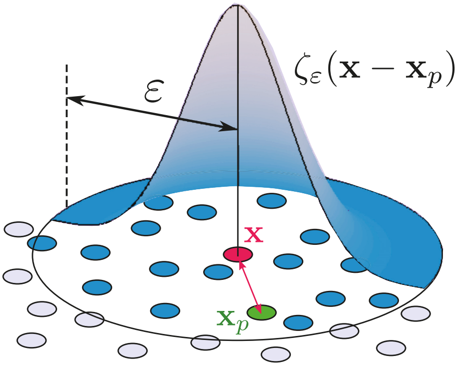

Figure 1. In Vortex blob methods, the vorticity ω^h at location $\mathbf{x}$ is approximated as the sum of the local circulations $\boldsymbol{\alpha}_p^h$ carried by the neighboring particles of volume v_p and located in the support of the ζ_ε mollified function.

2.2. Convergence Issues

What distinguishes vortex methods from grid-based methods is the fact that they are built in such a way that many inviscid flow invariants are conserved [22]. This makes them particularly interesting since they ensure a correct qualitative answer, even in the case of underresolved simulations. Besides this important feature, vortex methods indisputably belong to the category of plain numerical methods by means of their complete numerical analysis and their theoretical proofs of convergence.

The works of Hald in 1979 [34] and Beale and Majda in 1982 [35] provide the complete proof of convergence as part of the vortex blob method in two dimensions. Their analysis included the influence of the numerical parameters involved in the model, namely the blob radius ε (that is to say the cutoff width) and the particle spacing, denoted h. It turned out that the vortex blob trajectories tend to the exact one when the number of eddies increases, more precisely when $h = \mathcal{O}(\varepsilon)$. This result allows us to reach high orders of convergence in two dimensions. An extension of this convergence result to the three dimension case is also given in [35] as well as in the work of Cottet [29], giving birth to new high orders three dimensional vortex methods. The convergence condition $h = \mathcal{O}(\varepsilon)$ is also clearly highlighted numerically by the simulations performed by Knio and Ghoniem [36] concerning the propagation and stability of three-dimensional vortex rings. The temporal discretization is added for the first time in the convergence analysis of the 2D and 3D Euler equations by Anderson and Greengard in 1985 [28]. The most important result which came out of this study is the fact that these methods do not suffer from any Courant-Friedricks-Levy (CFL) condition, which constraints the time step to be related to the minimal grid size in Eulerian methods. Indeed, in vortex methods the stability constraint on the time step only depends on the velocity gradient:

$$\Delta t \leq \frac{C}{\|\nabla \mathbf{u}\|_\infty}, \tag{25}$$

where the constant C, also called LCFL number (for Lagrangian CFL), must be lower or equal to 1. This condition provides a much less restrictive constraint for the time step compared to purely grid-based schemes.

After this general presentation, one can distinguish several advantages using the discrete vortex method. First, its Lagrangian approach with particle discretization makes it intrinsically close to the flow physics it aims to model and provides a direct scheme to solve the transport of particles and the quantities they carry, based on ODEs systems, without numerical dissipation. Secondly, the vorticity field is a compact field compared to the velocity. It is therefore much more efficient to directly solve and simulate the vorticity field. Then, if the fluid density is constant, the Euler equations for incompressible flows does not contain pressure term in vorticity formulation. Furthermore, in the discrete vortex method the boundary condition at infinity can be automatically satisfied contrary to most grid-based approaches where external flows must be solved within a finite simulation domain. Finally, the stability condition (25) provided by the vortex method scheme allows larger time steps compared to grid-based methods.

3. Viscous Vortex Methods

The first numerical schemes including viscous effects in vortex methods were designed with the desire to conserve the Lagrangian framework. They were consequently purely based on particles. Before starting with the description of the very first viscous vortex method, namely the Random Walk method developed by Chorin in 1973 [37], it is necessary to introduce the concept of viscous splitting of the Navier-Stokes equations. For sake of clarity, in the rest of this paper the approximated quantities $\boldsymbol{\omega}_\varepsilon^h$, $\boldsymbol{\alpha}_\varepsilon^h$ and $\mathbf{u}_\varepsilon^h$ will be simply referred to as $\boldsymbol{\omega}$, $\boldsymbol{\alpha}$ and $\mathbf{u}$.

3.1. The Viscous Splitting and Random Walk Method

The original concept of viscous splitting was first introduced by Prandtl, in 1904 [38]. However, its design within the framework of vortex methods was originally proposed in the early 1970s by Chorin [37] in order to develop his Random Walk Method suited to model the diffusive phenomenon. The viscous diffusion equation is:

$$\frac{d\boldsymbol{\omega}}{dt} = \nu\Delta\boldsymbol{\omega}, \tag{26}$$

where ν denotes the viscosity of the fluid. This equation is coupled with the Biot-Savart Equation (24) in order to recover the velocity field from the vorticity.

The viscous splitting algorithm consists in performing substeps in which the advective and the diffusive effects are handled separately and successively. Thus, in the vortex method frame, the two steps of the viscous splitting algorithm for a two-dimensional flow are the following:
(1) advection:

$$\frac{d\mathbf{x}_p}{dt} = \mathbf{u}(\mathbf{x}_p) \tag{27}$$

$$\frac{d\omega_p}{dt} = 0, \tag{28}$$

(2) diffusion:

$$\frac{d\mathbf{x}_p}{dt} = 0 \tag{29}$$

$$\frac{d\omega_p}{dt} = \nu\Delta\omega(\mathbf{x}_p), \tag{30}$$

where in the first step, the particles locations ($\mathbf{x}_p$) are updated using the local flow velocity obtained with the Biot-Savart law and in the second one the vorticity (ω_p) is modified at these new positions by the diffusion. The convergence of the viscous splitting method was proved by Beale and Majda in 1981 [39].

Random Walk Method (RW)

The method of Random Walk, created by Chorin [37], consists in solving Equation (30) through the probabilistic interpretation of the Green's function, solution of the diffusion equation:

$$\omega(\mathbf{x}, t) = \int G(\mathbf{x} - \mathbf{y}, \nu t)\omega_0(\mathbf{y})\, d\mathbf{y}, \tag{31}$$

which, in d-dimensions is known to be explicitly equal to:

$$G(\mathbf{x}-\mathbf{y},\nu t)=\frac{1}{(4\pi\nu\Delta t)^{d/2}}\exp\left(\frac{-\|\mathbf{x}-\mathbf{y}\|^2}{4\nu\Delta t}\right). \tag{32}$$

As mentioned previously, the RW method is inherently related to the viscous splitting approach since the vorticity field obtained after the particle push (Equations (27) and (28)) is assigned as the initial condition of the diffusion Equation (30). The diffusion effects are then modeled imposing a Brownian motion to the flow particles whose positions are updated over a time step Δt according to the following scheme:

$$\mathbf{x}^{n+1}=\mathbf{x}^n+\Delta t\mathbf{u}^n+\mathbf{g}, \tag{33}$$

where $\mathbf{g}$ is a vector of independent random variables obtained through a Gaussian probability distribution with zero mean and a variance $\sigma=2\nu\Delta t$. Moving the particles in such a way creates a concentration field that converges to the above Green's function solution of the diffusion equation, as the number of particles tends to infinity. Marchioro and Pulvirenti [40], Goodman [41] and Long [42] successively proved the convergence of the Random Walk method.

Thank to its simplicity, its property to conserve the total circulation and also its capability to easily handle flows around complicated boundaries (see Section 5.1), this method has been extensively used. In terms of applications, we can cite the works of Chorin [37,43], Dommelen [44] and Stansby [45,46] who applied the Random Walk method for the simulations of flows around cylinders. We can also refer to Wang [47] who studied in his thesis several active flow control techniques to prevent the dynamic stall of airfoils and to Lewis [48] who used the Random Walk method to simulate flows over airfoil cascades. However, this viscous vortex method is a stochastic method: it therefore presents several drawbacks. First, it does not exactly conserve the mean position of the vorticity in free space. Next, the computed solutions are noisy due to the statistical errors. Indeed, increasing the viscosity ν makes the variance of the random variables larger and consequently deteriorates the solution. Finally, the stochastic feature of the Random Walk method limits its convergence capability. The error is indeed proportional to $1/\sqrt{N}$ as explained by Milinazzo and Saffman [49], where N is the number of particles. Therefore, accurate simulations need a very large number of fluid elements, which increases the computational cost and explains their rare application to three-dimensional simulations. One can however cite the use of RW method in the simulation of an impulsively started flow over a 3D cube at $Re_L=100$ performed by Gharakhani and Ghoniem [50] (with L the cube length)

As alternatives to RW, multiple deterministic schemes abounded. The most emblematic ones are described in the following.

3.2. Deterministic Viscous Vortex Schemes

3.2.1. Particle Strength Exchange Method (PSE)

Among all the viscous deterministic vortex methods, the PSE, introduced by Degond and Mas-Gallic in 1989 [51] from the previous connected works of Cottet and Mas-Gallic [52,53], is considered as one of the most popular. The mathematical description of the PSE method is here given in a two-dimensional framework but the main ideas of this approach remain the same in three dimensions:

1. Approximate the diffusion operator $\Delta\omega$ by an integral operator:

$$\Delta\omega(\mathbf{x})\approx\Delta_\varepsilon\omega(\mathbf{x})=\varepsilon^{-2}\int[\omega(\mathbf{y})-\omega(\mathbf{x})]\eta_\varepsilon(\mathbf{y}-\mathbf{x})\,d\mathbf{y}. \tag{34}$$

   where η_ε is a mollified diffusion kernel of order r, satisfying precise moment properties [22].

2. Substitute (34) in (26):

$$\frac{d\omega}{dt} = \nu\Delta\omega(\mathbf{x}) \approx \nu\varepsilon^{-2}\int[\omega(\mathbf{y}) - \omega(\mathbf{x})]\eta_\varepsilon(\mathbf{y}-\mathbf{x})\, d\mathbf{y}. \tag{35}$$

3. The particle approximation of the diffusion equation can be obtained from the numerical integration of (35). The resulting vortex scheme is given by:

$$\omega^h(\mathbf{x},t) = \sum_p v_p\omega_p^h(t)\delta(\mathbf{x}-\mathbf{x}_p^h), \tag{36}$$

where the particles trajectories $\mathbf{x}_p^h$ are computed from (27) (based on Biot-Savart law), and $\omega_p^h(t)$ satisfies the following ODEs:

$$\frac{d\omega_p^h}{dt} = \nu\varepsilon^{-2}\sum_q(v_q\omega_q^h - v_q\omega_p^h)\,\eta_\varepsilon(\mathbf{x}_q^h - \mathbf{x}_p^h), \tag{37}$$

where the right hand side is obtained from (35) through a discretization of the integral operator taking the particle positions as quadrature points.

Equation (37) can be interpreted as changes in the strength of particles due to the neighboring particles, which explains the name of "Particle Strength Exchange". Beyond its deterministic framework and its integral formulation, the accuracy and reliability of the PSE method is also based on its capability to conserve the natural invariants of the flow. Moreover, the method is not based on the viscous splitting algorithm, which therefore discards the intrinsic error of the time-steping process. The method exhibits an error bound of $\mathcal{O}(\varepsilon^2)$ for simple Gaussian smoothing. However, the quadrature rule used to discretize the integral makes the PSE method strongly dependent on the particles distribution, which has to respect the convergence condition $h = \mathcal{O}(\varepsilon)$ as well as possible. To circumvent this drawback, particle spatial adaptions often need to be added to the PSE method. This point will be addressed in details in Section 4.

A wide range of applications have been handled so far based on this deterministic approach which may be considered as one of the most efficient and accurate viscous Lagrangian vortex methods. Among them, one must cite the pioneer and reference works of Koumoutsakos and Leonard [54] who applied the PSE method to 2D viscous flows around translating and rotating cylinders for Reynolds numbers ranging from 40 to 9500. One can also cite the works of Ploumhans et al. [55] for the simulation of transient 3D flow past a sphere or those of Yokota et al. [56] for the study of 3D isotropic turbulence in a periodic domain. All these numerical studies highlight the necessity of particle spatial adaption in order to ensure the convergence of the vortex PSE method.

3.2.2. Core-Spreading Method (CSM)

This method is not based on integral operators approaching the Laplacian (like in PSE) but directly considers the exact solution of the diffusion Equation (26), given by the Green's function solution:

$$\boldsymbol{\omega}(\mathbf{x},t) = \frac{\boldsymbol{\alpha}_p}{(4\pi\nu t)^{d/2}}\exp\left(-\frac{|\mathbf{x}-\mathbf{x}_p|^2}{4\nu t}\right) \tag{38}$$

In order to discretize the diffusion equation with a vortex scheme, if one considers the numerical scheme provided by the vortex blob method described in the first section of this paper, one has:

$$\boldsymbol{\omega}_\varepsilon^h(\mathbf{x}) = \sum_p \boldsymbol{\alpha}_{p_\varepsilon}^h\zeta_\varepsilon(\mathbf{x}-\mathbf{x}_p^h), \tag{39}$$

where the smooth cutoff function ζ_ε distributes the vorticity on a blob of radius ε.

The core-spreading method, first introduced by Kuwahara and Takami in 1973 [57] and later reformulated in 1980 by Leonard [31] has its origin in the observation that, if one chooses ζ_ε as the Gaussian distribution:

$$\zeta_\varepsilon = \frac{1}{(2\pi\varepsilon^2)^{d/2}} \exp\left(-\frac{|\mathbf{x}_q - \mathbf{x}_p|^2}{2\varepsilon^2}\right) \tag{40}$$

then scheme (39) reduces to the solution of the heat Equation (38), provided the variance of the Gaussian blob distribution expands in time according to $\varepsilon^2 = 2\nu t$, which explains the denomination of "core-expansion" or "core-spreading" for the method. However, Greengard [58] highlighted that a the straightforward implementation of CSM lacked of consistency and could only give a converged approximation of the Navier-Stokes equations under the very restrictive limit of vanishing viscosity. Indeed, in a general point of view, the expansion in time of the vortex blobs radius is not in agreement with the convergence criterion stating that ε must be a small parameter. To circumvent this inconsistency, a spatial adaptation procedure was proposed by Rossi [59] in order to keep control on distance between particles. Based on this improvement (and provided a careful treatment of the local spatial adaptation further described in Section 4.1), the work of Barba et al. [60] demonstrated the means for using CSM in the case of a Lamb vortex dynamics study, and Yokota et al. [56] also used it successfully for their study of 3D isotropic turbulence. This approach conserves the deterministic treatment of the viscous diffusion equation and preserves the meshless framework of vortex methods.

3.2.3. Diffusion Velocity Method (DVM)

This method, first introduced by Fronteau and Combis in 1984 [61] and later used in the vortex methods framework by Ogami and Akamatsu in 1991 [62], relies on the idea that the diffusion of vorticity is handled within the advection process by absorbing the diffusion term into the advection one in the Navier-Stokes equations $\dfrac{\partial\omega}{\partial t} + \mathbf{u}\cdot\nabla\omega = \nu\Delta\omega$. This process gives rise to two different velocities: the advection velocity $\mathbf{u}$ and the diffusion velocity $\mathbf{u}_d$. The latter can be considered as an artificial velocity and is defined, in two-dimensions, as follows:

$$\mathbf{u}_d = \frac{\nu}{\omega}\left(\frac{\partial\omega}{\partial x}, \frac{\partial\omega}{\partial y}\right) \tag{41}$$

From this definition, the diffusion problem is now transformed into an advection equation:

$$\frac{\partial\omega}{\partial t} + \nabla(\omega\mathbf{u} + \omega\mathbf{u}_d) = 0 \tag{42}$$

Thus, the transport of vorticity (due to advection and diffusion effects) is modeled by the vortices' movement provoked by the advection velocities and the diffusion velocities. The DVM has been compared to PSE approach in the work of Beaudoin et al. [63] for the 2D simulations of pollutant transport in groundwater, featuring that for such dispersion problem the PSE tends to provide more accurate results while DVM seems to be more stable. However, the DVM requires an important particle overlapping, as precisely highlighted in [63] and in the earlier work of Clarke and Tutty [64] simulating the impulsively started two-dimensional flow past an arbitrary shaped body using DVM associated with a random walk (RW) procedure. Concerning the comparison of diverse vortex diffusion methods one finally refers to a very recent 2D study brought by Lucchesi et al. [65] confronting a direct differentiation approach (non-conservative), with three different PSE schemes and a DVM method (all conservative by construction). An extension to the three-dimensional formulation of the DVM was proposed by Rivoalen et al. [66], where a diffusion vorticity $\boldsymbol{\omega}_d$ (also called "viscous vorticity") has to be added to the problem, giving the new vorticity transport equation:

$$\frac{\partial \boldsymbol{\omega}}{\partial t} + \nabla \cdot ((\mathbf{u} + \mathbf{u}_d) \otimes \boldsymbol{\omega}) - (\boldsymbol{\omega} \cdot \nabla)\mathbf{u} - \boldsymbol{\omega}_d \times \boldsymbol{\omega} = 0 \tag{43}$$

which, in the Lagrangian framework, is solved according to the following system of ODEs:

$$\frac{d\mathbf{x}}{dt} = \mathbf{u}_p + \mathbf{u}_d \tag{44}$$

$$\frac{d\boldsymbol{\omega}_p}{dt} = (\boldsymbol{\omega}_p \cdot \nabla)\mathbf{u}_p - \boldsymbol{\omega}_d \times \boldsymbol{\omega}_p \tag{45}$$

However, it is important to notice that $\boldsymbol{\omega}_d$ needs the approximation of the Laplacian operator, which in practice in [66] is performed using a discretization of the integral approximation (as done in PSE method).

These three deterministic viscous methods, namely the PSE, the CSM and the DVM, represent the grid-free viscous approaches that allowed conservative and converged numerical simulations for two and three-dimensional problems. It is interesting however to mention several other methods that were proposed to solve the viscous diffusion equation with vortex schemes, despite their failure in successfully applying it to the three-dimensional case. One can for instance cite the one introduced by Fishelov in 1990 [67], called the Convolution of Cut-off Function method (CCF). It allows us to obtain the Laplacian operator by using explicitly second derivatives of the cutoff function, i.e., $\Delta\omega \approx \omega \star \Delta\zeta_\varepsilon$, in the vortex blob scheme:

$$\frac{d\omega_p^h}{dt} = \nu \sum_q (v_q \omega_q^h) \Delta\zeta_\varepsilon(\mathbf{x}_q^h - \mathbf{x}_p^h). \tag{46}$$

But this method encounters several weaknesses. It has been first observed to be more sensitive than PSE to particle field distortion, but overall, the formulation (46) lacks the correction term $-\omega_p \sum_q v_p \Delta\zeta_\varepsilon(\mathbf{x}_q^h - \mathbf{x}_p^h)$ and is therefore not conservative [22]. These reasons explain why this approach failed in giving rise to deeper research works.

Among the other vortex schemes proposed to solve the diffusion equation, one can also mention the Vortex Redistribution Method (VRM) of Shankar and van Dommelen (1996) [68]. This method was thought as an alternative to PSE with no need to perform particle rezoning. As PSE, the modeling of diffusion is built on the exchange of circulation between neighbor particles, but in VRM the scheme formulation in not based on integral operators. The exchange of circulation between particles in modeled through the computation of functions that will determine the amount of circulation each particle has to redistribute to its neighbors, located in the area limited by the typical diffusion distance. The definition of the redistribution fractions is designed such that local circulation as well as linear and angular momentum are conserved. However, their evaluation implies many parameters whose computation might be very costly (even more that the cost of velocity computation through Biot-Savart law [22]), which in practice makes this approach difficult to use.

For an exhaustive description about grid-free viscous vortex methods, one can refer the reader to the detailed literature survey given in Barba's thesis [69] and to Cottet and Koumoutsakos [22].

The important number of diverse viscous vortex schemes illustrates the difficulty of modeling viscous incompressible flows with a grid free vortex method. As emphasized in the present section, the main limitation of all the proposed schemes does not come from their capability of modeling the viscous effects themselves, but from the necessity to ensure particle overlapping throughout the whole calculation. Studies on spatial adaptation procedures were therefore developed in parallel in order to address this key point. We describe them in the following section.

4. Spatial Adaptation and Hybrid Vortex Methods

In pure Lagrangian method, the particle distribution may undergo distortion, that manifests itself by the clustering or spreading of the flow elements in high strain regions.

This accumulation or dispersion phenomenon is then translated in inaccurate computations because of a deteriorated communication between particles. As meaningful illustrations of the distortion effect one can cite the test case of the axisymmetric inviscid vortex patch, illustrated for instance by Rossinelli and Koumoutsakos [70]. In this example, one can observe the distortion of the initial and uniform particle distribution due to the important shear. One can also see in Henshaw et al. and in Krasny's studies [71,72] comparable behaviors concerning the appearance of non-physical small scales in vortex sheet calculations in the context of two dimensional inviscid flows. Therefore, and as mentioned in Section 2.2, the keypoint of vortex methods rely on the necessity of particle overlapping, that is to say, the need for the cutoff size ε to be at least of the order of h, the distance between particles.

Several solutions have been designed in order to overcome the distortion problem. One can separate these methods into two main classes.

4.1. The Meshless Rezoning Methods

The first class deals with methods involving a change in particle strength in order to correct the vorticity field such that the particle distribution better approximates the vorticity field. Among these methods one can first refer to the approach developed by Beale in 1988 [73] which consists in correcting the circulation at each time step through an iterative procedure. This technique has been successfully used by Chorin [74] to model incompressible viscous flow with a PSE scheme. However, the iterative process may be slow to converge in case of particle clustering or irregularities in the vorticity field. Both Beale and Chorin defined this circulation evaluation method as a problem of "scattered data interpolation".

In this spirit, Barba et al. [60] later proposed in 2005 a scattered data interpolation using Radial Basis Functions (RBF) as a rezoning approach in the context of vortex method. In this technique, as the vorticity $\boldsymbol{\omega}$ is known only over a finite number of positions $\mathbf{x}_p$, the objective is to find an approximation to the assumed piecewise continuous function $\boldsymbol{\omega}(\mathbf{x})$ as follows: $\boldsymbol{\omega}(\mathbf{x}) = \sum_{p=1}^{N} a_p \phi_p(\mathbf{x} - \mathbf{x}_p)$ where a_p denote the coefficients that have to be determined by collocation using the known values of $\boldsymbol{\omega}$ at $\mathbf{x}_p$, and where the basis functions ϕ_p have compact support and are often chosen to be univariate and only dependent on the distance between two particles (radial functions). The solution of such interpolation requires to solve a N-linear equation (one refers to [69] for a detailed description of the algorithmic issues about such approach). The RBF interpolation is a grid-free formulation and the new particles may be located in any spatial arrangement.

Another type of meshless rezoning techniques are the Free-Lagrange methods. The latter were initially designed to model the diffusion phenomenon but they actually offer a good framework to handle distortion problems. They consist in creating a triangulation, whose nodes are the particles locations, which is then used to interpolate the circulation carried by the flow elements. For instance, the Delaunay triangulation, suggested by Russo and Strain in 1994 [75] and obtained connecting the particles when they belong to adjacent polygons in a Voronoi diagram, enables to successfully avoid the distortion of the particle distribution and provides a second-order accurate vortex scheme. Another example among these Free-Lagrange methods is the adaptive quadrature method introduced by Strain in 1997 [76]. This approach allows us to increase the order of accuracy of the usual triangulation methods by considering sub-elements that would combine several triangles together.

One can also cite the strategy introduced by Schrader et al. in 2010 [77] which can be considered as a generalization of the PSE method. It indeed proposes to correct the method given by Eldredge et al. in 2002 [78] consisting in approximating the derivatives on scattered particles locations. This corrected framework of the PSE scheme enables one to achieve the convergence without any overlapping condition and regardless of the resolution. However, the convergence of the latter was limited to a certain range of resolutions.

Finally, we can refer to the recent approach proposed by Rossi et al. in 2015 [79], called the Regular Point Distributions (RPD). This technique, introduced within the Diffused Vortex Hydrodynamics method (DVH) designed by the same authors, consists in defining an appropriated set of points on which are generated the new particles after each diffusion steps. This set of points is generated with a "package" algorithm which, in the presence of an immersed obstacle, creates points regularly around the body (of any geometry) in order to accurately prescribe the no-slip boundary condition at the surface (the enforcement of boundary conditions in vortex methods will be addressed in details in the next main section).

4.2. The Remeshing Methods

The second class of methods designed in order to remedy the distortion problem are based on a frequent physical re-location of the particles onto new positions where the overlapping condition is satisfied. These methods allow us to directly control the distance between the particles, thus ensuring the convergence of the solution. The following of this section is dedicated to the description of the re-location methods principally used by now, based on the so called "remeshing" technique.

From the pioneer works of Huberson and Jollès (1990) [80] and Koumoutsakos and Leonard (1995) [54], the remeshing approach (also called "redistributing" or "regridding") has been widely and is still successfully used in vortex methods. It consists in redistributing the particles on an underlying Cartesian grid. The description of the regridding process is here proposed for the one-dimensional case. Let us denote by $\tilde{x}_q$ the position of the particle q carrying the circulation $\tilde{\Gamma}_q$ (or vorticity $\tilde{\omega}_q$). These particles are remeshed at the grid points x_k of a uniform Cartesian grid, with spacing h, using the interpolation kernel W of support $[-M_s,\ +M_s]$ like follows:

$$\Gamma_k = \sum_q \tilde{\Gamma}_q W\left(\frac{x_k - \tilde{x}_q}{h}\right). \tag{47}$$

In other words, this procedure means that every grid point k receives the sum of the weighted values of the circulation carried by the particles for which k is included in the interpolation support.

Let us recall that one of the strong advantages of the vortex methods lies in their capability to satisfy the conservation properties. In order to preserve this important feature, the interpolation kernel has to be constructed such that the successive moments are conserved. For instance, to satisfy the total circulation invariance (and more generally, the conservation of mass), W must ensure:

$$\sum_k W\left(\frac{x - x_k}{h}\right) = 1. \tag{48}$$

The conservation of the first p moments is given by the following conditions:

$$\sum_q x_q^{\alpha}\, W\left(\frac{x_q - x}{h}\right) = x^{\alpha}, \quad 0 \leq |\alpha| \leq p - 1, \tag{49}$$

and W is therefore an interpolation kernel of order p (we refer to [22] for the proof of this assessment). For $p = 0, 1$ and 2, the conservation of the total circulation, the linear impulse and the angular impulse are cumulatively ensured.

In the following, we will describe the different families of remeshing kernels W by giving their construction as well as their properties.

4.2.1. Remeshing Kernels

The Ordinary Interpolation Kernels

This group includes the kernels whose construction is only based on the satisfaction of conditions (49). These kernels, denoted Λ_p where p refers to the maximum order of conserved moments, are piecewise polynomial functions of degree p. Their construction requires the calculation of $p(p+1)$ coefficients, obtained from the relations (49). For $p = 1$, one gets the linear interpolation kernel, satisfying mass conservation:

$$\Lambda_1(x) = \begin{cases} 1 - |x| & \text{if} \quad |x| \leq 1 \\ 0 & \text{otherwise.} \end{cases} \tag{50}$$

As can be seen on Figure 2a where are also plotted Λ_2, Λ_3 and Λ_4, this type of kernels suffer from a lack of regularity. One can notice that Λ_2 is not even continuous, which is expected to lead to inaccurate solutions. In order to reduce the creation of oscillations due to the poor regularity of the kernels, Magni and Cottet [81,82] proposed to insert correction formulas in the expression of Λ_p.

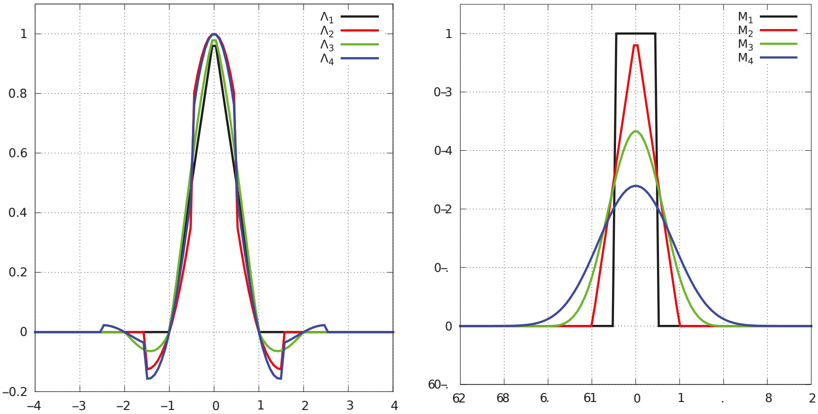

(**a**) Ordinary interpolation kernels (**b**) Kernels based on B-splines

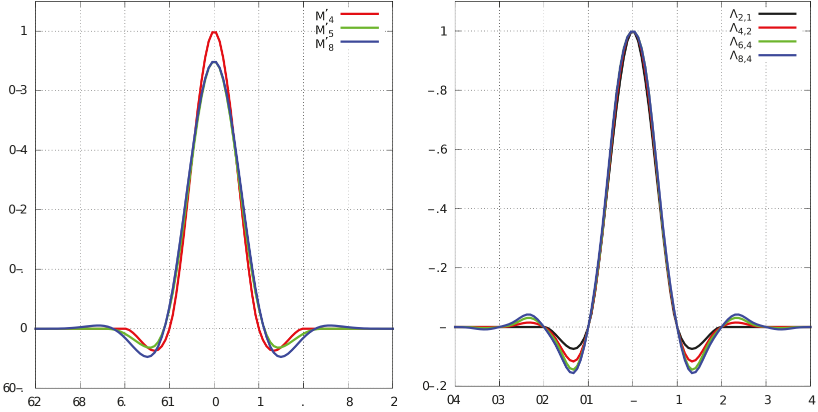

(**c**) Extrapolation of B-splines kernels (**d**) High order kernels

Figure 2. Graphical representation of the different families of remeshing kernels. For each family, several kernels of different orders are plotted (these plots have been constructed from the equations given in Section 4.2.1).

The B-Splines-Based Kernels

In 1946, Schoenberg [83] introduced smooth kernels, denoted M_p, obtained using B-splines :

$$M_p(x) = \frac{1}{2\pi} \int_{-\infty}^{\infty} \left(\frac{\sin \xi/2}{\xi/2} \right)^p e^{ix\xi}\, d\xi \tag{51}$$

For $p = 1$ one gets the top-hat function, M_1. The p-order kernels M_p thus correspond to the successive convolutions of M_1: $M_p = M_1^{(*p)}$ and each kernel M_p is of class $\mathcal{C}^{p-2}$ (Figure 2b). M_3 and M_5 particularly distinguish themselves for their non-oscillatory properties, as illustrated by Magni [84]. Nevertheless, the M_p kernels only ensure the conservation of the two first moments, which strongly limits the accuracy of the remeshing procedure.

Extrapolation of B-Splines-Based Kernels

In order to achieve higher order remeshing schemes while preserving their smoothness properties, Monaghan [85] proposed in 1985 an extrapolation of the M_p kernels. It consists in deriving linear combinations of the M_p kernels and their derivatives, more precisely $W = \sum_{l=0}^{p/2} \alpha_{l+1} x^l M_j^{(l)}$, such that the successive continuous moments of W are canceled:

$$\int y^\alpha W(y)\, dy = \begin{cases} 1 & \text{if} \quad \alpha = 0 \\ 0 & \text{if} \quad 1 \le \alpha \le p. \end{cases} \tag{52}$$

With this approach, Monaghan obtained the so-called M_4' kernel defined by:

$$W = M_4' = \frac{1}{2}\left(3M_4(x) + x\frac{dM_4}{dx}(x) \right) \tag{53}$$

$$= \begin{cases} 1 - \frac{5}{2}|x|^2 + \frac{3}{2}|x|^3 & \text{if} \quad |x| \le 1 \\ \frac{1}{2}(1-|x|)(2-|x|)^2 & \text{if} \quad 1 \le |x| \le 2 \\ 0 & \text{otherwise.} \end{cases} \tag{54}$$

This kernel is of class $\mathcal{C}^1$, it is piecewise cubic, and its support is of size 4 on $[-2,\ 2]$. Locally this kernel offers a third-order accurate scheme (although its global order is 2) and conserves the first three invariants when used in vortex methods (total circulation, linear impulse and angular impulse). In practice, the M_4' is a very good compromise between regularity, accuracy and computational cost, which explains that it is still widely used in vortex methods [6,8,86]. However, these extrapolated smooth kernels do not systematically satisfy the following interpolation property:

$$W(i) = \begin{cases} 1 & \text{if} \quad i = 0 \\ 0 & \text{otherwise.} \end{cases} \tag{55}$$

For instance, the M_4' kernel does satisfy this condition, but it is not the case of the one derived from M_8 (Figure 2c). Nevertheless, this property is essential since its dictates the algebraic conservation of the exact solution if the velocity is zero (that is to say if the particles do not move from their original location on the grid).

High Order Kernels

Much later, Bergdorf and Koumoutsakos [87] proposed in 2006 a higher order kernel, called M_6' and in 2014, Cottet et al. [88] used high order kernels in a systematic way. These high order kernels satisfy simultaneously the interpolation property, the smoothness and the moment conditions to any desired order. Their construction relies on the satisfaction of the five following properties:

- P1: W has support in $[-M_s,\ +M_s]$,
- P2: W is even and piecewise polynomial of degree M in intervals of the form $[i,\ i+1]$,
- P3: W is of class $\mathcal{C}^r$,
- P4: W satisfies the moment properties (49) for a given value of p
- P5: W satisfies the interpolation property (55).

In [88], a new global notation is proposed for these high order remeshing kernels and stands as $\Lambda_{p,r}$ where p denotes the order to which moment conditions are satisfied and r refers to the regularity of the kernel. Figure 2d depicts some of these kernels. In particular, the kernels $\Lambda_{2,1}$ and $\Lambda_{4,2}$ respectively correspond to M'_4 and M'_6.

4.2.2. The Directional Splitting

For multi-dimensions problems, the remeshing step is classically performed through a tensorial product of the chosen 1D kernel formula. For example, if the desired kernel has a 1D-support of $S = 2M_s$ points, then the number of operations needed to interpolate one particle on the grid is proportional to S^2 for a two-dimensional problem and to S^3 for a three-dimensional one. A new method was proposed in 2012 by Magni and Cottet [82] for the particle redistribution procedure. It consists in successively solving monodirectional sub-problems, including the advection and the remeshing step. In other words for a N-dimensional problem, one applies the following algorithm for each particle:

```
for d $\in \{1, ..., N\}$:
    advection in direction d
    remeshing in direction d
```

We refer to Figure 3 for a comparative pattern of tensorial product and directional splitting methods. As a consequence, if the chosen kernel contains S points in its 1D-support, the number of operations with the directional splitting method goes from $\mathcal{O}(S^2)$ to $\mathcal{O}(2S)$ in 2D and from $\mathcal{O}(S^3)$ to $\mathcal{O}(3S)$ in 3D. The directional splitting consequently allows for a drastic reduction of the computational cost in terms of regridding operations. The full convergence proof of the 1D advection-remeshing scheme, considering a smooth non-constant velocity and remeshing kernels of type $\Lambda_{p,r}$, was brought by Cottet et al. in 2014 [88], thus providing a robust and theoretical numerical framework to the directional splitting approach.

The increase of the time-order of the directional splitting scheme (limited to 1 in the form described above) was proposed by Magni and Cottet [82] through the so called Strang splitting scheme, which was successfully used by Cottet et al. [88] in the context of three-dimensional passive scalar advection problems. It consists in performing the directional advection/remeshing with half time steps, except for the last direction where one can gather the operations on $[t_n;\ t_{n+1/2}]$ and $[t_{n+1/2};\ t_{n+1}]$ together. The Strang splitting scheme is therefore of order 2 in time. The different substeps of this approach are given below for the 2D case (the same principle applies for the 3D case):

- advection + remeshing in the X-direction on $[t_n;\ t_{n+1/2}]$
- advection + remeshing in the Y-direction on $[t_n;\ t_{n+1}]$
- advection + remeshing in the X-direction on $[t_{n+1/2};\ t_{n+1}]$

With the Strang splitting method, a multidimensional remeshing thus costs $\mathcal{O}(3S)$ (respectively $\mathcal{O}(5S)$) operations per particle in 2D (respectively in 3D).

The introduction of an underlying grid in order to ensure particle overlapping modifies the essence of the original vortex methods and rapidly gave birth to the so-called “hybrid” vortex methods. The last part of this section is dedicated to the description of the two main families of hybrid vortex methods, namely the Domain Decomposition method on one side and the Vortex-Particle-Mesh (VPM) methods on the other side, with the Vortex-In-Cell (VIC) and the semi-Lagrangian vortex methods among the latter.

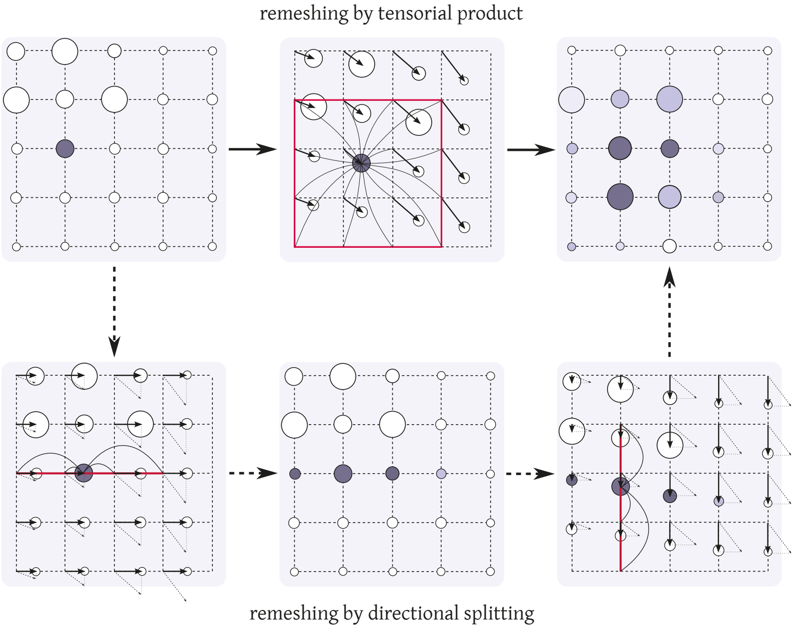

Figure 3. Remeshing steps using a tensorial product (on top, depicted by plain arrows) and a directional splitting [82] (on bottom, depicted by dashed arrows). The red lines indicate the support of the remeshing kernel. In this example, the kernel has a 1D-support of 4 points.

4.3. Hybrid Vortex Methods

Hybrid vortex methods were developed in order to overcome the main weaknesses of the pure Lagrangian vortex methods which essentially lie in the treatment of the viscous effects (see Section 3) and, as we will see in the next section, in the near wall boundary conditions. In order to preserve the robustness of the global scheme, characterized by minimal numerical dissipation, these methods still involve a Lagrangian framework for the advection process but they also handle a fixed grid. The presence of this grid facilitates the prescription of the no-slip boundary conditions as well as the modeling of the diffusive term, using Eulerian schemes (like finite-differences, finite-volumes, finite-elements or spectral methods) while ensuring the particle overlapping condition. In the following we will consider a vortex method as *hybrid* whenever the resolution of the vorticity transport equation and the velocity Poisson equation will be handled both on the particles and on an underlying grid.

Before introducing some hybrid vortex methods, we need to define the common thread between all of them which stands in the way to exchange information between Eulerian and Lagrangian schemes. More precisely, hybrid methods require us, on one hand, to transfer the values of the flow fields $\mathbf{a}$ from the particles to the grid points (we will denote it the *P2M* process, for *Particle to Mesh*) and, on the other hand, to transfer the values of $\mathbf{a}$ from mesh points to the particle distribution (we will denote it the *M2P* process, for *Mesh to Particle*). It is important to note that the *P2M* and *M2P* processes do not imply a physical particle relocation, they materialize an exchange of information.

Let us first define the *P2M* scheme, also called the assignment scheme. It is defined by the following scheme:

$$\mathbf{a}_k = \frac{1}{\mathbf{V}_k} \sum_p v_p \mathbf{a}_p \phi_k(\mathbf{x}_p), \tag{56}$$

where $\mathbf{V}_k$ corresponds to the volume surrounding the grid point $\mathbf{x}_k$ (this volume equals to h^3 if the mesh is Cartesian with a uniform mesh size h) and the basis function ϕ_k is defined by:

$$\phi_k(\mathbf{x}_p) = \phi\left(\frac{\mathbf{x}_p - \mathbf{x}_k}{h}\right), \tag{57}$$

and satisfies:

$$\sum_k \phi_k \equiv 1. \tag{58}$$

If the considered grid is Cartesian, the basis function ϕ may be taken as one of the M_p, M'_p or $\Lambda_{r,p}$ functions described in the previous subsection. In that case, the remeshing procedure presented previously may be considered as a particular case of the *P2M*.

On the other hand, the *M2P* scheme, also called the interpolation scheme, yields:

$$\mathbf{a}_p = \sum_k \mathbf{a}_k \phi_k(\mathbf{x}_p) \tag{59}$$

These *P2M* and *M2P* formula lead to conservative schemes. They are depicted in Figure 4.

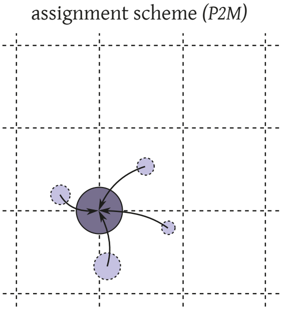

Figure 4. Assignment and interpolation schemes.

4.3.1. The Eulerian-Lagrangian Domain Decomposition Method

The first type of hybrid vortex approach presented in this section is the Eulerian-Lagrangian domain decomposition method, which was proposed by Cottet in 1991 [89] in the context of inviscid flows. The main idea relies on the fact that grid methods and Lagrangian methods are used in different parts of the computational domain. In the flow regions close to immersed obstacles, the use of grid-based schemes enables one to accurately impose the boundary conditions and on the other hand the grid-free vortex method, which is implemented elsewhere, ensures an accurate modeling of the advection-diffusion effects and also provides a simplified treatment of the domain boundary conditions. In the same spirit, Cottet et al. [90] considered an overlapping zone between the Eulerian (grid-based) domain Ω_1 and the Lagrangian (grid-free) domain Ω_2 (Figure 5), implying a Schwarz method in the overall algorithm. It is important to note that the remeshing procedure performed in the Lagrangian domain Ω_2 is not as crucial in this context as in a pure Lagrangian framework (cf. Section 3). Indeed, the distortion effects mainly occur in the vicinity of the wall boundaries, where the highest velocity gradients are observed.

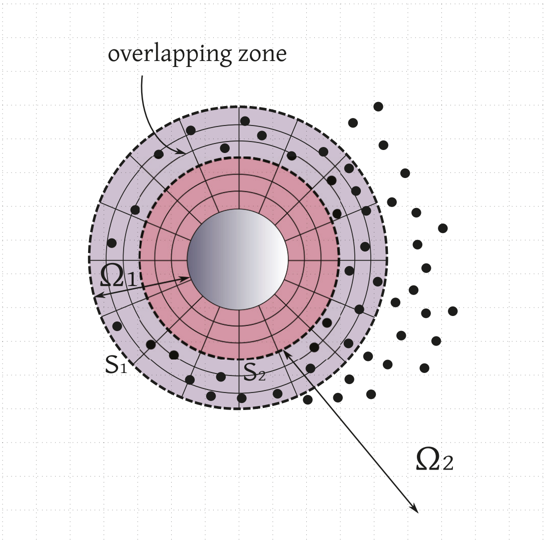

Figure 5. Domain decomposition for flow past a circular obstacle with overlapping Eulerian Ω_1 and Lagrangian Ω_2 domains. In this case, inspired from Cottet et al. [90], Ω_1 is defined by a polar mesh and a uniform Cartesian grid lies in Ω_2 for particle remeshing.

Huberson and Voutsinas [91] also report simulations of flows past circular cylinders realized with this Eulerian/Lagrangian decomposition method, as well as the example of a wind turbine operating in a non-axial wind flow, where a finite-differences scheme is used in the near wake region. One can cite as well the works of Guermond et al. who considered matching domains (no overlapping) [92], which makes the definition of interface boundary conditions more difficult but enables a reduction of computational operations.

4.3.2. From Vortex-In-Cell (VIC) to Semi-Lagrangian Vortex Methods

The Vortex-In-Cell is a hybrid vortex method which was proposed in the pioneer studies of Christiansen in 1973 [93]. It relies on dealing with an underlying Cartesian grid and using either Eulerian schemes (on the grid) or Lagrangian vortex schemes (on particles), according to their respective strengths, to solve the different parts of the governing equations. This method is based on a splitting algorithm (inspired from the Chorin's viscous splitting algorithm described in Section 3.1), also called a fractional step algorithm or an operator splitting algorithm. Concretely, in a VIC method, the advection is performed by updating the positions and the vorticity of the Lagrangian particles through a set of ODEs. On the other hand, Eulerian schemes are handled on the underlying grid to efficiently compute the particle velocities and to solve the diffusion terms for which pure vortex method encounter difficulties, as widely discussed in Section 3. For three dimensional flows, the stretching term is often resolved on the mesh for the sake of simplicity.

The general Vortex-In-Cell fractional step algorithm can be described as follows:

1. **Poisson equation**:
    (a) Assign particle vorticity values to the grid using a *P2M* formula.
    (b) Compute the velocity field solving the following equation on the grid:

$$\Delta \mathbf{u} = -\nabla \times \boldsymbol{\omega}. \tag{60}$$

2. **Advection**:
    (a) Interpolate the velocity field on the particles using a *M2P* formula.
    (b) Perform a Lagrangian advection of the particles and get their new positions and vorticity:
    $$\frac{d\mathbf{x}_p}{dt} = \mathbf{u}_p, \qquad \frac{d\boldsymbol{\omega}}{dt} = 0 \tag{61}$$
    (c) Assign vorticity values and element volumes to the grid using a *P2M* formula.
3. **Stretching** (in three-dimensions only):
    (a) Solve the stretching equation on the grid by differentiation of the velocity field:
    $$\frac{\partial \boldsymbol{\omega}}{\partial t} = (\boldsymbol{\omega} \cdot \nabla)\mathbf{u} \tag{62}$$
    Note: One can also write the stretching equation in its conservative form, namely
    $$\partial\boldsymbol{\omega}/\partial t = \mathrm{div}(\boldsymbol{\omega} : \mathbf{u}) \equiv (\boldsymbol{\omega} \cdot \nabla)\mathbf{u} - \mathbf{u}\mathrm{div}(\boldsymbol{\omega})$$
4. **Diffusion**:
    (a) Solve the diffusion equation on the grid and get the final grid values for the vorticity field:
    $$\frac{\partial \boldsymbol{\omega}}{\partial t} = \nu\Delta\boldsymbol{\omega} \tag{63}$$
    (b) Interpolate the particle values from the grid using a *M2P* formula.

As a typical example of study based on this type of VIC algorithm one can cite the work of Mortazavi and Giovannini [94]. In this study, dedicated to the simulation of 2D flow past thin and thick plates at $Re_H = 7000$ (with H the thickness of the plate), the Poisson equation (step 1) is solved with a finite element method (on a mesh), the advection (step 2) is solved with a usual vortex blob approach (where the core diameter is taken equal to the mesh size) and the diffusion (step 4) is realized through a Random Walk method. Besides, let us precise that the algorithm structure written above corresponds to the original version of the VIC algorithm, following the idea of Christiansen. We note that this initial version actually suffers from the same difficulties as the one experienced by purely Lagrangian approaches because of the distortion effects provoked by the Lagrangian resolution of the advection equation (step 2). The emergence of the remeshing technique in the mid 1990s allowed us to overcome this problem and the VIC method, also known nowadays as the "Vortex Particle-Mesh method" (VPM) (or "Remeshed Vortex methods") then became particularly attractive and efficient to handle very different types of applications [95–98]. One can find a wide range of differences among all the existing Vortex Particle-Mesh methods, which can be explained by the very modular structure of the fractional step algorithm they are based on. Concerning the resolution of steps 3 and 4, a common trend is to use a finite-differences scheme (like in the four references given above [95–98]), while the Poisson equation, in step 1, if often handled with a Fast Fourier Transform method or a Fast Multiple Method (FMM) (these algorithm aspects will be explained more precisely in Section 6.1). The numerical order of a VIC method therefore depends on the order of each scheme adopted in each substep of the operator splitting algorithm. An important difference between the diverse existing VIC schemes concerns the remeshing procedure in step 2. For example, in Caprace et al. [99], the particles are remeshed on the underlying Cartesian grid only every 5 times steps, while in Mimeau et al. [100] the remeshing procedure relocate the particles on the grid points every time steps, implying the presence of a particle at each node of the Cartesian mesh, at any time. In this particular latter case, one talks about "Semi-Lagrangian Vortex methods".

Today, the Vortex Particle-Mesh methods may be considered as one of the most commonly used types of hybrid vortex methods thanks to their relevant advantages we can recapitulate in the following list:

- Possibility to use Fast Poisson solvers for the velocity computation instead of direct summations using the Biot-Savart integral,
- Easy treatment of the viscous effects using finite-differences schemes on the grid (or finite-volumes schemes, spectral schemes) for the resolution of the diffusion equation,
- Easiness of implementation compared to domain decomposition methods,
- Basis for mixing VM with other methods, easy model coupling,
- Prevalence of the less restrictive Lagrangian CFL condition (Equation (25)) for the whole stability,
- Satisfaction of the particle overlapping condition all along the simulation through remeshing procedures, whose computational cost may be greatly decreased by the use of directional splitting schemes (see Section 4.2.2),
- Limitation of the diffusive effects in the advection step thanks to the Lagrangian framework (provided the use of regular and high order remeshing kernels like M_4' or more generally $\Lambda_{p,r}$).

For all these reasons, the VPM methods (i.e., VIC, semi-Lagrangian) have been extensively used in DNS (Direct Numerical Simulations) to discretize the three-dimensional Navier-Stokes equations, especially in the case of highly transitional regimes with Reynolds numbers ranging from 1000 to 10,000. Among the large quantity of CFD studies realized with VPMs, one can mention for example the work of van Rees et al. [97] who carried out the 3D Taylor-Green vortex case at $Re_\Gamma = 1/\nu = 1600$ and successively compared their results to the one obtained with spectral methods, as well as the studies of Morgenthal and Walther [101] or Kudela and Kozlowski [102] where a VIC method is used to model incompressible flows past cylinders up to $Re_D = 3000$ and $Re_D = 9500$ respectively (with D the cylinder diameter). One can moreover refer to the work of Cottet and Poncet [103] which proposed one of the first 3D flow control studies using VIC, where an optimal rotation of a 3D cylinder is designed in order to reduce the drag force. In terms of flow control one also notices the investigations of Creusé et al., based on a VIC method, concerning the active control of a flow over a backward-facing step using pulsing jets [104]. We refer the reader to Section 7 for further applications handled with VIC and semi-Lagrangian vortex methods that clearly highlight the above listed advantages of these methods.

Another type of hybrid vortex method one can also cite to conclude this section is the one designed recently by Kornev in 2018 [105] where the mesh-free simulation is embedded into the grid based one. It consists in representing the large scale field on the grid, whereas the small scale field is evaluated through a pure Lagrangian vortex method, the separation of the large scale vortices from the small ones being based on a LES (Large Eddy Simulation) filtering procedure. By far, this method has only been tested on simple two dimensional canonical flows and its application to more complex physics remains to prove.

5. Treatment of the Boundary Conditions

The ability of correctly handle boundary conditions in a very important issue for any numerical method in CFD. As is well known, the boundaries and the flow viscosity are the only source of vorticity, which explains the efforts made in order to design a method able to accurately model the flow behavior in this region, essentially governed by the no-slip boundary condition. In the context of vortex methods, the major difficulty lies in the fact that the no-slip boundary condition only involves the velocity field in its expression whereas these methods are based on a vorticity formulation of the Navier-Stokes equations. In this section we will give a global description of the main approaches dealing with boundary conditions in vortex methods. We will therefore consider the velocity-vorticity formulation of the Navier-Stokes equations and we will restrict this survey to solid and rigid obstacles.

In the context of Lagrangian vortex methods, the objective is to express the boundary conditions in terms of the vorticity field, equivalent to the no-slip boundary condition $\mathbf{u}(\mathbf{x}_s) = \mathbf{u}_s$, where $\mathbf{u}_s$ denotes the velocity of the solid body and $\mathbf{x}_s$ any location on the solid surface. To write these boundary conditions one may choose a Dirichlet formulation (wall vorticity) or a Neumann formulation (wall-normal vorticity flux). The Neumann form is often preferred since it directly governs the local production of vorticity at a solid wall. Indeed, the wall-normal vorticity flux, given by $\frac{\partial \boldsymbol{\omega}}{\partial \mathbf{n}}$, measures the vorticity that enters the flow from the boundaries. This flux is actually responsible for the total production of vorticity at the no-slip wall.

The approaches designed to model the boundary conditions can be divided into three main categories, exposed hereafter. The first family of methods belongs to pure Lagrangian methods; it is based on viscous splitting and mimics the vortex creation at the interface through the generation of vortex sheets. The two other families involve the presence of a mesh or a lattice and are therefore often used within Vortex-Particle-Mesh methods. The first one, known as the Boundary Elements Method (BEM) enforces the no-slip by defining vorticity flux boundary conditions on panels located at the wall, and the second one prescribes the boundary conditions by using Immersed Boundary Methods (IBM).

5.1. Boundary Treatment Based on Viscous Splitting and Vorticity Creation

The first successful approach designed to handle the boundary conditions in vortex methods for fluid flows is due to Chorin in 1973 [37], later improved by the same author in 1978 [106]. The method he introduced, called the vortex sheet/vortex blob method, uses the viscous splitting technique (described previously in Section 3.1) and relies on creating a vortex sheet at the solid boundary in order to vanish the slip velocity and thus to enforce the required no-slip boundary condition. Practically, the wall is discretized into segments. Each of these segments is associated to a local slip velocity where vortex elements are created at each time step to cancel it. We detail the different steps of the algorithm used in the improved method proposed in [106] to discretize the Navier-Stokes equations, with boundary conditions. More precisely, this approach is based on the coupling of the Prandtl boundary-layer equations near the surface with the Navier-Stokes equations everywhere else. The Prandtl equations are expressed in a coordinate system where x and y respectively denote the tangential and the normal coordinates, and where (u, v) corresponds to the velocity vector field in this system. The solid wall is assumed to be at $y = 0$ and the fluid domain is defined by the half-space $y \geq 0$. In the boundary region, the Prandtl boundary-layer equations rely on the assumption that vorticity diffusion mainly occurs in the direction normal to the wall and high velocity gradients are essentially along the component tangential to the wall (see Figure 6); they therefore can be written as:

$$\frac{\partial \omega}{\partial t} + u\frac{\partial \omega}{\partial x} + v\frac{\partial \omega}{\partial y} = \nu\frac{\partial^2 \omega}{\partial y^2} \tag{64}$$

$$\omega = -\frac{\partial u}{\partial y} \tag{65}$$

They are completed by the continuity equation and the following boundary conditions:

$$\mathbf{u} = 0 \;\text{ at }\; y = 0, \tag{66}$$

$$u(x, y_\infty) = u_\infty(x), \tag{67}$$

where Equation (66) imposes the no-slip boundary condition at $y = 0$ and Equation (67) expresses a far-field condition for the u component when $y \geq y_\infty$. The value y_∞ is often taken of the order of the boundary layer thickness.

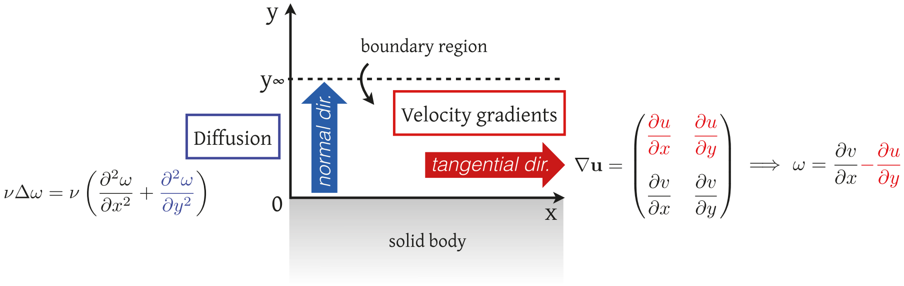

Figure 6. Graphical representation of the main directions driving the vorticity diffusion and the velocity gradients in the Prandtl boundary-layer.

Let us now consider a set of N vortex sheet elements $\mathcal{S}_i$ of strengths α_i. These elements should be seen as segments of a straight line, parallel to the x axis and of length ε, such that the two values of u at the extremities of $\mathcal{S}_i$ differ from each other by α_i. According to this definition, the vortex sheet approximation of ω is given by:

$$\omega \simeq \sum_j \alpha_j b_\varepsilon(x-x_j)\delta(y-y_j), \tag{68}$$

where b_ε is a one-dimensional cutoff function given by $b_\varepsilon = \varepsilon^{-1}b(x/\varepsilon)$ and where δ is the one-dimensional Dirac mass in the normal direction.

The u component of $\mathcal{S}_i$, due to the presence of the other surrounding segments, is then obtained from a direct integration of Equation (65), using the right-hand side of the above ω approximation (Equation (68)):

$$u(x,y) = u_\infty(x) + \sum_j \alpha_j b_\varepsilon(x-x_j)H(y_j-y) \tag{69}$$

where H is the Heavyside function. The expression of v can then be deduced from u, using the continuity equation:

$$v(x,y) = -\frac{\partial u_\infty(x)}{\partial x}y - \sum_j \alpha_j b'_\varepsilon(x-x_j)\min(y,y_j) \tag{70}$$

Based on these definitions, one can give the substeps constituting the algorithm of the Chorin's vortex sheet/vortex blob method (each of these steps are depicted in Figure 7):

1. Evaluation of the u and v components from formulations (69), (70) and advection of the vortex sheets with this velocity field.
2. Computation of u on the wall ($y=0$) and creation of new sheets at the boundary with strengths $\alpha_i = -u(x_i)dl$ in order to impose the no-slip boundary condition (these strength values directly come from the integration of Equation (65)). As explained by Chorin in [106], the velocity field is here extended across the wall by the anti-symmetry $u(x,-y) = -u(x,y)$. As a consequence $\omega(x,-y) = \omega(x,y)$ and a vortex sheet is generated at $y=0$.
3. Diffusion of the vortex sheets in the y direction using a Random Walk approach (see Section 3.1). If a sheet arises in the far-field region ($y \geq y_\infty$), it is transformed into a vortex blob. If a sheet crosses the boundary, moving into the body, it is reflected on the other side.

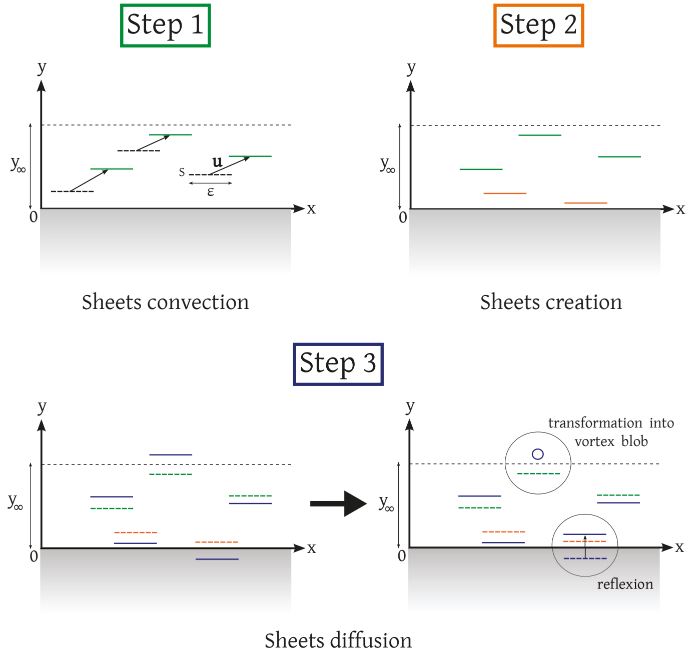

Figure 7. Steps of the vortex sheet/vortex blob algorithm.

In the pioneer version of Chorin's method [37], the cancellation of velocity at the boundary was realized by generating vortex blobs instead of vortex sheets. But, the overlap of vortex blobs with the solid boundary led to inconsistency. Thanks to its more natural framework implying vortex sheets in the boundary region, this random vortex sheet/vortex blob method turned out to be widely used to model slightly viscous flow past obstacles. For example, one can refer again to the work of Smith and Stansby [107] who studied flows around cylinder, to Sethian and Ghoniem [108] who performed a validation study of this technique for flow past a backward-facing step at different regimes or to Cheer [109] who carried out simulations of flows past airfoils and blunt bodies. One can moreover cite the numerical convergence study of the vortex sheet/vortex blob method carried out by Mortazavi et al. [110] which investigates the influence of three discretization parameters (the blob strength Γ, the core radius h and the time step Δt) on the accuracy. The role of the time step has specifically been outlined, with in particular the divergence of the numerical solution for too small values of Δt, due to the Random Walk Method.

The three dimensional version of the vortex sheet/vortex blob method was introduced shortly after, in 1980, by Chorin [111]. In this version, the vortex sheets within the boundary-layer region are now defined as "tiles". These tiles are rectangles, parallel to the wall and their motion is dictated by the straightforward extension of Equation (65) in 3D. Like in two dimensions, the tiles undergo random walk. They are transformed into vortex blobs (also referred to as vortex segments in 3D, as opposed to vortex filaments) when they leave the boundary layer. This method was successfully used in several studies, for instance by Fishelov [112] or Gharakhani and Ghoniem [113], who respectively dealt with flow past infinite plate and flow inside a cylinder equipped with an eccentric inlet port and a driven piston.

However, the Chorin's approach suffers from several limits. The first one, already pointed out in the two-dimensional case by Anderson and Reider [114], refers to the interface zone (in which vortex sheet turn into vortex blob) where the continuity of the tangential velocity value is guaranteed but not the one of the normal velocity, which can lead to spurious oscillations close to the interface. Secondly, the divergence free condition for the vorticity field is only satisfied approximately, which prevents from getting accurate application of vortex methods to three-dimensional flows. Finally, the last and main limitation stands on the fact that the Prandtl approximation makes such approach only valid for attached flows.

As a variant of Chorin's vortex sheet/vortex blob method, one can cite the approach proposed by Walther and Larsen in 1997 [115] were the determination of the surface vorticity in step 2 is no more based on the Prandtl approximation but on the kinematic relation between the velocity and the vorticity. This method has been successfully applied in 2D to flow past a fixed and harmonically oscillating flat plate at high Reynolds number ($Re_c = 10^4$, with c the chord length of the plate).

5.2. Boundary Treatment Based on Vorticity Flux Conditions

The type of method presented in this section was designed later and re-use the framework of algorithms based on viscous splitting and vorticity creation. However, contrary to the Chorin's method, detailed previously, it handles vorticity flux boundary conditions to enforce the no-slip condition on the walls, instead of vortex sheets or vortex blobs. In a first part we will give the expression of the corresponding continuous problem and secondly we will focus on the numerical schemes and techniques used to approximate the integral solution of this continuous problem.

5.2.1. The Continuous Problem

The idea of a vorticity creation method based on a vorticity flux boundary condition was independently proposed in 1994 by Cottet [116] and Koumoutsakos et al. [117]. The so-called vorticity flux boundary condition is characterized by a relation between the normal derivative of the vorticity and the time derivative of the tangential component of the velocity. To derive the global Navier-Stokes problem, we follow the development described in [116] starting with the 2D Stokes problem. Let us consider two vorticity fields ω_1 and ω_2 in the same time interval $[t^n, t^{n+1}]$. Each time step is initialized by the exact initial vorticity field ω^n and provides at the end the solution ω^{n+1} where ω_1 and ω_2 are the solutions of the 2 following sub-problems within the interval $[t^n, t^{n+1}]$:

$$\text{Sub-problem 1}: \begin{cases} \dfrac{\partial \omega_1}{\partial t} - \nu \Delta \omega_1 = 0 \quad \text{in } \Omega, \\ \omega_1(\cdot, t^n) = \omega^n \quad \text{in } \Omega, \\ \dfrac{\partial \omega_1}{\partial \mathbf{n}} = 0 \quad \text{on } S \end{cases} \tag{71}$$

$$\text{Sub-problem 2}: \begin{cases} \dfrac{\partial \omega_2}{\partial t} - \nu \Delta \omega_2 = 0 \quad \text{in } \Omega, \\ \omega_2(\cdot, t^n) = \omega^n \quad \text{in } \Omega, \\ \nu \dfrac{\partial \omega_2}{\partial \mathbf{n}} = -\dfrac{\partial}{\partial t}(\mathbf{u}_1 \cdot \mathbf{s}) \quad \text{on } S, \end{cases} \tag{72}$$

where $\mathbf{s}$ denotes the tangent vector to the surface S and $\mathbf{u}_1$ corresponds to the velocity field associated with ω_1. In other words, in sub-problem 1, the Stokes equations are solved with an homogeneous Neumann boundary condition, that is to say without creating any vortex sheet on the walls. Then, in sub-problem 2, vorticity is produced at the boundary thus enabling to cancel the slip resulting from sub-problem 1. At the end of the time step, ω^{n+1} is set to $\omega_2(\cdot, t^{n+1})$. We refer to [116] for the proof of equivalence with Chorin's algorithm and the proof of convergence using energy estimates. The generalization of the present algorithm to the Navier-Stokes problem is obtained straightforwardly by adding the advection term in Equations (71) and (72) and in replacing the vorticity flux boundary condition of (72) by:

$$\nu \frac{\partial \omega_2}{\partial \mathbf{n}} = -\left[\frac{\partial \mathbf{u}_1}{\partial t} + (\mathbf{u}_1 \cdot \nabla)\mathbf{u}_1 \right] \cdot \mathbf{s} \tag{73}$$

5.2.2. The Integral Formulation

The issue now lies on the resolution of the continuous problems derived above in order to obtain an explicit expression of the approximated vorticity field such that the no-slip boundary condition is satisfied. The general existing algorithms are based on a viscous splitting of the Stokes or Navier-Stokes equations and may be described by the following steps:

1. The Lagrangian advection is performed through the resolution of system (27) and (28),
2. The diffusion is solved in the domain with a PSE scheme for instance (the diffusion scheme needs to be based on a change of vorticity strength),
3. The vorticity flux boundary condition is expressed in terms of an integral formulation derived from the continuous problem (cf. (72) or (73)),
4. The PSE scheme in complemented by distributing this vorticity flux onto the existing vortex blobs so that vorticity enters the domain.

In the last step, particles just experience a change in their strength, they do not multiply themselves like in Chorin's vortex sheet method. In the following, we focus on steps 3 and 4.

Concerning step 3, the method designed to solve the continuous problem (72) was introduced and validated by Koumoutsakos et al. in [117] and [54]. It is denominated as boundary element method (BEM) or panels method. To present it, one re-writes the problem (72) by considering the vorticity diffusion equation supplemented with an homogeneous initial condition and a Neumann boundary condition:

$$\frac{\partial \omega}{\partial t} - \nu \Delta \omega = 0 \quad \text{in } \Omega \times [0,\ t], \tag{74}$$

$$\omega(\mathbf{x}, 0) = 0 \quad \text{in } \Omega, \tag{75}$$

$$\nu \frac{\partial \omega}{\partial \mathbf{n}} = F(\mathbf{x}, t) = -\frac{\partial}{\partial t}(\mathbf{u} \cdot \mathbf{s}) \quad \text{on } S \times [0,\ t]. \tag{76}$$

The integral solution of Equation (76) for the vorticity involves integrals over the surface S only. To discretize this integral, a boundary integral method is employed by defining S as a set of discrete panels, denoted with index i, length d and centered in $\mathbf{x}_i$. Then, the vorticity induced by a panel i can be given by the following integral:

$$\omega_i(\mathbf{x}, t) = \frac{1}{2} \int_0^t \mu_i(\tau) \phi(\mathbf{x} - \mathbf{x}_i, t - \tau)\, d\tau, \tag{77}$$

where, if one defines a coordinate system $\mathbf{x} = (x, y)$ with the x-axis parallel to the surface, the ϕ function yields:

$$\phi(\mathbf{x}, t - \tau) = \frac{e^{\frac{-y^2}{4\nu(t-\tau)}}}{\sqrt{4\pi\nu(t-\tau)}} \left(\operatorname{erf}\left[\frac{d + x}{\sqrt{4\nu(t-\tau)}} \right] + \operatorname{erf}\left[\frac{d - x}{\sqrt{4\nu(t-\tau)}} \right] \right), \tag{78}$$

and where $\mu(\mathbf{x}, t)$, the diffusion potential, can be approximated for points s along S by:

$$\mu_i(s) \approx -2F_i(s) \left[1 - \kappa(s)\sqrt{\pi\nu\Delta t} \right]^{-1} \approx -2\left(-\frac{(\mathbf{u} \cdot \mathbf{s})}{\Delta t}(s_i) \right) \left[1 - \kappa(s)\sqrt{\pi\nu\Delta t} \right]^{-1}, \tag{79}$$

with $\kappa(s)$ denoting the surface curvature at point s and $\gamma_i = -\dfrac{(\mathbf{u} \cdot \mathbf{s})}{\Delta t}(s_i)$ corresponding to the vortex sheet strength derived from (76). We refer the reader to [117] for a full description of the integral evaluation of Equation (77).

Then one jumps to the step 4 of the algorithm, where the strength $\Gamma_j = \omega(\mathbf{x}_j)v_j$ of the particles are modified by distributing the vorticity flux:

$$\Gamma_j(t) = \Gamma_j(0) + \frac{v_j \Delta t}{2} \sum_{i=1}^{N} \mu_i \phi\Big((\mathbf{x}_j - \mathbf{x}_i), \Delta t\Big), \tag{80}$$

with N denoting the number of panels on the surface of the body. Finally, replacing μ_i by approximation (79) in the above equation, the prescription of the no-slip boundary condition is realized through the following particle strength update:

$$\Gamma_j^{n+1} = \Gamma_j^n + v_j \Delta t \sum_{i=1}^{N} \frac{\gamma_i}{\Big(1 - \kappa(s)\sqrt{\pi \nu \Delta t}\Big)} \phi\Big((\mathbf{x}_j - \mathbf{x}_i), \Delta t\Big). \tag{81}$$

Concerning the 3D formulation, one distinguishes the flat surfaces (half-plane case) from the curved ones.

The first three-dimensional extension of the continuous formulation was given in the case of a flat plate. We note that in 3D, one must ensure that the vorticity is divergence free in order to satisfy the fundamental laws of the fluid mechanics. The direct 3D extension of problems (71) and (72) do guarantee this condition and we refer to Cottet and Koumoutsakos' book [22] for the proof. In order to solve the three-dimensional continuous problems, Casciola et al. [118] proposed a similar analysis as the one described in the above algorithm. First of all, this study supplies the expression of the integral equation for the vorticity creation. An approximation of such integral equation is then given and identified as the slip velocity at the surface of the flat body. Moreover, this work exposes an error estimate of the proposed approximation and also proves that the vorticity generated at the wall and then diffused in the flow is solenoidal.

The expression of three-dimensional continuous problems in the case of non-zero curvatures along the surface S has been first expressed for cylinders, where the curvature is constant and defined at $\kappa = 1/R$, where R is the cylinder radius. The natural coordinate system to consider herein is the cylindrical coordinate system where one denotes by $(\mathbf{e}_r, \mathbf{e}_z, \mathbf{e}_\theta)$ the basis vectors, respectively corresponding to the unit normal vector $(\mathbf{e}_r)$ and the tangent vectors to the cylinder surface $(\mathbf{e}_z, \mathbf{e}_\theta)$. According to Poncet and Cottet [119,120] it appears that the divergence free condition is ensured if the Neumann boundary condition $\partial\omega_\theta/\partial\mathbf{n}$ on the tangential component ω_θ is modified into a Robin type boundary condition, that is to say by $\kappa\omega_\theta + \partial\omega_\theta/\partial\mathbf{n}$. The three-dimensional numerical scheme giving the solution of such formulation is derived in the same two references and the validations carried-out herein show the accuracy of the vorticity flux boundary conditions.

In conclusion, the handling of the no-slip boundary condition using vorticity flux formula stands as a suitable and successful method. It indeed allows us to treat in an accurate way the high velocity gradients at the solid-fluid interface while overcoming the main drawbacks of the prior approaches. It is important to highlight the fact that the BEM technique is generally related to the presence of a lattice, first because of the use of a PSE scheme (that needs particle overlapping to ensure convergence, as evoked in Section 3.2) and most of all, because its design is based on the definition of panels on which the flux integrals are discretized. BEM is therefore very often used within Vortex-In-Cell/Vortex-Particle-Mesh algorithms, but not systematically as illustrates the completely mesh-free proposition of Cooper and Barba [121] based on the use of the radial basis function (RBF) collocation method (see Section 4.1). The latter method evaluates the ϕ function of Koumoutsakos (Equation (78)) and solves the diffusion equation by using the radial basis functions and therefore proposes a treatment of the boundary conditions without any panel.

5.2.3. Improvements of Vorticity Flux Boundary Conditions

Based on the pioneer works of Koumoutsakos and Leonard presented above, Ploumhans and Winkelmans proposed substantial improvements in [122] (2D study) and in [55] (3D extension) in the early 2000s. These advances may be separated into two categories.

First, they proposed to improve the step 2 described previously in the viscous splitting algorithm, concerning the diffusion process. Indeed, the authors point out that if the standard PSE scheme is used, namely:

$$\frac{d\omega_j}{dt} = \nu\varepsilon^{-2}\sum_i (v_i\omega_i - v_i\omega_j)\,\eta_\varepsilon(\mathbf{x}_i^h - \mathbf{x}_j^h), \tag{82}$$

then the particles j are completely and radially surrounded by other particles i, which is not true close to the wall. Thus, the use of standard PSE scheme induces spurious vorticity flux at the boundary (even if the total circulation is conserved). To overcome this problem, Ploumhans and Winkelmans [122] introduced a modified PSE scheme in which *image particles* are defined inside the body when the scheme is applied close to the wall. This process allows a zero vorticity flux during the PSE step, before computing it properly at step 3.

The second type of improvements are based on the fact that BEM (or panels methods) rely on grids to perform the particles remeshing. In Koumoutsakos and Leonard [54], the BEM was proposed in the particular case of a circular cylinder and the particle redistribution was performed on a body-fitted lattice, that followed the cylinder boundary, making it quite restrictive in terms of applications. In their work, Ploumhans and Winkelmans [122] propose on one side a regular lattice able to redistribute the particles in the case of any general geometry for the immersed obstacle, and on the other side, they introduce a mapping on non-uniform lattices, thus allowing a coarser and controllable resolution for the far wake regions.

All these advances have been validated in the 2D case [122] at different flow regimes for flow past a cylinder, a square and a generic geometry (2D "Apollo" capsule) as well as in the 3D case [55] with the simulation of flow past a sphere at transitional Reynolds numbers (from $Re_D = 300$ up to $Re_D = 1000$).

5.3. Boundary Treatment Based on Immersed Boundary Methods

Driven by the necessity to overcome the difficulties related to the body geometry, the Vortex-Particle-Mesh methods turned, in the early 2000s, to another strategy able to enforce boundary conditions without being constrained neither by the type of underlying mesh nor the obstacle geometry. This strategy lies in their coupling with Immersed Boundary Methods (IMB).

One of the first types of Immersed Boundary Vortex methods to be introduced was an approach in which the boundary conditions are in the form of local forcing terms in the right-hand side of the momentum equations. In this approach, the flow equations are discretized in a unique way in the computational domain, independently of the nature of the cells (i.e., fluid, solid or mixed cells). One can particularly cite the approach proposed in 2003 by Cottet and Poncet [120] in the context of a VIC method, where the no-slip boundary condition is enforced from source points that are located on the boundary itself on all grid points that are at a distance less than the grid-size from the boundary. Few years later, Poncet [123] proposed a revisited immersed boundary technique allowing to satisfy the no-through-flow boundary condition on a body of arbitrary geometry, in an implicit formulation. More precisely, the approach consists in solving the linear system associated to the source-to-flow-through linear application; this system is of reasonable size since it is only constituted by the discretization points of the surface, not all the grid cells. In Poncet's paper, this vortex IBM is applied to flow past a complete aircraft geometry and to the vorticity evolution around the complex geometry of a hollow bridge structure.

From this first approach arose other immersed boundary vortex methods, presented hereafter.

5.3.1. The Brinkman Vortex Penalization Method

The Brinkman penalization technique is part of the continuous forcing immersed boundary methods. It was first proposed in a context completely detached from vortex methods by Caltagirone in 1994 [124], further developed by Angot et al. [125] and was expressed and used in a vorticity formulation by Kevlahan and Ghidaglia in 2001 [126]. The resulting Brinkman-Navier-Stokes vorticity equations are:

$$\frac{\partial \boldsymbol{\omega}}{\partial t} + (\mathbf{u} \cdot \nabla)\boldsymbol{\omega} - (\boldsymbol{\omega} \cdot \nabla)\mathbf{u} - \nu\Delta\boldsymbol{\omega} = \nabla \times [\lambda\chi(\mathbf{u}_s - \mathbf{u})], \qquad \text{in } \Omega \times [0,t] \qquad (83)$$

$$\text{div } \mathbf{u} = 0, \qquad \text{in } \Omega \times [0,t] \qquad (84)$$

where the forcing term $\nabla \times [\lambda\chi(\mathbf{u}_s - \mathbf{u})]$ is the penalization term, in which χ denotes the characteristic function of the solid bodies, $\mathbf{u}_s$ corresponds to the velocity of the immersed obstacle and λ is the non-dimensionalized penalization factor. This penalization term actually comes from the Darcy equations that govern flows in porous media, and the factor λ is directly related, in the inverse proportion, to the permeability k of the considered media in the domain, i.e., $\lambda \sim 1/k$. The penalization factor λ is set to zero in the fluid region and to infinity in the solid ones. With such approach, the force is activated only inside the solids, making the velocity vanishing in these regions, and the no-slip boundary conditions are automatically satisfied. The condition $\mathbf{u} = \mathbf{u}_s$ is thus prescribed on the boundary and rigid motion is ensured within the solid.

In the 2010s arose the first resolutions of the vorticity-penalization Equations (83) and (84) through VPM methods. In practice, the penalization equation $\partial\boldsymbol{\omega}/\partial t = \nabla \times [\lambda\chi(\mathbf{u}_s - \mathbf{u})]$ is added to the fractional step algorithm and is solved on the grid, often using finite-differences and an implicit Euler scheme. In the last decade, this technique has been widely applied within VPMs to handle different types of problems involving boundaries. We can for instance cite the works of Gallizio [96] and Morency et al. [127] who coupled the penalization technique with a level-set method in order to handle moving bodies. Besides, in terms of fluid-structure interactions we can cite the works of Coquerelle and Cottet [128] who also coupled the penalization method with a level-set method and moreover with a collision model to simulate the interaction of an incompressible flow with rigid bodies. One also has to mention all the studies of Gazzola et al. focusing on obstacles' motion induced by vortical flow-structures [10] or dealing with fish schooling [6–8,86], where the penalization method is combined to a projection approach allowing to model the action of the fluid on the deforming fishes (more details are reported in Section 7 about these applications).

In terms of numerical advantages, the vortex penalization method naturally exhibits the ones of the immersed boundary methods, that is to say the absence of explicit prescription of the boundary conditions, the existence of a unique equation for the whole domain Ω and the possibility to handle complex geometries. Moreover, the Brinkman penalization method is particularly easy to implement and to parallelize. Finally, it allows the direct modeling of porous medium when giving intermediate values to the penalization factor, $0 < \lambda \lesssim 10^3$. Figure 8 depicts and summarizes the modeling of flow in solid-fluid-porous media with the Brinkman penalization method and we refer the reader to Section 7 for an example of related application. However, the major drawback of this approach lies in its first-order accuracy. Besides, performing relevant simulations imposes a restrictive overall time step Δt in the fractional step algorithm.

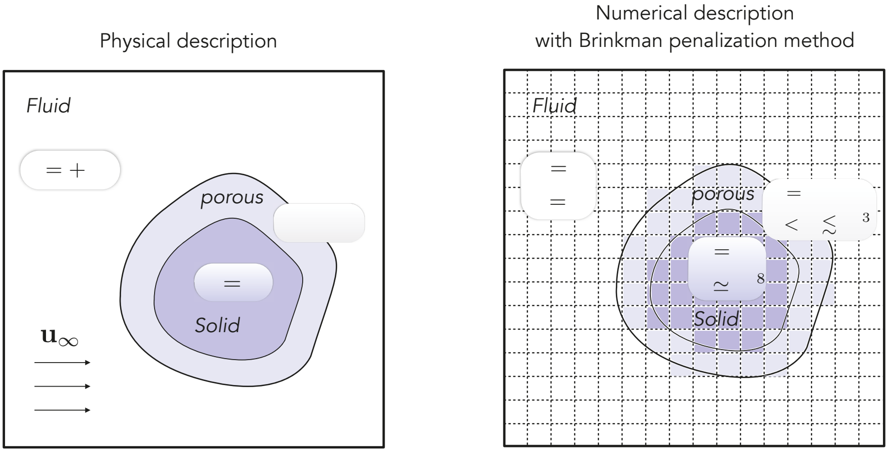

Figure 8. Schematic representation of the physical description (**left**) and its numerical parametrization (**right**) for flow past a solid-porous body using the Brinkman penalization method.

To remedy these weaknesses, Hejlesen et al. [129] introduced an iterative penalization scheme allowing to accurately enforce no-slip boundary conditions through sub-iterations of the penalty method. The proposed scheme imposes the resolution of a Poisson equation at each iteration to re-evaluate the penalized velocity, but it is applied only in the vicinity of the body, which on one hand reduces the computational cost of each Poisson sub-problem and on the other hand allows us to consider larger time-steps within the iterative penalization loop than the ones usually required in a standard Brinkman penalization. This iterative approach has proved to be more accurate for all the classical two-dimensional benchmarks tested by the authors (flow past an impulsively started cylinder at $Re_D = 9500$ and flow past a flat plate at different regimes). Another version of iterative penalization method was also proposed by Gillis et al. in [130] where they formulate the penalization problem as a linear system that is solved iteratively using a recycled Krylov subspaces.

5.3.2. The Immersed Interface Vortex Method

Despite the improvements brought by the iterative Brinkman penalization methods described previously, the latter keep on smearing the interface of the immersed body and are still first order convergence methods. To overcome these weaknesses, a third type of immersed boundary technique was proposed in 2016 by Marichal et al. [131] and in 2019 by Gillis et al. [132] to be coupled to VPM: the immersed interface method (IIM). In a general point of view, the immersed interface method (originally proposed by Leveque in 1994 [133]) consists in treating the flow discontinuities at the body's surface through finite-difference stencils, where the jumps are precisely taken into account inside the stencils thanks to modified Taylor series. These jump-corrected Taylor series allow us to evaluate the derivatives of the flow fields, which remain valid across the interface. The prescription of the desired boundary conditions is then realized by injecting them directly in the jump-corrected Taylor series discretizing the derivatives of the velocity field at each control point of the body's surface. In Gillis et al. [132], this approach is embedded in a two-dimensional VPM algorithm and tested in the case of flow past a 2D impulsively started cylinder at high Reynolds numbers (up to $Re_D = 40{,}000$). On one side the results show a second order spatial accuracy, up to the boundary region, and on the other side they reveal to be in good agreement with previous VPM computations based on Brinkman penalization performed by Rossinelli et al. [134], while considering an eight-fold coarser grid size near the wall.

6. Algorithmic Issues

All the sections written so far enabled to outline the landscape of the different families of Vortex Method, with their respective characteristics in terms of numerical convergence, accuracy and reliability. In this part we will now focus on the algorithmic and computational techniques developed to efficiently handle them. This point constitutes a crucial issue for any numerical method which aspires to be considered as a usable and challenging one.

6.1. Fast Vortex Methods

Regardless of which type of Vortex Methods one considers, it is admitted that the intrinsically most expensive operation in any vortex algorithm relies on the resolution of the Poisson problem. Indeed, for N particles, the classical discretization of the Poisson Equation (15) through the Biot-Savart Law (17) implies to compute the interactions between each particle and all the others, leading to a $\mathcal{O}(N^2)$ computational cost. A wide range of studies have been dedicated to the task of reducing this cost. They are mainly split into two categories: the strategies dedicated to the Vortex-Particle (Lagrangian) framework and the one dedicated to the Vortex-Particle-Mesh context.

Among the algorithms able to solve the Biot-Savart law, the most efficient one is certainly the Fast Multipole Method (FMM). This technique, introduced by Greengard and Rokhlin in 1987 [135], exploits in the context of vortex methods the geometrical distributions of the vortices to evaluate the velocity. The key point is that the velocity field induced by a group of particles clustered around a center does not need to be computed directly from its individual members, but it can be approximated by a finite number of multipole expansions. This approach, based on tree data structures, thus allows us to achieve a $\mathcal{O}(N)$ computational cost. Parallel multicores FMM implementations have been widely developed and used in the context of Lagrangian Vortex methods, like in the works of Marzouk and Ghoniem [136], Yokota et al. [137] or Giannopoulou et al. [138], to deal with the velocity resolution. Besides its capability to accelerate the evaluation of particle interactions, FMM was also used by Hu et al. [139] to reduce the time consumption of the stretching term calculation in the vorticity equation. However, the use of FMM algorithms is not restricted to Lagrangian Vortex approaches and was also implemented within Vortex-Particle-Mesh methods, as it will be illustrated in the last Section 7.

As one evokes the Vortex-Particle-Mesh methods (VIC, semi-Lagrangian), they particularly and naturally focused on fast grid-based Poisson solvers in order to take advantage of the presence of an underlying mesh. The latter are called fast Poisson solvers, as opposed to the traditional "slow" solvers based for instance on Jacobi, Gauss-Seidel, Conjugate Gradients or Successive Over Relaxation (SOR) methods. These fast Poisson solvers can be defined as hierarchical methods and among them, one can distinguish the direct solvers from the iterative ones. The most popular direct solvers are the Cyclic Reduction method, consisting in discretizing the Poisson equation by means of finite-differences method over a rectangle by a successive splitting of the initial problem, and the Fast Fourier Transform method, which consists in solving the Poisson equation in the Fourier space using FFTs. These two direct grid-based Poisson solvers present a $\mathcal{O}(N \log N)$ cost and have been widely used in VPM, for instance by Cottet and Poncet [120] for the Cyclic Reduction method (based on the `Fishpack` solver), or by Mimeau et al. [100] for the FFT approach (based on the `FFTW` fortran solver), where the computational cost of the Poisson problem was reduced to 5% within a whole time-step. On the other hand, one of the most famous iterative solvers relies on the Multigrid method, which recursively uses coarse discretizations of the Poisson problem to approximate its solution, following V-cycles. The complexity of Multigrid algorithms is $\mathcal{O}(N)$, which makes them very attractive in terms of computational cost. However, they may require more efforts in terms of implementation and use.

6.2. Performance-Computing Improvements Using GPUs

Because of their close link with computer graphics, the smooth particle hydrodynamics (SPH) methods were the first particle methods to have been implemented on graphic processors (GPUs) in the mid-2000s. Few years later, in 2008, arose the first implementation of Vortex methods in GPUs with the work of Rossinelli and Koumoutsakos [70]. In this pioneer contribution, the implemented 2D solver relies on a remeshed vortex method and runs exclusively on the GPU, including a periodic 2D multigrid Poisson solver developed for the GPU. This work, validated on 2D vortical flows was further successfully tested on 2D bluff body flows with vortex penalization techniques and a CUDA FFT library (`cuFFT`) by Rossinelli et al. [140]. It shown a good agreement and, above all, important speed-up with respect to identical simulations performed with prior solver based on CPU (Central Processing Unit) (up to 30 times speed-up of CPU-computations for flows past an impulsively started cylinder). In terms of GPU-simulations based on remeshed vortex methods, one can also cite the very recent work of Keck [141] who managed to solve a three-dimensional sediment flow on a 1537 × 512 × 512 Cartesian grid with a unique 32 gigabits `Nvidia® Tesla V100` node, within only 6 h (this work will be presented into more details in Section 7).

Regarding mesh-free approaches, Yokota and co-authors also developed in the late 2000s a FMM-GPU algorithm (inspired from the one first proposed by Gumerov and Duraiswami in 2008) to realize Lagrangian vortex method simulations of 3D isotropic turbulence [137]. Few years later, they proposed in [142] a comparison between a spectral method and a FMM-based vortex method on 4096 GPUs for the simulation of 3D homogeneous-isotropic fluid turbulence with 69 billions of grid nodes or particles. The authors highlight the limits of spectral methods in simulating problems on such a great number of GPUs and show that, in such configuration, the parallel FFM-GPU solver allows us to achieve a much better computational performance and efficiency than spectral methods, due to the non-local FFT-based operations of the latter, and show the relevance of advanced Lagrangian vortex solvers for the simulation of isotropic turbulence.

6.3. Adapted Grids, Multiresolution Aspects and LES Models

The Lagrangian framework of Vortex-Particle methods intrinsically allows us to spatially adapt the particle resolution according to the flow physics (provided the overlapping condition is satisfied). One can refer to the recent work of Giannopoulou et al. [138], based on the DVH method (already evoked in Section 4.1), where a self-adaptive particle resolution (also called *r*-adaptivity) is carried out in order to progressively reduce the particle size when getting closer to the boundaries. The method is tested in the cases of two-dimensional flows past cylinders with circular, elliptical and triangular sections, and successively compared to a Finite-Volume method. However the results reveal a higher computational cost with the DVM approach, which can be in particular explained by the large number of vortices required at the boundary compared to the number of cells required in Finite-Volume methods as well as the smaller time steps required by the explicit DVH approach.

Concerning hybrid vortex methods (i.e., Eulerian/Lagrangian domain decomposition or VPM methods like VIC and semi-Lagrangian vortex methods), they have encountered, as shown throughout this paper, a growing notoriety since the late 1990s and rapidly got concerned by the cost of the grid involved in their schemes. Like in Eulerian methods, questions related to adapted grids, multiresolution simulations or subgrid scale models therefore naturally arose in order to give VPM methods the opportunity to handle complex physical problems and/or turbulent flows, which require a high level of mesh refinement and thus a high computational cost.

6.3.1. Adaptive Mesh Refinement (AMR)

This technique consists in defining blocks of uniform grid sizes in a dynamic way from *a posteriori* estimates. It has been first introduced within a 2D remeshed vortex method by Bergdorf et al. in 2005 [143]. In this work the two-dimensional grid adaptivity obeys a criterion based on the velocity derivatives in order to refine the underlying mesh in the flow regions of high gradients. The simulation results are compared to those of a *r*-adaptive vortex method with global mappings for the inviscid evolution of an elliptical vortex of compact support in an unbounded domain. It turns out that AMR-based method seems to be usable in a wider range of problems since the refined regions can be created on demand based on any criterion (provided a stepwise refinement transition from coarse to fine grid-sizes), contrary to the method based on adaptive global mappings that must adapt smoothly to the flow physics involved in the problem. Rasmussen et al. [144] also proposed a 2D multiresolution VIC algorithm with Brinkman penalization and validated it in the case of classical benchmarks involving bluff bodies; in this study the local refinement is not adaptive but fixed *a priori*. In 2010, El Ossmani and Poncet [145] introduced a 3D adaptive mesh refinement based on multilevel sub-blocks that adapt to the flow evolution through the periodic evaluation of the quantity $\alpha|\boldsymbol{\omega}| + \beta|\nabla \times \boldsymbol{\omega}|$. They tested it to study 3D ellipsoid vortex dynamics and the wake development behind a sphere.

Based on these considerations, Bergdorf and Koumoutsakos [87] proposed in 2006 another multiresolution criteria for the grid adaptivity within remeshed vortex methods: the wavelets. The decomposition of a signal into wavelets (i.e., wave-like oscillations) is a mathematical tool complementary to Fourier transform. It is often used to extract information from data and to design compression/decompression algorithms. In the context of multiresolution analysis, the wavelet theory is applied to extract information from velocity and vorticity fields and to induce local refinements or compressions of the grid.

More precisely, the wavelet-based adaptivity proposed in [87] is performed using biorthogonal wavelets. The latter introduce a pair of analysis functions (involing the Fast Wavelet Transform) and a pair of synthesis functions (involving the inverse FWT). The velocity and vorticity field can therefore be decomposed in “scaling” and “detail” coefficients at different levels of resolution. Each point of the adaptive grid is thus represented by a scaling and a detail coefficient. The aim is to discard the detail coefficients which, compared to a fixed threshold, do not carry relevant information about the flow field. For each level of resolution, one only keeps the coefficients called active coefficients. To build up the wavelet-based AMR method, a block structure is used. Each block contains active coefficients situated at the same level of resolution and all blocks contain exactly the same number of active coefficients. These blocks are built so that they can be split into finer (refinement) or collapsed into coarser blocks (compression). In order to capture the emerging small scales, refinement of the grid is performed, written $\mathcal{R}(\boldsymbol{\omega}^n, \mathbf{u}^n)|_{t_r}$, based on a refinement threshold t_r at the beginning of each time step through inverse FWT. For compression, noted $\mathcal{C}(\boldsymbol{\omega}^{n+1}, \mathbf{u}^{n+1})|_{t_c}$, a threshold t_c is used at the end of each time step to truncate terms in reconstruction, retaining active coefficients and discarding detail coefficients which do not carry significant information. The blocks where these detail coefficients are located then collapsed into coarser ones performing FWT. Figure 9 depicts this process. The concept of wavelet adaptivity has been later implemented by Bergdorf, Koumoutsakos and co-authors in a 2D remeshed vortex library, called MRAG-I2D [134], where the space-adapted grids are also coupled with Local Time-Stepping (LTS) integration schemes in order to speedup the computational efficiency. These schemes, exploiting the time step locality imposed by the different stability conditions, allow us to integrate the coarser elements with larger time steps than the finer ones and thus enable one to perform fewer integration steps. Local time-stepping schemes are shown to speedup the computation by one order of magnitude at each level of resolution from a certain number of levels. The non-uniformity of the grid imposes the use of a Fast Multipole Method (FMM) to solve the velocity Poisson equation. The MRAG-I2D library efficiently maps these different algorithmic and numerical aspects onto heterogeneous CPU-GPU platforms. It has been used for the simulation of bluff body flows with Reynolds numbers ranging until 40,000, flow-mediated interactions between two solids, analysis of optimal shapes in anguilliform swimming and reinforcement learning in the context of self-propelled bodies (these applications will be further detailed in Section 7).

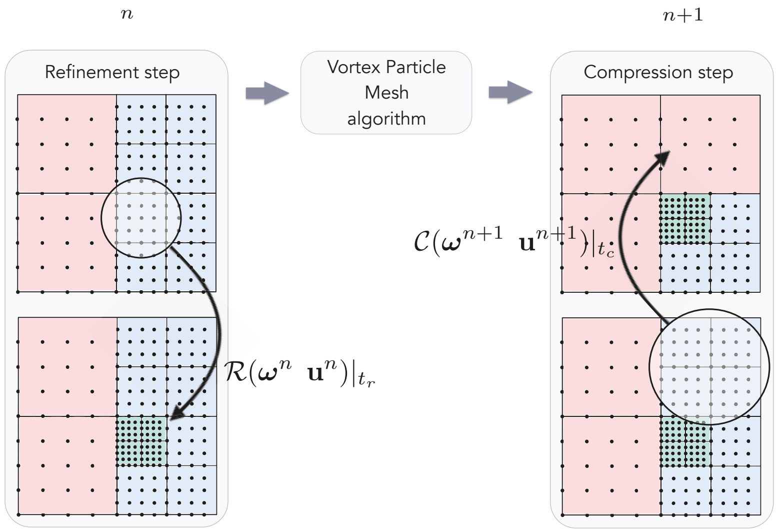

Figure 9. Sketch of refinement/computations/compression process within one time step of Vortex-Particle-Mesh method with wavelet-based Adaptive Mesh Refinement (AMR).

6.3.2. Subgrid Scale Vortex Methods

When the flow under study becomes turbulent, and therefore computationally expensive to simulate, the Large Eddy Simulations (LES) allow us to only capture and resolve the most energetic scales while modeling the effect of the Sub-Grid Scales (SGS) on the captured scales [146]. Before presenting some SGS vortex methods, let us first briefly introduce the general concept of LES methods. As evoked above, this approach consists in only resolving the smallest scales down to the cutoff length Δ of a chosen filter $\mathcal{F}$. Typically the spacial discretization is on the order of Δ. Thus the resolved (or filtered) quantity $\tilde{Q}$ is defined as:

$$\tilde{Q} = \mathcal{F}_{\Delta} \star Q(\mathbf{x}, t), \tag{85}$$

and the remaining smallest scales must be modeled. The filtered Navier-Stokes equations, written here in their velocity-pressure formulation, therefore can be written:

$$(\mathrm{NS}_{LES}) : \begin{cases} \dfrac{\partial \tilde{\mathbf{u}}}{\partial t} + (\tilde{\mathbf{u}} \cdot \nabla)\tilde{\mathbf{u}} = -\dfrac{1}{\rho}\nabla \tilde{p} + \nu \Delta \tilde{\mathbf{u}} - \nabla \cdot \boldsymbol{\tau} \\ \mathrm{div}(\tilde{\mathbf{u}}) = 0 \end{cases} \tag{86}$$

where $\tau_{ij} = \widetilde{u_i u_j} - \tilde{u}_i \tilde{u}_j$, referred to as the subgrid scale stress tensor, models the smallest scales behavior in the flow. Among the different classes of subgrid scale models, the eddy-viscosity models are the most commonly used as for instance the famous Smagorinsky model, given by:

$$\tau_{ij} = -2\nu_{sma}\tilde{S}_{ij} \qquad \text{with} \qquad \nu_{sma} \equiv (C\Delta)^2 |\tilde{\mathbf{S}}| \tag{87}$$

where C is a fixed constant, called the Smagorinsky coefficient, and $|\tilde{\mathbf{S}}|$ is the rate-of-strain tensor.

Vortex methods allow us to carry out under-resolved viscous simulations and large eddy dynamics. To illustrate this statement we will describe the guidelines of three different approaches.

The first one is the anisotropic subgrid scale model, based on Vortex method, proposed by Cottet in 1996 [147]. The 2D model derivation is based on the resolution of the regularized/smoothed Euler equations using vortex blob method (see Section 2.1):

$$\frac{\partial \omega}{\partial t} + \operatorname{div}(\mathbf{u}_\varepsilon \omega) = 0, \tag{88}$$

$$\mathbf{u}_\varepsilon = K_\varepsilon \star \omega \qquad \text{with} \qquad K_\varepsilon = K \star \zeta_\varepsilon, \tag{89}$$

where the function $\zeta_\varepsilon = \dfrac{\zeta(\mathbf{x}/\varepsilon)}{\varepsilon^2}$ results from a cutoff function ζ, that one assumes positive and decaying at infinity, of mean value 1 and with radial symmetry. The approximation of the exact vorticity field ω is then defined by the regularization $\omega_\varepsilon = \omega \star \zeta_\varepsilon$. In the spirit of LES methods, at a finite core size ε it is appropriate to interpret ω_ε as the filtered vorticity, and the core smoothing function ζ_ε as the spatial filter, of size $\Delta \equiv \varepsilon$. Performing the convolution of (88) with ζ_ε one gets:

$$\frac{\partial \omega_\varepsilon}{\partial t} + \operatorname{div}(\mathbf{u}_\varepsilon \omega_\varepsilon) = E(\mathbf{x}), \tag{90}$$

where E represents the truncation error resulting from the fact that the convolution was only applied on ω in the advection term $\operatorname{div}(\mathbf{u}_\varepsilon \omega)$. Based on the expression of error E, one can then derive an evaluation of the enstrophy production, given by:

$$\frac{d}{dt} \int \omega^2 \, d\mathbf{x} = - \iint [\omega(\mathbf{x}) - \omega(\mathbf{y})]^2 \, [\mathbf{u}(\mathbf{x}) - \mathbf{u}(\mathbf{y})] \cdot \nabla \zeta(\mathbf{x} - \mathbf{y}) \, d\mathbf{x} d\mathbf{y}. \tag{91}$$

where the subscript ε has been dropped for clarity. This expression indicates that the enstrophy will increase because of the exchange of vorticity between point $\mathbf{x}$ and $\mathbf{y}$ when they will satisfy:

$$[\mathbf{u}(\mathbf{x}) - \mathbf{u}(\mathbf{y})] \cdot \nabla \zeta(\mathbf{x} - \mathbf{y}) < 0. \tag{92}$$

meaning that the truncation error $E(\mathbf{x})$ in the mollified Euler equations intrinsically embed antidiffusive (or backscatter) mechanisms. The idea proposed in [147] is therefore to clip antidiffusivity while leaving contributions in the direction of dissipation untouched, leading to the following 2D anisotropic eddy viscosity model:

$$\frac{d\omega_p}{dt} = \varepsilon^{-2} \sum_q v_q (\omega_p - \omega_q) \{ [\mathbf{u}(\mathbf{x}_p) - \mathbf{u}(\mathbf{x}_q)] \cdot \nabla \zeta(\mathbf{x}_p - \mathbf{x}_q) \}_{-} \tag{93}$$

where the index—denotes the negative part of the quantity between brackets. This diffusion scheme, very reminiscent of PSE methods, is conservative. As explained by Cottet in [147] and in all the following works of the same author related to this subject, the proposed eddy viscosity model turns out to be more accurate than usual Smagorinsky-type models, which would produce stronger diffusion for identical flow problems.

A few times later, Mansfield et al. [148] proposed another development of a LES vortex scheme in order to model the effects of subfilter scale (SFS) velocity and vorticity fluctuations. To do so, the authors start from the 3D filtered vorticity transport equation:

$$\frac{\partial \tilde{\omega}_i}{\partial t} + \tilde{u}_j \frac{\partial \tilde{\omega}_i}{\partial x_j} = \tilde{\omega}_j \frac{\partial \tilde{u}_i}{\partial x_j} + \nu \Delta \tilde{\omega}_i - \frac{\partial R_{ij}}{\partial x_j} \tag{94}$$

where $\tilde{(\cdot)}$ denotes the low-pass filtered quantities and $R_{ij} = (\widetilde{\omega_i u_j} - \tilde{\omega}_i \tilde{u}_j) - (\widetilde{u_i \omega_j} - \tilde{u}_i \tilde{\omega}_j)$ is the subgrid scale vorticity stress. $\partial R_{ij} / \partial x_j$ refers to the subfilter scale torque $\mathbf{g}$. This SFS torque is modeled based on a Smagorinsky-like eddy diffusivity scheme:

$$\mathbf{g} = -\nabla \times (\nu_{sma} \nabla \times \tilde{\boldsymbol{\omega}}) \tag{95}$$

with $\nu_{sma} = (C\Delta)^2 |\tilde{\mathbf{S}}|$ the Smagorinsky eddy diffusivity. The authors then propose a particle discretization of this SFS model based on a vortex blob discretization and introduce a dynamic variation of the model coefficient C, directly evaluated in a Lagrangian way from the particles data. Based on this approach, the same authors performed dynamic LES of colliding three-dimensional vortex rings in [149]. The results coincide with experimental observations and highlight in particular the capability of the model to correctly simulate the generation of small-scale turbulent structures as well as the formation of small-scale ringlets propagating radially after collision. The same approach was also used by Pinon et al. [150] (with a fixed model-coefficient C) in order to perform LES of a 3D flow of a round-jet in a crossflow, providing results in good agreement with previous experimental and numerical studies.

With the increasing use of Vortex-In-Cell and semi-Lagrangian vortex methods, a novel way of performing LES within vortex methods appeared, where the subgrid scale vorticity stress in the rhs of the filtered vorticity transport equation is directly solved on the grid, using finite-differences schemes. This is what proposed Cocle et al. [151] who investigated several types of existing SGS models within a VIC method. Among the tested models, the usual Smagorinsky model is not able to be activated only during the complex phases of the flow, and turns out to be too diffusive, as expected. A good compromise highlighted in [151] is the use of the so called "regularized variational multiscale" model. In this approach, the artificial diffusion does not operate on the complete LES vorticity field, as in usual Smagorinsky models, but acts solely on the high frequency part of the LES vorticity field:

$$\frac{d\omega}{dt} = \nabla \cdot (\mathbf{u}\omega) + \nu\Delta\omega + \nabla \cdot (\nu_{sma}(\nabla\omega^s + (\nabla\omega^s)^T)) \tag{96}$$

with ω^s denoting the "small-scale" vorticity field defined as $\omega^s = \omega - \tilde{\omega}$ (where $\tilde{\omega}$ is the filtered vorticity obtained through a discrete filter of size Δ) and where the subgrid viscosity ν_{sma} is evaluated through a Smagorinsky model (see definition (87)). As reported in [151], this multiscale subgrid model included in a VIC method allows us to perform large eddy simulations with good spectral behavior. It indeed preserves the low and medium wavenumbers while ensuring the SGS dissipation at the high frequencies. This SGS model has been further used within others VPM methods, to handle challenging applications in aerodynamics (some of them are presented in Section 7).

All the algorithmic strategies exposed in this section, as well as the cited related works, are summarized in the diagram of Figure 10.

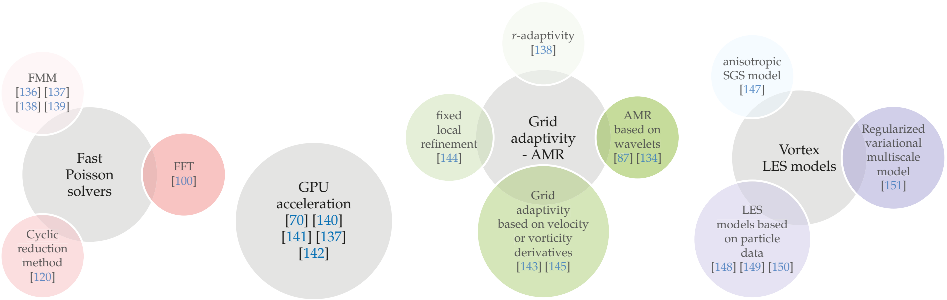

Figure 10. Algorithm issues in Vortex methods: summarize-diagram of Section 6.

7. Applications and Issues

Previous section illustrates the capability of purely meshless vortex methods to excel in the calculation of isotropic turbulence. They also proved their ability in simulating simple geometrical bluff body flows. Besides these types of applications, they seem to show a certain difficulty in handling complex flow physics implying the coupling of the Euler or Navier-stokes equations with other models.

On the contrary, hybrid vortex methods like Eulerian/Lagrangian domain decomposition or VPM methods, continually succeeded during the last two decades in undertaking more and more challenging applications. This last section proposes a non-exhaustive presentation of recent and advanced simulations performed with hybrid vortex methods in order to illustrate their capacities and their versatility. Table 1, given at the end of this section, outlines the main physical and numerical characteristics related to each of them.

7.1. Hydrodynamics

The simulations exposed hereafter deal with Vortex-Particle-Mesh methods used to study fluid-structure interactions in hydrodynamics and more specifically in fish schooling. The involved Reynolds numbers (based on the fish length L) stand in the range $100 \leq Re_L \leq 5000$.

Propelling and energy harvesting of articulated bodies (referred with number (#**1**) in Table 1) by Bernier et al., 2019 [9]. This study examines the hydrodynamics resulting from passive and actuated bodies in fluids. More precisely it consists in handling the passive propulsion of a free swimming articulated fish within the wake of a leading bluff body. The free swimmer is modeled by a multi-body articulated system including complex kinematic constraints like rotational joints and linear rails for self-propulsion as well as damper-like elements for energy harvesting. The parametric simulations show an efficient combination between power production (for the damped passive multi-body swimmer) and flow control (for the leading body).

Optimization of fish schooling (#**2**) by Gazzola et al., 2012b [86] and van Rees et al. 2013 [7]. The simulations performed in these two studies both include a CMA-ES (Covariance Matrix Adaptation Evolutionary Strategy) optimization algorithm within their VPM method in order to study optimal swimming regimes for anguilliformed robots. For the modeling of the swimming bodies, both study involve independent local deformable grids on which are defined the fish shapes and carrying the values of deformation velocities and characteristic/level-set functions, then interpolated on the underlying Cartesian computational grid. In [86], the CMA-ES algorithm is used to identify the fish shape-pattern which maximizes the escape distance. The resulting best motion kinematics exhibit the C-shape pattern as the optimal one, as confirmed by in vivo observations. In [7], the CMA-ES procedure is applied to the identification of the fastest and most efficient shapes for self-propelled swimmers. The results provide achievable robotic-shapes that allow us to outperform real larval zebrafish geometries by 40% and 135% for speed and efficiency, respectively.

Reinforcement learning for self-propelled swimmers (#**3**) by Novati et al., 2017 [152]. Another AI model-free procedure used by Novati et al. within a VPM method to optimize fish swimming lies in reinforcement learning (RL) algorithms. Their simulations involve two fishes, swimming in a synchronised tandem configuration (leader-follower). The coupling of a VPM with a Q-learning (RL) algorithm allows us to automatically define an optimal policy allowing the follower to maximize a desired and specified long-term reward (like the reduction in energy spent).

7.2. Aerodynamics

Vortex methods are known to be intrinsically well suited for advection-dominated flows. Problems related to aerodynamics are therefore natural applications for particle approaches. This subsection presents some studies showing the capability of hybrid vortex methods to perform LES of turbulent aerodynamic flow, characterized by Reynolds numbers higher than 10^4.

Dynamics of the wake of aircraft wings (#**4**) by Cocle et al., 2008 [14]. In this study the LES simulations, performed from a VPM method based on the SGS model (96), handle the 3D space-development of wake vortices behind an elliptically loaded wing in ground effect at $Re_c = 10{,}000$. They clearly depict the complex physics occurring in the wake region between primary and secondary vortex and the apparition of small-scales vortices due to the break down of the primary vortex under the effects of the secondary vortex spiral motion.

Dynamics of rotorcraft wakes (#**5**) by Caprace et al., 2020 [12]. Large eddy simulations of a 3D flow past an advancing helicopter rotor are realized through a VPM approach based on SGS model (96) and coupled with an Immersed Lifting Line (ILL) method. The latter, derived from the algorithms commonly used in wind energy community, is fully compatible with the Vortex-Particle-Mesh framework. It indeed consists in computing the vorticity corresponding to the local forces developed by the modeled wing/rotor and then in introducing this vorticity in the flow using vortex particles, that is to say in a Lagrangian fashion. The simulations performed in this study allowed, in particular, to precisely describe the vortex dynamics involved in the generation of the two main wake vortices of the rotorcraft thanks to thorough 3-D visualizations. For further details about the ILL approach in a VPM framework, one also refers to [99], by the same authors.

Dynamics of rotorcraft and finite aircraft wakes (#**6**) by Stock et al., 2010 [13]. Another type of large eddy simulations of rotorcraft wakes was earlier proposed by Stock et. al using a hybrid Eulerian/Langrangian decomposition domain approach (see Section 4.3). In the near-body region the computation is realized through a fully-compressible, Eulerian, Navier-Stokes flow solver based on a body-fitted structured grid. In the wake region, a pure Lagrangian vortex method is used, with the following characteristics: the velocity evaluation is performed through a GPU-FMM solver; since the Reynolds numbers considered in this study are in the order of $Re_c \approx 10^6$, no diffusion scheme is applied; a boundary element method (BEM) is used to set on each triangular panels the bound vortex sheet strength involved in velocity computation; an anisotropic SGS model based on Cottet's model [147] (3D extension of Equation (93)) is implemented for LES; finally, an overlap region and a coupling algorithm is carried out at the Eulerian/Lagrangian interface. LES of finite aircraft wing wakes are first performed, showing results that coincide rather well with experiments (showing however discrepancies in the region of the tip-vortex core), before presenting LES of 4-blades advancing rotor wakes for two angles of rotation of the whole device in forward flight.

7.3. Scalars Transport

Scalar advection problems involve the coupling of the Navier-Stokes equations with an advection-diffusion equation for the scalar transported at the flow velocity. In such problems, the production of small scales is dictated by the value of the Schmidt number, $Sc = \nu/\kappa$, defined as the ratio between the viscosity of the fluid and the diffusivity of the scalar. If $Sc > 1$, the size of the smallest scalar fluctuations is smaller than the smallest scale of the turbulent flow. In such situation, it appears quite natural therefore to perform numerical simulations involving different grid resolutions for the scalar and the momentum. The two following studies showcase the capability of VPM methods, more precisely here semi-Lagrangian vortex methods (see Section 4.3), to efficiently handle such problems.

Multi-scale solver for scalar turbulent transport on CPU-GPU (#**7**) by Etancelin et al. 2014 [153]. The computing strategy of this study is based on a semi-Lagrangian vortex method and consists in solving the Navier-Stokes equations (momentum and Poisson equation) on multi-CPUs while the scalar transport is computed on several GPUs. Passive scalar in a turbulent plane jet of $Sc = 10$ and $Re_w = 1000$ (with w the jet width) is simulated in a hybrid CPU/GPU computation with 128^3 and 512^3 grid points for the velocity and the scalar, respectively. In [154] a thorough HPC study is performed by the same author for turbulent jet problems (see Figure 6.13, p. 133) varying the respective grid sizes of the flow quantities and the scalar and varying the number of CPUs and GPUs in the parallel computation. It shows in particular that the computational time for the resolution of the scalar on a 1024^3 grid on 8 GPUs takes half the time needed for the resolution of the flow on a 256^3 grid on 32 CPUs.

Multi-scale solver for sediment transport on GPU (#**8**) by Keck 2019 [141]. This study examines the three-dimensional dynamics of sediment-laden fresh water above salt water. The modeling of such problem involves the coupling of the Navier-Stokes equations with two transport-diffusion equations concerning respectively the salinity S

and the sediment-particles concentration C. The Schmidt numbers considered in this study for the concentration C are $Sc_{(C)} = 3.5, 7, 14, 28$ and the ratio between the two scalars diffusivities is equal to 25. The problem is solved via a semi-Lagrangian vortex method, using GPU based computations. The obtained 3D sediment isocontours show, as expected from literature, salt fingers initially present on both sides of the sediment-laden water/salt water interface that then disappear under Rayleigh-Taylor instabilities for $Sc_{(C)} = 3.5$ and 7. For the two other Schmidt numbers $Sc_{(C)} = 14$ and 28, no more sediment fingers can be seen. They are replaced by downward moving sediment plumes of mushroom-shape, characteristic of Rayleigh-Taylor instabilities (see Figure 11 (a1 to a4)). These computations are performed on a lonely GPU core. An extension of this study to multi-scale hybrid CPU-GPU computations is envisioned.

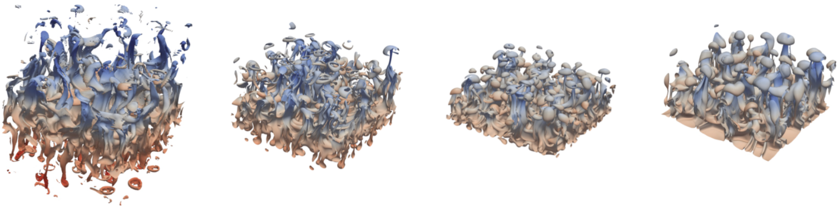

(a1) Sc = 3.5 (a2) Sc = 7.0 (a3) Sc = 14.0 (a4) Sc = 28.0

(b1) uncontrolled (b2) porous layer (b3) porous ring inlay

Figure 11. From a1 to a4 (case #8) *Courtesy of Keck* [141] Sediment isocontours showing moving fingers (downward w.r.t interface) at different Schmidt numbers. From b1 to b3 (case #9) Effect of porous-coating configuration on the wake of flow past a hemisphere at $Re_D = 1000$.

7.4. Porous Flows

The last examples given in this non-exhaustive list of applications focus on the ability of VPM, and more precisely hereafter of semi-Lagrangian vortex methods, to handle porous flows. This can be done through the coupling of the governing incompressible flow equations with Darcy or Brinkman equations, which are solved on the grid.

Passive flow control using porous media (**#9**) by Mimeau et al., 2014 and 2017 [20,155]. Based on the results obtained in the 2D case [155], the study [20] proposes to simulate 3D incompressible flows in solid-porous-fluid media through a semi-Lagrangian vortex method and then to perform passive control of bluff body flows by partially covering the body surface with a porous coating. The modeling of the physical problem is directly realized through the Brinkman-Navier-Stokes equation (Equation (83)) where the solid, porous and fluid regions are determined by defining characteristic functions and by setting specific values of the penalization factor λ in each region, knowing that intermediate values of λ enable to model a porous medium in which the flow has a Darcy velocity. The method is applied to the passive flow control of a hemisphere at transient Reynolds numbers. The results show that the effects of the added porous layer on the wake stabilization and drag reduction noticeably depend on the permeability and the location/geometry of the covering layer. The parametric simulations allow us to identify an efficient "porous ring-inlay" control device whose porous coating is only located in flow separation areas (see Figure 11 (b1 to b3)).

Table 1. The main physical and numerical characteristics of the simulations presented in Section 7.

	Application	Flow Regime	Governing Equations	Numerical Method	Particle Remeshing	Poisson Solver	Boundary Treatment	Grid Type	Simulation	Processor Type
#1 [9]	Swimming of articulated bodies	$Re_L = 100$, $Re_L = 200$	Navier-Stokes equations	VPM with multi-body solver	Tensorial M_4' scheme	FFT solver	Brinkman penalization	Cartesian uniform	2-D DNS	CPU
#2 [7,86]	Optimization of fish schooling	$Re_L = 500$	Navier-Stokes equations	VPM with CMA-ES algorithm	Tensorial M_4' scheme	FFT solver	Brinkman penalization	Cartesian uniform	3-D DNS	CPU
#3 [152]	Reinforcement learning for swimmers	$Re_L = 5000$	Navier-Stokes equations	VPM with RL algorithm	Tensorial M_4' scheme	FMM solver	Brinkman penalization	Wavelets-based AMR	2-D DNS	CPU
#4 [14]	Dynamics of aircraft wings wake	$Re_c = 10^4$	Navier-Stokes equations	VPM based on SGS model	Tensorial M_4' scheme	FMM solver	-	Cartesian uniform	3-D LES	CPU
#5 [12]	Dynamics of rotorcraft wakes	$Re_c = 4 \times 10^5$	Navier-Stokes equations	VPM based on SGS and ILL model	Tensorial M_4' scheme	FFT solver	ILL method	Cartesian uniform	3-D LES	CPU
#6 [13]	Dynamics of rotorcraft and aircraft wakes	$Re_c = 4.6 \times 10^5$, $Re_c = 1.5 \times 10^6$	Navier-Stokes equations	Hybrid method based on SGS model	-	FMM-GPU solver	BEM method	Body-fitted grid (near-body)	3-D LES	CPU-GPU
#7 [153]	Passive scalar turbulent transport	$Re_w = 1000$ $Sc = 10$	Navier-Stokes equations	Semi Lagrangian VM	Directional $\Lambda_{6,4}$ scheme	FFT solver	-	Cartesian uniform	3-D DNS	CPU-GPU
#8 [141]	Sediment flow	$Sc = 3.5, 7, 14, 28$	Navier-Stokes equations	Semi Lagrangian VM	Directional $\Lambda_{4,2}$ scheme	FFT solver	-	Cartesian uniform	3-D DNS	CPU-GPU
#9 [20,155]	Flow control using porous media	$Re_D = 300$, $Re_D = 1000$	Navier-Stokes equations	Semi Lagrangian VM	Directional $\Lambda_{4,2}$ scheme	FFT solver	Brinkman penalization	Cartesian uniform	3-D DNS	CPU
#10 [156]	Rock dissolution at pore-scale	Dissolution regime ($Pe = 0.7$)	Darcy Brinkman-Stokes equations	Semi Lagrangian method (for reaction equations)	Directional M_4' and M_4 schemes	FFT solver	penalization	Cartesian uniform	3-D DNS	CPU-GPU

Carbonate rock dissolution at pore-scale (**#10**) by Etancelin et al., 2020 [156]. Contrary to all the previous studies reported in this review paper, this last illustration of semi-Lagrangian capabilities deals with Darcy-Brinkman-Stokes equations, that is to say with problems not dominated by advection. More specifically, this last study aims to simulate dissolution processes at the pore scale of actual rocks. To do so, the authors couple a Lagrangian formulation of the chemical reaction equations (handled through a semi-Lagrangian solver) with the so called superficial velocity formalism (handled with an Eulerian scheme). The authors address the crucial issue of how to estimate the numerical diffusion induced by the remeshing step in the semi-Lagrangian solver and how to switch from a low-order to a high-order kernel in order to correctly adapt the physical diffusion. The 3D DNS simulations highlight the effects of fluid inclusions in a non-percolating and percolating carbonate rock.

8. Conclusions and Perspectives

8.1. Conclusions

The intensive development of the vortex methods between 1970 and the mid 1990s was motivated by the will to design robust and accurate numerical schemes able to overcome the main weaknesses of traditional grid methods, especially in the case of dominant advection effects in the flows. The major advantages arising from these pure Lagrangian methods are the following: appealing physical attributes, automatic adaptivity of the discretization elements (particles), compactness of vorticity support, accurate handling of boundary conditions at infinity, negligible numerical dissipation, conservation of the flow invariants, relaxed stability condition on the time step and usefulness of vorticity in terms of CFD results interpretations. However, during this period, vortex methods experienced some difficulties. First they had to face an inaccurate modeling of the viscous effects due to the particle distortion phenomenon. They were also confronted with the expensive resolution of the Poisson equation allowing to recover the velocity field from the vorticity. Finally, they failed in providing both accurate, efficient and generalized treatment of boundary conditions on solid walls due to the velocity formulation of the no-slip boundary conditions. For all these reasons, and despite the efforts made to design solutions to overcome the difficulties, these solutions remained partial and the purely Lagrangian vortex methods did not manage to become a common tool for the simulation of incompressible real and complex flows. In order to bypass their intrinsic limitations, they started to move towards hybrid formulations in the early 1990s, resulting in the introduction of underlying grids with remeshing. The presence of Cartesian grids indeed enables the use of Fast Poisson solvers as well as grid-based schemes for the discretization of the diffusion term, and makes possible the handling of immersed boundary methods for the treatment of the solid bodies, while ensuring a permanent control of the particle overlapping through regular redistribution operations on the grid. In the meantime, the particle discretization of the flow and the Lagrangian advection scheme allow us to keep most of the advantages of the Lagrangian methods. The introduction of grid and remeshing process in vortex methods marks the birth of hybrid methods, with among them the Eulerian-Lagrangian decomposition domain methods and the Vortex-Particle-Mesh methods (like the Vortex-In-Cell and the semi-Lagrangian vortex methods). All these advances allowed by the hybrid approaches increased the interest and potential of VM in handling challenging CFD problems. Important efforts were therefore supplied to design efficient algorithms in the context of hybrid vortex methods and eventually gave birth to high performance scientific libraries, able to perform simulations of complex real flows arising in diverse application fields like hydrodynamics, turbulent wake dynamics, scalars transport or porous flows.

8.2. Future Research Perspectives

As described before, the academic research on vortex methods has brought multiple achievements on the accuracy, stability and applicability of this family of approaches. They have also been boosted with powerful high performance computing tools increasing their capability to handle complex problems. Several perspectives appear to fill the future of the research related to this family of methods. The most current issue would be to strengthen their abilities for realistic and industrial applications. Below, some research perspectives are listed.

- Turbulent and high Reynolds number flow simulations. The recent researches highlight the road map for this target with two possibilities. The first option consists in proposing modern turbulence models for the velocity-vorticity filtered Navier-Stokes equations (i.e., LES-like approaches), based for example on those already developed by Mansfield et al. [148] on one side or Cocle et al. [151] on the other side. The second view, that takes its idea from the inherent nature of vortex methods, is the multi-resolution approach (based on the pioneer works of Cottet and Wray [147,157]) which consists in using two different levels of resolution for vorticity (fine level) and the velocity (coarse level). This multi-resolution would have a deep interest in problems where important Schmidt numbers are involved like in heat transfer (e.g., thermal conduction and convection [158]), passive-scalar transport [153] or sedimentation flows [141].
- Fluid Structure Interactions (FSI). The handling of no-slip boundary conditions has long been one of the main difficulties of vortex methods. The implementation of the Brinkman penalization method has significantly improved this drawback in the context of Vortex-Particle-Mesh methods. However, this approach is limited because of its low order and accuracy. The very recent introduction of immersed interface method (IIM) [131,132] and immersed lifting line approach (ILL) [12,99] introduced a real improvement and allows us to start a real progress in the challenging field of FSI.
- Environmental and industrial particular flows. Vortex methods belong to the family of particle methods with direct treatment of particles. Therefore, their application to problems like sediment transport [141,159] or internal multi-phase flows in industry with particle mixing, dispersion, deposition, and particle-wall collision [160], seems natural and deserves a special place in the future perspectives.
- Multi-phase flows. Besides the industrial fluid/particles two-phase flows evoked above, vortex methods also have a role to play in the handling of multi-phase flows in general, with for instance the development of models able to capture interfaces between two phases and to handle surface tension, variable fluid properties and high mass density-ratio flows. To the authors knowledge, only few works based on vortex methods have been dedicated to this topic [161].
- Finally, future vortex computations need to be continually strengthened with novel high performance computing parallelism techniques (hybrid multi-CPU/multi-GPU) and powerful algorithms (like the very recent 2D-3D Poisson solver released in 2021 by Caprace et al. [162]) in order to achieve more complex flow approximations.

Author Contributions: Conceptualization, C.M. and I.M.; investigation, C.M. and I.M.; writing-original draft preparation, C.M.; writing-review and editing, C.M. and I.M.; visualization, C.M. and I.M.; supervision, C.M. and I.M.; project administration, C.M. and I.M. All authors have read and agreed to the published version of the manuscript.

Funding: This research received no external funding.

Conflicts of Interest: The authors declare no conflict of interest.

Abbreviations

Here is the list of the abbreviations used in this manuscript, in order of appearance:

CFD	Computational fluids dynamics
ODE	Ordinary differential equation
VM	Vortex methods
SPH	Smooth particle hydrodynamics

CFL	Courant-Friedricks-Levy
LCFL	Lagrangian Courant-Friedricks-Levy
RW	Random walk
PSE	Particle strength exchange
CSM	Core spreading method
DVM	Diffusion velocity method
CCF	Convolution of cut-off function
VRM	Vortex redistribution method
RBF	Radial basis functions
RPD	Regular point distributions
DVH	Diffused vortex hydrodynamics
VPM	Vortex-particle-mesh
VIC	Vortex-in-cell
P2M	Particle to Mesh
M2P	Mesh to Particle
FMM	Fast multiple method
DNS	Direct numerical simulation
LES	Large eddy simulation
BEM	Boundary elements method
IBM	Immersed boundary method
FFT	Fast Fourier Transform
GPU	Graphics processing unit
CPU	Central processing unit
AMR	Adaptive mesh refinement
FWT	Fast wavelet transform
LTS	Local time stepping
SGS	Sub-grid scale
SFS	Sub-filter scale
CMA-ES	Covariance Matrix Adaptation - Evolutionary Strategy
RL	Reinforcement learning
ILL	Immersed lifting line
HPC	High performance computing
FSI	Fluid structure interaction

Nomenclature

in order of appearance

t	time
$\mathbf{x}, \mathbf{y}$	spacial locations
$\mathbf{Q}$	solution vector in given continuous system
$\mathbf{F}$	source term in given continuous system
Ω	computational domain
$\mathbf{u}$	velocity field
δ	Dirac distribution
p	particle
$\mathbf{v}_p$	volume of particle p (denoted v_p in 2D)
$\mathbf{x}_p$	location of particle p
W_ε	denomination of the smoothing radial symmetric function in Lagrangian methods
ε	radius of the smoothing radial symmetric function
Γ	circulation
$\times$	cross product
$\boldsymbol{\omega}$	vorticity field (denoted ω in 2D)
$\boldsymbol{\omega}_0$	initial vorticity field (denoted ω_0 in 2D)
$(\cdot)^h$	quantity approximation
$\mathbf{u}_\infty$	far-field velocity
$\boldsymbol{\alpha}_p$	local circulation around $\mathbf{x}_p$ (denoted α_p in 2D)
$\star$	convolution product

$\mathbf{G}$	Green's function
$\mathbf{K}$	$\equiv \nabla \mathbf{G}$
ζ	smooth cutoff function
ζ_ε	smoothing radial symmetric function in Vortex blobs methods (based on ζ and on blob radius ε)
$(\cdot)_\varepsilon$	quantity evaluated on mollified blob particles
h	particle spacing or grid spacing
Δt	time step
ν	fluid viscosity
Re	Reynolds number. Also Re_L, Re_c, Re_D and Re_w for Re based on *length, chord, diameter* and *width* respectively
η_ε	mollified diffusion kernel of given order, used in PSE schemes
$\mathbf{u}_d$	diffusion velocity
$\otimes$	tensor product
$\boldsymbol{\omega}_d$	viscous vorticity
W	interpolation/remeshing kernel
S	support of kernel W
M_s	half of grid points constituting the support of kernel W ($S = 2M_s$)
Λ_p	ordinary interpolation/remeshing kernel of maximum order p
M_p	B-splines interpolation/remeshing kernel of maximum order p
M'_4	Monaghan interpolation/remeshing kernel
$\Lambda_{p,r}$	interpolation/remeshing kernel of regularity r and maximum order p
ϕ_k	basis functions in interpolation/remeshing process
$\mathbf{u}_s$	velocity of the solid immersed body
$\mathbf{x}_s$	any location on the solid surface
$\partial\boldsymbol{\omega}/\partial\mathbf{n}$	wall normal vorticity flux
$\mathcal{S}$	surface of the solid body
$\mathcal{S}_i$	vortex sheet element at the surface
α_i	strength of vortex sheet element $\mathcal{S}_i$
H	Heavyside function
$\mathbf{s}$	tangent vector to the surface $\mathcal{S}$
$\kappa(s)$	surface curvature at point s
$(\mathbf{e}_r, \mathbf{e}_z, \mathbf{e}_\theta)$	basis vectors in cylindrical coordinate system
χ	characteristic function of the solid body
λ	non-dimensionalized Brinkman penalization factor
t_r, t_c	threshold for refinement and compression, respectively, in wavelet-based AMR method
$\mathcal{F}_\Delta$	spatial filter $\mathcal{F}$ of size Δ in LES
$\boldsymbol{\tau}$	subgrid scale stress tensor in LES
ν_{sma}	eddy viscosity in Smagorinsky model
C	coefficient in Smagorinsky model
$\lvert\tilde{\mathbf{S}}\rvert$	rate-of-strain tensor in Smagorinsky model
$\tilde{(\cdot)}$	low-pass filtered quantities in LES model
R_{ij}	subgrid scale vorticity stress in LES
$\mathbf{g} \equiv \partial R_{ij}/\partial x_j$	subfilter scale torque in LES
Sc	Schmidt number
κ	diffusivity of the advected scalar in transport problems.

References

1. Gingold, R.; Monaghan, J. Smoothed particle hydrodynamics: Theory and application to non-spherical stars. *Mon. Not. R. Astron. Soc.* **1977**, *181*, 375–389. [CrossRef]
2. Monaghan, J. Why particle methods work. *SIAM J. Sci. Stat. Comput.* **1982**, *3*, 422–433. [CrossRef]
3. Monaghan, J. Smoothed particle hydrodynamics. *Annu. Rev. Astron. Astrophys.* **1992**, *30*, 543–574. [CrossRef]
4. Shadloo, M.; Oger, G.; Le Touzé, D. Smoothed particle hydrodynamics method for fluid flows, towards industrial applications: Motivations, current state, and challenges. *Comput. Fluids* **2016**, *136*, 11–34. [CrossRef]
5. Lind, S.; Rogers, B.; Stansby, P. Review of smoothed particle hydrodynamics: Towards converged Lagrangian flow modelling. *Proc. R. Soc. A* **2020**, *476*, 20190801. [CrossRef]

6. Gazzola, M.; Chatelain, P.; van Rees, W.M.; Koumoutsakos, P. Simulations of single and multiple swimmers with non-divergence free deforming geometries. *J. Comput. Phys.* **2011**, *230*, 7093–7114. [CrossRef]
7. van Rees, W.; Gazzola, M.; Koumoutsakos, P. Optimal shapes for anguilliform swimmers at intermediate Reynolds numbers. *J. Fluid Mech.* **2013**, *722*. [CrossRef]
8. Gazzola, M.; Hejazialhosseini, B.; Koumoutsakos, P. Reinforcement Learning and Wavelet Adapted Vortex Methods for Simulations of Self-propelled Swimmers. *SIAM J. Sci. Comput.* **2014**, *36*, B622–B639. [CrossRef]
9. Bernier, C.; Gazzola, M.; Ronsse, R.; Chatelain, P. Simulations of propelling and energy harvesting articulated bodies via vortex particle-mesh methods. *J. Comput. Phys.* **2019**, *392*, 34–55. [CrossRef]
10. Gazzola, M.; Mimeau, C.; Tchieu, A.; Koumoutsakos, P. Flow mediated interactions between two cylinders at finite Re numbers. *Phys. Fluids* **2012**, *24*, 043103. [CrossRef]
11. Parthasarathy, T.; Chan, F.; Gazzola, M. Streaming-enhanced flow-mediated transport. *J. Fluid Mech.* **2019**, *878*, 647–662. [CrossRef]
12. Caprace, D.G.; Chatelain, P.; Winckelmans, G. Wakes of rotorcraft in advancing flight: A large-eddy simulation study. *Phys. Fluids* **2020**, *32*, 087107. [CrossRef]
13. Stock, M.; Gharakhani, A.; Stone, C. Modeling rotor wakes with a hybrid OVERFLOW-vortex method on a GPU cluster. In Proceedings of the 28th AIAA Applied Aerodynamics Conference, Chicago, IL, USA, 28 June–1 July 2010; p. 4553.
14. Cocle, R.; Winckelmans, G.; Daeninck, G. Combining the Vortex-In-Cell and parallel Fast Multipole methods for efficient domain decomposition simulations. *J. Comput. Phys.* **2008**, *227*, 9091–9120. [CrossRef]
15. Chatelain, P.; Duponcheel, M.; Caprace, D.G.; Marichal, Y.; Winckelmans, G. Vortex particle-mesh simulations of vertical axis wind turbine flows: From the airfoil performance to the very far wake. *Wind Energy Sci.* **2017**, *2*, 317–328. [CrossRef]
16. Balty, P.; Caprace, D.G.; Waucquez, J.; Coquelet, M.; Chatelain, P. Multiphysics simulations of the dynamic and wakes of a floating Vertical Axis Wind Turbine. *J. Phys. Conf. Ser.* **2020**, *1618*, 062053. [CrossRef]
17. Huberson, S.; Rivoalen, E.; Voutsinas, S. Vortex particle methods in aeroacoustic calculations. *J. Comput. Phys.* **2008**, *227*, 9216–9240. [CrossRef]
18. Samarbakhsh, S.; Kornev, N. Simulation of a free circular jet using the vortex particle intensified LES (VπLES). *Int J. Heat Fluid Flow* **2019**, *80*, 108489. [CrossRef]
19. Poncet, P.; Hildebrand, R.; Cottet, G.H.; Koumoutsakos, P. Spatially distributed control for optimal drag reduction of the flow past a circular cylinder. *J. Fluid Mech.* **2008**, *599*, 111–120. [CrossRef]
20. Mimeau, C.; Mortazavi, I.; Cottet, G.H. Passive control of the flow around a hemisphere using porous media. *Eur. J. Mech. B Fluids* **2017**, *65*, 213–226. [CrossRef]
21. Gustafason, K.; Sethian, J. (Eds.) *Vortex Methods and Vortex Motion*; SIAM: Philadelphia, PA, USA, 1991.
22. Cottet, G.H.; Koumoutsakos, P. *Vortex Methods—Theory and Practice*; Cambridge University Press: Cambridge, UK, 2000.
23. Yokota, R.; Obi, S. Vortex Methods for the Simulation of Turbulent Flows: Review. *J. Fluid Sci. Technol.* **2011**, *6*, 14–29. [CrossRef]
24. Mimeau, C. Conception and Implementation of a Hybrid Vortex Penalization Method for sOlid-Fluid-Porous Media: Application to the Passive Control of Incompressible Flows. Ph.D. Thesis, Université de Grenoble, Grenoble, France, 2015.
25. Prager, W. Die Druckverteilung an Korpern in ebener Potentialstromung. *Phys. Z.* **1928**, *29*, 865–869.
26. Rosenhead, L. The Formation of vortices from a surface of discontinuity. *Proc. R. Soc. Lond. Ser. A* **1931**, *134*, 170–192.
27. Chorin, A.J.; Bernard, P.S. Discretization of a Vortex Sheet, with an Example of Roll-Up. *J. Comput. Phys.* **1973**, *13*, 423–429. [CrossRef]
28. Anderson, C.; Greengard, C. On vortex methods. *SIAM J. Numer. Anal.* **1985**, *22*, 413–440. [CrossRef]
29. Cottet, G.H. A new approach for the analysis of Vortex Methods in two and three dimensions. *Annales de l'I. H. P. Analyse non Linéaire* **1988**, *5*, 227–285. [CrossRef]
30. Leonard, A. Numerical simulation of interacting vortex filaments. In Proceedings of the IV International Conference on Numerical Methods of Fluid Dynamics, Boulder, CO, USA, 24–28 June 1974; Springer: New York, NY, USA, 1975.
31. Leonard, A. Vortex methods for flow simulation. *J. Comput. Phys.* **1980**, *37*, 289–335. [CrossRef]
32. Leonard, A. Computing three-dimensional incompressible flows with vortex elements. *Ann. Rev. Fluid Mech.* **1985**, *17*, 523–559. [CrossRef]
33. Angelidis, A.; Neyret, F. Simulation of smoke based on vortex filament primitives. In Proceedings of the ACM-SIGGRAPH/EG Symposium on Computer Animation (SCA), Los Angeles, CA, USA, 29–31 July 2005.
34. Hald, O. Convergence of vortex methods II. *SIAM J. Numer. Anal* **1979**, *16*, 726–755. [CrossRef]
35. Beale, J.; Majda, A. Vortex methods II: High order accuracy in 2 and 3 dimensions. *Math. Comput.* **1982**, *32*, 29–52.
36. Knio, O.; Ghoniem, A.F. Numerical study of a three-dimensional vortex method. *J. Comput. Phys.* **1990**, *86*, 75–106. [CrossRef]
37. Chorin, A.J. Numerical study of slighly viscous flow. *J. Fluid Mech.* **1973**, *57*, 785–796. [CrossRef]
38. Prandtl, W. Uber Flussigkeitbewegung bei sehr kleiner Reibung. In Proceedings of the Fourth Mathematics Congress, Heidelberg, Germany, 8–13 August 1904; pp. 484–491.
39. Beale, J.T.; Majda, A. Rates of convergence for viscous splitting of the Navier-Stokes equations. *Math. Comput.* **1981**, *37*, 243–259. [CrossRef]
40. Marchioro, C.; Pulvirenti, M. Hydrodynamics in two dimensions and vortex theory. *Commun. Math. Phys.* **1982**, *84*, 483–503. [CrossRef]

41. Goodman, J. Convergence of the random vortex method. *Commun. Pure Appl. Math.* **1987**, *40*, 189–220. [CrossRef]
42. Long, D.G. Convergence of the random vortex method in two dimensions. *J. Am. Math. Soc.* **1988**, *1*, 779–804. [CrossRef]
43. Chorin, A.J. *Computational Fluid Mechanics*; Academic Press: New York, NY, USA, 1989.
44. van Dommelen, L.L. Computation of unsteady separation using Lagrangian procedures. In Proceedings of the IUTAM Symposium on Boundary Layer Separation, London, UK, 26–28 August 1986; pp. 73–87.
45. Smith, P.; Stansby, P. An efficient surface algorithm for random-particle simulation of vorticity and heat transport. *J. Comput. Phys.* **1989**, *81*, 349–371. [CrossRef]
46. Slaouti, A.; Stansby, P. Flow around two circular cylinders by the random-vortex method. *J. Fluids Struct.* **1992**, *6*, 641–670. [CrossRef]
47. Wang, S.C. Control of Dynamic Stall. Ph.D. Thesis, FAMU-FSU, College of Engineering, Tallahassee, FL, USA, 1995.
48. Lewis, R.I. *Vortex Element Methods for Fluid Dynamic Analysis of Engineering Systems*; Cambridge University Press: Cambridge, UK, 1990.
49. Milinazzo, F.; Saffman, P.G. The calculation of large Reynolds number two-dimensional flow using discrete vortices with random walk. *J. Comput. Phys.* **1977**, *23*, 380–392. [CrossRef]
50. Gharakhani, A.; Ghoniem, A. Three-Dimensional Vortex Simulation of Time Dependent Incompressible Internal Viscous Flows. *J. Comput. Phys.* **1997**, *134*, 75–95. [CrossRef]
51. Degond, P.; Mas-Gallic, S. The weighted particle method for convection-diffusion equations. *Math. Comput.* **1989**, *53*, 485–526.
52. Cottet, G.H.; Mas-Gallic, S. Une méthode de décomposition pour une équation de type convection-diffusion combinant résolution explicite et méthode particulaire. *C. R. Acad. Sci. Paris* **1983**, *297*, 133–136.
53. Cottet, G.H.; Mas-Gallic, S. A particle method to solve the Navier-Stokes system. *Numer. Math.* **1990**, *57*, 1–23. [CrossRef]
54. Koumoutsakos, P.; Leonard, A. High-resolution simulations of the flow around an impulsively started cylinder using vortex methods. *J. Fluid Mech.* **1995**, *296*, 1–38. [CrossRef]
55. Ploumhans, P.; Winckelmans, G.S.; Salmon, J.K.; Leonard, A.; Warren, M.S. Vortex Methods for Direct Numerical Simulation of Three-Dimensional Bluff Body Flows: Applications to the Sphere at $Re = 300$, 500 and 1000. *J. Comput. Phys.* **2002**, *178*, 427–463. [CrossRef]
56. Yokota, R.; Sheel, T.; Obi, S. Calculation of isotropic turbulence using a pure Lagrangian vortex method. *J. Comput. Phys.* **2007**, *226*, 1589–1606. [CrossRef]
57. Kuwahara, K.; Takami, H. Numerical studies of two-dimensional vortex motion by a system of point vortices. *J. Phys. Soc. Jpn.* **1973**, *34*, 247–253. [CrossRef]
58. Greengard, C. The core spreading vortex method approximates the wrong equation. *J. Comput. Phys.* **1985**, *61*, 345–348. [CrossRef]
59. Rossi, L.F. Resurrecting core spreading vortex methods: A new scheme that is both deterministic and convergent. *SIAM J. Sci. Stat. Comput.* **1996**, *17*, 370–397. [CrossRef]
60. Barba, L.; Leonard, A.; Allen, C. Advances in viscous vortex methods—Meshless spatial adaption based on radial basis function interpolation. *Int. J. Numer. Methods Fluids* **2005**, *47*, 387–421. [CrossRef]
61. Fronteau, J.; Combis, P. A lie admissible method of integration of Folkler-Plank equations with non linear coefficients (exact and numerical solutions). *Hadronic J.* **1984**, *7*, 911–930.
62. Ogami, Y.; Akamatsu, T. Viscous flow simulation using the discrete vortex model—The diffusion velocity model. *Comput. Fluids* **1991**, *19*, 433–441. [CrossRef]
63. Beaudoin, A.; Huberson, S.; Rivoalen, E. Simulation of anisotropic diffusion by means of a diffusion velocity method. *J. Comput. Phys.* **2003**, *186*, 122–135. [CrossRef]
64. Clarke, N.; Tutty, O. Construction and validation of a discrete vortex method for the two-dimensional incompressible Navier-Stokes equations. *Comput. Fluids* **1994**, *23*, 751–783. [CrossRef]
65. Lucchesi, M.; Allouch, S.; Le Maitre, O.; Mustapha, K.; Knio, O. Particle simulation of space–fractional diffusion equations. *Comput. Part. Mech.* **2020**, *7*, 491–507. [CrossRef]
66. Rivoalen, E.; Huberson, S.; Hauville, F. Simulation numérique des équations de Navier-Stokes 3D par une méthode particulaire. *C. R. Acad. Sci. Ser. IIB Mech. Phys. Chem. Astron.* **1997**, *324*, 543–549. [CrossRef]
67. Fishelov, D. A new vortex scheme for viscous flows. *J. Comput. Phys.* **1990**, *86*, 211–224. [CrossRef]
68. Shankar, S.; van Dommelen, L. A new diffusion procedure for vortex methods. *J. Comput. Phys.* **1996**, *127*, 88–109. [CrossRef]
69. Barba, L. Vortex Method for Computing High-Reynolds Number Flows: Increased Accuracy with a Fully Mesh-Less Formulation. Ph.D. Thesis, California Institute of Technology, Pasadena, CA, USA, 2004.
70. Rossinelli, D.; Koumoutsakos, P. Vortex methods for incompressible flow simulations on the GPU. *Vis. Comput.* **2008**, *24*, 699–708. [CrossRef]
71. Henshaw, W.; Kreiss, H.O.; Reyna, L. On the smallest scale for the compressible Navier-Stokes equations. *Theor. Comput. Fluid Dyn.* **1989**, *1*, 65–95.
72. Krasny, R. A study of singularity formation in a vortex sheet by the point vortex approximation. *J. Fluid Mech.* **1986**, *167*, 65–93. [CrossRef]
73. Beale, J.T. On the accuracy of vortex methods at large times. In *Computational Fluid Dynamics and Reacting Gas Flows*; Engquist, B., Majda, A., Luskin, M., Eds.; Springer: New York, NY, USA, 1988; pp. 19–32.

74. Choquin, J.P.; Lucquin-Desreux, B. Accuracy of a deterministic particle method for the Navier-Stokes equations. *Int. J. Numer. Fluids* **1988**, *8*, 1439–1458. [CrossRef]
75. Russo, G.; Strain, J. Fast triangulated vortex methods for the 2D Euler equations. *J. Comput. Phys.* **1994**, *111*, 291–323. [CrossRef]
76. Strain, J. Fast adaptive 2D vortex methods. *J. Comput. Phys.* **1997**, *132*, 108–122. [CrossRef]
77. Schrader, B.; Sbalzarini, I.; Redoux, S. Discretization correction of general integral PSE operators for particle methods. *J. Comput. Phys.* **2010**, *229*, 4159–4182. [CrossRef]
78. Eldredge, J.; Colonius, T.; Leonard, A. A general deterministic treatment of derivatives in particle methods. *J. Comput. Phys.* **2002**, *180*, 686–709. [CrossRef]
79. Rossi, E.; Colagrossi, A.; Bouscasse, B.; Graziani, G. The Diffused Vortex Hydrodynamics Method. *Commun. Comput. Phys.* **2015**, *18*, 351–379. [CrossRef]
80. Huberson, S.; Jollès, A. Correction de l'erreur de projection dans les méthodes particules/maillage. *La Recherche Aérospatiale* **1990**, *4*, 1–6.
81. Cottet, G.H.; Magni, A. TVD remeshing schemes for particle methods. *C. R. Acad. Sci. Paris* **2009**, *347*, 1367–1372. [CrossRef]
82. Magni, A.; Cottet, G.H. Accurate, non-oscillatory remeshing schemes for particle methods. *J. Comput. Phys.* **2012**, *231*, 152–172. [CrossRef]
83. Schoenberg, I.J. Contributions to the problem of approximation of equidistant data by analytic functions. *Q. Appl. Math.* **1946**, *4*, 112–141. [CrossRef]
84. Magni, A. Méthodes Particulaires Avec Remaillage: Analyse Numérique, Nouveaux Schémas Et Applications Pour La Simulation D'équations De Transport. Ph.D. Thesis, Université de Grenoble, Grenoble, France, 2011.
85. Monaghan, J. Extrapolating B-splines for interpolation. *J. Comput. Phys.* **1985**, *60*, 253–262. [CrossRef]
86. Gazzola, M.; van Rees, W.M.; Koumoutsakos, P. C-start: Optimal start of larval fish. *J. Fluid Mech.* **2012**, *698*, 5–18. [CrossRef]
87. Bergdorf, M.; Koumoutsakos, P. A Lagrangian particle-wavelet method. *SIAM Multiscale Model. Simul.* **2006**, *5*, 980–995. [CrossRef]
88. Cottet, G.H.; Etancelin, J.M.; Perignon, F.; Picard, C. High order Semi-Lagrangian particles for transport equations: Numerical analysis and implementation issues. *ESAIM Math. Model. Numer. Anal.* **2014**, *48*, 1029–1060. [CrossRef]
89. Cottet, G.H. Particle-grid domain decomposition methods for the Navier-Stokes equations in exterior domains. *Lect. Appl. Math. Ser. Am. Math. Soc. N. Y.* **1991**, *28*, 100–118.
90. Cottet, G.H.; Koumoutsakos, P.; Ould-Salihi, M. Vortex Methods with Spatially Varying Cores. *J. Comput. Phys.* **2000**, *162*, 164–185. [CrossRef]
91. Huberson, S.; Voutsinas, S. Particles and grid. *Comput. Fluids* **2002**, *31*, 607–625. [CrossRef]
92. Guermond, J.L.; Huberson, S.; Shen, W.Z. Simulation of 2D external viscous flows by means of a domain decomposition method. *J. Comput. Phys.* **1993**, *108*, 343–352. [CrossRef]
93. Christiansen, J. Numerical solution of hydrodynamics by the method of point vortices. *J. Comput. Phys.* **1973**, *13*, 363–379. [CrossRef]
94. Mortazavi, I.; Giovannini, A. The simulation of vortex dynamics downstream of a plate separator using a vortex-finite element method. *Int. J. Fluid Dyn.* **2001**, *5*, 31–48.
95. Ould-Salihi, M.; Cottet, G.H.; El Hamraoui, M. Blending finite-difference and vortex methods for incompressible flow computations. *SIAM J. Sci. Comp.* **2000**, *22*, 1655–1674. [CrossRef]
96. Gallizio, F. Analytical and Numerical Vortex Methods to Model Separated Flows. Ph.D. Thesis, Politecnico di Torino, Turin, Italy, 2009.
97. van Rees, W.M.; Leonard, A.; Pullin, D.; Koumoutsakos, P. A comparison of vortex and pseudo-spectral methods for the simulation of periodic vortical flows at high Reynolds numbers. *J. Comput. Phys.* **2011**, *230*, 2794–2805. [CrossRef]
98. Mimeau, C.; Gallizio, F.; Cottet, G.H.; Mortazavi, I. Vortex penalization method for bluff body flows. *Int. J. Numer. Meth. Fluids* **2015**, *79*, 55–83. [CrossRef]
99. Caprace, D.G.; Winckelmans, G.; Chatelain, P. An immersed lifting and dragging line model for the Vortex Particle-Mesh method. *Theor. Comput. Fluid Dyn.* **2020**, *34*, 21–48. [CrossRef]
100. Mimeau, C.; Cottet, G.H.; Mortazavi, I. Direct numerical simulations of three-dimensional flows past obstacles with a vortex penalization method. *Comput. Fluids* **2016**, *136*, 331–347. [CrossRef]
101. Morgenthal, G.; Walther, J.H. An immersed interface method for the Vortex-In-Cell algorithm. *Comput. Struct.* **2007**, *85*, 712–726. [CrossRef]
102. Kudela, H.; Kozlowski, T. Vortex-in-cell method for exterior problems. *J. Theor. Appl. Mech.* **2009**, *47*, 779–796.
103. Cottet, G.H.; Poncet, P. Simulation and control of three-dimensional wakes. *Comput. Fluids* **2004**, *33*, 697–713. [CrossRef]
104. Creusé, E.; Giovannini, A.; Mortazavi, I. Vortex simulation of active control strategies for transitional backward-facing step flows. *Comput. Fluids* **2009**, *38*, 1348–1360. [CrossRef]
105. Kornev, N. Hybrid method based on embedded coupled simulation of vortex particles in grid based solution. *Comput. Part. Mech.* **2018**, *5*, 269–283. [CrossRef]
106. Chorin, A.J. Vortex sheet approximation of boundary layers. *J. Comput. Phys.* **1978**, *27*, 428–442. [CrossRef]
107. Smith, P.; Stansby, P. Impulsively started flow around a circular cylinder by the vortex method. *J. Fluid Mech.* **1988**, *194*, 45–77. [CrossRef]

108. Sethian, J.A.; Ghoniem, A.F. Validation Study of Vortex Methods. *J. Comput. Phys.* **1988**, *74*, 283–317. [CrossRef]
109. Cheer, A.J. Numerical study of incompressible slightly viscous flow past blunt bodies and airfoils. *SIAM J. Sci. Stat. Comput.* **1983**, *4*, 685–705. [CrossRef]
110. Mortazavi, I.; Micheau, P.; Giovannini, A. Numerical convergence of vortex method for a high Reynolds number 2D bluff-body flow. *C. R. Mec.* **2002**, *330*, 409–416. [CrossRef]
111. Chorin, A.J. Vortex models and boundary layer instability. *SIAM J. Sci. Stat. Comput.* **1980**, *1*, 1–21. [CrossRef]
112. Fishelov, D. Vortex Methods for Slightly Viscous Three Dimensional Flow. *SIAM J. Sci. Stat. Comput.* **1990**, *3*, 399–424. [CrossRef]
113. Gharakhani, A.; Ghoniem, A. Simulation of the piston driven flow inside a cylinder with an eccentric port. *J. Fluids Eng.* **1998**, *120*, 319–326. [CrossRef]
114. Anderson, C.; Reider, M. Investigation of the use of Prandtl/Navier-Stokes Equation Procedures for Two-Dimensional Incompressible Flows. *Phys. Fluids* **1994**, *6*, 2380–2389. [CrossRef]
115. Walther, J.H.; Larsen, A. Two dimensional discrete vortex method for application to bluff body aerodynamics. *J. Wind Eng. Ind. Aerodyn.* **1997**, *67–68*, 183–193.
116. Cottet, G.H. A vorticity creation algorithm for the Navier-Stokes equations in arbitrary domain. In *Navier-Stokes Equations and Related Non-Linear Problems*; Sequeira, A., Ed.; Plenum Press Publishers: New York, NY, USA, 1994.
117. Koumoutsakos, P.; Leonard, A.; Pépin, F. Boundary conditions for viscous vortex methods. *J. Comput. Phys.* **1994**, *113*, 52–61. [CrossRef]
118. Casciola, C.M.; Piva, R.; Bassanini, P. Vorticity generation on a flat surface in 3D flows. *J. Comput. Phys.* **1996**, *129*, 345–356. [CrossRef]
119. Poncet, P. Méthodes Particulaires Pour la Simulation des Sillages Tridimensionnels. Ph.D. Thesis, Université Joseph Fourier–Grenoble I, Grenoble, France, 2001.
120. Cottet, G.H.; Poncet, P. Advances in direct numerical simulation of 3D wall-bounded flows by Vortex-In-Cell methods. *J. Comput. Phys.* **2003**, *193*, 136–158. [CrossRef]
121. Cooper, C.; Barba, L. Panel-free boundary conditions for viscous vortex methods. In Proceedings of the AIAA Computational Fluid Dynamics Conference, San Antonio, TX, USA, 22–25 June 2009.
122. Ploumhans, P.; Winckelmans, G.S. Vortex methods for high-resolution simulations of viscous flow past bluff bodies of general geometry. *J. Comput. Phys.* **2000**, *165*, 354–406. [CrossRef]
123. Poncet, P. Analysis of an immersed boundary method for three-dimensional flows in vorticity formulation. *J. Comput. Phys.* **2009**, *228*, 7268–7288. [CrossRef]
124. Caltagirone, J.P. Sur l'intéraction fluide-milieu poreux: Application au calcul des efforts exercés sur un obstacle par un fluide visqueux. *C. R. Acad. Sci. Paris* **1994**, *318*, 571–577.
125. Angot, P.; Bruneau, C.H.; Fabrie, P. A penalization method to take into account obstacles in incompressible viscous flows. *Numer. Math.* **1999**, *81*, 497–520. [CrossRef]
126. Kevlahan, N.; Ghidaglia, J.M. Computation of turbulent flow past an array of cylinders using a spectral method with Brinkman penalization. *Eur. J. Mech.* **2001**, *20*, 333–350. [CrossRef]
127. Morency, F.; Beaugendre, H.; Gallizio, F. Aerodynamic force evaluation for ice shedding phenomenon using vortex in cell scheme, penalisation and level set approaches. *Int. J. Comput. Fluid Dyn.* **2012**, *26*, 435–450. [CrossRef]
128. Coquerelle, M.; Cottet, G.H. A vortex level-set method for the two-way coupling of an incompressible fluid with colliding rigid bodies. *J. Comput. Phys.* **2008**, *227*, 9121–9137. [CrossRef]
129. Hejlesen, M.; Koumoutsakos, P.; Leonard, A.; Walther, J. Iterative Brinkman penalization for remeshed vortex methods. *J. Comput. Phys.* **2015**, *280*, 547–562. [CrossRef]
130. Gillis, T.; Winckelmans, G.; Chatelain, P. An efficient iterative penalization method using recycled Krylov subspaces and its application to impulsively started flows. *J. Comput. Phys.* **2017**, *347*, 490–505. [CrossRef]
131. Marichal, Y.; Chatelain, P.; Winckelmans, G. Immersed interface interpolation schemes for particle–mesh methods. *J. Comput. Phys.* **2016**, *326*, 947–972. [CrossRef]
132. Gillis, T.; Winckelmans, G.; Chatelain, P. A 2D immersed interface Vortex Particle-Mesh method. *J. Comput. Phys.* **2019**, *394*, 700–718. [CrossRef]
133. LeVeque, R.J.; Li, Z. The immersed interface method for elliptic equations with discontinuous coefficients and singular sources. *SIAM J. Numer. Anal.* **1994**, *31*, 1019–1044. [CrossRef]
134. Rossinelli, D.; Hejazialhosseini, B.; van Rees, W.M.; Gazzola, M.; Bergdorf, M.; Koumoutsakos, P. MRAG-I2D: Multi-resolution adapted grids for remeshed vortex methods on multicore architectures. *J. Comput. Phys.* **2015**, *288*, 1–18. [CrossRef]
135. Greengard, L.; Rokhlin, V. A fast algorithm for particle simulations. *J. Comput. Phys.* **1987**, *73*, 325–348. [CrossRef]
136. Marzouk, Y.M.; Ghoniem, A.F. K-means clustering for optimal partitioning and dynamic load balancing of parallel hierarchical N-body simulations. *J. Comput. Phys.* **2005**, *207*, 493–528. [CrossRef]
137. Yokota, R.; Narumi, T.; Sakamaki, R.; Kameoka, S.; Obi, S.; Yasuoka, K. Fast multipole methods on a cluster of GPUs for the meshless simulation of turbulence. *Comput. Phys. Commun.* **2009**, *180*, 2066–2078. [CrossRef]
138. Giannopoulou, O.; Colagrossi, A.; Di Mascio, A.; Mascia, C. Chorin's approaches revisited: Vortex Particle Method vs. Finite Volume Method. *Eng. Anal. Bound. Elem.* **2019**, *106*, 371–388. [CrossRef]

139. Hu, Q.; Gumerov, N.; Yokota, R.; Barba, L.A. Duraiswami, R. Scalable fast multipole methods for vortex element methods. In Proceedings of the 2012 SC Companion: High Performance Computing, Networking Storage and Analysis, Salt Lake City, UT, USA, 10–16 November 2012; pp. 1408–1409.
140. Rossinelli, D.; Bergdorf, M.; Cottet, G.H.; Koumoutsakos, P. GPU accelerated simulations of bluff body flows using vortex particle methods. *J. Comput. Phys.* **2010**, *229*, 3316–3333. [CrossRef]
141. Keck, J.B. Numerical Modelling and High Performance Computing for Sediment Flows. Ph.D. Thesis, Université Grenoble Alpes, Grenoble, France, 2019.
142. Yokota, R.; Barba, L.A.; Narumi, T.; Yasuoka, K. Petascale turbulence simulation using a highly parallel fast multipole method on GPUs. *Comput. Phys. Commun.* **2013**, *184*, 445–455. [CrossRef]
143. Bergdorf, M.; Cottet, G.H.; Koumoutsakos, P. Multilevel adaptive particle methods for convection-diffusion equations. *Multiscale Model. Sim.* **2005**, *4*, 328–357. [CrossRef]
144. Rasmussen, J.T.; Cottet, G.H.; Walther, J.H. A multiresolution remeshed Vortex-In-Cell algorithm using patches. *J. Comput. Phys.* **2011**, *230*, 6742–6755. [CrossRef]
145. El Ossmani, M.; Poncet, P. Efficiency of Multiscale Hybrid Grid-Particle Vortex Methods. *Multiscale Model. Simul.* **2010**, *8*, 1671–1690. [CrossRef]
146. Sagaut, P.; Deck, S.; Terracol, M. *Multiscale and Multiresolution Approaches in Turbulence. LES, DES and Hybrid RANS/LES Methods: Applications and Guidelines*; Imperial College Press: London, UK, 2013.
147. Cottet, G.H. Artificial Viscosity Models for Vortex and Particle Methods. *J. Comput. Phys.* **1996**, *127*, 199–208. [CrossRef]
148. Mansfield, J.; Knio, O.; Meneveau, C. A Dynamic LES Scheme for the Vorticity Transport Equation: Formulation and a Priori Tests. *J. Comput. Phys.* **1998**, *145*, 693–730. [CrossRef]
149. Mansfield, J.; Knio, O.; Meneveau, C. Dynamic LES of Colliding Vortex Rings Using a 3D Vortex Method. *J. Comput. Phys.* **1999**, *152*, 305–745. [CrossRef]
150. Pinon, G.; Bratec, H.; Huberson, S.; Pignot, G.; Rivoalen, E. Vortex method for simulation of a 3D round jet in a cross-stream. *J. Turbul.* **2005**, *6*, N18. [CrossRef]
151. Cocle, R.; Dufresne, L.; Winckelmans, G. Investigation of multiscale subgrid scale models for LES of instabilities and turbulence in wake vortex systems. In *Complex Effects in Large Eddy Simulations, Lecture Notes in Computational Science and Engineering (LNCSE)*; Springer: Berlin/Heidelberg, Germany, 2007; Volume 56.
152. Novati, G.; Verma, S.; Alexeev, D.; Rossinelli, D.; van Rees, W.; Koumoutsakos, P. Synchronisation through learning for two self-propelled swimmers. *Bioinspir. Biomim.* **2017**, *12*, 036001. [CrossRef]
153. Etancelin, J.M.; Cottet, G.H.; Pérignon, F.; Picard, C. Multi-CPU and multi-GPU hybrid computations of multi-scale scalar transport. In Proceedings of the 26th International Conference on Parallel Computational Fluid Dynamics, Trondheim, Norway, 20–22 May 2014; pp. 83–84.
154. Etancelin, J.M. Couplage de Modèles, Algorithmes Multi-échelles et Calcul Hybride. Ph.D. Thesis, Université de Grenoble, Grenoble, France, 2014.
155. Mimeau, C.; Mortazavi, I.; Cottet, G.H. Passive Flow Control Around a Semi-Circular Cylinder Using Porous Coatings. *Int. J. Flow Control* **2014**, *6*, 43–60.
156. Etancelin, J.M.; Moonen, P.; Poncet, P. Improvement of remeshed Lagrangian methods for the simulation of dissolution processes at pore-scale. *Adv. Water Resour.* **2020**, *146*, 103780. [CrossRef]
157. Cottet, G.H.; Wray, A. Anisotropic grid-based formulas for subgrid-scale models. In *Annual Research Briefs*; Center for Turbulence Research: Stanford, CA, USA, 1997.
158. Ostilla-Monico, R.; Yang, Y.; van der Poel, E.; Lohse, D.; Verzicco, R. A multiple-resolution strategy for Direct Numerical Simulation of scalar turbulence. *J. Comput. Phys.* **2015**, *301*, 308–321. [CrossRef]
159. Keck, J.B.; Cottet, G.H.; Meiburg, E.; Mortazavi, I.; Picard, C. Double-diffusive sedimentation at high Schmidt numbers: Semi-Lagrangian simulations. *Phys. Rev. Fluids* **2021**, to appear.
160. Iso, Y.; Kamemoto, K. A Grid-Free Lagrangian Approach of Vortex Method and Particle Trajectory Tracking Method Applied to Internal Fluid-Solid Two-Phase Flows. *J. Fluids Eng.* **2008**, *130*, 011401. [CrossRef]
161. Lorieul, G. Development and Validation of a 2D Vortex-Particle-Mesh Method for Incompressible Multi-Phase Flows. Ph.D. Thesis, Université Catholique de Louvain, Ottignies-Louvain-la-Neuve, Belgium, 2018.
162. Caprace, D.G.; Gillis, T.; Chatelain, P. FLUPS—A Fourier-based Library of Unbounded Poisson Solvers. *SIAM J. Sci. Comput.* **2021**, *43*, C31–C60. [CrossRef]

fluids

MDPI

Review

Theoretical Foundation of Rapid Distortion Theory on Transversely Sheared Mean Flows

Marvin E. Goldstein

NASA Glenn Research Center, Cleveland, OH 44135, USA; m.e.g@oh.rr.com

Received: 27 March 2020; Accepted: 18 April 2020; Published: 27 April 2020

Abstract: The focus of this paper is on Rapid Distortion Theory on transversely sheared mean flows, which is often used to investigate turbulence-solid surface interactions. The main purpose of the paper is to bring together and present in a consistent fashion a general theory that has been developed in several different papers that have been published in the Journal of Fluid Mechanics. The equations for the unsteady pressure and velocity flections (which decouple from the entropy fluctuations) are rewritten in terms of a gauge function in order to obtain expressions that involve two arbitrarily convected quantities. A pair of very general conservation laws are used to derive upstream boundary conditions that relate these quantities to the actual physical variables. The entropy fluctuations can be determined after the fact once the solutions for the pressure and velocity fluctuations are known. The result involves a third arbitrary convected quantity that is equal to the entropy fluctuations at upstream infinity and can, therefore, be specified as an additional upstream boundary condition. A secondary purpose of the paper is to summarize a number of applications of the theory that have also appeared in the literature and show how they compare with an experiment.

Keywords: turbulent flow; Rapid Distortion Theory; compressible flow; aeroacoustics; shear flow

1. Introduction

The interaction of turbulent shear flows with solid surfaces is clearly of great engineering interest [1–3] and too many papers have been written on the subject to be listed here. So, we mention only the well-known paper by Tufts, Wang and Wang [2] who used numerical methods to analyze the acoustic radiation produced by the interaction of an aerofoil with a turbulent shear layer. However, these types of interactions can also be studied analytically by using Rapid Distortion Theory (RDT).

RDT was developed to analyze relatively fast changes in turbulent flows such as those that occur in turbulence/solid surface interactions. It applies when the turbulence intensity is small and the interactions take place over length (or time) scales that are short compared to the decay time (or length) of the turbulent eddies [4–8]. These requirements make it possible to identify a distance that is very large (in fact, infinitely large when interpreted asymptotically) on the interaction scale, but still small on the length scale over which the turbulent eddies decay. The resulting flow will then be inviscid and non-heat conducting and will therefore be governed by the Euler equations linearized about an arbitrary nonlinear solution (often referred to as the base flow) to those equations.

1.1. The Kovasznay Result

The basic ideas are best understood by considering a uniform base flow. This case was first analyzed in the seminal paper by Kovasznay [9] which decomposed the unsteady isentropic motion on this flow into a vortical component that carries no pressure fluctuations and a solenoidal component that accounts for the pressure fluctuations. Möhring [10] pointed out that the latter, which is determined by a second-order wave equation in compressible flows, accounts for the acoustic component of the motion of these flows [10]. The former, which is a purely convected quantity in the sense that it moves downstream at the mean flow velocity, can then be interpreted as the hydrodynamic part of the motion. Two of its velocity components can be arbitrarily specified as (usually time-stationary) upstream boundary conditions for the unsteady motion. The Kovasznay decomposition has turned out to be very useful for analyzing turbulence/solid surface interactions on uniform mean flows [11–13], or on flows that become uniform far upstream [4–6], since the hydrodynamic component of the solution can be used to represent the incident turbulence in these analyses.

1.2. The Orr Result

The analysis becomes much more interesting when the entire base flow is allowed to be non-uniform. The simplest case is arguably a two-dimensional and incompressible flow with uniform mean shear so that the mean velocity, say U, is of the form

$$U = \Lambda y_2, \tag{1}$$

with constant $\Lambda \equiv dU/dy_2$ and $\{y_1, y_2, y_3\}$ denoting Cartesian coordinates, with y_1 in the mean flow direction. The unsteady motion is then determined by the linearized incompressible vorticity equation (the compressible case was analyzed by Möhring [10])

$$(\partial/\partial\tau + U\partial/\partial y_1)\omega'_3 = 0 \tag{2}$$

with τ denoting the time and ω'_3 denoting the spanwise vorticity perturbation. It was first pointed out by Orr [14,15] that Equation (2) or, equivalently, the two-dimensional Rayleigh equation

$$\frac{\partial}{\partial y_1}\left(\frac{\partial}{\partial\tau} + U\frac{\partial}{\partial y_1}\right)\omega'_3 = \left(\frac{\partial}{\partial\tau} + U\frac{\partial}{\partial y_1}\right)\left(\frac{\partial^2}{\partial y_1^2} + \frac{\partial^2}{\partial y_2^2}\right)v'_2 = 0, \tag{3}$$

which determines the unsteady cross-gradient velocity perturbation, $v'_2(y_2, \tau)$, can be integrated to show that the spanwise vorticity perturbation ω'_3 can be an arbitrary function, say $\omega_c(\tau - y_1/\Lambda y_2, y_2)$, of the indicated arguments and that v'_2 is determined by

$$\left(\frac{\partial^2}{\partial y_1^2} + \frac{\partial^2}{\partial y_2^2}\right)v'_2 = \frac{\partial}{\partial y_1}\omega_c\left(\tau - \frac{y_1}{\Lambda y_2}, y_2\right), \tag{4}$$

Orr [14] calculated the velocity and pressure fluctuations evolving from an initial state by solving an initial value problem associated with this equation. However, these solutions (or their long time limits) are not all that relevant to the time-stationary turbulent flows being considered here since the corresponding solutions to the full nonlinear equations can develop internal shear layers that can no longer be treated inviscidly and can support Kelvin–Helmholtz instabilities [16–18]. It is, however, not unreasonable to use the time-stationary or steady-state solutions given by Equation (4) to represent the turbulence in these flows. The relevant solution can then be written as

$$v'_2(\boldsymbol{x}, t) = \frac{\partial}{\partial x_1}\int_{-T}^{T}\int G_\perp(\boldsymbol{x}, t|\boldsymbol{y}, \tau)\,\omega_c\left(\tau - \frac{y_1}{\Lambda y_2}, y_2\right)d\boldsymbol{y}d\tau, \tag{5}$$

where $\boldsymbol{x} = \{x_1, x_2\}$ and $\boldsymbol{y} = \{y_1, y_2\}$ are two-dimensional Cartesian coordinates, T represents a large time interval and $G_\perp$ denotes the two-dimensional Green's function that is determined by the equation

$$\left(\frac{\partial^2}{\partial x_1^2} + \frac{\partial^2}{\partial x_2^2}\right)G_\perp(\boldsymbol{x}, t|\boldsymbol{y}, \tau) = \delta(t - \tau)\delta(\boldsymbol{y} - \boldsymbol{x}) \tag{6}$$

together with appropriate boundary conditions. The vorticity ω'_3, which is equal to the convected quantity $\omega_c(\tau - y_1/U(y_2), y_2)$, can now be specified as a boundary condition since Equation (5) will satisfy Equation (4) for any choice of this quantity.

The inner integral in Equation (5) is assumed to be carried out over an unbounded or semi-bounded region of space, with the Green's function $G_\perp$ required to satisfy appropriate transverse boundary conditions in the latter case and taken to be the free space Green's function $(4\pi)^{-1}\ln|\boldsymbol{x}-\boldsymbol{y}|^2\delta(t-\tau)$ in the former case. The transverse velocity perturbation $v'_2(\boldsymbol{x},t)$ will then be given by [19]

$$v'_2(\boldsymbol{x},t) = \int_{-\infty}^{\infty} \overline{G}_\perp\left(x_2\middle|y_2\right)\omega_c(t - x_1/\Lambda y_2)dy_2 \tag{7}$$

with

$$\overline{G}_\perp\left(x_2\middle|y_2\right) \equiv \frac{i}{2}(\mathrm{sgn}\omega)(\mathrm{sgn}y_2)e^{-|\omega||x_2-y_2|/\Lambda|y_2|} \tag{8}$$

when the convected vorticity $\omega_c(\tau - y_1/U(y_2), y_2)$ is taken to be the generic time-harmonic function

$$\omega_c\left(t - \frac{y_1}{U(y_2)}, y_2\right) = e^{i\omega[t-y_1/U(y_2)]}\widetilde{\Omega}_c(y_2 : \omega) \tag{9}$$

Figure 1, which is a plot of some typical values of v'_2 calculated from Equations (7)–(9) with $\widetilde{\Omega}_c(y_2 : \omega)$ taken to be

$$\widetilde{\Omega}_c(y_2 : \omega) = e^{-[a(y_2-y_0)]^2}, \tag{10}$$

shows that this quantity differs from the corresponding Kovasznay result on a uniform mean flow in that it now decays as $x_1 \to \pm\infty$.

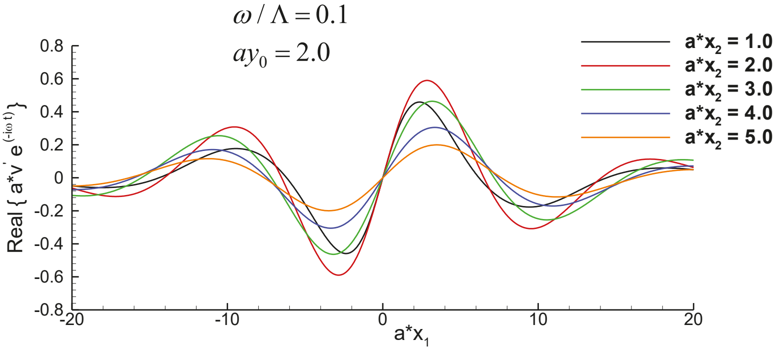

(**a**)

Figure 1. *Cont.*

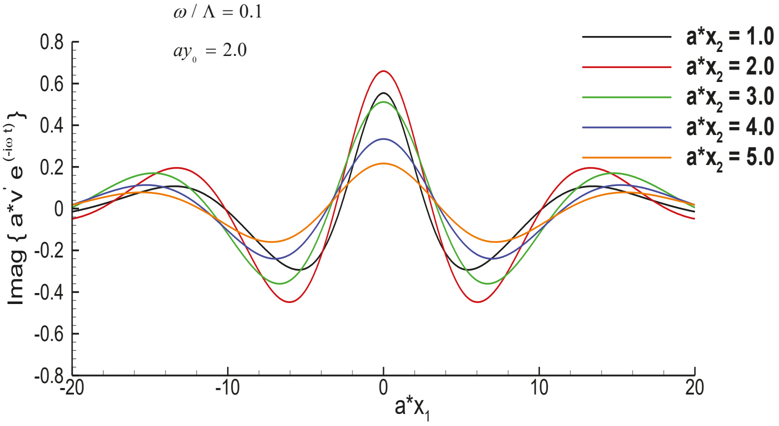

(**b**)

Figure 1. Transverse velocity fluctuations produced by the convected vorticity given by Equations (9) and (10) for the indicated values of the parameters. (**a**) Real part; (**b**) imaginary part. Reproduced with permission from [20].

This behavior will also occur in surface interaction problems, which might arise when a flat plate with a leading edge at $y_1 = 0$ is placed in the flow (see Figure 2). These considerations show that it is not possible to impose upstream boundary conditions by specifying v'_2 at the upstream infinity for this type of problem. However, it follows from Equation (4) that the Laplacian $\left(\partial^2/\partial y_1^2 + \partial^2/\partial y_2^2\right)v'_2$ is equal to the streamwise derivative of the convected quantity $\omega_c(\tau - y_1/U(y_2), y_2)$ and, therefore, does not decay. This means that the former quantity can be specified far upstream (infinitely far in an asymptotic sense) on the interaction length scale, which can still be small (infinitely small in an asymptotic sense) compared to the scale on which the turbulence evolves.

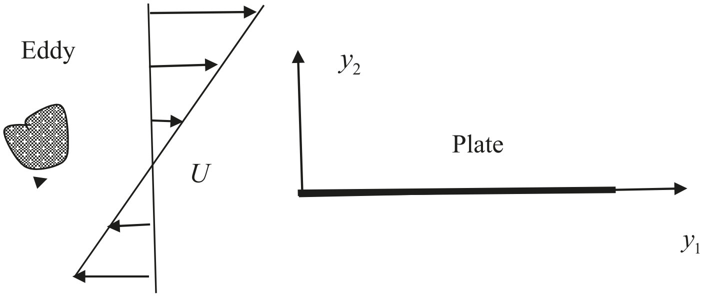

Figure 2. Leading edge scattering. Reproduced with permission from [20].

The key result is that the arbitrary function $\omega_c(\tau - y_1/U(y_2), y_2)$ can be determined by specifying an actual physical variable in a region where the flow is unaffected by the solid surface. The present paper shows that the situation is analogous but much more interesting for more complicated transversely sheared flows.

1.3. Scope of the Paper

A large number of papers [7,8,21,22] have used locally homogeneous RDT, which is a kind of local high-frequency approximation first introduced by Moffatt [23], to study the turbulent motion on planar shear flows. The assumption of local homogeneity eliminates the requirement for upstream boundary conditions, but the present paper is only concerned with non-homogenous RDT, which usually provides a much more realistic description of the flow. There are also a large number of papers on this subject that have appeared in the literature, but the focus of the present paper is on the much narrower topic of non-homogenous RDT on transversely sheared mean flows. Its primary purpose is to bring together and describe in an integrated fashion a general methodology that has been developed in a number of different papers [5,6,20,21] to deal with this phenomenon. Some significant new results are also presented.

The basic equations are rewritten in terms of a gauge function in Section 3 and a formal solution to the complete inhomogeneous RDT problem is given in Section 4. Section 5 discusses the role of causality and instability waves and shows that (as in the Kovasznay decomposition) the resulting formulas for the unsteady pressure and velocity fluctuations (which decouple from the entropy fluctuations) involve two convected quantities. However, unlike the Kovasznay result, they are not directly related to the physical flow variables. However, it is shown that they can be linked to these variables by using two very general conservation laws (derived in Appendix A and discussed in Section 7) that relate the convected quantities to the physical variables and a gradient-wise particle displacement (defined in Section 5). Appendix B shows that the latter quantity vanishes at upstream infinity and, therefore (as shown in Section 8), that conservation laws can be used to obtain a set of upstream boundary conditions that relate the convected quantities to the physical variables.

Spatially growing instability waves- which are usually associated with coherent structures in turbulent flows-may also appear in the solutions. However, their amplitudes cannot be determined by imposing upstream boundary conditions since they decay exponentially fast at upstream infinity. They can, however, be determined as part of the solution when causality is imposed on the flow, which appears to be particularly appropriate in the present context since Creighton [24,25] has shown that the imposition of causality is equivalent to imposing a Kutta condition at a trailing edge.

Section 6 shows that the entropy fluctuations can be determined from the particle displacement once the solution for the pressure and velocity fluctuations is known. The result brings in a third arbitrary convected function, which is equal to the entropy fluctuations at upstream infinity and can, therefore, be specified as a third upstream boundary condition.

Section 9 shows how these results can be used to relate turbulent pressure spectrum (which is of principal interest in acoustic and structural vibration problems) to the upstream turbulent velocity spectrum (usually specified as an upstream boundary condition in turbulent surface interaction problems) and an appropriate model for this spectrum is introduced. Some applications of the theory that have appeared in the literature are described in Section 11 and some brief conclusions are given in Section 12.

2. The Basic Equations

We consider the flow of an inviscid and non-heat conducting fluid which is assumed to be an ideal gas with squared sound speed $\gamma p/\rho$, and entropy $c_v \ln(p/\rho^\gamma)$ where p and ρ denote the pressure and density, respectively, and γ denotes the specific heat ratio c_p/c_v where c_p, c_v are the specific heats at constant pressure and volume, respectively.

The pressure $p' = p - p_0$ and mass flux

$$\boldsymbol{u} = \{u_1, u_2, u_3\} \equiv \rho\{v'_1, v'_2, v'_3\} \tag{11}$$

perturbations (where $\boldsymbol{v}' = \{v'_1, v'_2, v'_3\}$ is the actual velocity perturbation) on a transversely sheared mean flow whose velocity $U\left(\boldsymbol{y}_T\right)$ is in a single direction, whose pressure p_0 is equal to a constant, and whose mean sound speed squared $c^2\left(\boldsymbol{y}_T\right)$ depends only on the transverse coordinate $\boldsymbol{y}_T$, decouple from the entropy fluctuations and are governed by the linearized momentum and continuity equations

$$\frac{D_0 u_i}{D\tau} + \delta_{1i} u_j \frac{\partial U}{\partial y_j} + \frac{\partial}{\partial y_i} p' = 0, \ i = 1, 2, 3 \tag{12}$$

and

$$u_i \frac{D_0 p'}{D\tau} + \frac{\partial}{\partial y_j} c^2 u_j = 0 \tag{13}$$

where $\boldsymbol{y}_T \equiv \{y_2, y_3\}$, $\boldsymbol{y} \equiv \{y_1, y_2, y_3\} = \{y_1, \boldsymbol{y}_T\}$ and

$$\frac{D_0}{D\tau} \equiv \frac{\partial}{\partial \tau} + U(\boldsymbol{y}_T) \frac{\partial}{\partial y_1} \tag{14}$$

denote the convective derivative based on the source point (while $D_0/Dt \equiv \partial/\partial t + U(\boldsymbol{x}_T)\partial/\partial x_1$ denotes the convective derivative based on the observation point).

The entropy fluctuation s' depends on the momentum fluctuations and can be determined from the energy equation (Equation (11) of [26])

$$\frac{D_0 s'}{D\tau} = \frac{c_p}{\rho_0^2} u_i \frac{\partial \rho_0}{\partial y_i} \tag{15}$$

once u_i is known.

3. The Gauge Function Representation

The momentum Equation (12) will be identically satisfied for any arbitrary function ϕ and any purely convected function $\vartheta(\tau - (y_1/U), \boldsymbol{y}_T)$ when the pressure fluctuation p' and the momentum fluctuation.u_i are related to ϑ and ϕ by [27]

$$p' = -\frac{D_0^3 \phi}{D\tau^3}, \tag{16}$$

and

$$u_i = \frac{D_0}{D\tau} \lambda_i - \delta_{1i} \frac{\partial U}{\partial y_j} \lambda_j + \varepsilon_{ijk} \frac{1}{c^2} \frac{\partial U}{\partial y_j} \frac{\partial}{\partial y_k} \vartheta\left(\tau - \frac{y_1}{U}, \boldsymbol{y}_T\right), \text{ for } i = 1, 2, 3, \tag{17}$$

where ϕ plays the role of a gauge function,

$$\lambda_j \equiv \frac{\partial}{\partial y_j} \frac{D_0 \phi}{D\tau} + 2 \frac{\partial U}{\partial y_j} \frac{\partial \phi}{\partial y_1} \tag{18}$$

is a kind "pseudo-particle displacement", δ_{ij} denotes the Kronecker delta and ε_{ijk} denotes the Levi–Cevita permutation tensor.

Since the Gauge function ϕ is undetermined at this stage of the analysis it can be adjusted to ensure that the continuity Equation (13) is also satisfied by substituting Equations (16)–(18) into Equation (13) to obtain

$$\frac{D_0}{D\tau} L_a \phi = 0, \tag{19}$$

where L_a denotes the linear operator

$$L_a \equiv \frac{D_0^3}{D\tau^3} - \frac{\partial}{\partial y_i} c^2 \left(\frac{\partial}{\partial y_i} \frac{D_0}{D\tau} + 2 \frac{\partial U}{\partial y_i} \frac{\partial}{\partial y_1} \right) \tag{20}$$

As in the Orr analysis discussed in Section 1.2, this result can be integrated to show that the gauge function ϕ is determined by

$$L_a \phi = -\widetilde{\omega}_c \left(\tau - \frac{y_1}{U}, \boldsymbol{y}_T \right) \tag{21}$$

where $\widetilde{\omega}_c(\tau - y_1/U, \boldsymbol{y}_T)$ denotes a second arbitrary convected quantity.

4. Green's Function Solution of Gauge Function Equation

Eliminating the mass flux perturbation $\boldsymbol{u}$ between Equations (12) and (13) shows that the pressure fluctuation p' satisfies the well-known Rayleigh's equation [28]

$$L p' = 0, \tag{22}$$

where

$$L \equiv \frac{D_o}{D\tau}\left(\frac{\partial}{\partial y_i}c^2\frac{\partial}{\partial y_i} - \frac{D_o^2}{D\tau^2}\right) - 2\frac{\partial U}{\partial y_j}\frac{\partial}{\partial y_1}c^2\frac{\partial}{\partial y_j} \tag{23}$$

denotes the usual Rayleigh operator, which turns out to be adjoint to the operator L_a defined by Equation (20) since

$$\overline{v}L\overline{u} - \overline{u}L_a\overline{v} = \frac{\partial}{\partial y_i}c^2\left(\overline{u}\frac{\partial}{\partial y_i}\frac{D_0\overline{v}}{D\tau} + 2\overline{u}\frac{\partial U}{\partial y_i}\frac{\partial \overline{v}}{\partial y_1} - \frac{\partial \overline{u}}{\partial y_i}\frac{D_0\overline{v}}{D\tau}\right)$$

$$+\frac{D_0}{D\tau}\left(\overline{v}\frac{\partial}{\partial y_i}c^2\frac{\partial \overline{u}}{\partial y_i} + \frac{D_0\overline{u}}{D\tau}\frac{D_0\overline{v}}{D\tau} - \overline{u}\frac{D_0^2\overline{v}}{D\tau^2} - \overline{v}\frac{D_0^2\overline{u}}{D\tau^2}\right) - 2\frac{\partial}{\partial y_1}\left(c^2\frac{\partial U}{\partial y_j}\overline{v}\frac{\partial \overline{u}}{\partial y_j}\right) \tag{24}$$

for any functions $\overline{u}, \overline{v}$ [29].

Since, to our knowledge, all applications of non-homogeneous RDT have been to steady-state turbulent flows the focus here will be on the time-stationary solutions of Equation (21), we, therefore, suppose that ϕ is time stationary [30] and that initial conditions imposed in the distant past do not affect the solution at the finite time t.

Let $g(\boldsymbol{y},\tau|\boldsymbol{x},t)$ denote the Green's function for the Rayleigh operator L that satisfies

$$L\, g(\boldsymbol{y},\tau|\boldsymbol{x},t) = \delta(\boldsymbol{y}-\boldsymbol{x})\delta(\tau - t), \tag{25}$$

and behaves like an incoming wave as $|\boldsymbol{y}| \to \infty$. As usual we let the first two arguments of $g(\boldsymbol{y},\tau|\boldsymbol{x},t)$ represent the dependent variables and let the second two represent the source variables. Since $g(\boldsymbol{y},\tau|\boldsymbol{x},t)$ denotes value of the solution to Equation (25) at $(\boldsymbol{y},\tau)$ due to a point sink at $(\boldsymbol{x},t)$, it should be related to its adjoint $g_a(\boldsymbol{x},t|\boldsymbol{y},\tau)$ by the reciprocity relation [29,31]

$$g(\boldsymbol{y},\tau|\boldsymbol{x},t) = g_a(\boldsymbol{x},t|\boldsymbol{y},\tau) \tag{26}$$

Then since $g_a(\boldsymbol{x},t|\boldsymbol{y},\tau)$ satisfies Equation (21) with the source function $-\widetilde{\omega}_c(\tau - y_1/U, \boldsymbol{y}_T)$ replaced by $\delta(\boldsymbol{y}-\boldsymbol{x})\delta(\tau-t)$, and, therefore, corresponds to a direct Green's function in the present context, it reasonable to require that it satisfy the causality condition $g_a(\boldsymbol{x},t|\boldsymbol{y},\tau) = 0$, for all $\boldsymbol{t}<\tau$, which implies that the Green's function, $g(\boldsymbol{y},\tau|\boldsymbol{x},t)$, will vanish for all finite $\boldsymbol{y}$ as $\tau \to \infty$, since it vanishes for all $\tau > t$ by definition.

We can require that the solution $\phi(\boldsymbol{x},t)$ of the gauge function defined by Equation (21) along with its derivatives (and, therefore, the pressure fluctuations) vanish (for all finite times) as x_1 goes to plus or minus infinity when the source function $\widetilde{\omega}_c$ is reasonably compact—even for globally unstable base flows since the signal generated at $(\boldsymbol{y},\tau)$ cannot reach these locations when $t = T$ is finite. This means that gauge function $\phi(\boldsymbol{y},\tau)$ goes to zero as $y_1 \to \pm\infty$ for all finite τ. We also assume that the initial conditions are such that $\phi(\boldsymbol{y},\tau)$ and its derivatives vanish for all finite $\boldsymbol{y}$ as $\tau \to -\infty$.

Setting $\overline{u}$ equal to $g(\boldsymbol{y},\tau|\boldsymbol{x},t)$ in Equation (24), letting $\overline{v}$ denote a solution to Equation (21) and using the divergence theorem shows that Equation (21) possess the formal steady-state solution [27]

$$\phi(\boldsymbol{x},t) = -\int_{-T}^{T}\int_{V} g(\boldsymbol{y},\tau|x,t)\widetilde{\omega}_c\left(\tau - \frac{y_1}{U(\boldsymbol{y}_T)}, \boldsymbol{y}_T\right) d\boldsymbol{y}d\tau$$

$$+\int\limits_{-T}^{T}\int\limits_{S}\hat{n}_j c^2\left[g(\boldsymbol{y},\tau|x,t)\,\lambda_j-\frac{\partial g(\boldsymbol{y},\tau|x,t)}{\partial y_j}\frac{D_0\phi}{D\tau}\right]dS(\boldsymbol{y})\,d\tau \tag{27}$$

where T is a large but finite time, the volume V is assumed to be bounded by cylindrical surface(s) S that can be of finite, semi-infinite or infinite length in the streamwise direction, $\hat{n}=\{\hat{n}_i\}$ denotes the unit outward-drawn normal to S and λ_j is defined by Equation (18). Since $g(\boldsymbol{y},\tau|\boldsymbol{x},t)=0$ for $\tau>t$ we can replace the upper limit T by the time t.

Equation (27) expresses the solution to Equation (21) in terms of the volume source distribution $\widetilde{\omega}_c\left(\tau-y_1/U\left(\boldsymbol{y}_T\right),\boldsymbol{y}_T\right)$ and the gauge function ϕ distribution over one or more cylindrical surfaces S. The formulation is unconventional since the direct Green's function g now plays the role of an adjoint Green's function in the solution of Equation (27) for the Gauge function ϕ. The surface integral will not appear in Equation (27) and the Green's function g will be completely determined by Equation (25) together with the causality requirements given above when the integration volume V is all of space and will be incompletely determined by these requirements when it is not.

5. Integral Solution for the Physical Variables

5.1. The Pressure Fluctuation

Substituting Equation (27) into Equation (16) shows that the pressure fluctuation p' is given by

$$p'(\boldsymbol{x},t)=\int\limits_{-T}^{T}\int\limits_{V}G(\boldsymbol{y},\tau|x,t)\widetilde{\omega}_c\left(\tau-\frac{y_1}{U\left(\boldsymbol{y}_T\right)},\boldsymbol{y}_T\right)d\boldsymbol{y}d\tau$$

$$-\int\limits_{-T}^{T}\int\limits_{S}\hat{n}_j c^2\left[G(\boldsymbol{y},\tau|x,t)\lambda_j-\frac{\partial G(\boldsymbol{y},\tau|x,t)}{\partial y_j}\frac{D_0\phi}{D\tau}\right]dS(\boldsymbol{y})\,d\tau \tag{28}$$

where

$$G(\boldsymbol{y},\tau|\boldsymbol{x},t)\equiv\frac{D_0^3 g(\boldsymbol{y},\tau|x,t)}{Dt^3} \tag{29}$$

satisfies the reduced Rayleigh Green's function equation [27]

$$L\,\mathbf{G}(\boldsymbol{y},\tau|x,t)=\frac{D_0^3}{Dt^3}\delta(\boldsymbol{y}-\boldsymbol{x})\delta(\tau-t) \tag{30}$$

Equation (28) can be rewritten as

$$p'(\boldsymbol{x},t)=\int\limits_{-T}^{T}\int\limits_{V}G(\boldsymbol{y},\tau|x,t)\widetilde{\omega}_c\left(\tau-\frac{y_1}{U\left(\boldsymbol{y}_T\right)},\boldsymbol{y}_T\right)d\boldsymbol{y}d\tau$$

$$-\int\limits_{-T}^{T}\int\limits_{S}\left[G(\boldsymbol{y},\tau|x,t)\left(\hat{n}_j c^2\lambda_j\right)+\Gamma(\boldsymbol{y},\tau|x,t)p'(\boldsymbol{y},\tau)\right]dS(\boldsymbol{y})\,d\tau \tag{31}$$

by introducing the variable $\Gamma(\boldsymbol{y},\tau|\boldsymbol{x},t)$ defined to within some arbitrary convected quantities by

$$\frac{D_0^2\Gamma(\boldsymbol{y},\tau|x,t)}{D\tau^2}\equiv\hat{n}_j c^2\frac{\partial G(\boldsymbol{y},\tau|x,t)}{\partial y_j},\ \boldsymbol{y}\in S \tag{32}$$

and integrating by parts. Goldstein et al. [27] used this result to extend Equation (28) to flows with discontinuous velocity profiles downstream of the solid surfaces. They showed that the transverse component of the effective particle displacement $c^2\hat{n}_i\lambda_i$ and the pressure perturbation p' will be continuous across the discontinuities when $G(\boldsymbol{y},\tau|\boldsymbol{x},t)$ and $\Gamma(\boldsymbol{y},\tau|\boldsymbol{x},t)$ are required to satisfy the jump condition

$$\Delta[G] = \Delta[\Gamma] = 0, \text{ for } \boldsymbol{y}_T \in S_0 \tag{33}$$

where $\Delta[\cdot]$ denotes the jump in the indicated quantity across the surface/surfaces of discontinuity S_0 which will correspond to infinitely thin wakes or vortex sheets downstream of the solid surfaces when, as will usually be the case, they coincide with level surfaces of the mean flow.

5.2. Role of Instability Waves

It is well-known that inflectional base flows can support spatially growing instability waves, which are often used to represent the large-scale coherent structures in turbulent flows. Since all these instabilities (other than the singular neutral instability) decay exponentially fast at upstream infinity their amplitudes cannot be determined from by specifying upstream boundary conditions. However, as shown by Briggs [32] and Bers [33], they are uniquely determined as part of the solution when causality is imposed on the flow-which appears to be particularly appropriate in the present context since Creighton [24,25] has shown that the imposition of causality is equivalent to imposing a Kutta condition at the trailing edges.

5.3. The Pseudo-Particle Displacement

As is in the previous case the surface integrals drop out of Equation (31) and the Green's function G is then completely determined by Equation (30) together with the causality requirements given above when the doubly infinite surfaces S are all at infinity (i.e., when V represents all of space) but they can still be eliminated when they are not at infinity by requiring that G satisfy appropriate boundary conditions on these surfaces. The second term in square brackets drops out of the surface integral when

$$\Gamma(\boldsymbol{y},\tau|\boldsymbol{x},t) = 0 \text{ for } \boldsymbol{y} \in S \tag{34}$$

The remaining term will vanish when

$$\hat{n}_i\lambda_i c^2 = 0, \text{for } \boldsymbol{y} \in S \tag{35}$$

and the pressure perturbation p' will then be given by

$$p'(\boldsymbol{x},t) = \int_{-T}^{T}\int_{V} G(\boldsymbol{y},\tau|\boldsymbol{x},t)\widetilde{\omega}_c\left(\tau - \frac{y_1}{U(\boldsymbol{y}_T)}, \boldsymbol{y}_T\right) d\boldsymbol{y}d\tau \tag{36}$$

This means that the pressure fluctuation p' corresponding to a solution whose surface behavior is consistent with Equation (35) will be determined by Equation (36) when G satisfies Equations (33) and (34). It follows from Equation (17) that consistency with Equation (35) requires that the ϑ-independent component of the density-weighted velocity perturbation

$$\widetilde{u_i}(\boldsymbol{x},t) \equiv \frac{D_0}{D\tau}\lambda_i - \delta_{1i}\frac{\partial U}{\partial y_j}\lambda_j \tag{37}$$

vanish on S and, therefore, that the corresponding density-weighted normal surface velocity $\hat{n}_i u_i$ is given by

$$c^2\,\hat{n}_i u_i = \varepsilon_{ijk}\hat{n}_i\frac{\partial U}{\partial y_j}\frac{\partial}{\partial y_k}\vartheta\left(\tau - \frac{y_1}{U}, \boldsymbol{y}_T\right) = \varepsilon_{ij1}\,\hat{n}_i\frac{\partial U}{\partial y_j}\frac{\partial}{\partial y_1}\vartheta\left(\tau - \frac{y_1}{U}, \boldsymbol{y}_T\right) \text{ for } \boldsymbol{y} \in S \tag{38}$$

Since the surfaces S must be aligned with the mean flow. In fact they will usually coincide with the level $U =$ constant surfaces: in which case Equation (35) will be equivalent to requiring that the gradient-wise component

$$\lambda_{\perp}(\boldsymbol{y},\tau) \equiv (\partial U/\partial y_i)\lambda_i = \frac{\partial U}{\partial y_j}\left(\frac{\partial}{\partial y_j}\frac{D_0\phi}{D\tau} + 2\frac{\partial U}{\partial y_j}\frac{\partial \phi}{\partial y_1}\right) \tag{39}$$

of the pseudo-particle displacement λ_i vanish on S and Equation (38) will then imply that the (density-weighted) normal surface velocity $\hat{n}_i u_i$ vanishes on S, since the normal vector $\hat{\boldsymbol{n}}$ is then equal to $\nabla U/|\nabla U|$. Equation (38) shows that this will occur even when S does not coincide with a level $U =$ constant surface if

$$\vartheta\left(\tau - \frac{y_1}{U}, \boldsymbol{y}_T\right) = 0 \text{ for } \boldsymbol{y} \in S \tag{40}$$

Equations (18) and (27) show that the complete pseudo-particle displacement is given by

$$\lambda_i = -\int\limits_{-T}^{T}\int\limits_{V} \widetilde{G}_i(\boldsymbol{y},\tau|x,t)\widetilde{\omega}_c\left(\tau - \frac{y_1}{U(\boldsymbol{y}_T)}, \boldsymbol{y}_T\right) d\boldsymbol{y}d\tau$$

$$-\int\limits_{-T}^{T}\int\limits_{S}\left[\widetilde{G}_i(\boldsymbol{y},\tau|x,t)\left(\hat{n}_j c^2 \lambda_j\right) + \widetilde{\Gamma}_i(\boldsymbol{y},\tau|x,t)p'(\boldsymbol{y},\tau)\right] dS(\boldsymbol{y})\, d\tau, \text{ for } i = 1,2,3 \tag{41}$$

with $\widetilde{G}_i(\boldsymbol{y},\tau|\boldsymbol{x},t)$ determined by

$$\widetilde{G}_i(\boldsymbol{y},\tau|\boldsymbol{x},t) \equiv \frac{\partial}{\partial x_j}\frac{D_0 g}{Dt} + 2\frac{\partial U}{\partial x_j}\frac{\partial g}{\partial x_1}, \text{ for } i = 1,2,3 \tag{42}$$

and is, therefore, related to the Green's function derivative $\partial G(\boldsymbol{y},\tau|\boldsymbol{x},t)/\partial x_i$ of $G(\boldsymbol{y},\tau|\boldsymbol{x},t)$ by

$$\frac{D_0^2}{Dt^2}\widetilde{G}_i(\boldsymbol{y},\tau|\boldsymbol{x},t) = \frac{\partial}{\partial x_i}G(\boldsymbol{y},\tau|\boldsymbol{x},t), \text{ for } i = 1,2,3 \tag{43}$$

which means that $\widetilde{\Gamma}_i(\boldsymbol{y},\tau|\boldsymbol{x},t)$ is related to the transverse gradient of $\widetilde{G}_i(\boldsymbol{y},\tau|\boldsymbol{x},t)$ by

$$\frac{D_0^2\widetilde{\Gamma}_i(\boldsymbol{y},\tau|x,t)}{D\tau^2} \equiv \hat{n}_j c^2 \frac{\partial \widetilde{G}_i(\boldsymbol{y},\tau|x,t)}{\partial y_j} \tag{44}$$

5.4. The Density-Weighted Gradient-Wise Velocity Perturbation

It now follows from Equation (17) that the density-weighted gradient-wise velocity perturbation

$$u_{\perp} \equiv \frac{1}{|\nabla U|}\frac{\partial U}{\partial y_i}u_i \tag{45}$$

is related to the transverse particle displacement defined in Equation (39) by

$$u_{\perp} = \frac{1}{|\nabla U|}\frac{D_0\lambda_{\perp}}{D\tau}, \tag{46}$$

which is (like p') also independent of the second independent convected quantity $\vartheta\left(\tau - y_1/U, \boldsymbol{y}_T\right)$ and is explicitly given by

$$u_{\perp} = \int\limits_{-T}^{T}\int\limits_{V} G_{\perp}(\boldsymbol{y},\tau|x,t)\widetilde{\omega}_c\left(\tau - \frac{y_1}{U(\boldsymbol{y}_T)}, \boldsymbol{y}_T\right) d\boldsymbol{y}d\tau$$

$$-\int_{-T}^{T}\int_{S}\Big[G_{\perp}(\boldsymbol{y},\tau\big|x,t)\Big(\hat{n}_j c^2\lambda_j\Big)+\Gamma_{\perp}(\boldsymbol{y},\tau\big|x,t)p'(\boldsymbol{y},\tau)\Big]\,dS(\boldsymbol{y})\,d\tau \tag{47}$$

where $G_{\perp}(\boldsymbol{y},\tau\big|\boldsymbol{x},t)$ is defined by

$$G_{\perp}(\boldsymbol{y},\tau\big|\boldsymbol{x},t)\equiv-\frac{\nabla U}{|\nabla U|}\cdot\frac{D_0}{Dt}\left[\nabla\frac{D_0}{Dt}+2(\nabla U)\frac{\partial}{\partial x_1}\right]g(\boldsymbol{y},\tau\big|\boldsymbol{x},t). \tag{48}$$

with

$$\nabla\equiv\{\partial/\partial x_i\}. \tag{49}$$

and is, therefore, related to the gradient of $G(\boldsymbol{y},\tau\big|\boldsymbol{x},t)$ by

$$\frac{D_0}{Dt}G_{\perp}(\boldsymbol{y},\tau\big|\boldsymbol{x},t)=-\frac{\nabla U}{|\nabla U|}\cdot\nabla G(\boldsymbol{y},\tau\big|\boldsymbol{x},t) \tag{50}$$

The pseudo-particle displacement and gradient-wise velocity perturbation will be given by

$$\lambda_i=-\int_{-T}^{T}\int_{V}\widetilde{G}_i(\boldsymbol{y},\tau\big|x,t)\widetilde{\omega}_c\left(\tau-\frac{y_1}{U\big(\boldsymbol{y}_T\big)},\boldsymbol{y}_T\right)d\boldsymbol{y}d\tau \tag{51}$$

and

$$u_{\perp}=\int_{-T}^{T}\int_{V}G_{\perp}(\boldsymbol{y},\tau\big|x,t)\widetilde{\omega}_c\left(\tau-\frac{y_1}{U\big(\boldsymbol{y}_T\big)},\boldsymbol{y}_T\right)d\boldsymbol{y}d\tau \tag{52}$$

respectively, when boundary and jump conditions analogous to those given by Equations (33)–(35) are imposed. Equation (52) is clearly a generalization of the Orr result given by Equation (7). Similar equations can, of course, be obtained for the other components of $\boldsymbol{u}$.

Equation (27) is only formal in the sense that the integrals do not actually converge but the corresponding integrals for the physical variables given by Equations (31), (47), etc., do exist and these results will provide a proper solution to the original equations. However, as will be discussed in Appendix B, the integral in Equation (51) for the pseudo-particle particle displacement must be interpreted in terms of a principle value-like integral in order to remain finite, which may have some implications for the entropy fluctuations discussed below.

5.5. The Hydrodynamic Component of the Motion

These results can be used to calculate the sound radiation produced by turbulence -solid surfaceinteracions and many attempts have been made to follow Kovasznay [9] and isolate the acoustic component of the motion in applications of this type. However, the unsteady motion on a transversely sheared mean flow cannot be decomposed into distinct acoustic and hydrodynamic components. It is, on the other hand, possible to identify a hydrodynamic component of the motion by requiring that it does not produce any acoustic radiation at subsonic speeds. The remaining non-hydrodynamic component will then account for all the acoustic radiation. This suggests that the Rayleigh equation Green's function $g(\boldsymbol{y},\tau\big|\boldsymbol{x},t)$ that appears in the gauge function solution of Equation (27) be divided into two components, say

$$g(\boldsymbol{y},\tau\big|\boldsymbol{x},t)=g^{(0)}(\boldsymbol{y},\tau\big|\boldsymbol{x},t)+g^{(s)}(\boldsymbol{y},\tau\big|\boldsymbol{x},t). \tag{53}$$

where $g^{(0)}(\boldsymbol{y},\tau\big|\boldsymbol{x},t)$ is a particular solution of Equation (25), which is either defined on all space or satisfies appropriate homogeneous boundary conditions on an extension of the bounding surface S that goes from minus infinity to plus infinity in the direction of the mean flow direction. This breakdown implies the decompositions

$$G(\boldsymbol{y},\tau\big|\boldsymbol{x},t) = G^{(0)}(\boldsymbol{y},\tau\big|\boldsymbol{x},t) + G^{(s)}(\boldsymbol{y},\tau\big|\boldsymbol{x},t) \tag{54}$$

and

$$\widetilde{G}_i(\boldsymbol{y},\tau\big|\boldsymbol{x},t) = \widetilde{G}_i^{(0)}(\boldsymbol{y},\tau\big|\boldsymbol{x},t) + \widetilde{G}_i^{(s)}(\boldsymbol{y},\tau\big|\boldsymbol{x},t) \tag{55}$$

of the Green's function defined by Equation (29) and the Green's function derivative defined by Equation (43).

The decomposition displayed in Equation (54) then implies the pressure fluctuation decomposition

$$p'(\boldsymbol{x},t) = p'^{(0)}(\boldsymbol{x},t) + p'^{(s)}(\boldsymbol{x},t) \tag{56}$$

where $p'^{(0)}(\boldsymbol{x},t)$ (obtained by replacing $G(\boldsymbol{y},\tau\big|\boldsymbol{x},t)$ with $G^{(0)}(\boldsymbol{y},\tau\big|\boldsymbol{x},t)$ in Equation (28) and/or Equation (31), will not radiate any sound at subsonic speeds and can, therefore, be identified as the hydrodynamic component of the motion. The remaining component $p'^{(s)}(\boldsymbol{x},t)$ (given by Equations (28) and (31) with $G(\boldsymbol{y},\tau\big|\boldsymbol{x},t)$ replaced by $G^{(s)}(\boldsymbol{y},\tau\big|\boldsymbol{x},t)$ which is, in turn, determined by Rayleigh's equation (Equation (28)) along with suitable boundary/jump conditions) will then account for all of the acoustic components of the motion.

The decomposition of Equation (55) implies the decomposition

$$\lambda_i(\boldsymbol{x},t) = \lambda_i^{(0)}(\boldsymbol{x},t) + \lambda_i^{(s)}(\boldsymbol{x},t) \tag{57}$$

for the pseudo-particle displacement $\lambda_i(\boldsymbol{x},t)$ where $\lambda_i^{(0)}(\boldsymbol{x},t)$, which is given by Equation (41) with $\widetilde{G}_i(\boldsymbol{y},\tau\big|\boldsymbol{x},t)$ replaced by $\widetilde{G}_i^{(0)}(\boldsymbol{y},\tau\big|\boldsymbol{x},t)$.

Equations (47) and (52), which determine the physical variables p' and $u_\perp$, reduce the RDT problem to a boundary value problem for the Rayleigh's equation Green's function. The solutions $p'(\boldsymbol{x},t)$ and $u_\perp(\boldsymbol{x},t)$ will then be independent of the convected quantity $\vartheta\big(\tau - y_1/U, \boldsymbol{y}_T\big)$ (as well as the convected quantity $s_\infty\big(\tau - y_1/U, \boldsymbol{y}_T\big)$ defined below), which means that the resulting acoustic field will only depend on the single convected quantity $\widetilde{\omega}_c\big(\tau - y_1/U\big(\boldsymbol{y}_T\big), \boldsymbol{y}_T\big)$.

6. The Entropy Fluctuations

Since

$$\varepsilon_{ijk}\frac{1}{c^2}\frac{\partial U}{\partial y_j}\frac{\partial}{\partial y_k}\vartheta\Big(\tau - \frac{y_1}{U}, \boldsymbol{y}_T\Big) = \left(\delta_{ij}\frac{D_0}{D\tau} - \delta_{i1}\frac{\partial U}{\partial y_j}\right)\lambda_j^{(c)} \tag{58}$$

where

$$\lambda_j^{(c)} \equiv \frac{y_1}{Uc^2}\varepsilon_{jkl}\frac{\partial U}{\partial y_k}\frac{\partial}{\partial y_l}\vartheta\Big(\tau - \frac{y_1}{U}, \boldsymbol{y}_T\Big), \tag{59}$$

Equations (15) and (18) show that

$$\frac{D_0 s'}{D\tau} = \frac{c_p}{\rho_0^2}\frac{D_0}{D\tau}\frac{\partial \rho_0}{\partial y_i}\Big(\lambda_i + \lambda_i^{(c)}\Big) \tag{60}$$

which can be integrated to obtain

$$s' = \frac{c_p}{\rho_0^2}\frac{\partial \rho_0}{\partial y_i}\Big(\lambda_i + \lambda_i^{(c)}\Big) + s_\infty\Big(\tau - \frac{y_1}{U}, \boldsymbol{y}_T\Big) \tag{61}$$

where $s_\infty\big(\tau - y_1/U, \boldsymbol{y}_T\big)$ denotes a third arbitrary convected quantity. It, therefore, follows from Equation (59) that $s' \to \infty$ as $y_1 \to -\infty$ if $\varepsilon_{jkl}\big(\partial\rho_0/\partial y_j\big)(\partial U/\partial y_k)(\partial\vartheta/\partial y_l) \neq 0$ which makes the imposition of upstream boundary conditions can be somewhat problematic. However, when the level surfaces of mean density and velocity coincide, Equation (61) simplifies to

$$s' = \frac{\gamma}{\rho_0^2}\frac{\partial \rho_0}{\partial U}\lambda_\perp + s_\infty\left(\tau - \frac{y_1}{U}, \boldsymbol{y}_T\right) \tag{62}$$

with $\lambda_\perp$ given by Equation (39) which means that s' can remain finite in this case.

7. Conservation Laws

Like the Kovasznay decomposition discussed in Section 1.1 the present result involves two arbitrary convected quantities which we denoted by $\widetilde{\omega}_c\left(\tau - y_1/U, \boldsymbol{y}_T\right)$ and $\vartheta\left(\tau - y_1/U, \boldsymbol{y}_T\right)$. Equations (A2), (A6), (A8), (A13) and (39) show that these quantities are related to the physical variables and the gradient-wise particle displacement defined in Equation (39) by the conservation laws

$$\frac{\partial}{\partial y_1}\left(\widetilde{\omega}_c - p' - \frac{\partial N_i}{\partial y_i}\lambda_\perp\right) = -\varepsilon_{ijk}\frac{\partial}{\partial y_i}\left(\widetilde{\omega}_j N_k\right) \tag{63}$$

$$N_i\left(\widetilde{\omega}_i + \varepsilon_{ij1}\frac{\partial \lambda_\perp}{\partial y_j}\right) = 0 \tag{64}$$

where $\lambda_\perp$ is defined by Equation (39),

$$N_i \equiv \frac{c^2}{|\nabla U|^2}\frac{\partial U}{\partial y_i}, \tag{65}$$

denotes a scaled velocity gradient and

$$\widetilde{\omega}_i \equiv \varepsilon_{ijk}\frac{\partial \widetilde{u}_k}{\partial y_j} \tag{66}$$

denotes the density-weighted vorticity based on the $\vartheta-$ independent density-weighted velocity fluctuation $\widetilde{u}_i$ (defined by Equation (37)).

Equation (63) relates the arbitrary convected quantities $\widetilde{\omega}_c\left(\tau - y_1/U\left(\boldsymbol{y}_T\right), \boldsymbol{y}_T\right)$ and $\vartheta\left(\tau - y_1/U\left(\boldsymbol{y}_T\right), \boldsymbol{y}_T\right)$ to the pressure p', the gradient-wise particle displacement given by Equation(39) and the cross-gradient (density-weighted) vorticity components $\varepsilon_{ijk}\omega_j N_k$, where ω_j is defied by Equation (A2). Equation (64) relates the arbitrary convected quantity $\vartheta\left(\tau - y_1/U\left(\boldsymbol{y}_T\right), \boldsymbol{y}_T\right)$ to the gradient-wise vorticity component $\omega_j N_j$ and the gradient-wise particle displacement given by Equation (39) while Equation (62) relates the arbitrary convected quantity $s_\infty\left(\tau - y_1/U, \boldsymbol{y}_T\right)$ to the entropy fluctuation s' and the gradient-wise particle displacement given by Equation (39) in the important case where the level surfaces of mean pressure and velocity coincide.

8. Upstream Boundary Conditions

The conservation law Equations (63) and (64) cannot (by themselves) be used to relate the unknown convected quantities $\widetilde{\omega}_c$ and ϑ to the physical variables because they involve the cross-gradient particle displacement $\eta_\perp$ that is not actually a physical quantity, but we shall now show that $\eta_\perp \to 0$ (actually the hydrodynamic component of $\eta_\perp$) at upstream infinity and, therefore, that these equations can be used to obtain upstream boundary conditions that relate these quantities to those variables.

As in the classical Kovasznay decomposition discussed in Section 1.1, we suppose that it is the hydrodynamic component of the motion that should be related to physically measured variables and not the remaining scattered component. Appendix B shows that transverse components of the hydrodynamic portion of the pseudo-particle displacement behave like

$$\lambda_i^{(0)}(\boldsymbol{x}, t) \to \frac{1}{x_1}\boldsymbol{L}_i(t - x_1/U(\boldsymbol{x}_T), \boldsymbol{x}_T), \text{ for } i = 2, 3 \text{ as } x_1 \to -\infty \tag{67}$$

when causality is imposed on these flows. The purely convected quantity $\boldsymbol{L}_i(t - x_1/U(x_2), \boldsymbol{x}_T)$ is the Fourier transform of the function $\overline{\boldsymbol{L}}_i(\boldsymbol{x}_T, \omega)$ introduced in Appendix B.

Inserting Equation (67) into Equation (37) shows that the hydrodynamic component $\widetilde{u}_i^{(0)}(\boldsymbol{x},t)$ of the ϑ-independent component density-weighted velocity $u_i(\boldsymbol{x},t)$ behaves like

$$\widetilde{u}_i^{(0)}(\boldsymbol{x},t) \to \frac{1}{x_1^2}\widetilde{\boldsymbol{U}}_i(t - x_1/U(\boldsymbol{x}_T),\boldsymbol{x}_T),\ \text{for } i = 2,3 \text{ as } x_1 \to -\infty \tag{68}$$

where $\widetilde{u}_i^{(0)}$ is given by Equation (37) and $\widetilde{\boldsymbol{U}}_i(t - x_1/U(x_2),\boldsymbol{x}_T)$ has the obvious meaning.

Inserting Equation (68) into Equation (17) and using the result in the momentum Equation (12) shows that

$$\frac{\partial p'^{(0)}(\boldsymbol{x},t)}{\partial x_1} \to 0 \text{ as } x_1 \to -\infty, \tag{69}$$

It, therefore, follows from Equations (67) and (68) that the conservation law given by Equation (63) becomes

$$\frac{\partial \widetilde{\omega}_c}{\partial y_1} \to N_k \widetilde{\Gamma}_k^{(0)},\ \text{as } y_1 \to -\infty \tag{70}$$

where

$$\widetilde{\Gamma}_k^{(0)}(\boldsymbol{y},\tau) \equiv \nabla^2 \widetilde{u}_k^{(0)} - \frac{\partial}{\partial y_k}\nabla\cdot\widetilde{\boldsymbol{u}}^{(0)} \tag{71}$$

$$\frac{\partial}{\partial y_j}c^2 u_j = \frac{\partial}{\partial y_j}c^2 \widetilde{u}_j \tag{72}$$

the continuity Equation (13) shows that

$$\widetilde{\Gamma}_k^{(0)}(\boldsymbol{y},\tau) = \nabla^2 \widetilde{u}_k^{(0)} + \frac{\partial}{\partial y_k}\left[c^{-2}\left(\frac{D_0 p'^{(0)}}{D\tau} + \widetilde{u}_j^{(0)}\frac{\partial c^2}{\partial y_j}\right)\right] \tag{73}$$

It, therefore, follows Equations (68) and (69) that

$$\widetilde{\Gamma}_k^{(0)}(\boldsymbol{y},\tau) \to \nabla_\perp^2 \widetilde{u}_k^{(0)} \text{ for } k = 2,3 \text{ as } y_1 \to -\infty \tag{74}$$

where

$$\nabla_\perp^2 \equiv \frac{\partial^2}{\partial y_2^2} + \frac{\partial^2}{\partial y_3^2} \tag{75}$$

Equations (45), (46), (68), (70) and (74) then imply that

$$\begin{aligned}\frac{\partial \widetilde{\omega}_c}{\partial y_1} &= \frac{c^2}{|\nabla U|^2}\nabla_\perp^2\left(\frac{\partial U}{\partial y_k}u_k^{(0)}\right) + O\left(\frac{1}{y_1}\right) = \frac{c^2}{|\nabla U|^2}\nabla_\perp^2\left[\frac{1}{y_1^2}\frac{\partial U}{\partial y_k}\boldsymbol{U}_k\left(\tau - y_1/U,\boldsymbol{y}_T\right)\right] + O\left(\frac{1}{y_1}\right)\\ &\to \frac{c^2}{U^4}\frac{\partial U}{\partial y_k}\frac{\partial^2}{\partial \tau^2}\boldsymbol{U}_k\left(\tau - y_1/U,\boldsymbol{y}_T\right),\ \text{as } y_1 \to -\infty,\end{aligned} \tag{76}$$

which (upon neglecting unobserved tones due to the neutral instability wave) expresses $\widetilde{\omega}_c$ in terms of the transverse component of the hydrodynamic portion $\boldsymbol{u}^{(0)}$ of the physical velocity $\boldsymbol{u}$ at upstream infinity and, therefore, provides a suitable upstream boundary condition for determining the unknown convected quantity $\widetilde{\omega}_c$. Equation (76) can also be written as

$$\frac{\partial \widetilde{\omega}_c}{\partial y_1} \to \frac{c^2}{U^4}\frac{dU}{du}\frac{\partial^2}{\partial \tau^2}|\nabla u|\boldsymbol{U}_\perp\left(\tau - y_1/U(u),\boldsymbol{y}_T\right),\ \text{as } y_1 \to -\infty, \tag{77}$$

where

$$\boldsymbol{U}_\perp \equiv \frac{\partial u}{\partial y_k}\frac{\boldsymbol{U}_k}{|\nabla u|} \tag{78}$$

when there exists a function that forms an orthogonal coordinate system with the level surfaces $u\big(\boldsymbol{y}_T\big) =$ constant of the mean velocity $U = U(u)$.

9. Relation between the Pressure and Source Spectra

While these results can be used to that relates $\widetilde{\omega}_c$ to actual physical quantities, the interest in turbulent flows is on statistical and not instantaneous quantities. For example, the focus in aeroacoustics and structural vibration problems is usually on computing the pressure spectrum

$$I_\omega(\boldsymbol{x}) \equiv \frac{1}{2\pi}\int_{-\infty}^{\infty} e^{i\omega\widetilde{\tau}}\langle p'(\boldsymbol{x},t)p'(\boldsymbol{x},t+\widetilde{\tau})\rangle d\widetilde{\tau} \tag{79}$$

where the $\langle\cdot\rangle$ bracket denotes the time average

$$\langle p'(\boldsymbol{x},\tau)p'(\boldsymbol{x},\tau+\widetilde{\tau})\rangle \equiv \lim_{T\to\infty}\frac{1}{2T}\int_{-T}^{T} p'(\boldsymbol{x},\tau)p'(\boldsymbol{x},\tau+\widetilde{\tau})d\tau \tag{80}$$

Appendix C shows that this only depends on the turbulent fluctuations through source spectrum

$$S\big(\boldsymbol{y}_T\big|\widetilde{\boldsymbol{y}}_T\big) \equiv \frac{1}{2\pi}\int_{-\infty}^{\infty} e^{i\omega\widetilde{\tau}}\Big\langle\widetilde{\omega}_c\big(t,\boldsymbol{y}_T\big)\widetilde{\omega}_c\big(t+\widetilde{\tau},\widetilde{\boldsymbol{y}}_T\big)\Big\rangle d\widetilde{\tau} \tag{81}$$

which can be expressed in terms of the spectrum

$$\begin{gathered} \boldsymbol{S} \equiv \tfrac{1}{2\pi}\int_{-\infty}^{\infty} \exp i\omega\Big(\widetilde{\tau}-\Big[\widetilde{y}_1/U\big(\widetilde{\boldsymbol{y}}_T\big)-y_1/U\big(\boldsymbol{y}_T\big)\Big]\Big)\Big\langle\boldsymbol{U}_\perp\big(\tau-y_1/U\big(\boldsymbol{y}_T\big),\boldsymbol{y}_T\big)\times \\ \boldsymbol{U}_\perp\big(\tau-\widetilde{y}_1/U(\widetilde{y}_2)+\widetilde{\tau},\widetilde{\boldsymbol{y}}_T\big)\Big\rangle d\widetilde{\tau} \end{gathered} \tag{82}$$

of the transverse velocity amplitude in Equation (78) by Equation (A33) which ultimately has to be modeled in order to relate it to actual experimental measurements. An appropriate model for this quantity is given by Equation (A34) which leads to the model of Equation (A35) for the source spectrum given by Equation (81) that actually appears in the formula for the pressure spectrum given by Equation (79).

10. Calculating the Green's Function

It is, of course, necessary to determine the Green's function before numerical computations can be carried out. This will usually involve some numerical calculations, which can be very delicate when the mean flow includes shear layers that can sustain spatially growing instability waves. Baker and Peake [34] showed that the Wiener–Hopf technique [35] can be used to minimize these difficulties and developed efficient numerical algorithms for implementing this procedure.

However, experiments [36–40] show that the sound generated by solid surface interactions is often of low frequency in at least some applications of technological interest and the low-frequency Green's function, which can often be found analytically, can then be used in the calculations. Goldstein et al. [20,41,42] used the low-frequency Green's function to calculate acoustic radiation resulting from a jet interacting with a trailing edge. They eliminated the base flow velocity discontinuity by considering the case where the mean surface velocity was equal to zero. The Fourier transform of the resulting Green's function then turned out to be the same as the Fourier transform of zero-mean-flow Green's function in the low-frequency limit. However, their result still depended on the mean flow because the streamwise wave number of the Fourier transformed Green's function is set equal to $\omega/U\big(\boldsymbol{y}_T\big)$ in the final formula.

11. Application of the Theory

The general theory is applicable to a wide range of surface geometries and boundary conditions, such as lined surfaces which would be of interest in trailing edge noise reduction studies.

The acoustic radiation resulting from the interaction of a round jet with the trailing edge of a flat plate was measured by Olsen and Boldman [43] who compared their results with the RDT solution given in [5,21]. Their results showed that the shape of the radiation pattern and its change with jet velocity was accurately predicted by the theory which was not the case for alternative theories [12], that did not account for mean velocity gradients (e.g., [12]).

An earlier version of the theory given in [5] was used by Ayton and Peake [44] to calculate the high-frequency acoustic radiation resulting from the interaction of a periodic upstream disturbance with an airfoil embedded in a transversely sheared mean flow. Their results also showed that the radiated sound field was significantly affected by the mean shear. A more highly developed version of the theory given in [27] was used by Baker and Peake [45] to analyze the effect of boundary layer shear on trailing edge noise.

The authors of [20,46,47] used this latter version of the analysis to calculated he noise produced by the interaction of a large aspect ratio rectangular jet with the trailing edge of a flat plate (see Figure 3). They obtained an analytical formula relating the acoustic spectrum to the turbulence correlation function within the jet and represented this quantity by Equation (A35). The authors of [20] used experimental data to determine the parameters in this formula and compared the predicted sound field with experimental data taken over a broader range of polar angles and three different Mach numbers at Glenn research center [36–40]. As shown in Figure 4, the computed spectra turned out to be in good agreement with the experimental data. The predicted sound pressure levels would change by as much as 10 Db at the highest Mach number considered if the mean shear and the resulting proper treatment of the convection velocity were not accounted for.

The low-frequency Green's theory was used to predict the sound field produced by the interaction of circular jet with a trailing edge in [42] (see Figure 5). Their formulas turn out to be quite general and are expected to apply to many different flow configurations, such as the multiple jet configuration shown in Figure 6. They carried out computations over a range of azimuthal angles and three different Mach numbers and again obtained good agreement with experiment. Some typical comparisons are presented in Figure 7.

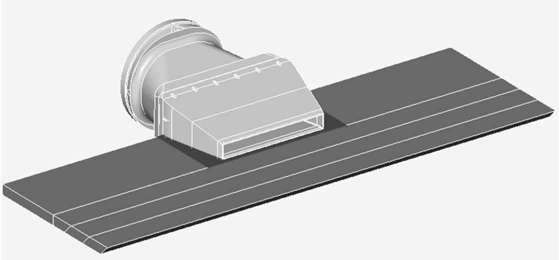

Figure 3. Rectangular jet interacting with the trailing edge of a flat plate.

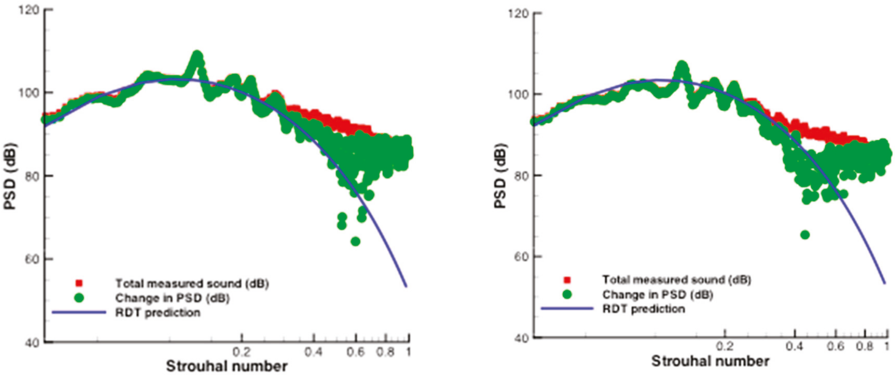

(**a**) (**b**)

Figure 4. Comparisons of theoretically predicted power spectral density (PSD), at various Strouhal numbers for a planar jet with experimental data of Brown [30] at an Acoustic Mach number of 0.9 based on the jet exit velocity and equivalent nozzle diameter at polar angles (**a**) $\theta = 95°$ and (**b**) $\theta = 105°$. Reproduced with permission from [20].

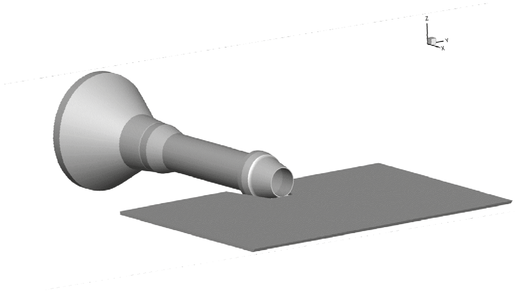

Figure 5. Round jet interacting with the trailing edge of a flat plate.

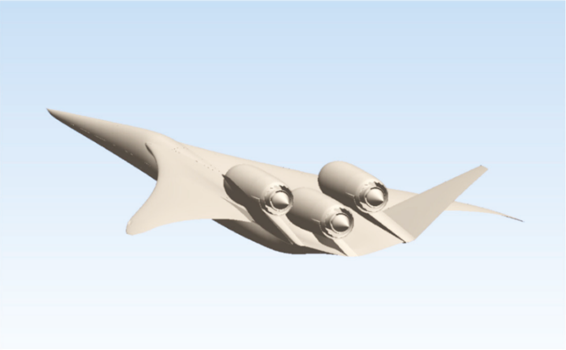

Figure 6. Supersonic cruise concept aircraft with top mounted engines. Reproduced with permission from Ramakrishnan et al. NASA CR-2018-219936 [48] (provided by Dr. James Bridges).

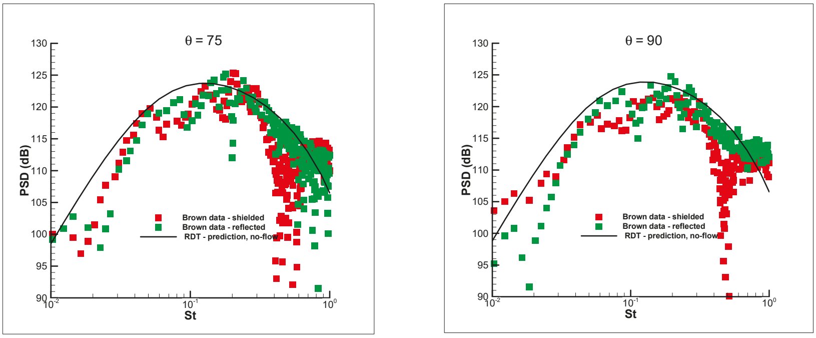

(**a**) (**b**)

Figure 7. Comparison of composite round jet Rapid Distortion Theory (RDT) solution with the power spectral density (PSD) of the far-field pressure fluctuation vs. Strouhal number, St, based on jet exit velocity and nozzle diameter at polar angles: (**a**) $\theta = 75°$ and (**b**) $\theta = 105°$ measured from the downstream jet axis by Brown [38,39]. The acoustic Mach number based on jet exit velocity is equal to 0.9. Reproduced with permission from [42].

12. Concluding Remarks

This paper was written to bring together and present in a consistent fashion a general theory for the unsteady motion on a transversely sheared mean flow that has been developed over the years in a number of papers published in the Journal of Fluid Mechanics. The relevant equations are reformulated in terms of a gauge function in order to obtain expressions of the unsteady velocity and pressure fluctuations (which decouple from the entropy fluctuations) that involve two arbitrarily convected quantities. A pair of very general conservation laws are then used to derive upstream boundary conditions that relate two of these quantities to experimentally measurable flow variables.

Inflectional base flows are able to support spatially growing instability waves, which are often associated with the coherent structures in turbulent flows. Their amplitudes cannot be determined by imposing upstream boundary conditions, but can be uniquely determined as part of the solution when causality is imposed on the flow-which appears to be particularly appropriate in the present context since Creighton [24,25] has shown that the imposition of causality is equivalent to imposing a Kutta condition at a trailing edge.

The entropy fluctuations can be determined after the fact once the velocity and pressure fluctuations are known by specifying a third arbitrary quantity. The results, which can be used to analyze the unsteady motion resulting from the interaction of turbulent shear flows with solid surfaces, are applicable to a wide range of flow–surface interaction problems.

Funding: This research received no external funding

Acknowledgments: I would like to thank the NASA Advanced Air Transport Program, Commercial Subsonic Technology Project for supporting this work. I would also like to thank James Bridges for proving the drawing shown in Figure 6 and Stewart Leib of the Ohio Aerospace institute for carrying out some of the computations.

Conflicts of Interest: The author declares no conflict of interest.

Appendix A

Equations (18), (20) and (21) show that the convected quantity $\widetilde{\omega}_c$ is related to the pressure perturbation p' and the pseudo-particle displacement λ_i by

$$\widetilde{\omega}_c = p' + \frac{\partial}{\partial y_i} c^2 \lambda_i \tag{A1}$$

while Equations (17) and (18) show that the density-weighted vorticity ω_i is related to λ_i by

$$\omega_i \equiv \varepsilon_{ijk}\frac{\partial u_k}{\partial y_j} = \frac{D_0}{D\tau}\varepsilon_{ijk}\frac{\partial \lambda_k}{\partial y_j} + \varepsilon_{ijk}\frac{\partial U}{\partial y_j}\frac{\partial \lambda_k}{\partial y_1} - \varepsilon_{ij1}\frac{\partial \eta_\perp}{\partial y_j} + \varepsilon_{knm}\varepsilon_{ijk}\frac{\partial}{\partial y_j}\frac{1}{c^2}\frac{\partial U}{\partial y_n}\frac{\partial \vartheta}{\partial y_m} \tag{A2}$$

where $\eta_\perp$ is given by Equation (39). However, since Equation (18) and the identities

$$\varepsilon_{ijk}\frac{\partial^2 U}{\partial y_j \partial y_k} = \varepsilon_{ijk}\frac{\partial^2 \phi}{\partial y_j \partial y_k} = 0 \tag{A3}$$

show that

$$\varepsilon_{ijk}\frac{\partial \lambda_k}{\partial y_j} = 2\varepsilon_{ijk}\frac{\partial U}{\partial y_k}\frac{\partial^2 \phi}{\partial y_1 \partial y_j} \tag{A4}$$

this can be written as

$$\omega_i = -\varepsilon_{ij1}\frac{\partial \eta_\perp}{\partial y_j} + \varepsilon_{ijk}\frac{\partial U}{\partial y_j}\frac{\partial}{\partial y_1}\left(\lambda_k - 2\frac{D_0}{D\tau}\frac{\partial \phi}{\partial y_k}\right) + \omega_i^{(c)} \tag{A5}$$

where $\omega_i^{(c)}$ is defined in terms of $u_i^{(c)}$ by

$$\omega_i^{(c)} \equiv \varepsilon_{ijk}\frac{\partial u_k^{(c)}}{\partial y_j} \tag{A6}$$

Equation (18) and the identity

$$\varepsilon_{ijk}\frac{\partial U}{\partial y_j}\frac{\partial U}{\partial y_k} = 0 \tag{A7}$$

can now be used to show that Equation (A5) can be written as

$$\omega_i = -\varepsilon_{ij1}\frac{\partial \eta_\perp}{\partial y_j} - \varepsilon_{ijk}\frac{\partial U}{\partial y_j}\frac{\partial \lambda_k}{\partial y_1} + \omega_i^{(c)} \tag{A8}$$

It, therefore, follows from Equation (39) that the cross product $\varepsilon_{ijk}\omega_j \partial U/\partial y_k$ can be written as

$$\begin{aligned}
\varepsilon_{ijk}\omega_j\frac{\partial U}{\partial y_k} &= -\varepsilon_{ijk}\varepsilon_{1jn}\frac{\partial \eta_\perp}{\partial y_n}\frac{\partial U}{\partial y_k} - \varepsilon_{ijk}\varepsilon_{jmn}\frac{\partial U}{\partial y_m}\frac{\partial \lambda_n}{\partial y_1}\frac{\partial U}{\partial y_k} + \varepsilon_{ijk}\omega_j^{(c)}\frac{\partial U}{\partial y_k} \\
&= -\left(\delta_1^i\delta_n^k - \delta_n^i\delta_1^k\right)\frac{\partial \eta_\perp}{\partial y_n}\frac{\partial U}{\partial y_k} + \left(\delta_m^i\delta_n^k - \delta_n^i\delta_m^k\right)\frac{\partial U}{\partial y_m}\frac{\partial \lambda_n}{\partial y_1}\frac{\partial U}{\partial y_k} + \varepsilon_{ijk}\omega_j^{(c)}\frac{\partial U}{\partial y_k} \\
&= -\delta_1^i\frac{\partial \eta_\perp}{\partial y_k}\frac{\partial U}{\partial y_k} + \frac{\partial U}{\partial y_i}\frac{\partial \eta_\perp}{\partial y_1} - \frac{\partial U}{\partial y_k}\frac{\partial U}{\partial y_k}\frac{\partial \lambda_i}{\partial y_1} + \varepsilon_{ijk}\omega_j^{(c)}\frac{\partial U}{\partial y_k}
\end{aligned} \tag{A9}$$

which can be solved for $\partial \lambda_i/\partial y_1$ to obtain

$$\frac{\partial \lambda_i}{\partial y_1} = \left[\frac{\partial U}{\partial y_i}\frac{\partial \eta_\perp}{\partial y_1} - \delta_{1i}\frac{\partial \eta_\perp}{\partial y_k}\frac{\partial U}{\partial y_k} - \varepsilon_{ijk}\left(\omega_j - \omega_j^{(c)}\right)\frac{\partial U}{\partial y_k}\right] / |\nabla U|^2 \tag{A10}$$

Inserting this into Equation (A1) shows that

$$\frac{\partial \widetilde{\omega}_c}{\partial y_1} = \frac{\partial}{\partial y_1}p' + \frac{\partial}{\partial y_i}\left\{\frac{c^2}{|\nabla U|^2}\left[\frac{\partial U}{\partial y_i}\frac{\partial \eta_\perp}{\partial y_1} - \delta_{1i}\frac{\partial \eta_\perp}{\partial y_k}\frac{\partial U}{\partial y_k} - \varepsilon_{ijk}\left(\omega_j - \omega_j^{(c)}\right)\frac{\partial U}{\partial y_k}\right]\right\} \tag{A11}$$

and, therefore, that

$$\frac{\partial\widetilde{\omega}_c}{\partial y_1}=\frac{\partial}{\partial y_1}p'+\left[\frac{\partial}{\partial y_i}\left(\frac{\partial U}{\partial y_i}\frac{c^2}{|\nabla U|^2}\right)\right]\frac{\partial\eta_\perp}{\partial y_1}-\varepsilon_{ijk}\frac{\partial}{\partial y_i}\left(\omega_j\frac{c^2}{|\nabla U|^2}\right)\frac{\partial U}{\partial y_k}+\varepsilon_{ijk}\frac{\partial}{\partial y_i}\left(\omega_j^{(c)}\frac{c^2}{|\nabla U|^2}\right)\frac{\partial U}{\partial y_k} \tag{A12}$$

or

$$\frac{\partial\widetilde{\omega}_c}{\partial y_1}=\frac{\partial}{\partial y_1}\left[p'+\eta_\perp\frac{\partial}{\partial y_i}\left(\frac{\partial U}{\partial y_i}\frac{c^2}{|\nabla U|^2}\right)\right]-\varepsilon_{ijk}\frac{\partial}{\partial y_i}\left[\frac{c^2}{|\nabla U|^2}\left(\omega_j-\omega_j^{(c)}\right)\frac{\partial U}{\partial y_k}\right] \tag{A13}$$

where the identity of Equation (A7) has again been used.

Appendix B

We suppose for definiteness that all solid surfaces are impermeable and that the Green's function is chosen so that the unsteady flow is governed by Equations (36) and (52). Taking the Fourier transform of the former equation, using the convolution theorem and noting that $G(\boldsymbol{x},t\middle|\boldsymbol{y},\tau)$, which is identically zero for all $\boldsymbol{t}<\tau$, satisfies the inhomogeneous Rayleigh Equation (30) and, therefore, depends on τ and t only in the combination $t-\tau$ shows that

$$\overline{p}'(x:\omega)=(2\pi)^2\int\limits_{A_T}e^{i\omega x_1/U(\boldsymbol{y}_T)}\overline{\overline{G}}\left(\boldsymbol{y}_T\middle|x:\omega,\omega/U\left(\boldsymbol{y}_T\right)\right)\overline{\Omega}^{(0)}\left(\boldsymbol{y}_T,\omega\right)d\boldsymbol{y}_T \tag{A14}$$

where A_T denotes the cross section of the volume V, $\alpha(x:\omega)=\lim\limits_{T\to\infty}\alpha(x:\omega;T)$ for $\alpha=\overline{p}',\,\overline{\Omega}$

$$\overline{p}'(x:\omega,T)\equiv\frac{1}{2\pi}\int\limits_{-T}^{T}e^{i\omega\,t}\overline{p'}(\boldsymbol{x},t)dt,\overline{\Omega}^{(0)}\left(\boldsymbol{y}_T:\omega,T\right)\equiv\frac{1}{2\pi}\int\limits_{-T}^{T}e^{i\omega\xi}\widetilde{\omega}_c\left(\xi,\boldsymbol{y}_T\right)dz \tag{A15}$$

and

$$\overline{\overline{G}}\left(\boldsymbol{y}_\perp|\boldsymbol{x};k,\omega\right)\equiv\frac{1}{(2\pi)^2}\iint e^{i[k(y_1-x_1)+\omega(t-\tau)]}G(\boldsymbol{y},\tau|\boldsymbol{x},t)d\tau dy_1 \tag{A16}$$

satisfies the reduced Rayleigh equation

$$\boldsymbol{L}\overline{\overline{G}}=i\frac{\delta\left(\boldsymbol{x}_\perp-\boldsymbol{y}_\perp\right)}{(2\pi)^2} \tag{A17}$$

where

$$\boldsymbol{L}\equiv\frac{\partial}{\partial y_j}\frac{c^2}{(kU-\omega)^2}\frac{\partial}{\partial y_j}+1-\frac{k^2c^2}{(kU-\omega)^2}\quad j=2,3 \tag{A18}$$

is the reduced Rayleigh operator and $\overline{\overline{\overline{G}}}_i$ is determined by

$$\left(U(\boldsymbol{x}_T)\frac{\partial}{\partial x_1}-i\omega\right)^2\overline{\overline{\overline{G}}}_i\left(\boldsymbol{y}_T\middle|x:\omega,k_1\right)\equiv\frac{\partial}{\partial x_i}\overline{\overline{G}}\left(\boldsymbol{y}_T\middle|x:\omega,k_1\right),\ i=2,3 \tag{A19}$$

Equation (A14) can be interpreted as a generalization of the classical Ffowcs Williams and Hall [49] equation (i.e., Equation (6) of that reference) which has often been used to study the sound produced by the turbulence trailing edge interaction. However, the present result accounts for mean flow interaction effects, which become important at the high Mach numbers of interest in aeronautical applications. There is, however, an even more significant difference between these formulations because, unlike the present result, the Ffowcs Williams and Hall equation does not predict the source convection velocity. It also does not account for the spatially growing instability waves discussed in Section 5.2. which are believed to represent coherent structures on the turbulent flow. Finally, it also does not account for the trailing edge vortex shedding which can have an important effect on the radiated sound.

The decompositions in Equations (54)–(57) imply the decomposition

$$\chi = \chi^{(0)} + \chi^{(s)} \tag{A20}$$

where the symbol χ is used to denote the Fourier transformed pressure fluctuation $\overline{p}'(x:\omega,T)$, the Fourier transformed pseudo-particle displacement $\overline{\lambda}_i(x:\omega,T)$, the reduced Rayleigh equation Green's functions $\overline{\overline{G}}\left(\boldsymbol{y}_T\middle|x:\omega,k_1\right)$ and

$$\overline{\overline{G}}_i\left(\boldsymbol{y}_T\middle|x_T:\omega,k_1\right) \equiv \frac{1}{i(k_1U(\boldsymbol{x}_T)-\omega)}\frac{\partial}{\partial x_i}\overline{\overline{G}}\left(\boldsymbol{y}_T\middle|x_T:\omega,k_1\right),\ i=2,3 \tag{A21}$$

with the $\overline{\overline{G}}^{(0)}\left(\boldsymbol{y}_T\middle|x:\omega,k_1\right)$ component of $\overline{\overline{G}}\left(\boldsymbol{y}_T\middle|x:\omega,k_1\right)$ either defined on all space or required to satisfy

$$\frac{\hat{n}_j}{\left[\omega-k_1U\left(\boldsymbol{y}_T\right)\right]^2}\frac{\partial}{\partial y_j}\overline{\overline{G}}^{(0)}\left(\boldsymbol{y}_T\middle|x:\omega,k_1\right)=0,\ \text{for } \boldsymbol{y}_T\in C_T \tag{A22}$$

(where C_T denotes the bounding curve/curves that generate the doubly infinite surface/surfaces that extend S from $y_1=-\infty$ to $y_1=+\infty$).

The Green's functions $\overline{\overline{G}}^{(0)}\left(\boldsymbol{y}_T\middle|x:\omega,k_1\right)$ and $\overline{\overline{G}}_i^{(0)}\left(\boldsymbol{y}_T\middle|x:\omega,k_1\right)$ are streamwise homogeneous and, therefore, depend on y_1 and x_1 only in the combination x_1-y_1-which means that we can write

$$\overline{\overline{G}}^{(0)}\left(\boldsymbol{y}_T\middle|x:\omega,k_1\right)=\overline{\overline{G}}^{(0)}\left(\boldsymbol{y}_T\middle|x_T:\omega,k_1\right). \tag{A23}$$

and it then follows from Equations (36), (51), (43) and (50) that

$$\overline{p}^{(0)}(x:\omega)=(2\pi)^2\int\limits_{A_T}e^{i\omega x_1/U(\boldsymbol{y}_T)}\overline{\overline{G}}^{(0)}\left(\boldsymbol{y}_T\middle|x:\omega,\omega/U\left(\boldsymbol{y}_T\right)\right)\overline{\Omega}^{(0)}\left(\boldsymbol{y}_T,\omega\right)d\boldsymbol{y}_T \tag{A24}$$

$$\overline{\lambda}_i^{(0)}(\boldsymbol{x},\omega)=-\frac{(2\pi)^2}{i\omega}\int\limits_{A_T}e^{i\omega x_1/U(\boldsymbol{y}_T)}\frac{U\left(\boldsymbol{y}_T\right)\overline{\overline{G}}_i^{(0)}\left(\boldsymbol{y}_T\middle|x_T:\omega,\omega/U\left(\boldsymbol{y}_T\right)\right)}{U(\boldsymbol{x}_T)-U\left(\boldsymbol{y}_T\right)}\overline{\Omega}^{(0)}\left(\boldsymbol{y}_T:\omega\right)d\boldsymbol{y}_T, \tag{A25}$$

Goldstein [2,19] and Goldstein et al. [17] show that $\overline{\overline{G}}^{(0)}\left(\boldsymbol{y}_T\middle|x_T:\omega,\omega/U\left(\boldsymbol{y}_T\right)\right)$ and $\overline{\overline{G}}_i^{(0)}\left(\boldsymbol{y}_T\middle|x_T:\omega,\omega/U\left(\boldsymbol{y}_T\right)\right)$ remain finite and continuous at $\boldsymbol{y}_T=\boldsymbol{x}_T$ but $\overline{\overline{G}}_i^{(0)}\left(\boldsymbol{y}_T\middle|x_T:\omega,\omega/U\left(\boldsymbol{y}_T\right)\right)/\left[U(\boldsymbol{x}_T)-U\left(\boldsymbol{y}_T\right)\right]$ becomes unbounded at $\boldsymbol{y}_T=\boldsymbol{x}_T$, since $\overline{\overline{G}}_i^{(0)}\left(\boldsymbol{y}_T\middle|x:\omega,\omega/U\left(\boldsymbol{y}_T\right)\right)$ will usually not vanish there. The integral in Equation (A25) can be made finite by imposing causality [20]. This can be accomplished by using the Briggs [33]–Bers [34] procedure which is equivalent to letting ω have a small positive imaginary part, say ε, and deforming the appropriate integration contour so that the solution remains continuous as $\varepsilon\to 0$. The singularity in Equation (A25) is the same as that in Equation (4.13) of [20] (the corresponding the formula for $\partial\overline{\lambda}_i^{(0)}(\boldsymbol{x},\omega)/\partial x_1$), so that the procedure used in Appendix C of that reference (which applies to any transversely sheared mean flow) can also be applied to Equation (A25) to show that

$$\overline{\lambda}_i^{(0)}(\boldsymbol{x},\omega)\to\frac{e^{i\omega x_1/U(\boldsymbol{x}_T)}}{x_1}\overline{\boldsymbol{L}}_i(\boldsymbol{x}_T,\omega),\ \text{for } i=2,3 \text{ as } x_1\to-\infty \tag{A26}$$

when causality is imposed: which, in turn, implies that the upstream behavior of the hydrodynamic component $\lambda_i^{(0)}(\boldsymbol{x},t)$ of the particle displacement $\lambda_i(\boldsymbol{x},t)$ is given by Equation (67).

Appendix C

It is appropriate to require that the source function $\widetilde{\omega}_c\left(\tau,\boldsymbol{y}_T\right)$ be a stationary random function of τ [30], since, as noted above, steady-state turbulent flows are usually time-stationary [50] and it then follows from Equation (36) that the pressure fluctuation $p'(t,\boldsymbol{x})$ should also be a function of this type. The pressure spectrum, can then be expressed in terms of the first Fourier transform of Equation (A15) by [30]

$$I_\omega(\boldsymbol{x}) = (2\pi)\lim_{T\to\infty}\left\{\overline{p}(x:\omega,T)[\overline{p}(x:\omega,T)]^*/2T\right\} \tag{A27}$$

Inserting the solution of Equation (A14) this result shows that

$$I_\omega(\boldsymbol{x}) = (2\pi)^2\int\limits_{A_T}\int\limits_{A_T} e^{i\omega x_1[1/U(\boldsymbol{y}_T)-1/U(\widetilde{\boldsymbol{y}}_T)]}\overline{\overline{G}}\left(\boldsymbol{y}_T\middle|x:\omega,\omega/U\left(\boldsymbol{y}_T\right)\right)\times$$

$$\overline{\overline{G}}^*\left(\widetilde{\boldsymbol{y}}_T\middle|x:\omega,\omega/U\left(\widetilde{\boldsymbol{y}}_T\right)\right)S\left(\boldsymbol{y}_T\middle|\widetilde{\boldsymbol{y}}_T\right)d\boldsymbol{y}_T d\widetilde{\boldsymbol{y}}_T \tag{A28}$$

and, therefore, that the pressure spectrum is related to the turbulent fluctuations through source spectrum defined by Equation (81) which can be expressed in terms of the Fourier transform $\overline{\Omega}^{(0)}\left(\boldsymbol{y}_T:\omega,T\right)$ by

$$S\left(\boldsymbol{y}_T\middle|\widetilde{\boldsymbol{y}}_T\right) = (2\pi)\lim_{T\to\infty}\left\{\left(\boldsymbol{y}_T:\omega,T\right)\left[\overline{\Omega}^{(0)}\left(\widetilde{\boldsymbol{y}}_T:\omega,T\right)\right]^*/2T\right\} \tag{A29}$$

where $\overline{\Omega}^{(0)}\left(\boldsymbol{y}_T:\omega,T\right)$ is given by Equation (A15) However, Equations (A15) and (77) imply that $\overline{\Omega}^{(0)}\left(\boldsymbol{y}_T:\omega,T\right)$ is related to the upstream gradient-wise velocity coefficient $\boldsymbol{U}_\perp\left(\xi,\boldsymbol{y}_T\right)$ in the arbitrary orthogonal curvilinear coordinate system $\{u,v\}\left(\boldsymbol{y}_T\right)$ by

$$\frac{i\omega}{U}\overline{\Omega}^{(0)}\left(\boldsymbol{y}_T:\omega,T\right)\to-\omega^2\frac{c^2}{U^4}|\nabla u|\frac{dU}{du}\overline{\boldsymbol{U}}_\perp\left(\boldsymbol{y}_T;\omega,T\right) \tag{A30}$$

where

$$\overline{\boldsymbol{U}}_\perp\left(\boldsymbol{y}_T;\omega,T\right)\equiv\frac{1}{2\pi}\int\limits_{-T}^{T}e^{i\omega\xi}\boldsymbol{U}_\perp\left(\xi,\boldsymbol{y}_T\right)d\xi \tag{A31}$$

The time average

$$\left\langle\boldsymbol{U}_\perp\left(\tau-y_1/U\left(\boldsymbol{y}_T\right),\boldsymbol{y}_T\right)\boldsymbol{U}_\perp\left(\tau-\widetilde{y}_1/U\left(\widetilde{\boldsymbol{y}}_T\right)+\widetilde{\tau},\widetilde{\boldsymbol{y}}_T\right)\right\rangle$$

$$=\left\langle\boldsymbol{U}_\perp\left(\tau,\boldsymbol{y}_T\right)\boldsymbol{U}_\perp\left(\tau+\widetilde{\tau}-\left[\widetilde{y}_1/U\left(\widetilde{\boldsymbol{y}}_T\right)-y_1/U\left(\boldsymbol{y}_T\right)\right],\widetilde{\boldsymbol{y}}_T\right)\right\rangle \tag{A32}$$

of $\boldsymbol{U}_\perp\left(\tau-y_1/U\left(\boldsymbol{y}_T\right),\boldsymbol{y}_T\right)$ will not only exist but will also be independent of τ when $\boldsymbol{U}_\perp$ is a stationary function of τ and therefore of $\tau-y_1/U\left(\boldsymbol{y}_T\right)$ [30].

The transverse velocity amplitude spectrum given by Equation (82) can then be written as

$$\boldsymbol{S}=(2\pi)\lim_{T\to\infty}\frac{\overline{\boldsymbol{U}}_\perp\left(\boldsymbol{y}_T;\omega,T\right)\left[\overline{\boldsymbol{U}}_\perp\left(\widetilde{\boldsymbol{y}}_T;\omega,T\right)\right]^*}{2T} \tag{A33}$$

and Equations (A30) and (A33), therefore, show that the source spectrum $S\left(\boldsymbol{y}_T\middle|\widetilde{\boldsymbol{y}}_T\right)$ of the convected quantity $\widetilde{\omega}_c$, is related to the normal velocity-like fluctuation $\boldsymbol{U}_\perp\left(\tau-y_1/U(u),\boldsymbol{y}_T\right)$ by

$$\begin{gathered}S\left(\boldsymbol{y}_T\middle|\widetilde{\boldsymbol{y}}_T\right)=\omega^2\frac{c^2\left(\boldsymbol{y}_T\right)c^2\left(\widetilde{\boldsymbol{y}}_T\right)}{U^3(u)U^3(\widetilde{u})}\frac{dU(u)}{du}\frac{dU(\widetilde{u})}{d\widetilde{u}}|\nabla u|\left|\widetilde{\nabla}\widetilde{u}\right|\int\limits_{-\infty}^{\infty}\exp\left\{i\omega\left(\widetilde{\tau}-\left[\widetilde{y}_1/U\left(\widetilde{\boldsymbol{y}}_T\right)-y_1/U\left(\boldsymbol{y}_T\right)\right]\right)\right\}\\ \times\left\langle\boldsymbol{U}_\perp\left(\tau-y_1/U(u),\boldsymbol{y}_T\right)\boldsymbol{U}_\perp\left(\tau-\widetilde{y}_1/U(\widetilde{u})+\widetilde{\tau},\widetilde{\boldsymbol{y}}_T\right)\right\rangle d\widetilde{\tau},\end{gathered} \tag{A34}$$

when there is function $v\left(\boldsymbol{y}_T\right)$ that forms an orthogonal coordinate system with the level surfaces $u\left(\boldsymbol{y}_T\right) =$ constant of the mean velocity $U = U(u)$.

However, it is necessary specify the cross correlation $\left\langle \boldsymbol{U}_\perp\left(\tau - y_1/U(u), \boldsymbol{y}_T\right) \times \boldsymbol{U}_\perp\left(\tau - \widetilde{y}_1/U(\widetilde{u}) + \widetilde{\tau}, \widetilde{\boldsymbol{y}}_T\right)\right\rangle$ of the upstream normal velocity derivative fluctuation before the source spectrum and, therefore, pressure spectrum can be determined. We are not aware of any experimental measurements of this quantity, but [32] used information about the gradient-wise velocity correlation to show that

$$\begin{aligned}\left\langle \boldsymbol{U}_\perp\left(\tau - y_1/U(u), \boldsymbol{y}_T\right) \boldsymbol{U}_\perp\left(\tau - \widetilde{y}_1/U(\widetilde{u}) + \widetilde{\tau}, \widetilde{\boldsymbol{y}}_T\right)\right\rangle = A\left(\boldsymbol{y}_T, \widetilde{\boldsymbol{y}}_T\right) l_2^4 \rho\left(\boldsymbol{y}_T\right) U\left(\boldsymbol{y}_T\right) \rho\left(\widetilde{\boldsymbol{y}}_T\right) U\left(\widetilde{\boldsymbol{y}}_T\right) \times \\ \exp - \sqrt{[f(\eta_2/l_2, \eta_3/l_3)]^2 + \{\widetilde{\tau} - [\widetilde{y}_1/U(\widetilde{u}) - y_1/U(u)]\}^2/\tau_0^2}\end{aligned} \tag{A35}$$

where $A\left(\boldsymbol{y}_T, \widetilde{\boldsymbol{y}}_T\right), f(\eta_2/l_2, \eta_3/l_3)$ are unspecified functions of the indicated arguments, τ_0, l_2, l_3 are constants and $\eta_2 \equiv u - \widetilde{u}, \eta_3 \equiv v - \widetilde{v}$, is expected to provide a good representation of this quantity. Since ρc^2 is constant in transversely sheared flows, Equation (27) of [51] can be used to show that the actual source spectrum defined by Equation (81) is given by [52]

$$\begin{aligned} S(u, \widetilde{u} : v, \widetilde{v}) = l_2^4\left(\rho_\infty c_\infty^2\right)^2 A\left(u, v \middle| \widetilde{u}, \widetilde{v}\right)\left[\frac{dU/du}{U^2(u)}\frac{dU/d\widetilde{u}}{U^2(\widetilde{u})}\omega^2 |\nabla u| \left|\widetilde{\nabla u}\right|\right] \times \\ \frac{1}{2\pi}\int\limits_{-\infty}^{\infty} e^{i\omega(\widetilde{\tau} - [\widetilde{y}_1/U(\widetilde{u}) - y_1/U(u)])} \exp - \sqrt{[f(\eta_2/l_2, \eta_3/l_3)]^2 + \{\widetilde{\tau} - [\widetilde{y}_1/U(\widetilde{u}) - y_1/U(u)]\}^2/\tau_0^2 d\widetilde{\tau}} \\ = l_2^4 A(u, v)\left(\rho_\infty c_\infty^2\right)^2\left[\frac{dU/du}{U^2(u)}\frac{dU/d\widetilde{u}}{U^2(\widetilde{u})}|\nabla u| \left|\widetilde{\nabla u}\right| \omega^2\right]\frac{\tau_0 f}{\pi\sqrt{1+\widetilde{\omega}^2}} K_1\left(f\sqrt{1+\widetilde{\omega}^2}\right)\end{aligned} \tag{A36}$$

where

$$\widetilde{\omega} \equiv \omega\tau_0, \tag{A37}$$

and K_1 denotes the modified Bessel function of the second kind.

References

1. Bilka, M.J.; Kerrian, P.; Ross, M.H.; Morris, S.C. Radiated Sound from a Circular Cylinder in a Turbulent Shear Layer. *Int. J. Aeroacoust.* **2014**, *13*, 511–532. [CrossRef]
2. Tufts, A.; Wang, K.; Wang, M. Computational study of sound by airfoil interaction with a turbulent shear layer, AIAA paper # 2018-0757. In Proceedings of the AIAA Aerospace Sciences Meeting, Kissimmee, FL, USA, 8–12 January 2018.
3. Ross, M.H. Radiated Sound Generated by Airfoils in a Single Stream Shear Layer. Master's Thesis, University of Notre Dame, Notre Dame, IN, USA, April 2009.
4. Hunt, J.C.R. A theory of turbulent flow round two-dimensional bluff bodies. *J. Fluid Mech.* **1973**, *61*, 625–706. [CrossRef]
5. Goldstein, M.E. Unsteady vortical and entropic distortions of potential flows round arbitrary obstacles. *J. Fluid Mech.* **1978**, *89*, 433–468. [CrossRef]
6. Goldstein, M.E. Turbulence generated by entropy fluctuation with non-uniform mean flows. *J. Fluid Mech.* **1979**, *93*, 209–224. [CrossRef]
7. Sagaut, P.; Cambon, C. *Homogeneous Turbulence Dynamics*; Cambridge University Press: Cambridge, UK, 2008.
8. Batchelor, G.K.; Proudman, I. The effect of rapid distortion of a fluid in turbulent motion. *Q. J. Mech. Appl. Math.* **1954**, *7*, 83–103. [CrossRef]
9. Kovasznay, L.S.G. Turbulence in Supersonic Flow. *J. Aeronaut. Sci.* **1953**, *20*, 657–674. [CrossRef]
10. Möhring, W. Über Schallwellen in Scherströmungen. In *Fortschritte der Akustik—DAGA*; VDI: Düsseldorf, Germany, 1976; Volume 76, pp. 543–546.
11. Sears, W.R. Some Aspects of Non-Stationary Airfoil Theory and Its Practical Application. *J. Aeronaut. Sci.* **1941**, *8*, 104–108. [CrossRef]
12. Amiet, R.K. Acoustic radiation from an Airfoil in a turbulent stream. *J. Sound Vib.* **1975**, *81*, 407–420. [CrossRef]

13. Paterson, R.W.; Amiet, R.K. Acoustic radiation and surface pressure characteristics ofan Airfoil due to incident turbulence, AIAA paper #76-571. In Proceedings of the AIAA Aeroacoustics Conference, Palo Alto, CA, USA, 20–23 July 1976.
14. Orr, W. The stability and instability of the steady motions of a perfect liquid and of a viscous liquid. *Proc. R. Irish Acad. A* **1907**, *27*, 69–138.
15. Drazin, P.G.; Reid, W.H. *Hydrodynamic Stability*; Cambridge University Press: Cambridge, UK, 1981; pp. 147–151.
16. Brinckman, K.W.; Walker, J.D.A. Instability in a viscous flow driven by streamwise vortices. *J. Fluid Mech.* **2001**, *432*, 127–166. [CrossRef]
17. Cowley, S.J. Laminar Boundary-layer Theory: A 20th Century Paradox? In Proceedings of the 20th International Congress of Theoretical and Applied Mechanics, Chicago, IL, USA, 27 August–2 September 2000; Kluwer: Dordrecht, The Netherlands, 2001; pp. 389–411.
18. Cassel, K.W.; Conlisk, A.T. Unsteady separation in vortex-induced boundary layers. *Philos. Trans. R. Soc. A Math. Phys. Eng. Sci.* **2014**, *372*, 20130348. [CrossRef] [PubMed]
19. Gradshteyn, I.S.; Ryzhik, I.M. *Table of Integrals Series and Products*; Academic Press: Cambridge, MA, USA, 1965; p. 406.
20. Goldstein, M.E.; Leib, S.J.; Afsar, M.Z. Generalized rapid-distortion theory on transversely sheared mean flows with physically realizable upstream boundary conditions: Application to trailing-edge problem. *J. Fluid Mech.* **2017**, *824*, 477–512. [CrossRef]
21. Goldstein, M.E. Scattering and distortion of the unsteady motion on transversely sheared mean flows. *J. Fluid Mech.* **1979**, *91*, 601–632. [CrossRef]
22. Xie, Z.; Karimi, M.; Girimaji, S.S. Small perturbation evolution in compressible Poiseulle flow-velocity interactions and obliqueness effects. *J. Fluid Mech.* **2017**, *814*, 249–276. [CrossRef]
23. Moffatt, H.K. Interaction of turbulence with strong wind Shear. In Proceedings of the Colloquium on Atmospheric Turbulence and Radio Wave Propagation, Moscow, Russia, 15–22 June 1965; Yaglom, A.M., Tatarski, V.I., Eds.; Nauka: Moscow, Russia, 1967; pp. 139–156.
24. Ayton, L.J.; Gill, J.; Peake, N. The importance of the unsteady Kutta condition when modelling gust–aerofoil interaction. *J. Sound Vib.* **2016**, *378*, 28–37. [CrossRef]
25. Crighton, D.G. The Kutta condition in unsteady flow. *Ann. Rev. Fluid Mech.* **1985**, *17*, 411–445. [CrossRef]
26. Goldstein, M.E. *Aeroacoustics*; McGraw-Hill Book Company: New York, NY, USA, 1976.
27. Goldstein, M.E.; Afsar, M.Z.; Leib, S.J. Non-homogeneous rapid distortion theory on transversely sheared mean flows. *J. Fluid Mech.* **2013**, *736*, 532–569. [CrossRef]
28. Haurwitz, B. Zur theorie der wellenbewegungen in luft und wasser. *Veroff. Geophys. Inst. Leipz.* **1931**, *6*, 324–364.
29. Morse, P.M.; Feshbach, H. *Methods of Theoretical Physics*; McGraw-Hill Book Company: New York, NY, USA, 1953; p. 870.
30. Weiner, N. The use of statistical theory to study turbulence. In Proceedings of the Fifth International Congress for Applied Mechanics, Cambridge, MA, USA, 12–16 September 1938; pp. 356–360.
31. Tam, C.K.W.; Auriault, L. Mean flow refraction effects on sound radiated from localized sources. *J. Fluid Mech.* **1998**, *370*, 149–174. [CrossRef]
32. Briggs, R.J. *Electron Stream Interaction with Plasmas*; MIT Press: Cambridge, MA, USA, 1964.
33. Bers, A. Linear waves and instabilities. In *Plasma Physics*; Dewitt, C., Perraud, J.D., Eds.; Gordon and Breach Science: New York, NY, USA, 1975; pp. 123–216.
34. Baker, D.J.; Peake, N. Scattering on rotational flows, Paper # AIAA-2019-2554. In Proceedings of the 25th AIAA/ACEAS Aeroacoustics Conference, Delft, The Netherlands, 20–23 May 2019.
35. Noble, B. *Methods Based on the Wiener-Hopf Technique for the Solution of Partial Differential Equations*; Pergamon: Oxford, UK, 1958.
36. Zaman, K.; Brown, C.A.; Bridges, J.E. Interaction of a Rectangular Jet with a Flat-plate placed parallel to the Flow. AIAA-2013-2184. NASA/TM-2013-217879 (E-18684). In Proceedings of the 19th AIAA/CEAS Aeroacoustics Conference, Berlin, Germany, 27–29 May 2013.
37. Bridges, J.; Brown, C.A.; Bozak, R. Experiments on Exhaust of Tightly Integrated Propulsion Systems, AIAA-2014-2904. In Proceedings of the 20th AIAA/CEAS Aeroacoustics Conference, Atlanta, GA, USA, 16–20 June 2014.

38. Brown, C.A. An Empirical Jet-Surface Interaction Noise Model with Temperature and Nozzle Aspect Ratio Effects. In Proceedings of the 53rd AIAA Aerospace Sciences Meeting, Kissimmee, FL, USA, 5–9 January 2015.
39. Brown, C. Jet-Surface Interaction Test: Far-Field Noise Results, ASME Paper GT2012-69639. In Proceedings of the ASME Turbo Expo 2012: Turbine Technical Conference and Exposition, Copenhagen, Denmark, 11–15 June 2012.
40. Bridges, J. Noise from Aft Deck Exhaust Nozzles—Differences in Experimental Embodiments. In Proceedings of the 52nd AIAA Aerospace Sciences Meeting, Nat'l Harbor, MD, USA, 13–17 January 2014.
41. Goldstein, M.E.; Afsar, M.Z.; Leib, S.J. *Structure of Small Amplitude Motion on Transversely Sheared Mean Flows, NASA/TM-2013-217862*; National Aeronautics and Space Administration (NASA): Washington, DC, USA, 2013.
42. Goldstein, M.E.; Leib, S.J.; Afsar, M.Z. Rapid distortion theory on transversely sheared mean flows of arbitrary cross-section. *J. Fluid Mech.* **2019**, *881*, 551–584. [CrossRef]
43. Olsen, W.; Boldman, D. Trailing edge noise data with comparison to theory, AIAA Paper # 79-1524. In Proceedings of the AIAA 12th Fluid and Plasma Dynamics Conference, Williamsburg, VA, USA, 23–25 July 1979.
44. Ayton, L.J.; Peake, N. An analytic approach to high-frequency gust-airfoil interaction noise in steady shear flows, Paper # AIAA-2014-2322. In Proceedings of the 20th AIAA/CEAS Aeroacoustics Conference, Atlanta, GA, USA, 16–20 June 2014.
45. Baker, D.I.; Peake, N. Effect of boundary-layer shear on trailing edge noise. Paper # AIAA-2017-3169. In Proceedings of the 23rd AIAA/CEAS Aeroacoustics Conference, Denver, CO, USA, 5–9 June 2017.
46. Afsar, M.Z.; Leib, S.; Bozak, R. Effect of de-correlating turbulence on the low frequency decay of jet-surface interaction noise in sub-sonic unheated air jets using a CFD-based approach. *J. Sound Vib.* **2017**, *386*, 177–207. [CrossRef]
47. Khavaran, A.; Bozak, R.F.; Brown, C.A. Jet Surface Interaction Noise in a Planar Exhaust, AIAA-2016-2863. In Proceedings of the 22nd AIAA/CEAS Aeroacoustics Conference, Lyon, France, 30 May–1 June 2016.
48. Ramakrishnan, K.; Paliath, U.; Pastouchencko, N.; Malcevic, I.; Pilon, A.; Morgenstern, J.; Buonanno, M.; Martinez, M.; Majjigi, M. *Evaluation of Low Noise Integration Concepts and Propulsion Technologies for Future Supersonic Civil Transports*; NASA CR-2018-219936; National Aeronautics and Space Administration (NASA): Washington, DC, USA, 2018.
49. Williams, J.E.F.; Hall, L.H. Aerodynamic sound generation by turbulent flow in the vicinity of a scattering half plane. *J. Fluid Mech.* **1970**, *40*, 657–670. [CrossRef]
50. Pope, S. *Turbulent Flows*, 1st ed.; Cambridge University Press: Cambridge, UK, 2000.
51. Leib, S.J.; Goldstein, M.E. Hybrid Source Model for Predicting High-Speed Jet Noise. *AIAA J.* **2011**, *49*, 1324–1335. [CrossRef]
52. Campbell, G.A.; Foster, R.M. *Fourier Integrals for Practical Applications*; D. Van Nostrand Co. Inc.: Princeton, NJ, USA, 1948; p. 111.

fluids

MDPI

Review

Fast Models of Hydrocarbon Migration Paths and Pressure Depletion Based on Complex Analysis Methods (CAM): Mini-Review and Verification

Ruud Weijermars [1,*], Aadi Khanal [1] and Lihua Zuo [2]

[1] Harold Vance Department of Petroleum Engineering, Texas A&M University, 3116 TAMU College Station, TX 77843-3116, USA; akhanal@tamu.edu

[2] Department of Mathematics, Texas A&M University-Kingsville, Kingsville, TX 78363, USA; lihuazuo@gmail.com

* Correspondence: R.Weijermars@TAMU.edu

Received: 13 November 2019; Accepted: 6 December 2019; Published: 5 January 2020

Abstract: A recently developed code to model hydrocarbon migration and convective time of flight makes use of complex analysis methods (CAM) paired with Eulerian particle tracking. Because the method uses new algorithms that are uniquely developed by our research group, validation of the fast CAM solutions with independent methods is merited. Particle path solutions were compared with independent solutions methods (Eclipse). These prior and new benchmarks are briefly summarized here to further verify the results obtained with CAM codes. Pressure field solutions based on CAM are compared with independent embedded discrete fracture method (EDFM) solutions. The CAM method is particularly attractive because its grid-less nature offers fast computation times and unlimited resolution. The method is particularly well suited for solving a variety of practical field development problems. Examples are given for fast optimization of waterflood patterns. Another successful application area is the modeling of fluid withdrawal patterns in hydraulically fractured wells. Because no gridding is required, the CAM model can compute the evolution of the drained rock volume (DRV) for an unlimited (but finite) number of both hydraulic and natural fractures. Such computations of the DRV are based on the convective time of flight and show the fluid withdrawal zone in the reservoir. In contrast, pressure depletion models are based on the diffusive time of flight. In ultra-low permeability reservoirs, the pressure depletion zones do not correspond to the DRV, because the convective and diffusive displacement rates differ over an order of magnitude (diffusive time of flight being the fastest). Therefore, pressure depletion models vastly overestimate the drained volume in shale reservoirs, which is why fracture and well spacing decisions should be based on both pressure depletion and DRV models, not pressure only.

Keywords: complex analysis methods; flow path models; pressure depletion; drained Rock volume; time of flight

---

1. Introduction

The petroleum industry is continually searching for faster tools to model and optimize field development methods. We developed a streamline simulator based on complex analysis methods (CAM) that is grid-less and therefore, can give instantaneous streamline solutions for flow tubes resulting from certain constant and/or variable well rates. Time-dependent flows can be modeled by time-stepping tracer particles through instantaneous velocity field solutions at different times. The method uses an Eulerian solution schedule for spatial velocity computations and time-tracking of fluid particle displacement. The Eulerian particle tracking method was first combined with CAM models by Weijermars [1]. The code was subsequently expanded to model the time of flight and sweep patterns in hydrocarbon reservoirs with vertical injection and producer wells, first in unbounded reservoirs [2], and then was adapted for fault-bounded reservoirs [3].

The CAM code became particularly powerful by the derivation of a new algorithm capable of modeling the flow near high-conductivity channels such as natural fractures embedded in a lower permeability matrix [4]. The superimposition of interval sources and sinks can account for the interference of fluid flow patterns between hydraulic fractures [5]. The method also is well-suited to compute the drained rock volume (DRV) in hydraulically fractured wells, with and without natural fractures [6–8]. The hydraulic fractures may be perfectly subparallel and normal to the wellbore [9,10], or bifurcate, which has been modeled with a fractal formulation based on the Lindenmayer system [11].

Recent studies based on CAM flow simulations have confirmed earlier contentions [12] that object-based upscaling of flow through fractured porous media is inaccurate, and that flow-based upscaling of the equivalent permeability is to be preferred [13]. For the upscaling of real field reservoirs with a large number of natural fractures, a newly proposed upscaling procedure first reduces the number of fractures by object-based upscaling, and next determines the equivalent permeability tensor based on flow-based upscaling [14].

Because of the strides made with the grid-less CAM code based on algorithms that are relatively new and developed by only our one research group, verification of the CAM results will help overcome the skepticism of practitioners and critics who are still unfamiliar with this modeling tool. Many reviewers of our prior work have expressed early disbelief that such advanced results could be obtained by superimposing flows that are completely governed by closed-form, analytical solutions. Of course, the superimposition of the linear equations due to the closed-form approach results in very intricate expressions that can only be solved with computerized numerical iteration schedules. However, the grid-less (and mesh-less) nature of the solution method is preserved throughout the coding schedule and leads to accurate solutions with infinite resolution (for any reservoir model with a certain initial state and chosen set of boundary conditions).

This paper briefly reviews some earlier key CAM results with particular emphasis on their verification with independent, currently accepted methods for modeling flow in hydrocarbon reservoirs. First, a brief review of the key algorithms used in this paper is given (Section 2), followed by a verification of convective time of flight models (Section 3), and diffusive time of flight models (Section 4). Brief examples are given of the visualization of the drained rock volume in hydraulically fractured wells, with and without natural fractures (Section 5). The strengths, limitations, and future potential of the CAM approach are discussed in some detail (Section 6), followed by conclusions (Section 7). The mathematical details (Section 2) of the method are only briefly stated in this concise review paper, to enable a discourse that focuses on the visual matches of the results, limiting assumptions, and future potential of the CAM approach. For an in-depth discussion of the key algorithms used, the reader is encouraged to consult our previous studies [1,2,4,15].

2. Brief Overview of CAM Methodology and Algorithms

The algorithms and background on CAM-based flow models have been extensively documented in our prior studies [4,9]; only a brief section, with major equations, suffices here. The instantaneous fluid particle paths of any 2D flow can be determined by integrating the system of ordinary differential equations [16,17]:

$$\frac{dx}{dt} = u(x,y) \text{ and } \frac{dy}{dt} = v(x,y) \left[\mathrm{m.s^{-1}}\right] \tag{1}$$

The challenge is to find the analytical function that adequately describes the vector field. A helpful step is to identify a valid complex potential, for which there exists a related analytical function, $f(z) = u(x,y) - iv(x,y)$, the conjugate of which solves the velocity field, $\overline{f(z)} = dz/dt$, in every location, $z = x + iy$. The flow paths can be solved from the parameterized solution of $z(t)$.

Numerous complex analytical functions which describe different physical flows have been discussed in our prior studies [18]. The real part of the time-dependent complex potential, $\Omega(z,t)$, yields the potential function, and the imaginary part represents the stream function. The velocity field vector $V(z,t)$ for a flow element can be obtained by differentiating the complex potential $\Omega(z,t)$ with respect to the relative position of fluid particles in the space (z). For this paper, the functions describing the flows in vertical production wells (point sinks) and injectors (point sources); and through natural fractures (areal doublets), are relevant. The complex potential for a source/sink flow of strength, $m(t)$ [$\mathrm{m}^2 \cdot \mathrm{s}^{-1}$], centered about an arbitrary location, z_d, is:

$$\Omega(z,t) = (m(t)/2\pi)\ln(z - z_d)\left[\mathrm{m}^2 \cdot \mathrm{s}^{-1}\right] \tag{2}$$

The source and sink flows are characterized by a positive and a negative value of the strength $m(t)$, respectively. Strength $m(t)$, for a well with productivity of $q(t)$ ($\mathrm{m}^3 \cdot \mathrm{s}^{-1}$) with a reservoir height of h (m), and reservoir porosity n, is:

$$m(t) = \frac{Bq(t)}{hn(1 - R_s)}\left[\mathrm{m}^2 \cdot \mathrm{s}^{-1}\right] \tag{3}$$

where m, h, R_s, B and n are the time dependent strength, the thickness of the reservoir, the residual oil saturation, the formation volume factor and the porosity respectively.

Similarly, the complex potential for a natural fracture element represented by an areal doublet is [4]:

$$\begin{array}{l}\Omega(z,t) = \frac{-i.v(t).e^{-i\gamma}}{2\pi.h.n.L.W}[(z - z_{a2}).\log(-e^{-i\gamma}(z - z_{a2})) - (z - z_{a1}).\log(-e^{-i\gamma}(z - z_{a1})) \\ +(z - z_{b1})\log(-e^{-i\gamma}(z - z_{b1})) - (z - z_{b2})\log(-e^{-i\gamma}(z - z_{b2}))]\end{array} \quad [\mathrm{m}^2 \cdot \mathrm{s}^{-1}] \tag{4}$$

where $v(t)(\mathrm{m}^4 \cdot \mathrm{s})$ is the strength of the natural fracture, L, W and h (m) are the length, width and height of the natural fracture, respectively, n is porosity, γ is the tilt angle of the natural fracture as shown in Figure 1. The corner points of the natural fracture domain are given by z_{a1}, z_{a2}, z_{b1}, and z_{b2}.

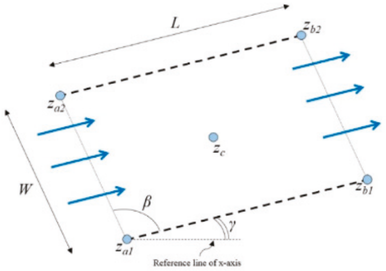

Figure 1. Natural fracture model. L and W are the length and width; z_c is the center; z_{a1}, z_{a2}, z_{b1}, and z_{b2} are the corners; β is the wall angles, while γ is the rotation angle of the natural fracture. Intended flow direction indicated with blue arrows. Reproduced with permission from [4].

The velocity fields for each of the analytical elements, represented by complex potentials in Equations (2) and (4), can be obtained by differentiating with respect to z. The corresponding generalized velocity potential, $V(z,t)$, for a point source/sink (well entry) and areal doublets (natural fractures), are given in Equations (5) and (6) respectively:

$$V(z,t) = \frac{m(t)}{2\pi(z - z_c)}\left[\mathrm{m} \cdot \mathrm{s}^{-1}\right] \tag{5}$$

$$\begin{array}{l}V(z,t) = \frac{-i.v(t).e^{-i\gamma}}{2\pi.h.n.L.W}[\log(-e^{-i\gamma}(z - z_{a2})) - \log(-e^{-i\gamma}(z - z_{a1})) \\ +\log(-e^{-i\gamma}(z - z_{b1})) - \log(-e^{-i\gamma}(z - z_{b2}))]\end{array} \quad [\mathrm{m}^2 \cdot \mathrm{s}^{-1}] \tag{6}$$

The CAM model developed in our study uses particle paths and time of flight contours (TOFC) generated by an Eulerian particle tracking method ($z_{n+1} \approx z_n + v(z_n)$). This method integrates the time-dependent flows by superimposing closed-form solutions for each state separated by a small-time increment. The selection of an appropriate time-step is a crucial decision in this method. An overly coarse time step in combination with sharply curving streamline will result in displacement vectors of the particles overshooting the actual path, resulting in an inaccurate particle path. However, if time steps are chosen sufficiently small, the solutions are highly accurate. A number of key examples is included in the present study. The velocities (v_x, v_y) of the fluid particles are mapped throughout the 2D flow plane using the real and imaginary parts of the complex potential:

$$V(z,t) = v_x - iv_y \left[\mathrm{m{\cdot}s^{-1}}\right] \tag{7}$$

Further details and derivation for Equation (7) are given in a previous study [9]. Equation (7) can be used to calculate the velocity field solutions from specific velocity field expressions defined for producer/injector and natural fracture, (Equations (5) and (6)). Tracing a particle path is accomplished by first choosing an initial position, $z_{0,}$ at time $t_0 = 0$ and calculating the local velocity. By choosing an appropriate time-step, Δt, the position $z_1(t_1)$ of the tracer at time $t_1 = t_0 + \Delta t$ is:

$$z_1(t_1) \approx z_0(t_0) + v(z_0(t_0))\Delta t \ [\mathrm{m}] \tag{8}$$

The position $z_j(t_j)$ of the tracer at any other time t_j is:

$$z_j(t_j) \approx z_{j-1}(t_{j-1}) + v(z_{j-1}(t_{j-1}))\Delta t \ [\mathrm{m}] \tag{9}$$

The particle paths are generated by tracking a sufficient number of particles for a certain flow period. The time of flight contour (TOFC) are next determined by plotting the location of all the tracers for a specific time step.

3. Flow Paths and Convective Time of Flight

The particle tracking using a formulation based on CAM can be used to contour both the advancing front of fluids injected into the reservoir, or reversely, trace the fluid withdrawal pattern by producer wells. The latter generally makes use of the principle of flow reversal, where fluid is injected back into the reservoir at the same rate as produced. Both applications have been modeled in detail, as briefly reviewed below with new detail added. Flood studies, including water cut quantification, and closed-loop optimization of the well rates are outlined in Section 3.1. CAM applications to model the flow in reservoirs with discrete fractures (both hydraulic and natural) are reviewed in Section 3.2. All the models below are based on computation of the convective time of flight for tracer particles. A complementary approach models the diffusive time of flight, which gives the pressure field solution as separately shown in Section 4.

3.1. Application in Flood Studies

The added value of water injection can be three-fold: (1) the volume of oil produced per time unit is accelerated, (2) the recovery factor is increased (because some residual oil that would otherwise not leave the reservoir is mobilized), and (3) well pressure is maintained which also contributes to an enhanced recovery factor. Optimization of the flood front arrival in producer wells is aimed at improving the sweep to ensure the maximum recovery factor is realized.

Improved oil recovery aimed for in water-flooding projects will commonly benefit from models predicting the rate of flood advance and water saturation in the production wells. Such models are even more useful when well rates can be adjusted to achieve the fastest sweep of the reservoir when none of the producer wells waters out prematurely. The optimum sweep will prevent premature decline of the oil saturation in the produced liquid. Fast affordable tools are currently limited to so-called capacitance resistance models (CRM), which provide a proxy for production optimization [19].

Models based on CAM present a fast alternative for the optimization of water injection programs. Eulerian solutions of the velocity field can track the water flood advance from injector wells to producer wells. Time-of-flight contours visualize the flood advance toward producers. Water cuts of each individual producer well for a given pump schedule can be predicted.

Our new approach may be particularly useful for application in smaller fields and in stripper-well operations. Without much financial room for any detailed data acquisition and analysis, water injection programs in stripper well fields often proceed without the support of any reservoir model or streamline simulation. Frequently, such operations cannot afford, due to little or limited subsurface data and low production margins, the development of advanced reservoir simulations. Many commercial reservoir simulators require filling fine-grid cells with well-defined reservoir properties and come at considerable expense due to time-consuming computations, dense input data requirement and in-depth reservoir modeling expertise. An alternative flood modeling method uses CAM, which can fill this technology gap. The linearity of the underlying algorithms makes grids redundant and allows fast and affordable streamline models to test various reservoir development strategies.

3.1.1. Case A—Sweep Patterns and Water Cut Ratios

A CAM model for the Quitman field has been presented in detail in a companion study [3]. The study revisited a classical waterflood simulation for an East Texas oil field [20]. The Quitman Field is situated in an 18 ft thick reservoir section of Harris sand inter-fingered with shales from the transgressive Eagle Ford formation [21]. All strata essentially can be modeled as sub-horizontal sheets, because the Quitman field is hosted on the southern flank of an extremely gentle dipping anticline (less than 3°; [22]). The reservoir is assumed bound by impenetrable formations below and above, and laterally by the fault offsets terminating the permeable sands against impermeable rocks. Normal faults strike parallel to the northeasterly trending axis of the anticlinal structure, which is caused by gentle doming above a salt pillow [23,24]. The well locations for the 8 producers and 4 injectors used in our flood model are confined to the Harris sand of the Eagle Ford [20].

The fluid transport in the bounded reservoir is controlled by the individual rates of injectors and producers. The particle paths in the fault bounded reservoir were modeled using Eulerian FRONTSIM Eclipse (Figure 2a–c) and compared with CAM (Figure 2d) solutions. Close matches were obtained for both the streamline patterns and the convective time of flight contours of the two methods (CAM and Eclipse). This type of verification refers to the accuracy of the solution of our computational models, according to the differentiation made between verification and validation in computational fluid dynamics [25]. After verification of a modeling code, one may proceed to verify the results with real world data, before one may claim a certain predictive capability of the model. Our aim in the present mini-review is to focus mostly on the verification of our results, while real world validation and forecasting of well productivity based on flow behavior in fractured porous media remain an integral part of our on-going research efforts.

As a result of the existing well placement, a production schedule with all four injectors flooding the field at the same rate, and all eight producers producing at the half the injector rate (for mass balance) will lead to premature water breakthrough in some of the wells. The CAM model for flood front tracking is capable of accurately predicting the first arrival of the flood front from a connected injector and quantifies the increasing water cut in each production well over time (Figure 3). For example, producers P1 and P2 have identical water cuts and are the first to completely water out at about $t^* = 70$. Well P3 will be last to water out, and much later so than all other wells.

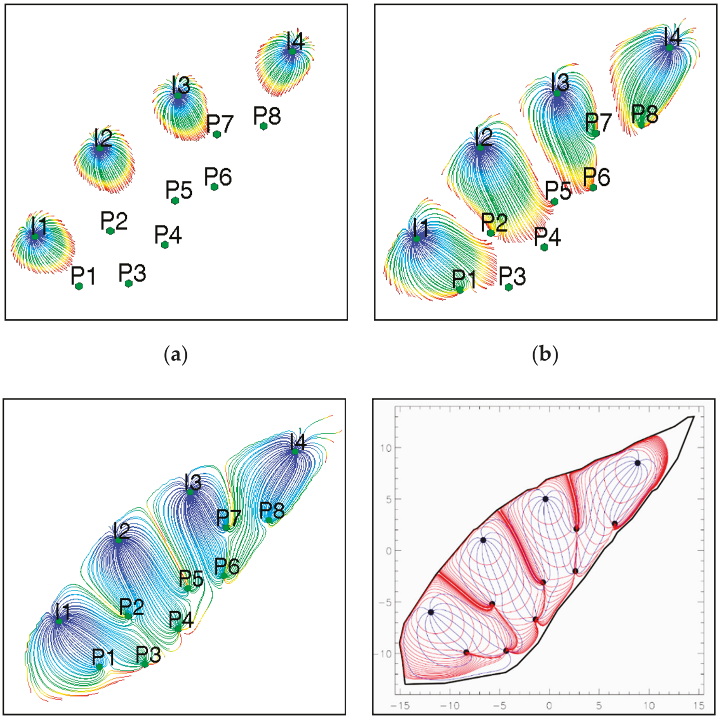

(**a**) (**b**)

(**c**) (**d**)

Figure 2. (**a**–**c**) Grid-based Eclipse simulations of progressive flooding starting from injector wells (I1-I4) in fracture-bounded reservoir space of the Quitman Field (East Texas). Particle paths delineate sweep front travel paths and convective time of flight (rainbow colors) toward the 8 producer wells (P1–P8). (**d**) A grid-less CAM simulation of the same injection pattern gives travel paths (blue lines) and the time of flight contours (red) that nearly perfectly match those of the Eclipse simulation. Reproduced with permission from [3].

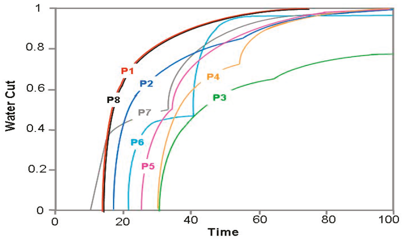

Figure 3. Water-cut (fraction) in individual producer wells (P1 to P8) versus non-dimensional time. Kink in curves for producers P2 to P7 is due to, and diagnostic for, the arrival of the flood front from a second injector well, connected to these producers. Computed using CAM. Reproduced with permission from [3].

Some important conclusions can be drawn from the CAM flood model. For example, the shapes of the water-cut profiles appear to be diagnostic for how many injectors communicate with a particular producer. Producers P6 and P7 show marked kinks in their water cut curves (Figure 3). Such kinks mark the moment in time when the stream tubes connected to the well start to receive water from a second injector. The arrival of water from a second injector in the producer well will further increase the well's water cut, and the water cut curves may show a rapid increase of water cut over a relatively short time. Producer wells P2 to P5 show only gentle kinks in their water-cut curves, but such kinks are equally diagnostic for the connectivity to a second injection well. The kink angles in the water cut curves also reveal how significant is the contribution of the second injection well for water supply to a producer. A gentle kink means the water cut in the producer (P2 to P5) due to the second injection well will only increase slowly (Figure 3). In contrast, a more pronounced, sharp kink in the water-cut curve (P6 and P7 in Figure 2) means that the water cut due to the second injection well will rapidly increase (Figure 3). If there is no kink in the curve of water ratio versus time of the producer well (P1 and P8), then such wells are connected to only one injector well.

In addition to the above results, the flooding compartments attributable to individual injectors (Figure 4a) and their complementary drainage patterns (Figure 4b) can be quantified and visualized with our new method. The only required inputs are the well rates. The Quitman Field example assumes fixed well rates, but rates may be transient, and the model results will still be accurate. For scaling of the dimensional time of the flood arrivals, additional inputs required are reservoir thickness, initial water saturation and porosity. With these few inputs all models in our original study were produced, and could accurately predict the resulting flood patterns and complementary drainage patterns and their evolution history [3].

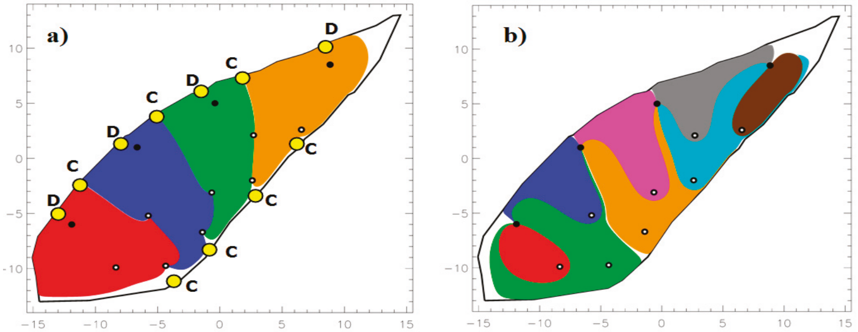

Figure 4. CAM simulations. (**a**) Injector partitions with colour segments showing individual sectors swept by each injector. Yellow dots are flow stagnation points with either divergent (D) or convergent (C) flow. (**b**) Producer partitions with colour segments marking individual sectors drained by each producer. Stagnation points occur along the periphery of the bounded domain and between producer wells. Reproduced with permission from [3].

A more comprehensive view of the sweep and drainage development is obtained by additionally plotting the evolution of the sweep area versus non-dimensional time (Figure 5a), and likewise, of the drainage area versus non-dimensional time (Figure 5b). The color codes of the sweep and drainage curves correspond to those used in Figure 4a,b. The sweep curves of individual injectors (Figure 5a) are bundling closely together and confirm their fairly uniform sweep areas (Figure 4a). In contrast, the drainage curves for individual producers (Figure 5b) show a much larger spread, indicating a fairly non-uniform drainage area (Figure 4b). Early in the flood program ($t^* = 15$), the drainage curves for each producer still coincide (Figure 5b), but these start to diverge after $t^* = 15$, due to the onset of premature water breakthrough of some wells, beginning with P7 and then cascading into water breakthrough in other wells (Figure 3).

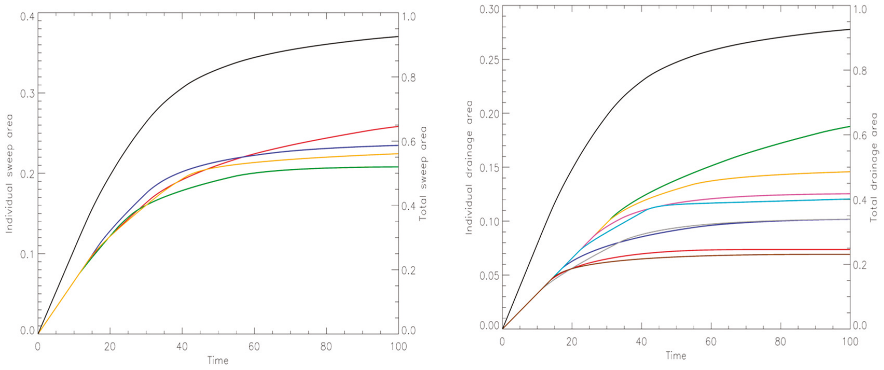

(**a**) (**b**)

Figure 5. CAM simulations. (**a**) Sweep area versus non-dimensional time attributed to individual injectors (percentage of total sweep area, left scale) and for all injectors combined (total sweep area, right scale). (**b**) Drainage area versus non-dimensional time attributed to individual producers (percentage of total drainage area, left scale) and for all producers combined (total drainage area, right scale). Reproduced with permission from [3].

The following observation rules are relevant for water saturation studies in any water flood program (Figure 4a): (1) Stagnation points near producer wells are always convergent (C), whereas stagnation points along the periphery of the bounded domain near the injection wells are alternating convergent (C) and divergent (D) (Figure 4a). (2) Producers (P) connected to only one stagnation point (either D as for P1, or C as for P8 in Figure 4a,b, compare with Figure 2d), will receive water from only one injector. (3) Two producers (P) connected to two adjacent stagnation points (D, as valid for producers P2 to P7 in Figure 4), will receive water from two injectors.

3.1.2. Case B—Closed-Loop Injection Rate Optimization

A great advantage of instantaneous streamline solutions in CAM models is that optimization of well rates for a certain waterflood injection pattern can be obtained after only a few time steps in the model. This is unlike gridded methods, where the full particle paths are only known after solving the flux from one grid cell to the next, which corresponds to real field times of months (or even years) and every iterative for optimization means the changed settings are only known for simulation times corresponding to later in the well life.

The principle of closed-loop optimization of injector well rates was demonstrated using CAM in synthetic models of a direct line drive with five injectors and five producers (Figure 6). The presence of heterogeneities, such as a region of enhanced reservoir permeability, will deflect the flood paths and result in water breakthrough times different from those originally anticipated (based on computations with limited information and homogeneous reservoir assumptions). Model pressures (as shown below) near the producer wells give sufficient information to readjust the well rates to improve the sweep in such heterogeneous reservoirs. Equal bottomhole pressures in free-flowing wells will give equal times for water–breakthrough in each well, which means that history matching of well pressures in the field is adequate to adjust the model to such well rates and prescribe adjustments to the well rates such that the field will be flooded with an optimized sweep pattern.

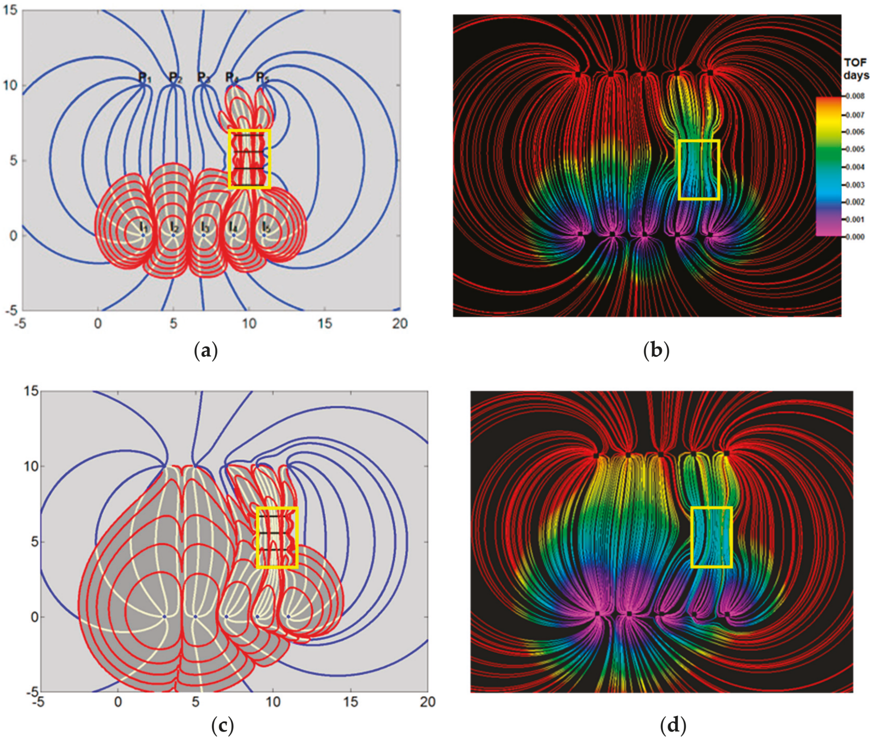

(**a**) (**b**)

(**c**) (**d**)

Figure 6. Grid-less CAM simulation (left images) before (**a**) and after (**c**) injector rate optimization of the five injector wells (bottom array I1-I5) in a direct line drive toward five producer wells (top array P1-P5). Grid-based Eclipse simulations (**b**,**d**) confirm the accuracy of CAM flow simulations and matching time of flight contours. Reproduced with permission from [26]. The high permeability zone in the rectangular space (yellow box) is 10 times more permeable than the ambient reservoir space (1000 mD as compared to ambient 100 mD).

A closed-loop adjustment of each of the five injector well rates based on an objective function that equalized pressures near all five producer wells can be quickly obtained in the CAM model (Figure 7). The optimized injection rates obtained with CAM ensured equal arrival times of the waterflood in the producer wells (Figure 6c). A grid-based Eclipse simulator does not allow for quick optimization based on pressure differentials near the producer wells. The optimized well rates obtained with CAM closed-loop optimization were fed into the Eclipse model. The latter used a streamline tracing algorithm developed to compute streamline trajectories and time of flight values using the methodology [27]. Finally, Eclipse results were imported into Petrel to visualize the particle paths and TOFC's and compare them with the CAM results. The CAM based simulations (Figure 6a,c) match closely with the Eclipse-based streamline simulations (Figure 6b,d). A very close match was obtained for both the streamline patterns and the convective time of flight contours of the waterflood front. The scaling rules that ensure kinematic similarity between the CAM and Eclipse model were detailed in an earlier study [26]. Note that an in-house developed streamline tracing algorithm was used in the Eclipse model instead of a commercial package (e.g., FRONTSIM) for better transparency when comparing the two models.

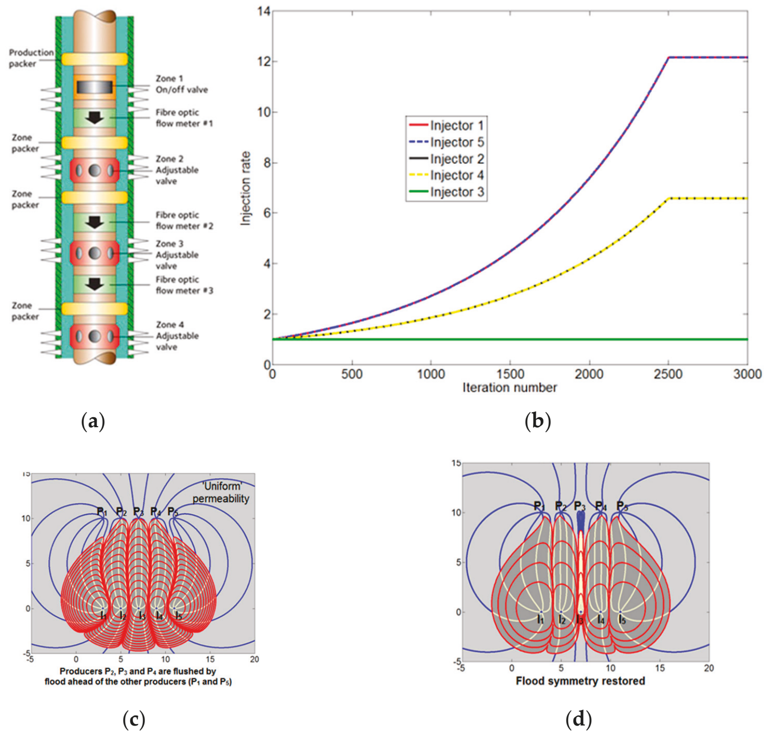

(**a**) (**b**)

(**c**) (**d**)

Figure 7. Closed-loop optimization of sweep efficiency using CAM. (**a**) Example of Inflow Control Valves (ICVs) with hydraulically operated sliding sleeves and flow meters such as first used in 2004 (for injection well A-11B at Statoil's Veslefrikk Field, North Sea). (**b**) Injection rates (non-dimensional) of wells I_1 to I_5 are iteratively adjusted by pressure monitoring of producer wells image (**c**) to achieve optimized sweep efficiency with equal flood arrival time at the producers as in (**d**). Reproduced with permission from [26].

3.2. Application to Fractured Reservoirs

Reservoir space may be heterogeneous and more often than not includes natural fractures that may deflect and impact the flow. In the present analysis a fracture is considered a domain bound by discrete linear, sub-parallel boundaries, forming so-called simple interfaces (cf., [28]), across which the permeability of the matrix abruptly changes. Fractures may consist of a void space (fully open cracks saturated with fluid) [29], and when very narrow, the hydraulic conductivity follows from a cubic law according to Boussinesq's solution of viscous flow through a narrow slot [30]. In many naturally fractured rocks, the fracture space may be containing rubble, mineralization of a mixture of gaps and altered rock fabric (partially open cracks) [29], in which case the fractures can be represented by lineaments of altered permeability relative to the matrix.

CAM simulations can accurately account for discrete fractures with a range of permeability. A new benchmark is included below for CAM versus Eclipse using the direct line drive model of Figure 6, but now with a high permeability fracture zone between the injector and producer wells (Case A). Examples of flow diversion in CAM models with impermeable faults are also included (Case B).

3.2.1. Case A—Permeable Fractures

Flow simulations based on finite difference volume discretization need to resort to time-consuming grid refinements and unstructured grids when modeling flow near fractures. The grid-less nature of CAM sidesteps such time-consuming gridding. What made the method extremely powerful for modeling flow in reservoirs with high permeability flow channels (such as natural fractures) was the development of a new algorithm to enable insertion of discrete natural fractures with higher permeability than the matrix [4]. Figure 8a–c show the CAM models of a high permeability zone (a natural fracture zone due to shear with an increased permeability) placed in the model of the direct line drive. Instead of the high permeability zone (Figure 6a), a fracture zone is placed obliquely between the injector and producer arrays (Figure 6a,b). The exaggerated finite width of the fracture zone helps to visualize the redirection of the particle paths in the high permeability zone as predicted by the Law of Streamline Refraction [31,32]. The same flow and flooding patterns are reproduced in an Eclipse model after much cumbersome gridding (Figure 8d). Close inspection of the two results reveals excellent matches between the streamline paths and the convective time of flight obtained by Eulerian tracking of tracer particles. Although the main focus of our brief review is on CAM results and capacity, we acknowledge that there are recent developments in the grid-based community that reduce the degree of cumbersome gridding [33–35].

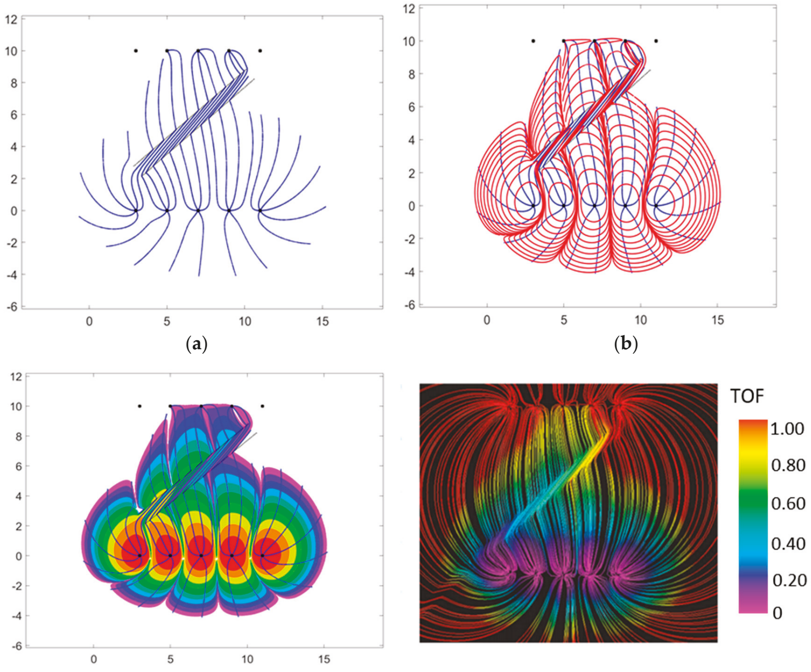

(**a**) (**b**)

(**c**) (**d**)

Figure 8. Refraction of flow paths in oblique high permeability fracture zone between a array of 5 injectors (at y = 0) and 5 producers (at y = 10). The permeability of the fracture zone is 10 times that of the ambient reservoir space. Grid-less CAM simulations (run time 5200 s and time step 0.01 s) show: (**a**) only streamlines, (**b**) streamlines with non-dimensional time of flight contours (12 TOFC, red) for advancing waterflood, and (**b**) same as (**b**) but now marked with rainbow color-coded TOFC. (**d**) Grid-based Eclipse simulation confirms the accuracy of CAM flow simulations and time of flight contours. (**a**–**c**): This study; (**d**): Reproduced with permission from [31].

3.2.2. Case B—Impervious Fractures

Impermeable fractures can be modeled most accurately by including images of no-flow boundaries using a Schwartz-Christoffel transformation (Figure 9a). When an impermeable fracture blocks the flow in the reservoir it turned out to be impossible to adjust well injection rates to achieve equal water breakthrough in all producers [26]. New producer wells would need to be drilled in the region that experiences stranded oil at the downstream side of the blocking fracture. Both the streamline paths and convective time of flight contours of the CAM model (Figure 9a) and Eclipse model (Figure 9b) are virtually identical. Additional CAM models for a large range of well patterns with impermeable fractures have been given in our earlier study [2].

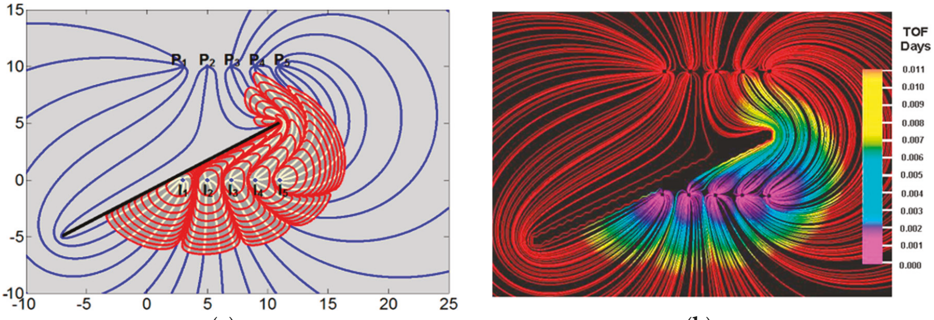

(**a**) (**b**)

Figure 9. Streamlines and TOFCs for waterflood advance in a homogeneous reservoir with an impervious fault. (**a**) CAM solution. (**b**) Eclipse solution. Reproduced with permission from [26].

4. Benchmarking Pressure Field Solutions

The pressures in CAM models are obtained by solving and scaling the potential function due to all superposed flow elements [5]. We compare the results from a CAM model to the results obtained from a discrete finite volume model. The MATLAB Reservoir Simulation Toolkit [36–39] was used to design simple examples of pressure deviations near a limited number of natural fractures. A fully resolved grid was first adopted where each fracture and matrix grid block are assigned a unique permeability. A fully resolved grid is more accurate than a dual porosity model to represent flow in naturally fractured reservoirs [40–42]. However, a fully resolved technique is computationally intensive, and careful gridding is required in order to match the reported dimensions of the natural fracture(s). Thus, an embedded discrete fracture model (EDFM) with two-point flux approximation (TPFA) was implemented (after first verifying fully resolved pressure plot and EDFM, which gave perfect matches).

EDFM represents the fractures explicitly by defining the fracture and matrix grids independently, which allows for intricate fracture networks without the need for complex matrix grid conformal with each fracture for fully resolved solution [39]. The complex fractures can be implemented in the conventionally structured grids without the need for a local grid refinement (LGR) around the fractures [43]. The LGR is computationally efficient only to represent hydraulic fractures, but is resource intensive to represent numerous discrete elements such as the natural fractures [44–46]. EDFM is based on a hybrid approach, where the dual-porosity model is used for the smaller fractures, and discrete fracture for the larger fractures [47]. Initially developed for planar 2D cases, EDFM has been recently expanded for 3D models with obliquely dipping fractures [48], for simulating the stimulated reservoir volume (SRV) to reduce the computational cost associated with LGR [49,50], and for assisted history matching in unconventional reservoirs [51]. Thus, efficient modeling of fluid flow in the natural fractures is possible with EDFM, using a limited number of cells for the pressure field benchmark cases (Figure 10a–c, top row).

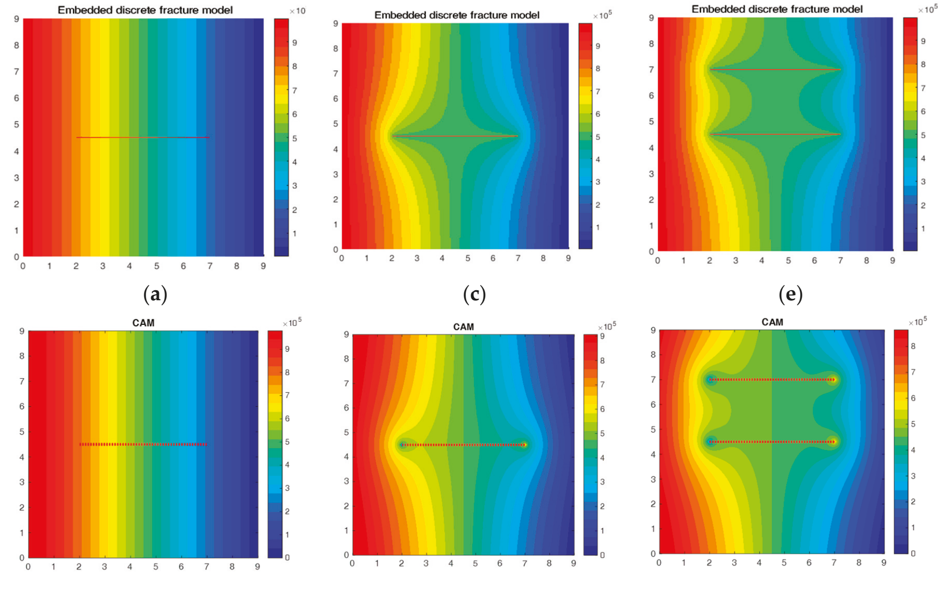

(**a**) (**c**) (**e**)

(**b**) (**d**) (**f**)

Figure 10. Pressure field solutions (scaled in Pa) around a non active fracture (**a**,**b**), active single fracture (**c**,**d**), and a pair of horizontal fractures (**e**,**f**). The reservoir space assumes a single phase 2D flow with the following boundary conditions and fluid properties: $P_{right} = 0$ Pa, $P_{left} = 10$ Pa, fluid viscosity is 0.1 Pa s (1 cP) and fluid density is 1 g/cm^3. (**a**, **c**, and **e**; Top row): Grid-based solutions using an embedded discrete fracture model (EDFM). (**b**, **d**, and **f**; Bottom row): Grid-less CAM solution of the same pressure field.

The pressure field solutions obtained with the fast CAM approach (Figure 10b,d,f, bottom row) closely match those obtained with EDFM. Although the pressures can be solved at infinite resolution by CAM, contouring of the pressures is fastest when gridded in our MATLAB code. The pattern of the pressure contours is nearly identical to those obtained by the independent EDFM method. Some minor mismatches of pressure occur at the fracture tips, which are artifacts of choices made about the spatial placement of branch cuts for integral solutions [18].

5. Application to Hydraulically Fractured Wells

The previous sections we believe conclusively verified the accuracy of fast CAM solutions for modeling fluid flow in hydrocarbon reservoirs. The method is particularly powerful for modeling, in considerable detail, the drained rock volume (DRV) in hydraulically fractured wells, with and without natural fractures. The convergence of particle paths due to discrete natural fractures with high permeability can be modeled by CAM using field-based well rates with both assumed natural fractures [8,13,18,52] as well as fractures based on fracture diagnostics [14].

Figure 11a–d show detailed examples of fluid withdrawal envelopes around hydraulic fractures constructed by computing the convective time of flight along each streamline. The well modeled (using public data of the Texas Railroad Commission) is Autobahn 34–117 1 H (Delaware Basin, West Texas), which has 17 fracture stages with a spacing of 250 ft and lateral well length of 4235 ft [53]. The individual hydraulic fractures have rates allocated by the history matched decline curve of the well.

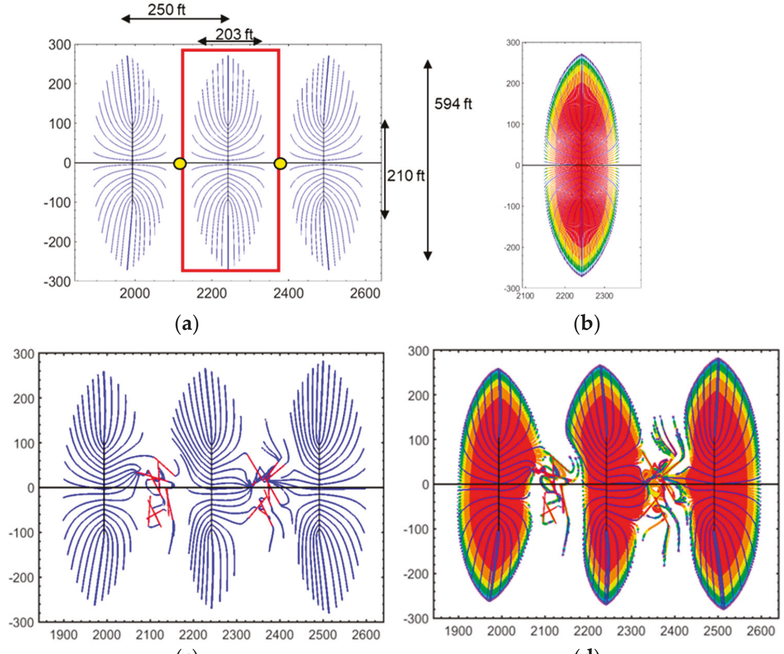

(**a**) (**b**)

(**c**) (**d**)

Figure 11. Flow simulations of fluid withdrawal paths around three hydraulic fractures in a horizontal well from the Permian Basin (map views). (**a**) Particle paths or fluid withdrawal paths based on well rate assuming homogenous reservoir (no natural fractures). (**b**) Drained rock volume after 30 years of production. Red region is drained in the first 3 years after which slower drainage occurs due to repaid decline of the well. (**c**,**d**): Distortions of flow paths and drained rock volume (marked by convective time of flight contours) due to presence of highly conductive natural fractures (red line segments) between the hydraulic fractures. Reproduced with permission from [53].

Figure 11a shows the migration path of hydrocarbons toward three central hydraulic fractures placed transverse to the horizontal well. Flow stagnation points occur between the fractures (yellow dots). The flow separation surfaces have been studied in detail elsewhere [5]. The DRV around the central fracture is given in Figure 11b. Much of the DRV region is drained in the first three years (red shaded region). The peripheral zones are drained much slower due to the rapid decline of the well (see decline curve details [53]).

The CAM models in Figure 11b,c show the impact if natural fractures were to occur near the fracture stages. Two clusters of natural fractures (red) are assumed in between the hydraulic fractures each comprising 10 discrete fractures. Particle paths (blue) are for 30 years of simulation. The TOFC are marked by color bands, each representing a 3-year production increment. The impact of natural fractures on both the flow paths (Figure 11c) and DRV (Figure 11d) can be compared to those in Figure 11a,b, which assumed no natural fractures are present in the reservoir. The presence of natural fractures shifts the DRV and results in hydraulic fracture interference (Figure 11d) as compared to the result without natural fractures (Figure 11b).

The conclusion is that high conductivity natural fractures will increase flow interference between hydraulic fractures. Likewise, natural fractures between adjacent wells will not only cause pressure communication [51], but also cause the DRV shape and location to shift [8,14].

6. Discussion

Previously, the potential of CAM models (which are based on potentiometric theory) was first explored in streamline application to oil fields [54], which were then computerized in the 1970s in several studies [20,55], and later in other studies [16,17]. The prior studies never unlocked the full potential of CAM due to (1) lack of computing power, and (2) no coupling of CAM with Eulerian particle tracking. The pairing of CAM with Eulerian particle tracking was first realized by Weijermars [1]. In addition, the introduction of new algorithms to model flow in natural fractures [4], solution of certain branch cut effects [18], and scaling of permeability contrast [13] provided crucial steps that are the basis of our current modeling capacity.

6.1. Model Strengths and Limitations

Obvious strengths of the CAM model for flow simulations are time gains due to (1) no need for gridding, and (2) high computational speed, while preserving the high resolution of closed–form solutions. The codes developed by our research group are as of yet proprietary, but may be made public at some time in the future. The method makes a number of simplifying assumptions. For example, fluid is assumed incompressible in the reservoir (but not in the fluid allocation based on well rates, where compressibility is actually accounted for) and remains in single phase flow.

Capillary effects are not accounted for neither are bubble point effects for highly saturated oil. Multiphase flow is inherently non-linear, which the linear superposition of CAM cannot account for unless some drastic localized scaling of flow would manage to correctly capture the pore-scale flow effects well enough to allow a verifiable globalized flow model. Initial efforts for study of two-phase flow and capillary effects with CAM were made to suggest that domainal oscillation functions may provide the required average velocity (or fluxes) in the pore-network model for use in a continuum model [56]. The oscillation function would need to be scaled on the basis of micro-fluidic pore network models or other physical models of the natural system to validate the results.

Prior limitations of CAM included the impossibility to account for heterogeneity, which we conclusively solved by developing new algorithms (Figures 6 and 8–11). The method works fastest in unbounded reservoir space, but can be adapted to account for finite reservoir space (Figure 2). The particle tracking enables streamline studies and nearly instantaneous optimization of well rate due to lack of grid cells (Figure 7). The convective time of flight contours can be constructed by connecting particles after certain flow periods (Figures 2 and 6–11). The visualization of drained rock volume around hydraulically fractured wells has revealed the importance of focusing on the convective time of flight. Pressure depletion plots alone (such as provided by CAM in addition to DRV) and as used in fast marching methods [57] cannot show the DRV.

Pressure depletion models are representative for the diffusive time of flight, but hydrocarbon molecules moving in the reservoir space outside the DRV will never reach the well [58]. The lag between the tracer time of flight and the diffusive time of flight has been noted before [27], but visualization of the DRV is first enabled by CAM. No other method has visualized the DRV before. The strength of CAM is that it allows visualization of the DRV at high resolution without any gridding effort.

One major limitation is that CAM models hitherto are limited to 2D flows. Quasi-3D flow solutions are possible by collocating 2D flow planes into 3D envelopes of the DRV [59]. Full 3D expansion of 2D complex potentials is theoretically possible but becomes intricate and the computational time gains over gridded methods will likely vanish, but 3D CAM should not be prematurely be dismissed.

6.2. Future Model Strengths and Limitations

CAM models are only in a nascent stage of their development, yet are capable of modeling flow in fractured porous media with high accuracy and speed, while saving cumbersome gridding time. Visualization of the DRV became possible by formulating hydraulic fracture strengths that are indexed to proppant concentration. One of our studies used fracture treatment pump rates from a field case

(Wolfcamp well, Midland Basin) to history match with a fracture propagation simulator the hydraulic conductivity of the created hydraulic fractures [59]. The latter study partitioned discrete segments of the hydraulic fractures corresponding to the hydraulic conductivity obtained by the fracture treatment history match. However, a continuous formulation is possible, which we are currently developing.

7. Conclusions

This review article summarizes the results from our previous CAM studies with several superposed analytical elements. In addition, this paper provides verification for both the particle path patterns and pressure solutions using a numerical reservoir simulator (Eclipse) and a widely used efficient numerical model (EDFM), respectively. The CAM results presented in this study provide a quick and computationally efficient method of reservoir simulation, which can be used to complement the traditional numerical simulators. The principal conclusions from this study are as follows:

1. CAM models can be used to study fluid flow in porous media, including hydrocarbon reservoirs, with a variety of attributes such as injectors, producers, hydraulic fractures and natural fractures.
2. The results from the CAM model match closely with those of established commercial reservoir simulators.
3. A newly developed algorithm, which can model fluid migration paths in naturally fractured reservoirs, was pressure-benchmarked against the widely used EDFM method.
4. Natural fractures may cause complex flow interference patterns between adjacent hydraulic fractures (or wells).
5. Fracture/well spacing optimization decisions should therefore be based on flow simulations that take into account the effect of natural fractures.
6. Pressure depletion plots provide accurate information for pressure depletion but, in low permeability reservoirs, cannot be used as a proxy for fluid withdrawal efficiency or drained rock volume.
7. Particle paths and time of flight contours constructed with CAM can convey a realistic picture of the drained rock volume.

Funding: This project was sponsored by startup funds of the senior author (R.W.) from the Texas A & M Engineering Experiment Station (TEES) and funds from the Crisman Institute at the Harold Vance Department of Petroleum Engineering at Texas A&M University.

Conflicts of Interest: The authors declare no conflict of interest.

References

1. Weijermars, R. Visualization of space competition and plume formation with complex potentials for multiple source flows: Some examples and novel application to Chao lava flow (Chile). *J. Geophys. Res. Solid Earth* **2014**, *119*, 2397–2414. [CrossRef]
2. Weijermars, R.; Van Harmelen, A. Advancement of sweep zones in waterflooding: Conceptual insight and flow visualizations of oil-withdrawal contours and waterflood time-of-flight contours using complex potentials. *J. Petrol. Explor. Prod. Technol.* **2017**, *7*, 785–812. [CrossRef]
3. Nelson, R.; Zuo, L.; Weijermars, R.; Crowdy, D. Applying improved analytical methods for modelling flood displacement fronts in bounded reservoirs (Quitman field, east Texas). *J. Pet. Sci. Eng.* **2018**, *166*, 1018–1041. [CrossRef]
4. van Harmelen, A.; Weijermars, R. Complex analytical solutions for flow in hydraulically fractured hydrocarbon reservoirs with and without natural fractures. *Appl. Math. Model.* **2017**, *56*, 137–157. [CrossRef]
5. Weijermars, R.; Harmelen, A.V.; Zuo, L.; Alves, I.N.; Yu, W. Flow Interference Between Hydraulic Fractures. *SPE Reserv. Eval. Eng.* **2018**, *21*, 0942–0960. [CrossRef]

6. Weijermars, R. Nascentes Alves, I. High-resolution visualization of flow velocities near frac-tips and flow interference of multi-fracked Eagle Ford wells, Brazos County, Texas. *J. Pet. Sci. Eng.* **2018**, *165*, 946–961. [CrossRef]
7. Khanal, A.; Weijermars, R. Pressure depletion and drained rock volume near hydraulically fractured parent and child wells. *J. Pet. Sci. Eng.* **2019**, *172*, 607–626. [CrossRef]
8. Khanal, A.; Weijermars, R. Visualization of drained rock volume (DRV) in hydraulically fractured reservoirs with and without natural fractures using complex analysis methods (CAMs). *Pet. Sci.* **2019**, *16*, 550–577. [CrossRef]
9. Weijermars, R.; van Harmelen, A.; Zuo, L.; Nascentes, I.A.; Yu, W. High-Resolution Visualization of Flow Interference Between Frac Clusters (Part 1): Model Verification and Basic Cases. In Proceedings of the SPE/AAPG/SEG Unconventional Resources Technology Conference, Denver, CO, USA, 22–24 July 2017. [CrossRef]
10. Weijermars, R.; van Harmelen, A.; Zuo, L. Flow Interference Between Frac Clusters (Part 2): Field Example from the Midland Basin (Wolfcamp Formation, Spraberry Trend Field) With Implications for Hydraulic Fracture Design. In Proceedings of the SPE/AAPG/SEG Unconventional Resources Technology Conference, Denver, CO, USA, 22–24 July 2017. [CrossRef]
11. Nandlal, K.; Weijermars, R. Drained rock volume around hydraulic fractures in porous media: Planar fractures versus fractal networks. *Pet. Sci.* **2019**, *16*, 1064–1085. [CrossRef]
12. Chen, T.; Clauser, C.; Marquart, G.; Willbrand, K.; Mottaghy, D. A new upscaling method for fractured porous media. *Adv. Water Resour.* **2015**, *80*, 60–68. [CrossRef]
13. Weijermars, R.; Khanal, A. High-resolution streamline models of flow in fractured porous media using discrete fractures: Implications for upscaling of permeability anisotropy. *Earth Sci. Rev.* **2019**, *194*, 399–448. [CrossRef]
14. Nandlal, K.; Weijermars, R. Impact on Drained Rock Volume (DRV) of Storativity and Enhanced Permeability in Naturally Fractured Reservoirs: Upscaled Field Case from Hydraulic Fracturing Test Site (HFTS), Wolfcamp Formation, Midland Basin, West Texas. *Energies* **2019**, *12*, 3852. [CrossRef]
15. Weijermars, R.; van Harmelen, A. Shale Reservoir Drainage Visualized for a Wolfcamp Well (Midland Basin, West Texas, USA). *Energies* **2018**, *11*, 1665. [CrossRef]
16. Strack, O.D.L. *Groundwater Mechanics*; Prentice-Hall: Englewood Cliffs, NJ, USA, 1989.
17. Sato, K. *Complex Analysis for Practical Engineering*; Springer International Publishing: Cham, Switzerland, 2015. [CrossRef]
18. Khanal, A.; Weijermars, R. Modeling Flow and Pressure Fields in Porous Media with High Conductivity Flow Channels and Smart Placement of Branch Cuts for Variant and Invariant Complex Potentials. *Fluids* **2019**, *4*, 154. [CrossRef]
19. Sayarpour, M.; Kabir, C.S.; Lake, L.W. Field Applications of Capacitance Resistance Models in Waterfloods. *SPE Annu. Tech. Conf. Exhib.* **2008**, *44*, 132–138. [CrossRef]
20. Doyle, R.E.; Wurl, T.M. Stream Channel Concept Applied to Waterflood Performance Calculations for Multiwell, Multizone, Three-Component Cases. *J. Pet Tech.* **1971**, *23*, 373–380. [CrossRef]
21. Scott, E.R. Quitman Oil Field, Wood County, Texas. In *Structure of Typical American Oil Fields: A Symposium of the Relation of Oil Accumulation to Structure AAPG Symposium, V. III.*; Howell, I.V., Ed.; American Association of Petroleum Geologists: Tulsa, OK, USA, 1947; pp. 419–431. ISBN 78-1-62981-248-9.
22. Smith, W.K. Quitman Field, Wood County, Texas. In *Occurrence of Oil and Gas in Northeast Texas*; Herald, F.A., Ed.; University of Texas Publication No.5116; Bureau of Economic Geology: Austin, TX, USA, 1951; pp. 315–319.
23. Miron, S. Quitman Field, Wood County. Texas. In *Occurence of Oil and Gas in Northeast Texas*; Eaton, R.W., Nichols, P.H., Eds.; East Texas Geological Society Publication No. 5; East Texas Geological Society: Tyler, TX, USA, 1964; Volume 1, pp. 58–78.
24. Wittick, T. Using 3-D Seismic Data to Find New Reserves in an Old Field Rejuvenation of Quitman Field, Wood County, Texas. In *Society of Exploration Geophysicists. Interpretation 2: Structural Case Histories*; Society of Exploration Geophysicists: Tulsa, OK, USA, 1996; pp. 352–355. [CrossRef]
25. Oberkampf, W.L.; Trucano, T.G. Verification and validation in computational fluid dynamics. *Prog. Aerosp. Sci.* **2002**, *38*, 209–272. [CrossRef]

26. Weijermars, R.; van Harmelen, A.; Zuo, L. Controlling Flood Displacement Fronts using a Parallel Analytical Streamline Simulator. *J. Pet. Sci. Eng.* **2016**, *139*, 23–42. [CrossRef]
27. Datta-Gupta, A.; King, M.K. *Streamline Simulation: Theory and Practice*; SPE Textbook Series; Society of Petroleum Engineers: Richardson, TX, USA, 2007; Volume 11.
28. Hassanizadeh, S.M.; Gray, W.G. Boundary and interface conditions in porous media. *Water Resour. Res.* **1989**, *25*, 1705–1715. [CrossRef]
29. Borst, R.D. Fluid flow in fractured and fracturing porous media: A unified view. *Mech. Res. Commun.* **2017**, *80*, 47–57. [CrossRef]
30. Witherspoon, P.A.; Wang, J.S.Y.; Iwai, K.; Gale, J.E. Validity of Cubic Law for fluid flow in a deformable rock fracture. *Water Resour. Res.* **1980**, *16*, 1016–1024. [CrossRef]
31. Zuo, L.; Weijermars, R. Rules for flight paths and time of flight for flows in heterogeneous isotropic and anisotropic porous media. *Geofluids* **2017**, *2017*, 5609571. [CrossRef]
32. Bear, J. *Dynamics of Fluids in Porous Media*; Elsevier: New York, NY, USA, 1972.
33. Gläser, D.; Helmig, R.; Flemisch, B.; Class, H. A discrete fracture model for two-phase flow in fractured porous media. *Adv. Water Resour.* **2017**, *110*, 335–348. [CrossRef]
34. Flemisch, B.; Berre, I.; Boon, W.; Fumagalli, A.; Schwenck, N.; Scotti, A.; Stefansson, I.; Tatomir, A. Benchmarks for single-phase flow in fractured porous media. *Adv. Water Resour.* **2018**, *111*, 239–258. [CrossRef]
35. Nordbotten, J.M.; Boon, W.M.; Fumagalli, A.; Keilegavlen, E. Unified approach to discretization of flow in fractured porous media. *Comput. Geosci.* **2019**, *23*, 225–237. [CrossRef]
36. Lie, K.-A.; Krogstad, S.; Ligaarden, I.S.; Natvig, J.R.; Nilsen, H.M.; Skaflestad, B. Open source MATLAB implementation of consistent discretisations on complex grids. *Comput. Geosci.* **2012**, *16*, 297–322. [CrossRef]
37. Krogstad, S.; Lie, K.-A.; Møyner, O.; Nilsen, H.M.; Raynaud, X.; Skaflestad, B. MRST-AD—An open-source framework for rapid prototyping and evaluation of reservoir simulation problems. In Proceedings of the 2015 Reservoir Simulation Symposium, Houston, TX, USA, 23–25 February 2015. [CrossRef]
38. Bao, K.; Lie, K.-A.; Møyner, O.; Liu, M. Fully implicit simulation of polymer flooding with MRST. *Comput. Geosci.* **2017**, *21*, 1219–1244. [CrossRef]
39. Lie, K.-A. *An Introduction to Reservoir Simulation Using MATLAB/GNU Octave: User Guide for the MATLAB Reservoir Simulation Toolbox (MRST)*; Cambridge University Press: Cambridge, UK, 2019; Available online: www.cambridge.org/9781108492430 (accessed on 12 September 2019).
40. Khoshghadam, M.; Khanal, A.; Lee, W.J. Numerical study of impact of nano-pores on gas-oil ratio and production mechanisms in liquid-rich shale oil reservoirs. In Proceedings of the 2015 Unconventional Resources Technology Conference, San Antonio, TX, USA, 20–22 July 2015. [CrossRef]
41. Khoshghadam, M.; Khanal, A.; Rabinejadganji, N.; Lee, W.J. How to Model and Improve Our Understanding of Liquid-Rich Shale Reservoirs with Complex Organic/Inorganic Pore Network. In Proceedings of the 2016 Unconventional Resources Technology Conference, San Antonio, TX, USA, 1–3 August 2016. [CrossRef]
42. Khoshghadam, M.; Khanal, A.; Yu, C.; Rabinejadganji, N.; Lee, W.J. Producing gas-oil ratio behavior of unconventional volatile-oil reservoirs, and its application in production diagnostics and decline curve analysis. In Proceedings of the 2017 Unconventional Resources Technology Conference, Austin, TX, USA, 24–26 July 2017. [CrossRef]
43. Yu, W.; Sepehrnoori, K. *Shale Gas and Tight Oil Reservoir Simulation*; Gulf Professional Publishing: Cambridge, MA, USA, 2018; pp. 155–200.
44. Khanal, A.; Khoshghadam, M.; Lee, W.J. Stochastic Study of Reservoir and Completion Parameters in Liquid Rich Shale. In Proceedings of the 2015 SPE Liquids-Rich Basins Conference—North America, Midland, TX, USA, 2–3 September 2015. [CrossRef]
45. Khanal, A.; Khoshghadam, M.; Lee, W.J. Accurate Forecasting of Liquid Rich Gas Condensate Reservoirs with Multiphase Flow. In Proceedings of the 2016 Unconventional Resources Technology Conference, San Antonio, TX, USA, 1–3 August 2016. [CrossRef]
46. Khanal, A.; Khoshghadam, M.; Lee, W.J.; Nikolaou, M. New forecasting method for liquid rich shale gas condensate reservoirs with data driven approach using principal component analysis. *J. Nat. Gas Sci. Eng.* **2017**, *38*, 621–637. [CrossRef]
47. Li, L.; Lee, S.H. Efficient field-scale simulation of black oil in a naturally fractured reservoir through discrete fracture networks and homogenized media. *SPE Reserv. Eval. Eng.* **2008**, *11*, 750–758. [CrossRef]

48. Moinfar, A.; Varavei, A.; Sepehrnoori, K.; Johns, R.T. Development of an efficient embedded discrete fracture model for 3D compositional reservoir simulation in fractured reservoirs. *SPE J.* **2014**, *19*, 289–303. [CrossRef]
49. Jiang, J.; Younis, R. Hybrid coupled discrete-fracture/matrix and multicontinuum models for unconventional-reservoir simulation. *SPE J.* **2016**, *21*, 1009–1027. [CrossRef]
50. Wang, K.; Liu, H.; Luo, J.; Wu, K.; Chen, Z. A comprehensive model coupling embedded discrete fractures, multiple interacting continua, and geomechanics in shale gas reservoirs with multiscale fractures. *Energy Fuels* **2017**, *31*, 7758–7776. [CrossRef]
51. Yu, W.; Tripoppoom, S.; Sepehrnoori, K.; Miao, J. An automatic history-matching workflow for unconventional reservoirs coupling MCMC and non-intrusive EDFM methods. In Proceedings of the PE annual technical conference and exhibition, Dallas, TX, USA, 24–26 September 2018. [CrossRef]
52. Khanal, A.; Weijermars, R. Estimation of Drained Rock Volume DRV and Pressure Depletion using Discrete Fracture Model and Complex Analysis Methods. In Proceedings of the 2019 SPE Europec Featured at 81st EAGE Conference and Exhibition, London, UK, 3–6 June 2019. [CrossRef]
53. Khanal, A.; Nandlal, K.; Weijermars, R. Impact of Natural Fractures on the Shape and Location of Drained Rock Volumes in Unconventional Reservoirs: Case Studies from the Permian Basin. In Proceedings of the 2016 Unconventional Resources Technology Conference, Denver, CO, USA, 22–24 July 2019. [CrossRef]
54. Muskat, M. The Theory of Potentiometric Models. *Trans. AIME* **1949**, *179*, 216–221. [CrossRef]
55. Higgins, R.V.; Leighton, A.J. Matching Calculated with Actual Waterflood Performance by Estimating Some Reservoir Properties. *J. Pet Tech.* **1974**, *26*, 501–506. [CrossRef]
56. Weijermars, R.; Khanal, A. Elementary Pore Network Models Based on Complex Analysis Methods (CAM): Fundamental Insights for Shale Field Development. *Energies* **2019**, *12*, 1243. [CrossRef]
57. Kulkarni, K.N.; Datta-Gupta, A.; Vasco, D.W. *A Streamline Approach for Integrating Transient Pressure Data into High-Resolution Reservoir Models*; Society of Petroleum Engineers: Richardson, TX, USA, 2001. [CrossRef]
58. Weijermars, R.; Nandlal, K.; Khanal, A.; Tugan, F.M. Comparison of Pressure Front with Tracer Front Advance and Principal Flow Regimes in Hydraulically Fractured Wells in Unconventional Reservoirs. *J. Pet. Sci. Eng.* **2019**, *183*, 106407. [CrossRef]
59. Parsegov, S.G.; Nandlal, K.; Schechter, D.S.; Weijermars, R. Physics-Driven Optimization of Drained Rock Volume for Multistage Fracturing: Field Example from the Wolfcamp Formation, Midland Basin. In Proceedings of the Unconventional Resources Technology Conference, Houston, TX, USA, 23–25 July 2018. [CrossRef]

MDPI
St. Alban-Anlage 66
4052 Basel
Switzerland
Tel. +41 61 683 77 34
Fax +41 61 302 89 18
www.mdpi.com

Fluids Editorial Office
E-mail: fluids@mdpi.com
www.mdpi.com/journal/fluids

MDPI
St. Alban-Anlage 66
4052 Basel
Switzerland

Tel: +41 61 683 77 34
Fax: +41 61 302 89 18

www.mdpi.com

ISBN 978-3-0365-2001-8